Published in Journals: Processes, Applied Sciences,
Materials, Sustainability and Toxics

Topic Reprint

New Research on Detection and Removal of Emerging Pollutants

Volume II

Edited by
Avelino Núñez-Delgado, Zhien Zhang, Elza Bontempi,
Mario Coccia, Marco Race and Yaoyu Zhou

mdpi.com/topics

MDPI

New Research on Detection and Removal of Emerging Pollutants—Volume II

New Research on Detection and Removal of Emerging Pollutants—Volume II

Editors

Avelino Núñez-Delgado
Zhien Zhang
Elza Bontempi
Mario Coccia
Marco Race
Yaoyu Zhou

MDPI

Basel • Beijing • Wuhan • Barcelona • Belgrade • Novi Sad • Cluj • Manchester

This is a reprint of articles from the Topic published online in the open access journals *Processes* (ISSN 2227-9717), *Applied Sciences* (ISSN 2076-3417), *Materials* (ISSN 1996-1944), *Sustainability* (ISSN 2071-1050), and *Toxics* (ISSN 2305-6304) (available at: https://www.mdpi.com/topics/Emerging_Pollutants).

For citation purposes, cite each article independently as indicated on the article page online and as indicated below:

Lastname, A.A.; Lastname, B.B. Article Title. *Journal Name* **Year**, *Volume Number*, Page Range.

Volume II
ISBN 978-3-7258-0827-4 (Hbk)
ISBN 978-3-7258-0828-1 (PDF)
doi.org/10.3390/books978-3-7258-0828-1

Set
ISBN 978-3-7258-0793-2 (Hbk)
ISBN 978-3-7258-0794-9 (PDF)

Contents

About the Editors

Avelino Núñez-Delgado

Avelino Núñez-Delgado, Ph.D., was born in O Barco de Valdeorras (Ourense province, Galicia, Spain). He obtained a Ph.D. in the Department of Soil Science and Agricultural Chemistry, at USC, in 1993. Between 1993 and 1996, he was a Post-doc Researcher in France (University of Montpellier) and Spain (USC), at the end of which he became a Professor in the Department of Soil Science and Agricultural Chemistry, Engineering Polytechnic School, Campus Lugo, University of Santiago de Compostela (USC), Spain, a position which he has covered to this day. He has nine patents, several research awards, and more than 400 publications to date (December 2023), around 200 of which are in D1 and Q1 JCR journals. He was the Principal Investigator and/or a collaborator in more than 40 research projects. He was listed among the top 2% of world researchers by the Stanford ranking system and among the world top researchers by Researchgate, Expertscape, Web of Sciences, Scopus, and other world research classifications. Currently, he is collaborating with a variety of research teams from various countries around the world. He is a Book Editor for Springer Nature, Elsevier, and other top scientific publishers. He is a Book Series Editor for Springer Nature, an Editor for various top research journals (covering roles such as Chief Editor, Associate Editor, Special Issues Editor, Managing Guest Editor, and Guest Editor), and a Reviewer for national and international research projects.

Zhien Zhang

Zhien Zhang is currently a Visiting Scientist at the University of Cincinnati. Prior to this position, he was a Research Assistant Professor at West Virginia University and a Senior Researcher at the Ohio State University. His research interests are in the following areas: carbon capture, utilization, and storage (cCuS); gas separation; absorption; membrane; gas hydrate; process modeling and simulation; and optimization. To date, he has published more than 120 peer-reviewed journal articles, 20 journal editorials, two books, and six book chapters (h-index of 53) and has been invited to and delivered more than 30 talks and seminars. He is an Editor in journals such as *Applied Energy, Environmental Chemistry Letters, Gas Science and Engineering*, and *Chemical Papers* and serves as a committee member in several international conferences. He was recognized as a Highly Cited Researcher by Clarivate in 2021 and 2022.

Elza Bontempi

Elza Bontempi has a permanent position at the University of Brescia, where she is currently a Full Professor teaching courses on the Fundamentals of Chemistry for Technology. She is responsible for the research line concerning eco-materials at the Chemistry for Technologies Laboratory. She has been responsible for several national and international research projects developing new technologies and sustainable materials from waste and by-products. In recent years, her scientific activity has focused on the recovery of critical raw materials from exhausted batteries, such as lithium and cobalt, in the context of the circular economy. She is the author of more than 300 peer-reviewed papers and several patents in the field of material recovery. She is included in the list of Unstoppable Women (the 1000 women who are changing Italy) and Top Italian Scientists in the field of natural and environmental sciences and in the list of 100 experts.

Mario Coccia

Mario Coccia is a social scientist acting as the Research Director in the National Research Council of Italy and as a visiting scholar at the Arizona State University (USA). He has been a researcher at the Max Planck Institute of Economics and a visiting professor at the Polytechnic of Torino and at the University of Piemonte Orientale (Italy). He has carried out scientific research at the Georgia Institute of Technology, Yale University, UNU-Maastricht Economic and Social Research Institute on Innovation and Technology (United Nations University-MERIT), RAND Corporation (Washington D.C.), University of Maryland (College Park), Bureau d'Économie Théorique et Appliquée (Strasbourg, France), Munk School of Global Affairs (University of Toronto, Canada), and the Institute for Science and Technology Studies (University of Bielefeld, Germany). He investigates via statistical analyses, models, experiments, and observational studies with an interdisciplinary scientific perspective in order to explain the evolutionary properties of science and technology in society, emerging research fields and the related scientific development, new technological trajectories, processes of coevolution between technologies, and the measurement of scientific and technological advances over time and space. He is a member of the Editorial Board of many international journals, and his research publications include more than 350 international papers on several disciplines.

Marco Race

Marco Race (Associate Professor) was born in Napoli, graduated with an M.Sc. in Environmental Engineering at the Università degli Studi di Napoli Federico II in May 2012, and obtained his Ph.D. in Environmental Systems Analysis at UNINA in 2016. Since 2022, he has been an Associate Professor at the University of Cassino. His main research fields concern the treatment of waste or wastewater treatments, the remediation of soil and groundwater, novel contaminant (bio)monitoring and risk assessment approaches, and trace metals and organics in biogeochemical cycles. He is the author of more than 100 papers published in international journals, conferences proceedings, and books chapters. He obtained an international award on soil reclamation.

Yaoyu Zhou

Dr. Yaoyu Zhou is a Full Professor in the College of Environment and Ecology, at the Hunan Agricultural University, Changsha, Hunan province, China. Prof. Zhou's academic background covers waste management and the decontamination of aqueous effluents. Prof. Zhou also has experience in fundamental soil science and the remediation of various contaminants in soils and sediments. Prof. Zhou is listed in Stanford's list of the top 2% of scientists in the world (2020). Together with some of his graduate students and colleagues, Prof. Zhou has published over 220 academic papers, 23 of which were ranked as ESI top papers (17 nominated as "Highly Cited Papers" and 8 nominated as "Hot Papers"). After being supported by the Hong Kong Scholar Program, Prof. Zhou worked in the Hong Kong Polytechnic University from 2018 to 2020. He also holds some international positions: he is a Member of the Editorial Board of Environmental Technology, Carbon Research, and Biochar and the Guest Editor of the *Journal of Environmental Management* (JCR Q1, New Research on Soil Degradation and Restoration) and *Science of the Total Environment* (JCR Q1, Antibiotics and Heavy Metal; and JCR Q1, BEEM conference 2019).

processes

MDPI

Editorial

Our Environment: Everything Is Natural on Earth, but . . . Editorial Piece on Current and Future Soil and Environmental Research

Avelino Núñez Delgado

Department Soil Science and Agricultural Chemistry, Engineering Polytechnic School, University Santiago de Compostela, 27002 Lugo, Spain; avelino.nunez@usc.es

When finishing the Topical Issue "New Research on Detection and Removal of Emerging Pollutants", some reflections came to my mind, which I include in the piece below.

According to what is generally accepted as a paradigm in current science, all the matter in the known universe derived from the big bang [1], which we will agree to consider as a natural event, without external intervention; therefore, we could say that everything that derived, derives, and will derive from that initial event, is natural.

This is the case with the formation and evolution of galaxies, including the Milky Way, and within it the Solar System, and in it the Earth.

The multiple impacts of meteorites and all sorts of other material entities received by our planet during its formation and past evolution undoubtedly qualify as natural events.

At one point, the events associated with atoms that interacted with others to form certain molecules that culminated in nucleic acids and some proteins, could be linked to the "miracle" of the emergence of life [2]. All this emerged from the original elements of the puzzle (the particles and/or forces derived from the big bang); therefore, it would continue to remain natural.

Later, specific living beings were able to drastically modify the planet's atmosphere by releasing oxygen as a result of their metabolic processes [3]. Perhaps that moment can be seen as the first time that living beings caused a major change in the Earth's atmosphere. It was itself natural, since its origin lay in beings made up of atoms derived from the particles generated/released at the time of the big bang.

Previous mass extinctions were related to past events, such as meteorite impacts, which can certainly be considered natural.

In the present, we see that different animals have the ability to build, be it nests (like those of various birds) [4] or termite mounds [5], while some others can use tools [6], grow mushrooms on fragments of vegetables [7], etc. Indeed, we can classify it as a natural process.

Of course, the lead in terms of construction is taken by human beings. However, the truth is that everything derived from the human mind, whether material objects or abstract constructions, such as ethics, morality, the concepts of good and evil, would be natural, since the human nervous system is made up of associations of molecules in turn made up of atoms, all of them derived from particles that began their evolution in the big bang.

On the other hand, both due to processes of struggle for survival and mutual aid (which can be observed from the level of microorganisms to others of greater complexity) [8,9], the current human adaptation to the environment, its future persistence and all its eventualities reach beyond evolution through mutations. As I comment in a book that is being prepared, certain behavioral, social and cultural changes, what we could call "social mutations", in the case of humans, give rise to much shorter term (and therefore accelerated) effects than mutations of a biological nature.

It is equally evident that what is achieved through science and technology (such as space travel) goes far beyond what exclusively biological evolution provides. Additionally,

Citation: Delgado, A.N. Our Environment: Everything Is Natural on Earth, but . . . Editorial Piece on Current and Future Soil and Environmental Research. *Processes* **2023**, *11*, 6. https://doi.org/10.3390/pr11010006

Received: 10 December 2022
Accepted: 16 December 2022
Published: 20 December 2022

the effects of technical and industrial processes sometimes mean new drastic changes at the environmental level, such as accelerated global warming in the troposphere. As noted above, other living beings gave rise to substantial modifications in the terrestrial gaseous sphere in the past, caused by the large-scale release of oxygen into our atmosphere.

Given that everything related to science, techniques and industry derives from our mind, with a nervous system made up of molecules and atoms derived from the big bang, everything is natural.

Therefore, weapons of mass destruction, all synthetic poisons, and any substance or anthropic process that can lead to extinction to humans and other species can also be considered as natural.

Whatever we do will derive from our thoughts; therefore, it will be natural. Whatever we do, it will be part of the future of our species, of our evolutionary course on this planet.

However, I believe that we still have some decision-making capacity over part of our future as living beings, as humans living in the environment of planet Earth.

Despite the awareness that we, as humans (more than 8 billion today), do not decide on something as crucial as our own survival as a species, and on the sustainability of life in general on the planet, but rather that a limited number of humans are the ones who make the decisions that affect the whole group, I think we can mention some related reflections on these ideas.

In some previous publications, I raised certain political and financial aspects that affect the management of waste and pollutants [10–12], as well as the need for politicians to intervene effectively to control risks and unsustainable processes for the planet [13]. The term "politicians" refers to actors who have the power to affect change. If, in practice, an elite (economic or of any other nature) has the power and capacity to act effectively, the restricted group should be the object of the interpellation.

Although ancient philosophers (such as Plato) characterized the government of philosophers as the panacea, I will not recommend a government of scientists as a solution to current problems. However, it should be mandatory that political decisions, at the level of states and supranational entities (of the UN style), consider the survival of the human species, of other species, of fundamental biodiversity, and of the planet, based on a mandatory (imperative for any state) and broad scientific consensus. On the other hand, if scientific consensus exists but no action is taken by individuals with power and the ability to bring about effective changes, such knowledge would remain decorative and non-functional.

Various authors have written interesting articles on the relationship between scientists and political power, such as de-Kerckhove et al. [14].

Beyond the above considerations, and as I comment in the book being prepared, I think it is clear that, at this point, the survival of humans as a species does not essentially and exclusively depend on the reproductive capacity of individuals. In fact, multiple social movements focus on or dedicate themselves to the care of people affected by physical and mental illnesses. In addition, some people opt for ways of life that do not involve their own reproduction. Additionally, these social movements and individuals contribute to making the planet's environment (and therefore also the humans who inhabit it and will inhabit it) more sustainable. Darwinian selective pressure and the positive effects of intra- and inter-species mutual aid may be complex, and perhaps inextricable today, as we intend to evaluate or predict the global effect in the medium and long term.

To conclude, I must say that on a personal level, as a person and as a scientist, I am hopeful about the viability and continuity of human beings and the planet as a whole.

Specifically, as a scientist, I believe that I should continue contributing "betting tickets" to what at one point could be a winning number of the "lottery" of positive results for the planet's environment, for biodiversity, and for the persistence of the human species within a sustainable framework.

Birth is often seen as a 'lottery'. However, in humans (and other species), individuals each contribute to society differently, with some contributions promoting the continued

survival of our species and the planet. In particular, I will continue working on investigating environmental issues, mainly continuing along the lines of research in which I have participated in recent years, including emerging pollutants and global risks due to pollutants of abiotic and biotic origin, through research projects and publications or by editing papers in scientific journals [15–23], including those in the Topical Issue "New Research on Detection and Removal of Emerging Pollutants" [24], as well as writing/editing books [25–27]. Sometimes, some of these tasks can be difficult, but I believe we should contribute as long as our work can be considered to be of value.

In view of the discussed factors, I continue to consider what I should work towards in the future. Specifically, despite the constraints we find, I will continue to expend as much energy as possible in researching, writing, reviewing, and editing in the fields of soil science and environmental science. Taking a hopeful and optimistic stance, I wish all of us luck in our scientific work and in its repercussions at the political level or in any instance where there exists effective power, as well as in the various individual and joint "lotteries" that affect life on our planet.

Data Availability Statement: Not applicable.

Conflicts of Interest: The author declares no conflict of interest. The funders had no role in the design of the study; in the collection, analyses, or interpretation of data; in the writing of the manuscript, or in the decision to publish the results.

References

1. CERN. Available online: https://www.exploratorium.edu/origins/cern/ideas/bang.html (accessed on 1 December 2022).
2. Sowerby, S.J.; Cohn, C.A.; Heckl, W.M.; Holm, N.G. Differential adsorption of nucleic acid bases: Relevance to the origin of life. *Proc. Natl. Acad. Sci. USA* **2001**, *98*, 820–822. [CrossRef] [PubMed]
3. Canfield, D.E. The Early History of Atmospheric Oxygen. Homage to Robert M. Garrels. *Annu. Rev. Earth Planet. Sci.* **2005**, *33*, 1–36. [CrossRef]
4. Mainwaring, M.C.; Hartley, I.R.; Lambrechts, M.M.; Deeming, D.C. The design and function of birds' nests. *Ecol. Evol.* **2014**, *4*, 3909–3928. [CrossRef] [PubMed]
5. Korb, J. Termite Mound Architecture, from Function to Construction. In *Biology of Termites: A Modern Synthesis*; Bignell, D., Roisin, Y., Lo, N., Eds.; Springer: Dordrecht, The Netherlands, 2010.
6. Seed, A.; Byrne, R. Animal Tool-Use. *Curr. Biol.* **2010**, *20*, R1032–R1039. [CrossRef]
7. Campbell, L.C.E.; Kiers, E.T.; Chomicki, G. The evolution of plant cultivation by ants. *Trends Plant Sci.* **2022**, 1–12. [CrossRef]
8. Foster, K.R.; Bell, T. Competition, Not Cooperation, Dominates Interactions among Culturable Microbial Species. *Curr. Biol.* **2012**, *22*, 1845–1850. [CrossRef]
9. Borrello, M.E. Mutual Aid and Animal Dispersion: An Historical Analysis of Alternatives to Darwin. *Perspect. Biol. Med.* **2004**, *47*, 15–31. [CrossRef]
10. Núñez-Delgado, A. Waste or gold? *J. Clean. Prod.* **2014**, *83*, 497. [CrossRef]
11. Núñez-Delgado, A. Take the waste and run (Correspondence on: Riding, M.J., Herbert, B.M.J., Ricketts, L., Dodd, I., Ostle, N., Semple, K.T. Harmonising conflicts between science, regulation, perception and environmental impact: The case of soil conditioners from bioenergy). *Environ. Int.* **2015**, *77*, 161. [CrossRef]
12. Núñez-Delgado, A. Welfare index, waste and expropriation. *J. Clean. Prod.* **2015**, *96*, 10–11. [CrossRef]
13. Núñez-Delgado, A. Scientists talking to politicians: Could you please save the environment? (Correspondence on Diamond et al. 2015. Exploring the planetary boundary for chemical pollution. Environment International 78, 8–15). *Environ. Int.* **2015**, *82*, 113. [CrossRef] [PubMed]
14. de Kerckhove, D.T.; Rennie, M.D.; Cormier, R. Censoring government scientists and the role of consensus in science advice. *EMBO Rep.* **2015**, *16*, 263–266. [CrossRef] [PubMed]
15. Conde-Cid, M.; Fernández-Calviño, D.; Nóvoa-Muñoz, J.C.; Núñez-Delgado, A.; Fernández-Sanjurjo, M.J.; Arias-Estévez, M.; Álvarez-Rodríguez, E. Experimental data and model prediction of tetracycline adsorption and desorption in agricultural soils. *Environ. Res.* **2019**, *177*, 108607–108620. [CrossRef] [PubMed]
16. Conde-Cid, M.; Ferreira-Coelho, G.; Fernández-Calviño, D.; Núñez-Delgado, A.; Fernández-Sanjurjo, M.J.; Arias-Estévez, M.; Álvarez-Rodríguez, E. Single and simultaneous adsorption of three sulfonamides in agricultural soils: Effects of pH and organic matter content. *Sci. Total Environ.* **2020**, *744*, 140872–140886. [CrossRef] [PubMed]
17. Santás-Miguel, V.; Díaz-Raviña, M.; Martín, A.; García-Campos, E.; Barreiro, A.; Núñez-Delgado, A.; Fernández-Sanjurjo, M.J.; Álvarez-Rodríguez, E.; Arias-Estévez, M.; Fernández-Calviño, D. Medium-term influence of tetracyclines on total and specific microbial biomass in cultivated soils of Galicia (NW Spain). *Spanish J. Soil Sci.* **2020**, *10*, 218–232. [CrossRef]

18. Cela-Dablanca, R.; Nebot, C.; Rodríguez-López, L.; Fernández-Calviño, D.; Arias-Estévez, M.; Núñez-Delgado, A.; Fernández-Sanjurjo, M.J.; Álvarez-Rodríguez, E. Efficacy of different waste and by-products from forest and food industries in the removal/retention of the antibiotic cefuroxime. *Processes* **2021**, *9*, 1151. [CrossRef]
19. Barreiro, A.; Cela-Dablanca, R.; Nebot, C.; Rodríguez-López, L.; Santás-Miguel, V.; Arias-Estévez, M.; Fernández-Sanjurjo, M.; Núñez-Delgado, A.; Álvarez-Rodríguez, E. Occurrence of Nine Antibiotics in Different Kinds of Sewage Sludge, Soils, Corn and Grapes After Sludge Spreading. *Spanish J. Soil Sci.* **2022**, *12*, 10741–10753. [CrossRef]
20. Rodríguez-López, L.; Santás-Miguel, V.; Núñez-Delgado, A.; Álvarez-Rodríguez, E.; Pérez-Rodríguez, P.; Arias-Estévez, M. Influence of pH, Humic Acids, and Salts on the Dissipation of Amoxicillin and Azithromycin Under Simulated Sunlight. *Span. J. Soil Sci.* **2022**, *12*, 10438. [CrossRef]
21. Núñez-Delgado, A.; Bontempi, E.; Coccia, M.; Kumar, M.; Farkas, K.; Domingo, J.L. SARS-CoV-2 and other pathogenic microorganisms in the environment. *Environ. Res.* **2021**, *201*, 111606. [CrossRef]
22. Dominguez, J.R.; Núñez-Delgado, A.; García-Rodríguez, J. Treatment technologies for emerging contaminants in water. *J. Environ. Manag.* **2021**, *286*, 112256. [CrossRef]
23. Núñez-Delgado, A.; Ahmed, W.; Bontempi, E.; Domingo, J.L. The environment, epidemics, and human health. *Environ. Res.* **2022**, *214*, 113931. [CrossRef] [PubMed]
24. Topical Issue. Available online: https://www.mdpi.com/topics/Emerging_Pollutants (accessed on 1 December 2022).
25. Núñez-Delgado, A. (Ed.) *Sorbents Materials for Controlling Environmental Pollution: Current State and Trends*; Elsevier: Amsterdam, The Netherlands, 2021.
26. Núñez-Delgado, A.; Arias-Estévez, M. (Eds.) *Emerging Pollutants in Sewage Sludge and Soils*; Springer: Cham, Switzerland, 2022.
27. Book Series. Available online: https://www.springer.com/series/11763 (accessed on 1 December 2022).

materials

MDPI

Article

Black Talc-Based TiO_2/ZnO Composite for Enhanced UV-Vis Photocatalysis Performance

Huan Shuai [1,2], Jiao Wang [2,*], Xianguang Wang [3,*] and Gaoxiang Du [1,*]

[1] School of Materials Science and Technology, China University of Geosciences, Beijing 100083, China; shuaihuan@email.cugb.edu.cn
[2] School of Basic Education, Beijing Polytechnic College, Beijing 100042, China
[3] Jiangxi Mineral Resources Guarantee Service Center, Nanchang 330025, China
* Correspondence: wj@bgy.edu.cn (J.W.); 13907090885@163.com (X.W.); dgx@cugb.edu.cn (G.D.)

Abstract: Herein, using black talc as a carrier, a ternary black talc-TiO_2/ZnO composite photocatalyst was prepared by the sol-gel method, and the effect of the black talc on the hetero-structure properties of the TiO_2 and ZnO was systematically studied. The prepared composite photocatalyst showed an excellent degradation performance of the pollutant, where black talc plays an important role in promoting the interface interaction by enhancing the contact area between the TiO_2 and ZnO. Moreover, the free carbon element doping in black talc favors the formation of more oxygen vacancies, thereby improving the response as a photocatalyst in visible light. In addition, the carbon in the black talc can also adsorb organic pollutants and enrich the surroundings of the photocatalyst with pollutants, so it further improves the catalytic efficiency of the photocatalyst. Under UV irradiation, the degradation rate of Rhodamine B on black talc-TiO_2/ZnO was found 3.3 times higher than that of black talc-TiO_2 with good stability.

Keywords: black talc carrier; heterostructure; photocatalyst; TiO_2; ZnO

Citation: Shuai, H.; Wang, J.; Wang, X.; Du, G. Black Talc-Based TiO_2/ZnO Composite for Enhanced UV-Vis Photocatalysis Performance. *Materials* **2021**, *14*, 6474. https://doi.org/10.3390/ma14216474

Academic Editors: Marco Race, Elza Bontempi, Avelino Núñez-Delgado, Zhien Zhang, Mario Coccia and Yaoyu Zhou

Received: 4 October 2021
Accepted: 18 October 2021
Published: 28 October 2021

1. Introduction

With the rapid development of the industries, organic pollutants in the air and water have been increased and brought a series of environmental problems [1–3] along with serious concern for human health [4]. Therefore, it is of great significance to investigate environmentally friendly, low-cost, facile-efficient pollutant treatment solutions including photocatalytic degradation, which offers cost-effective simple preparation and stable chemical properties devoid of secondary pollution [5–8]. As an important semiconductor material, TiO_2 has broad application prospects in energy conversion, catalysts, etc. [9–12].

However, some issues with TiO_2, such as being prone to agglomeration, low specific surface area, difficult to recycle, and having a high photo-generated electron–hole recombination rate and narrow range of wavelength for utilization of light, can limit its applications [13]. However, the construction of a heterojunction by coupling TiO_2 with other semiconductor photocatalysts such as ZnO, CdS, etc. can be an effective way to accelerate the separation of electron–hole pairs [14]. Meanwhile, the anchoring of catalyst particles on a suitable substrate can increase the contact area between the photocatalyst and pollutants, thereby increasing the photocatalytic activity.

On the other hand, ZnO, a semiconductor material with a bandgap of 3.37 eV, can only absorb ultraviolet (UV) light with a wavelength less than 378 nm [15,16]. The photogenerated electrons in ZnO are easy to recombine with holes, which reduce the concentration of the carriers that can migrate towards the surface, resulting in relatively low quantum efficiency [17]. As per the literature, the photocatalytic activity can be improved by combining two different semiconductors such as TiO_2 and ZnO to form heterojunction, which can expand the absorption spectrum from UV to visible light and improve the quantum

efficiency by accelerating the transfer of the photogenerated electrons and holes between the interface [18,19].

In comparison with a single-phase photocatalyst, the composite photocatalyst possesses higher catalytic activity, but is difficult to recycle. A suitable carrier, such as black talc, can be used to immobilize the composite photocatalyst. Thus far, black talc is one of the few layered silicate minerals with a well-defined lamellar structure, which can facilitate the hosting of the photocatalysts. The structure is shown in Scheme 1. The abundant hydroxyl groups on the surface of the black talc favor the nucleation of the supported photocatalyst, improve their dispersion and stability, and increase their contact area to the surrounding matter. More importantly, black talc is a sandwich structure with a graphene-like carbon layer embedded between the talc layers [20,21], where organic pollutants can be preferentially adsorbed on the carbon layer naturally, thereby increasing the concentrations of the pollutants near composite photocatalyst and improving the efficiency of the catalytic. The carbon in black talc can further dope with ZnO to generate more oxygen vacancies, thereby improving its response against visible light. In addition, the carbon-doped ZnO can inhibit the recombination of the photo-generated carriers and increase quantum efficiency [22–26].

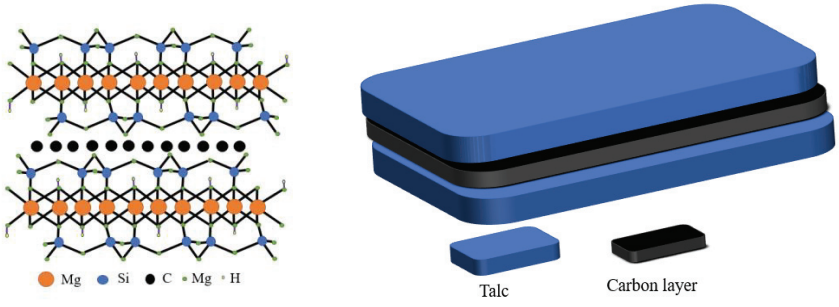

Scheme 1. Schematic diagram of black talc structure.

In order to increase specific surface area, catalytic efficiency, and adsorption of organic pollutants, and to achieve the synergistic catalytic effect, a new composite photocatalyst is an urgent requirement.

In this study, a black talc-TiO_2/ZnO composite photocatalyst with smaller particle size and larger specific surface area is prepared by the sol-gel method to provide the combination of large pollutant absorption capacity and high catalytic efficiency. The formed heterojunction between TiO_2 and ZnO provides significantly large charge transfer channels to favor high catalytic efficiency. The morphology, structure, and photocatalytic performance of the as-prepared black talc-TiO_2/ZnO composites have been thoroughly characterized, and the effect of the black talc on the interaction between TiO_2 and ZnO and output performance is systematically discussed. This study provides a new approach to synthesize novel and efficient hetero-structured photocatalysts in a facile and low-cost manner.

2. Materials and Methods

In this work, the materials and reagents were used as received, without further treatment. Black talc was purchased from Guangfeng, Jiangxi. Tetrabutyl titanate (TBOT), and zinc nitrate were purchased from Aladdin Reagent Co., Ltd. (Shanghai, China). The sulfuric acid, sodium hydroxide, and analytical pure ethanol were purchased from Beijing Chemical Plant (Beijing, China). Deionized water was used in the whole experimental process.

The black talc-TiO_2/ZnO composite was prepared by the sol-gel method. In a typical synthesis process, a 10.0% sulfuric acid solution was added to 325 mesh black talc powder and stirred for 2 h. Following this, the mixture was filtered via a suction filter, and the product was washed with deionized water three times. Next, the product was dried at 105 °C for 24 h prior to use and labeled as BT. The BT sample was calcined at 500 °C in a furnace purged with oxygen flow to obtain calcined black talc (CBT). Then, 8.5 g of TBOT was dissolved in 30 mL of absolute ethanol and stirred thoroughly to obtain solution A. Thereafter, 10 g of BT sample was added to solution A under stirring conditions. Finally, the mixture was placed in an oven at 105 °C for completely dry powder, and it was calcined in a tube furnace purged with nitrogen flow at 500 °C for 2 h before. Thus, the black talc-supported titanium dioxide composite photocatalyst was obtained and labeled as BT-T. The black talc-TiO_2/ZnO composite was prepared according to the following steps as shown in Scheme 2. Firstly, 5 g of zinc nitrate and 50 mL of sodium hydroxide solution (1 M) were evenly mixed and added to solution A, which was stirred for half an hour at room temperature. Afterward, the synthesized BT was added and stirred for half an hour before it was kept in an oven at 105 °C for drying. Finally, the dried product was placed in a tube furnace purged with nitrogen flow and calcined at 500 °C for 2 h, and the black talc supported titanium dioxide/zinc oxide composite photocatalyst was obtained and denoted as BT-T/Z.

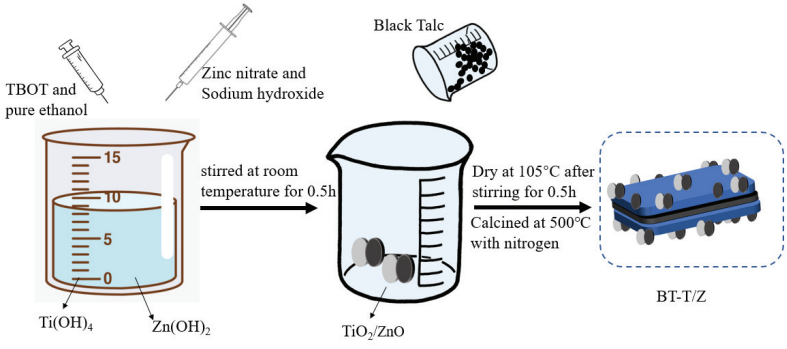

Scheme 2. Synthesis strategy for BT-T/Z composite photocatalyst.

3. Results

Figure 1 shows the XRD patterns for BT, BT-T, and BT-T/Z composite photocatalysts. The characteristic diffraction peaks for the anatase phase are observed in both BT-T and BT-T/Z samples at 25.3°, 37.8°, and 48.1°, which are attributed to the diffraction from (101), (104), and (200) planes of the anatase TiO_2, respectively [27]. Importantly, no characteristic peak is observed for the rutile TiO_2 phase. The results indicate that the anatase phase of the TiO_2 has been successfully synthesized on black talc in both BT-T and BT-T/Z samples. The characteristic diffraction peaks for the ZnO are observed in the BT-T/Z sample at 31.7°, 34.4°, and 56.6° from the (100), (002), and (110) diffraction planes for ZnO, respectively. The results show that the ZnO phase has been successfully coated onto the composite material. Meanwhile, the relative content of the black talc, i.e., BT sample is reduced with the formation of the TiO_2 and ZnO as the intensity of the characteristic peak becomes weak. However, all the diffraction peaks of the BT are stable, indicating that calcination at 500 °C cannot damage the black talc structure.

The SEM images are shown in Figure 2, where Figure 2a,b are captured for the BT sample while Figure 2c,d are captured for the photocatalyst BT-T/Z. It can be seen that the black talc exhibits a layered structure with small mineral particles of size less than 2 microns. The stacking of these flakes in the talc has a certain orientation along (001) planes in parallel to each other in a layered stack. From SEM images in Figure 2c,d, a large number of particles are agglomerated on the surface of the black talc mineral, especially at

its edge, with a relatively uniform size of about 20 nm. However, the lamellar structure for the black talc can be clearly seen after agglomeration. The compositional analysis of the elements by EDS confirms the existence of both TiO_2 and ZnO on the surface of the black talc mineral, depicting the composite phase. Figure 3 shows the EDS element probing for photocatalyst. And Figure 4 shows the EDS element mapping for photocatalyst.

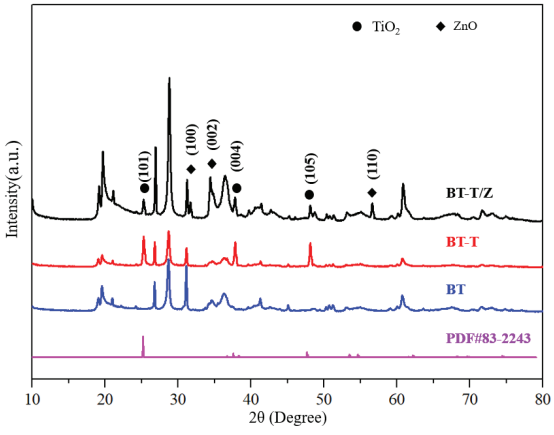

Figure 1. XRD diffraction pattern for photocatalytic material.

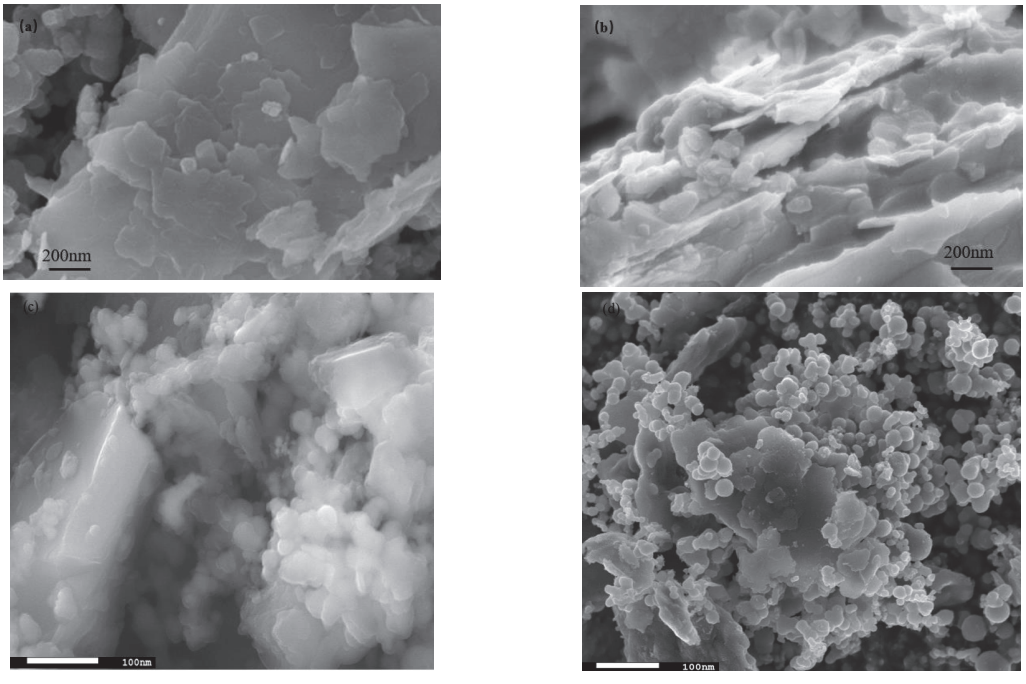

Figure 2. (**a**,**b**) SEM image of black talc, (**c**,**d**) SEM image of photocatalyst.

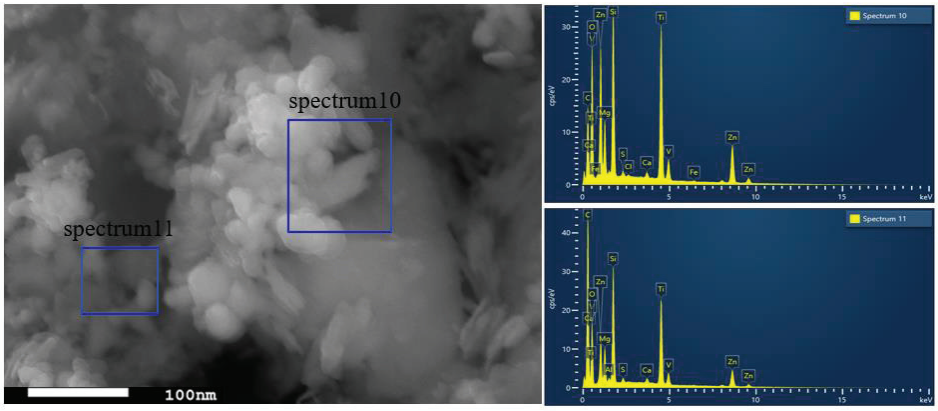

Figure 3. EDS element probing for photocatalyst.

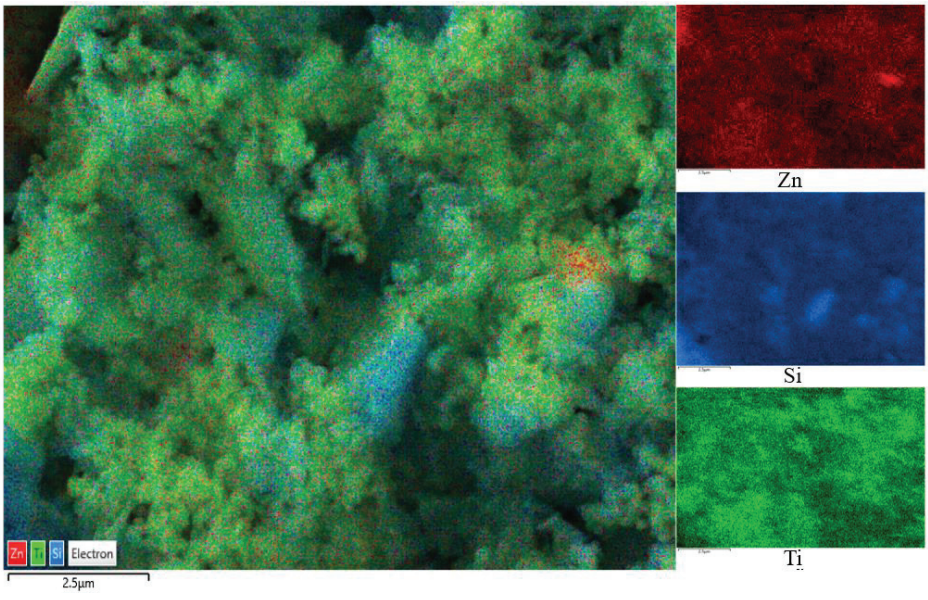

Figure 4. EDS element mapping for photocatalyst.

The profile obtained from X-ray photoelectron spectroscopy (XPS) for the BT-T/Z sample shows five chemical elements, namely Zn, O, Ti, C, and Si, as shown in Figure 5a. Figure 5b shows C 1s peaks for the BT-T/Z. The characteristic peak at 285.18 eV confirms the existence of C–C bonds in the sample. The narrow C 1s peaks in the BT-T and BT also appear at nearly 284 eV. As compared with the BT sample, the binding energy for the C element in the BT-T/Z and BT-T increases slightly due to the bound state of carbon atoms in TiO_2/ZnO heterojunction. In addition, the characteristic peak at 283.94 eV indicates that the formation of Zn–C bond on the black talc, i.e., C-doped ZnO [28,29].

Figure 5c shows the O 1s profile at 532.26 eV for Si-O-Si. The characteristic peaks at 529.51 eV and 530.35 eV are observed for Ti-O-Si, and that peak at 530.67 eV is attributed to the presence of oxygen defects or hydroxyl groups on the surface of the ZnO [30,31].

Figure 5d shows that the Zn 2p at 1022.41 eV is attributed to the Zn–O bond, while the Zn 2p1/2 peak appears at 1044.92 eV. The distance between the two peaks is observed at nearly 22 eV, corresponding to the featured profile of Zn^{2+} [32].

Figure 5e indicates that the Si 2p peak shifts to the blue end when the SiO_2 in black talc hybridized with TiO_2 and ZnO, confirming the effective combination of SiO_2 with TiO_2 and ZnO. Thus, a chemical bond is formed between TiO_2/ZnO and black talc.

Figure 5f shows the peaking at 464.02 eV and 458.25 eV are corresponding to the characteristic peaks of the Ti 2p1/2 and Ti 2p3/2, respectively. A span of 5.8 eV is observed between the two peaks, indicating Ti in its oxidation state of Ti^{4+} [33,34]. Comparably, the characteristic peak of Ti 2p in the BT-T/Z is much weaker than that of the BT-T due to the coating of the ZnO on the surface of the BT-T/Z composite. As the electronegativity of Si atoms is higher than that of Ti atoms, it can induce positively charged holes to move towards the Si-O-Ti interface and promote the directional diffusion of the photogenerated electrons and holes. With the increase in the contact area between TiO_2 and ZnO, a large number of electron transfer channels are generated at the interfaces due to the formation of TiO_2/ZnO heterostructure.

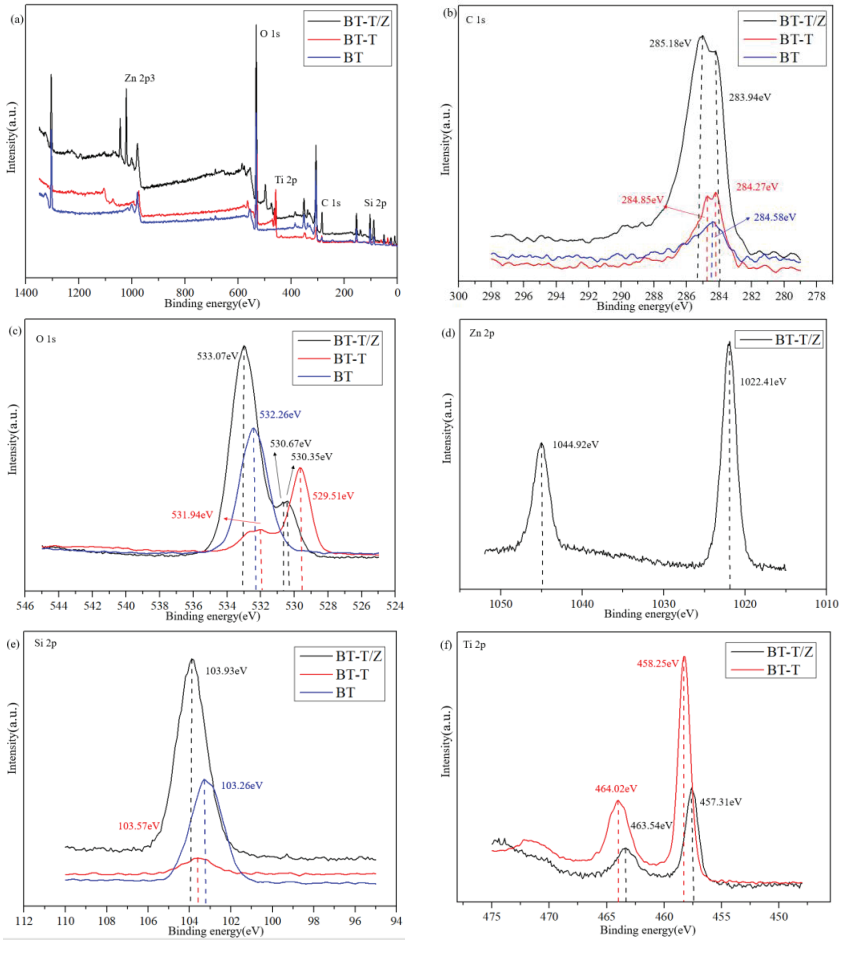

Figure 5. (**a**) XPS spectra of BT, BT-T, and BT-T/Z, (**b**) C 1s, (**c**) O 1s, (**d**) Zn 2p, (**e**) Si 2p, and (**f**) Ti 2p high-resolution energy spectrum.

In order to study the performance of the hetero-structure between TiO_2 and ZnO, the photocurrent transient response and electrochemical impedance spectroscopy (EIS) were measured, and the results are shown as Figure 6a,b, respectively. It can reflect the charge separation efficiency and charge transfer resistance of the BT-T and BT-T/Z.

Figure 6a shows that the BT-T/Z sample exhibits a higher photocurrent transient intensity than that of the BT-T sample, indicating that the coexistence of TiO_2 and ZnO is beneficial for the superior performance of the composite. Meanwhile, the TiO_2/ZnO composite exhibits a smaller arc radius (Figure 6b) in the counterpart of the BT-T sample, showing smaller charge transfer resistance. This indicates that defects contribute to the increase in donor density and the decrease in charge transfer resistance. Therefore, the close contact between TiO_2 and ZnO leads to the high mobility of the photogenerated electron-hole pair. The results confirm that the strong light response and small charge transfer resistance due to the formation of hetero-structure between the TiO_2 and ZnO can lead to a better photocatalytic performance from BT-T/Z composite than BT-T sample.

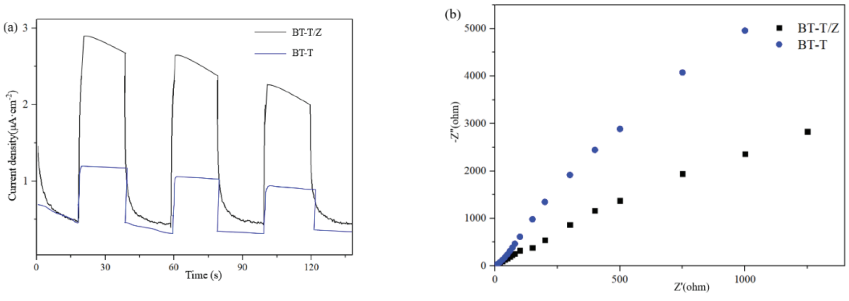

Figure 6. (**a**) Photoelectric conversion performances and (**b**) electrochemical impedance spectra.

Herein, Rhodamine B was used to mimic organic pollutants in the adsorption-degradation experiments. The determination of the degradation rate can be expressed as

$$\eta = (A_0 - A)/A_0 \times 100\% \quad (1)$$

where η is the decolorization rate for Rhodamine B. The absorbance, A_0, is determined for the rhodamine B solution before degradation, and A is the absorbance of the rhodamine B solution after degradation.

In a typical adsorption experiment, the four quartz test tubes were filled with 50 mL of rhodamine B solution (30 mg/L), respectively, and 50 mg of the BT, BT-T, and BT-T/Z are added to the mentioned three solutions, respectively, while the fourth was considered as a reference solution. Afterward, all the solutions were stirred at a constant speed with a magnet under dark conditions to ensure even mixing.

The mixtures were sampled every 20 min, and the supernatants obtained by centrifuging were measured three times for each sample by UV-vis at 554 nm to determine the change in the concentration of rhodamine B in the supernatant. According to the formula $(C_0 - C)/C_0$, the degradation rate of the Rhodamine B in a solution can be evaluated, and the outcomes are shown in Figure 7.

As shown in Figure 7, under dark conditions, the compound Rhodamine B itself is relatively stable with only 3% decay in the concentration. The adsorption rate of CBT is 4.3%, which is slightly higher than that of the control group. The adsorption rate of 16.8% of the BT-T to rhodamine B is observed, and it is 18.7% for BT-T/Z, which is slightly lower than that of BT (19.7%) as the adhesion of TiO_2 and ZnO affects the adsorption of Rhodamine B. After 120 min, the adsorption rate for each sample remains unchanged due to the saturation of the adsorption in the absence of photocatalytic degradation.

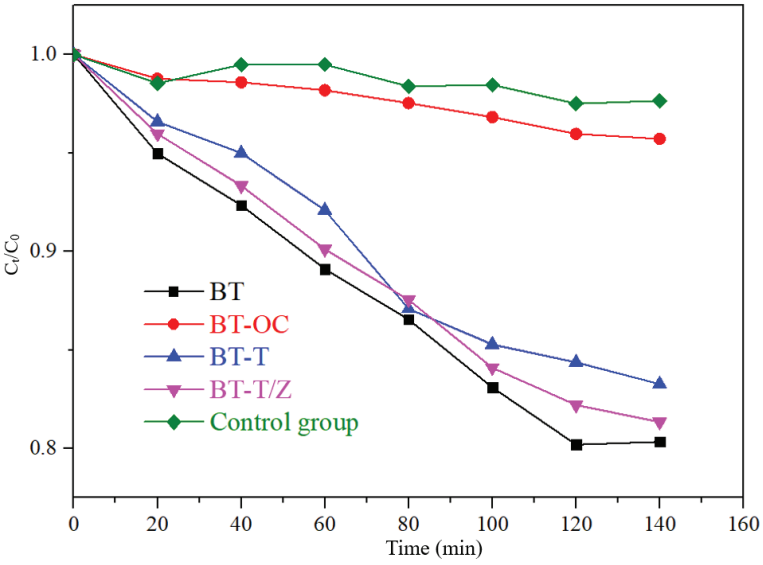

Figure 7. The adsorption effect of RhB on different samples under dark conditions.

The physical adsorption of Rhodamine B solution to black talc follows the quasi-first-order kinetic equation, as shown in Figure 8, where the adsorption performance for each sample can be quantitatively evaluated through the apparent rate constant k.

$$-\ln(C/C_0) = kt \quad (2)$$

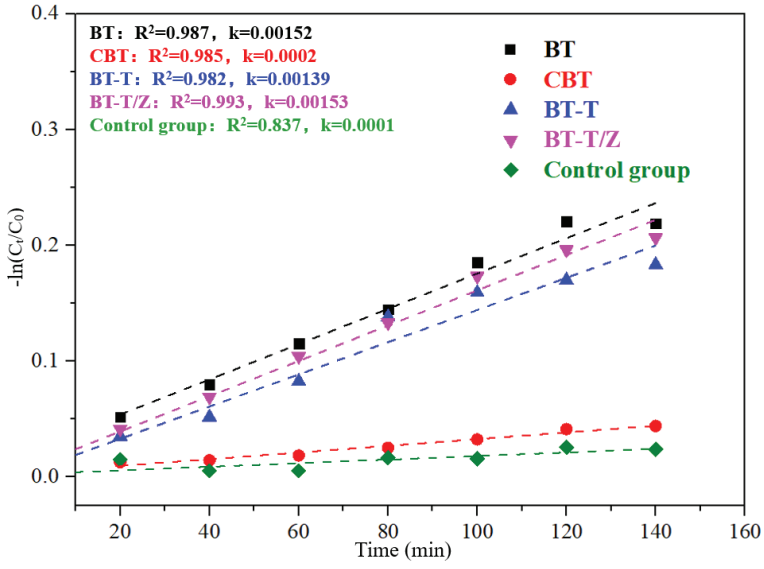

Figure 8. Kinetics fitting curves for the adsorption of Rhodamine B under dark conditions.

The photocatalytic degradation experiment was carried out using a high-pressure mercury lamp with a power of 300 W irradiating on the BT-T and BT-T/Z samples with a dominant wavelength of 365 nm. The whole reactor was immersed into a water circulation system to keep the temperature at 18 °C during the reaction. The successive sampling was taken at an interval of 20 min, and each sample was tested three times to obtain an average value. The initial concentration (absorbance) for Rhodamine B is denoted as C_0, and the concentration for the supernatant obtained at a different time is recorded as C so that the formula $(C_0 - C)/C_0$ can denote the degradation rate under this condition.

Figure 9 shows the degradation curves of Rhodamine B with the different photocatalyst under UV irradiation. Under UV irradiation, the concentration of Rhodamine B decreases less than 4% in the control group, indicating that Rhodamine B is quite stable under UV irradiation. The degradation rate reached 97.3% for BT-T/Z while 60% for BT-T after 140 min of irradiation. Obviously, the composite BT-T/Z showed the best photocatalytic performance, where TiO_2 and ZnO possess a synergistic effect in the photodegradation of Rhodamine B.

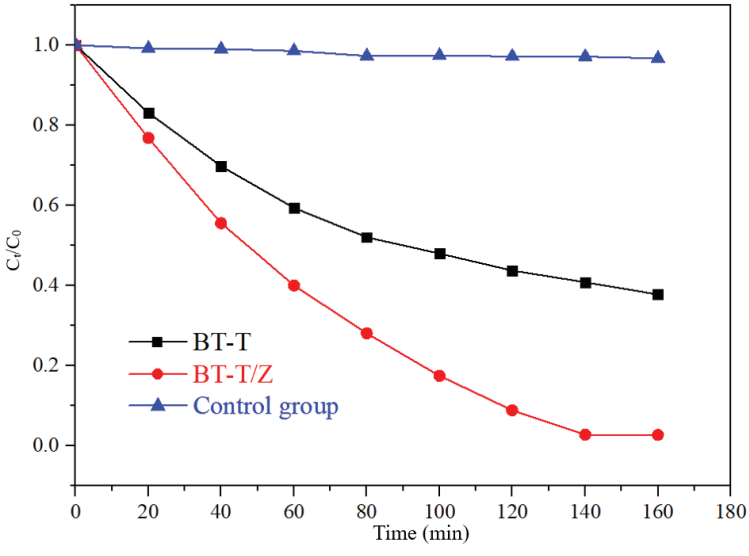

Figure 9. Degradation curves of Rhodamine B with the different photocatalyst under UV irradiation.

Figure 10 shows thekinetics fitting plots for the degradation of Rhodamine B under the irradiation with a wavelength of 365 nm.Through fitting kinetics, the apparent degradation rate constant of 0.00638 is evaluated for BT-T while 0.02087 for the BT-T/Z, where the degradation efficiency of the BT-T/Z is 3.3 times higher than that of the BT-T sample. This result confirms again that BT-T/Z is an excellent photocatalyst for organic pollutant degradation.

In order to further test the stability of the prepared photocatalyst, cyclic degradation tests were conducted. The experimental results are shown in Figure 11. The experimental results show that the adsorption–degradation rate for Rhodamine B being catalyzed by BT-T/Z was still around 88% after five cycles, indicating good stability and reusability.

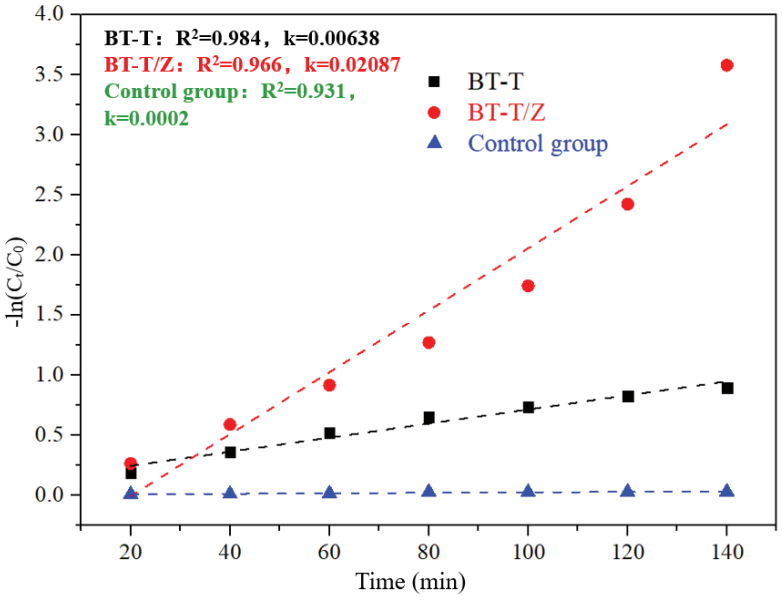

Figure 10. Kinetics fitting plots for the degradation of Rhodamine B under the irradiation with a wavelength of 365 nm.

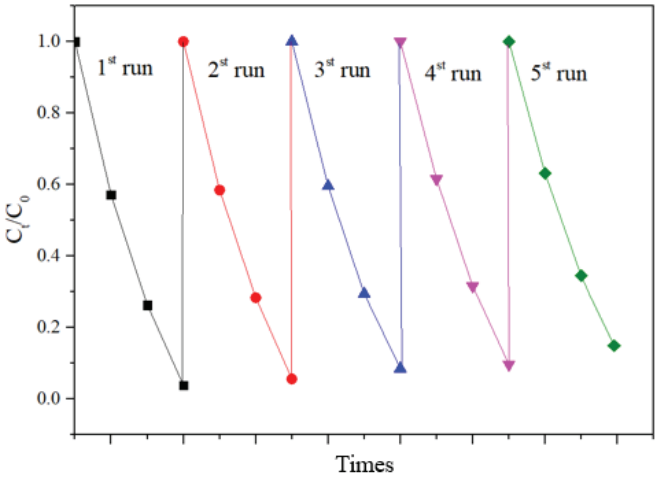

Figure 11. Cycling degradation test of Rhodamine B on BT-T/Z.

4. Discussion

As shown in Scheme 3, an efficient hetero-structure is formed between the TiO_2 and ZnO through their close interfacial combination with the substrate of BT. Under the photo-irradiation, the electrons in the valence band of the TiO_2 and ZnO are excited and transfer to their conduction band, whereas the holes remain in the valence band. The excited electrons in the ZnO recombine with the holes in the TiO_2 and weaken the electron–hole recombination extent for the TiO2, resulting in the majority of electrons surviving in the conduction band of the TiO2. Meanwhile, the holes accumulated in the valence band of the TiO2 take part in the oxidation reaction. The formation of hetero-structure between the TiO2 and ZnO can significantly improve the separation and transport efficiency of

the photogenerated carriers, which is one of the important factors, causing an improved photocatalytic redox performance for BT-T/Z in the counterparts of the BT-T. The black talc has abundant surface hydroxyl groups and high surface activity, playing a synergic role in improving photocatalytic performance. Compared with other studies [35–37], this experiment cleverly combined the construction of heterojunction and the loading of mineral materials to prepare a photocatalyst with good performance.

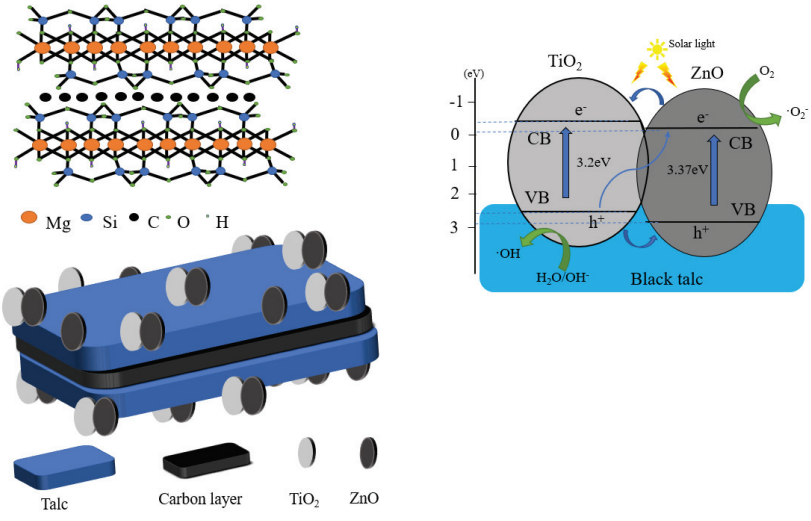

Scheme 3. The improved photocatalysis mechanism for BT-T/Z composite under photo-irradiation.

5. Conclusions

In summary, firstly, the presence of black talc reduces the particle size of the photocatalyst and increases its specific surface area. Therefore, more TiO_2 are exposed to contact and combine with ZnO, which causes more photocarriers to transfer pathways at their interface and favors an efficient photocarrier migration crossing at the interface between the TiO_2 and ZnO.

Moreover, a graphene-like carbon layer in black talc can adsorb and enrich organic pollutants, thereby increasing the catalytic efficiency. Finally, the free carbon in the black talc may participate in the doping, and it favors the formation of more oxygen vacancies and improves its response in visible light.

Finally, BT-T/Z composite photocatalyst has been prepared through the sol-gel method. Under UV irradiation, the degradation rate of Rhodamine B catalyzed by BT-T/Z composite was found 3.3 times higher than that of BT-T. The improved photocatalytic performance for BT-T/Z can be attributed to the synergistic effect of the characteristic adsorption of black talc and the formation of a high-efficiency TiO_2/ZnO hetero-structure. The existence of black talc can increase the specific surface area and light absorption and therefore further improve its photocatalytic efficiency. More importantly, the black talc can adsorb and enrich the pollutants around the photocatalyst, thereby increasing its catalytic efficiency. Consequently, black talc can be used as an effective carrier with multiple functions to improve the performance of the semiconductor photocatalysts. We believe that black talc can also be introduced into other semiconductor systems to form new high-efficiency composite photocatalysts, facilitating the development of high-efficiency and low-cost photocatalysts.

Author Contributions: Conceptualization, J.W. and G.D.; methodology, H.S., J.W. and G.D.; validation, H.S. and J.W.; formal analysis, H.S.; investigation, H.S. and X.W.; data curation, H.S.; writing—original draft preparation, H.S. and G.D.; writing—review and editing, H.S., J.W. and G.D.; visualization, H.S.; supervision, X.W.; project administration, X.W.; and funding acquisition, X.W. All authors have read and agreed to the published version of the manuscript.

Funding: The work was partly supported by the Beijing Municipal Education Commission Science and Technology Plan Key Project (No. KZ201910853043).

Institutional Review Board Statement: Not applicable.

Informed Consent Statement: Not applicable.

Data Availability Statement: The data presented in this study are available on request from the corresponding author.

Conflicts of Interest: The authors declare no conflict of interest.

References

1. Li, X.; Yu, J.; Jaroniec, M.; Chen, X. Cocatalysts for Selective Photoreduction of CO_2 into Solar Fuels. *Chem. Rev.* **2019**, *119*, 3962–4179. [CrossRef] [PubMed]
2. Qiao, B.; Chen, Y.; Tian, M.; Wang, H.; Yang, F.; Shi, G.; Zhang, L.; Peng, C.; Luo, Q.; Ding, S. Characterization of water soluble inorganic ions and their evolution processes during PM 2.5 pollution episodes in a small city in southwest China. *Sci. Total Environ.* **2019**, *650*, 2605–2613. [CrossRef] [PubMed]
3. Xue, J.; Kannan, K. Mass flows and removal of eight bisphenol analogs, bisphenol A diglycidyl ether and its derivatives in two wastewater treatment plants in New York State, USA. *Sci. Total Environ.* **2019**, *648*, 442–449. [CrossRef] [PubMed]
4. Gao, W.; Tian, J.; Fang, Y.; Liu, T.; Zhang, X.; Xu, X.; Zhang, X. Visible-light-driven photo-Fenton degradation of organic pollutants by a novel porphyrin-based porous organic polymer at neutral pH. *Chemosphere* **2020**, *243*, 125334. [CrossRef]
5. Yan, X.; Yuan, X.; Wang, J.; Wang, Q.; Zhou, C.; Wang, D.; Tang, H.; Pan, J.; Cheng, X. Construction of novel ternary dual Z-scheme Ag_3VO_4/C_3N_4/reduced TiO_2 composite with excellent visible-light photodegradation activity. *J. Mater. Res.* **2019**, *34*, 2024–2036. [CrossRef]
6. Ding, X.; Wang, W.; Zhang, A.; Zhang, L.; Yu, D. Efficient visible light degradation of dyes in wastewater by nickel–phosphorus plating–titanium dioxide complex electroless plating fabric. *J. Mater. Res.* **2019**, *34*, 999–1010. [CrossRef]
7. Prakash, J.; Sun, S.; Swart, H.C.; Gupta, R.K. Noble metals-TiO_2 nanocomposites: From fundamental mechanisms to photocatalysis, surface enhanced Raman scattering and antibacterial applications. *Appl. Mater. Today* **2018**, *11*, 82–135. [CrossRef]
8. Selcuk, S.; Zhao, X.; Selloni, A. Structural evolution of titanium dioxide during reduction in high-pressure hydrogen. *Nat. Mater.* **2018**, *17*, 923–928. [CrossRef]
9. Gaya, U.I.; Abdullah, A.H. Heterogeneous photocatalytic degradation of organic contaminants over titanium dioxide: A review of fundamentals, progress and problems. *J. Photochem. Photobiol. C Photochem. Rev.* **2007**, *9*, 1–12. [CrossRef]
10. Tsoukleris, D.S.; Maggos, T.; Vassilakos, C.; Falaras, P. Photocatalytic degradation of volatile organics on TiO_2 embedded glass spherules. *Catal. Today* **2007**, *129*, 96–101. [CrossRef]
11. Castro, R.H.R.; Wang, B. The Hidden Effect of Interface Energies in the Polymorphic Stability of Nanocrystalline Titanium Dioxide. *J. Am. Ceram. Soc.* **2011**, *94*, 918–924. [CrossRef]
12. Fujishima, A.; Rao, T.N.; Tryk, D.A. Titanium dioxide photocatalysis. *J. Photochem. Photobiol. C Photochem. Rev.* **2000**, *1*, 1–21. [CrossRef]
13. Lavanya, T.; Satheesh, K.; Dutta, M.; Jaya, N.V.; Fukata, N. Superior photocatalytic performance of reduced graphene oxide wrapped electrospun anatase mesoporous TiO_2 nanofibers. *J. Alloys Compd.* **2014**, *615*, 643–650. [CrossRef]
14. Li, C.; Sun, Z.; Zhang, W.; Yu, C.; Zheng, S. Highly efficient g-C_3N_4/TiO_2/kaolinite composite with novel three-dimensional structure and enhanced visible light responding ability towards ciprofloxacin and S. aureus. *Appl. Catal. B Environ.* **2018**, *220*, 272–282. [CrossRef]
15. Sampaio, M.J.; Lima, M.J.; Baptista, D.L.; Silva, A.M.T.; Silva, C.G.; Faria, J.L. Ag-loaded ZnO materials for photocatalytic water treatment. *Chem. Eng. J.* **2016**, *318*, 95–102. [CrossRef]
16. Sun, Y.B.; Xia, T.; Wu, H.; Zhang, W.J.; Zhu, Y.H.; Xue, J.X.; He, D.T.; Zhang, L.Y. Effects of nano zinc oxide as an alternative to pharmacological dose of zinc oxide on growth performance, diarrhea, immune responses, and intestinal microflora profile in weaned piglets. *Anim. Feed Sci. Technol.* **2019**, *258*, 114312. [CrossRef]
17. Wang, S.; Zhu, B.; Liu, M.; Zhang, L.; Yu, J.; Zhou, M. Direct Z-scheme ZnO/CdS hierarchical photocatalyst for enhanced photocatalytic H2-production activity. *Appl. Catal. B Environ.* **2018**, *243*, 19–26. [CrossRef]
18. Li, X.; Wang, C.; Xia, N.; Jiang, M.; Liu, R.; Huang, J.; Li, Q.; Luo, Z.; Liu, L.; Xu, W.; et al. Novel ZnO-TiO_2 nanocomposite arrays on Ti fabric for enhanced photocatalytic application. *J. Mol. Struct.* **2017**, *1148*, 347–355. [CrossRef]
19. Lin, J.; Luo, Z.; Liu, J.; Li, P. Photocatalytic degradation of methylene blue in aqueous solution by using ZnO-SnO_2 nanocomposites. *Mater. Sci. Semicond. Process.* **2018**, *87*, 24–31. [CrossRef]

20. Li, C.; Wang, R.; Lu, X.; Zhang, M. Mineralogical characteristics of unusual black talc ores in Guangfeng County, Jiangxi Province, China. *Appl. Clay Sci.* **2013**, *74*, 37–46. [CrossRef]
21. Li, C.; Wang, R.; Xu, H.; Lu, X.; Konishi, H.; He, K. Interstratification of graphene-like carbon layers within black talc from Southeastern China: Implications to sedimentary talc formation. *Am. Mineral.* **2016**, *101*, 1668–1678. [CrossRef]
22. Yang, X.; Li, W.X.; Hui, Y.; Ying, Y.; Ting, D.X. MOF-5 derived C-doped ZnO decorated with Cu cocatalyst for enhancing visible-light driven photocatalytic hydrogen evolution. *J. Phys. Chem. Solids* **2021**, *149*, 109793.
23. Wang, Y.; Ge, S.; Cheng, W.; Hu, Z.; Shao, Q.; Wang, X.; Lin, J.; Dong, M.; Wang, J.; Guo, Z. Microwave Hydrothermally Synthesized Metal-Organic Framework-5 Derived C-doped ZnO with Enhanced Photocatalytic Degradation of Rhodamine B. *Langmuir ACS J. Surf. Colloids* **2020**, *36*, 9658–9667. [CrossRef] [PubMed]
24. Yu, W.; Zhang, J.; Peng, T. New insight into the enhanced photocatalytic activity of N-, C- and S-doped ZnO photocatalysts. *Appl. Catal. B Environ.* **2016**, *181*, 220–227. [CrossRef]
25. Hu, C.; Hu, X.; Li, R.; Xing, Y. MOF derived ZnO/C nanocomposite with enhanced adsorption capacity and photocatalytic performance under sunlight. *J. Hazard. Mater.* **2020**, *385*, 121599. [CrossRef]
26. Hussain, M.Z.; Pawar, G.S.; Huang, Z.; Tahir, A.A.; Fischer, R.A.; Zhu, Y.; Xia, Y. Porous ZnO/Carbon nanocomposites derived from metal organic frameworks for highly efficient photocatalytic applications: A correlational study. *Carbon* **2019**, *146*, 348–363. [CrossRef]
27. Jaiswal, R.; Bharambe, J.; Patel, N.; Dashora, A.; Kothari, D.C.; Miotello, A. Copper and Nitrogen co-doped TiO_2 photocatalyst with enhanced optical absorption and catalytic activity. *Appl. Catal. B Environ.* **2015**, *168*, 333–341. [CrossRef]
28. Wang, B.; Zhang, G.; Leng, X.; Sun, Z.; Zheng, S. Characterization and improved solar light activity of vanadium doped TiO_2/diatomite hybrid catalysts. *J. Hazard. Mater.* **2015**, *285*, 212–220. [CrossRef]
29. Xia, Y.; Li, F.; Jiang, Y.; Xia, M.; Xue, B.; Li, Y. Interface actions between TiO_2 and porous diatomite on the structure and photocatalytic activity of TiO2-diatomite. *Appl. Surf. Sci.* **2014**, *303*, 290–296. [CrossRef]
30. Turner, N.H. X-Ray Photoelectron and auger electron spectroscopy. *Appl. Spectrosc. Rev.* **2000**, *35*, 203–254. [CrossRef]
31. Hsieh, P.-T.; Chen, Y.-C.; Kao, K.-S.; Wang, C.-M. Luminescence mechanism of ZnO thin film investigated by XPS measurement. *Appl. Phys. A* **2008**, *90*, 317–321. [CrossRef]
32. Jaramillo-Páez, C.; Navío, J.A.; Hidalgo, M.C.; Macías, M. High UV-photocatalytic activity of ZnO and Ag/ZnO synthesized by a facile method. *Catal. Today* **2016**, *284*, 121–128. [CrossRef]
33. Li, Y.; Yu, L.; Li, N.; Yan, W.; Li, X. Heterostructures of Ag_3PO_4/TiO_2 mesoporous spheres with highly efficient visible light photocatalytic activity. *J. Colloid Interface Sci.* **2015**, *450*, 246–253. [CrossRef] [PubMed]
34. Zhao, Z.; Wang, Y.; Xu, J.; Shang, C.; Wang, Y. AgCl-loaded mesoporous anatase TiO_2 with large specific surface area for enhancing photocatalysis. *Appl. Surf. Sci.* **2015**, *351*, 416–424. [CrossRef]
35. Xiaodong, C.; ZhongTao, Y.; Nannan, W.; Xin, G.; Gang, W.; Chunyu, S.; Yunfeng, L.; Lifeng, C. Fabrication of Ag/ZnO hollow nanospheres and cubic TiO_2/ZnO heterojunction photocatalysts for RhB degradation. *Nanotechnol. Rev.* **2021**, *10*, 1349–1358.
36. Mousa, H.M.; Fares, A.J.; Mohamed, I.M.A.; Yasin, A.S.; Hashem, A.-F.M.; Abdal-hay, A. Synthesis of TiO_2@ZnO heterojunction for dye photodegradation and wastewater treatment. *J. Alloys Compd.* **2021**, *886*, 161169. [CrossRef]
37. Gayathri, M.N.; Liya, G.; Tatiparti, S.S.V.; Suparna, M. Efficacy and reusability of mixed-phase TiO_2–ZnO nanocomposites for the removal of estrogenic effects of 17β-Estradiol and 17α-Ethinylestradiol from water. *J. Environ. Manag.* **2021**, *288*, 112340.

materials

MDPI

Article

Development of Flotation Device for Removing Unburnt Carbon in Fly Ash for Use in Hardened Cementitious Materials

Hangwei Lin, Koji Takasu *, Hidehiro Koyamada and Hiroki Suyama

Department of Architecture, Faculty of Environmental Engineering, The University of Kitakyushu, Kitakyushu 808-0135, Japan; a9dbb419@eng.kitakyu-u.ac.jp (H.L.); h-koyamada@kitakyu-u.ac.jp (H.K.); suyama@kitakyu-u.ac.jp (H.S.)

* Correspondence: takasu@kitakyu-u.ac.jp; Tel.: +80-093-695-3239

Abstract: The unburned carbon in fly ash inhibits the performance of concrete. A device using the flotation method to remove unburned carbon in fly ash was developed, and the operating condition of the device was experimentally examined. According to the results, the device was able to remove unburnt carbon from fly ash by using the installed micro bubble nozzles and a whirl-type pump. The removal efficiency of unburnt carbon improved when prior forced stirring was carried out by a concrete mixer for 3 min, and a scavenger was added into the fly ash slurry at a density of about 60 wt%. It has also been confirmed that the method of circulating water is more effective than the method of not circulating water. The elements of the modified fly ash slurry (MFAS) have also been experimentally confirmed as not being too different from untreated fly ash, except for the fact that the content of unburned carbon is reduced. The compressive strength and drying shrinkage characteristics of concrete made with MFAS were investigated. The use of MFAS will reduce the performance of concrete compared to that of ordinary concrete. This shows that in a certain range (15–30%), the influence of MFAS on drying shrinkage is constant. The static elastic modulus and dynamic elastic modulus were also investigated. The above results show that the application of MFAS prepared by the flotation method to concrete is feasible.

Keywords: flotation; fly ash; concrete; unburnt carbon

Citation: Lin, H.; Takasu, K.; Koyamada, H.; Suyama, H. Development of Flotation Device for Removing Unburnt Carbon in Fly Ash for Use in Hardened Cementitious Materials. *Materials* **2021**, *14*, 6517. https://doi.org/10.3390/ma14216517

Academic Editors: Marco Race, Elza Bontempi, Avelino Núñez Delgado, Zhien Zhang, Mario Coccia and Yaoyu Zhou

Received: 17 September 2021
Accepted: 25 October 2021
Published: 29 October 2021

1. Introduction

In Japan, the power supply includes renewable [1], thermal [2], and nuclear energy [3]; however, global environmental issues and the recent power supply situation mean that renewable energy is expected to expand substantially. Nevertheless, increasing the proportion of renewable energy in the energy mix will take time, and thermal power generation will still be required.

Coal-fired power generation has the second-highest utilization rate worldwide after liquefied natural gas power generation, but the treatment of the coal ash generated is a major problem. Fly ash is the fine residue generated by the combustion of ground or powdered coal and is transported through flue gasses. Global fly ash production is estimated to be 400–500 million tons per year and the utilization rate in cement and concrete components is about 30% [4,5]. The total amount of coal ash generated by Japan's electric power industry and general industry exceeded 10 million tons and 97.4% of the coal ash was used, and 96.3% of the total was used in the cement industry as a raw material.

The properties of recycled aggregate concrete (RAC) cause major problems globally and improving the properties of RAC is expected to increase the use of RAC in structures. Recycled aggregates generally increase the water absorption and drying shrinkage and reduce the modulus of elasticity, workability and compressive strength of RAC compared with concrete containing natural aggregate [6]. However, fly ash has a shrinkage-reducing effect on both ordinary concrete and RAC and can mitigate the increase in shrinkage caused by recycled aggregates [7]. For concrete with a water:cement ratio of 0.55, the dry shrinkage

of concrete prepared with 0%, 20%, 50%, and 100% recycled aggregate is reduced by 14%, 13%, 10%, and 7%, respectively [8]. When 35 wt% of cement is replaced with fly ash, the shrinkage strain of all types of concrete is decreased by 55×10^{-6} on average, and the shrinkage strain of concrete without fly ash is 15–20% higher than that with fly ash at an age of 112 days [9]. Using fly ash as an alternative to cement or as an additive that can improve the durability and workability of the concrete is the recommended approach and helps to protect the environment and reduce water consumption. The strength of concrete in which a percentage of cement is replaced by fly ash is lower at an early age, although its strength is higher than or similar to concrete without fly ash later on [10–12]. In general, concrete containing fly ash as an additive or to replace cement has improved durability. The higher compressive strength of concretes containing fly ash is related to the improved bonding between aggregates and slurry and the denser microstructure obtained by changing the pore size distribution [13].

Fly ash is classified into types I to IV according to Japanese Industrial Standard (JIS), and the quality of fly ash must be considered when it is used as an admixture for concrete. According to the Architectural Institute of Japan, type I or JASS5M-401 [14] fly ash is suitable for replacing cement, and types II or IV are suitable for replacing a proportion of fine aggregate. In other words, fly ash used as an admixture for concrete requires a loss on ignition (LOI) of 5.0% or less. This is because fly ash with an unburned carbon content of 5.0% or more may cause poor coagulation of cement, and that with an unburned carbon content of 3.0% or more, adsorbs admixtures and decreases the fluidity and workability of concrete, which prevents entrainment and adversely affects the concrete's quality [15].

Some fly ash discharged from coal-fired power plants has a LOI of more than 5.0%, but other qualities mainly conform to JIS standard. Even for fly ash with a LOI of less than 5.0%, the smaller the amount of unburned carbon, the smaller the effect on the fresh properties of concrete. Therefore, methods of separating unburned carbon from fly ash will help increase the use of fly ash as an admixture for concrete and the reuse of the fine unburned carbon, achieving more efficient use of waste fly ash and greater economic and environmental benefits compared with landfill disposal or storage. Methods for separating unburned carbon particles from fly ash and the effect of the method on the unburned carbon properties have been investigated.

In general, high-carbon fly ash can be beneficiated using dry and wet separation processes, such as froth flotation, electrostatic separation, fluidized bed reactors, oil agglomeration, density separation, and sieving [16–19]. Each separation method has disadvantages and advantages and can be adapted for different types of coal fly ash. For improved separation efficiency and higher purities of unburned carbon, a combination of several techniques is typically needed. For example, Bittner et al. [20] developed a processing system based on triboelectric charging and electrostatic separation, and Parallel and louvered plate separators were used for the beneficiation of fine coal fly ash particles by Soong et al. [21].

The flotation method is a conventional technique that is mainly used for coal beneficiation, ore beneficiation, and the deinking of used paper [22,23]. Hydrophobic particles are attached to the surface of bubbles and floated in the water, allowing for hydrophilic particles to be collected from the bottom. To improve the separation, a foaming agent and a collecting agent that improves particle adhesion to bubbles are often added [24,25]. Froth flotation is widely used in mineral processing and coal preparation industry [26]. The traditional Denver flotation cell has been used for the separation of unburned carbon in laboratory scale fly ash [16]. The existence of a large number of pores increases the consumption of diesel. During the adjustment process, the amount of diesel and the speed of the impeller have the greatest impact on the carbon recovery rate. Altun et al. [27] used a concurrent flotation column. Unburned carbon was separated from fly ash, and the effects of gas flow, pH value, the amount of collected kerosene and different types of fly ash on the separation performance were investigated. It was concluded that column flotation was an effective method. Li et al. [28] developed a flotation method, which is a novel device

with the characteristics of an internal recycling process and multiple mineralization steps. Uçurum et al. [29] found that in trials of a flotation method, unburned carbon was removed from the fly ash, but they did not determine the effectiveness of the removal effect. With the technique disclosed in past research, since separation cannot be performed efficiently, treatment requires a long time period, thus preventing sufficient productivity from being obtained and the floatation machine then becomes complicated and large, requiring extremely large installation space and a high facility cost. It is therefore impossible for small to medium fresh concrete factories to install such facilities.

In floating ore and coal beneficiation equipment, air bubbles are discharged from the bottom of a cylindrical container by an air diffuser and push the carbon over the top of the container. To use this equipment to remove unburned carbon from fly ash, the following factors must be studied: the effect of the bubble size; the methods for recovering fly ash from which the unburned carbon has been removed and for recovering the fly ash containing a large amount of unburned carbon; the method of recovering the fly ash from the fly ash slurry; the stirring method; the operating conditions of the device; and the types of device that can remove unburned carbon efficiently.

In this research, we prototyped an unburned carbon removal device for separating unburned carbon from fly ash by the flotation method. The first objective is to provide a floatation separation apparatus in a simple structure capable of efficiently separating materials to be treated, and the second objective is to provide a simple floatation separation method for efficiently separating unburnt carbon contained in fly ash. The third objective is to provide a simple manufacturing method for efficiently manufacturing a cement mixture using high-quality fly ash with a reduced unburnt carbon content. We investigated the size of bubbles suitable for removal and the operating conditions. We measured the effect of the conditions on the carbon removal and optimized the device design. Since the unburnt carbon content of the fly ash slurry thus obtained was decreased sufficiently, unburnt carbon-related problems hardly occur, even if a large amount is used, and whether such fly ash slurry can be used as various raw materials in large amounts is worthy of investigation. Therefore, the mechanical and physical properties of concrete containing 15% or 30% fly ash and modified fly ash slurry (MFAS) with unburned carbon removed with our device were measured.

2. Materials and Methods

2.1. Flotation Method Experiment

In the initial experiment, we examined the effects of the bubble diameter and the conditions on the unburned carbon removal to develop a base model of an unburned coal removal device, and the experiments described later were carried out step-by-step from devices I to III.

Table 1 shows the physical characteristics of the fly ash, which was generated from two thermal power plants. Fly ash a-2, a-3, a-5, and a-6 corresponded to JIS A 6201 [30] type II; a-4, b-1, b-2, and b-3 corresponded to type III; a-1 corresponded to type IV; and b-4 did not correspond to a defined type due to its high LOI.

Table 1. Physical characteristics of fly ash.

Fly Ash	LOI (%)	Density (g/cm^3)	Specific Surface Area (cm^2/g)
a-1	0.72	2.30	1510
a-2	0.42	2.27	2970
a-3	1.30	2.29	2790
a-4	6.99	2.30	4640
a-5	3.86	2.24	4250
a-6	2.22	2.25	4200
b-a	5.87	2.12	4590
b-2	7.39	2.27	4890
b-3	7.85	2.37	4620
b-4	12.92	2.24	4890
c	7.25	2.3	5560
d	9.85	2.11	6060
e	2.81	2.11	3470
f	3.36	2.26	3280

Experiment I was performed to examine the effect of bubble diameter. In device I, which had a capacity of 80 L, fly ashes from the 'a' series were used, and two general-purpose air diffusers Ø 70 mm × L200 mm in size were attached to the flotation device near the bottom (Figure 1 is based on the equipment used for coal flotation). The air was agitated at a rotation speed of 19 rpm, and the amount of air discharged from the air diffuser was 165 L/min. The most frequent bubble diameter was about 200 μm. The foaming agent was 0.3% pine oil and the unburned carbon collector was 5.0% kerosene. The device floated fly ash containing a large amount of unburned carbon near the water surface through aeration with the air diffuser, and then the floating material (foam ash) was removed and the fly ash that settled on the bottom after standing (tail ash) was collected. The experiment was performed as follows. The additives and tap water were inserted into the device and stirred for 5 min, fly ash was added to make a 20 wt% fly ash slurry and was stirred for 5 min, and then the mixture was aerated for 10 min before the foam ash was recovered. The tail ash was collected from the bottom of the device and dried in an electric furnace at 105 °C for 24 h and its LOI was measured. The unburned carbon removal rates of the ash types were determined based on the LOI measured by JIS A6201 [30].

Figure 1. The flotation device of the air diffuser.

Experiment II examined the effect of the bubble diameter and used fly ashes from the 'b' series, which had a larger LOI than fly ashes from the 'a' series. In device II, the fly ash was put into a 2 L plastic container (Figure 2). To prevent precipitation, a small mixer with a rotation speed of 250 rpm was used for mixing, and a high-speed rotary blade microbubble generator was used. The mode of the microbubble diameter was about 40 μm. In addition, in device II, a 60 wt% fly ash slurry and the collector were pre-stirred in a 0.6 L high-speed mixer before flotation due to the significant improvement in the separation performance of unburned carbon from coal fly ash [31]. Pretreatment has great importance for the flotation method. The kinetic energy that is dissipated in the stirred tank

could strengthen the interaction process between mineral particles and flotation reagents to improve the flotation efficiency in the presence of preconditioning [32]. Yu et al. [33] found in the flotation of coal that high intensity agitation, greater than 1200 rpm, reduces the kaolinite coating, which will lead to a higher combustibles recovery rate. The collecting agent and tap water were placed in the mixer (rotation speed 10,000 rpm), stirred for 1 min, the foaming agent was added, and the slurry concentration was increased to 20 wt%. Then, the air rotation was started and the floss ash was collected for 10 min. The additive addition rates were the same as those for experiment I. The device was left to stand, the tail ash was collected from the bottom of the device and dried, and then the LOI was measured in the same way as in experiment I.

Figure 2. Microbubble generator.

Experiment III was conducted to collect data for designing the actual device used in the industry and confirming the effectiveness of preprocessing based on the results of device II. The same fly ash as for device II was used as the material. Device III consisted of a 5 L metal container (Figure 3) and the fly ash slurry was circulated by a roller pump with a built-in orifice microbubble generator to prevent the ash from settling without using a stirrer. The experimental procedure was the same as that of experiment II, but the results with and without pre-stirring were compared.

Figure 3. Microbubble circulation device.

2.2. Concrete Specimen Fabrication

Concrete specimens were fabricated using MFAS and type II fly ash. Ordinary Portland cement was used, with sea sand as a natural fine aggregate, and crushed stone was used as a coarse aggregate. The properties of raw ash and MFA were tested (Table 2). Fly ash was used to partially replace cement. The JIS R 5210 [34] and JIS A 6201 [30] standards were followed.

Table 2. Properties of FA and MFA.

Type	MFA	Raw Ash
LOI (%)	1.75	13
Density (g/cm^3)	2.33	2.32
Blaine (cm^2/g)	3220	4830

The mixture proportions are shown in Table 3. The fine aggregate, cement, and fly ash were mixed for 30 s, water was added and mixed for 60 s, and coarse aggregate was added and mixed for 60 s.

Table 3. Mix proportion.

Type	W/C (%)	W/B (%)	Unit (kg/m^3)						
			W	C	FA	MFA	S	G	RG
C0F0F0	55	55	180	327	-	0	857	945	-
C0F0F15	65	55		278	49		840	945	-
C0F0F30	79	55		229	98		824	945	-
C0F0M15	65	55		278	-	49	842	945	-
C0F0M30	79	55		229	-	98	828	945	-
C100F0M15	65	55		278	-	49	842	-	885
C100F0M30	79	55		229	-	98	828	-	885

2.3. Concrete Specimen Tests

The compressive strength test was conducted using cylindrical specimens (Ø = 100 mm, h = 200 mm) according to JIS A 1108 [35]. For each mix, 12 cylinders were cast in a mold and kept in a chamber at 20 °C and 60% relative humidity for 24 h, after which they were demolded. The ages of the tested specimens were 1, 4, and 13 weeks. In addition, a specimen was tested immediately after the curing was complete. The load was applied at a uniform rate to avoid subjecting the specimen to impact loading; the loading rate was such that the compressive stress increased by 0.6 ± 0.4 N/mm^2 per second. During each test, the static elastic modulus specimens stored at the temperature and humidity specified for the test were tested (JIS A 1149 [36]).

The drying shrinkage test was conducted using a cuboid ($100 \times 100 \times 400$ mm^3) according to JIS A 1129-3 [37]. For each mix, three cuboids were cast in a steel mold and kept in a chamber at 20 °C and 60% relative humidity for 24 h until demolded. After demolding, the concrete specimens were immersed in water at 20 ± 2 °C and cured for 7 days. During the drying period, the specimens were kept at least 25 mm apart so as not to impede drying from the bottom of the specimen. Measurements were taken when a specimen was 7 days old, and this time was taken as the reference.

Dynamic elastic modulus tests were conducted using a cylinder or cuboid placed on a support base so that both ends could vibrate freely without being restrained. The output voltage of the amplified pickup was observed, and the frequency at which the indicator had a clear maximum vibration was defined as the primary resonance frequency of the longitudinal vibration according to JIS A 1127 [38].

3. Results and Discussion

3.1. Removal of Unburned Carbon by the Flotation Method

Figure 4 shows the LOI of untreated ash and tail ash for each device. When a diffuser tube was used in experiment I (Figure 4a), the LOI of the tail ash for all fly ash was slightly larger than that of the untreated ash in the range of this experiment, showing that the removal method had no effect. However, in experiment II (Figure 4b), the microbubble generator reduced the LOI and removed unburned carbon from the fly ash. In experiments I and II, it was not possible to compare samples from the same discharge source, but the decrease in LOI was due to the difference in equipment rather than the fly ash characteristics.

One reason for the larger LOI in experiment I was that the mode of the bubble diameter generated from the air diffuser was about 200 μm, which was about 10 times larger than that of the fly ash particles, and thus it was difficult to collect or raise the unburned carbon to the surface. In contrast, in experiment II, the mode of the microbubble diameter was 40 μm, which was about twice as large as that of the fly ash particles, allowing the unburned carbon to be efficiently collected and raised to the surface. Therefore, microbubbles were effective in removing unburned carbon in fly ash by the flotation method.

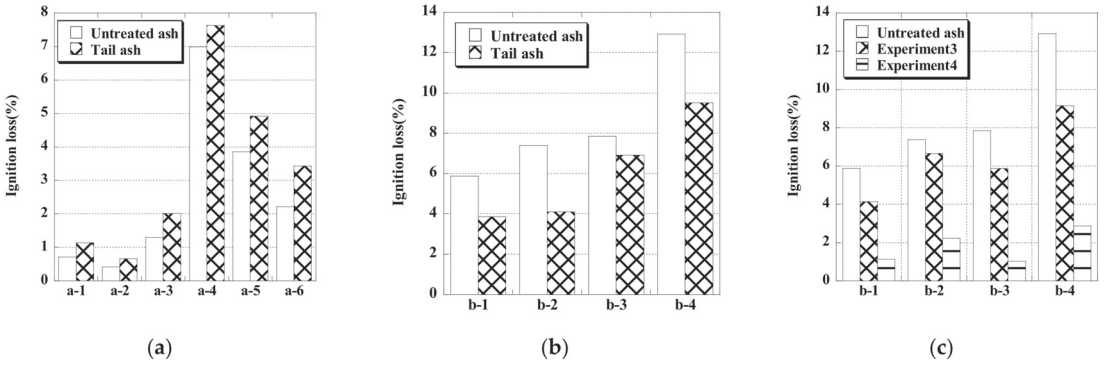

Figure 4. LOI of untreated ash and tail ash in experiment I (**a**), experiment II (**b**) and experiment III (**c**).

Next, we compare the results of experiment II, in which pre-stirring was performed, with those of experiment III. For fly ashes b-1 to b-4, the LOI was lower in experiment III than in experiment II. In particular, in experiment II, the LOI was reduced to 3.0% or less by using the circulating microbubble generator in device II, and the fly ash was modified to the equivalent of JIS type I. The circulating microbubble generator prevented the fly ash from settling without a stirrer, and the microbubbles were in uniform contact with the fly ash particles, and so the microbubbles enclosed the unburned carbon collected by the collector, which increased the effectiveness of the device. The effect of pre-stirring in the circulating microbubble generator was examined in experiment III. In the absence of pre-stirring, the LOIs of the tail ash of all types of fly ash were slightly lower than those of the untreated ash (Figure 4c). In contrast, when pre-stirring was performed, the LOIs of the tail ash were 3.0% or less for all types of fly ash, and the LOI could be decreased by up to 82%. Especially for fly ash b-4, the untreated ash did not correspond to a JIS type, but the tail ash had an LOI equivalent to JIS type I.

Figure 5 shows scanning electron microscope images of untreated ash and tail ash of b-1. Unburned carbon and other deposits were attached to the untreated fly ash particles, whereas the unburned carbon was physically removed from the surface of the tail ash particles. Pre-stirring most likely removed the unburned carbon from the fly ash particles and explained why pre-stirring decreased LOI substantially. Therefore, these results showed that for the flotation method using a microbubble generator, unburned carbon in the fly ash was effectively removed by pre-stirring using a mixer. The LOI of the foam ash was in the range of 55 to 70 wt%, indicating that it contained a large amount of unburned carbon and could be used as an auxiliary fuel after drying.

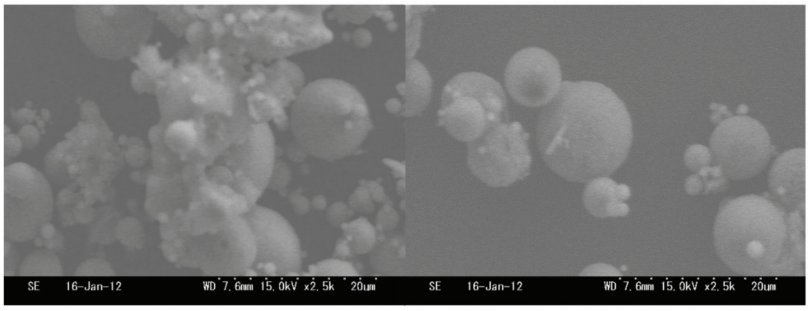

Figure 5. SEM images of raw ash and tail ash of b ash-1.

3.2. Base Model Development and Performance Verification

Based on the results of experiments I–III, we developed a base model of an unburned coal removal device that used the flotation method. Figure 6 shows the base model of the device, the spiral circulation pump, and the removal of foam ash. Figure 7 shows the draw of the base model of the device. The capacity of the device was 130 L. In experimental devices I–III, a roller pump was used to circulate the fly ash slurry, but in the base model, a spiral circulation pump with a higher circulation capacity was used. This type of pump can be used in an actual plant with a capacity of 10 m^3 or more. In the base model, the microbubble generator was placed eccentrically at the bottom of the side surface of the device to generate a vortex, and the top of the device was conical. This vortex attracts the foam ash to the center and causes the foam ash to flow from the upper part of the device so that it can be automatically discharged. The microbubble diameter was 40 μm, the pump output was 0.4 kW, the pump flow rate was 30 L/min, and the maximum air supply was 10 L/min. Compared with the traditional flotation technology, it does not need mechanical agitation and has the advantages of a more compact design and lower capital cost.

Figure 6. The medium unburned carbon removal device.

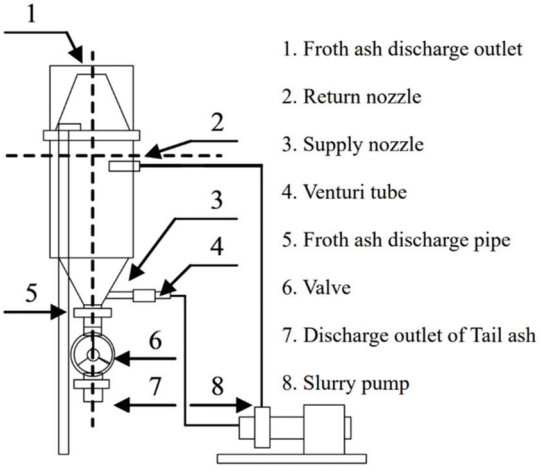

Figure 7. The draw of medium unburned carbon removal device.

Figure 8 shows the process of the flotation method using this device. The device is composed of the flotation tank, the circulating pump, and the microbubble generator. Fly ash, kerosene, and water are mixed as a prior process, and it is supplied to the flotation tank. The circulating pump is operated, and microbubbles are blown in from the lower side of the flotation tank. The froth ash that contains most of the unburned carbon accumulates and is expelled from the upper part of the flotation tank. The tail ash from which unburned carbon is removed accumulates below and is expelled from the lower side of the flotation tank.

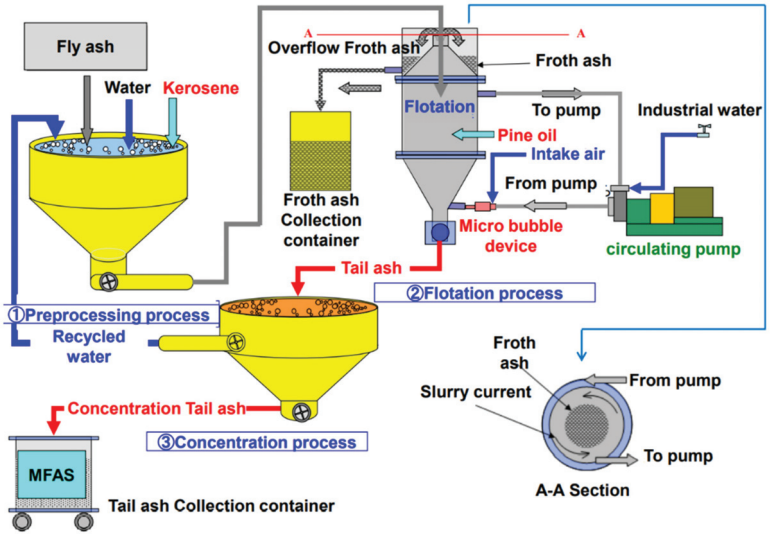

Figure 8. The flotation process of using medium unburned carbon removal device.

Fly ashes c and d generated from the two thermal power plants from Japan were used (Table 1). Fly ash c was equivalent to JIS type III, and fly ash d did not conform to JIS standards. The experimental procedure was the same as for experiment III with pre-stirring, but because the device capacity was 130 L and the number of input samples was large, pre-mixing was performed with a 50 L concrete mixer (MARUI & CO., LTD,

Daito, Japan) (speed 50 rpm) to eliminate the effect of the rotation speed caused by the insufficient capacity of the 0.6 L high-speed mixer. However, the rotation speed of the pre-stirring was 1/200th of that in experiment III. To make the total rotation speed of the mixer approximately the same as that in experiment III, the flotation beneficiation time was set to 30 min to consider the increased capacity of the device. The additive addition rate was the same as in experiment III.

Table 4 shows the physical characteristics of untreated ash and tail ash for fly ashes c and d. In all ashes, the LOI of the tail ash decreased to 3.0% or less compared with the untreated ash, the specific surface area decreased, and the density increased due to the removal of unburned carbon, which is porous and amorphous. Fly ash that is usable as various materials, preferably the fly ash with an unburnt carbon content as low as 5 wt%, and more preferably the fly ash with an unburnt carbon content as low as 3 wt%, can be obtained efficiently with a simple structure.

Table 4. Physical characteristics of untreated ash and tail ash.

Type		LOI (%)	Density (g/cm^3)	Specific Surface Area (cm^2/g)
C-ash	Untreated ash	7.25	2.30	5560
	Tail ash	2.31	2.31	4660
D-ash	Untreated ash	9.85	2.11	6060
	Tail ash	2.88	2.20	4520

Figure 9 shows the chemical composition of untreated ash and tail ash obtained by fluorescence X-ray analysis. The chemical composition was analyzed to measure the chemical effects of removing unburned carbon. Some components of the tail ash increased slightly when the LOI decreased, although none of the components changed substantially. Therefore, the unburned carbon removal device did not affect the chemical composition of the fly ash, other than removing the unburned carbon.

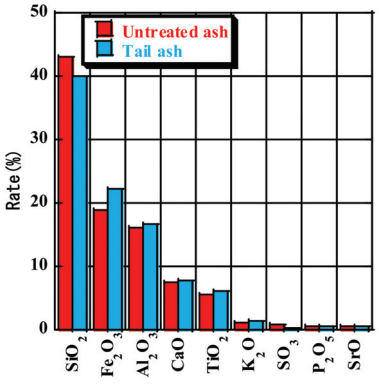

Figure 9. Chemical components of untreated ash and tail ash.

3.3. Treatment Conditions

Pre-stirring enhances the interaction between the collector and the fly ash. However, too much energy input from the stirring tank cannot improve the flotation efficiency. Flotation process factors of pre-stirring greatly affect the flotation capacity and efficiency. We examined the effect of the pre-stirring time, fly ash slurry concentration during flotation treatment, flotation processing time, and chemicals, and the optimum treatment conditions, such as the addition rate, in device III. Fly ash e was used in the tests (Table 1). Ash e was equivalent to JIS type II, but because the conditions strongly affect the removal of unburned

carbon, untreated ash with a low LOI was selected. First, the pre-stirring time and flotation processing time were examined. The concentration of the fly-ash slurry was set to 60%, and the slurry was pre-stirred using a concrete pan mixer (rotation speed 50 rpm). Then, the slurry concentration was adjusted to 6.6 wt%, and flotation was performed. The chemical addition rate was the same as for experiments I–III (collecting agent 5.0% and foaming agent 0.3% with respect to the fly ash mass). After determining the appropriate treatment time, the slurry concentration during the flotation treatment was changed to examine the treatment efficiency, and finally the chemical addition rate was changed. The microbubble diameter was 40 μm, the pump output was 0.4 kW, the pump flow rate was 30 L/min, and the maximum air supply was 10 L/min.

Figure 10a shows the LOI after 60 min of flotation treatment with 60 or 180 min of pre-stirring. The LOI was measured during the flotation treatment by sampling the tail ash from the tail ash outlet at 30 and 60 min without stopping the equipment. At 60 min, LOI was 0.12% lower for a pre-stirring time of 180 min; thus, the effect of the pre-stirring time on the reduction inLOI was small. After 30 min, there was a large reduction in LOI, and a smaller change after 60 min, which suggested that the flotation treatment time could be shortened to 30 min or less.

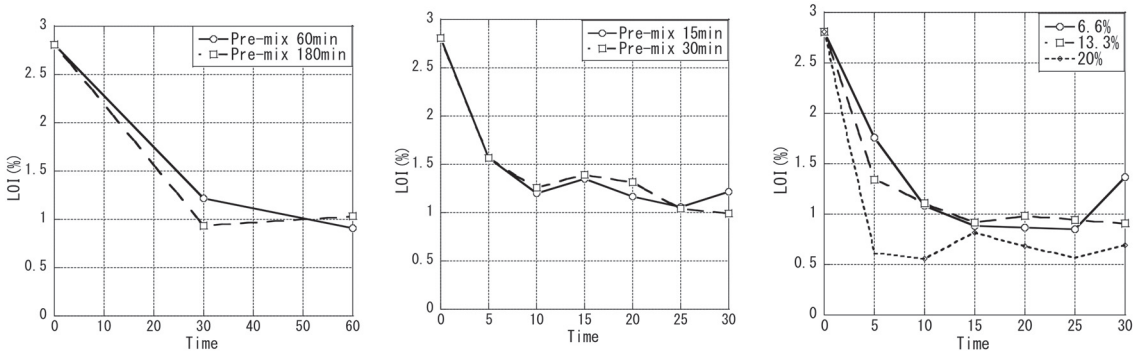

(**a**) (**b**) (**c**)

Figure 10. LOI of the flotation treatment with 60 or 180 min (**a**) and 15 or 30 min (**b**) pre-stirring, and at slurry concentrations of 6.6, 13.3, and 20.0 wt% (**c**).

Figure 10b shows the time course of the tail ash LOI sampled every 5 min up to a flotation time of 30 min with a pre-stirring time of 15 or 30 min. LOI was greatly reduced within 10 min. Because decreasing the pre-stirring time from 60 min to 15 min reduced the LOI, and there was almost no difference in LOI between pre-stirring times of 15 and 30 min, in the subsequent experiments the pre-stirring time and flotation treatment time were each set to 30 min for safety considerations.

In the flotation treatment, the efficiency of one treatment increased when the fly ash slurry concentration was increased. Therefore, we investigated the change over time in LOI at slurry concentrations of 6.6, 13.3, and 20.0 wt% (Figure 10c). At all fly ash slurry concentrations, the reduction in LOI was large within 10 min, and the smallest reduction was for a fly ash slurry concentration of 20.0 wt%. A preliminary experiment with a slurry concentration of 25.0 wt% showed that the reduction rate of LOI was lower than that at 20.0 wt% (data not shown). Therefore, the floating beneficiation method was efficient at a slurry concentration of 20.0 wt%.

The addition rates of the collecting agent and foaming agent were examined because they affect the processing cost. Flotation treatment was performed under a total of nine conditions at different mixing ratios. Here, we set the fly ash slurry concentration to 6.6 wt%. Figure 11 shows the relationship between the additive cost ratio and LOI under

each condition, where the additive cost for treatment with 5.0% collecting agent and 0.3% foaming agent is 1.0. The additive cost is the unit price when 18 L of the collecting agent and 18 L of the foaming agent are purchased as laboratory chemicals, and the LOI was measured after 30 min treatment by the flotation method. Assuming that the LOI control value was 1.0% or less, the best mixing ratio was 3.0% for the collecting agent and 0.2% for the foaming agent, which was a reduction of about 40% for the collector and about 33% for the foaming agent compared with the initial conditions. However, because the additive addition rate depends on the control value of LOI, the rate must be set at the operation stage, and the optimum mixing ratio can be determined by conducting the same experiment. In addition, the results show that the removal of unburned carbon was high for a ratio of 3.0% for the collecting agent and 0.3% for the foaming agent. The unburned carbon removal did not increase with the collection agent addition rate, whereas it did increase with the foaming agent addition rate. It is considered that there may be an optimum addition rate. Furthermore, the optimum additive addition rate is expected to depend on the type of fly ash and thus requires further study.

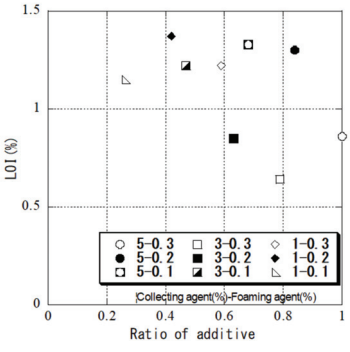

Figure 11. Relationship between the agent ratio and LOI under each condition.

3.4. Properties of Concrete with MFAS

The mechanical and physical properties of concrete with fly ash replacement ratios of 15% and 30% and different amounts of MFAS were measured.

Figure 12a shows the compressive strength of concrete containing recycled aggregate and fly ash or modified fly ash at 7–91 days. Using fly ash reduced the compressive strength of concrete at 7–91 days, and a 30% replacement ratio decreased the compressive strength with more than a 15% replacement ratio. For a replacement ratio of 15%, although the strength for modified fly ash concrete was lower than that for normal fly ash concrete, the modified fly ash concrete strength increased faster. At 7, 28, and 91 days, the strengths of F15 (15% fly ash) were 81.1%, 84.7%, and 97.5%, whereas the strengths of M15 (15% modified fly ash concrete) were 71.2%, 79.1%, and 92.5%, respectively. For the replacement ratio of 30%, the growth rate of the strength of fly ash and modified fly ash concrete was the same. At 7, 28, and 91 days, the strengths of F30 (30% fly ash) were 60.7%, 72.5%, and 86.6%, whereas the strengths of M30 (30% modified fly ash concrete) were 60.0%, 68.5%, and 82.5%, respectively.

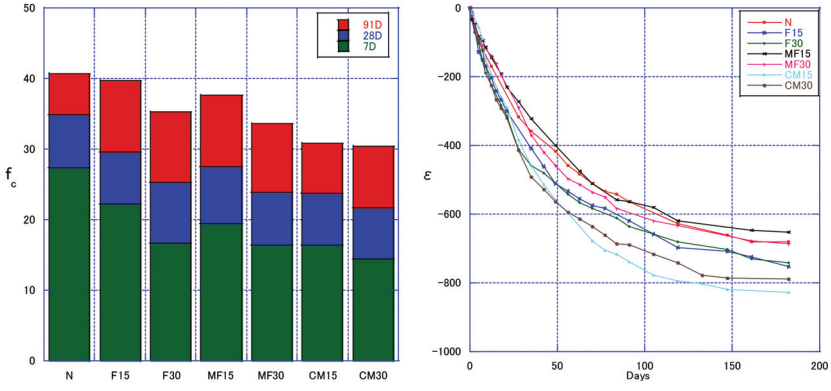

(**a**) (**b**)

Figure 12. Compressive strength (**a**) and drying shrinkage (**b**) of concrete with modified fly ash slurry.

The use of MFA had little effect on the strength of concrete. This is because the chemical characteristics of fly ash have a large effect on pozzolanic reactivity [39], and as discussed above, the flotation does not change the chemical characteristics of FA. Adding 30% of MFA or FA had a greater impact on the strength of concrete, increasing it by more than 15%. However, for recycled concrete, the two different mixing amounts of MFA or FA showed a very minor difference in strength. In words, the impact on the strength of recycled concrete was very minor.

Figure 12b shows the drying shrinkage of concrete specimens containing recycled aggregate and fly ash or modified fly ash up to 118 days—see the F15 line and F30 line in the figure, which are both below the red line. Fly ash increased the drying shrinkage of concrete compared with the control. The distance between these two lines is small. At fly ash replacement ratios of 15–30%, the replacement ratio did not affect the drying shrinkage—see the C100M15 line and C100M30 line, which are both below the red line. The distance between these two lines is small. At fly ash replacement ratios of 15–30%, and a recycled aggregate replacement ratio of 100%, the fly ash replacement ratio did not affect the drying shrinkage. The distance between the two lines is small. This suggests that within a certain range (15–30%), for non-mixed aggregates, the influence of fly ash on drying shrinkage is constant. Therefore, the carbon content of FA is different, and the effect on the drying shrinkage of concrete is different. However, the amount of FA mixed does not have a huge impact on the drying shrinkage.

Figure 13 shows the static elastic modulus and dynamic elastic modulus of concrete containing MFAS. The measurement of the static elastic modulus destroys the concrete test block, whereas the measurement of the dynamic elastic modulus does not; thus, measuring the dynamic elastic modulus is more convenient. Both measure the same characteristic of concrete, and thus showed consistent results. The effect of fly ash content on both moduli decreased as the fly ash content increased. The trend of the elastic modulus is consistent with the performance of the concrete's compressive strength, indicating that there is a certain correlation between the static elastic modulus and the compressive strength, and the trend of the dynamic elastic modulus is also consistent, meaning that when predicting the compressive strength of concrete, the dynamic elasticity modulus can also be used as an important factor, and is not limited to ordinary concrete. For example, when Farooq et al. [40] predicted self-compacting concrete, the dynamic elastic modulus was considered as a factor.

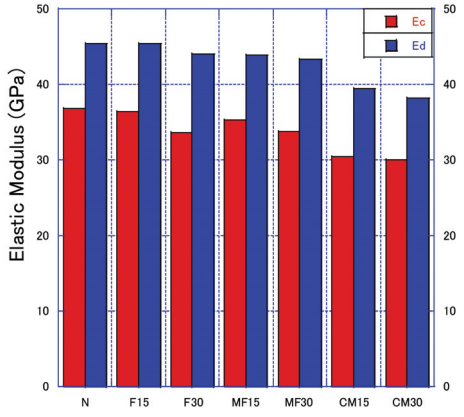

Figure 13. Static and Dynamic elastic Modulus.

4. Conclusions

We developed a prototype device for removing unburned carbon from fly ash by means of the flotation method and examined the operating conditions of the device experimentally. The fly ash was used in Portland cement concrete and the concrete properties were measured. Our findings are summarized as follows.

The base model, which used a circulating microbubble generator with a spiral pump, removed unburned carbon from fly ash by means of the froth flotation method without affecting the chemical composition of the fly ash. The removal efficiency was increased by adding a collecting agent to 60 wt% fly ash slurry and pre-stirring with a concrete mixer for 30 min. The LOI was greatly reduced within 10 min, and a treatment time of 30 min was sufficient. Flotation was improved by pre-stirring the sample and adding water to form a slurry with a concentration of 20 wt%.

MFAS was used in the mortar, and its properties were better than those of dry fly ash. MFAS reduced the compressive strength of concrete at 7–91 days. The drying shrinkage of concrete containing fly ash was greater than that of ordinary concrete; however, at fly ash replacement ratios of 15–30%, the replacement ratio did not affect the drying shrinkage.

Our results demonstrate that it is feasible to use modified fly ash prepared using the flotation method in concrete.

Author Contributions: Conceptualization, H.L. and K.T.; methodology, H.L.; validation, K.T., H.K. and H.S.; formal analysis, H.L.; investigation, H.L. and K.T.; resources, K.T., H.K. and H.S.; data curation, H.L.; writing—original draft preparation, H.L.; writing—review and editing, H.L.; visualization, H.L.; supervision, K.T.; project administration, K.T.; funding acquisition, K.T. All authors have read and agreed to the published version of the manuscript.

Funding: The research was funded by the fund of Environmental Restoration and Conservation Agency (JPMEERF20213G03) and Japan Society for the Promotion of Science KAKENHI (20H02300).

Institutional Review Board Statement: Not applicable.

Informed Consent Statement: Not applicable.

Data Availability Statement: The data presented in this study are available on request from the corresponding author. The data are not publicly available due to privacy restrictions.

Acknowledgments: The authors acknowledge the assistance in this work provided by Eiji Mikura.

Conflicts of Interest: The authors declare no conflict of interest.

References

1. Furubayashi, T. Design and analysis of a 100% renewable energy system for Akita prefecture, Japan. *Smart Energy* **2021**, *2*, 100012. [CrossRef]
2. Matsumoto, K.I. Economic Analysis of Introducing Renewable Energy in a Remote Island: A Case Study of Tsushima Island, Japan. 2021. Available online: https://ssrn.com/abstract=3880819 (accessed on 3 September 2021).
3. Kikuchi, M. Changing dynamics of the nuclear energy policy-making process in Japan. *Environ. Policy Gov.* **2020**, *31*, 116–124. [CrossRef]
4. Gollakota, A.R.; Volli, V.; Shu, C.-M. Progressive utilisation prospects of coal fly ash: A review. *Sci. Total. Environ.* **2019**, *672*, 951–989. [CrossRef] [PubMed]
5. Sancho, I.; Licon, E.; Valderrama, C.; de Arespacochaga, N.; López-Palau, S.; Cortina, J.L. Recovery of ammonia from domestic wastewater effluents as liquid fertilizers by integration of natural zeolites and hollow fibre membrane contactors. *Sci. Total. Environ.* **2017**, *584-585*, 244–251. [CrossRef] [PubMed]
6. Xiao, J.; Li, W.; Poon, C.S. Recent studies on mechanical properties of recycled aggregate concrete in China—A review. *Sci. China Ser. E Technol. Sci.* **2012**, *55*, 1463–1480. [CrossRef]
7. Guo, H.; Shi, C.; Guan, X.; Zhu, J.; Ding, Y.; Ling, T.-C.; Zhang, H.; Wang, Y. Durability of recycled aggregate concrete—A review. *Cem. Concr. Compos.* **2018**, *89*, 251–259. [CrossRef]
8. Kou, S.C.; Poon, C.S.; Chan, D. Influence of fly ash as a cement addition on the hardened properties of recycled aggregate concrete. *Mater. Struct.* **2007**, *41*, 1191–1201. [CrossRef]
9. Kou, S.C.; Poon, C.S.; Chan, D. Influence of fly ash as cement replacement on the properties of recycled aggregate concrete. *J. Mater. Civ. Eng.* **2007**, *19*, 709–717. [CrossRef]
10. Katar, I.; Ibrahim, Y.; Malik, M.A.; Khahro, S. Mechanical Properties of Concrete with Recycled Concrete Aggregate and Fly Ash. *Recycling* **2021**, *6*, 23. [CrossRef]
11. Shariati, M.; Mafipour, M.S.; Mehrabi, P.; Ahmadi, M.; Wakil, K.; Trung, N.T.; Toghroli, A.J.S.S. Systems, Prediction of concrete strength in presence of furnace slag and fly ash using Hybrid ANN-GA (Artificial Neural Network-Genetic Algorithm). *Smart Struct. Syst.* **2020**, *25*, 183–195. [CrossRef]
12. Oner, A.; Akyuz, S.; Yildiz, R. An experimental study on strength development of concrete containing fly ash and optimum usage of fly ash in concrete. *Cem. Concr. Res.* **2005**, *35*, 1165–1171. [CrossRef]
13. Wang, Q.; Wang, D.; Chen, H. The role of fly ash microsphere in the microstructure and macroscopic properties of high-strength concrete. *Cem. Concr. Compos.* **2017**, *83*, 125–137. [CrossRef]
14. Architectural Institute of Japan. *Japanese Architectural Standard Specification JASS 5 Reinforced Concrete Work*; Architectural Institute of Japan: Tokyo, Japan, 2009; p. 187, 672.
15. Feng, X.; Clark, B. In Evaluation of the physical and chemical properties of fly ash products for use in Portland cement concrete. In Proceedings of the World of Coal Ash (WOCA) Conference, Denver, CO, USA, 9–12 May 2011; pp. 1–8.
16. Zhang, W.; Honaker, R. Studies on carbon flotation from fly ash. *Fuel Process. Technol.* **2015**, *139*, 236–241. [CrossRef]
17. Yang, L.; Zhu, Z.; Li, D.; Yan, X.; Zhang, H. Effects of particle size on the flotation behavior of coal fly ash. *Waste Manag.* **2019**, *85*, 490–497. [CrossRef] [PubMed]
18. Walker, A.; Wheelock, T.D. Separation of Carbon from Fly Ash Using Froth Flotation. *Coal Prep.* **2006**, *26*, 235–250. [CrossRef]
19. Temuujin, J.; Surenjav, E.; Ruescher, C.H.; Vahlbruch, J.J.C. Processing and uses of fly ash addressing radioactivity (critical review). *Chemosphere* **2019**, *216*, 866–882. [CrossRef]
20. Bittner, J.; Hrach, F.; Gasiorowski, S.; Canellopoulus, L.; Guicherd, H. Triboelectric belt separator for beneficiation of fine minerals. *Procedia Eng.* **2014**, *83*, 122–129. [CrossRef]
21. Soong, Y.; Schoffstall, M.; Link, T. Triboelectrostatic beneficiation of fly ash. *Fuel* **2001**, *80*, 879–884. [CrossRef]
22. Ejtemaei, M.; Gharabaghi, M.; Irannajad, M. A review of zinc oxide mineral beneficiation using flotation method. *Adv. Colloid Interface Sci.* **2014**, *206*, 68–78. [CrossRef] [PubMed]
23. Ayhan, F.D.; Abakay, A.H.; Saydut, A. Desulfurization and Deashing of Hazro Coal via a Flotation Method. *Energy Fuels* **2005**, *19*, 1003–1007. [CrossRef]
24. Yang, L.; Li, D.; Zhang, L.; Yan, X.; Ran, J.; Wang, Y.; Zhang, H. On the utilization of waste fried oil as flotation collector to remove carbon from coal fly ash. *Waste Manag.* **2020**, *113*, 62–69. [CrossRef]
25. Drzymala, J.; Gorke, J.T.; Wheelock, T.D. A flotation collector for the separation of unburned carbon from fly ash. *Coal Prep.* **2005**, *25*, 67–80. [CrossRef]
26. Xia, Y.; Yang, Z.; Zhang, R.; Xing, Y.; Gui, X. Enhancement of the surface hydrophobicity of low-rank coal by adsorbing DTAB: An experimental and molecular dynamics simulation study. *Fuel* **2018**, *239*, 145–152. [CrossRef]
27. Altun, N.E.; Xiao, C.; Hwang, J.-Y. Separation of unburned carbon from fly ash using a concurrent flotation column. *Fuel Process. Technol.* **2009**, *90*, 1464–1470. [CrossRef]
28. Li, G.; Deng, L.; Liu, J.; Cao, Y.; Zhang, H.; Ran, J. A new technique for removing unburned carbon from coal fly ash at an industrial scale. *Int. J. Coal Prep. Util.* **2014**, *35*, 273–279. [CrossRef]
29. Uçurum, M. Influences of Jameson flotation operation variables on the kinetics and recovery of unburned carbon. *Powder Technol.* **2009**, *191*, 240–246. [CrossRef]

30. JIS A 6201, 2015. Fly Ash for Use in Concrete. Japanese Industrial Standard Committee, Japan. 2015. Available online: www.jisc.go.jp (accessed on 15 July 2021).
31. Yang, L.; Li, D.; Zhu, Z.; Xu, M.; Yan, X.; Zhang, H. Effect of the intensification of preconditioning on the separation of unburned carbon from coal fly ash. *Fuel* **2019**, *242*, 174–183. [CrossRef]
32. Yang, L.; Zhu, Z.; Qi, X.; Yan, X.; Zhang, H. The process of the intensification of coal fly ash flotation using a stirred tank. *Minerals* **2018**, *8*, 597. [CrossRef]
33. Yu, Y.; Cheng, G.; Ma, L.; Huang, G.; Wu, L.; Xu, H. Effect of agitation on the interaction of coal and kaolinite in flotation. *Powder Technol.* **2017**, *313*, 122–128. [CrossRef]
34. JIS R 5201, 2015. Physical Testing Methods for Cement. Japanese Industrial Standard Committee, Japan. 2015. Available online: www.jisc.go.jp (accessed on 21 July 2021).
35. JIS A 1108, 2018. Method of Test for Compressive Strength of Concrete. Japanese Industrial Standard Committee, Japan. 2018. Available online: www.jisc.go.jp (accessed on 28 July 2021).
36. JIS A 1149, 2017. Method of Test for Static Modulus of Elasticity of Concrete. Japanese Industrial Standard Committee, Japan. 2017. Available online: www.jisc.go.jp (accessed on 1 August 2021).
37. JIS A 1129-3, 2010. Methods of Measurement for Length Change of Mortar and Concrete−Part 3: Method with Dial Gauge. Japanese Industrial Standard Committee, Japan. 2010. Available online: www.jisc.go.jp (accessed on 3 August 2021).
38. JIS A 1127, 2010. Methods of Test for Dynamic Modulus of Elasticity, Rigidity and Poisson's Ratio of Concrete by Resonance Vibration. Japanese Industrial Standard Committee, Japan. 2010. Available online: www.jisc.go.jp (accessed on 6 August 2021).
39. Cho, Y.K.; Jung, S.H.; Choi, Y.C. Effects of chemical composition of fly ash on compressive strength of fly ash cement mortar. *Constr. Build. Mater.* **2019**, *204*, 255–264. [CrossRef]
40. Farooq, F.; Czarnecki, S.; Niewiadomski, P.; Aslam, F.; Alabduljabbar, H.; Ostrowski, K.A.; Śliwa-Wieczorek, K.; Nowobilski, T.; Malazdrewicz, S. A Comparative Study for the Prediction of the Compressive Strength of Self-Compacting Concrete Modified with Fly Ash. *Materials* **2021**, *14*, 4934. [CrossRef] [PubMed]

sustainability

MDPI

Review

Removal of Toxic Heavy Metals from Contaminated Aqueous Solutions Using Seaweeds: A Review

Edward Hingha Foday Jr [1,2,3], Bai Bo [1,2,4,5,*] and Xiaohui Xu [1,2]

[1] Key Laboratory of Subsurface Hydrology and Ecological Effects in Arid Region of the Ministry of Education, Chang'an University, Xi'an 710054, China; hinghaja@gmail.com (E.H.F.J.); xx4@princeton.edu (X.X.)
[2] Department of Environmental Engineering, School of Water and Environment, Chang'an University, Xi'an 710054, China
[3] Faculty of Education, Eastern Technical University of Sierra Leone, Combema Road, Kenema City 00232, Sierra Leone
[4] Key Laboratory of Tibetan Medicine Research, Northwest Institute of Plateau Biology, Chinese Academy of Sciences, Xining 810008, China
[5] Qinghai Provincial Key Laboratory of Tibetan Medicine Research, Xining 810001, China
* Correspondence: baibochina@163.com

Abstract: Heavy metal contamination affects lives with concomitant environmental pollution, and seaweed has emerged as a remedy with the ability to save the ecosystem, due to its eco-friendliness, affordability, availability, and effective metal ion removal rate. Heavy metals are intrinsic toxicants that are known to induce damage to multiple organs, especially when subjected to excess exposure. With respect to these growing concerns, this review presents the preferred sorption material among the many natural sorption materials. The use of seaweeds to treat contaminated solutions has demonstrated outstanding results when compared to other materials. The sorption of metal ions using dead seaweed biomass offers a comparative advantage over other natural sorption materials. This article summarizes the impact of heavy metals on the environment, and why dead seaweed biomass is regarded as the leading remediation material among the available materials. This article also showcases the biosorption mechanism of dead seaweed biomass and its effectiveness as a useful, cheap, and affordable bioremediation material.

Keywords: heavy metals; seaweed; biosorption; aqueous solution; remediation

Citation: Foday Jr, E.H.; Bo, B.; Xu, X. Removal of Toxic Heavy Metals from Contaminated Aqueous Solutions Using Seaweeds: A Review. *Sustainability* **2021**, *13*, 12311. https://doi.org/10.3390/su132112311

Academic Editors: Avelino Núñez-Delgado, Zhien Zhang, Elza Bontempi, Mario Coccia, Marco Race, Yaoyu Zhou and Marc A. Rosen

Received: 20 September 2021
Accepted: 5 November 2021
Published: 8 November 2021

1. Introduction

The severity of heavy metal pollution cannot be over-emphasized, as it has become a universal issue in recent years. The effects of heavy metals in the environment are harmful due to their high toxicity. Their release into the environment occurs as a result of various natural and anthropogenic activities. Unfortunately, most of these heavy metals, whether generated from human activities or nature, constantly undermine the existence and health of environmental resources. The toxicity, persistence, and non-biodegradable nature of these metal ions make them a threat to the environment [1,2]. These heavy metals are known to cause multiple and complicated health problems such as brain and lung damage, cancer, nausea, and vomiting [3,4]. Seaweed, also known as marine algae, serves as one of the major leading biosorption materials for the treatment of heavy metals [5]. Seaweed produces a variety of compounds such as xanthophylls, chlorophyll, carotenoids, vitamins, fatty acids, amino acids as well as antioxidants (such as halogenated compounds, alkaloids, and polyphenols), and polysaccharides (such as agar, alginate, carrageenan, proteoglycans, galactosyl glycerol, laminarin, rhamnan sulfate, and fucoidan) [6]. The presence of alginate in the seaweed makes it an effective eluted material for metal ion removal. Alginate, as well as fucoidan, has a high sorption capacity, which can mainly be attributed to polysaccharides found in the cell walls. The carboxylic and sulfonic acid functional groups are more active in the ion exchange process, and polysaccharides are

responsible for these functional groups [5,7]. On the whole, seaweed has proven to be one of the most outstanding and important biosorption materials for the remediation of metal ions. Its low cost, availability, and eco-friendliness, coupled with its high metal ion uptake capability, make it an ideal biosorption material compared to other sorption materials [6,8]. In this review, dead seaweed biomass is of particular interest, and because of the scant knowledge regarding its usefulness and biosorption mechanism, we seek to throw light on the importance of dead seaweed biomass as a sorption material and to summarize its biosorption mechanism. This review also pinpoints the toxic effects of heavy metals on environmental resources, as well as comparing dead seaweed biomass with other natural sorption materials in terms of heavy metal removal.

2. Heavy Metal Contamination in Water

Water is a universal solvent needed by all living organisms and is also good at dissolving both organic and inorganic compounds. Water resources are critically affected by heavy metal contamination, and this has seriously altered the aquatic ecosystem [9]. On a large scale, aquatic ecosystems are contaminated by heavy metals from industrial effluent, domestic sewage, and agricultural runoff [10]. Most rivers, streams, and lakes are polluted through erosion and leaching, while atmospheric deposition, metal corrosion, sediment resuspension, and metal evaporation are some of the ways the environment gets polluted [11,12]. The non-biodegradable character of heavy metals and their persistence in the environment have led to bioaccumulation through the food chain, leading to complicated health issues and environmental pollution [13]. The term heavy metals refer to metals and metalloids whose mass is over 5 g/cubic centimeters (g/cm^3) and are naturally occurring elements commonly found on earth [14]. They can be regarded as trace elements due to their trace concentrations in the environment. The set of environmental matrices for metal ion concentrations range from zero (0) ppb to ten (10) ppb [15,16]. Anthropogenic and natural activities such as mining, fossil fuel combustion, agriculture, volcanic eruptions, earthquakes, weathering of rocks, and industrial activity are the main causes of environmental contamination [17]. Direct contact with these heavy metals either through inhalation or ingestion poses serious health threats such as teratogenesis, cancer, and internal disorders [18]. Cadmium (Cd), Chromium (Cr), Lead (Pb), Mercury (Hg), and Arsenic (As) were identified by Tchounwou and team [16] as the most toxic heavy metals, and have been placed under the category "priority metals", which means they are metals of public concern, due to their toxic nature. These aforementioned metal ions are innately toxic and are capable of inducing damage to multiple organs even at minimal exposure levels. Reactive oxygen species (ROS) together with oxidative stress (OS) play key roles in the carcinogenic and toxic nature of these metal ions [16]. Zinc (Zn), Copper (Cu), Molybdenum (Mo), and several other metals have also been considered essential elements because they assist in biochemical reactions, although excess exposure above the required threshold can impair human health [19]. Against this background, international institutions like the United States Environmental Protection Agency (USEPA), the World Health Organization (WHO), the European Union (EU), etc. have set acceptable thresholds referred to as Maximum Contaminant Levels (MCLs). Table 1 shows the internationally accepted thresholds of metal ion concentrations in drinking water.

Table 1. Accepted thresholds of toxic metal ions in drinking water.

Drinking Water Acceptable Standards in (mg L^{-1})					
Metals	**WHO [20]**	**USEPA [21]**	**EU Standard [22]**	**MEE-China [23]**	**DWI-UK [24]**
Nickel (Ni)	0.07	-	0.020	0.000	0.02
Lead (Pb)	0.01	0.015	0.005	0.010	0.01
Zinc (Zn)	-	5.0	-	0.05	-
Copper (Cu)	2.0	1.0	2.000	1.000	2.0
Cadmium (Cd)	0.003	0.005	0.005	0.005	0.005
Mercury (Hg)	0.006	0.002	0.001	0.00005	0.001
Arsenic (As)	0.01	0.010	0.01	0.050	0.01
Chromium (Cr)	0.05	0.100	0.025	0.050	0.05
Antimony	0.02	-	0.01	-	0.005
Bromate	0.01	-	0.01	-	0.01
Uranium	0.03	0.03	0.03	-	-

The contamination of water bodies normally happens through leaching, erosion, wind, and other environmental means, thereby leading to negative health implications and risk to the ecosystem. Heavy metal pollution leaves a negative blueprint on the environment and people's lives. As shown in Figures 1 and 2, natural and anthropogenic sources are the known sources for heavy metal contamination. The natural sources for these toxic metals include volcanic eruptions, forest fires, biogenic sources, and the weathering of rock [25], while industrial estates, automobile exhaust, the spraying of insecticide, agricultural activities, transportation, and mining are the main anthropogenic sources of heavy metals pollution [26].

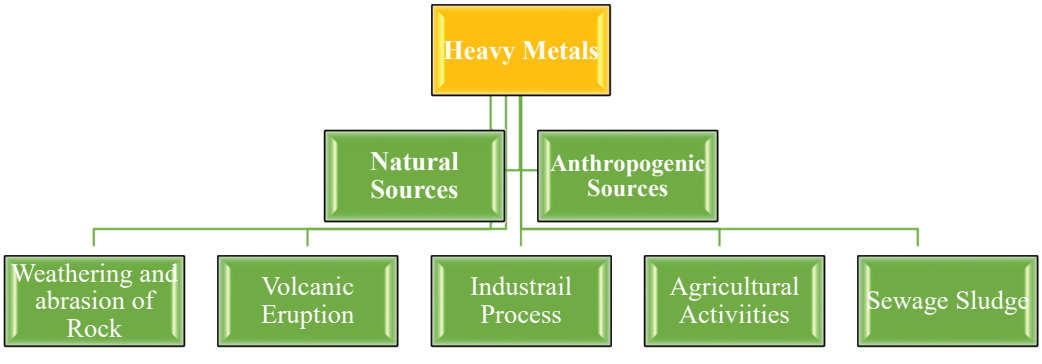

Figure 1. Categories of heavy metal sources.

As seen in Figure 3 below, topsoil and underground water are normally polluted by industrial activities, agricultural activities, weathering, volcanic eruptions, and other biogenic activities. The water bodies become contaminated as the topsoil is washed into them by either erosion, leaching, or landfill leakage. In turn, flora and fauna are affected as the polluted water bodies are consumed and accumulated into their systems, tissues, and organs. Human beings, on the receiving end, are exposed to multiple risks of biochemical disorder or organ failures following the ingestion of contaminated plants and animals.

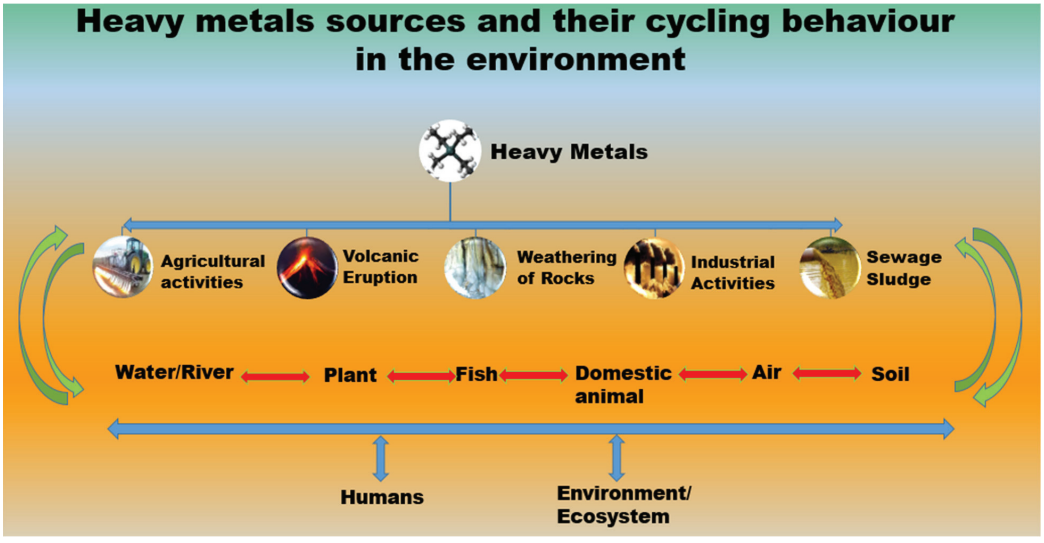

Figure 2. Sources of heavy metals.

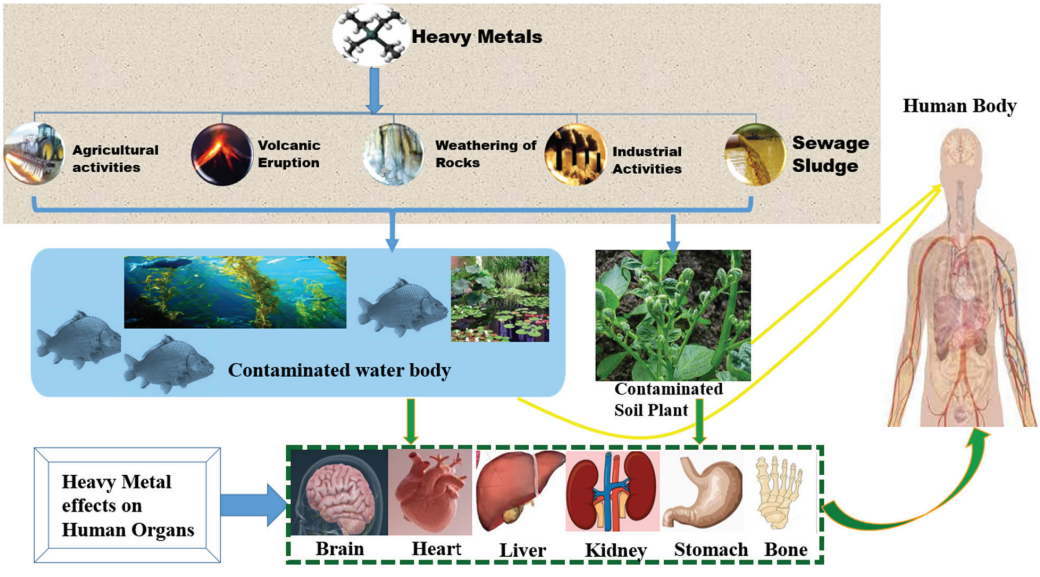

Figure 3. Heavy metal contamination in water.

3. Structure and Classification of Seaweed

Seaweed does not have roots, but rather has holdfasts that anchor the seaweed to the bottom of the sea or ocean. These root-like holdfasts are composed of many finger-like components known as Haptera and are supported by a stalk or stem called a Stipe. The structure of the stem or stipe can be hard, filled with gas, soft or flexible, short, or long, and in some cases, they may be completely absent depending on the type of seaweed [27]. These stipes or stem-like structures are either filled with gas or empty. These are referred to as pneumatocysts, while the entire body of the seaweed is referred to as the thallus. Seaweed has leaves called blades, which assist in photosynthesis, although some seaweed

species have only a single leaf, while others have many leaves. Figure 4 below shows the physical structure of seaweed.

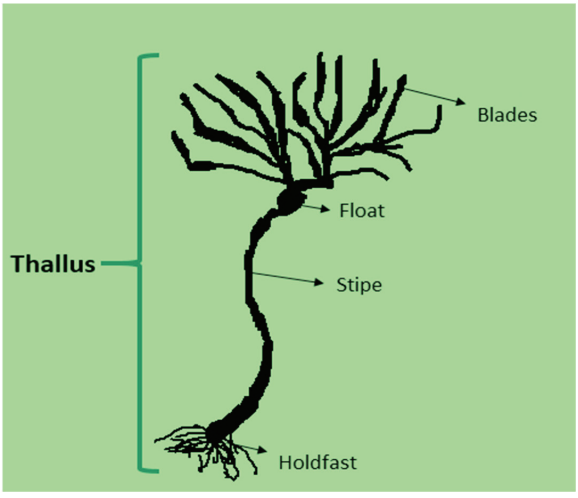

Figure 4. Structure of seaweed.

Seaweed is divided into three (3) main groups based on color characterization, namely: Brown (Phaeophyceae), Red (Rhodophyceae), and Green (Chlorophyceae) seaweeds [28]. Brown algae (Phaeophyta) have various physical appearances either in crust or filament form. Brown algae are multicellular and contain chlorophyll, which aids in photosynthesis, with fucoxanthin being the dominant pigment. Physically, brown algae can range from a large size (Kelp) of about 60 m long to as small as 60 cm [29]. Red algae (Rhodophyta) have chlorophyll in which phycocyanin and phycoerythrin are the dominant pigments responsible for red coloration. Red seaweeds are normally not actually red, but brownish-red or purple. Physically, red algae are smaller than brown algae in length [30]. Green seaweeds (chlorophyte) have chlorophyll, but with no dominant pigment justifying their green coloration; therefore, green seaweed is generally green. It is smaller in size than both red and brown seaweeds [5,31].

We further characterized seaweeds based on both their physical and chemical compositions as shown in Table 2. The alginate and the intercellular substance of the brown algae have high divalent cation uptakes. The cell walls of brown seaweeds are composed of cellulose, alginic acid, and polysaccharides, with alginates and sulfate being the dominant active groups [7]. The cell wall of red algae contains cellulose, but their biosorption capabilities can largely be attributed to sulfated polysaccharides made up of galactans. Similarly, the cell wall of the green algae contains cellulose with hydroxyl-proline glucosides; xylans and mannans are the main functional groups during biosorption [32,33].

Table 2. Characteristics of Seaweed.

Common Name (Phylum)	Body Form	Size	Pigments	Colour Composition	Cell Walls
Brown algae (Phaeophyta)	Multicellular	60 cm–60 m	Chlorophyll, Fucoxanthin, and several other xanthophylls	Golden-brown, Greenish-brown	Cellulose, Alginate, Fucoidan
Red algae (Rhodophyta)	Multicellular	50 cm–2 m	Chlorophyll, Phycocyanin, Phycoerythrin, and several xanthophylls	Brownish red, Purple	Cellulose, Xylans, Galactans
Green algae (Chlorophyta)	Unicellular, Colonial, Filamentous, Multicellular	1–1000 μm	a and b Chlorophyll and several xanthophylls	Green	Cellulose Hydroxyl –proline glucosides β- xylans, β-mannans

3.1. Seaweed: Metal Ion Biosorption Material

The treatment of contaminated solutions has been a burden to engineers and scientists over the years. Recently, seaweed has been proven to be more effective than other natural sorption materials. Some of the other natural sorption materials that have been used to elute metal ions are discussed in the next subsection. Remediation of aqueous solution from metal ions is of serious concern to environmentalists, considering the threat it poses to the purity of the natural environment [34]. The non-biodegradability, carcinogenicity, and toxicity of heavy metals make them harmful, and treatment of these heavy metals is essential [35]. Sorption has been proven to be a sustainable and effective method for treating heavy metals in aqueous solutions using natural biomass [36]. Based on these outstanding results, seaweed has emerged as the leading material, with a high rate of metal ion removal. The biosorption method is one of the simplest, cheapest, and most eco-friendly methods, and requires little or no nutrient addition. The effectiveness and efficiency of treatments for heavy metals are directly related to the type of sorbent used [37]. In short, the remediation of heavy metals using seaweed offers a more reliable, cheaper, and more effective means of heavy metal removal from aqueous solutions than the previous methods. Various mechanisms of seaweed biomass (electrostatic interaction, ion exchange, and complex formation) have been used in the biosorption process of heavy metals, and ion exchange has been widely used and is considered the most important among the list of mechanisms [38,39]. The cell walls of the algae possess polysaccharides and protein, which serve as binding sites for metal ion uptake [40]. There are several factors responsible for the sorption capability of a seaweed cell surface; among these factors are accessibility of binding groups for metal ions, the affinity constants of the metal with the functional group, the chemical state of these sites, the number of functional groups in the algae matrix, and the coordination number of the metal ion to be sorbed [41]. The metal biosorption ability of seaweed varies because of the heterogeneity of their respective cell wall composition. For example, as seen in Table 3, brown, green, and red algae have high affinities for lead (Pb), copper (Cu), and cobalt (Co), respectively [7]. Physical or chemical treatment can enhance heavy metal uptake by seaweed, and the cell wall surface is modified, thereby providing additional binding sites for biosorption [7,42]. The physical treatment includes freezing, crushing, heating, and drying, as these increase the surface area on which biosorption can be achieved [42]. The most common seaweed pretreatments are glutaraldehyde, calcium-chloride ($CaCl_2$), formaldehyde, sodium hydroxide (NaOH), and hydrogen-chloride (HCl). Pretreatment with calcium-chloride (CaCl2) enhances calcium binding with alginate, which plays a pivotal role in ion exchange [43]. The crosslinking bond between hydroxyl and amino group is strengthened by formaldehyde and glutaraldehyde [44]. The electrostatic interactions of metal ion cations are increased by sodium hydroxide (NaOH), while at the same time providing optimal conditions for ion exchange, while hydrogen-chloride

(HCl) dissolves the polysaccharides of the cell wall and also replaces light metal ions with a proton, thereby increasing the biosorption binding sites [7]. It is in this regard that we aim to showcase the comparative advantages of seaweed over other sorption materials in the removal of heavy metals.

Table 3. Different algae species for heavy metal removal.

Species of Algae	Metal Ions	qmax (mmol/g)	pH	References
Green Algae				
Ulva lactuca	Pb(II)	0.61	4.5	[45]
Cladophora glomerata		0.35	4.5	[45]
Ulva sp.		1.46	5.0	[33]
Codium vermilara		0.30	5.0	[46]
Spirogyra insignis		0.24	5.0	[46]
Spirogyra neglecta		0.56	5.0	[47]
Caulerpa lentillifera		0.13	5.0	[48]
Spirogyra sp.		0.43	5.0	[49]
Cladophora sp.		0.22	5.0	[49]
Ulva sp.	Cu(II)	0.75	5.0	[33]
Codium vermilara		0.26	5.0	[46]
Spirogyra insignis		0.30	4.0	[46]
Spirogyra neglecta		1.80	4.5	[47]
Ulva fasciata		1.14	5.5	[50]
Caulerpa lentillifera		0.08	5.0	[48]
Cladophora sp		0.23	5.0	[49]
Spirogyra sp		0.53	5.0	[51]
Ulva sp.	Cd(II)	0.58	5.5	[33]
Chaetomorpha linum		0.48	5.0	[52]
Codium vermilara		0.19	6.0	[46]
Spirogyra insignis		0.20	6.0	[46]
Ulva lactuca		0.25	5.0	[53]
Oedogonium sp.		0.79	5.0	[54]
Caulerpa lentillifera		0.04	5.0	[48]
Spirogyra sp.		0.006 a	-	[55]
Ulva sp.	Zn(II)	0.54	5.5	[33]
Codium vermilara		0.36	6	[46]
Spirogyra insignis		0.32	6	[46]
Caulerpa lentillifera		0.04	5	[48]
Spirogyra s		0.02 a	-	[55]
Ulva sp.	Ni(II)	0.29	5.5	[33]
Codium vermilara		0.22	6.0	[46]
Spirogyra insignis		0.29	6.0	[46]
Ulva lactuca		1.14	4.5	[56]
Red Algae				
Gracilaria corticata	Pb(II)	0.26	4.5	[45]
Gracilaria canaliculata		0.20	4.5	[45]
Polysiphonia violacea		0.49	4.5	[45]
Gracillaria sp.		0.45	5.0	[33]
Asparagopsis armata		0.30	4.0	[46]
Jania rubens		0.14	5.0	[57]
Pterocladia capillacea		0.16	5.0	[57]
Corallina mediterranea		0.31	5.0	[57]
Galaxaura oblongata		0.42	5.0	[57]
Asparagopsis armata		0.33	5.0	[46]
Chondrus crispus		0.63	4.0	[46]
Gelidium		0.51	5.3	[58]
Gracilaria changii		0.23	5.0	[52]
Gracilaria edulis		0.24	5.0	[52]

Table 3. *Cont.*

Species of Algae	Metal Ions	qmax (mmol/g)	pH	References
Gracilaria Salicornia		0.16	5.0	[52]
Asparagopsis armata		0.28	6.0	[46]
Ceramium virgatum		0.35	5.0	[59]
Mastocarpus stellatus		0.59	6.0	[60]
Jania rubens		0.27	5.0	[57]
Corallina mediterranea		0.57	5.0	[57]
Hypnea valentiae		0.15	6.0	[61]
Palmaria palmate	Cr	0.57 (Cr(III)) 0.65 (Cr(VI))	4.5 (Cr(III 2 (Cr(VI))	[62]
Polysiphonia lanosa		0.65 (Cr(III)) 0.88 (Cr(VI))	4.5(Cr(III)) 2 (Cr(VI))	[62]
Jania rubens		0.54 (Cr(III))	5.0 (Cr(III))	[57]
Pterocladia capillacea		0.66 (Cr(III))	5.0 (Cr(III))	[57]
Corallina mediterranea		1.35 (Cr(III))	5.0 (Cr(III))	[57]
Galaxaura oblongata		2.02 (Cr(III))	5.0 (Cr(III))	[57]
Jania rubens	Co(II)	0.55	5.0	[57]
Pterocladia capillacea		0.89	5.0	[57]
Corallina mediterranea		1.29	5.0	[57]
Galaxaura oblongata		1.25	5.0	[57]
Brown Algae				
Ascophyllum nodosum	Pb(II)	1.31	3.5	[63]
Fucus vesiculosus		1.11	3.5	[63]
Sargassum vulgare		1.10	3.5	[63]
Sargassum hystrix		1.37	4.5	[45]
Sargassum natans		1.14	4.5	[45]
Padina pavonia		1.04	4.5	[45]
Sargassum sp.		1.16	5.0	[33]
Padina sp.		1.25	5.0	[33]
Fucus vesiculosus		1.02	5.0	[38]
Fucus spiralis		0.98	3.0	[46]
Ascophyllum nodosu		0.86	3.0	[46]
Padina sp.	Cu(II)	1.14	5.0	[33]
Sargassum vulgarie		0.93	4.5	[64]
Sargassum fluitans		0.80	4.5	[64]
Sargassum filipendula		0.89	4.5	[64]
Fucus vesiculosus		1.66	5.0	[38]
Fucus spiralis		1.10	4.0	[46]
Ascophyllum nodosum		0.91	4.0	[46]
Sargassum filipendula		1.32	4.5	[65]
Fucus serratus		1.60	5.5	[66]
Sargassum sp.		1.13	5.5	[50]
Sargassum sp.	Cd(II)	0.76	5.5	[33]
Padina sp		0.75	5.5	[33]
Sargassum siliquosum		0.73	5.0	[52]
Sargassum baccularia		0.74	5.0	[52]
Padina tetrastomatica		0.53	5.0	[52]
Sargassum vulgarie		0.79	4.5	[64]
Sargassum fluitans		0.71	4.5	[64]
Sargassum muticum		0.68	4.5	[64]
Fucus vesiculosus		0.96	6.0	[38]
Fucus spiralis		1.02	6.0	[46]
Ascophyllum nodosum		0.78	6.0	[46]
Sargassum filipendula		1.17	5.0	[67]
Bifurcaria bifurcate		0.65	4.5	[68]
Saccorhiza polyschides		0.84	4.5	[68]

Table 3. *Cont.*

Species of Algae	Metal Ions	qmax (mmol/g)	pH	References
Ascophyllum nodosum		0.70	4.5	[68]
Laminaria ochroleuca		0.56	4.5	[68]
Pelvetia caniculata		0.66	4.5	[68]
Macrocystis pyrifera		0.89	3.0	[69]
Sargassum sp.	Zn(II)	0.50	5.5	[33]
Padina sp.		0.81	5.5	[33]
Fucus spiralis		0.81	6.0	[46]
Ascophyllum nodosum		0.64	6.0	[46]
Sargassum filipendula		0.71	5.0	[67]
Macrocystis pyrifera		0.91	4.0	[69]
Sargassum fluitans	Ni(II)	0.75	3.5	[63]
Ascophyllum nodosum		0.69	3.5	[63]
Sargassum natans		0.41	3.5	[63]
Fucus vesiculosus		0.39	3.5	[63]
Sargassum vulgare		0.09	3.5	[63]
Sargassum sp		0.61	5.5	[33]
Padina sp.		0.63	5.5	[33]
Cystoseria indica		0.85	6.0	[70]
Nizmuddinia zanardini		0.94	6.0	[70]
Sargassum glaucescensand		0.94	6.0	[70]
Padina australis		0.46	6.0	[70]
Fucus spiralis		0.85	6.0	[46]
Ascophyllum nodosum		0.73	6.0	[46]
Sargassum filipendula		1.07	4.5	[65]
Fucus vesiculosus	Cr	1.21 (Cr(III))	4.5 (Cr(III))	[62]
		0.82 (Cr(VI))	2 (Cr(VI))	
Fucus spiralis		1.17 (Cr(III))	4.5 (Cr(III))	[62]
		0.68 (Cr(VI))	2 (Cr(VI))	
Sargassum sp.		0.60 (Cr(VI))	2 (Cr(VI))	[71]
Sargassum muticum		3.77 (Cr(VI))	2 (Cr(VI))	[72]

a = Not maximum biosorption value.

Table 3 shows the different species of algae used in the removal of heavy metals. The numbers for metal ion uptake qmax (mmol/g) for the different species are in the range (0–4), especially the brown alga species (*Sargassum muticum*), while all uptake occurs between pH values of (2–6), and pH influences the dissociation of heavy metals from the solution using different alga species [48,73]. The pH impacts metal ion uptake, which is a result of the influence of the "functional group on the biomass' cell wall and the metal ions solution" [33]. The polysaccharides present in the cell wall of seaweeds are the most highly metal-binding sites [64].

3.2. Various Natural Materials Used for Sorption

In recent years, engineers and scientists have directed much effort towards identifying the most suitable biosorption materials. Among many materials, seaweed has been revealed to be the most suitable and effective natural material. Table 4 shows some of the various other materials that have been used for the removal of metal ions.

Table 4. Various natural materials used for the removal of metal ions.

Materials Used	Heavy Metals	References
Polymers	Fe and Cr	[74]
Sawdust and tree barks	Hg, Pb, and Zn	[75]
Electronic waste along with galvanic wastes	Cu, Ni, Mn, Pb, Sn	[76]
charcoal:	Cr(III)	[77]
Clay	Cr(III)	[78]
Fungi	Cr, Fe	[79]
Dead biomass	Cr	[80]
Peat moss	Cr, Fe	[81]
Peanut shells, Rice husk, Straw, and walnut cover	Cr, Cu, Ni	[82]
Cocoa shell	Al, Cd, Co, Cr, Cu, Fe, Mn, Ni, Pb, and Zn	[83]
Coconut husk	Cr, As	[82]
Caol and fly ashes	Cr, Cu, Ni	[84]
Banana pith and peels	Ni, Pb	[85]
Cassava fiber	Pb, Co	[86]
Chicken feathers	Al, As	[87]
Sheep manure wastes	Ca, Cd	[88]
Sunflower	Co, Cr	[89]
Rice byproducts	Cu, Fe	[90]
Orange peels	Cu, Fe, Hg	[91]
Palm kernel fiber	Fe, Hg	[82]
Grape stalks	Cr, Fe, Hg	[92]

As highlighted in Table 4, the use of different biomass (living or dead) for the removal of heavy metals has been studied over the years, and microalgae have stood out among the others. For non-living organisms, the cell surface involves different functional groups like amini, hydroxyl, sulfhydryl, phosphate, sulfate, and carboxyl groups [93]. Sawdust and tree barks are rich in tannin/lignin, and have been studied by Fiset and team [94], as they proved effective in metal adsorption. The tannin is an active species during the metal adsorption (ion exchange) process because of the polyhydroxy polyphenol groups [95]. Lignin, which is extracted from black liquor and is also a waste product of the paper industry, has been considered for the removal of metals (Hg, Pb, and Zn) [96]. Alcohols, acids, aldehydes, ketones, phenol, hydroxides, and ethers are all polar functional groups of lignin that have varying metal-binding capabilities [97]. Phytoremediation or phytofiltration of metal-contaminated effluents have been tested and proven successful. Some examples of aquatic plants with such ability are *Ceratophyllum demersum*, *Lemna minor, and Myriophyllum spicatum* [98]. Cellular components such as amide, imine, imidazol moieties, carboxyl, hydroxyl, sulfate, sulfhydryl, phosphate of these plants have high metal-binding properties, as reported by Gardea and team [99]. Chitin and chitosan have also been used to treat metal ions in wastewater. Chitin, which is the second-most abundant natural biopolymer after cellulose, is commonly found in the exoskeletons of crustaceans and shellfish, while Chitosan is produced by alkaline N-deacetylation of chitin [100]. Similarly, peat moss has been studied based on heavy metal decontamination of wastewater. It is a complex material with both lignin and cellulose as its main constituents, which contain polar functional groups [101]. Plenty of other agricultural waste, such as rice residues, fruit

and vegetable peels, tea/coffee residues, and coconut husks, have also been used for metal ion retention. Most of the materials have polyhydroxy, polyphenol, carboxylic, and amino groups, which play key roles in the metal adsorption process [83]. Animal bones, clay, human hair, and teeth have all been used to treat metal ions, but have not been effective or efficient when compared with seaweed [102]. In conclusion, the above-discussed natural sorption materials have not been effective either in terms of metal ions removal rate or socio-economic benefit when compared to seaweed.

4. Sorption Mechanism of Seaweed

Seaweed is characterized by both physical, biological, and chemical attributes, such as alginate, carrageenan, and photosynthesis features. It can also grow in extreme conditions, in the presence of heavy metals, salinity, and harsh temperatures. Owing to the aforementioned qualities, in addition to its high binding affinity, seaweed is considered a good bioremediation material for treating toxic metal ions in aqueous solutions [103]. Seaweed also has a "hormesis phenomenon feature", which refers to the toxic contamination of algae stimulating further algae growth [104]. Similarly, some cyanobacteria tend to grow in wastewater that is highly polluted with toxic heavy metals; examples of cyanobacteria include; spirogyra, oscillatoria, anabaena, and phormidium [105]. Seaweeds have both antioxidant enzymes and non-enzymatic antioxidants. Antioxidant enzymes include catalase, superoxide dismutase (SOD), ascorbate peroxidase, and reductase, while non-enzymatic antioxidants include glutathione (GHS), cysteine, proline, carotenoids, and ascorbic acid (ASC) [106]. During the sorption process, heavy metals in the seaweed ignite the phytochelatins (PCs) through biosynthesis. These phytochelatins are proteins and thiol-rich peptides that can minimize toxic metal ions through interaction [107]. Superoxide dismutase (SOD) performs a defensive role against the superoxide anion, which is exerted by breaking the superoxide anion into hydrogen peroxide and oxygen molecules. The catalase degrades hydrogen peroxide to oxygen and water molecules, while cysteine is the precursor for metallothioneins, phytochelatins (PCs), glutathione (GSH), and other sulfur-related compounds. [108]. The reduction of free radicals and reactive oxygen species (ROS) is performed by both glutathione (GSH) and ascorbic acid (ASC), which are endogenous antioxidants that are synthesized by seaweed [109]. Additionally, seaweed produces a high level of ascorbic acid (ASC) as "hydrophilic redox buffer", which protects cytosol against the threat of oxidation. Similarly, the seaweed is protected by glutathione (GSH) by enabling phytochelatins (PCs), scavenging free radicals, and ascorbic acid (ASC) synthesis alongside the restoration of substrate for other antioxidants [106,107]. The chemistry involved in the interaction between the biomass (seaweed) and the metal ions is shown in Figures 5 and 6, respectively.

As shown in Figure 5, the removal mechanism of heavy metals is performed in two folds. These two folds include biosorption, which is the "rapid extracellular passive adsorption", and the latter is bioaccumulation, which is the "slow intracellular positive diffusion and accumulation". Seaweeds' cell walls are made up of cellulose and alginate (polysaccharides) and lipids, while the organic protein offers amino, phosphate, hydroxyl, thiol-rich, and carboxyl (functional groups), which all possess good ability to bind metal ions [105]. Additionally, the cell wall is composed of laminarin, deprotonated sulphate, and monomeric alcohols capable of attracting both cationic and anionic species of metal ions [110]. Adsorption on the surface of seaweed occurs rapidly when compared to inside the seaweed. On the surface, adsorption takes place through ion exchange with the cell wall and covalent bonding with the ionized cell wall, resulting in "seaweed exopolysaccharides". Conversely, adsorption is slow inside, and phytochelatins, GSH, and metal transporter play a leading role in the binding of metal ions. This accumulation of metal ions inside is carried across the cell membrane to the cytoplasm before diffusion [110,111].

According to Figure 6, the biochemical constituent of seaweed is responsible for the sequestration of metal ions, which are composed of alginate and fucoidan in the cell wall. The cell wall of microalgae is made up of a fibrillary skeleton (cellulose) and

an amorphous embedded matrix (alginate) [5]. The cell wall of brown algae contain sulfated polysaccharides, while in red algae, galactans are found, and green algae, hydroxyl-proline [46].

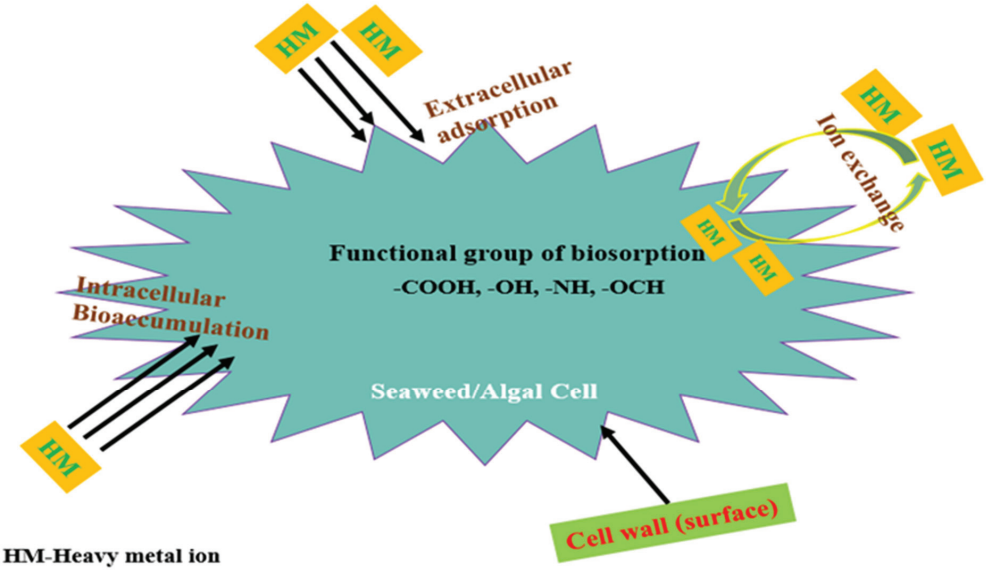

Figure 5. Mechanism of metal ion interaction with seaweed.

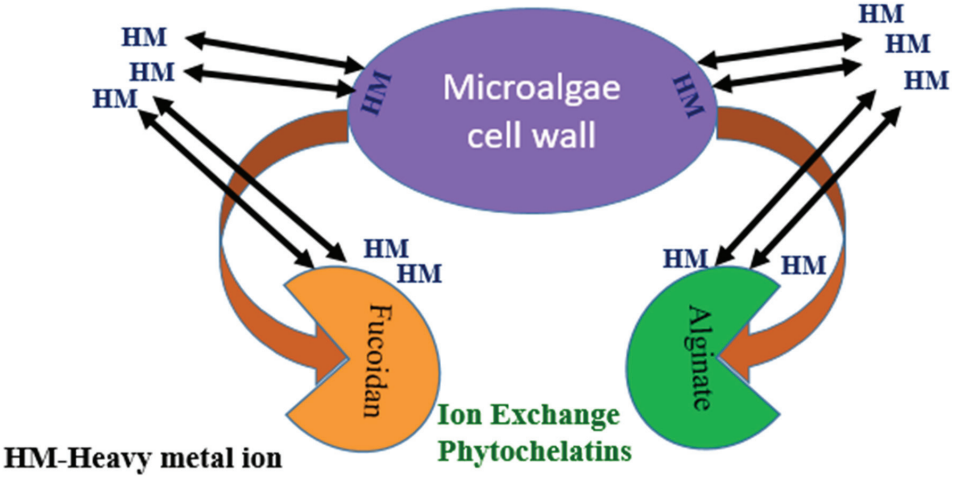

Figure 6. Interaction between metal ions and algal biomass.

5. Conclusions

The usage of seaweed as a sorption material has attracted the attention of many researchers in recent times. Seaweed's relevance is not only restricted to the treatment of heavy metals; it is a precious food that is prominent in basic balanced diets. Considering the current state of heavy metal pollution in our environment, seaweed has been proven to be an excellent, cheap, effective, abundantly available, eco-friendly, and efficient material for remediating the environment when compared to other natural sorption materials. This

multi-faceted and multi-dimensional seaweed has the potential to heal the world from various environmental menaces. It is evidence that seaweed could be economically prudent both for industrial and environmental uses. As seaweeds are among the most fascinating and resourceful species, more exploration is needed to reap the benefits of these unique species. For sorption purposes, seaweed has been proven to be a good biosorption material with high metal ion uptake (qmax (mmol/g)) within the range (0–4). The brown alga (*Sargassum muticum*) stands out efficiently at a pH value of 2 when compared to other natural sorption materials. The main biochemical interaction between the algae and the metal ions depends on the cell wall, with polysaccharides, lipids, and other organic proteins being the components that play the main roles during the sorption process. In conclusion, the sorption of metal ions using seaweed, especially brown algae, presents a solution that is more reliable, cheaper, and possesses more effective sorption ability than other natural sorption materials previously studied.

Author Contributions: Conceptualization—E.H.F.J., B.B.; Funding acquisition—B.B.; Methodology—E.H.F.J., B.B., X.X.; Resources—B.B.; Software—E.H.F.J.; Supervision—B.B., X.X.; Validation—X.X.; Writing—original draft—E.H.F.J.; Writing—review & editing—E.H.F.J., B.B., X.X.; Project administration—B.B. All authors have read and agreed to the published version of the manuscript.

Funding: This work was funded by the Natural Science Basic Research Program of Shaanxi (Program No. 2021SF-497), and the Fundamental Research Funds for Central Universities (CHD 300102291403).

Institutional Review Board Statement: Not applicable.

Informed Consent Statement: Not applicable.

Data Availability Statement: Not applicable.

Conflicts of Interest: This work has no conflict of interest.

References

1. Ajjabi, L.C.; Chouba, L. Biosorption of Cu^{2+} and Zn^{2+} from aqueous solutions by dried marine green macroalga *Chaetomorpha linum*. *J. Environ. Manag.* **2009**, *90*, 3485–3489. [CrossRef]
2. Bulut, Y.; Baysal, Z. Removal of Pb(II) from wastewater using wheat bran. *J. Environ. Manag.* **2006**, *78*, 107–113. [CrossRef]
3. Al-Rub, F.; El-Naas, M.; Benyahia, F.; Ashour, I. Biosorption of nickel on blank alginate beads, free and immobilized algal cells. *Process. Biochem.* **2004**, *39*, 1767–1773. [CrossRef]
4. Argun, M.E.; Dursun, S.; Ozdemir, C.; Karatas, M. Heavy metal adsorption by modified oak sawdust: Thermodynamics and kinetics. *J. Hazard. Mater.* **2007**, *141*, 77–85. [CrossRef] [PubMed]
5. Davis, T.A.; Volesky, B.; Mucci, A. A review of the biochemistry of heavy metal biosorption by brown algae. *Water Res.* **2003**, *37*, 4311–4330. [CrossRef]
6. He, J.; Chen, J.P. A comprehensive review on biosorption of heavy metals by algal biomass: Materials, performances, chemistry, and modeling simulation tools. *Bioresour. Technol.* **2014**, *160*, 67–78. [CrossRef] [PubMed]
7. Romera, D.E.; González, F.; Ballester, A.; Blázquez, M.L.; Muñoz, J.A. Biosorption with Algae: A Statistical Review. *Crit. Rev. Biotechnol.* **2006**, *26*, 223–235. [CrossRef]
8. Gupta, V.K.; Nayak, A.; Agarwal, S. Bioadsorbents for remediation of heavy metals: Current status and their future prospects. *Environ. Eng. Res.* **2015**, *20*, 1–18. [CrossRef]
9. Abrar, M.; Hussain, Z.; Akif, M.; Sok, K.; Muhammad, A.; Khan, A.; Khan, M. Textile effluents and their contribution towards aquatic pollution in the Kabul River (Pakistan). *J. Chem. Soc. Pak.* **2011**, *24*, 106.
10. Afzal, M.S.; Ashraf, A.; Nabeel, M. Characterization of industrial effluents and groundwater of Hattar industrial estate, Haripur. *Adv. Agric. Environ. Sci. Open Access (AAEOA)* **2018**, *1*, 70–77.
11. Yang, X.E.; Jin, X.F.; Feng, Y.; Islam, E. Molecular mechanisms and genetic basis of heavy metal toler-ance/hyperaccumulation in plants. *J. Integr. Plant Biol.* **2005**, *47*, 1025–1035. [CrossRef]
12. Nriagu, J.O. A global assessment of natural sources of atmospheric trace metals. *Nat. Cell Biol.* **1989**, *338*, 47–49. [CrossRef]
13. Yang, J.; Wei, W.; Pi, S.; Ma, F.; Li, A.; Wu, D.; Xing, J. Competitive adsorption of heavy metals by extracellular polymeric substances extracted from *Klebsiella* sp. J1. *Bioresour. Technol.* **2015**, *196*, 533–539. [CrossRef] [PubMed]
14. Duruibe, J.O.; Ogwuegbu, M.; Egwurugwu, J. Heavy metal pollution and human biotoxic effects. *Int. J. Phys. Sci.* **2007**, *2*, 112–118.
15. Bravo, S.; Amorós, J.; Pérez-de-los-Reyes, C.; García, F.; Moreno, M.; Sánchez-Ormeño, M.; Higueras, P. Influence of the soil pH in the uptake and bioaccumulation of heavy metals (Fe, Zn, Cu, Pb and Mn) and other elements (Ca, K, Al, Sr and Ba) in vine leaves, Castilla-La Mancha (Spain). *J. Geochem. Explor.* **2017**, *174*, 79–83. [CrossRef]

16. Tchounwou, P.B.; Yedjou, C.G.; Patlolla, A.K.; Sutton, D.J. Heavy Metal Toxicity and the Environment. *Mol. Clin. Environ. Toxicol.* **2012**, *101*, 133–164. [CrossRef]
17. Jaishankar, M.; Tseten, T.; Anbalagan, N.; Mathew, B.B.; Beeregowda, K.N. Toxicity, mechanism and health effects of some heavy metals. *Interdiscip. Toxicol.* **2014**, *7*, 60–72. [CrossRef]
18. Prasher, P.; Mudila, H.; Sharma, M. Biosorption and Bioaccumulation of Pollutants for Environmental Remediation. In *Microorganisms for Sustainability*; Springer International Publishing: Singapore, 2021; pp. 379–405.
19. World Health Organization. *Trace Elements in Human Nutrition and Health*; World Health Organization: Geneva, Swizerland, 1996.
20. World Health Organization. *Guidelines for Drinking-Water Quality, First Addendum to the Fourth Edition*; World Health Organization: Geneva, Swizerland, 2017.
21. United States Environmental Protection Agency (USEPA). Code of Federal Regulations-2003, Title 40-PART 141—NATIONAL PRIMARY DRINKING WATER REGULATIONS, Subpart B—Maximum Contaminant Levels. Available online: https://www.epa.gov/sites/default/files/2015-11/documents/howepargulates_cfr-2003-title40-vol20-part141_0.pdf (accessed on 30 October 2021).
22. European Union. Directive (EU) 2020/2184 of the European Parliament and of the Council of 16 December 2020 on the Quality of Water Intended for Human Consumption. *Off. J. Eur. Union* **2020**, *435*, 1–62.
23. The National Standards of the People's Republic of China. Environmental Quality Standards for Surface Water. Available online: http://english.mee.gov.cn/SOE/soechina1997/water/standard.htm (accessed on 30 October 2021).
24. Water, E.A.W. The Water Supply (Water Quality) Regulations 2016, PART 13 Amendments and Revocations. Available online: https://www.legislation.gov.uk/uksi/2016/614/pdfs/uksi_20160614_en.pdf (accessed on 30 October 2021).
25. Hayashi, K.; Rivai, I.F.; Herawati, N.; Suzuki, S.; Koyama, H. Cadmium, Copper, and Zinc Levels in Rice and Soil of Japan, Indonesia, and China by Soil Type. *Bull. Environ. Contam. Toxicol.* **2000**, *64*, 33–39. [CrossRef]
26. He, Z.L.; Yang, X.E.; Stoffella, P.J. Trace elements in agroecosystems and impacts on the environment. *J. Trace Elem. Med. Biol.* **2005**, *19*, 125–140. [CrossRef]
27. Mahadevan, K. Seaweeds: A sustainable food source. In *Seaweed Sustainability*; Elsevier BV: Manchester, UK, 2015; pp. 347–364.
28. Collins, K.G. An investigation of the prebiotic potential and gut health benefits of Irish seaweeds. *Univ. Coll. Cork* **2017**, *371*, 31–35.
29. Gade, R.; Tulasi, M.S.; Bhai, V.A. Seaweeds: A novel biomaterial. *Int. J. Pharm. Pharm. Sci.* **2013**, *5*, 975–1491.
30. Harbo, J.R.; Harris, J.W. Heritability in Honey Bees (Hymenoptera: Apidae) of Characteristics Associated with Resistance to *Varroa jacobsoni*(Mesostigmata: Varroidae). *J. Econ. Entomol.* **1999**, *92*, 261–265. [CrossRef]
31. Bittner, L.; Payri, C.; Couloux, A.; Cruaud, C.; De Reviers, B.; Rousseau, F. Molecular phylogeny of the Dictyotales and their position within the Phaeophyceae, based on nuclear, plastid and mitochondrial DNA sequence data. *Mol. Phylogenetics Evol.* **2008**, *49*, 211–226. [CrossRef]
32. Yalçın, S.; Sezer, S.; Apak, R. Characterization and lead (II), cadmium (II), nickel (II) biosorption of dried marine brown macro algae Cystoseira barbata. *Environ. Sci. Pollut. Res.* **2012**, *19*, 3118–3125. [CrossRef] [PubMed]
33. Sheng, P.X.; Ting, Y.-P.; Chen, J.P.; Hong, L. Sorption of lead, copper, cadmium, zinc, and nickel by marine algal biomass: Characterization of biosorptive capacity and investigation of mechanisms. *J. Colloid Interface Sci.* **2004**, *275*, 131–141. [CrossRef]
34. Adamu, C.; Nganje, T.; Edet, A. Heavy metal contamination and health risk assessment associated with abandoned barite mines in Cross River State, southeastern Nigeria. *Environ. Nanotechnol. Monit. Manag.* **2015**, *3*, 10–21. [CrossRef]
35. Badruddoza, A.Z.M.; Shawon, Z.B.Z.; Tay, W.J.D.; Hidajat, K.; Uddin, M.S. Fe3O4/cyclodextrin polymer nanocom-posites for selective heavy metals removal from industrial wastewater. *Carbohydr. Polymers* **2013**, *91*, 322–332. [CrossRef]
36. Turan, N.G.; Mesci, B. Use of Pistachio Shells as an Adsorbent for the Removal of Zinc(II) Ion. *CLEAN—Soil Air Water* **2011**, *39*, 475–481. [CrossRef]
37. Pozdniakova, T.A.; Mazur, L.P.; Boaventura, R.A.; Vilar, V.J. Brown macro-algae as natural cation exchangers for the treatment of zinc containing wastewaters generated in the galvanizing process. *J. Clean. Prod.* **2016**, *119*, 38–49. [CrossRef]
38. Mata, Y.; Blázquez, M.; Ballester, A.; González, F.; Muñoz, J.A. Characterization of the biosorption of cadmium, lead and copper with the brown alga Fucus vesiculosus. *J. Hazard. Mater.* **2008**, *158*, 316–323. [CrossRef] [PubMed]
39. Michalak, I.; Chojnacka, K. Interactions of metal cations with anionic groups on the cell wall of the macroalga *Vaucheria* sp. *Eng. Life Sci.* **2010**, *10*, 209–217. [CrossRef]
40. Gupta, V.; Rastogi, A. Biosorption of lead from aqueous solutions by green algae Spirogyra species: Kinetics and equilibrium studies. *J. Hazard. Mater.* **2008**, *152*, 407–414. [CrossRef]
41. Mehta, S.K.; Gaur, J.P. Use of Algae for Removing Heavy Metal Ions From Wastewater: Progress and Prospects. *Crit. Rev. Biotechnol.* **2005**, *25*, 113–152. [CrossRef]
42. Errasquín, E.L.; Vázquez, C. Tolerance and uptake of heavy metals by Trichoderma atroviride isolated from sludge. *Chemosphere* **2003**, *50*, 137–143. [CrossRef]
43. Bishnoi, N.R.; Kumar, R.; Kumar, S.; Rani, S. Biosorption of Cr(III) from aqueous solution using algal biomass *spirogyra* spp. *J. Hazard. Mater.* **2007**, *145*, 142–147. [CrossRef]
44. Ebrahimi, B.; Shojaosadati, S.; Ranaie, S.; Mousavi, S. Optimization and evaluation of acetylcholine esterase immobilization on ceramic packing using response surface methodology. *Process. Biochem.* **2010**, *45*, 81–87. [CrossRef]

45. Jalali, R.; Ghafourian, H.; Asef, Y.; Davarpanah, S.; Sepehr, S. Removal and recovery of lead using nonliving biomass of marine algae. *J. Hazard. Mater.* **2002**, *92*, 253–262. [CrossRef]
46. Romera, E.; González, F.; Ballester, A.; Blázquez, M.; Munoz, J. Comparative study of biosorption of heavy metals using different types of algae. *Bioresour. Technol.* **2007**, *98*, 3344–3353. [CrossRef] [PubMed]
47. Singh, R.K.; Chavan, S.L.; Sapkale, P.H. Heavy Metal Concentrations in Water, Sediments and Body Tissues of Red Worm (*Tubifex* spp.) Collected from Natural Habitats in Mumbai, India. *Environ. Monit. Assess.* **2006**, *129*, 471–481. [CrossRef]
48. Pavasant, P.; Apiratikul, R.; Sungkhum, V.; Suthiparinyanont, P.; Wattanachira, S.; Marhaba, T.F. Biosorption of Cu2+, Cd2+, Pb2+, and Zn2+ using dried marine green macroalga Caulerpa lentillifera. *Bioresour. Technol.* **2006**, *97*, 2321–2329. [CrossRef]
49. Lee, Y.-C.; Chang, S.-P. The biosorption of heavy metals from aqueous solution by Spirogyra and Cladophora filamentous macroalgae. *Bioresour. Technol.* **2011**, *102*, 5297–5304. [CrossRef]
50. Karthikeyan, S.; Balasubramanian, R.; Iyer, C. Evaluation of the marine algae Ulva fasciata and *Sargassum* sp. for the biosorption of Cu(II) from aqueous solutions. *Bioresour. Technol.* **2007**, *98*, 452–455. [CrossRef]
51. Rajfur, M.; Kłos, A.; Wacławek, M. Sorption of copper(II) ions in the biomass of alga *Spirogyra* sp. *Bioelectrochemistry* **2012**, *87*, 65–70. [CrossRef]
52. Hashim, M.; Chu, K. Biosorption of cadmium by brown, green, and red seaweeds. *Chem. Eng. J.* **2004**, *97*, 249–255. [CrossRef]
53. Sari, A.; Tuzen, M. Biosorption of Pb(II) and Cd(II) from aqueous solution using green alga (*Ulva lactuca*) biomass. *J. Hazard. Mater.* **2008**, *152*, 302–308. [CrossRef] [PubMed]
54. Gupta, V.; Rastogi, A. Equilibrium and kinetic modelling of cadmium (II) biosorption by nonliving algal biomass *Oedogonium* sp. from aqueous phase. *J. Hazard. Mater.* **2008**, *153*, 759–766. [CrossRef]
55. Rajfur, M.; Kłos, A.; Wacławek, M. Sorption properties of algae *Spirogyra* sp. and their use for determination of heavy metal ions concentrations in surface water. *Bioelectrochemistry* **2010**, *80*, 81–86. [CrossRef]
56. Zakhama, S.; Dhaouadi, H.; M'Henni, F. Nonlinear modelisation of heavy metal removal from aqueous solution using Ulva lactuca algae. *Bioresour. Technol.* **2011**, *102*, 786–796. [CrossRef] [PubMed]
57. Ibrahim, W.M. Biosorption of heavy metal ions from aqueous solution by red macroalgae. *J. Hazard. Mater.* **2011**, *192*, 1827–1835. [CrossRef]
58. Vilar, V.J.; Botelho, C.M.; Boaventura, R.A. Copper removal by algae Gelidium, agar extraction algal waste and granu-lated algal waste: Kinetics and equilibrium. *Bioresour. Technol.* **2008**, *99*, 750–762. [CrossRef] [PubMed]
59. Sari, A.; Tuzen, M. Biosorption of cadmium(II) from aqueous solution by red algae (*Ceramium virgatum*): Equilibrium, kinetic and thermodynamic studies. *J. Hazard. Mater.* **2008**, *157*, 448–454. [CrossRef] [PubMed]
60. Herrero, R.; Lodeiro, P.; García-Casal, L.J.; Vilariño, T.; Rey-Castro, C.; David, C.; Rodríguez, P. Full description of copper uptake by algal biomass combining an equilibrium NICA model with a kinetic intraparticle diffusion driving force approach. *Bioresour. Technol.* **2011**, *102*, 2990–2997. [CrossRef]
61. Rathinam, A.; Maharshi, B.; Janardhanan, S.K.; Jonnalagadda, R.R.; Nair, B.U. Biosorption of cadmium metal ion from simulated wastewaters using Hypnea valentiae biomass: A kinetic and thermodynamic study. *Bioresour. Technol.* **2010**, *101*, 1466–1470. [CrossRef] [PubMed]
62. Murphy, V.; Hughes, H.; McLoughlin, P. Comparative study of chromium biosorption by red, green and brown seaweed biomass. *Chemosphere* **2008**, *70*, 1128–1134. [CrossRef]
63. Holan, Z.R.; Volesky, B. Biosorption of lead and nickel by biomass of marine algae. *Biotechnol. Bioeng.* **1994**, *43*, 1001–1009. [CrossRef] [PubMed]
64. Davis, T.; Volesky, B.; Vieira, R. Sargassum seaweed as biosorbent for heavy metals. *Water Res.* **2000**, *34*, 4270–4278. [CrossRef]
65. Kleinübing, S.; Silva, E.; da Silva, M.G.C.; Guibal, E. Equilibrium of Cu(II) and Ni(II) biosorption by marine alga Sargassum filipendula in a dynamic system: Competitiveness and selectivity. *Bioresour. Technol.* **2011**, *102*, 4610–4617. [CrossRef]
66. Ahmady-Asbchin, S.; Andres, Y.; Gerente, C.; Le Cloirec, P. Biosorption of Cu(II) from aqueous solution by Fucus serratus: Surface characterization and sorption mechanisms. *Bioresour. Technol.* **2008**, *99*, 6150–6155. [CrossRef] [PubMed]
67. Luna, A.; Costa, A.; Da Costa, A.C.A.; Henriques, C. Competitive biosorption of cadmium(II) and zinc(II) ions from binary systems by Sargassum filipendula. *Bioresour. Technol.* **2010**, *101*, 5104–5111. [CrossRef]
68. Lodeiro, P.; Cordero, B.; Barriada, J.L.; Herrero, R.; de Vicente, M.S. Biosorption of cadmium by biomass of brown marine macroalgae. *Bioresour. Technol.* **2005**, *96*, 1796–1803. [CrossRef]
69. Cazón, J.P.; Bernardelli, C.; Viera, M.; Donati, E.; Guibal, E. Zinc and cadmium biosorption by untreated and calci-um-treated Macrocystis pyrifera in a batch system. *Bioresour. Technol.* **2012**, *116*, 195–203. [CrossRef]
70. Pahlavanzadeh, H.; Keshtkar, A.; Safdari, J.; Abadi, Z. Biosorption of nickel(II) from aqueous solution by brown algae: Equilibrium, dynamic and thermodynamic studies. *J. Hazard. Mater.* **2010**, *175*, 304–310. [CrossRef]
71. Yang, L.; Chen, J.P. Biosorption of hexavalent chromium onto raw and chemically modified *Sargassum* sp. *Bioresour. Technol.* **2008**, *99*, 297–307. [CrossRef] [PubMed]
72. Bermúdez, Y.G.; Rico, I.L.R.; Guibal, E.; de Hoces, M.C.; Martín-Lara, M.Á. Biosorption of hexavalent chromium from aqueous solution by Sargassum muticum brown alga. Application of statistical design for process optimization. *Chem. Eng. J.* **2012**, *183*, 68–76. [CrossRef]
73. Guo, D.; Mitchell, R.J.; Withington, J.M.; Fan, P.-P.; Hendricks, J.J. Endogenous and exogenous controls of root life span, mortality and nitrogen flux in a longleaf pine forest: Root branch order predominates. *J. Ecol.* **2008**, *96*, 737–745. [CrossRef]

74. Pathe, P.P.; Nandy, T.; Kaul, S.N.; Szpyrokwicz, L. Chromium recovery from chrome tan wastewater. *Int. J. Environ. Stud.* **1996**, *51*, 125–145. [CrossRef]
75. Lichtfouse, E.; Elbisser, B. 2nd European Meeting on Environmental Chemistry. In Proceedings of the 2nd European Meeting on Environmental Chemistry, Dijon, France, 12–15 December 2001; p. 273.
76. Vegliò, F.; Quaresima, R.; Fornari, P.; Ubaldini, S. Recovery of valuable metals from electronic and galvanic industrial wastes by leaching and electrowinning. *Waste Manag.* **2003**, *23*, 245–252. [CrossRef]
77. Dahbi, S.; Azzi, M.; Saib, N.; De la Guardia, M.; Faure, R.; Durand, R. Removal of trivalent chromium from tannery waste waters using bone charcoal. *Anal. Bioanal. Chem.* **2002**, *374*, 540–546. [CrossRef]
78. Park, S.-J.; Jung, W.-Y. Removal of chromium by activated carbon fibers plated with copper metal. *Carbon Lett.* **2001**, *2*, 15–21.
79. Bai, R.; Abraham, T. Studies on enhancement of Cr(VI) biosorption by chemically modified biomass of Rhizopus nigricans. *Water Res.* **2002**, *36*, 1224–1236. [CrossRef]
80. Chong, K.H.; Volesky, B. Metal biosorption equilibria in a ternary system. *Biotechnol. Bioeng.* **1996**, *49*, 629–638. [CrossRef]
81. Lee, S.-J.; Park, J.H.; Ahn, Y.; Chung, J.W. Comparison of Heavy Metal Adsorption by Peat Moss and Peat Moss-Derived Biochar Produced Under Different Carbonization Conditions. *Water Air Soil Pollut.* **2015**, *226*, 9. [CrossRef]
82. Ofomaja, A.; Ho, Y.-S. Effect of pH on cadmium biosorption by coconut copra meal. *J. Hazard. Mater.* **2007**, *139*, 356–362. [CrossRef]
83. Meunier, N.; Laroulandie, J.; Blais, J.; Tyagi, R. Cocoa shells for heavy metal removal from acidic solutions. *Bioresour. Technol.* **2003**, *90*, 255–263. [CrossRef]
84. Tan, L.C.; Choa, V.; Tay, J.H. The Influence of pH on Mobility of Heavy Metals from Municipal Solid Waste Incinerator Fly Ash. *Environ. Monit. Assess.* **1997**, *44*, 275–284. [CrossRef]
85. Foday Jr, E.H.; Ramli, N.A.S.; Ismail, H.N.; Malik, N.A.; Basri, H.F.; Aziz, F.S.A.; Nor, N.S.M.; Jumhat, F. Municipal solid waste characteristics in Taman Universiti, Skudai, Johore, Malaysia. *J. Adv. Res. Des.* **2017**, *38*, 13–20.
86. Abia, A.; Asuquo, E. Lead (II) and nickel (II) adsorption kinetics from aqueous metal solutions using chemically modified and unmodified agricultural adsorbents. *Afr. J. Biotechnol.* **2006**, *5*, 1475–1482.
87. Al-Asheh, S.; Banat, F.; Al-Rousan, D. Adsorption of Copper, Zinc and Nickel Ions from Single and Binary Metal Ion Mixtures on to Chicken Feathers. *Adsorpt. Sci. Technol.* **2002**, *20*, 849–864. [CrossRef]
88. Abu Al-Rub, F.A.; Kandah, M.; Al-Dabaybeh, N. Competitive Adsorption of Nickel and Cadmium on Sheep Manure Wastes: Experimental and Prediction Studies. *Sep. Sci. Technol.* **2003**, *38*, 483–497. [CrossRef]
89. Özdemir, N.; Horn, R.; Friedt, W. Construction and characterization of a BAC library for sunflower (*Helianthus annuus* L.). *Euphytica* **2004**, *138*, 177–183. [CrossRef]
90. Ajmal, M.; Rao, R.A.K.; Anwar, S.; Ahmad, J.; Ahmad, R. Adsorption studies on rice husk: Removal and recovery of Cd(II) from wastewater. *Bioresour. Technol.* **2003**, *86*, 147–149. [CrossRef]
91. Ajmal, M.; Rao, R.A.K.; Ahmad, R.; Ahmad, J. Adsorption studies on Citrus reticulata (fruit peel of orange): Removal and recovery of Ni(II) from electroplating wastewater. *J. Hazard. Mater.* **2000**, *79*, 117–131. [CrossRef]
92. Fiol, N.; Villaescusa, I.; Martínez, M.; Miralles, N.; Poch, J.; Serarols, J. Sorption of Pb (II), Ni (II), Cu (II) and Cd (II) from aqueous solution by olive stone waste. *Sep. Purif. Technol.* **2006**, *50*, 132–140. [CrossRef]
93. Kapoor, A.; Viraraghavan, T. Heavy metal biosorption sites in Aspergillus niger. *Bioresour. Technol.* **1997**, *61*, 221–227. [CrossRef]
94. Vaishya, R.; Prasad, S. Adsorption of copper (II) on sawdust. *Indian J. Environ. Prot.* **1991**, *11*, 284–289.
95. Vázquez, G.; Antorrena, G.; González-Álvarez, J.; Doval, M. Adsorption of heavy metal ions by chemically modified Pinus pinaster bark. *Bioresour. Technol.* **1994**, *48*, 251–255. [CrossRef]
96. Srivastava, S.K.; Gupta, V.K.; Mohan, D. Removal of Lead and Chromium by Activated Slag—A Blast-Furnace Waste. *J. Environ. Eng.* **1997**, *123*, 461–468. [CrossRef]
97. Bailey, S.E.; Olin, T.J.; Bricka, R.; Adrian, D. A review of potentially low-cost sorbents for heavy metals. *Water Res.* **1999**, *33*, 2469–2479. [CrossRef]
98. Keskinkan, O.; Goksu, M.; Basibuyuk, M.; Forster, C. Heavy metal adsorption properties of a submerged aquatic plant (*Ceratophyllum demersum*). *Bioresour. Technol.* **2004**, *92*, 197–200. [CrossRef]
99. Gardea-Torresdey, J.; Peralta-Videa, J.; Montes, M.; de la Rosa, G.; Corral-Diaz, B. Bioaccumulation of cadmium, chromium and copper by Convolvulus arvensis L.: Impact on plant growth and uptake of nutritional elements. *Bioresour. Technol.* **2004**, *92*, 229–235. [CrossRef]
100. Dumitriu, S. Polysaccharides as Biomaterials. In *Polymeric Biomaterials, Revised and Expanded*; CRC Press: New York, NY, USA, 2001; pp. 15–76.
101. Brown, P.; Gill, S.; Allen, S.J. Determination of optimal peat type to potentially capture copper and cadmium from solu-tion. *Water Environ. Res.* **2001**, *73*, 351–362. [CrossRef]
102. Celis, R.; Hermosín, M.C.; Cornejo, J. Heavy Metal Adsorption by Functionalized Clays. *Environ. Sci. Technol.* **2000**, *34*, 4593–4599. [CrossRef]
103. Cameron, H.; Mata, M.T.; Riquelme, C. The effect of heavy metals on the viability of Tetraselmis marina AC16-MESO and an evaluation of the potential use of this microalga in bioremediation. *PeerJ* **2018**, *6*, e5295. [CrossRef]

104. Sun, K.; Tang, J.; Gong, Y.; Zhang, H. Characterization of potassium hydroxide (KOH) modified hydrochars from different feedstocks for enhanced removal of heavy metals from water. *Environ. Sci. Pollut. Res.* **2015**, *22*, 16640–16651. [CrossRef] [PubMed]
105. Priatni, S.; Kosasih, W.; A Budiwati, T.; Ratnaningrum, D. Production of peptone from boso fish (Oxyeleotris marmorata) for bacterial growth medium. In *IOP Conference Series: Earth and Environmental Science*; IOP Publishing: Tangerang, Indonesia, 2017; p. 012009.
106. Upadhyay, A.; Singh, N.; Singh, R.; Rai, U. Amelioration of arsenic toxicity in rice: Comparative effect of inoculation of *Chlorella vulgaris* and *Nannochloropsis* sp. on growth, biochemical changes and arsenic uptake. *Ecotoxicol. Environ. Saf.* **2016**, *124*, 68–73. [CrossRef]
107. Gómez-Jacinto, V.; García-Barrera, T.; Gómez-Ariza, J.L.; Garbayo-Nores, I.; Vílchez-Lobato, C. Elucidation of the defence mechanism in microalgae Chlorella sorokiniana under mercury exposure. Identification of Hg–phytochelatins. *Chemi-Co-Biol. Interact.* **2015**, *238*, 82–90. [CrossRef]
108. Balaji, S.; Kalaivani, T.; Sushma, B.; Pillai, C.V.; Shalini, M.; Rajasekaran, C. Characterization of sorption sites and differ-ential stress response of microalgae isolates against tannery effluents from Ranipet industrial area—An application towards phycoremediation. *Int. J. Phytoremediat.* **2016**, *18*, 747–753. [CrossRef]
109. Devars, S.; Avilés, C.; Cervantes, C.; Moreno-Sánchez, R. Mercury uptake and removal by Euglena gracilis. *Arch. Microbiol.* **2000**, *174*, 175–180. [CrossRef] [PubMed]
110. Pradhan, P.; Costa, L.; Rybski, D.; Lucht, W.; Kropp, J.P. A systematic study of sustainable development goal (SDG) in-teractions. *Earth's Future* **2017**, *5*, 1169–1179. [CrossRef]
111. Ibuot, A.; Dean, A.P.; McIntosh, O.A.; Pittman, J.K. Metal bioremediation by CrMTP4 over-expressing Chlamydomonas reinhardtii in comparison to natural wastewater-tolerant microalgae strains. *Algal Res.* **2017**, *24*, 89–96. [CrossRef]

applied sciences

MDPI

Article

Smartphone-Based Colorimetric Detection of Chromium (VI) by Maleic Acid-Functionalized Gold Nanoparticles

Ahmed Mohamed [1], Xuemeng Li [2], Chengfei Li [2], Xuegang Li [2], Chao Yuan [2,*] and Hassan Barakat [3,4,*]

[1] Department of Biochemistry, Faculty of Agriculture, Benha University, Benha 13736, Egypt; ahmed.mohamed@fagr.bu.edu.eg
[2] College of Science, Huazhong Agricultural University, Wuhan 430070, China; xmli@mail.hzau.edu.cn (X.L.); guangqiangli@mail.hzau.edu.cn (C.L.); lixuegang@mail.hzau.edu.cn (X.L.)
[3] Department of Food Science and Human Nutrition, College of Agriculture and Veterinary Medicine, Qassim University, Buraydah 51452, Saudi Arabia
[4] Food Technology Department, Faculty of Agriculture, Benha University, Moshtohor 13736, Egypt
* Correspondence: yuanchao@mail.hzau.edu.cn (C.Y.); haa.mohamed@qu.edu.sa or hassan.barakat@fagr.bu.edu.eg (H.B.); Tel.: +86-134-371-522-58 (C.Y.); +966-547-141-277 (H.B.)

Abstract: Because of the significant environmental pollution produced by human activities, there is an ongoing need to develop transportable, simple, and reliable techniques for determining trace contaminants on the spot. This work reported a colorimetric detection method for aqueous Cr(VI) sensing by maleic acid-functionalized gold nanoparticles with high sensitivity and selectivity. The wine-red color of the probe solution can change to gray even in the presence of 1.0 μg L^{-1} of aqueous Cr(VI). Moreover, with the assistance of a smartphone installed with a commercially available color scan application software, its concentration of could be readily quantified on the spot without the help of UV-Vis spectrometer. The detection limit could reach as low as 0.1 μg L^{-1} with linear range from 0.2 to 2.0 μg L^{-1}. Most importantly, the coefficient variation of the proposed smartphone-based method was equivalent to that of colorimetry, demonstrating the high accuracy of the proposed method for accurate detection of Cr(VI) in resource-constrained countries. Conclusively, with the help of the smartphone, this nanomaterials-based probe demonstrated the potential in the field of environment monitoring for on-site quantitative detection of any pollutants in resource-constrained countries.

Keywords: Chromium; colorimetric measurement; smartphone-based detection; gold nanoparticles

Citation: Mohamed, A.; Li, X.; Li, C.; Li, X.; Yuan, C.; Barakat, H. Smartphone-Based Colorimetric Detection of Chromium (VI) by Maleic Acid-Functionalized Gold Nanoparticles. *Appl. Sci.* **2021**, *11*, 10894. https://doi.org/10.3390/app112210894

Academic Editor: Avelino Núñez-Delgado

Received: 15 October 2021
Accepted: 5 November 2021
Published: 18 November 2021

1. Introduction

As an important metal resource in the industrial community, Chromium generally exists in the natural environment in two oxidation states, VI as in CrO_4^{2-} and $Cr_2O_7^{2-}$ [1–7]. While Cr(III) plays a vital role in maintaining normal life activities [2–5,7,8], Cr(VI) is widely recognized as a highly toxic pollutant [2–4,6,7,9,10] with carcinogenic [2–5,7,8,11] and mutagenic effects [4,5,7]. Cr(VI) can cause metabolic disorders and damage to the kidney and other organs [5,10,12–16]. Fortunately, the existing methods, including atomic absorption spectroscopy, [2–4,6–10,17–20], inductively coupled plasma-mass spectrometry [7,8,10,20,21] and inductively coupled plasma-optical emission spectrometry, [7,10,22,23], could provide an extremely sensitive, selective and reliable way for the detection of Cr(III) and Cr(VI) in real samples [7]. However, these methods usually involve tedious sample preparation, expensive equipment use, and lab-based tests [2–4,6–11]. Therefore, there is always an urgent demand for the development of mobile, simple and reliable methods for rapid determination of trace Cr(VI) [2,3,8,11] and other pollutants.

Analytical methods employing Gold nanoparticles (Au NPs) include colorimetry, [6,7,24–32], surface-enhanced Raman scattering (SERS) [33,34], and surface plasmonic resonance (SPR) [7,35] offer improved performance compared to traditional methods. Some of them have already been commercialized for practical application. For

example, a portable device based on the SERS technique has been developed for on-site detection of pesticides on the surface of fruits with high selectivity and sensitivity [33]. Au NPs with rationally modified surfaces can be the base for colorimetric methods in which elaborate instrumentation is replaced by the naked eye [7,20,24–32]. Furthermore, due to their high extinction coefficient in the visible region, the Au NPs-based colorimetric method can be used to detect heavy metal ions selectively and sensitively [7,20,25,32,36–42]. For example, the Mirkin group has reported a highly selective probe for Hg^{2+} sensing, based on the strong coordination interaction between Hg^{2+} and thymine-rich DNA-functionalized Au NPs. [25] This method has a sensitivity of 20 ppb [25]. Recently, the Gao group developed a Pb^{2+} selective detection method using glutathione-modified Au NPs with a detection limit of about 10 nM [38]. However, a UV-Vis spectrometer is needed for quantitative colorimetric assays. The associated expense hampers practical use of the Au NPs-based visual detection method.

The smartphone, very portable and capable of high-resolution imaging, is a natural candidate for a powerful and convenient point-of-care analytical device. Specifically, smartphone-based colorimetric methods for environmental monitoring of heavy metal ions have been reported [2,11,43–53]. Herein, we describe an Au NPs-based colorimetric method for the detection of aqueous Cr(VI). Our assay involves an aggregation-induced color change of functionalized Au NPs in the presence of aqueous Cr(VI) (Figure 1). As we will show, with a color scan application, the smartphone can easily uncover nuances of color in solutions that the naked eye can not observe. Like the UV-Vis spectrophotometer a smartphone can quantify Cr(VI) in aqueous solution. Its detection limit can be as low as 0.1 μg L^{-1}.

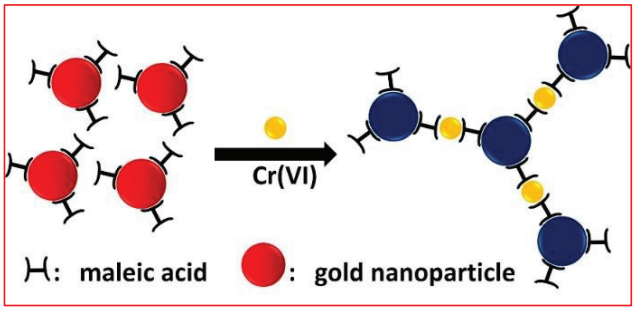

Figure 1. Color change of maleic acid-capped gold nanoparticles induced by Cr(VI).

2. Materials and Methods

2.1. Chemicals

Chloroauric acid hydrate ($HAuCl_4 \cdot 4H_2O$) and sodium citrate were obtained from Shanghai Reagent (analytical grade). Maleic acid (MA), various metal salts (Ba^{2+}, Ca^{2+}, Cd^{2+}, Co^{2+}, Cu^{2+}, Cr(III), $Cr_2O_7^{2-}$, Mg^{2+}, Mn^{2+}, Ni^{2+}, Pb^{2+}, Zn^{2+} and Al^{3+}) were obtained from Sinopharm Chemical Reagent. All chemicals used in the experiment were used as received without further purification, and solutions were prepared using high purity water purified through a Millipore system with a resistance of 18 MΩ cm^{-1}. All glassware was thoroughly cleaned with freshly prepared 3:1 HCl/HNO_3 and rinsed with high purity water before use.

2.2. Preparation and Functionalization of Au NPs

Au NPs were synthesized according to the classic citrate-mediated reduction method [54]. Briefly, 50 mL of water containing 1 mM of $HAuCl_4$ was heated to a boil under vigorous stirring, and 2 mL of 1% sodium citrate solution was then injected into boiling solution. After another 20 min of reaction, the boiling solution was allowed to cool down to room temperature under stirring. Finally, the obtained wine-red Au NPs colloid solution was

stored at 4 °C for further use. For the functionalization, 1 mL of citrate-capped Au NPs was mixed with C maleic acid (MA) under stirring, and the mixture was allowed to stir for 2 h at room temperature under rotation. The MA-functionalized Au NPs were then purified by centrifugation and the purified and functionalized Au NPs were then dissolved in 1 mL of ultrapure water for storage as the probe solution. For storage more than 2 months, the probe should be dispersed in 1 mL of DI water containing 0.1 mM maleic acid at 4 °C. The concentration of obtained MA-capped Au NPs was determined by its absorption at 525 nm with an extinction coefficient of 2.7×10^8 L·mol^{-1}·cm^{-1}.

2.3. Detection of Aqueous Cr(VI) by MA-Capped Au NPs

Briefly, 10 μL samples of Cr(VI) or other metal ion solutions including Ba^{2+}, Ca^{2+}, Cd^{2+}, Co^{2+}, Cu^{2+}, Cr(III), Mg^{2+}, Mn^{2+}, Ni^{2+}, Pb^{2+}, Zn^{2+}, and Al^{3+} stock solution prepared in water were added into 1 mL of MA-capped Au NPs and mixed thoroughly for 2 min by a pipette. A UV-Vis spectrophotometer was then used to collect the absorption spectrum of the solution. A smartphone equipped with color scan application software (ColorAssist Ver. 2.4, 2020 from Apple Store) was used to take the MA-capped Au NPs solution photo at room temperature. Typically, for photograph acquiring, the vial should be placed on a white paper together with white background, and glare should be avoided by changing the photographing direction. The camera should be parallel to the vial, and the distance can be adjusted according to the square pattern displayed by the app software; one need not adjust amount. The square pattern should just cover the whole transverse part of the vial. For real sample detection by the smartphone-based colorimetric method, aqueous samples collected from three local lakes (South Lake, Tangxun Lake, and Yezi Lake) were first filtered by a 0.22 μm Super filter. Atomic Absorption Spectroscopy method was then used to measure the absolute concentration of Cr(VI) in the three samples. As for smartphone sensing, 10 μL of the sample was added to 1 mL of MA-capped Au NPs, and the mixture was allowed to react for 2 min before photographing. Each measurement was done three times, and the average was presented with its standard deviation.

2.4. Characterization

The aggregation response of Au NPs after interaction with Cr(VI) was obtained by transmission electron microscopy (TEM, JEOL 2010, Tokyo, Japan) at an accelerating voltage of 200 kV. The absorption spectra of the colloid before and after interaction with metal ions were collected using a Shimadzu UV-2550 spectrometer (Shimadzu, Kyoto, Japan). A Canon-350D digital camera (Canon, Tokyo, Japan) takes optical photographs.

3. Results

3.1. Selectivity and Sensitivity Investigation of MA-Capped Au NPs to Aqueous Cr(VI)

The molecules used for Au NPs modification to effect colorimetric assays for heavy metal ions [7,32,55–57] all have carboxylic acid groups. Examples include 5,5-dithiobis(2-nitrobenzoic acid), [55] 1,4-dithiothreitol [56] and 5-thio-(2-nitrobenzoic acid) [57] can be used as the capping reagent for Cr(III) or Cr(VI) sensing. We used maleic acid (MA), another organic acid containing two carboxylic groups, was then used as the capping reagent for the functionalization of Au NPs. By incubating MA with citrate-prepared Au NPs for 2 h under rotation, MA-capped Au NPs could be obtained; MA at high concentration displaces the citrate. We compared the absorption spectra and aggregation response for Au NPs before and after MA functionalization, in the presence of a range of metal ions. See Figure 2A–C. While the citrate-bearing Au NPs solution showed poor selectivity to the metal ions, MA-treated Au NPs exhibited a highly selective response to Cr(VI) over other metal ions tested. As can be seen in Figure 2C, Ba^{2+}, Ca^{2+}, Cd^{2+}, Co^{2+}, Cu^{2+}, Cr(III), Mg^{2+}, Mn^{2+}, Ni^{2+}, Pb^{2+}, Zn^{2+}, and Al^{3+} can not cause a significant effect on the color of MA-capped Au NPs solution, while an obvious color change could occur in the presence of Cr(VI) at a concentration of 1.0 μg L^{-1}. We further recorded the UV-Vis spectra response of MA-capped Au NPs in the presence of different metal ions, which could further display the

excellent selectivity of our probe for aqueous Cr(VI) (Figure 2D,E). Our probe selectivity was found to be working well as well as the methods described by Kim et al., Xue et al., and Mao et al. [6,7,10]. Moreover, TEM images of MA-capped Au NPs in the presence and absence of Cr(VI) further confirmed their aggregation phenomenon induced by Cr(VI) (Figure 2F,G).

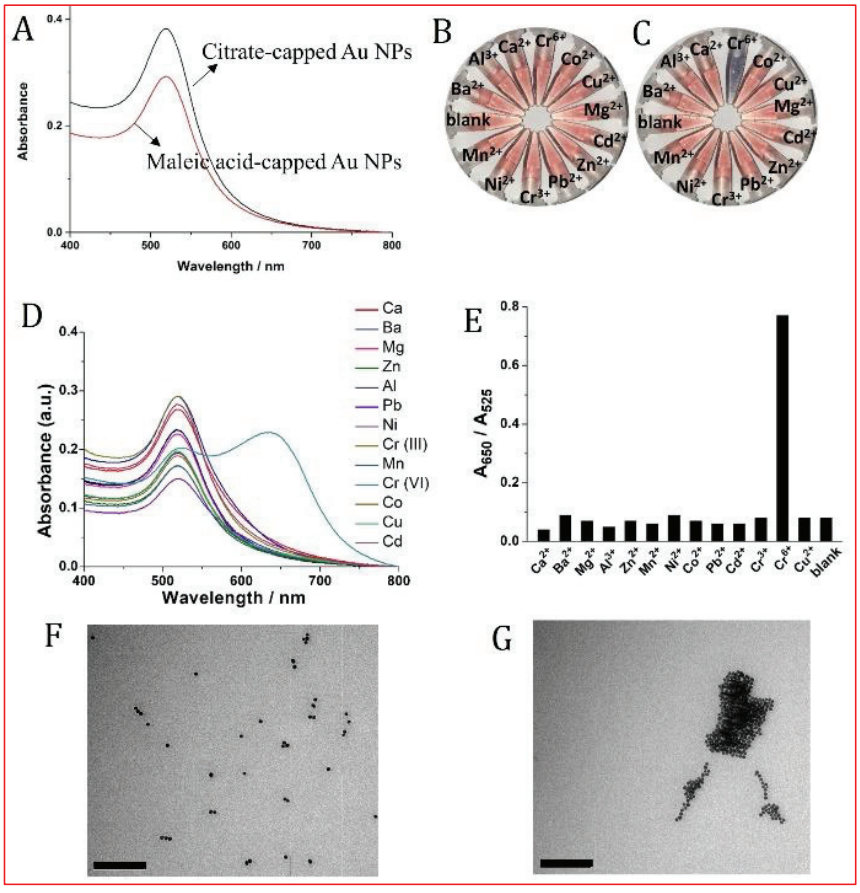

Figure 2. UV-Vis absorption spectra of citrate- and maleic acid-capped Au NPs (**A**). Optical responses of citrate-capped (**B**) and MA-capped (**C**) Au NPs to various metal ions, all the concentrations of metal ions are 1.0 μg L^{-1}. (**D**) UV-Vis spectra of MA-capped Au NPs in the presence of various metal ions and the corresponding A 650/A525 responses for those metal ions (**E**). (**F**,**G**) are the TEM images of MA-capped Au NPs in the absence and presence of 10 μg L^{-1} Cr(VI), respectively. Both of the two-scale bars are 200 nm.

The selectivity of our probe to Cr(VI) could be ascribed to the hypothesis that Cr(VI), existing in the form of $Cr_2O_7^{2-}$, could coordinate with the carboxyl group from maleic acid through hydrogen bond in an energetically favorable manner. In addition, this discrimination between Cr(VI) and Cr(III) could be ascribed to surface oxidation reaction between maleic acid and $Cr_2O_7^{2-}$ because of the strong oxidization ability of $Cr_2O_7^{2-}$. Figure 3A,B show the evolution of color and absorbance spectra after adding 10 μL of different concentrations of aqueous Cr(VI) into MA-capped Au NPs. A change in color already discernable by the naked eye is evident already at a concentration as low as 0.4 μg L^{-1} by the naked eye. According to Figure 3B, the absorption intensity at 520 nm declines and the

intensity at 650 nm grows as the concentration of Cr(VI) increases. Figure 3C shows plots of the absorption intensity ratio A650/A520 against the concentration of aqueous Cr(VI). Below about 2 μg L^{-1}, the limit beyond which the response reaches saturation, the plot is linear, described by the regression line (y = 0.40089 + 0.31557x) with a 0.94045 correlation coefficient (inset).

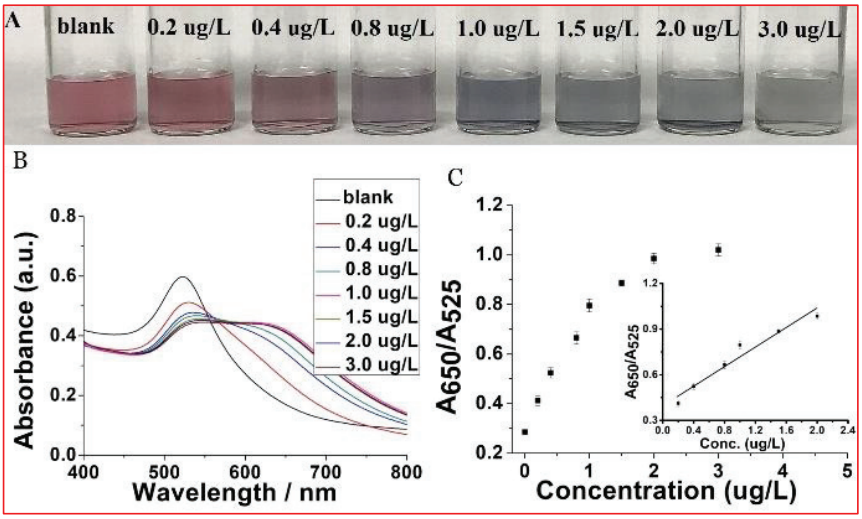

Figure 3. (**A**) Optical response of MA-capped Au NPs in the presence of different concentrations of Cr(VI) and their corresponding UV-Vis spectra (**B**). (**C**) The dose-response curve for Cr(VI) detection and the insert within is the linear calibration plot for Cr(VI) in the range of 0.2 to 2.0 μg L^{-1}.

3.2. Smartphone-Based Colorimetric Assay

The expensive, delicate, and costly UV-Vis spectrometer is not appropriate for on-site application. The portable, inexpensive, and sturdy smartphone is more suitable for point-of-care sensors [2,11], especially in resource-constrained countries. Therefore, we carried out the experiment assay with the help of a smartphone equipped with a color scan application software (ColorAssist), specially designed for photo analysis instead of a UV-Vis spectrometer. After taking, The software can analyze a photo of the MA-capped Au NPs solution producing a color card and RGB (red, green, and blue) values. As we know, colorimetry is a method that is used to determine the concentration of colored compound in solution by the application of the Beer-Lambert law, which is highly dependent on the use of UV-Vis spectrometer. Unlike colorimetry, RGB, as three primary of light, has been widely used in the field of image display since any color could be decoded by RGB value. The RGB components of light can represent any color, as shown in Figure 4. Small differences in the color of solutions of MA-capped Au NPs with different concentration of target could also be reflected by the ratio of green to red values displayed on the screen. Figure 5 shows that the ratio of green to red can be used to establish a correlation with Cr(VI) concentration. A linear calibration curve (y = 0.48297 + 0.49794x) was obtained and showed good linearity with a correlation coefficient of 0.99036 in the concentration range of 0.2 μg L^{-1} to 1 μg L^{-1}. The detection limit could reach as low as 0.1 μg L^{-1} based on the definition of three times the deviation of the blank signal (3 σ). Our detection limit was found to be very near to the limitations which were reported by Yingying Qi et al. (0.52 μg L^{-1}), Xiaolan Chen et al. (0.26 μg L^{-1}), and Kim et al. (0.4 μM) [2,7,32]. However, our detection limit was found to be more reliable than the method reported by Sushant D. Bamane et al. (1.3–11.6 μg L^{-1}) [11].

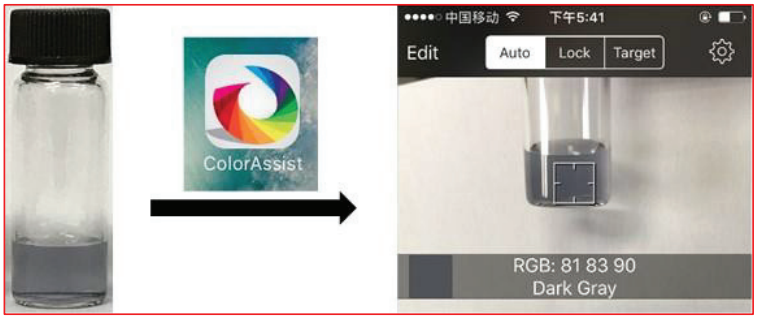

Figure 4. Photography showing the whole detection procedure by a smartphone pre-installed with the color scan application software ColorAssist. The color card and color values of RGB can be displayed on the screen simultaneously once the solution is placed in the scope that the smartphone's camera can photograph.

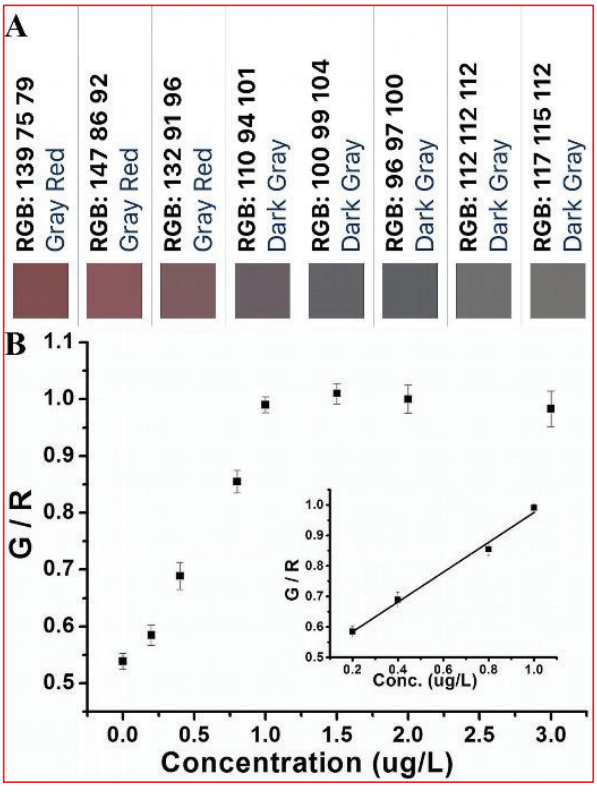

Figure 5. (**A**) Color cards of the solutions shown in Figure 2A obtained by a smartphone installed with a color scan application software. (**B**) Dose-response curve for Cr(VI) detection (G/R ratio vs. Cr(VI)) and the insert within is the linear calibration plot for Cr(VI) in the range of 0.2 to 1.0 μg L^{-1}.

3.3. Real Sample Detection Based on Smartphone Sensor

Samples collected from three local lakes were used to investigate the performance of our smartphone-based colorimetric method. The absolute concentrations of Cr(VI) in the three samples were measured by the traditional Atomic Absorption Spectroscopy (AAS) method. The samples were filtered through a 0.22 μm Super filter to remove any

particulate suspension before the Cr(VI) determination. As revealed by the results in Table 1, one can find that the concentrations of Cr(VI) in all the three lakes were in the detection range of our MA-capped Au NPs sensor, suggesting the samples could be used directly to interrogate the performance of our probe. As expected, the results obtained by the smartphone were consistent with the data obtained by AAS, suggesting the impurities within the samples did not cause serious interference for Cr(VI) detection in real samples collected. Compared to the AAS results, the recovery rate of our smartphone-based method for Cr(VI) detection was in the range of 84.9% to 115.8%. In addition, analytical precision was compared by analyzing the coefficient variations for UV-Vis and the proposed method, which revealed that the precision of smartphone-based assay was equivalent to that of colorimetry, demonstrating the potential of the proposed method for accurate detection of analyte in real world.

Table 1. Recovery test of Cr(VI) in a real water sample collected from three local lakes by the smartphone-based method and its coefficient variation comparison with conventional UV-Vis spectrometer [a].

Sample [b]	The Concentration of Cr(VI) ($\mu g\ L^{-1}$)		
	AAS Method	UV-Vis Method/CV	Smartphone/CV
South lake	1.01 ± 0.03	$0.95 \pm 0.06/12.43\%$	$1.08 \pm 0.04/14.48\%$
Yezhi lake	0.91 ± 0.04	$0.96 \pm 0.02/13.67\%$	$1.06 \pm 0.03/14.52\%$
Tangxun lake	1.04 ± 0.04	$1.00 \pm 0.03/12.28\%$	$0.88 \pm 0.02/13.88\%$

[a] Values shown were the calculated mean Cr(VI) concentration for each sample and were determined from three replicates. [b] all the sample were collected from the local lakes in Hongshan District of Wuhan city, China.

4. Conclusions

In this work, an MA-capped Au NPs based colorimetric method was developed for the rapid detection of aqueous Cr(VI) with high sensitivity and selectivity. The response of our probe to aqueous Cr(VI) could be simply observed with a color change from wine-red to gray, and the limit of detection could reach as low as 0.4 $\mu g\ L^{-1}$ by the naked eye. Moreover, with the help of a smartphone equipped with a color scan application software, Cr(VI) could be quantified on-site in a simple, portable, reliable, and rapid manner and detection liner range from 0.2 to 1.0 $\mu g\ L^{-1}$ with a detection limit as low as 0.1 $\mu g\ L^{-1}$. The coefficient variations obtained by the proposed method is comparable to that of conventional UV-Vis spectrometer, demonstrating the potential of the proposed method in heavy metal ion detection on site in resource-constrained countries. In the future, it is believed that assays in decentralized studies could be dramatically improved if smartphone were to be integrated with more powerful software for data collection. In addition, the proposed method reported here could potentially be adapted for the detection of any environmental pollutants as long as coordination reagents against it were available, therefore making smartphone-based method a versatile tool for environmental monitoring. Furthermore, this methodology is not confined to colorimetric assay, fluorescence-based assay combined with smartphone seems to be more suitable for on-site detection in real world from the perspective of detection sensitivity, which has been already intensely reported with high accuracy and sensitivity in the past decade.

Author Contributions: Conceptualization, A.M. and C.Y.; methodology, A.M., X.L. (Xuemeng Li) and C.L.; software, C.Y. and X.L. (Xuegang Li); validation, A.M., C.Y. and H.B.; formal analysis, A.M., X.L. (Xuemeng Li) and C.L.; investigation, A.M., X.L. (Xuemeng Li), C.L., C.Y., X.L. (Xuegang Li) and H.B.; data curation, A.M., X.L. (Xuemeng Li), C.L. and C.Y.; writing—original draft preparation, A.M. and C.Y.; writing—review and editing, A.M. and H.B.; visualization, A.M. and C.Y.; supervision, C.Y.; project administration, C.Y. and H.B.; funding acquisition, C.Y. and H.B. All authors have read and agreed to the published version of the manuscript.

Funding: This research received no external funding.

Institutional Review Board Statement: Not applicable.

Informed Consent Statement: Not applicable.

Data Availability Statement: The data presented in this study are available on request from the corresponding author.

Acknowledgments: Thanks to Carl Trindle of the University of Virginia for revising the English language for our paper.

Conflicts of Interest: The authors declare no conflict of interest.

References

1. Barceloux, D.G. Chromium. *Clin. Toxicol.* **1999**, *37*, 173–194. [CrossRef] [PubMed]
2. Chen, X.; Ma, C.; Kang, Q.; Chen, Y.; Shen, D. Field analysis of Cr(vi) in water samples by using a smartphone-based ultralong absorption path reflection colorimetric device. *New J. Chem.* **2021**, *45*, 2529–2535. [CrossRef]
3. Kumar, N.; Madhwal, D.; Jain, V.K.; Suman, A. POC device for on-the-spot detection of hexavalent chromium in wastewater. *J. Environ. Chem. Eng.* **2020**, *8*, 104342. [CrossRef]
4. Alula, M.T.; Madingwane, M.L. Colorimetric quantification of chromium(VI) ions based on oxidoreductase-like activity of Fe_3O_4. *Sens. Actuators B Chem.* **2020**, *324*, 128726. [CrossRef]
5. Zhai, H.M.; Zhou, T.; Fang, F.; Wu, Z.Y. Colorimetric speciation of Cr on paper-based analytical devices based on field amplified stacking. *Talanta* **2020**, *210*, 120635. [CrossRef]
6. Xue, Q.; Li, X.; Peng, Y.; Liu, P.; Peng, H.; Niu, X. Polyethylenimine-stabilized silver nanoclusters act as an oxidoreductase mimic for colorimetric determination of chromium(VI). *Mikrochim. Acta* **2020**, *187*, 263. [CrossRef] [PubMed]
7. Kim, D.; Choi, E.; Lee, C.; Choi, Y.; Kim, H.; Yu, T.; Piao, Y. Highly sensitive and selective visual detection of Cr(VI) ions based on etching of silver-coated gold nanorods. *Nano Converg.* **2019**, *6*, 34. [CrossRef]
8. Nghia, N.N.; Huy, B.T.; Lee, Y.I. Colorimetric detection of chromium(VI) using graphene oxide nanoparticles acting as a peroxidase mimetic catalyst and 8-hydroxyquinoline as an inhibitor. *Mikrochim. Acta* **2018**, *186*, 36. [CrossRef]
9. Ghayyem, S.; Swaidan, A.; Barras, A.; Dolci, M.; Faridbod, F.; Szunerits, S.; Boukherroub, R. Colorimetric detection of chromium(VI) ion using poly(*N*-phenylglycine) nanoparticles acting as a peroxidase mimetic catalyst. *Talanta* **2021**, *226*, 122082. [CrossRef]
10. Mao, Y.; Gao, S.; Yao, L.; Wang, L.; Qu, H.; Wu, Y.; Chen, Y.; Zheng, L. Single-atom nanozyme enabled fast and highly sensitive colorimetric detection of Cr(VI). *J. Hazard. Mater.* **2021**, *408*, 124898. [CrossRef]
11. Bamane, S.D.; Bhojwani, V.; Balkunde, P.L.; Bhattacharya, M.; Gupta, I.; Mohapatra, A.K.; Shekhar, A.; Singh, A. Smartphone-enabled field monitoring tool for rapid hexavalent chromium detection in water. *Anal. Bioanal. Chem.* **2021**, *413*, 3455–3469. [CrossRef] [PubMed]
12. Bagchi, D.; Stohs, J.S.; Downs, B.W.; Bagchi, M.; Preuss, H.G. Cytotoxicity and oxidative mechanisms of different forms of chromium. *Toxicology* **2002**, *180*, 5–22. [CrossRef]
13. Zhitkovich, A. Importance of Chromium-DNA Adducts in Mutagenicity and Toxicity of Chromium(VI). *Chem. Res. Toxicol.* **2005**, *18*, 3–11. [CrossRef] [PubMed]
14. Holmes, A.L.; Wise, S.S.; Wise, J.R. Carcinogenicity of hexavalent chromium. *Indian J. Med. Res.* **2008**, *128*, 353–372. [PubMed]
15. Costa, M.; Klein, C.B. Toxicity and Carcinogenicity of Chromium Compounds in Humans. *Crit. Rev. Toxicol.* **2008**, *36*, 155–163. [CrossRef] [PubMed]
16. Patlolla, A.K.; Barnes, C.; Yedjou, C.; Velma, V.R.; Tchounwou, P.B. Oxidative stress, DNA damage, and antioxidant enzyme activity induced by hexavalent chromium in Sprague-Dawley rats. *Environ. Toxicol.* **2009**, *24*, 66–73. [CrossRef] [PubMed]
17. Kiran, K.; Kumar, K.S.; Prasad, B.; Suvardhan, K.; Lekkala, R.B.; Janardhanam, K. Speciation determination of chromium(III) and (VI) using preconcentration cloud point extraction with flame atomic absorption spectrometry (FAAS). *J. Hazard Mater.* **2008**, *150*, 582–586. [CrossRef]
18. Wang, J.; Hansen, E.H. Coupling on-line preconcentration by ion-exchange with ETAAS A novel flow injection approach based on the use of a renewable microcolumn as demonstrated for the determination of nickel in environmental and biological samples. *Anal. Chim. Acta* **2000**, *424*, 223–232. [CrossRef]
19. Cordero, M.T.S.; Alonso, E.I.V.; de Torres, A.G.; Pavón, J.M.C. Development of a new system for the speciation of chromium in natural waters and human urine samples by combining ion exchange and ETA-AAS. *J. Anal. At. Spectrom.* **2004**, *19*, 398–403. [CrossRef]
20. Ejeta, S.Y.; Imae, T. Selective colorimetric and electrochemical detections of Cr(III) pollutant in water on 3-mercaptopropionic acid-functionalized gold plasmon nanoparticles. *Anal. Chim. Acta* **2021**, *1152*, 338272. [CrossRef]
21. Wen, B.; Shan, X.Q.; Lian, J. Separation of Cr(III) and Cr(VI) in river and reservoir water with 8-hydroxyquinoline immobilized polyacrylonitrile fiber for determination by inductively coupled plasma mass spectrometry. *Talanta* **2002**, *56*, 681–687. [CrossRef]
22. Menegário, A.A.; Smichowski, P.; Polla, G. On-line preconcentration and speciation analysis of Cr(III) and Cr(VI) using baker′s yeast cells immobilised on controlled pore glass. *Anal. Chim. Acta* **2005**, *546*, 244–250. [CrossRef]

23. Manzoori, J.L.; Shemirani, F. Determination of chromium(vi) and total chromium by inductively coupled plasma atomic emission spectrometry after preconcentration using solvent extraction and back-extraction. *J. Anal. At. Spectrom.* **1995**, *10*, 881–883. [CrossRef]
24. Rosi, N.L.; Mirkin, C.A. Nanostructures in biodiagnostics. *Chem. Rev.* **2005**, *105*, 1547–1562. [CrossRef] [PubMed]
25. Lee, J.S.; Han, M.S.; Mirkin, C.A. Colorimetric detection of mercuric ion (Hg^{2+}) in aqueous media using DNA-functionalized gold nanoparticles. *Angew. Chem.* **2007**, *46*, 4093–4096. [CrossRef] [PubMed]
26. Jiang, Y.; Zhao, H.; Lin, Y.; Zhu, N.; Ma, Y.; Mao, L. Colorimetric detection of glucose in rat brain using gold nanoparticles. *Angew. Chem.* **2010**, *49*, 4800–4804. [CrossRef]
27. Xu, X.; Han, M.S.; Mirkin, C.A. A gold-nanoparticle-based real-time colorimetric screening method for endonuclease activity and inhibition. *Angew. Chem.* **2007**, *46*, 3468–3470. [CrossRef]
28. Xu, S.; Ouyang, W.; Xie, P.; Lin, Y.; Qiu, B.; Lin, Z.; Chen, G.; Guo, L. Highly uniform gold nanobipyramids for ultrasensitive colorimetric detection of influenza virus. *Anal. Chem.* **2017**, *89*, 1617–1623. [CrossRef] [PubMed]
29. Zhang, Y.; Shen, H.Y.; Hai, X.; Chen, X.W.; Wang, J.H. Polyhedral oligomeric silsesquioxane polymer-caged silver nanoparticle as a smart colorimetric probe for the detection of hydrogen sulfide. *Anal. Chem.* **2017**, *89*, 1346–1352. [CrossRef]
30. Du, B.; Su, X.; Yang, K.; Pan, L.; Liu, Q.; Gong, L.; Wang, P.; Yang, J.; He, Y. Antibody-Free Colorimetric Detection of Total Aflatoxins in Rice Based on a Simple Two-Step Chromogenic Reaction. *Anal. Chem* **2016**, *88*, 3775–3780. [CrossRef]
31. Li, L.; Zhang, Y.; Zhang, L.; Ge, S.; Liu, H.; Ren, N.; Yan, M.; Yu, J. Paper-based device for colorimetric and photoelectrochemical quantification of the flux of H2O2 releasing from MCF-7 cancer cells. *Anal. Chem.* **2016**, *88*, 5369–5377. [CrossRef] [PubMed]
32. Qi, Y.; Ma, J.; Xiu, F.R.; Gao, X. Determination of Cr(VI) based on the peroxidase mimetic catalytic activity of citrate-capped gold nanoparticles. *Mikrochim. Acta* **2021**, *188*, 273. [CrossRef] [PubMed]
33. Li, J.F.; Huang, Y.F.; Ding, Y.; Yang, Z.L.; Li, S.B.; Zhou, X.S.; Fan, F.R.; Zhang, W.; Zhou, Z.Y.; Wu, D.Y.; et al. Shell-isolated nanoparticle-enhanced Raman spectroscopy. *Nature* **2010**, *464*, 392–395. [CrossRef]
34. Bodelon, G.; Montes-Garcia, V.; Lopez-Puente, V.; Hill, E.H.; Hamon, C.; Sanz-Ortiz, M.N.; Rodal-Cedeira, S.; Costas, C.; Celiksoy, S.; Perez-Juste, I.; et al. Detection and imaging of quorum sensing in Pseudomonas aeruginosa biofilm communities by surface-enhanced resonance Raman scattering. *Nat. Mater.* **2016**, *15*, 1203–1211. [CrossRef] [PubMed]
35. Mayer, K.M.; Hafner, J.H. Localized surface plasmon resonance sensors. *Chem. Rev.* **2011**, *111*, 3828–3857. [CrossRef] [PubMed]
36. Cao, G.; Xu, F.; Wang, S.; Xu, K.; Hou, X.; Wu, P. Gold nanoparticle-based colorimetric assay for selenium detection via hydride generation. *Anal. Chem.* **2017**, *89*, 4695–4700. [CrossRef]
37. Gao, Z.; Liu, G.G.; Ye, H.; Rauschendorfer, R.; Tang, D.; Xia, X. Facile colorimetric detection of silver ions with picomolar sensitivity. *Anal. Chem.* **2017**, *89*, 3622–3629. [CrossRef] [PubMed]
38. Yu, Y.; Hong, Y.; Gao, P.; Nazeeruddin, M.K. Glutathione modified gold nanoparticles for sensitive colorimetric detection of pb(2+) ions in rainwater polluted by leaking perovskite solar cells. *Anal. Chem.* **2016**, *88*, 12316–12322. [CrossRef]
39. Chai, F.; Wang, C.; Wang, T.; Li, L.; Su, Z. Colorimetric detection of Pb^{2+} using glutathione functionalized gold nanoparticles. *ACS Appl. Mater. Interfaces* **2010**, *2*, 1466–1470. [CrossRef]
40. Durgadas, C.V.; Lakshmi, V.N.; Sharma, C.P.; Sreenivasan, K. Sensing of lead ions using glutathione mediated end to end assembled gold nanorod chains. *Sens. Actuators B Chem.* **2011**, *156*, 791–797. [CrossRef]
41. Zhang, H.; Liu, Q.; Wang, T.; Yun, Z.; Li, G.; Liu, J.; Jiang, G. Facile preparation of glutathione-stabilized gold nanoclusters for selective determination of chromium (III) and chromium(VI) in environmental water samples. *Anal. Chim. Acta* **2013**, *770*, 140–146. [CrossRef] [PubMed]
42. Sung, H.K.; Oh, S.Y.; Park, C.; Kim, Y. Colorimetric detection of Co2+ ion using silver nanoparticles with spherical, plate, and rod shapes. *Langmuir* **2013**, *29*, 8978–8982. [CrossRef] [PubMed]
43. Wang, X.; Chang, T.W.; Lin, G.; Gartia, M.R.; Liu, G.L. Self-referenced smartphone-based nanoplasmonic imaging platform for colorimetric biochemical sensing. *Anal. Chem.* **2017**, *89*, 611–615. [CrossRef]
44. Wang, L.J.; Sun, R.; Vasile, T.; Chang, Y.C.; Li, L. high-throughput optical sensing immunoassays on smartphone. *Anal. Chem.* **2016**, *88*, 8302–8308. [CrossRef] [PubMed]
45. Rico-Yuste, A.; Gonzalez-Vallejo, V.; Benito-Pena, E.; de Las Casas Engel, T.; Orellana, G.; Moreno-Bondi, M.C. Furfural determination with disposable polymer films and smartphone-based colorimetry for beer freshness assessment. *Anal. Chem.* **2016**, *88*, 3959–3966. [CrossRef]
46. Zhang, L.; Yang, W.; Yang, Y.; Liu, H.; Gu, Z. Smartphone-based point-of-care testing of salivary alpha-amylase for personal psychological measurement. *Analyst* **2015**, *140*, 7399–7406. [CrossRef] [PubMed]
47. Nie, H.; Wang, W.; Li, W.; Nie, Z.; Yao, S. A colorimetric and smartphone readable method for uracil-DNA glycosylase detection based on the target-triggered formation of G-quadruplex. *Analyst* **2015**, *140*, 2771–2777. [CrossRef]
48. Abbas, M.; Hasan, B.; Sasan, A.; Nasim, F.; Abbas, A. New portable smartphone-based PDMS microfluidic kit for the simultaneous colorimetric detection of arsenic and mercury. *RSC Adv.* **2018**, *8*, 27091–27100. [CrossRef]
49. Ying, G.; Tao, L.; Qiongwen, H.; Longjie, Z.; Xinyi, W.; Hao, W.; Ping, W. In-situ detection of cadmium with aptamer functionalized gold nanoparticles based on smartphone-based colorimetric system. *Talanta* **2020**, *208*, 120231.
50. Mohd, F.S.; Soocheol, K.; Hyoil, J.; Taeho, K.; Chulmin, J.; Seungkyung, P. Miniaturized Sample Preparation and Rapid Detection of Arsenite in Contaminated Soil Using a Smartphone. *Sensors* **2018**, *18*, 777. [CrossRef]

51. Supattra, M.; Siriwan, T. On-site detection of heavy metals in wastewater using a single paper strip integrated with a smartphone. *Anal. Bioanal. Chem.* **2020**, *412*, 1395–1405.
52. Yuanyuan, C.; Yingnan, L.; Fan, L.; Shuwen, G.; Yuhang, S.; Hanyue, X.; Li, W. Portable colorimetric detection of copper ion in drinking water via red beet pigment and smartphone. *Microchem. J.* **2019**, *150*, 104176.
53. Mohd, F.S.; Zeeshan, A.K.; Hyoil, J.; Seungkyung, P. SPE based soil processing and aptasensor integrated detection system for rapid on site screening of arsenic contamination in soil. *Ecotoxicol. Environ. Saf.* **2020**, *196*, 110559.
54. Chen, W.; Cao, F.; Zheng, W.; Tian, Y.; Xianyu, Y.; Xu, P.; Zhang, W.; Wang, Z.; Deng, K.; Jiang, X. Detection of the nanomolar level of total Cr[(iii) and (vi)] by functionalized gold nanoparticles and a smartphone with the assistance of theoretical calculation models. *Nanoscale* **2015**, *7*, 2042–2049. [CrossRef]
55. Dang, Y.Q.; Li, H.W.; Wang, B.; Li, L.; Wu, Y. Selective detection of trace Cr3+ in aqueous solution by using 5,5′-dithiobis (2-nitrobenzoic acid)-modified gold nanoparticles. *ACS Appl. Mater. Interfaces* **2009**, *1*, 1533–1538. [CrossRef]
56. Tan, F.; Liu, X.; Quan, X.; Chen, J.; Li, X.; Zhao, H. Selective detection of nanomolar Cr(vi) in aqueous solution based on 1,4-dithiothreitol functionalized gold nanoparticles. *Anal. Methods* **2011**, *3*, 343–347. [CrossRef] [PubMed]
57. Lai, Y.J.; Tseng, W.L. Role of 5-thio-(2-nitrobenzoic acid)-capped gold nanoparticles in the sensing of chromium(vi): Remover and sensor. *Analyst* **2011**, *136*, 2712–2717. [CrossRef] [PubMed]

materials

MDPI

Article

Study on the Mechanical and Leaching Characteristics of Permeable Reactive Barrier Waste Solidified by Cement-Based Materials

Xuan Chen [1], Wenkui Feng [1], Hao Wen [2], Wei Duan [1], Chongxian Suo [1], Mingxing Xie [1] and Xiaoqiang Dong [1,*]

[1] College of Civil Engineering, Taiyuan University of Technology, Taiyuan 030024, China; c13546341719@163.com (X.C.); f15513682175@163.com (W.F.); duanwei@tyut.edu.cn (W.D.); Suochongxian0053@link.tyut.edu.cn (C.S.); star7822378@163.com (M.X.)

[2] School of Civil Engineering, Southwest Jiaotong University, Chengdu 610031, China; wenha0@yeah.net

* Correspondence: dongxiaoqiang@tyut.edu.cn

Abstract: The durability against wet-dry (w-d) cycles is an important parameter for the service life design of solidified permeable reactive barrier (PRB) waste. This study introduces the potential use of cement, fly ash, and carbide slag (CFC) for the stabilization/solidification (S/S) of PRB waste. In this study, solidified PRB waste was subjected to different w-d cycles ranging in times from 0 to 10. By analyzing the mass loss, the unconfined compressive strength (UCS), initial resistivity (IR), and the Mn^{2+} leaching concentration under different durability conditions, the results demonstrate that these variables increased and then tended to decrease with the number of w-d cycles. The UCS of contaminated soil is significantly correlated with IR. Moreover, scanning electron microscopy (SEM), energy dispersive spectroscopy (EDS), and X-ray diffraction (XRD) analyses indicate that the hydration products calcium silicate hydrate (C-S-H) and ettringite (AFt) are the main reasons for the enhancement of the UCS. However, the increase in Mn^{2+} concentration leads to a decrease in hydration products and the compactness of solidified soil, which has negative effects for the UCS and the leaching ion concentration. In general, the durability exhibited by the PRB waste treated with S/S in this paper was satisfactory. This study can provide theoretical guidance for practical engineering applications.

Keywords: PRB waste; wet-dry cycle; unconfined compressive strength; initial resistivity; leaching characteristics; microstructural characteristics

Citation: Chen, X.; Feng, W.; Wen, H.; Duan, W.; Suo, C.; Xie, M.; Dong, X. Study on the Mechanical and Leaching Characteristics of Permeable Reactive Barrier Waste Solidified by Cement-Based Materials. *Materials* **2021**, *14*, 6985. https://doi.org/10.3390/ma14226985

Academic Editor: Avelino Núñez-Delgado

Received: 13 October 2021
Accepted: 4 November 2021
Published: 18 November 2021

Publisher's Note: MDPI stays neutral with regard to jurisdictional claims in published maps and institutional affiliations.

1. Introduction

Acid mine drainage (AMD) is caused by the oxidation of sulfide minerals after being exposed to oxygen and water, which remains a serious environmental challenge for the mining industry [1,2]. Manganese is a major contaminant in AMD. Its toxicity is correlated with kidney, lung, and intestinal damage, and its chemical compounds can legitimately be predicted to be carcinogenic [3]. Numerous studies have been conducted by various experts and scholars on the safe disposal of manganese associated with acid mine drainage [2,4,5]. Permeable reactive barrier (PRB) technology is the most visible and influential [6,7]. PRBs can be used as removable, semipermanent, or permanent devices [8]. PRBs can eliminate heavy metal ions found in acid mine drainage to a tune of more than 95% [9,10]. PRB reaction materials are generally carbon/zero-valent iron (ZVI combination) [11], fly ash [12], red mud [13,14], or a mixture of various materials [15,16]. However, due to the active material's reactivity, durability, and site limits, the active material must be changed regularly. Additionally, because the heavy metal ions in PRB waste are in high quantities, removing the replacement material constitutes a new management concern.

In recent years, solidification/stabilization technology (S/S technology) has been more popular as a proven remediation solution for polluted sites and solid waste landfills [17].

Ordinary Portland cement is commonly employed as the fundamental cementitious material component in S/S technology because of its great strength, durability, and availability [18]. However, because the cement production process accounts for 5–10% of worldwide anthropogenic emissions, the cement industry must produce environmentally friendly, low-carbon, and effective cementitious materials for soil restoration in new and sustainable ways [19,20]. As a result, in the soil consolidation process, alternative materials such as fly ash, blast furnace slag, geopolymers, and activated magnesium oxide are utilized as partial or total alternatives for silicate cement [21]. When mixed with cement, these alkaline solid wastes can increase one or both of the mixture's strength and durability qualities [22] and their ability to effectively sequester. The w-d cycle can significantly impact the mechanical behavior of soils and their performance in a variety of geotechnical applications, including foundations, pavements, embankments, and engineered barriers in waste management systems [23,24]. Fly ash, a readily available industrial waste, can be employed as a suitable cementitious material additive in this context. Liao et al. [25] investigated the mechanical properties of cementitious materials exposed to the w-d cycle and discovered that cementitious materials' compressive strength, mass loss, and dynamic elastic modulus rose first and then declined. Wang et al. [26] investigated the hardening of cementitious materials using MgO-fly ash mixes. According to Wei et al. [27], the addition of fly ash to cellulose fiber concrete modifies the initial pore structure and increases its durability against sulfate. Wdah et al. [28] investigated the effects of w-d cycles on red mud waste solidified with desulfurization gypsum-fly ash. The effect of the cycle was investigated, and the practicality of employing resistivity response stress was confirmed. Du et al. [29] studied the effect of w-d cycles on the properties of calcium carbide slag-MgO stabilized kaolin and found that the UCS of cured soil decreased with increasing w-d cycles. Kampala et al. [30] studied the durability properties of calcium carbide slag and fly ash solidified silt under the action of w-d cycles and found that the mixture could be used for soil curing to obtain medium strength and better durability geological material. These earlier studies demonstrated that curing of contaminated waste with different composite solidified materials under the influence of w-d cycles showed good durability. However, very limited research has addressed the impacts of w-d cycles on the durability of composite materials solidified PRB wastes.

Accordingly, the objective of this study is to investigate the effect of w-d cycle on the durability of CFC solidified PRB waste. This study is based on a nonrecyclable PRB waste, consisting mainly of a 7:3 mixture of red mud and loess [31], solidified with CFC to investigate the mechanical and leaching properties under the influence of w-d cycles, and microscope analysis by scanning electron microscopy (SEM), energy dispersive spectroscopy (EDS), and X-ray diffraction (XRD). This research can provide feasible solutions for the use of PRB solid waste in practical engineering.

2. Materials and Methods

2.1. Materials

Acidic manganese-contaminated PRB waste (RLC) consisted of 7:3 red mud and loess. (The results of the study demonstrated that red mud and loess at 7:3 can be used as PRB material to adsorb more than 95% of heavy metal ions, as detailed in [31].) The initial moisture content of the RLC is 60%. The sieved RLC was placed in sieves with particle sizes less than 2 mm and combined with the acidic solution. The basic physical parameters of RLC were obtained by compaction tests according to standard for geotechnical testing method (GB/T 50123-2019), as shown in Table 1.

Table 1. Main physical properties of RLC.

Parameters	Values
Specific density	2.7
Liquid limit/%	27.2
Plastic limit/%	17.2
Plasticity index	10.0
Optimum water content/%	33.0
Maximum dry density/g·cm^{-3}	1.47
pH value	7.88–8.21

The RCL was formulated in the laboratory. The red mud used in this study (Figure 1a) was obtained from the Liulin aluminum plant in Taiyuan, Shanxi Province, China. The red mud employed in this work is a highly alkaline leftover from the Bayer process [32], which extracts alumina from produced bauxite, accounting for more than half of SiO_2 and Al_2O_3. The loess has a yellow appearance. Its plastic limit is 14.55%, the liquid limit value is 25.03%, and the plasticity index is 10.48%, which is typical of reconstituted loess from Shanxi (Figure 1b). According to Figure 2, the uniformity coefficients for red mud and loess were 6.68 and 8.32, respectively, and the curvature coefficients of red mud and loess were 1.401 and 1.648, respectively.

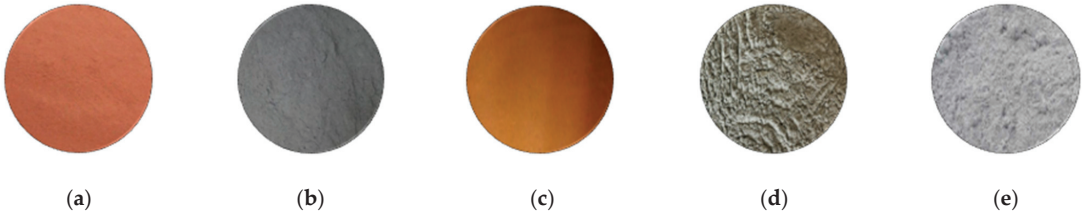

(**a**) (**b**) (**c**) (**d**) (**e**)

Figure 1. Test materials. (**a**) Red mud, (**b**) loess, (**c**) ordinary Portland cement, (**d**) fly ash, and (**e**) carbide slag.

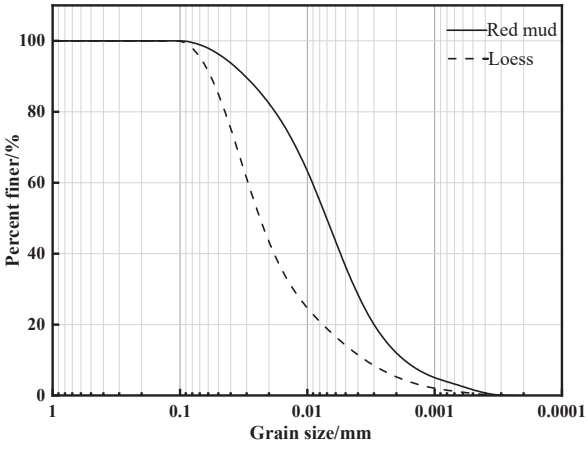

Figure 2. Particle size distribution of red mud and loess.

The ordinary Portland cement (Figure 1c) used in this study had a strength grade of 42.5 and came from the Taiyuan Lionhead Cement Plant. Fly ash (Figure 1d) was collected from Taiyuan No. 1. The thermal power plant, Taiyuan, Shanxi, China, contained large amounts of SiO_2 and Al_2O_3, which were used as partial cement replacements in this study. Carbide slag (Figure 1e) was collected from Yushe Chemical Co., Ltd, Taiyuan, Shanxi

Province, China. and was beige, with CaO as the main chemical composition. The chemical compositions of the three hardened materials are shown in Table 2.

Table 2. Chemical compositions of major materials.

Constituent	Cement/%	Fly Ash/%	Carbide Slag/%
SiO_2	20.96	50.10	3.0
Al_2O_3	4.98	26.50	2.5
CaO	64.03	4.10	59.5
Fe_2O_3	3.22	8.40	0.9
Na_2O	0.07	7.15	—
TiO_2	—	—	0.77
MgO	1.30	0.85	0.2
SO_3	2.60	1.40	0.89
K_2O	0.55	1.50	0.03

2.2. Specimen Preparation

First, the pH of the water sample was adjusted to approximately 3.0 using a dilute solution, and then two concentrations of Mn^{2+}(chemical reagent of choice $MnSO_4 \cdot H_2O$, analytical purity purchased by Tianjin Tianli Chemical Reagent Co, China) at 1000 mg·L^{-1} and 5000 mg·L^{-1} were added to simulate acidic mine drainage. A mixture of red mud and loess was placed in a soil column, and the RLC was removed after 30 days of soaking with simulated acid mine drainage, representing the waste at both pollutant concentrations. The RLC was dried at 60 °C, crushed, and passed through a 2mm sieve; cement, fly ash, and carbide slag were mixed at 8%, 8%, and 5% (results were obtained by orthogonal tests in the previous period) of the dry weight of RLC, respectively, and the optimum moisture content of 33% and maximum dry density of 1.47 g·cm^{-3} were obtained by compaction tests. The mixture was mixed to an optimum moisture content of 33%, and the specimens were prepared by the hydrostatic method to produce a dry density of 95% of the maximum dry density. The specimen was a cylinder of 50 mm in diameter and 50 mm in height. Cement-fly ash-carbide slag solidified in RLC is defined as FCCR1 and FCCR5. Three parallel samples were prepared for each group and placed in a curing chamber at a temperature of 20 °C ± 2 °C and relative humidity of 95% for 28 and 60 days, respectively.

Specimens for microscopic testing were immersed in alcohol to stop the hydration process [32], air-dried, and removed using 1 cm × 1 cm × 0.3 cm fine-grained sandpaper for SEM and XRD testing.

2.3. Testing Procedures

2.3.1. W-D Cycle Test

The specimens were tested for w-d cycles according to ASTM D4843-88 [33].

Step 1: Weigh the samples before the test.

Step 2: Place the samples into the oven at a temperature of 70 °C for 12 h, then take the sample from the oven and weigh it.

Step 3: Place and submerge the samples in distilled water for 24 h.

Step 4: Weigh the samples after removing them from distilled water.

The number of w-d cycles designed was 0, 1, 3, 5, 7, and 10. The mechanical and leaching characteristics and microstructural characteristics of the FCCR were analyzed at different cycle times.

2.3.2. UCS Test

The UCS test was performed on the test procedure for inorganic bonding materials for road engineering (JTG/T E51-2009) [34], which was conducted using an electonic universal testing machine. Subsequently, these samples were pressed at a rate of 1 mm/min until destruction.

2.3.3. Resistivity Test

The resistivity test was performed using a digital bridge (TH2828A) to record the IR as well as the process resistivity change [32]. The w-d test does not damage the sample, and the completed w-d test sample can be placed in the press for resistivity testing. After each w-d cycle, the sample surface was dried of moisture. Graphite was evenly applied to the surface of both ends of the sample, copper electrode pads were placed, and the leads were connected to a TH2828A-type LCR digital bridge for testing.

2.3.4. Leaching Concentration Test

The leaching toxicity test was performed using the sulfuric acid and nitric acid method of the solid waste leaching toxicity extraction method (HJ/T299-2007) [35]. The concentration of pollutants in the filtrate was determined by inductively coupled plasma emission spectrometer.

2.3.5. Microscopic Testing

XRD analysis was conducted on an FCCR to judge the formation of the new phase, and the natural drying samples were scanned with 2φ ranging between 10° and 70°. The specimens' pore structure and surface morphology were then observed at 5000×, 10,000×, and 20,000×. Moreover, SEM and EDS analysis were conducted using Hitachi TM3000 scanning electron microscope, Japan. The test flow is shown in Figure 3, and the experimental design is shown in Table 3.

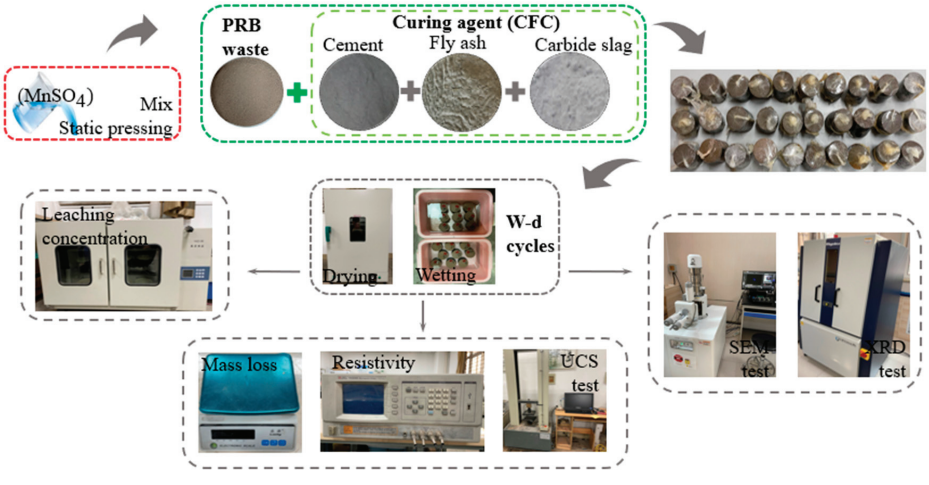

Figure 3. Testing process schematic.

Table 3. Experimental design.

W-d Cycles	Curing Time/d	Mn^{2+} Concentration/ $mg \cdot L^{-1}$	Test Procedures (with Equipment Type)
0,1,3,5,7,10	28	1000 5000	Mass loss—Electronic scales (LQ-C20002) and electric constant temperature blast drying oven (DHG-9246A, JiangSu, China)
		1000	UCS—Electronic universal testing machine (YSH-229WJ-50kN, ShangHai, China)
			Resistivity-Digital Bridge (TH2828A, ChangZhou, China)
	60	5000	Leaching concentration—Inductively coupled plasma emission spectrometer (Spetro Arcos, Kleve, Germany)
			SEM and EDS—Electron microscope (UltimaIV 2036E102, Tokyo, Japan)
			XRD—Ultima IV diffractometer (Nippon Rigaku, Tokyo, Japan)

3. Results and Discussion

3.1. UCS

The influence of the w-d cycle on the UCS of the specimens under various durability circumstances is shown in Figure 4. It is evident from the figure that the strength of the FCCR tends to rise with the number of w-d cycles, reaching a peak at the seventh w-d cycle. The inclusion of fly ash and carbide slag increased the specimen strength at first, but when the w-d cycle took effect, the time to achieve the intensity peak shifted back. The high-temperature environment encourages fly ash and carbide slag to enhance the hydration rate during the dry cycle [36]. In contrast, the aqueous environment favors the combination of fly ash and carbide slag to increase the hydration rate during the wet cycle [37]. At the same time, fly ash has a "filling effect" that can limit the soil's pore space, increasing its strength. This shows that fly ash changes the pore structure in solidified soil, resulting in decreased soil porosity and increased soil structure compactness. The influence of the early w-d cycle on solidified samples was reduced [38,39].

The samples' strength deteriorated after the seventh w-d cycle, notably as the Mn^{2+} content climbed from 1000 mg·L^{-1} to 5000 mg·L^{-1}. At 28 and 60 days, the maximal strength of the FCCR fell by 2.3% and 3.5%, respectively. The impact of manganese ions on FCCR strength is mainly due to a high concentration of ions slowing down the hydration process, lowering the hydration products and thus lowering the strength. The damage to the soil structure worsens from physical erosion as the number of w-d cycles rises, and cracks emerge in the pore structure and spread, leading to structural flaws and a fall in FCCR.

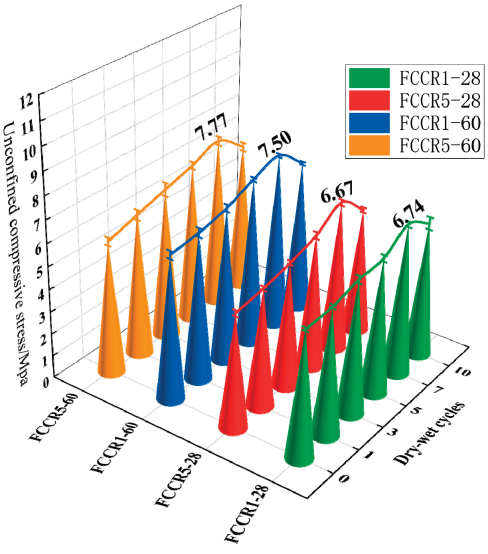

Figure 4. UCS of specimens under different durability conditions.

3.2. IR

Figure 5 depicts the IR trend as the number of w-d cycles increases. The IR increases with the number of w-d cycles. As seen in the graph, it then decreases, which is compatible with the law of change of UCS. The first seven w-d cycles show a rise in IR, and after the seventh w-d cycle, the IR displays a declining trend. This is because the pore space of the soil body expands, and cracks form throughout the w-d cycles. This is mainly because the soil generates fissures during the w-d cycle, and pore size becomes more prominent. Additionally, to a certain extent, it will block some of the conductive paths between soil

particles, and the soil particle orientation is weakened [40]. Thus, the conductivity between soil particles is reduced, and the resistivity shows an increasing trend.

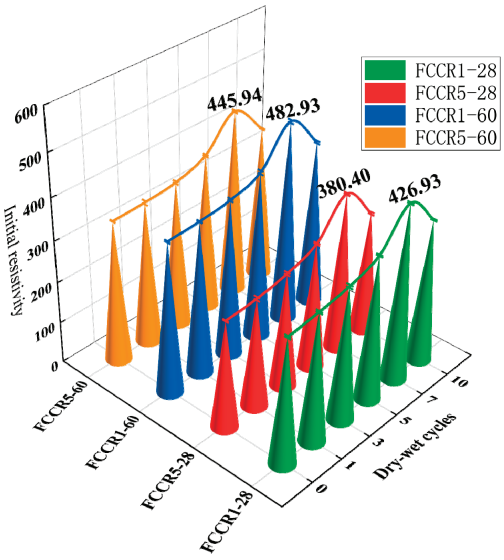

Figure 5. Curve of IR vs. different w-d cycles.

From the 7th w-d cycle, the degree on the soil gradually increases, the soil particle skeleton is compressed, the soil is damaged, the larger pores between particles are compressed into tiny pores, the pore water saturation increases, and the pore water conductivity is enhanced; thus, the resistivity shows an attenuation trend. As the pore water saturation rises and the pore water's electrical conductivity rises, the resistance falls. Because manganese ions are innately conductive, they affect FCCR resistivity. The stronger the conductivity and lower the resistivity of the soil, the higher the ion concentration in the pore solution, which is also consistent with the trend in UCS with ion concentration.

3.3. Correlation of UCS and IR

Figure 6 depicts the connection between the UCS and IR for various w-d cycles. It can be seen that the dark area near the fitted curve of UCS and IR is the 95% confidence interval of UCS, which includes more than half of the test data points in the 95% confidence interval, and includes basically all of the test data points in the whole 95% prediction interval, indicating that the test of IR of the test block can have 95% prediction to predict the UCS of the test block. The regression equations for the four fitted curves are listed in the Table 4. It can be deduced from the table and graphs that:

(a) At the same Mn^{2+} concentration, the resistance increases with curing time and IR.

(b) For a given IR, the higher the Mn^{2+} concentration is, the greater the compressive strength.

(c) For the same resistivity increment, the slope of the straight line increases with increasing Mn^{2+} concentration, showing that the compressive strength increases with increasing Mn^{2+} concentration.

Many researchers have studied and established the relationship between the UCS and IR of solidified soils [41–45] who discovered that the UCS and IR had a good linear relationship. The results of this paper are consistent with the above researchers. As a result, a resistivity method can be a valuable tool for assessing the quality of hardened soils and can be applied to various engineering tests.

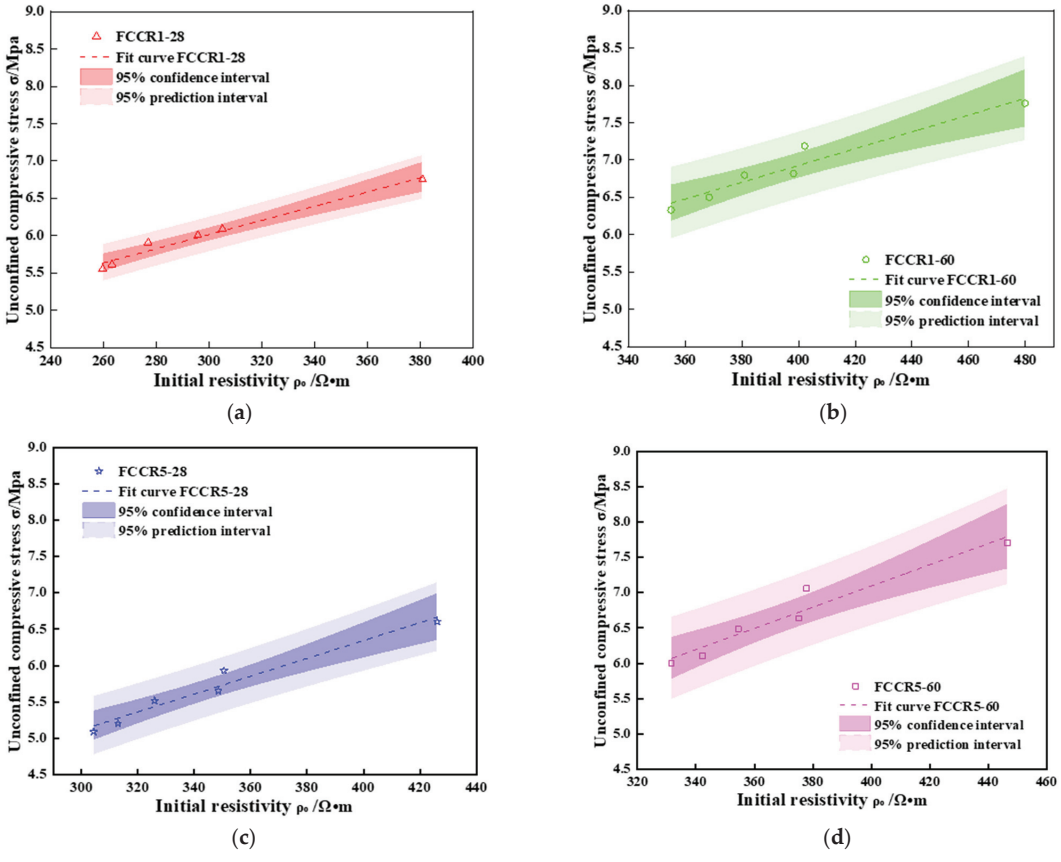

Figure 6. Relationship between UCS and IR. (**a**) UCS and IR fit curve of FCCR1-28; (**b**) UCS and IR fit curve of FCCR1-60; (**c**) UCS and IR fit curve of FCCR5-28; (**d**) UCS and IR fit curve of FCCR5-60.

Table 4. Fitting relationship between UCS and IR.

Curing Time/d	Mn^{2+} Concentration/mg·L^{-1}	Fitting Formula	Decision Coefficient R^2
28	1000	$q_u = 0.010\rho_0 + 1.740$	0.978
	5000	$q_u = 0.012\rho_0 + 2.378$	0.986
60	1000	$q_u = 0.011\rho_0 + 2.546$	0.947
	5000	$q_u = 0.015\rho_0 + 1.106$	0.920

Note: q_u is the UCS of the specimen and ρ_0 is the IR of the corresponding specimen.

3.4. Leaching Concentration

Figure 7 depicts the increase in Mn^{2+} leaching concentration as the number of w-d cycles increases. The leaching concentration of FCCR increases and then stabilizes as the number of w-d cycles increases, but all of these values are below the primary effluent discharge standard of 2.0 mg·L^{-1}, indicating that they will not harm the production and living environment or the human body [43]. The concentration of leached ions can detect a noticeable rise between zero and three cycles of the w-d cycle. This is because each w-d cycle develops small cracks on the surface and interior of the sample [46], resulting in increased ion leaching and FCCR mass loss. When the sample undergoes three w-d cycles, the leached concentration tends to stabilize or even decrease: with the continuous hydration process, hydration $Ca(OH)_2$ and calcium silicate hydrated (C-S-H) gelation

products were generated, among which $Ca(OH)_2$ and easily dissolved water-soluble Mn^{2+} formed precipitates. $Ca(OH)_2$ was easily oxidized to the more stable tetravalent manganese oxide in the alkaline environment, and the hydration products C-S-H and AFt increased after the large consumption of $Ca(OH)_2$ in the later phase. The system was mainly responsible for solidifying the continuously dissolved water-soluble Mn^{2+}: hydration products' physical adsorption and encapsulation. FCCR5-28 also had the largest concentration of leached Mn^{2+} and, as a result, the lowest UCS, implying that the initial Mn^{2+} concentration significantly impacts the FCCR's w-d cycle endurance.

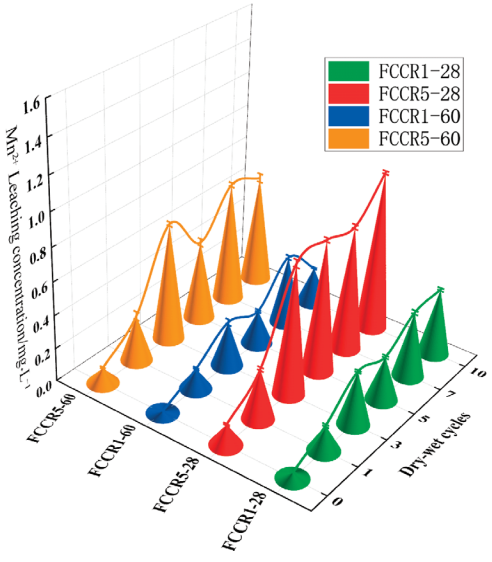

Figure 7. Leaching Mn^{2+} concentration under different durability conditions.

3.5. Mass Loss

As shown in Figure 8, capillary pores form on the surface of the FCCR, and tiny cracks appear; after ten w-d cycles, local detachment of the surface occurs, resulting in a mass change. The following two equations can calculate the mass change during w-d cycle action: Equation (1) is the mass loss for i w-d cycle actions, and Equation (2) is the cumulative mass loss for ten w-d cycle actions.

$$ML = \frac{(m_0 - m_i)}{m_0} \times 100\% \quad (1)$$

$$CML = \sum_{i=0}^{10} ML_i \quad (2)$$

where m_i is the mass of the specimen after i cycles and m_0 is the initial drying mass of the specimen.

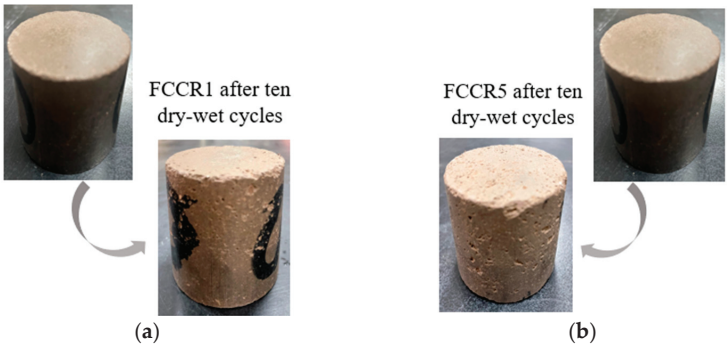

Figure 8. Surface features of FCCR after ten w-d cycles: (**a**) FCCR1 and (**b**) FCCR5.

Figure 9 represents the variation in the mass loss rate of FCCR with d-w cycles. From Figure 9a, it can be seen that the difference in the mass-loss rate per wetting cycle for FCCRs with two different pollutant concentrations at different maintenance ages is slight. During wet cycles 0–3, the mass-loss rate increased significantly with the action of the wet cycle. In the successive seven cycles, the mass loss rate of the specimens increased only slightly compared to the first three cycles and nearly stabilized. The specimen's structure has not yet reached a dense condition, and the internal pores are numerous at the start of the cycle. The water evaporates quickly after three drying cycles, and the mass loss rate is considerable. Between cycles 3 and 10, the gelling material generated by FCCR hydration fills the interior pores. The mass loss continues at a nearly constant rate while compressive strength declines and the leached ion concentration decreases. This conclusion is consistent with the findings of Guo et al. [47].

As shown in Figure 9b, under the effect of w-d cycles, the cumulative mass loss of FCCR at higher concentrations was much more significant than that at lower concentrations. Compared with the initial mass, the cumulative mass losses in the last w-d cycle (No. 10) increased by 2.97% for FCCR1-28, FCCR5-28, FCCR1-60, and FCCR5-60. This phenomenon occurs because the high concentration of Mn^{2+} invades the surface pores of the sample, resulting in peeling of the sample skin and loosening of the internal structure, leading to significant quality changes. The strength and leaching ion concentration of the soil sample also changes significantly.

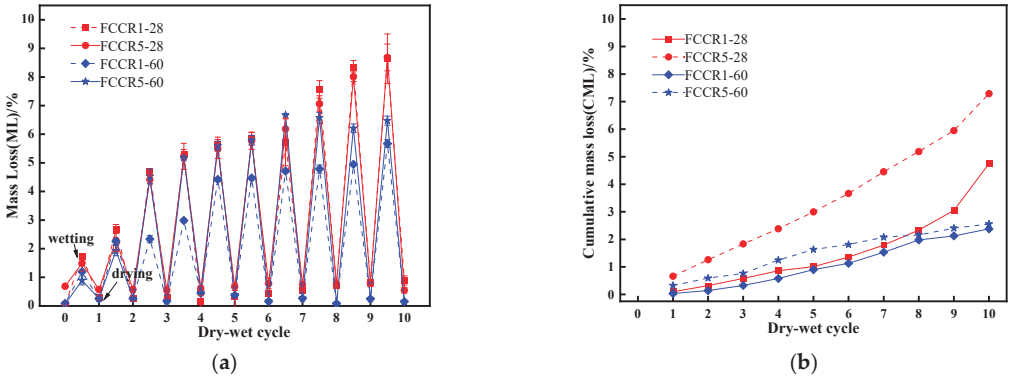

Figure 9. (**a**) Mass loss of specimens under different durability conditions; (**b**) cumulative mass loss of specimens under different durability conditions.

3.6. Microstructure Analysis

The extent of the effect of the w-d cycle on the hydration products of FCCR was further investigated by XRD analysis. Figure 10 displays the XRD graphs with various contaminant concentrations after 28 days of curing time under the effects of 0 and 10 w-d cycles. As can be observed in the figure, the comparison of the FCCR with the pure polluted waste identifies the development of new peaks, namely, the generation of calcium aluminosilicate hydrate (C-A-S-H) and ettringite (AFt) hydration products. The XRD plots for different numbers of w-d cycles show practically the same peaks, demonstrating that the effect of w-d cycles on the formation of gelling chemicals during the hydration process is negligible. The results of the analysis show that the hydration products of FCCR are mainly composed of calcium silicate hydrate (C-S-H), calcium aluminosilicate hydrate (C-A-S-H), and ettringite (AFt). In terms of XRD patterns, C-S-H gels are represented at the peaks of 2θ values corresponding to the vicinity of 32°, 42.5°, and 48.5°, which is consistent with existing studies [48,49]; also, C-A-S-H gels are likewise clearly observed near the 2θ values at 35.5°, 42.5°, and 45.5°, which is consistent with the results of existing studies [32,50]. The inclusion of fly ash and calcium carbide slag speeds up the hydration reaction process. It boosts the ionic activity, which helps to accelerate the volcanic ash reaction, carbonation reaction, and ion exchange reaction in the reaction system, resulting in more gelling material to strengthen the soil.

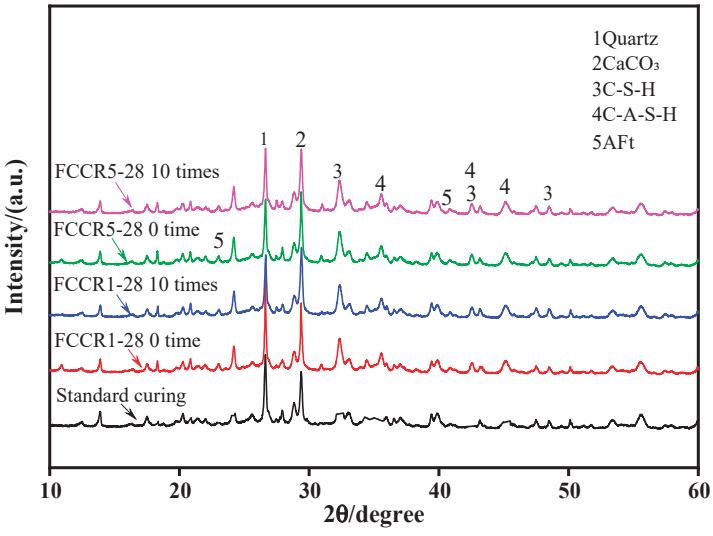

Figure 10. XRD pattern at 28 d of curing time under different durability conditions.

SEM images of specimens at 28 days of curing time were chosen. Figure 11a–d show SEM images at various magnifications without the w-d cycle, whereas Figures 10 and 11e show SEM images at various contaminant concentrations with the w-d cycle. The atomic Ca/Si ratio of C-S-H is an important composition parameter that affects nonstructural characteristics of C-S-H (usually Ca/Si between 1.0 and 1.7 represent C-S-H) [51]. Referring to EDS component analysis results (see Figure 12), it is evident that a large amount of needle/rock-like calcified material formed in the soil samples after 28 days of curing time, that is, a massive amount of C-S-H/C-A-S-H and AFt was generated [51–53]. Through hydration, the glass beads of fly ash and needle-like ettringite are wrapped or bonded together by the flocculent C-S-H/C-A-S-H gel component, which binds the different forms together to form a denser structure, which is the main reason for providing soil strength. At room temperature, tricalcium silicate dicalcium silicate (C_3S) and dicalcium aluminate (C_2S) in the cement hydrate create C-S-H and $Ca(OH)_2$. During the chemical reaction, fly

ash is activated over time by $Ca(OH)_2$ produced by the hydration of the cement and by $Ca(OH)_2$ contained in the calcium carbide slag itself, and OH^- from the pore fluid breaks Si-O-Si and Al-O-Al bonds, the hydrated calcium silicate C-S-H and hydrated calcium aluminosilicate C-A-S-H with Ca^{2+} are generated with gelling activity, and the C-A-S-H is excited by OH^-, SO_4^{2-}, Ca^{2+} to generate the water-hardened AFt. Fly ash is primarily responsible for filling the microporous aggregates and reducing the water consumption during the reaction [54]. The flocculent C-S-H/C-A-S-H gels produced in FCCR can bind fine particles together and further promote the assembly of agglomerates. Therefore, the appearance of C-S-H/C-A-S-H gels is a key factor to improve the strength and durability of FCCR, especially for samples with long-term curing, which is also consistent with the study of [55].

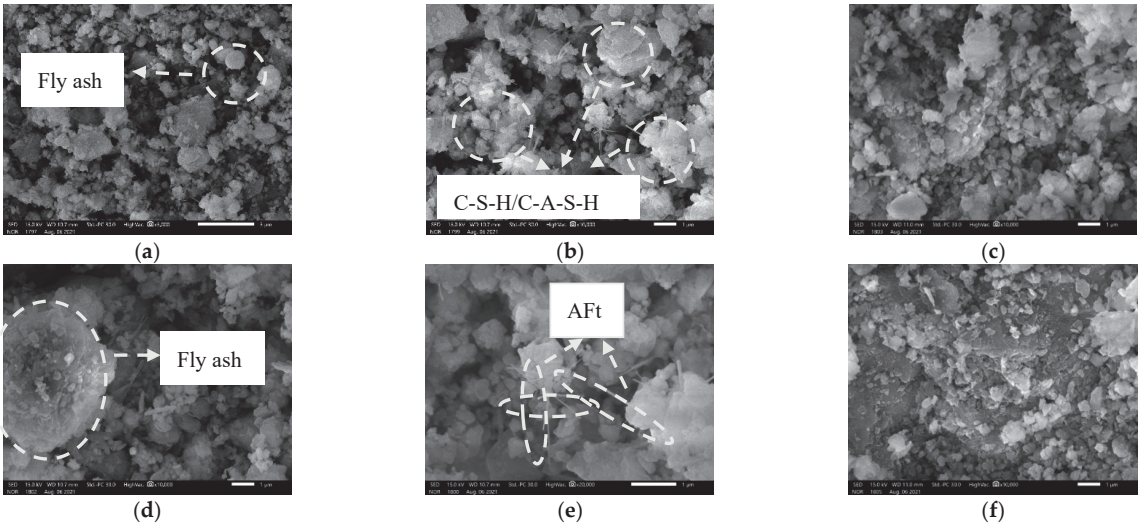

Figure 11. Microstructure after 28 d of curing: (**a**) × 5k; (**b**) × 10k; (**d**) × 10k; (**e**) × 20k. Microstructure after 10 w-d cycles: (**c**) FCCR1 × 10k; and (**f**) FCCR5 × 10k.

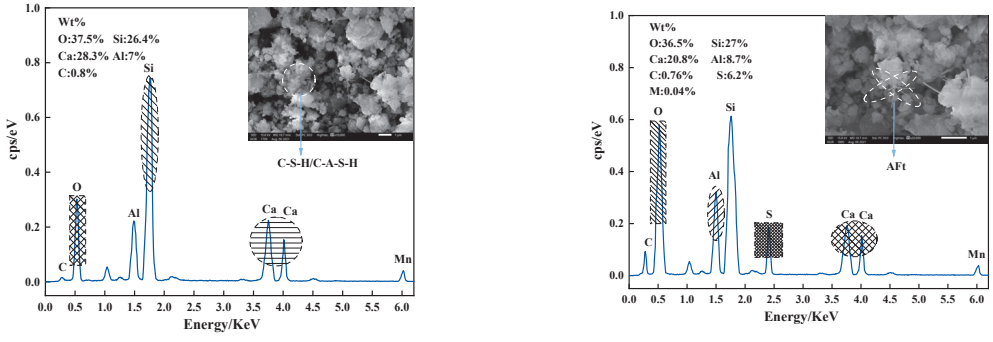

Figure 12. EDS images: (**a**) spectrum 1; (**b**) spectrum 2.

Figure 11e,f show SEM images of different FCCR concentrations after ten w-d cycles. A comparison of Figure 11c,d shows that after ten w-d cycles, there is a significant reduction in calcarenite hydration products in the specimen, as well as a significant reduction in C-A-S-H/C-S-H flocculent colloidal material and a significant reduction in compactness.

The pores between the particles become larger with the increasing of w-d cycles, which is the main reason for the variations in strength, indicating that the w-d cycle affected the soil to some extent [56]. From a geotechnical engineering perspective, FCCR has better durability against w-d cycling in addition to higher UCS values, which can be attributed to the increase in C-S-H/C-A-S-H and AFt during w-d. CFC can improve the short- and long-term UCS and durability of the fill material, which is beneficial for applications requiring practical engineering [57].

Figure 13 depicts a black-and-white binary image of the SEM processed with Image-Pro Plus, revealing which part of the soil has porosity. In the test block, porosity is defined as the ratio of the pore volume (area of the white zone in the black and white binary image) to the volume of the material (area of the black zone in the black and white binary image).

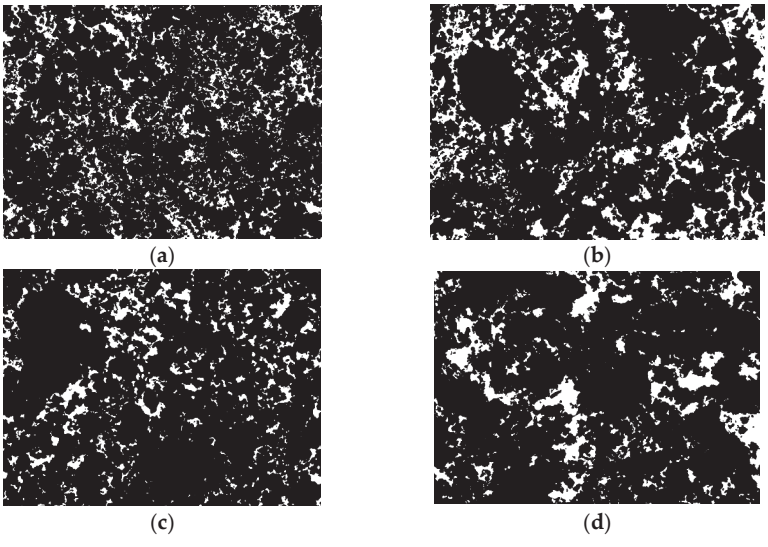

Figure 13. Black and white binary images of the specimens at 28 d of curing time: (**a**) RLC1-28 with 0 time; (**b**) RLC1-28 with 10 times; (**c**) RLC5-28 with 0 time; (**d**) RLC1-28 with 10 times.

According to Table 5, for various FCCR concentrations, the porosity rose by 37.42% and 28.11% after ten w-d cycles, respectively. This is due to varying degrees of loosening of the soil skeleton in response to w-d cycles. The specimen's hydration products formed are impacted and disrupted, creating a situation where the indicated pores become much more abundant. Although the porosity increases to varying degrees, the associated strengths are within the specification range, suggesting that FCCR is durable in both w-d cycles. This is also in line with the findings of the strength development program.

Table 5. Porosity ratio of specimens under different durability conditions at the age of 28 d.

Curing Time /d	Magnifying Power	Contaminant Concentration/mg·kg^{-1}	Cycle Times	Pore Area/μm^2	Soil Area /μm^2	Porosity Ratio	Growth Ratio /%
28	×5000	1000	0	166,358	1,024,066	0.162	37.42
			10	209,585	938,853	0.223	
		5000	0	135,532	1,087,255	0.125	28.11
			10	161,337	1,010,247	0.160	

3.7. Discussion of the Mechanism

The fundamental mechanism of the FCCR hydration process is depicted in Figure 14. Cement in the dry state is mainly composed of tricalcium silicate dicalcium silicate (C_3S), dicalcium aluminate (C_2S), tricalcium aluminate (C_3A), and a small amount of sulfate (potassium salt, sodium salt) and gypsum (calcium sulfate dihydrate). During the hydration of cement, C_3S, C_2S, and C_3A undergo complex hydration reactions with other components in cement to produce calcium alumina, i.e., ettringite AFt, calcium hydroxide, and C-S-H gel. C_3S in the cement dissolves quickly in water, causing hydration, the first stage in the cement hydration reaction, which results in C-S-H gels and $Ca(OH)_2$ crystals. Carbide slag adds OH^- to the system, breaking Si-O and Al-O bonds in the fly ash reactive body and providing the Ca^{2+} needed to make a hydraulic cementitious material [58,59] and make hydration products more stable and robust. ${SO_4}^{2-}$ in solution is primarily utilized to increase the fly ash's rate of active excitation and its degree of active excitation [19].

(a) The fly ash was stimulated by alkaline and sulfate interfaces, which formed hydrated calcium aluminate in addition to the C-S-H gel, and the fly ash's Al_2O_3 activity was effectively excited due to the coexistence of ${SiO_4}^{4-}$ and $Ca(OH)_2$.

(b) ${SO_4}^{2-}$ reacts with Ca^{2+} and ${AlO_2}^-$ trapped in the gel on the surface of the fly ash particles to create calcium bauxite, which is then released into the pore fluid. On the surface of the fly ash particles, calcium alumina creates a fibrous or cross-linked covering. The low density of this coating allows for easier ion dispersion and penetration, which boosts fly ash activity even more.

(c) ${SO_4}^{2-}$ ions can replace some of the ${SiO_4}^{4-}$ ions in the C-S-H gel, and the replaced ${SiO_4}^{4-}$ ions are released and react with Ca^{2+} outside the inclusions to form the C-S-H gel again, allowing further excitation of the active fly ash; at the same time, the solubility of the active Al_2O_3 increases significantly in the presence of ${SiO_4}^{4-}$, promoting the excitation of the active Al_2O_3.

In summary, the hydration reaction of FCCR has the following equation:

The equation for the hydration reaction of cement is:

$$CaO + H_2O = Ca(OH)_2 \quad (3)$$

$$3CaO{\cdot}SiO_2 + nH_2O = xCaO{\cdot}SiO_2{\cdot}(n - 3 + x)H_2O + (3 - x)Ca(OH)_2 \quad (4)$$

$$2CaO{\cdot}SiO_2 + nH_2O{\cdot}SiO_2{\cdot}(n - 2 + x)H_2O + (2 - x)Ca(OH)_2 \quad (5)$$

The hydration reaction between cement and $Ca(OH)_2$ contained in calcium carbide slag produces mainly C-S-H/C-A-S-H and Aft [30], thus continuously improving the strength of the cement system. Fly ash contains a large amount of reactive SiO_2, Al_2O_3, and other substances, and the hydration reaction with $Ca(OH)_2$ produced by the hydration of cement and $Ca(OH)_2$ contained in calcium carbide slag produces the following reaction equation:

$$SiO_2 + nCa(OH)_2 + xH_2O \rightarrow nCaO{\cdot}SiO_2{\cdot}xH_2O \quad (6)$$

$$Al_2O_3 + mCa(OH)_2 + yH_2O \rightarrow mCaO{\cdot}Al_2O_3{\cdot}yH_2O \quad (7)$$

$$Al_2O_3 + 3Ca(OH)_2 + 3(CaSO_4{\cdot}2H_2O) + 23H_2O = 3CaO{\cdot}Al_2O_3{\cdot}3CaSO_4{\cdot}32H_2O \quad (8)$$

With the processing of w-d cycles, the internal soil sample gradually generates tiny fissures under physical erosion: the pore space increases, and the wrapping force between soil particles decreases. The attached fine particles are scoured and reorganized under the action of dry and wet cycles. The soil strength gradually decays from the initial increase, corresponding to the surface appearance of the soil sample also causing the slag to fall off, leading to an increase in mass loss. In contrast, C-S-H/C-A-S-H and AFt act as wrapping adsorbents for Mn^{2+}, and most of the Mn^{2+} can replace the aluminum in the structure of hydration products and then solidify stably in the soil. The leaching ion concentration is stabilized or even decayed. In general, the mechanical and leaching characteristics of

FCCRs are affected to some extent by the w-d cycles. Still, they are all within the range of the specification so that FCCRs can provide good theoretical support for the application of practical projects.

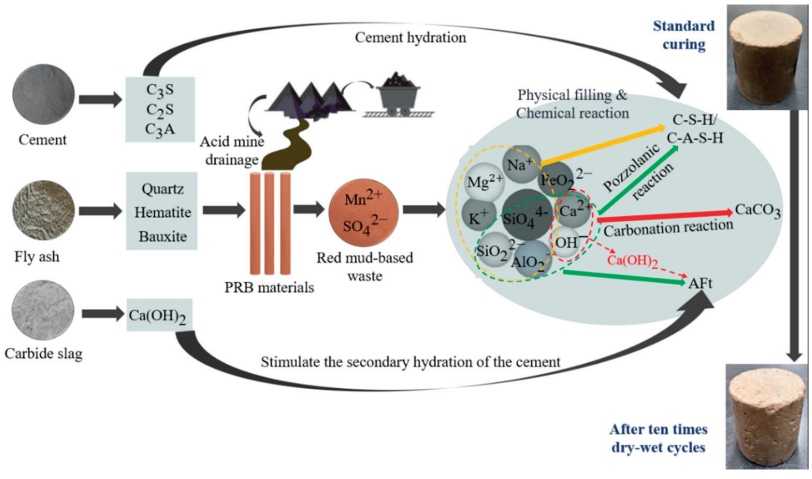

Figure 14. Schematic diagram of the mechanism.

4. Conclusions

This paper investigated the mechanical and leaching properties of FCCRs under w-d cycle conditions and SEM and XRD investigations of FCCRs. These results show that FCCR's mechanical and leaching properties are stable in both dry and wet conditions. Its durability is outstanding; the proposed resistivity method effectively predicts the quality of solidified soil. It can be easily and quickly applied to practical engineering applications. The following conclusions can be drawn:

(1) There was a clear trend of increasing intensity in the UCS of FCCR during the first seven cycles and then the intensity decreased. This cementitious curing agent, under the influence of wet and dry cycles, shows excellent durability.

(2) The mass-loss rate of FCCR tended to grow during the first three w-d cycles and then stabilized, demonstrating that the w-d cycles had little effect on FCCR morphology. The high concentration of Mn^{2+} had an inhibitory or suppressive effect on the specimens.

(3) A good linear relationship was demonstrated between the UCS and IR after adjusting the UCS of the FCCR to the IR; therefore, the resistivity method can effectively evaluate the quality of solidified soil for engineering applications.

(4) XRD and SEM results indicated that the hydration products of FCCR are mainly composed of C-S-H/C-A-S-H gel and AFt gel. These gelling substances are adsorbed on the surface of red mud and fly ash and fill the pores of the specimen, and their strength and ion leaching concentration are not affected much even under the influence of w-d cycles.

Author Contributions: X.C. and W.F.: Writing—original draft and data curation; W.F. and H.W.: Investigation and data curation; H.W. and W.D.: Writing—review and editing and validation; W.D., C.S. and X.D.: Project administration. C.S. and M.X.: writing—review and editing; X.C. and M.X.: Conceptualization and Methodology. X.D.: funding acquisition. All authors have read and agreed to the published version of the manuscript.

Funding: This work was funded by National Natural Science Foundation of China (Grant No. 51978438).

Institutional Review Board Statement: Not applicable.

Informed Consent Statement: Not applicable.

Data Availability Statement: Data presented in this study are available on request from the corresponding authors.

Conflicts of Interest: The authors declare no conflict of interest.

References

1. Sheoran, A.; Sheoran, V. Heavy metal removal mechanism of acid mine drainage in wetlands: A critical review. *Miner. Eng.* **2006**, *19*, 105–116. [CrossRef]
2. Kalin, M.; Fyson, A.; Wheeler, W.N. The chemistry of conventional and alternative treatment systems for the neutralization of acid mine drainage. *Sci. Total. Environ.* **2006**, *366*, 395–408. [CrossRef] [PubMed]
3. Bosco, S.M.D.; Jimenez, R.S.; Vignado, C.; Fontana, J.; Geraldo, B.; Figueiredo, F.; Mandelli, D.; Carvalho, W.A. Removal of Mn(II) and Cd(II) from wastewaters by natural and modified clays. *Adsorption* **2006**, *12*, 133–146. [CrossRef]
4. Neculita, C.M.; Rosa, E. A review of the implications and challenges of manganese removal from mine drainage. *Chemosphere* **2019**, *214*, 491–510. [CrossRef]
5. Le Bourre, B.; Neculita, C.M.; Coudert, L.; Rosa, E. Manganese removal processes and geochemical behavior in residues from passive treatment of mine drainage. *Chemosphere* **2020**, *259*, 127424. [CrossRef]
6. Tigue, A.A.S.; Malenab, R.A.J.; Promentilla, M.A.B. A Systematic Mapping and Scoping Review on Geopolymer and Permeable Reactive Barrier for Acid Mine Drainage Treatment Research. *Process. Integr. Optim. Sustain.* **2020**, *4*, 15–35. [CrossRef]
7. Indraratna, B.; Pathirage, P.U.; Banasiak, L.J. Remediation of acidic ground water by way of permeable reactive barrier. *Environ. Geotech.* **2014**, *4*, 284–298. [CrossRef]
8. Faisal, A.A.H.; Sulaymon, A.H.; Khaliefa, Q.M. A review of permeable reactive barrier as passive sustainable technology for groundwater remediation. *Int. J. Environ. Sci. Technol.* **2017**, *15*, 1123–1138. [CrossRef]
9. Miretzky, P.; Muñoz, C.; Carrillo-Chávez, A. Experimental Zn(II) retention in a sandy loam soil by very small columns. *Chemosphere* **2006**, *65*, 2082–2089. [CrossRef]
10. Jiangmin, S.; Guanxing, H.; Dongya, H.; Qinxuan, H.; Lin, G.; Meng, Z. A review of reactive media within permeable reactive barriers for the removal of heavy metal(loid)s in groundwater: Current status and future prospects. *J. Clean. Prod.* **2021**, *319*, 128644.
11. Alena, P.; Vojtěch, S.; Tomáš, P.; Jaroslav, N. Advanced remediation using nanosized zero-valent iron and electrical current in situ—A comparison with conventional remediation using nanosized zero-valent iron alone. *J. Environ. Chem. Eng.* **2021**, *9*, 106124.
12. Wang, X.; Jiang, H.; Fang, D.; Liang, J.; Zhou, L. A novel approach to rapidly purify acid mine drainage through chemically forming schwertmannite followed by lime neutralization. *Water Res.* **2019**, *151*, 515–522. [CrossRef]
13. López, E.; Soto, B.; Arias, M.; Núñez, A.; Rubinos, D.; Barral, M. Adsorbent properties of red mud and its use for wastewater treatment. *Water Res.* **1998**, *32*, 1314–1322. [CrossRef]
14. Jin, D.; Wang, X.; Liu, L.; Liang, J.; Zhou, L. A novel approach for treating acid mine drainage through forming schwertmannite driven by a mixed culture of Acidiphilium multivorum and Acidithiobacillus ferrooxidans prior to lime neutralization. *J. Hazard. Mater.* **2020**, *400*, 123108. [CrossRef] [PubMed]
15. Komnitsas, K.; Bartzas, G.; Paspaliaris, I. Efficiency of limestone and red mud barriers: Laboratory column studies. *Miner. Eng.* **2004**, *17*, 183–194. [CrossRef]
16. Franklin, O.N.; Johana, G.M.S.; Grzegorz, M. An overview of permeable reactive barriers for in situ sustainable groundwater remediation. *Chemosphere* **2014**, *111*, 243–259.
17. Qiushi, Z.; Xing, C.; Rui, M.; Shichang, S.; Lin, F.; Junhao, L.; Juan, L. Solid waste-based magnesium phosphate cements: Preparation, performance and solidification/stabilization mechanism. *Constr. Build. Mater.* **2021**, *297*, 123761.
18. Wang, D.; Zhu, J.; He, F. CO_2 carbonation-induced improvement in strength and microstructure of reactive MgO-CaO-fly ash-solidified soils. *Constr. Build. Mater.* **2019**, *229*, 116914. [CrossRef]
19. Elahi, T.E.; Rafat, S.A.; Shariful, I.M. Engineering characteristics of compressed earth blocks stabilized with cement and fly ash. *Constr. Build. Mater.* **2021**, *277*, 122367. [CrossRef]
20. Cai, G.H.; Liu, S.Y. Compaction and mechanical characteristics and stabilization mechanism of carbonated reactive MgO-stabilized silt. *KSCE J. Civ. Eng.* **2017**, *21*, 2641–2654. [CrossRef]
21. Wang, D.; Zentar, R.; Abriak, N.E. Durability and Swelling of Solidified/Stabilized Dredged Marine Soils with Class-F Fly Ash, Cement, and Lime. *J. Mater. Civ. Eng.* **2018**, *30*, 04018013. [CrossRef]
22. Elahi, A.; Basheer, P.A.M.; Nanukuttan, S.V.; Khan, Q.U.Z. Mechanical and durability properties of high performance concretes containing supplementary cementitious materials. *Constr. Build. Mater.* **2010**, *24*, 292–299. [CrossRef]
23. Wen, H.; Suo, C.; Hao, Y.; Fan, P.; Dong, X. Effect of Freezing-Thawing Cycle on the Mechanical Properties and Micromechanism of Red Mud-Calcium-Based Composite Cemented Soil. *Adv. Civ. Eng.* **2020**, *2020*, 1–14. [CrossRef]
24. Duan, W.; Cai, G.; Liu, S.; Puppala, A.J.; Chen, R. In-situ evaluation of undrained shear strength from seismic piezocone penetration tests for soft marine clay in Jiangsu, China. *Transp. Geotech.* **2019**, *20*, 100253. [CrossRef]
25. Liao, Y.D.; Yang, Y.C.; Jiang, C.H.; Feng, X.G.; Chen, D. Degradation of mechanical properties of cementitious materials exposed to wet–dry cycles of sulphate solution. *Mater. Res. Innov.* **2015**, *19*, S5-173–S5-177. [CrossRef]
26. Wang, D.; Wang, H.; Di, S. Mechanical properties and microstructure of magnesia–fly ash pastes. *Road Mater. Pavement Des.* **2018**, *20*, 1243–1254. [CrossRef]

27. Wei, Y.; Chai, J.; Qin, Y.; Li, Y.; Xu, Z.; Li, Y.; Ma, Y. Effect of fly ash on mechanical properties and microstructure of cellulose fiber-reinforced concrete under sulfate dry–wet cycle attack. *Constr. Build. Mater.* **2021**, *302*, 124207. [CrossRef]
28. Salih, W.; Yu, W.; Dong, X.; Hao, W. Study on stress-strain-resistivity and microscopic mechanism of red mud waste modified by desulphurization gypsum-fly ash under drying-wetting cycles. *Constr. Build. Mater.* **2020**, *249*, 118772. [CrossRef]
29. Du, Y.-J.; Bo, Y.-L.; Jin, F.; Liu, C.-Y. Durability of reactive magnesia-activated slag-stabilized low plasticity clay subjected to drying–wetting cycle. *Eur. J. Environ. Civ. Eng.* **2015**, *20*, 215–230. [CrossRef]
30. Kampala, A.; Horpibulsuk, S.; Prongmanee, N.; Chinkulkijniwat, A. Influence of Wet-Dry Cycles on Compressive Strength of Calcium Carbide Residue–Fly Ash Stabilized Clay. *J. Mater. Civ. Eng.* **2014**, *26*, 633–643. [CrossRef]
31. Lu, Y.S.; Wang, M.M.; Huang, G.; Dong, X.Q. Experimental Study on Treatment to Acid Mine Drainage by Modified Red Mud. *Non-Met. Mines* **2018**, *41*, 15–18.
32. Chen, R.; Cai, G.; Dong, X.; Mi, D.; Puppala, A.J.; Duan, W. Mechanical properties and micro-mechanism of loess roadbed filling using by-product red mud as a partial alternative. *Constr. Build. Mater.* **2019**, *216*, 188–201. [CrossRef]
33. American Society for Testing and Materials. *Standard Test. Standard Test Method for Wetting and Drying Test of Solid Wastes*; ASTM D4843-88; American Society for Testing and Materials: West Conshohocken, PA, USA, 2009.
34. People's Republic of China Industry Standards. *Standard Test. Test Methods of Materials Stabilized with Inorganic Binders for Highway Engineering*; JTG E51-2009; People's Republic of China Industry Standards: Beijing, China, 2009.
35. China's Environmental Protection Industry Standards. *Standard Test. Solid Waste-Extraction Procedure for Leaching Toxicity-Sulphuric Acid & Nitric Acid Method*; HJ/T299-2007; China's Environmental Protection Industry Standards: Beijing, China, 2007.
36. Li, H.; Zhuge, L.J.; Shi, S.; Xu, D.L. Hydration Products of Fly Ash Based Cementing Material Activated By NaOH. *J. Chin. Ceram. Soc.* **2012**, *40*, 234–239.
37. Eskisar, T. The role of carbide lime and fly ash blends on the geotechnical properties of clay soils. *Bull. Int. Assoc. Eng. Geol.* **2021**, *80*, 6343–6357. [CrossRef]
38. Zheng, D.-D.; Ji, T.; Wang, C.-Q.; Sun, C.-J.; Lin, X.-J.; Hossain, K.M.A. Effect of the combination of fly ash and silica fume on water resistance of Magnesium–Potassium Phosphate Cement. *Constr. Build. Mater.* **2016**, *106*, 415–421. [CrossRef]
39. Wang, Z.; Wei, B.; Wu, X.; Zhu, H.; Wang, Q.; Xiong, Z.; Ding, Z. Effects of dry-wet cycles on mechanical and leaching characteristics of magnesium phosphate cement-solidified Zn-contaminated soils. *Environ. Sci. Pollut. Res.* **2021**, *28*, 18111–18119. [CrossRef]
40. Chen, Y.C.; Huang, X.; Chen, X.J.; Ding, X.; Xu, K.Y. Relationship between unconfined compressive strength and electrical resistivity of red clay under dry and wet cycles. *J. Guangxi Univ. Nat. Sci. Ed.* **2020**, *45*, 1267–1275.
41. Tian, G.Y.; Chen, R.F.; Song, Z.W.; Dong, X.Q. Effect of Age on Detecting Shear Strength of Loess Improved by the Red Mud in Resistivity Method. *Bull. Chin. Ceram. Soc.* **2017**, *36*, 2337–2342.
42. Dong, X.Q.; Zhang, S.H.; Su, N.N.; Huang, X.E.; Bai, X.H. Effects of contaminated soil on electrical resistivity and strength of cemented soil. *China Civ. Eng. J.* **2015**, *48*, 91–98.
43. Zha, F.S.; Liu, J.J.; Xu, L.; Deng, Y.F.; Yang, C.B.; Chu, C.F. Electrical resistivity of heavy metal contaminated soils solidified/stabilized with cement-fly ash. *Rock Soil Mech.* **2019**, *40*, 4573–4580.
44. Zhang, D.W.; Cao, Z.G.; Liu, S.Y.; Chen, L. Characteristics and empirical formula of electrical resistivity of cement-solidified lead-contaminated soils. *China Civ. Eng. J.* **2015**, *37*, 1685–1691.
45. Zhang, D.W.; Cao, Z.G.; Liu, S.Y. Characteristics and an experiment modle of electrical resistivity of stabilized soils. *Chin. J. Rock Mech. Eng.* **2014**, *33*, 4139–4144.
46. Fakhrabadi, A.; Ghadakpour, M.; Choobbasti, A.J.; Kutanaei, S.S. Evaluating the durability, microstructure and mechanical properties of a clayey-sandy soil stabilized with copper slag-based geopolymer against wetting-drying cycles. *Bull. Int. Assoc. Eng. Geol.* **2021**, *80*, 5031–5051. [CrossRef]
47. Guo, X.; Xiong, G. Resistance of fiber-reinforced fly ash-steel slag based geopolymer mortar to sulfate attack and drying-wetting cycles. *Constr. Build. Mater.* **2021**, *269*, 121326. [CrossRef]
48. Kamruzzaman, A.H.; Chew, S.H.; Lee, F.H. Structuration and Destructuration Behavior of Cement-Treated Singapore Marine Clay. *J. Geotech. Geoenvironment. Eng.* **2009**, *135*, 573–589. [CrossRef]
49. Buchwald, A.; Hilbig, H.; Kaps, C. Alkali-activated metakaolin-slag blends—performance and structure in dependence of their composition. *J. Mater. Sci.* **2007**, *42*, 3024–3032. [CrossRef]
50. Kim, H.-S.; Lee, S.-H.; Moon, H.-Y. Strength properties and durability aspects of high strength concrete using Korean metakaolin. *Constr. Build. Mater.* **2007**, *21*, 1229–1237. [CrossRef]
51. Sargam, Y.; Wang, K. Quantifying dispersion of nanosilica in hardened cement matrix using a novel SEM-EDS and image analysis-based methodology. *Cem. Concr. Res.* **2021**, *147*, 106524. [CrossRef]
52. Jin, S.; Liu, K.; Zhang, G.; Shi, H.; Ding, Q.; Xu, W. Effect of Corrosive Ions (Cl−, SO42−, and Mg2+) on the Nanostructure and Chloride Binding Property of C-A-S-H Gel. *J. Wuhan Univ. Technol. Sci. Ed.* **2020**, *35*, 1061–1072. [CrossRef]
53. Cai, G.-H.; Liu, S.-Y.; Zheng, X. Influence of drying-wetting cycles on engineering properties of carbonated silt admixed with reactive MgO. *Constr. Build. Mater.* **2019**, *204*, 84–93. [CrossRef]
54. Neramitkornburi, A.; Horpibulsuk, S.; Shen, S.L.; Chinkulkijniwat, A.; Arulrajah, A.; Disfani, M.M. Durability against wetting–drying cycles of sustainable Lightweight Cellular Cemented construction material comprising clay and fly ash wastes. *Constr. Build. Mater.* **2015**, *77*, 41–49. [CrossRef]

55. Wang, D.; Gao, X.; Liu, X.; Zeng, G. Strength, durability and microstructure of granulated blast furnace slag-modified magnesium oxychloride cement solidified waste sludge. *J. Clean. Prod.* **2021**, *292*, 126072. [CrossRef]
56. Cai, G.-H.; Liu, S.-Y.; Zheng, X. Effects of Drying-Wetting Cycles on Durability of Carbonated Reactive Magnesia-Admixed Clayey Soil. *J. Mater. Civ. Eng.* **2019**, *31*, 04019276. [CrossRef]
57. Hoy, M.; Rachan, R.; Horpibulsuk, S.; Arulrajah, A.; Mirzababaei, M. Effect of wetting–drying cycles on compressive strength and microstructure of recycled asphalt pavement—Fly ash geopolymer. *Constr. Build. Mater.* **2017**, *144*, 624–634. [CrossRef]
58. Wang, Y.; Gao, S.; Liu, X.; Tang, B.; Mukiza, E.; Zhang, N. Preparation of non-sintered permeable bricks using electrolytic manganese residue: Environmental and NH_3-N recovery benefits. *J. Hazard. Mater.* **2019**, *378*, 120768. [CrossRef]
59. Zhou, H.Y.; Chen, P.; Zhao, Y.R.; Liu, R.J.; Wei, J.Z. Sulfate activation of electrolytic manganese residue on heat-stewed steel slag activity. *Inorg. Chem.Ind.* **2019**, *51*, 66–69.

materials

MDPI

Article

Preparation of Polystyrene Microsphere-Templated Porous Monolith for Wastewater Filtration

Nur Faezah Ibadat, Suryani Saallah, Clarence M. Ongkudon and Mailin Misson *

Bioprocess Engineering Research Group, Biotechnology Research Institute, Universiti Malaysia Sabah, Jalan UMS, Kota Kinabalu 88400, Sabah, Malaysia; nurfaezahibadat@gmail.com (N.F.I.); suryani@ums.edu.my (S.S.); clarence@ums.edu.my (C.M.O.)
* Correspondence: mailin@ums.edu.my

Abstract: Porous monoliths prepared using templates are highly sought after for filtration applications due to their good mass transport properties and high permeability. Current templates, however, often lead to the formation of dead-end pores and irregular pore distributions, which reduce the efficiency of the substrate flow across the monolith column. This study focused on the preparation of a microsphere-templated porous monolith for wastewater filtration. The optimal template/monomer ratio (50:50, 60:40, 70:30) was determined, and appropriate template removal techniques were assessed for the formation of homogenous pores. The physicochemical characteristics and pore homogeneity of the monoliths were examined. The 60:40 ratio was determined to result in monoliths with homogeneous pore distributions ranging from 1.9 μm to 2.3 μm. SEM and FTIR investigations revealed that solvent treatment was effective for removing templates from the resulting solid monolith. The water quality assessments revealed reductions in the turbidity and the total number of suspended particles in the tested wastewater of up to 96–99%. The findings of this study provide insightful knowledge regarding the fabrication of monoliths with homogenous pores that are beneficial for wastewater treatment.

Keywords: porous monolith; polymer; template; homogenous pore; water filtration

Citation: Ibadat, N.F.; Saallah, S.; Ongkudon, C.M.; Misson, M. Preparation of Polystyrene Microsphere-Templated Porous Monolith for Wastewater Filtration. *Materials* **2021**, *14*, 7165. https://doi.org/10.3390/ma14237165

Academic Editor: Alain Celzard

Received: 18 October 2021
Accepted: 12 November 2021
Published: 25 November 2021

1. Introduction

The past decade has witnessed the advancement of monoliths as an important technology in diverse applications including separation [1], filtration [2], biomolecule purification [3] and chromatography systems [4]. This is owing to their fascinating characteristics, which include high surface area, chemical stability, large pore volumes, high permeability and low flow resistance, which enable high-speed separation, making them promising for achieving high throughput, resolution, and separation in short run times. Sol–gel, free-radical polymerization and click reactions are among the methods employed for synthesizing monoliths comprising glycidyl methacrylate, porogen, initiator, and cross-linker [5]. There is much to discover regarding the fabrication of monoliths, as evidenced by the increasing number of studies in the reported literature on monolith applications. Interest in monoliths for wastewater treatment has markedly increased over the past decade, driven by their attractive features, which include interconnected pore structures and convective mass transfer. Gel-emulsion-templated polymeric monoliths have been employed for the efficient removal of particulate matter [6]. Chitosan/MOF composite [7] and porous polyurea [8] porous monoliths have also been used as adsorbents to remove pollutants in water. Cellular glassy porous monoliths have also been prepared using sacrificial paraffin spheres as the porogen and resorcinol-formaldehyde (RF) resin as the carbon precursor in order to achieve electrical and electromagnetic properties [9]. Compared to typical macrocellular materials, monoliths possess porosities in the range of 75–85 percent, and have narrow cell size distributions and microporosity, as well as high surface areas.

Monoliths are fabricated with interconnected macropores smaller than 2 nm in diameter and mesopores ranging from 2 nm to 50 nm in size [10]. The pore structure within monoliths formed using a template allows liquid to flow through the monolith at a reasonable pressure. Biodegradable polymers such as polylactide (Sun et al., 2017) and supramolecular aggregates are common templates that are frequently used in monolith fabrication [11]. The desired pore size, porosity, and pore morphology can be obtained by fine-tuning the properties of templates. However, the templates currently in use present several limitations, such as poor heat dissipation, uneven pore size distribution, the wall channel effect, and low mechanical strength, particularly when scaled up [12]. In addition, the formation of dead-end pores and uneven pore distribution due to partial reaction by free radical initiators lead to the formation of pressure inside the monolith, hampering its commercialization potential [12]. Therefore, templates that are able to produce homogenous and well-structured monolith pores are highly sought after.

Nischang (2013) presented a comprehensive review of the morphology, porosity, nanostructure and chromatographic performance of porous polymer monoliths. The most commonly used radically initiated cross-linking polymerization procedures require initiation in a homogeneous liquid polymerization precursor that contains monomers and porogenic solvent. Porogens have been used to synthesize monodisperse polystyrene microspheres (Vlakh et al., 2011). Porogens, however, have not been used as the directing template for the formation of pore structure, leading to monoliths with irregular pores. As a result, substances distributed in monoliths face complex pathways, thus limiting the efficiency of their adsorption and separation. According to Wu et al. (2012), monoliths with homogenous pore structures would have greater efficiency when employed as an HPLC column. Controlling the porous structure and properties of monoliths has been the main direction of research.

Microemulsion-based polymeric microspheres are a good candidate for monolith templates owing to their ability to fine-tune porosity and particle size. Microspheres are small spherical particles, sometimes referred to as microparticles, with particle diameters ranging from 1 to 1000 μm. Shameer and Nishath [13] generated polymer dispersions made of a variety of monomers, including styrene, butyl acrylate, and methyl methacrylate in the presence of a coupling comonomer. Different hybrid morphologies were obtained depending on the reaction conditions and the surfactants employed. A microemulsion is a thermodynamically stable and transparent system that can be prepared by means of several techniques, including solvent evaporation methods, spray drying, the solution-enhanced dispersion method and the hot melt technique. Among these techniques, the most frequently applied method, due to its ease of preparation, is the solvent evaporation method. Monteiro, et al. [14] discovered that microemulsion performs best with polymers such as polycaprolactone and polystyrene. The effects of the chemical precursor and surfactant concentration on the formation of particles were also reported in our previous study [15]. Among the tested polymers (polystyrene, polycaprolactone, polypropylene, polyethylene, and poly (vinyl-alcohol)), polystyrene was found to be the best chemical precursor for the formation of good particle morphologies with sizes ranging from 1.94 μm to 3.45 μm.

Polystyrene microspheres have been used extensively as hard templates for various hollow spherical materials [16] due to their good features, which include low density, high surface area, excellent charge capacity, and high permeability. These properties have made them highly applicable in various industrially important applications in biocatalysis and immobilization systems [13,17]. Until recently, monoliths with ordered structures prepared using microsphere templates had never been reported. Therefore, polystyrene-based microspheres were investigated as monolith templates in this study. It has traditionally been a major challenge to produce monoliths with a well-ordered structure. Uneven pore distributions can reduce the efficiency of monoliths in water filtration systems. Silica monoliths have been prepared via spinodal decomposition as a unique method for producing homogeneous interconnected pore networks, significantly enhancing mass transport [18].

According to Ali [19], during the templating process, a pre-formed template is filled with soft precursor material to form the desired shape before the precursor material is hardened via a chemical or physical process. The template is removed once the material resembles the shape of the template. Zhang, et al. [20] explained that calcination, chemical etching or special treatment can be employed for the removal of hard templates.

Template removal is also a critical step that requires major consideration. Incomplete template removal results in the drawback of poor pore interconnectivity. A facile procedure for template removal requiring moderate temperature and pressure is a technological interest that is being actively pursued by scholars and industrialists. Malik, et al. [21] successfully used high-temperature solvent extraction to produce physically robust nanostructured silica monoliths. However, their procedures required special equipment high pressures and temperatures (Pc and Tc, respectively), and long processing times.

Hence, in the present work, a procedure for preparing porous monoliths using polystyrene-based microsphere templates is reported. The strategy for incorporating the template with monolith monomers at the best ratio was studied. The removal of the template was carried out via solvent treatment and thermal treatment. The homogeneity of the resultant pores following template removal was investigated. Finally, the performance of the fabricated monolith for wastewater filtration to remove particulate matter was assessed.

2. Materials and Methods

2.1. Chemicals

Polystyrene, ethylene glycol dimethacrylate (EDMA) 98%, glycidyl methacrylate (GMA) 97%, azobisisobutyronitrile (AIBN) and Brij O10 surfactant were all purchased from Sigma Aldrich (Burlington, NJ, USA). Toluene, dimethylformamide (DMF) were purchased from Fisher Chemical (Hampton, NH, USA). Polyethylene glycol (PEG) was purchased from Tokyo Chemical Industries Co. Ltd. (Tokyo, Japan).

2.2. Preparation of Polystyrene Microsphere Template

Polystyrene microspheres were synthesized via solvent evaporation method as described in a previous study [15]. Polystyrene polymer at different concentrations (10–40 wt%) was dissolved in DMF solution. Brij O10 surfactant (7%) was added as a stabilizer. The solution mixture was mixed using a magnetic stirrer at a stirring rate of 1500 rpm at 80 °C (Favorit, PLT Scientific Instruments, Selangor, Malaysia) and left for 1 h under continuous stirring to evaporate the solvent. The resulting polymeric microspheres were kept at room temperature until further use as a monolith template.

2.3. Preparation of Microsphere-Templated Porous Monoliths

The preparation of porous monoliths using the synthesized microsphere template is schematically represented in Figure 1. The procedure consisted of two parts. Part I: the incorporation of the microsphere template into the monolith monomer. Part II: the removal of the template from the structure of the solid monolith, thus creating pores across the monolith structure.

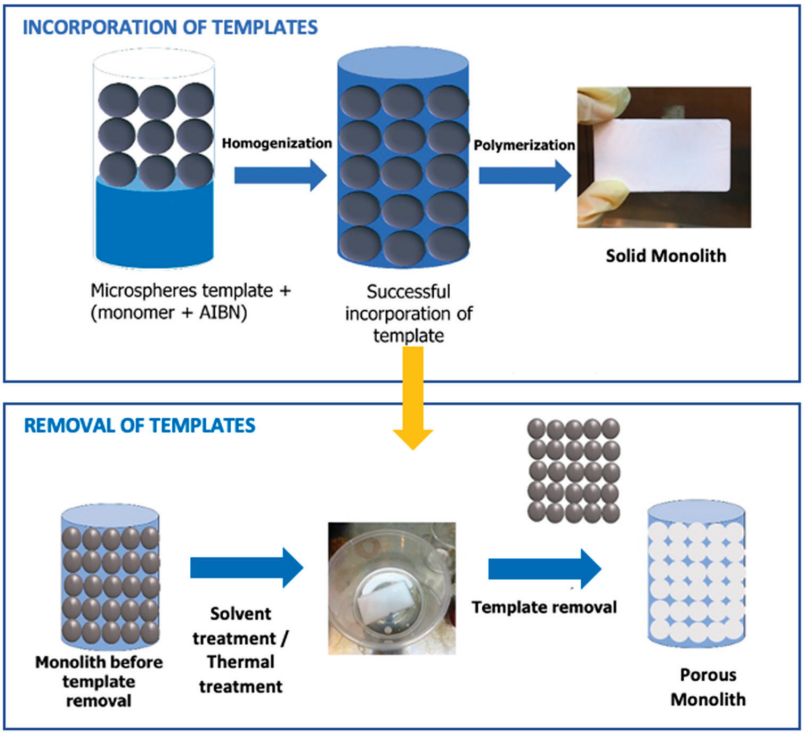

Figure 1. Schematic diagram of the preparation of porous monoliths using polystyrene microsphere particles as a pore-directing template. Part I: incorporation of the template into the monolith monomers. Part II: removal of the template via solvent treatment to produce a porous monolith.

Hierarchically porous polymethacrylate monoliths (PMMA) were synthesized through free-radical co-polymerization as described by [5] with slight modification (Figure 1; Part I). Glycidyl methacrylate and ethylene glycol dimethacrylate were used as monomers. Polymer solutions containing microspheres were mixed with the cross-linker, functional monomer and AIBN as an initiator to the reaction. Microsphere templates were added into the mixtures at varying template/monomer ratios (50:50, 60:40 and 70:30). The solution was sonicated at 20 °C for 20 min. Subsequently, the solution was inserted into a casting mold and heated at 60 °C for 3 h inside a water bath to allow the polymerization to occur [22]. The resulting solid monolith was removed and kept at room temperature until further use.

Next, the template was removed via solvent treatment and thermal treatment methods (Figure 1; Part II). The solvent treatment was conducted by soaking the monolith in toluene overnight. The monolith was washed with water to remove the solvent residues. Finally, the sample was oven-dried at 60 °C and kept at room temperature until further use [23]. For the thermal treatment method, the monolith was heated at 150 °C for 1 h in an oven. The physical structure of the monolith was observed after the first hour of exposure to high temperatures [24].

2.4. Characterization of Microsphere Template and Monoliths

The textural and morphological properties of the polystyrene microsphere templates were observed on a scanning electron microscope (Hitachi High Technologies America Inc. S-3400 Los Angeles, CA, USA) operated at 10 kV. Samples deposited on the sample holder were coated with a conductive gold before morphological examination. Successful incorporation and removal of the microsphere template on the monolith were also confirmed by

observing the monoliths using SEM. The average size of the polystyrene microsphere particles at different concentrations was determined using Dynamic Light Scattering (Nanoplus Micromeritics Instrument Corp, Tewkesbury, UK). The average pore size and the pore distribution of the monoliths obtained using different ratios were evaluated using Image J, 1.52 version software on the pre-captured image from SEM observation (Chan et al., [5]). The original SEM image was uploaded and binarized by altering the threshold. Particle size measurements were carried on based on the created particle outline. Fourier transform infrared spectroscopy (Agilents Technology Cary 630, Santa Clara, CA, USA) was used to characterize the functional groups in the monoliths after the incorporation and removal of the templates. The changes were observed by comparing the tested monoliths with a control monolith synthesized without the presence of a template.

2.5. Experimental Setup for Wastewater Filtration

The ability of the resultant porous monoliths to remove particulate matter in wastewater was tested (Figure 2). Wastewater samples showing a high level of turbidity were collected from an animal pond and laboratory waste. The animal pond wastewater was collected from the sea otter pond in Zoo Lok Kawi, Sabah, Malaysia, while the laboratory wastewater was collected from the Pilot Plant Laboratory at the Biotechnology Research Institute, Universiti Malaysia Sabah. A mini pump filtration system was developed (Figure 2a) consisting of a peristaltic pump, pressure gauge, monolith and flasks for the wastewater, clean water and waste residues. About 150 mL of wastewater samples were flowed through the monolith using a peristaltic pump with a pressure lower than 5 kPa. The actual setup of the monolith water filtration system is depicted in Figure 2b. The clean water was collected and tested for turbidity and total suspended solids (TSS) levels.

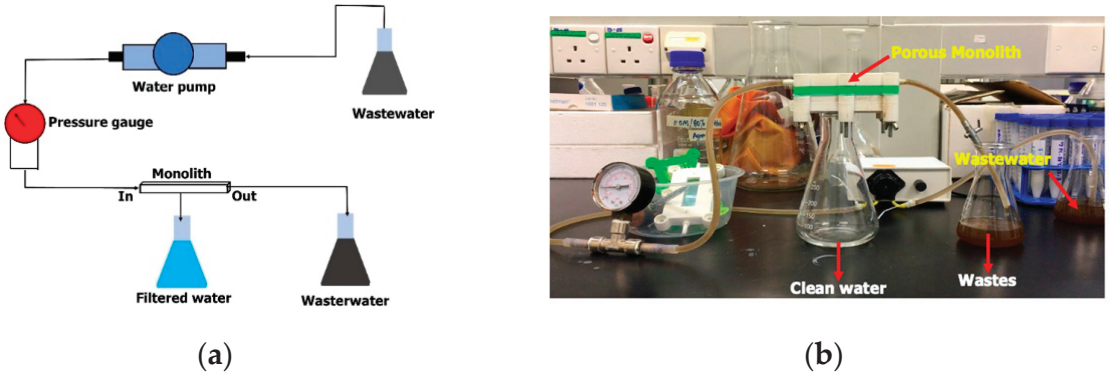

Figure 2. (**a**) Schematic representation of the monolith water filtration system. (**b**) Actual monolith water filtration system using the developed microsphere-templated porous monoliths.

2.6. Water Quality Analysis

Morphological analyses of the samples before and after the filtration process were conducted using an inverted microscope (40× magnification) to qualitatively observe the presence of particulate matter. The turbidity and total suspended solids (TSS) analyses of the samples were performed by an accredited laboratory for water quality surveillance located at the UMS-Water Analysis Laboratory Research Unit, Faculty of Science and Natural Resources, Universiti Malaysia Sabah. The TSS was analyzed using the APHA 2540 D 2012 method, while the turbidity test was carried out using the YSIProDSS method. The pH of the water samples was determined using a pH meter (Cyberscan, Thermo Fisher Scientific, MA, USA).

3. Results

3.1. Synthesis of Microsphere Particles as Monolith Templates

The average diameter and polydispersity index (PDI) of the polystyrene microspheres at different concentrations of polystyrene (10–40 wt%) are presented in Table 1. It can be seen that the particle diameter increased with increasing polymer concentration. The smallest particles were observed when using 10 wt% of polymer, with an average diameter of 0.9 μm. The particle size was also found to be in agreement with the PDI values. It can be observed that different polymer concentrations produced varying average microsphere diameters. The solution prepared at a lower concentration (10 wt%) produced an average diameter of 0.92 μm, with the lowest PDI value (0.537). According to Danaei, et al. [25], PDI values closer to 0.0 indicate monodisperse solutions, implying a homogenous system, while PDI values closer to 1.0 demonstrate polydisperse solutions, due to the presence of varying sizes of particles. Based on the findings reported by Ibadat, Ongkudon, Saallah and Misson [15], solutions prepared at 10 wt% polystyrene produce well-shaped microsphere particles compared to the formation of aggregated particles at a high concentration (40%). This is in agreement with the findings seen in this study, whereby increasing polymer concentration resulted in the formation of larger particles, ranging from 2.4 to 3.4 μm (Table 1). The experimental results showed that aggregation was more pronounced in the template prepared using a higher polymer concentration, probably as a result of the higher degree of viscosity of the polymer. The non-homogeneous conditions observed at higher concentrations of polystyrene can probably be attributed to the formation of irregular shapes and aggregated particles. This phenomenon was elucidated by Johansen and Schæfer [26], who suggested that polymer concentration strongly influences the viscosity of the solution, leading to particle aggregation.

Table 1. Pore size analysis of micro emulsion-based polystyrene microsphere templates prepared at different polymer concentrations.

Polymer Concentration (wt%)	Average Diameter (μm)	Polydispersity Index (PDI)
10	0.9	0.537
20	2.4	0.932
30	2.7	0.999
40	3.4	0.917

The findings show that polymer concentration significantly influences the pore distribution and homogeneity of the microsphere particles. With increasing concentration, non-homogenous particles were observed due to the formation of particle aggregation. Polystyrene at 10 wt% was found to be an optimal concentration for good-quality microspheres with a lower PDI value. Hence, this concentration was selected for further study on the preparation of porous monoliths.

3.2. Effect of Template/Monomer Ratio on Pore Distribution

Polymethacrylate monoliths were prepared by mixing cross-linker monomer, functional monomer, pore-directing agent and initiator using free-copolymerization. The synthesized polystyrene microsphere particles were used as templates for the monolith pore-directing agent. Pre-polymerization mixtures have been recognized as a factor influencing the morphology of the resultant monolith [13]. Therefore, the optimal ratio of the template and the monolith monomers (50:50, 60:40 and 70:30) for monolith fabrication was investigated. The physical structures of the resultant monoliths are presented in Figure 3. As can be observed, different monolith/template ratios produced monoliths with different physical structures. While the monoliths produced with the 50:50 and 60:40 ratios presented hard and solid physical structures, the monolith produced with the 70:30 ratio exhibited soft and brittle features.

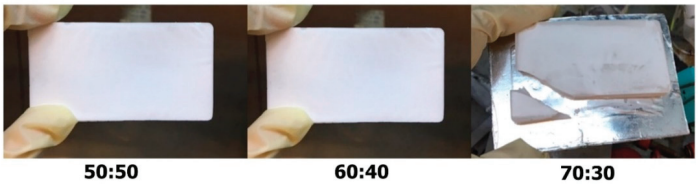

Figure 3. Physical observation of solid monoliths produced using different ratios of templates and monomers (50:50, 60:40, 70:30).

The internal structures of the three monoliths were further characterized. The pore distribution was observed at the outer, middle and inner monolith cross-sections (Figure 4). The images of each step of the ImageJ analysis are shown in Figures S1–S9. It can be observed from the 50:50 profile section (Figure 4a) that a smaller pore size can be found in the middle section (0.2 µm) of the monolith compared to the outer (1.8 µm) and inner (2.3 µm) sections. The outcomes seen here are in agreement with the image produced by the SEM, whereby smaller and non-interconnected pores were found in the monolith produced with a 50:50 ratio. Interconnectivity among pores is essential, as these connections allow the liquid to flow through the monolith, as well as permitting the occurrence of any sort of diffusion process [27]. The monolith produced with the 60:40 ratio exhibited homogenous particles, with particle diameter ranging from 1.9 µm to 2.3 µm in all sections (Figure 4b). In addition, good particle morphology with well-interconnected properties was observed compared to the particles in the monolith produced with the 50:50 ratio. The monolith produced with a 70:30 ratio demonstrated a lower degree of homogeneity than the 60:40 monolith. Larger particles were generated in the inner section, with sizes of 3.7 µm, followed by the outer (2.5 µm) and middle (2.3 µm) sections. The particles in the outer and middle sections were found to be slightly aggregated.

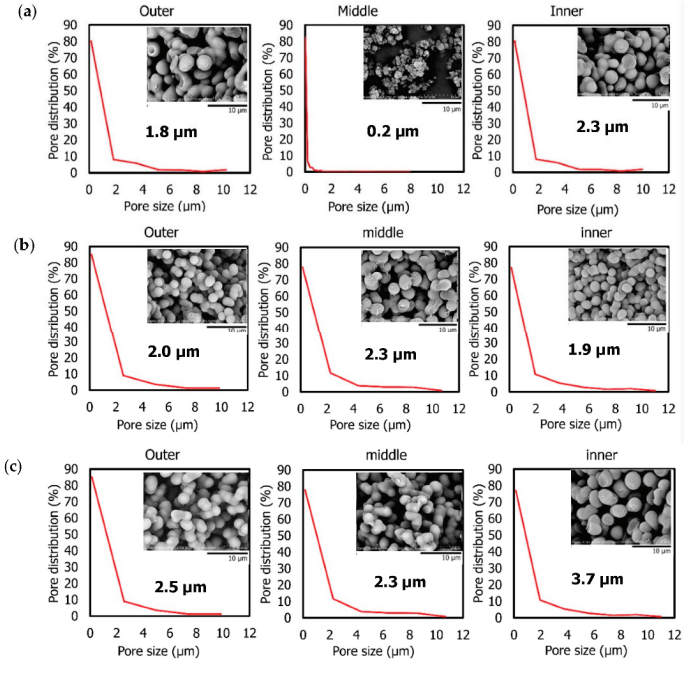

Figure 4. Pore distribution and SEM images (insert) of monolith cross-sections (outer, middle, inner) at different template/monomer ratios: (**a**) 50:50, (**b**) 60:40, (**c**) 70:30.

The physical and internal examinations of the monoliths prepared at various template/monomer ratios indicated the important role played by the template in the production of robust monoliths. The monolith produced with a 70:30 template/monomer ratio had the lowest degree of homogeneity (Figure 4c) and formed a fragile monolith structure (Figure 3). High amounts of template (70%) may result in insufficient reactivity for the building of linking pores throughout the monolith structure, resulting in non-homogeneous pore development, as seen in the SEM images. Some monolith constructions may not be completely covered by monomer components, meaning the structure can be readily shattered.

The ability of the monolith samples to allow water to flow through them was also further investigated. The results reveal that water failed to pass through the monolith with a 50:50 template/monomer ratio (data not shown), owing to the non-interconnected pore features, as shown in Figure 4a. Monolith synthesis using this ratio is not ideal for water filtration systems, since the tiny pore size in the inner section may prevent any substrate from flowing through the surface. According to Geise, et al. [28], simple filtration involves pore flow, whereby separation is predominantly accomplished via a size-sieving mechanism in which the solution is not allowed to flow when the pore size is too small. A similar observation was also found when using the monolith with a 70:30 ratio. Due to its non-homogeneous particles and fragile structure, it was similarly difficult for the water solution to flow through. The 60:40 template/monomer ratio, which exhibited a homogeneous pore distribution for all monolith cross-sections (outer, middle, and inner), was found to efficiently allow water to flow through it. The interconnectivity of the pores may allow liquid solutions to flow from one pore to another, which might be useful in water filtration systems; hence, it was chosen as the basis for future research.

3.3. Template Removal from the Monolith Structure

Following their incorporation into the monoliths, the templates are removed, resulting in the formation of pore structures resembling the shape of the templates. The efficiency of solvent treatment and thermal treatment for the removal of the incorporated microsphere templates in monolith structures was assessed and observed through SEM and FTIR analyses.

3.3.1. Morphological Structure Analysis

Figure 5a,b present the morphological characteristics of the monolith before and after template removal via the solvent treatment and the thermal treatment, respectively. The presence of template can be observed in the SEM images before template removal. After the solvent treatment, template was found to be absent from the images, indicating that the template had been successfully removed from the monolith structure. The monolith exhibited distinct morphologies before and after treatment with respect to the structure of the particles. In addition, a white solution appeared in the solvent, which was probably the microsphere template that had been successfully removed (Figure 5a). Meanwhile, some remaining template was present in the monolith after the thermal treatment (Figure 5b). This indicates that thermal treatment was unable to completely remove the template from the monolith. The findings of this study show that the solvent treatment is superior for the removal of templates from monolith structures. These findings are in agreement with the previous study conducted by Xu, et al. [29], in which it was reported that solvent treatment was superior for polymeric template removal. Solvent treatment has also been reported to be superior for the removal of organic templates from nanostructured silica monoliths, as described by Dabbs, et al. [30]. The resulting monoliths from both the Soxhlet and supercritical extraction methods were found to be mechanically robust, optically clear, and free of cracks. This technique offers the advantage of a moderate temperature and ambient pressure processing without the requirement of specialized equipment.

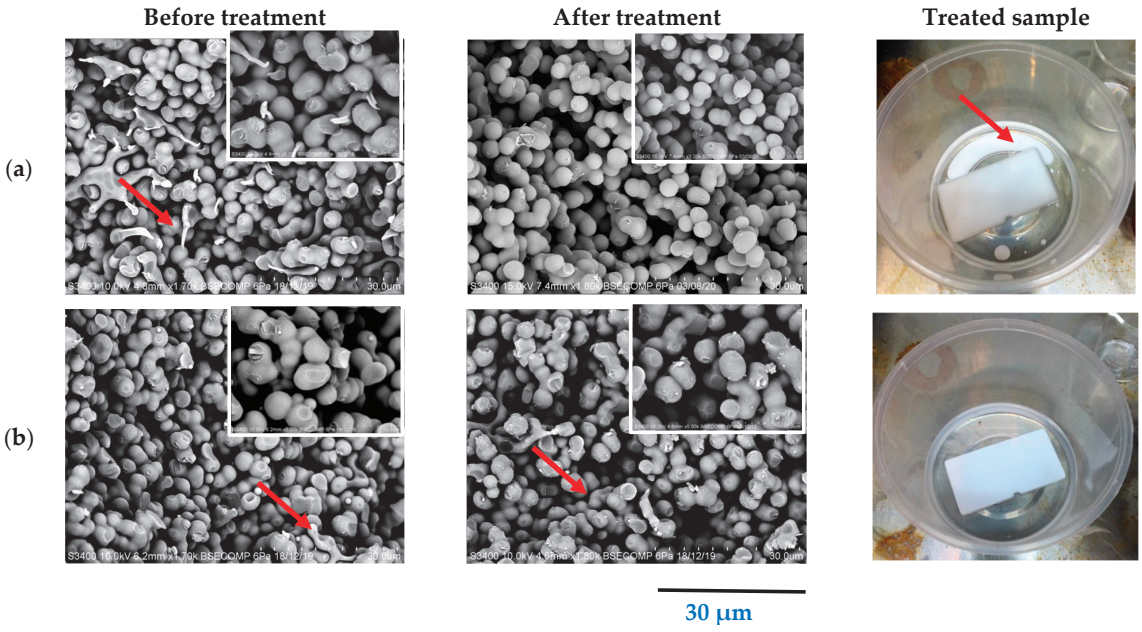

Figure 5. Physical observation and SEM images of monolith before and after template removal process via (**a**) solvent treatment and (**b**) thermal treatment. Red arrows indicate the microsphere template.

3.3.2. Chemical Composition Analysis

The efficiency of both treatments for template removal was further assessed using FTIR analysis (Figure 6). FTIR identifies the functional groups present in the monolith samples [13]. The absorbance of the samples was tested over a range from 600 cm^{-1} to 4000 cm^{-1}. As can be seen from the graph, some peaks disappeared, while some peaks demonstrated a reduced intensity in the solvent-treated monolith. The absorbance peak at 3593 cm^{-1} represents the O-H group of the template surfactant (oleyl alcohol) [31], which disappeared after the treatment process. No obvious peaks were observed within the range 1150–1650 cm^{-1}. The peaks at 1155 cm^{-1} and 1386 cm^{-1} represent the C-C and C-H stretching of polystyrene [32], respectively, while the peak at 1255 cm^{-1} corresponds to the C-N amide of dimethylformamide (DMF) [33], which was used as a solvent during the fabrication of the polystyrene template. These observations indicate the absence of the polystyrene template in the solvent-treated monolith, thus implying the complete removal of the template. On the other hand, most of the above-mentioned peaks remained in the monolith after thermal treatment. This observation is in agreement with the presence of template observed in the SEM images (Figure 5b). These findings indicate that the thermal treatment was inefficient for completely removing the template from the monoliths. In conclusion, on the basis of the SEM and FTIR analyses, the solvent treatment was found to be the best technique for the removal of the microsphere template.

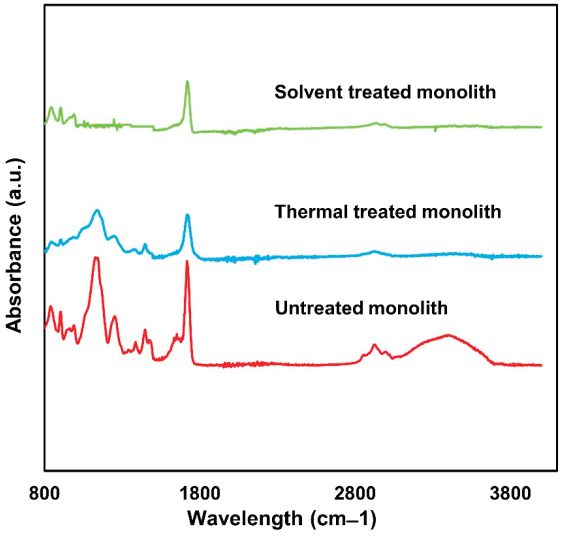

Figure 6. FTIR spectra of untreated monolith, thermal-treated monolith and solvent-treated monolith.

3.4. Thermal Stability of Microsphere-Templated Porous Monoliths

The thermal stability of the resulting solvent-treated microsphere-templated monoliths was further analyzed. Thermogravimetric analysis (TGA) determines the thermal stability of the material, indicating its stability against elevated temperature [22], as presented in Figure 7. The first deterioration of the monolith prepared using a 60:40 template/monolith ratio occurred at 243 °C, with the second degradation beginning at 332 °C. At 700 °C, the monolith samples had been completely degraded and converted into ashes. A previous study reported monolith degradation at a lower temperature of around 200 °C. That monolith was made of similar monomer chemicals, but was templated using porogen as prepared by Acquah, Danquah, Moy, Anwar and Ongkudon [22]. Yusuf, et al. [34] also reported initial monolith degradation at 210 °C in their study. These findings suggest that the thermal stability of the microsphere-templated monolith was slightly enhanced.

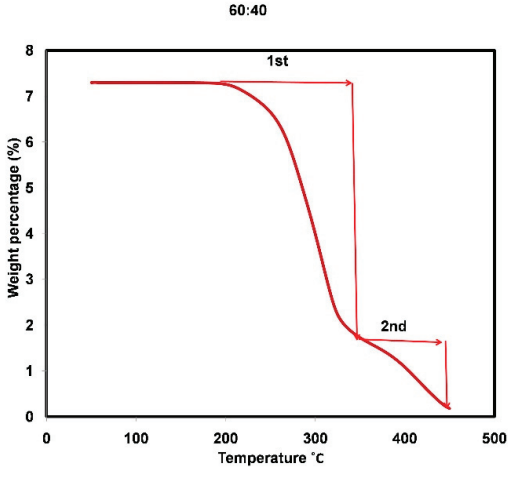

Figure 7. TGA analysis of the solvent-treated microsphere-templated monolith prepared at 60:40 template/monomer ratio at temperatures ranging from 50 to 700 °C.

3.5. Filtration Ability of Microsphere-Templated Porous Monoliths

Monoliths are employed for the removal of water-soluble dyes, heavy metal ions, and emulsified oils from water, and demonstrate a high separation efficiency [35,36]. In this study, the efficiency of the microsphere-templated porous polymethacrylate monoliths for removing particulate matter present in wastewater samples was evaluated by microscopic observation and the analysis of the pH value, turbidity and total suspended solids (TSS) of the samples (before and after treatment process). Figure 8 shows the distinguished optical and microscopic images of the wastewater samples before and after filtration. Before the filtration process, the presence of particulate matter can be clearly observed in both samples. The resultant filtered water samples became clear solutions following the filtration process.

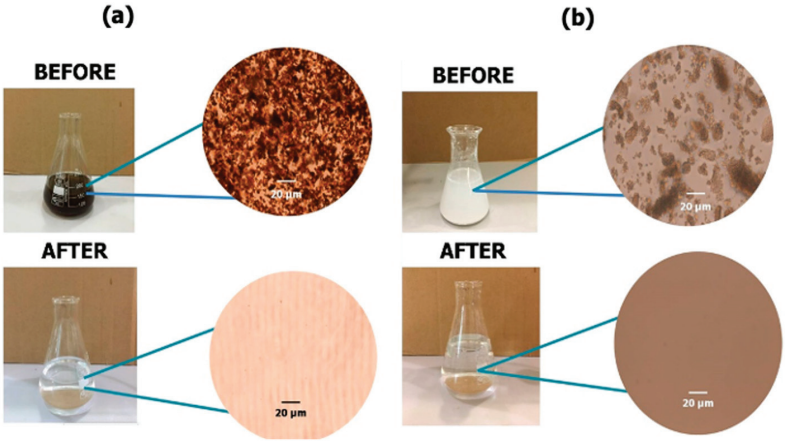

Figure 8. Microscopic images of (**a**) animal pond wastewater and (**b**) laboratory wastewater before and after the filtration process using the developed microsphere-templated porous monolith.

Both samples demonstrated an initial pH of 8.8 (Table 2). The turbidity and TSS of the animal pond wastewater were determined to be 80.7 mg/L and 52 mg/L, respectively. Meanwhile, the laboratory wastewater demonstrated turbidity of more than 1000 mg/L and TSS of 662 mg/L, indicating the presence of more particulate matter compared to the animal pond wastewater. According to Oliveira, et al. [37], the TSS value indicates the quality of the sample by indicating the presence of particulate matter in the water. Similar to TSS, turbidity represents the cloudiness of the water due to the presence of different types of particulates such as organic matter, clays, or silts, depending on the origin of samples [38].

Table 2. Water analysis of wastewater before and after filtration using monoliths prepared using template-directed porous monolith.

Water Quality	Animal Pond Wastewater		Laboratory Wastewater	
	before	**after**	**before**	**after**
Color	Dark brown	Clear	White	Clear
Presence of particulate matter	Yes	No	Yes	No
pH	8.8	8.9	8.8	8.9
Turbidity (mg/L)	80.7	2.69	>1000	0.91
Total suspended solid (mg/L)	52.00	1.60	662.0	0.50

The values of turbidity and TSS were reduced significantly, to 2.69 mg/L and 1.60 mg/L, respectively, as observed in the animal pond wastewater after the filtration. More interestingly, the laboratory wastewater, which presented a very high concentration of turbidity and TSS in initial testing, exhibited a drastic reduction to almost negligible values of turbidity and TSS (below 1.0 mg/L). The monolith demonstrated efficient filtration performance, successfully eliminating about 96.4–96.9% of the turbidity and TSS in the animal pond wastewater and 99.9% in the laboratory wastewater. The levels of turbidity and TSS are within the Class I category, which denotes water bodies with excellent quality based on the Interim National Water Quality Standard [39]. It is important to note that the laboratory-scale fabricated monolith was able to filter up to 3 L of wastewater in one cycle of the filtration process. The waste residues were remained on the surface of the monolith, as shown in Figure 9, and can be cleaned off by rinsing the monolith with water, enabling subsequent usage of the monolith.

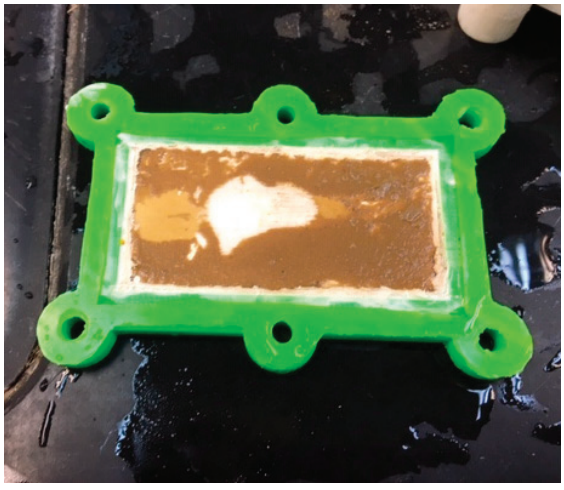

Figure 9. Waste residues on monolith surface upon completion of wastewater filtration.

The results of this study collectively demonstrate the suitability of the microsphere-templated monoliths for wastewater treatment. In future study, the efficiency of the monoliths for the removal of particulate matter can be tested on various types of wastewater, including residential and industrial effluents. Furthermore, their ability to remove other contaminants such as biochemical oxygen demand (BOD), chemical oxygen demand (COD), nitrate, phosphorus, and other organic compounds can be further evaluated.

4. Conclusions

The results presented in this study reveal that porous monoliths synthesized using polymeric microspheres as a template for pore development can be applied in wastewater treatment applications. A template/monomer ratio of 60:40 were demonstrated to be the best conditions for monolith fabrication, resulting in homogeneous pore distributions at all monolith cross-sections (inner, middle, and outer). Solvent treatment was found to be superior to thermal treatment for the removal of microsphere templates from monolith structures. The fabrication procedure successfully produced a monolith that was scalable and thermally stable at temperatures up to 243 °C. Furthermore, the newly fabricated monoliths were demonstrated to be efficient for the removal of particulate matter present in wastewater. The water quality analyses of the tested animal pond and laboratory wastewaters demonstrated the removal of up to 96–99% of TSS and turbidity. It can be concluded that the pores generated across the monolith structures are able to separate

larger and smaller molecules in mixture solutions, which is beneficial for water filtration applications, biomolecule separation, and chromatographic systems.

Supplementary Materials: The following are available online at https://www.mdpi.com/article/10.3390/ma14237165/s1, Figure S1: Images of monolith outer part at 50:50 template/monomer ratio. (a) Original SEM image, (b) threshold of the image set, and (c) the particle outline created with Image J software for the particle size measurement. Figure S2: Images of monolith middle part at 50:50 template/monomer ratio. (a) Original SEM image, (b) threshold of the image set, and (c) the particle outline created with Image J software for the particle size measurement. Figure S3: Images of monolith inner part at 50:50 template/monomer ratio. (a) Original SEM image, (b) threshold of the image set, and (c) the particle outline created with Image J software for the particle size measurement. Figure S4: Images of monolith outer part at 60:40 template/monomer ratio. (a) Original SEM image, (b) threshold of the image set, and (c) the particle outline created with Image J software for the particle size measurement. Figure S5: Images of monolith middle part at 60:40 template/monomer ratio. (a) Original SEM image, (b) threshold of the image set, and (c) the particle outline created with Image J software for the particle size measurement. Figure S6: Images of monolith inner part at 60:40 template/monomer ratio. (a) Original SEM image, (b) threshold of the image set, and (c) the particle outline created with Image J software for the particle size measurement. Figure S7: Images of monolith outer part at 70:30 template/monomer ratio. (a) Original SEM image, (b) threshold of the image set, and (c) the particle outline created with Image J software for the particle size measurement. Figure S8: Images of monolith middle part at 70:30 template/monomer ratio. (a) Original SEM image, (b) threshold of the image set, and (c) the particle outline created with Image J software for the particle size measurement. Figure S9: Images of monolith inner part at 70:30 template/monomer ratio. (a) Original SEM image, (b) threshold of the image set, and (c) the particle outline created with Image J software for the particle size measurement.

Author Contributions: N.F.I.; Methodology, formal analysis, investigation, data curation, writing—original draft preparation. S.S.; Methodology, supervision, writing—review and editing, supervision. C.M.O.; Methodology, writing—review and editing, supervision. M.M.; Conceptualization, methodology, resources, writing—review and editing, supervision, project administration, funding acquisition. All authors have read and agreed to the published version of the manuscript.

Funding: This research was funded by The Ministry of Higher Education Malaysia (MOHE) under research grant scheme FRGS0465-2017.

Institutional Review Board Statement: Not applicable.

Informed Consent Statement: Not applicable.

Data Availability Statement: Data availabilities are from the authors.

Acknowledgments: The authors acknowledge the research funding provided by MOHE and the facilities at Biotechnology Research Institute, Universiti Malaysia Sabah.

Conflicts of Interest: The authors declare no conflict interests.

References

1. Lynch, K.B.; Ren, J.; Beckner, M.A.; He, C.; Liu, S. Monolith columns for liquid chromatographic separations of intact proteins: A review of recent advances and applications. *Anal. Chim. Acta* **2019**, *1046*, 48–68. [CrossRef] [PubMed]
2. Hess, S.; Niessner, R.; Seidel, M. Quantitative detection of human adenovirus from river water by monolithic adsorption filtration and quantitative PCR. *J. Virol. Methods* **2021**, *292*, 114128. [CrossRef] [PubMed]
3. Almeida, A.M.; Queiroz, J.A.; Sousa, F.; Sousa, A. Minicircle DNA purification: Performance of chromatographic monoliths bearing lysine and cadaverine ligands. *J. Chromatogr. B* **2019**, *1118–1119*, 7–16. [CrossRef] [PubMed]
4. González-González, M.; Mayolo-Deloisa, K.; Rito-Palomares, M. Chapter 5—Recent advances in antibody-based monolith chromatography for therapeutic applications. In *Approaches to the Purification, Analysis and Characterization of Antibody-Based Therapeutics*; Matte, A., Ed.; Elsevier: Amsterdam, The Netherlands, 2020; pp. 105–116. [CrossRef]
5. Chan, Y.W.; Kansil, T.; Ongkudon, C.M. Analytical and preparative polymethacrylate monolith fabrication: Effect of porogen content and column size on pore morphology. *Colloid Polym. Sci.* **2017**, *295*, 2373–2382. [CrossRef]
6. Liu, J.; Li, M.; Wang, P.; Liu, K.; Fang, Y. Gel-emulsion templated polymeric monoliths for efficient removal of particulate matters. *Chem. Eng. J.* **2018**, *339*, 14–21. [CrossRef]

7. Wen, L.; Chen, X.; Chen, C.; Yang, R.; Gong, M.; Zhang, Y.; Fu, Q. Ice-templated porous polymer/UiO-66 monolith for Congo Red adsorptive removal. *Arab. J. Chem.* **2020**, *13*, 5669–5678. [CrossRef]
8. Lin, P.; Meng, L.; Huang, Y.; Liu, L. Synthesis of porous polyurea monoliths assisted by centrifugation as adsorbents for water purification. *Colloids Surf. A Physicochem. Eng. Asp.* **2016**, *506*, 87–95. [CrossRef]
9. Szczurek, A.; Fierro, V.; Plyushch, A.; Macutkevic, J.; Kuzhir, P.; Celzard, A. Structure and Electromagnetic Properties of Cellular Glassy Carbon Monoliths with Controlled Cell Size. *Materials* **2018**, *11*, 709. [CrossRef]
10. Juhl, A.C.; Elverfeldt, C.-P.; Hoffmann, F.; Fröba, M. Porous carbon monoliths with pore sizes adjustable between 10 nm and 2 µm prepared by phase separation—New insights in the relation between synthesis composition and resulting structure. *Microporous Mesoporous Mater.* **2018**, *255*, 271–280. [CrossRef]
11. Kamin, Z.; Abdulrahim, N.; Misson, M.; Chiam, C.K.; Sarbatly, R.; Krishnaiah, D.; Bono, A. Use of melt blown polypropylene nanofiber templates to obtain homogenous pore channels in glycidyl methacrylate/ethyl dimethacrylate-based monoliths. *Chem. Eng. Commun.* **2021**, *208*, 661–672. [CrossRef]
12. Gumba, R.E.; Saallah, S.; Misson, M.; Ongkudon, C.M.; Anton, A. Green biodiesel production: A review on feedstock, catalyst, monolithic reactor, and supercritical fluid technology. *Biofuel Res. J.* **2016**, *3*, 431–447. [CrossRef]
13. Shameer, P.M.; Nishath, P.M. Exploration and enhancement on fuel stability of biodiesel: A step forward in the track of global commercialization. In *Advanced Biofuels*; Woodhead Publishing: Sawston, UK, 2019; pp. 181–213.
14. Rodrigues, C.L.; Miguez, E.; Tavares, M.I. Development of Polycaprolactone/Poly(Vinyl Alcohol)/Clay Microparticles by Spray Drying. *Mater. Sci. Appl.* **2016**, *7*, 575–592.
15. Ibadat, N.F.; Ongkudon, C.M.; Saallah, S.; Misson, M. Synthesis and Characterization of Polymeric Microspheres Template for a Homogeneous and Porous Monolith. *Polymers* **2021**, *13*, 3639. [CrossRef] [PubMed]
16. Zhang, S.; Xu, L.; Liu, H.; Zhao, Y.; Zhang, Y.; Wang, Q.; Yu, Z.; Liu, Z. A dual template method for synthesizing hollow silica spheres with mesoporous shells. *Mater. Lett.* **2009**, *63*, 258–259. [CrossRef]
17. Misson, M.; Jin, B.; Chen, B.; Zhang, H. Enhancing enzyme stability and metabolic functional ability of β-galactosidase through functionalized polymer nanofiber immobilization. *Bioprocess Biosyst. Eng.* **2015**, *38*, 1915–1923. [CrossRef]
18. Galarneau, A.; Abid, Z.; Said, B.; Didi, Y.; Szymanska, K.; Jarzębski, A.; Tancret, F.; Hamaizi, H.; Bengueddach, A.; Renzo, F.D.; et al. Synthesis and Textural Characterization of Mesoporous and Meso-/Macroporous Silica Monoliths Obtained by Spinodal Decomposition. *Inorganic* **2016**, *4*, 9. [CrossRef]
19. Ali, S.I. Colloidal Templating: A Route towards Controlled Synthesis of Functional Polymeric Nanoparticles. Ph.D. Thesis, Technische Universiteit Eindhoven, Eindhoven, The Netherlands, 2010.
20. Zhang, Z.; Wang, F.; Ou, J.; Lin, H.; Dong, J.; Zou, H. Preparation of a butyl–silica hybrid monolithic column with a "one-pot" process for bioseparation by capillary liquid chromatography. *Anal. Bioanal. Chem.* **2013**, *405*, 2265–2271. [CrossRef]
21. Malik, A.S.; Dabbs, D.M.; Katz, H.E.; Aksay, I.A. Silica monoliths templated on L3 liquid crystal. *Langmuir* **2006**, *22*, 325–331. [CrossRef] [PubMed]
22. Acquah, C.; Danquah, M.K.; Moy, C.K.S.; Anwar, M.; Ongkudon, C.M. Parametric investigation of polymethacrylate monolith synthesis and stability via thermogravimetric characterisation. *Asia-Pac. J. Chem. Eng.* **2017**, *12*, 352–364. [CrossRef]
23. Pérez, N.; Olaizola, S. *Fabrication of 2D Silver Nanostructures from a Polystyrene Opal*; SPIE: Bellingham, WA, USA, 2006; Volume 6321.
24. Anceschi, A.; Binello, A.; Caldera, F.; Trotta, F.; Zanetti, M. Preparation of Microspheres and Monolithic Microporous Carbons from the Pyrolysis of Template-Free Hyper-Crosslinked Oligosaccharides Polymer. *Molecules* **2020**, *25*, 3034. [CrossRef]
25. Danaei, M.; Dehghankhold, M.; Ataei, S.; Hasanzadeh Davarani, F.; Javanmard, R.; Dokhani, A.; Khorasani, S.; Mozafari, M.R. Impact of Particle Size and Polydispersity Index on the Clinical Applications of Lipidic Nanocarrier Systems. *Pharmaceutics* **2018**, *10*, 57. [CrossRef] [PubMed]
26. Johansen, A.; Schæfer, T. Effects of interactions between powder particle size and binder viscosity on agglomerate growth mechanisms in a high shear mixer. *Eur. J. Pharm. Sci.* **2001**, *12*, 297–309. [CrossRef]
27. Svec, F. Porous polymer monoliths: Amazingly wide variety of techniques enabling their preparation. *J. Chromatogr. A* **2010**, *1217*, 902–924. [CrossRef]
28. Geise, G.M.; Lee, H.-S.; Miller, D.J.; Freeman, B.D.; McGrath, J.E.; Paul, D.R. Water purification by membranes: The role of polymer science. *J. Polym. Sci. Part B Polym. Phys.* **2010**, *48*, 1685–1718. [CrossRef]
29. Xu, H.F.; Zhang, H.J.; Chen, Q.Y.; Yuan, C.C.; Zhang, Q.; Huang, Y.D. Preparation of Hierarchical Porous Methylsilicone Monoliths with Monodisperse Polystyrene Microspheres as Template. *Adv. Mater. Res.* **2013**, *811*, 28–31. [CrossRef]
30. Dabbs, D.M.; Mulders, N.; Aksay, I.A. Solvothermal removal of the organic template from L 3 ("sponge") templated silica monoliths. *J. Nanopart. Res.* **2006**, *8*, 603–614. [CrossRef]
31. Munajad, A.; Subroto, C. Fourier Transform Infrared (FTIR) Spectroscopy Analysis of Transformer Paper in Mineral Oil-Paper Composite Insulation under Accelerated Thermal Aging. *Energies* **2018**, *11*, 364. [CrossRef]
32. Bhagat, R.N.; Sangawar, V.S. Synthesis and Structural Properties of Polystyrene Complexed with Cadmium Sulfide. *Int. J. Sci. Res. (IJSR)* **2017**, *6*, 361–365.
33. Shahali, Z.; Karbasi, S.; Avadi, M.R.; Semnani, D.; Zargar, E.N.; HashemiBeni, B. Evaluation of structural, mechanical, and cellular behavior of electrospun poly-3-hydroxybutyrate scaffolds loaded with glucosamine sulfate to develop cartilage tissue engineering. *Int. J. Polym. Mater.* **2017**, *66*, 589–602. [CrossRef]

34. Yusuf, K.; Badjah-Hadj-Ahmed, A.Y.; Aqel, A.; ALOthman, Z.A. Monolithic metal-organic framework MIL-53(Al)-polymethacrylate composite column for the reversed-phase capillary liquid chromatography separation of small aromatics. *J. Sep. Sci.* **2016**, *39*, 880–888. [CrossRef]
35. Fu, Q.; Zhang, L.; Zhang, H.; Chen, X.; Li, M.; Gong, M. Ice- and MOF-templated porous carbonaceous monoliths for adsorptive removal of dyes in water with easy recycling. *Environ. Res.* **2020**, *186*, 109608. [CrossRef] [PubMed]
36. Yang, J.; Xiao, Q.; Jia, X.; Li, Y.; Wang, S.; Song, H. Enhancement of wastewater treatment by underwater superelastic fiber-penetrated lamellar monolith. *J. Hazard. Mater.* **2021**, *403*, 124016. [CrossRef] [PubMed]
37. Oliveira, A.R.M.d.; Borges, A.C.; Matos, A.T.; Nascimento, M. Estimation on the concentration of suspended solids from turbidity in the water of two sub-basins in the doce river basin. *Eng. Agrícola* **2018**, *38*, 751–759. [CrossRef]
38. Roos, D.A.J.; Gurian, P.L.; Robinson, L.F.; Rai, A.; Zakeri, I.; Kondo, M.C. Review of Epidemiological Studies of Drinking-Water Turbidity in Relation to Acute Gastrointestinal Illness. *Environ. Health Perspect.* **2017**, *125*, 086003. [CrossRef] [PubMed]
39. Zainudin, Z. Benchmarking River Water Quality in Malaysia. *Jurutera* **2010**, *12*, 15.

applied sciences

MDPI

Article

Unstimulated Parotid Saliva Is a Better Method for Blood Glucose Prediction

Yangyang Cui [1,2,3,†], Hankun Zhang [1,2,3,†], Jia Zhu [3], Lu Peng [1,3], Zhili Duan [1,3], Tian Liu [1,3], Jiasheng Zuo [1,3], Lu Xing [1,3], Zhenhua Liao [3], Song Wang [3,*] and Weiqiang Liu [1,2,3,*]

[1] Tsinghua Shenzhen International Graduate School, Tsinghua University, Shenzhen 518055, China; cuiyy20@mails.tsinghua.edu.cn (Y.C.); zhanghk20@mails.tsinghua.edu.cn (H.Z.); pengl20@mails.tsinghua.edu.cn (L.P.); dzl20@mails.tsinghua.edu.cn (Z.D.); liut20@mails.tsinghua.edu.cn (T.L.); zjc20@mails.tsinghua.edu.cn (J.Z.); xingl20@mails.tsinghua.edu.cn (L.X.)
[2] Department of Mechanical Engineering, Tsinghua University, Beijing 100084, China
[3] Biomechanics and Biotechnology Lab, Research Institute of Tsinghua University in Shenzhen, Shenzhen 518057, China; zhuj@tsinghua-sz.org (J.Z.); liaozh@tsinghua-sz.org (Z.L.)
* Correspondence: wangs@tsinghua-sz.org (S.W.); weiqliu@hotmail.com (W.L.); Tel.: +86-0755-265-586-33 (S.W.); +86-0755-265-513-76 (W.L.)
† These authors contributed equally to this work.

Abstract: Objective: Saliva glucose has been widely used in diagnosing and monitoring diabetes, but the saliva collection method will affect saliva glucose concentration. So, this study aims to identify the ideal saliva collection method. Method: A total amount of six saliva collection methods were employed in 80 healthy participants in the morning. Besides, three unstimulated saliva methods were employed in another 30 healthy participants in the morning; in the meantime the blood glucose of these 30 participants was detected with a Roche blood glucose meter. The glucose oxidase method with 2, 4, 6-tribromo-3-hydroxybenzoic acid (TBHBA) as the chromogen has been improved to be suitable for healthy people, through the selection of the optimal pH value and ionic strength of the reaction system. This method was used for the detection of saliva glucose. Results: The improved method obtained absorbance at the wavelength of 520 nm, and the optimized parameter combination was pH 6.5 and 5 mg/dL NaCl. The lower limit of glucose detection was 0.1 mg/dL. Unstimulated saliva glucose concentration was higher than stimulated saliva glucose concentration. Unstimulated parotid saliva glucose concentration was the highest. Besides, unstimulated saliva glucose has a better normal distribution effect. Meantime, it was found that unstimulated parotid saliva was the most highly correlated with blood glucose (R^2 = 0.707). Conclusions: the saliva collection method was an important factor that affected saliva glucose concentration. Unstimulated parotid saliva was the most highly correlated with blood glucose, which provided a reference for prediction of diabetes mellitus.

Keywords: saliva; glucose; methods; diabetes mellitus; sample collection

Citation: Cui, Y.; Zhang, H.; Zhu, J.; Peng, L.; Duan, Z.; Liu, T.; Zuo, J.; Xing, L.; Liao, Z.; Wang, S.; et al. Unstimulated Parotid Saliva Is a Better Method for Blood Glucose Prediction. *Appl. Sci.* **2021**, *11*, 11367. https://doi.org/10.3390/app112311367

Academic Editor: Avelino Núñez-Delgado

Received: 13 October 2021
Accepted: 25 November 2021
Published: 1 December 2021

1. Introduction

Diabetes mellitus (DM) is a globally common chronic disease affecting humans, which remains one of the major health concerns of the 21st century [1]. Without urgent and sufficient action, it is predicted that 578 million people will have DM in 2030 and the number will increase by 51% reaching 700 million in 2045 [2,3]. Blood glucose measurement is an indispensable method for screening and controlling DM. However, routine blood glucose detection requires invasive venipuncture or acupuncture, which brings pain to the patient and affects the patient's enthusiasm for blood glucose monitoring [4,5]. Therefore, non-invasive blood glucose monitoring has attracted great attention. Among the most non-invasive methods, saliva glucose, replacing blood glucose, has major significance in monitoring these conditions. This research area has already generated a plethora of previous scholarly work [6,7]. Caixeta et al. [8] showed that saliva was a promising solution

for the detection and monitoring of DM. Rodrigue et al. [9] pointed out that saliva, like blood, can reflect changes in human physiological functions, so it may be a substitute for early detection and monitoring of DM. Meanwhile, saliva collection is convenient, safe, non-invasive, with no risk of infection, and painless to patients. Therefore, people pay more and more attention to it in experimental research and clinical use [10,11].

Although saliva glucose reflects the health of the human body, its use as a diagnostic fluid has been hindered and neglected, mainly because of the lack of standardized saliva collection methods [12,13]. Most studies use saliva in diagnosis using different collection methods and often lack clear sampling processes [14,15]. This makes it difficult to compare the results of different studies [16]. In general, most studies view saliva incorrectly as a homogeneous body fluid. However, saliva is not a solitary fluid and cannot be viewed as such. Instead, it is a complex mixture consisting of the secretions of three main glands (parotid, submandibular, and sublingual), each of which secretes a characteristic type of saliva, along with hundreds of small salivary glands, gingival crevicular fluids and debris [17]. It is also unstable, but constantly changing, and its composition is affected by other factors such as sampling method, environment, oral hygiene, psychological status and general health [18]. Thus, it is necessary to establish precise standards for saliva collection [19], such as the type of saliva glucose, i.e., saliva produced by whole saliva or specific glands, and whether the sample was collected after stimulation [20,21]. Besides, most of the carbohydrates that are present in saliva are either synthesized in situ in the salivary glands and/or transported from blood capillaries into saliva by diffusion, active transport and/or ultra-filtration [22]. The glucose in saliva may also undergo modifications due to underlying pathological conditions and/or as a result of exposure to drugs and other compounds or solutions. Our understanding of the glucose present in saliva during a normal healthy physiological state, as opposed to a pathological condition, requires further investigation in order for saliva to become a sample of choice for diagnostic and treatment purposes.

Therefore, this study aims to identify the ideal saliva collection method. A total of six saliva collection methods were employed in 80 healthy participants in the morning. Besides, three unstimulated saliva methods were employed in another 30 healthy participants in the morning; in the meantime, the blood glucose of these 30 participants were detected with a Roche blood glucose meter. The glucose oxidase method with 2, 4, 6-tribromo-3-hydroxybenzoic acid (TBHBA) as the chromogen has been improved to be suitable for healthy people, through the selection of the optimal pH value and ionic strength of the reaction system. This method was used for the detection of saliva glucose.

2. Materials and Methods

2.1. Participants

In this study, 110 healthy participants with a mean $\pm$ SD age of 37.5 $\pm$ 4.1 years were included. 80 of these only collected saliva, and another 30 healthy participants not only collected saliva, but also had their blood glucose detected with a glucose meter (Roche Ltd., Basel, Switzerland). Inclusion criteria were good general health, age $\geq$ 18 years, and body mass index (BMI) $\leq 30\,kg/m^2$. All the participants were free of fever or cold and maintained exceptional oral hygiene on the day of collection. If oral examination indicated poor oral hygiene, hyposalivation, oral complaints, or other oral diseases (e.g., mucosal lesions, clinical signs of ongoing periodontal diseases), they were directly excluded from further involvement in the study. All participants signed an informed consent form. The collection of human blood and saliva samples was approved by the local ethics committee at Tsinghua University.

2.2. Glucose Collection

Smoking, brushing teeth, and eating or drinking 30 min before collection were avoided. Then the mouth was rinsed with water before collection to remove food residues in the oral

cavity [23]. A salivette (Sarstedt, 51.5134) (including untreated swabs and swabs stimulated by citric acid) was used to collect saliva glucose, including six collection methods.

For each participant, samples of parotid, sublingual/submandibular, and whole saliva were collected with and without stimulation (as shown in Figure 1), respectively denoted as unstimulated whole saliva (UWS), stimulated whole saliva (SWS), stimulated parotid saliva (SPS), unstimulated parotid saliva (UPS), unstimulated sublingual/submandibular saliva (USS), and stimulated sublingual/submandibular saliva (SSS).

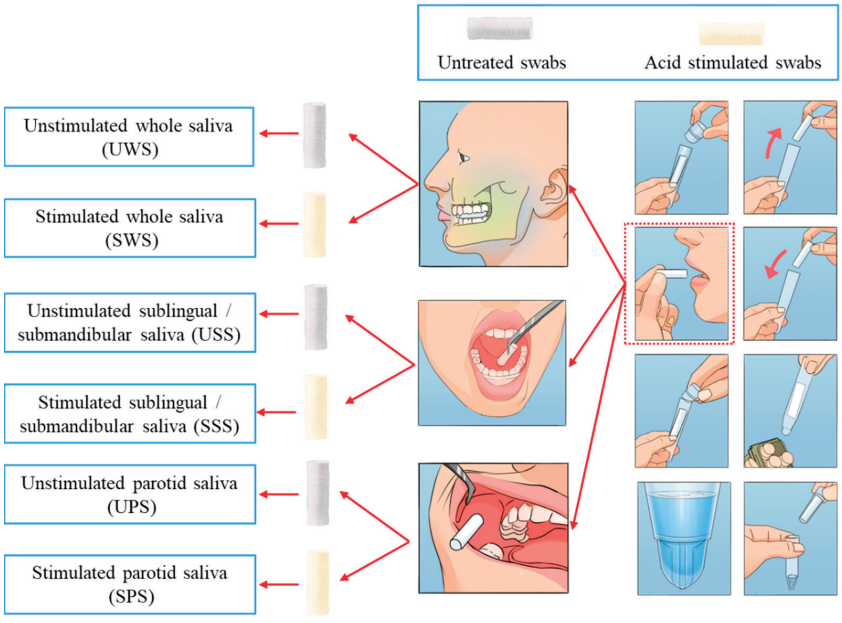

Figure 1. Six methods for collecting glucose; the swabs include untreated swabs and acid stimulated swabs, so the different swabs in parotid, sublingual/submandibular, and whole mouth represent unstimulated whole saliva (UWS), stimulated whole saliva (SWS), stimulated parotid saliva (SPS), unstimulated parotid saliva (UPS), unstimulated sublingual/submandibular saliva (USS), and stimulated sublingual/submandibular saliva (SSS).

All saliva glucose was collected in the same room in the morning. After completing the above steps, the cotton swab soaked with saliva was spit back into the collection tube, then the saliva was collected and weighed with an electronic balance (denoted as Q_1) after centrifugation, and was frozen directly at −20 °C for testing after collection [24]. The saliva flow rate (SFR) reflected the amount of saliva, calculated as in Equation (1).

$$\mathrm{SFR} = \frac{Q_1 - Q_2}{T} \quad (1)$$

SFR was the saliva flow rate, Q_1 was the gross weight, Q_2 was the weight of collection tube, and T was the collecting time.

2.3. Saliva Glucose Assay

The optimal pH and ionic strength of the reaction system were screened, and the glucose oxidase method using TBHBA as the chromogen was improved. Accurately, 20 mg of glucose was weighed before dissolving in artificial saliva (Phygene, pH = 7, Fuzhou, China), which was more than 99% similar to the saliva secreted by the real human body, then was transferred to a 100 mL volumetric flask, which was diluted to the mark to

obtain a 20 mg/dL artificial saliva glucose standard solution. Finally, it was diluted to 30 concentrations between 0.1–6 mg/dL, which were used for calibration of artificial saliva glucose solution measurements. Meanwhile, 0.25 mkat/LGOD and 0.17 mkat/LPOD as 1 mg/mL stock solutions according to the product instructions were prepared, and they were stored in aliquots and frozen at −20 °C. An appropriate amount was taken for each experiment and diluted to the required concentration with PBS. 4-aminoantibiotic Bilene (0.5 mmol/L) and TBHBA (5 g/L) were prepared by dissolving in PBS.

An ultra-micro ultraviolet spectrophotometer (Nano-Drop One Microvolume, Thermo Fisher Scientific, America) was used to obtain the absorbance spectrum of the sample. The wavelengths were selected at 500, 505, 510, 515, 520, 525, 530, 535 nm to obtain the absorbance spectrum of the sample, and the most relevant wavelength was selected. PBS with pH values of 5.6, 5.9, 6.2, 6.5, 6.8, 7.1, 7.4, 7.7, 8 were prepared. 0.1, 0.5, 0.9, 1.3, 1.7 and 2 mg/dL glucose sample were added to detection systems with different pH values, and the correlations were calculated. PBS (pH = 6.5) with NaCl concentration of 1, 3, 5, 7, 9, 11, 13, 15, 17 mg/dL were prepared. The sample group was set to 0.5, 1, and 1.5 mg/dL glucose sample, and the correlations were calculated.

The improved method was used to determine the linear range of glucose concentration detection using a newly constructed pH 6.5, NaCl concentration of 5 mg/dL reaction system to obtain the absorbance value of a glucose standard solution with concentrations of 0.1–6 mg/dL, the results obtained were drawn into a standard curve, and the method was used to measure the collected saliva samples.

Fasting blood glucose was tested before breakfast when all the saliva was collected using a glucose meter. Briefly, the index finger was disinfected with 70% alcohol, and a disposable sterile needle was used to obtain a drop of blood, which was collected on a glucose test strip and then inserted into the glucose meter. The blood glucose level was determined and recorded.

2.4. Statistics

SPSS was used to perform statistical analysis. The data were expressed as relative numbers, and χ^2 was used for comparison between groups. The measurement data were conformed to the normal distribution and expressed as mean ± standard deviation ($\overline{x} \pm s$), and the *t*-test was used for comparison between groups. The Shapiro-Wilk test was used to test the normality of sample data. Non-normally distributed data were described in terms of minimum and maximum numbers, and normally distributed data were described in terms of ($\overline{x} \pm s$). Hypothesis testing would have insufficient sensitivity when the sample size was small, which would cause the results to lose use value, and if the data deviates slightly from normality the final test result would not have much impact, so box plots and qq plots could also be combined to perform statistical analysis. $p < 0.05$ indicated that the difference was statistically significant.

3. Results

3.1. Saliva Detection Method

The reaction product of the improved methods had the highest absorbance value, measured at 510 and 520 nm wavelengths. However, at pH 6.5, the absorbance correlation was highest ($R^2 = 0.9948$) at 520 nm wavelength (as shown in Figure 2). Comprehensively, 520 nm of the maximum absorption wavelength and the pH 6.5 were chosen.

The correlations between different NaCl concentrations and absorbance when the glucose concentrations were 0.5 mg/dL, 1 mg/dL and 1.5 mg/dL are shown in Table 1. When NaCl were 5 mg/dL and 9 mg/dL, the correlations were the highest at 0.999, 0.999, but the Sy. x was the smallest at 5 mg/dL, and the correlation decreased when it was higher or lower than 5 mg/dL. Therefore, the optimal ion environmental concentration was selected as 5 mg/dL.

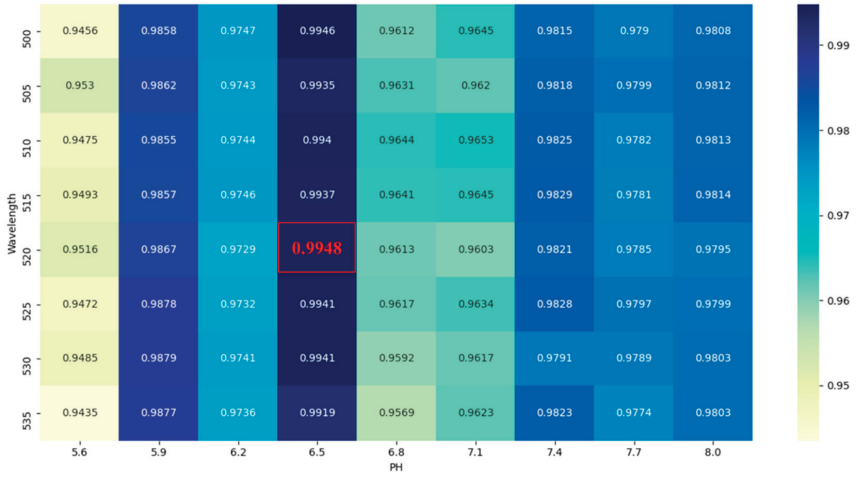

Figure 2. The influence of wavelength and pH on the absorbance of the sample. The red squared highlighting a value is the best result.

Table 1. Correlation between different NaCl concentration and absorbance with 520 nm wavelengths and pH 6.5.

NaCl Concentration	Absorbance of Different Glucose Concentration			R^2	Sy. x
	0.5 mg/dL	1 mg/dL	1.5 mg/dL		
1 mg/dL	0.268 ± 0.05	0.572 ± 0.15	0.762 ± 0.17	0.9826	0.04654
3 mg/dL	0.264 ± 0.09	0.474 ± 0.13	0.836 ± 0.28	0.977	0.06205
5 mg/dL	0.28 ± 0.09	0.558 ± 0.12	0.826 ± 0.27	0.9999 **	0.004082 **
7 mg/dL	0.3 ± 0.05	0.654 ± 0.28	0.75 ± 0.22	0.9012	0.1053
9 mg/dL	0.238 ± 0.03	0.564 ± 015	0.902 ± 0.23	0.9999 *	0.004899 *
11 mg/dL	0.262 ± 0.15	0.654 ± 0.25	1.302 ± 0.61	0.9802	0.1045
13 mg/dL	0.25 ± 0.15	0.592 ± 0.31	0.992 ± 0.45	0.998	0.02368
15 mg/dL	0.266 ± 0.07	0.504 ± 0.21	0.782 ± 0.36	0.998	0.01633
17 mg/dL	0.368 ± 0.19	0.53 ± 0.19	0.872 ± 0.24	0.9592	0.07348
19 mg/dL	0.254 ± 0.21	0.506 ± 0.11	0.744 ± 0.33	0.9997	0.005715

* Indicates the better result, ** Indicates the best result.

The absorbance was taken as the X axis and the glucose concentration as the Y axis, and linear regression was performed to obtain the standard curve equation as Y = 1.68X + 0.04, R^2 = 0.999, as shown in Figure 3. This showed that the improved method had a good linear relationship with the obtained absorbance value when the glucose concentration was in the range of 0.1–6 mg/dL. The lower limit of this range was 0.1 mg/dL, which fully met the sensitivity requirements for detecting the saliva glucose concentration of healthy people.

3.2. Sample Characteristics

Table 2 shows saliva glucose levels of the studied groups; the SFR in the unstimulated parotid saliva was the smallest, followed by the USS, and the largest was UWS. Stimulation of citric acid could also increase the SFR.

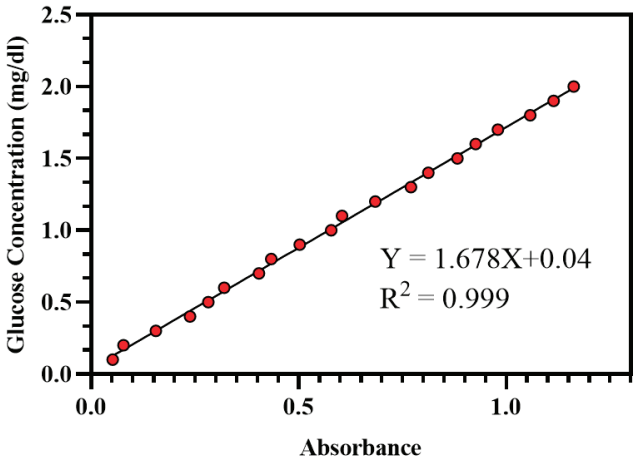

Figure 3. Standard curve of absorbance values of different concentrations of glucose.

Table 2. Saliva glucose levels of the studied groups.

Collection Methods	UWS	SWS	UPS	SPS	USS	SSS
SFR (μL/min)	1347 ± 322	1632 ± 314	113 ± 21	145 ± 55	413 ± 89	571 ± 111

SD: Standard Deviation, respectively denoted as unstimulated whole saliva (UWS), stimulated whole saliva (SWS), stimulated parotid saliva (SPS), unstimulated parotid saliva (UPS), unstimulated sublingual/submandibular saliva (USS), and stimulated sublingual/submandibular saliva (SSS).

Figure 4 shows absorbance of saliva glucose concentration at different saliva collection methods. It can be seen that the saliva concentration of unstimulated parotid saliva was significantly higher than the other five methods. At the same time, the stimulated saliva glucose concentration was significantly lower than the unstimulated saliva glucose concentration. In general, the amount of saliva collected by the stimulated method was much greater than that of the unstimulated method, but the stimulated saliva glucose concentration was lower than the unstimulated saliva glucose concentration.

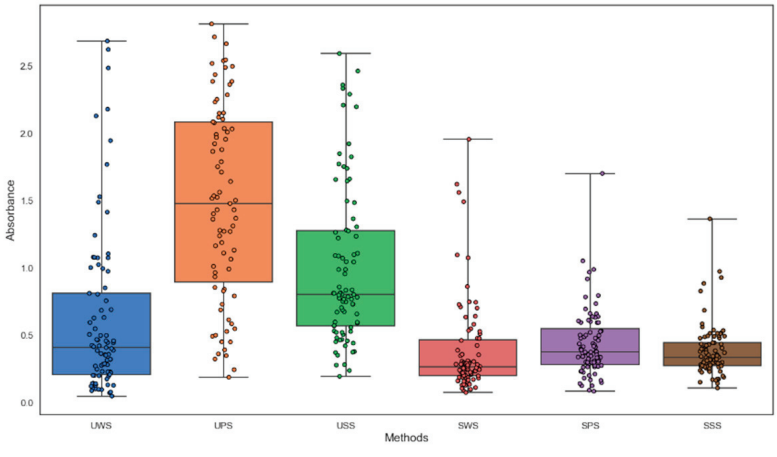

Figure 4. Absorbance of saliva glucose concentration at different saliva collection methods.

3.3. The Normal Distribution Curve of Each Collection Method

Figure 5 shows the normal distribution curve of different collection methods. The normal distribution curve reflected the distribution law of random variables, which indicated the potential of the data for saliva glucose testing. It can be seen that the unstimulated saliva methods had the better distribution law of random variables than the stimulated saliva methods. In general, unstimulated parotid saliva had better normal distribution than other saliva collection methods. So parotid glucose may be better used to respond to saliva glucose.

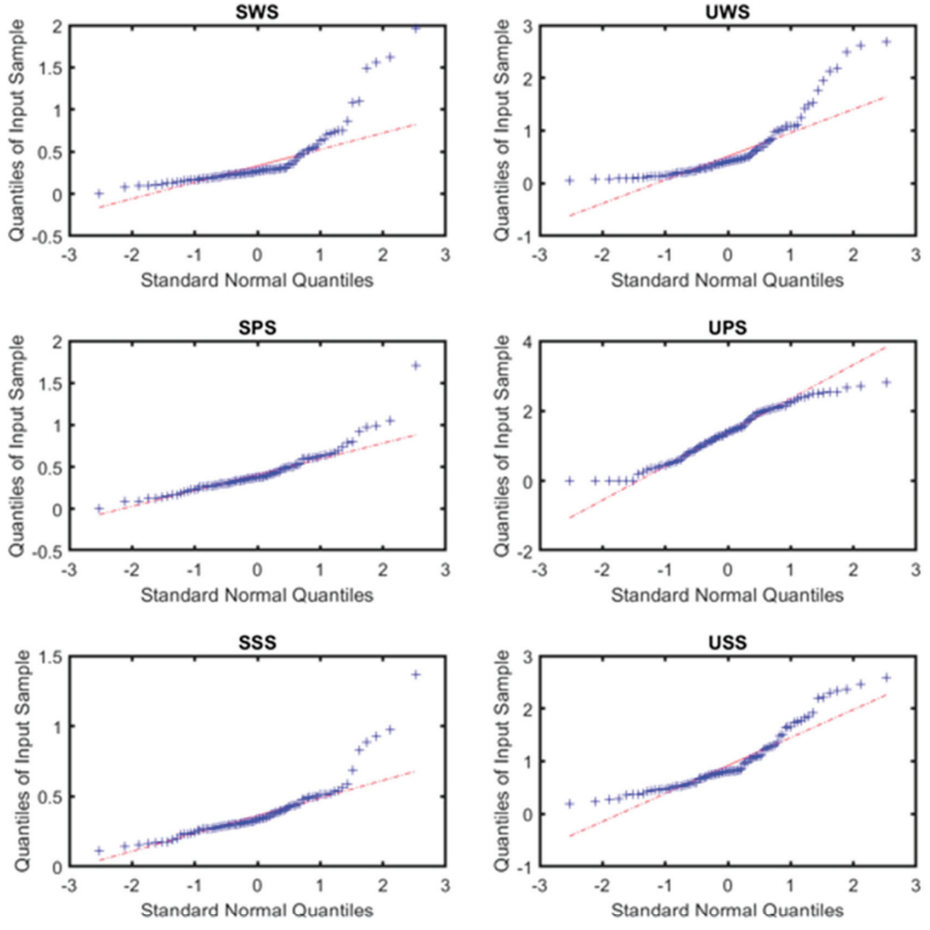

Shapiro-Wilk

Methods	Statistic	DF	SIG.	Methods	Statistic	DF	SIG.
SWS	0.733	64	0	UWS	0.792	65	0.004
SPS	0.799	65	0	UPS	0.973	61	0.189*
SSS	0.797	65	0	USS	0.878	65	0.011

Figure 5. The normal distribution curve of different collection methods. * Indicates that SIG is greater than 0.05 to accept the hypothesis. Respectively denoted as unstimulated whole saliva (UWS), stimulated whole saliva (SWS), stimulated parotid saliva (SPS), unstimulated parotid saliva (UPS), un-stimulated sublingual/submandibular saliva (USS), stimulated sublingual/submandibular saliva (SSS).

3.4. The Correlation of Blood Glucose and Unstiimulated Saliva Glucose

To assess the correlation of saliva glucose with human blood glucose levels, we performed a regression analysis. As shown in Figure 6, the linear regression equation for unstimulated parotid saliva glucose and blood glucose was $Y = 0.3435X + 4.671$, $R^2 = 0.7070$, $p < 0.0001$. The linear regression equation for unstimulated sublingual/submandibular saliva glucose and blood glucose was $Y = 0.4031X + 4.927$, $R^2 = 0.6211$, $p < 0.0001$. The linear regression equation for unstimulated whole saliva glucose and blood glucose was $Y = 0.4052X + 5.046$, $R^2 = 0.5114$, $p < 0.0001$.

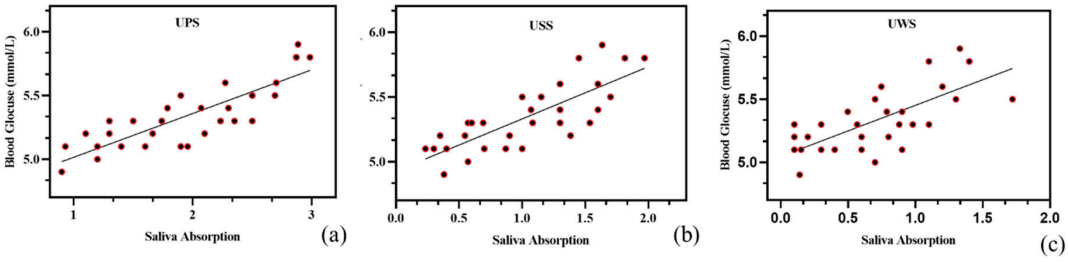

Figure 6. The correlation between saliva glucose and blood glucose: (**a**) unstimulated parotid saliva (UPS), (**b**) unstimulated sublingual/submandibular saliva (USS), (**c**) unstimulated whole saliva (UWS).

4. Discussion

Currently, non-invasive detection techniques based on saliva samples are basically targeted at DM patients. In this study, the glucose oxidase method with TBHBA as the chromogen has been improved to be suitable for healthy people. This method was used to compare the saliva glucose concentration of six different saliva collection methods for the first time.

This study found that the product has a maximum absorption at a wavelength of 520 nm, the optimal pH is 6.5, and the optimal NaCl concentration is 5 mg/dL. The environmental pH value will change or affect the dissociation state of the enzyme and the substrate to increase or decrease the enzyme activity. Therefore, the maximum activity of the enzyme requires the corresponding optimum pH value. The main catalytic enzymes in the test solution are GOD and POD. The activity of the former was in the range of pH 4.0 to 7.0, and the activity of the latter was in the range of pH 5.0 to 9.0. The optimal pH value of the reaction test solution measured in the experiment was 6.5, which was within the range of GOD activity and POD activity. Therefore, it was theoretically speculated that the pH value of 6.5 was the comprehensive optimal pH value of the same system where the two enzymes were located. Besides, it is found that its linear range, accuracy, and precision can meet the requirements of detection, and more importantly, makes the measurement process more standardized, reduces errors, and is simple and easy to implement.

Saliva, like plasma or serum, is a unique and complex body fluid. Sufficient saliva secretion is essential for maintaining oral health. The advantages of saliva assessment include the cost-effectiveness of non-invasive collection and screening of large populations [25]. Saliva is currently considered to be an excellent diagnostic biomarker for human characteristics [26]. In the present study, we found that the unstimulated saliva glucose levels were higher than in stimulated saliva, that unstimulated parotid saliva glucose level was higher than unstimulated sublingual/submandibular saliva, and that unstimulated whole saliva had the lowest level. The blood glucose and unstimulated parotid salivary glucose levels were significantly higher than levels in unstimulated sublingual/submandibular saliva and unstimulated whole saliva, and the glucose levels in parotid saliva were strongly correlated with blood glucose in healthy people. However, in another study, no correlation was found between saliva and plasma glucose levels [27]. Nonetheless, our study revealed a significant, strong correlation between parotid salivary and blood glucose levels but not between

mixed salivary and blood glucose levels, unstimulated sublingual/submandibular saliva and blood glucose; the glucose level in parotid saliva, but not that in unstimulated sublingual/submandibular saliva and unstimulated whole saliva, may thus reflect the blood glucose level. The different conclusions are mainly caused by different saliva collection methods. The six saliva collection methods in this study can make up for the shortcomings of existing research and provide the next step for the concentration of glucose in saliva. The determination of saliva has laid a good foundation and pointed out the direction for finding the most suitable method to collect saliva glucose.

The determination of saliva glucose concentration is a prerequisite for the development of saliva as a diagnostic and prognostic tool for DM biomarker discovery. In this case, it is important to keep the technical variability caused by sample collection and processing to a minimum so that inter-subject variability in health and disease states can be assessed reproducibly [28]. Single or mixed saliva can be collected. It should be noted that many unknown factors and unstable elements will affect the properties of mixed saliva. Saliva collected directly from a single gland is stable and not affected by oral conditions. Thus, it can accurately reflect blood glucose status. Saliva from the parotid gland is easily collected under unstimulated and stimulated conditions. Dhanya et al. [29] reported that, when saliva is collected under unstimulated conditions, the concentration of glucose in saliva is higher than under stimulated conditions, which is consistent with the conclusions obtained in this study. Other studies have found that there is no significant difference in the concentration of glucose in saliva collected under unstimulated and stimulated conditions [30], because participants may not be willing to accept acid stimulation, and the water concentration in stimulated saliva is higher. Besides, unstimulated saliva may be more representative of a normal physiological state. Takeda et al. [31] measured the saliva chemical concentration of healthy subjects under different conditions and found that, compared with stimulated saliva, almost all metabolites in unstimulated saliva were higher. Jha et al. [32] also found that, compared with stimulated saliva, the average saliva glucose level in unstimulated saliva of control and non-control DM patients was higher. Saliva collected directly from a single gland is stable and not affected by oral conditions. Therefore, it may accurately reflect blood glucose status. Moreover, as far as we know, this is the first study focused structurally on comparing the glucose expression of whole saliva and glandular saliva in a cohort of careful characterization and clinical examination. The results indicate that different collection methods provide significant differences in the snapshots of saliva glucose.

The limitation of our study is the relatively small sample size. Further studies with a larger sample size are necessary to confirm the correlation between blood glucose and saliva glucose, so as to design a saliva-based diagnostic test method for DM. In addition, there are still many problems in this study that need to be resolved and further explored. For example, the submandibular glands and sublingual glands are closely located, so it is difficult to separate saliva from these glands with certainty, which is why saliva is collected from both glands. How to distinguish sublingual saliva from submandibular saliva is also a direction that needs further research.

In summary, the results of this study indicate that different saliva collection methods provide significant differences in the snapshots of saliva glucose. Based on the comparison of unstimulated and stimulated saliva collection methods, it can be shown that, based on the simplicity and low variability of the collection method, UPS may be a preferred collection method. The results emphasize the importance of consistency when collecting saliva samples, which should be more important than the collection method itself.

5. Conclusions

In this study, the glucose oxidase method with TBHBA as the chromogen has been improved to become suitable for healthy people. The lower limit of the concentration range determined in this study was 0.1 mg/dL, which fully met the sensitivity requirements for detecting the concentration of saliva glucose in healthy people. The collection method was

an important factor that affected the saliva glucose concentration. This study demonstrated that parotid salivary glucose has potential as an indicator to monitor blood glucose.

Author Contributions: Conceptualization, Y.C.; methodology, H.Z.; software, J.Z. (Jia Zhu); validation, L.P.; formal analysis, Z.D.; investigation, T.L.; resources, L.X.; data curation, J.Z. (Jiasheng Zuo); writing—original draft preparation, Y.C.; writing—review and editing, H.Z.; visualization, H.Z.; supervision, S.W.; project administration, Z.L.; funding acquisition, W.L. All authors have read and agreed to the published version of the manuscript.

Funding: This project was supported by the Guangdong Basic and Applied Basic Research Foundation, the Innovation Commission of Science and Technology of Shenzhen Municipality and the Shenzhen Municipal Industrial and Information Technology Bureau.

Institutional Review Board Statement: The study was conducted according to the guidelines of the Declaration of Helsinki, and approved by the local ethics committee at Tsinghua University (protocol code 74 and date: 8 November 2021).

Informed Consent Statement: All study subjects signed an informed consent form, and the collection of human blood and saliva samples was approved by the local ethics committee at Tsinghua University.

Data Availability Statement: The study did not report any data.

Acknowledgments: This project was supported by the Guangdong Basic and Applied Basic Research Foundation (Grant No. 2020B1515120082), the Innovation Commission of Science and Technology of Shenzhen Municipality (Grant No. JCYJ20190807144001746, Grant No. JSGG20191129114422849) and the Shenzhen Municipal Industrial and Information Technology Bureau (Grant No. 20180309163834680).

Conflicts of Interest: The authors declare no conflict of interest.

References

1. Bauer, U.E.; Briss, P.A.; Goodman, R.A.; Bowman, B.A. Prevention of chronic disease in the 21st century: Elimination of the leading preventable causes of premature death and disability in the USA. *Lancet* **2014**, *384*, 45–52. [CrossRef]
2. Saeedi, P.; Petersohn, I.; Salpea, P.; Malanda, B.; Karuranga, S.; Unwin, N.; Colagiuri, S.; Guariguata, L.; Motala, A.A.; Ogurtsova, K.; et al. Global and regional diabetes prevalence estimates for 2019 and projections for 2030 and 2045: Results from the International Diabetes Federation Diabetes Atlas. *Diabetes Res. Clin. Pract.* **2019**, *157*, 107843. [CrossRef]
3. Jovanovi, J.; Mihailovi, M.; Uskokovi, A.; Grdović, N.; Dinić, S.; Vidaković, M. The Effects of Major Mushroom Bioactive Compounds on Mechanisms That Control Blood Glucose Level. *J. Fungi—Open Access Mycol. J.* **2021**, *7*, 58–65.
4. Meyhöfer, S.; Wilms, B.; Ihling, F.; Windjäger, A.; Kalscheuer, H.; Augustinov, A.; Herrmann, V.; Lehnert, H.; Schmid, S.M. Evaluation of a near-infrared light ultrasound system as a non-invasive blood glucose monitoring device. *Diabetes Obes. Metab.* **2020**, *22*, 694–698. [CrossRef]
5. Baghelani, M.; Abbasi, Z.; Daneshmand, M.; Light, P.E. Non-invasive continuous-time glucose monitoring system using a chipless printable sensor based on split ring microwave resonators. *Sci. Rep.* **2020**, *10*, 12980. [CrossRef]
6. Agrawal, R.P.; Sharma, N.; Rathore, M.S.; Gupta, V.B.; Jain, S.; Agarwal, V.; Goyal, S. Noninvasive method for glucose level estimation by saliva. *J. Diabetes Metab.* **2013**, *4*, 266.
7. Arakawa, T.; Kuroki, Y.; Nitta, H.; Chouhan, P.; Toma, K.; Sawada, S.-I.; Takeuchi, S.; Sekita, T.; Akiyoshi, K.; Minakuchi, S.; et al. Mouthguard biosensor with telemetry system for monitoring of saliva glucose: A novel cavitas sensor. *Biosens. Bioelectron.* **2016**, *84*, 106–111. [CrossRef]
8. Caixeta, D.C.; Aguiar, E.; Cardoso-Sousa, L.; Coelho, L.M.D.; Oliveira, S.W.; Espindola, F.S.; Raniero, L.; Crosara, K.T.B.; Baker, M.J.; Siqueira, W.L.; et al. Salivary molecular spectroscopy: A rapid and non-invasive monitoring tool for diabetes mellitus during insulin treatment. *PLoS ONE* **2019**, *15*, e0223461. [CrossRef] [PubMed]
9. Rodrigues, R.; Vieira, W.; Siqueira, W.L.; Agostini, B.A.; Moffa, E.B.; Paranhos, L.R. Saliva as a tool for monitoring hemodialysis: A systematic review and meta-analysis. *Braz. Oral Res.* **2021**, *35*, e016. [CrossRef] [PubMed]
10. Viswanath, B.; Choi, C.S.; Lee, K.; Kim, S. Recent trends in the development of diagnostic tools for diabetes mellitus using patient saliva. *TrAC Trends Anal. Chem.* **2017**, *89*, 60–67. [CrossRef]
11. Makaram, P.; Owens, D.; Aceros, J. Trends in nanomaterial-based non-invasive diabetes sensing technologies. *Diagnostics* **2014**, *4*, 27–46. [CrossRef]
12. Lee, H.; Hong, Y.-J.; Baik, S.; Hyeon, T.; Kim, D.-H. Enzyme-based glucose sensor: From invasive to wearable device. *Adv. Healthc. Mater.* **2018**, *7*, 1701150. [CrossRef]
13. Tang, L.; Chang, S.-J.; Chen, C.-J.; Liu, J.-T. Non-invasive blood glucose monitoring technology: A review. *Sensors* **2020**, *20*, 6925. [CrossRef] [PubMed]
14. Zhang, A.; Sun, H.; Wang, P.; Wang, X. Salivary proteomics in biomedical research. *Clin. Chim. Acta* **2013**, *415*, 261–265. [CrossRef]

15. Al-Tarawneh, S.K.; Border, M.B.; Dibble, C.F.; Bencharit, S. Defining salivary biomarkers using mass spectrometry-based proteomics: A systematic review. *Omics A J. Integr. Biol.* **2011**, *15*, 353–361. [CrossRef] [PubMed]
16. Matricali, G.A.; Dereymaeker, G.; Muls, E.; Flour, M.; Mathieu, C. Economic aspects of diabetic foot care in a multidisciplinary setting: A review. *Diabetes/Metab. Res. Rev.* **2007**, *23*, 339–347. [CrossRef] [PubMed]
17. Pedersen, A.M.L.; Sørensen, C.E.; Proctor, G.B.; Carpenter, G.; Ekström, J. Salivary secretion in health and disease. *J. Oral Rehabil.* **2018**, *45*, 730–746. [CrossRef] [PubMed]
18. Sigurðardóttir, Á.K. Self-care in diabetes: Model of factors affecting self-care. *J. Clin. Nurs.* **2005**, *14*, 301–314. [CrossRef]
19. Atkinson, K.R.; Lo, K.R.; Payne, S.R.; Mitchell, J.S.; Ingram, J.R. Rapid saliva processing techniques for near real-time analysis of salivary steroids and protein. *J. Clin. Lab. Anal.* **2008**, *22*, 395–402. [CrossRef]
20. Skálová, A.; Stenman, G.; Simpson, R.H.W.; Hellquist, H.; Slouka, D.; Svoboda, T.; Bishop, J.A.; Hunt, J.L.; Nibu, K.-I.; Rinaldo, A.; et al. The role of molecular testing in the differential diagnosis of salivary gland carcinomas. *Am. J. Surg. Pathol.* **2018**, *42*, e11–e27. [CrossRef]
21. Pappa, E.; Vastardis, H.; Rahiotis, C. Chair-side saliva diagnostic tests: An evaluation tool for xerostomia and caries risk assessment in children with type 1 diabetes. *J. Dent.* **2020**, *93*, 103224. [CrossRef]
22. Tettamanti, G.; Bassi, R.; Viani, P.; Riboni, L. Salvage pathways in glycosphingolipid metabolism. *Biochimie* **2003**, *85*, 423–437. [CrossRef]
23. Jurysta, C.; Bulur, N.; Oguzhan, B.; Satman, I.; Yilmaz, T.M.; Malaisse, W.J.; Sener, A. Salivary glucose concentration and excretion in normal and diabetic subjects. *J. Biomed. Biotechnol.* **2009**, *2009*, 430426. [CrossRef] [PubMed]
24. Vasconcelos, A.C.U.; Soares, M.S.M.; Almeida, P.C.; Soares, T.C. Comparative study of the concentration of salivary and blood glucose in type 2 diabetic patients. *J. Oral Sci.* **2010**, *52*, 293–298. [CrossRef] [PubMed]
25. Lee, Y.H.; Wong, D.T. Saliva: An emerging biofluid for early detection of diseases. *Am. J. Dent.* **2009**, *22*, 241.
26. Goudet, G.; Nadal-Desbarats, L.; Douet, C.; Savoie, J.; Staub, C.; Venturi, E.; Ferchaud, S.; Boulot, S.; Prunier, A. Salivary and urinary metabolome analysis for pre-puberty-related biomarkers identification in porcine. *Animal* **2019**, *13*, 760–770. [CrossRef]
27. Gupta, S.; Sandhu, S.V.; Bansal, H.; Sharma, D. Comparison of salivary and serum glucose levels in diabetic patients. *J. Diabetes Sci. Technol.* **2014**, *9*, 91–96. [CrossRef]
28. Panchbhai, A.S. Correlation of salivary glucose level with blood glucose level in diabetes mellitus. *J. Oral Maxillofac. Res.* **2012**, *3*, 3. [CrossRef]
29. Dhanya, M.; Hegde, S. Salivary glucose as a diagnostic tool in Type II diabetes mellitus: A case-control study. *Niger. J. Clin. Pract.* **2016**, *19*, 486–490. [CrossRef]
30. Vuletic, L.; Spalj, S.; Rogic, D.; Peros, K. The rise in glucose concentration in saliva samples mixed with test foods monitored using a glucometer: An observational pilot study. *J. Oral Biosci.* **2019**, *61*, 201–206. [CrossRef]
31. Takeda, I.; Stretch, C.; Barnaby, P.; Bhatnager, K.; Rankin, K.; Fu, H.; Weljie, A.; Jha, N.; Slupsky, C. Understanding the human salivary metabolome. *NMR Biomed.* **2010**, *22*, 577–584. [CrossRef] [PubMed]
32. Jha, S.K.; David, C.M.; Saluja, I.P.; Venkatesh, D.; Chaudhary, S.U. Estimation of salivary glucose level and plasma glucose level in subjects with and without diabetes mellitus: A comparative study. *Natl. J. Integr. Res. Med.* **2013**, *5*, 65–70.

materials

MDPI

Article

Microdome-Tunable Graphene/Carbon Nanotubes Pressure Sensors Based on Polystyrene Array for Wearable Electronics

Xingjie Su [1], Chunli Luo [1,*], Weiguo Yan [2], Junyi Jiao [1] and Dongzhou Zhong [3,*]

[1] School of Control and Mechanical Engineering, Tianjin Chengjian University, Tianjin 300384, China; abcsxj666@163.com (X.S.); junyi_0614@163.com (J.J.)
[2] School of Science, Tianjin Chengjian University, Tianjin 300384, China; yanweiguo@tcu.edu.cn
[3] School of Information Engineering, Wuyi University, Jiangmen 529020, China
* Correspondence: luocl@tcu.edu.cn (C.L.); zhongdz@wyu.edu.cn (D.Z.)

Abstract: Resistive pressure sensors are appealing due to having several advantages, such as simple reading mechanisms, simple construction, and quick dynamic response. Achieving a constantly changeable microstructure of sensing materials is critical for the flexible pressure sensor and remains a difficulty. Herein, a flexible, tunable resistive pressure sensors is developed via simple, low-cost microsphere self-assembly and graphene/carbon nanotubes (CNTs) solution drop coating. The sensor uses polystyrene (PS) microspheres to construct an interlocked dome microstructure with graphene/CNTs as a conductive filler. The results indicate that the interlocked microdome-type pressure sensor has better sensitivity than the single microdome-type and single planar-type without surface microstructure. The pressure sensor's sensitivity can be adjusted by varying the diameter of PS microspheres. In addition, the resistance of the sensor is also tunable by adjusting the number of graphene/CNT conductive coating layers. The developed flexible pressure sensor effectively detected human finger bending, demonstrating tremendous potential in human motion monitoring.

Keywords: resistive pressure sensors; self-assembly; polystyrene microspheres; tunable sensitivity

Citation: Su, X.; Luo, C.; Yan, W.; Jiao, J.; Zhong, D. Microdome-Tunable Graphene/Carbon Nanotubes Pressure Sensors Based on Polystyrene Array for Wearable Electronics. *Materials* **2021**, *14*, 7385. https://doi.org/10.3390/ma14237385

Academic Editor: Avelino Núñez-Delgado

Received: 19 October 2021
Accepted: 28 November 2021
Published: 2 December 2021

1. Introduction

Skin-inspired wearable devices hold tremendous potential in smart portable electronics' next generation due to their intriguing uses in human body movement monitoring, physiological signal detecting, soft robotics, and human–machine interfaces [1–6]. Among these wearable electronics, flexible pressure sensors based on various sensing mechanisms play an important role in detecting external pressure, for example, piezoelectricity [7–9], resistivity [10–13], and capacitance [14–16]. Due to their simplicity of signal processing and wide application range, resistive flexible pressure sensors have been extensively developed among these pressure sensors. Although great advancements have been made in the preparation of high-sensitivity pressure-sensing e-skins, the tradeoff between sensitivity and manufacturing cost has been the core of the research.

Resistive pressure sensors rely on two main aspects, which respond to various pressures. On the one hand, it depends on the resistivity of the sensing material. On the other hand, the microstructure of resistive pressure sensors is critical in improving the sensitivity [3,17]. Among sensing materials, graphene/CNTs exhibit some special advantages, including high electrical conductivity, inherent and structural flexibility, chemical and thermal stability [18–25]. These materials demonstrate outstanding mechanical and electrical characteristics, which make them viable candidates for wearing strain/pressure sensors. For example, Ho et al., using graphene, prepared a transparent and stretchable electronic skin sensor array, integrated the temperature, humidity, and pressure sensors via layer-by-layer superposition [18]. Dahiya Ravinder et al. reported a study on self-produced, flexible and transparent graphene tactile skin. A flexible capacitive touch sensor based on graphene was fabricated [19]. Professor D.H. Kim, using single-walled CNTs, fabricated

flexible and wearable capacitors, field-effect transistors, and gate logic devices or gate logic devices [25].

Introducing microstructure into the design of resistive pressure sensors is an important factor for improving sensitivity and decreasing stress concentration. Recently, several regular micro/nanostructures, including nanowire [26,27], pyramid [28,29], hemisphere [30,31], and microdome [32–35], were used to improve the sensitivity of resistive pressure sensors. For example, graphene films based on pyramidal microstructure arrays give the tactile sensors ultra-high sensitivity ($-5.5\ kPa^{-1}$) in a low-pressure range (<100 Pa) [28]; the sensitivity of the pressure sensor prepared using UV-patterned silver nanowire/polydimethylsiloxane (AgNW/PDMS) composite was $3.179\ kPa^{-1}$ (<2 kPa) [36]. The flexible pressure sensor based on interlocking microdome pattern PDMS showed high sensitivity ($-15\ kPa^{-1}$, <100 Pa) at low pressure [37]. Table 1 lists the sensitivity and sensing mechanisms by previously reported sensors with the microstructure. However, the metal film covering the microstructure surface is very easy to break during the bending motion of the sensor. Therefore, the graphene and CNT network, as a sensing layer, can overcome some shortcomings in fabricating resistive pressure sensors.

Table 1. Comparison of the sensitivity based on this work and previous reports.

Reference	Sensitivity (kPa^{-1})	Pressure Range (kPa)	Sensing Mechanism
[35]	0.533	0–2	Resistance
[36]	0.438	0–2	Resistance
[26]	0.034	0.1< or >10	Capacitive
[23]	0.0115	0–30	Capacitive
[37]	0.23×10^{-3}	0–3000	Resistance
This work	0.02	0–6.5	Resistance

Herein, we provide a unique and low-cost approach based on PS microsphere self-assembly and conductive solution drop coating to fabricate resistive pressure sensors. Graphene/CNT film as a conductive layer improves the bending resistance of a pressure sensor. PS microspheres increase the contact area of conductive film to improve the sensitivity. As a result, the pressure sensor's sensitivity can be adjusted by modifying the feature size of the microstructure. Moreover, the resistance value of the flexible pressure sensor can be flexibly adjusted via changing the number of layers of the graphene/CNTs conductive coating. The flexible sensor was successfully used to detect finger bending motion signals, showing its great application potential in wearable health monitoring system.

2. Experimental Section

2.1. Materials

PDMS was purchased from Dow Corning (Sylgard 184). The PS solution had diameters of 2 μm and 5 μm (Huge biotechnology Co., Ltd., Shanghai, China). Multi-walled CNTs (outer diameter 8–15 nm, inner diameter 3–5 nm, length 3–12 μm, specific surface area > 232 m^2/g, resistivity 1412 μΩm, purity > 95 wt%) and graphene (purity > 90 wt%, thickness ~2 nm, lamellar diameter < 10 μm) were purchased from Tanfeng Tech Co. Ltd., Jiangsu, China.

2.2. Fabrication of the PDMS Film

The liquid PDMS monomer and curing agent were mixed with the weight ratio of 10:1, then mechanically stirred for 10 min with a glass rod, and the mixture was left standing for 30 min to remove bubbles. Then, it was heated for 20 min in an air-blast drying oven at 80 °C to obtain an elastomer layer with a thickness of 2 mm. Then, the PDMS film was treated with oxygen plasma for 1 min to form a hydrophilic surface.

2.3. Preparation of the Monolayer PS Spheres Array

First, we cleaned the glass with detergent to increase the hydrophilicity of the surface. Then, the monodisperse PS spherical suspension (10 wt% in ethanol) was ultrasonically treated at a frequency of 40 kHz for 10 min. Then, the deionized water was dropped onto the clean glass substrate in the vessel to form a water film covering the whole glass surface. Next, we dropped the PS sphere suspension into the water surface and it self-assembled into a monolayer PS sphere array with a large area and close arrangement (Figure 1a). Then, clean water was injected into the vessel to float the PS array on the water surface in the vessel. Next, the PDMS substrate, which was bombarded with oxygen plasma, was held with tweezers and placed underneath the PS film floating on the water surface. Finally, the PDMS substrate slowly lifted up underneath and the monolayer PS sphere array was transferred to the top of the PDMS sheet (Figure 1b,c).

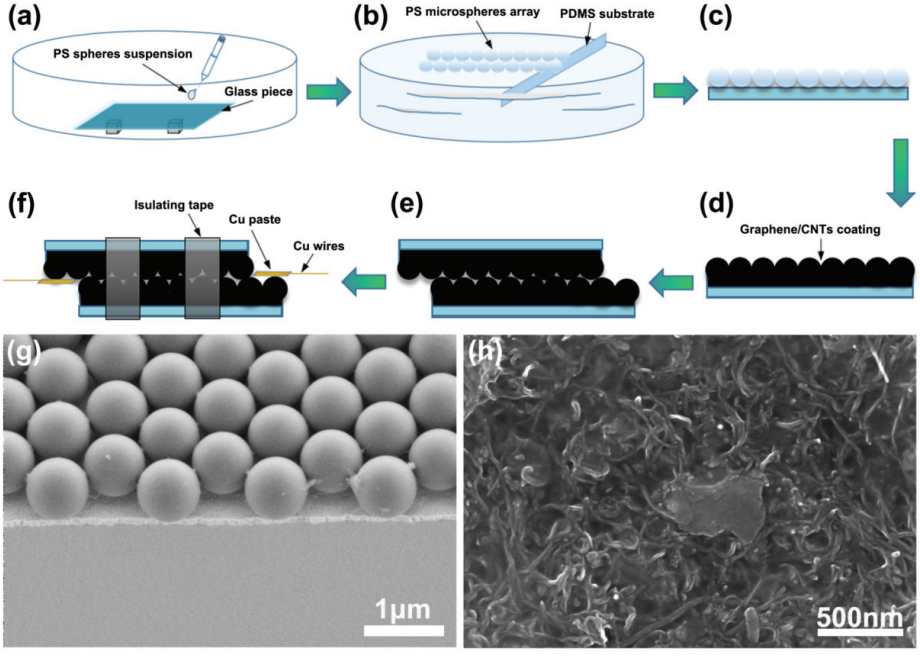

Figure 1. Sensor design and characterization. (**a**) Self-assembly of PS microspheres. (**b**) Assembling the microsphere on the PDMS substrate. (**c**) PDMS film coated with PS microsphere array. (**d**) Coating graphene/CNTs conductive solution on PS microsphere array. (**e**) Stack the two conductive sheets as shown in (**d**). (**f**) Flexible pressure sensor based on graphene/carbon nanotubes. (**g**) Scanning electron micrograph (SEM) of monolayer PS microsphere array. (**h**) SEM image of the surface of graphene/CNTs conductive coating.

2.4. Preparation of Graphene/CNTs Conductive Coating

Before pouring onto the monolayer PS spheres array, a weight ratio of 2:1 (graphene to carbon nanotube) was well mixed (Figure 1d). To guarantee that the coating's thickness was consistent, it was necessary to dip into a small amount of the graphene/CNTs solution with a thin plastic rod and apply it evenly on the PS microsphere array. Then, the sample was put into a 60 °C oven (DL-101, Zhonghuan Experimental Electric Furnace Co., Ltd., Tianjin, China) for 10 min.

2.5. Assembly of the Sensor

The top layer of the graphene/CNTs was attached with copper paste and copper wire to facilitate the electrical performance measurement of the pressure sensor. The electrode

was placed on one side of the graphene/CNTs conductive coating, the upper and lower plates were interlocked, and we stuck on the insulating tape to obtain a flexible pressure sensor (Figure 1e,f).

2.6. Characterizations of Graphene/CNTs Pressure Sensor

The morphologies and microstructures of the conductive coating were comprehensively studied using a field emission scanning electron microscope (FESEM) (Ultra Plus, Zeiss, Oberkochen, Germany) and Raman spectroscopy (532 nm laser source, XploRA, HORIBA Jobin Yvon, Paris, France). A UNI-T UT804 multimeter was used to test the resistance. A semiconductor parameter analyzer was used to assess the sensors' current-voltage (I–V) properties (4200A-SCS, Keithley, MO, USA).

2.7. Feasibility Analysis

First, regarding the preparation of microstructure arrays, we obtained monolayer PS microsphere arrays by simple self-assembly techniques, but traditionally, microstructures are obtained by Si micro-structured mold flip. The disadvantage is that the manufacturing of a silicon microstructure mold is relatively more difficult, which is highly dependent on the equipment and complicated manufacturing processes, such as exposure, soft baking, development, hard baking, photoresist coating, etching and stripping photoresist. Then, considering the manufacturing cost, when preparing the PS microsphere array, the main materials we need are a simple water tank, an ordinary glass sheet, 60–80 μL of monodispersed PS suspensions, and 60–160 μL of anhydrous ethanol solution, which cost very little. In contrast, Si micro-structured arrays rely on a Si mold that is very costly to prepare; a piece of Si micro-structured mold with a size of 1.5 cm × 1.5 cm, for example, costs RMB 3000 to manufacture. Most critically, regarding the flexibility of microstructure size regulation, the morphology of the microstructure layer of our prepared sensor can be tuned through tailoring monodispersed PS microspheres' diameter. As a result, the sensitivity of the pressure sensor may be altered by modifying the feature size of the microstructure. However, a Si micro-structured mold with microstructured surfaces may be utilized directly to recreate the microstructured patterns. Because of their inherent properties, the geometric parameters of microstructures are difficult to modify. A comparison regarding the manufacturing complexity, cost, PS microsphere size control and flexibility is shown in Table 2.

Table 2. Comparison of manufacturing complexity, cost, and flexibility in size control of PS microspheres.

	Microarray (1.5 cm × 1.5 cm)	
	PS Microspheres	**Silicon Template**
Manufacturing complexity	simple (self-assembly technology)	complex (photolithography)
Cost	low (RMB 2)	high (RMB 3000)
Size control flexibility of microstructure	easy to adjust geometric parameters	difficult to adjust geometric parameters

3. Results and Discussion

3.1. The Performance of the Graphene/CNTs Pressure Sensor

A monolayer PS microsphere array is prepared by microsphere self-assembly technology, and then transferred to a PDMS sheet, thereby obtaining a flexible substrate with a uniform dome-shaped microstructure; a single-layer PS microsphere array is shown in Figure 1g. The graphene/CNTs coating has excellent conductivity; Figure 1h shows the SEM view image of the coating. The Raman spectrum of graphene/CNTs conductive coating shows the characteristic spectrum with three main peaks centered at 1334, 1585, and 2691 cm^{-1}, which can be attributed to the D, G, and 2D bands, respectively (Figure 2a). The G band is due to the in-plane E2g mode, which arises from the stretching of the C–C bond, while D and D′bands can be attributed to the defects at the graphite edges.

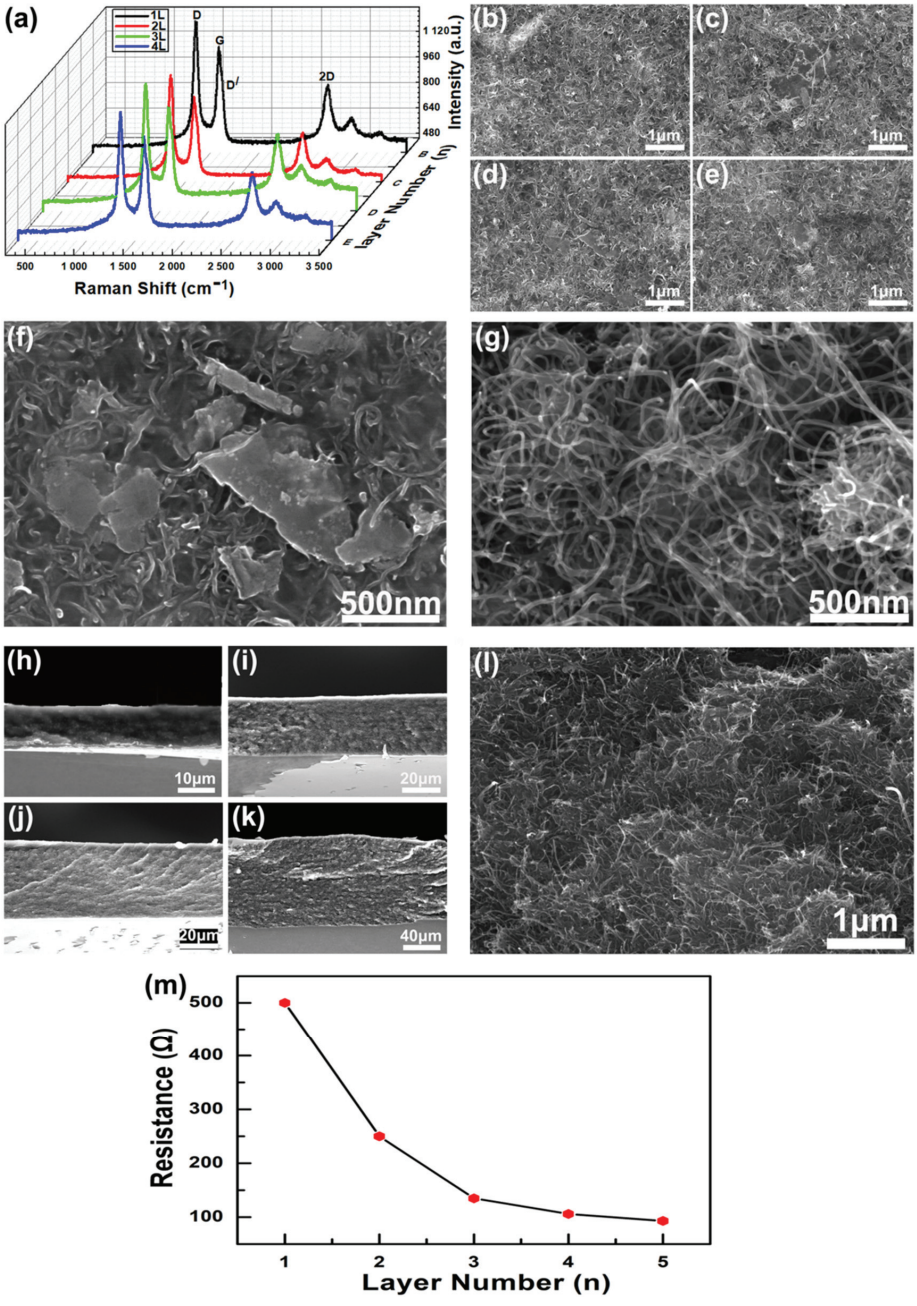

Figure 2. Characterization of graphene/CNTs conductive coating. (**a**) Raman spectra of graphene/carbon nanotube conductive coatings with different layers, respectively. (**b**–**e**) SEM image of 1~4-layer graphene/CNTs conductive coating surface. (**f**) SEM image of sheet-like multilayer graphene on conductive coating. (**g**) SEM image of multi-walled carbon nanotubes on conductive coating. (**h**–**k**) SEM side view of 1–4 layer graphene/CNTs conductive coating. (**l**) High magnification SEM side view of the conductive coating. (**m**) Relationship between the number of conductive coating layers and the resistance value of conductive layer.

The morphology and microstructure of the surface of 1–4 layers of graphene/CNTs conductive coating were characterized by the SEM top view image (Figure 2b–e). It can be seen that the surface morphology and microstructure of different layers of conductive coatings are different. Specifically, a conductive coating with a larger number of layers has a bulk conductor formed by stacking more graphene, as shown in Figure 2f. In addition, the multi-walled CNTs contained in the conductive coating are intertwined and woven together, as shown in Figure 2g. The greater the number of conductive coating layers, the more CNTs are contained, and the tighter the conductive mesh is interwoven. Figure 2h–k shows the SEM side views of 1–4 layers of graphene/CNTs conductive coatings respectively, where 2l is a side view with a larger magnification. Obviously, the coatings between adjacent layers are tightly bonded. With the increase in the number of graphene/CNT conductive coating layers, the conductivity is enhanced. In particular, in the process of increasing the number of layers from integer 1 to integer 3, the resistance is dropped significantly. This is because the two conductive materials, graphene and CNTs, combine more densely. Furthermore, it should be noted here that the sensitivity of the sensor is mainly controlled by the size of the PS microspheres. The increase in the number of conductive layers will slightly reduce the sensitivity of the sensor and slightly improve the mechanical strength, but it has little effect. Although increasing the number of conductive layers will enhance the conductivity of conductive layers, that is, the resistance will decrease, the resistance is not directly related to the sensitivity or mechanical strength. As shown in Figure 2m, it is the relationship between the number of conductive coating layers and the sensor resistance. Although the resistance value can be changed by adjusting the number of conductive layers, considering the cost and performance comprehensively, if there is no extremely high requirement for the conductivity of the conductive layers, the performance of the sensor made of a single conductive layer is good enough. Therefore, the pressure sensors in Figures 3–6 are all made of a single conductive layer.

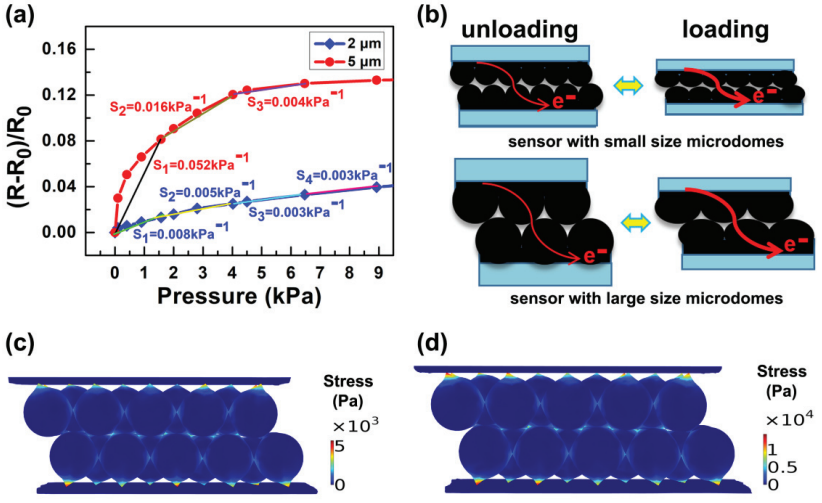

Figure 3. (**a**) Sensitivity of different pressure sensors based on 2 μm and 5 μm sized PS sphere. (**b**) Schematic illustration of the alterations that occur when the equal external pressure is applied to the pressure sensors based on 2 μm and 5 μm sized PS spheres. (**c**,**d**) Finite element modeling of the stress distribution and deformation of the sensors based on 2 μm and 5 μm diameter PS microspheres at 1 kPa applied pressure.

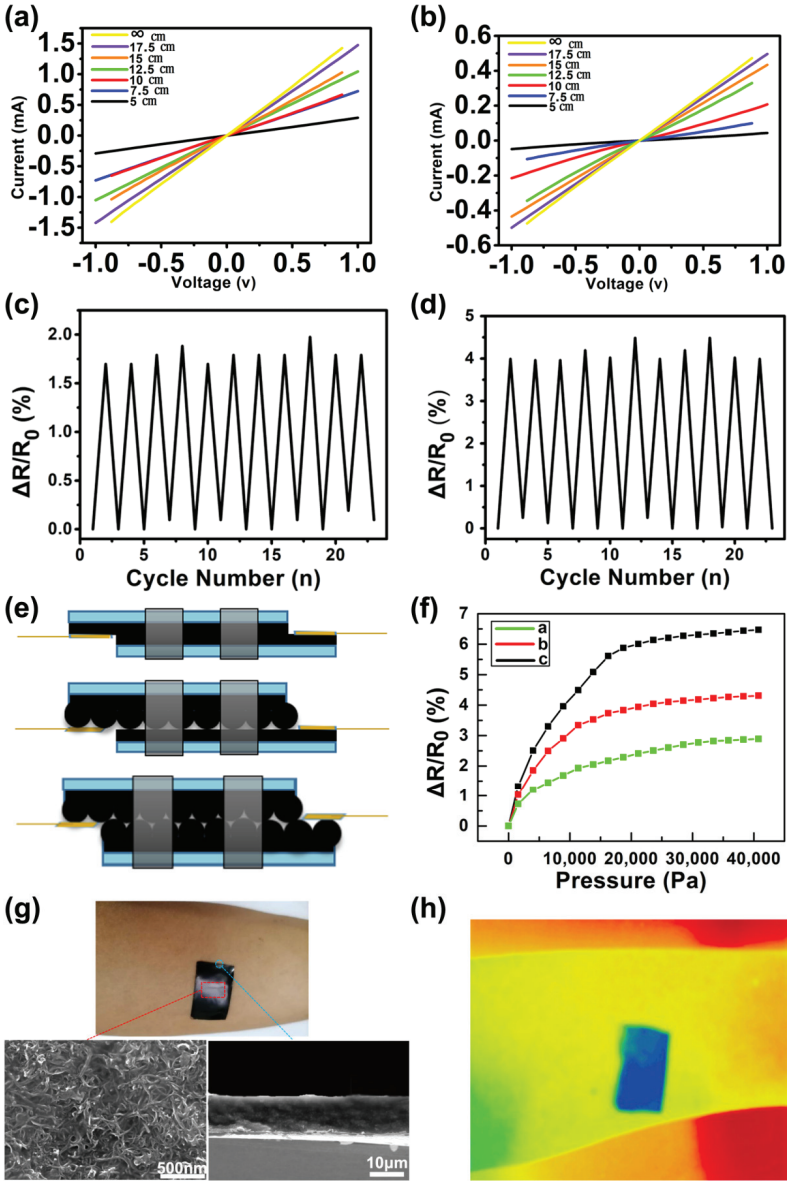

Figure 4. Performance test of graphene/CNTs pressure sensor. (**a**) The current-voltage (I–V) curve of a single planar pressure sensor without surface microstructure under different bending radii. (**b**) The I–V curve of the interlocking microdome pressure sensor under different bending radii. (**c**) The resistance change rate of a single planar pressure sensor without surface microstructure during cyclic bending. (**d**) The resistance change rate of the interlocking microdome pressure sensor during cyclic bending. (**e**) Pressure sensors of a single planar type without surface microstructure, a single microdome type, and an interlocking microdome type are all available. (**f**) The resistance change rate of pressure sensors with three different structures under pressure. (**g**) Test of the adhesion of the PDMS film with graphene/CNTs conductive coating to human skin. (**h**) Test of the infrared absorption effect of PDMS film with graphene/CNTs conductive coating.

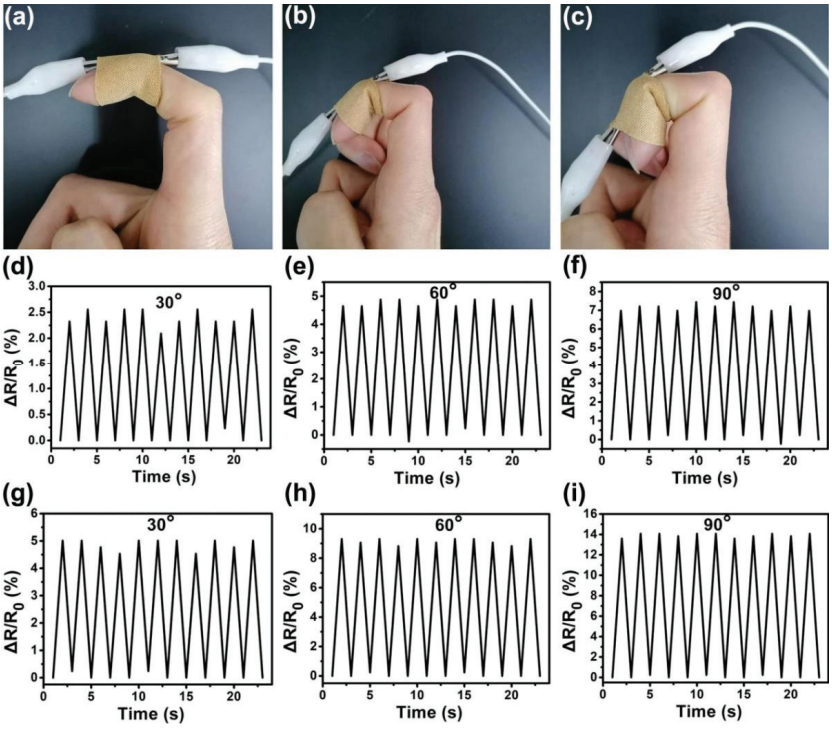

Figure 5. Response of pressure sensor to real-time human motions. (**a**–**c**) Pressure sensor fixed on the finger with a band-aid to monitor the bending motion of the joint at different angles. (**d**–**f**) The resistance change rate of a single planar pressure sensor with no surface microstructure when the finger performs 30, 60, and 90 degree cyclic bending motions. (**g**–**i**) The resistance change rate of the interlocking micro-dome pressure sensor when the finger performs 30, 60, and 90 degree cyclic bending motions.

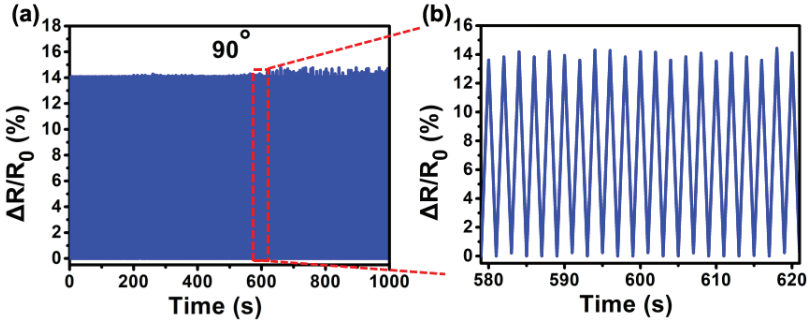

Figure 6. (**a**) The sensor is tested for 90° bending for 480 cycles. (**b**) The 21 cyclic tests extracted from the red region in (**a**).

The pressure-sensing abilities of the manufactured pressure sensors based on 5 μm and 2 μm diameter PS spheres are investigated by measuring relative resistance changes. The pressure sensitivity (S) may be calculated using the formula $S = \delta(\Delta R/R_0)/\delta P$, where P signifies the applied pressure, and R and R_0 signify the resistance change with load pressure and beginning resistance without pressure or load, respectively. The relative differences in resistance of the pressure sensors based on 5 μm and 2 μm diameter PS

sphere are shown in Figure 3a. When the sensor is subjected to the same pressure, the microstructure film with the bigger characteristic size will experience more significant deformation and a large relative change in resistance, as shown in Figure 3b. To explore the dimensional influence of dome-shaped structures on sensor performance systematically, the sensitivity within the low-pressure region may be approximated as:

$$S_{sen} = \frac{H}{S_0 E} \times 2\Pi r = \frac{\Pi}{4S_0 E} \times \left(D^2 + 4H^2\right)$$

where S_0 is the initial contact area between the microdomes, D is the dome's diameter, H is the dome's height, and E is the elastic modulus of PS. The height and diameter of the dome have a positive effect on the sensitivity in the low pressure range, which is clearly presented in the formula. Figure 3c,d depicts the stress distribution of the finite element simulated interlocked microdome sensor at 1 kPa applied pressure. Here, the monolayer microstructured films with microsphere diameters of 2 μm and 5 μm are assembled into interlocking dome pressure sensors in turn. The stress distribution graphic illustrates that as the load rises, the contact area S between interlocking microdomes grows and the dome height H decreases. Under the load applied state, the local stresses are focused on the contact faces between the interlocked microdomes. In addition, compared with the sensor with a microsphere diameter of 2 μm, the stress distribution range of the sensor with a microsphere diameter of 5 μm is wider.

In order to more clearly discuss the role of the PS microsphere size in the work, Table 3 records the sensitivity values of pressure sensors based on PS microspheres of 5 μm and 2 μm in different pressure ranges in detail. At low pressure (<1600 Pa), the sensitivity of the sensor based on 2 μm diameter PS microspheres is 0.00825 kPa^{-1}, while the sensitivity of the sensor based on 5 μm PS microspheres is as high as 0.05194 kPa^{-1}, the latter being more than 6 times more sensitive than the former. In particular, when the pressure is less than 100 Pa, the sensitivity of them is 0.04 kPa^{-1} and 0.3 kPa^{-1} respectively, the sensitivity is higher, and the disparity between them is larger. This is because the pressure sensor based on large PS microspheres can cause more severe deformation of the conductive film under the same pressure because of the larger size of the microspheres, while the sensor based on small size PS microspheres cannot cause obvious deformation and larger relative resistance change due to the size of the microspheres being much smaller than the thickness of the conductive film. In the medium pressure range (1600–4000 Pa), the sensitivity of the sensor based on small microspheres is 0.00495 kPa^{-1}, while that based on large microspheres is 0.01624 kPa^{-1}. Compared with the low pressure state, the sensitivity of PS microspheres is decreased to a greater extent, which is because the deformation of the PS microspheres is limited in a certain range and nonlinear, and the deformation of the PS microspheres is larger under the initial pressure. After increasing the pressure, the deformation increment gradually decreases, due to its own rigidity. On the other hand, because PS microspheres are covered on the flexible substrate of PDMS, the external pressure exerted on the sensor surface will be conducted down to the substrate through the PS microspheres. When the pressure is low, the substrate will sag down, which will cause greater bending deformation of the conductive film. However, as the pressure continues to increase, the upward reaction force of the substrate to the microspheres will also increase, and the deformation increment of the substrate will also decrease significantly. In the high pressure range (4000~6500 Pa), the sensitivities of both are 0.00317 kPa^{-1} and 0.00389 kPa^{-1}, respectively. With the increase in external pressure, the sensitivity of the sensor based on large-size microspheres decreases more rapidly, as, at this time, the sensitivity of both sensors is almost equal, and the sensor based on large-size microspheres reaches saturation pressure. The reason for the difference in sensitivity of pressure sensors based on different PS sphere sizes is related to the change in surface area of the conductive film. The microstructure conductive film with smaller feature size covers a large number of microspheres in the same area, and the microstructure array composed of microspheres with a smaller size is arranged more tightly, has a larger surface area, and has stronger

resistance to pressure. When the same pressure is applied, the deformation, contact area and resistance change of the sensor are smaller. At a higher pressure (6500~8900 Pa), because the sensor based on large-size microspheres has reached saturation pressure, it cannot respond to external pressure efficiently. However, the sensitivity of the sensor based on small-sized microspheres decreases relatively slowly with the increase in pressure, so the saturation pressure is higher, and the sensitivity is 0.00275 kPa^{-1} at this time. In summary, it is clear that the feature size of PS microspheres has a strong modulating effect on the sensitivity and pressure detection range of the sensor as well as the corresponding regulation mechanism.

Table 3. Experimental sensitivity values of the pressure sensor.

	Corresponding Pressure (Pa)			
Size of the microdomes (kPa^{-1})	0–1600	1600–4000	4000–6500	6500–8900
2 μm	0.00825	0.00495	0.00317	0.00275
5 μm	0.05194	0.01624	0.00389	0.0012

Figure 4a,b shows the pressure sensor's current–voltage (I–V) curves at the various radius of curvature. As the voltage is swept from −1 V to 1 V, the applied pressure remains constant. The slopes of the I–V curves reduce as the degree of bending increases, showing that resistance increases as curvature increases. The linearity of the I–V curves implies that Ohm's contact properties dictate the device's behavior. Among them, Figure 4a is the I–V curve of the pressure sensor without the PS microsphere array, and Figure 4b is the I–V curve of the PS microsphere array pressure sensor with a diameter of 2 μm. The resistance of the former increases by 11 times during the process from natural extension to bending to a radius of curvature of 5 cm. In the latter, under the same conditions, the resistance is increased by 5 times. Obviously, the interlocked microstructured sensor is more sensitive than the planar surface sensor. The curve of the resistance change rate of the pressure sensor without the PS microsphere array during the bending process is shown in Figure 4c, and Figure 4d is the resistance change rate curve of the pressure sensor with a 2 μm diameter PS microsphere array during the bending process. Three different pressure sensors were prepared, namely, single plane type, single microdome type and interlocking microdome type based on 2 μm diameter microspheres (Figure 4e), in order to study the influence of the surface micro-structure on sensor sensitivity. Figure 4f shows a comparison of their electrical resistance changes when subjected to external pressure, corresponding to the three curves: a, b, and c. Although all of them display an increase in resistance as pressure rises, the interlocking microdome sensors' responses differ significantly from those of the planar sensor. In reaction to pressure, we can notice a considerable reaction for the microstructured sensors. When the pressure is applied to 18,000 Pa, the resistance change rate of the interlocked microdome sensor is 5.87%, which is significantly higher than the resistance change rate of the non-structured sensor 2.29% and the single-microstructured sensor 3.83%. However, when the applied pressure is in the range of 18,000~40,000 Pa, as the pressure increases, the sensor resistance increases relatively slowly and tends to be stable. The PDMS flexible substrate of the pressure sensor has good adhesion to human skin (Figure 4g). In addition, as shown in Figure 4h, the graphene/CNTs hybrid coating of the pressure sensor can effectively absorb infrared rays. Therefore, the flexible pressure sensor possesses extensive use outlooks in wearable medical monitoring devices, electronic skin, artificial intelligence, and soft robotics [23].

3.2. The Specific Application of the Graphene/CNTs Pressure Sensor

The graphene/CNTs pressure sensor was fixed on the finger through a band-aid to monitor the bending motion of the joint at different angles (Figure 5a–c). At the same time, real-time resistance changes were recorded (Figure 5d–i). The resistance change rate of the pressure sensor without the PS microsphere array in the cyclic bending of the finger at

different angles is shown in Figure 5d–f. Figure 5g–i corresponds to the resistance change rate of the pressure sensor with a 2 μm diameter PS microsphere array. It was found that the resistances of the sensor showed corresponding increases or decreases with the deformation of the finger. Furthermore, under the same conditions, the resistance change rate of the interlocking microstructure sensor was almost twice that of flat surface sensor.

There is a significant difference in sensitivity between them, providing more contact area under the same applied pressure, which is the reason why the interlocking microstructure sensor is far more sensitive than the sensor with flat surface. As a consequence, as compared to a pressure sensor composed of an unstructured substrate, the structured sensor's sensitivity to outside pressure may be effectively boosted. The decreased contact resistance between the two interlocked conductive films caused by the increased contact area under outside load is the main reason for this result. The amazing sensing performance of our sensor is due to the changing in the contact zone, which is generated by the deformation of the microstructure.

To investigate the long-term stability, a pressure sensor based on a 2 μm diameter PS sphere was fixed on the finger and bent at 90°/released 480 times. As shown in Figure 6a, after 480 cycles, the change in relative resistance showed almost no change, and only after the 290th cycle, the change rate of resistance increased slightly during bending. Figure 6b shows 21 random cycle tests extracted from the red region in Figure 6a; the curves of each bending–releasing cycle are almost the same, and the high reproducibility and durability of the microstructure sensor are proved by the very similar amplitude and waveform. We ascribe this exceptional endurance to the PS microspheres' and PDMS substrate's strong elasticity, which can resist numerous mechanical deformation cycles.

4. Conclusions

In summary, a novel graphene/CNTs resistive pressure sensor based on interlocking microdome structure was successfully fabricated and showed to be significantly improved in adjusting sensitivity. Graphene/CNTs are used as the conductive layer to enhance the bending resistance of the sensor, and the PS microsphere array changes the contact area of the conductive film to adjust the sensitivity. By introducing PS microspheres with a larger feature size, the sensitivity of the sensor was significantly improved. The resistive pressure sensor was successfully used for real-time monitoring of finger bending motion. In addition, 480 cycles of the bending test were carried out on the pressure sensor fixed on the finger; the consistency of the curve of relative resistance change rate showed that the sensor has high stability and good durability. Therefore, this work provides a novel strategy for manufacturing flexible pressure sensors with high performance and low cost through the use of carbon nanomaterials and microstructure construction.

Author Contributions: Conceptualization, C.L. and W.Y.; methodology, X.S.; software, J.J.; validation, X.S.; formal analysis, J.J.; investigation, X.S., W.Y. and D.Z.; resources, C.L.; data curation, C.L.; writing—original draft preparation, X.S.; writing—review and editing, D.Z. All authors have read and agreed to the published version of the manuscript.

Funding: This research was funded by National Natural Science Foundation, grant number 62075168; Guang Dong Basic and Applied Basic Research Foundation, grant number 2020A1515010088; Major Project of Basic Research and Applied Research for Natural Science in Guang Dong Province, grant number 2017KZDXM086; Special project in key fields of Guangdong Provincial Department of Education of China, grant number 2019KZDZX1025, 2020ZDZX3052.

Institutional Review Board Statement: Not applicable.

Informed Consent Statement: Not applicable.

Data Availability Statement: The data presented in this study are available on request from the corresponding author.

Conflicts of Interest: The authors declare no conflict of interest.

References

1. Xu, K.; Lu, Y.; Takei, K. Multifunctional Skin-Inspired Flexible Sensor Systems for Wearable Electronics. *Adv. Mater. Technol.* **2019**, *4*, 1800628. [CrossRef]
2. Zang, Y.; Zhang, F.; Di, C.-A.; Zhu, D. Advances of flexible pressure sensors toward artificial intelligence and health care applications. *Mater. Horiz.* **2015**, *2*, 140–156. [CrossRef]
3. Lee, G.-H.; Moon, H.; Kim, H.; Lee, G.H.; Kwon, W.; Yoo, S.; Myung, D.; Yun, S.H.; Bao, Z.; Hahn, S.K. Multifunctional materials for implantable and wearable photonic healthcare devices. *Nat. Rev. Mater.* **2020**, *5*, 149–165. [CrossRef]
4. Boutry, C.M.; Beker, L.; Kaizawa, Y.; Vassos, C.; Tran, H.; Hinckley, A.C.; Pfattner, R.; Niu, S.; Li, J.; Claverie, J.; et al. Biodegradable and flexible arterial-pulse sensor for the wireless monitoring of blood flow. *Nat. Biomed. Eng.* **2019**, *3*, 47–57. [CrossRef]
5. Mishra, R.K.; Goud, K.Y.; Li, Z.H.; Moonla, C.; Mohamed, M.A.; Tehrani, F.; Teymourian, H.; Wang, J. Continuous Opioid Monitoring along with Nerve Agents on a Wearable Microneedle Sensor Array. *J. Am. Chem. Soc.* **2020**, *142*, 5991–5995. [CrossRef]
6. Ji, S.; Wan, C.; Wang, T.; Li, Q.; Chen, G.; Wang, J.; Liu, Z.; Yang, H.; Liu, X.; Chen, X. Water-Resistant Conformal Hybrid Electrodes for Aquatic Endurable Electrocardiographic Monitoring. *Adv. Mater.* **2020**, *32*, e2001496. [CrossRef]
7. Chorsi, M.T.; Curry, E.J.; Chorsi, H.T.; Das, R.; Baroody, J.; Purohit, P.K.; Ilies, H.; Nguyen, T.D. Piezoelectric Biomaterials for Sensors and Actuators. *Adv. Mater.* **2019**, *31*, e1802084. [CrossRef] [PubMed]
8. Cha, Y.; Chung, J.; Hur, S.-M. Torsion Sensing on a Cylinder Using a Flexible Piezoelectric Wrist Band. *IEEE/ASME Trans. Mechatron.* **2019**, *25*, 460–467. [CrossRef]
9. Shen, M.-L.; Zhang, Y. Flexible sensor and energy storage device based on piezoelectric nanogenerator. *Acta Phys. Sin.* **2020**, *69*, 170701. [CrossRef]
10. Pang, C.; Lee, G.-Y.; Kim, T.-I.; Kim, S.M.; Kim, H.N.; Ahn, S.-H.; Suh, K.-Y. A flexible and highly sensitive strain-gauge sensor using reversible interlocking of nanofibres. *Nat. Mater.* **2012**, *11*, 795–801. [CrossRef]
11. Park, J.; Lee, Y.; Hong, J.; Lee, Y.; Ha, M.; Jung, Y.; Lim, H.; Kim, S.Y.; Ko, H. Tactile-Direction-Sensitive and Stretchable Electronic Skins Based on Human-Skin-Inspired Interlocked Microstructures. *ACS Nano* **2014**, *8*, 12020–12029. [CrossRef]
12. Fu, X.; Dong, H.; Zhen, Y.; Hu, W. Solution-Processed Large-Area Nanocrystal Arrays of Metal-Organic Frameworks as Wearable, Ultrasensitive, Electronic Skin for Health Monitoring. *Small* **2015**, *11*, 3351–3356. [CrossRef]
13. Park, H.; Jeong, Y.R.; Yun, J.; Hong, S.Y.; Jin, S.; Lee, S.-J.; Zi, G.; Ha, J.S. Stretchable Array of Highly Sensitive Pressure Sensors Consisting of Polyaniline Nanofibers and Au-Coated Polydimethylsiloxane Micropillars. *ACS Nano* **2015**, *9*, 9974–9985. [CrossRef]
14. He, Z.; Chen, W.; Liang, B.; Liu, C.; Yang, L.; Lu, D.; Mo, Z.; Zhu, H.; Tang, Z.; Gui, X. Capacitive Pressure Sensor with High Sensitivity and Fast Response to Dynamic Interaction Based on Graphene and Porous Nylon Networks. *ACS Appl. Mater. Interfaces* **2018**, *10*, 12816–12823. [CrossRef] [PubMed]
15. Wan, Y.; Qiu, Z.; Huang, J.; Yang, J.; Wang, Q.; Lu, P.; Yang, J.; Zhang, J.; Huang, S.; Wu, Z.; et al. Natural Plant Materials as Dielectric Layer for Highly Sensitive Flexible Electronic Skin. *Small* **2018**, *14*, e1801657. [CrossRef] [PubMed]
16. Qiu, Z.; Wan, Y.; Zhou, W.; Yang, J.; Yang, J.; Huang, J.; Zhang, J.; Liu, Q.; Huang, S.; Bai, N.; et al. Ionic Skin with Biomimetic Dielectric Layer Templated from Calathea Zebrine Leaf. *Adv. Funct. Mater.* **2018**, *28*, 1802343. [CrossRef]
17. Tang, X.; Wu, C.; Gan, L.; Zhang, T.; Zhou, T.; Huang, J.; Wang, H.; Xie, C.; Zeng, D. Multilevel Microstructured Flexible Pressure Sensors with Ultrahigh Sensitivity and Ultrawide Pressure Range for Versatile Electronic Skins. *Small* **2019**, *15*, e1804559. [CrossRef] [PubMed]
18. Ho, D.H.; Sun, Q.; Kim, S.Y.; Han, J.T.; Kim, D.H.; Cho, J.H. Stretchable and Multimodal All Graphene Electronic Skin. *Adv. Mater.* **2016**, *28*, 2601–2608. [CrossRef] [PubMed]
19. Núñez, C.G.; Navaraj, W.T.; Polat, E.O.; Dahiya, R. Energy-Autonomous, Flexible, and Transparent Tactile Skin. *Adv. Funct. Mater.* **2017**, *27*, 1606287. [CrossRef]
20. Pyo, S.; Choi, J.; Kim, J. Flexible, Transparent, Sensitive, and Crosstalk-Free Capacitive Tactile Sensor Array Based on Graphene Electrodes and Air Dielectric. *Adv. Electron. Mater.* **2018**, *4*, 1700427. [CrossRef]
21. Tang, X.; Yang, W.; Yin, S.; Tai, G.; Su, M.; Yang, J.; Shi, H.; Wei, D.; Yang, J. Controllable Graphene Wrinkle for a High-Performance Flexible Pressure Sensor. *ACS Appl. Mater. Interfaces* **2021**, *13*, 20448–20458. [CrossRef]
22. Sahoo, B.N.; Woo, J.; Algadi, H.; Lee, J.; Lee, T. Superhydrophobic, Transparent, and Stretchable 3D Hierarchical Wrinkled Film-Based Sensors for Wearable Applications. *Adv. Mater. Technol.* **2019**, *4*, 4. [CrossRef]
23. Kim, S.Y.; Park, S.; Park, H.W.; Park, D.H.; Jeong, Y.; Kim, D.H. Highly Sensitive and Multimodal All-Carbon Skin Sensors Capable of Simultaneously Detecting Tactile and Biological Stimuli. *Adv. Mater.* **2015**, *27*, 4178–4185. [CrossRef] [PubMed]
24. Cui, J.; Nan, X.; Shao, G.; Sun, H. High-Sensitivity Flexible Pressure Sensor-Based 3D CNTs Sponge for Human–Computer Interaction. *Polymers* **2021**, *13*, 3465. [CrossRef]
25. Son, D.; Koo, J.H.; Song, J.-K.; Kim, J.; Lee, M.; Shim, H.J.; Park, M.; Lee, M.; Kim, J.H.; Kim, D.-H. Stretchable Carbon Nanotube Charge-Trap Floating-Gate Memory and Logic Devices for Wearable Electronics. *ACS Nano* **2015**, *9*, 5585–5593. [CrossRef]
26. Chen, X.; Shao, J.; An, N.; Li, X.; Tian, H.; Xu, C.; Ding, Y. Self-powered flexible pressure sensors with vertically well-aligned piezoelectric nanowire arrays for monitoring vital signs. *J. Mater. Chem. C* **2015**, *3*, 11806–11814. [CrossRef]
27. Xu, X.; Wang, R.; Nie, P.; Cheng, Y.; Lu, X.; Shi, L.; Sun, J. Copper Nanowire-Based Aerogel with Tunable Pore Structure and Its Application as Flexible Pressure Sensor. *ACS Appl. Mater. Interfaces* **2017**, *9*, 14273–14280. [CrossRef] [PubMed]
28. Zhu, B.; Niu, Z.; Wang, H.; Leow, W.R.; Wang, H.; Li, Y.; Zheng, L.; Wei, J.; Huo, F.; Chen, X. Microstructured Graphene Arrays for Highly Sensitive Flexible Tactile Sensors. *Small* **2014**, *10*, 3625–3631. [CrossRef] [PubMed]

29. Yang, J.C.; Kim, J.-O.; Oh, J.; Kwon, S.Y.; Sim, J.Y.; Kim, D.W.; Choi, H.B.; Park, S. Microstructured Porous Pyramid-Based Ultrahigh Sensitive Pressure Sensor Insensitive to Strain and Temperature. *ACS Appl. Mater. Interfaces* **2019**, *11*, 19472–19480. [CrossRef] [PubMed]
30. Mahata, C.; Algadi, H.; Lee, J.; Kim, S.; Lee, T. Biomimetic-inspired micro-nano hierarchical structures for capacitive pressure sensor applications. *Measurement* **2020**, *151*, 107095. [CrossRef]
31. Lee, K.Y.; Yoon, H.; Jiang, T.; Wen, X.; Seung, W.; Kim, S.-W.; Wang, Z.L. Fully Packaged Self-Powered Triboelectric Pressure Sensor Using Hemispheres-Array. *Adv. Energy Mater.* **2016**, *6*, 1502566. [CrossRef]
32. Huang, K.-H.; Tan, F.; Wang, T.-D.; Yang, Y.-J. A Highly Sensitive Pressure-Sensing Array for Blood Pressure Estimation Assisted by Machine-Learning Techniques. *Sensors* **2019**, *19*, 848. [CrossRef] [PubMed]
33. Huang, K.-H.; Tan, F.; Wang, T.-D.; Yang, Y.-J. A tactile sensing array integrated with tension sensor for continuously monitoring blood pulse waves. *Microelectron. Eng.* **2019**, *218*, 218. [CrossRef]
34. Jeong, Y.; Gu, J.; Byun, J.; Ahn, J.; Byun, J.; Kim, K.; Park, J.; Ko, J.; Jeong, J.; Amjadi, M.; et al. Ultra-Wide Range Pressure Sensor Based on a Microstructured Conductive Nanocomposite for Wearable Workout Monitoring. *Adv. Health Mater.* **2021**, *10*, 2001461. [CrossRef] [PubMed]
35. Park, J.; Lee, Y.; Hong, J.; Ha, M.; Jung, Y.-D.; Lim, H.; Kim, S.Y.; Ko, H. Giant Tunneling Piezoresistance of Composite Elastomers with Interlocked Microdome Arrays for Ultrasensitive and Multimodal Electronic Skins. *ACS Nano* **2014**, *8*, 4689–4697. [CrossRef]
36. Xiao, T.; Gao, Y.; Yu, G.; Qian, M.; Tan, J.; Xuan, F. Wearable pressure sensor using UV-patternable silver nanowire/polydimethylsiloxane composite. *Mater. Res. Express* **2019**, *6*, 095087. [CrossRef]
37. Zhang, Y.; Hu, Y.; Zhu, P.; Han, F.; Zhu, Y.; Sun, R.; Wong, C.-P. Flexible and Highly Sensitive Pressure Sensor Based on Microdome-Patterned PDMS Forming with Assistance of Colloid Self-Assembly and Replica Technique for Wearable Electronics. *ACS Appl. Mater. Interfaces* **2017**, *9*, 35968–35976. [CrossRef]

sustainability

MDPI

Article

Carbon Dioxide Separation by Polyethylene Glycol and Glutamic Acid/Polyvinyl Alcohol Composite Membrane

Angus Shiue [1,†], Ming-Jie Yin [2,†], Min-Hsuan Tsai [1], Shu-Mei Chang [1,3,*] and Graham Leggett [4]

[1] Graduate Institute of Organic and Polymeric Materials, National Taipei University of Technology, Taipei 106, Taiwan; angusshiue@gmail.com (A.S.); minhsuantsai@ntu.edu.tw (M.-H.T.)
[2] Beijing Key Laboratory for Green Catalysis and Separation, Department of Environmental and Chemical Engineering, Beijing University of Technology, Beijing 100124, China; yinmj@bjut.edu.cn
[3] Department of Molecular Science and Engineering, Research and Development Center for Smart Textile Technology, National Taipei University of Technology, Taipei 106, Taiwan
[4] LI-COR Biosciences, Cambridge CB4 0WS, UK; graham.leggett@licor.com
* Correspondence: f10914@mail.ntut.edu.tw; Tel.: +886-2-2771-2171 (ext. 2408)
† Denotes equal contribution.

Abstract: In this study, Polyvinyl alcohol (PVA) blended with Polyethylene glycol (PEG), Monosodium glutamate (MSG) and Glutamic acid (GA) was cast on a reverse osmosis membrane to form a composite membrane. It is expected that the ether group can increase the CO_2 affinity of the membrane. Sodium tetraborate (Borax) as a crosslinker can increase membrane basicity and glutamic acid (salt) can provide an enhanced transport mechanism, thereby improving the permeability and selectivity of carbon dioxide. FTIR spectra show that the thickness of coating is sufficiently low, while SEM results show that PVA-PEG series have a dense surface, and particles are observed on the surface of MSG/GA series. The gas permeance and separation performance of the composite membrane was tested using a single gas. Results showed that CO_2 had higher permeance (GPU) at lower pressure differential. PEG with an ether group had the greatest effect on improving CO_2 permeance and selectivity. However, MSG and GA with amine groups could not effectively improve CO_2 selectivity due to solubility. The best coating solution was provided by PVA-PEG-1.2. The CO_2 selectivity of the composite membrane was 10.05 with a pressure differential of 1.00 bar in a humid environment and no obvious deterioration was observed over a 10-day period. Borax can improve selectivity, water absorption, and thermal stability while avoiding the need for high temperature and long crosslinking time of aldehydes, which makes it possible to be used in a PVA carbon dioxide separation membrane.

Keywords: carbon dioxide; polyvinyl alcohol; polyethylene glycol; Borax; monosodium glutamate; glutamic acid; reverse osmosis membrane

Citation: Shiue, A.; Yin, M.-J.; Tsai, M.-H.; Chang, S.-M.; Leggett, G. Carbon Dioxide Separation by Polyethylene Glycol and Glutamic Acid/Polyvinyl Alcohol Composite Membrane. *Sustainability* **2021**, *13*, 13367. https://doi.org/10.3390/su132313367

Academic Editors: Avelino Núñez-Delgado, Zhien Zhang, Elza Bontempi, Mario Coccia, Marco Race and Yaoyu Zhou

Received: 6 October 2021
Accepted: 30 November 2021
Published: 2 December 2021

1. Introduction

The increasing demand for energy and an associated need to improve efficiency of energy consuming processes has led to a growing global willingness to use membrane materials as a potential long-term solution to reduce greenhouse gas emissions and prevent global warming. With global energy consumption expected to double by 2050, current fossil fuel reserves are under increasing environmental and economic pressure. The energy sector must unequivocally overcome the many technological barriers between membrane production, utilization, and potential applications. Polymer substrate membranes are one of the most popular separation materials in the industry, but their low temperature and chemical stability greatly limit their application. Despite these limitations, demand for inorganic gas permeable membranes is increasing in many cases. Carbon membranes are particularly useful in gas separation through adsorption and molecular screening mechanisms, even between gases of very similar molecular size [1–4]. However, in industrial applications, they suffer from low penetration and poor mechanical strength. To date,

the utilization of polymer membranes in pilot plants and at industrial scales has been limited due to higher manufacturing costs. Therefore, to compensate for the high cost, manufacturers have explored ways to improve the separation performance of membrane materials for various gases [5,6].

Each membrane material has its advantages and challenges in terms of material cost, separation performance, and service life. The development of advanced membrane materials to increase cost-effectiveness is critical to reducing CO_2 capture costs. Each membrane material has its own separation characteristics, thermochemical stability, and mechanical strength [7]. In general, most polymer membrane have good separation properties and relatively low costs, but the low stability of the membrane is a negative performance factor when exposed to acidic gases and harsh conditions (high temperature and high pressure), typical in many industrial processes.

Existing gas separation membranes must further improve permeability and selectivity to expand their market share and compete with traditional separation technologies. Since gas permeability is inversely proportional to the thickness of the dense layer, a high multilayered material must be selected, or the thickness of the dense selective layer reduced to prepare a more efficient membrane. However, highly permeable materials typically exhibit low selectivity due to the trade-off between the permeability and selectivity of polymer materials [8,9]. Porous membranes may consist of a thin film composite (TFC) consisting of one or more layers of a porous substrate to maximize selectivity, permeability, and mechanical crosslinking, or a more traditional asymmetric film construction where a fine porous skin layer is applied to a thick microporous underlying layer. TFC construction offers a low skin advantage: (1) only a small amount of selective layer material, less than 2 g/m^2, is required to coat the surface of a porous substrate, compared to approximately 50 g/m^2 required to manufacture the overall skinning of an asymmetric film—therefore, the cost of materials is reduced when applying TFC construction; (2) depending on the product requirements, each layer of the membrane layer can be tuned for optimal separation; (3) as long as the main body of the membrane can form or deposit on the surface of the substrate thin layer, its mechanical properties and machinability restrictions are less. However, the manufacture of high-performance, defect-free TFC materials is challenging: (1) there are some challenges in the influence of substrate resistance; (2) performance is compromised if the thickness of the ultra-thin selective layer is inconsistent; (3) material intrusion substrategy; (4) ultra-thin selective layers accelerate aging and plasticization, and these harmful problems may degrade the performance of TFC [10–13].

Compared with the membrane after the solution diffusion mechanism, the promotion of the transmission mechanism contributes to high CO_2 separation and CO_2/N_2 selectivity. In convenient transport, the CO_2 separation capacity of a mobile carrier is higher than that of a fixed carrier, but lacks carrier stability [14]. Polyallylamine (PAA) is one of the fixed carriers used for CO_2 separation and is mixed with other polymers, either without change or in the form of bit resistance [15–21]. PAA is primarily amine-based, which is very fragile and cannot form a membrane under dry conditions. The polyvinyl alcohol (PVA), in combination with PAA, is widely used as a fixed position in CO_2 substrates and mixing bases [18]. Temperature and humidity influence the transport mechanism. PVA is soluble in water and at higher humidity a decrease in CO_2 emission performance may be observed at temperatures lower than 70 °C [15].

Polyethylene oxide (PEO) membranes are considered attractive materials for CO_2 separation because the polymer chain has polar ether-oxygen bonds and therefore it has a strong CO_2 affinity [22]. Great efforts have been made in the design and synthesis of polymers containing PEO. Hirayama et al. [23] synthesized films containing PEO and crosslinking polymers with a CO_2/N_2 selectivity of 69 and a CO_2 penetration rate of 62 Barrer. Potreck et al. [24] argue that PEO-based block congregations provide an attractive way to integrate CO_2 separation using thin-film technology because of the high interaction between CO_2 and its polar ether connections.

In this study, polyvinyl alcohol was chosen to make the main polymer. It is a convenient polymer to use, being non-toxic and water soluble. Polyglycol was selected to increase the solubility coefficient and CO_2 affinity. To avoid high molecular weight leading to crystallization and reduction in the permeability of CO_2, liquid PEG200 was used in the preparation of the membrane. In addition, consideration was given to the pH value of the membrane and reduction of cross-link reaction time and temperature. To this end, polyvinyl alcohol was chosen, as cross-linking occurs at room temperature. In addition, tetraborate (Borax) was employed as a crosslinking agent. Once prepared, the composite membrane was tested to determine carbon dioxide permeability and selectivity in both dry and humid environments. Monosodium glutamate (MSG), which is expected to promote transport mechanisms and therefore increase CO_2 permeability and selectivity of the composite membrane was also tested, while glutamic acid (GA) was also used in experiments to compare the effects of glutamic acid (salt).

2. Materials and Methods

2.1. Chemicals and Equipment

Polyvinyl alcohol (PVA) (M_w = 31,000–55,000 g/mol, 98.0~98.8% hydrolyzed), polyethylene glycol (PEG) (M_w = 200 g/mol), sodium tetraborate (Borax), monosodium glutamate (MSG), and glutamic acid (GA) were purchased from Acros Organics, Geel, Belgium. All chemicals were used as received without treatment and deionized water was used as the solvent during preparation. The reverse osmosis membrane was purchased from Film Tec Corp. Minneapolis, MN, USA. N_2 and CO_2 applied in the experiments were purchased from Chin-Fung Ltd., Taipei, Taiwan.

2.2. Structure of Composite Membrane

Reverse osmosis membrane was used as a substrate and coated with a polymer-mixed solution to make a composite membrane. The uppermost layer of this composite membrane was dominated by polyvinyl alcohol (PVA), mixed with polyethylene glycol (PEG). Monosodium glutamate (MSG) or glutamic acid (GA) was an optional layer to contact the air, interacting with CO_2 via its quadrupole moment. Gas penetration and separation were achieved via a dissolve diffusion mechanism. The reverse osmosis membrane was a polyamide layer about 200 nanometers thick and had approximately a 15 nanometers aperture from top to bottom, followed by a porous polysulfone (PSU) layer approximately 40 microns thick, with polyester at the bottom as a support layer approximately 120 microns thick.

2.3. Preparation of Polymer-Mixed Solution

In this experiment, a fixed PVA intake was configured in different proportions by adjusting the amount of PEG, MSG, GA, Borax, and deionized water. The polymer-mixed solution was divided into four preparation methods: (a) only used PVA and Borax (b) added PEGs and adjusted the combination of proportions (c) added MSGs and adjusted the combination of proportions and (d) added GA and adjusted the combination of proportions.

2.4. Preparation of Self-Supporting Membrane

A polymer-mixed solution was prepared with a micro straw of 10 mL, transferred to a petri dish and left in a drying chamber for 48 h, then placed in a vacuum oven (-700 mmHg) to dry for 24 h at 35 °C. The membrane was removed and baked in a hot air oven for 1 h at a temperature of 105 °C to remove the remaining moisture. This completed the preparation of the self-supporting membrane.

2.5. Preparation of Composite Membrane

A substrate reverse osmosis membrane (about 15 × 20 cm) was fixed to the glass plate, and then the prepared polymer-mixed solution was applied to this membrane with a plastic form coated rod. The modified substrate was placed in a drying oven for 24 h

before being transferred to a vacuum oven (-00 mmHg) at 35 °C where it was further dried for 24 h. This process resulted in a polymer membrane formed on the substrate surface. After making a polymer membrane, Fourier-Transform Infrared Spectroscopy-Attenuated Total Reflection (FTIR-ATR, using SHIMADZU IRSpirit with QATR-S module), Thermogravimetric Analysis (TGA, using NETZSCH TG 209 F3), and Scanning Electron Microscopy (SEM, using HITACHI TM4000Plus) were used to confirm surface modification on the reverse osmosis membrane.

2.6. CO_2 Permeation Test

The gas membrane permeation system device is shown in Figure 1. Pure N_2 or pure CO_2 gas enters the line via a float flow control valve. The inlet pressure into the system is controlled by means of a precision pressure control valve, with pressure measured by a pressure meter. The pipeline is divided into two paths. One path is through a deionized water humidifier. The humidifier consists of a water vessel immersed in a thermostatic tank set at 35 °C. Gas is passed through the water to achieve a relative humidity (RH) of approximately 80%. After the humidifier, the gas and moisture enter the gas penetration device which contains the membrane to be tested. The gas penetration device is placed in the hot air oven and this is set to a fixed temperature. This temperature is maintained for the duration of the experiment to reduce any changes in membrane performance that may arise from temperature fluctuations. The lower end of the gas penetration device is connected with a three-way valve and the mass flow meter (Brooks Instrument, Hatfield, PA, USA) of the two gases is attached at each end, allowing evaluation of the performance of the membrane under test. During operation, the test gas can be humidified or dry, depending on the selected flow path as shown in Figure 2.

When a gas passes through a dense membrane, transport is mostly explained by the solution-diffusion model. A formula describing the passing properties of the gas, called permeability of the gas, is derived from Fick's first law of diffusion theorem.

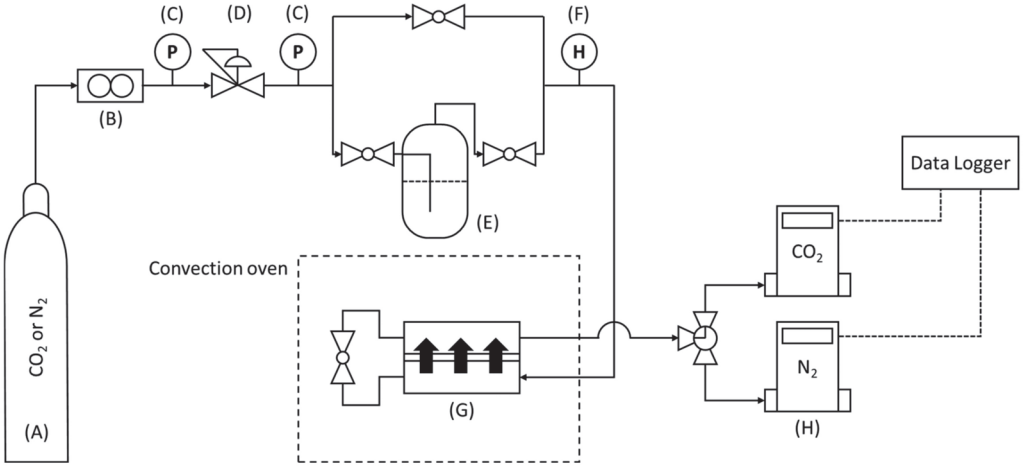

Figure 1. Schematic diagram of the polymer membrane separation system. (**A**) N_2 or CO_2, (**B**) floating flow controller, (**C**) pressure gauge, (**D**) precision regulator, (**E**) humidifier, (**F**) temperature and humidity meter, (**G**) membrane separation system, and (**H**) mass flow meter.

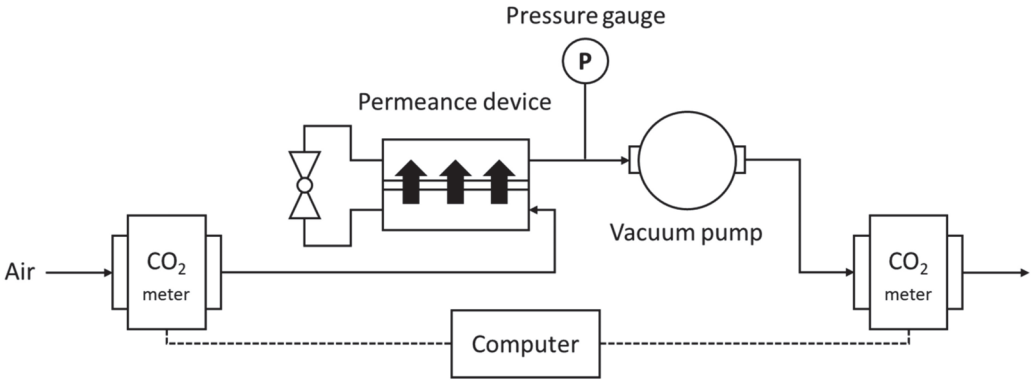

Figure 2. CO_2 membrane separation energy measurement system.

2.7. Principle

When a gas passes through a dense membrane, its behavior is mostly explained by the solution-diffusion model, and the membrane material itself has a formula for the passing properties of the gas, called the permeability of the gas, which is derived from Fick's first law of diffusion theorem:

$$J = -D\frac{\partial c}{\partial x} \tag{1}$$

where J is the gas flux (cm^{-2} s^{-1}), D is the gas diffusion coefficient in the membrane (cm^2 s^{-1}), and $\frac{\partial c}{\partial x}$ is the concentration gradient (cm^{-4}).

The boundary condition is

$$x = 0, C = C_1 \tag{2}$$

$$x = L, C = C_2 \tag{3}$$

where x is length scale of the system (m), and L is the thickness of the membrane (cm). The concentration distribution of gas molecules in the membrane (mol m^{-3}) can be solved by boundary conditions as shown in the following equation:

$$\frac{C - C_1}{C_2 - C_1} = \frac{x}{L} \tag{4}$$

Equation (4) is substituted into Equation (3) to obtain the gas flux (J).

$$J = -D\frac{(C_1 - C_2)}{L} \tag{5}$$

The physical significance of the gas flux is the area per unit, the number of gas molecules passed in a unit time:

$$J = \frac{1}{A}\frac{\partial n}{\partial t} \tag{6}$$

Combine Equations (5) and (6) to obtain:

$$\frac{1}{A}\frac{\partial n}{\partial t} = -D\frac{(C_2 - C_1)}{L} \tag{7}$$

Assuming that the dissolution and evaporation of the gas is balanced, the concentration at the membrane interface is related to the dispensing of the components in the gas and it must comply with Henry's Law:

$$C' = Sp \tag{8}$$

where C' is the solubility of a gas at a fixed temperature (mL gas L^{-1}), S is the solubility coefficient of the gas for the membrane (mL gas L^{-1}), and p is the partial pressure of the gas (atm).

At constant temperature, $S_1 = S_2 = S$, Equation (8) substituted into (7) obtains:

$$\frac{1}{A}\frac{\partial n}{\partial t} = -D\frac{(S_2p_2 - S_1p_1)}{L} = DS\frac{(p_1 - p_2)}{L} \tag{9}$$

The defined permeability coefficient is:

$$P = DS \tag{10}$$

Equation (10) substituted into (9) obtains:

$$\frac{1}{A}\frac{\partial n}{\partial t} = P\frac{(p_1 - p_2)}{L} \tag{11}$$

The gas permeability coefficient P is arranged as:

$$P = \frac{L}{(p_1 - p_2)A}\frac{\partial n}{\partial t} \tag{12}$$

Measurements are usually made in Barrer units:

$$1\text{Barrer} = 10^{-10}\frac{cm^3{}_{(STP)} \cdot cm}{cm^2 \cdot \sec \cdot cmHg} \tag{13}$$

In addition to permeability, the overall permeability of the membrane is often expressed as a gas permeability (Permeance), which is the gas penetration coefficient divided by the membrane thickness L as follows:

$$\text{Permeance} = \frac{\text{Permeability}}{L} = \frac{1}{(p_1 - p_2)A}\frac{\partial n}{\partial t} \tag{14}$$

Its physical significance is described as:

$$\text{Permeance} = \frac{\text{Gas amount}}{\text{Pressure difference} \times \text{Surface Area}} \tag{15}$$

From Equation (15), permeance units can be expressed as $\frac{cm^3{}_{(STP)} \cdot cm}{cm^2 \cdot \sec \cdot cmHg}$. Because this number is small, it is usually expressed in gas Permeance Units (GPUs).

$$1GPU = 10^{-6}\frac{cm^3{}_{(STP)} \cdot cm}{cm^2 \cdot \sec \cdot cmHg} \tag{16}$$

In addition, the film can be obtained by dividing the gas permeability or gas permeability coefficient of the two gases to obtain membrane selectivity:

$$\text{Selectivity} = \frac{\text{Permeance(Gas1)}}{\text{Permeance(Gas 2)}} = \frac{\text{Permeability(Gas1)}}{\text{Permeability(Gas 2)}} \tag{17}$$

3. Results and Discussion

3.1. FTIR Analysis

3.1.1. Infrared Spectrum of Polyvinyl Alcohol Cross-Linked Borax

Polyvinyl alcohol membrane stretch vibrations of O-H and C-O are found at 3100–3600 and 1730 cm^{-1}, respectively. At 2850–2950 cm^{-1} two C-H symmetrical and asymmetric stretch vibrations are observed, which may result from the undehydrated ethylene acetate group on polyvinyl alcohol. It can be seen that there is a C-H bending vibration at 1350 cm^{-1}, and C-O

stretch vibration feature peaks at 1140 and 1090 cm^{-1}. Cross-linked membranes that have added Borax display similar absorption features, and are shown in Figure 3 and Table 1.

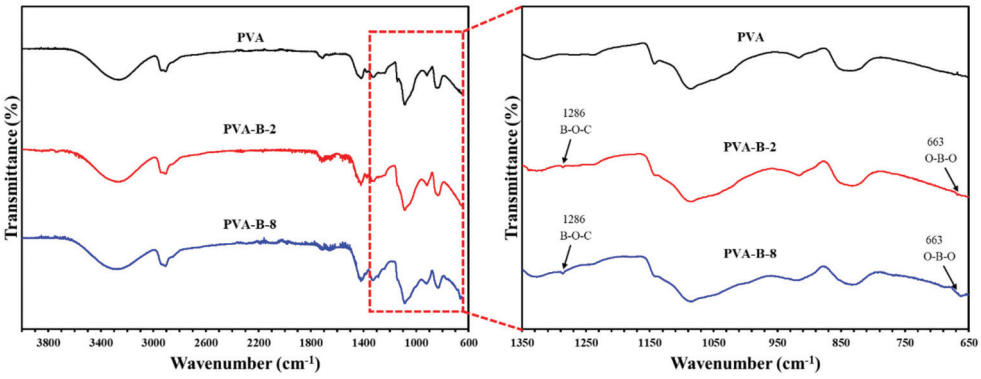

Figure 3. Infrared spectrum of PVA, PVA-B-2, and PVA-B-8 samples.

Table 1. Peak assignments of PVA and cross-linked PVA.

Peak Position (cm^{-1})		Peak Assignment
PVA	**PVA-B-Series**	
3100–3600	3100–3600	O-H stretching
2850–2950	2850–2950	C-H symmetric/asymmetric stretching
1730	1730	C=O stretching
1350	1350	C-H bending
1140	1140	C-O stretching
1090	1090	C-O stretching
	1286	B-O-C stretching
	663	O-B-O stretching

Since Borax in PVA-B-2 is only 2 percent of its weight relative to polyvinyl alcohol, to further determine the effects of Borax, a self-supporting membrane of PVA-B-8 sample with Borax content of 8 percent is formulated and adjusted. The instrument scanning parameters were measured at a resolution of 0.9 cm^{-1} and absorption peaks could be seen at 1286 cm^{-1} and 663 cm^{-1}, while the PVA-B-2 membrane had a slight decrease in penetration in both locations. The two absorption peaks correspond to B-O-C and O-B-O stretching vibrations, representing boric acid from borax dissolved in water, acting as a cross-linker between polyvinyl alcohols in the process of forming a membrane. This was also observed and reported in previous studies [25–27] as shown in Figure 3 and Table 1.

3.1.2. Experimental Coating and Infrared Spectrum

Because the gas permeability is related to the thickness of the separation membrane under the condition that the gas permeability is constant, the thicker the separation membrane, the lower the gas permeability, and vice versa. FTIR, using a half-attenuation full-reflection device, was used as a means to make a preliminary confirmation that the membrane selection layer was thin enough. A polyvinyl alcohol self-supporting membrane, a reverse osmosis membrane and the experimental method of polyvinyl alcohol as a selection layer, coated as a support layer on the reverse osmosis membrane prepared composite membrane were analyzed.

The reverse osmosis membrane is itself a composite membrane of polyamide and polysulfone. From the spectrum in Figure 4 and Table 2, the reverse osmosis membrane prior to modification is seen to have stretching vibrations of O-H, C-H with alkane, N-H,

C=C, and C-O at 3500–3200, 2966 and 1236, 1560, 1500, and 1050 cm^{-1}, respectively. Characterized absorption that may come from a polycyclic group is: stretching vibration of C=C, C-O-C, O-S-O, C-H, and C-S-C at 1585 cm^{-1} and 1487, 1236, 1149, 1014, and 831 cm^{-1}, respectively [26,28].

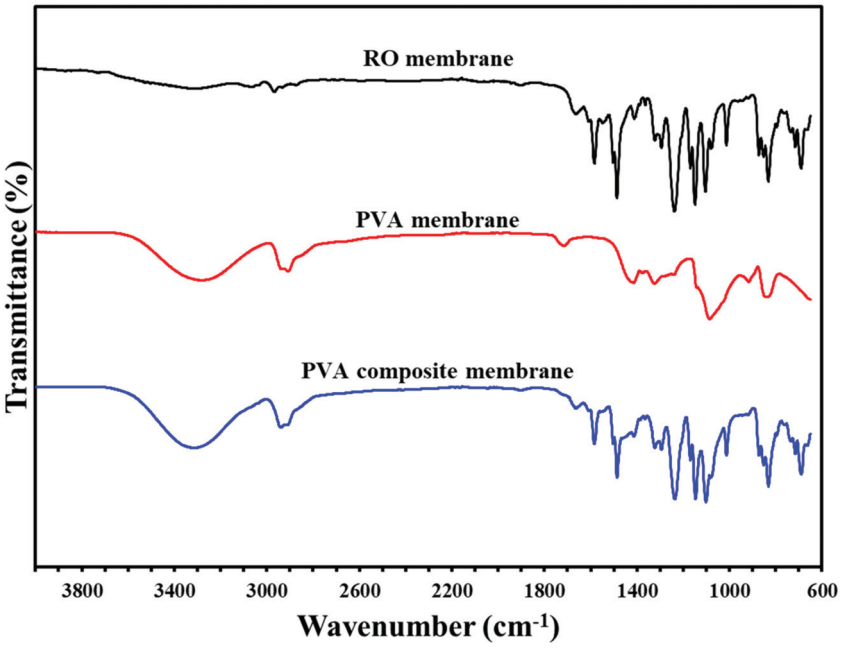

Figure 4. The infrared spectrum of the components of the composite membranes and each layer.

Table 2. Peak assignments of composite membrane.

Peak Position (cm^{-1})	Peak Assignment
3600–3000	O-H stretching
2966	C-H stretching
2950–2850	C-H symmetric asymmetric stretching
1585	C=C stretching
1560	N-H stretching
1500	C=C stretching
1487	C=C stretching
1236	C-O-C stretching
1149	O-S-O stretching
1050	C-O stretching
1014	C-H stretching
831	C-H stretching
690	C-S-C stretching

It is found that the absorption peaks of the reverse osmosis membrane prior to modification is concentrated below 1800 cm^{-1}, although there are absorption peaks above 2700 cm^{-1}, but not strong, while polyvinyl alcohol at 3600–3000 cm^{-1} displays a strong absorption peak of O-H stretching vibration, and there is an absorption peak resulting from the C-H stretching vibration near 2950 cm^{-1}. Therefore, if coated with polyvinyl alcohol, the prepared composite membrane should display absorption features at 3000 cm^{-1} associated with O-H and at 2950 cm^{-1} resulting from C-H groups. The visible composite film results in features in the infrared spectrum, while at the same time peaks associated

with the polyvinyl alcohol selection layer and reverse osmosis membrane support layer are also present. Since infrared spectral measurements are carried out by half-attenuation full reflection, the depth range of infrared light entering the sample is approximately 0.5 to 3 μm (related to the crystal refractive index, sample refractive index, incident angle and number of incident light waves used in the device). From this it can be inferred that the thickness of the coated polyvinyl alcohol selection layer should be less than 3 μm, as shown in Figure 4 and Table 2.

3.1.3. Infrared Spectrum of Polyvinyl Alcohol-Polyethylene Glycol

A fixed amount of polyvinyl alcohol was mixed with different volumes of polyethylene glycol and applied to a self-supporting membrane. The resulting materials were analyzed using ATR-FTIR; results are shown in Figure 5. The main absorption peaks of polyethylene glycol are C-H and C-O stretching vibrations at 2800–2900, and 1350 and 1090 cm^{-1}, respectively. From the spectrum, it is observed that increasing the polyglycol addition results in strengthening of the absorption features associated with polyethylene glycol. This is especially evident for C-H and C-O stretching vibrations at 2800–2900 and 1090 cm^{-1}, respectively.

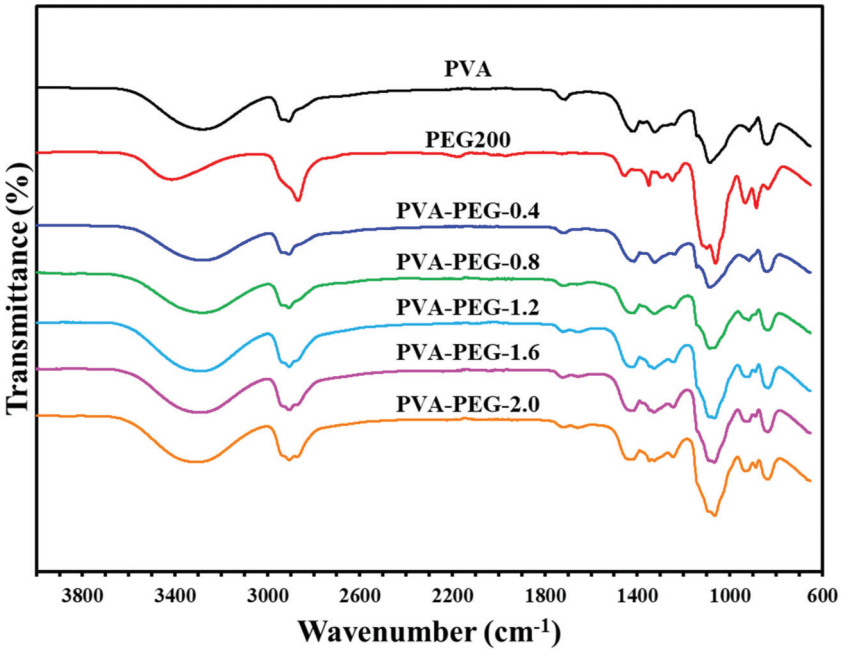

Figure 5. Infrared spectrum of polyvinyl alcohol-polyethylene glycol self-supporting membranes.

A mixed solution of polyvinyl alcohol and polyethylene glycol was coated on the reverse osmosis membrane to prepare a composite membrane. ATR-FTIR was used to analyze the resulting materials; results are shown in Figure 6. The characteristic absorption features of the reverse osmosis membrane are observed, confirming that the coating is thin enough to allow infrared light to penetrate the selection layer to the reverse osmosis membrane. The strength of the absorption line at 1090 cm^{-1} is dependent on the amount of polyglycol in the sample.

3.1.4. Infrared Spectrum of Polyvinyl Alcohol–Sodium Glutamate

A fixed amount of polyvinyl alcohol was mixed with different weights of monosodium glutamate and prepared into a self-supporting membrane, which was analyzed by ATR-FTIR; results are shown in Figure 7. The presence of MSG is evident from the peaks at 1602 and 1395 cm^{-1} from the absorption of C-O stretching vibrations. It can be found that as the amount of added MSG increases, so the strength of the characteristic absorption feature associated with monosodium glutamate increases, resulting from the self-supporting membrane of PVA-MSG.

Polyvinyl alcohol is mixed with monosodium glutamate and coated in a reverse osmosis membrane to form a composite membrane; its infrared spectra are shown as Figure 8. Compared with the original reverse osmosis membrane, the composite membrane spectrum displays polyvinyl alcohol absorption lines, and the sodium glutamate C-O stretching vibration of 1602 cm^{-1}. Penetration also decreased with an increase in the content of sodium glutamate, and from another C-O stretching vibration at 1395 cm^{-1}, it can be seen that the absorption peak becomes more obvious, representing an increase in the MSG content in the selection layer.

3.1.5. Infrared Spectrum of Polyvinyl Alcohol–Glutamic Acid

Since a layer of crystallization is observed on the surface of the membrane when it is prepared for self-supporting membranes, only composite membrane spectra are shown in Figure 9 and Table 3. The glutamic acid itself is visible from absorption lines at 2950–3050 cm^{-1} from C-H, N-H or COOH, symmetrical N-H, and symmetrical COOH stretching vibration at 1635, 1500, and 1400 cm^{-1}, respectively [29]. However, the absorptions resulting from these groups are not strong. The glutamate acid addition is low and thus an increase in strength of absorption features associated with this compound are not observed as the added amount is increased. There is also no change in penetration related to the added amount.

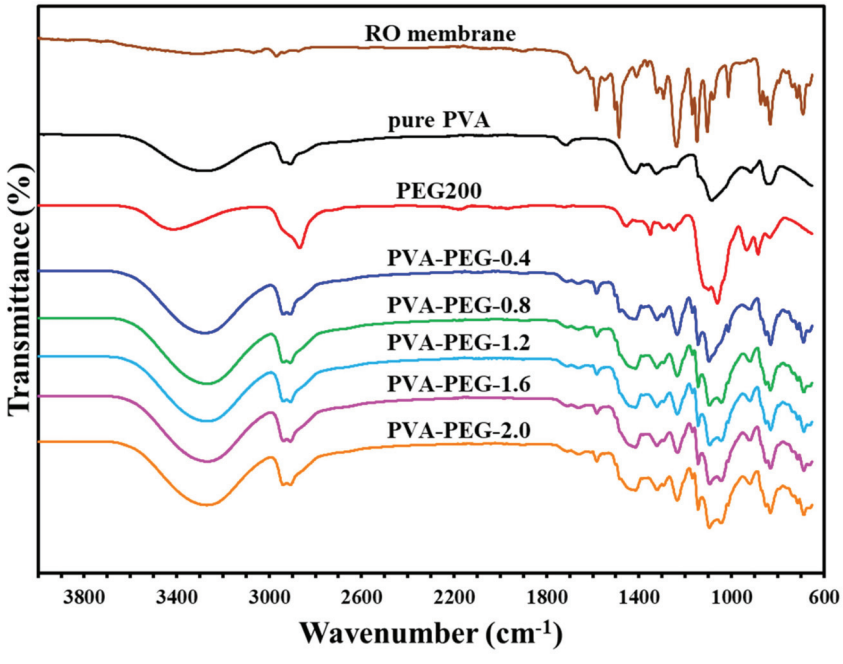

Figure 6. Infrared spectrum of polyvinyl alcohol–polyethylene glycol composite membranes.

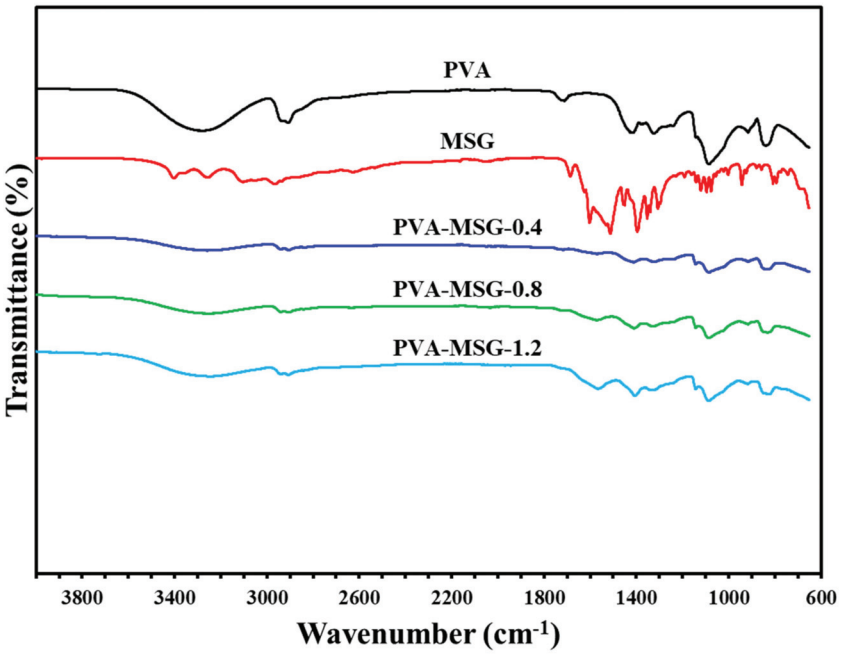

Figure 7. Infrared spectrum of polyvinyl alcohol–sodium glutamate self-supporting membranes.

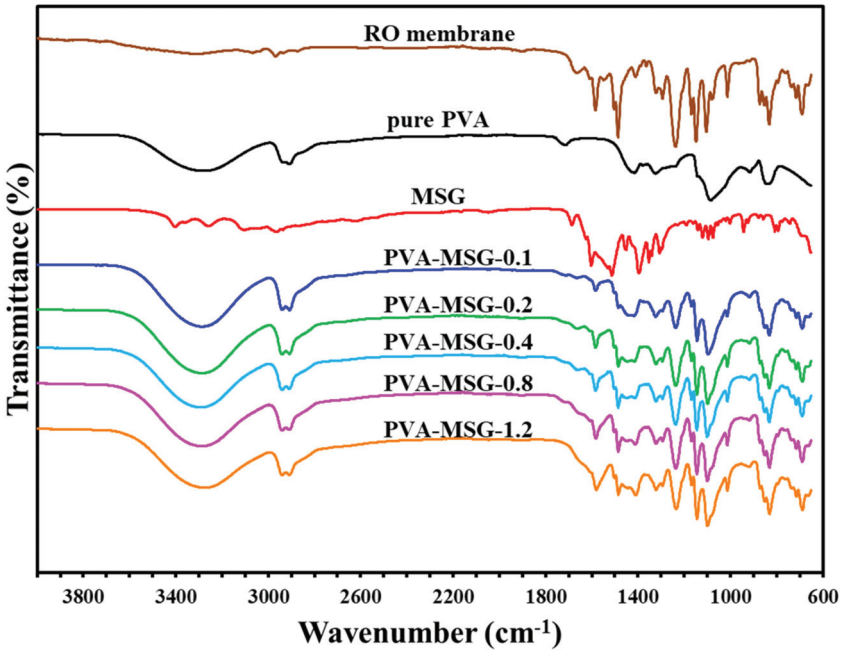

Figure 8. Infrared spectrum of polyvinyl alcohol-sodium glutamate composite membranes.

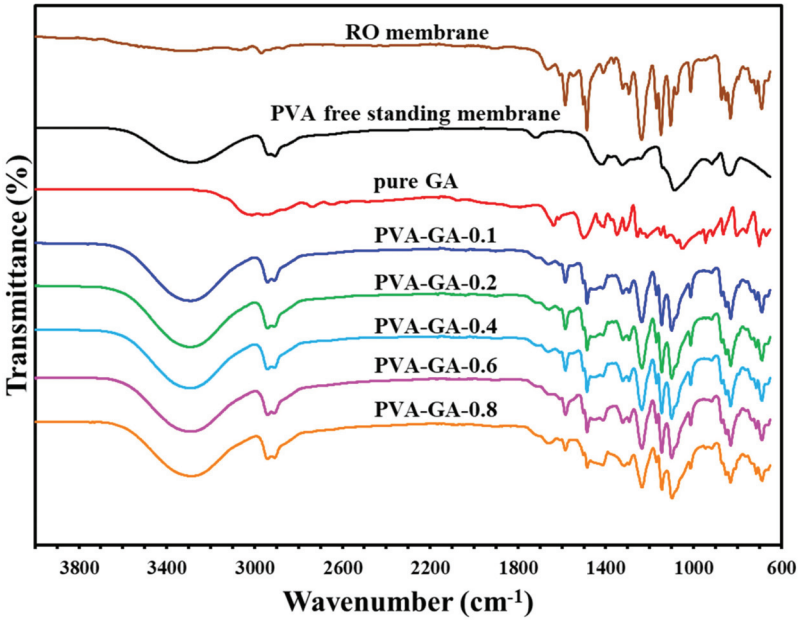

Figure 9. TGA diagram of polyvinyl alcohol–glutamic acid composite membranes.

Table 3. Peak assignments of PVA-X composite membranes.

Peak Position (cm^{-1})			Peak Assignment
PVA-PEG	**PVA-MSG**	**PVA-GA**	
3000–3600	3000–3600	3000–3600	O-H stretching
2800–2900	2950–3050	2950–3050	C-H stretching
		1635	N-H stretching
	1602		C-O stretching
		1500	N-H stretching, symmetric
		1400	COOH stretching, symmetric
	1395		C-O stretching
1350			C-O stretching
1090			C-O stretching

3.2. Thermogravimetric Analysis

To avoid a weight increase associated with increased thickness of the support material, the polyester support layer in the composite membrane is torn off, leaving only three layers of mixed polymer, polyamide and polyurethane. The thermal stability of the composite membrane is tested under an argon atmosphere with a temperature ramp increasing to 900 °C. Polyvinyl alcohol (PVA)-polyglycol (PEG) composite membrane thermal stability experimental results are shown in Figure 10 and Table 4. It is observed that the reverse osmosis membrane as a substrate has a significant weight loss only at 500–550 °C, which should be associated with the polysulfone that acts as a support layer. The composite membrane coated with PVA-PEG shows three stages of weight change. The first stage weight change at 150–250 °C comes from the loss of composite membrane moisture and PEG cracking, the second stage at 275–350 °C comes from PVA cracking, and the third stage at 500–550 °C is the same as the reverse osmosis membrane which is caused by PSU lysis. The experimental results of the polyvinyl alcohol-glutamic acid (salt) composite membrane thermal analysis are shown in Figure 11. In addition to PSU cracking, a weight change can be seen at 275–375 °C. From Figure 12, the maximum cleavage rate temperatures of

glutamic acid (salt) and PVA are approximately 300–400 °C, so this temperature change should be as a result of the degradation of glutamate acid and PVA.

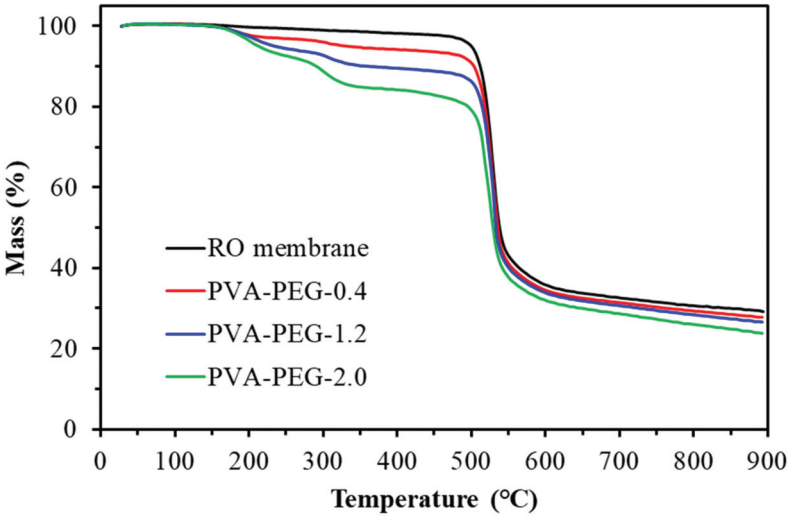

Figure 10. TGA diagram of polyvinyl alcohol-polyethylene glycol composite membranes.

Table 4. Thermal gravimetric analysis.

Sample	1st Degradation		2nd Degradation		3rd Degradation	
	T_1 (°C)	Weight Loss (%)	T_2 (°C)	Weight Loss (%)	T_3 (°C)	Weight Loss (%)
RO	500–550	50	-	-	-	-
PVA-PEG-2.0	150–250	7.3	275–350	5.8	500–550	45.8
PVA-MSG-1.2	275–375	7.7	500–550	51.1	-	-
PVA-GA-0.8	275–375	5.9	500–550	54.0	-	-

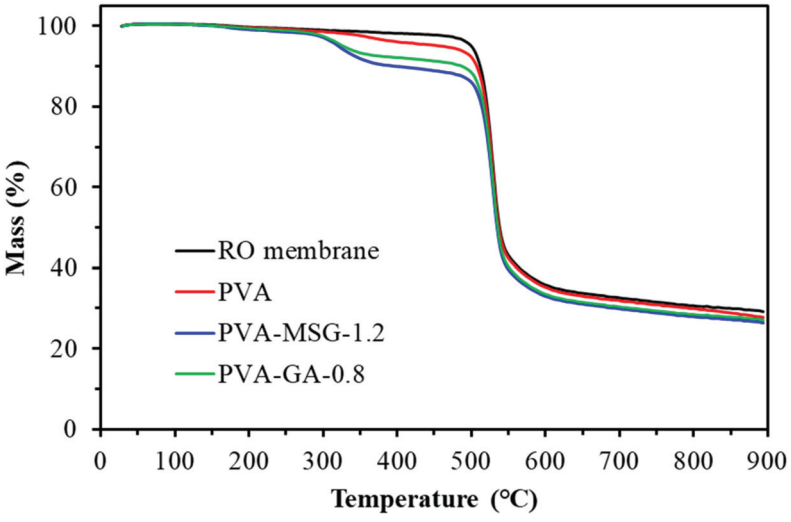

Figure 11. TGA diagram of polyvinyl alcohol-glutamic acid (salt) composite membranes.

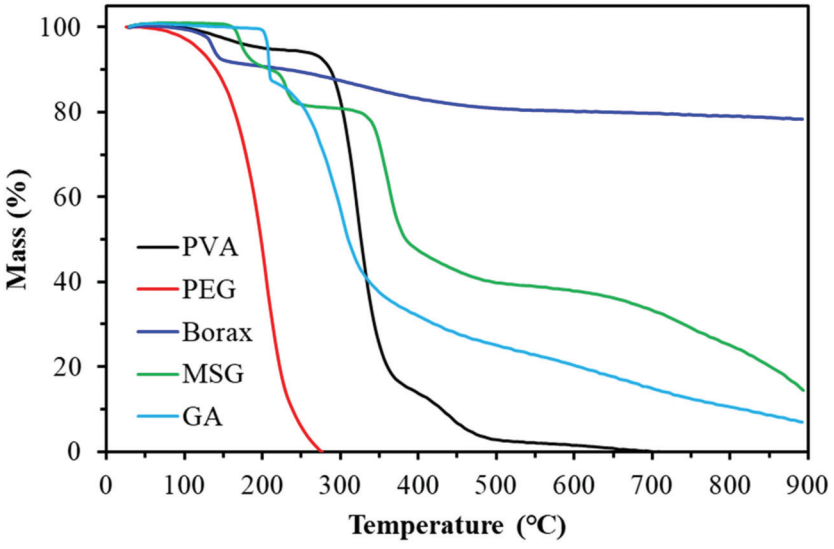

Figure 12. TGA diagram of experimental chemicals.

3.3. SEM Analysis

SEM was used to observe the membrane surface pattern and showed that the polyamide layer distribution as a substrate had many holes, as shown in Figure 13A. When the composite membrane surface is coated with a polyvinyl alcohol solution (PVA-B-2), the original rough surface is covered by PVA and converted to a dense surface as shown in Figure 13B.

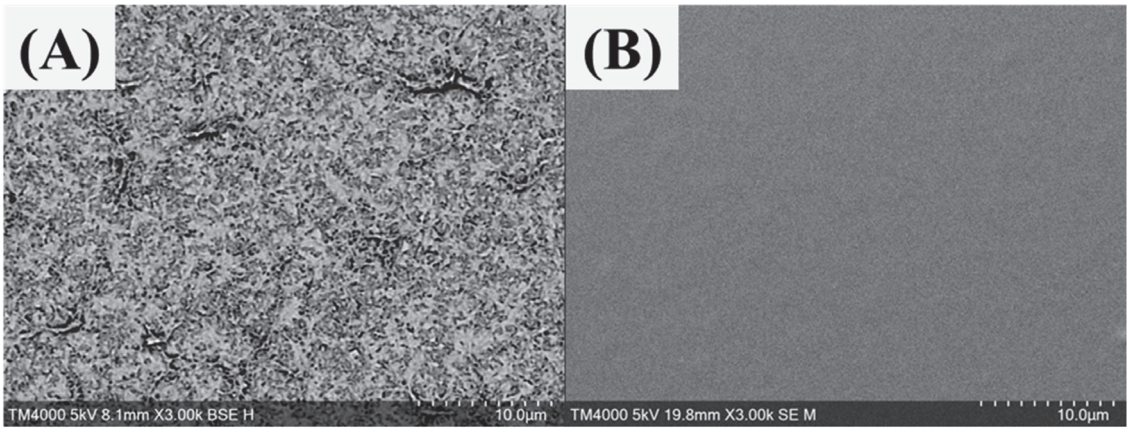

Figure 13. SEM diagrams of (**A**) reverse osmosis film and (**B**) PVA-B-2 coated film.

In the PVA-PEG series of polyvinyl alcohols with different proportions of polyglycol, the surface of the coated composite membrane remains dense, no different from the PVA-B-2 condition of the original polyethylene glycol addition as shown in Figure 14.

A PVA-MSG series of samples of polyvinyl alcohol with added sodium glutamate, whose surfaces remain dense when MSG is less than 9 wt% (PVA-MSG-0.4) as shown in Figure 15A–C. From Figure 15D–F, as the MSG addition increases, particles are observed on the membrane surface, and as the amount added increases further, so the particle size becomes larger and more widely distributed. The particles are crystalized MSG distributed on the membrane surface.

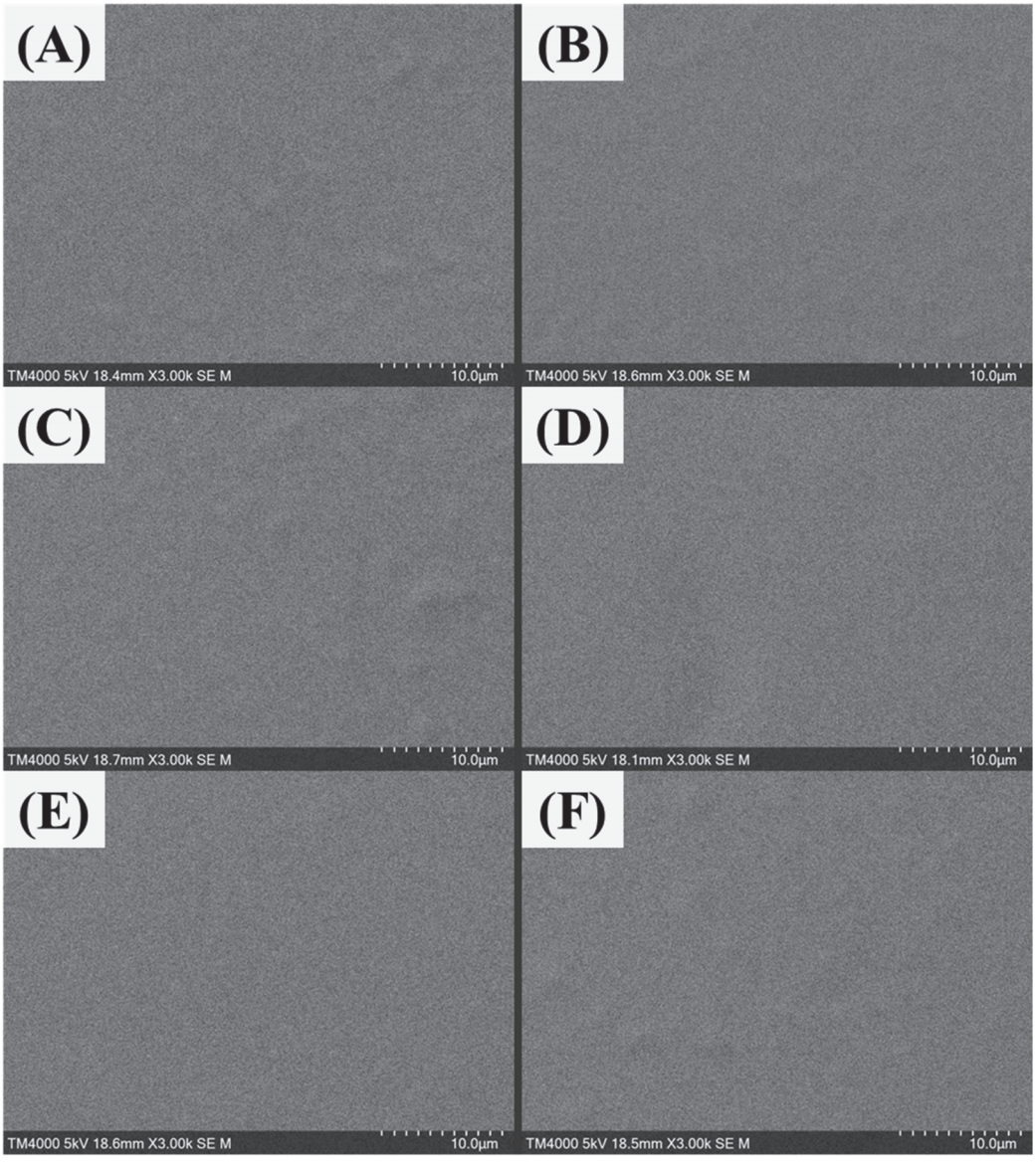

Figure 14. SEM diagrams of different PEG content PVA-PEG composite membranes: (**A**) no additional PEG, (**B**) 10 wt%, (**C**) 18 wt%, (**D**) 24 wt%, (**E**) 30 wt%, and (**F**) 35 wt%.

The coating solution is changed to polyvinyl alcohol to add glutamate acid PVA-GA series samples. The GA addition amount is less than 9 wt% (PVA-GA-0.4). Its surface also appears to be in a dense state as shown in Figure 16A–D. From Figure 16E,F, as the GA addition continues to be increased above 13 wt% (PVA-GA-0.6), granular fluctuations are found on the surface, while at 17 wt%, GA will have larger particles, which result from GA aggregation.

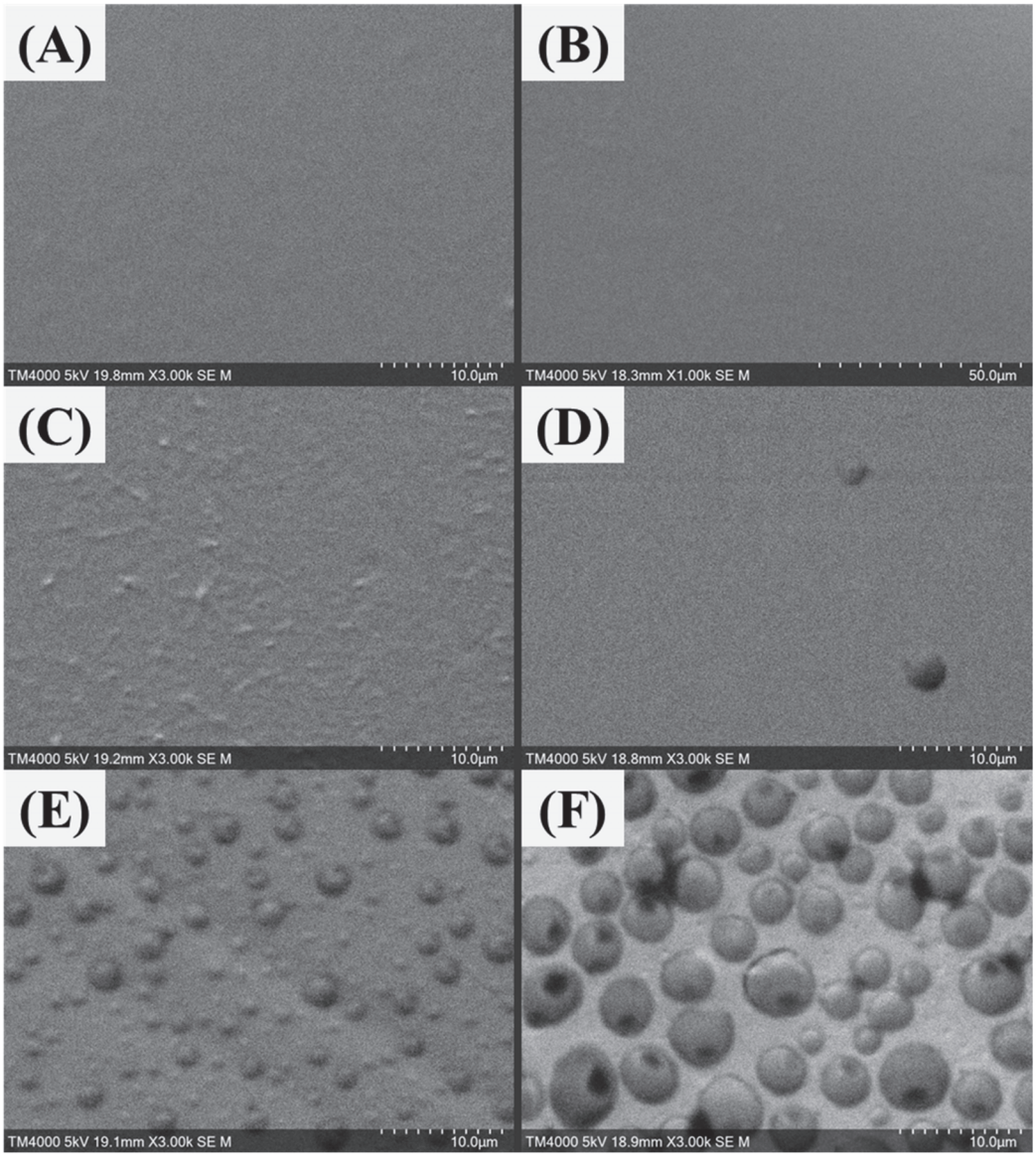

Figure 15. SEM diagrams of different MSG content PVA-MSG composite membranes: (**A**) no additional MSG, (**B**) 2 wt%, (**C**) 5 wt%, (**D**) 9 wt%, (**E**) 17 wt%, and (**F**) 23 wt%.

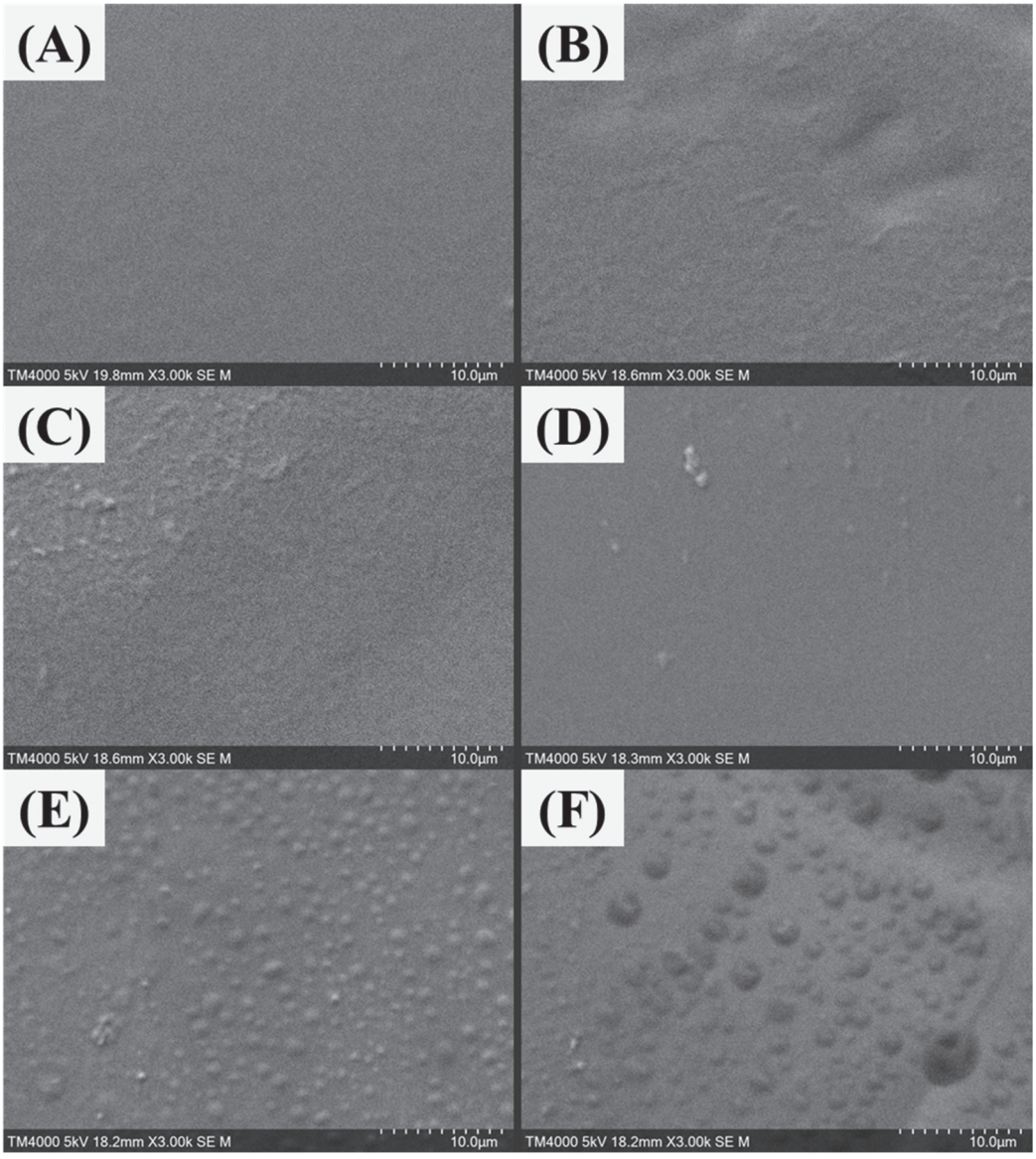

Figure 16. SEM diagrams of different GA content PVA-GA composite membranes: (**A**) no additional GA, (**B**) 2 wt%, (**C**) 5 wt%, (**D**) 9 wt%, (**E**) 13 wt%, and (**F**) 17 wt%.

3.4. Effect of Moisture on the Separation Efficiency of Polyvinyl Alcohol-Polyglycol Composite Membrane

The experimental results are shown in Figure 17 and Tables 5 and 6. In wet environments, CO_2 permeability is improved compared to dry environments, while N_2 permeability decreases slightly compared to dry environments, resulting in a significant improvement in CO_2/N_2 selectivity in wet environments compared with dry environments. This can be attributed to the ambient humidity increasing moisture content in the hydrophilic polyvinyl alcohol membrane, so that CO_2 can react with the water to produce

bicarbonate, accelerating the transmission of CO_2 in the membrane. CO_2 permeability increases, compared with N_2, since water solubility for the latter is small [30,31], making CO_2/N_2 more selective in humid environments than in dry environments.

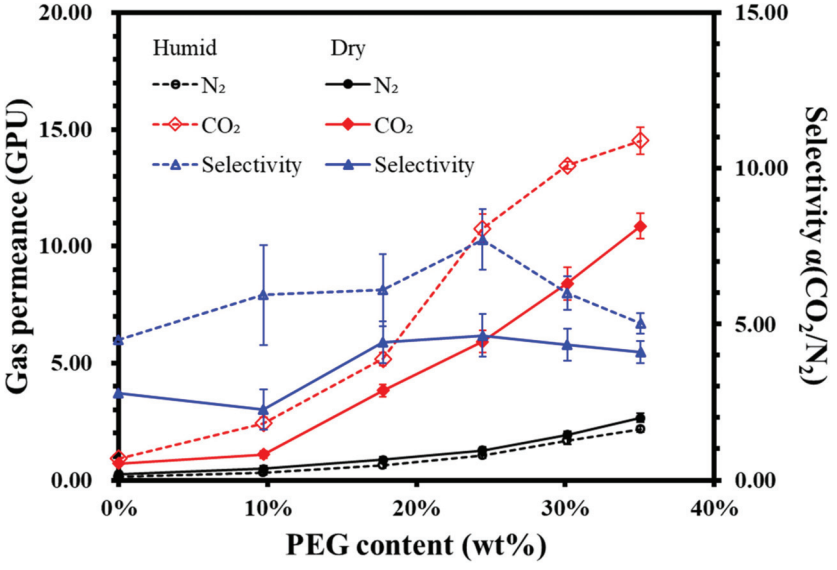

Figure 17. Effect of PEG content on the gas permeability of composite membrane in a dry or humid environment.

Table 5. Gas permeability and selectivity in a dry environment *.

Sample	PEG (wt%)	Permeance (GPU)		Selectivity (CO_2/N_2)
		CO_2	N_2	
PVA-B-2	0	0.71 ± 0.12	0.26 ± 0.12	2.80 ± 1.36
PVA-PEG-0.4	10	1.10 ± 0.16	0.48 ± 0.12	2.26 ± 0.63
PVA-PEG-0.8	18	3.83 ± 0.28	0.87 ± 0.12	4.41 ± 0.68
PVA-PEG-1.2	24	5.72 ± 0.25	1.26 ± 0.08	4.53 ± 0.34
PVA-PEG-1.6	30	8.42 ± 0.70	1.94 ± 0.16	4.34 ± 0.51
PVA-PEG-2.0	35	10.86 ± 0.54	2.65 ± 0.19	4.10 ± 0.36

* Feed gas pressure: 1.00 bar.

Table 6. Gas permeability and selectivity in a humid environment *.

Sample	PEG (wt%)	Permeance (GPU)		Selectivity (CO_2/N_2)
		CO_2	N_2	
PVA-B-2	0	0.92 ± 0.15	0.15 ± 0.08	6.00 ± 3.16
PVA-PEG-0.4	10	2.42 ± 0.25	0.31 ± 0.08	7.92 ± 2.14
PVA-PEG-0.8	18	5.18 ± 0.27	0.64 ± 0.12	8.12 ± 1.55
PVA-PEG-1.2	24	11.34 ± 0.41	1.13 ± 0.13	10.05 ± 1.22
PVA-PEG-1.6	30	13.46 ± 0.15	1.68 ± 0.15	8.00 ± 0.73
PVA-PEG-2.0	35	14.54 ± 0.58	2.17 ± 0.12	6.71 ± 0.45

* Feed gas pressure: 1.00 bar.

PVA-PEG-1.2 has the best gas selectivity. This composite film was tested under different pressure difference conditions, with results shown in Figure 18 and Table 7. It is observed that the nitrogen permeability of the composite film does not change appreciably, while CO_2 permeability and gas selectivity increase slightly with decreasing pressure difference. This decrease in pressure differential and increase in gas permeability are

usually caused by the promotion of transmission mechanisms [30,32]. This occurs when the gas is passed through the membrane by the dissolve-diffusion mechanism, since its driving force comes from different pressures at both ends of the membrane, resulting in a gas concentration gradient. Calculation of permeability requires division of the pressure difference at both ends, with permeability in the simple solubility-diffusion mechanism assuming no gradient. For a small pressure difference, the proportion of promoting transmission mechanism is larger, and when the pressure difference gradually increases, the carrier molecules with CO_2 gradually reach saturation. At this point, the system is converted from the dissolved-diffusion mechanism to account for a larger proportion. CO_2 permeability will gradually tend to stabilize the constant [32]. There is a negative correlation between CO_2 permeability and the pressure difference.

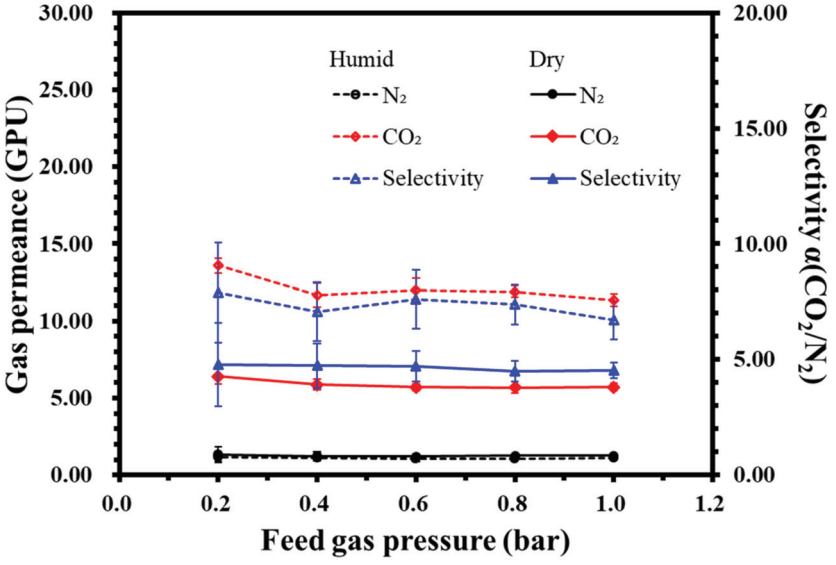

Figure 18. The relationship between gas permeability/selectivity and the pressure of the PVA-PEG-1.2 composite membrane in a dry or humid environment.

Table 7. The gas permeability and selectivity of PVA-PEG-1.2 membrane in varied pressure.

Pressure (bar)	Permeance (GPU)				Selectivity	
	Dry		Humid		Dry	Humid
	CO_2	N_2	CO_2	N_2	(CO_2/N_2)	
1.00	5.72 ± 0.25	1.26 ± 0.08	11.34 ± 0.41	1.13 ± 0.13	4.53 ± 0.34	10.05 ± 1.22
0.80	5.69 ± 0.37	1.27 ± 0.09	11.91 ± 0.39	1.08 ± 0.12	4.49 ± 0.44	11.07 ± 1.29
0.60	5.71 ± 0.22	1.21 ± 0.16	11.99 ± 0.79	1.05 ± 0.16	4.71 ± 0.66	11.39 ± 1.89
0.40	5.88 ± 0.33	1.24 ± 0.25	11.67 ± 0.78	1.10 ± 0.18	4.73 ± 0.98	10.61 ± 1.90
0.20	6.41 ± 0.48	1.34 ± 0.49	13.58 ± 0.49	1.15 ± 0.31	4.79 ± 1.80	11.83 ± 3.25

The experimental results show that there should be a transmission mechanism in the polyvinyl alcohol-polyethylene glycol membrane, which may be derived from moisture in the membrane. This is because polyvinyl alcohol is cross-linked, and the relative humidity of the dry environment set by the experiment is still approximately 40%. Whether in a dry environment or humid environment, the membrane still retains moisture to promote the transmission mechanism, so that in the case of reduced CO_2 pressure, CO_2 permeability can increase slightly.

3.5. Effect of Additional Sodium Glutamate and Glutamic Acid on Gas Separation Efficiency

Results from testing additional sodium glutamate in the PVA-MSG membrane are shown in Figure 19 and Table 8. It is observed that with increased MSG content, CO_2 and N_2 permeability also increase. Gas selectivity did not increase appreciably, especially when the MSG content is 23 wt%. N_2 permeability is greatly increased, with gas selectivity falling close to 1. SEM analysis of the composite membrane shows the presence of crystalline MSG on the membrane surface. This results in gaps between PVA and MSG, making it easier for gas to pass through the membrane, thus reducing selectivity [18].

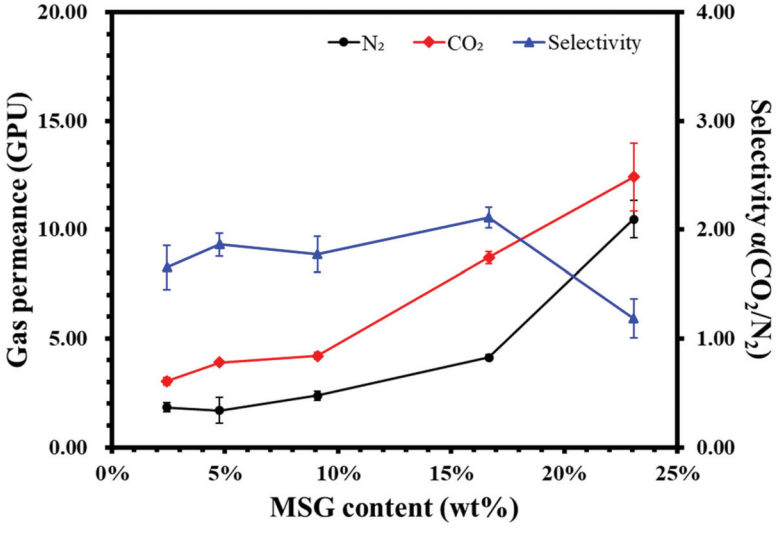

Figure 19. Effect of sodium glutamate content on the gas permeability of composite membrane.

Table 8. Gas permeability of polyvinyl alcohol-sodium glutamate composite membranes *.

Sample	MSG (wt%)	Permeance (GPU)		Selectivity (CO_2/N_2)
		CO_2	N_2	
PVA-MSG-0.1	2	3.03 ± 0.16	1.84 ± 0.20	1.65 ± 0.20
PVA-MSG-0.2	5	3.91 ± 0.08	1.69 ± 0.60	1.86 ± 0.10
PVA-MSG-0.4	9	4.21 ± 0.15	2.37 ± 0.20	1.77 ± 0.16
PVA-MSG-0.8	17	8.72 ± 0.27	4.13 ± 0.13	2.11 ± 0.09
PVA-MSG-1.2	23	12.42 ± 1.55	10.48 ± 0.85	1.18 ± 0.18

* Feed gas pressure: 1.00 bar, wet condition.

Results from testing additional glutamate acid in the PVA-GA membrane are shown in Figure 20 and Table 9. Similar to the addition of MSG, CO_2 and N_2 permeability increase with the additional content, but gas selectivity does not increase appreciably. Gas selectivity falls to approximately 1, the reason assumed to be the same as for the PVA-MSG membrane.

Table 9. Gas permeability of polyvinyl alcohol/glutamic acid composite membranes *.

Sample	GA (wt%)	Permeance (GPU)		Selectivity (CO_2/N_2)
		CO_2	N_2	
PVA-GA-0.1	2	2.78 ± 0.19	1.76 ± 0.08	1.58 ± 0.13
PVA-GA-0.2	5	2.83 ± 0.15	1.63 ± 0.56	1.46 ± 0.12
PVA-GA-0.4	9	5.43 ± 0.20	2.81 ± 0.12	1.94 ± 0.11
PVA-GA-0.6	13	7.06 ± 0.27	3.85 ± 0.12	1.83 ± 0.09
PVA-GA-0.8	17	7.88 ± 0.20	6.15 ± 0.23	1.28 ± 0.06

* Feed gas pressure: 1.00 bar, wet condition.

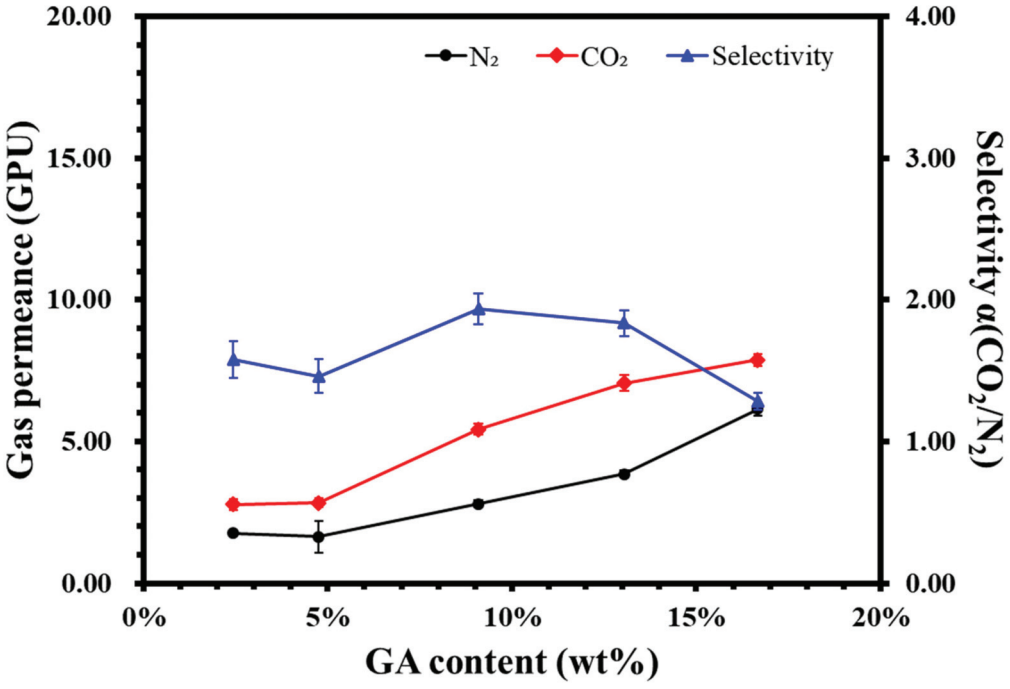

Figure 20. Effect of glutamic acid content on the gas permeability of composite membrane.

3.6. Separation Efficiency of CO_2

Separation efficiency tests for PVA-PEG-1.2, PVA-MSG-0.8, and PVA-GA-0.4 composite membranes were completed. Experimental results are shown in Figure 21 and Table 10. Experiments show that the polyvinyl alcohol-polyethylene glycol as a selection layer coated on the reverse osmosis membrane can improve the concentration of CO_2 passing through this composite membrane. PVA-PEG-1.2 can increase the concentration of CO_2 to approximately 32.6 ppm (composite membrane concentration difference-reverse osmosis membrane concentration difference). The PVA-MSG-0.8 composite membrane and PVA-GA-0.4 composite membranes increased CO_2 concentration by approximately 8.6 ppm and 5.0 ppm, respectively. These results show that the addition of glut amine or glutamate is not a viable option to affect a significant increase in CO_2 concentration.

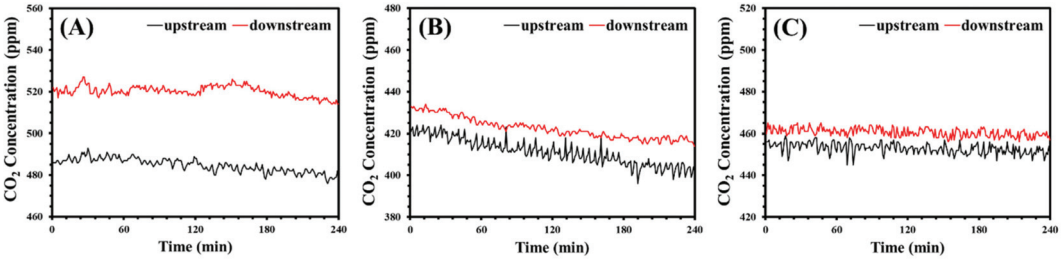

Figure 21. The concentration difference of CO_2 in the composite membranes: (**A**) PVA-PEG-1.2, (**B**) PVA-MSG-0.8, and (**C**) PVA-GA-0.4.

Table 10. Separation efficiency of the composite membranes.

Sample	Pressure Difference (mmHg)	CO_2 Concentration (ppm)
blank	-	2.43 ± 2.08
reverse osmosis membrane	700	2.73 ± 1.43
PVA-PEG-1.2	700	35.37 ± 3.15
PVA-MSG-0.8	700	11.32 ± 3.32
PVA-GA-0.4	700	7.70 ± 2.76

3.7. Water Absorption of the Membrane

The experimental results of water absorption measurement of the self-supporting membrane are shown in Table 11. The results show that compared with pure polyvinyl alcohol PVA membrane, water absorption of the PVA-B-2 membrane with Borax was increased from 52.3% to 60.7%, while the PVA-PEG-1.2 membrane with polyethylene glycol resulted in a higher increase to 72.1%. In contrast, water absorption of PVA-MSG-0.8 membrane with sodium glutamate decreased.

Table 11. Water absorption measurement of the self-supporting membranes.

Sample	Water Uptake (%)
PVA	52.3 ± 1.4
PVA-B-2	60.7 ± 1.3
PVA-PEG-1.2	72.1 ± 1.6
PVA-MSG-0.8	39.9 ± 1.3
PVA-GA-0.4	N/A

There are two reasons for the decrease in water absorption associated with the addition of sodium glutamate. Firstly, because the water absorptivity of sodium glutamate is less than that of polyvinyl alcohol, the addition of sodium glutamate results in an overall decrease in water absorptivity. Secondly, as observed via SEM analysis, sodium glutamate forms particles on the surface of the membrane, thus reducing the contact area between the membrane and moisture in the space. This results in a decrease in water absorption of the PVA-MSG-0.8 membrane over the same period.

The addition of sodium tetraborate increases water absorption. Sodium tetraborate dissolves in water to form a mixed solution of boric acid and hydrogen and oxygen root ions, increasing the overall pH In previous studies [30,31] researchers also found that when the PVA membrane is partially alkaline, water absorption of the membrane increased. Polyethylene glycol and polyvinyl alcohol are hydrophilic, while also reducing the crystallization of polyvinyl alcohol [33]. Therefore, water absorption of the PVA-PEG-1.2 membrane is higher than that of the PVA-B-2 membrane.

3.8. The Deterioration Measurement of the Selectivity of CO_2 Membrane

In this experiment, the highest CO_2 selectivity sample of each group, namely PVA-PEG-1.2, PVA-MSG-0.8 and PVA-GA-0.4 composite membrane, were teste. CO_2 selectivity for each material was tested after 48, 96, 144, 192, and 240 h to determine whether the composite membrane has deteriorated over the 10-day period. Experimental results are shown in Figure 22 and Table 12.

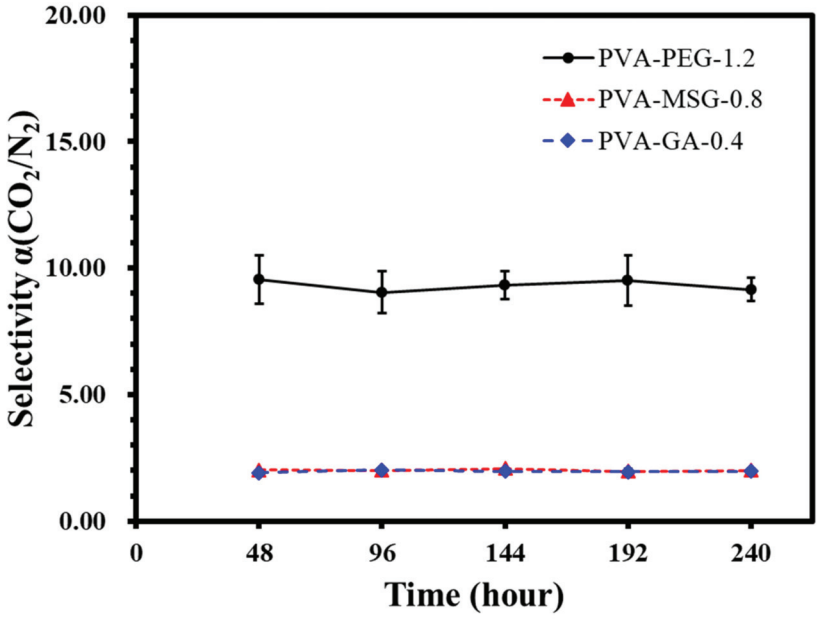

Figure 22. The selectivity of PVA-PEG-1.2, PVA-MSG-0.8, and PVA-GA-0.4 composite membranes.

Table 12. The selectivity $\alpha(CO_2/N_2)$ of PVA-X composite membranes.

Time (hour)	PVA-PEG-1.2	PVA-MSG-0.8	PVA-GA-0.4
48	9.59 ± 0.97	2.10 ± 0.08	1.91 ± 0.09
96	9.56 ± 0.95	2.02 ± 0.13	2.01 ± 0.04
144	9.04 ± 0.83	2.01 ± 0.15	1.97 ± 0.11
192	9.33 ± 0.54	1.97 ± 0.09	1.95 ± 0.14
240	9.51 ± 0.99	2.01 ± 0.10	1.97 ± 0.09

Polyvinyl alcohol-polyethylene glycol is measured using PVA-PEG-1.2 composite membrane. The results showed that the selectivity of the gas composite membrane is approximately 9.5. There was no upward or downward trend, and no significant change occurred in 10 days.

Polyvinyl alcohol-sodium glutamate is measured using PVA-MSG-0.8 composite membrane. The results showed that the selectivity of the gas composite membrane is approximately 2.0. There was no upward or downward trend, and no significant change occurred in 10 days.

Polyvinyl alcohol-glutamic acid is measured using PVA-GA-0.4 composite membrane. The results showed that the selectivity of the gas composite membrane is approximately 1.9–2.0. There was no upward or downward trend, and no significant change occurred in 10 days.

3.9. Add Sodium Tetraborate (Borax) Crosslinking Effect

The best gas selectivity PVA-PEG-1.2 was selected as the control group. The material was also formulated using the same polyvinyl alcohol, polyethylene glycol ratio. The sample without Borax, PVA-PEG-1.2-NB, was prepared but with 15 mL Borax solution replaced by deionized water. Its formulation ratio is shown in Table 13. Gas permeability, gas selectivity and moisture adsorption measurement results are shown in Table 14. The experimental results showed that PVA-PEG-1.2 samples with Borax were higher in

PVA-PEG-1.2-NB without Borax, but the gas selectivity was lower and moisture absorption was reduced.

Table 13. The composition of samples with or without Borax.

Sample	PVA (g)	PEG (mL)	Borax (g)
PVA-PEG-1.2	4.00	1.20	0.08
PVA-PEG-1.2-NB	4.00	1.20	-

Table 14. The gas separation and adsorption properties of samples with or without Borax.

Sample	Permeance (GPU)		Selectivity (CO_2/N_2)	Water Uptake (%)
	CO_2	N_2		
PVA-PEG-1.2	10.76 ± 0.61	1.05 ± 0.12	10.05 ± 1.22	72.1 ± 1.6
PVA-PEG-1.2-NB	13.95 ± 0.42	1.66 ± 0.12	8.42 ± 0.65	66.9 ± 1.7

The PVA-PEG-1.2 composite membrane with Borax added may have better CO_2/N_2 separation than PVA-PEG-1.2-NB without Borax: (1) It can be seen that the power radius of CO_2 is 3.30, and the power radius of nitrogen is 3.64, so crosslinking may cause the membrane aperture and quantity to decrease. The result is that the gas dynamic radius of N_2 is more affected, and permeability decreases more than for CO_2, resulting in a selective increase in CO_2/N_2, as shown in Table 15. (2) It can be seen from the water adsorption experiment that PVA-PEG-1.2 is slightly higher than that of PVA-PEG-1.2-NB, which means it is easier to dissolve into the membrane because of the high solubility of CO_2 in water, resulting in a selectivity increase in CO_2/N_2.

Table 15. Gas dynamic radius.

Molecule	Kinetic Diameter (Å)
CO_2	3.30
N_2	3.64

Simulation results of a linear addition of thermal weight changes in each component are shown in Figure 23. It can be seen that PVA-PEG produced significant weight changes in three stages. These occurred at approximately 125 °C, 200–350 °C and 375–450 °C, corresponding to moisture loss, lysis of polyglycol and polyvinyl alcohol branch chains, and cracking of polyvinyl alcohol main chains, respectively [25,34–36].

Comparing the simulated thermal weight loss with the actual experimental results, it is found that with polyethylene glycol mixed into polyvinyl alcohol, the original lysis of polyethylene glycol occurs at a reduced temperature of approximately 200 °C. Secondly, comparing PVA-PEG-1.2 with sodium tetraborate and PVA-PEG-1.2-NB without sodium tetraborate, it can be found that the residual weight of PVA-PEG-1.2 is slightly higher than PVA-PEG-1.2-NB. In addition, the residual weight of PVA-PEG-1.2 is higher before and after 400 °C, which is approximately 10% higher than the simulated thermal weight loss. The B-O-C bond is produced by the crosslinking of boric acid and hydroxyl, so that the polyvinyl alcohol branch chain is less, which could be cracked in this temperature range, resulting in a higher residual weight. Therefore, the use of Borax as a polyvinyl alcohol crosslinking agent can improve the thermal stability of the membrane.

From the experimental results, it can be seen that the use of Borax as a polyvinyl alcohol crosslinking agent, results in a slight decrease in carbon dioxide permeability, and an improvement in CO_2/N_2 selectivity, moisture adsorption and thermal stability. Polyvinyl alcohol is an improvement over other crosslinkers since, unlike formaldehyde, dialdehyde and other commonly used compounds, it can function at room temperature. Therefore, Borax and polyvinyl alcohol can be recommended for the purpose of manufacturing composite membranes suitable for CO_2 separation.

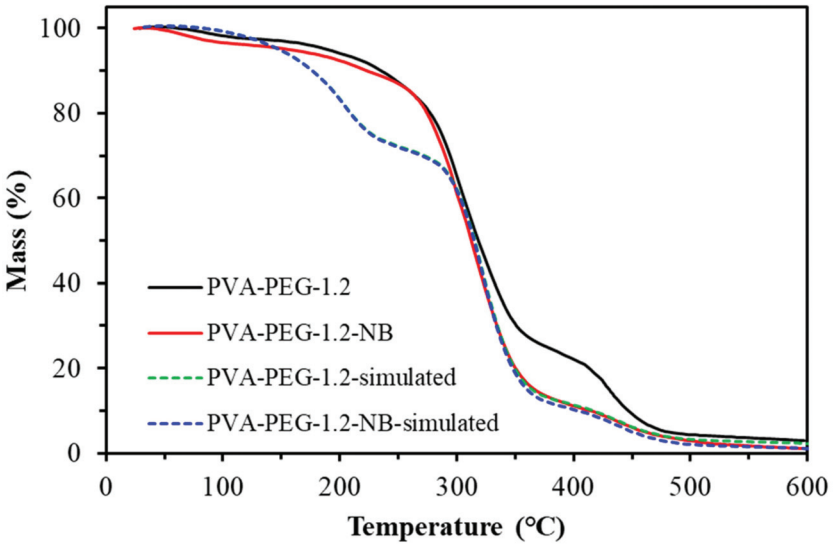

Figure 23. Thermal mass of the PVA-PEG-1.2 composite membrane.

4. Conclusions

In this study, the use of polyethylene glycol, glutamic acid, monosodium glutamate, water as a solvent and polyvinyl alcohol formulated a polymer mixing solution, coated to the surface of the dry reverse osmosis membrane, thereby improving carbon dioxide permeability and CO_2/N_2 selectivity. The addition of polyethylene glycol and glutamic acid (salt) to polyvinyl alcohol films can increase CO_2 permeability. In a humid environment, because moisture promotes the composite membrane transmission mechanism, CO_2 permeability and gas selectivity are higher than in a dry environment. PVA-PEG-1.2 composite membrane is the best selection for CO_2 separation under the condition of a pressure difference of 1.00 bar and a humid environment, the selectivity reaching to 10.05. As PEG content continues to increase, nitrogen permeability increases by more than CO_2 permeability, which leads to a decrease in selectivity. Glutamic acid (salt) may crystallize due to low solubility. The solubility of the amine-based acid itself should be considered when using amine-based acids in polyvinyl alcohol membrane preparation. During the 10-day test, the CO_2/N_2 selectivity of polyvinyl alcohol complex membranes, whether added to polyethylene glycol, sodium glutamate or glutamic acid, remained stable without degradation. Borax can be cross-linked at room temperature and can improve CO_2/N_2 selectivity, water absorption and thermal stability, which can be used by polyvinyl alcohol as the main CO_2 separation membrane.

Author Contributions: Conceptualization, S.-M.C.; data curation, M.-H.T.; formal analysis and investigation, A.S. and M.-H.T.; project administration, S.-M.C. and M.-J.Y.; supervision, S.-M.C. and M.-J.Y.; writing—original draft, M.-H.T. and A.S.; writing—review and editing, S.-M.C. and G.L. All authors have read and agreed to the published version of the manuscript.

Funding: This research was funded by the Ministry of Science and Technology of Taiwan (MOST-107-2221-E-027-027) and the National Taipei University of Technology - Beijing University of Technology Joint Research Program (NTUT-BJUT-110-03; BJUT-NTUT-110-03).

Institutional Review Board Statement: Not applicable.

Informed Consent Statement: Not applicable.

Conflicts of Interest: The authors declare no conflict of interest.

References

1. Lu, J.G.; Cheng, M.; Ji, Y.; Hui, Z. Membrane-based CO_2 absorption into blended amine solutions. *J. Fuel Chem. Technol.* **2009**, *37*, 740–746. [CrossRef]
2. Bernardo, P.; Drioli, E.; Golemme, G. Membrane Gas Separation: A Review/State of the Art. *Ind. Eng. Chem. Res.* **2009**, *48*, 4638–4663. [CrossRef]
3. Metz, B.; Davidson, O.; De Coninck, H.C.; Loos, M.; Meyer, L. *IPCC Special Report on Carbon Dioxide Capture and Storage, Intergovernmental Panel on Climate Change (IPCC)*; Cambridge University Press: Cambridge, UK, 2005; p. 442.
4. Suleman, M.S.; Lau, K.K.; Yeong, Y.F. Plasticization and Swelling in Polymeric Membranes in CO_2 Removal from Natural Gas. *Chem. Eng. Technol.* **2016**, *39*, 1604–1616. [CrossRef]
5. Lin, H.; Freeman, B.D. Materials selection guidelines for membranes that remove CO_2 from gas mixtures. *J. Mol. Struct.* **2005**, *739*, 57–74. [CrossRef]
6. Klaassen, R.; Feron, P.H.M.; Jansen, A.E. Membrane Contactors in Industrial Applications. *Chem. Eng. Res. Des.* **2005**, *83*, 234–246. [CrossRef]
7. He, X.; Yu, Q.; Hägg, M.B. CO_2 Capture. In *Encyclopedia of Membrane Science and Technology*; Hoek, E.M.V., Tarabara, V.V., Eds.; Wiley: Hoboken, NJ, USA, 2013.
8. Freeman, B.D. Basis of permeability/selectivity tradeoff relations in polymeric gas separation membranes. *Macromolecules* **1999**, *32*, 375–380. [CrossRef]
9. Robeson, L.M. The upper bound revisited. *J. Membr. Sci.* **2008**, *320*, 390–400. [CrossRef]
10. Baker, R.W.; Low, B.T. Gas separation membrane materials: A perspective. *Macromolecules* **2014**, *47*, 6999–7013. [CrossRef]
11. Chung, T.S. A review of microporous composite polymeric membrane technology for air-separation. *Polym. Polym. Compos* **1996**, *4*, 269–283.
12. Dai, Z.; Ansaloni, L.; Deng, L. Recent advances in multi-layer composite polymeric membranes for CO_2 separation: A review. *Green Energy Environ.* **2016**, *1*, 102–128. [CrossRef]
13. Li, P.; Chen, H.Z.; Chung, T.S. The effects of substrate characteristics andpre-wetting agents on PAN-PDMS composite hollow fiber membranes for CO_2/N_2 and O_2/N_2 separation. *J. Membr. Sci.* **2013**, *434*, 18–25. [CrossRef]
14. Xie, K.; Fu, Q.; Qiao, G.G.; Webley, P.A. Recent progress on fabrication methods of polymeric thin film gas separation membranes for CO_2 capture. *J. Membr. Sci.* **2019**, *572*, 38–60. [CrossRef]
15. Sun, J.; Yi, Z.; Zhao, X.; Zhou, Y.; Gao, C. CO_2 separation membranes with high permeability and CO_2/N_2 selectivity prepared by electrostatic self-assembly of polyethylenimine on reverse osmosis membranes. *RSC Adv.* **2017**, *7*, 14678–14687. [CrossRef]
16. Zou, J.; Ho, W.S.W. CO_2-selective polymeric membranes containing amines in crosslinked poly(vinyl alcohol). *J. Membr. Sci.* **2006**, *286*, 310–321. [CrossRef]
17. Zhao, Y.; Ho, W.S.W. CO_2-Selective Membranes Containing Sterically Hindered Amines for CO_2/H_2 Separation. *Ind. Eng. Chem. Res.* **2013**, *52*, 8774–8782. [CrossRef]
18. Zhao, Y.; Ho, W.S.W. Steric hindrance effect on amine demonstrated in solid polymer membranes for CO_2 transport. *J. Membr. Sci.* **2012**, *415–416*, 132–138. [CrossRef]
19. Xing, R.; Ho, W.S.W. Crosslinked polyvinylalcohol–polysiloxane/fumed silica mixed matrix membranes containing amines for CO_2/H_2 separation. *J. Membr. Sci.* **2011**, *367*, 91–102. [CrossRef]
20. Zhao, Y.; Jung, B.T.; Ansaloni, L.; Ho, W.S.W. Multiwalled carbon nanotube mixed matrix membranes containing amines for high pressure CO_2/H_2 separation. *J. Membr. Sci.* **2014**, *459*, 233–243. [CrossRef]
21. Mondal, A.; Mandal, B. Synthesis and characterization of crosslinked poly (vinyl alcohol)/poly(allylamine)/2-amino-2-hydroxymethyl-1,3-propanediol/polysulfone composite membrane for CO_2/N_2 separation. *J. Membr. Sci.* **2013**, *446*, 383–394. [CrossRef]
22. Cai, Y.; Wang, Z.; Yi, C.; Bai, Y.; Wang, J.; Wang, S. Gas transport property of polyallylamine–poly(vinyl alcohol)/polysulfone composite membranes. *J. Membr. Sci.* **2008**, *310*, 184–196. [CrossRef]
23. Brunetti, A.; Scura, F.; Barbieri, G.; Drioli, E. Membrane technologies for CO_2 separation. *J. Membr. Sci.* **2010**, *359*, 115–125. [CrossRef]
24. Hirayama, Y.; Kase, Y.; Tanihara, R.; Sumiyama, Y.; Kusuki, Y.; Haraya, K. Permeation properties to CO_2 and N_2 of poly(ethylene oxide)-containing and crosslinked polymer films. *J. Membr. Sci.* **1999**, *160*, 87–99. [CrossRef]
25. Potreck, J.; Nijmeijer, K.; Kosinski, T.; Wessling, M. Mixed water vapor/gas transport through the rubbery polymer PEBAX (R) 1074. *J. Membr. Sci.* **2009**, *338*, 11–16. [CrossRef]
26. Chen, C.; Chen, Y.; Xie, J.; Xu, Z.; Tang, Z.; Yang, F.; Fu, K. Effects of montmorillonite on the properties of cross-linked poly(vinyl alcohol)/boric acid films. *Prog. Org. Coat.* **2017**, *112*, 66–74. [CrossRef]
27. Lim, M.; Kwon, H.; Kim, D.; Seo, J.; Han, H.; Khan, S.B. Highly-enhanced water resistant and oxygen barrier properties of cross-linked poly(vinyl alcohol) hybrid films for packaging applications. *Prog. Org. Coat.* **2015**, *85*, 68–75. [CrossRef]
28. Rashidzadeh, M.; Fathi, A.; Ehsani, N.; Baharvandi, H.; Rahimnejad Yazdi, A. Synthesis of Boron Carbide Nano Particles Using Polyvinyl Alcohol and Boric Acid. *Ceram-Silikaty* **2012**, *56*, 32–35.
29. Singh, K.; Devi, S.; Bajaj, H.C.; Ingole, P.; Choudhari, J.; Bhrambhatt, H. Optical Resolution of Racemic Mixtures of Amino Acids through Nanofiltration Membrane Process. *Sep. Sci. Technol.* **2014**, *49*, 2630–2641. [CrossRef]

30. Roddick-Lanzilotta, A.D.; McQuillan, A.J. An in situ Infrared Spectroscopic Study of Glutamic Acid and of Aspartic Acid Adsorbed on TiO_2: Implications for the Biocompatibility of Titanium. *J. Colloid Interface Sci.* **2000**, *227*, 48–54. [CrossRef]
31. Saeed, M.; Rafiq, S.; Bergersen, L.H.; Deng, L. Tailoring of water swollen PVA membrane for hosting carriers in CO_2 facilitated transport membranes. *Sep. Purif. Technol.* **2017**, *179*, 550–560. [CrossRef]
32. Saeed, M.; Deng, L. Carbon nanotube enhanced PVA-mimic enzyme membrane for post-combustion CO_2 capture. *Int. J. Greenh. Gas. Control.* **2016**, *53*, 254–262. [CrossRef]
33. Deng, L.; Kim, T.J.; Hägg, M.B. Facilitated transport of CO_2 in novel PVAm/PVA blend membrane. *J. Membr. Sci.* **2009**, *340*, 154–163. [CrossRef]
34. Entezam, M.; Daneshian, H.; Nasirizadeh, N.; Khonakdar, H.A.; Jafari, S.H. Hybrid Hydrogels Based on Poly(vinyl alcohol) (PVA)/Agar/Poly (ethylene glycol) (PEG) Prepared by High Energy Electron Beam Irradiation: Investigation of Physico-Mechanical and Rheological Properties. *Macromol. Mater. Eng.* **2017**, *302*, 1600397. [CrossRef]
35. Barooah, M.; Mandal, B. Enhanced CO_2 separation performance by PVA/PEG/silica mixed matrix membrane. *J. Appl. Polym. Sci.* **2018**, *135*, 46481. [CrossRef]
36. Dilshad, M.R.; Islam, A.; Sabir, A.; Shafiq, M.; Butt, M.T.Z.; Ijaz, A.; Jamil, T. Fabrication and performance characterization of novel zinc oxide filled cross-linked PVA/PEG 600 blended membranes for CO_2/N_2 separation. *J. Ind. Eng. Chem.* **2017**, *55*, 65–73. [CrossRef]

processes

MDPI

Article

Efficient Removal of Azlocillin Sodium from Water by Polystyrene Anion Exchange Resin Supported MIL-53

Yi Qian [1,*], Haoyan Fu [1], Long Li [2,*], Wenyuan Su [1], Jiayin Li [2] and Yihao Zhang [2]

[1] College of Chemical Engineering, Qingdao University of Science and Technology, Qingdao 266042, China; fuhaoyanfhy@163.com (H.F.); suwenyuan1226@163.com (W.S.)
[2] College of Environment and Safety Engineering, Qingdao University of Science and Technology, Qingdao 266042, China; lijiayin085@163.com (J.L.); 18832623721@163.com (Y.Z.)
* Correspondence: qianyi@qust.edu.cn (Y.Q.); lli@yic.ac.cn (L.L.)

Abstract: Due to the widespread use of antibiotics in medical treatment, animal husbandry and aquaculture, a large number of antibiotics are discharged into the environment as metabolites or in their original state, causing pollution to water bodies, which is a serious issue. In this study, a novel nanocomposite adsorbent MIL-53/D201 was successfully prepared by hydrothermal synthesis. This approach overcomes the disadvantage of easy dissociation of MOF material in the water phase and realizes the efficient removal of antibiotic azlocillin sodium in water. The crystal morphology and basic structure of the composites were characterized by X-ray diffraction (XRD), Fourier transform infrared spectroscopy (FTIR), scanning electron microscopy (SEM), energy scattering spectroscopy (EDS), and specific surface area and porosity analyzer (BET). The results showed that MIL-53 was successfully synthesized in situ in D201. The results of adsorption experiments show that the maximum saturated adsorption capacity of the composite is 122.3 mg/g when the dosage of the composite is 1.0 g/L. Compared with pure MIL-53 material, the composite material exhibits greater stability and efficient adsorption performance for target pollutants at different pH values. The adsorption process accords with the quasi-second-order kinetic adsorption model and Langmuir adsorption isothermal model. After five cycles of adsorption and desorption, the removal rate of MIL-53/D201 to azlocillin sodium was still above 87%.

Keywords: MOF; polystyrene macroporous resin; adsorption; antibiotics; in situ synthesis

Citation: Qian, Y.; Fu, H.; Li, L.; Su, W.; Li, J.; Zhang, Y. Efficient Removal of Azlocillin Sodium from Water by Polystyrene Anion Exchange Resin Supported MIL-53. *Processes* **2021**, *9*, 2195. https://doi.org/10.3390/pr9122195

Academic Editor: Avelino Núñez-Delgado

Received: 7 November 2021
Accepted: 30 November 2021
Published: 6 December 2021

1. Introduction

As a result of the aggravation of water pollution and the upgrade in the national environmental protection strategy, research into purification methods for water pollutants has become a popular topic in the environmental field [1]. Antibiotics are also commonly used in aquaculture because of intensive farming. Compared with other pollutants, antibiotics have higher bioavailability and longer environmental retention time, and can thus pose a significant threat to the aquatic ecosystem at the PPM and ppb levels. As a result, these issues have attracted extensive attention in recent years [2–5]. As an oxygen-containing anion antibiotic, azlocillin sodium is widely used in various infections caused by Gram-positive and -negative bacteria and Pseudomonas aeruginosa infection. Its uses include treatment of sepsis, meningitis, the gastrointestinal tract, the bile duct, the urinary tract, reproductive organs, skin burns, and other diseases, and it cannot be effectively removed by biodegradation. When azlocillin sodium enters the human body, 30% to 90% of its active ingredients are excreted without changing their properties. These substances may directly or indirectly enter the water system environment, thus causing pollution. In addition, the massive influx of antibiotics into water bodies has led to an increase in antibiotic-resistant bacteria, known as "antibiotic resistance pollution" [6]. At present, many treatment processes have been proposed to solve these problems, such as chemical precipitation, flocculation, advanced oxidation, and membrane filtration. However, these

methods have a high cost, readily produce secondary pollution, and cannot easily remove pollutants to acceptable concentrations. These challenges limit their practical application. For example, membrane separation is not suitable for large-scale applications because of its short lifetime, limited performance at low pressure, and poor stability in acid gas environments [7]. Compared with the above methods, adsorption technology is favored by scientific research and engineering fields because of its advantages of lower cost, easy design, and regeneration [1,8]. Unfortunately, improvement is required in traditional adsorption materials such as zeolite, activated carbon, and hydrotalcite in terms of adsorption capacity and adsorption selectivity [9–11], and the development of new efficient adsorbent materials for water pollutants remains an urgent unresolved problem.

The metal-organic framework (MOF) is a new kind of nano-adsorption material, which is a porous crystal material formed by metal ion clusters and organic ligands through coordination links. The transition metal ions provide the catalytic center for MOF, and the organic ligands provide the functional branch chain structure [12]. Therefore, MOF material is more abundant in structural changes and has significant advantages in adsorption capacity and selectivity compared with other adsorbents [13,14]. In addition, MOF is one of the most promising adsorbents, having the advantages of large specific surface area, channel tunability, and small particle size for rapid water filtration [15–17]. For example, Lee and colleagues previously developed a series of robust MOFs with a 3D framework and high surface area volume ratio, showing excellent antibacterial activity against *Escherichia coli* and *Staphylococcus aureus*. This is highly relevant to the current work [18,19]. Ma and coworkers synthesized three iron-based MOFs for adsorption of a typical volatile organic compound, toluene [20]. However, the particle size of MOF material is mostly at the micron level, and it is difficult to separate from the water phase after adsorption. Therefore, when used as the filler of a rapid filtration device, the pressure drop is large; thus, the hydrodynamic performance is poor. Secondly, due to the size of the organic ligand, most MOF materials are microporous, and the diffusion rate of the adsorbent is slow during the adsorption process, resulting in poor adsorption kinetic performance [21–23]. Thirdly, the structural integrity of MOF material depends on the coordination between organic ligands and metal ion clusters, and it is easily dissociated in the water phase [24–26]. MIL-53 is a three-dimensional porous solid linked by numerous -Fe-O-O-Fe-O-Fe- bonds and crosslinked by terephthalate. Its chemical structure is shown in Figure 1, and it has the advantages of low cost and non-toxicity. MIL-53 also shows considerable adsorption and photocatalytic activity in wastewater treatment, which makes it a potential candidate material for environmental remediation [27,28]. However, MIL-53 is extremely unstable in an aqueous solution. It is a challenge to achieve optimal performance of MIL-53 by directly suspending it in water as an adsorbent to remove organic pollutants [29]. To overcome the above shortcomings of MOF, there is an urgent need to find a stable polymer material as a carrier, and fix MOF onto this carrier to prepare more stable and efficient composite adsorption materials. Polystyrene macroporous resin (for example, D201 resin is an anion exchange resin) has high mechanical and chemical stability and excellent hydrodynamics performance. The covalently linked quaternary ammonium groups on the polystyrene framework can preconcentrate the target ions through ion exchange [30]. By loading inorganic adsorption materials into macroporous resins, a variety of efficient composite adsorption materials can be developed [31–33]. However, little research has been done on impregnating MOF into macroporous anion exchange resins to remove contaminants from water.

In summary, in this study, MIL-53 material was in situ synthesized in D201 macroporous resin to prepare MIL-53/D201 composite material, for use in the adsorption of azlocillin sodium in water. The preparation method of the composite was systematically studied by investigating the microstructure, surface properties, and internal structure of the composite. Based on the properties of pores, specific surface area, and ion exchange capacity, the experimental conditions were optimized to prepare the composite with good properties. The composite material was used for the adsorption of azlocillin sodium, and

the effects of adsorption time, adsorbent dosage, solution PH, and different interfering ions on the adsorption performance of MIL-53/D201 composite were studied. The adsorption performance was investigated by batch adsorption experiments, the relevant thermodynamic parameters were obtained, and the adsorption mechanism was explored.

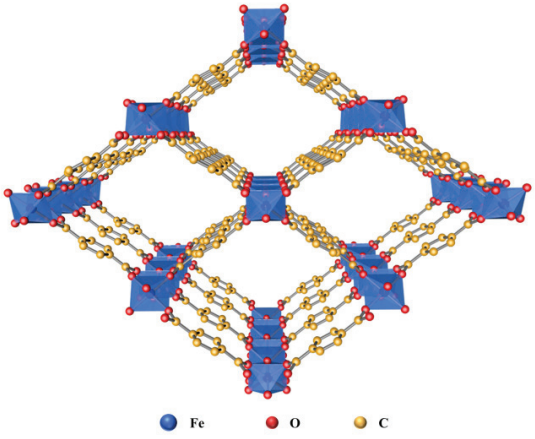

Figure 1. The schematic 3D representation of MIL-53.

2. Materials and Methods

2.1. Materials

Ferric chloride hexahydrate ($FeCl_3 \cdot 6H_2O$, 99%), N, N-dimethylformamide (DMF, 99%), terephthalic acid (H_2BDC, 99%), and ethanol (C_2H_5OH) was purchased from Shanghai Maclin Biochemical Technology Co., LTD (Shanghai, China). Sodium hydroxide (NaOH) and nitric acid (HNO_3) were purchased from Shanghai Aladdin Chemical Reagent Co., LTD. Azlocillin sodium was purchased from Sinopharm Chemical Reagent Co., LTD (Shanghai, China). These reagents were analytical grade and used without further purification. D201 macroporous resin was purchased from Zhengzhou Kelisen Chemical Technology Co., LTD (Zhengzhou China). Ultra-pure water was used in all experiments.

2.2. Preparation of MIL-53/D201 Composite

MIl-53/D201 composite was prepared by the hydrothermal synthesis method (Figure 2). D201 was extracted with acetone in a Soxhlet apparatus to remove possible residual impurities and dried in an oven at 60 °C for later use. First, ferric chloride hexahydrate (5 mmol) and D201 macroporous resin (0.5 g) were dissolved in N, N-dimethylformamide solution (30 mL) and stirred at room temperature for 1 h, denoted as solution 1. Then, terephthalic acid (5 mmol) was dissolved in N, N-dimethylformamide solution (30 mL), and ultrasound was performed for 20 min, denoted as solution 2. Solution 1 and solution 2 were quickly mixed, fully stirred at room temperature for 2 h, then transferred to a 100 mL Teflon reactor and heated at 150° for 15 h. After the reactor was cooled to room temperature, the product was centrifuged and washed several times with N, N-dimethylformamide, and finally placed in a 60° vacuum drying oven overnight to obtain MIL-53/D201 composite.

2.3. Characterizations

X-ray diffraction (XRD) testing was performed with a Rigaku X-ray Diffractometer (Shimadzu Corporation of Japan, Tokyo, Japan), which uses Cu-Kα tubes and Ni filters (λ = 0.1542 nm). Fourier transform infrared spectroscopy (FTIR) in the wavelength range of 500–4000 cm^{-1} was recorded on a Nicolet-6700 FTIR spectrometer (PerkinElmer, Waltham, MA, USA). The JMS-6700 scanning electron microscope (SEM) and energy spectrum (EDS) were used to analyze and test the samples. The tested sample was sprayed with gold five times, and the acceleration voltage was 10 kV. The N_2 adsorption-desorption process of the

composite was tested at 77 K by ASAP2020 specific surface area and porosity analyzer (BET), and N_2 adsorption and desorption isotherms and pore size distribution were obtained.

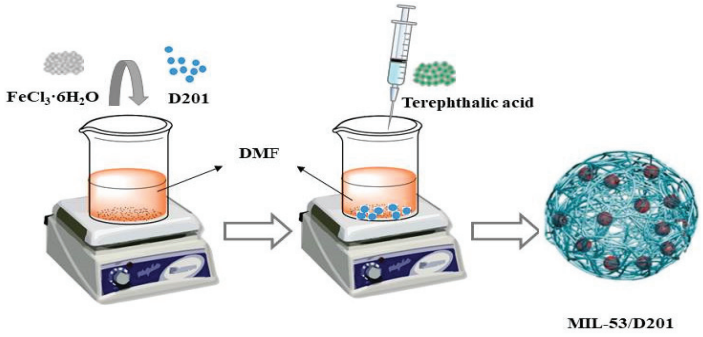

Figure 2. Schematic illustration of preparation process of MIL-53/D201 composite material.

2.4. Adsorption Experiment and Regeneration Experiment

In order to study the mass ratio with high adsorption performance, a certain amount of MIl-53/D201 composite material was placed in a 250 mL conical flask, and 200 mL sodium azlocillin solution (1 mmol/L) was added at the same time and adsorbed by a water bath shaker under constant temperature (25 °C). The solution pH was adjusted with 0.1 mol/L nitric acid (analytically pure) and 0.1 mol/L sodium hydroxide (analytically pure), and the adsorption of MIL-53 and MIL-53/D201 composite in the pH range (1.0 to 11.0) was investigated. Considering that the actual wastewater treatment is more complicated, Cl^-, SO_4^{2-}, and SiO_3^{2-} were selected as interference ions. The adsorption experiments were carried out by adding 100 mg MIL-53/D201 composite material to 200 mL of azlocillin sodium solution with different concentrations of three interfering ions. In order to determine the recoverability of MIL-53/D201 composite adsorbent, the adsorbent after adsorption balance was washed with deionized water and soaked in ethanol solution at room temperature for 24 h for desorption, so as to completely eliminate the adsorbed azlocillin sodium. The regenerated MIL-53/D201 composite was used in the adsorption experiment again, and the cycle was repeated five times. All of the above adsorption and regeneration experiments were carried out at room temperature (25 °C) with a water bath shaker at a speed of 350 RPM. The solution was centrifuged in a conical flask. The supernatant was extracted using an injection filter (hydrophobic, 0.5 μm) and the concentration of the remaining azlocillin sodium solution was analyzed by UV spectrum. The adsorption capacity and efficiency of the adsorbent can be calculated by the following equations:

$$q_e = \frac{(C_0 - C_e)V}{m}, \quad (1)$$

$$E(\%) = \frac{C_0 - C_e}{C_0} \times 100\%, \quad (2)$$

where C_0 and C_e (g/mL) were the initial and equilibrium concentrations of azlocillin sodium, respectively. q_e represents adsorption capacity (mg/g); V represents the volume of solution (mL); and M represents adsorbent mass (g).

3. Results and Discussions

3.1. Characterization

XRD is usually used to characterize the crystal structure of materials. Figure 3a shows X-ray diffraction patterns of D201, MIL-53, and MIL-53/D201 composite. It can be seen from the figure that although D201 has no obvious characteristic peak, it has characteristic fluctuation in the range 2θ = 15–25. The crystal structure of MIL-53 has sharp and clear characteristic peaks at 2θ = 9.3, 12.6, 16.8, 17.9, 25.5, 27.32, 29.8, 30.28, and 36.18. This

indicates that the prepared MIL-53 material has a good crystal structure, which is consistent with the results reported in the literature [34]. In addition, in the XRD patterns of MIL-53/D201 composite, we can see that the material at 2θ = 9.3, 12.6, 16.8, 17.9 and 25.5 has the characteristic peaks of MIL-53 and the characteristic fluctuations of D201. The results showed that MIL-53/D201 composite was successfully synthesized.

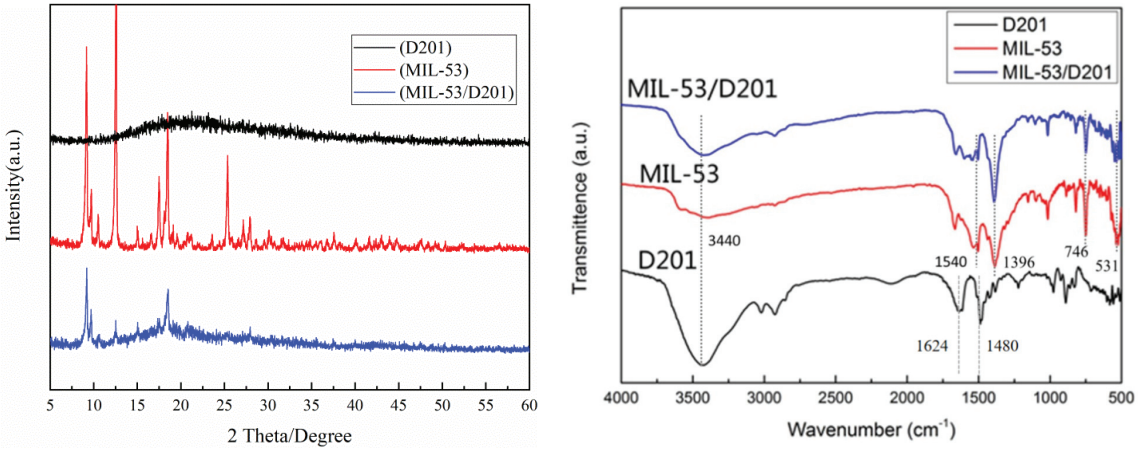

(**a**) (**b**)

Figure 3. XRD (**a**) and FT−IR (**b**) of MIL-53/D201 composite and their components.

FTIR study further confirmed the successful synthesis of MIL-53/D201 composite (Figure 3b). These results showed that the infrared absorption spectra of MIL-53 are highly consistent with the data reported in the literature [35]. The peaks at 746 and 533 cm^{-1} correspond to the vibration of the C-H bond in the benzene ring and the formation of the metal-oxygen bond between the carboxyl group of terephthalic acid and Fe^{3+}, respectively. The region between 1300 and 1700 cm^{-1} is associated with carboxylic acid ligands, indicating the coordination of H_2BDC with iron centers. The two peaks of MIL-53 at 1540 and 1380 cm^{-1} correspond to the asymmetric vibration of the carboxyl group and the symmetric vibration of the carboxyl group, respectively, which proves the existence of dicarboxylic acid bonds in the sample. The wide peak centered at 3440 cm^{-1} is related to the stretching vibration of the water-adsorbed O-H. The characteristic peaks of D201 macroporous resin at 1624 and 1480 cm^{-1} are mainly related to the $-N^{+}(CH_3)_3$ group.

By comparing the FTIR spectra of the MIL-53/D201 composite, it was found that the stretching vibration of the characteristic bond of MIL-53 and D201 anion exchange resin was shown in the FTIR spectra of MIL-53/D201 composite, which further demonstrated the successful preparation of the composite adsorption material.

As shown in Figure 4, the morphology of MIL-53, D201 macroporous resin, and MIL-53/D201 composite material was analyzed by SEM. MIL-53 was observed to have an irregular blocky structure (Figure 4a) dominated by a rod-like structure with smooth surfaces and straight edges (Figure 4b), which is consistent with previously reported results [36]. The parent anion exchange resin bead has a smooth surface and is free of any particles (Figure 4c) [37]. There are many dense pores in the D201 macroporous resin (Figure 4d). Figure 4e,f show SEM images of the surface and cross section of MIL-53/D201 composite material, respectively. It can be seen that MIL-53 is evenly dispersed on the surface of D201 resin. MIL-53 still maintains a clear rod-like structure inside the resin and has close interface contact with the resin.

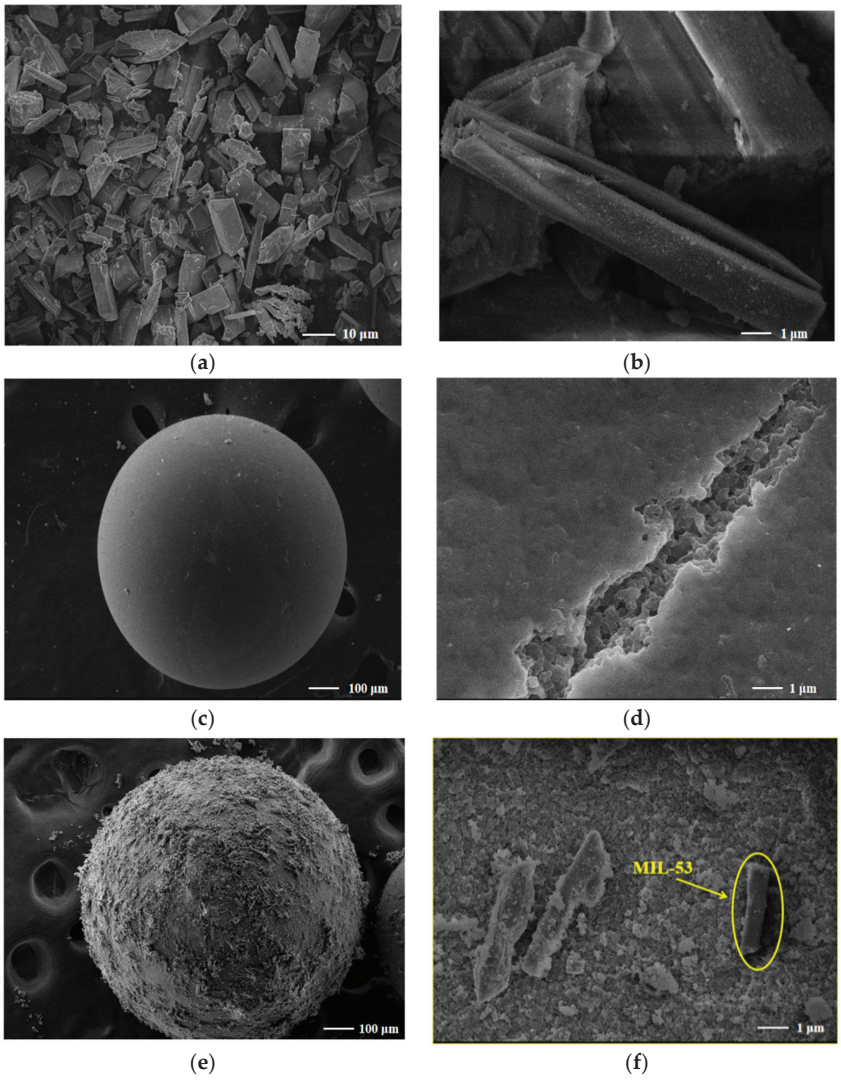

Figure 4. SEM image of MIL-53 (**a**,**b**), D201 (**c**,**d**), MIL-53/D201 composite (**e**), and MIL-53/D201 composite transverse section (**f**) at different magnifications.

Figure 5 shows the element distribution diagram and energy spectrum analysis diagram of MIL-53/D201 composite in cross section. Figure 5a,b of the element distribution in the cross section shows that Fe and Cl are not only distributed on the outside of the resin, but also on the inside of the resin, indicating that MIL-53 was successfully synthesized in situ inside the resin. Figure 5c clearly shows that the main components of MIL-53/D201 composite are C, O, N, Fe, and Cl. The presence of Cl in the material sample of MIL-53/D201 composite is due to the random absence of organic ligands in the entire material frame, resulting in charge and coordination defects, which can be compensated for by Cl^-.

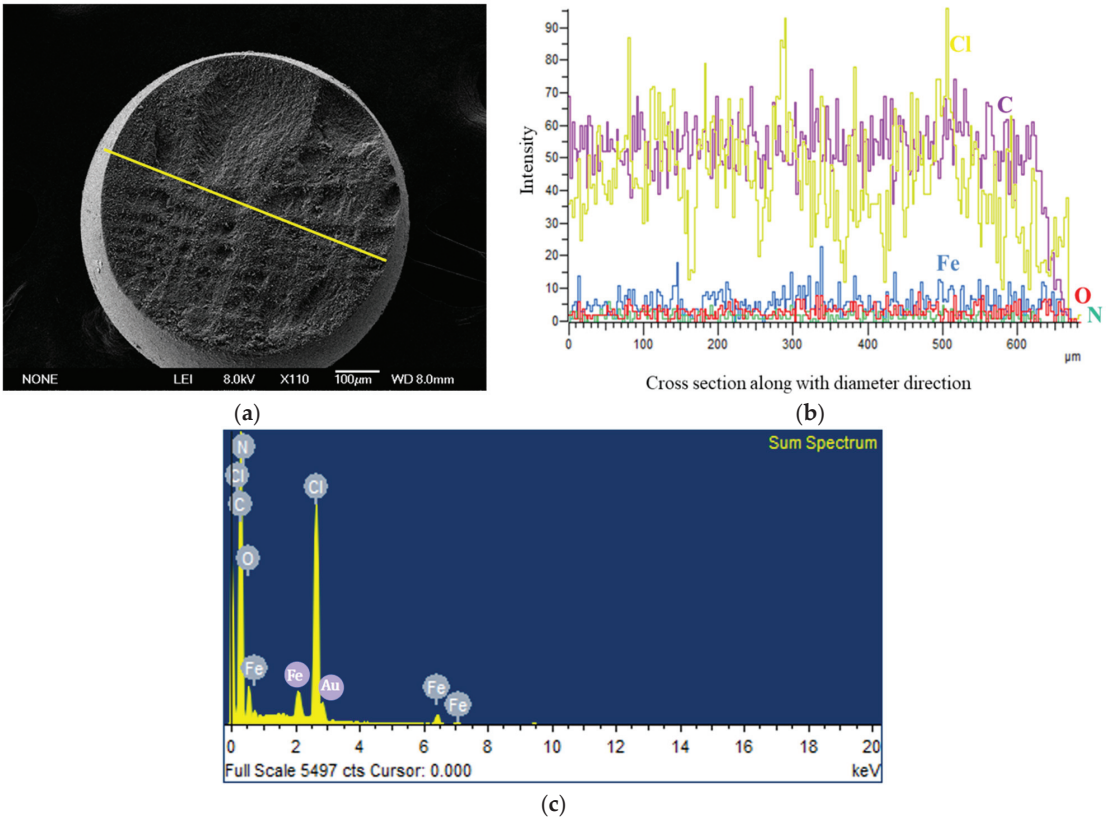

Figure 5. Cross section SEM image (**a**), element distribution diagram (**b**), and EDS spectrum analysis diagram (**c**) of MIL-53/D201.

Based on BET test analysis of MIL-53/D201 composite anion-exchange resin composite, N_2 adsorption and desorption isotherms (Figure 6a) and BJH pore size distribution (Figure 6b) were obtained. The total specific surface area of composites was calculated by the BET equation. The BET equation is as follows:

$$\frac{P}{V\,(P_0 - P)} = \frac{1}{V_M C} + \frac{C-1}{V_M C} \times \frac{P}{P_0}, \quad (3)$$

where P and P_0 represent nitrogen saturated vapor pressure at nitrogen partial pressure and liquid nitrogen temperature, respectively. V represents the actual adsorption amount of nitrogen on the sample surface; V_M represents the saturated adsorption capacity of the nitrogen monolayer; C is a constant related to the adsorption capacity of the sample. According to IUPAC classification criteria, the N_2 adsorption-desorption isotherms of MIL-53/D201 composite are intermediate between type I and type IV in the relative pressure range, with hysteresis rings corresponding to micropores [38]. The pore size distribution curve of BJH shows that the pore sizes are concentrated at 2.9 and 141 nm, corresponding to micropores and macropores, respectively.

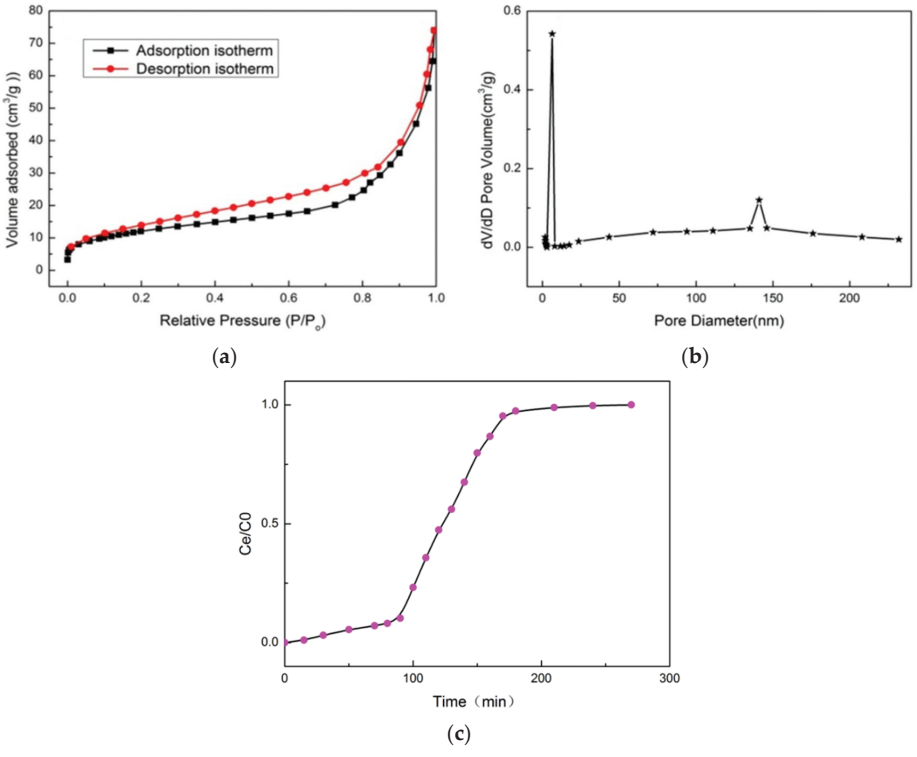

Figure 6. N_2 adsorption-desorption isotherms (**a**) and BJH pore size distributions (**b**), and penetration curve of azlocillin sodium (**c**).

3.2. Penetration Curve

One of the main parameters in the selection of adsorbents for industrial applications is the adsorption penetration time. In the whole adsorption process, when the simulated wastewater flows out of the penetrating column with adsorbent under the condition of constant liquid concentration, the corresponding point of the corresponding penetration curve when the outflow concentration Ce reaches 5% of the initial concentration C_0 ($C_e/C_0 = 0.05$) is called the penetration point [39]. When the outlet concentration of the adsorption column is equal to 95% of the initial concentration of the solution ($C_e/C_0 = 0.95$), the adsorption saturation is achieved. The penetration time is the time required from the beginning of adsorption to the point of penetration [40]. The time from the beginning of adsorption to the composite material to reach the adsorption saturation time is the adsorption saturation time. The penetration curve of MIL-53/D201 composite material adsorbing azlocillin sodium solution (1 mmol/L) at a constant flow rate was studied (Figure 6c). Figure 6c shows that, before 165 min, the adsorption capacity of MIL-53/D201 composite continued to increase because MIL-53/D201 composite has a large specific surface area and a large number of active adsorption sites. These active adsorption sites were occupied over time and reached equilibrium after 165 min. When MIL-53/D201 composite material adsorbed sodium azlocillin, the $C_e/C_0 = 0.05$ time was about 40 min (Table 1), and the adsorption saturation time was about 165 min.

Table 1. Penetration time and saturation time of azlocillin sodium.

Adsorbate (0.1 mmol/L)	Penetration Time (min)	Saturation Time (min)
Azlocillin sodium	40	165

3.3. *Effect of the Adsorbent Addition Amount*

Figure 7a shows the adsorption effect of MIL-53/D201 composite material on azlocillin sodium solution at different dosages (20, 40, 100, and 200 mg). With the increase in dosage, the adsorption capacity of MIL-53/D201 composite adsorbent to azlocillin sodium increased gradually, but the unit adsorption capacity showed a decreasing trend. This is because, as the dosage increases, the specific surface area and active adsorption site provided by the adsorbent increase, but the amount of adsorbate (azlocillin sodium) in the solution remains constant. It was observed that when the dosage was 20 and 40 mg, the adsorption of azlocillin sodium on the composite was basically saturated at 240 min. When the dosages were 100 and 200 mg, the adsorption of azlocillin sodium on the composites reached saturation after 120 min. The comparative experiment showed that when the dosage is 100 mg, the adsorption effect can be improved, and the adsorbent will not be wasted.

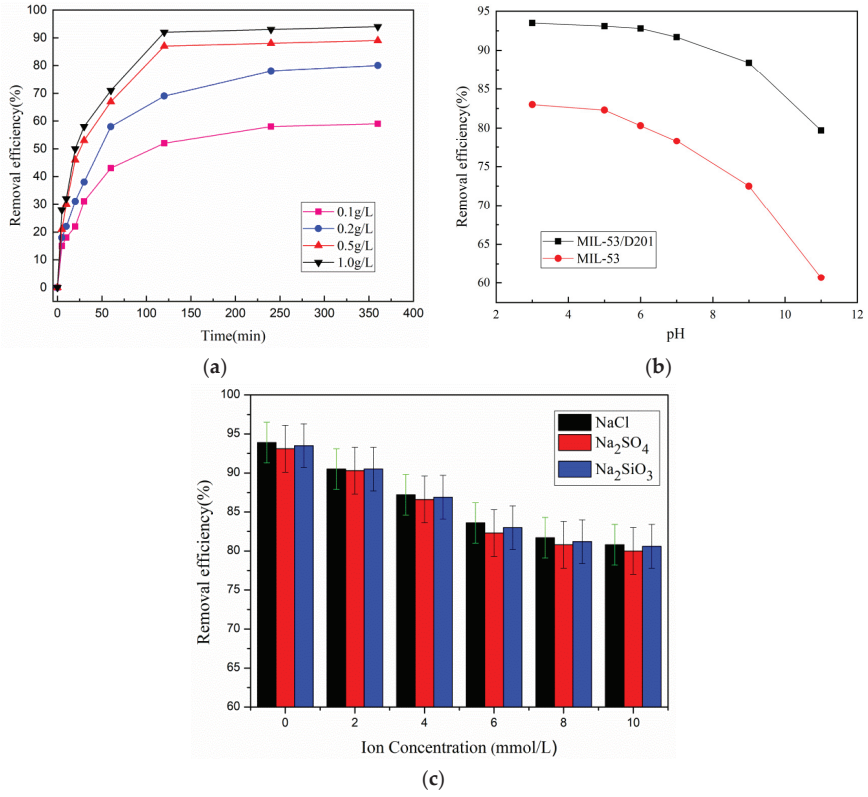

Figure 7. The effect of the addition amount of MIL-53/D201 (**a**), solution pH (**b**), and interfering ions (**c**) on the removal of azlocillin sodium.

3.4. *Effect of pH of the Solution*

The adsorption of the adsorbent in the pollutant solution depends largely on the pollutant solution's pH. In this experiment, the influence of the pH on the removal rate of MIL-53/D201 composite and MIL-53 was investigated. This influence determines the existence form of the target ion and the possible change in the surface charge of the adsorbent. As shown in Figure 7b, the adsorption of MIL-53/D201 composite and MIL-53 adsorbents on azlocillin sodium solution under different pH conditions was investigated. The results showed that the adsorption effects of the two adsorbents were significantly improved under weak acid conditions, and the maximum removal rates were 93.9% and

83.3%, respectively. For MIL-53, this is because a lower pH value facilitates the release of a higher concentration of H^+, and MIL-53 has a positive potential. Azlocillin sodium in aqueous solution is an anionic ligand with the ability to give a pair of electrons (Lewis base), and has a strong electrostatic interaction with the central Fe^{3+} (Lewis acid) in the MIL-53 framework. This explains the high adsorption capacity of MIL-53 for azlocillin sodium under acidic conditions. However, the π-π interaction between MIL-53 and the benzene ring of azlocillin sodium and the respiratory effect of MIL-53 may also be the existing mechanism [41]. For MIL-5/D201 composite, not only was the adsorption performance of MIL-53 improved, but its D201 macroporous resin was able to preconcentrate target anions through quaternary amine groups, so as to achieve more efficient adsorption. As a result of the increase in pH value, the adsorption capacity of MIL-53 decreased significantly, because the increasing OH^- in the solution can compete with the anions in azlocillin sodium, reducing the adsorption capacity of MIL-53. In addition, the number of negatively charged sites also increases. MOF materials are unstable in strong alkali conditions (especially in the case of terephthalic acid as the linker) and will gradually dissolve and reduce the adsorption performance.

It is worth noting that MIL-53/D201 composite also has a high adsorption capacity under alkaline conditions. This stability is attributed to the protection of crosslinked polystyrene matrix, so the adsorption capacity of MIL-53/D201 composite to azlocillin sodium is significantly higher than MIL-53 at the same pH value.

3.5. Effect of Interfering Ions in Solution

The adsorption process of adsorbents is affected by other ions in water. The results show that the adsorption properties of D201 resin are affected differently by different kinds and concentrations of anions. In general, a greater concentration of anions will affect the resin adsorption. This is because the anions occupy the active adsorption site on the resin, hindering the resin adsorption of the adsorbent; this phenomenon is competitive adsorption. Therefore, Cl^-, SO_4^{2-}, and SiO_3^{2-} were selected as interfering ions in this experiment to explore the adsorption effect of MIL-53/D201 composite on azlocillin sodium (Figure 7c). It can be seen from Figure 7c that the influence of these three interfering ions on the adsorption efficiency of MIL-53/D201 composite is $SO_4^{2-} > SiO_3^{2-} > Cl^-$. With the increase in the concentration of interfering ions, the removal efficiency of MIL-53/D201 composite adsorbent decreased successively. However, when the concentration of interfering ions increased to 8 mmol/L, the removal efficiency of MIL-53/D201 composite basically did not decrease any further, because the interfering ions engaged in competitive adsorption with anions in azlocillin sodium. The selective adsorption of target anions by D201 macroporous resin is hindered, and the greater the concentration of interfering ions is, the more obvious it is. Due to the presence of MIL-53 in the composite adsorbent, the adsorption of target anions can be continued through electrostatic interaction, which effectively indicates that when the concentration of interfering ions increases to a certain extent, the removal efficiency of MIL-53/D201 composite does not continue to decrease.

3.6. Adsorption Kinetics

In order to better study the adsorption process of MIL-53/D201 on azlocillin sodium, Lagergren's pseudo-first-order and pseudo-second-order dynamics were used for fitting analysis, and the simulation diagram of adsorption kinetics is shown in Figure 8a. The adsorption kinetic parameters (Table 2) were obtained from the pseudo-first-order model equation (Formula (4)) and the pseudo-second-order model equation (Formula (5)), where the first-order kinetic coefficient R^2 was 0.942.

$$\mathrm{Log}(q_e - q_t) = \mathrm{Log}q_e - \frac{k_1 t}{2.303}, \tag{4}$$

$$\frac{t}{q_t} = \frac{1}{k_2 q_e^2} + \frac{t}{q_e}, \tag{5}$$

where k_1 and k_2 represent the rate constant of the pseudo-first-order model ($L \cdot min^{-1}$) and pseudo-second-order model ($g \cdot mg^{-1} \cdot min^{-1}$) respectively. q_e and q_t are the adsorption capacity at equilibrium ($mg \cdot g^{-1}$) and adsorption capacity at t ($mg \cdot g^{-1}$), respectively. It can be seen from the comparison that the equilibrium adsorption amount obtained in the actual experiment is quite different from the equilibrium adsorption amount obtained by the fitting results. Therefore, the adsorption process of MIL-53/D201 composite is not suitable to be described by pseudo-first-order kinetics; that is, the adsorption of MIL-53/D201 composite is not simple physical adsorption of azlocillin sodium. It can be seen from Table 2 that the R^2 correlation coefficient of the quasi-second-order kinetic equation is 0.957, and the equilibrium adsorption amount obtained in the actual experiment is closer to that obtained through fitting results, indicating that the adsorption process is more consistent with the quasi-second-order kinetic adsorption model. This indicates that the chemisorption of MIL-53/D201 composite to azlocillin sodium is dominant. The fitting results show that the whole adsorption process of MIL-53/D201 composite followed the quasi-second-order kinetic model; that is, chemical adsorption was the main process.

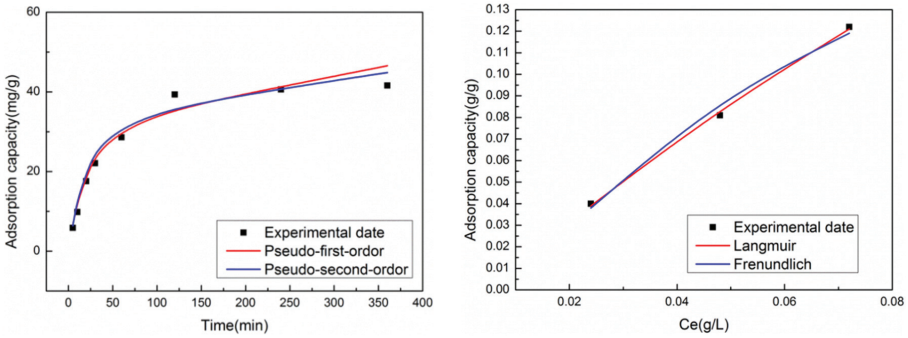

(**a**) (**b**)

Figure 8. Kinetic fitting diagram (**a**) and thermodynamic fitting diagram (**b**) of adsorption of azlocillin sodium by MIL-53/D201 composite.

Table 2. Kinetic fitting parameters and thermodynamic fitting parameters of azlocillin sodium adsorption by MIL-53/D201 composite.

	R^2	K
Pseudo-first-order	0.942	0.254
Pseudo-second-order	0.957	0.084
Langmuir	0.993	2.056
Freundlich	0.987	0.182

3.7. Thermodynamics of Adsorption

The Langmuir isothermal adsorption model (Formula (6)) and Freundlich isothermal adsorption model (Formula (7)) were used to combine the adsorption data of MIL-53/D201 composite for azlocillin sodium solution. The thermodynamic fitting diagram is shown in Figure 8b, and the fitting parameters are shown in Table 2. The Langmuir thermodynamic fitting parameter R^2 was 0.993, which was larger than the Freundlich thermodynamic fitting parameter R^2, indicating that the adsorption process of MIL-53/D201 composite material for sodium azlocillin followed the Langmuir adsorption isothermal model; that is, monolayer adsorption was predominant. The maximum saturated adsorption capacity was 122.3 mg/g. The linearized Langmuir model is expressed by the following equation:

$$\frac{C_e}{q_e} = \frac{1}{q_m K_1} + \frac{C_e}{q_m}, \quad (6)$$

where C_e is the equilibrium concentration (mg/L). q_e and q_m represent the adsorption capacity (mg/g) and maximum adsorption capacity (mg/g) at equilibrium, respectively. K_1 is the Langmuir adsorption constant (L/mg). The parameters q_m, K_1, and correlation coefficient R^2 are determined by the linear regression between C_e/q_e and C_e. The Freundlich model can also be applied to non-ideal systems, including multilayer adsorption on heterogeneous media surfaces, expressed by the following equation:

$$q_e = K_F C_e^{\frac{1}{n}}, \quad (7)$$

where C_e and q_e represent equilibrium concentration (mg/L) and adsorption capacity (mg/g), respectively. K_F and n represent the Freundlich constant. The parameters K_F, 1/n, and correlation coefficient R^2 are determined by the linear regression relationship between q_e and log C_e [42]. An n value between 1 and 10 indicates that adsorption is favorable. A low n value indicates that there are bad adsorption conditions and competitive adsorption may exist.

3.8. Adsorption Regeneration

In practical applications, the reusability of adsorbents is a very important parameter in terms of cost effectiveness. Compared with powdered MOF, MOF/D201 composite adsorbent not only has higher adsorption performance, but also can achieve adsorption regeneration through simple ethanol immersion. The used ethanol can still be used for the next cycle, effectively avoiding waste. In this study, ethanol was used as a desorption agent for MIL-53/D201 composite after adsorption. After five sorption-desorption cycles, the results obtained are shown in Figure 9a. After four cycles, the removal efficiency tended to be stable, and was still about 83%. These results indicate that MIL-53/D201 adsorbent has good reusability and can be used in water treatment for a long period.

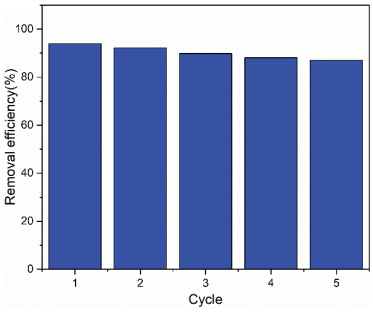

(**a**)

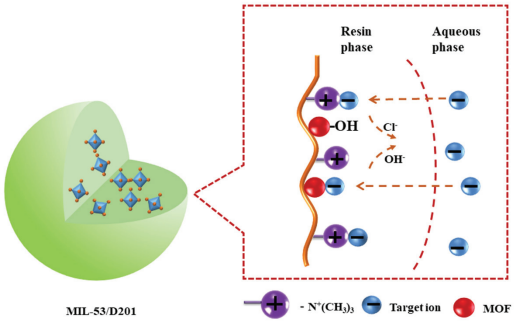

(**b**)

Figure 9. Adsorption regeneration diagram (**a**) and adsorption mechanism diagram (**b**) of removing azlocillin sodium by MIL-53/D201.

4. Conclusions

In this paper, MIL-53 was in situ synthesized in D201 anion exchange resin by the hydrothermal synthesis method. A new MIL-53/D201 composite was prepared and the adsorption effect of the composite on azlocillin sodium in solution was studied. The structural characteristics, functional groups, and thermal analysis of MIL-53 and MIL-53/D201 composite were studied by XRD, SEM, EDS, and BET. The results showed that D201 as the carrier not only did not destroy the original structure of MOF material, but also caused the composite material to have a larger specific surface area and more stable and efficient adsorption performance.

Through the adsorption exploration experiment, it was found that the composite material can overcome the disadvantages of MOF material instability in the water phase and easy dissociation in strongly alkaline conditions. The composite was also shown to have the characteristics of stable and efficient adsorption. The adsorption mechanism can be explained by electrostatic interaction between -NR_3^+ in D201 resin and anions in pollutants, the π-π interaction between the MIL-53 aromatic ring and azlocillin sodium, and the coordination of MIL-53 and hydrogen bonding (Figure 9). The adsorption process was more consistent with the quasi-second-order kinetic adsorption model and Langmuir isothermal adsorption model; that is, chemical adsorption and monolayer adsorption were the main adsorption processes, and the maximum saturated adsorption capacity was 122.3 mg/g. In conclusion, this study provides an idea for the fixation of MOF materials in stable carriers, and this novel composite adsorbent material can be used as a potential material for the degradation of target anionic pollutants in water.

Author Contributions: Conceptualization, Y.Q. and L.L.; Data curation, H.F.; Formal analysis, H.F.; Funding acquisition, Y.Q.; Investigation, L.L.; Methodology, H.F.; Resources, Y.Q.; Software, H.F., W.S. and J.L.; Validation, Y.Z.; Visualization, W.S., J.L. and Y.Z.; Writing—original draft, H.F.; Writing—review & editing, H.F. All authors have read and agreed to the published version of the manuscript.

Funding: This work was financially supported by the Shandong Provincial Natural Science Foundation, China (No. ZR2021ME170 and ZR2021MB028) and the Foundation of State Key Laboratory of High-efficiency Utilization of Coal and Green Chemical Engineering (2022-K26).

Institutional Review Board Statement: Not applicable.

Informed Consent Statement: Not applicable.

Data Availability Statement: Not applicable.

Acknowledgments: This work was supported by the This work was supported by the Shandong Provincial Natural Science Foundation, China and the Foundation of State Key Laboratory of High-efficiency Utilization of Coal and Green Chemical Engineering.

Conflicts of Interest: The authors declare no conflict of interest.

References

1. Xie, H.; Du, J.; Chen, J. Concerted Efforts Are Needed to Control and Mitigate Antibiotic Pollution in Coastal Waters of China. *Antibiotics* **2020**, *9*, 88. [CrossRef]
2. Li, J.; Wang, X.; Zhao, G.; Chen, C.; Chai, Z.; Alsaedi, A.; Hayat, T.; Wang, X. Metal-organic framework-based materials: Superior adsorbents for the capture of toxic and radioactive metal ions. *Chem. Soc. Rev.* **2018**, *47*, 2322–2356. [CrossRef] [PubMed]
3. Bobbitt, N.S.; Mendonca, M.L.; Howarth, A.J.; Islamoglu, T.; Hupp, J.T.; Farha, O.K.; Snurr, R.Q. Metal-organic frameworks for the removal of toxic industrial chemicals and chemical warfare agents. *Chem. Soc. Rev.* **2017**, *46*, 3357–3385. [CrossRef] [PubMed]
4. Mon, M.; Bruno, R.; Ferrando-Soria, J.; Armentano, D.; Pardo, E. Metal-organic framework technologies for water remediation: Towards a sustainable ecosystem. *J. Mater. Chem. A* **2018**, *6*, 4912–4947. [CrossRef]
5. Hasan, Z.; Jhung, S.H. Removal of hazardous organics from water using metal-organic frameworks (MOFs): Plausible mechanisms for selective adsorptions. *J. Hazard. Mater.* **2015**, *283*, 329–339. [CrossRef] [PubMed]
6. Martínez, J.L. Antibiotics and antibiotic resistance genes in natural environments. *Science* **2008**, *321*, 365–367. [CrossRef] [PubMed]
7. Gaikwad, S.; Cheedarala, R.K.; Gaikwad, R.; Kim, S.; Han, S. Controllable Synthesis of 1,3,5-tris (1H-benzo [d] imidazole-2-yl) Benzene-Based MOFs. *J. Appl. Sci.* **2021**, *11*, 9856. [CrossRef]

8. Howarth, A.J.; Liu, Y.; Hupp, J.T.; Farha, O.K. Metal-organic frameworks for applications in remediation of oxyanion/cation-contaminated water. *CrystEngComm* **2015**, *17*, 7245–7253. [CrossRef]
9. Zou, Y.; Wang, X.; Khan, A.; Wang, P.; Liu, Y.; Alsaedi, A.; Hayat, T.; Wang, X. Environmental remediation and application of nanoscale zero-valent iron and its composites for the removal of heavy metal ions: A review. *Environ. Sci. Technol.* **2016**, *50*, 7290–7304. [CrossRef]
10. Wu, X.; Tan, X.; Yang, S.; Wang, P.; Liu, Y.; Alsaedi, A.; Hayat, T.; Wang, X. Coexistence of adsorption and coagulation processes of both arsenate and NOM from contaminated groundwater by nanocrystallined Mg/Al layered double hydroxides. *Water Res.* **2013**, *47*, 4159–4168. [CrossRef] [PubMed]
11. Hadi, P.; To, M.H.; Hui, C.W.; Lin, C.S.K.; McKay, G. Aqueous mercury adsorption by activated carbons. *Water Res.* **2015**, *73*, 37–55. [CrossRef]
12. Hoskins, B.F.; Robson, R. Infinite polymeric frameworks consisting of three dimensionally linked rod-like segments. *J. Am. Chem. Soc.* **1989**, *111*, 5962–5964. [CrossRef]
13. Colinas, I.R.; Silva, R.C.; Oliver, S.R.J. Reversible, selective trapping of perchlorate from water in record capacity by a cationic metal-organic framework. *Environ. Sci. Technol.* **2016**, *50*, 1949–1954. [CrossRef]
14. Zhu, L.; Xiao, C.; Dai, X.; Li, J.; Gui, D.; Sheng, D.; Chen, L.; Zhou, R.; Chai, Z.; Albrecht-Schmitt, T.E.; et al. Exceptional perrhenate/pertechnetate uptake and subsequent immobilization by a low-dimensional cationic coordination polymer: Overcoming the hofmeister bias selectivity. *Environ. Sci. Technol. Lett.* **2017**, *4*, 316–322. [CrossRef]
15. Bhadra, B.N.; Seo, P.W.; Khan, N.A.; Jhung, S.H. Hydrophobic cobalt-ethylimidazolate frameworks: Phase-pure syntheses and possible application in cleaning of contaminated water. *Inorg. Chem.* **2016**, *55*, 11362–11371. [CrossRef] [PubMed]
16. Farha, O.K.; Eryazici, I.; Jeong, N.C.; Hauser, B.G.; Wilmer, C.E.; Sarjeant, A.A.; Snurr, R.Q.; Nguyen, S.T.; Yazaydin, A.O.; Hupp, J.T. Metal-organic framework materials with ultrahigh surface areas: Is the sky the limit? *J. Am. Chem. Soc.* **2012**, *134*, 15016–15021. [CrossRef]
17. Alaerts, L.; Maes, M.; Giebeler, L.; Jacobs, P.A.; Martens, J.A.; Denayer, J.F.; Kirschhock, C.E.; De Vos, D.E. Selective Adsorption and Separation of Ortho-Substituted Alkylaromatics with the Microporous Aluminum Terephthalate MIL-53. *J. Am. Chem. Soc.* **2008**, *130*, 14170–14178. [CrossRef] [PubMed]
18. Gwon, K.; Han, I.; Lee, S.; Kim, Y.; Lee, D.N. Novel metal–organic framework-based photocrosslinked hydrogel system for efficient antibacterial applications. *ACS Appl. Mater. Interfaces* **2020**, *12*, 20234–20242. [CrossRef]
19. Gwon, K.; Kim, Y.; Cho, H.; Lee, S.; Yang, S.H.; Kim, S.J.; Lee, D.N. Robust Copper Metal–Organic Framework-Embedded Polysiloxanes for Biomedical Applications: Its Antibacterial Effects on MRSA and In Vitro Cytotoxicity. *Nanomaterials* **2021**, *11*, 719. [CrossRef] [PubMed]
20. Ma, X.; Wang, W.; Sun, C.; Li, H.; Sun, J.; Liu, X. Adsorption performance and kinetic study of hierarchical porous Fe-based MOFs for toluene removal. *Sci. Total Environ.* **2021**, *793*, 148622. [CrossRef] [PubMed]
21. Shen, K.; Zhang, L.; Chen, X.; Liu, L.; Zhang, D.; Han, Y.; Chen, J.; Long, J.; Luque, R.; Li, Y.; et al. Ordered macro-microporous metal-organic framework single crystals. *Science* **2018**, *359*, 206–210. [CrossRef]
22. Ou, R.; Zhang, H.; Wei, J.; Kim, S.; Wan, L.; Nguyen, N.S.; Hu, Y.; Zhang, X.; Simon, G.P.; Wang, H. Thermoresponsive amphoteric metal-organic frameworks for efficient and reversible adsorption of multiple salts from water. *Adv. Mater.* **2018**, *30*, 1802767. [CrossRef] [PubMed]
23. Valizadeh, B.; Nguyen, T.N.; Smit, B.; Stylianou, K.C. Porous Metal-Organic Framework@ Polymer Beads for Iodine Capture and Recovery Using a Gas-Sparged Column. *Adv. Funct. Mater.* **2018**, *28*, 1801596. [CrossRef]
24. McHugh, L.N.; McPherson, M.J.; McCormick, L.J.; Morris, S.A.; Wheatley, P.S.; Teat, S.J.; McKay, D.; Dawson, D.M.; Sansome, C.E.F.; Ashbrook, S.E.; et al. Hydrolytic stability in hemilabile metal-organic frameworks. *Nat. Chem.* **2018**, *10*, 1096–1102. [CrossRef]
25. Hynek, J.; Brázda, P.; Rohlíček, J.; Londesborough, M.G.; Demel, J. Phosphinic acid based linkers: Building blocks in metal-organic framework chemistry. *Angew. Chem. Int. Ed.* **2018**, *57*, 5016–5019. [CrossRef]
26. Yuan, S.; Feng, L.; Wang, K.; Pang, J.; Bosch, M.; Lollar, C.; Sun, Y.; Qin, J.; Yang, X.; Zhang, P.; et al. Stable metal-organic frameworks: Design, synthesis, and applications. *Adv. Mater.* **2018**, *30*, 1704303. [CrossRef]
27. Liang, R.; Jing, F.; Shen, L.; Qin, N.; Wu, L. MIL-53(Fe) as a highly efficient bifunctional photocatalyst for the simultaneous reduction of Cr(VI) and oxidation of dyes. *J. Hazard. Mater.* **2015**, *287*, 364–372. [CrossRef]
28. Du, J.; Yuan, Y.; Su, J.; Peng, F.; Jiang, X.; Qiu, L.; Xie, A.; Shen, Y.; Zhu, J. New photocatalysts based on MIL-53 metal-organic frameworks for the decolorization of methylene blue dye. *J. Hazard. Mater.* **2011**, *190*, 945–951. [CrossRef] [PubMed]
29. Zhu, B.J.; Yu, X.Y.; Jia, Y.; Peng, F.M.; Sun, B.; Zhang, M.Y.; Lou, T.; Liu, J.H.; Huang, X.J. Iron and 1, 3, 5-benzenetricarboxylic metal-organic coordination polymers prepared by solvothermal method and their application in efficient As (V) removal from aqueous solutions. *J. Phys. Chem. C* **2012**, *116*, 8601–8607. [CrossRef]
30. Molinari, A.; Varani, G.; Polo, E.; Vaccari, S.; Maldotti, A. Photocatalytic and catalytic activity of heterogenized W10O324—In the bromide-assisted bromination of arenes and alkenes in the presence of oxygen. *Mol. Catal. A Chem.* **2007**, *262*, 156–163. [CrossRef]
31. Zhang, X.; Cheng, C.; Qian, J.; Lu, Z.; Pan, S.; Pan, B. Highly efficient water decontamination by using sub-10 nm FeOOH confined within millimeter-sized mesoporous polystyrene beads. *Environ. Sci. Technol.* **2017**, *51*, 9210–9218. [CrossRef]
32. Zhang, X.; Wu, M.; Dong, H.; Li, H.; Pan, B. Simultaneous oxidation and sequestration of As (III) from water by using redox polymer-based Fe (III) oxide nanocomposite. *Environ. Sci. Technol.* **2017**, *51*, 6326–6334. [CrossRef] [PubMed]

33. Liu, F.; Shan, C.; Zhang, X.; Zhang, Y.; Zhang, W.; Pan, B. Enhanced removal of EDTA-chelated Cu (II) by polymeric anion-exchanger supported nanoscale zero-valent iron. *J. Hazard. Mater.* **2017**, *321*, 290–298. [CrossRef]
34. Araya, T.; Jia, M.; Yang, J.; Zhao, P.; Cai, K.; Ma, W.; Huang, Y. Resin modified MIL-53 (Fe) MOF for improvement of photocatalytic performance. *J. Appl. Catal. B Environ.* **2017**, *203*, 768–777. [CrossRef]
35. Ai, L.; Zhang, C.; Li, L.; Jiang, J. Iron terephthalate metal-organic framework: Revealing the effective activation of hydrogen peroxide for the degradation of organic dye under visible light irradiation. *Appl. Catal. B Environ.* **2014**, *148*, 191–200. [CrossRef]
36. Gao, Y.; Li, S.; Li, Y.; Yao, L.; Zhang, H. Accelerated photocatalytic degradation of organic pollutant over metal-organic framework MIL-53 (Fe) under visible LED light mediated by persulfate. *Appl. Catal. B Environ.* **2017**, *202*, 165–174. [CrossRef]
37. Huang, W.; Liu, N.; Zhang, X.; Wu, M.; Tang, L. Metal organic framework g-C_3N_4/MIL-53 (Fe) heterojunctions with enhanced photocatalytic activity for Cr (VI) reduction under visible light. *Appl. Surf. Sci.* **2017**, *425*, 107–116. [CrossRef]
38. Zhang, N.; Yuan, L.Y.; Guo, W.L.; Luo, S.Z.; Chai, Z.F.; Shi, W.Q. Extending the use of highly porous and functionalized MOFs to Th (IV) capture. *ACS Appl. Mater. Interfaces* **2017**, *9*, 25216–25224. [CrossRef]
39. Yao, M.; Dong, Y.; Feng, X.; Hu, X.; Jia, A.; Xie, G.; Hu, G.; Lu, J.; Luo, M.; Fan, M. The effect of post-processing conditions on aminosilane functionalizaiton of mesocellular silica foam for post-combustion CO_2 capture. *Fuel* **2014**, *123*, 66–72. [CrossRef]
40. Wan, D.; Ma, X.; Sentorun-Shalaby, C.; Song, C. Development of carbon-based "molecular basket" sorbent for CO_2 capture. *Ind. Eng. Chem. Res.* **2012**, *51*, 3048–3057.
41. Haque, E.; Jun, J.W.; Jhung, S.H. Adsorptive removal of methyl orange and methylene blue from aqueous solution with a metal-organic framework material, iron terephthalate (MOF-235). *J. Hazard. Mater.* **2011**, *185*, 507–551. [CrossRef]
42. Bandura, L.; Kołodyńska, D.; Franus, W. Adsorption of BTX from aqueous solutions by Na-P1 zeolite obtained from fly ash. *Process Saf. Environ. Prot.* **2017**, *109*, 214–223. [CrossRef]

materials

MDPI

Article

Analysis of Exhaust Gas Content for Selected Biofuel-Powered Combustion Engines with Simultaneous Modification of Their Controllers

Marietta Markiewicz [1,*], Michał Pająk [2] and Łukasz Muślewski [1]

[1] Faculty of Mechanical Engineering, Bydgoszcz University of Science and Technology, Alley of Professor S. Kaliskiego 7, 85-796 Bydgoszcz, Poland; lukasz.muslewski@utp.edu.pl
[2] Faculty of Mechanical Engineering, University of Technology and Humanities in Radom, Stasieckiego 54, 26-600 Radom, Poland; m.pajak@uthrad.pl
* Correspondence: marmar000@utp.edu.pl

Abstract: The use of renewable resources for powering self-ignition engines in European Union countries involves a high demand for renewable energy which is not accompanied by the development of its production infrastructure. The application of biofuel in vehicle powering is supposed to provide reductions in greenhouse gas emissions and an increase in the share of renewable energy resources in the total energy consumption. The study includes the analyses of power unit exhaust components, such as oxygen, carbon monoxide, nitric oxides, carbonizers, carbon dioxide and a quantity of exhaust particles contained in exhaust gases. Tests using an exhaust gas analyzer and a vapor analyzer were conducted. Three high-pressure engines, characterized by direct fuel injection, were tested. The vehicle computer software adjustments included increasing the fuel dose and the air load. Mixtures of diesel oil and fatty acid methyl esters were used in the tests. Based on the results, a statistical analysis was performed and an assessment model was developed to understand the functioning of the research objects fueled with these mixtures, with simultaneous software changes in the vehicle computers. On the basis of the conducted analysis, it was found that only 30% of fatty acid methyl ester additives to diesel oil reduced the performance parameters of the drive units.

Keywords: combustion engine; biofuel; renewable energy sources; components of combustion engine exhaust gases; controllers of a vehicle computer

Citation: Markiewicz, M.; Pająk, M.; Muślewski, Ł. Analysis of Exhaust Gas Content for Selected Biofuel-Powered Combustion Engines with Simultaneous Modification of Their Controllers. *Materials* **2021**, *14*, 7621. https://doi.org/10.3390/ma14247621

Academic Editors: Avelino Núñez-Delgado, Zhien Zhang, Elza Bontempi, Mario Coccia, Marco Race and Yaoyu Zhou

Received: 26 October 2021
Accepted: 7 December 2021
Published: 10 December 2021

1. Introduction

Nowadays, the protection of the planet environment and its natural resources is an important issue. The addition of biocomponents to diesel oil recommended by the European Union makes it possible to decrease the use of fossil fuels. Structural solutions of the combustion engine structure make it possible for engines to be modernized and adjusted for the application of plant oils. There are a few arguments in favor of biofuels. The first argument is related to the exhaustibility of petroleum-derived fuels; the second consists in relieving the market of petroleum-derived product delivery; and the third one regards the intensification of rural areas. Although the prognoses regarding the exhaustion of fossil fuels are more optimistic than before, there are still many social, economic and political factors that indicate the need to carry out tests on the suitability of plant oils to be used for combustion engine powering. Another argument in favor of using plant oils as engine fuel is CO_2 emission reduction. The emission of toxic substances from transport is a significant problem, especially because, in the European Union countries, it was reported to be 0.4 g/km in 2019.

The basic fuel used in self-ignition engines is diesel oil. Due to the rising prices of petroleum-derived fuels and the exhaustion of natural resources, the idea of renewable fuels has been revived. Renewable fuels (of natural origin) include rape oil, sunflower oil,

soya oil, peanut oil and animal fats [1]. Plant fuels (biofuels) need to undergo chemical processing to achieve physical–chemical properties similar to those of diesel oil. Due to technical, structural and economic factors, it is rape oil that finds the widest application [2,3]. Biogas from fruit, vegetables and meat production waste can also be used for powering self-ignition engines [4–6]. Alternative fuels that are produced from unfit-for-use food products are referred to as second-generation fuels. Another source of biofuel are microalgae (third-generation fuels), whose cultivation involves only CO_2 and solar energy [4,7,8]. Numerous scientific and industrial centers deal with testing fatty acid methyl ester additives to diesel oil. The test results indicate that their physical–chemical properties are the most similar to those of a diesel oil.

The literature provides the results of tests on engine operation efficiency, fuel consumption and the amounts of substances in exhaust gases, including solid particles. Measurements of the operation efficiency of engines powered with first-generation biofuel have already been performed by many scientific units. The results confirm changes in the power-unit performance parameters, including fuel density, increase in fuel flow resistance and reduction in engine power [9–11]. The results of the tests indicate an increase in fuel consumption when using mixtures of diesel oil and biocomponents for powering engines [12–15]. The quantities which describe a combustion engine performance (performance parameters) are indicators of its operation and their analysis provides information on its characteristics. The criteria for the assessment of self-ignition engines powered with mixtures of diesel oil and biocomponents are based on the information available in the literature [16–21]. Figure 1 shows their graphical interpretation.

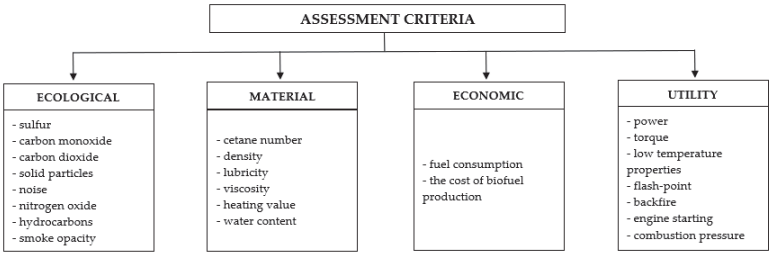

Figure 1. Criteria for assessment of transport means drive unit [16].

The most frequently used indicators of a self-ignition engine operation assessment are power output, torque, fuel consumption, composition of exhaust gases and exhaust smoke. According to scientific publications, the use of biofuels for engine powering contributes to a decrease in the emission of carbon monoxides, hydrocarbons and solid particles [22–28] and an increase in nitric oxides by several percent, as compared to diesel oil [13]. These quantities are largely affected by the fuel physical–chemical properties, which are presented in Table 1. This study presents a comparison of the results for diesel oil, biodiesel and vegetable oil that had not been chemically treated for use as diesel fuel. However, the presented biodiesel comprised fatty acid methyl esters or vegetable oil that had been transesterified.

Table 1. Comparison of fuel physical chemical properties.

Property	Diesel Oil	Biodiesel	Plant Oil
Viscosity ($mm^2 \times s^{-1}$)	2.0–4.5	3.5–5.5	7.2
Sulfur content ($mg \times kg^{-1}$)	$\leq$35	$\leq$10	no
Density ($g \times cm^{-3}$)	0.82–0.45	0.86–0.90	0.88
Cetane number	$\geq$51	$\geq$47	>40
Calorific value (MJ/kg)	43	41	37.6
Ignition point (°C)	$\geq$55	$\geq$101	$\geq$220

The study presents the results of fuel component tests and content of solid particles in exhaust gases of combustion engines powered with mixtures of diesel oil and fatty acid methyl esters. Moreover, the computer software of the analyzed power units was modified by changing the fuel dose and air load. The purpose of the tests was to check how the fuel mixture and reprogramming of the computer controllers affected the analyzed fuel component amounts. The study is also an attempt to demonstrate the content of fatty acid methyl esters added to diesel fuel from the point of view of the power-unit performance parameters.

2. Materials and Methods

The tested objects were three self-ignition engines with identical technical parameters. The engines are widely used in car transport. They are mounted in passenger and delivery cars of different makes. The engines used for the tests were popular models that are found in vehicles. Three identical power units were used to provide reliable results. The tests covered engines with power output 81 kW, characterized by indirect fuel injection and a common rail fuel injection system. The tested engines were mounted in vehicles, thanks to which it was possible to simulate road conditions. An image of one of the analyzed engines, which was installed in a vehicle, is presented in Figure 2, whereas technical specifications of particular engines are presented in Table 2.

Figure 2. Combustion engine used in tests.

Table 2. Technical specifications of combustion engines used in the tests.

Type of Engine	With Self-Ignition
Kind of fuel	Diesel oil
Power output of engine	81 kW
Engine cubic capacity	1560 cm^3
Maximal torque	240 Nm
Number of cylinders	4
Diameter of cylinder	73 mm
Piston stroke	88.3 mm
Number of valves	16
Particulate filter	none
Compression ratio	16.0:1

The research objects were modified by adjusting the fuel supply system which enabled noninvasive exchange of the fuel mixture. These changes covered the fuel supply system and involved the installation of an additional fuel tank. The modifications had no direct effect on the engine structure. The changes involved the installation of an external fuel tank while disconnecting the liquid flow from the vehicle internal tank. No additional filters or fuel pumps were fixed. The fuel supply system was connected from an additional tank directly to the engine. Standard filters suitable for a given engine model were added. The excess of fuel returned to the external tank through a return fuel tank. Each time after a mixture was exchanged, the engines worked for 10 min with the gears in neutral in order to remove the remains of the previous fuel from the fuel filter and the fuel supply system.

The research material was a 'virgin' diesel oil (ON) and fatty acid methyl esters of rape oil (RME). Diesel oil without a biocomponent additive was the virgin diesel oil used in the tests. The composition of the analyzed mixtures and their markings are presented in Table 3. Fatty acid methyl esters are plant oils that have been subjected to catalytic esterification. Such substances are commonly referred to as biocomponents. The fatty acid methyl esters of rape oil used in the tests were provided by domestic producers and the plants for their production were obtained from regional suppliers.

Table 3. Composition of fuel mixtures.

Composition of Fuel Mixture	Symbol of Mixture
"virgin" diesel oil	ON
90% diesel oil, 10% fatty acid methyl esters	BIO10
70% diesel oil, 30% fatty acid methyl esters	BIO30
50% diesel oil, 50% fatty acid methyl esters	BIO50

Based on the analysis of the literature and the authors' own tests for various proportions of the tested mixtures, it was decided to use the mixtures with the composition presented in Table 4. First, selected properties of the tested mixtures were determined, such as viscosity, calorific value, heat of combustion and cetane number. The obtained results are presented in Table 4. The table shows the mean values for 30 measurements.

Table 4. Properties of the tested mixtures.

Properties	ON	BIO10	BIO30	BIO50
Viscosity	6.46	6.26	7.8	8.56
Calorific value (J/g)	43,097.33	43,199.33	41,959.00	40,590.00
Heat of combustion (J/g)	44,277.33	44,379.00	43,139.00	41,770.00
Cetane number (mPa × s)	53.33	54.94	55.92	58.40

The engines were also modified by adjusting the electronic system through modification of computer software. The introduction of computer software changes was performed to find out whether and how the number of exhaust components and the number of solid particles emitted to the environment changed. Due to the specificity of the electronic system, the software changes required dismantling the deck computer and mounting it on the modification stand, as shown in Figure 3.

Software modifications were introduced according to an earlier prepared schedule. They involved increasing the dose of fuel and the air load. The tests were performed for four fuel injection controller settings, which are presented in Table 5.

Figure 3. Stand for modification of vehicle computer software.

Table 5. Composition of fuel mixtures.

Modifications of Computer Software	Marking of Setting
Factory settings	I
Fuel dose increased by 2% and air load increased by 50 hPa	II
Fuel dose increased by 4% and air load increased by 50 hPa	III
Fuel dose increased by 6% and air load increased by 50 hPa	IV

Each fuel injection setting required the generation of a new fuel injection characteristic. Four characteristics were created for each fuel dose and fuel injection pressure. One of the characteristics is presented in Figure 4.

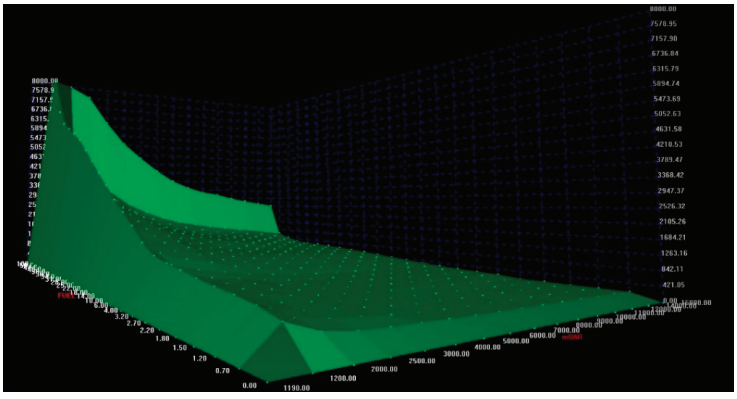

Figure 4. Stand for modification of vehicle computer software.

The experiment involved measuring the pressure of the exhaust gas component concentration and the number of solid particles. The measurement of the exhaust gas concentration was performed by means of an MGT-5 exhaust gas analyzer. The analysis of the exhaust gases enabled determination of the amounts of exhaust substances which were discharged into the environment in the form of exhaust gases. The described device was used for the measurement of the toxicity degree of a self-injection engine exhaust and was designed for the determination of the values of compounds such as hydrocarbons (HC), carbon dioxide (CO_2), nitric oxides (NO_2) and carbon oxide (CO). The analyzer can also be used for determination of exhaust gas components which are not environmentally harmful including oxygen (O_2), and a coefficient of air excess ƛ. The measurement of solid particles with dimensions exceeding 100 mm was performed by means of an MPM-4 analyzer. An optical method involving measuring the intensity of a light beam passing

through the stream of exhaust gases was used for the measurement of the mass of solid particles contained in the exhaust gases.

The tests were conducted with the use of a load-bearing chassis dynamometer with an eddy current brake which allowed us to simulate road conditions and apply proper loads to the vehicles.

3. Analysis of Test Results

3.1. Statistical Analyses of the Test Results

A linear multi-factor regression equation was developed to assess the dependence of the power unit performance parameter values Y for fuel mixtures, dependent on the fuel injection modification X. Six performance parameters (fuel components and solid particles) were tested for the four settings of combustion engine computer software and four fuel mixtures. The test results were averaged for the three analyzed power units. Since numerous calculations had to be performed, the study includes an exemplary regression equation for the 'solid particles' parameter based on the vehicle computer software settings. The graphic interpretation of the obtained results is shown in Figure 5 as follows: a chart shows the empirical points, while a graphical chart is depicted as a determinant of theoretical parameters.

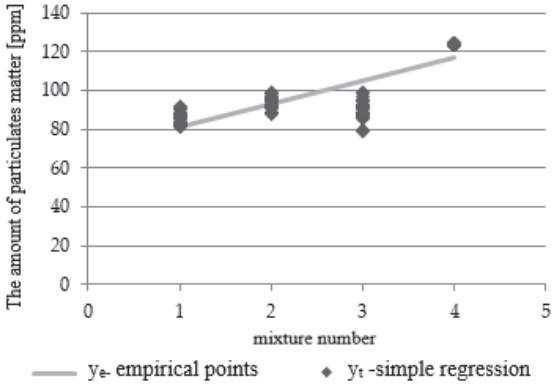

Figure 5. Diagram of linear regression for the analyzed parameter.

The values of the estimators were determined by means of the method of the smallest squares. The differences between the measurement values, their mean values and the values of the defined functions were also calculated. Based on this, a straight of regression was estimated, which, for setting III, takes the following form:

$$y = 0.1431x + 88.015 \quad (1)$$

The correlation coefficient for an increased regression equation was r = 0.5151. Testing the H_0: a = 0 hypothesis yielded $p < 0.0001$, which means that the analyzed dependence was statistically significant.

The distribution of the obtained results was verified prior to the analysis of linear regression performed by means of X^2 Pearson and λ Kołmogorov consistency tests. The distribution was found to be normal. A variance analysis was also performed. The test involved comparing the mean values for the four mixtures of diesel oil and fatty acid methyl esters. Four tests were conducted for each engine software setting (I, II, III and IV) to investigate relevant parameters of the analyzed power units. Equal mean values of all the mixtures were accepted to be the zero hypothesis.

3.2. Figures, Tables and Schemes

This study takes into consideration ecological parameters, evaluated in terms of environmental impact. These parameters were chosen due to their environmental impact and functioning of combustion engines, which are powered with mixtures of diesel oil and fatty acid methyl esters. The physical–chemical properties of these mixtures, such as calorific value, viscosity and cetane number, were also tested.

The aim of the tests was to compare power units powered with different mixtures of virgin diesel oil and fatty acid methyl esters. The assessment of the power units was performed on the basis of their significant characteristics [29]. The assessment covered the distinguished ecological parameters and those described earlier. It was a normalized comparative assessment which referred to the accepted point of reference. In the analyzed case, the values of the characteristics describing the analyzed parameters could be lower or higher than the values of characteristics that represented the point of reference.

In the presented model, variable X means unidimensional vector (tested parameters of power units), which was accepted to be a random variable. Vectors ($X_1 \div X_7$) represent an assessment of power units powered with different fuel mixtures. The considered vector takes the following form:

$$X_i = <X_1, X_2, X_3, X_4, X_5, X_6, X_7> \quad (2)$$

where the vector components include the following:

X_1—particulates contained in exhaust gases;
X_2—carbon monoxide;
X_3—carbon dioxide;
X_4—hydrocarbons;
X_5—oxygen;
X_6—nitric oxides;
X_7—air excess coefficient.

The assessment process was performed with the use of a multi criteria optimization analysis (MOA) [30]. The multi criteria optimization analysis enabled us to compare the same parameters of power units powered with different fuel mixtures. Although the characteristics of the analyzed mixtures are hardly comparable, they had a significant impact on the research object's functioning and the natural environment. The analysis included different variants of the environmental criterion. The variants evaluated within a given criterion were arranged in a specified order. The quality of particular variants was also defined by assigning appropriate results to them. The application of this method enabled the determination of a qualitative criterion, a system of weights for particular variants and the performance of the whole assessment for the environmental criterion, as well as its interpretation. The method of analytical hierarchy process (AHP) was used during the MOA analysis for the determination of the weights for each variant [31,32].

A random variable was defined for the research object as follows:

$$Z_x = \alpha_1 X_1 + \alpha_2 X_2 + \alpha_3 X_3 + \alpha_4 X_4 + \alpha_5 X_5 + \alpha_6 X_6 + \alpha_7 X_7 \quad (3)$$

where α refers to the values of the weights for particular parameters.

The developed assessment system includes seven criteria defined on the basis of the power-unit parameters. The mean value of 30 measurements was the assessed value. The criteria argument scopes were limited by the highest and the lowest values provided by the tests. All the criteria were accepted in the form of MINSIMP, which means that the lowest values, consistent with the lowest emission of a given substance, were found to be the most optimal. The weights of particular criteria were defined during the tests and are presented in Table 6.

Table 6. Values of weights for particular parameters.

Marking	Weight
α_1	0.19365
α_2	0.16125
α_3	0.16125
α_4	0.16125
α_5	0.1291
α_6	0.16125
α_7	0.03225

A comparison of the tested mixtures of diesel oil and fatty acid methyl esters based on the evaluation of particular variants allowed us to refer the parameter values of to a 'virgin' diesel oil that, in this study, was assumed to be the point of reference. The performed assessment is expressed as an arithmetic mean, this being the most effective, unburdened estimator of an unknown expected value [33], and is presented in Table 7 with a division into particular variants.

Table 7. Assessment of the tested parameter values for particular fuel mixtures.

Number of Variant	Symbol of Mixture	Number of Setting	PM	CO	CO_2	HC	O_2	NO_2	Lambda
1	ON	1	04174	1	0.4234	0.4598	0.4234	0.4771	0.6522
2	ON	2	0.4147	1	0.7443	0.5527	0.7443	0.4645	0.6710
3	ON	3	0.4202	1	0.6657	0.6512	0.6657	0.4622	0.6418
4	ON	4	0.4193	1	0.6865	0.6581	0.6865	0.4658	0.6236
5	BIO10	1	0.4167	1	0.4439	0.6181	0.4439	0.4717	0.6047
6	BIO10	2	0.4214	1	0.6810	0.6744	0.6810	0.4717	0.6242
7	BIO10	3	0.4164	1	0.6429	0.6868	0.6443	0.4745	0.6193
8	BIO10	4	0.4280	1	0.6887	0.6671	0.6887	0.4726	0.5990
9	BIO30	1	0.4185	1	0.5393	0.9937	0.5393	0.4614	0.5741
10	BIO30	2	0.4153	1	0.6580	1	0.6579	0.4627	0.6169
11	BIO30	3	0.4107	1	0.5843	0.7872	0.5843	0.4720	0.6035
12	BIO30	4	0.4132	1	0.6196	0.6732	0.6196	04630	0.5875
13	BIO50	1	0.4168	1	0.6081	0.4161	0.6081	0.4482	0.5996
14	BIO50	2	0.4106	1	0.6317	0.4018	0.6317	0.4121	0.6126
15	BIO50	3	0.4152	1	0.6317	0.5624	0.6317	0.4678	0.5802
16	BIO50	4	0.4153	1	0.6317	0.4834	0.6317	0.4726	0.5935

The results presented in the table present the ratings for individual operational parameters and sixteen variants of the mixture–controller setting. The graphic interpretation of these results is shown in Figure 6.

The measurements performed for four mixtures of diesel oil with fatty acid methyl esters and four computer software modifications of the analyzed vehicles allowed us to obtain 16 variants and provide a complete assessment for all the analyzed criteria, which is presented in Table 8.

The graphical interpretation of the obtained scores for individual variants is shown in Figure 7.

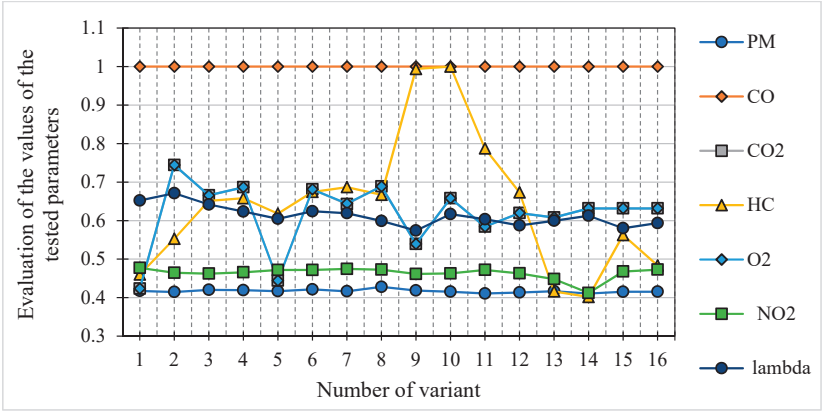

Figure 6. Assessment of the tested parameter values for particular fuel mixtures.

Table 8. Complete assessment for particular variants.

Number of Variant	Symbol of Mixture	Number of Setting	Complete Assessment
1	ON	1	5.4968
2	ON	2	6.0378
3	ON	3	6.1121
4	ON	4	6.0511
5	BIO10	1	5.7727
6	BIO10	2	6.1647
7	BIO10	3	6.1391
8	BIO10	4	6.0970
9	BIO30	1	6.5388
10	BIO30	2	6.6417
11	BIO30	3	6.1993
12	BIO30	4	5.9829
13	BIO50	1	5.7043
14	BIO50	2	5.5627
15	BIO50	3	5.7302
16	BIO50	4	5.7067

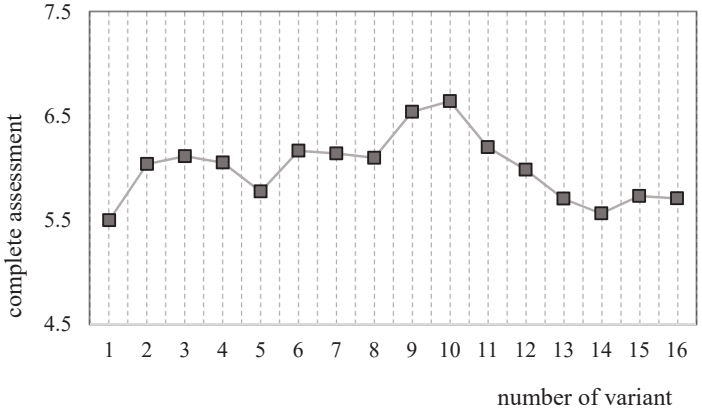

Figure 7. Complete assessment for particular variants.

In terms of the assessment criteria, variant number 10, that is, a BIO30 mixture with an increased fuel dose of 4% and air load of 50 hPa, which was 6.6417, was found to be the best one. The use of BIO30 fuel to power the engine enabled to obtain the best assessment results for all computer software adjustments. By using the virgin oil-powered engine to be a reference point, it was found that the use of the BIO10 and BIO30 mixtures improved the performance quality of the analyzed power units in terms of the accepted criteria.

It needs to be emphasized that, by referring the assessment result scatter to a possibly higher scatter of assessment results, which can be obtained using this method (from 4 to 10), an exchange of a mixture involves, approximately, a 19% change in the tested object performance quality. Hence, this issue has a significant impact on the rationalization of the process of self-ignition combustion engine operation.

The test results allowed us to define the vector components quantities. The determination of these components enabled us to perform the geometric interpretation of the parameter mean values. For the purpose of transparency and unequivocality of the results, their values were normalized into the interval <0 ÷ 10> for the set of the analyzed parameters <0 ÷ 10>, using the following dependency:

$$10 \times \frac{(X_i - X_{min})}{(X_{max} - X_{min})} \quad (4)$$

Variability intervals were also determined for the analyzed parameter set. The vector components were analyzed for the four tested fuel mixtures with averaged modifications of the fuel injection controller. The minimal values obtained from experimental tests were accepted to be the most desired result for the tested parameters. The normalized results of the particular vector components are presented in Table 9.

Table 9. Assessment of the tested parameter values for respective fuel mixtures.

Vector Components	Symbol of Mixture			
	ON	**BIO10**	**BIO30**	**BIO50**
X_1	1.361	2.249	1.801	2.819
X_2	7.287	8.867	8.267	6.933
X_3	4.701	5.211	3.589	2.844
X_4	1.759	1.745	4.275	6.755
X_5	7.281	8.695	7.081	0.265
X_6	7.951	6	4.9	4.467
X_7	7.052	8.244	9.104	1.433

The results are presented in a normalized form in such a way that number 0 means the lowest score, whereas 10 means the highest one. Thus, the minimal score is the best one for the considered power unit parameters. The results obtained for the analyzed parameters in particular variants (fuel mixtures) are presented in a geometric interpretation in Figures 8–10. The blue color was used for marking 'virgin' diesel oil, which, in the analyzed case, was the point of reference for the remaining fuel mixtures. The other colors (orange, green and violet) were used to mark the tested mixtures of diesel oil and fatty acid methyl esters—respectively, BIO10, BIO30 and BIO50. The analyzed power units are the vector components in a graphic interpretation.

The above-presented schemes show that the lowest parameter values were found for the BIO50 mixture (except for the parameters of solid particles and hydrocarbons). For the BIO10 mixture, the analyzed parameters had higher values than the reference point, that is, 'virgin' diesel oil. A drop in the value of certain parameters was observable for BIO30, these being carbon dioxide and nitric oxides. An analysis of the data showed that only a 30% additive of fatty acid methyl esters to diesel oil decreased the number of components in exhaust gases which can have a negative influence on the natural environment. It is the

optimal amount of the biocomponent that should be added to diesel fuel in order to lower the engine parameters.

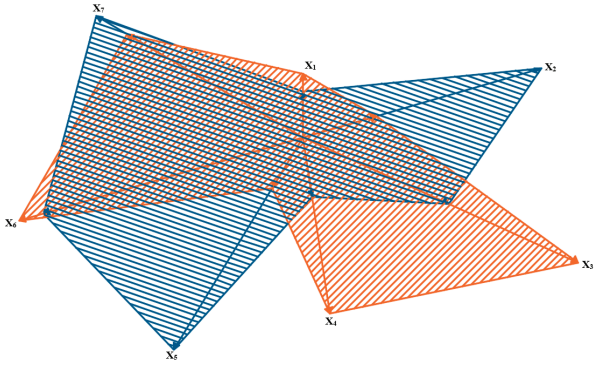

Figure 8. Graphic interpretation of comparative analysis of results of particular component parameters for BIO 10 and 'virgin' diesel oil.

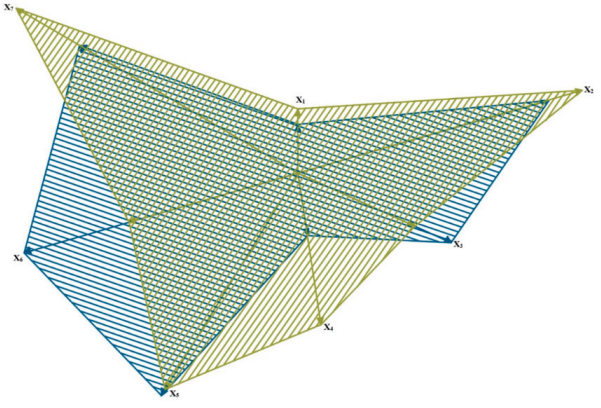

Figure 9. Graphic interpretation of comparative analysis of results for particular parameters of components for BIO 30 and 'virgin' diesel oil.

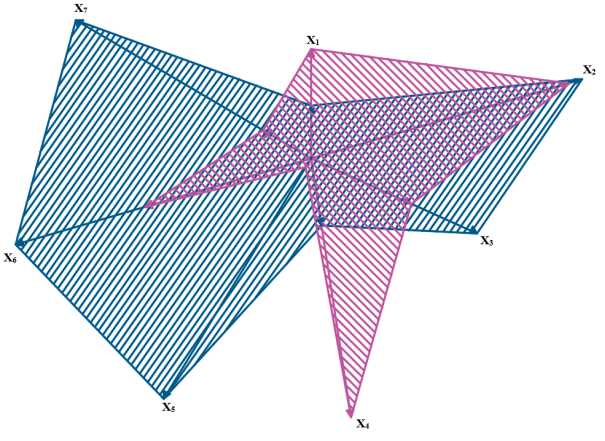

Figure 10. Graphic interpretation of comparative analysis of results for particular parameters of components for BIO 50 and 'pure' diesel oil.

The mean values of the results provided for the three analyzed research objects allowed us to define the quantity of random variable Z_x. The standardized results of the random variable are presented in Figure 11.

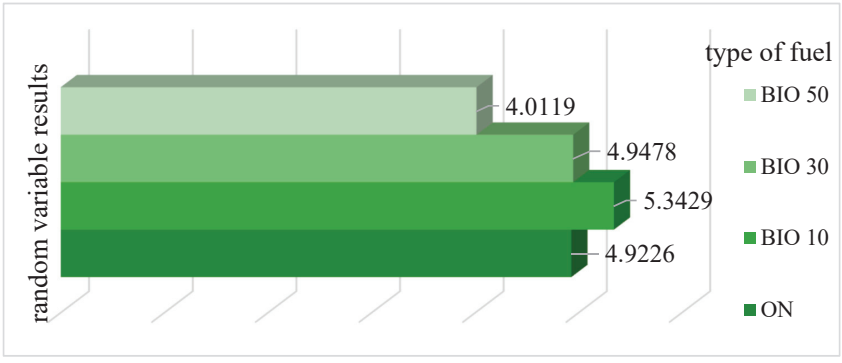

Figure 11. Standardized results of random variable.

The values of the random variable Z_x for particular fuel mixtures (ON, BIO10, BIO30 and BIO50) reflect the sum of the vector component products and assign them weights. The ON mixture ('virgin' diesel oil) was the point of reference. As can be seen in the chart, the random variable determined for the BIO10 mixture (90% of diesel oil and 10% of fatty acid methyl esters) and BIO30 mixture (70% of diesel oil and 30% of fatty acid methyl esters) is higher than that of the point of reference. The random variable of the BIO50 mixture is lower by approximately 18% than that of the point of reference. The obtained results indicate a beneficial effect of the BIO50 mixture.

3.3. Verification of the Proposed Assessment Model

One of the problems of the assessment process is the determination of only those parameters which significantly affect the assessment from the point of view of the analyzed parameter set; the selected parameters provide the basis for further analyses. A set of seven parameters was distinguished in the proposed model. To verify this model, the method of mean fuzzy charts was used. The application of elements of fuzzy logic allowed us to correct the redundancy of the parameter set and to determine the significance of these parameters. In order to analyze real data, the value established for the cross-section by measuring points was fuzzified. The belonging of the measuring point to a given cross-section was rendered in the form of a Gauss function. Original software was used to perform the analyses. The value of the membership function coefficient range was 20%. The number of fuzzy cross-sections was established to be seven and a method was developed for the scatter calculation as a mean square value. The value 0.01 was accepted to be the significance limit [33,34]. By providing all the analyzed performance parameters with identical parameters, it was found which ones were the most significant from the point of view of the experiment. The test result mean values of the analyzed fuel mixtures performance parameters and fuel injection controller settings are presented in Table 10.

The results achieved in this way were analyzed through the determination of fuzzy means to identify the change in sensitive parameters. Figure 12 shows a gradient form of fuzzy means. The analyzed parameters are demonstrated in a decreasing manner according to the values of their scattering.

Table 10. Assessment of mean values for the accepted variants.

Symbol of Mixture	Number of Setting	Particulates	Carbon Monoxide	Carbon Dioxide	Hydrocarbons	Oxygen	Nitric Oxides	Excess Air Coefficient
ON	I	9400	13	1196	5147	1727	22,723	1355
	II	9593	10	1214	3083	581	25,040	1324
	III	8667	6	1178	1953	684	25,460	1372
	IV	12,890	6	1184	1900	646	24,813	1402
BIO10	I	8573	16	1199	2210	1578	23,717	1433
	II	9370	4	1170	1773	656	23,723	1427
	III	9067	8	1203	1677	723	23,200	1409
	IV	12,392	2	1127	1830	642	23,563	1444
BIO30	I	7503	7	1189	903	1025	23,777	1526
	II	8997	8	1210	863	698	25,367	1413
	III	9323	12	1240	1237	861	23,663	1435
	IV	12,035	8	1224	1783	768	25,310	1482
BIO50	I	6643	6	1200	6500	789	28,040	1442
	II	8567	9	1241	6943	746	34,683	1420
	III	9437	11	1211	5067	746	24,077	1506
	IV	12,105	4	1231	4413	746	23,547	1462

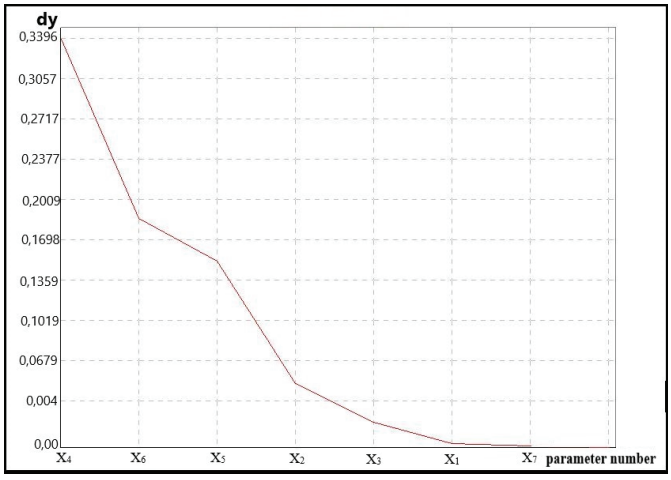

Figure 12. Spectral form.

Based on data analysis, it can be accepted that the parameters whose scatter value is lower than 0.04 were not sensitive to the changes introduced in engine computer software and their values did not undergo statistically significant change depending on the fuel mixture used. The values of scatter obtained for particular parameters, defining their sensitivity to the fuel mixture change and the power unit computer software, are demonstrated in Table 11.

The test results make it possible to find out which of the analyzed parameters was sensitive to the changes and whether it can be omitted in further research. Exemplary charts of the most sensitive parameter X_4 and little sensitive X_7 are presented in Figures 13 and 14.

Table 11. Values of fuzzy mean scatter for the tested parameters.

Marking of Parameter	Value of Fuzzy Mean Scatter
X_1	0.0032
X_2	0.0491
X_3	0.0210
X_4	0.3396
X_5	0.1524
X_6	0.1886
X_7	0.0014

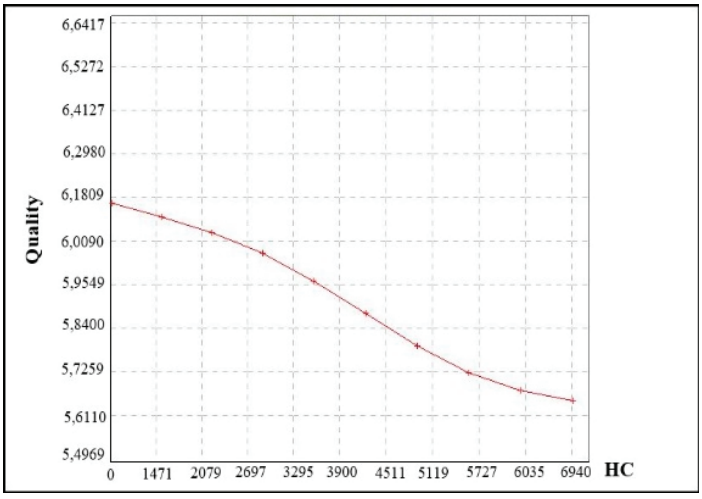

Figure 13. A chart of fuzzy means for sensitive data on the basis of parameter X_4.

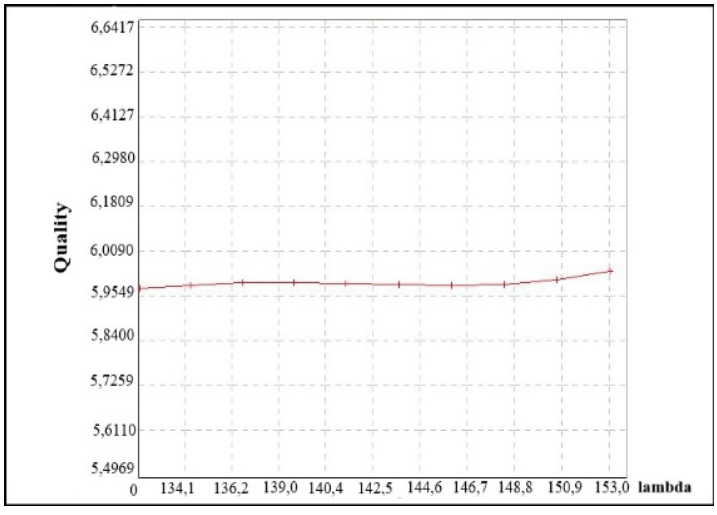

Figure 14. A chart of fuzzy means for little sensitive data on the basis of parameter X_7.

4. Discussion

The need to reduce the emission of harmful fuel components from self-ignition engines raises interest in research on new power supply solutions. The test results prove that the

use of mixtures of diesel oil and fatty acid methyl esters contributes to the reduction in the amount of fuel components emitted into the environment, which has also been confirmed by many authors [35–39]. The test results involve different settings of power-unit computer software. The literature does not provide data on the subject of fuel injection controller adjustment that would enable us to match a given setting to obtain optimal performance of the power unit powered with a mixture of diesel oil and fatty acid methyl ester. Adjustments of vehicle computer software would allow us to decrease the number of exhaust gas components. The most important aspect of the study is the assessment of engine performance depending on the fuel mixture composition. This was possible by obtaining the measurements for fatty acids of diesel oil, those of the ester service and service updates for 16 updates and the evaluation of methyl services. The conducted assessment shows the last grade of the coal assessment and the lowest grade for the assessment performed. The assessment of the significant it is the most unstable, its results ranging around 1, as well as being equal for the equation that contains lambda. The ratings for the experiments vary between 0.4 and 0.7. Location data should be analyzed in two ways; in addition to the analysis of the operational parameters, the verification of the variant sample should be carried out as follows: the first assessment should be performed for the second, eighth and tenth variants, while the lowest assessment should be performed for the first, thirteenth and fourteenth variants. From the analysis of the evaluation scores, out of all them, the evaluation scores of the controls for the tenth variant were lower than the previous one. The article also presents the verification of individual performance parameters in terms of assessment. On the basis of the control performed, changes to the settings were made.

5. Conclusions

An analysis of the values of particular parameters, based on the random variable defined for each research object, showed that the best results were obtained for the BIO10 mixture and the worst ones for BIO50. It can be observed that the best mixture was the one with 70% of diesel oil and 30% of fatty acid methyl esters. Changes in the analyzed parameter properties were represented in a vector-based form which enabled the simultaneous analysis of their changes. From the point of view of exhaustibility of petroleum, the use of alternative solutions for powering combustion engines is justified. The application of fatty acid methyl esters makes it possible to reduce the consumption of diesel oil. According to the established 10-point rating scale, the assessment of the impact of the fuel injection controller settings on the values of the performance parameters of engines fed with mixtures of fatty acid methyl esters and diesel oil is as follows: In the case of setting I for mixture III, the assessment was 8 and the difference between the highest and the lowest rating for individual mixes was about 16%, while, in the case of setting II for mix V, the assessment was 8 and the difference between the highest and the lowest rating for individual mixtures was about 36%. In the case of setting III for mixture V, the assessment was 8.2 and the difference between the highest and the lowest grade for individual mixtures was about 6%, whereas, in the case of setting the IV for mixture V, the assessment was 8.3 and the difference between the highest and the lowest grade for individual mixtures was about 13%. Finally, in the case of setting V for mixture V, the assessment was 8 and the difference between the highest and the lowest grade for individual mixtures was about 17%. This means that there is a correlation between the fuel mixture composition and the fuel injection controller settings. The applied method of fuzzy diagrams is an important tool to be used for the assessment of the influence of fatty acid methyl esters addition to diesel oil on transport means power-unit functioning, including the optimal setting of the fuel injection controller. The test results confirm advisability of using alternative fuels with appropriate component proportions and adequate settings of the power unit fuel injection controller.

Author Contributions: Conceptualization, Ł.M., M.M., M.P.; formal analysis, M.M. and M.P.; investigation, M.M.; methodology, Ł.M. and M.M.; resources, M.M.; visualization, M.M.; writing—original draft, M.M.; writing—review and editing, M.M. All authors have read and agreed to the published version of the manuscript.

Funding: The research study did not receive external financing.

Conflicts of Interest: The authors declare no conflict of interest.

References

1. Varuwel, E.G.; Mrad, M.; Tazerout, M.; Aloui, F. Experimental Analysis of Biofuel as an Alternative Fuel for Diesel Engines. *Appl. Energy* **2012**, *94*, 224–231. [CrossRef]
2. Hirkude, J.B.; Padalkar, A. Performance and emission analysis of a compression ignition: Engine operated on waste fried oil methyl esters. *Appl. Energy* **2012**, *90*, 68–72. [CrossRef]
3. Masera, K.; Hossain, A. Biofuels and thermal barrier: A review on compression ignition engine performance, combustion and exhaust gas emission. *J. Energy Inst.* **2019**, *92*, 783–801. [CrossRef]
4. Wierzbicki, S. Biogas as A Fuel for Diesel Engines. *J. Kones Powertrain Transp.* **2012**, *19*, 477–482. [CrossRef]
5. Zivkovic, S.; Veljković, M. Environmental impacts the of production and use of biodiesel. *Environ. Sci. Pollut. Res.* **2017**, *25*, 191–199. [CrossRef]
6. Singh, J. Commercialization Petential of Microalgae for Biofuels Production. *Renew. Sustain. Energy Rev.* **2010**, *14*, 2596–2610. [CrossRef]
7. Naik, S.; Goud, V.; Rout, P.; Dalai, A. Production of First and Second Generation Biofuels: A Comprenensive Review. *Renew. Sustain. Energy Rev.* **2010**, *14*, 578–597. [CrossRef]
8. Nigam, P.; Singh, A. Production of Liquid Biofuel from Renewable Resource. *Prog. Energy Combust. Sci.* **2011**, *37*, 52–68. [CrossRef]
9. Asadia, A.; Zhangb, Y.; Mohammadi, H.; Khorand, H.; Rui, Z.; Hossein Doranehgard, M.; Bozorge, M. Combustion and Emission Characteristics of Biomass Derived Biofuel, Premixed in A Diesel Engine: A CFD Study. *Renew. Energy* **2019**, *138*, 79–89. [CrossRef]
10. Mofijur, M.; Rasul, M.; Hyde, J.; Bhuyia, M. Role of Biofuels on IC Engines Emission Reduction. *Energy Procedia* **2015**, *75*, 886–892. [CrossRef]
11. Gang, W.; Guohe, J.; Zhiyuan, Y.; Zhijian, H. Emission Characteristics for Waste Cooking Oil Biodiesel Blend in A Marine Diesel Propulsion Engine. *Pol. J. Environ. Stud.* **2019**, *28*, 2911–2921.
12. Azoumah, Y.; Blin, J.; Daho, T. Exergy efficiency applied for the performance optimization of a direct injection compression ignition (CI) engine using biofuels. *Renew. Energy* **2009**, *34*, 1494–1500. [CrossRef]
13. Tompkins, B.; Song, H.; Bittle, J.; Jacobs, T. Efficiency considerations for the use of blended biofuel in diesel engines. *Appl. Energy* **2012**, *98*, 209–218. [CrossRef]
14. Fontaras, G.; Karavalakis, G.; Kousoulidou, M.; Tzamkiozis, T.; Ntziachristos, L.; Bakeas, E.; Stournas, S.; Samaras, Z. Effects of Biodiesel on Passenger Car Fuel Consumption, Regulated and Non-Regulated Pollutant Emissions Over Legislated and Real-World Driving Cycles. *Fuel* **2009**, *88*, 1608–1617. [CrossRef]
15. Markiewicz-Patalon, M.; Muślewski, Ł.; Kaszkowiak, J.; Knopik, L. Analysis of Selected Operating Parameters of Engine Powered by A Mixture of Biocomponents And Diesel Oil. *J. Kones Powertrain Transp.* **2018**, *25*, 239–244. [CrossRef]
16. Markiewicz, M.; Muślewski, Ł.; Pająk, M. Impact of Biocomponent Additive to Diesel Oil on Values of Elected Functional Parameters of Transport Means. *Pol. J. Environ. Stud.* **2020**, *29*, 3475–3483. [CrossRef]
17. Markiewicz, M.; Muślewski, Ł. The Impact of Powering an Engine with Fuels from Renewable Energy Sources Including Its Software Modification on A Drive Unit Performance Parameters. *Sustainability* **2019**, *11*, 6585. [CrossRef]
18. Markiewicz, M.; Muślewski, Ł. Survey performance and emission parameters of diesel engine powered by diesel oil and fatty acid methyl esters using fuzzy logic techniques. *Fuel* **2020**, *277*, 118179. [CrossRef]
19. Landowski, B.; Baran, M. Analysis of selected results of engine oil tests. In Proceedings of the 18th International Conference Diagnostics of Machines and Vehicles, MATEC Web of Conferences, Sibiu, Romania, 5–7 June 2019; Volume 302.
20. Landowski, B.; Pająk, M.; Żółtowski, B.; Muślewski, Ł. Method of building a model of operational changes for the marine combustion engine describing the impact of the damages of this engine on the characteristics of its operation process. *Pol. Marit. Res.* **2017**, *24*, 67–76. [CrossRef]
21. Landowski, B.; Muślewski, Ł.; Pająk, M.; Polishchuk, O. Method for initial assessment of unit costs of public city transport means operation. In Proceedings of the MATEC Web of Conferences, 17th International Conference Diagnostics of Machines and Vehicles, Bydgoszcz, Poland, 25–26 September 2018; pp. 1–7. [CrossRef]
22. Karthickeyan, V. Experimental investigation on combined effect of ignition promoters and ceramic coating fuelled with papaya seed oil methyl ester in DI diesel engine. *Renew. Energy* **2020**, *148*, 772–789. [CrossRef]
23. Man, X.; Cheung, C.; Ning, Z.; Wei, L.; Huang, Z. Influence of Engine Load And Speed on Regulated and Unregulated Emissions of a Diesel Engine Fueled with Diesel Fuel Blended with Waste Cooking Oil Biodiesel. *Fuel* **2016**, *180*, 41–49. [CrossRef]
24. Chauhan, B.; Kumara, N.; Chob, H.; Limc, H. A Study on The Performance and Emission of a Diesel Engine Fueled with Karanja Biodiesel and Its Blends. *Energy* **2013**, *56*, 1–7. [CrossRef]
25. Hoekman, S.; Robbins, C. Review of The Effects of Biodiesel on Nox Emissions. *Fuel Process. Technol.* **2012**, *96*, 237–249. [CrossRef]

26. Necati, A.; Canakci, O. Determination of Performance and Combustion Characteristics of a Diesel Engine Fueled with Canola and Waste Palm Oil Methyl Esters. *Energy Convers. Manag.* **2011**, *52*, 108–116.
27. Özener, O.; Yüksek, L.; Ergenç, A.T.; Özkan, M. Effects of soybean biodiesel on a DI diesel engine performance, emission and combustion characteristics. *Fuel* **2014**, *115*, 875–883. [CrossRef]
28. Rajak, U.; Nashine, P.; Singh, T.S.; Verma, T.N. Numerical investigation of performance, combustion and emission characteristics of various biofuels. *Energy Convers. Manag.* **2018**, *156*, 235–252. [CrossRef]
29. Muślewski, Ł. Evaluation Method of Transport Systems Operation Quality. *Pol. J. Environ. Stud.* **2009**, *7*, 18.
30. Lootsma, F.A. A model for the relative importance of the criteria in the multiplicative AHP and Smart. *Eur. J. Oper. Res.* **1996**, *94*, 467–476. [CrossRef]
31. Saaty, T.L. The Analytic Hierarchy Process. In *Planning, Priority Setting and Resource Allocation*; Mc. Graw-Hill: New York, NY, USA, 1980.
32. Plucińska, A.; Pluciński, E. *Probabilistyka*; WNT: Warszawa, Poland, 2000.
33. Landowski, B. Numerical Simulation of the Process of a Technical Object State Changes. *J. Konbin* **2017**, *44*, 119–140. [CrossRef]
34. Pająk, M. Genetic-Fuzzy system of power units maintenance schedules generation. *J. Intell. Fuzzy Syst.* **2015**, *28*, 1577–1589. [CrossRef]
35. Agarwal, A.K.; Srivastava, D.K.; Dhar, A.; Maurya, R.K.; Shukla, P.C.; Singh, A.P. Effect of fuel injection timing and pressure on combustion, emissions and performance characteristics of a single cylinder diesel engine. *Fuel* **2013**, *111*, 374–383. [CrossRef]
36. Mehregan, M.; Moghiman, M. Effects of nano-additives on pollutants emission and engine performance in a urea-SCR equipped diesel engine fueled with blended-biodiesel. *Fuel* **2018**, *222*, 402–406. [CrossRef]
37. Hoseinia, S.; Najafia, G.; Ghobadiana, B.; Mamat, R.; Sidikc, N.; Azmib, W. The effect of combustion management on diesel engine emissions fueled with biodiesel-diesel blends. *Renew. Sustain. Energy Rev.* **2017**, *73*, 307–331. [CrossRef]
38. Giakoumis, E.; Rakopoulos, C.; Dimaratos, A.M.; Rakopoulos, D.C. Exhaust emissions of diesel engines operating under transient conditions with biodiesel fuel blends. *Prog. Energy Combust. Sci.* **2012**, *38*, 691–715. [CrossRef]
39. Ospina, G.; Selim, M.Y.; Al Omari, S.A.; Ali, M.I.H.; Hussien, A.M. Engine roughness and exhaust emissions of a diesel engine fueled with three biofuels. *Renew. Energy* **2019**, *134*, 1465–1472. [CrossRef]

sustainability

MDPI

Article

A New Collaborative Multi-Agent Monte Carlo Simulation Model for Spatial Correlation of Air Pollution Global Risk Assessment

Mustafa Hamid Hassan [1,2], Salama A. Mostafa [1,*], Aida Mustapha [3], Mohd Zainuri Saringat [1], Bander Ali Saleh Al-rimy [4], Faisal Saeed [5], A.E.M. Eljialy [6] and Mohammed Ahmed Jubair [1,2]

[1] Faculty of Computer Science and Information Technology, Universiti Tun Hussin Onn Malaysia, Parit Raja 84600, Malaysia; mustafa.hamed@sadiq.edu.iq (M.H.H.); zainuri@uthm.edu.my (M.Z.S.); mohammed.a@sadiq.edu.iq (M.A.J.)
[2] College of Information Technology, Imam Ja'afar Al-Sadiq University, Al-Muthanna 66002, Iraq
[3] Faculty of Applied Sciences and Technology, Universiti Tun Hussein Onn Malaysia, Panchor 84500, Malaysia; aidam@uthm.edu.my
[4] School of Computing, Faculty of Engineering, Universiti Teknologi Malaysia, Johor Bahru 81310, Malaysia; bander@utm.my
[5] School of Computing and Digital Technology, Birmingham City University, Birmingham B4 7XG, UK; alsamet.faisal@gmail.com
[6] Department of Information System, College of Computer Engineering & Sciences, Prince Sattam Bin Abdulaziz University, Alkharj 11942, Saudi Arabia; ae.mohammed@psau.edu.sa
* Correspondence: salama@uthm.edu.my

Citation: Hassan, M.H.; Mostafa, S.A.; Mustapha, A.; Saringat, M.Z.; Al-rimy, B.A.S.; Saeed, F.; Eljialy, A.; Jubair, M.A. A New Collaborative Multi-Agent Monte Carlo Simulation Model for Spatial Correlation of Air Pollution Global Risk Assessment. *Sustainability* **2022**, *14*, 510. https://doi.org/10.3390/su14010510

Academic Editors: Avelino Núñez-Delgado, Zhien Zhang, Elza Bontempi, Mario Coccia, Marco Race and Yaoyu Zhou

Received: 29 October 2021
Accepted: 27 December 2021
Published: 4 January 2022

Abstract: Air pollution risk assessment is complex due to dynamic data change and pollution source distribution. Air quality index concentration level prediction is an effective method of protecting public health by providing the means for an early warning against harmful air pollution. However, air quality index-based prediction is challenging as it depends on several complicated factors resulting from dynamic nonlinear air quality time-series data, such as dynamic weather patterns and the verity and distribution of air pollution sources. Subsequently, some minimal models have incorporated a time series-based predicting air quality index at a global level (for a particular city or various cities). These models require interaction between the multiple air pollution sensing sources and additional parameters like wind direction and wind speed. The existing methods in predicting air quality index cannot handle short-term dependencies. These methods also mostly neglect the spatial correlations between the different parameters. Moreover, the assumption of selecting the most recent part of the air quality time series is not valid considering that pollution is cyclic behavior according to various events and conditions due to the high possibility of falling into the trap of local minimum and poor generalization. Therefore, this paper proposes a new air pollution global risk assessment (APGRA) prediction model for an air quality index of spatial correlations to address these issues. The APGRA model incorporates an autoregressive integrated moving average (ARIMA), a Monte Carlo simulation, a collaborative multi-agent system, and a prediction algorithm for reducing air quality index prediction error and processing time. The proposed APGRA model is evaluated based on Malaysia and China real-world air quality datasets. The proposed APGRA model improves the average root mean squared error by 41%, mean and absolute error by 47.10% compared with the conventional ARIMA and ANFIS models.

Keywords: air quality index; air pollution; risk assessment; autoregressive integrated moving average; Monte Carlo simulation; multi-agent system

1. Introduction

Air quality has drawn much attention in recent years because it seriously affects people's health. At present, monitoring stations in a city can provide real-time air quality measures [1]. Nonetheless, people strongly desire air quality prediction, which is

challenging as it depends on several complicated factors, such as weather patterns and spatial-temporal dependencies of air quality. Air pollution risk assessment is complex due to its dynamic data and distributed pollution sources [2]. For instance, predicting air quality on weekdays and weekends may be different due to the difference in anthropic emissions [3]. Air Quality Index (AQI) effectively protects public health by communicating early warnings of harmful air pollutants. However, the prediction is challenging because it depends on several complex factors, such as weather patterns, nonlinear time series of air quality data, and distribution of air pollution sources [4,5]. The dynamic data and distributed air pollution risk assessment sources need to be estimated relying on two phases. The first phase is utilized to predict the AQI of a local area. The second phase is employed to assess the global risk level based on the AQIs of local areas [6,7].

Air quality prediction aims to predict the future state of air quality in a specified location based on existing data, like historical air quality and meteorological data. Many types of research have been conducted to tackle the problem of assessing air pollution risk. Some examples are the works of [4,7,8]. Each of these has mostly focused on assessing the concentration of a specific pollutant parameter such as $PM_{2.5}$, CO, and PM_{10} [7,9]. However, some approaches have been focused on predicting the level of certain parameters that directly impact the state of pollution [6,10]. The literature provides a significant number of works in air pollution prediction models either for a specific location or specific variables. Feng et al. [11] combine air mass trajectory analysis and wavelet transformation with artificial neural network (ANN) to improve the prediction accuracy of daily average concentrations of $PM_{2.5}$. Tong et al. [8] deploy Monte Carlo simulation (MCS) to estimate health risks related to the concentration of dust-induced occupational conditions.

Prasad et al. [12] used an adaptive neuro-fuzzy inference system (ANFIS) for predicting the concentration of several AQI parameters. However, these models predict air pollution concentrations based on the most recent part of the time series. This mechanism requires larger data for producing proper prediction results. It is highly possible to fall into the trap of local minimum [4,10]. Moreover, the learning or training of these models with short-term prediction situations may never converge due to the training data/time insufficiency, which might cause the algorithms to be trapped in an infinite training situation [13]. Because of these constraints, the statistical approach represents the best option. One of the best statistical approaches that deal with short-term time series prediction is the autoregressive integrated moving average (ARIMA) algorithm, as it only requires prior data of a time series to generalize the prediction of the AQI model [4]. However, the ARIMA algorithm does not produce satisfactory results for certain air pollution parameters (i.e., PM_{10} and CO), even for a short prediction period [14–16].

Many approaches have tackled the problem of weather variable prediction and forecasting as well as pollution estimation and alarming. Each one has concentrated on one aspect, while some strategies have focused on predicting the level of a certain variable that has a critical impact on the pollution state [6]. Others have dealt with the issue of lacking adequate measurement stations across countries [9]. Moreover, some approaches have focused on building models for estimating air pollution more accurately based on feature selection or neural networks. Others have built one-step-ahead forecasting models [11,14,15] and have used fuzzy models for alarming air pollution [4,7]. Hence, a set of neural networks and simple auto-regression forecasters can be used, such as in the work of Westerlund et al. [17] that is validated to be superior over a single forecaster. The literature has revealed that very limited models have been constructed to assess the global (interaction between the pollution sources) level of air pollution. However, the dynamic nature and high spatiotemporal variability of AQI represent a complex predicting problem. Hence, none-of the existing models are able to incorporate time-series data to provide dynamic forecasting of various weather variables. This can be achieved by tackling the global interaction of different locations using wind direction and speed for enabling contextual forecasting added to the mathematical model. Consequently, the research gap

lies in the absence of interaction between air pollution parameters under investigation and finding the global prediction level of the dynamic and distributed air pollution risk.

This paper identifies that the global interaction among meteorological parameters such as wind speed and wind direction at the different areas is essential in air pollution prediction and risk assessment due to the nature of dynamic weather and air pollution time series at various locations. The study in this paper aims to fill this gap by searching for ways to overcome the conditional heteroscedasticity problem. The contributions of this paper are represented by: (i) to develop ARIMA-based MCS prediction algorithm that integrates ARIMA and MCS algorithms for reducing AQI prediction error; (ii) to propose an air pollution global risk assessment (APGRA) model that incorporates the ARIMA-based MCS algorithm into a multi-agent system (MAS) for dynamic and distributed assessment of multiple sources of AQI risk levels; and (iii) to test and evaluate the performance of APGRA models in terms of prediction error and time by using China and Malaysia air quality datasets.

The remaining parts of the paper are organized as follows: Section 2 provides Materials and Methods. Section 3 describes the Monte Carlo method to be used in accommodating the uncertainty of the forecast. It then presents a proposed APGRA model. Section 4 discusses the results of the APGRA model, and Section 5 provides conclusions and future research.

2. Materials and Methods

This section covers the materials and methods which are used in this paper. At the same time, it first explains the air pollution datasets divided into two case studies: Malaysia and China. Second, it explains the prediction algorithms that are used in the local risk assessment, such as MCS and ARIMA. Third, it explains several performance measures such as root mean square error (RMSE) and mean absolute error (MAE) used to evaluate this work.

2.1. Air Pollution Datasets

This study utilizes two real-world air pollution datasets of Malaysia and China. The data layout is presented as a matrix $D = \left\{x_t^{i,j}\right\}$, where $i = 1, 2 \ldots M, j = 1, 2 \ldots N$, M indicates the number of variables, and M indicates the number of cities, t represents the time, sampled as hourly. The data is fed into the framework for one of two goals, forecasting one of the time series within a certain defined time horizon or evaluating a given model configuration in terms of its forecasting accuracy in a certain time interval. Another element of the data is the map combined with longitude and latitude for all cities with their time series included in matrix D. The datasets are described in the following subsections.

2.1.1. Malaysia Air Pollution Dataset

This paper applies the heterogeneous data set, including the one-dimension series data and the multi-dimension panel data. The one-dimension series data is composed of the value of AQI concentrations with the change of time. For the panel data, the Sulphur Dioxide (SO_2), Nitrogen Dioxide (NO_2), Carbon Monoxide (CO), Sulfur Dioxide ($SO_{2,}$) and Ozone (O_3) concentrations, temperature, relative humidity (RH), wind speed (WS), and PM_{10} concentrations of the previous hour are selected as the input variables. The AQI concentrations of the current hour are the output variable of the forecasting model. The Malaysia air quality monitoring network gathers the PM_{10}, SO_2, NO_2, CO, and O_3 concentrations data. The air quality monitoring stations include ten stations, as illustrated in Figure 1.

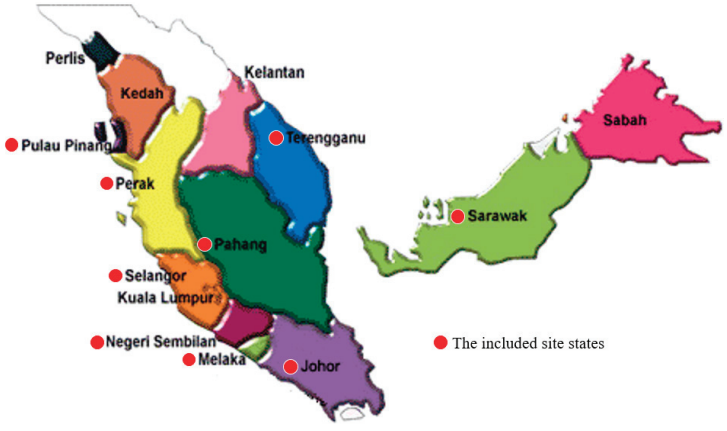

Figure 1. The geographic position of the Malaysia case study.

The data of air pollutant concentrations are collected from the different cities of Malaysia. Table 1 shows the locations of the included states in this study. Hourly air quality data have been collected from the eight air pollution monitoring stations during the ten years from 2006 to 2016 in Malaysia. These stations record data of some important AQI parameters such as the CO, NO_2, O_3, and "Particulate Matter (PM_{10})". These parameters are used to calculate the AQI. AQI is a commonly used indicator defined by the United States Environmental Protection Agency (EPA) to use air quality conditions. In order to calculate AQI for a location, an indicator value of AQI is calculated for each of the observed pollutant concentrations (CO, NO_2, O_3, and PM_{10}) using Equation (1) [18].

$$AQI = \frac{I_{high} - I_{low}}{C_{high} - C_{low}} * (C - C_{low}) + I_{low} \quad (1)$$

Table 1. Area of air quality data in Malaysia.

NO	Site State	Site ID	Location	Latitude	Longitude	Type
1	Johor	CAS 001	SM Pasir Gudang 2, Pasir Gudang, Johor	N01° 28.225	E103° 53.637	Residential
2	Terengganu	CAE 002	SRK Bukit Kuang, Teluk Kalung, Kemaman.	N04° 16.260	E103° 25.826	Residential
3	Pulau Pinang	CAN 003	Sek. Keb. Cenderawasih, Tmn. Inderawasih, Perai	N05° 23.470	E100° 23.213	Residential
4	Sarawak	CAK 004	Medical Store, Kuching, Sarawak	N01° 33.734	E110° 23.329	Residential
5	Melaka	CAS 006	Sek. Men. Keb. Bukit Rambai, Melaka	N02° 15.510	E102° 10.364	Residential
6	Pahang	CAE 007	Pej. Kajicuaca, Batu Embun, Jerantut, Pahang	N03° 58.238	E102° 20.863	Residential
7	Perak	CAN 008	SM Jalan Tasek, Ipoh, Perak	N04° 37.781	E101° 06.964	Residential
8	Pulau Pinang	CAN 009	SK Seberang Jaya II, Perai, Pulau Pinang	N05° 23.890	E100° 24.194	Residential
9	Negeri Sembilan	CAC 010	Taman Semarak (Phase II), Nilai, N.Sembilan	N02° 49.246	E101° 48.877	Residential
10	Selangor	CAC 011	SM(P) Raja Zarina, Klang, Selangor	N03° 00.620	E101° 24.484	Residential

2.1.2. China Air Pollution Dataset

The Beijing multi-site air-quality dataset comprises hourly AQI parameters from 10 measured air pollution monitoring locations countrywide [1]. The AQI data character-

izes the Beijing public environmental areas for the 24-h care center. The climatological and meteorological data in the AQI site are coordinated with China's climatological management's adjacent climate monitoring site. The historical time is from March 2013 to February 2017. Table 2 and Figure 2 show descriptive information related to the dataset.

Table 2. Area of air quality data in China.

Dataset Characteristics	Multivariate, Time-Series
Number of Instances:	420,768
Area:	Physical
Number of Attributes:	18
Attribute Characteristics:	Integer, Real
Missing Values?	Yes
Associated Tasks:	Regression

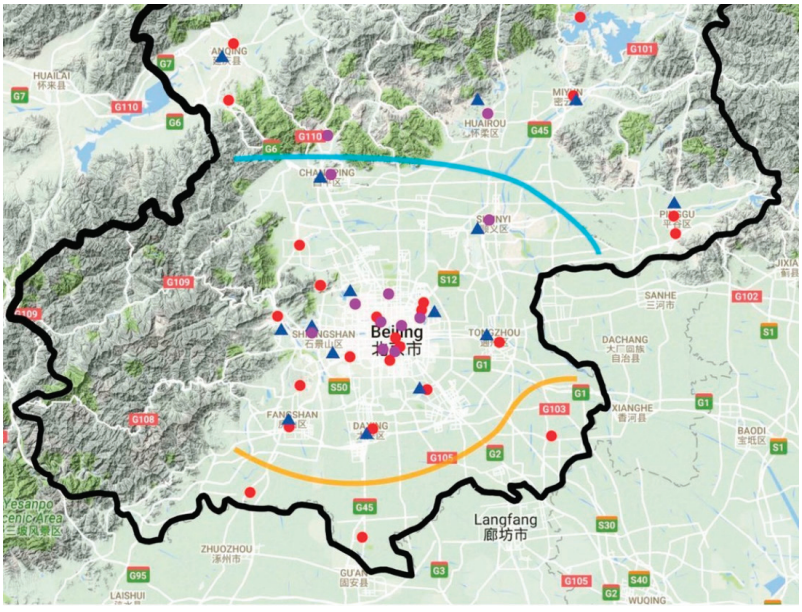

Figure 2. The geographic position of the China air pollution case study [1].

The response AQI is classified into four categories: AQI $\leq$ 35 μgm^{-3} (green), 35 μgm^{-3} < $PM_{2.5}$ $\leq$ 75 μgm^{-3} (yellow), 75 μgm^{-3} < AQI $\leq$ 150 μgm^{-3} (orange) and AQI > 150 μgm^{-3} (red). The four numbers inside each colored node indicate the proportions of the AQI categories at each layer of the branch, and the percentage represents the marginal proportion of the sample at the node. Figure 2 shows the position of 36 air quality monitoring sites marked as purple and red circles and 15 metrological sites marked as blue triangles.

2.2. Prediction Methods

2.2.1. Descriptive Statistics

Descriptive statistics are used to quantitatively describe or summarize each monitoring station data's features for further explaining their implication. Mean and median are statistical terms introduced to understand the central tendency of the data. Minimum and maximum show the amplitude of the time series. Standard deviation is a measure for quantifying the amount of variation or dispersion of the data values. A low standard

deviation indicates that the data points tend to be close to the data set's mean, while a high standard deviation indicates that the data points are spread out over a wider range of values. Skewness and kurtosis are applied to judge whether the sampling distribution is normal or not. Moreover, standard error of skewness (SES) and standard error of kurtosis (SEK) are presented to show the deviation between Skewness or Kurtosis's values.

2.2.2. ARIMA Algorithm

ARIMA, short for the auto-regressive integrated moving average, is actually a class of models that explains a given time series based on its own past values, that are its own lags and the lagged forecast errors so that the equation can be used to forecast future values. Any "non-seasonal" time series that exhibits patterns and is not a random white noise can be modeled with ARIMA models [4]. An ARIMA model is characterized by three terms: p, d, and q. Where p is the order of the AR term, q is the order of the MA term, and d is the number of differences required to make the time series stationary. If a time series has seasonal patterns, then seasonal terms are added, becoming SARIMA, short for seasonal ARIMA. The first step to building an ARIMA model is to make the time series stationary because the term "Auto Regressive" (AR) in ARIMA means it is a linear regression model that uses its own lags as predictors. Linear regression models work best when the predictors are not correlated and are independent of each other. The most common approach is to subtract the previous value from the current value. Sometimes, depending on the complexity of the series, differences might be needed. Therefore, the value of d is the minimum number of differences needed to make the series stationary. If the time series is already stationary, then $d = 0$. "p" is the order of the AR term. It refers to the number of lags of Y to be used as predictors. And "q" is the order of the "Moving Average" (MA) term. It refers to the number of lagged forecast errors that should go into the ARIMA Model. We adopt for forecasting the famous ARIMA model that is given by the Equation:

$$d^I x_t^{i,j} = \alpha_1 d^I x_{t-1}^{i,j} + \alpha_2 d^I x_{t-2}^{i,j} + \ldots \alpha_p d^I x_{t-p}^{i,j} + u_t + \beta_1 u_{t-1} + \ldots \beta_q u_{t-q} \quad (2)$$

2.2.3. Monte Carlo Simulation

Monte Carlo simulation (MCS) algorithms are mainly used in three problem classes: optimization, numerical integration, and generating draws from a probability distribution. MCS is one of the most common methods used to accommodate the uncertainties associated with many risk-related problems [8,19,20]. It has been recognized as a means of quantifying variability and uncertainty in risk assessments by the National Academy of Sciences and USEPA. This method provides a quantitative way to estimate the probability distributions for exposure risks and provides more information for making decisions related to risk protection. The widespread use of MCS in risk assessment promises a significant improvement in the scientific rigor of these assessments [20]. The MCS method generally requires three main steps, which are intended as follows:

Step 1 Construct a descriptive procedure to the probabilistic process:

- Build an appropriate probability model according to the simulated object's characteristics;
- Find a suitable distribution function to the desired solution.

Step 2 Achieve sampling method from a known probability distribution:

- Generate a random variable (or random vector) with a known probability distribution;
- Generate a random variable of a sample;
- Establish the sampling method of the random distribution.

Step 3 Establish various statistical estimators:

- Simulate a random variable as the solution to the object problem;
- Find the unbiased estimator.

Many statistics problems involve nested expectations and thus do not permit conventional MCS estimation. For such problems, a nest estimator, terms in an outer estimator,

involve calculating a separate and nested expectation [19]. Nested expectations occur in a wide variety of portfolio risk management problems [21]. Tackling such problems requires some form of nested estimation scheme in the MCS. In this approach, MCS simulated as an interest in estimating quantities of the form:

$$E_Z = [F(E(W|Z)] \tag{3}$$

where Z represents deferent risk scenarios, and $E[W \mid Z]$ represents exposure, depending on the scenario.

2.3. Modeling Dynamic and Distributed Behavior

Dynamic and distributed problem solving is achieved by employing a MAS that has the behaviors and methods of interaction, communication, and collaboration [22,23]. The dynamic behaviors of the agent help the statistical methods such as ARIMA or MCS to perform dynamic prediction tasks and assess the risk with the availability of dynamic data sources [24,25]. The term "agent", or software agent, has found its way into many technologies and has been widely used, for example, in artificial intelligence [26], data processing [25], operating systems [27], and healthcare and computer networks [28] literature. An agent can execute several behaviors concurrently. However, it is important to note that the scheduling of behaviors in an agent is collaborative rather than preemptive (as for running threads). This means when behavior is scheduled for execution, its action method is not called but runs until it returns, dynamically deliberating the selection of action options based on the agent and the environmental conditions [22,29].

The problem of distributed risk assessment, however, depends on the communication agent and collaboration features. Each agent represents a location or city in multiple city environments in which the agents need to communicate with each other to assess the global risk of air pollution [23,30]. Agent communication is probably the most utilized feature of the Java Agent Development Framework (JADE) [31]. The communication paradigm is based on asynchronous message passing. Thus, each agent has a "mailbox" (the agent message queue) where the JADE run-time posts messages sent by other agents [30]. The receiving agent is notified whenever a message is posted in the mailbox message queue. However, the agent picking up the message from the queue for processing is a design choice of the agent programmer. This process is depicted in Figure 3.

Each message includes the following fields: (i) the sender of the message; (ii) the list of receivers; and (iii) the communicative act (also called the "performative") indicating what the sender intends to achieve by sending the message. For instance, if the performative is REQUEST, the sender wants the receiver to act, if it is INFORM, the sender wants the receiver to be aware of a fact. The content containing the actual information to be exchanged by the message (e.g., the action to be performed in a REQUEST message, or the fact that the sender wants to disclose in an INFORM message, etc.). The content language indicates the syntax used to express the content. Both the sender and the receiver must be able to encode and parse expressions compliant with this syntax for the communication to be effective.

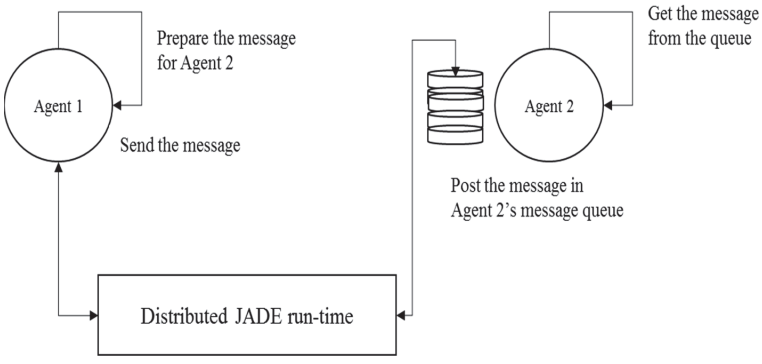

Figure 3. The asynchronous message passing in a MAS [31].

2.4. Evaluation Metrics

In order to evaluate the performance of a forecasting system, we use several model performance measures such as MAE, RMSE [25]. The formulas of the statistical measures used herein are as follows:

$$MAE = \frac{1}{n}\sum_{i=1}^{n}|Yi - yi| \tag{4}$$

$$RMSE = \sqrt{\frac{\sum_{i=1}^{n}(Y_i - y_i)}{n}} \tag{5}$$

Y_i and y_i are the forecast value and the observed value, respectively. MAE and RMSE are applied as the performance criterion of the prediction model to quantify the errors of forecasting values. In general, the smaller the values, the better the prediction or the closer the estimator approaches the actually observed ones.

3. Air Pollution Global Risk Assessment (APGRA) Model

The Air Pollution Global Risk Assessment (APGRA) model consists of local air pollution risk assessment and Global air pollution risk assessment. The local air pollution risk assessment has an improved ARIMA-based MCS algorithm that performs local forecasting to the AQI risk of a particular area or city. Subsequently, in the Global AQI risk assessment, the APGRA model offers more accurate and global-oriented AQI forecasting through deploying MAS architecture in which agents are controlling the ARIMA-based MCS algorithm of cities. The APGRA model performs based on agent interaction and processing of the AQIs' parameters.

3.1. Air Pollution Local Risk Assessment

This section explains the usage of the MCS to accommodate the uncertainty of the forecasting method presented in the ARIMA-based MCS algorithm. The concept of using MCS is to exploit the repeated sampling of the operation of the ARIMA outcomes to provide a more accurate description of the forecasting results of the local air pollution risk assessment. The ARIMA-based MCS algorithm defines a set of parameters that describe our usage of the MCS. Firstly, the algorithm selects the time interval that is used to fit the simulation model. The $ARIMA(p, I, q, i, j)$ function has the p, q, I, which are the same as presented earlier, and i, j represents the subject time series type and city that is under simulation. Secondly, the algorithm selects the time interval T_past that is used for fitting $ARIMA(p, I, q, i, j)$, and users assign it. Thirdly, the ARIMA-based MCS algorithm selects the time horizon T_future that the forecasting model uses. Fourthly, the algorithm selects the number of runs N_runs that MCS uses.

Algorithm 1 shows the ARIMA-based MCS. The main task of the MCS is to execute the forecasting of the ARMIA that is fitted in the requested T_past for the requested T_future.

This procedure is repeated several times equal to *N_runs*, representing the number of simulations. After accumulating all the forecasted time series, we calculated the random process summarized by the distribution of the predicted time series. Assuming that the distribution is normal, the ARIMA-based MCS algorithm offers two series, *y_forecasted*, which provides the forecasted time series, and *σ_forecasted*, which provides the indicator of the confidence or risk of the local AQI forecasting.

Algorithm 1 Air Pollution Local Risk Assessment Algorithm

Input
initial input < *ARIMA* (*p*, *I*, *q*, *i*, *j*); *T_past*; *T future*; *N_runs*; *y_history* >;
initial output < *y_forecasted*, *σ_forecasted* >;
Output
Y = []; *y_forecasted*; *σ_forecasted*;
Start
prediction model = fit*ARIMA* (*p*, *I*, *q*, *i*, *j*, *T_past*, *N_runs*, *y_history*);
for t = 1 until No_runs do:
y_forecasted = forecast (model, T_past, T_future);
Y = add(*y_forecasted*);
end
σ_forecasted = sqrt(variance(Y));
y_forecasted = avg(Y);
End

3.2. Air Pollution Global Risk Assessment

The issue with the previous algorithm of the ARIMA-based MCS algorithm is its non-awareness of the global aspect regarding possible interaction between individual cities. In order to overcome this matter, the APGRA model is designed to assess a global value of the AQI that takes into account dynamic parameters reading at multiple, distributed local stations. The global model is developed based upon a MAS architecture consisting of many local agents representing a specific city. Local AQI forecast values are aggregated into the APGRA model based on the city's wind speed and direction under study. Figure 4 depicts the single-agent processing and how to be communicated with MAS.

The decisions affect the interval of training the agent models and the horizon of forecasting and prediction. Each agent is equipped with an ARIMA-based MCS algorithm. The concept of collaborative MAS is essentially in estimating the global air pollution risk. In collaboration, agents work together to solve a complex problem of global risk while achieving their personal goals of local risk. The risk assessment visualization is a module used to present the risk assessment results for local and global risks. Based on Figure 4, the inputs of the APGRA model come from two sources, data provider and risk level, as shown in Figure 5. Firstly, the data provider is the historical time series data of various pollution and weather variables collected across all cities in the last T_y years. Secondly, the risk level is used to feed the data to the model by a mediator agent. The data fed into each city's computation layer is a combination of N agents, where N denotes the number of variables provided. Each agent is responsible for using the data to build the corresponding variable and the city's primary prediction algorithm. The agents are denoted as *Ai*,*j* where $i = 1,2 \ldots M$ and $j = 1,2 \ldots$ N indicates the number of variables, and M indicates the number of cities.

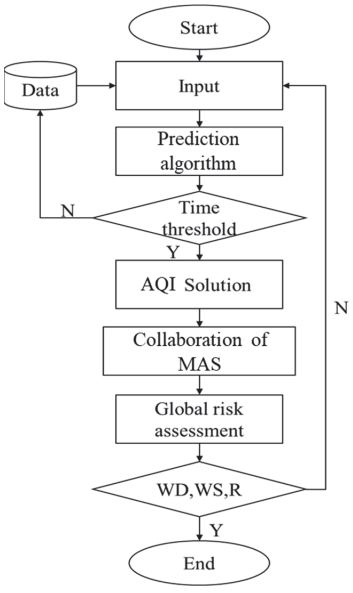

Figure 4. A single agent processing cycle.

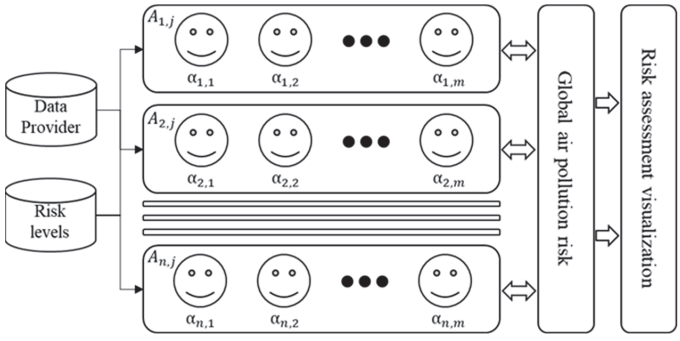

Figure 5. Air Pollution Global Risk Assessment (APGRA) model.

Figure 6 illustrates an example of local air pollution prediction and global air pollution assessment. The example consists of two neighboring cities that have an interaction effect. Each city has different local and global parameters with variable concentrations or values used to predict the local and global risk. The local pollution parameters are CO, NO_2, O_3, SO_2, and PM_{10}. In contrast, the global meteorological parameters are wind direction and wind speed. The local parameters are used to predict the local air pollution risk via utilizing the ARIMA-based MCS algorithm. Next, assess the global air pollution risk levels based on wind direction and wind speed by using the APGRA model.

Agents communicate with each other, and the coordinator agent (mediator Agent) is responsible for interacting with the user and commanding two components; global AQI reading and local ARIMA-based MCS forecasts. This model includes the global risk assessment agent, which interacts with other agents to estimate the global risk. The pseudo-code in Algorithm 2 begins by scanning the cities, one by one, using the loop given in line number 1. Next, each subject city builds a circle around itself with radius R, and checks the wind speed and direction. If the wind speed is higher than a predefined threshold speed and the wind direction is towards the subject city, then it will be regarded as a source of effect to the subject city. Then the algorithm goes through the time series of the subject city,

one by one, and changes them to include the effect of the corresponding time series of the subject city. A coefficient factor named alpha is used for adding the effect. After summing the effects of all source cities for a certain time series, it will be added to the subject city.

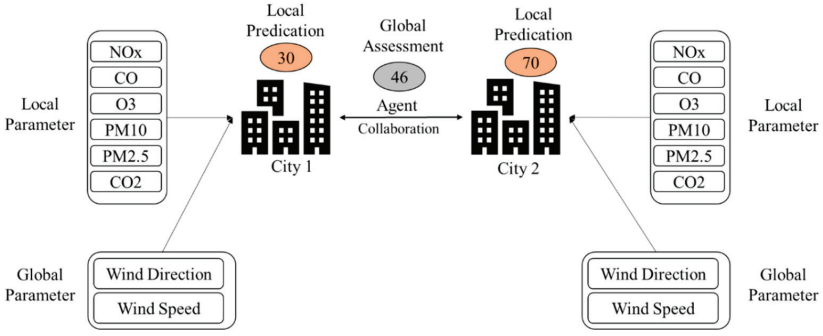

Figure 6. An example application of the APGRA model.

Algorithm 2 Air Pollution Global Risk Assessment Algorithm

```
Input
    A(i, j) // I = 1, 2, ..., n umber of cities; j = 1, 2, ..., m number of time series // this represents
    the original agent's models
    WS(i) // wind speed at city i
    WD(i) // wind direction at city i
    R // Radius of interaction
    SpeedT // lower speed effec
Output
    AI (i, j) // this represents the model after modifying with global interaction
Start
    for i = 1: n // to go through all cities
      cities = find Cities (i, R) // for each city we find influencing city
      for k = 1: length(cities)
        if(WS(k) > SpeedT and WD(i) is toward location of city k)
          for j = 1:m
            AI (i, j) = alpha*WS(k)*A (k, j) // to change all-time
            series to be affect by the source city
          end
          AI (i, j) = A (i, j) + AI (i, j)
      end
    end
  end
End
```

Based on Algorithm 2, assuming that the $A_s(i,j)$ represents the agent that is responsible for forecasting. When a request for forecasting is given to $A_s(i,j)$, a circle with a radius R will be created around the city i. Hence the surrounding cities will be taken as the source of effect to the subject model of $A_s(i,j)$. The effect source is represented as $SE(i,j) = (a_{j1}, a_{j2}, \ldots a_{je})$. Next, a vector of influence factors for each of the agent $SE(i,\ j)$ is created based on the wind direction and speed described by the pseudocode.

This vector is called $fWE(i,j) = (w_{j1}, w_{j2}, \ldots w_{je})$. Then the forecasting model at the city i and the variable j will be as shown in Equation (6).

$$A_{gs}(i,j) = A_s(i,j) + w_{j1} \times a_{j1} + w_{j2} \times a_{j2} + ..w_{je} \times a_{je} = A_s(i,j) + SE.WE \quad (6)$$

3.3. Risk Forecasting

The role of the APGRA is to issue an alarm when the AQI reaches a certain time series that indicates high risk. This alarm will be issued in a probabilistic way using the results of the ARIMA-based MCS and has been calculated using Equation (5).

$$P_{L_i} = P(y(t) > L_i) = \frac{N_{L_i}}{N_S} \tag{7}$$

3.4. Correlation Analysis

Correlation analysis is used to quantify the degree of relationship between two continuous variables, such as in between an independent and a dependent variable or between two independent variables. The correlation analysis is meant to prove or validate the correctness of the air pollution risk assessment operation. Figure 7a–e highlights the correlation between AQI reading and the concentrations of the parameters that affect air quality in the Malaysia case study, which are O_3, PM_{10}, NO_2, CO, and SO_2. The figures show that O_3, NO_2, and CO concentrations are around 0.2, with SO_2 having an even lower correlation of 0.08. These concentrations indicate a very low relationship with the AQI reading but will alert the prediction system if the concentrations increase. The highest correlation between the concentrations and the AQI is of PM10, which correlates with around 0.7. This indicates a high presence of particulate matter <10 μm in Malaysian air.

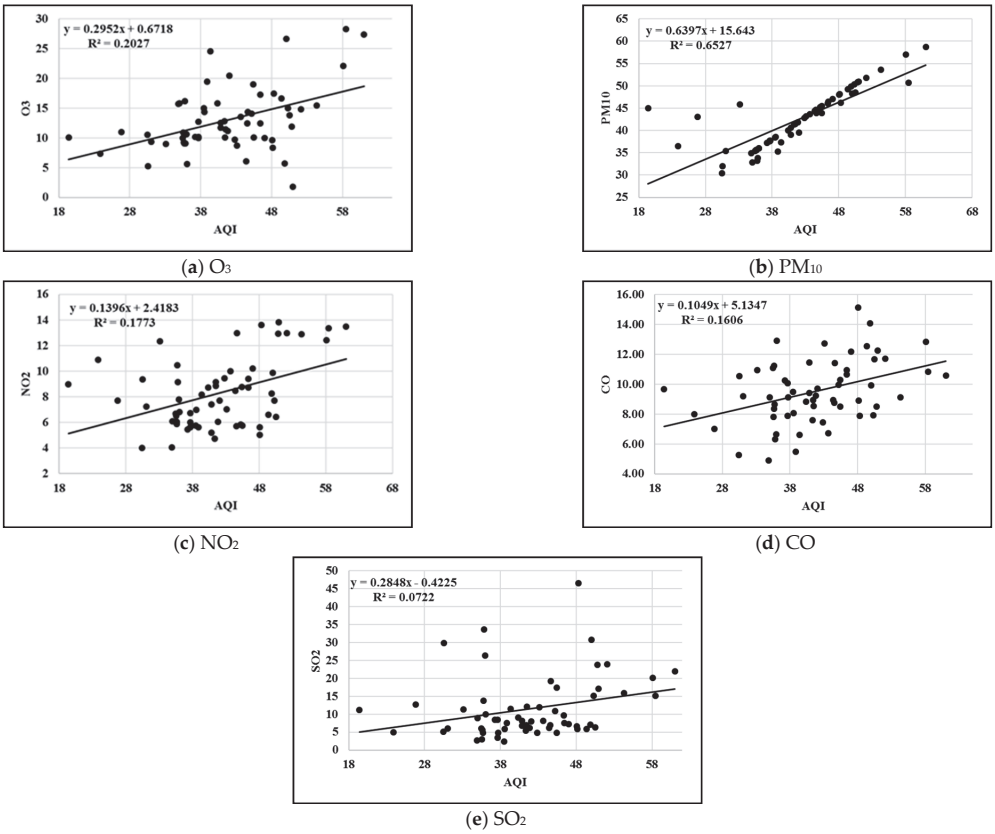

Figure 7. Correlation between AQI levels and all parameters in Malaysia.

Next, Figure 8a–e highlights the correlation between AQI reading and all parameters that affect air quality in the China case study, which are O_3, PM_{10}, NO_2, SO_2, and $PM_{2.5}$. From the figures, it can be seen that most of the concentration correlations are higher in China compared to Malaysia. Correlations of O_3 and NO_2 are low, around 0.2 and 0.3, respectively. Other parameters show a high correlation with AQI in China, with SO_2 around 0.6, while $PM_{2.5}$ and PM_{10} are both around 0.9.

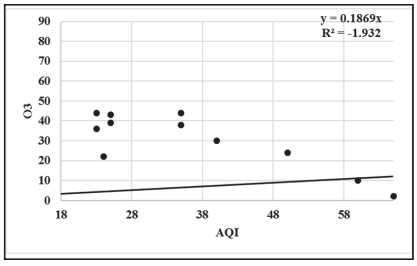

(**a**) O_3

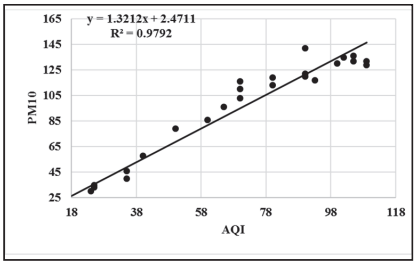

(**b**) PM_{10}

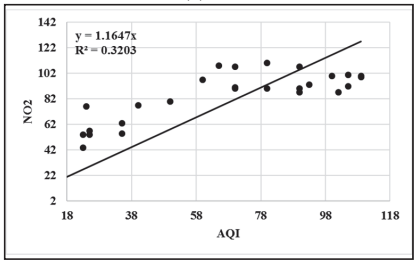

(**c**) NO_2

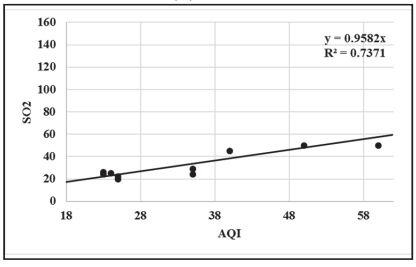

(**d**) SO_2

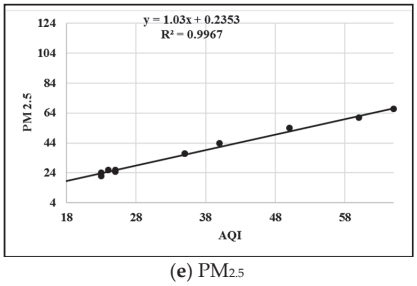

(**e**) $PM_{2.5}$

Figure 8. Correlation between AQI levels and all parameters in China.

For both case studies in Malaysia and China, the correlation analysis shows that the particulate matter, which is small enough to be suspended in the air, has a high degree of relationship with the AQI. In general, particle matter less than 10 μm in diameter can get deep into the lungs and, in some cases, into the bloodstream, which must be monitored closely by both countries. This implies that $PM_{2.5}$, tiny particles in the air that are two and one half microns or less in width, pose the greatest risk to health as compared to PM_{10}. Studies show that ambient $PM_{2.5}$ concentrations were significantly associated with influenza-like illness (ILI) risk in Beijing, China [11].

4. Results and Discussion

Prediction of the air pollutant concentrations represents a complex spatio-temporal problem due to the dynamic nature and high spatio-temporal variability in air pollution data. This section presents the results of the AQI prediction between three models: (i) the base model ARIMA; (ii) the ANFIS model of Prasad et al. [12]; and (iii) the improved ARI

APGRA model by MA-based MCS algorithm. Prediction model performance is evaluated according to accuracy based on MAE and RMSE as well as prediction ability based on the coefficient of determination R_2.

4.1. Comparison between AQI Prediction Models

The experiments aim to examine the proposed model effectiveness in predicting AQI concentrations for one day and two days in advance. The results are compared between the real AQI values against the base models of ARIMA, ANFIS, and the APGRA models for two separate case studies from Malaysia and China. Based on Table 3, the best prediction in the Malaysia case study achieved for one-day prediction is at City 10, and two-day prediction is at City 7. The prediction of the first day yields a lower error than the second day since the prediction error for one day in advance is brought into the next day's prediction. The APGRA model produced the best results compared to the direct approach in the APGRA and ANFIS models for both one-day and two-day predictions. This shows that the APGRA model plays an important role in obtaining good prediction results with approximately 41% improvement on RMSE. This is attributed to incorporating uncertainty into the prediction, which allows for exploiting the repeated sampling of the operation that improves the accuracy of the forecasting. From the aspect of absolute errors, as measured by RMSE and MAE, the best prediction for one day is achieved by City 10 using MCS. The fact that City 10 produced lower absolute error than other cities indicates the importance of the local environment where a station is located. City 10 is located in the zone of "clean source". Therefore, the low variability of AQI concentrations makes it easier to predict than other cities. Nevertheless, the best R_2 is achieved for both one-day and two-day predictions at City 8, which indicates that the relative measure can objectively evaluate the prediction model in different backgrounds. The AQI prediction results showed a good R_2. Moreover, ARIMA produced better results than the APGRA model and ANFIS approach for both one-day and two-day prediction in terms of processing time. The result shows that the best algorithm among the three is the APGRA model in terms of RMSE and MAE as it achieves an average R_2 of 0.772, RMSE of 1.891, MAE of 1.642 and time of 7.57. The basic ARIMA average is R_2 of 0.571, RMSE of 3.22, MAE of 2.874, and time of 5.97. The ANFIS benchmark average R_2 of 0.48, RMSE of 3.7, MAE of 3.33 time of 10.37.

Based on Table 4, the best prediction in the China case study is achieved for one-day in City 1, and two-day is at City 3. The prediction values of the first day yield lower error rates than the second day. This can be explained by the theory of error accumulation since the forecasting error for one day in advance is brought into the next day's prediction. The ARIMA-based MCS yields better results than the direct approach ARIMA and ANFIS models for both one-day and two-day forecasts. This confirms the ability of the Monte Carlo simulation to accurately reproduce the sample, which boosts the predictive power of ARIMA. The results show that the ARIMA-based MCS algorithm plays an important role in obtaining good prediction results with approximately 47% improvement on RMSE. As measured by RMSE and MAE, the best prediction is achieved for one day using the APGRA model from the aspect of absolute error. Nevertheless, the best R_2 is achieved for both one-day and two-day predictions, which indicates that the relative measure can evaluate the prediction model in different backgrounds.

Subsequently, the APGRA model provides the best solution among the three in terms of RMSE, MAE, and R_2. The model achieves an average R_2 of 0.852, RMSE of 7.509, MAE of 5.909, and time of 3.34. The basic ARIMA average R_2 of 0.718, RMSE of 14.14, MAE of 11.86, and time of 2.65. The ANFIS benchmark model achieves an average R_2 of 0.615, RMSE of 13.426, MAE of 11.4146, and time of 7.7.

Table 3. Comparison between the three AQI prediction algorithms in Malaysia dataset.

AQI 1-Day Advance Prediction											
	Metric	**City 1**	**City 2**	**City 3**	**City 4**	**City 5**	**City 6**	**City 7**	**City 8**	**City 9**	**City 10**
ARIMA	R_2	0.83	0.24	0.33	0.47	0.87	0.34	0.48	0.92	0.89	0.34
	RMSE	3.84	2.83	4.99	2.66	3.78	2.77	2.18	3.11	4.71	1.33
	MAE	3.45	2.69	4.40	2.32	3.40	2.26	2.04	2.78	4.30	1.10
	Time	7.20	6.30	5.20	6.30	6.50	4.70	3.80	6.60	6.90	6.20
MCS	R_2	0.91	0.75	0.50	0.64	0.89	0.88	0.73	0.94	0.92	0.56
	RMSE	2.15	1.08	2.05	1.24	3.08	1.92	1.02	2.47	3.10	0.80
	MAE	1.90	1.03	1.89	1.06	2.60	1.60	0.88	2.11	2.70	0.65
	Time	8.40	8.30	6.20	8.30	7.50	6.70	6.80	7.50	7.90	8.10
ANFIS	R_2	0.8	0.6	0.4	0.3	0.8	0.1	0.1	0.9	0.7	0.1
	RMSE	4.3	3.3	5	3.2	4.5	4	2.3	3.4	5	2
	MAE	4	3.1	4.4	2.7	4.1	3.5	2	3	4.8	1.7
	Time	10.40	12.30	9	11	9	9	9	11	12	11
AQI 2-Day Advance Prediction											
	Metric	**City 1**	**City 2**	**City 3**	**City 4**	**City 5**	**City 6**	**City 7**	**City 8**	**City 9**	**City10**
ARIMA	R_2	0.12	0.20	0.30	0.39	0.01	0.02	0.25	0.82	0.80	0.10
	RMSE	19.40	9.20	5.90	22.30	14.80	8.10	3.60	6.76	12.60	16.20
	MAE	15.30	7.20	5.31	16.80	12.00	6.90	3.36	3.80	10.50	11.38
	Time	9.20	7.40	7.20	7.30	7.50	6.70	6.80	8.80	8.30	7.30
MCS	R_2	0.20	0.50	0.40	0.40	0.89	0.08	0.75	0.90	0.88	0.49
	RMSE	10.90	5.36	4.52	11.30	4.47	2.50	1.72	4.14	9.00	4.60
	MAE	7.96	3.75	3.77	8.51	3.54	1.95	1.42	2.66	7.00	2.80
	Time	9.80	9.40	9.80	9.50	9.20	8.70	8.30	9.80	9.30	9.30
ANFIS	R_2	0.1	0.4	0.6	0.4	0.1	0.1	0.3	0.9	0.8	0.2
	RMSE	19	9.3	3.9	22	14	8	2.7	3.2	12	16.4
	MAE	15.6	7.4	3.3	17	12	7	2.3	2.9	10	11.7
	Time	13	15	14	15	14	13	14	15	15	14

4.2. Results of Global Air Pollution Risk Assessment Model

The APGRA model is the best prediction algorithm because it scores the lowest error from the earlier analysis. However, the AQI's prediction poses a distributed problem because the pollution risks are distributed in multiple places of cities. In turn, the process of risk as a prediction model is important to aggregate the risks from various local stations as represented in cities in both Malaysia and China case studies. Moreover, finding the risk level from AQI of various parameters is one of the main objectives of this research. As a result, this paper proposes a Global Air Pollution Risk Assessment (APGRA) model based on a collaborative multi-agent architecture where each city is modeled as a collaborative agent. This model, therefore, aggregates risk input from multiple agents residing in distributed cities to produce a single global air pollution prediction value. An APGRA model is implemented in a system for testing and evaluation to achieve this. Figure 9a shows the mediator agent in APGRA with a dynamic selection of the number of agents to work with. The mediator agent in the APGRA model is responsible for decision-making depending on the information that comes from multiple agents (cities). The information that comes from the multi-agents includes the configuration of the main agent, the direction of the wind, the threshold for the error of prediction, the amount of data, the information sent between agents, the main city understudy, and other cities affected by the main city. The main agent aggregates all risk information calculated by the multi-agents depending on the individual AQI level in each city. The parameter of different forms of air pollution in this research depends on the case study. Malaysia, for example, does not measure $PM_{2.5}$ in all cities. The mediator agent in APGRA monitors and visualizes the current range of data as determined by the user, along with options to filter data by year, month,

and day. APGRA also provided the option to choose the model for calculating local AQI prediction, such as the ARIMA-based MCS. This model relies on cooperative multi-agents to produce the global assessment of air pollution. Figure 9b shows the cooperation process among the single agents representing a single city. Assessment becomes more complex and challenging, resulting in a global air pollution risk.

Table 4. Comparison between the three AQI prediction algorithms in China dataset.

AQI 1-Day Advance Prediction											
	Metric	**City 1**	**City 2**	**City 3**	**City 4**	**City 5**	**City 6**	**City 7**	**City 8**	**City 9**	**City 10**
ARIMA	R_2	0.97	0.94	0.55	0.89	0.58	0.45	0.66	0.40	0.81	0.93
	RMSE	4.45	9.78	6.14	10.0	5.46	20.2	21.4	30.4	19.1	14.24
	MAE	3.32	8.39	5.38	8.54	4.88	15.1	16.7	26.3	17.4	12.46
	Time	2.70	3.00	2.50	2.80	2.30	2.70	2.70	2.80	2.90	2.10
MCS	R_2	0.98	0.95	0.83	0.91	0.73	0.81	0.93	0.50	0.91	0.97
	RMSE	2.70	4.64	2.95	5.70	2.30	16.7	9.80	11.0	12.9	6.40
	MAE	1.80	3.75	2.40	4.54	2.00	11.7	7.10	9.80	10.7	5.30
	Time	3.10	3.90	3.10	3.90	3.10	3.10	3.90	3.10	3.10	3.10
ANFIS	R_2	0.8	0.8	0.40	0.79	0.63	0.25	0.69	0.14	0.73	0.92
	RMSE	4.43	10.3	6.09	8.99	6.12	13.3	19.7	30.0	20.5	14.7
	MAE	3.22	8.6	5.1	7.9	5.41	10.8	15.9	26	18.3	12.9
	Time	7	8	7	8	8	7	8	9	8	7
AQI 2-Day Advance Prediction											
	Metric	**City 1**	**City 2**	**City 3**	**City 4**	**City 5**	**City 6**	**City 7**	**City 8**	**City 9**	**City 10**
ARIMA	R_2	0.90	0.86	0.69	0.64	0.89	0.74	0.52	0.30	0.58	0.817
	RMSE	15.8	22.1	11.1	15.0	13.2	30.3	25.2	38.7	21.6	18.98
	MAE	9.91	17.2	8.42	11.1	9.38	25.6	21.5	30.3	20.1	16.25
	Time	3.20	4.10	4.10	4.10	4.30	3.20	3.20	3.20	4.30	4.30
MCS	R_2	0.94	0.87	0.76	0.75	0.96	0.85	0.82	0.40	0.81	0.90
	RMSE	11.6	15.7	7.20	11.2	9.70	21.9	15.0	27.0	13.7	11.50
	MAE	6.80	10.6	4.70	7.40	6.00	17.9	11.8	17.0	12.1	9.00
	Time	4.10	4.90	4.80	4.90	4.80	4.80	4.80	4.10	4.80	4.10
ANFIS	R_2	0.9	0.8	0.5	0.6	0.8	0.7	0.5	0.5	0.5	0.8
	RMSE	16	22	11	15	13.5	30	24	39	23	19
	MAE	10	17	8	11	9.5	26	21	30	20	16
	Time	9	9	8	8	9.20	9.30	9.20	9.40	8.90	8.60

Figure 10a,b show the global AQI values from all cities in the different case studies (Malaysia and China). Note that the proposed ARIMA-based MCS algorithm conducted local prediction of AQI levels. Subsequently, the APGRA model under this multi-agent architecture produces a singular global air pollution risk prediction value.

The APGRA model depends on the wind data, which are wind speed and wind directions, to produce the global prediction value. This is important to illustrate the dynamic changes of air pollution risks for a specific city concerning other cities. Wind direction determines the direction of pollution, while wind speed determines the zone pollution. There exists a direct correlation between the pollution zone and wind speed. When the wind speed increases, the zones of pollution increases as well, and this relationship can be shown by the APGRA. Figure 11 explains how the APGRA model work relies on wind data in several cities in Malaysia with a ring of pollution zone between 0.5 km to 5 km.

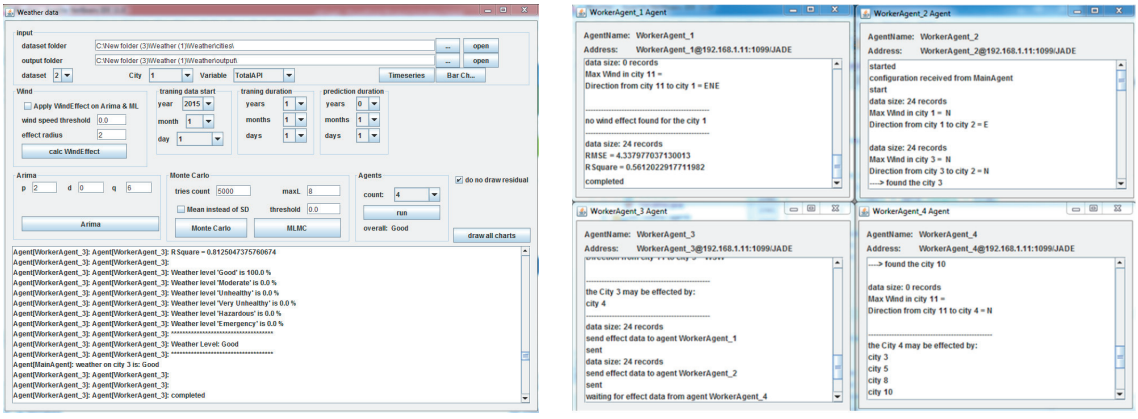

(**a**) (**b**)

Figure 9. The implementation results of the APGRA model. (**a**) The GUI of the mediator agent; (**b**) Cooperation among agents.

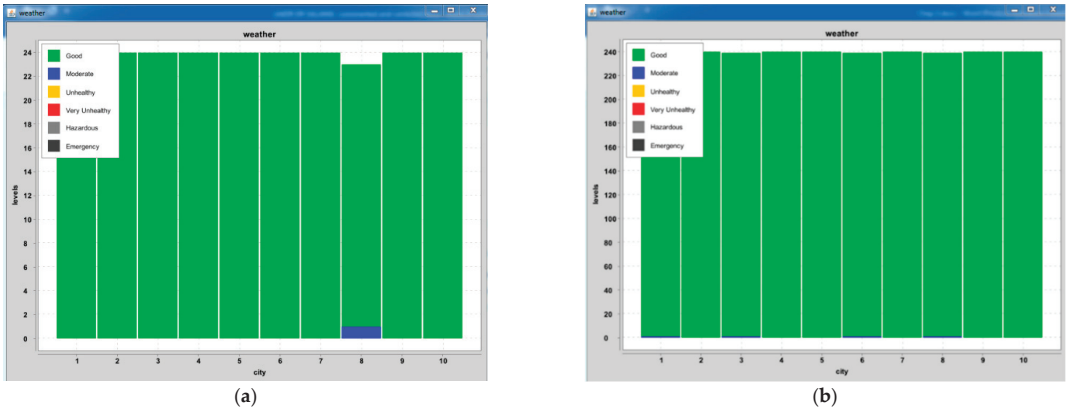

(**a**) (**b**)

Figure 10. The AQI levels of different cities.(**a**) Global AQI level in Malaysia dataset; (**b**) Global AQI levels in China dataset.

Based on Figure 11, if the wind speed is normal at 5 km/h, the zone pollution will be 0.5 km (refer to Figure 11a). If the wind speed is between 10 to 20 km/h, the zone pollution will be 1 km (refer to Figure 11b). If the wind speed is between 20 to 30 km/h, the zone pollution will be 2 km (refer to Figure 11c). Finally, if the wind speed is more than 30 km/h, the zone pollution will be 5 km (refer to Figure 11d).

Table 5 explains the results of the global air pollution risk assessment model that depends on wind data to calculate the interaction pollution among cities for two case studies (Malaysia and China). The proposed model calculates the air pollution level for each city then calculates the global air pollution level for all cities. The wind speed corresponds to the area of pollution zones, whereas the area of pollution zone increases proportionally according to the increase of wind speed. The wind direction responds to the direction of pollution, which might also affect the other cities. The obtained results of the APGRA model are compared with the actual data of the ten cities in both case studies. The estimated risk levels of the 10 cities in both case studies have a full match. This indicates that the APGRA model correctly predicts global risk levels. This is attributed to the ability of APGRA to assess the global value of the AQI and take into account dynamic parameter readings at multiple, distributed local stations. Therefore, the prediction model becomes

aware of the global aspect regarding possible interaction between individual cities, which improves the proposed APGRA.

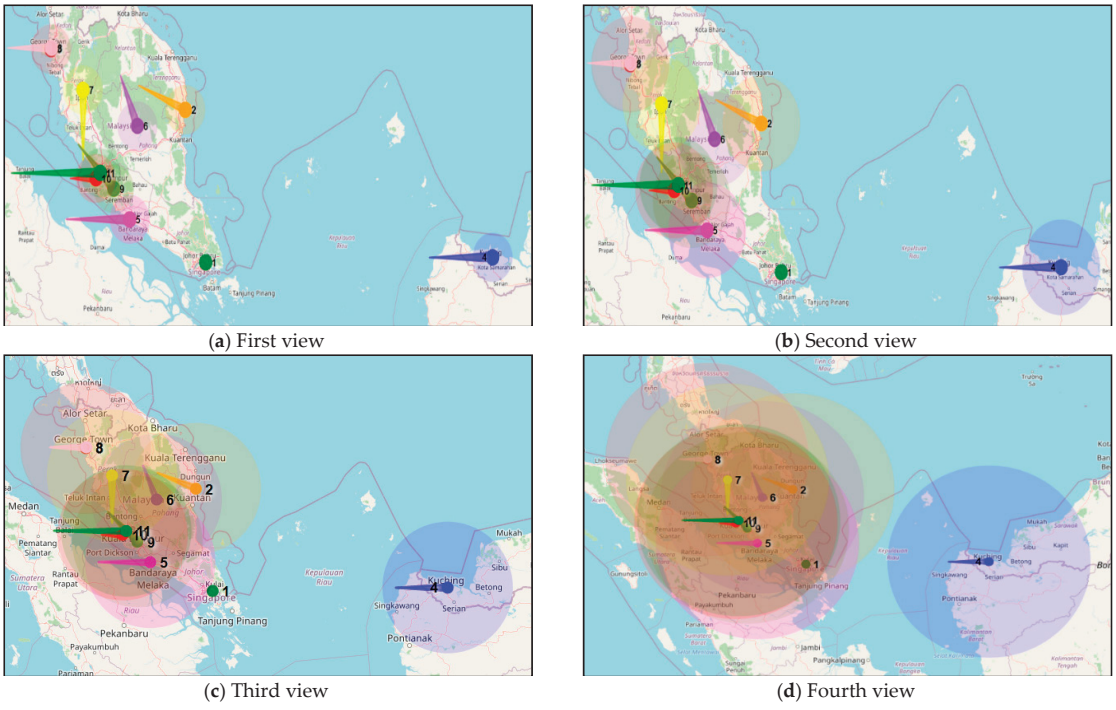

(**a**) First view (**b**) Second view

(**c**) Third view (**d**) Fourth view

Figure 11. The radius of pollution.

Table 5. Sample of global air pollution risk levels.

AQI 1-Day Advance Assessment of Risk Level in Malaysia Dataset										
Results	**City 1**	**City 2**	**City 3**	**City 4**	**City 5**	**City 6**	**City 7**	**City 8**	**City 9**	**City 10**
Risk level	good	good	moderate	good	good	good	good	moderate	moderate	good
Affected by	none	none	7,9	none	3,8	none	none	7,9	none	9
Effect on	none	none	5	none	none	none	3	5	7,3,10	none
Effect zone	1	2	0.5	1	1	0.5	2	2	2	1
R_2	0.9	0.6	0.5	0.8	0.7	0.6	0.6	0.7	0.8	0.6
RMSE	1.06	2.6	2.98	1.7	1.8	2	2.2	3.1	1.3	1.9
MAE	0.7	1.2	1.7	1.2	1.37	1.5	1.55	1.78	0.9	1.3
Time	3.20	5.30	4.20	3.30	3.20	4.90	4.80	3.20	3.90	5.10
AQI 1-Day Advance Assessment of Risk Level in China Dataset										
Results	**City 1**	**City 2**	**City 3**	**City 4**	**City 5**	**City 6**	**City 7**	**City 8**	**City 9**	**City 10**
Risk level	moderate	good	moderate	good	good	moderate	good	moderate	good	good
Affected by	none	9	4	none	none	none	none	4	none	4
Effect on	none	none	none	8,3,10	none	none	none	none	2	none
Effect zone	0.5	0.5	1	1	0.5	0.5	0.5	2	0.5	0.5
R_2	0.6	0.6	0.8	0.8	0.9	0.5	0.7	0.7	0.8	0.9
RMSE	2.8	3.2	4.5	5	5.2	5.1	4.8	5.8	6.8	4
MAE	2.1	2.4	3.2	3.75	4.1	3.6	3.4	4	4.5	2.8
Time	3.70	3.20	3.10	3.20	3.20	3.20	3.20	3.70	3.90	3.20

Table 5 appointed the RMSE, MAE, R_2, and processing time. The APGRA model matches greatly with actual data, representing R_2, that showed low errors, good processing time, good ability, and flexibility. At the same time, the Malaysia case study's average performance metrics are R_2 of 0.7, RMSE of 2.064, MAE of 1.32, and time of 4.11. Likewise, China's case study average performance metrics are R_2 of 0.73, RMSE of 4.72, MAE of 3.385, and a time of 3.36.

5. Conclusions

This paper proposed a new air pollution global risk assessment (APGRA) model for predicting spatial correlation AQI risk assessment to address these issues. The APGRA model incorporates the autoregressive integrated moving average (ARIMA), Monte Carlo simulation (MCS), the collaborative multi-agent system (MAS), and the prediction algorithm for reducing AQI prediction error and time. The proposed APGRA model was evaluated based on Malaysia and China's two real-world air quality datasets. The APGRA model improved the average Root Mean Squared Error (RMSE) by 41%, and the Mean and Absolute Error (MAE) by 47.10% when compared to the conventional ARIMA model and ANFIS model. The accuracy level of the ARIMA-based MCS algorithm was stably higher than that of ARIMA. In particular, RMSE and MAE of ARIMA-based MCS algorithm generated significant improvements, which helps to estimate the variation trend of the AQI concentrations. The proposed model provided the variance prediction in addition to AQI concentrations prediction, expressing more information on the forecasting target. We analyzed and explained the AQI concentrations prediction with the ARIMA-based MCS algorithm, and the simulation results proved outstanding in adapting to the proposed model. The ARIMA-based MCS algorithm can be applied to other AQI forecasting if the model's appropriate input variables are selected. Some issues still need further investigation. This includes study areas that their $PM_{2.5}$ emission data was not available. The $PM_{2.5}$ with complex components exhibits a high correlation with the other AQIs. It is rather remarkable that the influence of $PM_{2.5}$ on AQI should be considered in the forecasting system. The $PM_{2.5}$ with complex components is another issue that exhibits a high correlation with the other AQIs. Therefore, it is rather remarkable that the influence of different AQIs on $PM_{2.5}$ should be considered in the forecasting system. As we mentioned before, the APGRA model solves the global pollution interaction between cities depending on a local ARIMA-based MCS algorithm developed in this paper and some additional parameters such as wind speed and wind direction. The issue with the ARIMA-based MCS algorithm is the cost of the simulation, resulting from the need to apply significant values of p and q that led to consuming processing time.

Author Contributions: Conceptualization, M.H.H. and S.A.M.; methodology, M.H.H., S.A.M. and A.M.; software, M.H.H. and M.A.J.; validation, M.H.H., S.A.M. and M.Z.S.; formal analysis, M.H.H. and B.A.S.A.-r.; investigation, M.H.H. and S.A.M.; resources, M.Z.S., F.S. and A.E.M.E.; data curation, M.H.H.; writing—original draft preparation, M.H.H., S.A.M. and A.M.; writing—review and editing, M.H.H., S.A.M. and M.A.J.; visualization, M.H.H., F.S. and B.A.S.A.-r.; supervision, S.A.M. and A.M.; project administration, M.Z.S., S.A.M. and A.M.; funding acquisition, M.Z.S., S.A.M. and A.E.M.E. All authors have read and agreed to the published version of the manuscript.

Funding: The authors express appreciation to the Malaysia Ministry of Higher Education (MoHE). This research was funded by the Fundamental Research Grant Scheme (FRGS/1/2019/ICT04/UTHM/03/1) grant vot number K209.

Informed Consent Statement: Not applicable.

Data Availability Statement: The used dataset of this research is available online and has a proper citation within the paper contents.

Acknowledgments: The authors would like to thank the Department of Environment (DOE) for providing the required data and assistance for this work. The authors also would like to thank the Center of Intelligent and Autonomous Systems (CIAS) at the Faculty of Computer Science and Information Technology (FSKTM), Universiti Tun Hussein Onn Malaysia (UTHM) for supporting this work.

Conflicts of Interest: The authors declare that they have no conflict of interest to be addressed related to this work.

References

1. Zhang, S.; Guo, B.; Dong, A.; He, J.; Xu, Z.; Chen, S.X. Cautionary tales on air-quality improvement in Beijing. *Proc. R. Soc. A Math. Phys. Eng. Sci.* **2017**, *473*, 20170457. [CrossRef] [PubMed]
2. Liu, Y.S.; Cao, Y.; Hou, J.J.; Zhang, J.T.; Yang, Y.O.; Liu, L.C. Identifying common paths of CO_2 and air pollutants emissions in China. *J. Clean. Prod.* **2020**, *256*, 120599. [CrossRef]
3. Li, J.; Tartarini, F. Changes in air quality during the COVID-19 lockdown in Singapore and associations with human mobility trends. *Aerosol Air Qual. Res.* **2020**, *20*, 1748–1758. [CrossRef]
4. Nyoni, T.; Mutongi, C. Modeling and forecasting carbon dioxide emissions in China using Autoregressive Integrated Moving Average (ARIMA) models. *EPRA Int. J. Multidiscip. Res.* **2019**, *5*, 215–224.
5. Bakhtavar, E.; Hosseini, S.; Hewage, K.; Sadiq, R. Air pollution risk assessment using a hybrid fuzzy intelligent probability-based approach: Mine blasting dust impacts. *Nat. Resour. Res.* **2021**, *30*, 2607–2627. [CrossRef]
6. Siwek, K.; Osowski, S. Data mining methods for prediction of air pollution. *Int. J. Appl. Math. Comput. Sci.* **2016**, *26*, 467–478. [CrossRef]
7. Yang, Z.; Wang, J. A new air quality monitoring and early warning system: Air quality assessment and air pollutant concentration prediction. *Environ. Res.* **2017**, *158*, 105–117. [CrossRef]
8. Tong, R.; Cheng, M.; Zhang, L.; Liu, M.; Yang, X.; Li, X.; Yin, W. The construction dust-induced occupational health risk using Monte-Carlo simulation. *J. Clean. Prod.* **2018**, *184*, 598–608. [CrossRef]
9. Song, C.; Fu, X. Research on different weight combination in air quality forecasting models. *J. Clean. Prod.* **2020**, *261*, 121169. [CrossRef]
10. Yang, H.; O'Connell, J.F. Short-term carbon emissions forecast for aviation industry in Shanghai. *J. Clean. Prod.* **2020**, *275*, 122734. [CrossRef]
11. Feng, X.; Li, Q.; Zhu, Y.; Hou, J.; Jin, L.; Wang, J. Artificial neural networks forecasting of PM2.5 pollution using air mass trajectory based geographic model and wavelet transformation. *Atmos. Environ.* **2015**, *107*, 118–128. [CrossRef]
12. Prasad, K.; Gorai, A.K.; Goyal, P. Development of ANFIS models for air quality forecasting and input optimization for reducing the computational cost and time. *Atmos. Environ.* **2016**, *128*, 246–262. [CrossRef]
13. Zio, E. Challenges in the vulnerability and risk analysis of critical infrastructures. *Reliab. Eng. Syst. Saf.* **2016**, *152*, 137–150. [CrossRef]
14. Wang, P.; Zhang, H.; Qin, Z.; Zhang, G. A novel hybrid-Garch model based on ARIMA and SVM for PM2. 5 concentrations forecasting. *Atmos. Pollut. Res.* **2017**, *8*, 850–860. [CrossRef]
15. Hernandez-Matamoros, A.; Fujita, H.; Hayashi, T.; Perez-Meana, H. Forecasting of COVID19 per regions using ARIMA models and polynomial functions. *Appl. Soft Comput.* **2020**, *96*, 106610. [CrossRef] [PubMed]
16. Benvenuto, D.; Giovanetti, M.; Vassallo, L.; Angeletti, S.; Ciccozzi, M. Application of the ARIMA model on the COVID-2019 epidemic dataset. *Data Brief* **2020**, *29*, 105340. [CrossRef] [PubMed]
17. Westerlund, J.; Urbain, J.P.; Bonilla, J. Application of air quality combination forecasting to Bogota. *Atmos. Environ.* **2014**, *89*, 22–28. [CrossRef]
18. Mannshardt, E.; Benedict, K.; Jenkins, S.; Keating, M.; Mintz, D.; Stone, S.; Wayland, R. Analysis of short-term ozone and PM2. 5 measurements: Characteristics and relationships for air sensor messaging. *J. Air Waste Manag. Assoc.* **2017**, *67*, 462–474. [CrossRef] [PubMed]
19. Qazi, A.; Shamayleh, A.; El-Sayegh, S.; Formaneck, S. Prioritizing risks in sustainable construction projects using a risk matrix-based Monte Carlo Simulation approach. *Sustain. Cities Soc.* **2021**, *65*, 102576. [CrossRef]
20. Zhao, L.; Ji, Y.; Yao, J.; Long, S.; Li, D.; Yang, Y. Quantifying the fate and risk assessment of different antibiotics during wastewater treatment using a Monte Carlo simulation. *J. Clean. Prod.* **2017**, *168*, 626–631. [CrossRef]
21. Gordy, M.B.; Juneja, S. Nested simulation in portfolio risk measurement. *Manag. Sci.* **2010**, *56*, 1833–1848. [CrossRef]
22. Mostafa, S.A.; Ahmad, M.S.; Annamalai, M.; Ahmad, A.; Gunasekaran, S.S. A dynamically adjustable autonomic agent framework. In *Advances in Information Systems and Technologies*; Springer: Berlin/Heidelberg, Germany, 2013; pp. 631–642.
23. Hassan, M.H.; Mostafa, S.A.; Mustapha, A.; Abd Wahab, M.H.; Nor, D.M. A survey of multi-agent system approach in risk assessment. In Proceedings of the 2018 International Symposium on Agent, Multi-Agent Systems and Robotics (ISAMSR), Putrajaya, Malaysia, 27–28 August 2018; Institute of Electrical and Electronics Engineers (IEEE): Putrajaya, Malaysia, 2018; pp. 1–6.

24. Mostafa, S.A.; Ahmad, M.S.; Ahmad, A.; Annamalai, M. Formulating situation awareness for multi-agent systems. In Proceedings of the 2013 International Conference on Advanced Computer Science Applications and Technologies, Kuching, Malaysia, 23–24 December 2013; Institute of Electrical and Electronics Engineers (IEEE): Kuching, Malaysia, 2013; pp. 48–53.
25. Kashinath, S.A.; Mostafa, S.A.; Mustapha, A.; Mahdin, H.; Lim, D.; Mahmoud, M.A.; Yang, T.J. Review of data fusion methods for real-time and multi-sensor traffic flow analysis. *IEEE Access* **2021**, *9*, 51258–51276. [CrossRef]
26. Mostafa, S.A.; Hazeem, A.A.; Khaleefahand, S.H.; Mustapha, A.; Darman, R. A collaborative multi-agent system for oil palm pests and diseases global situation awareness. In Proceedings of the Future Technologies Conference, Vancouver, BC, Canada, 13–14 November 2018; Springer: Cham, Switzerland, 2018; pp. 763–775.
27. Mostafa, S.A.; Mustapha, A.; Gunasekaran, S.S.; Ahmad, M.S.; Mohammed, M.A.; Parwekar, P.; Kadry, S. An agent architecture for autonomous UAV flight control in object classification and recognition missions. *Soft Comput.* **2021**, 1–14. [CrossRef]
28. Khalaf, B.A.; Mostafa, S.A.; Mustapha, A.; Mohammed, M.A.; Mahmoud, M.A.; Al-Rimy, B.A.S.; Marks, A. An Adaptive Protection of Flooding Attacks Model for Complex Network Environments. *Secur. Commun. Netw.* **2021**, *2021*. [CrossRef]
29. Mostafa, S.A.; Gunasekaran, S.S.; Ahmad, M.S.; Ahmad, A.; Annamalai, M.; Mustapha, A. Defining tasks and actions complexity-levels via their deliberation intensity measures in the layered adjustable autonomy model. In Proceedings of the 2014 International Conference on Intelligent Environments (IE '14), Shanghai, China, 30 June–4 July 2014; Institute of Electrical and Electronics Engineers (IEEE): Shanghai, China, 2014; pp. 52–55.
30. Mostafa, S.A.; Mustapha, A.; Mohammed, M.A.; Ahmad, M.S.; Mahmoud, M.A. A fuzzy logic control in adjustable autonomy of a multi-agent system for an automated elderly movement monitoring application. *Int. J. Med. Inform.* **2018**, *112*, 173–184. [CrossRef] [PubMed]
31. Bellifemine, F.L.; Caire, G.; Greenwood, D. *Developing Multi-Agent Systems with JADE*; John Wiley & Sons: Chichester, UK, 2007.

processes

MDPI

Article

A Water Surface Contaminants Monitoring Method Based on Airborne Depth Reasoning

Wei Luo [1,2,3], Wenlong Han [1], Ping Fu [4], Huijuan Wang [1], Yunfeng Zhao [1,2,3], Ke Liu [1,2,3], Yuyan Liu [1,2,3], Zihui Zhao [1,2,3,5,*], Mengxu Zhu [1], Ruopeng Xu [1] and Guosheng Wei [1]

[1] North China Institute of Aerospace Engineering, Langfang 065000, China; luowei@radi.ac.cn (W.L.); m17803269306@163.com (W.H.); wanghj@nciae.edu.cn (H.W.); nanhchao@163.com (Y.Z.); liuke1176@163.com (K.L.); lyy@nciae.ac.cn (Y.L.); mengxu_zhu@163.com (M.Z.); sam970125@163.com (R.X.); convwei@163.com (G.W.)
[2] Aerospace Remote Sensing Information Processing and Application Collaborative Innovation Center of Hebei Province, Langfang 065000, China
[3] National Joint Engineering Research Center of Space Remote Sensing Information Application Technology, Langfang 065000, China
[4] Key Laboratory of Advanced Motion Control, Fujian Provincial Education Department, Minjiang University, Fuzhou 350108, China; shirkl@163.com
[5] School of Geography, Hebei Normal University, Shijiazhuang 050024, China
* Correspondence: 13770765697@163.com

Abstract: Water surface plastic pollution turns out to be a global issue, having aroused rising attention worldwide. How to monitor water surface plastic waste in real time and accurately collect and analyze the relevant numerical data has become a hotspot in water environment research. (1) Background: Over the past few years, unmanned aerial vehicles (UAVs) have been progressively adopted to conduct studies on the monitoring of water surface plastic waste. On the whole, the monitored data are stored in the UAVS to be subsequently retrieved and analyzed, thereby probably causing the loss of real-time information and hindering the whole monitoring process from being fully automated. (2) Methods: An investigation was conducted on the relationship, function and relevant mechanism between various types of plastic waste in the water surface system. On that basis, this study built a deep learning-based lightweight water surface plastic waste detection model, which was capable of automatically detecting and locating different water surface plastic waste. Moreover, a UAV platform-based edge computing architecture was built. (3) Results: The delay of return task data and UAV energy consumption were effectively reduced, and computing and network resources were optimally allocated. (4) Conclusions: The UAV platform based on airborne depth reasoning is expected to be the mainstream means of water environment monitoring in the future.

Keywords: deep learning; edge computing; machine learning; open source unmanned aerial vehicle; plastic waste detection; remote sensing; water environment protection

Citation: Luo, W.; Han, W.; Fu, P.; Wang, H.; Zhao, Y.; Liu, K.; Liu, Y.; Zhao, Z.; Zhu, M.; Xu, R.; et al. A Water Surface Contaminants Monitoring Method Based on Airborne Depth Reasoning. *Processes* **2022**, *10*, 131. https://doi.org/10.3390/pr10010131

Academic Editors: Avelino Núñez-Delgado, Zhien Zhang, Yaoyu Zhou, Marco Race, Elza Bontempi and Mario Coccia

Received: 14 December 2021
Accepted: 3 January 2022
Published: 10 January 2022

1. Introduction

Plastic refers to a type of high polymer compound that is characterized by differing compositions and shape flexibility. It exhibits several advantages (e.g., impact resistance, wear resistance, good insulation and low cost), nonetheless, it has significant defects. Additionally, plastic cannot be effectively recovered through classification. As indicated from the report of the voice of economy, the industrial ecology team of the University of California estimated the overall amount of plastics available on Earth. Since it was invented in 1909, mankind has produced approximately nine billion tons of plastics, equated with 25,000 Empire State buildings in New York and the sum of one billion elephants (e.g., plastic bottles, plastic bags and other plastic products). Merely 30% of plastic is recycled, and 70% of plastic turns out to be garbage, most of which is buried under the land.

According to the team of California scientists, considerable garbage floats in the ocean. Plastic is suggested to be not biodegradable. Over time, macro plastic pieces degrade into increasingly smaller pieces, termed microplastic (less than five millimeters long) [1]. Microplastic can be swallowed by various water surface organisms and then rise through the food chain, ending up on our dinner tables [2]. Water surface plastic waste pollution is a major challenge to the global ecology and impacts numerous fields (e.g., economics, ecology, public health and aesthetics).

The amount of plastic waste in the ocean has reached 150 million tons, nearly one fifth of the total weight of marine fish [3]. It is estimated that the weight of plastic in the ocean will exceed that of fish by 2050. The international community has made some efforts to build a standardized monitoring method, including Oslo and Paris Conventions (OSPAR) (OSPAR commission, 2020) [4], Commonwealth Scientific and Industrial Research Organization (CSIRO) [5], National Oceanic and Atmospheric Administration (NOAA) [6], as well as United Nations Environment Programme/Intergovernmental Oceanographic Commission (UNEP/IOC) [7]. However, little knowledge has been acquired from the total quantity and spatial-temporal distribution of water surface plastic waste, and the monitoring method remains in the preliminary stage. Mauro et al. [8] inserted 190 FTIR spectra of plastic samples in a digital database and submitted those to Independent Component Analysis (ICA) to extract the "pure" plastic polymers present. In addition, they established the similarity with unknown plastics by employing the correlation coefficient (r), and the cross-correlation function (CC). Topouzelis K. et al. [9] adopted worldview-2 images to examine the optical properties exhibited by wet and dry plastics, as well as assessed the possibility of multispectral images for floating plastic detection in water. Kyriacos et al. [10] set seven indices for satellite image processing, which were examined to verify whether they are capable of detecting plastic waste in water. Furthermore, the authors examined two novel indices to be applied for processing satellite images, i.e., the Plastics Index (PI) and the Reversed Normalized Difference Vegetation Index (RNDVI). The novel Plastic Index (PI) is capable of detecting plastic objects floating on the water surface, and it has been proven as the most effective index to detect the plastic waste target in the sea. By mounting the equipment on a C-130 aircraft that surveyed the Great Pacific Garbage Patch, Shungudzemwoyo et al. [11] captured red, green and blue (RGB) and hyperspectral SWIR imagery. Furthermore, they explored SWIR spectral information acquired by employing a SASI-600 imager (950−2450 nm) and then examined the potential of SWIR remote sensing technology in detecting and quantifying ocean plastic.

Unmanned Aerial Vehicles (UAVs) have been demonstrated as an effective low-cost image-capturing platform capable of accurately monitoring aquatic environments [12,13]. Gil et al. [14] proposed an Unmanned Aerial System (UAS)-based process for automated water surface litter mapping under a beach-dune system. The very high-resolution orthophoto produced from UAS images was automatically screened by the random forest machine learning method to characterize the water surface litter load on beach and dune areas. A. Deidun et al. [15] optimized the protocol to monitor the identical litter along coastal stretches within an MPA in the Maltese Islands through aerial drones, with the aim of generating density maps for the beached litter. The mentioned process can help detect the identical litter and mainstream such a methodology in national and regional programs for monitoring water surface waste. UAVs have been exploited to capture geo-referenced RGB images in the selected zone of a protected water surface area (the Migliarino, Massacciuccoli and San Rossore Park near Pisa, Italy) in a long-term (ten month) monitoring program. A post-processing system based on visual interpretation of the images can be applicable to localizing and detecting the anthropogenic water surface debris in the scanned area, as well as estimating their spatial and temporal distributions in different beach zones [16].

Over the past few years, deep learning theory and the practice of theory have been trailblazing, and the theory has been applied for detecting water surface plastic waste. The deep learning model can automatically select image features, which is considered an advantage of the model. VGGNet [17], FCN [18], Faster R-CNN [19], Yolo [20], U-Net [21]

and other models exhibit the most advanced accuracy in detecting floating plastic waste in UAV images. Kyriaki et al. [22] proposed a macro plastic recognition model by complying with the convolutional neural network (CNN). When the classifier is trained on three identical types of plastic water surface garbage (i.e., plastic bottles, plastic buckets and plastic straws), it is capable of recognizing novel plastic objects well, and the verification accuracy reaches approximately 86%. Jun Ichiro et al. [23] explored the method of exploiting autonomous robots (e.g., commercial UAVs and AUVs) to monitor water surface environments. Moreover, they adopted the deep learning target detection algorithm Yolov3 to detect underwater water surface organisms and floating debris on the sea, achieving the respective average accuracies of 69.6% and 77.2%. However, they ignored the top-level spatial information, thereby causing the lack of accurate positioning and class boundary characterization. Furthermore, the mentioned methods are primarily offline analysis methods based on aerial photography data acquired by using UAVs, i.e., UAVs acquire real-time information from the surrounding environment by turning on the camera or sensor while synchronously pushing it to the ground station. Subsequently, the ground station transmits the video or image information acquired to the special image analysis server (workstation) for subsequent analysis. All the above process is considered a significant resource-intensive task. The model network is sophisticated with considerable parameters and low efficiency, and the degree of real-time is largely determined by the bandwidth and stability of the transmission network.

The strategy of edge computing can address the mentioned problems. Edge computing decomposes the large-scale services originally processed by the central node and disperses them to the edge nodes closer to the user terminal equipment. It is capable of expediting the data processing and sending and reducing the delay. Kang Z. et al. [24] used the flight points calculated by UAV to fly in turn to cover a convex polygon area. The detailed solving process of flight point was given, while the programming, simulation and actual flight experiment of the proposed method were performed. Zhang Z. et al. [25] first used the deep learning model to preprocess the captured image and extracts useful information. Subsequently, they transmitted these data to the edge server on the ground for further analysis. Compared with the direct transmission of the original data, this method is capable of significantly reducing the communication load.

The existing airborne image processing board has limited computing power, so it cannot easily perform large-scale target solving tasks. As a typical one-stage algorithm, Yolo series of target detection algorithms exhibit high precision and are fast and lightweight. According to the latest yolov5, the fast reasoning time of the respective image is up to 0.007 s and 140 frames per second (FPS). Yolov5, an extremely lightweight target recognition network, solves the problems of low efficiency of the full convolution model network, as well as the difficulty in ensuring the classification effect. As indicated from the verification of several public datasets, its accuracy is equivalent to that of EfficientDet and yolov4, whereas the model size is only one tenth of the latter [26,27]. It is an ideal choice to carry out edge computing on UAVs, unmanned ships and other platforms.

The rest of this study is organized below. First, in the second section, the research area of the water surface plastic waste monitoring experiment is introduced, as well as the photoelectric pod and target detection model applied by the aerial robot. Subsequently, in the third section, the computer configuration of Aerial Robot and the training method of target detection model is presented. To solve the problems of River waste monitoring, this study proposed three optimization strategies, compared and analyzed the models and discussed the recognition results of different models. Lastly, in the fourth section, the specific challenges and future development trend of Aerial Robot are summarized for real-time monitoring of plastic waste on the water surface.

2. Materials and Methods

2.1. Study Area and UAV Trajectory Planning

The experiment of this study was conducted at the East Zhangwu Wetland Section of Longhe river in Anci District, Langfang City, Hebei Province. The longitude amplitude of the research area ranged from 116.69° N to 116.80° N, while the latitude amplitude was from 39.41° E to 39.48° E. Longhe River refers to an interprovincial and intermunicipal drainage channel, originating from Daxing District of Beijing and entering Yongding River flooding area via a dike protection road in East Zhangwu of Langfang City. The river exhibits a total length of 68.42 km and a drainage area of 577.94 km^2, of which 256 km^2 is in Beijing and 322 km^2 is in Langfang. The Longhe river serves as a vital barrier to protect the ecological balance of the capital city.

The main water surface environmental protection method in East Zhangwu Wetland section of Longhe River aims at irregular manual inspections and fishing as assisted by a diesel-powered fishing boat (Figure 1). As impacted by the long river length, there are often people picnicking and camping along its shores, so the possibility of sudden plastic waste pollution is high. The existing salvage vessels have slow speeds (<20 km/h), the number of operators is small (2 people) and the emergency response ability to sudden pollution is low. Furthermore, if the number of inspections is extremely frequent, the exhaust gas emitted by the vessels causes secondary pollution to the wetland environment.

Figure 1. Salvage vessel for water surface waste inspection on the Longhe River.

The aerial robot can substitute for the salvage vessel to irregularly inspect the river environment and send the waste detection results to the ground station on the salvage vessel in real time. When the waste loading [28] reaches a certain degree, the salvage vessel can perform accurate salvage in accordance with the waste position fed back by the aerial robot. It is capable of significantly increasing the efficiency of salvage and saving capital and labor costs while reducing the exhaust pollution attributed to repeated vessel inspections.

QGroundControl software was adopted to design the flight route of the survey area. QGroundControl can offer full flight control and the vehicle setup for PX4 or ArduPilot-powered vehicles. To yield the optimal resolution, numerous experiments were performed, and the optimal altitude of 7 m was determined. The speed was set at 5 m/s, the course overlap rate was 80% and the side overlap rate was 75%. The flight route was perpendicular to the river flow direction (Figure 2).

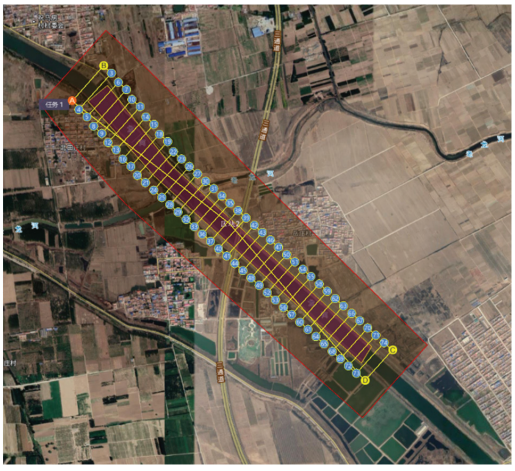

Figure 2. Distribution of survey area.

2.2. Data Acquisition

The remote sensing images of the study area were captured with an Intel d435i binocular depth camera on a Feisi x450 UAV (Figure 3a) developed by Beijing Droneyee Intelligent Technology Co., Ltd., Beijing, China. There were four round holes on the front of the d435 camera (Figure 3b). From left to right, the first and third were IR stereo cameras, while the second and the fourth were an IR projector and a color camera, respectively. The maximal distance of camera capture was 10 m, and the video transmission rate could be up to 90 FPS. Feisi x450. The UAV is also equipped with a TX2 airborne visual processing board, capable of performing visual navigation, target recognition and target following. Other tasks will be introduced in Section 3.1.

(**a**) (**b**)

Figure 3. Data acquisition equipment of the study. (**a**) FEISI X450 UAV; (**b**) Intel d435i binocular camera.

From the UAV survey, 10,000 UAV remote sensing images were selected area as the sample database, with an image resolution of about 1 cm and a size of 2048 × 1080 pixels. Of the 10,000 images, 7000 were employed as the training samples, and the remaining 3000 were employed as test samples to verify the recognition results. The data of this research are available in ScienceDatabank (doi:10.11922/sciencedb.01121). This study used professional labeling software in the UAV images to mark common plastic waste (e.g., plastic bottles, plastic bags and plastic foam). The coordinates of the upper left corner and the lower right corner of the rectangle box were recorded in an XML document.

As impacted by the small amount of plastic waste in the UAV remote sensing image, to obtain higher training effect, the data were partially downloaded from the public dataset as a supplement. Moreover, the data were randomly cut, rotated, scaled and flipped

to generate multiple similar images. Data enhancement is capable of compensating for incomplete data, effectively reducing the overfitting, making the model more applicable to novel samples and improving the generalization utility of the model. Lastly, UAV images were converted into datasets of visual object class format for pretraining of the deep learning model.

2.3. Overall Research Framework

The overall research framework of this study is shown in Figure 4. First, the model was pretrained by the open dataset. Subsequently, the model was trained and reasoned by the labeled (interpretation object) training set. Given the characteristics exhibited by plastic waste, the deep learning model was regulated to achieve a more effective solution and then packaged. By building the intelligent analysis platform of edge computing UAV, the encapsulated deep learning model was transplanted to the airborne image processing board.

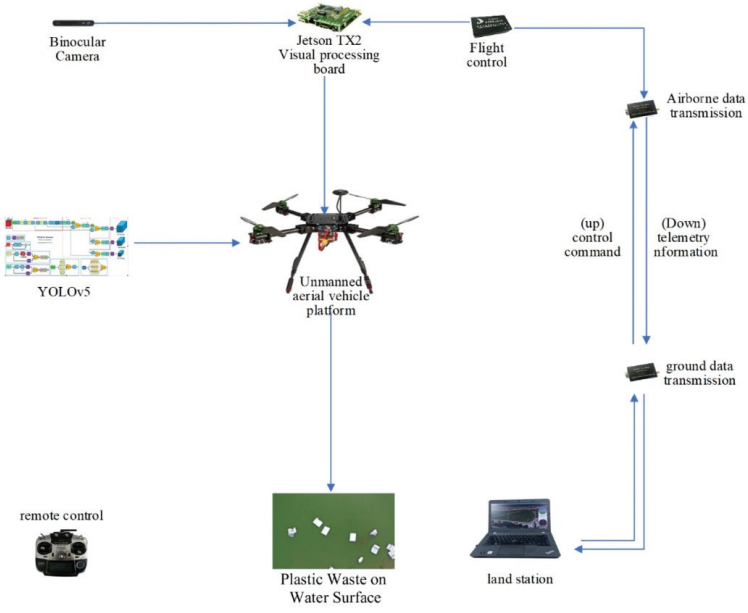

Figure 4. Research framework of this study.

The UAV processed and analyzed the plastic waste targets while capturing aerial photos. In addition, it detected and counted the types and quantities of plastic waste while transmitting the detection results back to the ground workstation on the salvage vessel via data transmission. The operator decided when to perform the fishing work in accordance with the quantity and position of plastic waste on the water surface obtained by the workstation in real time.

2.4. Deep Network

The target detection of a flowing river is significantly challenging. There are many challenges attributed to continuous plastic movement (e.g., low amount of training data, high imbalance of dataset, frequent target location and scene changes). This study took yolov5 as the baseline algorithm and proposed various optimization strategies to address the problems in target detection. The overall flow chart of the algorithm is presented in Figure 5.

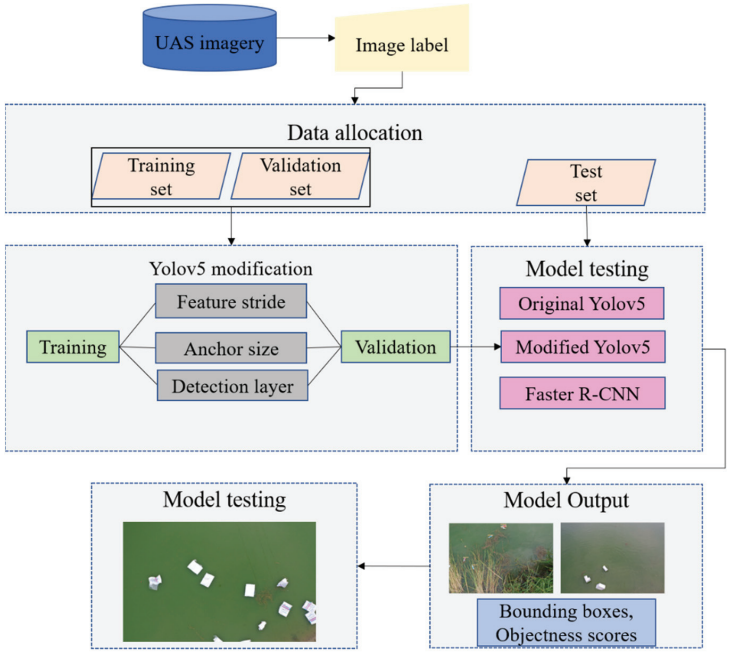

Figure 5. Algorithm block diagram.

In this study, a novel deep learning network for target detection, yolov5, was adopted to detect the labeled training set image. Yolov5 refers to the network exhibiting the smallest depth and feature map width in the target detection series, with its accuracy equivalent to that of yolov4, whereas the model is nearly 90% smaller than that of yolov4. Yolov5 is considered a prominent lightweight network with fast convergence on multiple datasets and high customizability. The relevant source code can be referenced from https://github.com/ultralytics/YOLOv5 accessed on 9 April 2021. Yolov5 was implemented by complying with the Python framework. Yolov5 operations place a novel focus on changing the image into a feature map after slicing. Two CSP structures were applied in the backbone extraction network. With yolov5's network as an example, a csp1_ X structure was applied to the backbone network, i.e., another type of csp2. The X structure was used in the neck. The FPN + pan structure was selected as the neck. The csp2 structure designed by cspnet was employed to improve the ability of network feature fusion.

CSP structure divides the feature map into two parts, and then merges it through the proposed cross stage hierarchy. By splitting the gradient flow, the gradient flow propagates through different network paths. It can greatly reduce the amount of calculation and improve the reasoning speed and accuracy. Two CSP structures, csp1, are used in yolov5 network_ X for backbone feature extraction network, csp1_ X uses the residual structure module to speed up the backbone feature extraction and network feature extraction capability. CSP2_ X is used for the neck network, FPN + pan structure is selected as the neck, and csp2 is used_ X structure to improve the ability of network feature fusion.

Yolo, a highly typical target detection algorithm, refers to a single-stage algorithm integrating target proposal stage and classification stage, and its detection rate is higher than that of the two-stage RNN algorithm. Yolov5 is regarded as the latest version of the Yolo architecture. Yolov5 architecture comprises four architectures, i.e., Yolov5s, Yolov5m, Yolov5l and Yolov5x. To prevent the model from being extreme and overfitting, this study selected Yolov5s with a relatively simple structure as the baseline model.

On the whole, Yolov5s framework comprises three parts (i.e., backbone network, neck network and detection network). The backbone network aims to aggregate different

convolutional neural network images, as an attempt to form image features. To be specific, the first layer of the backbone network is the focus module. First, the respective input UAV image fell to four slices, and the slice operation was used to reduce the amount of model calculation and increase the training speed without image loss. Second, the four parts were deeply connected by concat operation to output the size of the characteristic graph. Subsequently, the results were outputted to the next layer via the convolution layer (conv2d + BN + leakyrelu activation function, CBL) composed of 32 convolution cores.

The third layer of the backbone network refers to the BottleNeckCSP module used to more effectively extract the deep features of the image. The Bottleneck CSP module primarily consists of the bottleneck module. It connects the 1×1 CBL and 3×3 residual network architecture of CBL. The ninth layer of the backbone network is the SPP module (spatial pyramid pooling), converting any size feature map into a fixed size feature vector to optimize the receptive field of the network. First, the neck network is the feature map output after the convolution layer. The feature map is linked to the sub sampling depth of the output feature map via three parallel maxpooling layers. The output feature map is capable of retrieving the final output feature map via a convolution layer.

The neck network, a series of hybrid feature aggregation layer image features, is largely exploited to generate a feature pyramid network and subsequently transmit the output feature map to the detection network. The feature pyramid network structure optimizes the bottom-up path, improves the transmission of low-level features and facilitates the detection of floating plastic waste at different scales. Thus, the same target object with different sizes and scales can be accurately detected. The detection network was primarily applied for the last detection part of the model. The anchor box was applied into the feature map output on the neck network, and a vector was outputted (e.g., the category probability of the target object, the score of the object and the position of the bounding box around the object). The detection network of Yolov5s architecture comprises three detection layers, which are adopted to detect image objects of different sizes. Lastly, the respective detection layer outputted a vector while generating and marking the prediction boundary box and category of the target in the original image to detect plastic waste in the UAV image.

To increase the accuracy of water surface garbage detection, the original model was converted to the modified Yolov5:

1. Modifying anchor structure

Anchor structure, a vital part of the Yolo series target detection algorithm, produces suggestions for predicting potential objects. The original anchor structure exhibits high performance in detecting various objects in the dataset (e.g., coco). However, the size of these anchors is not applicable to small objects. The average size of plastic waste in the UAV image here was less than 30 cm, and the total area of the image was only approximately 1% of the overall image area. In small target detection, setting a small anchor scale is considered a feasible solution to solve the mentioned problem. However, it is arbitrary to assess the performance of the model by comparing the anchor size and sample size, and the model is also capable of finding a more appropriate size by the bounding box regression. To select the appropriate anchor size, the anchor size selection setting was optimized by a K-means clustering algorithm and then set experimentally [45,62; 25,20; 16,28], [13,9; 31,44; 10,26], [24,54; 15,21; 23,30]. Three groups of anchor structures were tested for the target (Figure 6).

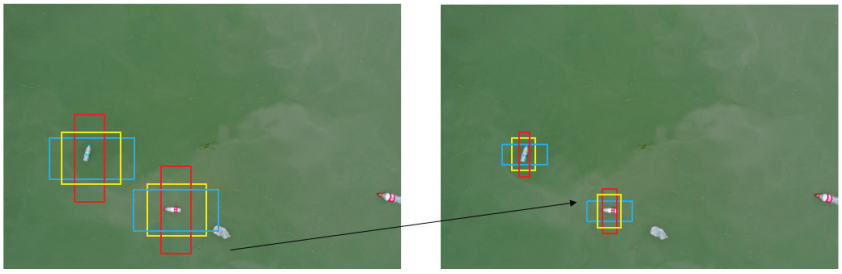

Figure 6. Modification of anchor structure.

2. Modify step size

Between the convolution layer and the aggregation layer of deep learning in the network, several layers have steps larger than 1, thereby performing the down-sampling operation and generating a series of smaller feature maps. The category and location of small objects are difficult to predict in large step down-sampling. A simple and effective method can be used to reduce the feature step for tackling down the down-sampling problem in the small target detection. The 16strides was modified to 8strides to make the feature extraction network accurately extract the plastic garbage in the UAV network (Figure 7).

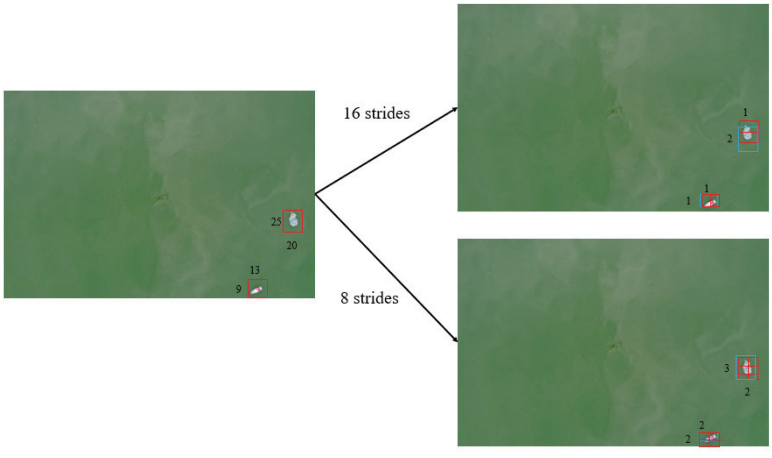

Figure 7. Step comparison chart.

3. Mechanism of increasing attention

The spatial information of river plastic waste is changeable, and the target is difficult to detect. To detect river plastic waste, an attention mechanism was introduced efficiently and accurately into the model, thereby ignoring irrelevant information and stressing localized effective information. Common attention mechanism modules consist of the se module and CBAM module, among others. This study introduced the Yolov5 model into the CBAM module. The CBAM module is lightweight, with the structural features presented in Figure 8. Given an intermediate feature graph, this study inferred the attention weight by complying with the two dimensions of space and channel, and then multiplied it with the original feature graph to adaptively regulate the feature. Since CBAM is a lightweight general module, it can be seamlessly integrated to any CNN architecture, and the extra overhead is negligible. Moreover, it can be trained end-to-end with basic CNN, and

the results can make the model more sensitive to channel and spatial features, and the performance can be enhanced with a small amount of computation.

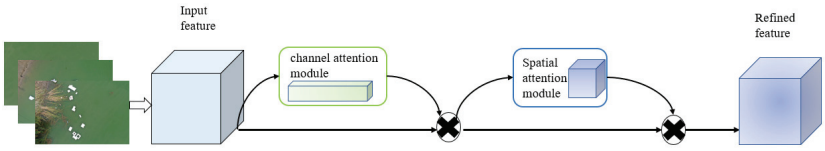

Figure 8. CBAM structure diagram.

3. Results

3.1. Experimental Platform

The airborne image processing board applied experimentally was a TX2 embedded platform for unmanned intelligent field launched by NVIDIA company (Figure 4). It was a modular AI supercomputer, with the GPU of NVIDIA Pascal™ Architecture with 256 CUDA cores. Its CPU covers six cores, consisting of a dual-core denver2 processor and a four-core arm cortex-a57. TX2 is powerful in performance and small in shape. It is significantly applicable to intelligent edge equipment (e.g., a robot, a UAV and an intelligent camera). After training the Yolov5 model on a virtual machine, the model was imported into the TX2 processing board via an SD card. Through the corresponding path of the trained model, the processing results were yielded.

3.2. Model Training Results

In this study, the Pascal VOC matrix reported by Everingham et al. [29] was used as the evaluation protocol to verify false positives (FP), true positives (TP) and false negatives (FN). When a predicted bounding box corresponds to a unique real bounding box, it is counted as a TP when it has the largest IOU with a specific real bounding box and reaches the IOU threshold (0.8). Otherwise, the predicted bounding box is considered a FP. When the real bounding box cannot be combined with the predicted bounding box when the IOU reaches the IOU threshold (0.8), it is considered a FN. The prediction of plastic waste in our study is evaluated based on recall (R) and precision (P), which are defined as follows:

$$\text{Precision} = \text{TP}/(\text{TP} + \text{FP}) \tag{1}$$

$$\text{Recall} = \text{TP}/(\text{TP} + \text{FN}) \tag{2}$$

Recall provides insight into the predicted coverage of plastic floating waste, while accuracy evaluates the accuracy of the predicted total. Since the recall rate and precision only reflect one aspect of the model's performance, the average precision (AP) and F1 score were used to comprehensively evaluate the results. AP can be simply regarded as the area under the accurate recall curve or expressed mathematically as:

$$\text{AP} = \Sigma_{i=1}^{n}\text{Precision}_i(\text{Recall}_i - \text{Recall}_{i-1}), \text{with} \text{Recall}_{i=0} = 0 \tag{3}$$

The average accuracy of the whole class represents the average value of the whole class mAP, it shows the ability of the target detection model to distinguish different floating plastic wastes.

$$\text{mAP} = \Sigma_{i=1}^{n}\text{AP}/n \tag{4}$$

The score threshold of the algorithm was set to 0.8 to suppress low score prediction. High score predictions were compared with surface facts to yield a set of TP, FP, FN, precision, recall and AP, mAP.

Deep learning models (i.e., Fast-RCNN, YOLOv5 and modified YOLOv5) were adopted to train three types of plastic waste datasets (i.e., plastic bottles, plastic bags and foam

plastics), respectively, on GTX 1080. The data were annotated through 100 iterations of 100 models, and the Yolov5 model P, R, AP and mAP curves were modified (Figure 9).

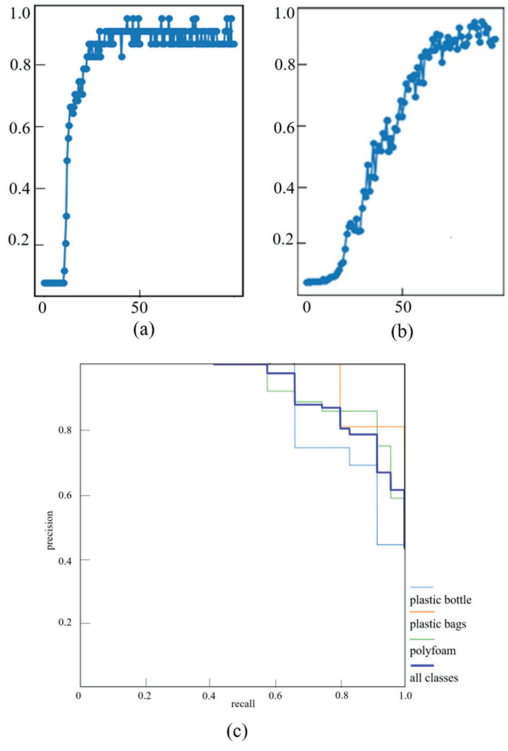

Figure 9. The modified YOLOv5 accuracy evaluation. (**a**) Precision curve; (**b**) recall curve; (**c**) AP, mAP curve.

The P curve has converged in the iteration to about 50 generations, and the R curve converged in the iteration to 75 generations. The accuracy of AP and mAP remained more than 80%, which shows that the model converged and the detection effect was good.

a. Performance Evaluation

1. Recognition results

Given the training results, three types of marine plastic waste were detected, and the results are illustrated in Figure 10.

Because the garbage target was smaller, the local part was enlarged, the yellow border was detected as a plastic bottle, green was plastic foam, purple was plastic bag, the three plastic waste scores were all above 0.8 and the detection results were more accurate.

2. Accuracy comparison

All experimental models were migrated to the development board for experimental comparison. As assisted by FPS (frames per second), AP, mAP and size of model, a comparison was drawn for the accuracy of the detection results generated by Fast RCNN, SDD, Yolov3, Yolov5 and the modified Yolov5 model (Table 1). After the modified Yolov5 model was transferred to the TX2 development board, FPS could reach 45, and mAP was 94.55%, which indicated optimal overall performance. Thus, the requirements of users to obtain the analysis results of the deep learning model in real time could be more effectively met.

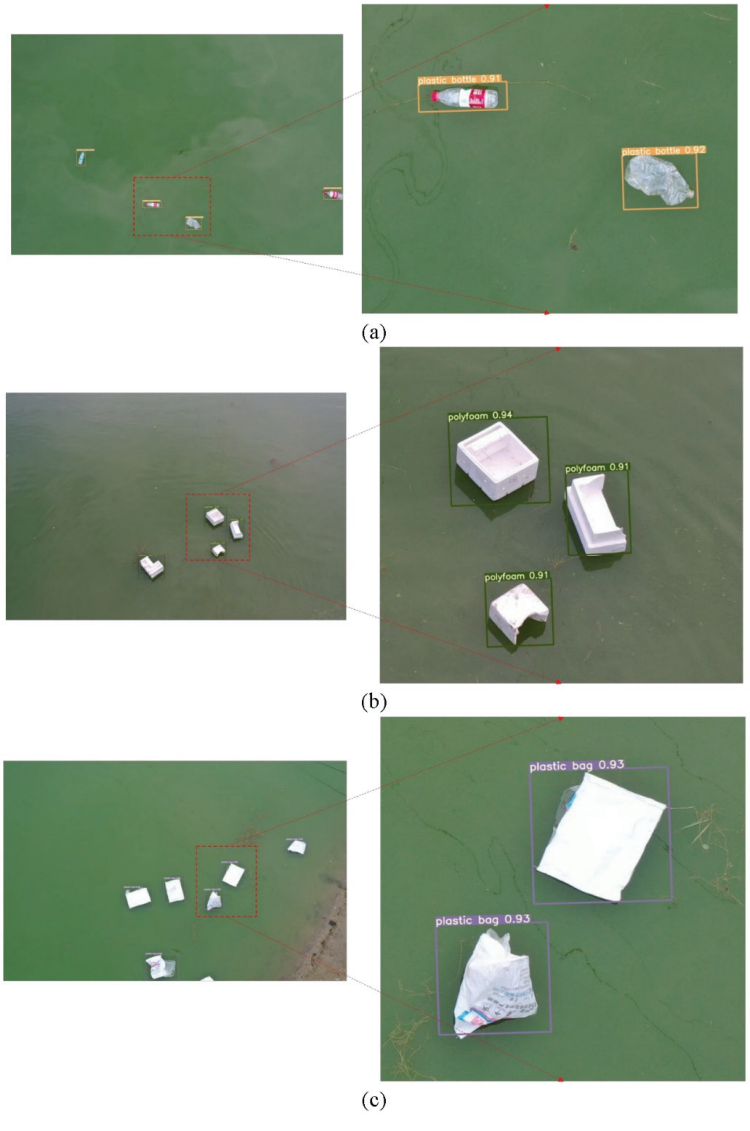

Figure 10. Marine litter monitoring results. (**a**) Plastic bottles; (**b**) polyfoam; (**c**) plastic bags.

Table 1. Detection results of the dataset.

Network	FPS	P	R	AP_{bottle}	AP_{bag}	$AP_{polyfoam}$	mAP	Size of Model
Faster-CNN	10.24	0.88	0.87	0.82	0.88	0.86	0.85	345 MB
SSD	26.24	0.69	0.65	0.62	0.68	0.65	0.65	35.6 MB
Yolov3	35.62	0.73	0.76	0.71	0.73	0.75	0.73	236 MB
Yolov5	46.37	0.80	0.82	0.81	0.82	0.80	0.81	14.5 MB
Modified Yolov5	43.63	0.86	0.89	0.80	0.89	0.87	0.86	15.2 MB

4. Discussion

The Yolov5 network acts as a prominent lightweight network structure. The Yolov5 network's far better performance is primarily attributed to focus structure slice pictures,

extract features of cspnet and optimization strategies of giou using output. Although the fast RCNN detection accuracy was equated with that of the optimized Yolov5, FPS was only about 10 due to the calculation burden attributed to its two-stage structure, so it could not easily meet the real-time requirements of data analysis. By modifying the original Yolov5, the three optimization strategies had different degrees and exerted different effects on the plastic detection classification. The adjustment of the anchor frame and the step length of the anchor frame primarily aimed to address the problem of difficult recognition of small target river waste by adopting the K-means clustering algorithm. The algorithm placed its focus on the plastic waste target in the UAV image more efficiently by introducing an attention detection layer while integrating the information of the plastic waste. Although the optimized Yolov5 increased the model parameters and calculation amount, only 3 FPS were lost, whereas the model's accuracy was elevated by nearly 5%, thereby satisfying the real-time performance and improving the reliability of the results. Furthermore, as verified by the experimentally achieved results, the optimized Yolov5 outperformed other detection algorithms.

The high-precision detection model increased the accuracy in the detection of marine plastic waste, though some plastic waste was not detected due to the influence of the photo environment and angle. On the whole, the recognition accuracy of plastic foam and plastic bags was high, and the recognition accuracy of plastic bottles was slightly lower. The former primarily resulted from the single recognition type and being easy to distinguish, while the latter was largely attributed to the large number of shapes, colors and types, which limited the recognition accuracy. Accordingly, the model could be further optimized by increasing the scale of the dataset and collecting data from different environments.

As indicated from the experimentally achieved results, modified Yolov5 outperformed other target detection methods. High-speed garbage detection can process images in real time and offer floating garbage information for UAV in time in a changeable and complex water environment. Although the fast RCNN achieves high accuracy, it cannot achieve real-time performance due to the computational burden of a two-stage network, and the model size is 345 mb. The huge model hinders the deployment of a UAV algorithm. Yolov5 adopts the focus structure to slice the image, thereby improving the model detection speed without image information loss. The model size is 14.5 mb, meeting the real-time requirements. High-precision plastic detection can help the UAV platform complete the task more accurately, reliably and stably. SSD and Yolov3 are far less accurate than the Yolov5 network. The backbone feature extraction network exerts a certain effect on the performance of the target detection model. The backbone feature extraction network of SSD refers to the classic vgg16 and res101 network, the backbone feature extraction network of Yolov3 is Darknet, and the backbone feature extraction network of Yolov5 is BottleNetCSP. The performance of BottleNetCSP is noticeably better than that of conventional vgg16, res101 and other networks. Its performance is equated with that of the Darknet classifier, yet it has fewer floating-point operations and faster speed, thereby satisfying the practical needs of speed and accuracy.

Yolov5 is prominent in accuracy and speed, so the rising space will not be significant when improving. Accordingly, our goal is to achieve high speed while at least improving the original accuracy. The anchor box reclustered by the K-means clustering algorithm will be more applicable to three types of micro water surface garbage monitoring. Reducing the step size can make the Yolov5 model find water surface plastic garbage better. Introducing a CBAM attention detection layer enabled the target detection algorithm to focus on the plastic garbage targets in UAV images more quickly. The three strategies improved the accuracy of Yolov5. The optimized Yolov5 increased the model parameters and complicated the calculation, and the model size was 15.2 mb; the FPS lost was only 3, whereas the model accuracy increased by about 5%. It was also verified that the performance of the optimized Yolov5 was better than that of other detection algorithms.

Some plastic wastes were not detected by the modified Yolov5 due to the influence of photographing environment and angle. On the whole, the detection accuracy of plastic foam

and plastic bag was high, and the recognition accuracy of plastic bottles was slightly lower. The former was mainly due to the single recognition type and being easy to distinguish, while the latter was primarily attributed to more shapes, colors and types, which limited the recognition accuracy. Accordingly, the model could be further optimized by increasing the scale of the dataset and collecting data from different environments.

The Yolov5 network comprises different sizes of four architectures (i.e., Yolov5s, Yolov5m, Yolov5l and Yolov5x). Users can select specific models with appropriate sizes for development and application. In the present study, the selection and design of the recognition algorithm largely considered its application environment in surface garbage, i.e., the application deployment of detection algorithm on UAV, as an attempt to recognize plastic floating garbage targets in real time. The advantages of light weight (very small model size) and high detection speed of the Yolov5s network will downregulate the deployment cost of the detection model, which shows that the detection model based on the optimized Yolov5s has great potential to be deployed in the edge computing equipment of UAV, and the algorithm can be built by training and strategy selection by complying with different task requirements.

5. Conclusions

In this study, the optimized Yolov5 was used to detect three types of common surface plastic waste. As indicated from the experimentally achieved results, the accuracy was further improved compared with that of the original structure though three optimization strategies (i.e., regulating the anchor frame, increasing the detection layer and shortening the step length) that also made the FPS slightly lower. The accuracy of the fast CNN model was equated with that of the Yolov5 model, but the FPS was low and inefficient. In addition, by transferring the trained Yolov5 model to the UAV platform equipped with a TX2 development board, the average accuracy was 86%, and the FPS was 35%. Compared with the existing methods, the method adopted in this study could avoid the significant occupation of network bandwidth attributed to the return video and the lack of information attributed to the analysis delay. In addition, it could effectively achieve the real-time detection and result feedback of all types of water surface plastic waste while significantly increasing monitoring efficiency. The high-intelligence UAV platform is expected to be the mainstream means of water environment monitoring in the future.

Author Contributions: Conceptualization and writing—original draft preparation, W.L.; methodology, Z.Z.; software, W.H.; validation, H.W.; formal analysis, M.Z.; investigation, K.L.; data curation, Y.Z.; writing—review and editing, G.W.; visualization, R.X.; supervision, Y.L.; funding acquisition, P.F. All authors have read and agreed to the published version of the manuscript.

Funding: This research was funded by National Key Research and Development Program of China, No. 2017YFC0506501; Strategic Priority Science and Technology Special Project of Chinese Academy of Sciences, No. XDA23100203; Key Laboratory of Surveying and Mapping Science and Geospatial Information Technology of Ministry of Natural Resources Open Research Fund Project (2020-2-5); Scientific Research Key Project of Hebei Provincial Department of Education (Grant No. ZD2020161) and Science and Technology Project of Hebei Education Department (QN2019213).

Institutional Review Board Statement: Not applicable.

Informed Consent Statement: Not applicable.

Data Availability Statement: Data for this research are available in ScienceDatabank (doi:10.11922/sciencedb.01121).

Acknowledgments: This research was supported by Beijing Droneyee Intelligent Technology Co., Ltd.

Conflicts of Interest: The authors declare no conflict of interest.

References

1. Lebreton, L.; van der Zwet, J.; Damsteeg, J.W.; Slat, B.; Andrady, A.; Reisser, J. River plastic emissions to the world's oceans. *Nat. Commun.* **2017**, *8*, 1–10. [CrossRef]
2. Gordana, J.; Govedarica, M.; Alvarez-Taboada, F. A Deep Learning Model for Automatic Plastic Mapping Using Unmanned Aerial Vehicle (UAV) Data. *Remote Sens.* **2020**, *12*, 1515.
3. Haward, M. Plastic pollution of the world's seas and oceans as a contemporary challenge in ocean governance. *Nat. Commun.* **2018**, *9*, 667. [CrossRef] [PubMed]
4. Da Costa, J.P.; Mouneyrac, C.; Costa, M.; Duarte, A.C.; Rocha-Santos, T. The Role of Legislation, Regulatory Initiatives and Guidelines on the Control of Plastic Pollution. *Front. Environ. Sci.* **2020**, *8*, 104. [CrossRef]
5. Hardesty, B.D.; Lawson, T.J.; van der Velde, T.; Lansdell, M.; Wilcox, C. Estimating quantities and sources of water surface debris at a continental scale. *Front. Ecol. Environ.* **2016**, *15*, 18–25. [CrossRef]
6. Burgess, H.K.; Herring, C.E.; Lippiatt, S.; Lowe, S.; Uhrin, A.V. *NOAA Marine Debris Monitoring and Assessment Project Shoreline Survey Guide*; NOAA Technical Memorandum NOS OR&R 56; NOAA: Washington, DC, USA, 2021; 20p. [CrossRef]
7. Cheshire, A.C.; Adler, E.; Barbière, J.; Cohen, Y.; Evans, S.; Jarayabhand, S.; Jeftic, L.; Jung, R.T.; Kinsey, S.; Kusui, E.T.; et al. *UNEP/IOC Guidelines on Survey and Monitoring of Water Surface Litter. UNEP Regional Seas Reports and Studies. No. 186*; UNEP: Nairobi, Kenya, 2009; p. 120.
8. Mecozzi, M.; Pietroletti, M.; Monakhova, Y.B. FTIR spectroscopy supported by statistical techniques for the structural characterization of plastic debris in the marine environment: Application to monitoring studies. *Mar. Pollut. Bull.* **2016**, *106*, 155–161. [CrossRef]
9. Topouzelis, K.; Papakonstantinou, A.; Garaba, S.P. Detection of floating plastics from satellite and unmanned aerial systems (Plastic Litter Project 2018). *Int. J. Appl. Earth Obs. Geoinf.* **2019**, *79*, 175–183. [CrossRef]
10. Kyriacos, T.; Papoutsa, C.; Michaelides, S.; Hadjimitsis, D. Investigating Detection of Floating Plastic Litter from Space Using Sentinel-2 Imagery. *Remote Sens.* **2020**, *12*, 2648.
11. Garaba, S.P.; Aitken, J.; Slat, B.; Dierssen, H.M.; Lebreton, L.; Zielinski, O.; Reisser, J. Sensing Ocean Plastics with an Airborne Hyperspectral Shortwave Infrared Imager. *Environ. Sci. Technol.* **2018**, *52*, 11699–11707. [CrossRef]
12. Gray, P.C.; Fleishman, A.B.; Klein, D.J.; McKown, M.W.; Bezy, V.S.; Lohmann, K.J.; Johnston, D.W. A Convolutional Neural Network for Detecting Sea Turtles in Drone Imagery. *Methods Ecol. Evol.* **2019**, *10*, 345–355. [CrossRef]
13. Hong, S.-J.; Han, Y.; Kim, S.-Y.; Lee, A.-Y.; Kim, G. Application of Deep-Learning Methods to Bird Detection Using Unmanned Aerial Vehicle Imagery. *Sensors* **2019**, *19*, 1651. [CrossRef]
14. Gonçalves, G.; Andriolo, U.; Pinto, L.; Bessa, F. Mapping marine litter using UAS on a beach-dune system: A multidisciplinary approach. *Sci. Total Environ.* **2020**, *706*, 135742. [CrossRef] [PubMed]
15. Deidun, A.; Gauci, A.; Lagorio, S.; Galgani, F. Optimising beached litter monitoring protocols through aerial imagery. *Mar. Pollut. Bull.* **2018**, *131*, 212–217. [CrossRef]
16. Merlino, S.; Paterni, M.; Berton, A.; Massetti, L. Unmanned aerial vehicles for debris survey in coastal areas: Long-term monitoring programme to study spatial and temporal accumulation of the dynamics of beached marine litter. *Remote Sens.* **2020**, *12*, 1260. [CrossRef]
17. Simonyan, K.; Zisserman, A. Very deep convolutional networks for large-scale image recognition. *arXiv* **2014**, arXiv:1409.1556.
18. Long, J.; Shelhamer, E.; Darrell, T. Fully convolutional networks for semantic segmentation. In Proceedings of the IEEE Conference on Computer Vision and Pattern Recognition, Boston, MA, USA, 8–10 June 2015; pp. 3431–3440.
19. Ren, S.; He, K.; Girshick, R.; Sun, J. Faster R-CNN: Towards Real-Time Object Detection with Region Proposal Networks. *IEEE Trans. Pattern Anal. Mach. Intell.* **2017**, *39*, 1137–1149. [CrossRef] [PubMed]
20. Redmon, J.; Divvala, S.; Girshick, R.; Farhadi, A. You only look once: Unified, real-time object detection. In Proceedings of the IEEE Conference on Computer Vision and Pattern Recognition, Las Vegas, NV, USA, 27 June–1 July 2016; pp. 779–788.
21. Ronneberger, O.; Fischer, P.; Brox, T. U-net: Convolutional networks for biomedical image segmentation. In *International Conference on Medical Image Computing and Computer-Assisted Intervention*; Springer: Cham, Switzerland, 2015; pp. 234–241.
22. Kyriaki, K.; Ioannis, K.A.; Constantinos, H. Identifying floating plastic water surface debris using a deep learning approach. *Environ. Sci. Pollut. Res.* **2019**, *26*, 17091–17099.
23. Junichiro, W.; Yang, S.; Naoto, M. Underwater and airborne monitoring of water surface ecosystems and debris. *J. Appl. Remote Sens.* **2019**, *13*, 044509.
24. Kang, Z.; Ling, H.; Zhu, T.; Luo, H. Coverage Flight Path Planning for Multi-rotor UAV in Convex Polygon Area. In Proceedings of the 2019 Chinese Control And Decision Conference (CCDC), Nanchang, China, 3–5 June 2019.
25. Zhang, Z.; Njilla, L.L.; Yu, S.; Yuan, J. Edge-Assisted Learning for Real-Time UAV Imagery via Predictive Offloading. In Proceedings of the 2019 IEEE Global Communications Conference (GLOBECOM), Waikoloa, HI, USA, 9–13 December 2019.
26. Redmon, J.; Farhadi, A. YOLOv3: An Incremental Improvement. *arXiv* **2018**, arXiv:1804.02767.
27. Bochkovskiy, A.; Wang, C.Y.; Liao, H.Y.M. YOLOv4: Optimal Speed and Accuracy of Object Detection. *arXiv* **2020**, arXiv:2004.10934.

28. Castro-Jiménez, J.; González-Fernández, D.; Fornier, M.; Schmidt, N.; Sempéré, R. Macro-litter in surface waters from the Rhone River: Plastic pollution and loading to the NW Mediterranean Sea. *Mar. Pollut. Bull.* **2019**, *146*, 60–66. [CrossRef] [PubMed]
29. Everingham, M.; Van Gool, L.; Williams, C.K.I.; Winn, J.; Zisserman, A. The Pascal Visual Object Classes (VOC) Challenge. *Int. J. Comput. Vis.* **2010**, *88*, 303–338. [CrossRef]

processes

MDPI

Article

Physicochemical Characterization of Santa Barbara Amorphous-15 (SBA-15) and Its Functionalization with Polyaniline for Phenol Adsorption

Lady Johana Cárdenas [1], Liliana Giraldo [1] and Juan Carlos Moreno-Piraján [2,*]

[1] Grupo de Investigación en Calorimetría, Departamento de Química, Facultad de Ciencias, Universidad Nacional de Colombia, Bogota 111711, Colombia; lacardenas@unal.edu.co (L.J.C.); lgiraldogu@unal.edu.co (L.G.)

[2] Grupo de Investigación en Sólidos Porosos y Calorimetría, Departamento de Química, Facultad de Ciencias, Universidad de los Andes, Bogota 111711, Colombia

* Correspondence: jumoreno@uniandes.edu.co

Abstract: The chemical surface of Santa Barbara Amorphous-15 (SBA-15) was functionalized with polyaniline (SBA-15/PA) and was prepared using aniline and ammonium persulfate as the modifying agent and oxidant. The samples were characterized by N_2 physical adsorption at 77 K. SBA-15's surface area was 654.5 $m^2\ g^{-1}$, changing to 254.6 $m^2\ g^{-1}$. The total acidity and basicity were determined using a modified Boehm's method, and the point of zero charge pH (pH_{pzc}) was determined. Immersion calorimetry in water, benzene, and NaOH, HCl, and phenol (100 mg L^{-1}) solutions was performed, producing values ranging from −15.1 to −174.1 J g^{-1} related to the chemical surface, pH_{pzc}, and acid and base group values. Finally, the phenol adsorption capacity was found to be higher for the modified polyaniline silica, at 138 mg g^{-1}.

Keywords: SBA-15; phenol; functionalization; adsorption; immersion calorimetry

Citation: Cárdenas, L.J.; Giraldo, L.; Moreno-Piraján, J.C. Physicochemical Characterization of Santa Barbara Amorphous-15 (SBA-15) and Its Functionalization with Polyaniline for Phenol Adsorption. *Processes* **2022**, *10*, 188. https://doi.org/10.3390/pr10020188

Academic Editors: Avelino Núñez-Delgado, Zhien Zhang, Yaoyu Zhou, Marco Race, Elza Bontempi and Mario Coccia

Received: 27 October 2021
Accepted: 11 January 2022
Published: 18 January 2022

1. Introduction

According to the Environmental Protection Agency (EPA) [1], phenol is considered a priority pollutant, dangerous for the environment due to its high toxicity even at low concentrations. In Colombia, according to the Ministry of Environment and Sustainable Development in resolution 631 of 2015, the maximum permissible limit for phenol in wastewater discharges is 0.2 mg L^{-1}. The most common sources of phenol in water are effluents from industries that manufacture iron, rubber, resins, plastics, fibers, adhesives, and synthetic fuels. Phenol can be found in air and water because of the use and disposal of products that contain this substance; in the soil it tends to move into groundwater. Phenol-contaminated water sources have a bad taste and odor, so it is necessary to remove it in order to avoid repercussions for human health and the ecosystem [1,2]. According to the World Health Organization (WHO), the treatments to be carried out to produce safe water depend on the quality that is desired; a process to achieve basic levels of sanitation requires up to four barriers to eliminate traces of organic compounds: a typical water treatment scheme includes physical separation, passage through a membrane bioreactor or activated sludge, followed by treatment, such as advanced oxidation, activated carbon adsorption, or membrane filtration [2,3]. As mentioned in the first paragraph of this introduction, in Colombia, as in many Latin American countries, phenol is one of the compounds found in aquifer systems, generating major health problems for the entire population, especially the most unprotected, and mainly children. Several methods have been developed for the removal of phenol from water, such as photocatalytic degradation, electrochemical oxidation, solvent extraction, and biological degradation and adsorption, which is one of the most widely used methods for decontamination [4–11].

Adsorption on porous adsorbents is an alternative to processes like advanced oxidation, chlorination, and ozonation which involve reactive molecules, such as drugs, which can result in the production of more toxic compounds if agents such as hydrogen peroxide, ozone, and chlorine are present, giving rise to organochlorine compounds, furans, dioxins, and chloroform—molecules that have greater persistence and low degradability in the environment. Activated carbon is considered a non-reactive barrier that retains organic and inorganic compounds due to its physicochemical properties, such as high surface area, porosity, and the presence of surface chemical groups that allow it to interact with compounds that have several chemical characteristics [5–7].

According to scientific studies for Colombia, there is evidence for the presence of several kind of molecules, including those for pharmaceutical use, in water sources, generating a great problem that is concerning for state, environmental, political, and academic organizations in the context of evaluating solutions from different areas. One of the processes endorsed by the WHO in the guide for the production of safe water is adsorption on porous solids because it is considered an alternative to chemical processes that change the properties of pharmaceutical compounds, turning them into more toxic substances with greater difficulty of removal [7,10].

Colombia has a serious problem in the form of phenol contamination in water, which manifests itself by causing a noticeable unpleasant taste and odor change through the chlorination of water, despite the fact that its concentration is at ppm level and even less than that. Most phenols and their derivates are corrosive to skin and eye. In Colombia, as well as in other countries in the area, coal distillation and organic synthesis waste flows bearing coal entities contain large amounts of phenols and their derivatives, as well as phenolic compounds, which are present in wastewater from pulp and paper-bleaching facilities, and from resin, pesticide, insecticide, paint, and solvent industries. That is why it is very important to face this problem and generate solutions that can be scaled to the most vulnerable populations; it is a social duty for academia [8,9].

The adsorption process of phenolic compounds has been evaluated in several studies. The main conclusions shared by these works are that the adsorption process depends on factors such as the physical nature of the adsorbent (porous structure, surface chemistry), the physical nature of the adsorbate (pKa, polarity, size), and conditions of the solution (pH, ionic strength, adsorbate concentration) [2–6].

Regarding the adsorbent, factors such as geometric and chemical heterogeneity have been considered from the initial composition of the precursor, which affect the phenol adsorption process due to the presence of pores of different sizes that modify not only the kinetics of the process but also the adsorption capacity, since by increasing the volume of the micropores the amount of phenol adsorbed decreases [4]. On the other hand, the presence of narrow microporosity may not favor the process because phenol can form aggregates with water and increase its size, presenting diffusive restrictions in very small pores, as indicated by the kinetic data reported in the literature [5,7].

The analysis of the influence of surface chemistry on the adsorption capacity of phenol has also been evaluated. Studies conclude that activated carbon surfaces that have been subjected to oxidative treatments have lower adsorption capacities due to an increase in polarity in the surface which raises the affinity for the solvent, generating a blockage of the pores, so that the phenol interacts with the activated carbon through interactions with π electrons. However, an excess of oxidized groups can generate an inductive effect of electrons, also weakening the formation of interactions of this type [2,6].

Another of the postulated mechanisms for the adsorption of phenol on other adsorbents, such as activated carbons, is the electron donor–acceptor interaction, where the carbonyl groups of activated carbon are electron donors and the aromatic ring of phenol is the acceptor. Some authors have reported [7] the effect of heat treatment of activated carbons on phenol adsorption. According to the data, the process is favored in an activated carbon subjected to heat treatment at 1173 K, followed by treatment at 973 K, and finally at 1373 K. The author attributes this behavior to the increase in surface area caused by

the increase in porous structures generated in the heat treatment; however, an excess of temperature leads to the collapse of the porous structure. When comparing the adsorption capacities of activated carbon without heat treatment and with treatment at 1173 K for different temperatures for the adsorption system (298 K, 313 K, 328 K), it was found that the adsorption capacity does not vary with temperature but the heat treatment for the sample favors the process ($1.27 < 1.54$ mmol g^{-1}) [7–11].

On the other hand, other authors have reported [8] that the isosteric heat of adsorption decreased when the concentration increased from -78 kJ mol^{-1} to -5.5 kJ mol^{-1}; likewise, the immersion enthalpies showed the same trend and varied between -2152 and 82.8 J g^{-1}.

At basic pH, the presence of oxygenated groups on activated carbon decreases phenol adsorption capacity due to a strong repulsive effect between phenolate and acidic chemical groups that are ionized with negative charge; however, oxygenated groups of a basic nature, such as pyrones, can contribute to form adsorbate–adsorbent interactions because they are not dissociated [2,9].

Another study [10] indicated that phenol adsorption involves three phases: adsorption at infinite dilution, filling of micropores, and filling of larger micropores. In the first phase, there is a correlation between the number of oxygenated groups and a decrease in adsorption capacity, which is associated with an increase in the affinity of the surface for the solvent, which is corroborated by an increase in the immersion enthalpy in water with respect to the amount of acid groups. This same author affirms that aromatic compounds, such as phenol, present three mechanisms by which adsorption on activated carbon is carried out from the aqueous phase: interactions by dispersion of π electrons, formation of hydrogen bonds, and formation of electron donor–acceptor complexes [11].

Most phenol–adsorbent interactions are due to physisorption; however, the oxidative coupling of phenol on activated carbon is associated with chemisorption.

From the thermodynamic point of view, the adsorption of phenol on activated carbon is considered exothermic, with enthalpy values between -6.03 and -30.4 kJ mol^{-1}, according to [5]. The process presents a low energy barrier to be carried out given that the activation energies are around 13 kJ mol^{-1}, which confirms that the process is a physisorption. The entropy change values are positive and depend on the surface chemistry of the adsorbent and the chemistry of the solution [10,11].

The adsorption processes have made it possible to address this type of research during the last few years. A great variety of materials, such as activated carbons [12–16], silica [12,17,18], polymeric resins [12,19,20], fly ash [21], clays including kaolinite [22], and zeolites [23–27], have been explored in detail for the removal of phenolic pollutants from wastewater. Among these materials, some authors [12] have reported that materials such as zeolite adsorbents have been regarded as an alternative to activated carbon due to their adsorption–regeneration properties. They say that although they have attracted special attention in sorption processes, their use in this field is limited by their pore size diameter with regards to the size of the organic pollutants [12]. As such, the use of mesoporous materials seems to be promising because of their larger pore volume and diameter, their high surface area, and their regular channel type structures [28,29]. The interest in the potential utilization of mesoporous materials as sorbents is increasing due to the need for economical and efficient adsorbents to remove organic contaminants from wastewater.

According to the literature, the chemical modification of mesoporous adsorbents by introducing functional groups into the matrixes enhances their adsorption capacity for phenol-containing materials [30]. For example, organically functionalized mesoporous silica materials, such as MCM41 and SBA-15, have already been reported by Brunel et al. and Stein et al. [12,31,32]. However, information on mesoporous materials interacting with toxic phenolic compounds is still limited.

In some research published by renowned researchers, Mangrulkar et al. [12,33] have used MCM-41 to remove phenol from an aqueous solution and observed that the removal of phenols from water is strongly dependent on the type of species (dissociated or molecular), as dissociated species are more polar than molecular compounds and interact preferentially

with water rather than with MCM-41. Their works have allowed them to establish that the most important features involved in the investigation of adsorption phenomenon are: (i) interface characteristics, (ii) the adsorbate–adsorbent interactions, and (iii) adsorption isotherm [12]. It is worth mentioning that the physicochemical mechanisms in these materials are not very well described; no simple theory of adsorption could adequately describe experimental results. The adsorption phenomenon depends on interactions between the surface of the adsorbent and the adsorbed species. These interactions may be due to (i) chemical bonding, (ii) hydrogen bonding, (iii) hydrophobic bonding, or (iv) Van der Waals force. It was observed that the adsorption of substituted benzene depends on the electronic effect of the substituent. However, during the adsorption of dioxane on non-porous, mesoporous, and microporous silica, it was observed that adsorption on microporous silica is governed by pore volume and dimension.

SBA-15 material (Santa Barbara Amorphous No 15) is a mesoporous silica that has been increasing in importance due to its textural properties, regular mesoporous structure, high specific surface area, thermal and mechanical stability, distribution, and pore size. Its high uniformity allows for its potential use in the removal of inorganic and organic contaminants in aqueous solutions [34]. The functionalization of the silica generates an increase in the adsorption capacity because, upon including functional groups, the active sites increase and the conditions on the chemical surface improve [29].

This work was developed with the objective of preparing and functionalizing SBA-15 with polyaniline to increase the capacity to adsorb phenol from the liquid phase, enabling the study of its interactions through the enthalpy of the immersion of solids in benzene, water, and solutions of 0.1 M NaOH, 0.1 M HCl, and phenol, and the elucidation of the relationships that exist between the enthalpies of the immersion of silica and its modification, along with its physicochemical properties, such as surface area, total acidity and basicity, and pH at the point of charge zero. The phenol adsorption capacity of SBA-15 and SBA-15/PA was determined using the adsorption isotherms for aqueous solutions.

2. Materials and Methods

2.1. SBA-15 Synthesis

SBA-15 was synthesized according to the method reported by Zhao et al. [35]. Initially, 18 g of pluronic 123 (Sigma-Aldrich, St. Louis, MO, USA) and 135 g of water were weighed and dissolved, and the mixture was left while stirring for 24 h. This solution was then placed in a water bath at 37 °C, a solution of HCl (72 mL of concentrated hydrochloric acid in 450 mL of water) was added slowly, and then 42 mL of TEOS (tetraethylorthosilicate) (Aldrich) was added. Finally, the mixture was left while stirring for 20 h, washed with plenty of water, dried at 70 °C for 24 h, and calcined at 540 °C for 6 h.

2.2. Modification with Polyaniline

SBA-15 was modified with polyaniline, as reported by Weng et al. [36]. A solution of 42.9 mL of 0.55 M hydrochloric acid and 1.95 mL of aniline was prepared, followed by the addition of 2 g of SBA-15. This was stirred for 30 min in an ice-water bath at 0 °C, a solution of ammonium persulfate, APS (4.45 g of APS in 19.5 mL of water), was added dropwise, and the mixture was left to stand for 3 h. Subsequently, it was filtered and washed three times with water, acetone, and a 0.55 M hydrochloric acid solution. Finally, it was dried at 70 °C for 24 h. The solid obtained was called SBA-15/PA.

2.3. Textural Characterization

The surface area and pore volume were determined by weighing approximately 100 mg of the sample, which had been degassed at 250 °C for 24 h, followed by N_2 fission at 77 K on a Quantachrome Autosorb IQ2 sortometer. The surface area was determined by

applying the Brunauer–Emmett–Teller (BET) model. The most common form of the BET equation is:

$$\frac{\frac{P}{Po}}{n\left(1-\frac{P}{Po}\right)} = \frac{1}{n_m C} + \frac{C-1}{n_m C}\left(\frac{P}{Po}\right);\ C = \mathrm{Exp}\left(\frac{q1-q2}{RT}\right) \quad (1)$$

where n is the specific amount of gas adsorbed at the relative pressure P/P_o, n_m is the adsorption capacity in the monolayer, P is the pressure, P_o is the saturation pressure of a substance that is adsorbed at the adsorption temperature, and C is the BET constant that is exponentially related to the monolayer adsorption energy [37]. Micropore volume (V_o) was calculated using Dubinin–Radushkevich (D–R) equation; mesopore volume (V_{meso}), total volume, and pore diameter were calculated using the density functional theory (DFT) method.

2.4. Chemical Characterization

The total acidity and basicity were determined according to the method proposed by Boehm [38] with modifications. First, 0.1 g of the sample was mixed with 50 mL of 0.05 M NaOH and 50 mL 0.05 M HCl. The mixture was left under constant stirring for five days. Subsequently, an aliquot of 10 mL of the solution was titrated with previously standardized acid or base using a CG 840B Schott automatic titrator. The zero-charge point (pH_{pzc}) was determined using the mass titration method. Quantities between 0.1 and 0.6 g of the samples were weighed, and 10 mL of 0.1 M NaCl was added. They were left under constant stirring for 48 h; then, the pH of each solution was measured with a pH meter, a CG 840B Schott [39].

2.5. Determination of Immersion Enthalpy

The immersion enthalpies of SBA-15 and its modification in benzene, water, and solutions of 0.1 M NaOH, 0.1 M HCl, and phenol (100 mg L^{-1}) were determined using a heat-conduction microcalorimeter [40–45]. For the determinations, 0.1 g of a sample was weighed and placed in a glass vial that was fitted inside the equipment cell. Then, 10 mL of the liquid was placed in a stainless steel cell, the temperature was stabilized, and thermal recording was initiated by an electrical potential signal from the sensors; then, the sample was immersed in the liquid. The resulting thermal changes were recorded, and, finally, electrical calibration was performed.

2.6. Adsorption Isotherms

In order to investigate the influence of adsorption conditions on the adsorption ability of mesoporous SBA-15 and SBA-15/PA composites, including the initial concentration of phenol, adsorption temperature and pH value, batch adsorption experiments were conducted previously (these results are not shown here; they were taken as a basis to establish the experimental conditions of this investigation). Firstly, a series of phenol aqueous solutions with concentrations ranging from 20 to 150 mg L^{-1} were prepared by dissolving different amounts of phenol in deionized water. Then, a series of phenol aqueous solutions with the same phenol concentration (150 mg L^{-1}) and various pH values in the range of 2–10 were also prepared by introducing different amounts of HCl or NaOH solutions. Then, for each experiment, the adsorbent was separated from the mixture by centrifugation, and the residual concentration of phenol solution was measured using an ultraviolet–visible (UV–vis) spectrometer (Thermo Nicolet Nexus) at a characteristic adsorption wavelength of 271.0 nm. In addition, for studying the effect of adsorption temperatures on the uptake capacity of the mesoporous composite, 0.06 g of adsorbent was added to 100 mL of 150 mg L^{-1} phenol solution and stirred at 15, 25, 30, 35, and 40 °C, respectively. Then, the residual phenol concentrations were measured using the same method as mentioned above. Moreover, the adsorption capacity of pristine SBA-15 silica was also analyzed for studying the effect of polyaniline modification on the removal of phenol. Typically, 0.02 g of pristine SBA-15 and SBA-15/PA composite was, respectively,

added into 100 mL of phenol solutions with initial concentrations of 20–150 mg L^{-1} under stirring at 25 °C. After 15 h, the adsorbent was separated by centrifugation, and the residual resorcinol concentrations were measured using the UV–vis spectrometer. Finally, they were left stirring for 58 hours until they reached equilibrium. The samples were filtered and the phenol concentrations were determined on a UV–Vis Thermo Nicolet Nexus spectrophotometer at 271 nm. The equilibrium concentration, C_e (mg L^{-1}) and the amounts adsorbed on the adsorbent at equilibrium, q_e (mg g^{-1}), were calculated. The initial pH of phenol solutions is 6.9 in SBA-15 and 3.0 in SBA-15/PA, and these values were maintained during each of the experiments.

3. Results

3.1. Textural Characterization

Figure 1 shows the nitrogen adsorption isotherms obtained for SBA-15 and SBA-15/PA; the samples presented type IV(a) isotherms according to the updated IUPAC classification [39–41]. At medium relative pressures, capillary condensation began and H1-type hysteresis loops were generated, which are associated with mesoporous solids with cylindrical pore channels. For SBA-15/PA, the hysteresis loop is H5 type, which is associated with pore structures containing open and partially blocked mesopores. The incorporation of polyaniline in the pores of the silica explains the decrease in the amount of nitrogen adsorbed; this behavior is due to the limitation of the diffusion of nitrogen molecules that generate the surface groups located in the openings of the pores [42].

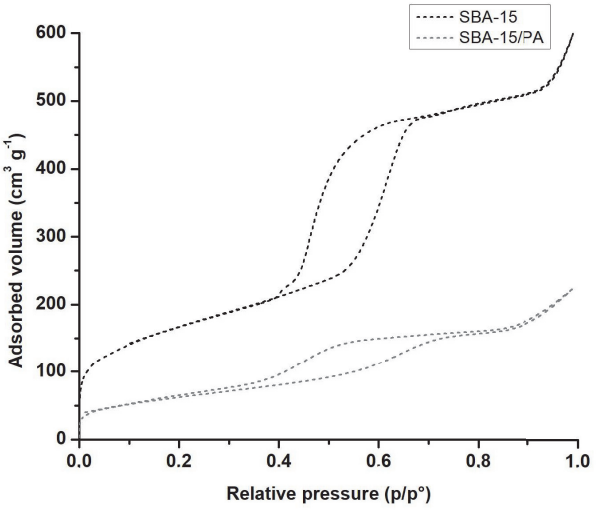

Figure 1. Nitrogen adsorption isotherms at 77 K for SBA-15 and SBA-15/PA.

The textural parameters of the BET surface area, micropore volume (V_o), mesopore volume (V_{meso}), total volume, and pore diameter were calculated from the experimental data of the N_2 adsorption–desorption isotherm and are shown in Table 1. The surface area value for SBA-15 was 654.5 $m^2 g^{-1}$ and its pore diameter was 6.08 nm; after the surface modification, the surface area and pore diameter values were reduced to 215.3 m^2 g^{-1} and 5.28 nm, respectively. Likewise, the total pore volume changed from 0.84 to 0.33 cm^3 g^{-1} due to the partial blocking of the pore channels of SBA-15 by polyaniline, supporting the idea that polymerization took place primarily within the pores of SBA-15 [42–44].

Table 1. Textural parameters of SBA-15 and SBA-15/PA determined from the N_2 isotherms at 77K.

Sample	Surface Area (m^2 g^{-1}) BET	V_o (cm^3 g^{-1})	V_{meso} (cm^3 g^{-1})	Total V (cm^3 g^{-1})	Average Pore Diameter (nm)
SBA-15	655	0.22	0.61	0.84	6.08 ± 0.06
SBA-15/PA	215	0.07	0.26	0.33	5.28 ± 0.05

The precision for the surface area values was ± 1 m^2 g^{-1}, and that for the pore volume was ± 0.01 $cm^3 g^{-1}$, according to the characteristics of the Quantachrome Autosorb IQ2 sortometer.

3.2. Chemical Characterization

Using the methodology proposed by Boehm, the acid–base character of the surface of the silica was determined depending on the amount of acidic or basic sites that it contained. Table 2 shows the results obtained for the acidity, basicity, and the point of zero-charge for SBA-15 and SBA-15/PA. SBA-15 has total acid groups of 0.026 meq g^{-1} and a pH at the point of zero charge of 6.5. According to these values, the acidity of the surface is related to the deprotonation of the silanols; after their modification, there is evidence of a decrease in the amount of acid sites to 0.011 meq g^{-1} and in the pH_{pzc} to 3.0, these values being attributed to the decrease in silanol groups present on the surface of SBA-15. The pH at the point of zero charge of the two samples is acidic, such that if the solids were put in contact with solutions whose pHs were lower than the pH_{pzc}, the charges on their surfaces would be positive, on average [45,46].

Table 2. Acidity, basicity, and pH at zero charge point of SBA-15 and its modification.

Sample	Acidic Sites (meq g^{-1})	Basic Sites (meq g^{-1})	pH_{pzc}
SBA-15	$0.026 \pm 1.0 \times 10^{-4}$	$0.010 \pm 1.2 \times 10^{-4}$	6.5 ± 0.01
SBA-15/PA	$0.011 \pm 1.2 \times 10^{-4}$	$0.006 \pm 0.8 \times 10^{-4}$	3.0 ± 0.01

3.3. Immersion Enthalpy Measurements

Immersion enthalpy is a thermodynamic parameter that correlates the pore structure and the surface chemistry of the solid. Table 3 shows the values obtained in the calorimetric determinations; all the immersion enthalpies are negative, which indicates that these processes are exothermic. Figures 2–4 show the electric potential curves as a function of time for the immersion process of samples and their modification into benzene, water, NaOH (0.1 M,) HCl (0.1 M), and phenol solution (100 mgL^{-1}) to evaluate the interaction between the silica, the solvents, and the solutions used. This information allows the magnitude of the interaction in the adsorption to be established.

Table 3. Enthalpies of immersion for SBA-15 and its modification in water, benzene, and solutions of HCl, NaOH, and phenol.

Sample	$-\Delta H_{Exp.}$ Water (J g^{-1})	$-\Delta H_{Exp.}$ Benzene (J g^{-1})	$-\Delta H_{Exp.}$.HCl (J g^{-1})	$-\Delta H_{Exp.}$ NaOH (J g^{-1})	$-\Delta H_{Exp.}$ Phenol Solution (J g^{-1})
SBA-15	31.2 ± 0.5	28.1 ± 0.4	62.2 ± 0.8	174.1 ± 2.3	41.0 ± 0.6
SBA-15/PA	20.4 ± 0.3	15.1 ± 0.2	58.7 ± 0.8	167.7 ± 2.2	18.5 ± 0.3

Figure 2 shows the potentiograms from the immersion calorimetry in water and benzene of SBA-15 and its modification. The polarity of the surface of the silicas could be evaluated based on the fact that the proportion of hydrophobicity and hydrophilicity of a surface can be estimated using the relationship with the enthalpies of immersion in a polar and a nonpolar liquid, such as water and benzene. As the values of the enthalpy of immersion in water of SBA-15 and SBA-15/PA were greater than those of the enthalpy of

immersion in benzene, the surfaces were considered hydrophilic. However, the formation of hydrogen bonds between the water molecules and the silanol groups of SBA-15 generated an enthalpy value of 31.2 J g^{-1}, and upon reducing the amount of silanol groups in SBA-15/PA by shielding the polyaniline molecules located in the polar sites of the surface of the silica, the enthalpy of immersion in water was reduced to 20.4 J g^{-1} [39–49].

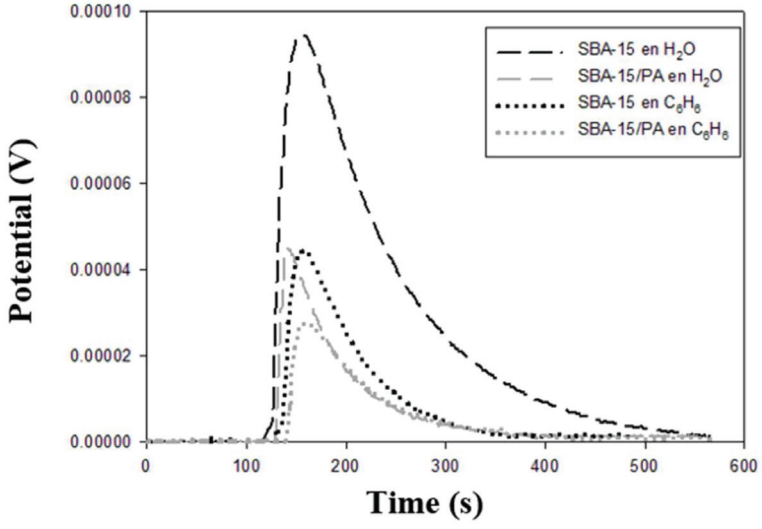

Figure 2. Potentiogram of immersion of the SBA-15 and its modification in water and benzene.

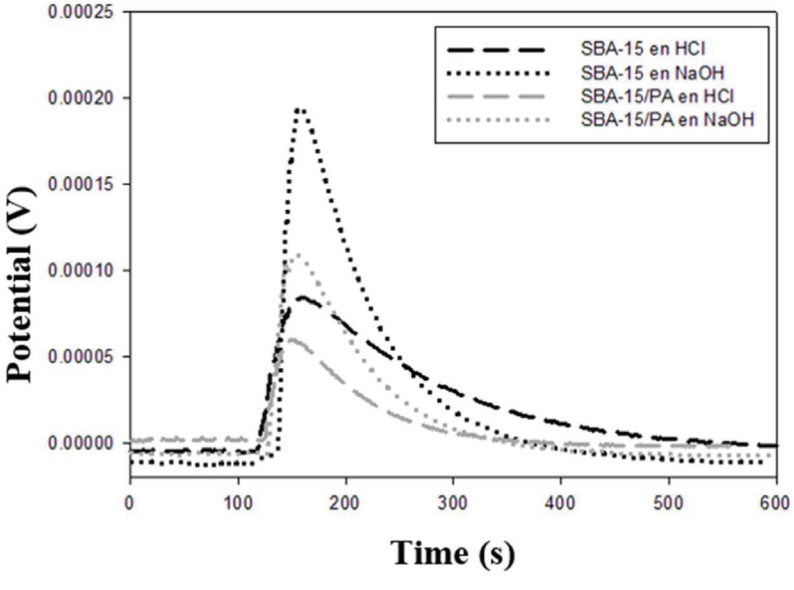

Figure 3. Immersion potentiogram for SBA-15 and its modification in HCl and NaOH.

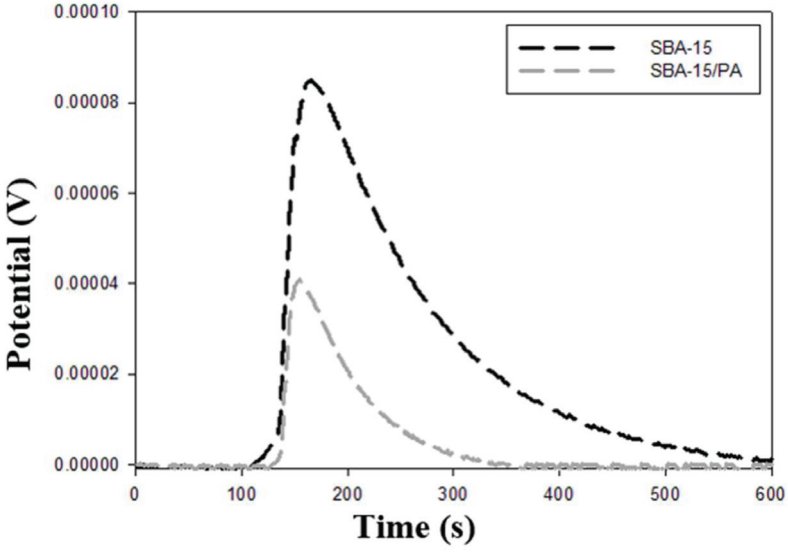

Figure 4. Immersion potentiogram for SBA-15 and its modification in 100 mg L^{-1} phenol solution.

The absolute values of the enthalpy of SBA-15 and SBA-15/PA were higher for immersion in the sodium hydroxide solution, as observable in Figure 3, confirming a greater interaction with the acidic sites of the silicas. As the enthalpy of immersion of the silicas in the solutions were related to the acidity and total basicity of the former, it is evident that, in the case of the immersion enthalpy being a function of the content of acid groups, there was an increase in the value of the enthalpy of immersion of SBA-15 when the acidity increased, with a value of 0.026 meq g^{-1}, and an immersion enthalpy in NaOH of 174.1 J g^{-1}, decreasing after functionalization with polyaniline to values of 0.011 meq g^{-1} and 167.7 J g^{-1}. With respect to the basic groups, it should be noted that they were related to the values for the immersion enthalpy of the silicas in HCl solution, since the values for the basic groups were lower than those for the acid groups. The same was observed with the values of the immersion enthalpy in HCl being lower than the enthalpy in NaOH [41,49–51].

Another characteristic of silicas is the pH at the point of zero charge, pH_{pcc}, which establishes the charge on the surface of the materials and is related to surface chemistry, and which, in turn, affects the energetic interactions that occur between the solid and the immersion liquid. For this reason, it corresponds to the enthalpy of immersion in benzene and a linear behavior is obtained; as the value of the enthalpy of immersion increases, the pH at the point of zero charge also increases, with 28.1 J g^{-1} being the immersion enthalpy of SBA-15, with a pH_{pcc} of 6.5; for SBA-15/PA, the enthalpy decreases to 15.1 J g^{-1}, as does the pH_{pcc} to 3.0 [47–49].

There is a directly proportional relationship between the enthalpy of immersion and the surface area of the silicas, with the greater 28.1 J g^{-1} enthalpy of immersion for SBA-15, because when there is a wider space for the entrance of molecules, greater interaction of the adsorbate with the porous structure is generated. The immersion enthalpy value for SBA-15/PA decreased to –15.1 J g^{-1}. This shows that there was a reduction in porosity due to the fixation of the functional groups on the surface [45–49].

The degree and nature of the interactions at the solid–liquid interface in processes such as adsorption can be determined using the immersion enthalpy, because, for some molecules, it can vary according to the specific interactions between the immersion liquid and the surface of the solid. The immersion enthalpy of SBA-15 in the 100 mg L^{-1} phenol solution was higher than that of SBA-15/PA. Figure 4 shows that the thermal effect obtained for SBA-15 was high and corresponded to the sum of various interactions, such as the

wetting of the solid surface by the solvent, the interaction of the solvents with the chemical groups on the surface, and the interaction of phenol with the surface and its groups. In SBA-15/PA, the access of the molecules to the surface decreased in such a way that there was a considerably low thermal effect; however, it continued to present an exothermic enthalpy, correlated with the processes of the interaction of the aniline monomers and the surface of the solid. The adsorbed amount and immersion enthalpy were affected by the contents of total acid and base groups on the surface of SBA-15 and its modification. It is known that, upon decreasing the content of acid groups, the adsorbed amount of the phenolic compound increased [45–49].

3.4. Adsorption Isotherms

In order to evaluate the effectiveness of the adsorbents, the equilibrium phenol adsorption (q_e) was studied as a function of the equilibrium concentration (C_e). Adsorption isotherms are modeled by different adsorption isotherms from aqueous solutions.

Adsorption isotherms from aqueous solutions

There are several theoretical models for the description of adsorption isotherms with different considerations, such as the starting hypotheses and the number of characteristic parameters of each of them. The models used in adsorption studies in single-component solid–liquid systems are related to thermodynamic models obtained from theoretical adsorption models based on the thermodynamic properties of the adsorbent and the fluid phase. The others are semi-empirical models, which are the result of an adjustment of experimental data to certain mathematical functions, although with a thermodynamic basis. The models commonly used for the adjustment and interpretation of the experimental data obtained in adsorption studies for solid–liquid single-component systems are detailed below.

Two-parameter isotherm models.

3.4.1. Langmuir Model

This is an empirical model that assumes monolayer adsorption and uniform adsorption energy on the surface [50–52]. There is no transmigration of the adsorbate in the plane of the surface [31]. Adsorption only occurs in a finite and fixed number of defined and localized sites that are identically equivalent and in which there are no lateral interactions or steric hindrance between the same adsorbed molecules on the adjacent sites [50]. Adsorption is homogeneous and each molecule has constant enthalpy and activation energy of sorption (all sites have the same affinity for adsorbate) [50–52].

$$q_e = \frac{q_m K_L C_e}{1 + K_L C_e}$$

where q_e = the amount of solute adsorbed per unit weight of adsorbent at equilibrium (mg g^{-1}), C_e = the equilibrium concentration of solute in solution volume (mg L^{-1}), q_m = the maximum adsorption capacity (mg g^{-1}), and K_L = the adsorption equilibrium constant of Langmuir (L mg^{-1}).

3.4.2. Freundlich Model

The equation being exponential, the model assumes that the adsorbate concentration increases on the surface of the adsorbent and that it is a multilayer adsorption [53,54]. It describes reversible and non-ideal adsorption with non-uniform distribution of heat of adsorption and affinity on the heterogeneous surface [53]. The amount adsorbed is the sum of the adsorption of all the sites.

$$q_e = K_F C_e^{1/n}$$

where q_e = the amount of solute adsorbed per unit weight of adsorbent at equilibrium (mg g^{-1}), C_e = the equilibrium concentration of solute in solution volume (mg L^{-1}), K_F = the Freundlich constant related to the relative adsorption capacity of the adsorbent

($mg^{1-(1/n)}$ $L^{1/n}$ g^{-1}), and n = the heterogeneity factor, related to the constant that indicates the intensity of the adsorption. If $n = 1$, it is a linear adsorption. If $n > 1$, it is a physical adsorption and it is favorable. If $n < 1$ it is a chemical adsorption. On the other hand, if the value of $1/n < 1$ indicates a normal Langmuir-type isotherm and if $1/n > 1$, cooperative adsorption is indicated.

Two-parameter isotherm models.

3.4.3. Sips Model

The Sips model is a combined form of the Langmuir and Freundlich expressions deduced to predict systems with heterogeneous adsorption and overcome the limitations at high concentrations of the Freundlich equation [55–58]. At low concentrations, the adsorbate is reduced to the Freundlich isotherm, whereas at high concentrations a monolayer adsorption is predicted, characteristic of the Langmuir isotherm. As a general rule, the parameters of the equation are mainly governed by adsorption conditions, such as pH, temperature, and concentration [55,56].

$$q_e = \frac{q_{mS}(K_S C_e)^{\frac{1}{n_S}}}{1 + (K_S C_e)^{\frac{1}{n_S}}}$$

where q_e = the amount of solute adsorbed per unit weight of adsorbent at equilibrium (mg g^{-1}), C_e = the equilibrium concentration of solute in solution volume (mg L^{-1}), q_{ms} = the Sips maximum adsorption capacity (mg g^{-1}), K_s = the Sips equilibrium constant, and n_s = the Sips model exponent.

3.4.4. Tóth Model

This is an empirical equation modified from the Langmuir equation that reduces the error between the experimental data and the predicted values of the equilibrium adsorption data [54–58]. The application of this equation is more appropriate for multilayer adsorption and for heterogeneous adsorption systems that satisfy the low and high concentration ranges [57,58]. Its correlation assumes an asymmetric quasi-Gaussian distribution, with most sites having an adsorption energy lower than the maximum peak or the mean value [57,58].

$$q_e = q_{mT} \frac{C_e}{\left[\frac{1}{K_T} + C_e^{m_T}\right]^{1/m_T}}$$

where q_e (mmol g^{-1}) and C_e (mmol L^{-1}) have the same meaning as in the above equations, q_{mT} (mmol g^{-1}) = the Tóth maximun adsorption capacity, K_T = the Tóth equilibrium constant, and mT = the model exponent. When mT is equal to 1, Toth's equation is reduced to Langmuir's equation, with which it can be deduced that this parameter is related to the heterogeneity of the system.

3.4.5. Redlich–Peterson Model

Similar to the Sips model, this takes into account the characteristics of the Langmuir and Freundlich isotherms in a single equation, indicating that the adsorption mechanism is a combination of both models. Due to its versatility, it allows the representation of an adsorption system in equilibrium for a wide range of concentrations and can be applied for both homogeneous and heterogeneous systems. The model is represented by the following equation [57,58].

$$q_e = \frac{K_{RP} C_e}{1 + \alpha_{RP} C_e^{\beta}}$$

where K_{RP} (L g^{-1}), $\dashv_{RP}$ (L mg^{-1})$^{-\beta}$ and the exponent β (dimensionless) are Redlich–Peterson parameters. The β value is between 0 and 1 and it determines the degree of heterogeneity of the surface. This equation is transformed into a linear isotherm (Henry's

equation) at low surface coverage (β = 0), it is reduced to the Langmuir isotherm when β = 1, and becomes the Freundlich isotherm when K_{RP} y α_{RP} >> 1 y β = 1.

The results shown in Figure 5 for the SBA-15 and SBA-15/PA samples were analyzed and evaluated according to the aforementioned models using the ANOVA analysis of variance optimization method, included in the Sigma-Plot® v.10.0 software for each adjustment function according to each model. These results correspond to experimental data in the equilibrium data of phenol that were adjusted with the mathematical expressions which represent the corresponding isotherms in their linear form for each model, and their results are presented in Tables 4 and 5.

The associated error analysis shows that the Freundlich model is the most appropriate for representing the adsorption process, as it had excellent correlations of $R^2 > 0.99$ and low standard mean error percentages, ε < 1.2%. Likewise, the Langmuir model, with R^2 correlations greater than 0.97 and ε errors less than 2.9%, can represent the isotherms in an acceptable manner, as shown when representing the experimental data in Figure 5 by the dotted lines in the experimental adsorption data. The measure of the heterogeneity of the surface 1/n in the Freundlich model in SBA-15/PA is 0.3296; as this is less than 1, it is established that the adsorption process is favorable and indicates that the surface is heterogeneous; the relative adsorption capacity of the SBA-15 modified with polyaniline is 24.07 times higher than the relative adsorption capacity of SBA-15. The maximum adsorption capacity values calculated using the Langmuir model were 138 and 85.54 mg g^{-1} for SBA-15/PA and SBA-15, respectively, again indicating an increase in adsorption effectiveness upon the inclusion of the polyaniline groups in the structure.

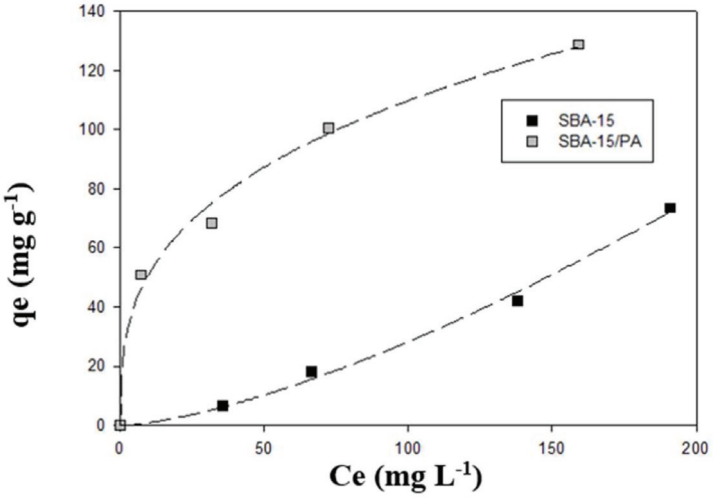

Figure 5. Isotherms for phenol adsorption from experimental data from aqueous solutions on silica and its modification.

Table 4. Langmuir and Freundlich (two-parameter isotherms) parameters on silica and its modification.

Model	Parameter	SBA-15	SBA-15/PA
Langmuir	q_m	85.54	138
	K_L	0.0024	0.0463
	R^2	0.992	0.972
	ε (%)	2193	2929
Freundlich	K_F	0.0347	24.07
	1/n	1.4552	0.3296
	R^2	0.9971	0.9962
	ε (%)	1289	1376

Table 5. Sips, Tóth and *Redlich–Peterson* (three-parameter isotherms) parameters on silica and its modification.

Model Isotherms Parameters	SBA-15	SBA-15/PA
Sips		
q_{ms} (mg g^{-1})	67.37	78.97
K_s (L^m mg^{-m})	4.32×10^{-4}	3.23×10^{-3}
m_s	1988	0.902
R^2	0.9769	0.9804
Tòth		
q_{mT} (mg g^{-1})	67.34	96.45
K_T	0.467	0.134
m_T	3.691	0.928
R^2	0.9587	0.9601
Redlich–Peterson		
K_{RP}	6.4326	3.6784
α	1.6785	1.7865
β	0.2745	0.3215
R^2	0.9587	0.9301

The phenol isotherms in SBA-15 and SBA-15/PA are shown in Figure 5. It was observed that the adsorption order in terms of the amount adsorbed was greater in SBA-15/PA than in SBA-15. This can be explained by the fact that large amounts of polyaniline macromolecules were fixed on the walls of the pores of SBA-15, and since phenol is a weak acid and polyaniline a weak base, acid–base interactions occurred in the adsorption process. SBA-15/PA, having an acidic surface, interacts with the phenol solution, while the amino groups of the aniline interact with the hydroxyl group through hydrogen bonds [49–58]. When you have the value of n ($0 < 1\ n < 1$) for the Freundlich model, this suggests that the adsorbent surface is heterogeneous. In this study, it is interesting that by modifying the SBA-15 with polyaniline, one went from a surface that was not homogeneous to a more homogeneous one. This had an impact on the adsorption capacity of phenol.

In summary, it can be said that for the two-parameter models, the sample with the best fit between these two models was the SBA-15 sample, and, under the experimental conditions of this research work, there is a greater fit to the Freundlich model compared to Langmuir's, taking from now on the regression coefficient R^2 as a criterion for the analysis of all models.

Regarding the three-parameter models, neither of the two shows a behavior that allows an affirmation that one fits better than one of the abovementioned models, despite having three parameters. If we slightly amplify the R^2 criterion in qualitative way, it can be said that the SBA-15/PA sample has a relative fit to the Sips model.

This result is consistent if it is taken into account that the Sips model is derived from a mathematical treatment between the Langmuir and Freundlich models. For this reason, the adsorption of phenol on the SBA-15/PA samples and even that of SBA-15 can be explained by this model. This result turns out to be very interesting and should be further explored at different phenol concentrations and temperatures.

The experimental results with the adsorbents at a constant temperature in equilibrium conditions were tested with various isotherm models (Langmuir, Freundlich, Sips, Tòth, and Redlich–Peterson isotherms) to establish the adsorption mechanisms. The testing of Langmuir and Freundlich isotherms is essential, since it reveals whether the adsorbent surface has a specific number of active sites which come in contact with adsorbates to form a permanent attachment. The test of the Langmuir isotherm ascertains physical adsorption, whereas the test of the Freundlich isotherm determines chemical adsorption, and they also facilitate the determination of adsorption mechanisms. SBA-15 and SBA-15/PA had interesting adsorption capacities and comparable adsorption capacities with respect to other adsorbents; therefore, these adsorbents are suitable for practical use.

4. Conclusions

SBA-15 was modified using polyaniline on the pore wall according to textural and chemical characterization. Novel adsorbents were synthesized to effectively remove phenol pollutants from aqueous solutions. SBA-15 and SBA-15/PA mesoporous composites were synthesized by successfully modifying polyaniline on the pore wall of SBA-15 silica. The experimental results demonstrate that these composite materials are very promising candidates for the removal of phenol.

The experimental results demonstrated that SBA-15/PA is a promising candidate for the removal of phenol with an adsorption capacity of 138 mg g^{-1} compared with 85.54 mg g^{-1} for SBA-15. The surface area of SBA-15 was 654.5 m^2 g^{-1}, and when it was modified this decreased to 254.6 m^2 g^{-1}; the micropore volume, mesopore volume, total volume, and pore diameter presented the same behavior due to the fact that large amounts of polyaniline macromolecules were fixed on the walls of the pores of SBA-15. Increasing behavior of the immersion enthalpy for SBA-15 and SBA-15/PA in benzene was observed with respect to the increase of BET surface area, explained by its same porous nature. According to the enthalpies in water and benzene, the surfaces of the silicas were considered hydrophilic. There was an increase in the enthalpy when the acidity increased. The adsorbed amount and immersion enthalpy were affected in such a way that, as the content of acid groups decreased, the adsorbed amount of the phenolic compound increased.

Author Contributions: Conceptualization, L.G. and L.J.C.; methodology and formal analysis, L.J.C., L.G. and J.C.M.-P.; investigation and writing—original draft preparation, L.G. and L.J.C.; writing—review and editing, L.J.C., L.G. and J.C.M.-P. All authors have read and agreed to the published version of the manuscript.

Funding: This research received no external funding.

Institutional Review Board Statement: Not Applicable.

Informed Consent Statement: It does not apply to this research.

Data Availability Statement: We do not report any data.

Acknowledgments: The authors thank the framework agreement between Universidad Nacional de Colombia and Universidad de los Andes (Bogotá, Colombia) under which this work was carried out. Juan Carlos Moreno-Piraján thanks for an award the Facultad de Ciencias of Universidad de los Andes, number INV-2021-128-2257, and the support of "Publica tus Nuevos Conocimientos y Expón tu Nuevas Creaciones", de la Vicerrectoría de investigaciones de la Universidad de los Andes (Bogotá, Colombia).

Conflicts of Interest: The authors declare that they have no known competing financial interests or personal relationships that could appear to have influenced the work reported in this paper.

References

1. Biglari, H.; Afsharnia, M.; Alipour, V.; Khosravi, R.; Sharafi, K.; Mahvi, Y. A review and investigation of the effect of nanophotocatalytic ozonation process for phenolic compound removal from real effluent of pulp and paper industry. *Environ. Sci. Pollut. Res.* **2017**, *24*, 4105–4116. [CrossRef] [PubMed]
2. Dąbrowski, A.; Podkościelny, P.; Hubicki, Z.; Barczak, M. Adsorption of phenolic compounds by activated carbon—A critical review. *Chemosphere* **2005**, *58*, 1049–1070. [CrossRef] [PubMed]
3. Kuśmierek, K.; Świątkowski, A.; Skrzypczyńska, K.; Błażewicz, S.; Hryniewicz, J. The effects of the thermal treatment of activated carbon on the phenols adsorption. *Korean J. Chem. Eng.* **2017**, *34*, 1081–1090. [CrossRef]
4. Lorenc-Grabowska, E. Effect of micropore size distribution on phenol adsorption on steam activated carbons. *Adsorption* **2016**, *22*, 599–607. [CrossRef]
5. Rincón-Silva, N.G.; Moreno-Piraján, J.C.; Giraldo, L. Equilibrium, kinetics and thermodynamics study of phenols adsorption onto activated carbon obtained from lignocellulosic material (Eucalyptus Globulus labill seed). *Adsorption* **2016**, *22*, 33–48. [CrossRef]
6. Vargas, D.P.; Giraldo, L.; Moreno-Piraján, J.C. Effect of textural and chemical characteristics of activated carbons on phenol adsorption in aqueous solutions. *Pol. J. Chem. Technol.* **2017**, *19*, 87–93. [CrossRef]
7. Zhang, D.; Huo, P.; Liu, W. Behavior of phenol adsorption on thermal modified activated carbon. *Chin. J. Chem. Eng.* **2016**, *24*, 446–452. [CrossRef]

8. Carvajal-Bernal, A.M.; Gómez-Granados, F.; Giraldo, L.; Moreno-Pirajan, J.C. Application of the Sips model to the calculation of maximum adsorption capacity and immersion enthalpy of phenol aqueous solutions on activated carbons. *Eur. J. Chem.* **2017**, *8*, 112–118. [CrossRef]
9. Gaber, D.; Haija, M.A.; Eskhan, A.; Banat, F. Graphene as an Efficient and Reusable Adsorbent Compared to Activated Carbons for the Removal of Phenol from Aqueous Solutions. *Water Air Soil Pollut.* **2017**, *228*, 320. [CrossRef]
10. Kowalczyk, P.; Deditius, A.; Ela, W.P.; Wiśniewski, M.; Gauden, P.A.; Terzyk, A.P.; Neimark, A.V. Super-sieving effect in phenol adsorption from aqueous solutions on nanoporous carbon beads. *Carbon* **2018**, *135*, 12–20. [CrossRef]
11. Cheng, W.; Gao, W.; Cui, X.; Ma, J.; Li, R. Phenol adsorption equilibrium and kinetics on zeolite X/activated carbon composite. *J. Taiwan Inst. Chem. Eng.* **2016**, *62*, 192–198. [CrossRef]
12. Toufaily, J.; Koubaissy, B.; Kafrouny, L.; Hamad, H.; Magnoux, P.; Ghannam, L.; Karout, A.; Hazimeh, H.; Nemra, G.; Hamieh, M.; et al. Functionalization of SBA-15 materials for the adsorption of phenols from aqueous solution. *Cent. Eur. J. Eng.* **2013**, *3*, 126–134. [CrossRef]
13. Nakagawa, K.; Namba, A.; Ariayadejwanich, P.; Tanthapanichakoon, W. Adsorption of phenol and reactive dye from aqueous solution on activated carbons derived from solid wastes. *Water Res.* **2004**, *38*, 1791–1798. [CrossRef]
14. Papadimas, S.P.; Sorial, G.A.; Suidan, M.T.; Speth, T.F. The effect of molecular oxygen on the activated carbon adsorption of natural organic matter in Ohio river water. *Water Res.* **1995**, *29*, 551–562.
15. Su, F.; Lv, L.; Hui, T.M.; Zhao, X.S. Phenol adsorption on zeolite-templated carbons with different structural and surface properties. *Carbon* **2005**, *43*, 1156–1164. [CrossRef]
16. Pan, B.C.; Zhang, X.; Zhang, W.M.; Zhang, Q.X. Adsorption of phenolic compounds from aqueous solution onto a macroporous polymer and its aminated derivative: Isotherm analysis. *J. Hazard. Mater.* **2005**, *121*, 233–241. [CrossRef] [PubMed]
17. Zhao, Z.G.; Zhang, L.H.; Lin, Y. Thermodynamics of Adsorption of Organic Compounds at the Silica Gel/Nonpolar Solvent Interfaces. *J. Colloid Interface Sci.* **1994**, *166*, 23–28. [CrossRef]
18. Parida, S.; Dash, S.; Patel, S.; Mishra, B. Adsorption of organic molecules on silica surface. *Adv. Colloid Interface Sci.* **2006**, *121*, 77–110. [CrossRef]
19. Zhang, W.; Chen, J.; Pan, B.; Zhang, Q. Modeling cooperative adsorption of aromatic compounds in aqueous solutions to nonpolar adsorbent. *Sep. Purif. Technol.* **2006**, *49*, 130–135. [CrossRef]
20. Delval, F.; Crini, G.; Vebrel, J. Removal of organic pollutants from aqueous solutions by adsorbents prepared from an agroalimentary by-product. *Bioresour. Technol.* **2006**, *97*, 2173–2181. [CrossRef]
21. Wang, S.; Boyjoo, Y.; Choueib, A.; Zhu, Z.H. Removal of dyes from aqueous solution using fly ash and red mud. *Water Res.* **2005**, *39*, 129–138. [CrossRef]
22. Alkaram, U.F.; Mukhlis, A.A.; Al-Dujaili, A.H. The removal of phenol from aqueous solutions by adsorption using surfactant-modified bentonite and kaolinite. *J. Hazard. Mater.* **2005**, *169*, 324–332. [CrossRef]
23. Koubaissy, B.; Toufaily, J.; Kafrouny, L.; Joly, G. Industrial water treatment, by adsorption, using organized mesoporous materials. *Phys. Procedia* **2011**, *21*, 228–233. [CrossRef]
24. Khalid, M.; Joly, G.; Renaud, A.; Magnoux, P. Removal of Phenol from Water by Adsorption Using Zeolites. *Ind. Eng. Chem. Res.* **2004**, *43*, 5275–5280. [CrossRef]
25. Koubaissy, B.; Joly, G.; Magnoux, P. Adsorption and Competitive Adsorption on Zeolites of Nitrophenol Compounds Present in Wastewater. *Ind. Eng. Chem. Res.* **2008**, *47*, 9558–9565. [CrossRef]
26. Koubaissy, B.; Joly, G.; Batonneau-Gene, I.; Magnoux, P. Adsorptive Removal of Aromatic Compounds Present in Wastewsssgater by Using Dealuminated Faujasite Zeolite. *Ind. Eng. Chem. Res.* **2011**, *50*, 5705–5713. [CrossRef]
27. Koubaissy, B.; Toufaily, J.; El-Murr, M.; Daou, T.J.; Joly, G.; Magnoux, P.; Hamieh, T. Adsorption Kinetics and Equilibrium of Phenol Drifts on three Zeolites. *Cent. Eur. J. Eng.* **2012**, *2*, 435–444. [CrossRef]
28. Zhao, D.Y.; Feng, J.; Huo, Q.; Melosh, N. Triblock copolymer syntheses of mesoporous silica with periodic 50 to 300 angstrom pores. *Science* **1998**, *279*, 548–552. [CrossRef]
29. Zhao, D.Y.; Huo, Q.; Feng, J.; Chmelka, B.F. Nonionic Triblock and Star Diblock Copolymer and Oligomeric Surfactant Syntheses of Highly Ordered, Hydrothermally Stable Mesoporous Silica Structures. *J. Am. Chem. Soc.* **1998**, *120*, 6024–6036, Erratum in *J. Am. Chem. Soc.* **2014**, *136*, 10546. [CrossRef]
30. Zhang, L.X.; Yu, C.C.; Zhao, W.R.; Hua, Z.L. Preparation of multi-amine-grafted mesoporous silicas and their application to heavy metal ions adsorption. *J. Non-Cryst. Solids* **2007**, *353*, 4055–4061. [CrossRef]
31. Brunel, D. Functionalized micelle-templated silicas (MTS) and their use as catalysts for fine chemicals. *Microporous Mesoporous Mater.* **1999**, *27*, 329–344. [CrossRef]
32. Stein, A.; Melde, B.J.; Schroden, R.C. Hybrid Inorganic-Organic Mesoporous Silicates-Nanoscopic Reactors Coming of Age. *Adv. Mater.* **2000**, *12*, 1403–1419. [CrossRef]
33. Mangrulkar, P.A.; Kamble, S.P.; Meshramb, J.; Rayalu, S.S. Adsorption of phenol and o-chlorophenol by mesoporous MCM-41. *J. Hazard. Mater.* **2008**, *160*, 414–421. [CrossRef] [PubMed]
34. Zhai, Q.; Li, X. Efficient removal of cadmium (II) with SBA-15 nanoporous silica: Studies on equilibrium, isotherm, kinetics and thermodynamics. *Appl. Water Sci.* **2019**, *9*, 143. [CrossRef]
35. Kjellman, T.; Reichhardt, N.; Sakeye, M.; Smått, J.H.; Lindén, M.; Alfredsson, V. Independent Fine-Tuning of the Intrawall Porosity and Primary Mesoporosity of SBA-15. *Chem. Mater.* **2013**, *25*, 1989–1997. [CrossRef]

36. Weng, S.; Lin, Z.; Zhan, Y.; Chen, L.; Zhou, J. Facile synthesis of SBA-15/polyaniline nanocomposites with high electrochemical activity under neutral and acidic conditions. *React. Funct. Polym.* **2009**, *69*, 130–136. [CrossRef]
37. Filip, A.; Macdonald, T.; Martis, V.; Parkin, I. Evaluation of the BET theory for the characterization of meso and microporous MOFs. *Small Methods* **2018**, *2*, 11.
38. Boehm, H. Chemical Identification of Surface Groups. *Adv. Catal.* **1966**, *16*, 179–274.
39. Babić, B.; Milonjić, S.; Polovina, M.; Kaludierović, B. Point of zero charge and intrinsic equilibrium constants of activated carbon cloth. *Carbon* **1999**, *37*, 477–481. [CrossRef]
40. Moreno, J.; Giraldo, L. Determination of the immersion enthalpy of activated carbon by microcalorimetry of the heat conduction. *Instrum. Sci. Technol.* **2000**, *28*, 171–178. [CrossRef]
41. Thommes, M.; Kaneko, K.; Neimark, A.V.; Olivier, J.P.; Rodriguez-Reinoso, F.; Rouquerol, J.; Sing, K.S. Physisorption of gases, with special reference to the evaluation of surface area and pore size distribution (IUPAC Technical Report). *Pure Appl. Chem.* **2015**, *87*, 1117. [CrossRef]
42. Takamori, D.; Bizeto, M.; Fantini, A.; Rubinger, C.; Faez, R.; Martins, T. Polyaniline inclusion into ordered mesoporous silica matrices: Synthesis, characterization and electrical transport mechanism. *Microporous Mesoporous Mater.* **2019**, *274*, 212–219. [CrossRef]
43. Boukoussa, B.; Hakiki, A.; Nunes-Beltrao, A.; Hamacha, R.; Azzouz, A. Assessment of the intrinsic interactions of nanocomposite polyaniline/SBA-15 with carbon dioxide: Correlation between the hydrophilic character and surface basicity. *J. CO2 Util.* **2018**, *26*, 171–178. [CrossRef]
44. Santos, S.; Cecilia, J.; Vilarrasa-García, E.; Silva Junior, I.; Rodríguez-Castellón, E.; Azevedo, D. The effect of structure modifying agents in the SBA-15 for their application in the biomolecules adsorption. *Microporous Mesoporous Mater.* **2016**, *232*, 53–64. [CrossRef]
45. Rodríguez-Estupiñán, P.; Giraldo, L.; Moreno-Piraján, J.C. Calorimetric study of amino-functionalised SBA-15. *J. Therm. Anal. Calorim.* **2015**, *121*, 127–134. [CrossRef]
46. Navarrete, L.; Giraldo, L.; Moreno, J.C. Influence of surface chemistry on the immersion enthalpy of activated carbons in aqueous solutions of phenol and 4-nitro phenol. *Rev. Colomb. Chem.* **2006**, *35*, 215–224.
47. Rodríguez-Estupiñán, F.; Giraldo, L.; Moreno-Piraján, J.C. Relationship between immersion enthalpies of activated carbons modified in their surface chemistry in different liquids and their physicochemical characteristics. *Afinidad Rev. Quím. Teór. Apl.* **2015**, *72*, 114–119.
48. Vargas, D.; Giraldo, L.; Moreno-Piraján, J.C. Characterization of granular activated carbon prepared by activation with $CaCl_2$ by means of gas adsorption and immersion calorimetry. *Adsorption* **2016**, *22*, 717–723. [CrossRef]
49. Carvajal-Bernal, A.; Gómez-Granados, F.; Giraldo, L.; Moreno-Piraján, J.C. A study of the interactions of activated carbon-phenol in aqueous solution using the determination of immersion enthalpy. *Appl. Sci.* **2018**, *8*, 843. [CrossRef]
50. Asmaly, H.; Ihsanullah; Abussaud, B.; Saleh, T.; Laoui, T.; Gupta, K.; Ali, M. Adsorption of phenol on aluminum oxide impregnated fly ash. *Desalin. Water Treat.* **2016**, *57*, 6801–6808. [CrossRef]
51. Li, Q.; Yu, H.; Song, J.; Pan, X.; Liu, J.; Wang, Y.; Tang, L. Synthesis of SBA-15/polyaniline mesoporous composite for removal of resorcinol from aqueous solution. *Appl. Surf. Sci.* **2014**, *290*, 260–266. [CrossRef]
52. Kundu, S.; Gupta, A.K. Arsenic adsorption onto iron oxide-coated cement (IOCC): Regression analysis of equilibrium data with several isotherm models and their optimization. *Chem. Eng. J.* **2006**, *122*, 93–106. [CrossRef]
53. Freundlich, H.M.F. Over the adsorption in solution. *J. Phys. Chem.* **1906**, *57*, 385–471.
54. Adamson, A.W.; Gast, A.P. *Physical Chemistry of Surfaces*, 6th ed.; Wiley Interscience: New York, NY, USA, 1997.
55. Hamdaoui, O.; Naffrechoux, E. Modeling of adsorption isotherms of phenol and chlorophenols onto granular activated carbon. Part II. Models with more than two parameters. *J. Hazard. Mater.* **2007**, *147*, 401–411. [CrossRef] [PubMed]
56. Ho, Y.S.; Porter, J.F.; Mckay, G. Equilibrium isotherm studies for the sorption of divalent metal ions onto peat: Copper, nickel and lead single component systems. *Water Air Soil Pollut.* **2002**, *141*, 1–33. [CrossRef]
57. Prasad, R.K.; Srivastava, S.N. Sorption of distillery spent wash onto fly ash: Kinetics and mass transfer studies. *Chem. Eng. J.* **2009**, *146*, 90–97.
58. Gimbert, F.; Morin-Crini, N.; Renault, F.; Badot, P.M.; Crini, G. Adsorption isotherm models for dye removal by cationized starch-based material in a single component system: Error analysis. *J. Hazard. Mater.* **2008**, *157*, 34–46. [CrossRef]

sustainability

MDPI

Article

Caesium-133 Accumulation by Freshwater Macrophytes: Partitioning of Translocated Ions and Enzyme Activity in Plants and Microorganisms

Laura Zorza [1,2], Maris Bertins [3], Kristine Saleniece [2,4], Gunta Kizane [2], Andrejs Grinbergs [1,2], Ugis Eismonts [2,4], Ingars Reinholds [2,3,*], Arturs Viksna [3] and Olga Muter [1,2]

[1] Institute of Microbiology and Biotechnology, University of Latvia, 1 Jelgavas Str., 1004 Riga, Latvia; laura.zorza@lu.lv (L.Z.); andrejsg2@inbox.lv (A.G.); olga.mutere@lu.lv (O.M.)
[2] Institute of Chemical Physics, University of Latvia, 1 Jelgavas Str., 1004 Riga, Latvia; kristine.saleniece@lu.lv (K.S.); gunta.kizane@lu.lv (G.K.); ugis.eismonts@lu.lv (U.E.)
[3] Faculty of Chemistry, University of Latvia, 1 Jelgavas Str., 1004 Riga, Latvia; maris.bertins@lu.lv (M.B.); arturs.viksna@lu.lv (A.V.)
[4] Faculty of Medicine, University of Latvia, 1 Jelgavas Str., 1004 Riga, Latvia
* Correspondence: ingars.reinholds@lu.lv; Tel.: +371-2680-2448

Abstract: The potential of aquatic plants to accumulate Cs may be of notable importance in the environmental monitoring of radioactive wastes. This study aimed to evaluate the accumulation of Cs-133 by freshwater macrophytes *Bacopa amplexicaulis*, *Elodea densa*, *Ceratophyllum submersum*, and *Limnobium laevigantum* after a 10-day incubation period with CsCl (1–1000 μM). The partitioning of Cs and other elements, including 21 metals, such as P, B, and As, was analyzed using inductively coupled plasma mass spectrometry combined with principal component analysis (PCA). The enzymatic activity of plant crude extracts and aquatic microorganisms was characterized. The transfer factor (TF) reached the highest values of 0.13 and 0.10 for *C. submersum* and *L. laevigantum*, respectively, at 1000 μM Cs. The TFs in the other sets were below 0.1. In the presence of Cs-133, there was a significant increase in dehydrogenase activity ($p < 0.05$) and a decrease in the activity of the Folin–Ciocalteu assay. A three-fold decrease in culturable microorganisms was found in plants with 1000 μM Cs. PCA analysis revealed the species-specific elemental distribution in plant biomass and the aquatic phase. A negative correlation between Na, Ca (2.0–2.5, PC1) and Mg, K, and P (−2, PC1) was found. Certain enzyme groups can serve as bioindicators of Cs pollution in aquatic ecosystems.

Keywords: Cs-133; element analysis; antioxidant activity; enzymes; ICP-MS; macrophytes; transfer factor

Citation: Zorza, L.; Bertins, M.; Saleniece, K.; Kizane, G.; Grinbergs, A.; Eismonts, U.; Reinholds, I.; Viksna, A.; Muter, O. Caesium-133 Accumulation by Freshwater Macrophytes: Partitioning of Translocated Ions and Enzyme Activity in Plants and Microorganisms. *Sustainability* **2022**, *14*, 1132. https://doi.org/10.3390/su14031132

Academic Editors: Avelino Núñez-Delgado, Zhien Zhang, Elza Bontempi, Mario Coccia, Marco Race and Yaoyu Zhou

Received: 29 November 2021
Accepted: 28 December 2021
Published: 19 January 2022

1. Introduction

The growing global demand for nuclear energy poses the risk of the accidental release of nuclear products into the environment. According to data published by the European Nuclear Society in 2021, Europe has 176 nuclear power plants in operation, raising concerns about potential nuclear waste in the coming decade. Recently, a large amount of data on this topic was reported by Japanese researchers due to their experience with nuclear incidents affecting the release of Cs radionuclides into the environment. The Fukushima Daiichi Nuclear Power Plant disaster in 2011 resulted in radioactive caesium adsorption by soil and plants as a result of the transfer of radionuclides to livestock [1–5]. Other sites of nuclear mishaps, e.g., Ignalina [6] and Chernobyl, have been reported [7,8]. The accumulation risks of the disposal of radioactive wastes can also be attributed to Latvia and other post-Soviet countries due to the presence of old nuclear power plant facilities and their nuclear wastes located in these countries' territory [9].

In this respect, the health and ecological effects of radionuclide contamination are of great interest to various fields of research, including biomedicine, ecology, and biotechnology techniques for the removal of toxic metal compounds. Among radionuclides, radiocaesium (Cs-137, Cs-134) raises the most concern due to the relatively long half-life of Cs-137 (> 30 years) and the high degree of mobility and bioavailability of Cs^+ ions [10,11]. Anoxic remobilization of Cs from sediments and the release of Cs by macrophytes should be considered in order to understand and predict Cs distribution in the water column [12,13].

The partitioning of Cs among the abiotic and biotic compounds of aquatic ecosystems depends on many factors, e.g., mineralogical composition of suspended and bottom sediments, abundance of monovalent cations, and the characteristic geochemistry of water [10,11]. Many studies have been conducted with stable Cs-133 due to the similarities in the distribution of radiocaesium and Cs-133 in soil, sediment, and water [3,13–15].

The present study particularly focused on Cs distribution in aquatic environments and accumulation by macrophytes for the development of water treatment technologies, including wetlands, ponds, hydroponics, and other approaches [13,16]. In 1993, the overall accumulation of Cs-137 by macrophytes in a small, drainless lake in Belarus constituted 5% of its stock in the lake's water mass [8]. The quantification of Cs contamination in the field experiment showed that the contributions of the suspended particle fraction and aquatic biota were 80 and 20%, respectively [17]. Studies on Cs accumulation by plants have demonstrated a broad heterogeneity in results depending on species characteristics and environmental factors [1,3,13,18].

Moreover, the presence and accumulation of other metals in plants may have a significant impact on plant properties and indicate environmental contamination, which could help determine technological solutions. For example, in their experiments with water hyacinth (*Eichhornia crassipes*), Du et al. [19] found that, despite a good Me absorption capacity, the concentration of metals in leaves was low due to a low translocation factor. Therefore, after the remediation stage, the leaves of water hyacinth can be used as animal feed [19].

In this study, the accumulation of Cs by freshwater macrophytes was evaluated, in addition to concentrations of other elements in plant biomass. The processes of metal accumulation and remobilization in plants are supposed to be species-specific and distinct depending on the initial Cs concentration in water. An emphasis on extra-low concentrations of Cs (i.e., 1 μM) in water will bring this study closer to real water contamination with micropollutants, particularly radionuclides. The macrophytes *Bacopa amplexicaulis*, *Elodea densa*, *Ceratophyllum submersum*, and *Limnobium laevigantum* were selected for the study due to their reported potential to accumulate different metals in considerable quantities, whereas no data on Cs accumulation thus far have been reported in these studies [20–27]. Thus, it was critical to evaluate, within laboratory testing, whether these plans could be used to determine Cs accumulation.

The aim of this study was to analyse the accumulation of non-radioactive Cs (Cs-133) in freshwater macrophytes and to evaluate the potential toxic impact of caesium on plant species. It was hypothesized that this knowledge would have a necessary impact on a more detailed evaluation of the effect of radiocaesium (Cs-137, Cs-134) on the environment, including the accumulation in plant species, to exclude or confirm the summary effect of chemical toxicity and the impact on radiation. For this reason, the main evaluation in this study was provided solely by testing Cs-133 at different concentrations.

The experiment was performed in self-sustaining aquarium water for 10 days, with added initial caesium chloride (CsCl) concentrations ranging from 1 to 1000 μM. Plant responses to Cs-133 accumulation was evaluated by a range of enzyme groups, which are involved in antioxidant activities and metabolism, and the effect of multivariate factors, such as elemental contents and enzyme activity, was compared by statistical analysis.

2. Materials and Methods

2.1. Plants, Chemicals, and Reagents

Representative freshwater aquatic higher plants, namely, *B. amplexicaulis*, *E. densa*, *C. submersum*, and *L. laevigantum*, were purchased from local professional suppliers in Latvia. All the chemicals purchased for testing were of analytical grade and were used as received without any further purification. Ascorbic acid, CsCl, fluorescein diacetate (FDA), 3-methyl-2-benzothiazoninone hydrazine (MBTH), TRIS-HCl, 4-methylcatehol, polyvinylpyrrolidone (PVP), and Standard Count Agar (SCA) were purchased from Sigma-Aldrich (St. Lois, MO, USA). Guaiacol was purchased from Scharlau (Barcelona, Spain). Iodonitrophenyl formazan (INTF) was purchased from Fluka Analytical (Vienna, Austria). $Na_2HPO_4 \times 12H_2O$ and Na_2CO_3 were purchased from Lachema (Brno, Czech Republic). KH_2PO_4, acetone, Bradford reagent, 35% H_2O_2, Folin-Ciocalteau reagent were purchased from Enola (Riga, Latvia). L-3,4-dihydroxyphenylalanine dopaquinone (L-DOPA) was purchased from Alfa Aesar (Lancashire, UK).

2.2. Experimental Setup

The four plant species were cultured in a 56 L freshwater aquarium under sustainable conditions for six months. Then, each of the plant species was submerged in a 120 mL polypropylene flask containing 100 ml of aquarium water amended with 0, 1, 10, 500, and 1000 μM CsCl water solution. Samples were taken in triplicate to evaluate the range of element contents and provide microbiological and biochemical testing. The amount of plant biomass per flask was approximately 10% of the liquid volume. The experimental flasks were randomly placed and incubated at 23 °C for 10 days with a 12:12-h dark–light cycle and periodic shaking. Additional control sets were prepared with the same concentrations of CsCl added to the water samples without the plants. At the end of the incubation period, the volume of the aquatic phase was justified to the initial level by adding deionized water due to evaporation. Afterwards, the liquid phase and plant were separated and kept frozen until testing.

2.3. Physicochemical Characteristics of the Aquatic Phase

The water used in the study was considered to be self-sustaining aquarium water, derived from the freshwater aquarium, which had a sustained ecosystem (plants, fish, snails, shrimps, gravel with biofilm) for at least three months. The water pH was 6.8, conductivity was 563 μS/cm, concentrations of sodium, potassium, calcium, phosphorous, and magnesium in the freshwater were 28.97 mg/L, 4.61 mg/L, 3.64 mg/L, 74.46 μg/L, and 18.98 mg/L, respectively. Concentrations of nitrites and nitrates were below the level of detection (LOD) (data not shown).

2.4. Element Analysis

Before analysis, the moisture content was determined in plant species by drying partial samples at 105 °C until a constant weight, according to laboratory practices of plant nutritional analysis [28].

The analysis of elemental composition (e.g., 21 metals, B, P, and As) was conducted using an Agilent 8900 (USA) inductively coupled plasma triple quadrupole mass spectrometry (ICP-QQQ-MS) device equipped with a MicroMist nebulizer. The results of determined element concentrations, except Cs, are summarized in Figure S4 of the Supplementary Material. The instrumental parameters of ICP-MS were set as follows: RF power —1.550 W; auxiliary gas flow—0.90 mL/min; plasma gas flow—15.0 L/min; He cell gas flow—5.0 mL/min; and sampling depth—8 mm. The analytical standard stock solutions were purchased from TraceCert®(Sigma-Aldrich, Burlington, MA, USA) for ICP (100 mg/L). The instrumental limit of detection (LOD) for the determined elements was 0.02 μg/L and the limit of the quantification (LOQ) was 0.06 μg/L. The linear range for the measurements by the ICP-MS method was up to 10 mg/L. The relative standard deviation (RSD) within the analysis of one sample replicate did not exceed 6%. For the calibration

graph, standard solutions in the concentration ranged from 0.1 to 100.0 µg/L. Calibration solutions were prepared from stock standard solutions. A calibration graph with blank correction was used to calculate the concentrations of elements in the samples. An internal standard mix solution from Agilent Technologies (10 g/mL) was used as an internal standard. A stability check of the ICP-MS system was performed by using two standard solutions after every 10 samples. For quality control of the analytical procedures, the same elements were also determined using reference material IAEA-336 provided by the International Atomic Energy (Vienna, Austria) containing 45 elements.

The reference material sample was included at the beginning and end of each analytical sequence. The differences between the certified and measured values did not exceed 10%. Three replicates of each sample were used for the analysis. A Mass Hunter workstation programme, together with its Instrument control and Offline data analysis programmes, was used.

The transfer factor (TF) of Cs-133 from the aquatic phase to plants was calculated according to [29], with minor modifications, as stated in Equation (1):

$$TF = \frac{(final\ metal\ concentration\ in\ plant) - (initial\ metal\ concentration\ in\ plant)}{metal\ concentration\ in\ aquatic\ phase} \quad (1)$$

2.5. Microbiological Analysis

The number of colony-forming units (CFU) was determined by the microdilution plating method. Sample dilutions (10^{-1} to 10^{-6}) were prepared for each sample in microplates. Using a multichannel pipette, 10 µL of each sample dilution was used to inoculate Petri dishes containing SCA medium. The plates were incubated at 30 °C for 48 h. The data obtained were processed in triplicate and determined as CFU/mL.

2.6. Testing of Enzyme Activity in the Aquatic Phase and Crude Plant Extracts

2.6.1. Aquatic Phase

The enzyme activity of microorganisms in water was measured by the FDA hydrolysis assay according to the procedure reported, with some modifications [30]. The water samples were transferred to a 12-well microplate (600 µL per well). After the addition of 2.4 mL FDA reaction mixture (4 mg FDA, 2 mL acetone, 48 mL 60 mM phosphate buffer) to each well, the plate was incubated for 48 h at 37 °C. Afterwards, the reaction was stopped by the addition of 600 µL acetone. The samples were transferred to 1.5 mL reaction microtubes and centrifuged at 10,000 rpm for 5 min. The supernatant was transferred to a 96-well microplate (200 µL per well). The hydrolysed FDA concentration was determined photometrically using a TECAN Infinite F50 microplate reader at OD492 (Männedorf, Switzerland).

2.6.2. Plant Crude Extract

Preparation of the Plant Crude Extract

Frozen plant samples were washed twice with distilled water. Ten grams of the plant sample was cut into thin slices and homogenized in buffer medium (50 mL 100 mM sodium phosphate buffer (pH 7.0) containing 1 mM ascorbic acid and 0.5% (w/v) PVP) for 5 min at 4 °C. The homogenate was filtered through three layers of cheesecloth. The filtrate was then centrifuged at 5000× g for 15 min, and the supernatant was collected according to the procedure reported by [31].

Protein Concentration

The concentration of proteins in crude plant extracts was determined using the Bradford assay. The measurement was performed in 96-well microplates with 200 µL Bradford [32] reagent and 100 µL of sample per well. The calibration curve was prepared using bovine albumin with good linearity (R^2 = 0.96). Before testing the enzyme activity, plant crude extracts were justified by protein concentrations.

DOPA-MBTH Assay

The assay measures the pink pigment formed by the reaction of Besthorn's hydrazone (MBTH) with dopaquinone, the product of oxidation of L-DOPA by tyrosinase [33]. The reaction mixture of 45 mg L-DOPA and 10 mg MBTH was dissolved in 25 mL 50 mM phosphate buffer at pH 6.0, and 500 µL crude extract in a total volume of 3.0 mL was prepared at 23 °C. The increase in absorption was measured photometrically at 492 nm. The assay was carried out in triplicate.

Dehydrogenase Activity

The dehydrogenase (DHA) activity was determined by the reduction of 2-p-iodo-3-nitrophenyl-5-phenyltetrazolium chloride (INT) to iodo-nitrophenyl formazan (INTF), according to [34] with some modifications. Two mL of the crude plant extract sample was centrifuged at 10,000 rpm for five minutes. The supernatant was discarded. The reaction was performed on a concentrated sample by adding 200 µL of the reaction mixture (20 mL of 0.25 M TRIS-HCl, 40 mg INT, 10 mg glucose). The samples were incubated for 24 h at 28 °C in triplicate, after which the absorption was measured at 492 nm using a Tecan Infinite F50 microplate reader (Switzerland).

Peroxidase Activity

The peroxidase activity was determined using 4-methylcatechol as the substrate. The reaction mixture (100 mM sodium phosphate buffer (pH 7.0), 5 mM 4-methylcatechol, 5 mM H_2O_2, and 500 µL of crude extract in a total volume of 3.0 mL) was prepared at 23 °C. The increase in the absorption caused by oxidation of 4-methylcatechol by H_2O_2 was measured photometrically at 420 nm [35]. The assay was carried out in triplicate.

The Folin–Ciocalteu Assay

The Folin–Ciocalteu (F-C) reaction is an antioxidant assay based on electron transfer, which measures the reductive capacity of an antioxidant. A plant extract aliquot was mixed with a diluted Folin–Ciocalteau reagent (2.5 mL, 10%) and Na_2CO_3 (4%, 2.0 mL) aqueous solution, as described by [36]. After 24 h in the dark, absorbance was measured at 740 nm using a spectrophotometer. A control sample was performed with 500 µL distilled water, 2.5 mL Folin–Ciocalteau reagent, and 2 mL Na_2CO_3 solution. The assay was carried out in triplicate.

Guaiacol Peroxidase Activity

Guaiacol peroxidase is involved in many important biosynthetic processes and defence against stress, e.g., exposure to polycyclic aromatic hydrocarbons, heavy metals, and herbicides [37]. The reaction mixture contained 80 mM guaiacol and 10 mM H_2O_2 in 0.066 M K-Na phosphate buffer (pH = 7.4), with the addition of polyvinylpyrrolidone according to [38]. The enzymatic reaction was started by adding 0.1 mL of the crude plant extract to 3 mL of the reaction mixture. The activity of guaiacol peroxidase was measured photometrically at 492 nm. The assay was carried out in triplicate.

2.7. Statistical Analysis

A one-way analysis of variance (ANOVA) was applied to evaluate the differences between the obtained results. The level of significance was set to $p < 0.05$. All statistical analyses were performed using Microsoft Excel and CAT (Chemometrics agile tool) software (Gruppo di Chemiometria della Divisione di Chimica Analitica della Società Chimica Italiana).

For multivariate statistical analysis, Statistica for Windows 6.0 software packages (StatSoft, Tulsa, OK, USA) were used. The calculation of mean concentrations of macro- and trace elements in plants and water samples and the analysis of variance to estimate statistically significant differences between groups of samples were carried out. To estimate the relationships between element concentrations in plants, Pearson's correlation coeffi-

cients were calculated. Additionally, principal component analysis (PCA) was applied to the experimental data sets. The data for PCA were normalized to unit concentration to avoid misclassifications caused by different orders of magnitude in the variables. The combination of PCA can assess the contribution of specific factors that may affect the variations in the elements in different plant parts and appreciate the mechanisms influencing the element distribution in each plant species regarding the effect of CsCl concentration.

3. Results

3.1. Accumulation of Cs and Other Metals by Aquatic Plants

The accumulation of Cs by macrophytes was measured after 10 days of incubation. As shown in Figure 1A, the initial Cs concentration greatly influenced the intensity of Cs accumulation in the plant biomass. Thus, the amount of Cs in biomass in the sets with 1000 μM Cs was 1.5–2.0 orders higher than that with 10 μM Cs. This trend was shown for all tested plants. At the lowest Cs concentration (i.e., 1 μM), its accumulation in plants was negligible, particularly 29.1, 35.3, 22.0, and 28.1 mg/kg dw for *B. amplexicaulis*, *E. densa*, *C. submersum*, and *L. laevigantum*, respectively (Figure 1A). One of the most important criteria for evaluating the metal-accumulation potential of plants is the transfer factor (TF) of Cs-133 in the plants. The data on Cs TF values for the macrophytes under the tested conditions are summarized in Table 1. The highest TF values were detected for *C. submersum* and *L. laevigantum* at 1000 μM Cs, which reached 0.13 and 0.10, respectively. Other measurements of TF for different initial Cs concentrations and four tested plants were below 0.1 (Table 1).

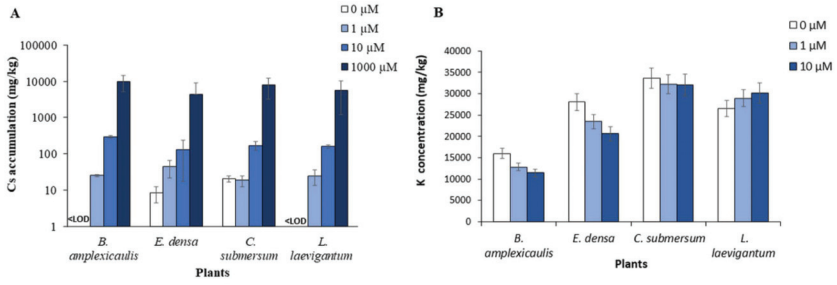

Figure 1. Accumulation of Cs (**A**) and K (**B**) in aquatic plants after incubation with different concentrations of CsCl for 10 days. <LOD values are below the LOD limit of detection.

Table 1. The transfer factor of Cs-133 after the 10-day incubation of macrophytes in the aquatic phase with different Cs concentrations.

Initial Cs Concentration (μM)	Plants			
	B. amplexicaulis	*E. densa*	*C. submersum*	*L. laevigantum*
1	0.09	0.00	0.05	0.06
10	0.09	0.05	0.09	0.04
1000	0.02	0.04	0.13	0.10

Our data on Cs and K concentrations in plant biomass have been tested for their possible correlation depending on the initial Cs concentrations. Putting together all the data related to 0, 1, 10, and 1000 μM Cs, the correlation analysis showed a strong species-specific effect. In particular, the concentrations of Cs and K in plant biomass were positively correlated in *B. amplexicaulis* ($R^2 = 0.61$) and *E. densa* ($R^2 = 0.50$), while not correlated in *C. submersum* ($R^2 = -0.00$) and negatively correlated in *L. laevigantum* ($R^2 = -0.79$) (Figure S1).

3.2. Microbial Abundance and Enzyme Activity in an Aquatic Phase Depending on the Cs Concentration

As was reported earlier, direct biological Cs accumulation from water/sediment/soil occurs readily due to primary producers (i.e., plants) and microorganisms [10,11]. At the beginning of the experiment, an aquatic phase contained a sustained microbial consortium. Therefore, further incubation of different plants with Cs was expected to change the microbial activity. The FDA hydrolysis activity assay was applied for estimation of microbial response towards Cs-133 in an aquatic phase during the 10-day experiment. As shown in Figure 2A, FDA hydrolysis activity did not show any trend with increasing Cs concentration in the aquatic phase. No significant plant species-specific differences were revealed. Another parameter that could indicate the effect of Cs on the microbial community is the number of culturable microorganisms. As shown in Figure 2B, a decrease in the CFU count by three orders in the presence of 1000 μM Cs was found compared to the control set without Cs. The exceptions were the sets with *E. densa* and non-planted sets, where the inhibition of culturable microorganisms by 1000 μM Cs was negligible (Figure 2B).

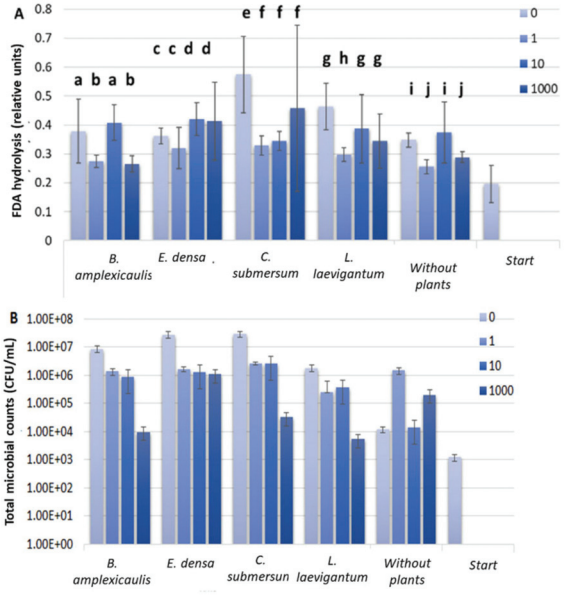

Figure 2. Fluorescein diacetate (FDA) hydrolysis assay (**A**) and CFU counts (**B**) in an aquatic phase before and after plant incubation with different concentrations of CsCl for 10 days. Concentrations of CsCl: 0, 1, 10, and 1000 μM. The FDA hydrolysis assays were incubated for 72 h. For variables with different letters, the difference between the means is statistically significant ($p < 0.05$). The differences are shown within the dataset for one plant individually.

3.3. Changes in Enzyme Activity in Plant Crude Extract after Plant Incubation with Cs

In our study, the physiological response of macrophytes to Cs-133 was assessed by the changes of different groups of enzymes, i.e., DHA, which reflects the electron transport system activity, correlated with the respiration rate [39]; peroxidase and guaiacol peroxidase–enzymatic antioxidants [40], L-DOPA+MBTH assay–phenol oxidases activity [41], and Folin–Ciocalteu–polyphenols–nonenzymatic antioxidants [40]. Some of these reactions developed relatively slowly and were thus measured after 24 h incubation (Figure 3), while others reacted immediately after the addition of the enzyme substrate and monitored for the first 15 min (Figure 4).

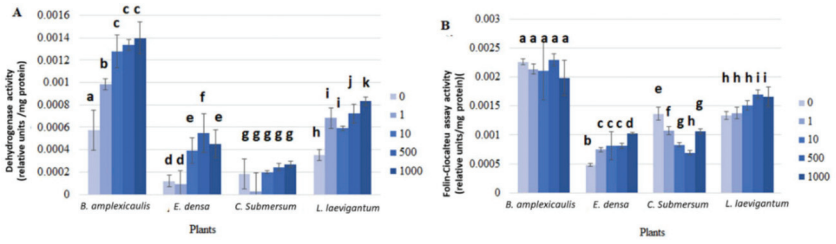

Figure 3. Dehydrogenase (**A**) and Folin–Ciocalteu (**B**) assays with crude plant extracts after plant incubation with different concentrations of CsCl for 10 days. Concentrations of CsCl: 0, 1, 10, and 1000 μM. A—Dehydrogenase; B—Folin–Ciocalteu assay. Enzyme activity was measured after 24 h of incubation. For variables with different letters, the difference between the means is statistically significant ($p < 0.05$). The differences are shown within the dataset for one plant individually.

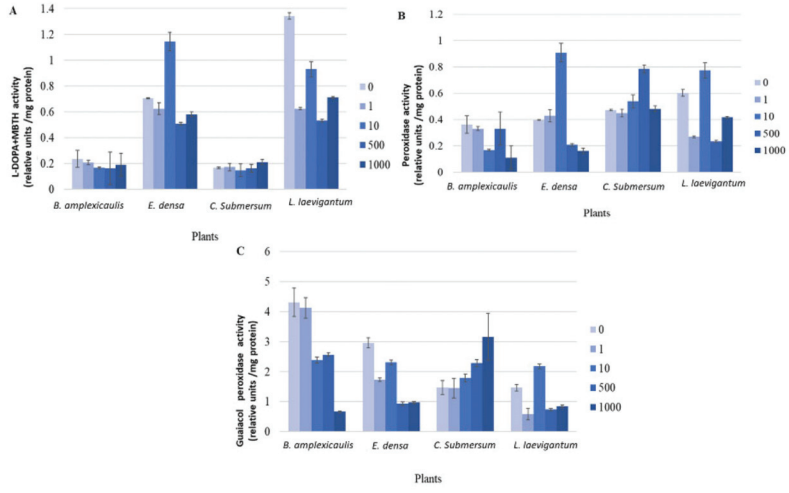

Figure 4. L-DOPA + MBTH (**A**), peroxidase (**B**), and guaiacol peroxidase (**C**) assays with crude plant extracts after plant incubation with different concentrations of CsCl for 10 days. Concentrations of CsCl: 0, 1, 10, and 1000 μM. Enzyme activity of crude plant extracts is presented in units defined as a 0.001 change in absorbance per minute.

The activity of DHA gradually increased in the crude plant extract with increasing Cs concentration in the aquatic phase. In particular, the enzyme activity in *B. amplexicaulis*, *E. densa*, *C. submersum*, and *L. laevigantum* after incubation at 1000 μM Cs was 142, 279, 48 and 137% higher, respectively, than in the control without Cs (Figure 3A). An increase of DHA activity in the presence of 1 μM Cs was significant ($p < 0.05$) in the sets with *Bacopa* sp. and *Limnobium* sp. compared with the control. A further significant ($p < 0.05$) increase in DHA activity with increasing Cs concentration from 1 to 10 μM Cs was observed for *B. amplexicaulis* and *E. densa* (Figure 3A).

The FC assay revealed a slight Cs activation effect for *E. densa* and *L. laevigantum*, while no effect and a gradual decrease in *B. amplexicaulis* ($p > 0.05$) and *C. submersum*, respectively, were detected (Figure 3B). Specifically, a gradual significant ($p < 0.05$) decrease in the activity was detected in *C. submersum* at 1, 10, and 500 μM Cs (Figure 3B).

The fast development of a colour reaction in the L-DOPA, peroxidase, and guaiacol peroxidase assays revealed the more precise differences in the kinetics of antioxidant response in four tested plants depending on the Cs concentration (Figures S2–S4 of the Supplementary Material). A considerable increase of enzyme activity at 10 μM Cs, compared with

the control, was shown in *E. densa* in DOPA and peroxidase assays and in *L. laevigantum* in a guaiacol peroxidase assay (Figures S2 and S3). More precisely, quantification of these differences (i.e., change in absorbance per minute) showed an increase in the mentioned enzymes 1.61, 2.28, and 1.49 times compared to the control, respectively (Figure 4).

3.4. Principal Component Analysis

Previous studies showed that in the case of a large amount of multivariate data, PCA can be effectively used to indicate covariation in different measured parameters between different plant species [42].

PCA of the studied plants after plant incubation with different concentrations of CsCl showed that the most variability we observed was in Component 1 (PC1, 41.4% of variance). Cs (−0.1 on PC1) is not the main factor that varies in different samples. The differences in PC1 are explained by the different elemental patterns of each plant species. There is good separation of different species on PC1. *C. submersum* forms a separate cluster with a centre at −3.4 on PC1, *L. laevigantum* and *E. densa* with a centre at 0 on PC1, and *B. amplexicaulis* with a centre at +3.2 on PC1. The main differences are related to the negative correlation of Na and Ca (1.8–2.6, PC1) and Mg, K, and P (−1.8–−2.6, PC1). Component 2 (PC2, 17.4%) shows the impact of increasing the Cs concentration on different plant species. There is practically no impact of increasing the Cs concentration on *L. laevigantum*, while there is a negative correlation between Cs and Mg content in *C. submersum* and a negative correlation between Cs and Mg content in *B. amplexicaulis*. Significant changes in the content of macroelements for *C. submersum*, *B. amplexicaulis*, and *E. densa* appear at a very high Cs content (1000 µM CsCl) (Figure 5). The accumulation of different elements in plant biomass after the 10-day incubation is shown in Figure S1 of the Supplementary Material. PCA also shows that the dehydrogenase and Folin–Ciocalteu assays covariate with Cs concentration and are most expressed in *B. amplexicaulis*. Guiacol peroxidase increases with increased Cs concentration and is most expressed in *C. submersum* L-DOPA + MBTH, and peroxidase activity decreases with the increase in Cs concentration. These changes are more expressed in *E. densa* and *L. laevigantum*.

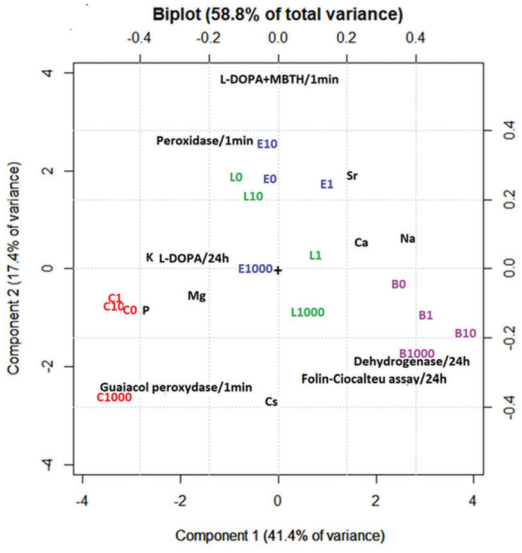

Figure 5. Principal component analysis (PCA) of macroelements in the studied plants (B—*B. amplexicaulis*, C—*C. submersum*, E—*E. densa*, and L—*L. laevigantum*) after plant incubation with different concentrations of CsCl for 10 days. Concentrations of CsCl: 0, 1, 10, and 1000 µM.

4. Discussion

Our results showed that the amount of Cs accumulated by macrophytes depended on the initial Cs concentrations in an aquatic phase. This observation is in good agreement with [14], who reported that concentrations of endogenous Cs were correlated with those in the environment, particularly sediments [14]. In this respect, the possible adsorption mechanisms of Cs-133 can explain the dependence of Cs accumulation on the initial concentration of Cs in water. This mechanism was proposed by [14] in model experiments with *E. densa* in hydroponics with predominant localization of Cs-133 in the cell wall or apoplectic regions. The same dependence was also reported to be attributed to other metals, e.g., Co [43]. However, the non-even distribution of Cs-133 in plant organs with greater amounts of Cs in younger parts of stems and leaf blades indicated the selective sorption of Cs by plants [4]. Vacula et al. [15] recently reported on Cs accumulation by *C. demersum* L. under laboratory and field conditions with a Cs concentration range comparable with that in our study. Thus, in the sets with initial Cs concentrations of 8 and 1067 μM after 8 days, the plant biomass accumulated on average 78 and 6248 mg/kg Cs, respectively [15]. In our study, after 10 days, at initial Cs concentrations of 10 and 1000 μM, 201.3 and 8763.2 mg/kg Cs, respectively, were accumulated by *C. submersum* (Figure 1A).

The possible mechanisms responsible for metal accumulation in submerged plants have been summarized by [44]. This review demonstrated a broad variability of the extent of metal accumulation in aquatic plants, depending on plant species, environmental conditions (including metal abundance and concentration), and experiment design. Among the protective functions of submerged plants against metal cytotoxicity, access control, rapid translocation, efficient accumulation, and detoxification are indicated [44]. The key roles in metal homeostasis and tolerance use such proteins as heavy metal-transporting ATPases, natural resistance-associated macrophage proteins, cation diffusion facilitator family proteins, and multidrug and toxin efflux proteins [45].

The values of TF are species-specific and greatly depend on the environmental conditions and the period of plant contact with metals [3,15]. For example, the TF of Cs from soil by shoots and brown rice ranged from 0.018 to 0.068 and 0.004 to 0.065, respectively [1]. Shinano et al. [3] compared the TF of radiocaesium (Cs-137, Cs-134) in 33 varieties of terrestrial *Amaranthus* spp. and indicated species-specific differences, which varied in the range from 0.048 to 0.170 [3]. Among the TF, other parameters are widely used in aquatic toxicology, e.g., bioconcentration and bioaccumulation factors. These factors are calculated by similar equations however differ by considering either only the dissolved phase or both the dissolved and particulate phases of a contaminant in the environment [46]. In addition, root and shoot accumulation factors, as well as translocation factors, are used for distinguishing metal localization in the plant [47].

Most of the studies focusing on Cs uptake by plants also emphasized Cs and K interrelations in the plants. In particular, the removal of Cs from water/sediments/soil often correlated with the K concentration. Absorption of Cs^+ into the roots was suggested to have occurred using two types of K^+ transporters (i.e., high affinity and low affinity) [48]. Our results indicate a strong species-specific effect. This fact is concordant with the studies of other authors [49]. In a study on Cs-137 and K-40 distribution in a lake, a negative correlation of Cs accumulation by *Phragmites australis* and K concentration was found [7]. Another field trial for 552 days in a pond reservoir spiked with Cs-133 demonstrated a correlation of Cs-133 removal with a period of increasing K concentration in the water, e.g., in winter [12]. As reported by [43], a high discrimination of the K+ transporter against Cs+ on the plant cell membranes takes place at enhanced K concentrations, i.e., above 0.3 mM. In our study, the K concentration in water did not exceed 0.1 mM (p.2.3), so it is unlikely to affect Cs accumulation in plants under the tested conditions. Inhibition of Cs uptake by plants can also occur in the presence of divalent ions, i.e., Ca^{2+}, Mg^{2+}, and Ba^{2+} [50,51].

Another factor that could facilitate Cs removal from aquatic environments is microbial activity. Microorganisms can directly interact with and change the physicochemical properties of certain elements [44,52].

The response of microorganisms to Cs-133 in an aquatic phase in our study was evaluated by enzyme activity and CFU count. The FDA hydrolysis assay is based on the ability of bacteria or fungi to split the FDA molecule using several enzymes (e.g., esterases, lipases, proteases) [39]. FDA hydrolysis activity may correlate with the total physiological activity of heterotrophic microorganisms in environmental samples, which reflects local/microhabitat conditions [53]. Interestingly, FDA hydrolysis activity was not significantly changed at different Cs concentrations, while the number of CFU decreased by three orders of magnitude at 1000 μM CsCl. The mechanisms of interrelations "Cs: microorganisms" are still poorly understood. Nevertheless, some interesting data can be found for explaining the physiological processes occurring in microbial cells under Cs stress. Thus, in the study on yeast response to Cs and other monovalent cations, the yeast's ability to substitute for K in the activation of several enzymes was assessed [54]. Pyruvate kinase from *Rhodotorula rubra* was more inhibited by cations, whose ionic radii are smaller (e.g., Na^+ (97 pm) and Li^+ (78 pm)) or larger (Cs^+ (166 pm) compared to K^+ (133 pm). At the same time, an abundance of Cs of up to 100 mM did not affect a pyruvate kinase from *Saccharomyces cerevisiae* [54]. These observations support the hypothesis on species specificity in microbial response to metal stress.

As previously reported in the discussion, the influx of Cs into the plant biomass occurs via K^+ transporters. Potassium regulates the osmotic pressure of cells, which in turn is essential for enzymatic reactions. In cases where the increased Cs concentrations replace K in cells, the cytotoxicity increases due to inhibition of enzymes [51,55,56]. The results obtained in this study indicated that the dependence of K concentration in the plant tissues on Cs accumulation was plant species-specific. In this respect, the changes in enzyme activity in the plant crude extract after incubation with Cs in different concentrations would bring new insight into plant ecotoxicological response towards Cs.

L-DOPA is known to be one of the most used substrates for phenol oxidase (PO) and peroxidase assays in soil and other environmental samples [41]. The effect of divalent metals (up to 800 mM) on PO activity in soil was tested by [57]. PO activities were stimulated by Mg(II), Mn(II), and Zn(II) and were inhibited by other metals [57]. Thus far, no data on the Cs effect on PO activity in aquatic plants under metal stress has been reported. Our data corroborate with other studies, which showed that Cs-133 affects plant functioning via activating the defence mechanism against oxidative stress [58,59].

In a recent study with a freshwater macro-algae *Nitella pseudoflabellata*, an increased activity of catalase and guaiacol peroxidase was observed at 0.75 μM Cs-133 compared to the control [58]. This effect is also attributable to other metals. Thus, an increasing activity of antioxidant enzymes has also been detected in macrophyte *Hydrilla verticillate* when exposed to cobalt (up to 100 μM) for seven days [43]. However, in the study with *Elodea* sp., activation of antioxidant enzymes was detected during the first eight hours of exposure to nickel, which corresponds to the passive binding of metal ions (chemisorption) [60].

Nevertheless, the metal-induced activation of antioxidant enzymes in plants is determined by species-specific characteristics. In the comparative study on Cd accumulation by the semi-aquatic plant *Nymphoides peltata* and the aquatic plant *Nymphaea* sp., a similar level of Cd accumulation was shown; however, the plant resistance towards Cd differed. In particular, Nymphaea had greater peroxidase activity and was more resistant to Cd than *N. peltata* [61]. In our study, the highest concentration of Cs, i.e., 1000 μM, resulted in the strongest inhibition of peroxidase and guaiacol peroxidase activity in *B. amplexicaulis*. However, no linear dependence of enzyme activity on Cs concentration was observed.

5. Conclusions

The accumulation of caesium in macrophytes was greatly influenced by an initial concentration added during the aquatic phase. The amount of Cs in biomass in the sets with

1000 μM Cs was 1.5–2.0 orders higher than that with 10 μM Cs. This trend was indicated for all tested plants. The PCA analysis revealed a species-specific elemental distribution in plant biomass and the aquatic phase. The main differences could be related to the negative correlation of Na and Ca (2.0–2.5, PC1) and Mg, K, and P (−2, PC1).

An inhibitory effect of 1000 μM Cs on aquatic microorganisms was detected; specifically, the CFU count was decreased by up to three orders of magnitude, as compared to the set without Cs. Nevertheless, FDA hydrolysis activity did not show any considerable changes after incubation with different Cs concentrations.

The activity of DHA gradually increased in the crude plant extract with increasing Cs concentration in the aquatic phase. Importantly, this effect was also detected at 1 μM Cs in the sets with *B. amplexicaulis* and *L. laevigantum* compared with the control ($p < 0.05$).

A considerable increase in antioxidative enzyme activity at 10 uM Cs, compared with the control, was shown in *E. densa* in DOPA+MBTH (1.61 times) and peroxidase assays (2.28 times) and in *L. laevigantum* in a guaiacol peroxidase assay (1.49 times) compared with the control.

This study has revealed certain enzyme groups in the tested aquatic plants that specifically respond to the presence of Cs in water, e.g., dehydrogenase and guaiacol peroxidase. These parameters could serve as bioindicators for the ecotoxicological evaluation of Cs-contaminated sites. Further intensive research is needed to describe the mechanisms of Cs accumulation in aquatic plants in environmental, technological, and ecotoxicological aspects. These results provide important information about the effect of Cs ions and can also be attributed to the evaluation of radioactive Cs accumulation in plants. It can be concluded that there is a low effect of Cs-133 on plant species at low concentrations; thus, in the case of Cs-137, radioactivity may be the main factor affecting plant species and should be addressed in further studies.

Supplementary Materials: The following are available online at https://www.mdpi.com/article/10.3390/su14031132/s1, Figure S1. Accumulation of different elements in *B. amplexicaulis*, *E. densa*, *C. submersum*, and *L. laevigantum*. Biomass after 10-day incubation in the presence of 0, 1, 10, and 1000 μM CsCl. Figure S2. Dopaquinone and 3-methyl-2-benzothiazoninone hydrazine (DOPA+MBTH) activity of crude plant extracts (A—*B. amplexicaulis*, B—*E. densa*, C—*C. submersum*, D—*L. laevigantum*) after plant incubation with 0 to 1000 μmol/L (μM) CsCl for 10 days. Figure S3. Peroxidase activity of crude plant extracts (A—*B. amplexicaulis*, B—*E. densa*, C—*C. submersum*, D—*L. laevigantum*) after plant incubation with 0 to 1000 μmol/L (μM) CsCl for 10 days. Figure S4. Guaiacol peroxidase activity of crude plant extracts (A—*B. amplexicaulis*, B—*E. densa*, C—*C. submersum*, D—*L. laevigantum*) after plant incubation with 0 to 1000 μmol/L (μM) of CsCl for 10 days.

Author Contributions: Conceptualization, O.M., A.G., A.V. and I.R.; methodology, O.M., I.R. and M.B.; software, I.R. and M.B.; validation, A.V., A.G. and M.B.; formal analysis, L.Z., K.S. and U.E.; investigation, L.Z., O.M., I.R., A.G., A.V. and M.B.; resources, G.K. and M.B.; data curation, A.V. and A.G.; writing—original draft preparation, L.Z., O.M., M.B. and I.R.; writing—review and editing, I.R., O.M., L.Z., M.B., A.G. and A.V.; visualization, O.M., I.R. and M.B.; supervision, A.G., A.V. and I.R.; project administration, I.R. and G.K.; funding acquisition, G.K. and I.R. All authors have read and agreed to the published version of the manuscript.

Funding: This research was funded by the Latvian Council of Science: Project No. lzp-2020/2-0213 "Application of modified cellulose fiber sorbents for concentration of radioactive hydrogen (tritium) and other radionuclides from contaminated environments and evaluation of toxic properties: approbation of the method for purification of water residues from nuclear reactors stored in Latvia."

Institutional Review Board Statement: Not applicable.

Informed Consent Statement: Not applicable.

Data Availability Statement: Not applicable.

Acknowledgments: The Latvian Council of Science is acknowledged for supporting this study and the further research based on these results. The fluent English speaker, M. Semjonova-Reinholde and the MDPI English editor provided proofreading.

Conflicts of Interest: The authors declare no conflict of interest.

References

1. Kondo, M.; Maeda, H.; Goto, A.; Nakano, H.; Kiho, N.; Makino, T.; Sato, M.; Fujimura, S.; Eguchi, T.; Hachinohe, M.; et al. Exchangeable Cs/K ratio in soil is an index to estimate accumulation of radioactive and stable Cs in rice plant. *Soil Sci. Plant Nutr.* **2014**, *61*, 133–143. [CrossRef]
2. Sawajiri, M.; Miyamoto, S.; Yamanouchi, K.; Wada, S.; Srimawong, P.; Nomura, Y.; Uchida, T. Drinking high-energy electrolytic water decreases internal radiation exposure caused by the Fukushima Daiichi Nuclear power plant disaster. *Nucl. Technol. Radiat. Prot.* **2016**, *31*, 173–178. [CrossRef]
3. Shinano, T.; Watanabe, T.; Chu, Q.; Osaki, M.; Kobayashi, D.; Okouchi, T.; Matsunami, H.; Nagata, O.; Okazaki, K.; Nakamura, T. Varietal difference in radiocesium uptake and transfer from radiocesium deposited soils in the genus *Amaranthus*. *Soil Sci. Plant Nutr.* **2014**, *60*, 809–817. [CrossRef]
4. Kang, D.-J.; Seo, Y.-J.; Ishii, Y. Distribution of cesium and cationic mineral elements in napiergrass. *SN Appl. Sci.* **2019**, *1*, 1665. [CrossRef]
5. Nagakawa, Y.; Uemoto, M.; Kurosawa, T.; Shutoh, K.; Hasegawa, H.; Sakurai, N.; Harada, E. Comparison of radioactive and stable cesium uptake in aquatic macrophytes affected by the Fukushima Dai-ichi Nuclear Power Plant accident. *J. Radioanal. Nucl. Chem.* **2018**, *319*, 185–196. [CrossRef]
6. Marčiulionienė, D.; Mazeika, J.; Paškauskas, R.; Jefanova, O. Specific patterns of 137Cs, 60Co, and 54Mn accumulation by macrophytes and bottom sediments. *Zool. Ecol.* **2014**, *24*, 168–176. [CrossRef]
7. Krolak, E.; Golub, G.; Barczak, K. Caesium-137 and potassium-40 in selected oxbow lakes of the border Bug River more than 20 years after the Chernobyl accident. *Water Int.* **2012**, *37*, 75–85. [CrossRef]
8. Pavlyutin, A.P.; Babitskii, B.A. Higher Aquatic Plants in a Lake Contaminated with Radionuclides: Composition, distribution, storage, and accumulation of Cesium-137. *Hydrobiol. J.* **1998**, *34*, 1–9. [CrossRef]
9. Riekstina, D.; Berzins, J.; Krasta, T.; Kizane, G.; Rudzitis, J. Impact of the former Salaspils Nuclear Reactor on the surrounding territory. *Latv. J. Phys. Tech. Sci.* **2016**, *53*, 67–76. [CrossRef]
10. Ashraf, M.A.; Akib, S.; Maah, M.J.; Yusoff, I.; Balkhair, K. Cesium-137: Radio-chemistry, fate, and transport, remediation, and future concerns. *Crit. Rev. Environ. Sci. Technol.* **2014**, *44*, 1740–1793. [CrossRef]
11. Avery, S. Fate of caesium in the environment: Distribution between the abiotic and biotic components of aquatic and terrestrial ecosystems. *J. Environ. Radioact.* **1996**, *30*, 139–171. [CrossRef]
12. Pinder, J.E.; Hinton, T.; Whicker, F. Contrasting cesium dynamics in neighboring deep and shallow warm-water reservoirs. *J. Environ. Radioact.* **2010**, *101*, 659–669. [CrossRef] [PubMed]
13. Jeong, H.; Miller, V.; Hinton, T.G.; Johnson, T.E.; Pinder, J.E. Model-based analyses of the cesium dynamics in the small mesotrophic reservoir, Pond 4. I. Estimating the inventories of and the fluxes among the pond's major biotic components. *J. Environ. Radioact.* **2018**, *189*, 282–296. [CrossRef] [PubMed]
14. Kowata, H.; Nagakawa, Y.; Sakurai, N.; Hokura, A.; Terada, Y.; Hasegawa, H.; Harada, E. Radiocesium accumulation in *Egeria densa*, a submerged plant – possible mechanism of cesium absorption. *J. Anal. At. Spectrom.* **2014**, *29*, 868–874. [CrossRef]
15. Vacula, J.; Komínková, D.; Pecharová, E.; Doksanská, T.; Pechar, L. Uptake of 133Cs and 134Cs by *Ceratophyllum demersum* L. under field and greenhouse conditions. *Sci. Total. Environ.* **2020**, *720*, 137292. [CrossRef]
16. Moogouei, R.; Chen, Y. Removal of cesium, lead, nitrate and sodium from wastewater using hydroponic constructed wetland. *Int. J. Environ. Sci. Technol.* **2020**, *17*, 3495–3502. [CrossRef]
17. Sansone, U.; Belli, M.; Riccardi, M.; Alonzi, A.; Jeran, Z.; Radojko, J.; Smodis, B.; Montanari, M.; Cavolo, F. Adhesion of water-borne particulates on freshwater biota. *Sci. Total Environ.* **1998**, *219*, 21–28. [CrossRef]
18. Burger, A.; Lichtscheidl, I. Stable and radioactive cesium: A review about distribution in the environment, uptake and translocation in plants, plant reactions and plants' potential for bioremediation. *Sci. Total Environ.* **2018**, *618*, 1459–1485. [CrossRef] [PubMed]
19. Du, Y.; Wu, Q.; Kong, D.; Shi, Y.; Huang, X.; Luo, D.; Chen, Z.; Xiao, T.; Leung, J.Y. Accumulation and translocation of heavy metals in water hyacinth: Maximising the use of green resources to remediate sites impacted by e-waste recycling activities. *Ecol. Indic.* **2020**, *115*, 106384. [CrossRef]
20. Rai, U.; Sinha, S.; Tripathi, R.D.; Chandra, P. Wastewater treatability potential of some aquatic macrophytes: Removal of heavy metals. *Ecol. Eng.* **1995**, *5*, 5–12. [CrossRef]
21. Abdussalam, A.K.; Ratheesh-Chandra, P. Bio-accumulation of heavy metals in *Bacopa monnieri* (L.) Pennell growing under different habitat. *Int. J. Ecol. Dev.* **2010**, *15*, 66–73.
22. Kumar, N.; Bauddh, K.; Dwivedi, N.; Barman, S.C.; Singh, D.P. Accumulation of metals in selected macrophytes grown in mixture of drain water and tannery effluent and their phytoremediation potential. *J. Environ. Biol.* **2012**, *33*, 923–927. [PubMed]
23. Gouder de Beauregard, A.C.; Mahy, G. Phytoremediation of heavy metals: The role of macrophytes in a stormwater basin. *Int. J. Ecohydrol. Hydrobiol.* **2002**, *2*, 1–4.
24. Maleva, M.G.; Nekrasova, G.F.; Bezel, V.S. The response of hydrophytes to environmental pollution with heavy metals. *Russ. J. Ecol.* **2004**, *35*, 230–235. [CrossRef]

25. Pasichnaya, Y.A.; Gorbatiuk, L.O.; Arsan, O.M.; Platonov, N.A.; Burmistrenko, S.P.; Godlevska, O.; Gopinath, A. Assessment of a possibility of the use of aquatic macrophytes for biomonitoring and phytoindication of the contamination of natural waters by heavy metals. *Hydrobiol. J.* **2020**, *56*, 81–89. [CrossRef]
26. Arán, D.S.; Harguinteguy, C.A.; Fernandez-Cirelli, A.; Pignata, M.L. Phytoextraction of Pb, Cr, Ni, and Zn using the aquatic plant *Limnobium laevigatum* and its potential use in the treatment of wastewater. *Environ. Sci. Pollut. Res.* **2017**, *24*, 18295–18308. [CrossRef]
27. Pamila, D.; Sivalingam, A.; Thirumarimurugan, M. Green revolution- phytoremediation of heavy metals from industrial effluent by water hyacinth. *Eng. Technol. India* **2016**, *7*, 56–64. [CrossRef]
28. Thamkaew, G.; Sjöholm, I.; Galindo, F.G. A review of drying methods for improving the quality of dried herbs. *Cri. Rev. Food Sci. Nutr.* **2021**, *61*, 1763–1786. [CrossRef] [PubMed]
29. Prabasiwi, D.S.; Murniasih, S.; Rozana, K. Transfer factor as indicator of heavy metal content in plants around adipala steam power plant. *J. Physics: Conf. Ser.* **2020**, *1436*, 012133. [CrossRef]
30. Chen, W. The role of microbial activity in suppression of damping-off caused by *Pythium ultimum*. *Phytopathology* **1988**, *78*, 314–322. [CrossRef]
31. Alici, E.H.; Arabaci, G. Determination of SOD, POD, PPO and CAT enzyme activities in *Rumex obtusifolius* L. *Annu. Res. Rev. Biol.* **2016**, *11*, 1–7. [CrossRef]
32. Technical Bulletin. Available online: https://2020.igem.org/wiki/images/1/19/T--IIT_Roorkee--documents--WetLab_Protocols_Bradford.pdf (accessed on 1 December 2021).
33. Winder, A.J. A stopped spectrophotometric assay for the dopa oxidase activity of tyrosinase. *J. Biochem. Biophys. Methods* **1994**, *28*, 173–183. [CrossRef]
34. Camiña, F.; Trasar-Cepeda, C.; Gil-Sotres, F.; Leirós, C. Measurement of dehydrogenase activity in acid soils rich in organic matter. *Soil Biol. Biochem.* **1998**, *30*, 1005–1011. [CrossRef]
35. Onsa, G.H.; Saari, N.; Selamat, J.; Bakar, J. Purification and characterization of membrane-bound peroxidases from Metroxylon sagu. *Food Chem.* **2004**, *85*, 365–376. [CrossRef]
36. Singleton, V.L.; Orthofer, R.; Lamuela-Raventós, R.M. Analysis of total phenols and other oxidation substrates and antioxidants by means of Folin-Ciocalteu Reagent author links open overlay panel. *Met. Enzymol.* **1999**, *299*, 152–178.
37. Erofeeva, E.A. Dependence of guaiacol peroxidase activity and lipid peroxidation rate in drooping birch (*Betula pendula* Roth) and tillet (*Tilia cordata* Mill) leaf on motor traffic pollution intensity. *Dose-Response* **2015**, *13*, 13. [CrossRef]
38. Shevyakova, N.I.; Stetsenko, L.A.; Meshcheryakov, A.B.; Kuznetsov, V.V. The activity of the peroxidase system in the course of stress-induced CAM development. *Russ. J. Plant Physiol.* **2002**, *49*, 598–604. [CrossRef]
39. Fontvieille, D.; Outaguerouine, A.; Thevenot, D. Fluorescein diacetate hydrolysis as a measure of microbial activity in aquatic systems: Application to activated sludges. *Environ. Technol.* **1992**, *13*, 531–540. [CrossRef]
40. Haida, Z.; Hakiman, M. A comprehensive review on the determination of enzymatic assay and nonenzymatic antioxidant activities. *Food Sci. Nutr.* **2019**, *7*, 1555–1563. [CrossRef]
41. Bach, C.E.; Warnock, D.D.; Van Horn, D.J.; Weintraub, M.; Sinsabaugh, R.L.; Allison, S.D.; German, D.P. Measuring phenol oxidase and peroxidase activities with pyrogallol, l-DOPA, and ABTS: Effect of assay conditions and soil type. *Soil Biol. Biochem.* **2013**, *67*, 183–191. [CrossRef]
42. Shtangeeva, I.; Vīksna, A.; Bērtiņš, M.; Ryumin, A.; Grebnevs, V. Variations in the concentrations of macro- and trace elements in two grasses and in the rhizosphere soil during a day. *Environ. Pollut.* **2020**, *262*, 114265. [CrossRef] [PubMed]
43. Sridhar, A.; Khader, P.A.; Ramasamy, T. Assessment of cobalt accumulation effect on growth and antioxidant responses in aquatic macrophyte *Hydrilla verticillata* (L.f.) Royle. *Biology* **2020**, *75*, 2001–2008. [CrossRef]
44. Geng, N.; Wu, Y.; Zhang, M.; Tsang, D.; Rinklebe, J.; Xia, Y.; Lu, D.; Zhu, L.; Palansooriya, K.N.; Kim, K.-H.; et al. Bioaccumulation of potentially toxic elements by submerged plants and biofilms: A critical review. *Environ. Int.* **2019**, *131*, 105015. [CrossRef] [PubMed]
45. Clemens, S.; Ma, J.F. Toxic heavy metal and metalloid accumulation in crop plants and foods. *Annu. Rev. Plant Biol.* **2016**, *67*, 489–512. [CrossRef] [PubMed]
46. Wang, W.X. Chapter 4—Bioaccumulation and biomonitoring. In *Marine Ecotoxicology*; Blasco, J., Chapman, P., Campana, O., Hampel, M., Eds.; Elsevier: New York, NY, USA; London, UK, 2016; pp. 99–119.
47. Ortiz-Oliveros, H.B.; Cruz, D.; Flores-Espinosa, R.M.; Santillán-Malaquías, I.; Zarazúa-Ortega, G.; Villalva, A. Evaluation of the bioaccumulation of heavy metals and 137Cs in succulent plants *Echeveria elegans*. *Int. J. Environ. Sci. Technol.* **2021**, 1–14. [CrossRef]
48. Shaw, G.; Bell, J. The kinetics of Caesium absorption by roots of winter wheat and the possible consequences for the derivation of soil-to-plant transfer factors for radiocaesium. *J. Environ. Radioact.* **1989**, *10*, 213–231. [CrossRef]
49. Zhu, Y.; Smolders, E. Plant uptake of radiocaesium: A review of mechanisms, regulation and application. *J. Exp. Bot.* **2000**, *51*, 1635–1645. [CrossRef]
50. Smolders, E.; Sweeck, L.; Merckx, R.; Cremers, A. Cationic interactions in radiocaesium uptake from solution by spinach. *J. Environ. Radioact.* **1997**, *34*, 161–170. [CrossRef]
51. Rai, H.; Kawabata, M. The dynamics of radio-cesium in soils and mechanism of cesium uptake into higher plants: Newly elucidated mechanism of cesium uptakei into rice plants. *Front. Plant Sci.* **2020**, *11*, 528. [CrossRef]

52. Muter, O.; Patmalnieks, A.; Rapoport, A. Interrelations of the yeast *Candida utilis* and Cr(VI): Metal reduction and its distribution in the cell and medium. *Process. Biochem.* **2001**, *36*, 963–970. [CrossRef]
53. Piscart, C.; Genoel, R.; Doledec, S.; Chauvet, E.; Marmonier, P. Effects of intense agricultural practices on heterotrophic processes in streams. *Environ. Pollut.* **2009**, *157*, 1011–1018. [CrossRef] [PubMed]
54. Perkins, J.; Gadd, G.M. Caesium toxicity, accumulation and intracellular localization in yeasts. *Mycol. Res.* **1993**, *97*, 717–724. [CrossRef]
55. Maathuis, F.J. Physiological functions of mineral macronutrients. *Curr. Opin. Plant Biol.* **2009**, *12*, 250–258. [CrossRef] [PubMed]
56. White, P.J.; Broadley, M.R. Mechanisms of caesium uptake by plants. *New Phytol.* **2000**, *147*, 241–256. [CrossRef]
57. Carine, F.; Enrique, A.-G.; Stéven, C. Metal effects on phenol oxidase activities of soils. *Ecotoxicol. Environ. Saf.* **2009**, *72*, 108–114. [CrossRef] [PubMed]
58. Atapaththu, K.S.S.; Rashid, H.; Asaeda, T. Growth and oxidative stress of brittlewort (*Nitella pseudoflabellata*) in response to cesium exposure. *Bull. Environ. Contam. Toxicol.* **2016**, *96*, 347–353. [CrossRef]
59. Nayek, S.; Gupta, S.; Saha, R. Effects of metal stress on biochemical response of some aquatic macrophytes growing along an industrial waste discharge channel. *J. Plant Interact.* **2010**, *5*, 91–99. [CrossRef]
60. Maleva, M.G.; Malec, P.; Prasad, M.N.V.; Strzałka, K. Kinetics of nickel bioaccumulation and its relevance to selected cellular processes in leaves of *Elodea canadensis* during short-term exposure. *Protoplasma* **2015**, *253*, 543–551. [CrossRef] [PubMed]
61. Lavid, N.; Schwartz, A.; Lewinsohn, E.; Tel-Or, E. Phenols and phenol oxidases are involved in cadmium accumulation in the water plants *Nymphoides peltata* (Menyanthaceae) and Nymphaeae (Nymphaeaceae). *Planta* **2001**, *214*, 189–195. [CrossRef]

materials

MDPI

Article

Porous $ZnCl_2$-Activated Carbon from Shaddock Peel: Methylene Blue Adsorption Behavior

Hongxia Zhao [1], Haihong Zhong [1], Yu Jiang [2], Huiyu Li [1], Pinggui Tang [1], Dianqing Li [1] and Yongjun Feng [1,*]

[1] State Key Laboratory of Chemical Resource Engineering, College of Chemistry, Beijing University of Chemical Technology, Beijing 100029, China; hxzhaochemistry@163.com (H.Z.); hzhong@mail.buct.edu.cn (H.Z.); huiyuli@buct.edu.cn (H.L.); tangpg@mail.buct.edu.cn (P.T.); lidq@mail.buct.edu.cn (D.L.)

[2] Beijing Municipal Construction Group Co., Ltd., A40 Xingshikou Road, Haidian District, Beijing 100195, China; jy558833@126.com

* Correspondence: yjfeng@mail.buct.edu.cn; Tel.: +86-10-6443-6992; Fax: +86-10-6442-5385

Abstract: It is of great interest and importance to resource utilization of waste biomass to produce porous carbon for environmental treatments. Pore structure and properties of the obtained carbon mainly relate to carbonization conditions and biomass types. In this work, a series of porous, biomass-activated carbons (AC) were prepared using shaddock peel, with $ZnCl_2$ as a pore-forming agent. The effect of carbonization temperature and the mass ratio between $ZnCl_2$ and shaddock peel were thoroughly investigated. The material composition, surface chemical properties, and surface structures of samples were carefully characterized. The specific surface area and adsorption capacity to methylene blue (MB) of adsorbents were changed with the carbonization temperature and the mass ratios between $ZnCl_2$ and shaddock peel; when the temperature was at 1000 °C and the mass ratio was equal to 2:1, the resulting adsorbent had the largest specific surface area of 2398.74 m^2/g and average pore size of 3.04 nm, which showed the highest adsorption capacity to MB to be 869.57 mg/g. The adsorption processes of biomass AC adsorbent matched the pseudo-second-order kinetic model and Langmuir isotherm model. This efficient and environmentally friendly biomass AC adsorbent from shaddock peel, activated by $ZnCl_2$, is a promising candidate for the treatment of water pollution.

Keywords: biomass carbon; adsorption; porous structure; $ZnCl_2$-activated carbon

Citation: Zhao, H.; Zhong, H.; Jiang, Y.; Li, H.; Tang, P.; Li, D.; Feng, Y. Porous $ZnCl_2$-Activated Carbon from Shaddock Peel: Methylene Blue Adsorption Behavior. *Materials* **2022**, *15*, 895. https://doi.org/10.3390/ma15030895

Academic Editor: Avelino Núñez-Delgado

Received: 8 December 2021
Accepted: 18 January 2022
Published: 25 January 2022

1. Introduction

Organic dyes have greatly enriched human life, with widespread applications in textile, papermaking, leather [1], and printing industries [2]. Due to excessive use and uncontrollable discharge, dye pollution is threatening human health and the ecological system. According to statistics, ca. 7×10^5 tons of dye is produced in the world every year [3]. Among them, methylene blue (MB), a heterocyclic aromatic chemical compound ($C_{16}H_{18}C_lN_3S_3H_2O$), is one kind of toxic cationic dye [4] that not only cause diseases, such as heart disease, tissue necrosis, emesis, shock, and others [5], but also has a negative impact on aquatic animals and plant growth due to the reduced photosynthesis [6]. Therefore, it is critical to limit new discharges and remove existing pollution from water bodies using various technologies.

Many technologies, such as electrochemical [7], photoelectrochemical [8], microbial degradation [9], ions exchange [10,11], Fenton reaction [2], membrane separation [12], adsorption [13], and so on, have been developed to remove organic dyes from polluted water. In comparison, adsorption technology is widely used due to its low cost, ease of operation, and high efficiency [14]. Metal oxides [15], carbon materials [16], metalorganic frameworks (MOF) [17], graphene [18], zeolites [19], and polymers [20] have all been used as adsorbents in the treatment of polluted water. Among them, activated carbon (AC) is one of the most commonly used adsorbents, which is one kind of low-cost adsorbent, and the corresponding adsorption performance is primarily determined by the carbon pore

structure, which is derived by the carbon resource and carbonization process. Recently, shaddock peel, a type of biomass resource, has piqued the interest of AC investigators due to its abundant supply, low cost, and abundant functional groups [21]. Various types of carbon adsorbents have been synthesized from shaddock peel and used in the energy storage [22,23], gas detection [24], catalysis [25], and adsorption fields [26–28]. Usually, the chemical activation method can contribute to the porous structure and chemical properties of carbon surface. KOH [29], H_2SO_4 [30], HNO_3 [31], $CaCO_3$ [32–34], and so on, have been used as activating agents for the preparation of biomass carbon. Recently, $ZnCl_2$ has attracted increasing interest as a high-performance chemical activation agent for fabricating porous carbon materials from various biomass, because $ZnCl_2$ acts as a Lewis acid and can be used as a dehydration agent to selectively remove the H and O from biomass to restrain the formation of tar and contribute to the formation of high surface area and porous structure [35,36]. As examples, $ZnCl_2$ was used to activate olive solid waste to produce AC with a 10 times higher specific surface area of 1480 m^2/g and enhanced nitrate adsorption capacity of 5.5 mg/g [37]; $ZnCl_2$ was used to activate coconut shell to produce active, magnetic, activated carbon with a more than 275 times improved specific surface area of 935.46 m^2/g, and an increased maximum adsorption capacity of 156.25 mg/g for MB [38]. Therefore, $ZnCl_2$ is a potential activating agent to improve the specific surface area and porosity of carbon materials. It is of great necessity and importance to investigate the influence of $ZnCl_2$ in the carbonization of shaddock. Particularly, the adsorption performance of these adsorbents, activated by $ZnCl_2$, remains to be improved; moreover, optimizing the pore structure of carbon from shaddock peel and the enhancement of its adsorption performance remains a significant challenge, and few reports on the activation behavior of $ZnCl_2$, based on shaddock peel, have been published to date.

In this study, a series of porous ACs were prepared from shaddock peel with $ZnCl_2$ as an activating agent. The effects of carbonization and $ZnCl_2$ dosage were investigated to get porous structure activated carbon adsorbents. The obtained AC adsorbents with high specific surface area and porous structure were applied for the removal of MB in aqueous solution, and the kinetic and isotherm adsorptions were carefully investigated. The carbonization temperature and $ZnCl_2$ dosage are important in optimizing pore structure and enhancing adsorption performance. The use of shaddock peel as a carbon precursor, and of $ZnCl_2$ as an activating agent, is a low-cost and environmentally friendly method for practical applications of sewage treatment.

2. Materials and Methods

2.1. Materials

The zinc chloride ($ZnCl_2$) used in this study was of analytical grade, received from Beijing Tongguang Fine Chemical Co., and was used without further purification. Deionized water was used throughout.

2.2. Preparation of Activated Carbon

A series of porous AC adsorbents were prepared using shaddock peel as the carbon resource and $ZnCl_2$ as the activation agent, with carbonization temperatures ranging from 600 to 1000 °C, and the mass ratios of $ZnCl_2$ to shaddock peel at 0 to 6:1. Prior to carbonization, shaddock peel without yellow skin was washed with deionized water, cut into ca. 1×1 cm^2 pieces, and dried in a 90 °C oven at for 12 h. For instance, 10.00 g $ZnCl_2$ was dissolved in 150 mL deionized water to form a $ZnCl_2$ solution, and then 5.00 g shaddock peel was added to the above solution. The resulting suspension was then kept for another 4 h with vigorous magnetic stirring. Later, the mixed suspension was dried in an oven at 90 °C for another 12 h. The dried sample was placed in a tube furnace under N_2 atmosphere and carbonized at 800 °C for 2 h with a heating rate of 5 °C/min. The obtained biomass carbon was washed with deionized water, until no Cl^- was detected using a 1 wt.% $AgNO_3$ aqueous solution. It was ground into a 100 μm powder by a mortar, and collected as 2:1-800, indicating that the collected AC sample was synthesized with a $ZnCl_2$

to shaddock mass ratio of 2:1 and a carbonization temperature of 800 °C. Some samples were fabricated at different carbonization temperatures ranging from 600 to 1000 °C at a mass ratio 2:1, following the same procedure, and recoded as 2:1-600, 2:1-700, 2:1-800, 2:1-900, 2:1-1000. Others were performed at 1000 °C with different mass ratios between $ZnCl_2$ and shaddock peel, such as 0 (without $ZnCl_2$), 1:1, 2:1, 4:1, and 6:1, and labeled as 0-1000, 1:1-1000, 2:1-1000, 4:1-1000, and 6:1-1000, respectively.

2.3. Characterization

Crystalline structures were characterized on Bruker D8 Advance powder X-ray diffractometer (Cu Kα1 radiation, λ = 0.15406 nm) from 10 to 70°/2θ at a scan speed of 10° min^{-1}. Morphologies were captured using a Hitachi S-4700 scanning electron microscope (SEM) operating at 30 kV, which was also used to record the elemental mapping and spectrum of energy dispersive X-ray spectrometry (EDXS). The transmission electron microscopy (TEM) images were obtained on a HITACHI HT 7700 transmission electron microscope with an accelerating voltage of 100 kV. Specific surface area and pore properties were calculated based on low-temperature N_2 adsorption–desorption isothermal curves, recorded at 77 K on Micromeritics ASAP 2460 (Norcross, GA, USA), where the specific surface area was evaluated by the Brunauer–Emmett–Teller (BET) method from the adsorption curve, and both the pore size distribution and the pore volume were analyzed using the density functional theory (DFT) method. Micromeritics Auto Pore IV 9500 (Norcross, GA, USA) was used to characterize the macroporous structure. Fourier transform infrared spectra (FT-IR) curves were collected from Bruker Vector 22 spectrophotometer (Karlsruhe, Germany) with mass ratio between sample and potassium bromide at 1:100 following homogeneous mixture.

2.4. Batch Adsorption Experiments

The adsorption kinetic experiments on the fabricated AC towards MB were performed in 100 mL conical beakers in a thermostated shaker at 30 °C. Typically, 0.020 g AC powder was dispersed in 40 mL MB aqueous solution with initial concentration of 500 mg/L at nature pH with a shaking speed of 150 rpm, then 1.0 mL of the suspension was extracted after certain time intervals (e.g., 5, 10, 20, 30, 45, 60, 120, 180, 240, 300, 360, and 420 min) through a microfiltration membrane (Φ = 0.22 μm, pore diameter) and the MB concentration in the filtrate was tested by UV-vis spectrophotometer at λ_{max} = 664 nm. The adsorption quantity of the AC towards MB at time t, q_t (mg/g) was calculated by the following equation:

$$q_t = \frac{(C_0 - C_t) \times V}{m} \quad (1)$$

where C_0 (mg/L) represents the initial MB concentration, C_t (mg/L) is the MB concentration at time t, V (L) is the volume of MB solution, and m (g) refers to the mass of AC.

In addition, the adsorption isotherm experiments of AC to MB were carried out in conical beakers by dispersing 0.01 g of the AC in each 20 mL MB solution with an initial concentration ranging from 300 to 700 mg/L. After 7 h of shaking at a speed of 150 rpm at 30 °C, the concentration of MB in the solution was measured using a UV-vis spectrophotometer at λ_{max} = 664 nm, the adsorption quantity of the AC to MB at equilibrium, q_e (mg/g), was calculated as follows:

$$q_e = \frac{(C_0 - C_e) \times V}{m} \quad (2)$$

where C_0 (mg/L) represents the initial concentration of MB solution, C_e is the equilibrium concentration of MB solution, and V (L) and m (g) refer to the volume of MB solution and the mass of the AC, respectively.

All of the adsorption experiments were repeated three times, and the corresponding average values were used for analysis.

3. Results and Discussion

3.1. Structure and Morphologies

A series of porous AC adsorbents were synthesized using shaddock peel as the carbon resource and $ZnCl_2$ as the activation agent at various carbonization temperatures (T) ranging from 600 to 1000 °C, and with mass ratios between $ZnCl_2$ and shaddock peel scaling from 0 to 6:1. Figure 1 shows powder X-ray diffraction (PXRD) patterns of all the prepared AC adsorbents. As the temperature rises from 600 °C to 800 °C, a series of typical Bragg diffraction peaks for ZnO in the range of 10–70°/2θ were observed, as marked in the graph, which matched well to PDF card No. 79-2205 [39]. Furthermore, the intensity of the related diffraction peak decreased with increasing T from 700 °C to 800 °C, owing to the production of Zn from the reduction between ZnO and carbon [40]. When the T was beyond 900 °C, a broad peak at 2θ = 23° occurred in all AC adsorbents, which was assigned to the (002) plane of carbon carbonized from shaddock peel; a peak at 2θ = 43.8° corresponded to the (100) plane of graphite crystal, and no diffraction peak of ZnO was detected [41], implying complete volatilization of Zn, as reported in the literature [40]. This phenomenon is also verified by the EDXS mapping results in Figure S1 and Table S1; Zn was observed in the samples prepared below 900 °C, when the carbonization increased to 1000 °C, no Zn was observed, and only carbon adsorbents appeared. The 2 diffraction peaks at 23 and 43.8° also existed in all AC samples at different mass ratios when the temperature was fixed at 1000 °C.

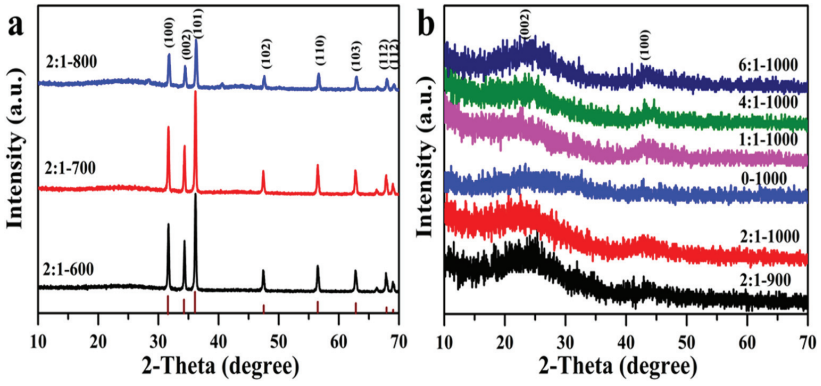

Figure 1. Powder X-ray diffraction patterns (PXRD) of different AC adsorbents prepared at different carbonization temperatures (**a**) and mass ratios (**b**).

Figure 2 furthermore demonstrates the FT-IR spectra of all AC adsorbents in the range of 4000–400 cm^{-1}. In all cases, 2 main typical adsorption bonds were observed: 1 at 3433 cm^{-1} attributed to stretching vibration of the hydroxyl group, the other at 1044 cm^{-1}, which belonged to the stretching and vibration peak of C-O for alcohols, phenols, or ester groups. For the 3 samples at T = 600–800 °C, 1 adsorption band centered at 529 cm^{-1}, which is described as the vibration of the Zn-O bond, which is consistent with the results shown in Figure 1.

Furthermore, Figure 3 shows SEM images of all the AC samples as a function of carbonization temperature and mass ratios between $ZnCl_2$ and shaddock peel, with significantly different morphologies and pore structures. On the one hand, a high carbonization temperature favors the formation of large pore. For example, the carbon surface was smooth and dense at T = 600 and 700 °C; at T from 800 to 1000 °C, the carbon surface varied from crude to porous and the pore size increased with carbonization temperature, with the increase in temperature, the dehydration and gasification of Zn also showed gradually increasing tendency. On the other hand, increasing the use of $ZnCl_2$ aided in the production of more macrospores at 1000 °C. For instance, when no $ZnCl_2$ was used, there were fewer pores; when the mass ratio was increased from 1:1 to 6:1, more hierarchical pores with varying pore sizes, particularly micrometer-level

macrospores, were observed. Besides, Figure S2 shows the TEM images of AC adsorbents. Some differences were observed but it was difficult to distinguish them. We may pay special attention to this issue in the future. Generally, macrospores provide transport channels and increase the exposure of active adsorption sites, since more macrospores may improve adsorption rate and increase adsorption capacity [42]. Enhancing carbonization temperature and a suitable $ZnCl_2$ dosage is beneficial for the formation of an optimized porous structure.

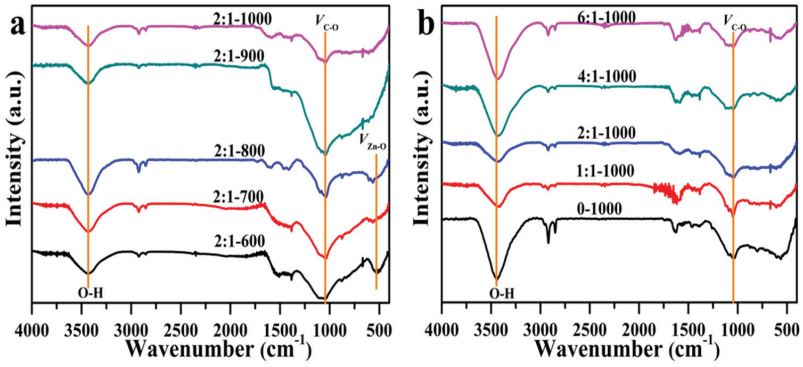

Figure 2. FT-IR curves of different AC adsorbents synthesized with various carbonization temperatures (**a**) and mass ratios (**b**).

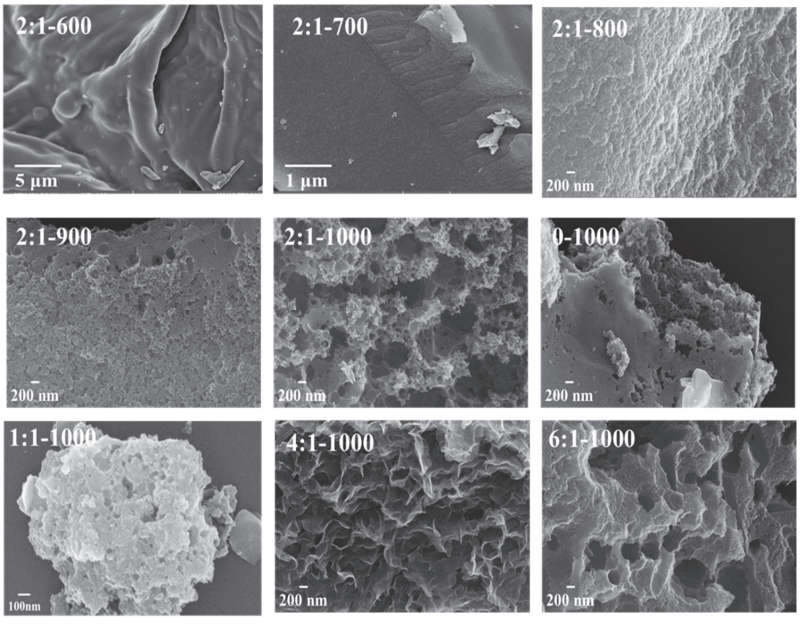

Figure 3. SEM images of AC adsorbents synthesized at various carbonization temperatures (from 600 to 1000 °C) and mass ratios (0, 1:1, 2:1, 4:1, 6:1).

3.2. Pore Structure

In the case of porous adsorbents, pore structure is crucial in terms of adsorption rate and maximum adsorption capacity, which are related to pore size and size distribution, as well as surface area. Figure 4 further displays the low-temperature nitrogen adsorption–desorption isotherm curves of AC adsorbents determined at 77 K and a pore diameter distribution graph, as calculated based on the desorption curve from the DFT

method. Table 1 also lists the corresponding BET results derived from the desorption curves. According to IUPAC, the isotherm curves of 2:1-600, 2:1-700, 2:1-800, and 2:1-900 (c.f., Figure 4a,b) exhibit a typical IV with a H3 hysteresis loop, indicating that the pore structures were irregular; the isotherm curves in Figure 4c,d show a typical IV with an H4 hysteresis loop for 0-1000, 1:1-1000, 2:1-1000, 4:1-1000, and 6:1-1000, indicating that the pore structures were mainly composed of micropores and mesopores, as observed from the calculated pore diameter distribution [43]. In the case of the 2:1 T samples, the specific surface area increased from 764.30 to 2398.74 m^2/g and the pore volume increased from 0.40 to 1.82 cm^3/g as the temperature rose from 600 to 1000 °C; for the mass ratios ranging from 0 to 6:1 at 1000 °C, the specific surface area first increased from 1280.51 m^2/g to 2398.74 m^2/g and then decreased to 1560.85 m^2/g—the optimized mass ratio was 2:1, based on specific surface area and pore volume. In addition, the pore diameter distribution of all the adsorbents can be divided into three ranges: (1) 0.3–2, (2) 2–10, and (3) 10–100 nm, as shown in Figure 4e,f.

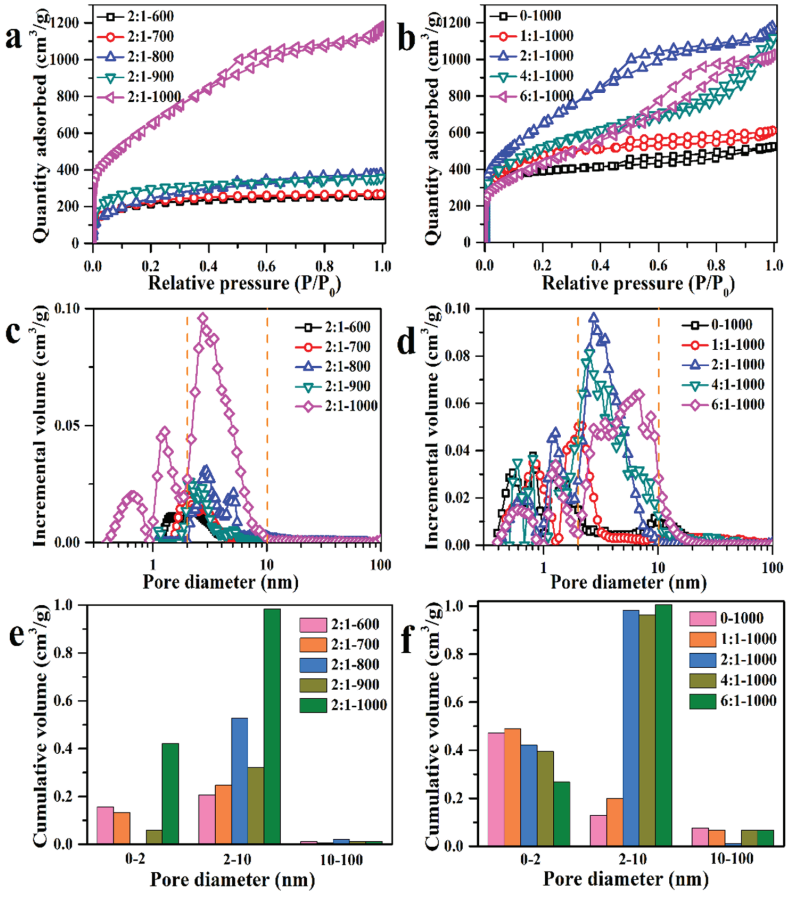

Figure 4. (**a**) N_2 adsorption–desorption isotherms of various AC adsorbents prepared with different carbonization temperatures and (**b**) mass ratios; (**c**) pore size distribution of various AC adsorbents prepared with different carbonization temperatures and (**d**) mass ratios; (**e**) pore volume distribution of various AC adsorbents prepared with different carbonization temperatures and (**f**) mass ratios.

Table 1. BET results of various AC adsorbents with different carbonization temperatures and mass ratios.

Samples	Surface Area (m^2/g)	Average Pore Size (nm)	Pore Volume (cm^3/g)	Samples	Surface Area (m^2/g)	Average Pore Size (nm)	Pore Volume (cm^3/g)
2:1-600	764.30	2.10	0.40	0-1000	1280.51	2.53	0.81
2:1-700	789.10	2.07	0.41	1:1-1000	1663.74	2.27	0.94
2:1-800	881.20	2.65	0.58	2:1-1000	2398.74	3.04	1.82
2:1-900	988.90	2.23	0.55	4:1-1000	1810.08	3.59	1.62
2:1-1000	2398.74	3.04	1.82	6:1-1000	1560.85	4.07	1.31

The calcined temperature is important in forming richly porous structures before the volatilization temperature of Zn metal, and the addition of $ZnCl_2$ favors the formation of mesopores and macropores after the volatilization temperature. For example, the pore diameter of the adsorbents was mainly located at the range of 2–10 nm and expanded to 0.3–2 nm at 1000 °C, which is favorable for the increase in specific surface area and adsorption quantity. The adsorbents synthesized at 1000 °C with a mass ratio of 2:1 exhibited the highest specific surface area of 2398.74 m^2/g with an average pore diameter of 3.04 nm. To some extent, the high specific surface area and appropriate pore diameter distribution will contribute to the adsorption process.

As shown in Figure 3, macropore structure existed in AC adsorbents synthesized at 1000 °C with different mass ratios. Therefore, the mercury intrusion method was employed to evaluate the macropore structure of AC adsorbents. The corresponding results and pore parameters are shown in Figure 5 and Table 2. From 0.1 μm to 900 μm, the pore size distribution was divided into 3 sections: (1) 0.1–6 μm, (2) 6–50 μm, and (3) 50–900 μm. The 2:1-1000 sample had the highest Hg intrusion volume of 7.61 mL/g, the strongest porosity of 79.26%, and the maximum cumulative volumes at all 3 pore size sections. Therefore, the 2:1-1000 showed perfect hierarchical porous structure and possessed the largest macroporous volume, which contributed to the adsorption performance on MB, because the macropore exposes more adsorption sites and provides transport channels for adsorbate, thereby accelerating the mass transfer into the inner surface of adsorbent [42].

Table 2. The pore parameters of AC adsorbents from different mass ratios at 1000 °C.

Sample	Hg Intrusion Pore Volume (mL/g)	Porosity (%)
0-1000	3.43	74.72
1:1-1000	3.32	67.78
2:1-1000	7.61	79.26
4:1-1000	3.88	75.28
6:1-1000	3.28	74.26

3.3. Adsorption Kinetics

The adsorption behavior of all AC adsorbents towards MB in aqueous solution, synthesized at different temperatures and mass ratios, was thoroughly investigated. Figure 6a,c show the effects of contact time on the adsorption of all AC adsorbents toward MB. The adsorption quantity increased with contact time, and all samples reached equilibrium when the contact time surpassed 120 min. However, the adsorption rate increased with carbonization temperature, indicating that the carbonization temperature had an effect on the adsorption property.

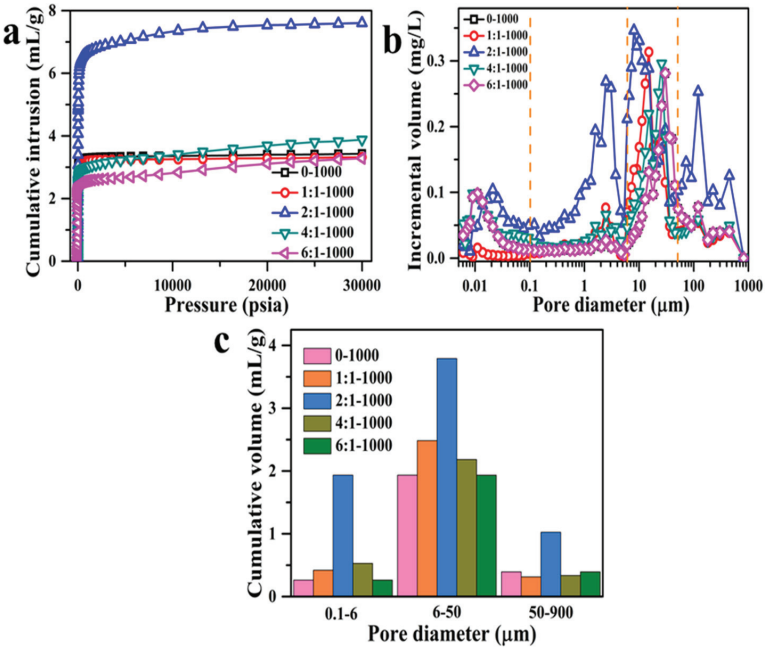

Figure 5. The variation of cumulative intrusion with pressure (**a**), macropore distribution (**b**), and pore volume distribution (**c**) of AC adsorbents from 0-1000 to 6:1-1000 with different mass ratios at 1000 °C.

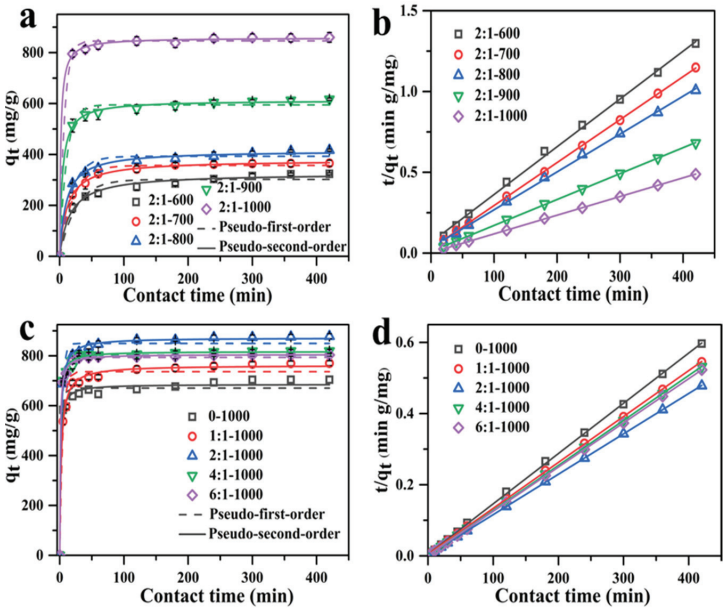

Figure 6. (**a**) The nonlinear fitting of adsorption kinetics and (**b**) linear fitting of pseudo-second-order kinetics of MB for AC adsorbents from different carbonization temperatures. (**c**) The nonlinear fitting of adsorption kinetics and (**d**) linear fitting of pseudo-second-order kinetics of MB for AC adsorbents from different mass ratios.

The nonlinear and linear fitting of kinetics adsorption were described by frequently used, pseudo-first-order and pseudo-second-order adsorption kinetics models, as follows:

$$\lg(q_e - q_t) = \lg(q_e) - \frac{k_1}{2.303}t \quad (3)$$

$$\frac{t}{q_t} = \frac{1}{k_2 \times {q_e}^2} + \frac{t}{q_e} \quad (4)$$

where the q_t (mg/g) represents the adsorption quantity at time t (min), q_e (mg/g) is the equilibrium adsorption quantity, and k_1 (min^{-1}) and k_2 (mg g^{-1} min^{-1}) are the adsorption rate constants of pseudo-first-order and pseudo-second-order kinetics models, respectively.

To determine the optimal carbonization temperature, the adsorption kinetic experiments of AC adsorbents toward MB were carried out. Figure 6a,b show the nonlinear fitting results for two kinetic models, as well as the linear fitting results of the pseudo-second-order kinetic model on MB by AC at various carbonization temperatures, while Figure S3a demonstrates the linear fitting of pseudo-first-order kinetic model. The corresponding adsorption kinetic parameters are listed in Tables 3 and S2. According to the adsorption kinetic parameters, the pseudo-second-order kinetic model is more suitable for the description of the adsorption performance of the AC adsorbents, since it displays a higher R^2 value than the pseudo-first-order kinetic model, which is better suited to describe the adsorption behavior of adsorbents synthesized at different temperatures. In addition, the theoretical adsorption quantity values ($q_{e,cal}$) of the pseudo-second-order kinetic model are closer to the experimental values ($q_{e,exp}$) than that of the pseudo-first-order model. The adsorption rate increased as the carbonization temperature rose from 600 to 1000 °C, and the 2:1-1000 AC adsorbent reached equilibrium adsorption sooner than that at other temperatures. Moreover, the calculative adsorption quantity increased from 325.87 to 870.37 mg/g as the temperature rose from 600 to 1000 °C, which was in accordance with the increased specific surface area from 764.30 m^2/g to 2398.74 m^2/g. More adsorption active sites for MB were provided by the higher specific surface area and more porous structure.

Table 3. Nonlinear fitting parameters of pseudo-first-order and pseudo-second-order adsorption kinetics of AC adsorbents with different carbonization temperatures for MB adsorption.

Sample	$q_{e,exp}$ (mg/g)	Pseudo-First-Order			Pseudo-Second-Order		
		$q_{e,cal}$ (mg/g)	k_1	R^2	$q_{e,cal}$ (mg/g)	k_2	R^2
2:1-600	324	313.55	0.03838	0.7184	325.87	3.436×10^{-4}	0.8935
2:1-700	366	341.80	0.08742	0.6893	364.01	3.998×10^{-4}	0.9066
2:1-800	417	373.27	0.01104	0.7854	404.09	4.048×10^{-4}	0.9469
2:1-900	617	609.43	0.1979	0.6909	615.85	6.104×10^{-4}	0.9152
2:1-1000	879	849.55	0.2952	0.9809	871.87	7.567×10^{-4}	0.9979

Furthermore, the mass ratio of AC adsorbents at 1000 °C was optimized. Here, Figure 6c,d exhibit the nonlinear and linear fitting results of pseudo-second-order adsorption kinetic curves of AC adsorbents synthesized from different mass ratios, respectively, while Figure S3b displays the linear fitting of pseudo-first-order kinetic model. Table 4 and Table S3 list the calculated adsorption kinetic parameters. The adsorption quantity increased with time and the adsorption reached an equilibrium at ca. 100 min. Based on the R^2 values of the two models, the pseudo-second-order model matched the adsorption kinetic process more closely, and the theoretical adsorption quantity values ($q_{e,cal}$) of the pseudo-second-order kinetic model were closer to the experimental values ($q_{e,exp}$). The equilibrium adsorption quantity firstly increased with the mass ratios from 0 to 2:1, then decreased from 2:1 to 6:1. Among the 5 samples investigated, the largest equilibrium adsorption capacity of 870.37 mg/g was achieved at a mass ratio of 2:1, which was consistent with the results of specific surface area, so the appropriate mass ratio between $ZnCl_2$ and shaddock peel was determined at 2:1.

Table 4. Nonlinear fitting parameters of pseudo-first-order and pseudo-second-order adsorption kinetics of biomass carbon adsorbents with different mass ratios for MB adsorption.

Sample	$q_{e,exp}$ (mg/g)	Pseudo-First-Order			Pseudo-Second-Order		
		$q_{e,cal}$ (mg/g)	k_1	R^2	$q_{e,cal}$ (mg/g)	k_2	R^2
0-1000	704	670.45	0.3701	0.9747	685.56	1.310×10^{-3}	0.9908
1:1-1000	771	736.28	0.2198	0.9714	762.22	5.541×10^{-4}	0.9958
2:1-1000	879	849.55	0.2952	0.9809	871.87	7.567×10^{-4}	0.9979
4:1-1000	822	802.70	0.3849	0.9895	817.13	1.320×10^{-3}	0.9981
6:1-1000	803	793.32	0.3879	0.9946	805.43	1.490×10^{-3}	0.9992

3.4. Adsorption Isotherm

The adsorption isotherm experiments on MB of AC adsorbents synthesized with different mass ratios were carried out, as described in the experimental section. The nonlinear and linear adsorption isotherm fitting results were described by the widely used Langmuir (5) and Freundlich (6) isotherm models.

$$\frac{C_e}{q_e} = \frac{1}{K_L q_m} + \frac{C_e}{q_m} \tag{5}$$

$$\lg q_e = \lg K_F + \frac{1}{n} \lg C_e \tag{6}$$

where q_e (mg/g) and q_m (mg/g) are the equilibrium and maximum adsorption quantity, C_e (mg/L) is the concentration at equilibrium time, K_L (L/mg) and K_F are the Langmuir and Freundlich adsorption constants, respectively, and n is the adsorption intensity.

Figure 7 shows the nonlinear and linear fitting results of the Langmuir and Freundlich isotherm models and Figure S4 describes the linear fitting of Freundlich isotherm for AC adsorbents with varying mass ratios. Tables 5 and S4 list the adsorption isotherm parameters of nonlinear and linear adsorption isotherm. The adsorption quantity increased with the increase in equilibrium concentration from 13.31 to 333.79 mg/g, then remained constant. This is due to the fact that the initial concentration was the primary driving force for breaking through the mass transfer resistance between the solid and liquid phases. Because a low concentration of MB cannot occupy all the adsorption sites in the early stage of adsorption, the adsorption quantity was low; as the MB concentration increased, the adsorption quantity increased gradually. However, when the concentration increased to a certain value, the adsorption sites of AC adsorbents became saturated, leading to the unchanged adsorption quantity. According to the adsorption isotherm parameters listed in Tables 5 and S4, the Langmuir model exhibited higher R^2 value compared with that of the Freundlich model for both nonlinear and linear fitting modes, implying that the Langmuir model is better suited to describe the adsorption process of the AC adsorbents, demonstrating the monolayer adsorption process of the AC adsorbents [44]. The AC adsorbent synthesized at the mass ratio of 2:1 exhibited a maximum adsorption quantity (q_m) of 859.81 mg/g. This result was in line with the largest specific surface area and appropriate pore size of the 2:1-1000 AC adsorbent's honeycomb hierarchical porous morphology, which is beneficial for the adsorption behavior toward MB.

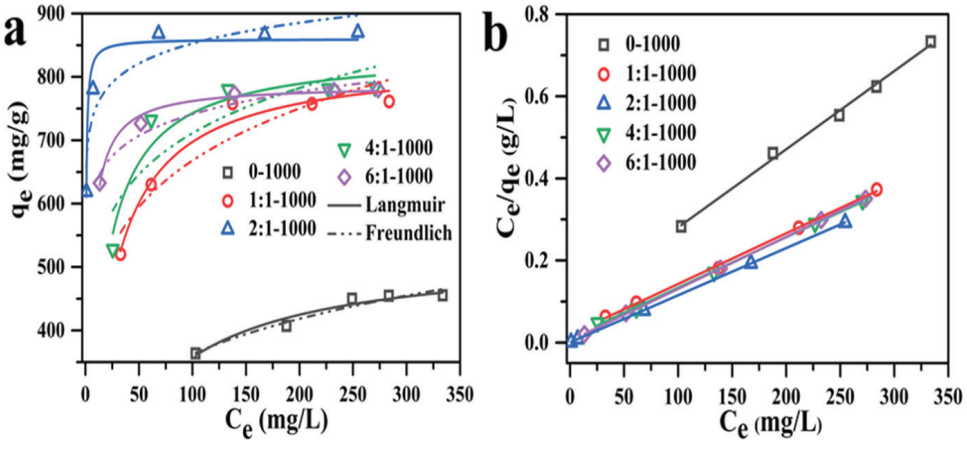

Figure 7. (**a**) The nonlinear fitting of adsorption isotherm; linear fitting of (**b**) Langmuir isotherm for AC adsorbents, prepared with different mass ratios.

Table 5. Nonlinear fitting parameters of Langmuir and Freundlich adsorption isotherm of AC adsorbents with different mass ratios for MB adsorption.

Samples	Langmuir Isotherm			Freundlich Isotherm		
	q_m (mg/g)	K_L (L/mg)	R^2	K_F (mg/g)	n	R^2
0-1000	523.96	0.02141	0.9420	139.99	0.2067	0.9383
1:1-1000	829.90	0.05261	0.9663	309.22	0.1673	0.8448
2:1-1000	859.81	2.9518	0.9429	663.85	0.05437	0.8535
4:1-1000	841.48	0.07507	0.9167	377.04	0.1378	0.6932
6:1-1000	787.23	0.2988	0.9825	543.48	0.06735	0.9181

Table 6 lists the specific surface area and adsorption quantity for MB by different adsorbents synthesized from different carbon sources in other publications. As can be seen, the 2:1-1000 AC adsorbent synthesized from shaddock peel in this work shows a superb specific surface area of 2398.74 m^2/g and a high adsorption capacity of 859.81 mg/g, which is the highest adsorption quantity found among the literature listed. As a result of the high specific surface area, as well as the appropriate pore size, the adsorbent synthesized in our method shows a promising removal performance toward MB.

3.5. Post-Analyses Investigation

In order to further investigate the adsorption behavior toward MB, the 2:1-1000 AC adsorbent was characterized by FT-IR and BET before and after MB adsorption. As depicted in Figure 8a, compared with the FT-IR spectra before adsorption, the FT-IR spectrum of 2:1-1000 adsorbent after adsorption of MB exhibits new characteristic peaks at 873, 1320, and 1381 cm^{-1}, which belong to the characteristic adsorption peak of =C-H (aromatics ring) and C-N stretching vibration peaks. Besides, after adsorption, the intensity of the peak at 1595 cm^{-1}, attributing to the characteristic adsorption peak of C=C (aromatic ring), increases. These four characteristic peaks also can be found in the same location of the FT-IR spectrum of MB [10]. Therefore, this result indicates that the MB has been successfully adsorbed on the adsorbents via physical adsorption through the abundant porous structure.

Table 6. Comparison the adsorption capacity of different adsorbents for MB.

Adsorbent	Activating Agent	Carbonizatin Temperature (°C)	Specific Surface Area (m^2/g)	Adsorption Capacity (mg/g)	Ref.
Corncob AC	KOH	700	1405.00	636.94	[45]
Coconut AC	NaOH	600	876.14	200.01	[46]
Wood AC	H_3PO_4	500	1161.29	159.89	[47]
Soybean dregs AC	$ZnCl_2$	500	643.58	225.10	[48]
Walnut shells AC	$ZnCl_2$	450	1800.00	315.00	[49]
Banana peel AC	NaOH	400	432.00	232.50	[50]
Palm shell AC	-	-	731.50	163.30	[51]
Peanut shell AC	NaOH	800	868.75	555.60	[52]
Sewage sludge and Coconut shell AC	KOH	700	873.54	623.37	[53]
Magnetic coal-based AC	KOH	1000	1188.00	238.56	[54]
Shaddock peel AC	$ZnCl_2$	1000	2398.74	859.81	This work

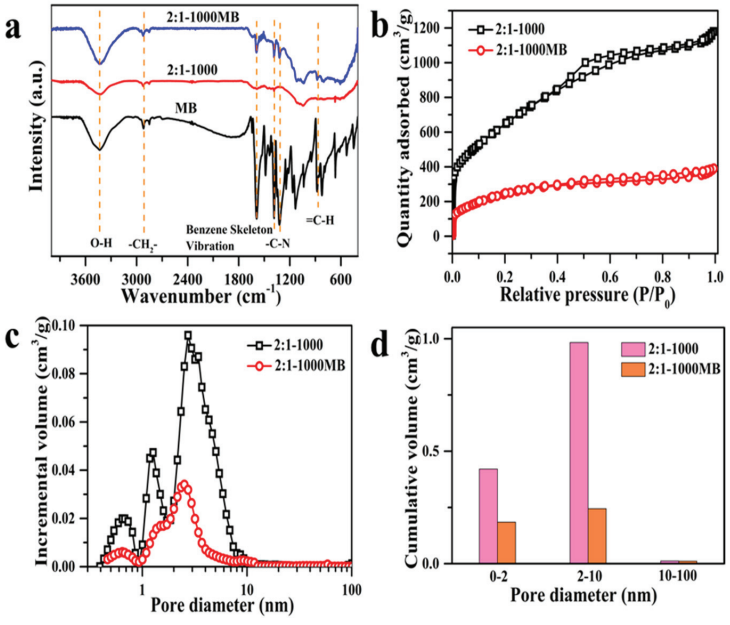

Figure 8. (**a**) FT-IR spectra of MB and 2:1-1000 AC adsorbent before and after the adsorption of MB; (**b**) N_2 adsorption–desorption isotherm of 2:1-1000 AC adsorbent before and after MB adsorption; (**c**) pore size distribution of 2:1-1000 AC adsorbent before and after the adsorption of MB; (**d**) pore volume distribution of 2:1-1000 AC adsorbent before and after MB adsorption.

Figure 8b–d shows the N_2 adsorption–desorption isotherm, pore size distribution, and pore volume distribution of 2:1-1000 AC adsorbent. The isotherms of 2:1-1000 before and after MB adsorption show a typical IV with a H4 hysteresis loop, indicating that the micropores and mesopores pores remained in the AC adsorbent, even after MB adsorption. Indeed, after MB adsorption, the specific surface area of 2:1-1000 AC adsorbent decreased from 2398.74 to 899.30 m^2/g, with a decreased average pore size from 3.04 to 2.67 nm, suggesting that MB had been adsorbed in the inner pore of 2:1-1000 AC adsorbent and occupied the pore space. As shown in Figure 8d, after MB adsorption, the population of the microspore and mesoporous pores decreased dramatically, especially the mesoporous pore. These results reveal that the porous structure, especially the size range of 2–10 nm, makes a significant contribution to the MB adsorption process.

3.6. Practical Implications of This Study

Globally, humans have been facing the great challenges of environmental pollution and excessive waste biomass. Novel treatment technologies will be explored including high-efficiency adsorption and separation, which mainly depend on porous adsorbents. It is one of the promising routes of resource utilization of waste biomass to produce porous materials for pollution treatments. Undoubtedly, this work provides a revealing paradigm on the design of efficient adsorbents based on waste biomass in pollution treatment applications.

4. Conclusions

In this work, we synthesized a series of activated carbon (AC) adsorbents from shaddock peel by using zinc chloride ($ZnCl_2$) as a pore-forming agent, with various carbonization temperatures and mass ratios between $ZnCl_2$ and shaddock peel. All of the synthesized AC adsorbents showed good adsorption performance toward MB, and the adsorption process followed the pseudo-second-order kinetics model and Langmuir adsorption isotherm model. The 2:1-1000 AC adsorbent, synthesized at a temperature of 1000 °C and a mass ratio of 2:1, had the highest specific surface area of 2398.74 m^2/g, a suitable average pore size of 3.06 nm, and the highest MB adsorption capacity of 859.81 mg/g. This demonstrates the importance of a high specific surface area and a proper pore structure for MB adsorption. To summarize, the AC adsorbent, prepared from shaddock peel with $ZnCl_2$ as the activator, shows potential for treating water pollution in an economical and efficient manner.

Supplementary Materials: The following supporting information can be downloaded at: https://www.mdpi.com/article/10.3390/ma15030895/s1, Figure S1: The EDXS mappings of 2:1-600, 2:1-700, 2:1-800, 2:1-900 and 2:1-1000, Figure S2: The TEM images of AC adsorbents synthesized at various carbonization temperatures (from 600 to 1000 °C) and mass ratios (0, 1:1, 2:1, 4:1, 6:1), Figure S3: The linear fitting of pseudo-first-order kinetics for MB by AC adsorbents from (a) different carbonization temperatures and (b) different mass ratio, Table S1: The element percentage of C, O, Zn in adsorbents prepared with different carbonization temperatures, Table S2: Linear fitting parameters of pseudo-first-order and pseudo-second-order adsorption kinetics of biomass carbon adsorbents with different carbonization temperatures for MB adsorption, Figure S4: The linear fitting adsorption isotherm of Freundlich adsorption isotherm for AC adsorbents prepared with different mass ratios, Table S3: Linear fitting parameters of pseudo-first-order and pseudo-second-order adsorption kinetics of AC adsorbents with different mass ratios for MB adsorption, Table S4: Linear fitting parameters of Langmuir and Freundlich adsorption isotherm of AC adsorbents with different mass ratios for MB adsorption.

Author Contributions: Methodology, investigation, writing—original draft preparation, H.Z. (Hongxia Zhao); conceptualization, writing—review and editing, Y.F., H.Z. (Haihong Zhong) and H.L.; supervision, D.L. and P.T.; validation, Y.J. All authors have read and agreed to the published version of the manuscript.

Funding: This research received no external funding.

Institutional Review Board Statement: Not applicable.

Informed Consent Statement: Not applicable.

Data Availability Statement: Not applicable.

Acknowledgments: The authors are very grateful for Beijing Engineering Center for Hierarchical Catalysts, and Fundamental Research Funds for the Central Universities (No. ZY2117).

Conflicts of Interest: The authors declare no conflict of interest.

References

1. Yagub, M.T.; Sen, T.K.; Afroze, S.; Ang, H. Dye and its removal from aqueous solution by adsorption: A review. *Adv. Colloid Interface Sci.* **2014**, *209*, 172–184. [CrossRef]
2. Zhang, H.; Xue, G.; Chen, H.; Li, X. Magnetic biochar catalyst derived from biological sludge and ferric sludge using hydrothermal carbonization: Preparation, characterization and its circulation in Fenton process for dyeing wastewater treatment. *Chemosphere* **2017**, *191*, 64–71. [CrossRef]

3. Lawagon, C.P.; Amon, R.E.C. Magnetic rice husk ash 'cleanser' as efficient methylene blue adsorbent. *Environ. Eng. Res.* **2019**, *25*, 685–692. [CrossRef]
4. Al-Mokhalelati, K.; Al-Bakri, I.; Wattar, N.A.S.A. Adsorption of methylene blue onto sugarcane bagasse-based adsorbent materials. *J. Phys. Org. Chem.* **2021**, *34*, 4193–4201. [CrossRef]
5. Dinh, V.-P.; Huynh, T.-D.-T.; Le, H.M.; Nguyen, V.-D.; Dao, V.-A.; Hung, N.Q.; Tuyen, L.A.; Lee, S.; Yi, J.; Nguyen, T.D.; et al. Insight into the adsorption mechanisms of methylene blue and chromium(iii) from aqueous solution onto pomelo fruit peel. *RSC Adv.* **2019**, *9*, 25847–25860. [CrossRef]
6. Saratale, R.; Saratale, G.D.; Chang, J.; Govindwar, S. Bacterial decolorization and degradation of azo dyes: A review. *J. Taiwan Inst. Chem. Eng.* **2011**, *42*, 138–157. [CrossRef]
7. Kabdaşlı, I.; Arslan, T.; Olmez-Hanci, T.; Arslan-Alaton, I.; Tünay, O. Complexing agent and heavy metal removals from metal plating effluent by electrocoagulation with stainless steel electrodes. *J. Hazard. Mater.* **2009**, *165*, 838–845. [CrossRef]
8. Divyapriya, G.; Singh, S.; Martínez-Huitle, C.A.; Scaria, J.; Karim, A.V.; Nidheesh, P. Treatment of real wastewater by photoelectrochemical methods: An overview. *Chemosphere* **2021**, *276*, 130188–130219. [CrossRef]
9. Katheresan, V.; Kansedo, J.; Lau, S.Y. Efficiency of various recent wastewater dye removal methods: A review. *J. Environ. Chem. Eng.* **2018**, *6*, 4676–4697. [CrossRef]
10. Huang, R.; He, L.; Zhang, T.; Li, D.; Tang, P.; Zhao, Y.; Feng, Y. Fabrication and Adsorption Behavior of Magnesium Silicate Hydrate Nanoparticles towards Methylene Blue. *Nanomaterials* **2018**, *8*, 271. [CrossRef]
11. Hassan, M.M.; Carr, C.M. A critical review on recent advancements of the removal of reactive dyes from dyehouse effluent by ion-exchange adsorbents. *Chemosphere* **2018**, *209*, 201–219. [CrossRef]
12. Nguyen, T.A.; Juang, R.-S. Treatment of waters and wastewaters containing sulfur dyes: A review. *Chem. Eng. J.* **2013**, *219*, 109–117. [CrossRef]
13. Guo, Z.; Zhang, X.; Kang, Y.; Zhang, J. Biomass-Derived Carbon Sorbents for Cd (II) Removal: Activation and Adsorption Mechanism. *ACS Sustain. Chem. Eng.* **2017**, *5*, 4103–4109. [CrossRef]
14. Sahraei, R.; Pour, Z.S.; Ghaemy, M. Novel magnetic bio-sorbent hydrogel beads based on modified gum tragacanth/graphene oxide: Removal of heavy metals and dyes from water. *J. Clean. Prod.* **2017**, *142*, 2973–2984. [CrossRef]
15. Ahmed, S.; Guo, Y.; Huang, R.; Li, D.; Tang, P.; Feng, Y. Hexamethylene tetramine-assisted hydrothermal synthesis of porous magnesium oxide for high-efficiency removal of phosphate in aqueous solution. *J. Environ. Chem. Eng.* **2017**, *5*, 4649–4655. [CrossRef]
16. Cha, J.S.; Park, S.H.; Jung, S.-C.; Ryu, C.; Jeon, J.-K.; Shin, M.-C.; Park, Y.-K. Production and utilization of biochar: A review. *J. Ind. Eng. Chem.* **2016**, *40*, 1–15. [CrossRef]
17. Mousavi, D.V.; Ahmadipouya, S.; Shokrgozar, A.; Molavi, H.; Rezakazemi, M.; Ahmadijokani, F.; Arjmand, M. Adsorption performance of UiO-66 towards organic dyes: Effect of activation conditions. *J. Mol. Liq.* **2020**, *321*, 114487–114496. [CrossRef]
18. Olszewski, R.; Nadolska, M.; Łapiński, M.; Prześniak-Welenc, M.; Cieślik, B.M.; Żelechowska, K. Solvent-Free Synthesis of Phosphonic Graphene Derivative and Its Application in Mercury Ions Adsorption. *Nanomaterials* **2019**, *9*, 485. [CrossRef]
19. Abdellaoui, Y.; El Ibrahimi, B.; Oualid, H.A.; Kassab, Z.; Quintal-Franco, C.; Giácoman-Vallejos, G.; Gamero-Melo, P. Iron-zirconium microwave-assisted modification of small-pore zeolite W and its alginate composites for enhanced aqueous removal of As(V) ions: Experimental and theoretical studies. *Chem. Eng. J.* **2021**, *421*, 129909–129924. [CrossRef]
20. Toprak, A.; Hazer, B. Novel porous carbon microtubes and microspheres produced from poly(CL-b-VbC) triarm block copolymer as high performance adsorbent for dye adsorption and separation. *J. Mol. Liq.* **2018**, *314*, 113565–113574. [CrossRef]
21. Xiao, L.; Ye, F.; Zhou, Y.; Zhao, G. Utilization of pomelo peels to manufacture value-added products: A review. *Food Chem.* **2021**, *351*, 129247–129264. [CrossRef]
22. Wang, Z.; Zheng, P.; Guo, J. Pomelo peel-derived lamellar carbon with surface oxygen functional groups for high-performance supercapacitors. *Appl. Surf. A* **2021**, *5*, 127–323. [CrossRef]
23. Sun, N.; Liu, H.; Xu, B. Facile synthesis of high performance hard carbon anode materials for sodium ion batteries. *J. Mater. Chem. A* **2015**, *3*, 20560–20566. [CrossRef]
24. Wang, L.; Zhang, Y.; Yu, J.; He, J.; Yang, H.; Ye, Y.; Song, Y. A green and simple strategy to prepare graphene foam-like three-dimensional porous carbon/Ni nanoparticles for glucose sensing. *Sens. Actuators B Chem.* **2017**, *239*, 172–179. [CrossRef]
25. Lu, L.; Yu, J.; Wu, Z.; Fan, J.; Lei, W.; Ouyang, Y.; Xia, X.; He, G.; Hao, Q. Shaddock peel derived nitrogen and phosphorus dual-doped hierarchical porous carbons as high-performance catalysts for oxygen reduction reaction. *Int. J. Hydrogen Energy* **2019**, *44*, 26982–26991. [CrossRef]
26. Huang, Z.; Xiong, C.; Zhao, M.; Wang, S.; Zhou, Y.; Dai, L.; Zhang, L. Surface-functionalized pomelo peel-derived biochar with mercapto-1,2,4-triazloe for selective elimination of toxic Pb (II) in aqueous solutions. *Adv. Powder Technol.* **2021**, *31*, 1013–1022. [CrossRef]
27. Dong, F.-X.; Yan, L.; Zhou, X.-H.; Huang, S.-T.; Liang, J.-Y.; Zhang, W.-X.; Guo, Z.-W.; Guo, P.-R.; Qian, W.; Kong, L.-J.; et al. Simultaneous adsorption of Cr (VI) and phenol by biochar-based iron oxide composites in water: Performance, kinetics and mechanism. *J. Hazard. Mater.* **2021**, *416*, 125930–125941. [CrossRef]
28. Li, H.; Sun, Z.; Zhang, L.; Tian, Y.; Cui, G.; Yan, S. A cost-effective porous carbon derived from pomelo peel for the removal of methyl orange from aqueous solution. *Colloids Surf. A* **2016**, *489*, 191–199. [CrossRef]

29. Liang, H.; Song, B.; Peng, P.; Jiao, G.; Yan, X.; She, D. Preparation of three-dimensional honeycomb carbon materials and their adsorption of Cr (VI). *Chem. Eng. J.* **2019**, *367*, 9–16. [CrossRef]
30. Sudha, R.; Srinivasan, K.; Premkumar, P. Removal of nickel (II) from aqueous solution using Citrus Limettioides peel and seed carbon. *Ecotoxicol. Environ. Saf.* **2015**, *117*, 115–123. [CrossRef]
31. Jin, J.; Li, S.; Peng, X.; Liu, W.; Zhang, C.; Yang, Y.; Han, L.; Du, Z.; Sun, K.; Wang, X. HNO_3 modified biochars for uranium (VI) removal from aqueous solution. *Bioresour. Technol.* **2018**, *256*, 247–253. [CrossRef] [PubMed]
32. Block, I.; Günter, C.; Rodrigues, A.D.; Paasch, S.; Hesemann, P.; Taubert, A. Carbon Adsorbents from Spent Coffee for Removal of Methylene Blue and Methyl Orange from Water. *Materials* **2021**, *14*, 3996. [CrossRef] [PubMed]
33. Campos, G.A.F.; Perez, J.P.H.; Block, I.; Sagu, S.T.; Celis, P.S.; Taubert, A.; Rawel, H.M. Preparation of Activated Carbons from Spent Coffee Grounds and Coffee Parchment and Assessment of Their Adsorbent Efficiency. *Materials* **2021**, *9*, 1396. [CrossRef]
34. Kamedulski, P.; Gauden, P.A.; Lukaszewicz, J.P.; Ilnicka, A. Effective Synthesis of Carbon Hybrid Materials Containing Oligothiophene Dyes. *Materials* **2019**, *12*, 3354. [CrossRef] [PubMed]
35. Li, F.; Zimmerman, A.R.; Hu, X.; Yu, Z.; Huang, J.; Gao, B. One-pot synthesis and characterization of engineered hydrochar by hydrothermal carbonization of biomass with $ZnCl_2$. *Chemosphere* **2020**, *254*, 126866–126871. [CrossRef]
36. Ozdemir, I.; Şahin, M.; Orhan, R.; Erdem, M. Preparation and characterization of activated carbon from grape stalk by zinc chloride activation. *Fuel Process. Technol.* **2014**, *125*, 200–206. [CrossRef]
37. Nassar, H.; Zyoud, A.; El-Hamouz, A.; Tanbour, R.; Halayqa, N.; Hilal, H.S. Aqueous nitrate ion adsorption/desorption by olive solid waste-based carbon activated using $ZnCl_2$. *Sustain. Chem. Pharm.* **2020**, *18*, 100335–100343. [CrossRef]
38. Yağmur, H.K.; Kaya, I. Synthesis and characterization of magnetic $ZnCl_2$-activated carbon produced from coconut shell for the adsorption of methylene blue. *J. Mol. Struct.* **2021**, *1232*, 130071–130082. [CrossRef]
39. Guo, Z.; Huo, W.; Cao, T.; Liu, X.; Ren, S.; Yang, J.; Ding, H.; Chen, K.; Dong, F.; Zhang, Y. Heterojunction interface of zinc oxide and zinc sulfide promoting reactive molecules activation and carrier separation toward efficient photocatalysis. *J. Colloid Interface Sci.* **2020**, *588*, 826–837. [CrossRef]
40. Chen, W.; Zhang, Y.; Zhang, S.; Lu, W.; Xu, H. Pyrolysis Behavior and Pore-Forming Mechanism During Reuse of Textile Waste Flax by Activation. *Waste Biomass Valoriz.* **2020**, *11*, 4259–4268. [CrossRef]
41. Sharma, M.; Joshi, M.; Nigam, S.; Shree, S.; Avasthi, D.K.; Adelung, R.; Srivastava, S.K.; Mishra, Y. ZnO tetrapods and activated carbon based hybrid composite: Adsorbents for enhanced decontamination of hexavalent chromium from aqueous solution. *Chem. Eng. J.* **2019**, *358*, 540–551. [CrossRef]
42. Huang, R.; Wu, M.; Zhang, T.; Li, D.; Tang, P.; Feng, Y. Template-free Synthesis of Large-Pore-Size Porous Magnesium Silicate Hierarchical Nanostructures for High-Efficiency Removal of Heavy Metal Ions. *ACS Sustain. Chem. Eng.* **2017**, *5*, 2774–2780. [CrossRef]
43. Sangwichien, C.; Aranovich, G.; Donohue, M. Density functional theory predictions of adsorption isotherms with hysteresis loops. *Colloids Surf. A* **2002**, *206*, 313–320. [CrossRef]
44. Li, L.; Wu, M.; Song, C.; Liu, L.; Gong, W.; Ding, Y.; Yao, J. Efficient removal of cationic dyes via activated carbon with ultrahigh specific surface derived from vinasse wastes. *Bioresour. Technol.* **2021**, *322*, 124540–124572. [CrossRef]
45. Zhou, D.; Li, D.; Li, A.; Qi, M.; Cui, D.; Wang, H.; Wei, H. Activated carbons prepared via reflux-microwave-assisted activation approach with high adsorption capability for methylene blue. *J. Environ. Chem. Eng.* **2020**, *9*, 104671–104681. [CrossRef]
46. Islam, A.; Ahmed, M.; Khanday, W.; Asif, M.; Hameed, B. Mesoporous activated coconut shell-derived hydrochar prepared via hydrothermal carbonization-NaOH activation for methylene blue adsorption. *J. Environ. Manag.* **2017**, *203*, 237–244. [CrossRef]
47. Danish, M.; Ahmad, T.; Hashim, R.; Said, N.; Akhtar, M.N.; Mohamad-Saleh, J.; Sulaiman, O. Comparison of surface properties of wood biomass activated carbons and their application against rhodamine B and methylene blue dye. *Surf. Interfaces* **2018**, *11*, 1–13. [CrossRef]
48. Li, Y.; Li, Y.; Zang, H.; Chen, L.; Meng, Z.; Li, H.; Ci, L.; Du, Q.; Wang, D.; Wang, C.; et al. $ZnCl_2$-activated carbon from soybean dregs as a high efficiency adsorbent for cationic dye removal: Isotherm, kinetic, and thermodynamic studies. *Environ. Technol.* **2018**, *41*, 1–24. [CrossRef]
49. Yang, J.; Qiu, K. Preparation of activated carbons from walnut shells via vacuum chemical activation and their application for methylene blue removal. *Chem. Eng. J.* **2010**, *165*, 209–217. [CrossRef]
50. Maia, L.S.; Duizit, L.D.; Pinhatio, F.R.; Mulinari, D.R. Valuation of banana peel waste for producing activated carbon via NaOH and pyrolysis for methylene blue removal. *Carbon Lett.* **2021**, *31*, 749–762. [CrossRef]
51. Wong, K.T.; Eu, N.C.; Ibrahim, S.; Kim, H.; Yoon, Y.; Jang, M. Recyclable magnetite-loaded palm shell-waste based activated carbon for the effective removal of methylene blue from aqueous solution. *J. Clean. Prod.* **2016**, *115*, 337–342. [CrossRef]
52. Ahmad, M.A.; Yusop, M.F.M.; Zakaria, R.; Karim, J.; Yahaya, N.K.E.; Yusoff, M.A.M.; Hashim, N.H.F.; Abdullah, N.S. Adsorption of methylene blue from aqueous solution by peanut shell based activated carbon. *Mater. Today Proc.* **2021**, *47*, 1246–1251. [CrossRef]

53. Tu, W.; Liu, Y.; Xie, Z.; Chen, M.; Ma, L.; Du, G.; Zhu, M. A novel activation-hydrochar via hydrothermal carbonization and KOH activation of sewage sludge and coconut shell for biomass wastes: Preparation, characterization and adsorption properties. *J. Colloid Interface Sci.* **2021**, *593*, 390–407. [CrossRef]
54. Liu, Y.; Zhu, Z.; Cheng, Q.; Ren, H.; Wang, S.; Zhao, Y.; Li, J.; Zhu, J.; Kong, L.B. One-step preparation of environment-oriented magnetic coal-based activated carbon with high adsorption and magnetic separation performance. *J. Magn. Magn. Mater.* **2021**, *521*, 167517–167523. [CrossRef]

materials

MDPI

Article

Identification of Olfactory Nuisance of Floor Products Containing Bitumens with the TD–GC–MS/O Method

Mateusz Kozicki

Building Research Institute, Filtrowa 1 Street, 00-611 Warsaw, Poland; m.kozicki@itb.pl; Tel.: +22-57-96-187

Abstract: The adopted TD–GC–MS/O method helps determine the correlation between the odour signals and compounds separated on the chromatographic column, from the analysed gas mixture. It is possible to compare the retention times at which the odour signals were identified with the retention time of eluting compounds, when the test system and matrix are known. The presented study describes the details of representative samples obtained from (1) indoor air samples from a room where floor materials containing bitumen are present, (2) wooden floor staves placed in an emission chamber, and (3) fragments (chips) of the materials mentioned above, placed in glass tubes, exposed to an elevated desorption temperature. The results, presented in the paper, describe the identified odours and their intensity and assign chemical compounds to each odour, indicating their likely source of origin. The results presented in the manuscript are intended to show what methodology can be adopted to obtain intense odours from the tested samples, without losing the sensitivity derived from GC–MS. The manuscript presents representative results—case studies. The results for various types of samples were not very reproducible, related to the complex matrix of bituminous products. The enormity of compounds present in tar adhesives makes it possible to indicate only the groups of compounds that emit from these systems. They include, primarily, aliphatic, aromatic and heteroaromatic hydrocarbons, particularly Naphthalene and Phenol derivatives.

Keywords: olfactometry; bitumens; odourant; TD–GC–MS; emission; IAQ

Citation: Kozicki, M. Identification of Olfactory Nuisance of Floor Products Containing Bitumens with the TD–GC–MS/O Method. *Materials* **2022**, *15*, 959. https://doi.org/10.3390/ma15030959

Academic Editors: Avelino Núñez-Delgado, Zhien Zhang, Elza Bontempi, Mario Coccia, Marco Race and Yaoyu Zhou

Received: 7 December 2021
Accepted: 24 January 2022
Published: 26 January 2022

1. Introduction

Establishing unambiguous criteria for olfactory nuisance is hugely challenging. Construction products and interior design objects, which emit volatile organic compounds (VOC), are the most common causes of indoor air pollution in buildings [1–4]. The indoor air quality influences the inhabitants' health and comfort. Studies by Wargocki et al. [5,6] and Shaughnessy et al. [7], show that poor air quality has a negative impact on office staff's performance. This is why a growing demand is observed for technical equipment to measure, maintain and control indoor air quality. VOCs are responsible for the odour sensed by the users, on the condition that their concentration exceeds the odour detection threshold [8]. The intensity of an odour mixture, such as an air sample, can be determined based on the intensity of individual odours in the mixture. This way, at concentrations exceeding the detection threshold, the mixture's odour intensity is lower than the total odour intensity of individual ingredients. The phenomenon is called hyperaddition or synergism [9].

The paper presents the results of air quality tests in a renovated office room, for the presence of compounds formed in wooden structures impregnated with tar compositions and bituminous sealants, containing hydrocarbon-based solvents. In order to confirm the source of VOC emission, the material samples were collected in the same rooms where air measurements were performed and tested in emission chambers. The most volatile polycyclic aromatic hydrocarbon, naphthalene, is a popular compound related to indoor air contamination, with the abovementioned materials [10]. A growing number of papers describe the harmfulness and effects of inhalation exposure to naphthalene

and its derivatives [11–13]. Long-term exposure may occur among smokers and non-smokers exposed to tobacco in their environment, as well as among people working in areas where high concentrations of naphthalene are present (production of mothballs or creosote impregnating facilities) [14].

There are many methods of air sampling for the testing and identification of compounds in the collected samples, which help identify a potential source of unpleasant odour and understand the problem, once combined with other information, concerning the sampling location. The methodology of the likelihood of determination was established as part of the standardisation of the olfactometric measurement procedures. It is described by EN 13725:2003 [15]. However, the procedure focuses mainly on the air sampling methods in open spaces and is principally used for field tests, in response to people's complaints about odours from agriculture, production, services, catering etc. According to the data provided by the Central Statistical Office [16], animal breeding and rearing is the agricultural domain with the highest odour nuisance. The following areas were identified as problematic olfactorily: meat and animal feed production plants—18% of complaints; poultry and swine breeding—12% of complaints and municipal waste and sewage—16% of complaints [16]. The standard [15] specifies exact requirements for persons who assess the odour (selection procedure), the minimum number of people in the assessing teams, the number of repetitions required and other conditions for odour detection threshold tests (individual and team values). A team is a group of at least four people with a similar sense of smell. Odour assessors who fulfil specific selection criteria are accepted into the teams. Therefore, stating, according to the method and conditions set out in the standard, that P = 0.5, means that one European Odour Unit (ouE) is present in one cubic metre. The likelihood of detecting the odour of air containing any pollutants is then the same as the likelihood of detecting the odour of air containing 123 μg of n-butanol (reference odourant).

Dynamic olfactometry is divided into direct (field) olfactometry, where measurements are carried out in real time (field measurements), with no delay. The stream of fragrant gas reaches the diluting apparatus and is diluted with a stream of neutral gas. This helps avoid errors related to sampling in analysis bags and changes in the sampled mixture's composition during transport. Indirect (laboratory) olfactometry is the other type, where gas is sampled into foil bags and transported for analysis; this method is only used for high concentrations because odourants vary in time too much for low concentrations. In addition, transporting samples long distances poses some problems because of the chemical reactions occurring in the analysis bags [15,17].

Generally, the measurements are divided into short- and long-term ones (based on diffusion samples). Active sampling is among the short-term air sampling methods involving aspiration of known air volumes with aspirators (suction apparatuses) onto sorption tubes, with standardised dimensions. A GC–MS system, coupled with a thermal desorption (TD) system, is used to determine volatile organic compound content in the samples. In addition, the so-called cold-trap system, where compounds are concentrated by freezing, helps determine low concentrations.

The ISO 16000 series standards apply to different aspects of indoor air testing. Currently, the series contains 44 parts. The odour tests on construction materials are covered by ISO 16000-28: 2012 [18]. The referenced standard specifies the requirements for collecting air samples for odour assessment described in ISO 16000-9: 2006 [19]. The standard [18] uses two odour acceptability aspects, which determine the odour nuisance or acceptance on a −1 to +1 scale, and the perceived odour intensity that determines the odour intensity, regardless of its type and nuisance, compared to the odour intensity of air mixture with reference substances, such as acetone or n-butanol on a *pi* scale. A hedonic tone is an alternative to determine if the odour is perceived as pleasant or unpleasant on a nine-point perception scale, from −4 to +4. The standard [18] assumes that the odour assessment interface consists of a diffuser connected to the chamber outlet but also accepts other interfaces, such as odour masks, used in situations where the airflow rate in the test chambers does not fulfil the requirements for the airflow rate from the diffuser, e.g., for large construction

products. Diffusers and masks must be airtight, made of odourless materials, such as stainless steel or glass, non-adsorptive (must not adsorb compounds on their surface), and the interface must not have its own emission that could come into contact with the tested air sample (non-permeable). Sample containers intended for collecting and transferring the samples from the test chamber to the place of their detection by panellists have to fulfil similar requirements. The materials recommended for transferring the samples include the tetrafluoroethylene hexafluoropropylene copolymer (FEP), polyvinyl fluoride (PVF) and polyethylene terephthalate (PET). It is assumed that the assessment should be made as quickly as possible after collecting the samples (up to 6 weeks) [18].

The GC–MS/O [20–24] method can be used for identifying the compounds released from construction materials, including the odour type and intensity recognition. The adopted methodology allows for the determination of the correlation between the chemical character and the concentration of specific fragrant compounds, owing to the human perception of odour. Each of the perceived compounds is identified based on retention time, reference compounds and spectra database. The sense of smell of the people assessing the signal leaving the analyser fulfils the detector's role.

Olfactometry, which is a part of sensory analysis, measures the odourant perception thresholds, determines the odour intensity, recognises the type of smell and determines its hedonic tone [25–30]. This paper presents analyses concerning direct dynamic olfactometry, which is a method of objective determination of odour concentration in gas samples, where a fragrant gas sample is diluted with odourless gas and presented to the testing persons, who are the detectors.

The GC–MS/O hybrid method helps solve the sensory analysis problem of the odour synergy of a mixture, such as the analysed air sample. There is a valve at the chromatographic column end, where the fragrant gas sample is split into two streams. One of them is mixed with humid air and fed through a thermostat-featured conduit onto the odour assessment port, while the other stream goes to the MS detector. Consequently, a chemical compound can be identified on the chromatograph and simultaneously correlated with an odour stimulus, imaged with an aromagram. The intensity of aromagraphic signals depends on the recording method and may vary depending on the applied system (turning a knob, intensity assessment with voice recordings or pushing buttons on controllers). It is a complex issue in laboratory practice, and odour signals occur before the chromatographic identification peaks, causing their mutual offset [8,22].

Qualitative and quantitative odour assessment can be performed for each identified compound leaving the column. Still, quantitative assessment is relative, and a rank (weight) can be assigned, according to the assumed intensity scale. Odour presence alone is the evidence of its concentration exceeding the threshold triggering odour sensation for the particular compound. The duration of the sensory activity of odour stimuli is further information provided by an olfactometric analysis.

2. Materials and Methods

The analyses were carried out using a GCMS-QP2010 gas chromatograph (Shimadzu, Tokyo, Japan) featured with TD20 thermal desorption (Shimadzu, Tokyo, Japan) and connected to an olfactometric port enabling odour detection (Phaser, GL Sciences, the Netherlands). An olfactometric port consists of a glass cone blown through with air previously humidified with water (to protect the mucous membrane in the nose). A computational software or pneumatic system's control module, which enables automatic setting according to the stream division, and offers a much more convenient and accurate setting of the parameters, can be used for calculating the stream's flow and determining the split ratio of the gas between the olfactometric port and MS detector. A pneumatic system's control module was used for the tests presented in the paper. The analyses were carried out on Rxi-5Sil MS capillary chromatographic column (30 m $\times$ 0.25 mm $\times$ 0.25 μm). A two-position four-way valve was installed downstream on the column, offering two operation modes. Position A was used for operation skipping the olfactometric port, owing to which the entire stream is

directed to MS. A part of the stream was fed onto the olfactometric port in position B, while the rest went to MS. The split ratio between MS and OLF depends on the pre-set gas flow rates and pressures. In order to obtain the required stream split values, it was necessary to install two restrictors with the correct lengths and diameters (1.5 m × 0.25 m and 5 m × 0.15 m), which helped achieve the desired pressure values. The MS: OLF stream split ratio amounted to 1:10 in the tests presented in the study.

For such an array configuration, it was assumed that two analyses needed to be performed to obtain the most accurate analytical information for two positions (A and B) of the installed two-position valve. The measurements in position B enabled orienting a larger part of the stream onto the olfactometric port, which results in odour stimuli amplification (higher concentration). Unfortunately, the MS spectrum, which is simultaneously recorded, provides a low-intensity signal. Owing to the MS spectrum in position B and MS spectrum in position A, we gained information about the mutual offset of the spectra for both positions of the valve. Position A skips the olfactometric port directing the entire stream onto the MS detector, providing detailed spectra information on the test sample. Summing up, to obtain the most accurate information, odour signals were collected in position B, while the result from the measurement in position A was used for interpreting the mass spectra. Two samples had to be collected for the analyses. Regardless of the valve position, the measurements were carried out in the splitless mode, which enabled amplification of the odour and mass spectra signals.

Figure 1 shows the system's configuration used for the tests presented in the paper. Figure 2 shows a diagram of a two-position four-way diagram in positions A and B, with restrictors marked.

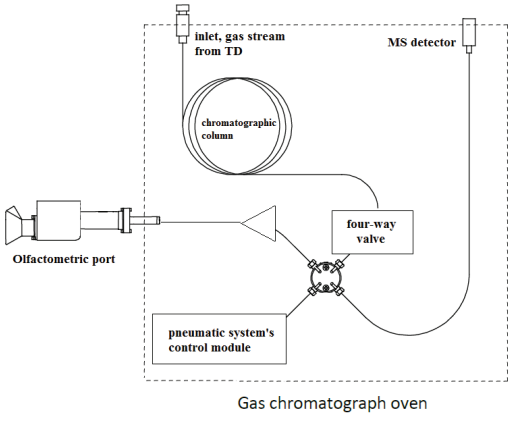

Figure 1. Simplified diagram of the TD–GC–MS/O chromatographic array used for the tests.

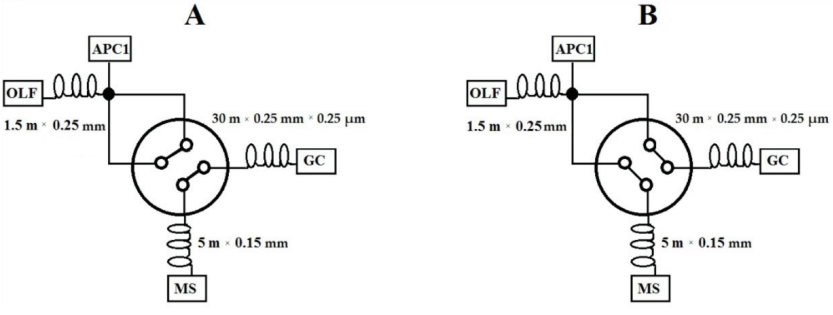

Figure 2. Diagram of a two-position four-way valve in positions (**A**) and (**B**), with the marked chromatographic column and applied restrictors.

The adopted TD–GC–MS/O methodology helps determine the correlation between the chemical compounds and odour signal. This is possible owing to the comparison of the retention times for which the odours were identified with the chemical compounds assigned with the mass spectra available in the NIST 2011 database, assuming the offset between them. All the compounds with the mass spectra matching factors $p \geq 80\%$ were regarded as identified. The author described the odour substances according to subjective perception and previous experience [31].

The shifts of the odour signals may result from the pressure differences arising on the GC–MS system, among others, as follows, by: use of a restrictor; the time it takes for the gas stream to travel to the restrictor; the experimenter's reflexes; passage of the gas stream through the transfer line; human olfactory system responses; information to the brain and finally the decision to record the signal by experimenter.

2.1. Air Samples Collected during Renovation and in a Non-Renovated Office Room

The air samples were collected with a dynamic method into tubes filled with Tenax TA© absorber. The samples were simultaneously collected at three measurement points with electronic mass flow controllers from Aparatura Pomiarowa Ochrony Środowiska (local manufacturer). Accredited calibration laboratories regularly calibrate the mass flow controllers. The volume of the collected air samples was 10 L. The sampling rate amounted to 10 L/h. The flow time was measured with an electronic timer.

The chemical compounds captured on the Tenax TA© absorber were desorbed in a thermal desorber in the following conditions: the heated valve's temperature, 250 °C; feeding line's temperature, 250 °C; desorption time, five min; helium flow rate, 60 mL/min. After cryogenic focusing, they were released to the carrier gas stream directed to the gas chromatograph.

Chromatographic analysis was performed at the following temperature programme of the GC heater: the initial temperature of 40 °C was maintained for five min and then increased from 10 °C/min to 260 °C; the end temperature amounted to 260 °C and was maintained for one min. The splitless mode was used. The determination limit of the applied method is 1 $\mu g/m^3$.

A slightly chemical odour was present in the renovated room's air, at the stage of removing the floor staves. The odour originated from the floor layers disturbed during their dismantling, which resulted in increased concentrations of fragrant compounds in the air. The odour had been detectable for the room users before the renovation, but it was less intense.

Air samples from a non-renovated office room used daily were collected for comparison. The room was furnished with plywood racks, desks and chairs. The floor was covered with a fitted carpet. The measurements were carried out in naturally ventilated rooms. All doors and windows had been closed twenty-four hours before the measurement—the rooms were not used or ventilated. The air samples were collected at three representative measurement points located 1.5 m above the floor, away from windows, doors, potential emission sources, or direct sunlight. The temperature in the tested rooms where the samples were collected amounted to 17.7–24.0 °C, and the RH was 29.8–45.2%.

In an office room, a tar adhesive under the parquet flooring was detected. Tar adhesives are purified fractions of raw coal tars and mixtures of raw coal tar or tar oil with coal pitch, having specific physicochemical properties, useful in practical applications. They were used for waterproofing ceilings of buildings as well as for gluing floor slats to the concrete substrate. They included the following: aliphatic, aromatic and heteroaromatic hydrocarbons and Phenol derivatives. Tar adhesives show the highest vapor emissions of Naphthalene, methylnaphthalenes, ethylnaphthalenes, Acenaphthalene, biphenyls, Dibenzofuran, Fluorene, Phenanthrene or Anthracene.

2.2. Floor Staves Placed in the Emission Chamber

Several floor staves covered with bitumen-based (Figure 3A) products were collected from the renovated room where the air was sampled for the tests. Then, the staves were placed in a stainless emission chamber with 100 L volume. Finally, the test samples were laid on an inert material—fibre cement panels (Figure 3B). The dimensions of the tested material were suited to the test chamber size and the loading factor, which amounts to L = 0.4 for flooring products. The loading factor is the ratio of the tested material's area in the reference room to the reference room's volume (m^2/m^3). The overall dimensions of the test sample amounted to 20 cm × 20 cm. The values of the chamber loading factors, reference room's volume, acceptable size of the test chamber and other test parameters are described in PN-EN 16516 + A1:2020 [32]. The standard assumes air collection from an empty chamber (background) 7 and 28 days after placing the material in the chamber at the specified air flow rate. The absence of the airflow through the chamber to accumulate the compounds released from the test material differed from the standard [32] assumptions.

(**A**) (**B**)

Figure 3. (**A**) Wooden floor staves coated with bitumen, collected from the renovated office room (**B**) The same floor staves placed in the emission chamber.

Moreover, the air samples were collected from the chamber three days into the seasoning. Five Liters of air were collected from each chamber; the collection rate was 10 L/h for 30 min. Two air samples were collected at the same time. The flow time was measured with an electronic timer. Chromatographic analysis of the air samples collected from the chamber was conducted in the same conditions as the air samples collected in the rooms.

2.3. Fragments (Chips) of the Materials Placed in Thermal Desorption Tubes

Small fragments (chips) were planed from the wooden staves coated with bituminous products and placed in thermal desorption tubes (Figure 4). The weight of the samples was ca. 0.3 g. The samples were subjected to thermal desorption in the following conditions: heated valve's temperature 250 °C; feeding line's temperature 250 °C; block's temperature 70 °C; desorption time 10 min; helium flow rate 60 mL/min. The chromatographic analysis of the collected air samples was performed in the same conditions as the air samples from the rooms and emission chamber.

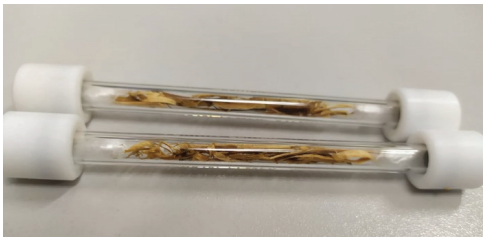

Figure 4. Chips planed from wooden floor staves coated with bituminous products, ready for thermal desorption tests.

3. Results

3.1. Air Samples Collected during the Renovation and in a Non-Renovated Office Room

Figure 5 and Table 1 show the test results obtained for the air sample collected in a renovated office room. Three air samples were collected, but only one representative spectrum was selected for the description below and carefully analysed. The chromatographic spectra of all the collected samples differed slightly (minor differences in the intensity of individual peaks). However, more significant differences occurred in the odour signals' identification, which is why the spectrum containing the highest number of identified odours was selected for the analysis presented below.

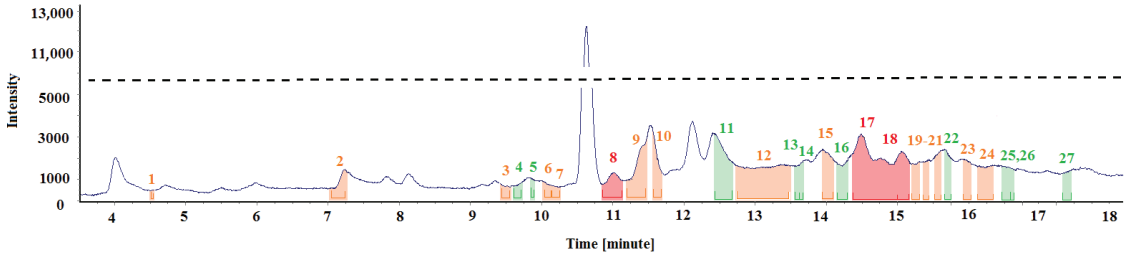

Figure 5. Chromatographic spectrum with the applied odour signals obtained for the air sample collected from the office room during renovation.

Table 1. Identification of odour signals obtained for the air sample collected in an office room during renovation.

No.	Signal Beginning	Signal End	Intensity	Odour Description	Assigned Compound
1	4514	4541	Medium	n/a	n/a
2	7047	7227	Medium	solvent, chemical	m-Xylene
3	9434	9567	Medium	fat, oil, resin	Alpha-Pinene
4	9601	9721	Weak	tar, wood	Camphene
5	9851	9894	Weak	aa	n/a
6	10,017	10,114	Medium	fat, tallow	n/a
7	10,121	10,231	Medium	pine, resin	Beta-pinene
8	10,864	11,141	Strong	pine, resin, forest	3-Carene
9	11,191	11,470	Medium	unpleasant	n/a
10	11,564	11,674	Medium	aa	n/a
11	12,434	12,684	Weak	solvent	Acetophenone
12	12,750	13,500	Medium	spice, orange, citrus	Linalool
13	13,517	13,524	Weak	n/a	n/a
14	13,564	13,670	Weak	solvent	Cis-Verbenol
15	13,970	14,097	Medium	n/a	n/a
16	14,154	14,294	Weak	medicinal	Pinocarvone
17	14,370	14,934	Strong	naphthalene	Naphthalene
18	14,944	15,160	Strong	medicinal, chemical	D-verbenone
19	15,200	15,290	Medium	aa	n/a
20	15,364	15,427	Medium	aa	n/a
21	15,540	15,610	Medium	aa	n/a

Table 1. *Cont.*

No.	Signal Beginning	Signal End	Intensity	Odour Description	Assigned Compound
22	15,674	15,720	Weak	aa	n/a
23	15,940	16,010	Medium	aa	n/a
24	16,120	16,334	Medium	chemical, tar, mothball	1-Methylnafthalene
25	16,480	16,577	Weak	n/a	n/a
26	16,587	16,620	Weak	n/a	n/a
27	17,317	17,427	Weak	n/a	n/a

aa—as above; n/a—not applicable.

Figure 5 shows the spectra fragments (marked with different colours) during which specific odours were perceived. The colour type indicates the odour signal's intensity (strength). The "weak" odours are marked in green, odours with "medium" intensity are orange, and "strong" odours are marked in red. Table 1 summarises the identified odour signals, according to the ordinal number above the peak. The odour description complies with the study author's subjective perception and previous experiences working with an olfactometric port and the tested matrix.

For comparison, Figure 6 and Table 2 show the test results for an air sample collected in a non-renovated office room. Three air samples were also collected in the room, and one representative spectrum was thoroughly analysed, as in the previous case. The chromatographic spectra of all the collected samples were nearly identical (except for the intensity of some peaks).

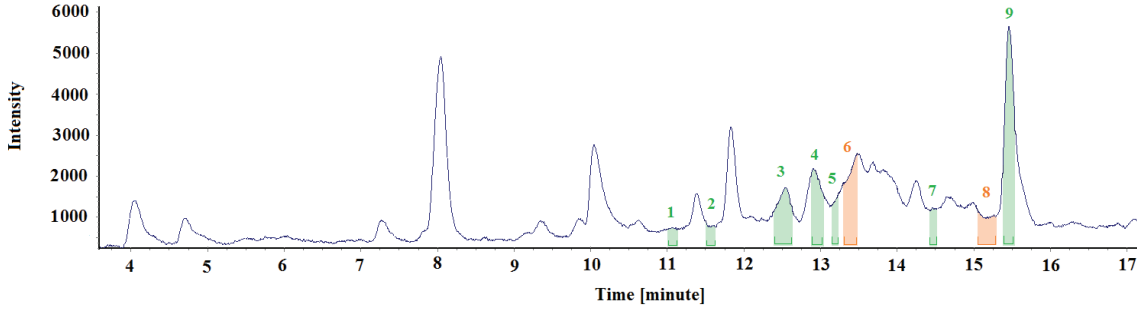

Figure 6. Chromatographic spectrum with the applied odour signals obtained for the air sample collected from the non-renovated office room.

Table 2. Identification of the signals obtained for the air sample collected from the non-renovated office room.

No.	Odour Beginning	Odour End	Intensity	Odour Description	Assigned Compound
1	11,024	11,117	Weak	chemical	n/a
2	11,514	11,584	Weak	citrus	3-Carene
3	12,411	12,611	Weak	chemical	2-Ethyl-1-hexanol
4	12,897	13,024	Weak	a/a	n/a
5	13,154	13,214	Weak	naphthalene	n/a
6	13,304	13,444	Medium	plastic	2-Butoxyethyl acetate
7	14,444	14,507	Weak	plasticine	n/a
8	15,060	15,267	Medium	chemical	Benzoic acid
9	15,404	15,517	Weak	plastic	1-(2-butoxyethoxy)ethanol

aa—as above: n/a—not applicable.

Figure 6 shows the spectra fragments, marked with different colours, where specific odours were perceived. The same colour code as described in the previous paragraph was used to identify odour intensities.

3.2. Samples of Floor Staves in the Emission Chamber

Figure 7 and Table 3 show the test results obtained for the air sample collected in an emission chamber, where the floor staves were placed. Two air samples were collected three days into their seasoning, but only one representative spectrum was selected for a detailed analysis. The chromatographic spectra of both collected samples differed slightly (minor differences in the intensity of individual peaks).

Figure 7 shows the spectra fragments (marked with different colours) during which specific odours were perceived. The colour type indicates the odour signal's intensity (strength). The "weak" odours are marked in green, odours with "medium" intensity are orange, and "strong" odours are marked in red. Table 3 summarises the identified odour signals according to the ordinal number above the peak.

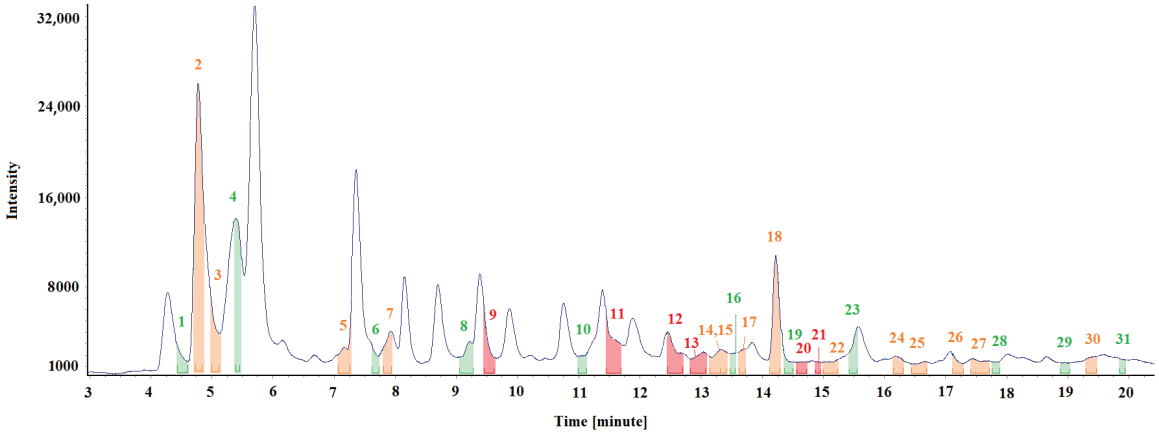

Figure 7. Chromatographic spectrum with the applied odour signals obtained for the air sample collected from the emission chamber after three days.

Table 3. Identification of the signals obtained for the air sample collected from the emission chamber.

No.	Odour Beginning	Odour End	Intensity	Odour Description	Assigned Compound
1	4471	4578	Weak	fat, tallow	n/a
2	4731	4841	Medium	acetic	Acetic acid
3	5001	5114	Medium	n/a	n/a
4	5381	5448	Weak	butter	n/a
5	7094	7238	Medium	plastic	Methylcyclohexane
6	7638	7718	Weak	butter, camphor	Methyl Isobutyl Ketone
7	7808	7928	Medium	a/a	a/a
8	9084	9231	Weak	plastic	m-Xylene
9	9468	9611	Strong	unpleasant	n/a
10	11,008	11,108	Weak	mushroom, musty	Heptanoic acid
11	11,464	11,671	Strong	citrus, fruit, fresh	3-Carene
12	12,468	12,704	Strong	tar, naphthalene	Phenol

Table 3. *Cont.*

No.	Odour Beginning	Odour End	Intensity	Odour Description	Assigned Compound
13	12,874	13,091	Strong	a/a	m-Cresol
14	13,144	13,324	Medium	a/a	n/a
15	13,331	13,451	Medium	plastic	n/a
16	13,491	13,568	Weak	alcohol, solvent	n/a
17	13,571	13,708	Medium	wood, musty	Acetophenone
18	14,174	14,328	Medium	wood	n/a
19	14,368	14,511	Weak	plastic	n/a
20	14,534	14,724	Strong	naphthalene	Nafthalene
21	14,864	14,988	Strong	naphthalene	Nafthalene
22	14,994	15,234	Medium	tar, wood	n/a
23	15,441	15,541	Weak	n/a	n/a
24	16,161	16,291	Medium	tar, wood	1-Methylnafthalene
25	16,471	16,667	Medium	pleasant	n/a
26	17,121	17,287	Medium	n/a	n/a
27	17,414	17,744	Medium	tar, wood	2-Methylnaphthalene
28	17,757	17,874	Weak	forest fruit	n/a
29	18,891	18,997	Weak	mold, musty	n/a
30	19,321	19,454	Medium	pleasant	n/a
31	19,864	19,911	Weak	plasticine	n/a

aa—as above; n/a—not applicable.

3.3. Fragments (Chips) of the Materials Placed in Thermal Desorption Tubes

In order to obtain extra analytical information about the tested array, Figure 8 and Table 4 show the test results obtained for the wooden floor staves' fragments (chips), exposed to emissions at an elevated desorption temperature of 70 °C (Section 2).

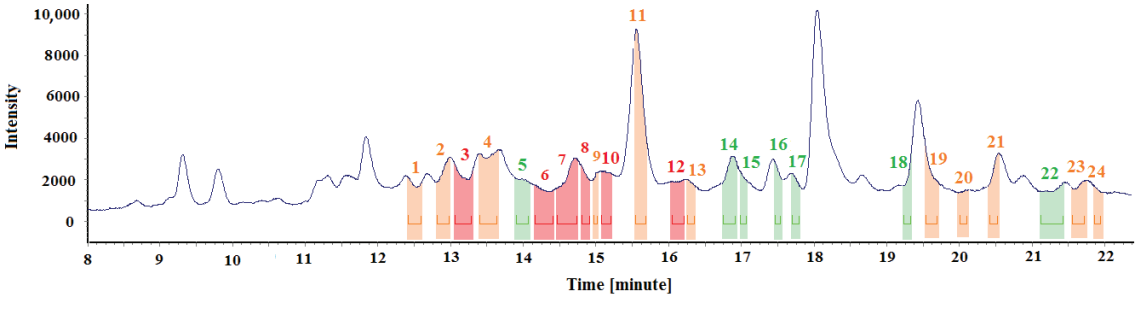

Figure 8. Chromatographic spectrum with the applied odour signals obtained for the samples of floor staves exposed to elevated desorption temperature.

Figure 8 contains the spectra fragments (marked with different colours) during which specific odours were perceived. The same colour code as previously described was used to identify odour intensities. Table 4 summarises the exact durations of the odour signals and the chemical compounds responsible for them, assigned based on spectral data (where applicable).

Table 4. Identification of the signals obtained for the samples of floor staves exposed to elevated desorption temperature.

No.	Odour Beginning	Odour End	Intensity	Odour Description	Assigned Compound
1	12,421	12,587	Medium	chemical, medicine	Phenol
2	12,817	12,981	Medium	unpleasant	n/a
3	13,064	13,281	Strong	unpleasant	m-Cresol
4	13,397	13,630	Medium	unpleasant	n/a
5	13,904	14,067	Weak	n/a	n/a
6	14,164	14,407	Strong	chemical	o-Cresol
7	14,464	14,740	Strong	unpleasant	n/a
8	14,810	14,917	Strong	unpleasant	2,3-Dimethylphenol
9	14,967	15,017	Medium	pleasant, sweet	n/a
10	15,080	15,207	Strong	naphthalene	Naphthalene
11	15,550	15,684	Medium	n/a	n/a
12	16,054	16,207	Strong	wood	n/a
13	16,257	16,350	Medium	wood	2-Ethyl-5-methylphenol
14	16,757	16,917	Weak	plant, herbal	n/a
15	16,990	17,064	Weak	unpleasant	4-Ethyl-2-methoxyphenol
16	17,464	17,540	Weak	n/a	n/a
17	17,697	17,797	Weak	unpleasant	1-Methylnaphthalene
18	19,237	19,330	Weak	n/a	n/a
19	19,537	19,694	Medium	wood	2,6-Dimethylnaphthalene
20	20,004	20,104	Medium	n/a	n/a
21	20,420	20,527	Medium	n/a	n/a
22	21,120	21,427	Weak	n/a	n/a
23	21,560	21,724	Medium	naphthalene	Dibenzofuran
24	21,857	21,940	Medium	n/a	n/a

aa—as above; n/a—not applicable.

4. Discussion

4.1. Air Samples Collected during Renovation and in a Non-Renovated Room

A slight chemical odour was perceived in the renovated room's air, at the stage of the floor staves' removal. The odour originated from the floor layers disturbed during dismantling and resulted in a higher airborne concentration of fragrant compounds from bituminous products and wood. An onerous odour, described by the room users even before the renovation, was less intense.

Comparing chromatographs and odour signals from the air samples collected in the non-renovated and renovated room of the same intended use, reveals that the odour signals diversity was higher in the latter ones, and there were more medium and strong intensity signals. Three strong signals, fourteen medium signals and ten weak signals were identified in the renovated room. In the non-renovated room, despite seven weak-intensity signals, two odours were identified to which medium intensity was assigned. Moreover, the compounds identified in the renovated room are present in more significant amounts, confirmed by the intensity scale values.

Terpene hydrocarbons (mostly pleasant odours), such as α-Pinene, Camphene, β-Pinene, 3-Carene, Acetophenone, Linalool, Cis-Verbenol and Pinocarvone were assigned to the odour signals identified in the samples from the renovated room. They are natural com-

pounds of many essential oils, originating from evergreen trees (carenes, pinenes). Moreover, unpleasant odour signals were also identified. They are associated with the smell of naphthalene, tar and old wood. Naphthalene and 1-Methylnaphthalene were assigned to them in the spectrum (Figure 5).

The compounds mentioned above, present in the renovated room's air, could have originated from the floor materials, i.e., wooden floor staves and insulation and moisture barriers, such as tar paper and adhesive. The released quantities of the compounds were higher because their structures were disturbed.

3-Carene was also identified in the non-renovated room, although in lower concentrations. Moreover, odours were identified coming from glycol ether derivatives, used in industry as solvents for paints, varnishes (released from varnish coats applied to wooden surfaces), dyes and adhesive agents, and components of cleaning agents.

4.2. Samples of Floor Staves in the Emission Chamber

The floor panel samples (Figure 3) emitted a strong unpleasant odour, characteristic of bituminous materials. The airflow through the chamber was switched off to accumulate the compounds emitted from the floor materials because the test assumption was to determine the qualitative, rather than quantitative, characteristics of the emitted compounds. As expected, the intensity values of the chromatographic peaks were higher than the values obtained for the air samples collected in the room.

A representative chromatograph was selected for a detailed analysis. An olfactometric analysis helped identify six strong-intensity signals, fourteen medium-intensity signals and eleven weak-intensity signals. However, assigning the likely compounds was impossible for many odour signals, so they were marked as n/a. In such cases, the experimenter's sense of smell was more sensitive than the sensitivity threshold of the testing apparatus or the non-identified odour signals resulting from the odour synergy or the "echo" of the preceding signals.

The odour signals identified in the air samples collected from the emission chamber, where the floor staves from the renovated room were placed, were mainly assigned to simple aromatic cyclic compounds, such as xylene, phenol, and naphthalene methyl derivatives. Bicyclic aromatic hydrocarbons are characteristic of tar products from coal processing (pitch, coal tar, adhesive, oil from coal tar distillation) and are evidence of the tar adhesive's presence in the test samples. Tricyclic aromatic hydrocarbons have a high molecular weight and are non-volatile at room temperature; hence, they were not identified in the study.

4.3. Fragments (Chips) of the Materials Placed in Thermal Desorption Tubes

The results presented in Figure 8 and Table 4 suggest that wood chip tests contain many odour signals, and their intensity is highly diversified. An olfactometric analysis helped identify six strong signals, eleven medium-intensity signals and seven weak signals. An unpleasant odour of naphthalene characterised most of the signals to which chemical compounds were assigned. The odours were described as chemical, naphthalene, old wood, unpleasant, etc. Since the samples were exposed to a higher temperature than the room temperature during the desorption, heavier and more branched derivatives of aromatic compounds were released from them, including 2,3-Dimethylphenol, 2-Ethyl-5-methylphenol, 4-Ethyl-2-methoxyphenol, 2,6-Dimethyl naphthalene and dibenzofuran.

Desorption was performed at 70 °C. Observations, previous tests and experiments [31] revealed that heating the samples to higher temperatures causes their thermal destruction, manifested by a burnt material odour released from the olfactometric port. Moreover, interpreting the signals present then in the chromatographs is impossible, because either the signals originate from the samples' thermal degradation products or there are too many signals, especially in the high spectral range.

5. Conclusions

Based on the measurements, the conclusion was drawn that the method of collecting the samples and their preparation for the tests is the key aspect of the experiment and must be highly repeatable. Tables 1–4 and Figures 5–8 describe all the odours that were identified during the measurements presented in the article. Apparently, the rest of the compounds present in the test samples were odourless or the odour detection threshold of these compounds was higher than their concentrations in the test samples. Each compound has its own detection threshold; hence, it can be concluded that a high GC–MS signal does not mean a strong odour intensity and vice versa. A low GC–MS signal may correspond to a very intense odour.

The experiment series led to the conclusion that, in order to correlate the odour leaving the olfactometric port with a clear chromatographic signal, two samples, collected simultaneously at two positions of the high-temperature two-position four-way valve, should be analysed. This results from the fact that for valve position B (Section 2), most of the tested gas stream is subjected to sensory analysis. At such an apparatus setting, one-tenth of the stream reaches the MS detector, which results in the spectrum's weak signal. In such cases, we get a strong odour and insufficient information in the chromatographic spectrum (weak intensity). Therefore, to correlate numerous odour signals with eluting compounds, additional analysis should be carried out on a sample collected simultaneously at the other valve position (position A). A spectrum obtained in this way is applied to the odour signals from the olfactometric port, and hence, the complete information presented in this paper is provided [12–14].

In some situations, the human nose is more sensitive than chromatographic detection, which is why an odour stimulus cannot be assigned to any of the eluting compounds.

The quality of the analytes' chromatographic splitting, meaning the GC–MS analysis conditions, matters for the qualitative assessment of odour. A human is a proper detector in the described method. That is why the factors affecting the assessment have to be stable, i.e., laboratory free of odours, stable temperature and pressure, sequence of the analysed samples, their repeatability and scale used for the odour intensity assessment.

Based on the presented and previous studies [31], the author demonstrated that such compounds as naphthalene, methyl naphthalenes, dimethyl naphthalenes, biphenyl and acenaphthene could be identified in the air, in rooms where tar or asphalt binder was present, and in rooms where the wood was impregnated with chloronaphthalene-based agents [31]. This article [31] provides quantitative and qualitative results, and explains more about the differences between emissions from wooden structures, which were impregnated with tar compositions (creosote oil and Xylamite oil containing tar products), and buildings in which bituminous seal containing hydrocarbon solvents was used. The enumerated compounds seem responsible for the naphthalene-like odour of the air in the rooms.

The fact that some odours are repeated in the different spectra and other odours are not, is related to (1) different concentrations of compounds in the tested samples, (2) various odour detection thresholds and (3) the type of selected detection method (from indoor air, emission chamber, thermal desorption).

In indoor air research, fewer compounds can be identified, compared to materials research. Despite the fact that the odour is often clearly felt in the tested rooms, analytical results often do not show high concentrations of components derived from tar adhesives. The repeatability for air samples taken in one room, at the same time, is practically identical, whereas for samples taken from different rooms, the results are different.

Analyses performed on samples placed in emission chambers or subjected to thermal desorption provide more information on the detectable odours originating from this type of material. The emissions from tar adhesives show a greater concentration and variety of compounds because they are isolated in the test chambers (chamber background subtraction was also used). Besides, the research concerned the floor layers disturbed during their dismantling. The repeatability for the air samples taken from test chambers for the same

products is practically identical, whereas, for different tar adhesive products, the emissions differ from each other. This is related to complex tar adhesive compositions.

The fragments (chips) of the materials were subjected to desorption temperatures in which organic compounds are more concentrated. The reproducibility of these chip test results from one sample is very high, but the results are not identical. One should remember that wood chip samples are subjected to thermal desorption at a temperature higher than the temperature in office rooms, so the results supplement the results obtained for air samples tests and tests in emission chambers.

Funding: This work was financially supported by the statutory fund of the Building Research Institute in Warsaw.

Institutional Review Board Statement: Not applicable.

Informed Consent Statement: Not applicable.

Acknowledgments: I would like to thank Katarzyna Komorowska for her support and numerous substantive conversations that motivated me to take further actions and inspired new ideas. I would also like to thank Waldemar Kurek, the Shimadzu service engineer, for many hours of interesting and educational conversations about the TD–GC–MS/O system and his help configuring the system.

Conflicts of Interest: The author declares no conflict of interest.

References

1. Harčárová, K.; Vilčeková, S.; Balintova, M. Building Materials as Potential Emission Sources of VOC in the Indoor Environment of Buildings. *Key Eng. Mater.* **2020**, *838*, 74–80. [CrossRef]
2. Kozicki, M.; Piasecki, M.; Goljan, A.; Deptuła, H.; Niesłochowski, A. Emission of Volatile Organic Compounds (VOCs) from Dispersion and Cementitious Waterproofing Products. *Sustainability* **2018**, *10*, 2178. [CrossRef]
3. Kotzias, D. Built environment and indoor air quality: The case of volatile organic compounds. *AIMS Environ. Sci.* **2021**, *8*, 135–147. [CrossRef]
4. Kozicki, M.; Guzik, K. Comparison of VOC Emissions Produced by Different Types of Adhesives Based on Test Chambers. *Materials* **2021**, *14*, 1924. [CrossRef] [PubMed]
5. Wargocki, P.; Wyon, D.P.; Fanger, P.O. The performance and subjective responses of call-center operators with new and used supply air filters at two outdoor air supply rates. *Indoor Air* **2004**, *14*, 7–16. [CrossRef]
6. Frontczak, M.; Wargocki, P. Literature survey on how different factors influence human comfort in indoor environments. *Build. Environ.* **2011**, *46*, 922–937. [CrossRef]
7. Shaughnessy, R.J.; Haverinen-Shaughnessy, U.; Nevalainen, A.; Moschandreas, D. A preliminary study on the association between ventilation rates in classrooms and student performance. *Indoor Air* **2006**, *16*, 465–468. [CrossRef]
8. Kostyrko, K.B.; Wargocki, P. *Pomiary Zapachów i Odczuwalnej Jakości Powietrza w Pomieszczeniach*; Instytut Techniki Budowlanej: Warszawa, Poland, 2012.
9. Kostyrko, K.B.; Kozicki, M. Kierunki rozwoju pomiarów zapachu i zawartości związków mVOC we wnętrzach budynków. *Zesz. Nauk. Wydz. Elektrotechniki I Autom. Politech. Gdańskiej.* **2018**, *2018*, 97–102. [CrossRef]
10. Jia, C.; Batterman, S. A Critical Review of Naphthalene Sources and Exposures Relevant to Indoor and Outdoor Air. *Int. J. Environ. Res. Public Health* **2010**, *7*, 2903–2939. [CrossRef]
11. National Toxicology Program. *NTP Technical Report on the Toxicology and Carcinogenesis Studies of Naphthalene in F344/N Rats (Inhalation Studies)*; National Toxicology Program Technical Report Series; National Institutes of Health: Durham, NC, USA, 2000.
12. Ad Hoc Working Group on Chlorinated Naphthalenes under the POPs Review Committee of the Stockholm Convention. Stockholm Convention on Persistent Organic Pollutants. In Proceedings of the 2012 Stockholm Convention, Geneva, Switzerland, 15–19 October; 2012; pp. 1–38.
13. Preuss, R.; Drexler, H. Naphthalene—An environmental and occupational toxicant. *Int. Arch. Occup. Environ. Health* **2003**, *76*, 556–576. [CrossRef]
14. Buckpitt, K.K.; Kephalopoulos, A.; Naphthalene, S. *WHO Guidelines for Indoor Air Quality: Selected Pollutants*; World Health Organization: Geneva, Switzerland, 2010. Available online: https://www.ncbi.nlm.nih.gov/books/NBK138704/ (accessed on 1 December 2021).
15. Technical Committee: CEN/TC 264, EN 13725:2003/AC:2006. *Air Quality—Determination of Odour Concentration by Dynamic Olfactometry*; National Standards Authority of Ireland: Dublin, Ireland, 2003.
16. Kośmider, J.; Mazur-Chrzanowska, B. *Odory. Wyd. 1*; Wydawnictwo Naukowe PWN: Warsaw, Poland, 2002.
17. Kośmider, J.; Krajewska, B. Normalizacja Olfaktometrii Dynamicznej. Podstawowe Pojęcia i Jednostki Miar. *Normalizacja* **2005**, *1*, 15–22.

18. Technical Committee: ISO/TC 146/SC 6. *Indoor Air, International Standard, ISO 16000-282012 Indoor Air—Part 28: Determination of Odour Emissions from Building Products Using Test Chambers*; ISO: Geneva, Switzerland, 2003; p. 13.
19. Technical Committee: ISO/TC 146/SC 6, ISO 16000-9:2006. *Indoor Air—Part 9: Determination of the Emission of Volatile Organic Compounds from Building Products and Furnishing—Emission Test Chamber Method*; ISO: Geneva, Switzerland, 2006.
20. Knudsen, H.; Clausen, P.; Wilkins, C.; Wolkoff, P. Sensory and chemical evaluation of odorous emissions from building products with and without linseed oil. *Build. Environ.* **2007**, *42*, 4059–4067. [CrossRef]
21. Bitter, F.; Müller, B.; Müller, D. Estimation of odour intensity of indoor air pollutants from building materials with a multi-gas sensor system. *Build. Environ.* **2010**, *45*, 197–204. [CrossRef]
22. Zhang, S.; Cai, L.; Koziel, J.A.; Hoff, S.J.; Schmidt, D.R.; Clanton, C.J.; Jacobson, L.D.; Parker, D.B.; Heber, A.J. Field air sampling and simultaneous chemical and sensory analysis of livestock odorants with sorbent tubes and GC–MS/olfactometry. *Sens. Actuators B Chem.* **2010**, *146*, 427–432. [CrossRef]
23. Brattoli, M.; Cisternino, E.; de Gennaro, G.; Giungato, P.; Mazzone, A.; Palmisani, J.; Tutino, M. Gas chromatography analysis with olfactometric detection (gc-o): An innovative approach for chemical characterizatio of odor active volatile organic compounds (vocs) emitted from a consumer product. *Chem. Eng. Trans.* **2014**, *40*, 121–126. [CrossRef]
24. Suchorab, Z.; Frąc, M.; Guz, Ł.; Oszust, K.; Łagód, G.; Gryta, A.; Bilińska-Wielgus, N.; Czerwiński, J. A method for early detection and identification of fungal contamination of building materials using e-nose. *PLoS ONE* **2019**, *14*, e0215179. [CrossRef]
25. Wardencki, W.; Chmiel, T.; Dymerski, T.; Biernacka, P.; Plutowska, B. Application of gas chromatography, mass spectrometry and olfactometry for quality assessment of selected food products. *Ecol. Chem. Eng. S* **2009**, *16*, 287–300.
26. Luo, S.; Li, Q.; Chen, A.; Liu, X.; Pu, B. The Aroma Composition of Baby Ginger Paocai. *J. Food Qual.* **2017**, *2017*, 7653791. [CrossRef]
27. Cai, L.; Rice, S.; Koziel, J.A.; Dharmadhikari, M. Development of an Automated Method for Selected Aromas of Red Wines from Cold-Hardy Grapes Using Solid-Phase Microextraction and Gas Chromatography-Mass Spectrometry-Olfactometry. *Separations* **2017**, *4*, 24. [CrossRef]
28. Rice, S.; Koziel, J.A. The relationship between chemical concentration and odor activity value explains the inconsistency in making a comprehensive surrogate scent training tool representative of illicit drugs. *Forensic Sci. Int.* **2015**, *257*, 257–270. [CrossRef]
29. Kobayashi, N.; Nishimura, O. Availability of Detection Frequency Method Using Three-Port Gas Chromatography-Olfactometry for Rapid Comparison of Whole Milk Powders. *Food Sci. Technol. Res.* **2014**, *20*, 809–814. [CrossRef]
30. De-La-Fuente-Blanco, A.; Ferreira, V. Gas Chromatography Olfactometry (GC-O) for the (Semi)Quantitative Screening of Wine Aroma. *Foods* **2020**, *9*, 1892. [CrossRef] [PubMed]
31. Kozicki, M.; Niesłochowski, A. Materials Contamination and Indoor Air Pollution Caused by Tar Products and Fungicidal Impregnations: Intervention Research in 2014–2019. *Sensors* **2020**, *20*, 4099. [CrossRef] [PubMed]
32. *PKN/KT 308, PN-EN 16516+A1:2020-12*; Construction Products: Assessment of Release of Dangerous Substances—Determination of Emissions into Indoor Air. Polish Committee for Standardization: Warsaw, Poland, 2020.

processes

MDPI

Article

Radioactive Elements Detected in Abandoned Oil Tank Farms

Stefan Petrache [1], Timur Chis [2,*], Ancaelena Eliza Sterpu [2] and Olga Valerica Săpunaru [2]

[1] Ph. D. School, Oil and Gas University Ploiesti, Bucuresti Blv, 37, 100680 Ploiesti, Romania; mihstepetrache@gmail.com
[2] Chemical and Chemical Engineering Department, Ovidius University Constanta, Mamaia Blv, 224, 900450 Constanta, Romania; asterpu@univ-ovidius.ro (A.E.S.); olgutasapunaru@yahoo.com (O.V.S.)
* Correspondence: tchis@univ-ovidius.ro; Tel.: +40-723-670-107

Abstract: Oil fields in Romania were active in the period 1900–2020, some of which will close due to declining oil production and especially due to reduced processing after the application of European Community recommendations to give up fossil fuels and the use of renewable fuel. The rehabilitation of the soil affected by hydrocarbon pollution is carried out with public funds. This is why, when transferring the land to the local community, an oil pollution assessment study is carried out. If the hydrocarbon content is less than 1000 mg/kg dry matter, the soil is not depolluted. In the Moinesti oil area, Romania, against the background of the increased incidence of breast cancers in women who worked in oil facilities, a study was conducted on the natural radioactivity of abandoned oil areas. The results of this analysis are presented and discussed in this article. It is the first study of radioactivity of the oil tank farm affected by oil pollution, its purpose being to draw attention in detecting radioactive elements when handing over land affected by oil pollution (but which respects the maximum levels of pollutant) to the local community.

Keywords: radioactive elements; oil; pollution; soil

Citation: Petrache, S.; Chis, T.; Sterpu, A.E.; Săpunaru, O.V. Radioactive Elements Detected in Abandoned Oil Tank Farms. *Processes* **2022**, *10*, 374. https://doi.org/10.3390/pr10020374

Academic Editors: Avelino Núñez-Delgado, Zhien Zhang, Elza Bontempi, Mario Coccia, Marco Race and Yaoyu Zhou

Received: 1 November 2021
Accepted: 10 February 2022
Published: 15 February 2022

1. Introduction

Exploitation of deposits of raw materials may cause exposure to ionizing radiation of workers and the environment, due to the presence of naturally occurring radioactive materials, the most exposed sectors being [1–3]:

a. oil and gas production,
b. geothermal energy production,
c. coal-fired power plants,
d. groundwater filtration installations,
e. extraction of ores other than uranium ores.

As can be seen from NORM (Naturally Occuring Radioactive Materials) standards, oil and gas extraction is an industry that can radioactively pollute the work environment.

A risk assessment for radioactive exposure [2–4] identifies the oil and gas extraction industry as an industry with:

- low risk of internal exposure of workers due to closed processing of these products,
- high risk of internal exposure of workers due to the need to measure flows and the quality of final products and extraction products,
- medium risk in case of environmental pollution, as the crude oil and gas processing systems have an environmental protection management system.

The first articles on the identification of radioactive pollution in the oil and gas industry were published in 1904 [4] when radionuclide Ra-226 has been identified during separation of natural gas from crude oil.

In Romania, the effects of radioactive radiation on employees and the resident population in oil and natural gas extraction areas were analyzed after the closure of oil fields (as a result of the increase in diseases in the area) [5].

European Community has European Council issued directives to identify minimum levels of exposure by naturally radioactive materials and radiological risk for the employees or the population [6].

Radionuclides identified as occurring in hydrocarbon explorations and extractions processes in higher concentration values are Ra-226, K-40, and Ac-228 [7–11].

Their half-life is very long, and they are present in the earth's crust with activity concentration that depends on the type of rock.

Hydrocarbon exploration and exploitation processes achieve NORM accumulation through the following potential routes of exposure [9–11]:

- detritus resulting from well drilling,
- the drilling fluid used to make the wells,
- field water,
- accumulated sediments, such as sand and sludge deposited in separators and storage tanks,
- crusts formed on pipelines and in reinforcements (Figure 1),
- condensed gases,
- the fluid used in the interventions and repairs to the wells.

Figure 1. Crust of oil installations (photo provided by Stefan Petrache) [8].

The natural radioactivity of the Moinesti geological area has been studied.

The Moinești area is located in the northeast of Romania, being an area with crude oil, gas, and coal deposits, exploited since 1600 (geographical coordinates 46°30′48″ N 26°35′51″ E).

In the last period of time, due to the reduction of crude oil quantities and the reduction of the use of coal, most of the oil, gas, and coal operations have been abandoned.

Magma from the volcanic mountains (Harghita) was detected in the coal mines, located about 10 km from the oil extraction area.

These radioactive elements were transported by oil during its extraction.

Crude oil from the Oligocene geological era was extracted from 21 wells at depths of 280–1024 m and treated at an oil tank farm.

In this article, the authors aimed for:

a. Detection of the presence of radioactive elements in the areas where the extracted crude oil has been treated and stored,
b. analysis of radioactive elements present in the area of abandoned tank farms for the treatment and storage of extracted crude oil,
c. the level of pollution with radioactive elements in the area of treatment and storage of the extracted crude oil,
d. the level of pollution with radioactive elements in the Moinești extraction area.

2. Materials and Methods

The apparatus used to measure the Equivalent Dose (H) was the computerized portable radiation contaminant INSPECTOR (Geiger–Mueller tube to detect radiation-IMI Inspector Alert) and the VICTOREEN 451P ionization chamber dosimeter.

Gamma dose flow rates were measured by measuring the area of interest.

In the area of interest, we collected samples by soil at 5 cm and 100 cm depth.

For equipment, the determination was made at their contact and at a distance of 100 cm and a height of 150 cm.

The apparatus used to measure the Equivalent Dose Rate (H—the dose absorbed in the tissue or organ, weighted by the type and quality of radiation R) was the computerized portable radiation contaminant INSPECTOR (Geiger–Mueller tube to detect radiation-IMI Inspector Alert).

To perform soil spectrometric analyses, 50 soil samples were taken from 25 sampling points, from depths of 5 cm and 100 cm, respectively.

The soil samples were prepared in the laboratory in order to determine the concentration of gamma-emitting radionuclides.

The samples were dried in an oven at 100 °C, after which it was crushed and homogenized. These were taken mainly around installations with a high potential for NORM contamination and from areas where NORM contamination was identified following the measurement of radiation fields.

The analysis was performed by gamma spectrometry, by the multichannel analyzer spectrometric chain technique with a germanium detector.

Each measurement performed was repeated at least 5 times.

The arithmetic mean was calculated and the relative error of these measurements compared to the average value was established, being 1%.

The collected samples were divided into 5 analysis cells, and also the relative error was determined compared to the average value (being 0.08%).

3. Measuring Results

The measurement and sampling points within the analysis area (a crude oil and gas treatment plant and a storage facility for petroleum products) are shown in Table 1.

The presence of radionuclides in the soil samples is listed in Table 2.

Table 3 shows the concentration of natural radionuclides for the study area.

Table 1. Equivalent Dose Rate (H) values of the equipment.

Measuring Point		H Contact, μSv/h	H at 100 cm, μSv/h
Mentenance house	BP	0.17	0.14
Fire equipment point	PSI	0.14	0.11
Oil tank 250 m^3	P	2.40	0.19
Pumps	HI	0.20	0.17
Tank water and oil	R1	0.90	1.16
Salt water tank 20 m^3	R2	1.80	0.18
Salt water tank 200 m^3	R3	2.10	0.15
Oil tank 17 m^3	R4	3.50	0.27
Oil and water tank 20 m^3	R5	2.30	0.16
Oil tank 20 m^3,	R6	2.50	0.12
Oil tank 20 m^3,	R7	2.20	0.11
Pipe oil blending	CSF	3.10	0.23
Separator biphasic oil-gas	SVB1	2.10	0.14

Table 1. *Cont.*

Measuring Point		H Contact, μSv/h	H at 100 cm, μSv/h
Separator biphasic oil-gas	SVB2	1.70	0.17
Separator biphasic oil-gas	SVB3	1.80	0.13
Separator biphasic oil-gas	SVB3	1.90	0.11
Pipe oil, gas and water blending	CSS	1.60	0.14

Table 2. Activity concentrations (Bq/kg) of Ra-226, Ac-228 and K-40 in soils.

Sampling Point	Radionuclide Concentration Ra-226, Bq/kg	Radionuclide Concentration Ra-226, Bq/kg	Radionuclide Concentration Ac-228, Bq/kg	Radionuclide Concentration Ac-228, Bq/kg	Radionuclide Concentration K-40, Bq/kg	Radionuclide Concentration K-40, Bq/kg
	Depth, 5 cm, Ra-226_5	Depth, 100 cm, Ra-226_100	Depth, 5 cm, Ac-228_5	Depth, 100 cm, Ac-228_100	Depth, 5 cm, K-40_5	Depth, 100 cm, K-40_100
1	1150	702	53	49	709	980
2	2768	609	61	53	801	809
3	142	209	42	33	387	334
4	98	62	48	51	448	636
5	96	70	49	33	579	782
6	115	76	69	60	499	602
7	3147	5203	395	468	1009	1018
8	143	77	41	34	781	690
9	98	90	84	77	690	670
10	426	301	180	98	703	781
11	200	99	81	67	697	700
12	98	65	53	44	440	445
13	48	39	27	37	599	589
14	56	58	28	22	692	702
15	62	66	37	40	409	449
16	43	51	33	82	301	305
17	115	75	57	77	407	395
18	987	98	257	301	708	838
19	1830	407	576	409	883	777
20	432	201	100	61	730	463
21	398	291	191	155	620	533
22	849	555	338	222	501	602
23	591	91	101	99	402	444
24	4398	901	453	298	1096	999
25	327	78	77	62	607	621

Table 3. Natural radionuclide concentrations for the year 2020 in the city area at 100 mm depth and 5 km north of oil tank farm [8].

Radionuclide	Concentration Natural Background, Bq/kg
Ra-226	9.76
Ac-228	15.05
K-40	259.09

The natural background dose rate for a neighboring area not affected by NORM contamination is 0.110 μSv/h [8,10].

4. Evaluation of the Dose of Ground Exposure to Personnel and the Resident Population

Exposure to contaminated soil for park staff and residence population is analysis in concordance with Radioactively Contaminated Land Exposure Assessment Method (RCLEA), recommended by the Department of Environment Food and Rural Affairs for Environment Food and Rural Affairs (DEFRA) in the UK [12].

The scenario used to calculate the effective annual doses for employees was based on the following assumptions:

- for the calculation of the annual effective dose, the area most polluted with radioactive elements was taken, namely point 7 and a depth of 100 cm,
- soil contamination with radionuclides: Ra-226 (activity concentration 5203 Bq/kg), Ac-228 (activity concentration 468 Bq/kg) and K-40 (activity concentration 1018 Bq/kg),
- contaminated area: 970 m^2,
- type of land: commercial/industrial,
- type of building: concrete/brick,
- age of the recipient: adult,
- sex of the recipient: male.

The routes of exposure are as follows:

- external irradiation of the whole body,
- soil ingestion,
- external irradiation of the skin,
- inhalation,
- inhalation of Rn-222 gas inside the building.

The resulting effective annual dose was 22 mSv/annum, with the following contributions:

- External irradiation of the whole body: $\mathbf{1.24 \cdot 10^{-1}}$ mSv/annum,
- Soil ingestion: $\mathbf{3.05 \cdot 10^{-3}}$ mSv/annum,
- External irradiation of the skin: $\mathbf{5.56 \cdot 10^{-5}}$ mSv/annum,
- inhalation: $\mathbf{7.10 \cdot 10^{-4}}$ mSv/annum,
- Rn-222 gas inhalation inside the building: $\mathbf{2.20 \cdot 10}$ mSv/qn.

The scenario used to calculate the effective annual doses for population was based on the following assumptions:

- contaminated area: 107 m^2,
- type of land: residential with products grown at home,
- type of building: wood,
- age of the recipient: infant,
- sex of the recipient: female.

The routes of exposure are as follows:

- external irradiation of the whole body,
- ingestion of external skin irradiation of the skin,

- inhalation,
- vegetable intake,
- ingestion of soil on plants,
- inhalation of Rn-222 gas inside the building.

The resulting effective annual dose was 5.8 mSv/annum, with the following contributions:

- External irradiation of the whole body: $\mathbf{4.01 \cdot 10^{-1}}$ mSv/annum,
- Soil ingestion: $\mathbf{3.71 \cdot 10^{-3}}$, mSv/annum,
- External irradiation of the skin: $\mathbf{2.39 \cdot 10^{-5}}$, mSv/annum;,
- inhalation: $\mathbf{6.55 \cdot 10^{-4}}$, mSv/annum,
- Rn-222 gas inhalation inside the building: $\mathbf{5.75 \cdot 10}$ mSv/annum.

5. Analysis of the Correlation between Radionuclide Activity Concentrations and Dosing Rates from Contact Equipment

In order to observe the dispersion of the determined concentrations of the three radionuclides in part, for the depths of 5 cm and 100 cm, we analyzed the correlation of the data series (Figures 2–4):

- r(Ra-226_5, Ra-226_100) = 0.6083,
- r(Ac-228_5, Ac-228_100) = 0.9334,
- r(K-40_5, K-40_100) = 0.8414.

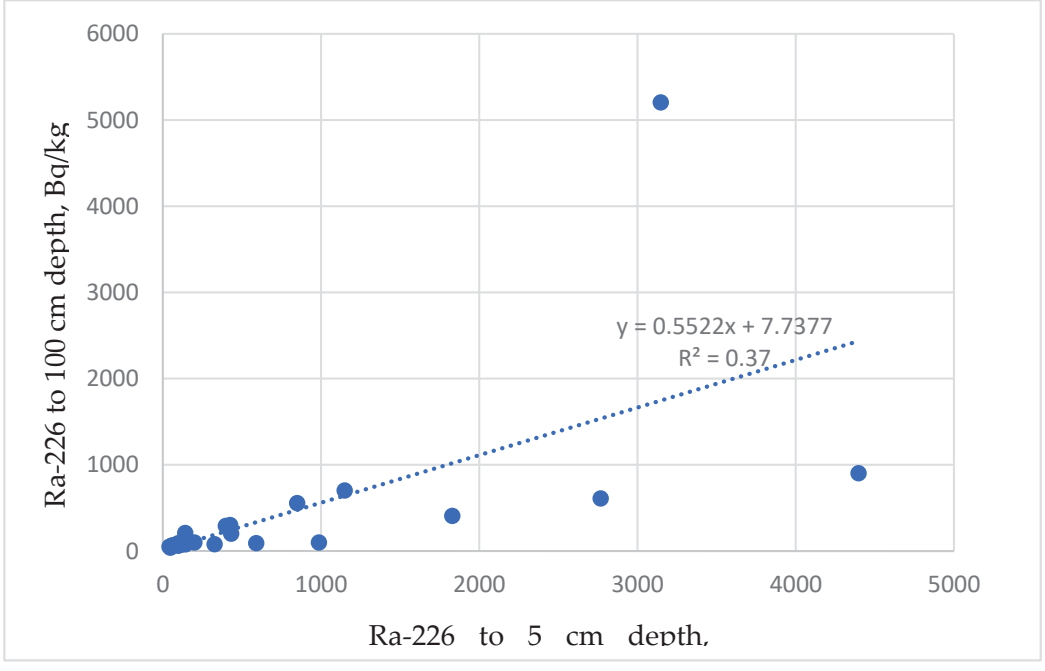

Figure 2. Variation of natural radionuclide concentrations (Ra-225) to 5 and 100 cm depth.

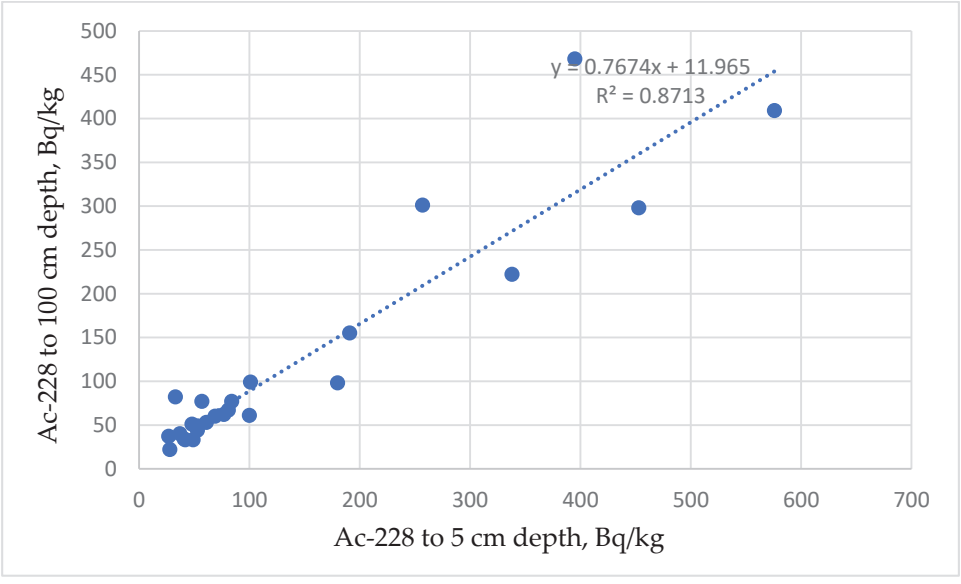

Figure 3. Variation of natural radionuclide concentrations (Ac-228) to 5 and 100 cm depth.

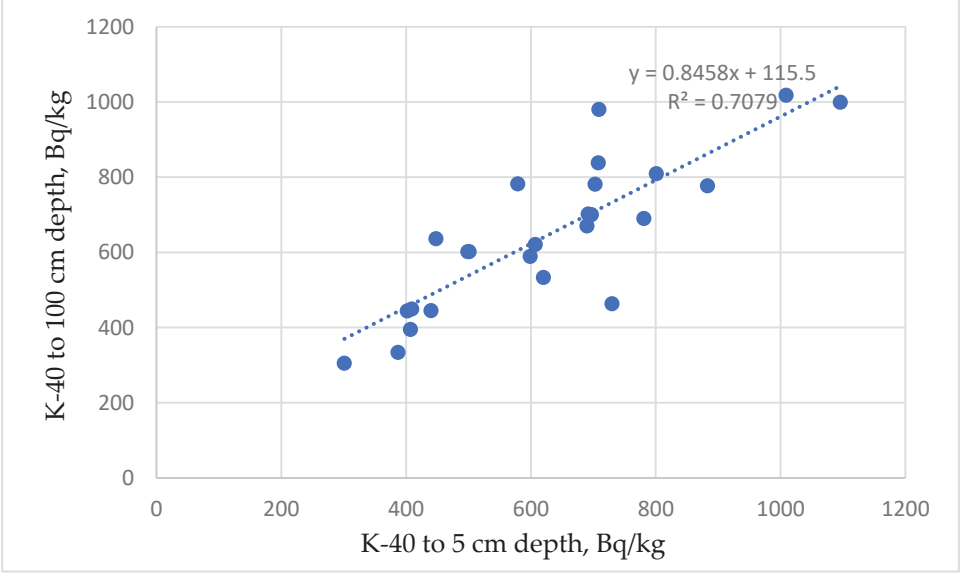

Figure 4. Variation of natural radionuclide concentrations (K-40) to 5 and 100 cm depth.

We also analyzed the correlation for the Equivalent Dose Rate (H) data series (at contact and 100 cm) (Figure 5):

- r(Equivalent Dose Rate (H) at contact, Equivalent Dose Rate (H) at 100 cm) = 0.145.

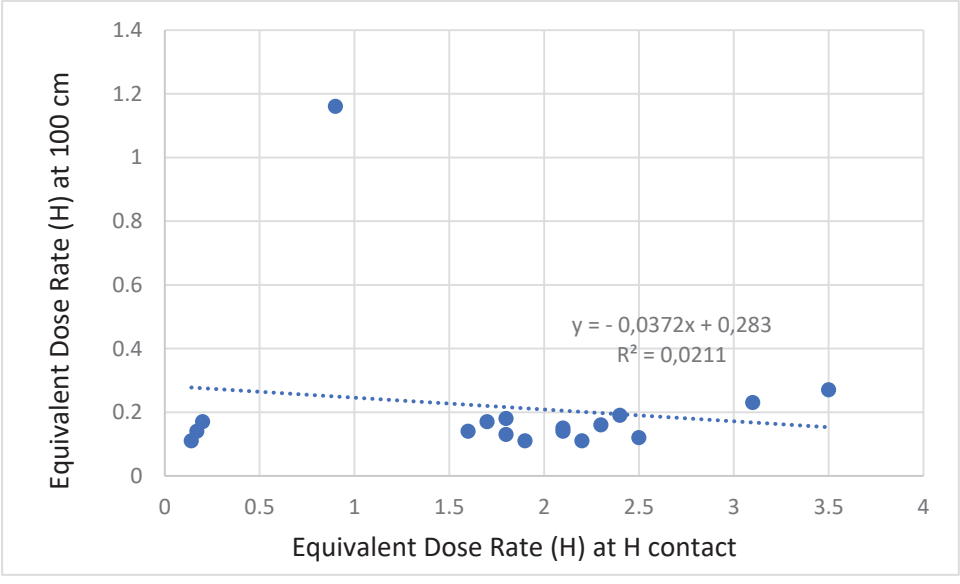

Figure 5. Equivalent Dose Rate (H) to H contact and 100 cm.

The first three data series show a strong correlation, which confirms the dependence on radionuclides contamination of the soil, for depths of 5 cm and 100 cm (Figures 2–4):

- r(Ra-226_5, Ra-226_100) = 0.6083 shows a positive correlation between bot variables. The regression line shows that concentrations at 5 cm depth are greater than at 100 cm. This is consistent with vertical migration of Ra-226, but the bigger fraction remains at 5 cm depth (Figure 2).
- r(Ac-228_5, Ac-228_100) = 0.9334 shows a strong positive correlation. The regression line shows that concentrations at 5 cm depth are slightly bigger than at 100 cm. This is consistent with vertical migration of Ac-228, but the fraction at 5 cm depth is slightly bigger (Figure 3).
- r(K-40_5, K-40_100) = 0,8414, shows a strong positive correlation. The regression line shows that K-40 concentration at 5 cm and 100 cm depth are very similar. This is consistent with the conservative abundance of K in nature (Figure 4).

The analysis of soil samples from a depth of 100 cm suggests that a deep contamination can be discussed, this being present on the entire depth, in differentiated layers (Figure 5).

6. Areas of Radioactive Pollution

In order to establish the area contaminated with NORM, the following steps were completed:

- scale definition of the perimeter of the fleet of separators—tanks,
- division of the perimeter into 1 m × 1 grids,
- DDE dispersion measurement for each perimeter,
- performing three measurements for each perimeter at four time periods on the day of collection (6:00 a.m., 12:00 a.m, 6:00 p.m. and 12:00 p.m.),
- statistical verification of the data collected (reading error was below 1%),
- sampling and analysis,
- integration of data collected by full perimeter scanning with previously collected data.
- The measurements were aimed at:
- integration of DDE values for equipment at their contact and at a distance of 100 cm,
- integration of DDE values for measuring points at a height of 5 cm and 100 cm, respectively,

- integration of the concentration values of the three radionuclides for the sampling points, respectively, Ra-226, Ac-228, and K-40, for the depths of 5 cm and 100 cm.

The collected data were graphically integrated with the help of a software developed by the authors and which has the role of graphically drawing the scanned environmental measurements. In addition, the exclusion perimeter was achieved by summing the radioactive elements and joining the maximum points.

The DDE dispersion map at a height of 5 and 100 cm (Figures 6 and 7) highlights the influence of soil contamination with NORM on the values determined by area dosimetric measurements.

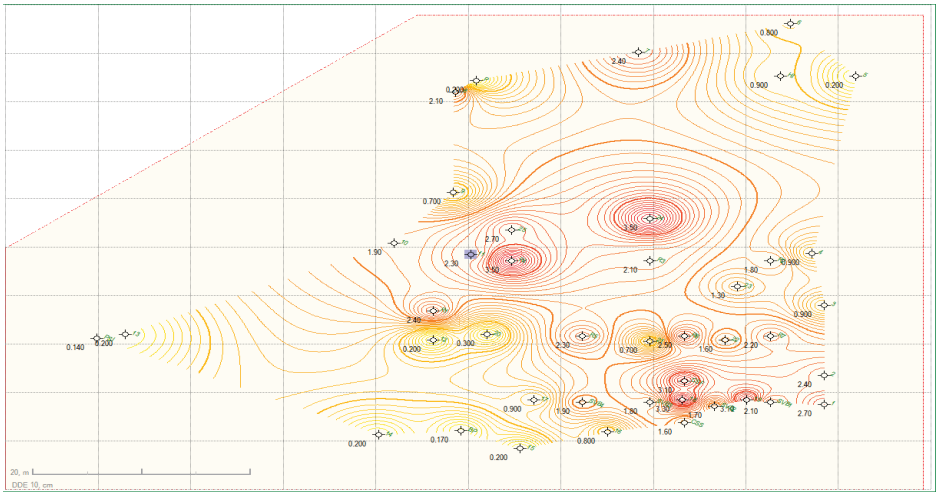

Figure 6. Modeling the dispersion of the Equivalent Dose Rate in contact with the equipment.

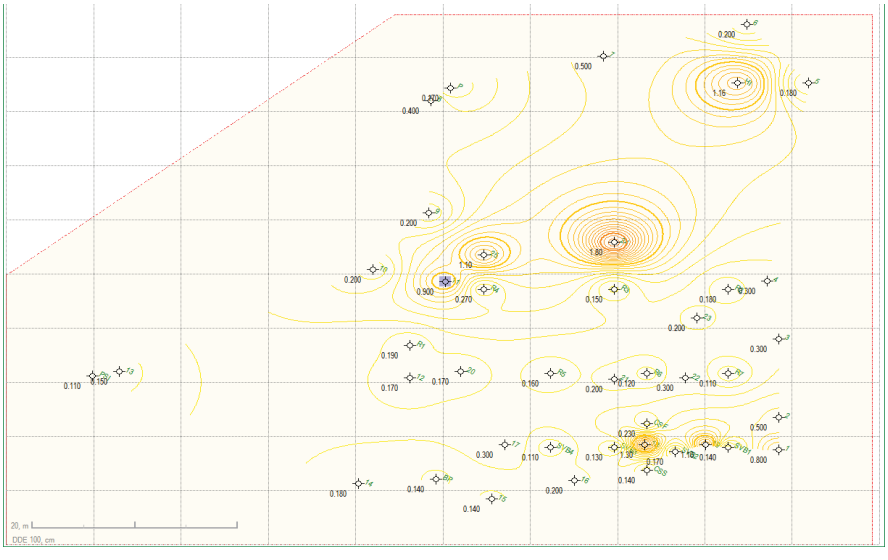

Figure 7. Modeling the dispersion of the Equivalent Dose Rate at 100 cm from the equipment.

Figures 8–13 show the dispersion maps for the concentrations of radionuclides Ra-226, Ac-228 and K-40, within the perimeter of the park (tank farm), for depths of 5 cm and 100 cm, respectively.

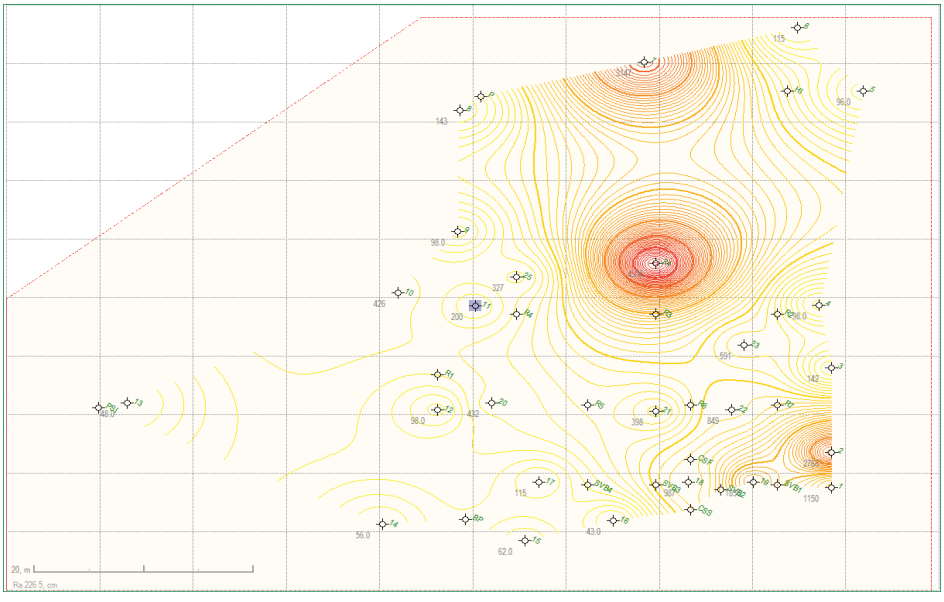

Figure 8. Dispersion map of Ra-226 at a depth of 5 cm.

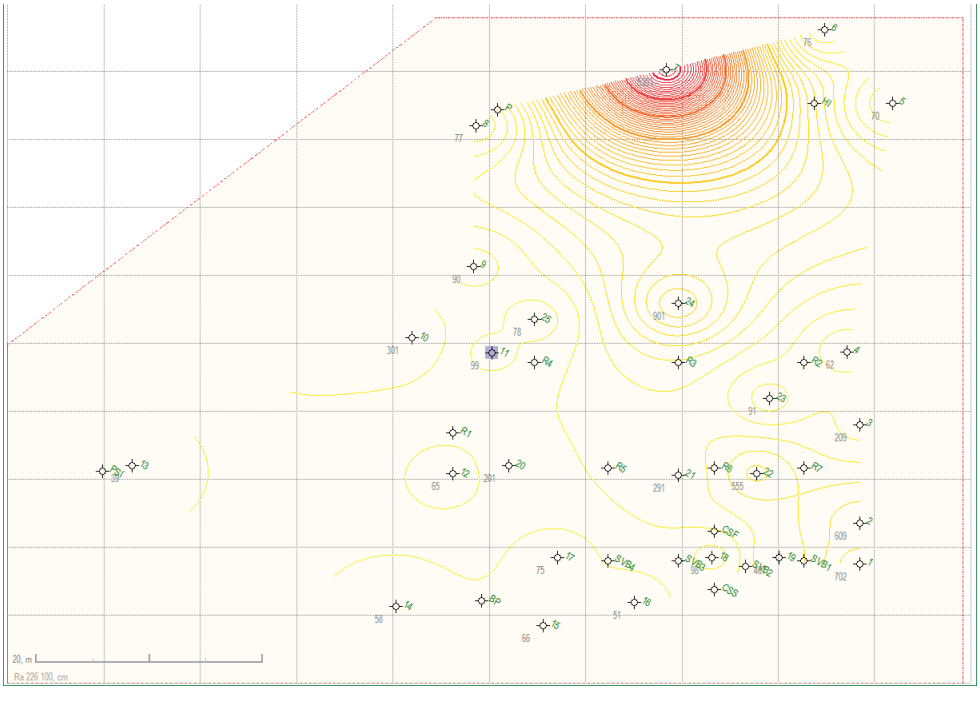

Figure 9. Dispersion map of Ra-226 at a depth of 100 cm.

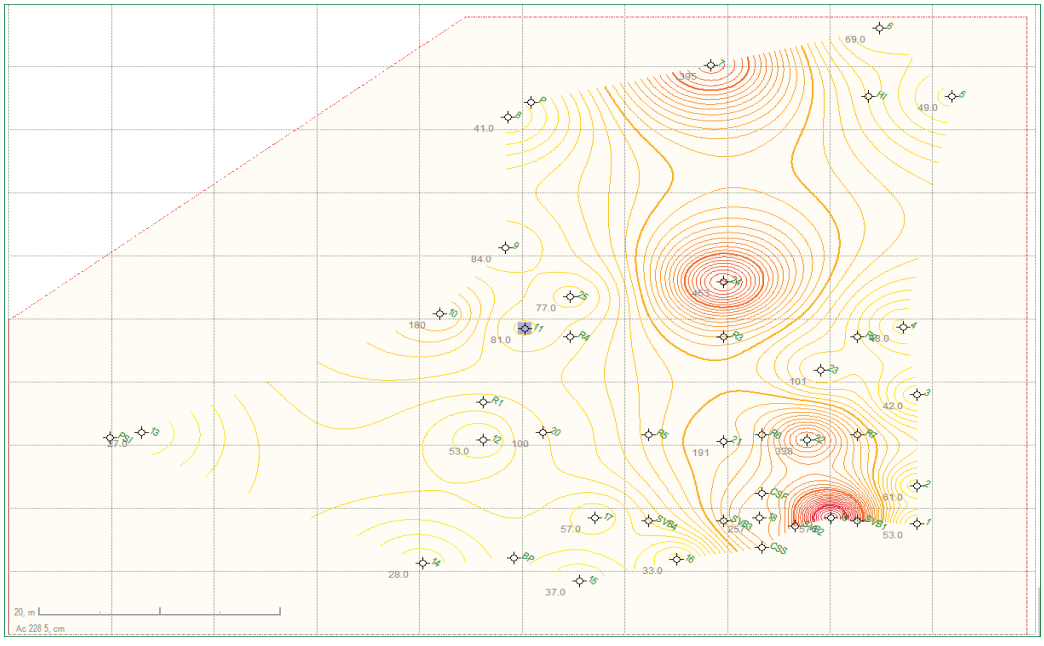

Figure 10. Dispersion map of Ac-228 at a depth of 5 cm.

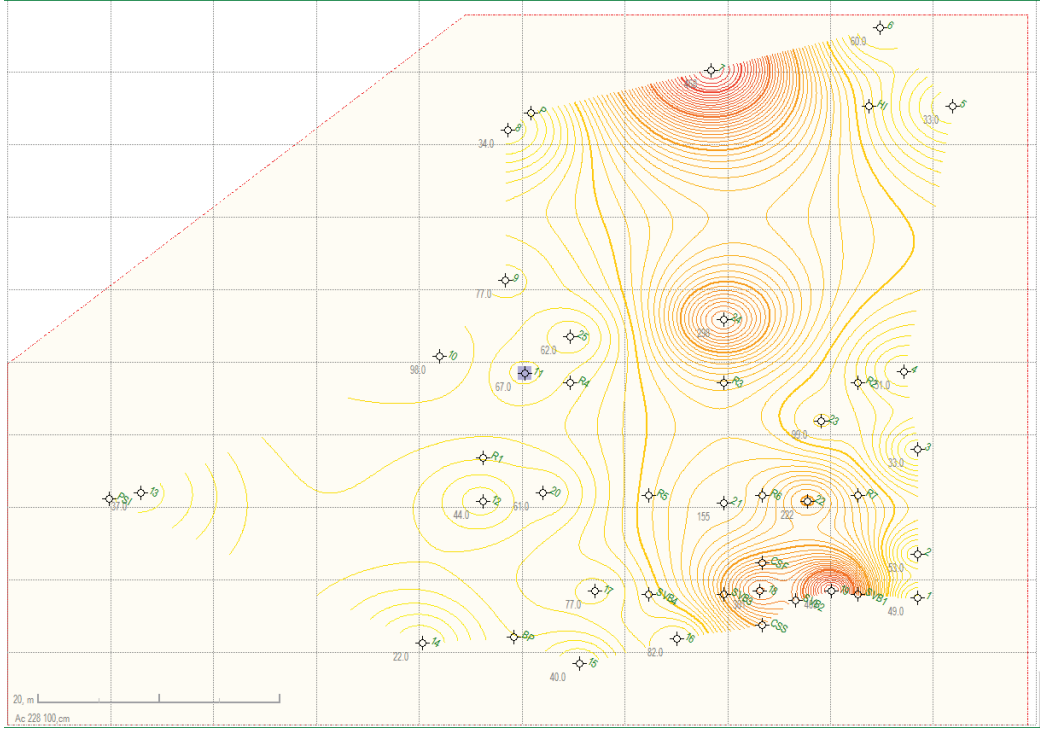

Figure 11. Dispersion map of Ac-228 at a depth of 100 cm.

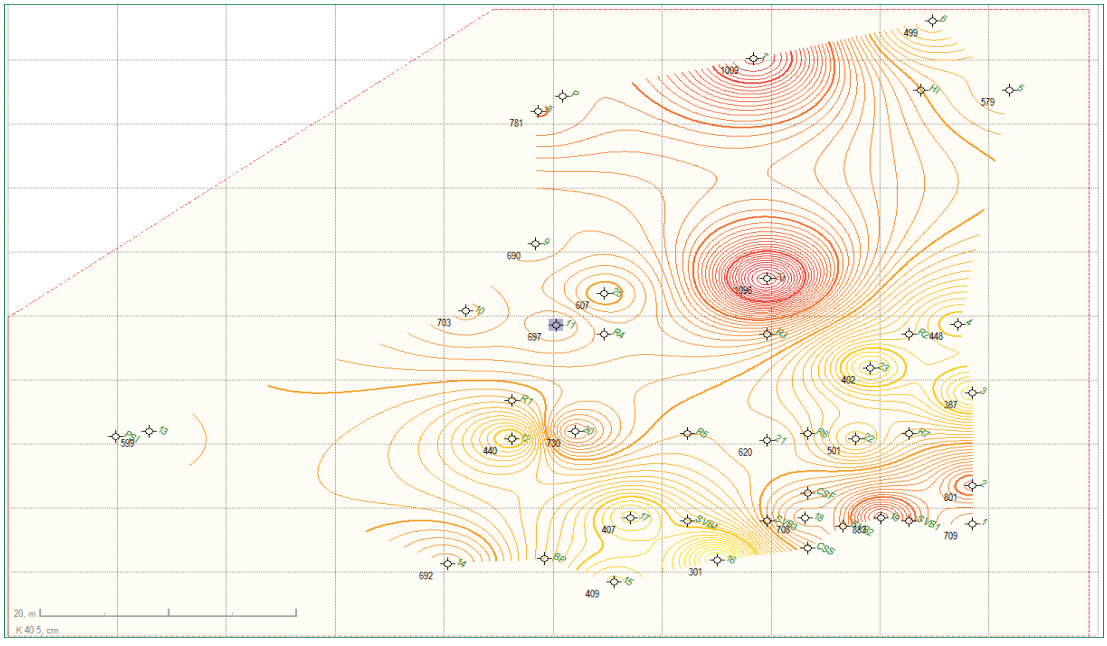

Figure 12. Dispersion map of K-40 at a depth of 5 cm.

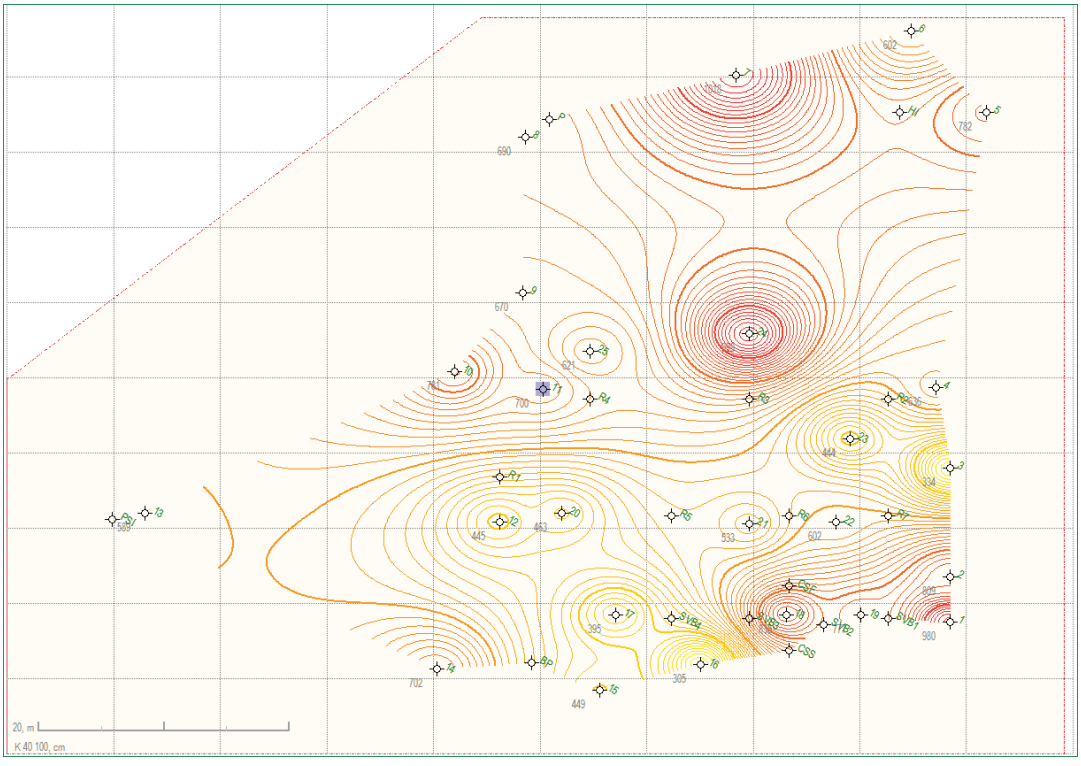

Figure 13. Dispersion map of K-40 at a depth of 100 cm.

7. Discussion

The extraction of crude oil took place between 1960–2000, after which it was abandoned.

No soil decontamination was performed because the concentration in petroleum substances was below the intervention threshold, i.e., below 1000 mg/kg dry matter (the land being a less sensitive area) [7,8].

This soil area is at this moment public property being identified as a playground.

Considering the results of the research carried out in the case study, the following recommendations can be formulated:

- prohibiting public access to the contaminated area until decommissioning and carrying out soil remediation works (Figure 14),
- limiting the access of park employees to the contaminated area and their dosimetric monitoring for a period of at least one year, in order to have a projection on the annual absorbed dose,
- decommissioning of equipment under radiological control and their transport for decontamination, within authorized locations for these types of activities.

As can be seen, the extraction of crude oil entails radioactive pollution.

Analyzing the state of radioactive pollution of the land, we observe the following:

A. For Ra-226, most sampling points have concentrations above the national allowed limit of 76 Bq/kg, except points number 4, 5, 12, 13, 14, 15, 16, and 17.
B. However, all values determined for Ra-226 are at least 399% higher than the natural background (9.76 Bq/kg).
C. For the radionuclide concentration for K-40, the allowed limit (259.09 Bq/kg) is exceeded by at least 118%.
D. The concentration of Ac-228 exceeds the allowed limit (15.05 Bq/kg) by at least 142%.
E. The most visible pollution is in the area of the pump and biphasic separators where there have usually been leaks of gases and liquids into the ground and absorbed by the vegetation (Figure 14).

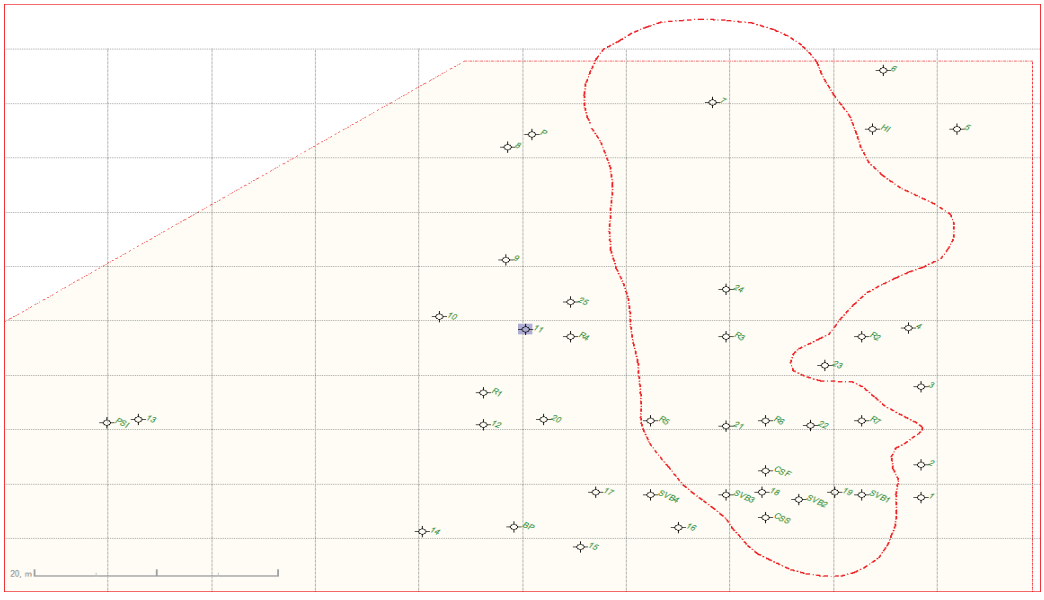

Figure 14. Map of the surface contaminated with radionuclides.

Author Contributions: Conceptualization, S.P. and T.C.; methodology, O.V.S.; software, T.C.; validation, S.P., O.V.S. and A.E.S.; formal analysis, T.C.; investigation, T.C.; resources, T.C.; data curation, T.C.; writing—original draft preparation, T.C.; writing—review and editing, T.C.; visualization, S.P.; supervision, O.V.S.; project administration, T.C.; funding acquisition, T.C. All authors have read and agreed to the published version of the manuscript.

Funding: This research received no external funding. This project was part of the doctoral and postdoctoral research program.

Institutional Review Board Statement: The study was conducted in accordance with the Declaration of Helsinki, and approved by the Ethics Committee of Ovidius University.

Informed Consent Statement: Informed consent was obtained from all subjects involved in the study.

Data Availability Statement: The data contained in this study are original and are part of the environmental protection analysis, without affecting companies, local communities and government authorities. The study is in accordance with the legislation in force, being in accordance with the requirements of the local community and sustainable development policies.

Conflicts of Interest: The authors declare no conflict of interest.

References

1. Council Directive 2013/59/EURATOM of 5 December 2013. Laying Down Basic Safety Standards for Protection against the Dangers Arising from Exposure to Ionising Radiation, and Repealing Directives 89/618/Euratom, 90/641/Euratom, 96/29/Euratom, 97/43/Euratom and 2003/122/Euratom. Available online: https://eur-lex.europa.eu/legal-content/en/ALL/?uri=CELEX%3A31999R2587 (accessed on 22 September 2021).
2. Petrache, Ş. The Environmental Impact of NORM for an Oil and Gas Production Facility. In Proceedings of the 2nd International Colloquium Energy and Environmental Protection, Ploieşti, România, 9–11 November 2016; pp. 20–24.
3. Sharma, P.V. *Environmental and Engineering Geophysics*; Cambridge University Press: Cambridge, UK, 1997; pp. 22–45.
4. International Atomic Energy Agency. *Radiation Protection and the Management of Radioactive Waste in the Oil and Gas Industry*; International Atomic Energy Agency: Vienna, Austria, 2003; pp. 1–30, (Safety reports series), no. 34, STI/PUB/1171; ISBN 92-0-114003–7. ISSN 1020–6450.
5. European Commission. *Current Practice of Dealing with Natural Radioactivity from Oil and Gas Production in EU Member States*; Final Report; European Commission: Brussels, Belgium, 1997; pp. 1–40.
6. Conference of Radiation Control Program Directors, Inc. *E-42 Task Force Report: Review of TENORM in the Oil&Gas Industry*; Conference of Radiation Control Program Directors, Inc.: Frankfort, KY, USA, 2015; pp. 5–50.
7. Petrache, Ş. Problems in well drilling abandonment programs-radioactivity aspects. In Proceedings of the Balkan Mining Congress, Petroşani, România, 20–23 September 2015.
8. Petrache, Ş. Environment Aspects of Oil Exploration and Exploitation Abandonment. Ph.D. Thesis, Oil and Gas University, Ploiesti, România, 2021.
9. Naturally Occurring Radioactive Material (NORM VI). In Proceedings of the Sixth International Symposium on Naturally Occurring Radioactive Material, Organized by The Hassan II University of Mohammedia and the Cadi Ayyad University of Marrakesh in Cooperation with the International Atomic Energy Agency, Marrakesh, Morocco, 22–26 March 2010; pp. 103–109.
10. Naţional Comision of Radiaoctivity Worker. *NSR-01 Norms to Radioactivity Measurenment*; Naţional Comision of Radiaoctivity Worker: Bucureşti, Romania, 2000; pp. 20–60.
11. International Association of Oil&Gas Producers. *Report 412: Managing Naturally Occuring Radioactive Material (NORM) in the Oil and Gas Industry*; International Association of Oil&Gas Producers: London, UK, 2016; pp. 100–200.
12. Environment Agency. *The Radioactively Contaminated Land Exposure Assessment Methodology—Technical Report*; CLR-14 Version 1.2 May 2011; Environment Agency: London, UK, 2014; pp. 1–40. Available online: https://assets.publishing.service.gov.uk/government/uploads/system/uploads/attachment_data/file/316279/Radioactively_Contaminated_Land_Exposure_Assessment_Methodology_Technical_Report.pdf (accessed on 22 September 2021).

processes

MDPI

Review

Imaging Method by Matrix-Assisted Laser Desorption/Ionization Mass Spectrometry (MALDI-MS) for Tissue or Tumor: *A Mini Review*

Jiawen Wu [1], Ze Rong [2], Peng Xiao [3] and Yuanzhe Li [4,*]

[1] Department of Chemistry, Queen's University, Kingston, ON K7L 3N6, Canada; 15524244086@163.com
[2] School of Mathematical and Physical Sciences, University College London, London WC1E 6BT, UK; r_ongze@126.com
[3] Faculty of Public Health, Mahidol University, Nakhon Pathom 73170, Thailand; eric2015aei@gmail.com
[4] School of Materials Science & Engineering, Nanyang Technological University, Singapore 639798, Singapore
* Correspondence: yuanzhe001@e.ntu.edu.sg

Abstract: Matrix-assisted laser desorption/ionization mass spectrometry (MALDI-MS) is an advanced technique that uses minimum fragmented ions from complex molecules for mass spectrometry (MS) analysis (tissue profiling by mass spectrometry). It is able to analyze spatially resolved tissue or tumor sections at the molecular level. It has become a valuable tool for tumor and tissue imaging, due to its ease of operation and high mass resolution, but it still has vast room for development in the instrumentation of larger proteins in some tissues. In this review, we focus on the main components of MALDI-MS instrumentation, sample handling and processing, the working principle of MALDI-MS, and its applications in diagnostic and prognostic assessments, tumor removal and drug development. Although it is less effective at detecting larger proteins in some tissues, it still shows huge potential because of its advancements in instrumentation and processing protocols. This article may benefit those who have interests in MALDI-MS for tissue or tumor imaging.

Keywords: matrix-assisted laser desorption/ionization mass spectrometry (MALDI-MS); tissue or tumor imaging; instrumentation; processing protocol; working principle

Citation: Wu, J.; Rong, Z.; Xiao, P.; Li, Y. Imaging Method by Matrix-Assisted Laser Desorption/Ionization Mass Spectrometry (MALDI-MS) for Tissue or Tumor: *A Mini Review*. *Processes* **2022**, *10*, 388. https://doi.org/10.3390/pr10020388

Academic Editors: Avelino Núñez-Delgado, Zhien Zhang, Elza Bontempi, Mario Coccia, Marco Race and Yaoyu Zhou

Received: 24 January 2022
Accepted: 15 February 2022
Published: 17 February 2022

1. Introduction

Matrix-assisted laser desorption/ionization (MALDI) is an ionization process that utilizes a laser irradiation absorbing matrix to produce minimum fragmented ions from complex molecules for mass spectrometry (MS) analysis (tissue profiling by mass spectrometry). In 1994, the first use of MALDI-MS in an imaging context, for matrix crystals containing the neuropeptide P, was reported by Spengler et al. [1] (Small molecule MALDI MS imaging: Current technologies and future challenges). With the development of MALDI-MS, its application areas have rapidly expanded. MALDI-MS is a powerful analytical technique that combines the high sensitivity and selectivity of mass spectrometry with the spatial distribution data of molecules in tumors or tissues [2]. It is target free; therefore, it does not need to choose a certain protein analyte ahead of time. Although biased detections may occur sometimes, it is fully multiplex, and it measures all ions from a tissue sample simultaneously. Therefore, using MALDI-MS, protein localization can be determined, with molecular specificity, directly from tissue parts [1]. Furthermore, since the MALDI laser does not ablate any of the tissue, and molecules are desorbed from the surface, cellular and molecular integrity is maintained, with minimal effects on most of the cells. Oppenheimer's report provides an overview of the workflow of the analysis, providing a detailed introduction of the instrumentation and applications to clinical oncology and pharmaceutical development [3]. As a general outline, the analysis uses a matrix that absorbs energy at the irradiating laser's wavelength. The sample molecule is combined

with the matrix, then dried on an electrically conductive glass slide. Matrix–analyte co-crystals develop during the drying process. Such crystals are then exposed to UV laser light, allowing the sample molecule to desorb and ionize. Then, in a time-of-flight (TOF) mass analyzer, a mass-to-charge (m/z) ratio is generated [4]. Finally, a 2D ion intensity map can be constructed based on the signals obtained at x, y coordinates. It should be noted that, due to the limited coverage of various aspects, such as data analysis techniques and other types of detectors, the TOF mass analyzer within this paper only represents one representative example of MALDI imaging.

This article overviews the sample preparation for MALDI-MS, the three main components, and the principle of MALDI-MS for tissue or tumor imaging, and explores its limitations and future applications in diagnostic and prognostic assessments, tumor removal and drug development.

2. Sample Handling and Processing

2.1. Tissue Storage

After a tissue or tumor sample is extracted, it needs to be frozen immediately to maintain its morphology and prevent protein degradation, which is essential to keep the sample in a native condition. Next, aluminum foil is used to wrap the tissue biopsy loosely. To store the sample for a longer time, the temperature should be kept at −80 °C or lower [3], which can preserve tissue or tumor samples in a native state for over a year. In addition to this method, the tissue can also be preserved by submerging it in formalin or a variety of alcohols [3]. The tissue is typically preserved as paraffin blocks. This method is called fixation. Freshly frozen and FFPE tissues are commonly used for MALDI imaging. [4].

2.2. Sectioning

The next process is sectioning the tissue specimens. For most applications, the tissue is cut into 5–20 µm-thick slices at −15 °C. The thickness and cutting temperature are based on the type of tissue. It is crucial to use an embedding medium to keep the specimen in place on a cryostat head during the cutting process [5].

2.3. Mounting

After sectioning, the tissue section needs to be mounted. The tissue sections should be placed on a cooled target plate that has a similar temperature to the previously sliced section. Next, the tissue section can be steadily warmed by placing a hand under the plate. The surface needs to be electrically conductive to allow for the high voltage potential from the ion source of MALDI-MS. Indium tin oxide (ITO)-coated glass slides are very suitable for this kind of analysis [6].

2.4. Pretreatment of Samples

Sample pretreatments are useful for improving the sensitivity of the interest analytes prior to matrix implementation. The pretreatment measures include the removal of impurities, on-tissue digestion, and on-tissue derivatization. Salts and fats affect the analysis of proteins and peptides [7]. The normal protocol requires a 30 s wash in 70% ethanol, a 30 s wash in 90% ethanol, and a final 30 s wash in 95% ethanol. Then, the sample is dried. This washing technique will remove all impurities from the sliced samples, without disrupting the texture of the tissues [8]. For on-tissue digestion, this washing technique is especially beneficial for the study of the samples because the peptide fragments need to be released from the cross-linked tissue [8]. During this procedure, trypsin solution is added to the samples; wet samples are kept in a humid environment at room temperature, or 37–50 °C, to preserve the surface solution and provide adequate time for the peptide fragments to be released [4,9]. For on-tissue derivatization, the washing technique is performed by manually spraying TCDI on the tissue sections. Then, the matrix is added to the tissue section by sublimation [8].

2.5. Matrix Deposition

A chemical matrix can absorb the laser irradiation and transports the sample to a gas phase, facilitating the mechanism of ionization [10]. 2,5-dihydroxybenzoic acid (DHB) [11], α-cyano-4-hydroxycinnamic acid (CHCA) [12], and 3,5-dimethoxy-4-hydroxycinnamic acid (SA, sinapinic acid) [13] are three commonly used matrices. There are two methods to apply matrices. One method is continuous manual matrix coating, and the other method is discrete matrix coating, utilizing automatic matrix spotting tools, such as robotic sprayers. For manual matrix deposition, droplets as tiny as 200 nL can be deposited onto the sections. Normally, the sections need to be spotted twice, in order to enhance the crystal density. The MALDI crystals will form after the solvent has evaporated completely [8].

2.6. Staining

Staining is an optional step; however, it is necessary to identify the interested parts of the tissues. It can be performed before the application of the matrix to the tissue [5]. However, staining procedures have variables that may alter the molecular composition of the tissues or tumors. Alternatively, section staining can be performed after MALDI−MS analysis [6]. Hematoxylin and eosin (H&E) staining is a common protocol to color sections. Prior to H&E staining, the matrices must be removed from the sections by submerging the sections in a 70% ethanol solution, as most matrices are soluble in a diluted ethanol solution. After the matrices have been removed, the sections need to be dehydrated in graded ethanol. Finally, the sections can be stained [14,15].

3. Instrumentation

Most MALDI-MS imaging work is performed by a time-of-flight (TOF) instrument because the high mass-to-charge (m/z) ratio values of this type of mass spectrometer are suitable for large molecules, such as proteins. Although MALDI-MS instruments have been commercialized now, improvements in these instruments are still in progress. Zavalin et al. demonstrated a new transmission geometry MALDI source, and the capability of this system was demonstrated by imaging an axon fiber at a step size of 2.5 μm. Generally, a mass spectrometer has the following three main components: the ion source, the mass analyzer and the detector. The ion source is used for the creation and fragmentation of ions. The analyzer is used to separate the ions, and there is usually a reflectron to improve the mass resolving power of the analyzer. Ions are separated by their mass-to-charge ratio, spatially or in time. The detector is used to measure the quantities of separated ions.

3.1. Ion Source (MALDI)

Matrix-assisted laser desorption/ionization (MALDI) is an ion source that utilizes a laser irradiation absorbing matrix to produce minimum fragmented ions from complex molecules [1]. Firstly, the emission of a UV laser beam to the matrix–analyte mixture leads to desorption and ablation of the top layer of the matrix. The matrix is ionized by adding a proton, or losing a proton, during the absorption of the laser radiation. After the matrix is desorbed, ionized and ablated, a hot plume that includes neutral molecules and matrix ions, and protonated and deprotonated matrix molecules, is generated. Secondly, the analyte is ionized by transferring the charges from the matrix. Quasimolecular ions are produced after this step. To date, MALDI ion sources can be used in a high vacuum environment or under atmospheric pressure [16]. A general description of how the analytes are ionized is shown in Figure 1 [17].

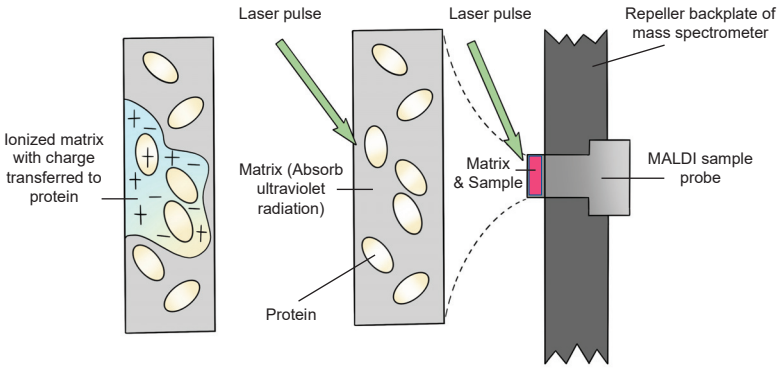

Figure 1. Schematic diagram of the general procedure of ionization.

3.2. Mass Analyzer

The pulsed nature of laser desorption renders MALDI ion sources ideal for time-of-flight (TOF) analyzers [18]. After the ions are produced by the ion source, they move to the mass analyzer, which separates the ions. At approximately 3000 to 20,000 times per second, 20,000 V is added to the backplate to accelerate the ions to the drift region from the source region. If the kinetic energies of the ions are the same when they are ejected from the source, on the TOF mass spectrometer, they can be observed as just a straight tube between the source and the detector on two sides. In this situation, ions ejected from the source transmit to the detector, according to their mass. The lighter ions move quicker and vice versa. However, normally, the ions do not have identical kinetic energies because the ions formed next to the backplate are accelerated by a larger voltage, and will gain more kinetic energy, than those positioned closer to the grid. In addition, the kinetic energies are distributed unequally among the ions [17]. As a result, ions may enter the detector at the same time, though they have different m/z ratios. To overcome this problem, a reflectron (or ion mirror) can be added to the mass analyzer. The design of the TOF mass spectrometer is shown in Figure 2 [18]. The reflectron is a sequence of hollow rings, kept at a progressive positive potential, and a grid whose potential is more positive than the accelerated potential on the source backplate. When the ions enter the reflectron region, they are decelerated, stopped and reflected out to the left. Faster ions, with more kinetic energy, migrate deeper through the reflectrons and vice versa. Then, all ions with the same mass enter the grid at the same moment, even though their kinetic energies are not identical.

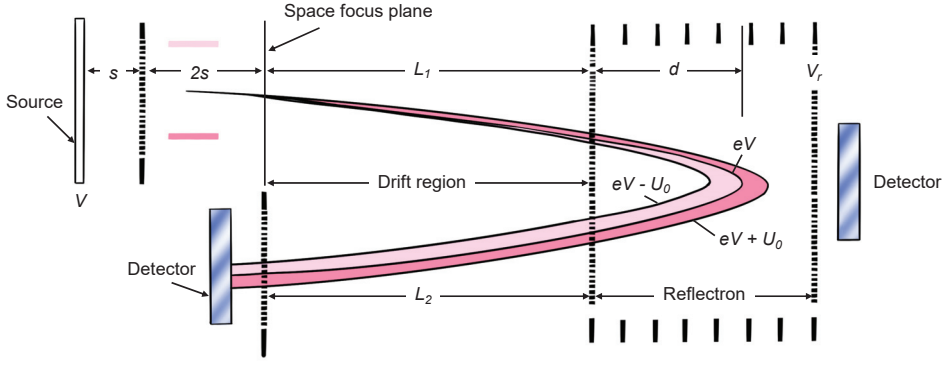

Figure 2. The schematic diagram of TOF mass spectrometer including "reflectron" [18].

3.3. Detector

The detector is the last part of a mass spectrometer. It plays a crucial role in the mass spectrometer. It tracks and records the induced charges as the ions move through, or reach, a surface [16]. There are many kinds of detectors, such as the electron multiplier, Faraday cup, photographic plate, scintillation counter and channel electron multiplier, etc. [19]. An effective detector should have high amplification, a fast time response, low noise, a high collection capacity, low expense, low response spread, the same response for all masses, a wide dynamic range, long-term reliability, and the ability to be mounted outside the vacuum [20,21]. There is not a certain type of detector that is required to complete tumor or tissue imaging using MALDI-MS. All these detectors have their own advantages and drawbacks. Finally, a spectrum of the signal intensity of the ions vs. the mass-to-charge ratio is displayed by the detector [22,23].

4. Principle of MALDI-MS for Tissue or Tumor Imaging

The general workflow of how MALDI-MS works to produce images of tumors and tissue is shown in Figure 3 [24]. Firstly, a sliced tissue or tumor is pretreated, and a matrix is needed to cover it. Then, the mass spectrometer analyzes the tissue specimen (with a spatial resolution varying from approximately 200 μm to 20 μm), producing a mass spectrum for each measurement spot.

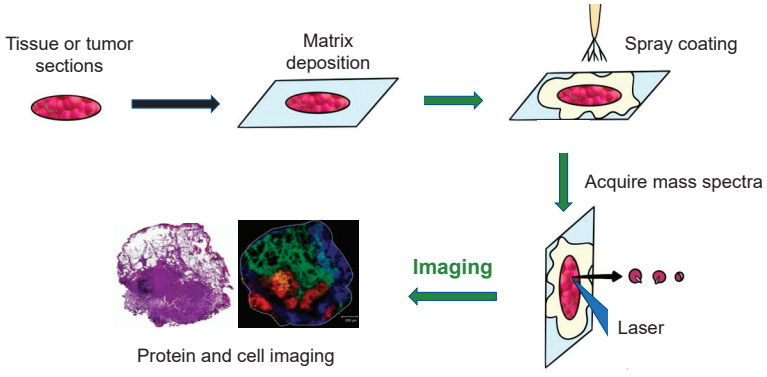

Figure 3. The principal workflow of the MALDI imaging and profiling experiments [24].

An Ultraflex II MALDI-TOF-MS (Bruker Daltonics, Billerica, MA, USA), equipped with a SmartBeam TM laser, can be used for tissue or tumor imaging. Using this machine, a total of 400 laser shots are obtained for each matrix spot, in increments of 50 shots, starting at the middle of each spot and randomly rastering at various locations inside the spot. An evaluation of the relative coordinates of each matrix spot from the optical picture of the MALDI plate is required for automated acquisition of the profile. Then, the x, y coordinates of each spot are written on a file in the native target geometry of the mass spectrometer control program. Three positions from the outer corners of the array are chosen for final alignment of the plate [3]. Finally, plotting the intensities of each signal at its x, y coordinates can create a two-dimensional morphological image of the ion profiles. Since the sliced tissue or tumor can be stained, the observed mass signals can then be observed as color intensity maps and can be used to investigate molecules in certain cell types. Using these colored signals, the distribution of different molecules in the tissues can be visualized [8].

5. Limitations and Future Applications

MALDI-MS analyses are successful for most tumors and tissues. Due to the limitation of the article length, the protocol described above is only suitable for peptides (proteins), but is not suitable for small molecules. Similarly, the method that describes rinsing with

ethanol and adding trypsin are optional for proteins targeted by MALDI-MS, but not for small molecules. Moreover, it is less effective at detecting larger proteins in some tissues because the mass range of such a methodology is limited by laser ionization and ablation processes, which lead to the fragmentation of larger molecules, such as cytokines, growth factors, enzymes and receptors that have molecular weights exceeding 25 kDa, and because MALDI-MS is vulnerable to detector saturation when studying complicated mixtures. This limitation could be overcome by using a high mass detector, but this would generate a significant chemical background, which would affect any losses of sensitivity. Hence, a high mass detector that can withstand the high chemical background of MALDI-MS is required [22]. In addition, due to the limitations of this mini-review, only limited coverage of various aspects, such as data analysis techniques and detector coverage, is included within this paper. Such examples may only indicate the distribution of three molecules, rather than illustrating how to use the technique to diagnose via tumor subtyping.

5.1. Diagnostic and Prognostic Assessment in Clinical Pathology

Recently, MALDI-MS has been applied to cancer research, including human non-small-cell lung tumors, gliomas, breast cancer and ovarian tumors. The general method employed by these studies is to compare the mass spectral characteristics (m/z peaks) with a range of patient data, to classify specific molecular alterations related to disease progression [21]. The spatial proteomic characterization of tissue and tumor recognition contributes to better diagnoses and individual predictive trends of therapy response [23].

Generally, 1 μL of extracted serum peptide may be mixed with 1 μL of saturated α-cyano-4-hydroxycinnamic acid matrix (dissolved with 0.1% trifluoroacetic acid, 50% acetonitrile), spotted on a target plate and dried at room temperature; the target plate is placed in the mass spectrometer; the instrument is calibrated with standards, and then the standards are detected to obtain a mass-to-charge ratio (m/z) peptide peak, consisting of different mass-to-charge ratios (m/z). The mass spectra of the peptide peaks with different mass-to-charge ratios (m/z) are then obtained. In order to avoid system errors and human errors, standards (peptide mixtures) are used before each specimen is tested, and the specimens are only tested when the results are consistent with the composition of the standards, indicating that the test system is working properly, thus ensuring reliable and reproducible results.

One segment example of lung cancer tissue, displaying various areas identified by the distinct molecular content of the tissue, is shown in the bottom right of Figure 3 [24]. The left side of the figure shows the H&E staining of the segment after MALDI-MS analysis. The right side of the figure shows a fibrotic region of the tumor cells (m/z = 1117.1, yellow), a tumor region (m/z = 1822.5, red), a non-tumor region (m/z = 1530.4, blue), and a peritumoral inflammatory field (m/z = 1429.1, green). This example illustrates how to use the technique to diagnose disease.

5.2. Tumor Removal

In clinical oncology, completely removing tumors is crucial. Research shows that some of the tumor's molecular features are represented in histologically healthy tissue neighboring the tumors, due to molecular modifications before phenotypic changes. MALDI-MS can aid in the interpretation of alterations in tumors and neighboring healthy tissues' environments, as well as provide an approximation of how far these changes extend beyond the histologically defined margins [25]. As a result, the tumors can be resected completely.

5.3. Drug Development

MALDI-MS can be used to investigate the distribution of drugs in human and animal tumor tissues [26]. This technique has improved selectivity and sensitivity, which is ideal for analyzing how effective drugs are and for improving drug design. One study used MALDI-MS to deliver paclitaxel to a mouse with a tumor. Paclitaxel (PTX) was combined with micelle (NK105) and delivered to the tumor tissue of the mouse. Using MALDI-MS,

this section was compared with the tumor section treated with PTX alone, as well as the untreated mouse. The PTX concentration delivered from NK105 was significantly higher than the free PTX and untreated tumor tissue, meaning that the anticancer efficacy of NK105 is higher than PTX alone [27].

6. Conclusions

MALDI-MS is a powerful analytical technique that has become a valuable tool for tumor and tissue imaging, due to its ease of operation and high mass resolution, but it still has vast room for development in instrumentation for larger proteins in some tissues. Overall, the potential of MALDI-MS for tumor and tissue imaging is high, and advancements in instrumentation and processing protocols can offer new developments and observations for molecular processes, including for health and disease.

Author Contributions: Conceptualization, J.W. and Y.L.; methodology, J.W. and Z.R.; software, J.W. and Y.L.; validation, J.W., Z.R. and P.X.; formal analysis, Y.L.; investigation, Z.R. and P.X.; resources, J.W. and Y.L.; data curation, J.W. and Y.L.; writing—original draft preparation, J.W., Z.R. and P.X.; writing—review and editing, Z.R. and Y.L.; visualization, J.W. and Y.L.; supervision, Y.L.; project administration, Y.L.; funding acquisition, Y.L. All authors have read and agreed to the published version of the manuscript.

Funding: This research received no external funding. And the APC was funded by Wu, J., Rong, Z. and Li, Y.

Institutional Review Board Statement: Not applicable.

Informed Consent Statement: Not applicable.

Data Availability Statement: All data related to this study are publicly available upon reasonable request to the corresponding author.

Conflicts of Interest: The authors declare no conflict of interest.

References

1. Gessel, M.; Norris, J.; Caprioli, R.M. MALDI imaging mass spectrometry: Spatial molecular analysis to enable a new age of discovery. *J. Proteom.* **2014**, *107*, 71–82. [CrossRef] [PubMed]
2. Hillenkamp, F.; Karas, M.; Beavis, R.C.; Chait, B.T. Matrix-assisted laser desorption/ionization mass spectrometry of biopolymers. *Anal. Chem.* **1991**, *63*, 1193–1203. [CrossRef]
3. Oppenheimer, S.R.; Mi, D.; Sanders, M.E.; Caprioli, R.M. Molecular Analysis of Tumor Margins by MALDI Mass Spectrometry in Renal Carcinoma. *J. Proteome Res.* **2010**, *9*, 2182–2190. [CrossRef] [PubMed]
4. Du, Y.; Du, Y.; Cui, M.; Liu, Z. Characterization of the Noncovalent Interactions between Lysozyme and Panaxadiol Glycosides by Intensity-Fading—Matrix-Assisted Laser Desorption Ionization—Mass Spectrometry (IF-MALDI-MS). *Anal. Lett.* **2021**, *54*, 2387–2394. [CrossRef]
5. Chaurand, P.; Latham, J.C.; Lane, K.B.; Mobley, J.; Polosukhin, V.V.; Wirth, P.S.; Nanney, L.B.; Caprioli, R.M. Imaging Mass Spectrometry of Intact Proteins from Alcohol-Preserved Tissue Specimens: Bypassing Formalin Fixation. *J. Proteome Res.* **2008**, *7*, 3543–3555. [CrossRef]
6. Treu, A.; Römpp, A. Matrix ions as internal standard for high mass accuracy matrix-assisted laser desorption/ionization mass spectrometry imaging. *Rapid Commun. Mass Spectrom.* **2021**, *35*, e9110. [CrossRef]
7. Wang, C.; Bi, H.; Xie, J. Visualization of the Distance among Fishes by MALDI MS for Rapid Determination of the Taxonomic Status of Fish Fillets. *J. Agric. Food Chem.* **2020**, *68*, 8438–8446. [CrossRef]
8. Norris, J.; Caprioli, R.M. Analysis of Tissue Specimens by Matrix-Assisted Laser Desorption/Ionization Imaging Mass Spectrometry in Biological and Clinical Research. *Chem. Rev.* **2013**, *113*, 2309–2342. [CrossRef]
9. Lemaire, R.; Desmons, A.; Tabet, J.C.; Day, R.; Salzet, M.; Fournier, I. Solid Ionic Matrixes for Direct Tissue Analysis and MALDI Imaging. *Anal. Chem.* **2006**, *78*, 809–819. [CrossRef]
10. Karas, M.; Krüger, R. Ion Formation in MALDI: The Cluster Ionization Mechanism. *Chem. Rev.* **2003**, *103*, 427–440. [CrossRef]
11. Tsuchida, S.; Umemura, H.; Nakayama, T. Current Status of Matrix-Assisted Laser Desorption/Ionization–Time-of-Flight Mass Spectrometry (MALDI-TOF MS) in Clinical Diagnostic Microbiology. *Molecules* **2020**, *25*, 4775. [CrossRef] [PubMed]
12. Beavis, R.C.; Chaudhary, T.; Chait, B.T. α-Cyano-4-hydroxycinnamic acid as a matrix for matrixassisted laser desorption mass spectrometry. *Org. Mass Spectrom.* **1992**, *27*, 156–158. [CrossRef]
13. Beavis, R.C.; Chait, B.T.; Standing, K.G. Matrix-assisted laser-desorption mass spectrometry using 355 nm radiation. *Rapid Commun. Mass Spectrom.* **1989**, *3*, 436–439. [CrossRef] [PubMed]

14. Zhang, X.; Wu, C.; Tan, W. Brain Lipid Dynamics in Amyloid Precursor Protein/Presenilin 1 Mouse Model of Early Alzheimer's Disease by Desorption Electrospray Ionization and Matrix Assisted Laser Desorption Ionization–Mass Spectrometry Imaging Techniques. *J. Proteome Res.* **2021**, *20*, 2643–2650. [CrossRef] [PubMed]
15. Chaurand, P.; Norris, J.L.; Cornett, D.S.; Mobley, J.A.; Caprioli, R.M. New Developments in Profiling and Imaging of Proteins from Tissue Sections by MALDI Mass Spectrometry. *J. Proteome Res.* **2006**, *5*, 2889–2900. [CrossRef]
16. Han, X. *Lipidomics: Comprehensive Mass Spectrometry of Lipids*; Wiley: Hoboken, NJ, USA, 2016.
17. Harvey, J. Analysis of carbohydrates and glycoconjugates by matrix-assisted laser desorption/ionization mass spectrometry: An update for 2013–2014. *Mass Spectrom. Rev.* **2018**, *37*, 353–491. [CrossRef] [PubMed]
18. Lan, J.; Zenobi, R. Characterizing the iron loading pattern of ferritin using high-mass matrix-assisted laser desorption ionization mass spectrometry. *Rapid Commun. Mass Spectrom.* **2019**, *33*, 1855–1860. [CrossRef] [PubMed]
19. Mamyrin, B.A.; Karataev, V.I.; Shmikk, D.V.; Zagulin, V.A. Mass reflection: A new nonmagnetic time-of-flight high resolution mass- spectrometer. *Sov. Phys. Tech. JETP* **1973**, *37*, 5.
20. Khatri, N.; Gupta, A.; Taneja, R.; Bilandi, A.; Beniwal, P. A Review on Mass Spectrometry Detectors. *Int. Res. J. Pharm.* **2012**, *3*, 33–42.
21. Thurner, G.C.; Debbage, P. Molecular imaging with nanoparticles: The dwarf actors revisited 10 years later. *Histochem. Cell Biol.* **2018**, *150*, 733–794. [CrossRef]
22. Yang, J.; Caprioli, R.M. Matrix pre-coated targets for high throughput MALDI imaging of proteins. *Biol. Mass Spectrom.* **2014**, *49*, 417–422. [CrossRef] [PubMed]
23. Schaepe, K.; Bhandari, D.R.; Werner, J.; Henss, A.; Pirkl, A.; Kleine-Boymann, M.; Rohnke, M.; Wenisch, S.; Neumann, E.; Janek, J.; et al. Imaging of Lipids in Native Human Bone Sections Using TOF–Secondary Ion Mass Spectrometry, Atmospheric Pressure Scanning Microprobe Matrix-Assisted Laser Desorption/Ionization Orbitrap Mass Spectrometry, and Orbitrap–Secondary Ion Mass Spectrometry. *Anal. Chem.* **2018**, *90*, 8856–8864. [CrossRef] [PubMed]
24. Balluff, B.; Schöne, C.; Höfler, H.; Walch, A. MALDI imaging mass spectrometry for direct tissue analysis: Technological advancements and recent applications. *Histochem. Cell Biol.* **2011**, *136*, 227–244. [CrossRef] [PubMed]
25. Wu, N.; Jiao, L.; Bütikofer, M.; Zeng, Z.; Zenobi, R. High-Mass Matrix-Assisted Laser Desorption/Ionization Mass Spectrometry for Absolute Quantitation of Noncovalent Protein–Protein Binding Interactions. *Anal. Chem.* **2021**, *93*, 10982–10989. [CrossRef]
26. Römpp, A.; Spengler, B. Mass spectrometry imaging with high resolution in mass and space. *Histochem. Cell Biol.* **2013**, *139*, 759–783. [CrossRef]
27. Yasunaga, M.; Furuta, M.; Ogata, K.; Koga, Y.; Yamamoto, Y.; Takigahira, M.; Matsumura, Y. The significance of microscopic mass spectrometry with high resolution in the visualisation of drug distribution. *Sci. Rep.* **2013**, *3*, 3050. [CrossRef]

applied sciences

MDPI

Article

The Effect of Sample Preparation and Measurement Techniques on Heavy Metals Concentrations in Soil: Case Study from Kraków, Poland, Europe

Agnieszka Operacz [1], Adrianna Bigaj [2,*], Karolina Hap [1] and Tomasz Kotowski [1]

[1] Department of Sanitary Engineering and Water Management, Faculty of Environmental Engineering and Geodesy, University of Agriculture in Kraków, 31-120 Krakow, Poland; agnieszka.operacz@urk.edu.pl (A.O.); karolina.hap@urk.edu.pl (K.H.); tomasz.kotowski@urk.edu.pl (T.K.)

[2] Department of Fuel Technology, Faculty of Energy and Fuels, AGH University of Science and Technology in Kraków, 30-059 Krakow, Poland

* Correspondence: adwojcik@agh.edu.pl

Abstract: Accurate and reliable laboratory results are an extremely important and integral part of conducting scientific research. Many factors influence the results obtained, including the type of determination method, accuracy and precision of measurements, and laboratory equipment used for the tests. This paper presents the results of measurements of heavy metal concentration in soil using two methods for adding soil components into solution and different laboratory methods and types of measuring equipment. The first method used was hot digestion of soil samples with a mixture of concentrated HNO_3 and $HClO_4$, after prior ashing of organic matter (IUNG method). The second method was a two-stage decomposition, where soil samples were hot digested, initially with oxidizing acid (HNO_3) and subsequently with non-oxidizing acid (HF) (two-stage decomposition). The concentrations of selected heavy metals (Cr, Cu, Fe, Mn, Ni, Pb and Zn) were determined in solutions obtained by both digestion methods. The solutions obtained from soil decomposition were determined twice using atomic absorption spectrometry (AAS) and inductively coupled plasma mass spectrometry (ICP MS) methods in different laboratories using different types of spectrometers. In most cases, the measured concentrations of heavy metals are the highest for the two-stage solution samples and the measurements of their concentrations carried out using ICP. The exceptions are the measurements of Cu and Ni concentrations. In the case of Cu, lack of significant differentiation in concentrations of this metal may result from different forms of occurrence of Cu in soil than in the case of other metals. For Ni, however, a reversal of the trends seen for the other metals is observed and the type of spectrometer used for measurements is important. There may be an interference of the spectrometric spectrum of Ni with the spectra of the other determined metals. However, this is not clear at the present stage of the study. In conclusion, the results of this study indicate that the choice of soil sample preparation and the type of spectrometer used for measurements can, in many cases, determine the value of laboratory results, even if it is in an expected range of standard material. Research of published papers proved that most of them show only results based on one selected course of methodology without comparison with others. The novelty of the paper is the comparison of the measurements of heavy metal concentration in soil using two methods for adding soil components into solution and different laboratory methods and types of measuring equipment. Additionally, the article includes a discussion of the importance of methodology. We believe that the conclusions may help to better understand how sample preparation and measurement methods applied may influence the results obtained.

Keywords: heavy metals; soil; determination methodology; sample preparation; spectrometry

Citation: Operacz, A.; Bigaj, A.; Hap, K.; Kotowski, T. The Effect of Sample Preparation and Measurement Techniques on Heavy Metals Concentrations in Soil: Case Study from Kraków, Poland, Europe. *Appl. Sci.* **2022**, *12*, 2137. https://doi.org/10.3390/app12042137

Academic Editor: Avelino Núñez-Delgado

Received: 17 January 2022
Accepted: 17 February 2022
Published: 18 February 2022

1. Introduction

Accurate and reliable laboratory results are essential for scientific research. Results can be affected by many factors, including the test methods used, the accuracy and precision of the test performed, and the laboratory equipment used [1]. Measurements of concentrations of various chemical compounds/elements are carried out, among others, to study the composition of soils. Soil is a complex three-phase solid-liquid-gas system, in which continuous processes of decomposition and synthesis of mineral and organic compounds and their transfer between different soil horizons take place. The infiltration of compounds into the soil is made possible by infiltrating water. Rainwater percolates through the different soil layers, dissolving and/or transporting dissolved substances and suspended solids to deeper soil layers. From an agronomic point of view, the soil must be protected and used in such a way that it is possible to continuously produce sufficient quantities of high-quality plant raw materials [2]. Heavy metals play an important role here as excessive accumulation of these elements in soils may cause far-reaching, often irreversible chemical degradation of soils. In the short term, negative effects of heavy metal pollution may be hardly noticeable, however, their gradual accumulation may lead to exceeding the sorption capacity of soils and, as a consequence, release of those metals into the environment. This can be a source of significant contamination of the water-soil environment and consequently the food chain. Contaminants accumulating in soils may also affect soil organisms and/or plants, which may lead to a reduction in biodiversity or decrease in soil vegetation cover, and consequently to an increase in water and aeolian erosion processes [3,4]. In times of rapid economic development, the content of heavy metals in soil can be significant. The biggest amount of heavy metals are emitted to the environment in the areas of mining and metallurgical processing of metal ores, cement production and industrial combustion of fossil fuels. The environment can also be a source of toxic substances. An example is Pb, which can be leached from the rock environment or derived from geothermal H_2S sources [4,5]. All over the world, the problem of heavy metal contamination of soils is common, which is a frequent subject of scientists' research, e.g., in Europe [6,7] or in Asia, including, among others, China [8,9], in Mongolia [10], in Tibet [11], India [12], and Pakistan [13].

Heavy metal ions are retained in the surface layer of soils mainly due to sorption, and their movement into the soil profile is relatively slow. Excessive accumulation of heavy metals in the surface layer of soils is one of the basic causes of chemical degradation of soils and pollution of soil-soil and surface waters. Heavy metals occurring in the soil lead to an imbalance in the recycling of soil nutrients and a decline in soil quality [13,14]. Furthermore, heavy metals are characterised by the easy accumulation in soils of different types [15,16]. The occurrence of elevated concentrations of heavy metals in agricultural soils and consequently also in food poses a threat to animal and human health. For example, too high concentrations of Cu can cause liver cirrhosis and chronic anaemia. Apart from affecting soft tissues, heavy metals can also accumulate in bone tissue, Pb being one example. Cr is also worth mentioning. Its deficiency in the body may be manifested by diabetic symptoms, while compounds of this element on high oxidation levels (+4, +6) are directly toxic and carcinogenic for humans. Based on a comprehensive analysis of heavy metal hazards, the United Environmental Protection Agency has listed eight heavy metals (Pb, Cd, Cr, Hg, As, Cu, Zn, Ni) as major contaminants of the groundwater environment [17]. Due to the high danger of heavy metals contained in soils, numerous studies have been undertaken on soil contamination with these elements e.g., [18–20]. There are many indicators determining the level of heavy metal contamination in soils, such as the pollution index [21], geo-accumulation index [22], Nemerow integrated pollution index [23], enrichment factor [24], and potential ecological risk index [25].

There are many methods used for the determination of heavy metal content in dissolved soil samples. For example, pulsed differential stripping voltammetry (DP ASV) is one of the most sensitive instrumental methods that can achieve very low limits of quantification for metal cations [26–28]. For surface samples, X-ray analysis (XRD) is used

to determine the elemental composition. The percentages of the main mineral components of soils are determined by means of pattern analysis, the number of radiation pulses and the intensity of reflections [5]. Spectroscopy methods based on the interpretation of spectra produced by the interaction of radiation with matter, especially atoms (atomic spectrometry), are widely used. Methods based on atomic spectra can be divided into absorption and emission methods. An example of the former is atomic absorption spectrometry (AAS). The principle of this method is based on determining the relation between absorption of electromagnetic radiation for a particular line of the determined element and its concentration, which is quantitatively expressed by Lambert-Beer law [5,13,26]. Atomic emission methods include, among others, the historically first atomic excitation technique: flame photometry. The concentration of elements in solutions after the previous extraction can also be determined using the technique of Inductively Coupled Plasma Optical Emission Spectrometry (ICP-OES) [29]. The inductively coupled plasma mass spectrometry (ICP-MS) technique was developed by Gray in 1978, and the first instruments to use it was built in 1978 [30,31]. The first instruments for its application appeared several years later than the ICP-OES technique. ICP-MS spectrometers enable fast multi-element analysis (up to 70 elements within a few minutes). The technique is characterised by high sensitivity, selectivity, low limit of quantification and rapidity of determinations. Inductively coupled plasma analytical instruments are widely used for the determination of trace amounts of metals in environmental samples such as drinking water, wastewater and groundwater. It can also be used for the determination of trace amounts of metals in petrochemical samples, soil samples, or food products.

Environmental studies require a wide variety of fieldwork and laboratory determinations. In order for the results to be a basis for further considerations and interpretation they should be characterised by sufficient accuracy and reliability. During both the field and laboratory stages of the study, there are possibilities of errors that may distort the results obtained. In order to control the precision of the determinations it is recommended to take duplicate samples and to assess the precision of laboratory determinations. Unfortunately, even if these recommendations are followed, it may be difficult to obtain fully valid test results since, depending on the preparation and measurement technique/apparatus used, significantly different results may be obtained for the same environmental samples [32]. In Poland, the information on soil contamination is scarce and selective. Usually, the information concerns larger agglomerations, i.e., Warszawa, Łódź, or Wrocław [33–36], and mainly characterise concentrations of heavy metals in soils. The information on soil contamination in towns of medium and small size (<100,000 inhabitants) is sporadic. There is also a lack of literature reports on sample preparation and measurement techniques, which may influence the variability of heavy metal determination results in soil. In this context, the methodology of determinations, the accuracy and precision of the measurements performed, and the laboratory equipment used for the studies are important. Taking into account the above observations, the aim of this study was to determine the influence of the method of sample preparation and the applied measurement methods on the variation in the determination of heavy metal concentrations in soils. The study area was the area directly adjacent to the Arcelor Mittal metallurgical plant near Kraków in southern Poland. This area is characterised by a significantly polluted soil environment as a result of many years of operation of the steelworks. Soil samples prepared by two methods were analysed and the solutions obtained were determined using two analytical methods and different types of spectrometers. The contents of heavy metals in soil determined using two selected methods commonly used in this type of study, i.e., AAS and ICP-MS, were compared.

Wide research of the published articles proves that most of them show only results based on one selected course of methodology without comparison with others. Many of them are based only on the influence of preparation methodology in plants, i.e., on *Pleurozium schreberi* moss samples prior to use in active biomonitoring studies [37]. Four different methodologies were tested across four different sample locations with the conclusion that of the four methods used to prepare mosses for later exposure in active biomonitoring,

the best method is averaging with simultaneous conditioning of mosses in demineralised water. Another published paper shows evaluation and comparison between a conventional acid digestion method and a microwave digestion system for heavy metals determination in *Mentha* samples by ICP-MS [38]. The concentrations of selected heavy metals were measured in the stems and leaves of the *Artemisia herba-alba* medicinal plant and soil samples were evaluated by Massadeh et al. [39]. Results showed different results in heavy metal concentrations of washed and unwashed parts of plants, which is still the preparation method. The results of this study [39] revealed that there is a correlation between heavy metal levels in medicinal plants and their concentrations in soil. Usually, authors show that results depend on the preparation but choose only one measurement method.

The novelty of the paper is the comparison of the measurements of heavy metal concentration in soil using two methods for adding soil components into solution and different laboratory methods and types of measuring equipment. Additionally, the article includes a discussion of the importance of the methodology. We believe that the conclusions may help to better understand how sample preparation and measurement methods applied may influence the results obtained.

Innovation of our research is the comparison of the selected methods which shows how the methodology is important. Results are highly dependent on the preparation and measurement methods applied. We believe that the conclusions based on the comparison may help to better understand how the methodology applied may influence the results obtained.

2. Study Area

The study area covers 6200 ha and is located directly at the eastern border of the Arcelor Mittal (formerly W. Lenin) steelworks in the Kraków area (southern Poland, Central Europe). The study area was subjected to almost 70 years of the direct impact of the steelworks. The steelworks mainly emit dust-gas pollutants, which reach the ground surface in the form of wet and dry precipitation (Figure 1). The main pollutants are gaseous sulphur compounds and heavy metals (Cr, Cu, Fe, Mn, Ni, Pb, Zn) occurring in various chemical forms (including elemental form). The technological development of the steelworks and changes in the volume of steel production directly affected the emission of pollutants. In the initial years of the steelworks existence (mainly 1950s to 1980s), the emission of pollutants to the environment was very high. At present, the modern technologies applied have considerably reduced it. However, the pollutants emitted during many years of the steelworks existence still constitute a serious environmental problem and the explanation of the processes they undergo in the water and soil environment is a key issue for the assessment of the condition of the natural environment in the studied area. Among the pollutants emitted by the steelworks, heavy metals are potentially the greatest hazard to the environment. The following were selected for detailed analyses: Cr, Cu, Fe, Mn, Ni, Pb and Zn, while the main source of these metals in the study area was/is the emission from the steelworks.

The study area is characterised by high homogeneity of soil types—the parent rocks of soils are mainly Quaternary loess sediments related to the Vistula glaciation. Soils developed on outcrops of Cretaceous marls (Figure 2) occur only subordinately in small areas of the NE part of the study area. Besides the mentioned primary loess deposits, alluvial and deluvial deposits occur in narrow stream valleys. Very small fragments of stream valleys are occupied by mud and peat deposits. The areas of particular types and subtypes calculated on the basis of planimetric measurements (Table 1) confirm the domination of soils developed on loess.

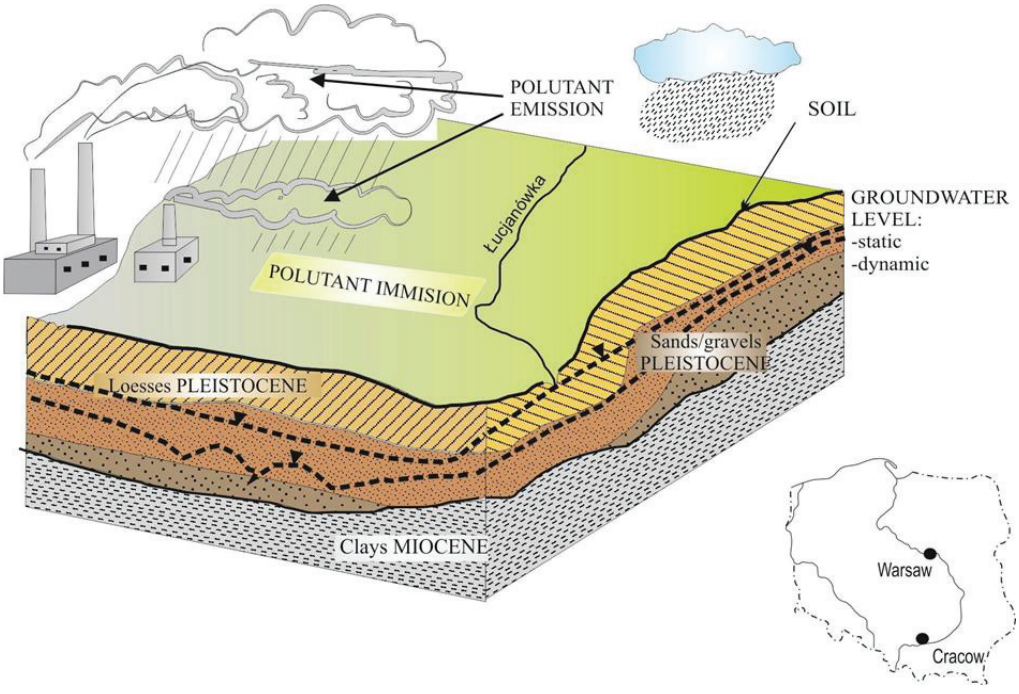

Figure 1. Study area layout and location.

Table 1. Soil types of the study area [40].

Soil Types and Subtypes	Share [%]
brown soils developed from loess and loess loam formations	22.4
proper deluvial brown soils developed from loessial and loessial clay formations	3.0
alkaline lignite soils developed from loess and clay formations	2.3
proper chernozem developed from ordinary loess formations	0.9
proper deluvial chernozems developed from loess and loess loam formations	13.4
degraded chernozem developed from loess and loess loam formations	51.4
silts formed from alluvial deposits of silt and clayey silt composition	5.1
clayey loess soils	0.7
rendzina soil formed from chalky marls	0.5
mud-peat and peat-silt soils	0.3
Total	100.0

Only in the NE part of the study area are soils developed on marl outcrops (Cretaceous), but they occupy only 0.5% of the study area (Figure 2).

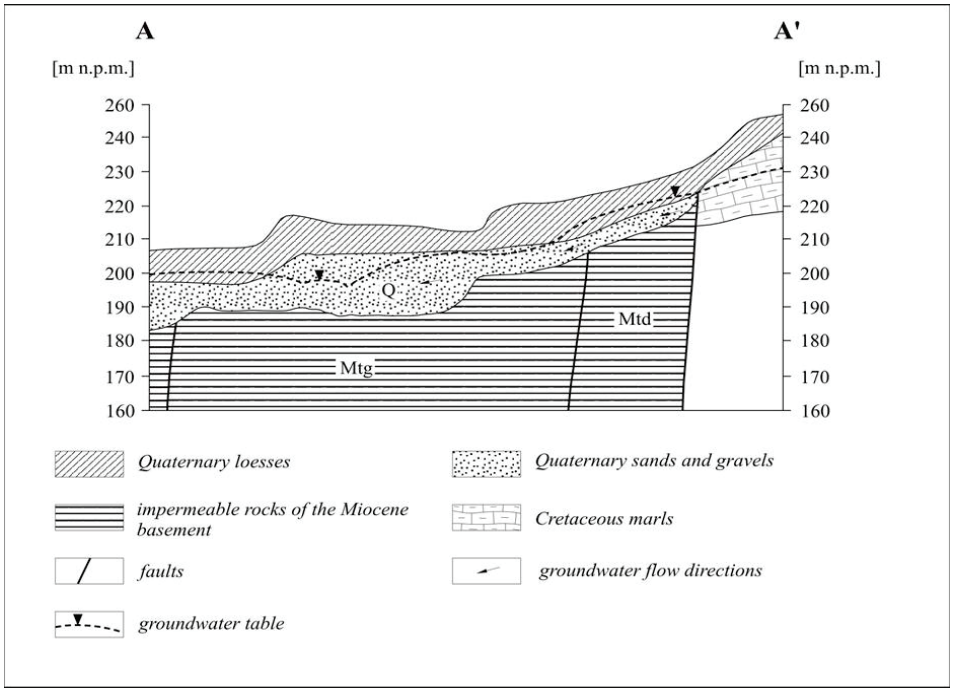

Figure 2. Simplified hydrogeological cross-section A-A′ (acc. to [41] modified).

There is also an underground water intake located in the immediate vicinity of the steelworks, which is used as a source of drinking water. This intake consists of 13 wells exploiting a shallow valley water-bearing horizon. The aquifer is mainly composed of alluvial sediments of various grains. Within the studied area, the aeration zone of the aquifer is formed mainly by poorly permeable loess sediments with a thickness of several metres on average. Consequently, the aeration zone is characterised by high retention capacity due to its considerable thickness and poor permeability properties, which determines the relatively long infiltration time of rainwater. The average infiltration velocity value obtained on the basis of interpretation of natural (SO_4^{2-} ions) and artificial (Br^- ions) tracer movements in the aeration zone profile is 0.53 m·year^{-1} [42–47]. As a result, at least some part of heavy metals may be absorbed. It is significant because infiltration waters are the basic source of supply for the aquifer system in the study area. The study area is predominantly used for agricultural purposes. Arable fields cover the vast majority of the area. The agricultural character of land use has a major impact on soil conditions, especially on pH and humus content. This determines the ability of the soil to retain contaminants. Heavy metals are subject to a number of different physical and chemical reactions in the soil layer, which can cause significant delays in their migration into the aquifer system and often even stop their migration [30]. Heavy metal concentrations in soils also depend on the type of soil itself. In the studied area the soils are mainly characterised by neutral and alkaline reactions, which favour retention of heavy metal migration [48]. Precipitation with pH < 5 occurs sporadically only in April and May, which is not a significant factor that could trigger the leaching of metals from the soil cover.

3. Materials and Methods

An area of over 60 km^2 was sampled (Figure 3). Samples were collected in a kilometre grid using a bucket sampler. There were 65 samples taken from the arable soil layer (0–20 cm).

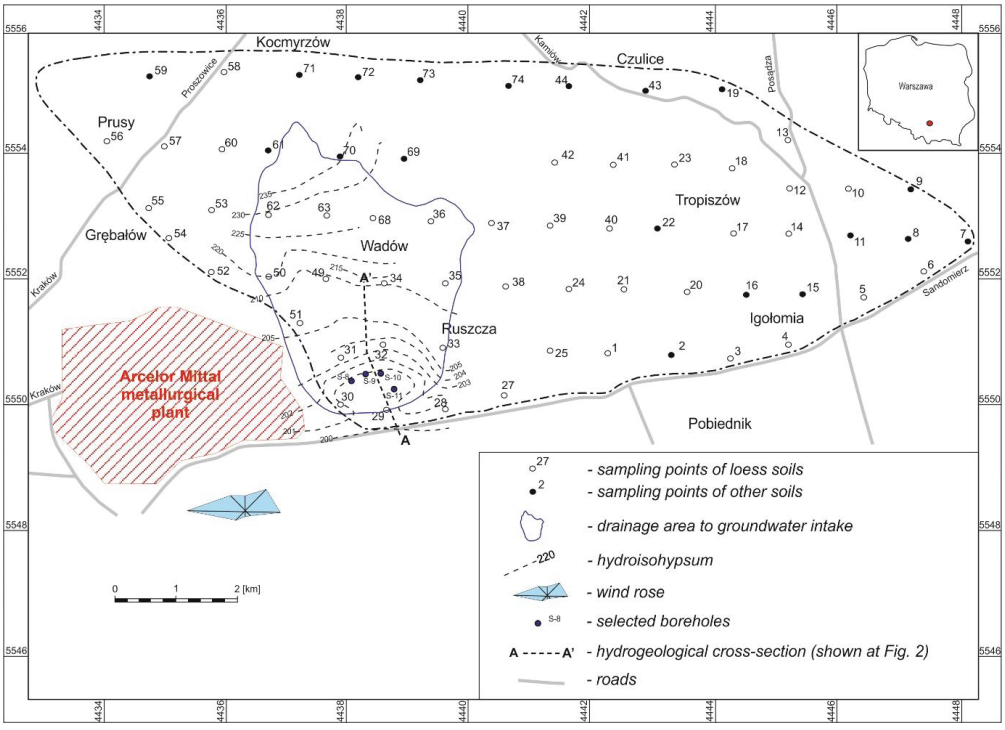

Figure 3. Sampling sites.

At 9 points, duplicate samples were taken following the same procedure as for the other soil samples. Duplicate samples accounted for 13% of all soil samples collected. Additionally, the standard material as San Joaquin soil was used and the results were sufficient. This preliminary test was necessary for further investigation. Results were in the range of expected values but some differences were observed (Table 2). It was an impulse to create the presented manuscript.

Table 2. Standard material analyses [40].

mg/kg	Standard San Joaquin Soil	AAS_1	$ICP\text{-}MS_1$
Cr	60–115 (79)	67	78.8
Cu	26–40 (32)	27	29.3
Fe	-	19.18	29.528
Mn	-	282	292.9
Ni	65–90 (78)	84	79.9
Pb	12–18 (13)	13	14.4
Zn	87–120 (100)	87	97.6

3.1. Sampling and Methods for Decomposition of Mineral Soil Components

The samples collected in linen bags in an air-dry state were transported to the Institute of Soil Science, Plant Cultivation and Fertilisation in Puławy, where preliminary operations were performed, consisting of manual grinding of air-dry samples in a porcelain mortar and sieving them through a sieve with a mesh diameter of 1 mm (which is equivalent to separation into so-called earthy and skeletal parts). The samples were then crushed in

a 12-min cycle in an electric agate mortar to a grain diameter of <0.1 mm. The soil dust obtained as a result of grinding was stored in paper bags in an air-dry state. The material thus prepared was used for further studies. The concentrations of heavy metals in the soils of the study area were determined using two methods of transferring components from soil to solution:

- with the IUNG method of hot digestion of soil material with a mixture of concentrated HNO_3 and $HClO_4$ after incineration of organic matter [49];
- with a two-step decomposition method, i.e., oxidative acid digestion followed by non-oxidative acid digestion (HNO_3 and HF, respectively) in a microwave oven [50].

Complete decomposition of soil minerals is a relatively difficult operation, so cold or hot leaching of soil components with mineral acids and mixtures is often used. The chemical components brought into solution by strong acids during hot leaching are assumed to be close to their total content in the soil [49]. In soils with a similar grain size distribution, the relation between the amount of chemical components in the digestion solution and their total content is relatively constant. To determine the so-called total content of individual elements in the soil, the method of hot digestion of soil material with a mixture of concentrated HNO_3 and $HClO_4$ was adopted. Acid digestion of organic soils is preceded by the ashing of the organic matter. Soil ashing releases components bound in the organic matter. Digestion of the incineration residue with a mixture of HNO_3 and $HClO_4$ causes decomposition of most of the soil minerals and the passage of the constituents into solution. In the following part of the article, this decomposition is referred to as the IUNG method and was carried out at the Department of Soil Science and Soil Erosion of the IUNG in Puławy. The second method of decomposition was a two-stage decomposition, i.e., digestion with oxidizing acid and then with non-oxidizing acid (HNO_3 and HF, respectively), hot, in a microwave, which was carried out in the laboratory of the Department of Hydrogeology and Water Protection of the AGH University of Science and Technology (AGH) in Kraków.

3.2. Methods for the Determination of Heavy Metals in Soil and Assessment of the Precision of These Determinations

The concentrations of selected heavy metals (Zn, Pb, Cu, Fe, Mn, Ni, Cr) were determined in solutions obtained by both digestion methods. The solutions obtained from the decomposition by the IUNG method were determined twice: by the AAS method (AA500 flame, PG Instruments, Leicestershire, UK) in the IUNG laboratory and by the ICP MS method (ELAN 6100 Perkin Elmer, Waltham, USA) in the AGH laboratory. Solutions obtained from two-stage decomposition were analysed only on ICP MS in the AGH laboratory.

To assess the precision of determinations based on results of determinations in duplicate samples, hydrogeochemical simplified methods were applied [1], i.e., correlation plot and percentile diagram. Duplicate samples should constitute at least 6% of the total number of normal samples and should be taken randomly [51]. The described graph for estimating precision is based on percentiles 50, 90, and 99 of the $\sigma c = 0.05$ c function, plotted on a logarithmic grid. The diagrams (Figure 4) should be viewed considering the position of individual points in relation to the lines limiting the likely percentage of differences between samples for the assumed model (in this case for a precision of 5%). If more than 50% of the points are below the 50% line and less than 10% are above the 90% line, it can be considered that the assumed precision has been achieved.

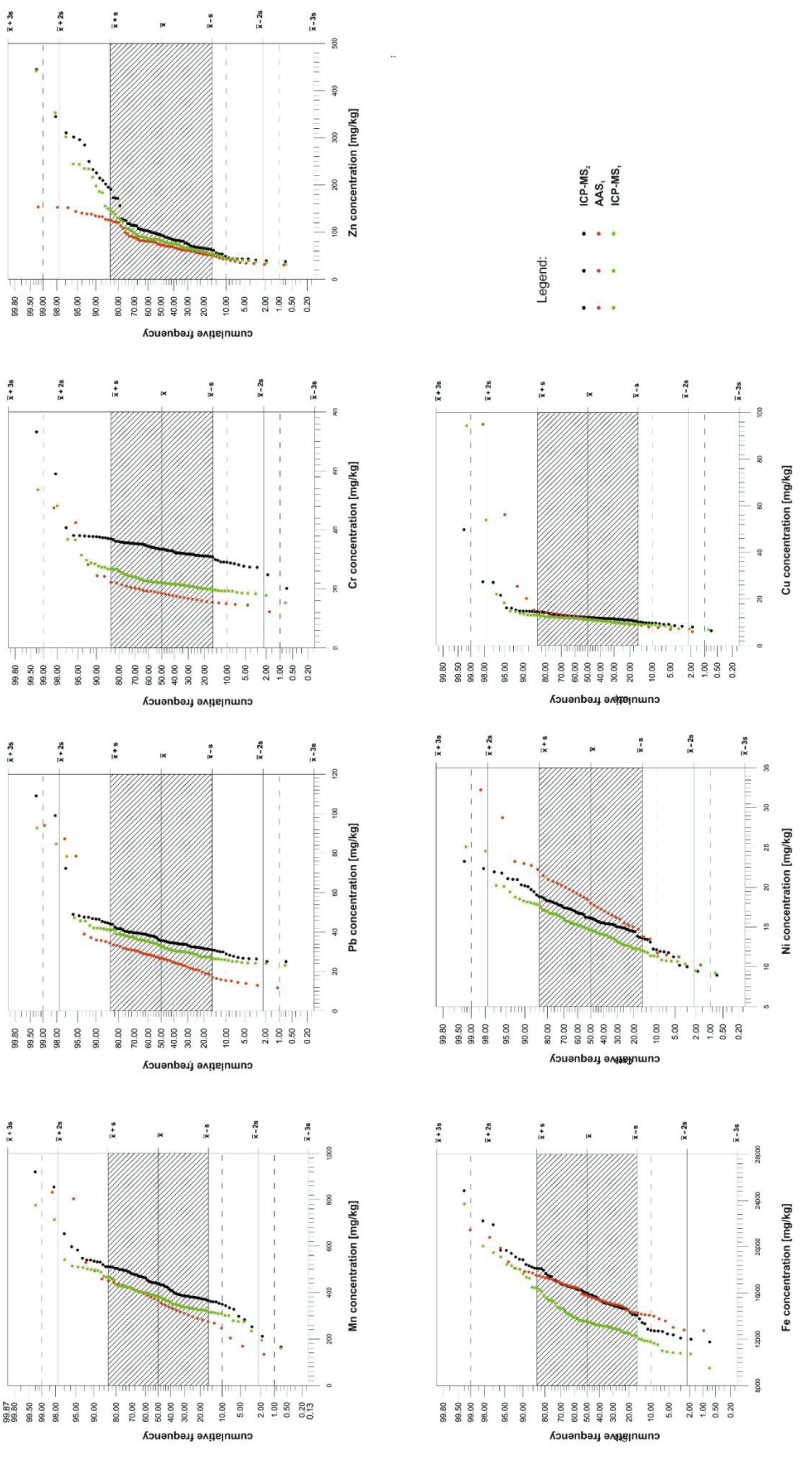

Figure 4. Frequency plot of cumulative heavy metal content determined by different methods in soil samples.

In order to determine whether the variation in heavy metal concentrations in individual soil samples statistically significantly differs depending on the analytical method used and/or sample preparation, analysis of variance with Repeated Measures Anova (hereafter referred to as RMA) was applied. In this analysis, the null hypothesis of equality of means of individual measurements is tested. Rejection of the null hypothesis indicates the presence of significant differences between the means in successive repeated measurements. RMA, apart from the assumptions typical for the analysis of variance (normality, homogeneity of variance), also requires the assumption of sphericity of variance to be met. This assumption was checked using the Mauchly test to determine the equality of variances for differences between individual measurements. If a significant violation of sphericity is found, it is recommended to perform multivariate tests, which are much more resistant to violation of sphericity.

4. Results and Discussion

The soil organic matter is characterised by significant sorption capacity, consisting of binding various components, including heavy metals, which limits their migration in the soil environment and their toxicity. The results of the content of humus in the samples indicated that the vast majority of soils were characterised by medium and high humus content (Table 3). Very high and low humus soils were of minor importance (in the order of a few percent).

Table 3. Content of hummus in soil samples.

Content of Hummus %	<1.0 Low	1.01–2.00 Medium	2.01–3.50 High	>3.51 Very High
percent of samples %	9.2	40.2	47.2	3.4

The pH value is a very important parameter characterising the soil's ability to retain heavy metals. The results of the pH in KCl for soil samples are presented in Table 4. The general pH of the analysed soils was mostly neutral and slightly acidic.

Table 4. pH values in soil samples.

pH (in KCl)	<4.5 Very Acidic	4.6–5.5 Acidic	5.6–6.5 Slightly Acidic	6.6–7.2 Neutral	>7.2 Alcaline
percent of samples %	9.2	17.2	26.4	34.6	12.6

The concentrations of heavy metals in soil samples depend on many factors and are time-varying. The assessment of heavy metals accumulation and the self-cleaning ability of the soil environment as a heavy metal storage medium is a complex issue. The process of migration of pollutants can be divided into two stages. The first one is related to the direct supply of pollutants as a result of increased anthropopressure and their accumulation in the environment. The second stage is the duration of the operation of the processes to which the stored pollutants are subject after the anthropopressure has ceased or markedly diminished. Due to the slow migration of some pollutants, such as the heavy metals considered, the system can naturally reduce the mass, toxicity, concentration and mobility of pollutants without human intervention. Such entrusting to nature of some or all of the self-cleaning processes has been defined by the Office of Solid Waste and Emergency Response (OSWER) of the EPA as Natural Attenuation (also known as intrinsic remediation or natural restoration) [52].

Soil air is characterised by an increased content of CO_2, which, by changing the gas balance of infiltrating waters, leads to an increase in the content of HCO_3^- ions in the waters percolating through the unsaturated zone [53]. Solid phases, usually amorphous and/or cryptocrystalline, are also formed in the soil zone. For this reason, they are more

soluble than the crystalline phases. In general, the soil also experiences a radical change in pH and Eh conditions, which affects the migration capacity of many elements along with infiltration waters. Water migration of elements in the soil zone is also dependent on the amount and nature of the organic substance, which creates various types of complex compounds, protective colloids, etc. In the area covered by the research, brown soils and chernozems, characterized by a high degree of enrichment in organic matter, predominate. Sorption processes take place in the soils, in which colloids, clay minerals and organic matter participate. This study focuses only on the physicochemical processes occurring in the soil, with the omission of biological processes. However, it is worth noting their significant role in modifying the chemistry of the soil.

Being aware of the complexity of the processes, the ranges of concentrations of analysed metals in soils determined in the study were measured and are presented in Table 5.

Table 5. Ranges of heavy metal concentrations in soils in the study area [mg/kg].

	IUNG Distribution Designation on the AAS (AAS_1)	**IUNG Distribution Determination on ICP-MS ($ICP\text{-}MS_1$)**	**Two-Step Decomposition Determination on ICP-MS ($ICP\text{-}MS_2$)**	**Geochemical Background to Loess Soils (According to Kabata-Pendias A., 1993)**
Zn	30.5–138	32.1–442	37.8–445	30–360 65 on average
Pb	11.8–94	23.1–92.8	25.0–109	19–49 25 on average
Cu	6–95	6.9–94.4	6.4–49.8	4.0–53.0 19.0 on average
Cr	15.3–47.5	15.3–53.7	20.2–73.3	14.0–80.0 38.0 on average
Ni	10.3–32.3	9.5–25.1	8.9–23.3	10–104 25 on average
Fe	12,756–21,460	9510–20,055	11,771–24,854	Fe (%) 0.8–2.78 on average 1.2
Mn	134–832	161–776	166–920	380–700 560 on average

Graphical comparison of metal concentrations determined by individual methods and spectrometer types from soil samples prepared from both IUNG and two-stage decomposition is shown in Figure 4.

It can be observed that both the type of decomposition method and laboratory determination methods noticeably affected the determined concentration value of almost all the analysed heavy metals. Generally, heavy metal concentrations were higher for the two-stage decomposition than for the IUNG method. The exception was Ni, where samples prepared by the IUNG method and determined by AAS were higher than in the other methods of preparation and/or laboratory determinations. In the case of Cu, sample preparation with both methods leads to practically the same results regardless of the method of laboratory determination.

In order to confirm whether the variation in heavy metal concentrations in individual soil samples statistically significantly differs depending on the applied method of laboratory determinations and/or sample preparation, analysis of variance with repeated measurements (RMA) was applied. The results of normality tests (Shapiro-Wilk) indicate that in most cases (>92%), the analysed data are characterised by a distribution more or less deviating from normal. Therefore, an attempt was made to normalise the data using the Box-Cox transformation. Unfortunately, this did not give satisfactory results and only for two metals (Zn and Fe), a normal distribution was obtained for determinations performed

by all methods (AAS_1, ICP-MS_1 and ICP-MS_2). At the same time, the results of Mauchly's test indicate a significant violation of sphericity for all analysed data and therefore further analysis was carried out using Pillais, Hotelling and Roy's multivariate tests. The results of these tests indicate statistically significant variation in the concentrations of all heavy metals depending on the analytical method and/or sample preparation used. For in-depth data analysis, conservative post-hoc tests (Scheffé's test) were additionally performed. These tests showed that Cu concentrations in soil samples do not differ significantly depending on the chosen laboratory test method and/or sample preparation. In contrast, the other results of the post-hoc tests are consistent with the results of the multivariate tests. This ambiguity in the results may be due to the fact that even if the multivariate tests are significant, this may only apply to a limited part of the data population. In this case, the significant variation in Cu concentrations shown by the multivariate test may be the result of the presence of anomalous concentrations of this metal in some soil samples. Conservative post-hoc tests, such as the Scheffé test, are more resistant to the occurrence of anomalous values and, except for Cu, no lack of differentiation of concentrations of the analysed metals depending on the method of their determination was observed. Similar observations can be made from the analysis of the expected values of the marginal averages (Figure 5).

Similar results were presented by Jablonska et al. [54]. These authors noted that even the method of mineralisation can influence the test results, with metals such as As, Cd or Zn. As they state, when dealing with the solution of soil samples for determination of Co, Mn and Cu, total mineralization with both $HF/HCl/HNO_3$ and $H_2O_2/HF/HNO_3$ mixtures can be successfully applied due to the lack of significant differences in obtained analyses by ICP-MS and AAS techniques, however, in the case of heavily contaminated samples, it is best to use total distribution with $H_2O_2/HF/HNO_3$. Additionally, at extremely high metal contents, the absorption of fluorescent radiation is equally important as well as the primarily determined metal, which may be the cause of the so-called matrix effect consisting of the change of chemical composition of the sample matrix [54].

The precision determined from the duplicate samples for the determination of heavy metals is shown using a probabilistic plot in Figure 6.

The precision of heavy metal determinations was found to be satisfactory for all metals determined on both AAS and ICP-MS except Cr determined on AAS. For all determinations, more than half of the points lay below the 50% line. For Mn, Cr, Cu and Pb, individual points were just above the 99% line but did not represent more than 10% of all samples. This indicated adequate precision of determinations of metal concentrations in the studied soil samples. Only the determination of Cr concentrations by AAS showed precision slightly lower than expected (Figure 6). Concentrations of other metals were determined with precision equal to 5%.

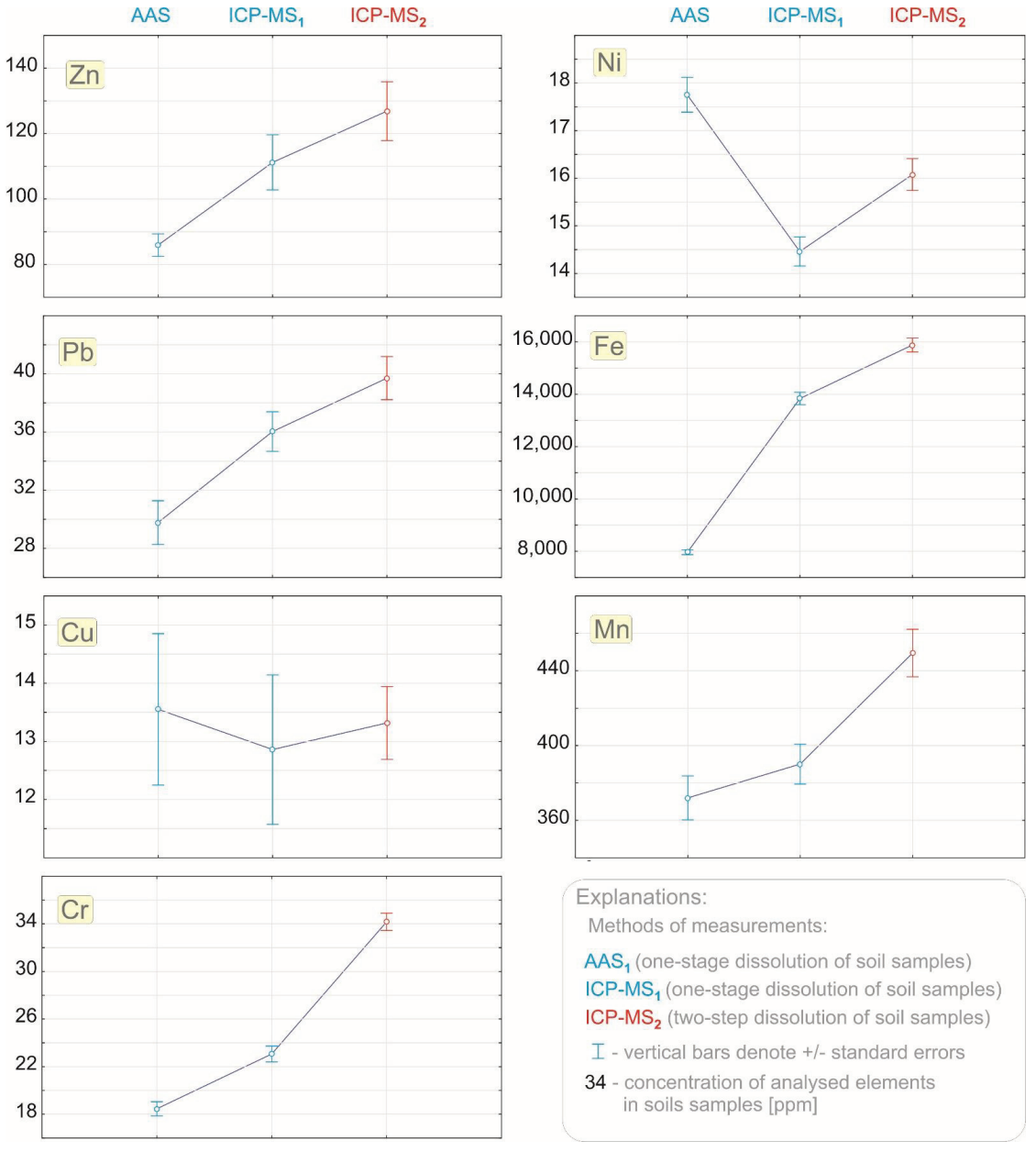

Figure 5. The Least-squares means for analysed metals.

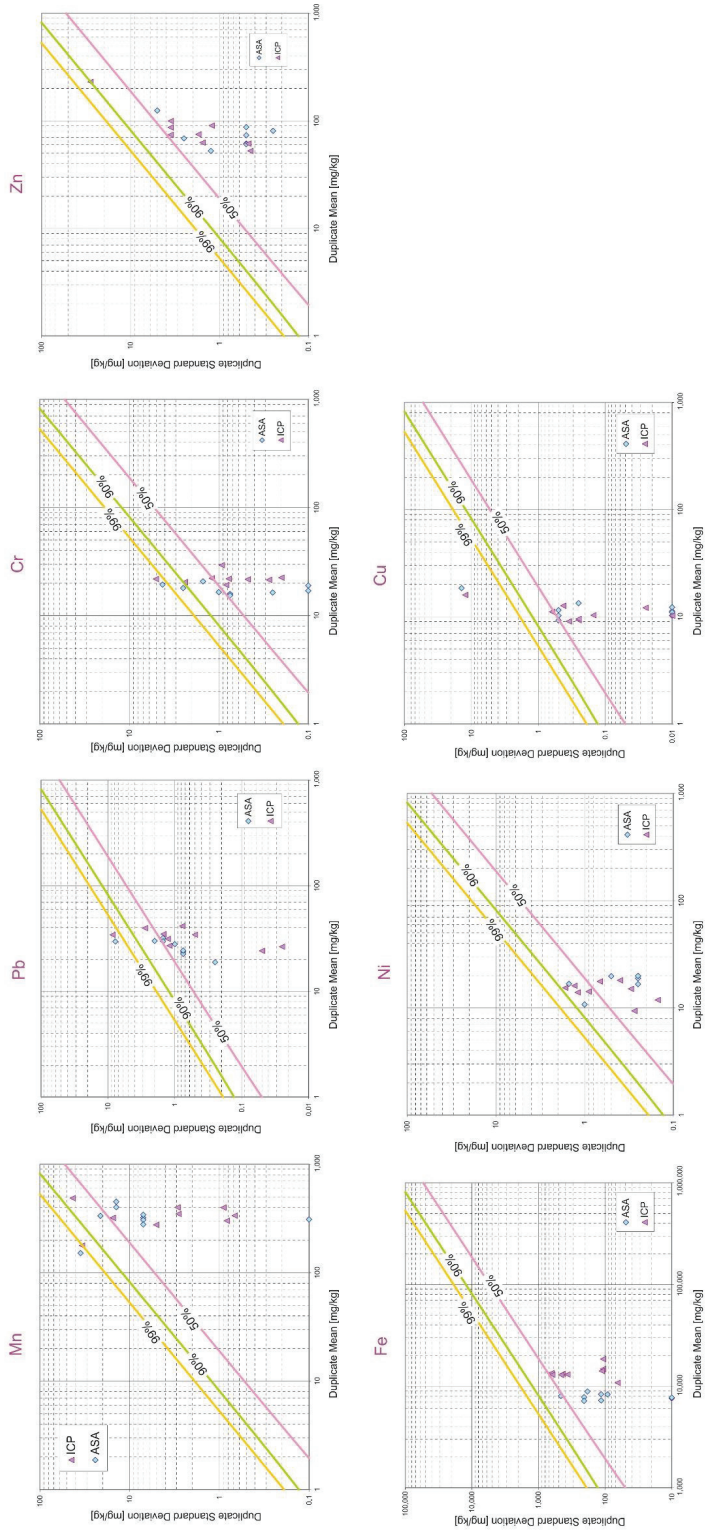

Figure 6. Precision of heavy metal determinations.

5. Conclusions

The results of the conducted studies indicate the occurrence of significant statistical differentiation of heavy metal concentrations in soil depending on the sample preparation method and/or the applied determination method. In most cases, the concentrations of heavy metals are the highest for samples digested in two stages, and their concentrations are measured using ICP-MS. However, this does not apply to Cu and Ni. In the case of Cu, the lack of significant differentiation of this metal concentration may result from different forms of Cu occurrence in the soil than the other metals. Unfortunately, the forms of occurrence of the analysed metals in soils are not known at present and it requires further studies. For Ni, however, a kind of reversal of trends seen in the case of other metals is observed and the highest concentrations are observed in the case of AAS determinations, while the lowest in the case of two-stage dissolution samples and their concentrations measured with ICP-MS. As in the case of Cu, the speciation of this metal may be important, but it seems more likely that in the case of Ni, the type of spectrometer used for the measurements may be important. It is possible that in the case of AAS, the spectrometric spectrum of Ni interferes with the spectra of the other determined metals, however, this is not fully clear at the present stage of the study, and further studies in this direction are planned.

Author Contributions: A.O.: conceptualization, methodology, formal analysis, writing—original draft preparation, writing—review and editing, visualization, funding acquisition, A.B.: writing—original draft preparation; K.H.: writing—original draft preparation; T.K.: conceptualization, writing—original draft preparation. All authors have read and agreed to the published version of the manuscript.

Funding: This study constitutes a part of status research of Department of Hydrogeology and Water Protection AGH University of Science and Technology, financed by KBN—contract 11.11.140.251 and research project—Scientific Research Committee (KBN) no. 5T12B01224.

Institutional Review Board Statement: Not applicable.

Conflicts of Interest: The authors declare no conflict of interest. The funders had no role in the design of the study; in the collection, analyses, or interpretation of data; in the writing of the manuscript, or in the decision to publish the results.

References

1. Thompson, M.; Howarth, R.J. Duplicate analysis in geochemical practice: Part I. Theoretical approach and estimation of analytical reproducibility. *Analyst* **1976**, *101*, 690–698. [CrossRef]
2. Kiedrzyńska, E.; Wagner-Łotkowska, I.; Zalewski, M. Quantification of phosphorus retention efficiency by floodplain vegetation and a management strategy for a eutrophic res-ervoir restoration. *Ecol. Eng.* **2008**, *33*, 15–25. [CrossRef]
3. Siebielec, S.; Siebielec, G.; Sugier, P.; Woźniak, M.; Grządziel, J.; Gałązka, A.; Stuczyński, T. Activity and diversity of microorganisms in root zone of plant species spontaneously inhabiting smelter waste piles. *Molecules* **2020**, *25*, 5638. [CrossRef] [PubMed]
4. Manahan, S.E.; Boczoń, W.; Koroniak, H. *Environmental Toxicology: Chemical and Biochemical Aspects*; Wydawnictwo Naukowe PWN: Warsaw, Poland, 2011.
5. Cabała, J. *Heavy Metals in the Soil Environment of the Olkusz Zn-Pb Ore Mining Region*; Wydawnictwo Uniwersytetu Śląskiego: Katowice, Poland, 2009.
6. Kompiš, M.; Ballová, Z.K. The influence of preferred habitat and daily range of the European hare on its contamination by heavy metals: A case study from the West Carpathians. *Environ. Sci. Pollut. Res.* **2021**, *28*, 52093–52105. [CrossRef]
7. Silva, H.F.; Silva, N.F.; Oliveira, C.M.; Matos, M.J. Heavy metals contamination of urban soils—A decade study in the city of lisbon, portugal. *Soil Syst.* **2021**, *5*, 27. [CrossRef]
8. Yang, Q.; Li, Z.; Lu, X.; Duan, Q.; Huang, L.; Bi, J. A review of soil heavy metal pollution from industrial and agricultural regions in China: Pollution and risk assessment. *Sci. Total Environ.* **2018**, *15*, 690–700. [CrossRef]
9. Huang, Y.; Wang, L.; Wang, W.; Li, T.; He, Z.; Yang, X. Current status of agricultural soil pollution by heavy metals in China: A meta-analysis. *Sci. Total Environ.* **2019**, *651*, 3034–3042. [CrossRef]
10. Guo, W.; Sun, W.H.; Zhao, R.X.; Zhao, W.J.; Fu, R.Y.; Zhang, J. Characteristic and evaluation of soil pollution by heavy metal in different functional zones of Hohhot. *Huanjing Kexue/Environ. Sci.* **2013**, *34*, 1561–1567.
11. Wu, J.; Lu, J.; Li, L.; Min, X.; Luo, Y. Pollution, ecological-health risks, and sources of heavy metals in soil of the northeastern Qinghai-Tibet Plateau. *Chemosphere* **2018**, *201*, 234–242. [CrossRef]
12. Lokeshwari, H.; Chandrappa, G.T. Impact of heavy metal contamination of Bellandur Lake on soil and cultivated vegetation. *Curr. Sci.* **2006**, *91*, 622–627.

13. Ashraf, I.; Ahmad, F.; Sharif, A.; Altaf, A.R.; Teng, H. Heavy metals assessment in water, soil, vegetables and their associated health risks via consumption of vegetables, District Kasur, Pakistan. *SN Appl. Sci.* **2021**, *3*, 552. [CrossRef]
14. Cao, H.; Chen, J.; Zhang, J.; Zhang, H.; Qiao, L.; Men, Y. Heavy metals in rice and garden vegetables and their potential health risks to inhabitants in the vicinity of an industrial zone in Jiangsu, China. *J. Environ. Sci.* **2010**, *22*, 1792–1799. [CrossRef]
15. Burges, A.; Epelde, L.; Garbisu, C. Impact of repeated single-metal and multi-metal pollution events on soil quality. *Chemosphere* **2015**, *120*, 8–15. [CrossRef] [PubMed]
16. Zhang, J.; Hua, P.; Krebs, P. Influences of land use and antecedent dry-weather period on pollution level and ecological risk of heavy metals in road-deposited sediment. *Environ. Pollut.* **2017**, *228*, 158–168. [CrossRef] [PubMed]
17. U.S. Environmental Protection Agency. Guidelines for the Health Risk Assessment of Chemical Mixtures. *Fed. Regist.* **1986**, *51*, 34014–34025.
18. Liu, G.; Yu, Y.; Hou, J.; Xue, W.; Liu, X.; Liu, Y.; Wang, W.; Alsaedi, A.; Hayat, T.; Liu, Z. An ecological risk assessment of heavy metal pollution of the agricultural ecosystem near a lead-acid battery factory. *Ecol. Indic.* **2014**, *47*, 210–218. [CrossRef]
19. Tian, K.; Huang, B.; Xing, Z.; Hu, W. Geochemical baseline establishment and ecological risk evaluation of heavy metals in greenhouse soils from Dongtai, China. *Ecol. Indic.* **2017**, *72*, 510–520. [CrossRef]
20. Chai, L.; Wang, Y.; Wang, X.; Ma, L.; Cheng, Z.; Su, L. Pollution characteristics, spatial distributions, and source apportionment of heavy metals in cultivated soil in Lanzhou, China. *Ecol. Indic.* **2021**, *125*, 107507. [CrossRef]
21. Yi, Y.; Yang, Z.; Zhang, S. Ecological risk assessment of heavy metals in sediment and human health risk assessment of heavy metals in fishes in the middle and lower reaches of the Yangtze River basin. *Environ. Pollut.* **2011**, *10*, 2575–2585. [CrossRef]
22. Fei, X.; Xiao, R.; Christakos, G.; Langousis, A.; Ren, Z.; Tian, Y.; Lv, X. Comprehensive assessment and source apportionment of heavy metals in Shanghai agricultural soils with different fertility levels. *Ecol. Indic.* **2019**, *106*, 105508. [CrossRef]
23. Zhang, P.; Qin, C.; Hong, X.; Kang, G.; Qin, M.; Yang, D.; Pang, B.; Li, Y.; He, J.; Dick, R.P. Risk assessment and source analysis of soil heavy metal pollution from lower reaches of Yellow River irrigation in China. *Sci. Total Environ.* **2018**, *633*, 1136–1147. [CrossRef] [PubMed]
24. Buat-Menard, P.; Chesselet, R. Variable influence of the atmospheric flux on the trace metal chemistry of oceanic suspended matter. *Earth Planet. Sci. Lett.* **1979**, *42*, 399–411. [CrossRef]
25. Hakanson, L. An ecological risk index for aquatic pollution control a sedimentological approach. *Water Res.* **1980**, *14*, 975–1001. [CrossRef]
26. Linnert, A.; Musiał, J. Investigation of the content of selected heavy metals—Lead and cadmium in a soil section. *Analit* **2019**, *7*, 32–43.
27. Kubiak, W.W.; Piech, R. *Introduction to Polarography and Voltammetry*, 16th ed.; AGH University of Science and Technology: Kraków, Poland, 2006.
28. Górka, A.; Kogut, A.; Krzystyniak, A. Contents of selected heavy metals—Lead and cadmium in soils, and their toxic effects on plant development. *Analit* **2017**, *3*, 32–39.
29. Nadgórska-Socha, A.; Wójcik, A.; Spiler, J.; Dabioch, M. Assessment of the degree of heavy metal accumulation in common dandelions and soil using ICP-OES technique. *Wydaw. Uniw. Śląskiego* **2017**. Available online: https://rebus.us.edu.pl/handle/20.500.12128/7839 (accessed on 16 January 2022).
30. Gray, A.L.; Date, A.R. Inductively coupled plasma source mass spectrometry using continuum flow ion extraction. *Analyst* **1983**, *108*, 1033–1050. [CrossRef]
31. Gray, A.L. Solid sample introduction by laser ablation for inductively coupled plasma source mass spectrometry. *Analyst* **1985**, *110*, 551–556. [CrossRef]
32. Karpińska-Rzepa, A. The Role of Soil and Aeration Zone in the Processes of Self-Purification of Groundwater Environment Degraded by Industrial Emissions in the Area of Tadeusz Sendzimir Steelworks. Ph.D. Dissertation, AGH University of Science and Technology, Kraków, Poland, 2009.
33. Czarnowska, K. Level of some heavy metals in soils and tree leaves of the city of Łódź. *Soil Sci. Annu.* **1997**, *48*, 49–61.
34. Czarnowska, B.; Gworek, K. The state of zinc, lead and copper contamination of the soils of Warszawa. *Soil Sci. Annu.* **1991**, *42*, 49–56.
35. Dąbkowska-Naskręt, S.; Różański, H. Accumulation of heavy metals and physico-chemical properties of urbanozems from Bydgoszcz agglomeration. *Ecol. Chem. Eng.* **2002**, *9*, 1313–1318.
36. Karczewska, A.; Bogda, A.; Wolszczak, M.; Gałka, B.; Szopka, K. Kabała Copper, lead and zinc in soils of the industrial part of the Różanka housing estate in Wrocław. *Ochr. Sr. Zasobów Nat.* **2009**, *41*, 516–522.
37. Świsłowski, P.; Kosior, G.; Rajfur, M. The influence of preparation methodology on the concentrations of heavy metals in Pleurozium schreberi moss samples prior to use in active biomonitoring studies. *Environ. Sci. Pollut. Res.* **2021**, *28*, 10068–10076. [CrossRef] [PubMed]
38. Alsehli, B.R.M. Evaluation and Comparison between a Conventional Acid Digestion Method and a Microwave Digestion System for Heavy Metals Determination in Mentha Samples by ICP-MS. *Egypt. J. Chem.* **2021**, *64*, 869–881. [CrossRef]
39. Massadeh, A.M.; El-Rjoob, O.A.; Omari, M.N. Investigation of Metal levels in Artemisia herba-alba Medicinal Plant and Soil Samples Collected from Different Areas in Jordan Country. *Soil Sediment Contam. Int. J.* **2021**, *30*, 216–230. [CrossRef]

40. Karpińska-Rzepa, A. The role of soil and aeration zone in self-purification processes of groundwater environment degraded by industrial emissions in the area of Tadeusz Sendzimir Metallurgical Plant. Final report on the implementation of the research project of the State Committee for Scientific Research No. 5T12B01224. 2005; Unpublished work.
41. Witczak, S.; Zuber, A.; Kleczkowski, A.S.; Myszka, J. Efficiency and mineralization of water intake from the Vistula high terrace east of Kraków in the light of isotopic research. In *Contemporary Problems Hydrogeologic*; AGH: Kraków, Poland, 1985; pp. 187–196.
42. Operacz, A.; Karlikowska, J. Soil and unsaturated zone as a store of the contaminants and protective barrier for groundwater. In *Prace Naukowe. Chemia i Ochrona Środowiska*; Akademia im. Jana Długosza w Częstochowie: Częstochowa, Poland, 2008; Volume 12, pp. 163–173.
43. Witczak, S.; Operacz, A. Soil and aeration zone testing programme for assessing the resistance of groundwater of GZWP 450 to pollution. Jakość i podatność wód podziemnych na zanieczyszczeń. *Pr. Nauk. Uniw. Śląskiego* **2002**, *22*, 81–88.
44. Operacz, A. Hydrogeochemical profile of loess pore waters in the area of Tadeusz Sendzimir Steelworks in Kraków. *Contemp. Probl. Hydrogeol.* **2003**, *11*, 179–182.
45. Witczak, S.; Operacz, A.; Musiał, M. Construction of a large-diameter dug well in the profile of unsaturated zone as a good database of percolating water composition. In Proceedings of the 11th Magdeburg seminar on Waters in Central and Eastern Europe, Leipzig, Germany, 18–22 October 2004; pp. 244–245.
46. Operacz, A. Migration velocity of infiltrating waters through loess aeration zone determined from stable isotope and tritium studies. *Hydrogeochemistry* **2005**, *5*, 68–73.
47. Duliński, W.S.M.; Kapusta, M.; Operacz, A.; Różański, K. Evolution of carbon isotopic composition of 13C, 12C, 14C dissolved carbonates in the aeration zone. *Contemp. Probl. Hydrogeol.* **2007**, 65–75. Available online: https://www.researchgate.net/publication/320101138_Evolution_of_Carbon_Isotope_Composition_13C12C_14C12C_of_Dissolved_Carbonates_in_Unsaturated_Zone (accessed on 16 January 2022).
48. Operacz, A.; Kurek, K.; Młyński, D.; Bugajski, P. Untypical draining barriers efficiency as a method of pollutants limiting in the groundwater reservoir. *J. Ecol. Eng.* **2019**, *20*, 67–76. [CrossRef]
49. Ostrowska, A.; Gawlinski, S.; Szczubiałka, Z. *Metody Analizy i Oceny Właściwości Gleb i Roślin*; Instytut Ochrony Srodowiska: Warsaw, Poland, 1991.
50. Matusiewicz, H. Wet decomposition methods for samples. In *Nowe Horyzonty i Wyzwania w Analityce i Monitoringu środowiskowym*; Namieśnik, J., Chrzanowski, W., Szpinek, P., Eds.; CEEAM: Gdańsk, Poland, 2003.
51. Witczak, S.; Bronders, J.; Kania, J.; Kmiecik, E.; Różański, K.; Szczepańska, J. Summary Guidance and Recommendations on Sampling, Measuring and Quality Assurance. BRIDGE. 2006. Available online: https://scholar.google.com/citations?view_op=view_citation&hl=en&user=-jfz0AQAAAAJ&cstart=20&pagesize=80&sortby=pubdate&citation_for_view=-jfz0AQAAAAJ:UebtZRa9Y70C (accessed on 16 January 2022).
52. U.S. Environmental Protection Agency. Office of Solid Waste and Emergency Response. Data Quality Objectives Process for Superfund. EPA-540/R-93-071; September 1993. Available online: https://nepis.epa.gov/Exe/ZyNET.exe/2000E40J.TXT?ZyActionD=ZyDocument&Client=EPA&Index=1991+Thru+1994&Docs=&Query=&Time=&EndTime=&SearchMethod=1&TocRestrict=n&Toc=&TocEntry=&QField=&QFieldYear=&QFieldMonth=&QFieldDay=&IntQFieldOp=0&ExtQFieldOp=0&XmlQuery=&File=D%3A%5Czyfiles%5CIndex%20Data%5C91thru94%5CTxt%5C00000008%5C2000E40J.txt&User=ANONYMOUS&Password=anonymous&SortMethod=h%7C-&MaximumDocuments=1&FuzzyDegree=0&ImageQuality=r75g8/r75g8/x150y150g16/i425&Display=hpfr&DefSeekPage=x&SearchBack=ZyActionL&Back=ZyActionS&BackDesc=Results%20page&MaximumPages=1&ZyEntry=1&SeekPage=x&ZyPURL (accessed on 16 January 2022).
53. Apello, C.A.J.; Postma, D. *Geochemistry, Groundwater and Pollution*, 2nd ed.; Balkema, A.A., Ed.; CRC Press: Boca Raton, FL, USA, 2005.
54. Jablonska, K.; Nocoń, M.S.S. ICP-MS and ASA as a useful tool in creating reference materials used in EDXRF technique. *Eng. Environ. Prot.* **2011**, *14*, 121–135.

applied sciences

MDPI

Article

Release of Microplastics from Reusable Kitchen Plasticware and Generation of Thermal Potential Toxic Degradation Products in the Oven

Juri Jander [1], Darius Hummel [1], Sophie Stürmer [1], Adrian Monteleone [1], Tizian Neumaier [1], Felix Broghammer [1], Uta Lewin-Kretzschmar [2], Thomas Brock [2], Martin Knoll [3] and Andreas Siegbert Fath [1,4,*]

[1] Faculty of Medical and Life Sciences, Hochschule Furtwangen, 78054 Villingen-Schwenningen, Germany; juri.jander@gmail.com (J.J.); d.hummel@uni-hohenheim.de (D.H.); sophie.katharina.stuermer@hs-furtwangen.de (S.S.); adrian.monteleone@hs-furtwangen.de (A.M.); tizian.neumaier@hs-furtwangen.de (T.N.); felix.broghammer@hs-furtwangen.de (F.B.)
[2] Employer's Liability Insurance Association of Raw Materials and Chemical Industry—(Competence Center Hazardous Substances and Biological Agents), 06237 Leuna, Germany; uta.lewin-kretzschmar@bgrci.de (U.L.-K.); thomas.brock@bgrci.de (T.B.)
[3] Department of Earth and Environmental Systems, University of the South, Sewanee, TN 37383, USA; mknoll@sewanee.edu
[4] Faculty of Medical and Life Sciences, Institute of Applied Biology, Hochschule Furtwangen, 78120 Villingen-Schwenningen, Germany
* Correspondence: fath@hs-furtwangen.de

Citation: Jander, J.; Hummel, D.; Stürmer, S.; Monteleone, A.; Neumaier, T.; Broghammer, F.; Lewin-Kretzschmar, U.; Brock, T.; Knoll, M.; Fath, A.S. Release of Microplastics from Reusable Kitchen Plasticware and Generation of Thermal Potential Toxic Degradation Products in the Oven. *Appl. Sci.* **2022**, *12*, 2535. https://doi.org/10.3390/app12052535

Academic Editors: Avelino Núñez-Delgado, Zhien Zhang, Elza Bontempi, Mario Coccia, Marco Race and Yaoyu Zhou

Received: 3 February 2022
Accepted: 24 February 2022
Published: 28 February 2022

Publisher's Note: MDPI stays neutral with regard to jurisdictional claims in published maps and institutional affiliations.

Abstract: Plastics are one of the most important technical materials at present, yet they are associated with a whole series of environmental problems such as micro-and nanoplastics or their plasticizers, which have become increasingly relevant in recent years. While there are many studies that focus on microplastics (MPs) introduced into the human body through commercially produced food, there are nearly none that consider the MPs we ingest through homemade food made with plastic kitchen utensils such as mixing bowls. To investigate this, samples were obtained by exposing different plastic bowls made of acrylonitrile–butadiene–styrene (ABS), polypropylene (PP), melamine, polyethylene (PE), polystyrene (PS), and styrene–acrylonitrile (SAN), to mechanical stress and then analyzed via infrared spectroscopy. This not only raises the question of whether microplastics are incorporated into foods but also the extent to which the degradation products produced by thermal stress in an oven could play a toxicological role. Degradation products were generated by pyrolysis and analyzed afterwards using gas chromatography mass spectrometry. There were differences in the number of microplastic particles abraded by the different types of plastic, with the most consisting of melamine (898 particles) and the least consisting of low-density polyethylene (331 particles). There were also differences in the number and relevance of the thermal degradation products for the different plastics, so that a human toxicological assessment would have to be evaluated in further work.

Keywords: microplastic; microplastic analysis; kitchen plastic bowl; pyrolysis; GC-MS; abrasion

1. Introduction

Since the industrialization of plastics in the 1950s, their applications have also increased, and they have become an important technical material in the world, but the waste they produce has become an increasing global problem over the years. The high durability of plastic makes it highly resistant to degradation; hence, disposing of plastic poses a big challenge [1]. Therefore, plastics accumulate in the environment and landfills, and it is projected that by the year 2050, 12 billion metric tons of plastics will be distributed throughout both settings [2]. Plastics that end up in the environment are broken down by mechanical [3], chemical [4], or biological [5] processes into smaller pieces. For that reason, microplastic can be passed into the human body through the consumption of contaminated

food. It has been suggested that exposure to microplastic through the consumption of food can influence growth, behavior, and histopathological changes [6]. It is unknown if the ingestion of microplastics released from take-out food containers poses a risk to human health [7], but recently published studies on mice [8] demonstrate the ability of polystyrene microplastic particles to cross the blood–brain barrier and affect the immune system. Plastics even present a risk for human health as sorbents for different drugs such as X-ray contrast agents [9], antibiotics [10], or trace elements [11,12]. While there are many studies that focus on MPs introduced into the human body through commercially produced food [13–16], there are nearly none that consider the MPs we ingest through homemade food made with plastic kitchen utensils such as mixing bowls. This not only raises the question of whether microplastics are incorporated into foods but also the extent to which the degradation products produced by thermal stress in an oven could play a toxicological role.

To investigate these questions, six commercially available plastic bowls and a glass bowl were tested for abrasion with a mixing machine. In addition, the effect on the abrasion of plastic and microplastic particle count of granular or crystalline substances such as sugar or salt were investigated. Fourier transform infrared spectrometer (FTIR-spectrometer) analysis was used to count and specifically determine the type of plastic particles produced (microplastics over 25 μm). Plastic samples were cut out from the bowls and prepared with a cryo-mill for the determination of volatile degradation products originating between 200 and 250 °C. These products were treated using pyrolysis, analyzed by gas chromatography mass spectrometry (GCMS), and subsequently measured.

2. Materials and Methods

2.1. Sample Material

For the experiments, we used commercially available kitchen mixing bowls made of six different types of plastic, which were to provide a range of abraded microplastics as well as thermally released pollutants during general baking. The indicated plastic type for each bowl was double checked via IR spectroscopy using the Bruker polymer database. The six bowls were made of the following materials: bowl 1 of styrene–acrylonitrile copolymers (SAN), bowl 2 of melamine, bowl 3 polystyrene (PS), bowl 4 of acrylonitrile butadiene styrene (ABS), bowl 5 of low-density polyethylene (LDPE), and lastly, bowl 6 of polypropylene (PP). The selection of plastics also demonstrates different properties such as the Rockwell hardness of engineering materials, which can play a role in mechanical abrasion (Table 1).

Table 1. The range of Rockwell hardness of selected polymers.

Polymeric Material	Minimum Rockwell Hardness	Maximum Rockwell Hardness
Acrylonitrile–butadiene styrene (ABS)	2.00	70.00
Low-density polyethylene (LDPE)	1.00	20.00
Melamine	67.00	86.00
Polypropylene (PP)	1.00	20.00
Polystyrene (PS)	60.00	75.00
Styrene–acrylonitrile copolymers (SAN)	10.00	80.00

2.2. Sample Preparation

To assess the extent to which microplastics can be abraded during everyday uses of kitchen bowls, several steps were taken. First, all six individual bowls were treated in the same manner with a hand mixer (Q4835DE, Bosch, Stuttgart, Germany). The mixer was used for a total of 2 min at 200 rpm, which was intended to abrade microplastic particles. Then, 100 mL of purified water was added to each bowl, which was followed by three repetitions of abrasion runs. An additional sample run was conducted with salt in the bowl in order to gauge the influence of granular ingredients on abrasion. This

additional test was carried out with the ABS bowl (ABS I), in which 5 g of rock salt (Steinsalz, Herbaria, München, Germany) was added to the purified water. This rock salt, unlike marine salt, is completely free of microplastics [12,13]. Furthermore, a glass bowl was included in the analysis as a negative control, whereby the environmental parameters such as contamination from air and the water used were established to normalize the results. To investigate if the detected MP particles were in fact from the plastic bowls, two different blank samples were made. The first was to determine if the particles originated from the hand mixer components. For this, 100 mL of water was mixed for 2 min at 200 rpm in a glass bowl. The second blank sample was made to check if there was any MP contamination in the tap water used. For that, 100 mL of tap water was utilized. After these steps, the water was removed from the bowls, filtered, and the filtrate was prepared for analysis with the Perkin Elmer Frontier Fourier transform infrared spectrometer (Perkin Elmer Frontier and Perkin Elmer Spotlight, FTIR-spectrometer). The sample suspensions were filtered through a high-purity aluminum oxide membrane with a pore size of 0.2 µm (Anodisc™ 25, Diameter 25 mm, GE Healthcare UK limited, Little Chalfont Buckinghamshire, Amersham Place, UK) and was afterwards dried at 40 °C overnight. Then, the particles on the aluminum oxide membrane were ready for further analysis with the FTIR spectrometer (Section 2.3 Microplastic Analysis).

Finally, the kitchen bowl plastics had to be prepared as controls for the thermal decomposition products with the pyrolysis, which was followed by GC-MS. To be able to identify decomposition products that can arise during pyrolysis in the oven, a 2–3 g sample of each of the six-plastic bowls was separated with a heavy metal knife and then processed into powder using a cryogenic mill. To crush different plastic types, 3 sequences of the cryogenic mill were performed: pre-cooling, crushing, and intercooling. Pre-cooling lasted 90 s at a frequency of 5 Hz with one cycle, the crushing lasted 300 s at 30 Hz for two cycles, and intercooling lasted 30 s at 5 Hz for one cycle. To generate the required microplastic particles, 2–3 g of each plastic were comminuted by a one-cycle process using a cryogenic swinging mill (CryoMill, Retsch GmbH, Haan, Germany). In contrast to the other plastics, the parameters described above for the plastic LDPE had to be extended by an additional cycle to produce a finer powder. The powder thus obtained from the various plastic bowls could now be used for analysis with the pyrolysis, which was followed by GC-MS (Section 2.4 Analysis of thermal decomposition products).

2.3. Microplastic Analysis (FT-IR Spectroscopy)

In order to determine the specific plastic of the particles on the aluminum membrane, the FTIR spectrometer was used. Sixteen scans per particle were performed to detect individual particles to reduce the noise of the spectral data obtained. Only particles with a diameter larger than 25 µm were included in the analysis, since no qualitative high-quality spectra can be obtained below this limit for this purpose. Due to the technical equipment of the FTIR used, an automated measurement of a complete sample filter with a filter area of 490 mm^2 was not possible, as this measurement would be very time consuming and additionally susceptible to measurement interruptions. For this reason, statistical extrapolation from square grid fields to the complete filter had to be applied. For this purpose, three square fields (side lengths of 2 mm) with an area of 4 mm^2 were measured for each sample at the same positions of the complete round sample filter (490 mm^2), and the plastics were identified and counted. Absorption spectra of the measured particles were created through the microscope, and these were compared with the existing plastic databases using a "search function". Based on the number of particles in these three square areas of 4 mm^2 each, an extrapolation was made to the total area of the sample filter 490 mm^2 [17]. The calculated and extrapolated particle counts with the error bars are shown in Figure 1.

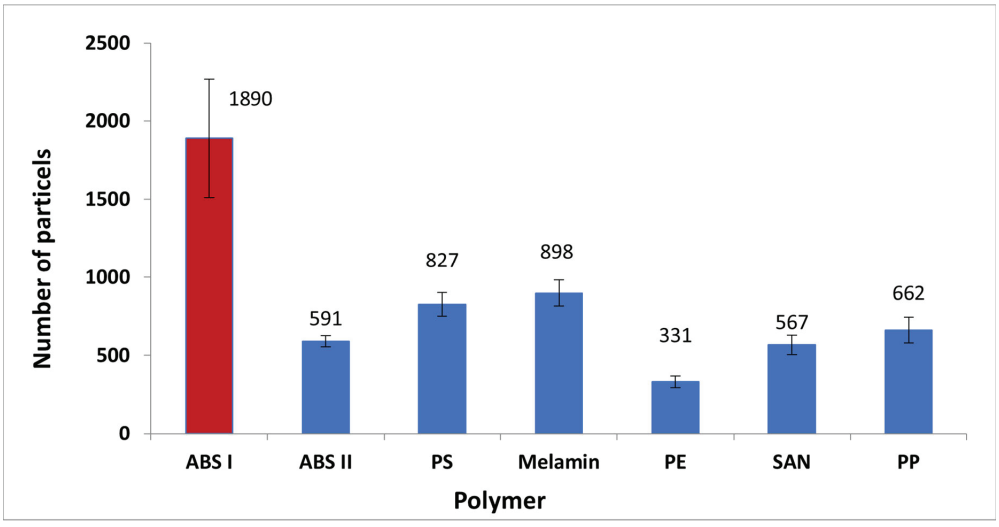

Figure 1. FTIR spectrometer microplastic analysis of the different plastic bowls listed according to the type of material. Red bar = use of water and salt. Blue bar = use of water only.

2.4. Analysis of Thermal Decomposition Products

For the analysis of the thermal decomposition products resulting from the mixing-derived microplastics during baking, a pyrolysis of polymers was performed, and the products were analyzed afterwards by GC-MS. To detect volatile compounds, 0.5 g of the material samples were weighed, placed into vials, and heated to 200 °C and 250 °C in the thermal block (Liebisch Labortechnik, Bielefeld, Germany). After 30 min, 500 µL samples were taken from the vapor space above the samples with a gas-tight syringe, and then, these were chromatographed and analyzed by mass spectrometry. Under these conditions, water was released from all materials, which is not explicitly mentioned below. For this purpose, a gas chromatograph (6890N, Agilent Technologies, Palo Alto, CA, USA) with split/splitless injector and mass-selective detector (5973N, Agilent Technologies, Palo Alto, CA, USA) was used. The separation was performed with fused silica capillaries (Zebron ZB-624, from Phenomenex) with a length of 60 m, inner diameter of 0.32 mm, film thickness of 1.8 µm, and helium as a carrier gas (0.9 mL/min in constant flow). The heating process was carried out in 4 steps: (1) initial temperature 50 °C (isothermal for 8 min); (2) heating rate I: 5 °C/min to 100 °C (isothermal for 5 min); (3) heating rate II: 10 °C/min to final temperature; and (4) final temperature at 180 °C for 5 min isothermal. The mass spectrometry used electron impact ionization at 70 eV, and the temperatures were 230 °C for the ion source and transfer line.

3. Results and Discussion

3.1. Microplastic Analysis (FTIR Spectroscopy)

The results of counting the microplastic particles via FTIR spectrometry of the six different plastic bowls, as well as the bowl made of ABS (ABSI) with the salt treatment, are shown in Figure 1. The IR microscope recognized some particles within the first blank sample, but none of them matched with the references found in the database, which means they were not MP. These particles were probably lime from the faucet. In the second blank sample, only one particle was found, which matched the database. The one particle had a 60% correlation to polyurethane. Due to only one plastic particle in the reference samples for the glass bowl and the used water, which does not correspond to the plastic types used, no normalization of the values in Figure 1 was performed. For the sake of comparison, the samples treated with only water show abraded particles in descending order from

Melamine with 898 particles > PS with 827 > PP with 662 > ABS 591 > SAN with 567 > PE with only 331 particles. The effect of the salt test on the plastic ABS shows an increase from 591 particles (ABS II) of about 320% to 1890 particles (ABS I).

3.2. Analysis of Thermal Decomposition Products (Pyrolysis and GC-MS)

The Py-GCMS showed different results for the included plastics, which are described in the next paragraphs. In performing pyrolysis, the heating of the polymers revealed which substances were produced in abundance and in trace amounts as a result of the process.

Acrylonitrile–butadiene–styrene copolymer (ABS). The same spectrum of pollutants was obtained at both temperatures, although the intensities of most pollutants were higher at 250 °C than at 200 °C. The complete table of degradation products for the temperature 200 °C (Table S1) and 250 °C (Table S2) can be found in the Supporting Information. Styrene was the main component detected in the vapor space under these conditions. Furthermore, benzaldehyde, acrolein, n-alkanals (acetaldehyde to n-nonanal), acetophenone, 2-phenylisopropanol, methylstyrene, ethylbenzene, toluene, cumene, 2-methyl-1-propene, and a mixture of other unsaturated aliphatic hydrocarbons (highest single concentration: 1-tridecene) were detected. In low concentrations, there was evidence of acrylonitrile, 4-vinylcyclohexene, and acetone, as well as traces of benzene, ethanol, furan, tert-butanol, 2-butanone, propanenitrile, phenol, and other alkanals and alkyl aromatics.

Low-density polyethylene (LDPE). Under these conditions (Tables S3 and S4), acetaldehyde was detected as the main component in the vapor space, and at 200 °C, acetic acid and formic acid were also detected. Furthermore, n-butane, 2-butanone, and n-alkanals (n-propanal to n-nonanal) were also detected. In low concentrations, there were indications of ethanol, acrolein, acetone, propane, further n-alkanes (n-pentane to n-dodecane), as well as traces of methanol, n-propanol, n-butanol 2-and 3-alkanones and, at 200 °C, dihydro-2(3H)-furanone (butyrolactone).

Polypropylene (PP). The main components detected under these conditions in the vapor space were acetone and, at 200 °C (Table S5), acetic acid and formic acid. The latter could not be detected at 250 °C (Table S6) and acetic acid was detected only in low concentrations. With the exception of some ketones, the concentrations of the other contaminants were higher at 250 °C. A complex mixture of saturated and unsaturated aldehydes (highest concentrations: methacrolein, acetaldehyde), saturated and unsaturated hydrocarbons (highest concentrations: 2,4-dimethyl-1-heptene, 2-methyl-1-pentene, 2-methyl-1-propene, n-pentane), saturated and unsaturated ketones (highest concentrations: 2,4-pentanedione, 2-pentanone, 4-methyl-2-heptanone, methyl isobutyl ketone), and alcohols (highest concentrations: methanol and higher branched alcohols that could not be clearly identified) were detected.

Styrene–acrylonitrile copolymer (SAN). At 200 °C (Table S7), the main components detected in the vapor space under these conditions were styrene and ethylbenzene. Hydrogen cyanide, acrylonitrile, benzaldehyde, acetophenone, phenol, and other aromatic hydrocarbons (e.g., xylenes, cumene, propylbenzene) were detectable in traces, and there was evidence of a complex mixture of unsaturated aliphatic hydrocarbons (C number range approximately C11 to C12). At 250 °C (Table S8), the main components detected in the vapor space were styrene, benzaldehyde, ethylbenzene, and acetophenone. Hydrogen cyanide and phenol were detectable in low concentrations, and there was evidence of 2-phenylpropenal and a complex mixture of unsaturated aliphatic hydrocarbons (C number range approximately C11 to C12). Other aromatic hydrocarbons (e.g., benzene, xylenes, cumene, propylbenzene, methylstyrene), acrylonitrile, acetaldehyde, acetone, and benzonitrile were identified in trace amounts.

Melamine. At both temperatures (Tables S9 and S10), formaldehyde and methanol were detected as the main components in the vapor space under these conditions. Acetaldehyde, methyl formate, and 2,3-butanedione were identified in low concentrations and, additionally, at 250 °C, furfural, furfuryl alcohol, acetic acid, hydroxyacetone, butyrolactone, 2(5H)-furanone, 5-methylfurfural, acetone, and benzaldehyde (which could only

be detected in trace amounts at 200 °C). At 250 °C, there was also evidence of further furan compounds, ketones, and formaldehyde derivatives, which could not be clearly identified.

Polystyrene (PS). A similar spectrum of pollutants was obtained at both temperatures (Tables S11 and S12), although the concentrations of most pollutants were higher at 250 °C than at 200 °C. The main components determined in the vapor space under these conditions were styrene and benzaldehyde. Furthermore, acetophenone, 2-phenylpropenal, ethylbenzene, methylstyrene, cumene, propylbenzene, phenol, phenylacetaldehyde and phenyloxirane were detected. Benzene, formaldehyde, acetic acid, acetaldehyde, benzyl alcohol and a propyl toluene were identified in low concentrations at 250 °C, which could only be detected in the trace range at 200 °C or not at all in the case of acetic acid. In the trace range, there were also indications of n-alkanals, 2-alkanones, benzyl methyl ketone, unsaturated ketones, other aromatic hydrocarbons, and alcohols, in particular at 250 °C.

4. Discussion/Conclusions

4.1. Microplastic Analysis (FTIR Spectroscopy)

When assessing the results generated, several parameters must be associated with each other and, if possible, correlated. One is the type and hardness of the plastics as well as the influence of friction-enhancing granular or crystalline substances and the resulting effect on the number of microplastics. The resulting number of microplastics influences the potential amount of degradation products generated by thermal stress in the oven. Meaning for real application that abraded mass of plastic particles from the production of for example cake or bread in plastic kitchenware are approximately proportional to their thermal decomposition products in the oven. The amount of the produced microplastic particles is shown for each polymer (Figure 1). This makes it possible to determine which material was the most resistant to mechanical force. The plastics melamine and PS show the highest abrasion without salt treatment, which can be explained by considering the Rockwell hardness, which, compared to the other plastics, is in the high range for melamine (898 particles) between 67.00 and 86.00 and PS (827 particles) at 60.00–75.00 (Table 1). The plastics ABS and SAN show a relatively similar range of Rockwell hardness of 20.00–70.00 (ABS) and 10.00–80.00 for SAN, which is reflected in the only 4% difference in microplastic count. LDPE has the lowest microplastic count with only 331 particles, which can be explained by a very low Rockwell hardness value of 1.00–20.00. Furthermore, the influence of friction-increasing substances such as salt or other components, which could occur in the added ingredients when mixing in a plastic bowl, was tested. It was found that adding salt to the plastic ABS when stirring in water can cause a tripling of the microplastic count from 591 particles to 1890 particles. This means that the type of ingredients and the type of processing in a plastic bowl can also have an influence on the microplastic content.

4.2. Analysis of Thermal Decomposition Products (Pyrolysis and GC-MS)

In performing pyrolysis, the heating of the polymers revealed which substances were produced in abundance and in traces. From these results, initial predictions can then be made about the risk of such plastic particles and their degradation products in various baked foods. However, not all parameters needed for a specific toxicological assessment could be considered in this study, and further studies are needed for a complete estimation.

In the case of the ABS polymer, the main substances detected were styrene, benzaldehyde, and acrolein. This is concerning, as all these substances are considered carcinogenic [18,19]. Furthermore, substances such as acetophenone, methylstyrene, and ethylbenzene were found. These substances are also harmful to health, as they can irritate the respiratory system [18,19]. In addition, it was possible to detect traces of substances such as ketones, phenols, alkenes, and aromatics. However, they can be neglected due to their low concentrations. Analysis of the PS polymer revealed mainly benzaldehydes and styrenes as products. Benzaldehydes are only considered harmful to health in higher quantities. In the case of styrenes, there is a risk of them being converted into styrene oxides when ingested [20,21]. These are extremely dangerous, as they are potentially muta-

genic and carcinogenic [18–20]. Substances such as benzene or benzyl alcohol were found in traces.

The results of the analysis of the melamine polymer are extremely worrying, as the major products were the very toxic and carcinogenic substance formaldehyde [18,19] and the toxic and highly hazardous substance methanol [18,19]. This was observed when pyrolysis was carried out at both temperatures of 200 °C and 250 °C. In addition, the presence of acetaldehydes, methyl formates, and 2,3-butanedione could be determined at a temperature of 250 °C. At the temperature of 200 °C, these could only be found in traces. In Germany, it is forbidden to heat products containing melamine to over 70 °C, since formaldehyde is released at this temperature [22]. Regarding the LDPE polymer, the formation of the substance acetaldehyde, which is harmful to health and carcinogenic, was one the main products. Acetic acid was also synthesized in higher quantities. The acid has an irritating effect on mucous tissues [18,19]. Formic acid was also released, which is considered dangerous, especially in high concentrations, as it is irritating to the eyes and can cause respiratory distress if inhaled [18,19]. Butane was also formed, which has a fatiguing effect [23], as well as aldehydes, which can potentially cause allergies [18,19]. Traces of acroleine, propane, ketones, and short-chain alcohols were detected. However, in the second pyrolysis experiment at a temperature of 250 °C, both acetic acid and formic acid were not formed.

Pyrolysis products of SAN polymer have been identified primarily as styrene and ethybenzene. These are both considered hazardous to health, as they can cause cancer. However, when pyrolysis was carried out at 250 °C, acetophenones and benzaldehydes were also formed in larger concentrations. The trace substances formed at both 200 °C and 250 °C included hydrocyanic acid and phenols as well as other aromatic hydrocarbons and acetophenone. More trace substances were found during pyrolysis at 250 °C. When examining the resulting products concerning the polymer PP, acetone as well as formic and acetic acid could be identified in large quantities. Acetone is extremely harmful because it is particularly irritating to the eyes. The same applies to acetic acid. Formic acid is very damaging if it is ingested and, in addition, it has a severe corrosive effect on tissues. In addition, methanol was detected. This is hazardous to health when inhaled, touched, or ingested.

By comparing particle amounts and hazard classifications of main components, we deduce that LDPE seems to be the safest plastic to be used in a common household mixing bowl. Apart from acetaldehyde, which is damaging to organs in higher concentrations, its other components are not as hazardous in comparison. Additionally, the number of particles measured following the abrasion process was the lowest of all available plastics. This study shows the extent to which the various plastics (microplastics) are decomposed by thermal stress to harmful or questionable substances. It is not evident whether these substances volatilize in the oven or accumulate in foodstuffs through adsorption or absorption. As already mentioned, no conclusive toxicological assessment can be given yet, since for this the dose, the exposure times of the intake and the bioaccumulation in the organism of the resulting substances would have to be considered. Thus, studies on the ad- or absorbed or bound substances in the prepared food would have to be carried out, which should be addressed in future research work.

Supplementary Materials: The following supporting information can be downloaded at: https://www.mdpi.com/article/10.3390/app12052535/s1, Tables S1–S12: The complete table of degradation products for both temperatures (PDF).

Author Contributions: Formal analysis, U.L.-K., T.B.; investigation, J.J., D.H., T.N., F.B.; writing—review and editing, S.S., M.K.; supervision, A.M.; project administration, A.S.F. All authors have read and agreed to the published version of the manuscript.

Funding: The article processing charge was funded by the Baden-Württemberg Ministry of Science, Research and Culture and the Furtwangen University in the funding programme Open Access Publishing.

Acknowledgments: We would like to thank the summer semester 2021 course of study "Biology & Process technology" in the faculty of medical & life sciences within the lecture "scientific writing" for their contribution to the manuscript.

Conflicts of Interest: The authors declare no conflict of interest.

References

1. Sivan, A. New perspectives in plastic biodegradation. *Curr. Opin. Biotechnol.* **2011**, *22*, 422–426. [CrossRef] [PubMed]
2. Geyer, R.; Jambeck, J.R.; Law, K.L. Production, use, and fate of all plastics ever made. *Sci. Adv.* **2017**, *3*, e1700782. [CrossRef] [PubMed]
3. Chubarenko, I.; Efimova, I.; Bagaeva, M.; Bagaev, A.; Isachenko, I. On mechanical fragmentation of single-use plastics in the sea swash zone with different types of bottom sediments: Insights from laboratory experiments. *Mar. Pollut. Bull.* **2020**, *150*, 110726. [CrossRef] [PubMed]
4. Andrady, A.L. Microplastics in the marine environment. *Mar. Pollut. Bull.* **2011**, *6*, 1596–1605. [CrossRef] [PubMed]
5. Kooi, M.; van Nes, E.H.; Scheffer, M.; Koelmans, A.A. Ups and Downs in the Ocean: Effects of Biofouling on Vertical Transport of Microplastics. *Environ. Sci. Technol.* **2017**, *51*, 7963–7971. [CrossRef] [PubMed]
6. Hantoro, I.; Löhr, A.J.; van Belleghem, F.G.A.J.; Widianarko, B.; Ragas, A.M.J. Microplastics in coastal areas and seafood: Implications for food safety. *Food Addit. Contam. Part A. Chem. Anal. Control. Expo Risk Assess.* **2019**, *36*, 674–711. [CrossRef] [PubMed]
7. Du, F.; Cai, H.; Zhang, Q.; Chen, Q.; Shi, H. Microplastics in take-out food containers. *J. Hazard. Mater.* **2020**, *399*, 122969. [CrossRef] [PubMed]
8. Kwon, W.; Kim, D.; Kim, H.Y.; Jeong, S.W.; Lee, S.G.; Kim, H.C.; Lee, Y.J.; Kwon, M.K.; Hwang, J.S.; Han, J.E.; et al. Microglial phagocytosis of polystyrene microplastics results in immune alteration and apoptosis in vitro and in vivo. *Sci. Total Environ.* **2022**, *807*, 150817. [CrossRef] [PubMed]
9. Kormos, J.L.; Schulz, M.; Ternes, T.A. Occurrence of iodinated X-ray contrast media and their biotransformation products in the urban water cycle. *Environ. Sci. Technol.* **2011**, *45*, 8723–8732. [CrossRef] [PubMed]
10. Cheng, D.; Ngo, H.H.; Guo, W.; Chang, S.W.; Nguyen, D.D.; Liu, Y.; Wei, Q.; Wei, D. A critical review on antibiotics and hormones in swine wastewater: Water pollution problems and control approaches. *J. Hazard. Mater.* **2020**, *387*, 121682. [CrossRef] [PubMed]
11. Binda, G.; Spanu, D.; Monticelli, D.; Pozzi, A.; Bellasi, A.; Bettinetti, R.; Carnati, S.; Nizzetto, L. Unfolding the interaction between microplastics and (trace) elements in water: A critical review. *Water Res.* **2021**, *204*, 117637. [CrossRef] [PubMed]
12. Bussan, D.D.; Snaychuk, L.; Bartzas, G.; Douvris, C. Quantification of trace elements in surgical and KN95 face masks widely used during the SARS-COVID-19 pandemic. *Sci. Total Environ.* **2022**, *814*, 151924. [CrossRef] [PubMed]
13. Cox, K.D.; Covernton, G.A.; Davies, H.L.; Dower, J.F.; Juanes, F.; Dudas, S.E. Human Consumption of Microplastics. *Environ. Sci. Technol.* **2019**, *53*, 7068–7074. [CrossRef] [PubMed]
14. Schwabl, P.; Koppel, S.; Konigshofer, P.; Bucsics, T.; Trauner, M.; Reiberger, T.; Liebmann, B. Detection of various microplastics in human stool: A prospective case series. *Ann. Intern. Med.* **2019**, *171*, 453–457. [CrossRef] [PubMed]
15. Diaz-Basantes, M.F.; Conesa, J.A.; Fullana, A. Microplastics in Honey, Beer, Milk and Refreshments in Ecuador as Emerging Contaminants. *Sustainability* **2020**, *12*, 5514. [CrossRef]
16. Karami, A.; Golieskardi, A.; Keong Choo, C.; Larat, V.; Galloway, T.S.; Salamatinia, B. The presence of microplastics in commercial salts from different countries. *Sci. Rep.* **2017**, *7*, 46173. [CrossRef] [PubMed]
17. Jander, J. Mikroplastik in Flüssen und Lebensmitteln. Bachelor's Thesis, Hochschule Furtwangen University, Villingen-Shwenningen, Germany, 2021.
18. Institut für Arbeitsschutz der Deutschen Gesetzlichen Unfallversicherung. GESTIS-Stoffdatenbank. Available online: https://gestis.dguv.de/ (accessed on 11 January 2022).
19. European Union, Eurpean Chemicals Agency. Available online: https://echa.europa.eu/de/home (accessed on 11 January 2022).
20. Conti, B.; Maltoni, C.; Perino, G.; Ciliberti, A. Long-term carcinogenicity bioassays on styrene administered by inhalation, ingestion and injection and styrene oxide administered by ingestion in Sprague-Dawley rats, and para-methylstyrene administered by ingestion in Sprague-Dawley rats and Swiss mice. *Ann. N. Y. Acad. Sci.* **1988**, *534*, 203–234. [CrossRef] [PubMed]
21. Linhart, I.; Šmejkal, J.; Mládková, I. Stereochemical aspects of styrene biotransformation. *Toxicol. Lett.* **1998**, *94*, 127–135. [CrossRef]
22. Bundesinstitut für Risikobewertung. *Freisetzung von Melamin und Formaldehyd aus Geschirr und Küchenutensilien*; Bundesinstitut für Risikobewertung: Berlin, Germany, 2011; pp. 1–5.
23. Committee on Acute Exposure Guideline Levels; Committee on Toxicology; Board on Environmental Studies and Toxicology; Division on Earth and Life Studies; National Research Council. *Butane: Acute Exposure Guideline Levels for Selected Airbone Chem*; National Academies Press: Washington, DC, USA, 2012; p. 12. [CrossRef]

processes

MDPI

Article

Selective Adsorption of Pb^{2+} in the Presence of Mg^{2+} by Layer-by-Layer Self-Assembled MnO_2/Mxene Composite Films

Hongjing Qu [1], Jiayan Deng [2], Dan Peng [1], Tong Wei [2], Hang Zhang [2] and Ruichao Peng [2,*]

[1] Central-Southern Safety & Environment Technology Institute Co., Ltd., Wuhan 430051, China; whukobe@126.com (H.Q.); dfdzm@126.com (D.P.)
[2] College of Chemistry & Molecular Sciences, Wuhan University, Wuhan 430072, China; dengjiayan@whu.edu.cn (J.D.); 2018302030048@whu.edu.cn (T.W.); 2018302030049@whu.edu.cn (H.Z.)
* Correspondence: prc@whu.edu.cn

Abstract: A self-assembled MnO_2/Mxene composite film was compounded with MXene nanosheets and layered crystalized MnO_2 nanosheets using surfactant sodium dodecyl sulfate (SDS) as a soft template. The obtained material was characterized by XRD, SEM, XPS, and FT-IR, which showed that the films have large surface-active functional groups and metal ion flow channels, indicating that the MnO_2/Mxene composite films were capable of both the chemical and physical adsorption of the target heavy metal ions. The analysis of adsorption performance showed that the Pb^{2+} removal rate reached 98.3% at pH 6 and an initial Pb^{2+} concentration of 30 mg/L, while the maximum adsorption capacity could reach 1235 μmol/g. In addition, the MnO_2/Mxene composite film had specific selectivity and recyclability. The reuse study verified that the Pb^{2+} removal rate reached 96.4% after five cycles, confirming that the MnO_2/Mxene composite films had practical application prospects.

Keywords: MnO_2/MXene composite film; Pb^{2+} adsorption; selective adsorption

Citation: Qu, H.; Deng, J.; Peng, D.; Wei, T.; Zhang, H.; Peng, R. Selective Adsorption of Pb^{2+} in the Presence of Mg^{2+} by Layer-by-Layer Self-Assembled MnO_2/Mxene Composite Films. *Processes* **2022**, *10*, 641. https://doi.org/10.3390/pr10040641

Academic Editors: Avelino Núñez-Delgado, Zhien Zhang, Elza Bontempi, Mario Coccia, Marco Race and Yaoyu Zhou

Received: 28 February 2022
Accepted: 22 March 2022
Published: 25 March 2022

1. Introduction

The presence of heavy metal ions (e.g., Pb^{2+}, As^{3+}, Cu^{2+}) in water poses a significant threat to human health through food chain transfers due to their toxicity and the tendency for bioaccumulation. Several approaches have been developed and used to remove aqueous heavy metals, such as adsorption, membrane separation, precipitation, ion exchange, photocatalysis, and electrochemical removal [1–5]. These commonly used technologies have some specific advantages as well as some inherent disadvantages. For example, precipitation is very effective and simple to operate, but the process generates a large amount of sludge, leading to secondary pollutants. Membrane separation, ion exchange, and electrochemical removal have the advantages of high efficiency and selectivity. However, they all have very high operation costs, while membrane and ion exchange also make regeneration difficult [6–8]. Of these methods, adsorption is considered one of the most efficient and effective means of removing heavy metal ions; it also has a good tolerance for a wide range of pH values and can be easily operated [9]. Currently, cheap and readily available carbon-based materials are widely used for the adsorption of heavy metal ions [10–12], but their adsorption capacity is not ideal due to the limited specific surface area. Moreover, the adsorption of heavy metal ions is not selective, so that other metal ions can easily interfere in the process owing to competitive adsorption effects.

Metal oxides, especially manganese oxide, show strong adsorption properties for metal ions due to their highly active sites. Their adsorption capacities are higher than carbon-based materials due to physical and chemical adsorption [13–15]. For example, Ma Jun et al. compounded graphene with δ-MnO_2 and used it as an adsorbent to remove Pb^{2+} and Cu^{2+} from water. The maximum adsorption capacity could reach 781 μmol/g and 1620 μmol/g, respectively, where Pb^{2+} and Cu^{2+} could be adsorbed on the surface of the composite and enter the inter-layers of MnO_2 to cause adsorption [12]. Eun-Ju Kim et al. synthesized a

three-dimensional MnO_2 loaded with magnetic Fe_3O_4 by a hydrothermal method, and its maximum adsorption capacity for Cd is 53.2 mg/g. In addition, the adsorption rate for different metal ions follower the order Cu(II) > Pb(II) > Cd(II) > Zn(II) [16]. However, the following problems exist when using manganese oxide as an adsorbent for heavy metal ions, making it a challenge to meet the needs of practical applications. First, the adsorption effect of manganese oxide is often disturbed by other cations in the solution, and the selective adsorption characteristics are not prominent. Second, manganese oxide has good dispersibility, which facilitates adsorption but makes recycling difficult.

MXene is a carbon-based compound with a two-dimensional crystal structure obtained by etching an intermediate metal layer from the MAX phase material. Due to its typical layered structure and rich surface characteristics, MXene shows excellent adsorption properties for heavy metal ions and organic pollutants [17–21]. Unlike other carbon-based adsorbents, MXene can selectively adsorb metal ions from water. For instance, the selective adsorption properties of two-dimensional titanium carbide on Pb^{2+} were investigated by Tian Yongjun et al. Their results showed that the hydroxyl functional group on the surface of titanium carbide gives it excellent selective adsorption properties for Pb^{2+}, even if high concentrations of Mg^{2+} or Ca^{2+} cations existing in the solution [22].

In this paper, a wet-chemistry method was used to synthesize monolayer manganese oxide nanosheets under the induction of surfactants. Moreover, MXene, which is currently on the cutting edge of material science research, was applied to modify and functionalize the MnO_2 nanosheet to tackle the difficulties mentioned above and improve the selectivity and regeneration ability of the absorbent. Therefore, monolayer MnO_2 nanosheets were self-assembled layer by layer with MXene nanosheets to form a self-supporting MnO_2/MXene composite film and then used for the selective adsorption of Pb^{2+}. The adsorption characteristics of the MnO_2/MXene composite film were systematically investigated with various experimental parameters, such as solution pH value, adsorption time, and initial metal ion concentration. Meanwhile, the removal rate of Pb^{2+} over five cycles and the effects of other metal cations on the adsorption properties of Pb^{2+} were also investigated. The results proved that the MnO_2/MXene composite film has a high adsorption capacity and some degree of adsorption selectivity and stability for Pb^{2+}. It also has the advantages of being easy to recycle and reuse.

2. Materials and Methods

2.1. Synthesis of Monolayer Manganese Oxide Nanosheets

Three grams of SDS powder was dissolved in 100 mL of deionized water, magnetically stirred well; then, 1.5 mL of H_2SO_4 was added and stirred to obtain a clear and transparent solution. Afterward, the solution was heated and stirred in an oil bath at 90 °C for 15 min and 0.8 g of $KMnO_4$ powder was added, and the reaction was performed at that temperature for 1 h. Finally, the mixture was cooled and washed with deionized water to remove excess surfactant and freeze-dried to obtain the monolayer MnO_2 nanosheets [23].

2.2. Preparation of MnO_2/MXene Composite Films

Ten milligrams of the above single-layer MnO_2 nanosheets were weighed and dispersed in 100 mL of deionized water; then, 2 mg of commercially available MXene solution was added, and after ultrasonic dispersion for 30 min, vacuum filtration was performed to obtain a MnO_2/MXene composite self-supporting film [24].

2.3. Characterization Test

Field emission scanning electron microscope (SEM, Zeiss SIGMA, Carl Zeiss AG, Jena, Germany), and transmission electron microscope (TEM, JEM-2100, JEOL, Tokyo, Japan) were applied for the morphological characterization of the MnO_2/MXene composite film, while the X-ray diffraction patterns were recorded on the X-ray diffractometer (XRD, XPert Pro, PANalytical Corporation, Malvern, UK) and fully automatic rapid comparison on the Surface area and porosity analyzer (BET, ASAP 2020, McMerritik (Shanghai) In-

strument Co., Ltd., Shanghai, China) The photoelectron spectra were recorded on X-ray photoelectron spectrometer (XPS, ESCALAB 250Xi, Thermo Fisher, Waltham, MA, USA), continuous light source atomic absorption spectrometer (contrAA700, Analytik Jena AG, Thuringia, Germany), while the IR spectra were recorded on a Thermo FT-IR 5700 IR spectrometer (KBr).

2.4. Heavy Metal Ion Adsorption Test

To start, 30 mg/L Pb^{2+} solution was taken as the target heavy metal ion solution, and 12 mg of MnO_2/MXene composite film was weighed and placed in 100 mL of Pb^{2+}-containing solution as the pH value was adjusted from 3 to 7, and adsorption equilibrium was reached by stirring at a low speed at room temperature. Atomic absorption spectrometry was used to measure the changes in the concentration of heavy metal ions (Pb^{2+}) in different pH environments and at different adsorption times, and the adsorption capacity and removal rate were calculated. In addition, the adsorption characteristics of MnO_2/MXene composite films were also investigated when the solution pH was 6 and the initial concentration of Pb^{2+} was from 10 to 90 mg/L to evaluate the influence of different initial concentrations on the adsorption efficiency of the films.

Adsorption capacity was calculated by using the mass balance equation for the adsorption (1):

$$q = \frac{(C_0 - C_e) \times V}{m} \quad (1)$$

In addition, the *removal rate* (%) was calculated from the Equation (2):

$$Removal\ rate(\%) = \frac{(C_0 - C_e) \times 100\%}{C_0} \quad (2)$$

where q is the adsorption capacity (mg/g) at equilibrium, C_0 and C_e are the initial and the equilibrium concentrations (mg/L), respectively, V is the volume (L) of the solution, and m is the mass (g) of the adsorbent used [25].

3. Results

3.1. Morphology and Structure Characterization

Figure 1A–C shows the cross-sectional and surface SEM images of the commercially available MXene solution after filtration. As MXene has a typical two-dimensional nanosheet structure, a layer-by-layer self-assembled film can be formed by suction filtration. What can be seen from Figure 1C is that the surface of MXene still maintains a good nanosheet morphology after suction filtration. Figure 1D–E shows the cross-sectional SEM images of the MnO_2/Mxene composite films, with the self-assembled films obtained by filtration after the addition of MnO_2 nanosheets. In comparison with the cross-sectional figures of the MXene films, it can be seen that the stacking of nanosheets in the MnO_2/MXene composite films is more fluffy; this provides more adsorption sites than the dense MXene films and is more conducive to the flow and adsorption of metal ions between the nanosheet layers. In addition, the cross-sectional surface sweep result of the MnO_2/MXene composite films shows that all the elements can be uniformly distributed in the composite films (as shown in Figure 1F), indicating that MnO_2 and MXene are alternately stacked. In addition, Ti and C were derived from MXene (TiC), Mn and O originated from MnO_2 nanosheets, while K was introduced by the MnO_2 preparation process and was present between the lattice layers of MnO_2, supporting its layered crystal structure and maintaining charge balance.

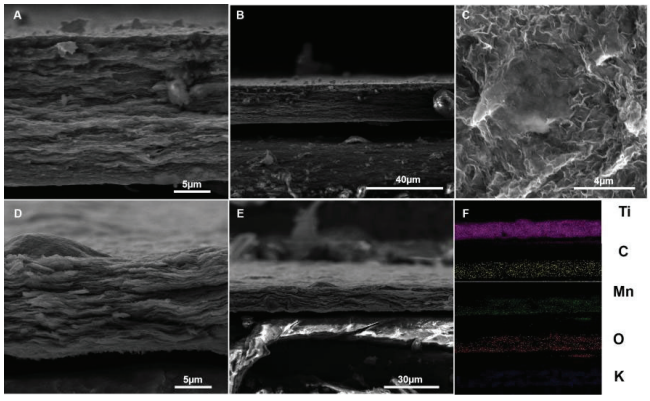

Figure 1. (**A**–**C**) SEM images of the cross-section and surface of the commercially available MXene solution after suction filtration. (**D**,**E**) SEM images of the cross-section of the MnO_2/MXene composite film. (**F**) Element distribution in the MnO_2/MXene composite film.

Figure 2 shows the XRD pattern of the MnO_2/MXene composite film. The peaks at 5.6° and 27.1° are characteristic of 2D Ti_3C_2, where 5.6° corresponds to the crystal plane (002), indicating a layer spacing of 1.56 nm for Ti_3C_2. Similarly, 17.1°, 29.2°, and 36.3° correspond to the characteristic peaks of 2D MnO_2. No characteristic peaks of other heterogeneous phases were observed, indicating that the prepared material was the pure-phase MnO_2/Mxene composite.

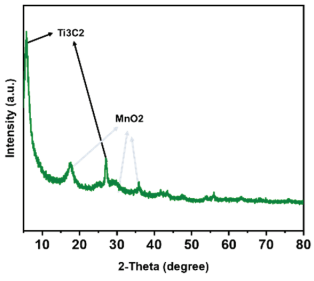

Figure 2. XRD patterns of MnO_2/MXene composite films.

Furthermore, the XPS of the MXene, MnO_2, and MnO_2/MXene composite films were tested to characterize their surface or near-surface valence information. For MXene (Figure 3), it is evident from the XPS pattern that it contains a certain amount of O and F in addition to the elements Ti and C. More specifically, for Ti2p, the characteristic peaks consist of Ti-O-Ti, Ti-OH, and Ti-C, while those of C1s are derived from C impurities introduced during the testing process in addition to Ti-C and C-OH, and the characteristic peaks of O1s consist of Ti-O-Ti, Ti-OH, and C-OH. The above test results indicate that the surface of MXene contains a large amount of surface functional groups, such as C-OH, Ti-OH, and F^-, which are all capable of bonding heavy metal ions in water to achieve efficient adsorption. The surface valence properties of the prepared MnO_2 nanosheets were characterized by XPS, as shown in Figure 4, where the characteristic peak of Mn2p indicates that the surface is composed of Mn^{3+} and Mn^{4+}. The presence of Mn^{3+} makes the surface of MnO_2 negatively charged and causes oxygen defects, which is beneficial for the adsorption of positively charged metal cations in solution to achieve charge balance. The O1s characteristic peak, on the other hand, consists of Mn-O-Mn, Mn-OH, and the adsorbed water on the surface. As shown in Figure 5, after compounding, the MnO_2/Mxene composite film results in the

characteristic peaks of both MXene and MnO_2. Therefore, it has the surface properties of both MXene and MnO_2.

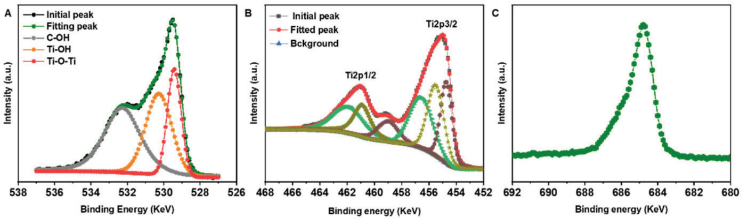

Figure 3. XPS spectra of MXene: (**A**) is O1s, (**B**) is Ti2p, and (**C**) is F1s.

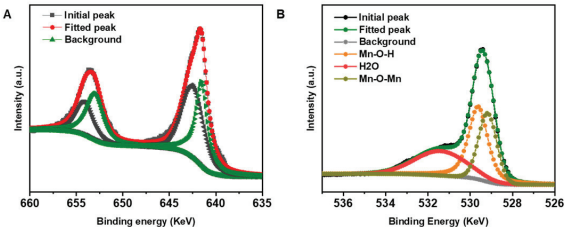

Figure 4. XPS spectrum of MnO_2. (**A**) is Mn2p and (**B**) is O1s.

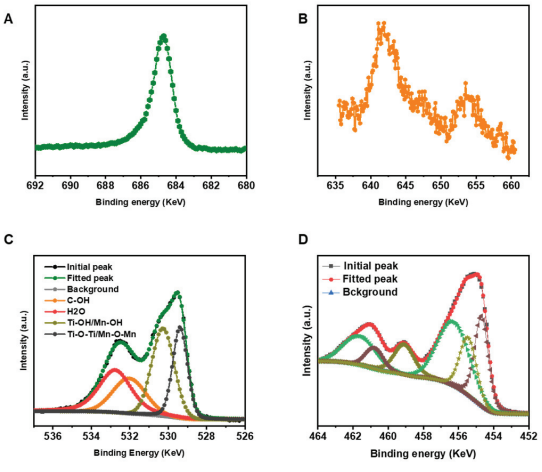

Figure 5. XPS spectrum of MnO_2/MXene composite films: (**A**) is F1s, (**B**) is Mn2p, (**C**) is O1s, and (**D**) is Ti2p.

As shown in the FT-IR spectrum (Figure 6), the wide bands at 1640 and 3292 cm^{-1} in the MnO_2/MXene composite film represents the bending vibration of water molecules and the O-H contraction vibration of water molecules, respectively, while the characteristic peaks of Mn-O and Ti-C are found between 600 and 700 cm^{-1} [26].

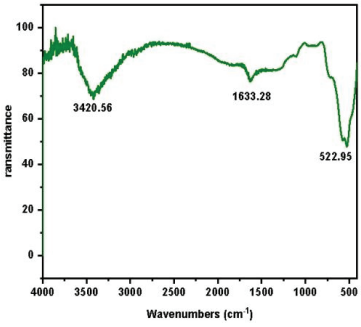

Figure 6. FT-IR spectrum of MnO_2/MXene composite films.

3.2. Study of Adsorption Performance

The above characterizations show that the synthesis of MnO_2 nanosheets using surfactants as soft templates and their composites with MXene nanosheets can self-assemble into thin films, which combines the surface properties of MnO_2 and MXene with abundant surface active sites. In addition, both MnO_2 and MXene are typical two-dimensional crystalline structures with large layer spacing; indeed, the layer spacing of MXene can reach 1.56 nm, which provides more adsorption channels for metal ion adsorption. Moreover, the microscopic morphology of the stacked layers can also provide adsorption channels for metal ions (Figure 7).

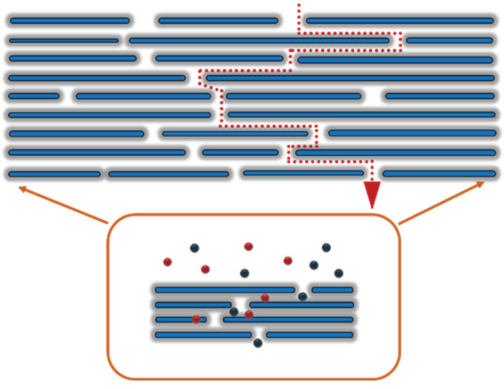

Figure 7. Schematic diagram of adsorption of heavy metal ions by MnO_2/MXene composite film [27].

3.2.1. Effect of pH on Adsorption Performance

Figure 8 shows the adsorption characteristics of the MnO_2/Mxene composite film at different pH values. It can be seen that the MnO_2/Mxene composite film can be used in a wide range of pH solutions, and that the removal rate of Pb^{2+} increases as the pH value rises. The removal rate was 28.3% when the pH was 3 and leveled off at pH 6 (reaching 98.3%), indicating that the pH of the solution has a significant effect on the adsorption of Pb^{2+}. As the surface of the MnO_2/Mxene composite film has abundant -OH groups, the negative charge on its surface increases as the pH value increases. Therefore, at low pH values, the adsorption of Pb^{2+} is low and gradually increases with the increase in pH value as H^+ in solution competes for the adsorption of -OH on the surface of the MnO_2/Mxene composite film.

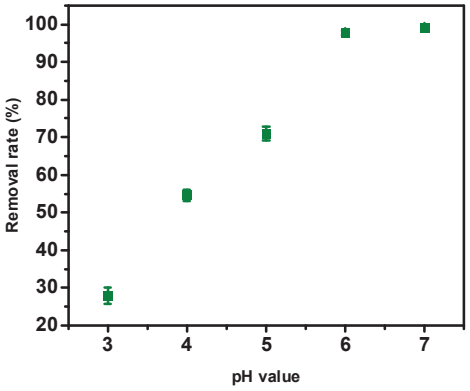

Figure 8. Removal rate of Pb^{2+} under different pH values. (Experimental conditions: MnO_2/Mxene composite films 12 mg, solution volume 100 mL $C_{Pb}{}^{2+}$ = 30 mg/L, 25 °C).

3.2.2. Effect of Adsorption Time on Adsorption Performance

The adsorption kinetics experiments of MnO_2/MXene composite films were investigated when the solution pH was 6 (Figure 9). The removal of Pb^{2+} was only 27.4% within the initial hour. However, the removal increased to 98.3% after 8 h of reaction and reached adsorption equilibrium. Compared to other conventional powder adsorbents, the MnO_2/MXene composite film took longer to reach adsorption saturation due to the lower specific surface area of the MnO_2/MXene composite film, which exposed a smaller amount of metal ions in a short period. However, over time, heavy metal ions were able to flow in the inter-layer channels of the MnO_2/MXene composite film and achieve the adsorption of metal ions. Therefore, although the time to achieve adsorption equilibrium was prolonged, the MnO_2/MXene composite film still had a high Pb^{2+} removal rate. Furthermore, the longer adsorption equilibrium time also indicated that the chemical adsorption mechanism plays a decisive role in the adsorption rate of the reaction during the adsorption of Pb^{2+} by the MnO_2/Mxene composite film.

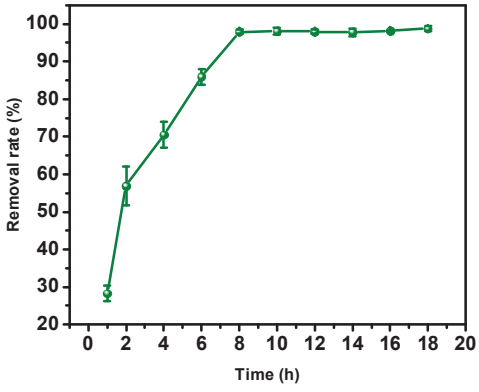

Figure 9. The removal rate of Pb^{2+} at different adsorption times. (Experimental conditions: pH = 6, MnO_2/Mxene composite films 12 mg, solution volume 100 mL, $C_{Pb}{}^{2+}$ = 30 mg/L, 25 °C).

3.2.3. Effect of Initial Concentration on the Adsorption Capacity

Figure 10 explores the effect of the initial concentration on the adsorption capacity when the pH is 6. The MnO_2/MXene composite film adsorption capacity was 401.4 μmol/g when the initial concentration of Pb^{2+} was 10 mg/L and reached 1187 μmol/g at 30 mg/L and 1235 μmol/g at 90 mg/L. As the initial concentration of Pb^{2+} continued to increase,

the adsorption capacity did not increase significantly. The excellent adsorption properties of MnO_2/MXene composite films can be attributed to two factors. First, the -OH, F^- and defects on the surface of the MnO_2/Mxene composite film can act as ligands for metal ions, thus achieving chemical complex adsorption. Second, the MnO_2/Mxene composite film has a layered crystal structure, and its layer spacing and two-dimensional channels formed by layer stacking further provide adsorption sites.

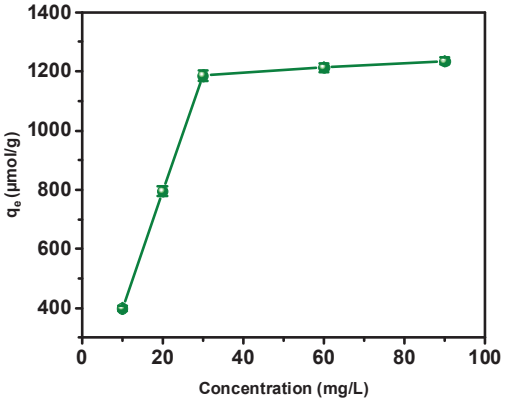

Figure 10. The adsorption capacity of Pb^{2+} under different initial concentrations. (Experimental conditions: pH = 6, MnO_2/Mxene composite films 12 mg, solution volume 100 mL, 25 °C).

3.2.4. Cycling Performance Test of Mno_2/Mxene Composite Film

In addition, MnO_2/Mxene composite films can easily be recycled after use for heavy metal ion adsorption. Compared with traditional powder adsorbents, film-based adsorbents do not possess advantages in terms of adsorption time, but can be easily recycled without causing secondary contamination of water bodies. After the adsorption test, the MnO_2/Mxene composite film was regenerated to verify its recycling characteristics. As shown in Figure 11, the Pb^{2+} removal rate remained at 96.4% after five cycles, and the adsorption performance was only 1.9% lower than the first adsorption, demonstrating the excellent stability of the material to cycling.

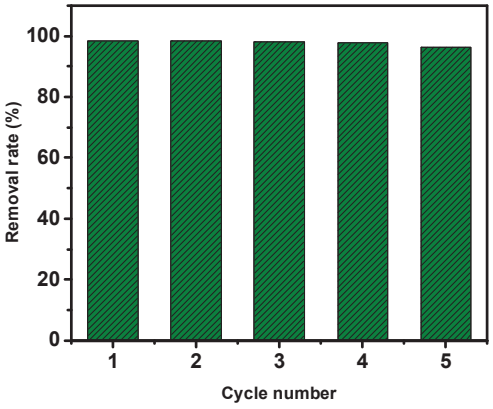

Figure 11. The removal rate of Pb^{2+} during cycling. (Experimental conditions: pH = 6, MnO_2/Mxene composite films 12 mg, solution volume 100 mL $C_{Pb}{}^{2+}$ = 30 mg/L, 25 °C).

3.2.5. The Effect of Other Metal Cations on the Adsorption Performance

Actual industrial wastewater contains large amounts of heavy metal ions and other metal cations, such as Mg^{2+}, Ca^{2+}, and K^{+}. These unavoidable cations can interfere with the adsorption of Pb^{2+} and affect the adsorption capacity. In order to explore the effect of other metal cations on the adsorption performance of Pb^{2+} by MnO_2/Mxene composite films, a mixed solution containing both Mg^{2+} and Pb^{2+} was served as the target solution to determine the adsorption characteristics at different Mg^{2+} contents. The concentration of Pb^{2+} in the fixed mixed solution was 30 mg/L. As shown in Figure 12, the Pb^{2+} removal rate decreased as the concentration of Mg^{2+} increased in the mixed solution. Although the Mg^{2+} content was much larger than that of Pb^{2+}, showing that the MnO_2/Mxene composite film still had excellent adsorption characteristics for Pb^{2+}. For example, when the concentration ratio of Mg^{2+}/Pb^{2+} was 10:1, the removal rate of Pb^{2+} could still reach 61.7%. This result indicated that although there was a certain degree of competition of Mg^{2+} on the adsorption of Pb^{2+}, the MnO_2/MXene composite film retains a selectivity for the adsorption of Pb^{2+}, proving its promising prospects for practical wastewater treatment applications.

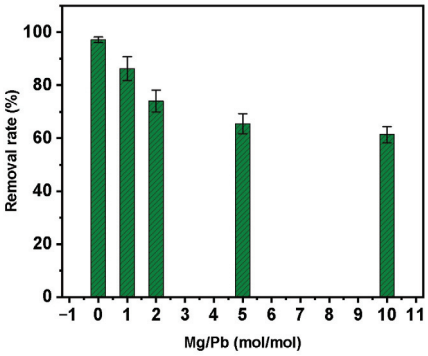

Figure 12. Pb^{2+} removal rate at different concentrations of Mg^{2+}. (Experimental conditions: pH = 6, MnO_2/Mxene composite films 12 mg, solution volume 100 mL, $C_{Pb}{}^{2+}$ = 30 mg/L, 25 °C).

3.2.6. Adsorption Kinetic of MnO_2/Mxene Composite Films

The modeling of adsorption kinetics was conducted by using pseudo-second-order models with linear fitting (Figure 13):

$$\frac{t}{q_t} = \frac{1}{k\,q_e^2} + \frac{1}{q_e}t \tag{3}$$

where k is the pseudo-second-order adsorption rate constant ($g \cdot mmol^{-1} \cdot min^{-1}$); t is the adsorption time, q_e and q_t are the adsorption rate ($mmol \cdot g^{-1}$) at equilibrium and at time t, respectively.

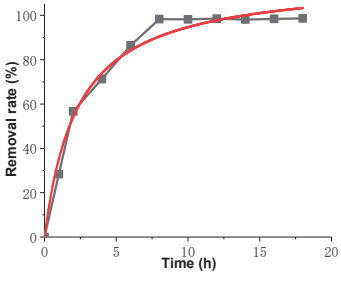

Figure 13. Pseudo-second-order models with linear fitting.

According to the Table 1 and Figure 13, the mechanism of the adsorption contains both physical adsorption and chemical adsorption, and the long adsorption equilibrium time also indicates that the MnO_2/MXene composite film on Pb^{2+} is the chemical adsorption mechanism plays a decisive role in the adsorption rate of the reaction.

Table 1. Kinetic parameters for the pseudo-second-order models for the adsorption.

q_e	k	R^2
116.53	0.433	0.98462

3.2.7. Comparison of Various MnO_2-Based Adsorbents for Pb(II)

The comparison of the maximum adsorption capacities of the obtained MnO_2/MXene composite films and various MnO_2-based adsorbents for Pb^{2+} is listed in Table 2, which shows that the MnO_2/MXene composite films might be an ideal adsorbent for aqueous Pb(II).

Table 2. Comparison of the maximum adsorption capacities of various MnO_2-based adsorbents for Pb(II).

Adsorbent	Adsorption Capacity (mg/g)	Reference
ε-MnO_2 nanoflowers	239.7	[28]
g-C_3N_4/MnO_2 composite	204	[29]
α-MnO_2	124.87	[25]
MnO_2 modified magnetic graphitic carbon nitride composite	187.6	[30]
graphene nanosheet/δ-MnO_2	781 μmol/g (161.6 mg/g)	[27]
MnO_2/MXene composite films	1235 μmol/g (255.6 mg/g)	This work

4. Conclusions

In this paper, the MnO_2/Mxene composite films were prepared by a layer-by-layer self-assembly process using SDS as a soft template and applied to the adsorption of Pb^{2+} in water. The effects of solution pH, adsorption time, initial concentration, and impurity ions on the adsorption of Pb^{2+} were investigated.

(1) The pH value of the solution, adsorption time, and initial concentration all significantly affect the adsorption of Pb^{2+}. The removal of Pb^{2+} by the MnO_2/Mxene composite film reached 98.3% at pH 6 and reached adsorption equilibrium at 8 h. Increasing the content of Pb^{2+} in the initial solution can enhance the adsorption capacity of the MnO_2/Mxene composite film, which reached 1235 μmol/g when the initial concentration of Pb^{2+} was 90 mg/L.

(2) The MnO_2/MXene composite film has a particular selectivity for Pb^{2+} adsorption, and the removal rate of Pb^{2+} can still reach 61.7% in the solution with high Mg^{2+} content (Mg^{2+}/Pb^{2+} = 10:1).

(3) The MnO_2/Mxene composite film has the property of easy recovery; after five cycles of testing, its Pb^{2+} removal rate can still reach 96.4%.

(4) The process of Pb^{2+} adsorption of by the MnO_2/Mxene composite film is consistent with the pseudo-second-order models.

Author Contributions: H.Q.; writing—original draft preparation, J.D.; writing—review and editing, D.P.; investigation; T.W.; investigation; H.Z.; investigation; R.P.; supervision. All authors have read and agreed to the published version of the manuscript.

Funding: This research received no external funding.

Conflicts of Interest: The authors declare no conflict of interest.

References

1. Sunil, K.; Karunakaran, G.; Yadav, S.; Padaki, M.; Zadorozhnyy, V.; Pai, R.K. Al-Ti_2O_6 a mixed metal oxide based composite membrane: A unique membrane for removal of heavy metals. *Chem. Eng. J.* **2018**, *348*, 678–684. [CrossRef]
2. Xu, L.; Wang, T.; Wang, J.; Lu, A. Occurrence, speciation and transportation of heavy metals in 9 coastal rivers from watershed of Laizhou Bay, China. *Chemosphere* **2017**, *173*, e61–e68. [CrossRef] [PubMed]
3. Xu, Y.; Zhang, C.; Zhao, M.; Rong, H.; Zhang, K.; Chen, Q. Comparison of bioleaching and electrokinetic remediation processes for removal of heavy metals from wastewater treatment sludge. *Chemosphere* **2017**, *168*, e1152–e1157. [CrossRef]
4. Sounthararajah, D.P.; Loganathan, P.; Kandasamy, J.; Vigneswaran, S. Removing heavy metals using permeable pavement system with a titanate nano-fibrous adsorbent column as a post treatment. *Chemosphere* **2017**, *168*, e467–e473. [CrossRef] [PubMed]
5. Tag El-Din, A.F.; El-Khouly, M.E.; Elshehy, E.A.; Atia, A.A.; El-Said, W.A. Cellulose acetate assisted synthesis of worm-shaped mesopores of MgP ionexchanger for cesium ions removal from seawater. *Microporous Mesoporous Mater.* **2018**, *265*, 211–218. [CrossRef]
6. Barakat, M.A. New trends in removing heavy metals from industrial wastewater. *Arab. J. Chem.* **2011**, *4*, 361–377. [CrossRef]
7. Nguyen, T.A.H.; Ngo, H.H.; Guo, W.S.; Zhang, J.; Liang, S.; Yue, Q.Y.; Li, Q.; Nguyen, T.V. Applicability of agricultural waste and byproducts for adsorptive removal of heavy metals from wastewater. *Bioresour. Technol.* **2013**, *148*, 574–585. [CrossRef]
8. Xu, J.; Cao, Z.; Zhang, Y.L.; Yuan, Z.L.; Lou, Z.M.; Xu, X.H.; Wang, X.K. A review of functionalized carbon nanotubes and graphene for heavy metal adsorption from water: Preparation, application, and mechanism. *Chemosphere* **2018**, *195*, 351–364. [CrossRef]
9. Sarma, G.K.; Sen Gupta, S.; Bhattacharyya, K.G. Nanomaterials as versatile adsorbents for heavy metal ions in water: A review. *Environ. Sci. Pollut. Res.* **2019**, *26*, 6245–6278. [CrossRef]
10. Yao, H.; Zhang, X.F.; Hu, Z.H. The advantages of Shanglu biochar for Pb ion adsorption. *J. Shihezi Univ. (Nat. Sci.)* **2021**, *39*, 668–673.
11. Zhai, F.J.; Zhang, C.; Song, G.F.; Jiang, S.X.; Shan, B.Q.; Song, Z.X. The adsorption mechanism of kapok biochar on Cr(VI) in aqueous solution. *Acta Sci. Circumstantiae* **2021**, *41*, 1891–1900.
12. Wei, Z.P.; Zhu, Y.L.; Zhao, C.T.; Tang, J.X.; Gao, Y.X.; Li, M.X. Research Advances on Biochar Adsorption Mechanism for Heavy Metals and its Application Technology. *Chin. J. Soil Sci.* **2020**, *51*, 741–747.
13. Peng, R.C.; Li, H.; Chen, Y.T.; Ren, F.P.; Tian, F.Y.; Gu, Y.W.; Zhang, H.L.; Huang, X.R. Highly efficient and selectivity removal of heavy metal ions using single-layer $Na_xK_yMnO_2$ nanosheet: A combination of experimental and theoretical study. *Chemosphere* **2021**, *275*, 130068. [CrossRef]
14. Song, Y.Q.; Tan, Q.; Lin, B.Y.; Liao, L.; Zeng, C.; He, Z.Z.; Lin, B.Y.; Qiu, W.M. Controllable synthesis of MnO_2 with different crystal structures and their adsorption activity for heavy metals. *Inorg. Chem. Ind.* **2018**, *50*, 40–42, 53.
15. Peng, Q.; Guo, J.X.; Zhang, Q.R.; Xiang, J.Y.; Liu, B.Z.; Zhou, A.G.; Liu, R.P.; Tian, Y.J. Unique Lead Adsorption Behavior of Activated Hydroxyl Group in Two-Dimensional Titanium Carbide. *J. Am. Chem. Soc.* **2014**, *136*, 4113–4116. [CrossRef]
16. Ma, C.X.; Huangfu, X.L.; Ma, J.; Huang, R.X.; He, Q.; Liu, C.H.; Zhou, J.; Jiang, J.; Zhu, Y.Y.; Huang, M.H. Deposition Kinetics of Nanosized Manganese Dioxide in Presence of Divalent Cations. *China Water Wastewater* **2018**, *34*, 31–35.
17. Kim, E.J.; Lee, C.S.; Chang, Y.Y.; Chang, Y.S. Hierarchically Structured Manganese Oxide-Coated Magnetic Nanocomposites for the Efficient Removal of Heavy Metal Ions from Aqueous Systems. *ACS Appl. Mater. Interfaces* **2013**, *5*, 9628–9634. [CrossRef] [PubMed]
18. Zhang, W.J.; Kou, M. Applications of two dimensional material MXene in water treatment. *J. Mater. Eng.* **2021**, *49*, 14–26.
19. Hou, J.H.; Yang, M.Y.; Sun, A.; Cao, C.B. Application of MXenes and their composite materials in the field of environment. *Fine. Chemicals.* **2021**, *38*, 2422–2431.
20. Fan, M.; Wang, L.; Zhang, Y.J.; Pei, C.; Chai, Z.; Shi, W. Research progress of MXene materials in radioactive element and heavy metal ion sequestration. *Sci. Sin. Chim.* **2019**, *49*, 27–38. [CrossRef]
21. Leng, Y.Y.; Zhang, S.Y.; Zong, X.X.; Li, Y.F. Research Progress on New Low Dimensional Materials MXene. *Chem. Adhes.* **2016**, *38*, 450–454.
22. Wan, H.; Nan, L.; Geng, H.; Zhang, W.; Shi, H. Green Synthesis of A Novel MXene–CS Composite Applied in Treatment of Cr(VI) Contaminated Aqueous Solution. *Processes* **2021**, *9*, 524. [CrossRef]
23. Liu, Z.; Xu, K.; Sun, H.; Yin, S. One-Step Synthesis of Single-Layer MnO_2 Nanosheets with Multi-Role Sodium Dodecyl Sulfate for High-Performance Pseudocapacitors. *Small* **2015**, *11*, 2182–2191. [CrossRef]
24. Chen, S.; Xiang, Y.; Xu, W.; Peng, C. A novel MnO_2/MXene composite prepared by electrostatic self-assembly and its use as an electrode for enhanced supercapacitive performance. *Inorg. Chem. Front.* **2019**, *6*, 199–208. [CrossRef]
25. Dinh, V.P.; Le, N.C.; Nguyen, T.P.; Nguyen, N.T. Synthesis of α-MnO_2 Nanomaterial from a Precursor γ-MnO_2: Characterization and Comparative Adsorption of Pb(II) and Fe(III). *J. Chem.* **2016**, *2016*, 8285717. [CrossRef]
26. Zhao, Q.N.; Li, X.L.; Zhu, J.F.; Jiao, H.Y.; Huang, J.X. Manganese Dioxide Morphology on Electrochemical Performance of $Ti_3C_2T_X$@MnO_2 Composites. *J. Inorg. Mater.* **2020**, *35*, 119–125. [CrossRef]
27. Ren, Y.; Yan, N.; Feng, J.; Ma, J.; Wen, Q.; Li, N.; Dong, Q. Adsorption mechanism of copper and lead ions onto graphene nanosheet/δ-MnO_2. *Mater. Chem. Phys.* **2012**, *136*, 538–544. [CrossRef]
28. Lin, M.; Chen, Z. A facile one-step synthesized epsilon-MnO_2 nanoflowers for effective removal of lead ions from wastewater. *Chemosphere* **2020**, *250*, 126329. [CrossRef]

29. Guo, J.; Chen, T.; Zhou, X.; Zheng, T.; Xia, W.; Zhong, C.; Liu, Y. Preparation and Pb (II) adsorption in aqueous of 2D/2D g-C_3N_4/MnO_2 composite. *Appl. Organomet. Chem.* **2019**, *33*, e5119. [CrossRef]
30. Xia, W.; Liu, Y. Preparation of MnO_2 modified magnetic graphitic carbon nitride composite and its adsorption toward Pb(II) in waste water. *Water Pract. Technol.* **2021**, *16*, 1498–1509. [CrossRef]

processes

MDPI

Article

Leaching Kinetics of Aluminum from Alkali-Fused Spent Cathode Carbon Using Hydrochloric Acid and Sodium Fluoride

Jie Yuan *, Huijin Li and Shuang Ding

School of Chemistry and Materials Engineering, Liupanshui Normal University, Liupanshui 553004, China; xihu1101@126.com (H.L.); xiaoxiangzi0927@163.com (S.D.)
* Correspondence: yuanjieedu@163.com

Abstract: Abundant carbon resides in spent cathode carbon (SCC) of aluminum electrolysis and its high-purity carbon powder is conducive to high-value recycling. The alkali-fused SCC was separated and effectively purified using an HCl/NaF solution. Effects of particle size, leaching temperature, time, initial acid concentration, and sodium fluoride dosage, on the purity of carbon powder and aluminum removal rate, were investigated. Using aluminum as the research object, kinetics of aluminum acid leaching were examined by single-factor experiments. Results showed that under an initial 4 M HCl concentration, particle size D(50) = 67.49 μm, liquid-solid ratio of 15:1, 333 K, 120 min, 0.3 M NaF, carbon powder with ash level below 1% were obtained in subsequent purification of SCC. The leaching process was described by Avram equation, the model characteristic parameter was 0.75147 and the apparent activation energy was 22.056 kJ/mol, which indicated a mixed control mechanism between chemical reactivity and diffusion. The kinetic reaction equation of leaching aluminum from alkali-fused SCC in a mixed HCl/NaF system was established.

Keywords: spent cathode carbon of aluminum electrolysis; acid leaching; kinetics; Avrami equation

Citation: Yuan, J.; Li, H.; Ding, S. Leaching Kinetics of Aluminum from Alkali-Fused Spent Cathode Carbon Using Hydrochloric Acid and Sodium Fluoride. *Processes* **2022**, *10*, 849. https://doi.org/10.3390/pr10050849

Academic Editor: George Z. Kyzas and Guining Lu

Received: 22 March 2022
Accepted: 21 April 2022
Published: 25 April 2022

1. Introduction

Aluminum is an indispensable nonferrous metal critical for national economic development. Electrolysis of molten salt produces elemental aluminum via the Hall–Héroult process [1]. As the primary component of a reduction cell, carbon cathode used during aluminum electrolysis is prepared by anthracite, asphalt coke, natural and artificial graphite, roasted at high temperature. Cracks and corrosion pits form as the cathodic carbon block corrodes due to high-temperature liquid metal, molten alkaline electrolyte, and metallic sodium. High-temperature melt in the cell permeates the crevices and pits, which results in efficacy losses at the carbon cathode [2,3]. Additionally, secondary products (NaF, NaCN, β-Al_2O_3, etc.) occur via reactions between air and chemical species (sodium, aluminum, cryolite, etc.) attached to the cathode surface or crevices at high temperatures [4], which further aggravate carbon cathode failure. Generally, the electrolytic cell requires an overhaul and replacement of the cathode every 3–10 years [5]. Spent cathodic carbon is solid waste produced from electrolytic cell overhaul. In addition to large amounts of carbon [6](about 60~80 wt%), sodium fluoride (NaF), cryolite, and alumina removed during conventional alkali or acid leaching, there are some intractable non-carbon components such as complex aluminates and aluminosilicates in SCC from aluminum reduction cells. Non-carbon impurities primarily involve the high-temperature reaction products of alumina, cryolite, and silicon dioxide. These impurities make it difficult to improve the purity of carbon powder recovered from SCC, which is not conducive to high-value utilization of carbon powder [7].

Traditionally, comprehensive treatment of SCC from aluminum electrolysis focused on flotation [8], the pyrometallurgy process [9], and hydrometallurgical processes [10]. SCC is used as a fuel substitute in the cement [11] and nonferrous metallurgy industries [12]; however, despite utilizing the combustion characteristics of carbon, high-purity carbon

was not obtained. The thermal behavior of fluorides and cyanides in SCC was studied based on a TG/DSC-MS system by Li [13], who reported that fluorides were volatilized, and cyanides decomposed at high temperature, so non-hazardous treatment of SCC was conducted. Yao [14] purified SCC via NaOH-Na_2CO_3 binary molten salt roasting and water leaching and obtained a treated carbon purity of 96.98%. Leaching is a common hydrometallurgical method, and SCC treated by hydrothermal acid-leaching resulted in an aluminum leaching rate of ~80% under optimal conditions. The removal rates of impurities were not perfect, but the novel idea of silicon carbide preparation with hydrothermal acid leached coal gangue, and the waste cathode was reported [15].

A three-step process separated cryolite from SCC [16] via leaching with acidic anodizing wastewater, and a valuable, high-purity carbon (95.5%), was obtained. Lisbona [17] obtained carbon powder (purity ~95%) in various solutions. Defluorination of SCC was researched in an acidic iron-containing solution [18]. Low caustic leaching and liming (LCL&L) process developed by Rio Tinto Aluminum [19] is a typical method for SCC treatment. These conventional processes can remove some impurities from SCC; however, the carbon powder purities obtained were unsatisfying. Moreover, valuable carbonaceous materials were unrecoverable via pyrometallurgical techniques and new solid waste by-product residues were produced. Hydrometallurgy treatments are complex, produce low purity carbon powder, and novel, undesirable by-products. Recently, vacuum distillation, high-temperature graphitization, and others that improve carbon powder purity have been reported. For example, Xie [20] treated SCC in a joint controlling temperature-vacuum process, and optimized conditions produced a carbon purity of 97.89%. Wang [21] separated and recovered SCC by vacuum distillation. Cryolite, NaF, and sodium were separated effectively. At 1200 °C, the separation rate exceeded 80%, and the carbon powder purity > 91%. Patent CN108050848b [22] discloses a high-temperature continuous electric calcining furnace. It treats 2–50 mm of SCC particles at a feed rate of 500–600 kg/h to produce graphite with a fixed carbon content of >98%. Limited to high energy consumption and high-temperature resistant equipment, these technologies are difficult to apply in large-scale industrial treatment. Therefore, there is a strong incentive to investigate the deep purification process of spent cathode carbon.

In this study, SCC pretreated by sodium hydroxide alkali fusion was purified by a mixture of hydrochloric acid and NaF to remove acid-soluble inorganic impurities. Effects of initial acid concentration, reaction temperature, and NaF addition on the purification were studied. An acid leaching impurity and aluminum removal models were established based on a previous experimental procedure, and its apparent activation energy was calculated to clarify the leaching mechanism of impurities in a mixed acid solution.

2. Materials and Methods

2.1. Materials

SCC used in the work was discharged from an electrolytic aluminum plant in China. After crushing and grinding, the powder at different particle sizes was dried in an oven at 105 °C for 24 h to remove water. Sodium hydroxide, hydrochloric acid, and NaF were of analytical purity and obtained from Sinopharm Chemical Reagent Co., Ltd. (Beijing, China).

2.2. Procedure

Dried SCC, sodium hydroxide, and deionized water were mixed, stirred into a paste, and soaked for an additional 2 h. The mixture was loaded into a corundum crucible. After water evaporation, the powder was kept at 550 °C for 3 h under a nitrogen (99.99%) atmosphere in a muffle furnace (TF1200-100, Kejing Material Technology Co., Ltd.,Hefei, China, ~1200 °C). The sample was cooled, washed, and dried with deionized water until the filtrate was neutral. The final analysis and mineral content of the alkali-fusion treated powder are listed in Table 1 and Figures 1 and 2.

Table 1. Ultimate analysis of untreated and alkali-fused SCC/%.

Element		C	F	Na	Al	Ca	Si	O	Others
content	untreated	61.06	14.37	8.71	7.09	1.35	0.43	5.47	1.52
	treated	93.26	0.74	0.48	1.46	2.38	0.57	0.73	0.38

Figure 1. SCC after alkali fusion treatment.

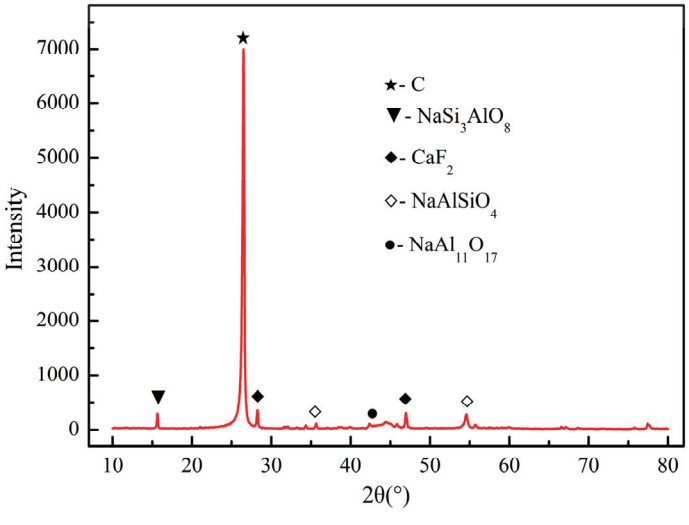

Figure 2. XRD pattern of alkali-fused SCC.

The alkali-fusion treated carbon powder was leached in a solution of hydrochloric acid and NaF. Leaching took place in a plastic beaker at constant temperature. Experimental

factors such as leaching temperature (303~333 K), time (~120 min), initial hydrochloric acid concentration (1~4 M), and NaF addition (0.1~0.4 M) on the ash levels of the leaching residue and aluminum leaching rate were investigated.

After alkali fusion and acid leaching, the powder was dried in a blast drying oven at 105 °C for 24 h, followed by ash content detection. To improve test efficiency and reduce experiment complexity, the ash content was expressed by the residual amount of purified carbon powder upon combustion at 800 °C in air for 4 h. Ash levels were calculated using Equation (1).

$$\eta_a = m_a / m_s \times 100\% \quad (1)$$

where η_a is the ash content of purified SCC, (%) m_a is the ash mass of purified SCC heated at 800 °C in the air for 4 h, g; m_s is the mass of purified SCC combusted at 800 °C in air for 4 h, g.

The aluminum leaching rate was calculated using Equation (2).

$$\eta_A = (C_{A0} - C_A)/C_{A0} \times 100\% \quad (2)$$

where η_A is aluminum leaching rate, %; C_{A0} is the aluminum content in alkali fused SCC, %; C_A is the aluminum level of SCC after alkali fusion and acid leaching, %.

2.3. Characterization

SCC was analyzed by X-ray fluorescence spectrometry (XRF). Carbon levels were determined by elemental analysis (EA, Vario E1 III, Elementar Company, Hanau, Germany) before XRF analysis. The samples with certain carbon, volatile matter, and moisture levels were burned in a muffle furnace at 800 °C for 4 h, followed by XRF analysis of the ash. Element levels were calculated from previous analysis results. Sample phases were detected by X-ray diffraction (XRD, Riguka D/max 2500 X-ray diffractometer, Japan Electronics Co., Ltd., Tokyo, Japan). Solid materials were broken into—200 mesh powder and dried at 105 °C for 12 h. Phase and microcrystalline structures were analyzed by XRD using a working voltage of 40 mV and a 100-mA current; Cu irradiation (Kα) was used at a step size of 10°/min from 10° to 80°. Scanning electron microscope analysis (SEM) and energy dispersive spectrometer analysis (EDS) were synchronous instruments in this study. A JSM-6360 LV scanning electron microscope made by Japan Electronics Co., Ltd. observed and analyzed the micro morphologies of the solid materials. EDS analysis was performed using an EDX-QENESIS 60S X-ray spectrometer (EDAX company, Philadelphia, PA, USA). A laser particle size analyzer (MS2000, Malvern, UK) was used for solid particle size analysis. Alcohol was the diffusing agent and the refractive index referenced to graphite.

3. Results and Discussion

3.1. Characterization and Analysis

SCC subjected to alkali-fusion treatment is illustrated in Figure 1; the carbon powder was fluffy and expansive. Results of the complete analysis and phase characterization of carbon residue from alkali fused and washed SCC powder are given in Table 1 and Figure 2, respectively. Those results show the alkali fused residue contains some products soluble in strong acids and is consistent with initial exploratory experiments. From SCC purification results previously reported [23] and impurity reactivity in alkali fusion, there were three kinds of inorganic impurities in the alkali-fused carbon powder. The first type was unreacted hydroxide M(OH)x and oxide M_2O_x (M was element Al, Fe, Mg, Ca, etc.) compounds. The second type included inorganics like calcium fluoride and complex aluminosilicates that do not react during alkali leaching. The last group includes products such as Na_2SiO_3, SiO_2, and $NaAlO_2$. Because they comprised less than 5 wt.%, inorganic impurities are not displayed in the XRD pattern accurately and comprehensively.

3.2. Thermodynamic Calculations

To improve the purity of carbon powder after alkali fusion treatment, a mixed solution of hydrochloric and hydrofluoric acids was used to leach the residue even further, according to types and properties of complex inorganics existing in alkali fused SCC powder. The possible reactions in acid leaching process are expressed in Equations (3)–(17). Figure 3 shows the relationship of ΔG vs. T during acid leaching, as calculated using HSC-Chemistry 6.0 (Outotec).

$$Fe(OH)_3 + 3HCl = FeCl_3 + 3H_2O \quad (3)$$

$$Al(OH)_3 + 3HCl = AlCl_3 + 3H_2O \quad (4)$$

$$Mg(OH)_2 + 2HCl = MgCl_2 + 2H_2O \quad (5)$$

$$Ca(OH)_2 + 2HCl = CaCl_2 + 2H_2O \quad (6)$$

$$Fe_2O_3 + 6HCl = 2FeCl_3 + 3H_2O \quad (7)$$

$$Al_2O_3 + 6HCl = 2AlCl_3 + 3H_2O \quad (8)$$

$$MgO + 2HCl = MgCl_2 + H_2O \quad (9)$$

$$CaO + 2HCl = CaCl_2 + H_2O \quad (10)$$

$$CaF_2 + 2HCl = CaCl_2 + 2HF \quad (11)$$

$$NaAlSiO_4 + 4HCl = NaCl + AlCl_3 + SiO_2 + 2H_2O \quad (12)$$

$$SiO_2 + 6HF = H_2SiF_6 + 2H_2O \quad (13)$$

$$CaSiO_3 + 6HF + SiO_2 = CaSiF_6 + 2H_2O \quad (14)$$

$$H_2SiO_3 + 4HF = SiF_4(g) + H_2O \quad (15)$$

$$Na_2SiO_3 + 2HCl = 2NaCl + H_2SiO_3 \quad (16)$$

$$CaSiF_6 + HCl = H_2SiF_6 + CaCl_2 \quad (17)$$

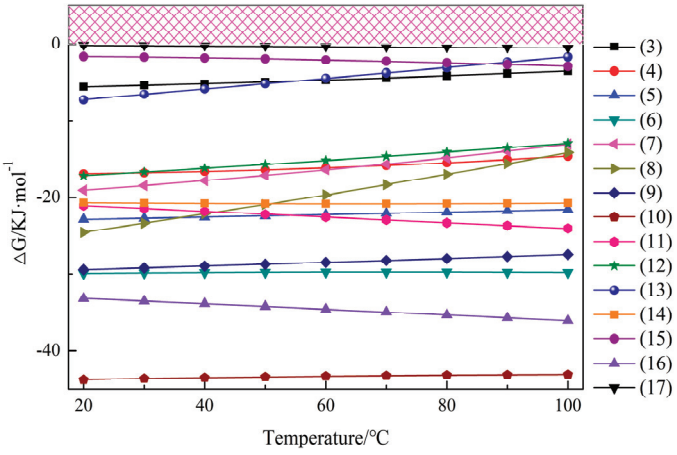

Figure 3. Relationship of functions' ΔG vs. T in acid leaching process.

Thermodynamic calculation results in Figure 3 show the possible chemical reactions of inorganic impurities in alkali-fused carbon powder in hydrochloric acid and NaF mixed solution are thermodynamically feasible and reasonable. From 20−100 °C, acid leaching reactions are relatively simple; the products primarily contain water-soluble compounds or gaseous substances such as SiF_4. Thermodynamic analysis results provide theoretical

support for the effective removal of impurities in alkali-fused carbon powder in the mixed acid solution.

3.3. Effect of Experimental Factors on Leaching Efficiency

3.3.1. Particle Size

Dried SCC powders with different particle sizes [−10~+60 mesh (D(50) = 304.36 μm), −60~+100 mesh (D(50) = 175.49 μm), −100~+200 mesh (D(50) = 94.56 μm), −200 mesh (D(50) = 55.51 μm)] were subjected to alkali fusion and mixed acid leaching for deep purification according to the experimental procedures outlined in Section 2.2. Experimental conditions of acid leaching were as follows: initial hydrochloric acid concentration of 4 M, liquid-solid ratio of 15:1 (constant), 333 K, and 0.3 M NaF. Effects of raw material particle size on carbon level in the purified powder and extraction rate of elemental aluminum during acid leaching were investigated. Figure 4 shows those experimental results.

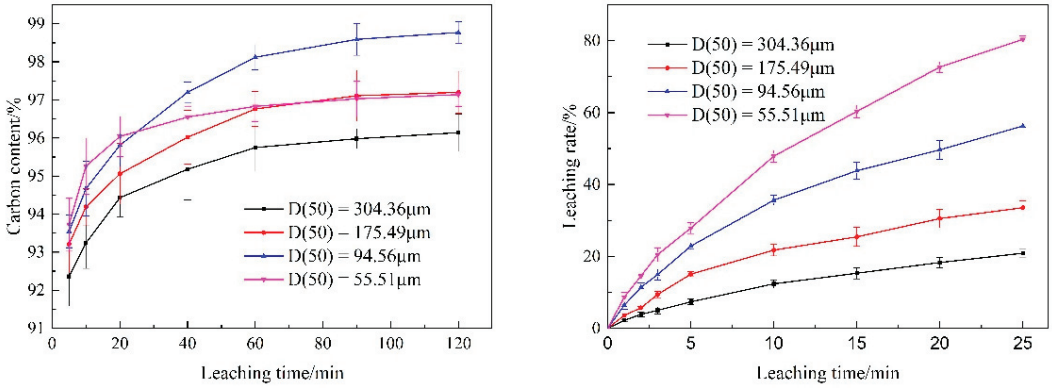

Figure 4. Effect of particle size on carbon content (**left**) and Al leching rate (**right**) (initial HCl concentration 4 mol/L, 333 K, NaF dosage 0.3 mol/L).

Sample particle size has a clear influence on the separation and leaching behavior of inorganic impurities. Smaller particle sizes correspond with faster reaction rates [24]. Higher impurity decomposition rates correspond to higher carbon powder purity and aluminum removal for leaching time less than 25 min. The highest purity was obtained from purification of −100 to +200 mesh (D(50) = 94.56 μm) raw materials at time above 60 min. The reason was that large particle size inorganic impurities were not exposed sufficiently, and impurities were readily trapped by carbon and lowered the acid reaction rate. When particle size was <200 mesh, according to the previous analysis [25], more impurities would disperse into the SCC powder. Therefore, considering experimental convenience and energy consumption, −100 mesh (D(50) = 67.49 μm) was the optimal particle size.

3.3.2. Initial HCl Concentration

Figure 5 shows the effect of initial hydrochloric acid concentration on carbon powder purification after sodium hydroxide fusion treatment. Inorganic impurities in the alkali-fused SCC were effectively separated and removed in acid solution. The purity of carbon powder increased with the initial HCl concentrations, and the leaching rate of element aluminum also rose. At an initial concentration of 1 M, carbon powder purity increased from 92.41% after 5 min to 98.08% after 120 min, and aluminum leaching rate rose from 4.39% after 1 min to 49.61% after 25 min. At 4 M, carbon powder purity increased from 94.32% after 5 min to 98.81% after 120 min, and the aluminum leaching rate rose from 18.57% after 1 min to 81.06% after 25 min. Increasing the initial HCl concentration improved both carbon powder purity and aluminum leaching rate.

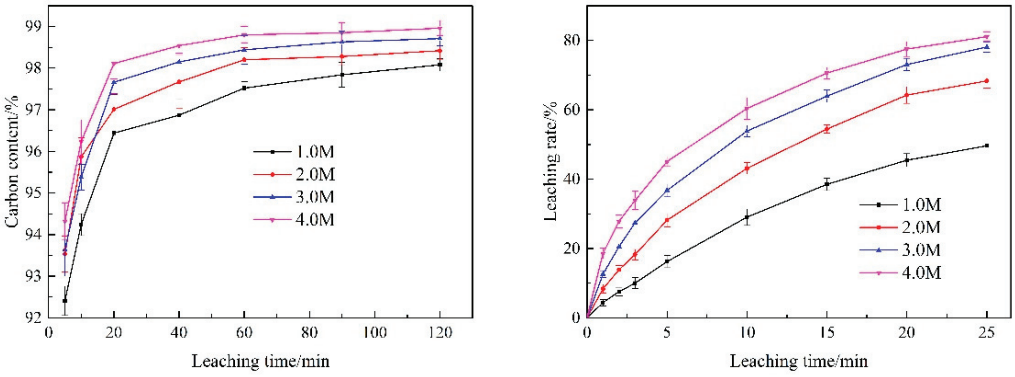

Figure 5. Effect of initial HCl concentration on carbon content (**left**) and Al leching rate (**right**) (particle size D(50) = 67.49 μm, 333 K, NaF 0.3 mol/L).

3.3.3. Temperature

Temperature played an important role in removing impurities by acid leaching [26]. The effects of acid leaching temperature on the carbon content of purified SCC and the aluminum removal rate were tested, and the results are illustrated in Figure 6. The purification efficiency of SCC increased with the gradual increase of reaction temperature. Carbon powders with purities > 98.9% and an aluminum leaching rate of 81.08% were obtained at temperatures above 333 K. Impurities in alkali fused and the washed carbon powder mainly included calcium fluoride and complex aluminosilicates. Calcium fluoride dissolves in acidic solutions, and aluminosilicate minerals react with acid to produce silicic acid and other substances. When temperature was above 323 k and leaching time was longer than 60 min, acid leaching temperature changes had little effect on impurity removal. There was an experimental phenomenon in which carbon content of the leaching residue decreased slightly at higher temperatures, primarily due to the increased volatility of hydrochloric acid caused by high temperatures. Volatilization by heating not only causes environmental pollution, but also reduces the acid concentration, which slightly impacts removal efficacy. Therefore, the optimal temperature of 60 °C was used.

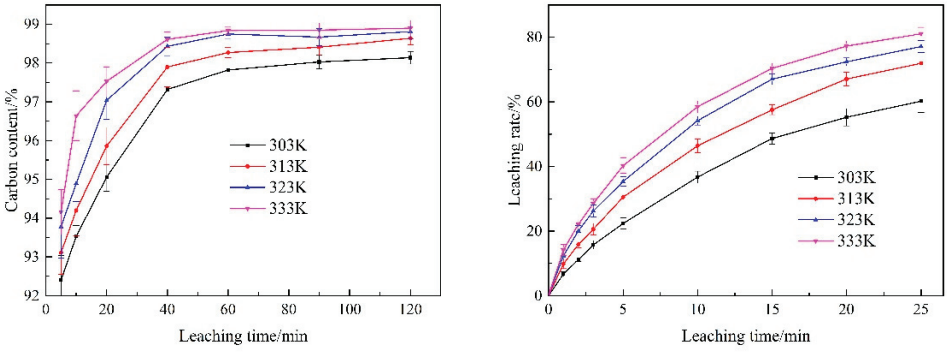

Figure 6. Effect of temperature on carbon content (**left**) and Al leching rate (**right**) (initial HCl concentration 4 mol/L, particle size D(50) = 67.49 μm, NaF 0.3 mol/L).

3.3.4. Sodium Fluoride Addition

As shown in Figure 7, carbon in the leaching residue increased significantly with added NaF in the acid leaching solution. The carbon levels increased in 20 min as NaF addition grew from 0.1–0.3 M, the corresponding purity increased from 97.12% to 97.99%. Increasing

the NaF dosage to 0.4 M increased the purity to 98.14% before trending downward. At an NaF concentration of 0.3 mol/L, the purity of purified carbon powder increased from 93.85% after 5 min to 98.92% after 120 min. NaF levels positively impacted the separation of inorganic impurities. With added NaF, hydrofluoric acid concentrations increased, which improved impurity removal.

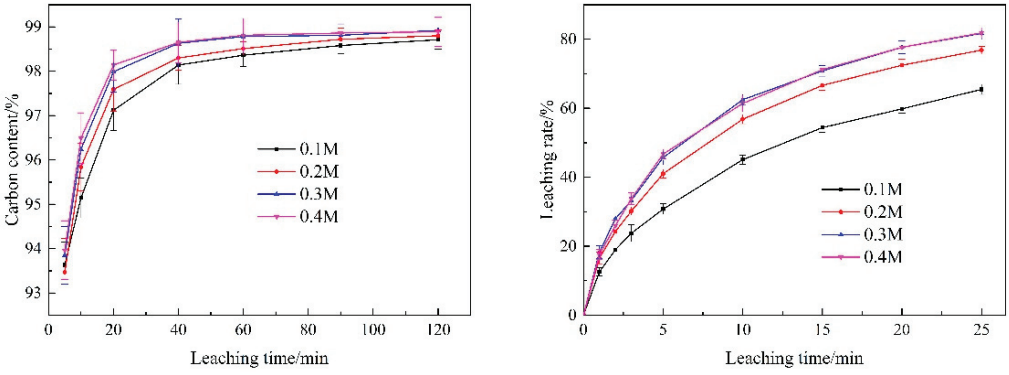

Figure 7. Effect of NaF addition on carbon content (**left**) and Al leching rate (**right**) (initial HCl concentration 4 mol/L, particle size D(50) = 67.49 μm, 333 K).

During acid leaching of fly ash, the leaching rate of aluminum improved significantly when using hydrochloric acid as a leaching agent and NaF as an additive. Fluoride ion in solution reacts with silicon in aluminum silicon glass to produce fluorinated silicon compounds that destroy the glass and improves aluminum reaction activity greatly. Reaction equations are as follows [27]:

$$H^+ + NaF = HF + Na^+ \quad (18)$$

$$Al_2O_3 \cdot SiO_2 + 4HF = SiF_4(g) + Al_2O_3 + 2H_2O \quad (19)$$

$$3Al_2O_3 \cdot SiO_2 + 6HF = H_2SiF_6 + 3Al_2O_3 + 2H_2O \quad (20)$$

$$H_2SiF_6 = SiF_6^{2-} + 2H^+ \quad (21)$$

$$Al_2O_3 + 6H^+ = 2Al^{3+} + 3H_2O \quad (22)$$

Reaction activities of some SCC impurities such as SiO_2, $NaAl_{11}O_{17}$, and $NaAlSiO_4$ are weak in hydrochloric acid systems, but solubilizing some of these impurities increases in hydrofluoric acid systems. Therefore, upon addition of NaF, carbon levels in the leaching residue showed a continuous upward trend (Figure 7). When NaF addition exceeded 0.3 M, residual impurities in SCC were not effectively removed in the existing leaching system; all impurities in the waste cathode were not removed completely in an HCl/HF solution, and the change of treated carbon powder purity was not obvious. In addition, NaF solubility in water is low and additional NaF in solution may complicate purified carbon powder washing. Solid carbon powder provided crystal nucleation sites, and porous carbon adsorbed on those crystalline particles. So, the optimal amount of NaF was 0.3 M.

3.3.5. Purified SCC Analysis

High purity carbon powder with ash levels below 1% was obtained by acid leaching the alkali-fused SCC in a hydrochloric acid/sodium fluoride solution. Figure 8 shows the XRD analysis of SCC and carbon powder after acid leaching, and Figure 9 shows the SEM-EDS results. After treatment, the ash content of purified carbon powder was less than 1%.

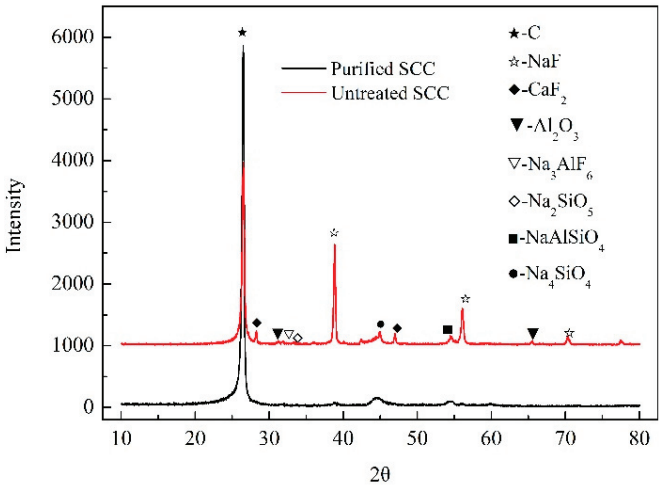

Figure 8. XRD patterns of SCC.

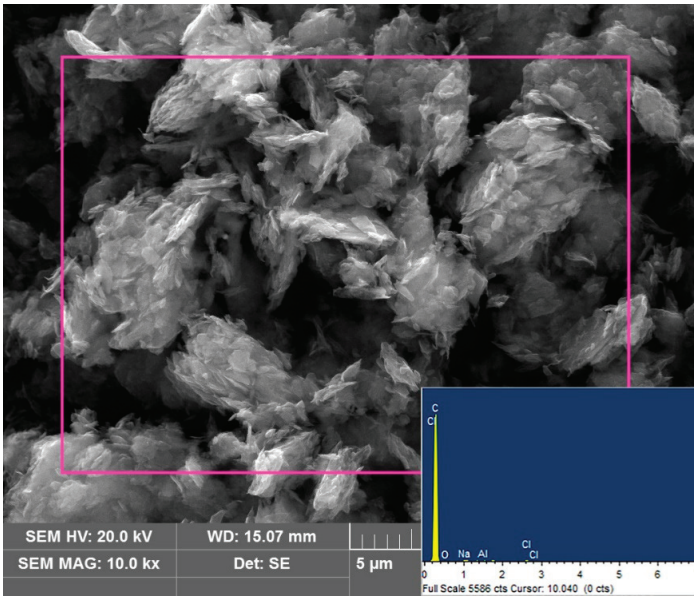

Figure 9. SEM-EDS images of SCC after alkali fusion-acid leaching treatment.

3.4. Leaching Kinetic Analysis

3.4.1. Kinetic Model

Aluminum, a primary element of SCC, was selected to explore the extraction efficiency during leaching; the leaching reaction mechanism was explained kinetically.

The Avrami Equation [28] was first used in the kinetics of nucleus growth in heterogeneous chemical reactions; it now uses in the leaching of many metals and metal oxides [29]. Equation (23) shows this equation:

$$-\ln(1-\eta) = kt^n \quad (23)$$

where k is the apparent reaction rate constant; η is leaching rate, %; t is leaching time, min; n is reaction characteristic parameter.

The reaction characteristic parameter depends on mineral grain property and geometry, which reflects the leaching reaction mechanism. It relates only to the properties and geometry of solid grains and remains unchanged with reaction conditions [30]. As $n < 1$, the initial reaction rate is very high and decreases with leaching progress. As $n > 1$, the initial reaction rate approaches 0.

Taking the natural logarithm on both sides of Equation (23) yields the following Equation (24):

$$\ln[-\ln(1-\eta)] = \ln k + n\ln t \quad (24)$$

3.4.2. Determination of Leaching Model Parameters

Results in Figure 4 (right) were substituted into Equation (24), and variations of $\ln[-\ln(1-\eta)]$ with lnt were plotted for the particle sizes as shown in Figure 10. The good linear correlation in Figure 10 indicated the Avrami model effectively describes the aluminum extraction from alkali-fused cathode carbon under different particle sizes. The linear fitting regression equations and correlation coefficient values are listed in Table 2.

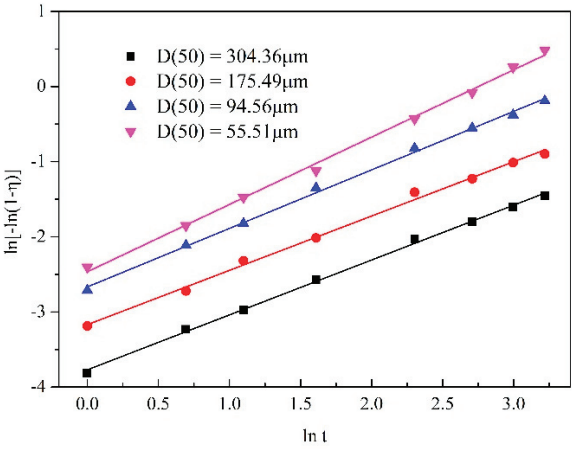

Figure 10. Plots of $\ln[-\ln(1-\eta)]$ vs. lnt in alkali fused SCC leaching process under different particle sizes.

Table 2. Fitting results between $\ln[-\ln(1-\eta)]$ and lnt under different particle size.

Particle Size	Regression Equation	R^2
D(50) = 304.36 μm	$\ln[-\ln(1-\eta)] = 0.73058\ln t - 3.76902$	0.99799
D(50) = 175.49 μm	$\ln[-\ln(1-\eta)] = 0.72284\ln t - 3.16824$	0.99552
D(50) = 94.56 μm	$\ln[-\ln(1-\eta)] = 0.77899\ln t - 2.66602$	0.99755
D(50) = 55.51 μm	$\ln[-\ln(1-\eta)] = 0.89611\ln t - 2.46394$	0.99666

The apparent reaction rate constant, k, relates to solution concentration, mineral particle size, and temperature. Combined with the Arrhenius equation, k is expressed as shown in Equation (25).

$$k = k_0 C_{HCl}^{a} C_{NaF}^{b} D^{d} \exp(-Ea/RT) \quad (25)$$

where k_0 is the frequency factor; C_{HCl} is the initial concentration of hydrochloric acid, M; C_{NaF} is NaF addition, M; D is the particle size, μm; Ea is the activation energy, J/mol; T is temperature, K; R is the universal gas constant, 8.314 J/(K·mol); a is the hydrochloric acid concentration reaction order; b is the NaF concentration reaction order; d is the particle size influence index.

Taking logarithms of Equation (25) yielded Equation (26).

$$\ln k = \ln k_0 + a\ln C_{HCl} + b\ln C_{NaF} + d\ln D - Ea/RT \quad (26)$$

Based on Equation (26), others were fixed conditions and variable particle size, variations of lnk with lnD were plotted in Figure 11. The slope of the straight line was −0.82962, which was the particle size influence index.

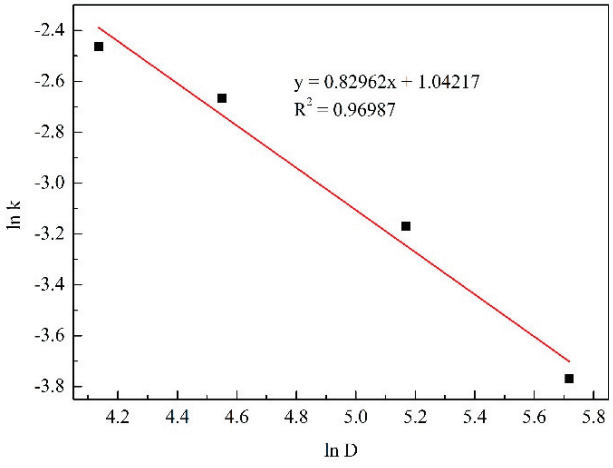

Figure 11. Plot of lnk vs. lnD in alkali fused SCC leaching process.

Results shown in Figure 5(right) were substituted into Equation (24), and the variations of ln[−ln(1 − η)] with lnt were plotted for initial acid concentrations in Figure 12. The linear fitting regression equations and correlation coefficients are listed in Table 3. The straight lines in Figure 12 and fitting curve correlation coefficients R^2 in Table 3 showed good linear correlations between ln[−ln(1 − η)] and lnt under different initial acid concentrations.

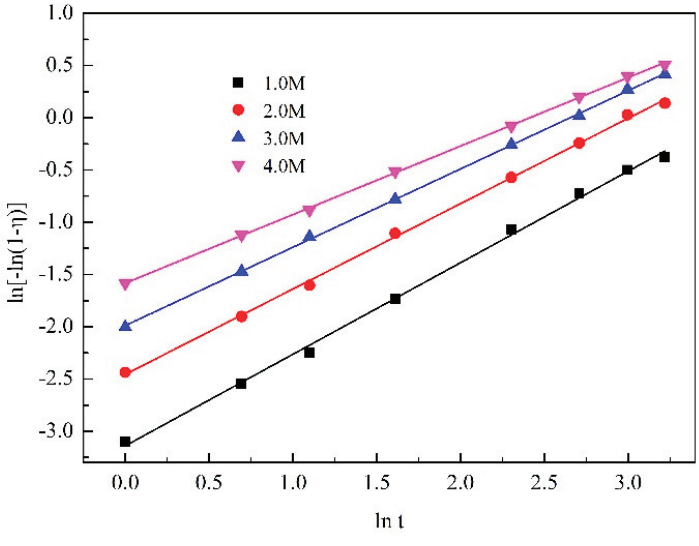

Figure 12. Plots of ln[−ln(1 − η)] vs. lnt in alkali fused SCC leaching process under different acid concentrations.

Table 3. Fitting results between ln[−ln(1 − η)] and lnt under different acid concentrations.

Initial Acid Concentration	Regression Equation	R^2
1 mol/L	y = 0.87611x − 3.13885	0.99762
2 mol/L	y = 0.81689x − 2.45518	0.99885
3 mol/L	y = 0.74951x − 1.98818	0.99964
4 mol/L	y = 0.65595x − 1.58231	0.99957

Varying the initial acid concentration while fixing the other variables gave variations of lnk with $\ln C_{HCl}$ and are plotted in Figure 13. The slope of the straight line was 1.10841, which was the hydrochloric acid concentration influence index.

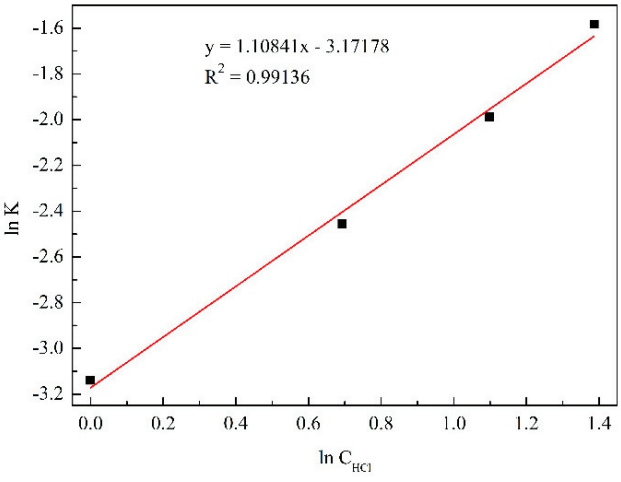

Figure 13. Plot of lnk vs. $\ln C_{HCl}$ in alkali fused SCC leaching process.

Results shown in Figure 6(right) were substituted into Equation (24), and variations of ln[−ln(1 − η)] with lnt were plotted as a function of leaching temperature (Figure 14). The linear fitting regression equations and correlation coefficients are listed in Table 4.

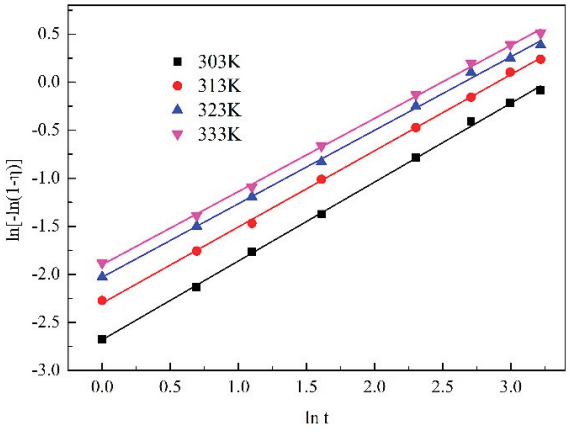

Figure 14. Plots of ln[−ln(1 − η)] vs. lnt in alkali fused SCC leaching process under different temperatures.

Table 4. Fitting results between ln[−ln(1 − η)] and lnt under different temperatures.

Temperature	Regression Equation	R^2
303 K	y = 0.82056x − 2.67984	0.99899
313 K	y = 0.79246x − 2.29784	0.9993
323 K	y = 0.76404x − 2.02802	0.99847
333 K	y = 0.7609x − 1.89813	0.99900

Varying temperature and keeping other variables fixed yielded the variations of lnk with 1/T, which were plotted and shown in Figure 15. The slope of the straight line was 1.10841, which was hydrochloric acid concentration influence index. The slope was −Ea/R, and an apparent reaction activation energy Ea 22.056 kJ/mol was obtained. In general, diffusion controls most metallurgical processes when the apparent activation energy is less than 10 kJ/mol; chemical reactivity primarily controls processes with apparent activation energies > 40 kJ/mol. However, there is mixed control when the apparent activation energy ranges between 10–40 kJ/mol. Therefore, the leaching process of alkali-fused SCC in an HCl/NaF system was controlled by a mixed mechanism of chemical reactivity and diffusion.

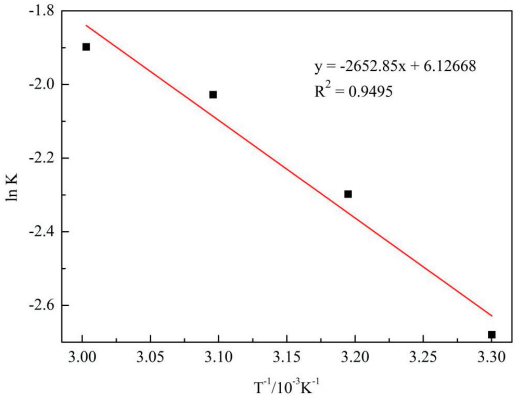

Figure 15. Plot of lnk vs. T^{-1} in alkali fused SCC leaching process.

Results shown in Figure 7 (right) were substituted into Equation (24) to yield the fitting results given in Figure 16 and Table 5.

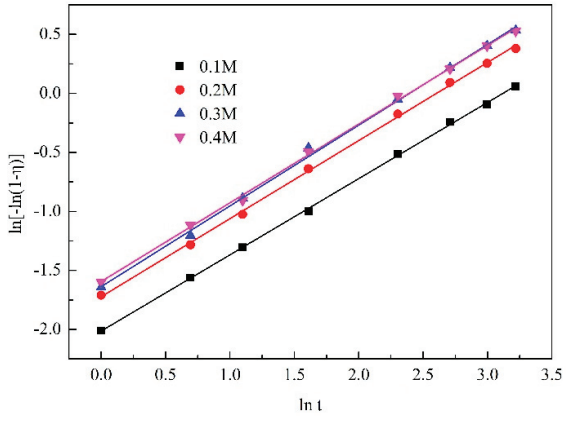

Figure 16. Plots of ln[−ln(1 − η)] vs. lnt in alkali fused SCC leaching process under different NaF additions.

Table 5. Fitting results between ln[−ln(1 − η)] and lnt under different NaF additions.

NaF Concentration	Regression Equation	R^2
0.1 mol/L	y = 0.64577x − 2.01349	0.99951
0.2 mol/L	y = 0.66183x − 1.72284	0.99899
0.3 mol/L	y = 0.68402x − 1.63707	0.99782
0.4 mol/L	y = 0.66698x − 1.59361	0.99858

NaF addition varied, and others were fixed; the variations of lnk with $\ln C_{NaF}$ are plotted in Figure 17. The NaF addition influence index was 0.30758.

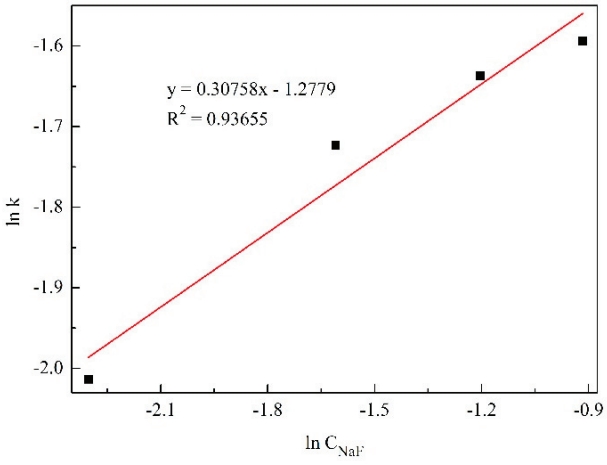

Figure 17. Plot of lnk vs. $\ln C_{NaF}$ in alkali fused SCC leaching process.

3.4.3. Determination of the Kinetic Equation

Tables 2–5 show a good linear relationship between ln[−ln(1 − η)] and lnt. According to the data fitted by all Avrami equations, the average reaction characteristic parameter *n* value was 0.75147. Based on Equations (23) and (25), variations of $-\ln(1-\eta)$ with $C_{HCl}^{1.10841}C_{NaF}^{0.30758}D^{-0.82962}\exp(-2652.85/T)\,t^{0.75147}$ were plotted in Figure 18. The slope of the straight line obtained by fitting was the frequency factor, k_0 (2.78788).

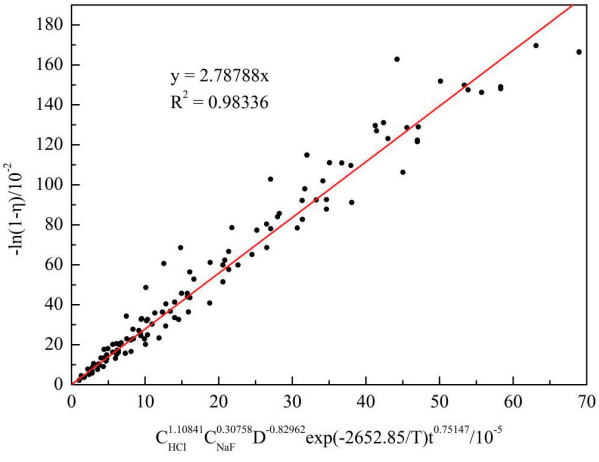

Figure 18. Plot of $-\ln(1-\eta)$ vs. $C_{HCl}^{1.10841}C_{NaF}^{0.30758}D^{-0.82962}\exp(-2652.85/T)\,t^{0.75147}$.

Equation (27) gives the kinetic equation of aluminum extraction from alkali-fused SCC from aluminum smelters by leaching in an HC/NaF mixture.

$$-\ln(1-\eta) = 2.78788 C_{HCl}^{1.10841} C_{NaF}^{0.30758} D^{-0.82962} \exp(-2652.85/T) t^{0.75147} \quad (27)$$

4. Conclusions

Spent cathode carbon of aluminum electrolysis was treated with alkali fusion and then purified deeply in an HCl/NaF solution. Useful results have been achieved.

(1) Alkali-fused SCC powders from aluminum electrolysis were purified in a mixed solution of hydrochloric acid and sodium fluoride; the residual ash content was <1%.
(2) Leaching of alkali fusion treated SCC powder in a hydrochloric acid and sodium fluoride system is described by the Avrami equation. The reaction characteristic parameter was 0.75147 and the apparent activation energy was 22.056 kJ/mol. Leaching was controlled by a mixed mechanism of chemical reaction and diffusion.
(3) Kinetic equation of aluminum extraction was: $-\ln(1-\eta) = 2.78788 C_{HCl}^{1.10841} C_{NaF}^{0.30758} D^{-0.82962} \exp(-2652.85/T) t^{0.75147}$.

Author Contributions: Conceptualization, J.Y.; methodology, J.Y.; software, H.L. and S.D.; formal analysis, H.L.; investigation, J.Y. and H.L.; resources, J.Y.; data curation, H.L.; writing-original draft preparation, J.Y. and S.D.; writing-review and editing, S.D.; visualization, J.Y.; supervision, S.D.; project administration, J.Y.; funding acquisition, J.Y. All authors have read and agreed to the published version of the manuscript.

Funding: This research was supported by National Natural Science Foundation of China (51904150), Basic Research Program of Guizhou Province ([2020]1Y225), Guizhou Province Ordinary Universities Scientific Talents Project (KY [2019]056), Liupanshui Key Laboratory of Aluminum Production and Application (52020-2019-05-09), Liupanshui Normal University Scientific Research Foundation (LPSSYKYJJ201904).

Conflicts of Interest: The authors declare that there is no conflict of interest regarding the publication of this paper.

References

1. Lu, F.; Su, X.; Huang, F.; Wang, J.; Wang, H. Co-Treatment of Spent Pot-Lining and Red Mud for Carbon Reutilization and Recovery of Iron, Aluminum and Sodium by Reductive Roasting Process. *Metall. Mater. Trans. B* **2020**, *51*, 1564–1575. [CrossRef]
2. Liu, F.; Xie, M.; Liu, W.; Zhao, H. Footprint of harmful substances in spent pot lining of aluminum reduction cell. *Trans. Nonferrous Met. Soc.* **2020**, *30*, 1956–1963. [CrossRef]
3. Nunez, P. Developing Guidance to Support Sustainable Spent Pot Lining (SPL) Management Across the Aluminum Industry. *JOM* **2020**, *72*, 3334–3340. [CrossRef]
4. Li, J.; Li, J.; Zhang, H.; Li, T.; Xiao, J. Structural characteristics and sodium penetration behaviors in anthracite cathodes: A combination study using Monte Carlo and molecular dynamics simulations. *Carbon Lett.* **2019**, *30*, 259–269. [CrossRef]
5. Holywell, G.; Breault, R. An Overview of Useful Methods to Treat, Recover, or Recycle Spent Potlining. *JOM* **2013**, *65*, 1441–1451. [CrossRef]
6. Senanu, S.; Wang, Z.; Ratvik, A.; Grande, T. Carbon Cathode Wear in Aluminium Electrolysis Cells. *JOM* **2019**, *72*, 210–217. [CrossRef]
7. Sun, G.; Zhang, G.; Liu, J.; Xie, W.; Evrendilek, F.; Buyukada, M. (Co-)combustion behaviors and products of spent potlining and textile dyeing sludge. *J. Clean. Prod.* **2019**, *224*, 384–395. [CrossRef]
8. Ren, H.; Zhang, C.; Chang, Q.; Cheng, H.; Li, D.; Zhang, D. Optimization of flotation conditions for spent pot lining carbon of aluminum reduction. *Light Met.* **2017**, 26–31.
9. Yang, K.; Gong, P.; Tian, Z.; Lai, Y.; Li, J. Recycling spent carbon cathode by a roasting method and its application in Li-ion batteries anodes. *J. Clean. Prod.* **2020**, *261*, 121090. [CrossRef]
10. Xiao, J.; Yuan, J.; Tian, Z.; Yang, K. Comparison of ultrasound-assisted and traditional caustic leaching of spent cathode carbon (SCC) from aluminum electrolysis. *Ultrason. Sonochem.* **2018**, *40*, 21–29. [CrossRef]
11. Ghenai, C.; Inayat, A.; Shanableh, A.; Al-Saraira, E.; Janajreh, I. Combustion and emissions analysis of Spent Pot lining (SPL) as alternative fuel in cement industry. *Sci. Total Environ.* **2019**, *684*, 519–526. [CrossRef]
12. Flores, I.V.; Fraiz, F.; Lopes Junior, R.A.; Bagatini, M.C. Evaluation of spent pot lining (SPL) as an alternative carbonaceous material in ironmaking processes. *J. Mater. Res. Technol.* **2019**, *8*, 33–40. [CrossRef]

13. Li, R.; Lu, T.; Xie, M.; Liu, F. Analysis on thermal behavior of fluorides and cyanides for heat-treating spent cathode carbon blocks from aluminum smelters by TG/DSC-MS & ECSA(R). *Ecotox. Environ. Safe* **2020**, *189*, 110015.
14. Yao, Z.; Xiao, J.; Mao, Q.; Wang, G.; Tang, L.; You, Z.; Zhong, Q. Detoxification and Recovery of Spent Carbon Cathodes via NaOH–Na_2CO_3 Binary Molten Salt Roasting-Water Leaching: Toward a Circular Economy for Hazardous Solid Waste from Aluminum Electrolysis. *ACS Sustain. Chem. Eng.* **2020**, *8*, 16912–16923. [CrossRef]
15. Xiao, J.; Zhang, L.; Yuan, J.; Yao, Z.; Tang, L.; Wang, Z.; Zhang, Z. Co-utilization of spent pot-lining and coal gangue by hydrothermal acid-leaching method to prepare silicon carbide powder. *J. Clean. Prod.* **2018**, *204*, 848–860. [CrossRef]
16. Li, X.; Yin, W.; Fang, Z.; Liu, Q.; Cui, Y.; Zhao, J.; Jia, H. Recovery of Carbon and Valuable Components from Spent Pot Lining by Leaching with Acidic Aluminum Anodizing Wastewaters. *Metall. Mater. Trans. B* **2019**, *50*, 914–923. [CrossRef]
17. Lisbona, D.F.; Somerfield, C.; Steel, K.M. Leaching of spent pot-lining with aluminium nitrate and nitric acid: Effect of reaction conditions and thermodynamic modelling of solution speciation. *Hydrometallurgy* **2013**, *134–135*, 132–143. [CrossRef]
18. Nie, Y.; Guo, X.; Guo, Z.; Tang, J.; Xiao, X.; Xin, L. Defluorination of spent pot lining from aluminum electrolysis using acidic iron-containing solution. *Hydrometallurgy* **2020**, *194*, 105319. [CrossRef]
19. Birry, L.; Leclerc, S.; Poirier, S. The LCL&L process: A sustainable solution for the treatment and recycling of Spent potling. *TMS* **2016**, 467–471.
20. Xie, M.; Li, R.; Zhao, H.; Liu, W.; Lu, T.; Liu, F. Detoxification of spent cathode carbon blocks from aluminum smelters by joint controlling temperature-vacuum process. *J. Clean. Prod.* **2020**, *249*, 119370. [CrossRef]
21. Wang, Y.; Peng, J.; Di, Y. Separation and Recycling of Spent Carbon Cathode Blocks in the Aluminum Industry by the Vacuum Distillation Process. *JOM* **2018**, *70*, 1877–1882.
22. Tang, H. High-Temperature Continuous Electric Calciner. Patent CN201711147639, 17 November 2017.
23. Yuan, J.; Xiao, J.; Tian, Z.; Yang, K.; Yao, Z.; Zhang, L. Optimization of purification treatment of spent cathode carbon from aluminum electrolysis using response surface methodology (RSM). *Asia-Pac. J. Chem. Eng.* **2018**, *13*, e2164. [CrossRef]
24. Hodge, H.; Hayes, P.C.; Hawker, W.; Vaughan, J. The DSP concentrate sinter-leach process for aluminium and sodium recovery 2: Leaching behaviour. *Miner. Process. Extr. Metall.* **2020**, *131*, 341–353. [CrossRef]
25. Yuan, J.; Xiao, J.; Tian, Z.; Yang, K. Optimization of spent cathode carbon purification process under ultrasonic action using Taguchi method. *Ind. Eng. Chem. Res.* **2018**, *57*, 7700–7710. [CrossRef]
26. Zhang, H.; Chen, G.; Cai, X.; Fu, J.; Yu, H. The leaching behavior of copper and iron recovery from reduction roasting pyrite cinder. *J. Hazard. Mater.* **2021**, *420*, 126561. [CrossRef]
27. Wang, B. Study on High-Purity Aluminum Oxide Recovered from Aluminum Dross by Acid Leaching. Master's Thesis, Zhengzhou University, Zhengzhou, China, May 2016.
28. Guía-Tello, J.C.; Garay-Reyes, C.G.; Ruiz-Esparza-Rodríguez, M.A. Effect of plastic deformation on the precipitation reaction in 2024 alloys. *Mater. Chem. Phys.* **2021**, *271*, 124927. [CrossRef]
29. Xu, Z.; Guo, X.; Li, D. Leaching kinetics of tellurium-bearing materials in alkaline sulfide solutions. *Miner. Process. Extr. Metall. Rev.* **2018**, *41*, 1–10. [CrossRef]
30. Turunen, K.; Yazdani, M.R.; Santasalo-Aarnio, A.; Seppl, A. Exceptional cold-crystallization kinetics of erythritol-polyelectrolyte enables long-term thermal energy storage. *Sol. Energy Mater. Sol. Cells* **2021**, *230*, 111273. [CrossRef]

materials

MDPI

Article

Amoxicillin Retention/Release in Agricultural Soils Amended with Different Bio-Adsorbent Materials

Raquel Cela-Dablanca [1,*], Ana Barreiro [1], Lucia Rodríguez-López [2], Vanesa Santás-Miguel [2], Manuel Arias-Estévez [2], María J. Fernández-Sanjurjo [1], Esperanza Álvarez-Rodríguez [1] and Avelino Núñez-Delgado [1]

[1] Department Soil Science and Agricultural Chemistry, Engineering Polytechnic School, University Santiago de Compostela, 27002 Lugo, Spain; ana.barreiro.bujan@usc.es (A.B.); mf.sanjurjo@usc.es (M.J.F.-S.); esperanza.alvarez@usc.es (E.Á.-R.); avelino.nunez@usc.es (A.N.-D.)

[2] Soil Science and Agricultural Chemistry, Faculty Sciences, University Vigo, 32004 Ourense, Spain; lucia.rodriguez.lopez@uvigo.es (L.R.-L.); vsantas@uvigo.es (V.S.-M.); mastevez@uvigo.es (M.A.-E.)

* Correspondence: raquel.dablanca@usc.es; Tel.: +34-982823145

Abstract: The antibiotic amoxicillin (AMX) may reach soils and other environmental compartments as a pollutant, with potential to affect human and environmental health. To solve/minimize these hazards, it would be clearly interesting to develop effective and low-cost methods allowing the retention/removal of this compound. With these aspects in mind, this work focuses on studying the adsorption/desorption of AMX in different agricultural soils, with and without the amendment of three bio-adsorbents, specifically, pine bark, wood ash and mussel shell. For performing the research, batch-type experiments were carried out, adding increasing concentrations of the antibiotic to soil samples with and without the amendment of these three bio-adsorbents. The results showed that the amendments increased AMX adsorption, with pine bark being the most effective. Among the adsorption models that were tested, the Freundlich equation was the one showing the best fit to the empirical adsorption results. Regarding the desorption values, there was a decrease affecting the soils to which the bio-adsorbents were added, with overall desorption not exceeding 6% in any case. In general, the results indicate that the bio-adsorbents under study contributed to retaining AMX in the soils in which they were applied, and therefore reduced the risk of contamination by this antibiotic, which can be considered useful and relevant to protect environmental quality and public health.

Keywords: antibiotics; bio-adsorbents; emerging pollutants; soil pollution

Citation: Cela-Dablanca, R.; Barreiro, A.; Rodríguez-López, L.; Santás-Miguel, V.; Arias-Estévez, M.; Fernández-Sanjurjo, M.J.; Álvarez-Rodríguez, E.; Núñez-Delgado, A. Amoxicillin Retention/Release in Agricultural Soils Amended with Different Bio-Adsorbent Materials. *Materials* **2022**, *15*, 3200. https://doi.org/10.3390/ma15093200

Academic Editor: Elisabetta Loffredo

Received: 24 March 2022
Accepted: 27 April 2022
Published: 28 April 2022

1. Introduction

Emerging pollutants include a wide range of chemical compounds, such as various pharmaceutical products, and specifically antibiotics [1,2]. In 2020, in the European Union (EU), the average total consumption of anti-bacteria compounds for systemic use (ATC Group J01) was 16.4 defined daily doses (DDD) per 1000 inhabitants [3]. These compounds are not fully absorbed in the intestine, causing them to be excreted in significant amounts (up to 90%) through urine and feces [4,5], thus passing to wastewater in the case of humans, and to manure pits or manure accumulations in the case of animal farms. These contaminants can pass into various environmental compartments and may directly cause undesirable effects in soils [6], including the promotion of antibiotic resistance [7–9], and/or be absorbed by plants used for human or animal consumption, entering the food chain, as has been shown for lettuce and other vegetables [7,10,11].

One of the most widely used antibiotics in both human and veterinary medicine is amoxicillin (AMX), which is frequently used as a first-choice drug for the treatment of serious infections [12]. Between 80 and 90% of this antibiotic is excreted due to its poor absorption [13], then reaching the environment, and achieving concentrations of 127.49 ng L^{-1} in wastewater [14].

Different authors point out that antibiotics are frequently detected in treated wastewater, because they come from human use, but also from other sources such as agriculture and livestock production [15–18]. In this regard, one of the current strategies to alleviate water scarcity is the reuse of previously treated wastewater, which could result in public health issues due to the presence of different chemical pollutants and microbes [19]. Wastewater treatment tries to decrease nutrient loads [20] and pathogens [21], among other contaminants, but many current treatments are not sufficiently effective in retaining and inactivating pharmaceuticals such as antibiotics [22,23].

Current EU and United States (US) legislations do not include concentration limits for antibiotics in treatment plant effluents [24,25], making it more probable that antibiotics reach soils through WWTP-purified water used in irrigation [26]. In addition, antibiotics may be spread on soils through WWTP sludge used as fertilizer in agricultural crops and silvo-pastoral systems [27], and can subsequently be incorporated into the food chain.

Soils have a relevant buffering capacity and filtering potential due to the colloids present in the clay fraction and in organic matter, which help in preventing environmental pollution [28–30]. The dynamics followed by antibiotics in the soil depends on their physicochemical properties, as well as on those of the soil, and also on the time of application of the residual materials, as well as weather conditions [31–33]. Among the various processes that antibiotics can undergo in the soil environment, it is worth highlighting mineralization, degradation, volatilization, leaching, surface runoff, bioaccumulation, and adsorption.

The specific behavior of the antibiotic AMX in the soil is highly conditioned by the pH of the medium, which affects the ionization of the compound and the surface charge of the soil colloids [34,35]. In this regard, it is highly relevant that AMX has amphoteric properties due to three functional groups present in its structure: $-NH_2$, -COOH, and -OH [36]. The dissociation constants (pk_a) of a molecule indicate its ionization state as a function of pH [37]. In the case of AMX, pk_{a1} corresponds to carboxyl groups (-COOH), pk_{a2} is represented by amine groups ($-NH_2$), while pk_{a3} corresponds to phenolic groups (where hydroxyl (-OH) is attached to a C atom integrated in an aromatic ring), so that, at different pH values, AMX may appear as a cation, anion, or zwitterion [38]. Specifically, at $pH < pk_{a1}$ AMX will appear as a cation, at $pH > pk_{a3}$ it will appear as an anion, while at pH values between pk_{a1} and pk_{a3} it will appear as a zwitterion [39].

The presence of antibiotics in soils and water that have received the spreading/disposal of wastewater and/or sewage sludge is a matter of concern [40], so different investigations have focused on the design of a variety of systems intended to its removal [41]. Several technologies have been proposed to achieve antibiotics removal during wastewater treatment, such as the use of ozone [42] or advanced oxidation [39], although these methods tend to generate unwanted toxic side-products. In contrast, adsorption is considered a rather simple and sustainable alternative [43]. In this way, commonly used adsorbents include mineral and biological materials, as well as activated carbon, with this last adsorbent being widely used, although it has a high cost and regeneration issues [44]. In view of this, there is increasing interest in using low-cost adsorbents, such as industrial waste or by-products, for which it is necessary to determine their pollutant adsorption capacity, and in particular their potential to retain/remove antibiotics [45,46].

Among them, certain residues/by-products from the food industry, such as mussel shell, and from the forestry industry, such as pine bark and wood ash, are abundant, easily accessible and low-cost, making it interesting to determine their capacity to adsorb contaminants such as antibiotics that reach different environmental compartments. These three bio-adsorbent materials could be added to the soil or used in modules specifically designed and installed in wastewater treatment plants, to minimize the risk of dispersion of these pollutants in the environment. Mussel shell, pine bark and wood ash have already been studied previously regarding their ability to retain heavy metals, inorganic anions and antibiotics from the group of tetracyclines and sulfonamides, obtaining very promising results [47–56]. There are also previous studies dealing with the adsorption of AMX present in wastewater by means of adsorbents such as wheat grain, almond shell ash, palm bark,

bentonite or activated carbon [36]. However, there are no previous publications that have focused on evaluating the effects on AMX retention derived from amending crop soils with pine bark, wood ash and mussel shell. In fact, the efficacy of these bio-adsorbents to increase the adsorption of antibiotics in soils has been previously proven for sulfonamides in the case of pine bark [57], while wood ash and mussel shell showed worse results. In addition, mussel shell has been widely studied as a bio-adsorbent in soils contaminated with heavy metals [58], and wood ash has also been investigated for this purpose (for example [59]), but studies on the application of these materials in the retention of pharmaceutical products are very scarce.

In view of the above background, the present study was performed to investigate for the first time AMX adsorption and desorption on/from different agricultural soils with and without the presence of the bio-adsorbents pine bark, wood ash and mussel shell, assessing their potential to decrease the dispersion of this antibiotic, which can be considered of relevance with regard to environmental preservation and public health protection.

2. Materials and Methods

2.1. Soils and Bio-Adsorbents

Four agricultural soils, devoted to maize and vineyard cultivation, located in different areas of Galicia (NW Spain), were selected in function of their pH values and organic matter (OM) contents. All four were characterized as detailed in the Supplementary Materials. Table S1 (Supplementary Materials) shows values corresponding to soil properties., Within them, soil pH_{water} was between 5.01 and 6.04, while organic matter (OM) content was in the range 3.06–4.59%. The texture of two of the soils (soils M1 and M2) was clay loam, while it was sandy clay loam for the other two soils (soils M3 and VO).

In addition, the following materials were used as bio-adsorbents/amendments: (a) two forest by-products: pine bark (commercially distributed by Geolia, Madrid, Spain), and wood ash (from a local boiler at Lugo, Spain); (b) mussel shell (crushed at <1 mm), from Abonomar (Pontevedra, Spain). These bio-adsorbents were characterized as indicated in the Supplementary Materials, with results shown in Table S2. Some additional data regarding characteristics of these materials have been included in previous publications [55,56].

Different soil + amendment mixtures were elaborated adding the bio-adsorbents to soil samples at doses of 48 t ha^{-1}, followed by 72 h of stirring at 50 rpm using a rotatory shaker, and further homogenization by means of a Retsch splitter (Haan, Germany), all this carried out at stable temperature of 25 ± 2 °C. The pH of the different soil + bio-adsorbent mixtures was analysed, with results shown in Table 1.

Table 1. pH values of the different soils and soil + bio-adsorbent mixtures. VO: vineyard soil; M: maize soils; A: wood ash; MS: mussel shell; PB: pine bark. Average values (n = 3), with coefficients of variation always <5%.

Soils and Mixtures	pH	Soils and Mixtures	pH
M1	5.33	M3	5.01
M1 + A	6.93	M3 + A	6.93
M1 + MS	5.29	M3 + MS	5.46
M1 + PB	4.92	M3 + PB	4.79
M2	5.65	VO	6.04
M2 + A	7.04	VO + A	7.81
M2 + MS	5.76	VO + MS	5.92
M2 + PB	5.24	VO + PB	5.35

2.2. Chemical Reagents

The antibiotic AMX used (with purity ≥ 95%) was from Sigma-Aldrich (Barcelona, Spain), while acetonitrile (purity ≥ 99.9%) and phosphoric acid (85% extra pure) were from Fisher Scientific (Madrid, Spain), and $CaCl_2$ (95% purity) was from Panreac (Barcelona,

Spain). All the solutions needed for HPLC analyses were prepared using milliQ water (from Millipore, Madrid, Spain).

2.3. Adsorption and Desorption Experiments

AMX adsorption and desorption were studied by means of batch experiments, performed on the different soils amended with the bio-adsorbent materials, which were added to the soils in doses of 48 t ha^{-1}. For this, 2 g of the soil + bio-adsorbent mixtures was weighed, then adding a volume of 5 mL of a solution with different concentrations of the antibiotic (2.5, 5, 10, 20, 30, 40, 50 μmol L^{-1}), which also contained 0.005 M $CaCl_2$ as background electrolyte. The resulting suspensions were shaken for 48 h in the dark, using a rotary shaker. Previous kinetic tests indicated that the 48 h period is enough to reach equilibrium (data not shown). This step was followed by centrifuging the suspensions (15 min at 4000 rpm), and by subsequent filtration of the supernatants through 0.45 μm nylon syringe filters. Finally, AMX concentration was quantified using specific HPLC-UV equipment (an LPG 3400 SD device, by Thermo-Fisher Scientific, Madrid, Spain). Details on AMX HPLC determinations are provided in Supplementary Materials. Additionally, example chromatograms are shown in Figure S1 (Supplementary Materials).

Regarding desorption, it was studied adding 5 mL of 0.005 M $CaCl_2$ to the material derived from the adsorption experiments, then repeating the procedure performed for the previous adsorption phase. In all cases, triplicate determinations were carried out.

2.4. Data Treatment

The experimental adsorption data were fitted to the Freundlich (Equation (1)), Langmuir (Equation (2)) and Linear (Equation (3)) models [60].

$$q_e = K_F C_{eq}^n \quad (1)$$

$$q_e = \frac{q_m K_L C_{eq}}{1 + K_L C_{eq}} \quad (2)$$

$$K_d = q_e / C_{eq} \quad (3)$$

with q_e being the amount of AMX retained, which was calculated as the difference between the concentration added and that remaining in the equilibrium; C_{eq} is the AMX concentration in the equilibrium solution; K_F is the Freundlich parameter related to the adsorption capacity; n is a Freundlich parameter related to the degree of heterogeneity in adsorption; K_L is the Langmuir adsorption constant; q_m is the maximum adsorption capacity in the Langmuir model; and K_d is the partition coefficient in the Linear model.

The fitting of the experimental data to the Langmuir, Freundlich and Linear models was studied by means of the SPSS Statistics 21 software (IBM, Armonk, NY, USA).

3. Results

3.1. Adsorption

As shown in Figure 1, as well as in data included in Table S3 (Supplementary Materials), pine bark performed as a very effective material for increasing AMX adsorption in the soils amended with this bio-adsorbent. Table 1 shows that the pH of each soil changes when the different bio-adsorbents are added. Specifically, pine bark (which has pH = 3.99) generally causes an acidification of the amended soil.

Table 2 presents the values of the parameters corresponding to AMX adsorption as per the Freundlich, Langmuir and Linear models.

Considering R^2 values, all the non-amended soils (except M1) presented an overall good fit to all three models, given that $R^2 > 0.90$ for VO and M3, and $R^2 > 0.80$ for M2. Focusing on both the non-amended soils and those amended with bio-adsorbents, the errors in some parameters of the Linear model, and especially in the Langmuir model, were

too high, invalidating the adjustment in those cases, so the Freundlich's model shows the best results.

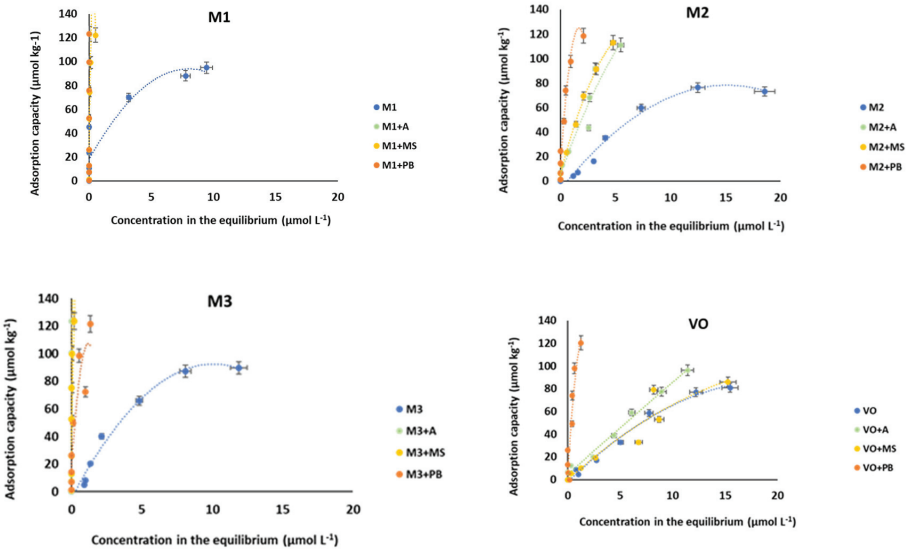

Figure 1. Adsorption curves for AMX in unamended and bio-adsorbent-amended soils. Average values (n = 3), with coefficients of variation always <5%.

Table 2. Values of the adsorption parameters corresponding to the Freundlich (K_F, expressed in L^n $\mu mol^{1-n} kg^{-1}$, and n–dimensionless-), Langmuir (K_L, expressed in L μmol^{-1}, and q_m -μmol kg^{-1}-) and Linear (K_d, expressed in L kg^{-1}) models. M: maize soil; VO: vineyard soil; A: wood ash; MS: mussel shell; PB: pine bark; –: fitting not possible.

	Freundlich					Langmuir					Linear		
Sample	K_F	**Error**	n	**Error**	R^2	K_L	**Error**	q_m	**Error**	R^2	K_d	**Error**	R^2
M1	50.79	34.56	0.274	0.344	0.723	–	–	–	–	–	3.699	0.122	0.983
M1 + A	–	–	–	–	–	0.78	0.209	2066.7	0	0.344	1525.8	358.85	0.344
M1 + MS	139.24	36.56	0.191	0.145	0.745	27.983	29.168	129	30.23	0.746	–	–	–
M1+ PB	–	–	–	–	–	–	–	–	–	–	–	–	–
M2	11.81	4.224	0.676	0.141	0.896	0.074	0.039	140.85	40.68	0.935	5.057	0.568	0.813
M2 + A	31.042	6.881	0.758	0.16	0.932	–	–	–	–	–	22.265	1.671	0.911
M2 + MS	40.022	3.142	0.672	0.062	0.986	0.183	0.064	243.06	53.74	0.984	26.378	1.625	0.939
M2 + PB	91.91	6.984	0.391	0.108	0.923	1.725	0.795	154	27.49	0.934	69.95	11.36	0.633
M3	19.17	4.626	0.67	0.114	0.928	0.124	0.049	161.82	34.48	0.961	3.084	0.113	0.978
M3 + A	–	–	–	–	–	0.05	0	–	–	–	–	–	–
M3 + MS	107.418	7.279	0	0.038	0.978	103.812	287.076	–	–	–	–	–	–
M3 + PB	98.89	11.05	0.282	0.15	0.85	7.342	6.343	112.88	20.25	0.85	94.94	15.65	0.622
VO	9.579	2.155	0.806	0.091	0.974	0.037	0.017	232.67	75.91	0.982	5.934	0.312	0.957
VO + A	10.99	2.246	0.892	0.094	0.982	–	–	–	–	–	8.694	0.313	0.979
VO + MS	10.25	4.764	0.795	0.196	0.893	–	–	–	–	–	6.287	0.571	0.875
VO + PB	109.63	14.06	0.766	0.214	0.815	–	–	–	–	–	112.34	13.83	0.778

Figure 2 shows the AMX adsorption results (expressed as percentage values) for the different soils with or without bio-adsorbents. It is evident that, in general, adsorption is lower in the vineyard soil, and in the four soils studied, the amount of AMX adsorbed increases when amending with the bio-adsorbents, especially for the three highest concentrations of antibiotic added (30, 40 and 50 μmol L^{-1}). In three of the soils (VO, M2 and M3), adsorption increases when amending with the bio-adsorbents, and this takes place for any of the AMX concentrations added; however, in soil M1, this increase occurs just for the

three highest concentrations of antibiotic, because for lower concentrations the soil adsorbs 100% of the added antibiotic. These graphs show that the greatest increases in adsorption occur in both VO and M2 soils, especially after the addition of pine bark, while in soils M1 and M3, no differences were found regarding adsorption onto the different bio-adsorbents (Figure 2).

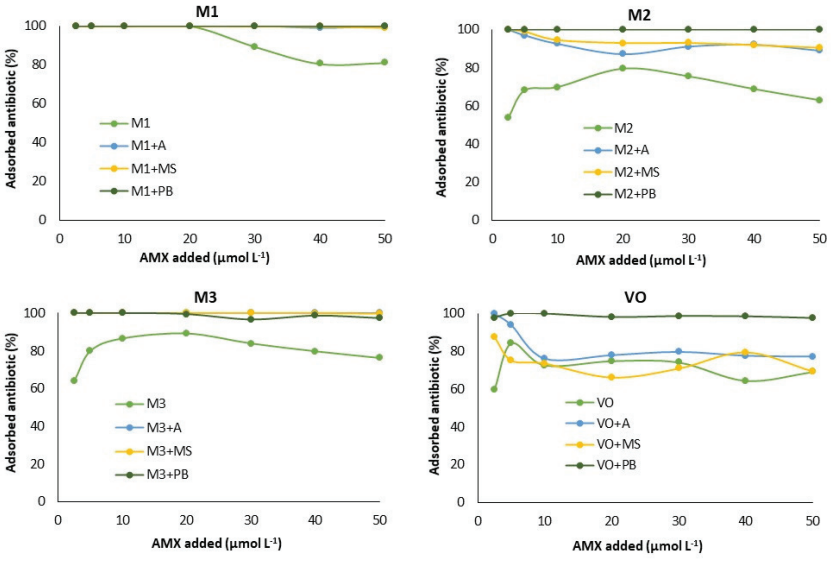

Figure 2. Adsorbed antibiotic (%) for each soil and the mixtures soil + bio-adsorbent in relation to the concentration of AMX added. M: maize soil; VO: vineyard soil; A: wood ash; MS: mussel shell; PB: pine bark; AMX: amoxicillin. Average values (n = 3), with coefficients of variation always <5%.

3.2. Desorption

Table 3 shows the values of AMX desorption from the different soils depending on the concentration of antibiotic added and the bio-adsorbent used. In general, the higher the concentration of antibiotic added, the greater the desorption from soils, both with and without bio-adsorbent amendments. In some soils, this progressive increase is observed up to 40 μmol L^{-1} of AMX added, with further increase being very scarce or null from this concentration up to 50 μmol L^{-1}. In most cases, desorption was lower in soils with one bio-adsorbent than in soils without bio-adsorbents.

Table 3. AMX desorption, in μmol kg^{-1} and in percentage between brackets, from the soils studied, with or without bio-adsorbents, as a function of the concentration of antibiotic added (C_0). M: maize soils; VO: vineyard soil; A: wood ash; MS: mussel shell; PB: pine bark; –: no value. Average values (n = 3), with coefficients of variation always <5%.

	C_0 (μmol L^{-1})						
Sample	**2.5**	**5**	**10**	**20**	**30**	**40**	**50**
M1	0.349 (10.9)	1.181 (12.5)	2.331 (12.8)	2.819 (11.1)	4.781 (7.2)	4.816 (11.6)	6.21 (16.9)
M1 + A	0 (0)	0 (0)	0 (0)	0.414 (0.79)	1.698 (2.26)	2.482 (2.51)	5.062 (4.10)
M1 + MS	0 (0)	0 (0)	0 (0)	0.233 (0.44)	2.259 (3.05)	3.943 (3.98)	6.105 (4.99)
M1 + PB	0 (0)	0 (0)	0 (0)	0 (0)	0.824 (1.09)	0.834 (0.84)	1.851 (1.50)
M2	0.767 (9.25)	1.339 (12.19)	3.029 (16.12)	5.032 (13.17)	5.211 (6.07)	11.504 (8.07)	18.489 (8.36)
M2 + A	0 (0)	0 (0)	0 (0)	0 (0)	0 (0)	0 (0)	0.935 (0)
M2 + MS	0 (0)	0.047 (0.34)	0.176 (0.77)	–	0.69 (0.99)	1.061 (1.16)	3.488 (3.09)
M2 + PB	–	0.164 (1.13)	0.329 (1.35)	0.713 (1.46)	1.075 (1.46)	1.788 (1.83)	2.597 (2.19)

Table 3. *Cont.*

	C_0 (μmol L^{-1})						
Sample	**2.5**	**5**	**10**	**20**	**30**	**40**	**50**
M3	0.384 (7.45)	0.828 (8.88)	2.6 (10.40)	4.639 (6.11)	–	6.151 (9.33)	6.107 (9.67)
M3 + A	0.283 (3.82)	0.313 (2.45)	–	0.949 (1.80)	1.055 (1.40)	2.319 (2.31)	–
M3 + MS	–	0.258 (2.01)	–	2.488 (4.74)	2.694 (3.58)	–	4.684 (3.79)
M3 + PB	0 (0)	0 (0)	0 (0)	0 (0)	0 (0)	0.14 (0.14)	1.276 (1.05)
VO	0.357 (7.67)	0.735 (13.41)	2.115 (13.85)	2.446 (8.58)	4.741 (8.15)	8.139 (6.26)	8.682 (7.68)
VO + A	0 (0)	0 (0)	0 (0)	0 (0)	0 (0)	0 (0)	0 (0)
VO + MS	0 (0)	0 (0)	0 (0)	0 (0)	0 (0)	0 (0)	0 (0)
VO + PB	0 (0)	0 (0)	0 (0)	0 (0)	0.219 (0.30)	0.712 (0.73)	–

4. Discussion

4.1. Adsorption

In the current study pine bark (with pH 3.99) generally causes an acidification of the amended soil. In this regard, it must be noted that greater acidification is associated with more pronounced AMX adsorption increases, as occurs in soils VO and M2. In previous studies, Githinji et al. [61] found a decrease in AMX adsorption as pH increased from 3.5 to 8.5, whereas other researchers also described a decrease in adsorption for pH values > 5, using pistachio shell [62] or activated carbon [63] as adsorbents.

In the current piece of research, the pH of the soils is above 5, and it was expected that lowering it by incorporating acid adsorbents would facilitate AMX adsorption. In this regard, it is worth noting that, depending on the environmental acid-base conditions, most antibiotics can behave as cations, anions or zwitterions [64], and in the case of AMX the electrical charge of the molecule changes depending on the pH, associated with the charge density present in different functional groups. For AMX, when the pH is lower than its pk_{a1} value (2.98), the amine groups are protonated and the molecule acquires a positive charge; when the pH value is between pk_{a1} (2.98) and pk_{a2} (7.4), the molecule behaves like a zwitterion, with deprotonated carboxyl groups (negative charge density) and protonated amine groups (positive charge density); on the other hand, at pH values between pk_{a2} (7.4) and pk_{a3} (9.6), deprotonated carboxyl and amine groups predominate (with negative charge density); and, finally, at pH > pk_{a3} the phenolic groups are also deprotonated, and the charge is even more negative [65]. When soil pH decreases due to amending with acidic bio-adsorbents (such as pine bark), more positive charges appear on the variable-charge components of those soils, which are summed to those present on the bio-adsorbents, thus being able to bind functional groups of AMX with negatively charged sites, due to electrostatic interactions.

In the current study, the wood ash amendment increased the pH of all soils, while the addition of mussel shell clearly increased the pH of only two of them (M2 and M3) (Table 1). However, an increase in AMX adsorption was also observed with these two amendments (wood ash and mussel shell), similarly to what was achieved when pine bark was added. This is due to the fact that the increase in pH derived from the addition of wood ash and mussel shell causes the appearance of a large number of negative charges in organic matter and in the non-crystalline minerals of the soil, which are very abundant in the soils of this study (Table S1, Supplementary Materials), to be summed to the fact that non-crystalline minerals are also very abundant in wood ash (Table S2, Supplementary Materials). Thus, these negative charges present in the soils and in the bio-adsorbents will facilitate bonds with deprotonated carboxyl groups of the AMX molecule, stablished through cationic bridges (in which Ca probably plays an important role, given its abundance both in wood ash and in mussel shell, Table S2, Supplementary Materials). However, it should be noted that, in the VO soil, despite the fact that wood ash and mussel shell increase the pH, the increase in AMX adsorption is clearly lower than that achieved by amending with pine

bark, because organic matter and non-crystalline mineral contents are much lower in this soil than in the other three.

Regarding the fittings to adsorption models, starting with the Linear model the values of the distribution coefficient (K_d) were in the range between 1 and 1525.76 L kg^{-1} in maize soils, and between 5.93 and 112.34 L kg^{-1} in the vineyard soil (Table 2). These values are lower than those reported in previous studies for tetracycline antibiotics [54], but are higher than for sulfonamides [66]. This would indicate that the interactions with soils that give rise to AMX adsorption are weaker than those taking place with tetracycline antibiotics, but stronger than those affecting sulfonamides. Regarding the Freundlich model, the K_F values (affinity coefficient, related to adsorption capacity) vary between 1 and 139.24 L^n μmol^{1-n} kg^{-1} in maize soils, and between 9.58 and 109.63 L^n μmol^{1-n} kg^{-1} in the vineyard soil. These results are also lower than those obtained by other authors [56] for tetracyclines, but higher than those obtained for sulfonamide [64]. As for the Freundlich's n values, in the case of maize soils they are between 0 and 0.926, while in the vineyard soil they range between 0.298 and 0.892. These n values are lower than 1 in all soils, which would indicate that adsorption is not linear, coinciding with that obtained by other authors [61] for other materials. In fact, values of $n < 1$ indicate the presence of heterogeneous adsorption sites and a non-linear and concave curve, which means that the number of available adsorption sites decreases when the concentration of the added contaminant increases, occupying firstly the high energy adsorption sites [67,68]. Regarding the Langmuir model, the K_L values range between 0.05 and 103.81 L μmol^{-1} in maize soils, and between 0.037 and 0.975 L μmol^{-1} in vineyard soils (Table 2).

As shown in Figure 1 and in Table S3 (Supplementary Materials), both soils M1 and M3 have very high AMX adsorption scores (sometimes close to 100%) for most of the antibiotic concentrations added. For these two soils, the incorporation of bio-adsorbents causes modifications in adsorption that are lower than the results reached in the other two soils. In the soils that adsorb less AMX (VO and M2), the mixtures with wood ash, mussel shell or pine bark generally continue to present high R^2 values (>0.80) for the three models (Table 2), but the high errors associated with the estimation of some parameters invalidate the fittings in several cases (especially in the Langmuir model).

4.2. Desorption

Regarding desorption, focusing on the maximum concentration added (50 $\mu mol\ L^{-1}$), unamended soils desorb between 6% and 17% of the AMX previously adsorbed, while the release of the antibiotic from the mixtures of soil + bio-adsorbent was always lower than 6%. The greatest decrease in desorption occurred in soil M2 when adding pine bark, going from 17% to 2.5%. Similar results were obtained previously for tetracyclines and sulfonamides [56,66], by researchers who added pine bark to different soils, detecting a decrease in desorption of up to 12% for tetracyclines, and up to 17% for sulfonamides. In this regard, a previous study [69] indicated that the presence of tannins in pine bark favors adsorption (and decreases desorption). It should be noted that AMX desorption has been mainly studied in wastewater, while most of the studies on the adsorption of this antibiotic in soils omit desorption processes. In aqueous matrices, the reported AMX desorption values went from 5% when almond shell ashes were added [70] up to 40% in cases where clay materials were used as adsorbents [71].

5. Conclusions

The pH and the abundance of non-crystalline minerals and organic matter are the most determining factors in the adsorption processes of the antibiotic amoxicillin (AMX) in the soils evaluated in this study, both alone and amended with the three tested bio-adsorbents (pine bark, wood ash and mussel shell). It was evidenced that AMX adsorption increased when the crop soils used (devoted to maize and vineyard cultivation) were mixed with the different bio-adsorbents. This increase was higher when pine bark (the bio-adsorbent with the most acidic pH) was added. In addition, AMX desorption decreased when the bio-

adsorbent materials were incorporated into the soil, reaching values that did not exceed 6%. The overall results obtained in the current research show that, regarding its applicability, the incorporation of the three bio-adsorbents into agricultural soils contaminated by AMX reduced the risk of transport and passage of the antibiotic to surface and groundwater, and therefore to the food chain, which in fact entails important implications for the environment and public health. In future studies, it would be interesting to evaluate the effect of other bio-adsorbents, as well as soils with different characteristics compared to those used here. Furthermore, possible additional studies could delve into the mechanisms that explain the retention and release processes of AMX when it reaches the environment as a pollutant.

Supplementary Materials: The following supporting information can be downloaded at: https://www.mdpi.com/article/10.3390/ma15093200/s1. Table S1. Values corresponding to the basic parameters determined in the various soils studied. M: maize soils; VO: vineyard soils; OC: organic carbon; OM: organic matter; eCEC: effective cation exchange capacity; Cae, Mge, Nae, Ke, Ale: elements in the exchange complex; o subindex: non-crystalline form; pyr subindex: crystalline form. Average values (n = 3), with coefficients of variation always <5%.; Table S2. Characteristics of the bio-adsorbent materials. Cae, Mge, Nae, Ke, Ale: elements in the exchange complex; Sat. Al: Al-saturation in the exchange complex; eCEC: effective cation exchange capacity; XT: total content of the element (X); Alo, Feo: non-crystalline Al and Fe; <LD: below detection level. Average values (n = 3), with coefficients of variation always <5%.; Table S3. AMX adsorption, expressed in μmol kg^{-1} (and in percentage between brackets), for the various soils studied, with or without bio-adsorbents, as a function of the concentration of antibiotic added. M: maize (corn) soils; VO: vineyard soils; A: ashes; MS: mussel shell; PB: pine bark. Average values (n = 3), with coefficients of variation always <5%.; Figure S1. Example chromatograms corresponding to AMX adsorption onto soils amended with bio-adsorbents

Author Contributions: Conceptualization, E.Á.-R., M.J.F.-S., A.N.-D. and M.A.-E.; methodology, E.Á.-R., M.J.F.-S., A.N.-D., M.A.-E., R.C.-D. and A.B.; software, E.Á.-R. and R.C.-D.; validation, E.Á.-R., M.J.F.-S., A.N.-D., M.A.-E. and A.B.; formal analysis, R.C.-D.; investigation, E.Á.-R., M.J.F.-S., R.C.-D. and A.B.; resources, E.Á.-R., M.J.F.-S. and M.A.-E.; data curation, E.Á.-R., M.J.F.-S., A.N.-D. and A.B.; writing—original draft preparation, E.Á.-R., M.J.F.-S., A.B. and R.C.-D.; writing—review and editing, A.N.-D.; visualization, E.Á.-R., M.J.F.-S., A.N.-D., M.A.-E., R.C.-D., L.R.-L., V.S.-M. and A.B.; supervision, E.Á.-R., M.J.F.-S. and A.B.; project administration, E.Á.-R., M.J.F.-S. and M.A.-E.; funding acquisition, E.Á.-R., M.J.F.-S. and M.A.-E. All authors have read and agreed to the published version of the manuscript.

Funding: This research was funded by Spanish Ministry of Science, Innovation and Universities, grant numbers RTI2018-099574-B-C21 and RTI2018-099574-B-C22.

Institutional Review Board Statement: Not applicable.

Informed Consent Statement: Not applicable.

Data Availability Statement: Not applicable.

Conflicts of Interest: The authors declare no conflict of interest. The funders had no role in the design of the study; in the collection, analyses, or interpretation of data; in the writing of the manuscript, or in the decision to publish the results.

References

1. Conde-Cid, M.; Núñez-Delgado, A.; Fernández-Sanjurjo, M.J.; Álvarez-Rodríguez, E.; Fernández-Calviño, D.; Arias-Estévez, M. Tetracycline and Sulfonamide Antibiotics in Soils: Presence, Fate and Environmental Risks. *Processes* **2020**, *8*, 1479–1519. [CrossRef]
2. Khan, N.A.; Khan, S.U.; Ahmed, S.; Farooqi, I.H.; Yousefi, M.; Mohammadi, A.A.; Changani, F. Recent trends in disposal and treatment technologies of emerging-pollutants—A critical review. *Trends Anal. Chem.* **2020**, *122*, 115744–115759. [CrossRef]
3. ECDC. *European Centre for Disease Prevention and Control. Antimicrobial Consumption in the EU/EEA (ESAC-Net)—Annual Epidemiological Report 2020*; European Centre for Disease Prevention and Control: Stockholm, Sweden, 2021.
4. Duan, H.; Li, X.; Mei, A.; Li, P.; Liu, Y.; Li, X.; Li, W.; Wang, C.; Xie, S. The diagnostic value of metagenomic next-generation sequencing in infectious diseases. *BMC Infect. Dis.* **2021**, *21*, 62–69. [CrossRef]

5. Russell, J.N.; Yost, C.K. Alternative, environmentally conscious approaches for removing antibiotics from wastewater treatment systems. *Chemosphere* **2021**, *263*, 128177–128187. [CrossRef] [PubMed]
6. Santás-Miguel, V.; Díaz-Raviña, M.; Martín, A.; García-Campos, E.; Barreiro, A.; Núñez-Delgado, A.; Fernández-Sanjurjo, M.J.; Álvarez-Rodríguez, E.; Arias-Estévez, M.; Fernández-Calviño, D. Medium-term influence of tetracyclines on total and specific microbial biomass in cultivated soils of Galicia (NW Spain). *Span. J. Soil Sci.* **2020**, *10*, 2017–2232. [CrossRef]
7. Christou, A.; Agüera, A.; Bayona, J.M.; Cytryn, E.; Fotopoulos, V.; Lambropoulou, D.; Manaia, C.M.; Michael, C.; Revitt, M.; Schöder, P.; et al. The potential implications of reclaimed wastewater reuse for irrigation on the agricultural environment: The knowns and unknowns of the fate of antibiotics and antibiotic resistant bacteria and resistance genes—A review. *Water Res.* **2017**, *123*, 448–467. [CrossRef] [PubMed]
8. Krzeminski, P.; Tomei, M.C.; Karaolia, P.; Langenhoff, A.; Almeida, C.M.R.; Felis, E.; Gritten, F.; Andersen, H.R.; Fernandes, T.; Manaia, C.M.; et al. Performance of secondary wastewater treatment methods for the removal of contaminants of emerging concern implicated in crop uptake and antibiotic resistance spread: A review. *Sci. Total Environ.* **2019**, *648*, 1052–1081. [CrossRef]
9. Salam, L.B.; Obayori, O.S. Structural and functional metagenomics analyses of a tropical agricultural soil. *Span. J. Soil Sci.* **2019**, *9*, 1–23. [CrossRef]
10. Ahmed, M.B.M.; Rajapaksha, A.U.; Lim, J.E.; Vu, N.T.; Kim, I.S.; Kang, H.M.; Lee, S.S.; Ok, Y.S. Distribution and accumulative pattern of tetracyclines and sulfonamides in edible vegetables of cucumber, tomato, and lettuce. *J. Agric. Food Chem.* **2015**, *63*, 398–405. [CrossRef]
11. Azanu, D.; Mortey, C.; Darko, G.; Weisser, J.J.; Styrishave, B.; Abaidoo, R.C. Uptake of antibiotics from irrigation water by plants. *Chemosphere* **2016**, *157*, 107–114. [CrossRef]
12. Yazidi, A.; Atrous, M.; Soetaredjo, F.E.; Sellaoui, L.; Ismadji, S.; Erto, A.; Bonilla-Petriciolet, A.; Dotto, G.L.; Lamine, A.B. Adsorption of amoxicillin and tetracycline on activated carbon prepared from durian shell in single and binary systems: Experimental study and modeling analysis. *Chem. Eng. J.* **2020**, *379*, 122320. [CrossRef]
13. Kidak, R.; Doğan, Ş. Medium-high frequency ultrasound and ozone based advanced oxidation for amoxicillin removal in water. *Ultrason. Sonochem.* **2018**, *40*, 131–139. [CrossRef] [PubMed]
14. Kim, C.; Ryu, H.; Chung, E.G.; Kim, Y. Determination of 18 veterinary antibiotics in environmental water using high-performance liquid chromatography-q-orbitrap combined with on-line solid-phase extraction. *J. Chromatogr. B* **2018**, *1084*, 158–165. [CrossRef] [PubMed]
15. Cacace, D.; Fatta-Kassinos, D.; Manaia, C.M.; Cytryn, E.; Kreuzinger, N.; Rizzo, L.; Karaolia, P.; Schwartz, T.; Alexander, J.; Merlin, C.; et al. Antibiotic resistance genes in treated wastewater and in the receiving water bodies: A pan- European survey of urban settings. *Water Res.* **2019**, *162*, 320–330. [CrossRef] [PubMed]
16. Bilal, M.; Mehmood, S.; Rasheed, T.; Iqbal, H.M. Antibiotics traces in the aquatic environment: Persistence and adverse environmental impact. *Curr. Opin. Environ. Sci. Health* **2020**, *13*, 68–74. [CrossRef]
17. Parra-Saldivar, R.; Bilal, M.; Iqbal, H.M.N. Life cycle assessment on wastewater treatment technology. *Curr. Opin. Environ. Sci. Health* **2020**, *13*, 80–84. [CrossRef]
18. Rizzo, L.; Gernjak, W.; Krzeminski, P.; Malato, S.; McArdell, C.S.; Perez, J.A.S.; Schaar, H.; Fatta-Kassinos, D. Best available technologies and treatment trains to address current challenges in urban wastewater reuse for irrigation of crops in EU countries. *Sci. Total Environ.* **2020**, *710*, 136312–136329. [CrossRef]
19. Adegoke, A.A.; Amoah, I.D.; Stenström, T.A.; Verbyla, M.E.; Mihelcic, J.R. Epidemiological evidence and health risks associated with agricultural reuse of partially treated and untreated wastewater: A review. *Front. Public Health* **2018**, *6*, 337–357. [CrossRef]
20. Carey, R.O.; Migliaccio, K.W. Contribution of wastewater treatment plant effluents to nutrient dynamics in aquatic systems: A review. *Environ. Manag.* **2009**, *44*, 205–217. [CrossRef]
21. Payment, P.; Plante, R.; Cejka, P. Removal of indicator bacteria, human enteric viruses Giardia cysts and *Cryptosporidium* oocysts at a large wastewater primary treatment facility. *Can. J. Microbiol.* **2001**, *47*, 188–193. [CrossRef]
22. Rizzo, L.; Manaia, C.; Merlin, C.; Schwartz, T.; Dagot, C.; Ploy, M.C.; Michael, I.; Fatta-Kassinos, D. Urban wastewater treatment plants as hotspots for antibiotic resistant bacteria and genes spread into the environment: A review. *Sci. Total Environ.* **2013**, *447*, 345–360. [CrossRef] [PubMed]
23. Oliveira, N.A.L.; Gonçalves, B.H.; Lee, S.; Oliveira, C.A.F.; Corassin, C.H. Use of antibiotics in animal production and its impact on human health. *J. Food Chem. Nanotechnol.* **2020**, *6*, 40–47. [CrossRef]
24. Grenni, P.; Ancona, V.; Caracciolo, A.B. Ecological effects of antibiotics on natural ecosystems: A review. *Microchem. J.* **2018**, *136*, 25–39. [CrossRef]
25. Kovalakova, P.; Cizmas, L.; McDonald, T.J.; Marsalek, B.; Feng, M.; Sharma, V.K. Occurrence and toxicity of antibiotics in the aquatic environment—A review. *Chemosphere* **2020**, *251*, 126351–126366. [CrossRef]
26. Piña, B.; Bayona, J.M.; Christou, A.; Fatta-Kassinos, D.; Guillon, E.; Lambropoulou, D.; Michael, C.; Polesel, F.; Sayen, S. On the contribution of reclaimed wastewater irrigation to the potential exposure of humans to antibiotics, antibiotic resistant bacteria and antibiotic resistance genes—NEREUS COST Action ES1403 position paper. *J. Environ. Chem. Eng.* **2020**, *8*, 102131–102134. [CrossRef]
27. Chen, Q.; An, X.; Li, H.; Su, J.; Ma, Y.; Zhu, Y. Long-term field application of sewage sludge increases the abundance of antibiotic resistance genes in soil. *Environ. Int.* **2016**, *92–93*, 1–10. [CrossRef]

28. López-Periago, E.; Núñez-Delgado, A.; Díaz-Fierros, F. Attenuation of groundwater contamination caused by cattle slurry: A plot-scale experimental study. *Bioresour. Technol.* **2002**, *84*, 105–111. [CrossRef]
29. Núñez-Delgado, A.; López-Períago, E.; Díaz-Fierros-Viqueira, F. Pollution attenuation by soils receiving cattle slurry after passage of a slurry-like feed solution: Column experiments. *Bioresour. Technol.* **2002**, *84*, 229–236. [CrossRef]
30. Xie, T.; Wang, M.; Su, C.; Chen, W. Evaluation of the natural attenuation capacity of urban residential soils with ecosystem-service performance index (EPX) and entropy-weight methods. *Environ. Pollut.* **2018**, *238*, 222–229. [CrossRef]
31. Dong, J.; Xie, H.; Feng, R.; Lai, X.; Duan, H.; Xu, L.; Xia, X. Transport and fate of antibiotics in a typical aqua-agricultural catchment explained by rainfall events: Implications for catchment management. *J. Environ. Manag.* **2021**, *293*, 112953–112963. [CrossRef]
32. Kemper, N. Veterinary antibiotics in the aquatic and terrestrial environment. *Ecol. Indic.* **2008**, *8*, 1–13. [CrossRef]
33. Pan, M.; Chu, L.M. Fate of antibiotics in soil and their uptake by edible crops. *Sci. Total Environ.* **2017**, *599–600*, 500–512. [CrossRef] [PubMed]
34. Putra, E.K.; Ismadji, S. Performance of activated carbon and bentonite for adsorption of amoxicillin from wastewater: Mechanisms, isotherms and kinetics. *Water Res.* **2009**, *43*, 2419–2430. [CrossRef]
35. Zha, S.X.; Zhou, Y.; Jin, X.; Chen, Z. The removal of amoxicillin from wastewater using organobentonite. *J. Environ. Manag.* **2013**, *129*, 569–576. [CrossRef]
36. Anastopoulos, I.; Pashalidis, I.; Orfanos, A.O.; Manariotis, I.D.; Tatarchuk, T.; Sellaoui, L.; Bonilla-Petriciolet, A.; Mittal, A.; Núñez-Delgado, A. Removal of caffeine, nicotine and amoxicillin from (waste) waters by various adsorbents. *A review. J. Environ. Manag.* **2020**, *261*, 110236. [CrossRef] [PubMed]
37. Felix, I.M.B.; Moreira, L.C.; Chiavone-Filho, O.; Mattedi, S. Solubility measurements of amoxicillin in mixtures of water and ethanol from 283.15 to 298.15 K. *Fluid Phase Equilib.* **2016**, *422*, 78–86. [CrossRef]
38. Shakak, M.; Rezaee, R.; Afshin, M.; Jafari, A.; Safari, M.; Shahmoradi, B.; Daraei, H.; Lee, S. Synthesis and characterization of nanocomposite ultrafiltration membrane (PSF/PVP/SiO2) and performance evaluation for the removal of amoxicillin from aqueous solutions. *Environ. Technol.* **2020**, *17*, 100529–100543. [CrossRef]
39. Homayoonfal, M.; Mehrnia, M.R. Amoxicillin separation from pharmaceutical solution by pH sensitive nanofiltration membranes. *Sep. Purif. Technol.* **2014**, *130*, 74–83. [CrossRef]
40. Lyu, J.; Yang, L.; Zhang, L.; Ye, B.; Wang, L. Antibiotics in soil and water in China—A systematic review and source analysis. *Environ. Pollut.* **2020**, *266*, 115147–115159. [CrossRef]
41. Ding, H.; Wu, Y.; Zou, B.; Lou, Q.; Zhang, W.; Zhong, J.; Lu, L.; Dai, G. Simultaneous removal and degradation characteristics of sulfonamide, tetracycline, and quinolone antibiotics by laccase-mediated oxidation coupled with soil adsorption. *J. Hazard. Mater.* **2016**, *307*, 350–358. [CrossRef]
42. Ata, R.; Sacco, O.; Vaiano, V.; Rizzo, L.; Tore, G.Y.; Sannino, D. Visible light active N-doped TiO_2 immobilized on polystyrene as efficient system for wastewater treatment. *J. Photochem. Photobiol. A Chem.* **2017**, *348*, 255–262. [CrossRef]
43. Zhang, C.; Wang, W.; Duan, A.; Zeng, G.; Huang, D.; Lai, C.; Tan, X.; Cheng, M.; Wang, R.; Zhou, C.; et al. Adsorption behavior of engineered carbons and carbon nanomaterials for metal endocrine disruptors: Experiments and theoretical calculation. *Chemosphere* **2019**, *222*, 184–194. [CrossRef]
44. Crisafully, R.; Millhome, M.A.L.; Cavalcante, R.M.; Silveira, E.R.; De Keukeleire, D.; Nascimento, R.F. Removal of some polycyclic aromatic hydrocarbons from petrochemical wastewater using low-cost adsorbents of natural origin. *Bioresour. Technol.* **2008**, *99*, 4515–4519. [CrossRef] [PubMed]
45. Cela-Dablanca, R.; Nebot, C.; Rodríguez López, L.; Fernández-Calviño, D.; Arias-Estévez, M.; Núñez-Delgado, A.; Fernández-Sanjurjo, M.J.; Álvarez-Rodríguez, E. Efficacy of Different Waste and By-Products from Forest and Food Industries in the Removal/Retention of the Antibiotic Cefuroxime. *Processes* **2021**, *9*, 1151. [CrossRef]
46. Núñez-Delgado, A.; Álvarez-Rodríguez, E.; Fernández-Sanjurjo, M.J.; Nóvoa-Muñoz, J.C.; Arias-Estévez, M.; Fernández-Calviño, D. Perspectives on the use of by-products to treat soil and water pollution. *Micropor. Mesopor. Mater.* **2015**, *210*, 199–201. [CrossRef]
47. Ramírez-Pérez, A.M.; Paradelo, M.; Nóvoa-Muñoz, J.C.; Arias-Estévez, M.; Fernández-Sanjurjo, M.J.; Álvarez-Rodríguez, E.; Núñez-Delgado, A. Heavy metal retention in copper mine soil treated with mussel shells: Batch and column experiments. *J. Hazard. Mater.* **2013**, *248–249*, 122–130. [CrossRef]
48. Seco-Reigosa, N.; Peña-Rodríguez, S.; Nóvoa-Muñoz, J.C.; Arias-Estévez, M.; Fernández Sanjurjo, M.J.; Álvarez-Rodríguez, E.; Núñez-Delgado, A. Arsenic, chromium and mercury removal using mussel shell ash or a sludge/ashes waste mixture. *Environ. Sci. Pollut. Res.* **2013**, *20*, 2670–2678. [CrossRef]
49. Seco-Reigosa, N.; Bermúdez-Couso, A.; Garrido-Rodríguez, B.; Arias-Estévez, M.; Fernández Sanjurjo, M.J.; Álvarez-Rodríguez, E.; Núñez-Delgado, A. As(V) retention on soils and forest by-products and other waste materials. *Environ. Sci. Pollut. Res.* **2013**, *20*, 6574–6583. [CrossRef]
50. Seco-Reigosa, N.; Cutillas-Barreiro, L.; Nóvoa-Muñoz, J.C.; Arias-Estévez, M.; Fernández-Sanjurjo, M.J.; Álvarez-Rodríguez, E.; Núñez-Delgado, A. Mixtures including wastes from the mussel shell processing industry: Retention of arsenic, chromium and mercury. *J. Clean Prod.* **2014**, *84*, 680–690. [CrossRef]
51. Cutillas-Barreiro, L.; Ansias-Manso, L.; Fernández-Calviño, D.; Arias-Estévez, M.; Nóvoa-Muñoz, J.C.; Fernández Sanjurjo, M.J.; Álvarez-Rodríguez, E.; Núñez-Delgado, A. Pine bark as bio-adsorbent for Cd, Cu, Ni, Pb and Zn: Batch-type and stirred flow chamber experiments. *J. Environ. Manag.* **2014**, *144*, 258–264. [CrossRef]

52. Otero, M.; Cutillas-Barreiro, L.; Nóvoa-Muñoz, J.C.; Arias-Estévez, M.; Fernández Sanjurjo, M.J.; Álvarez-Rodríguez, E.; Núñez-Delgado, A. Cr (VI) sorption/desorption on untreated and mussel-shell-treated soil materials: Fractionation and effects of pH and chromium concentration. *Solid Earth* **2015**, *6*, 373–382. [CrossRef]
53. Romar, A.; Nóvoa, J.C.; Arias, M.; Fernández-Sanjurjo, M.J.; Álvarez, E.; Núñez, A. Controlling risks of P water pollution by sorption on soils, pyritic material, granitic material, and different by-products: Effects of pH and incubation time. *Environ. Sci. Pollut. Res.* **2018**, *26*, 11558–115564. [CrossRef] [PubMed]
54. Quintáns-Fondo, A.; Ferreira-Coelho, G.; Paradelo, R.; Nóvoa, J.C.; Arias, M.; Fernández-Sanjurjo, M.J.; Álvarez, E.; Núñez, A. F sorption/desorption on two soils and on different by-products and waste materials. *Environ. Sci. Pollut. Res.* **2016**, *23*, 14676–14685. [CrossRef] [PubMed]
55. Quintáns-Fondo, A.; Ferreira-Coelho, G.; Arias-Estévez, M.; Nóvoa-Múñoz, J.C.; Fernández-Calviño, D.; Álvarez-Rodríguez, E.; Fernández-Sanjurjo, M.J.; Núñez-Delgado, A. Chromium VI and fluoride competitive adsorption on different soils and by-products. *Processes* **2019**, *7*, 748–761. [CrossRef]
56. Conde-Cid, M.; Ferreira-Coelho, G.; Arias-Estévez, M.; Álvarez-Esmorís, C.; Nóvoa Muñoz, J.C.; Núñez-Delgado, A.; Fernández-Sanjurjo, M.J.; Álvarez-Rodríguez, E. Competitive adsorption/desorption of tetracycline, oxytetracycline and chlortetracycline on pine bark, oak ash and mussel shell. *J. Environ. Manag.* **2019**, *250*, 109509–109519. [CrossRef] [PubMed]
57. Conde-Cid, M.; Cela-Dablanca, R.; Ferreira-Coelho, G.; Fernández-Calviño, D.; Núñez-Delgado, A.; Fernández-Sanjurjo, M.J.; Arias-Estévez, M.; Álvarez-Rodríguez, E. Sulfadiazine, sulfamethazine and sulfachloropyridazine removal using three different porous materials: Pine bark, "oak ash" and mussel shell. *Environ. Res.* **2021**, *195*, 110814–110820. [CrossRef]
58. Núñez-Delgado, A.; Fernández-Sanjurjo, M.J.; Álvarez-Rodríguez, E.; Arias-Estévez, M.; Conde-Cid, M.; Fernández-Calviño, D. Chapter 25—Sorbents to control soil pollution. In *Sorbents Materials for Controlling Environmental Pollution*; Núñez-Delgado, A., Ed.; Elsevier: Amsterdam, The Netherlands, 2021; pp. 691–700. [CrossRef]
59. Rivas-Pérez, I.M.; Conde-Cid, M.; Nóvoa-Muñoz, J.C.; Arias-Estévez, M.; Fernández-Sanjurjo, M.J.; Álvarez-Rodríguez, E.; Núñez-Delgado, A. As(V)/Cr(VI) retention on un-amended and waste-amended soil samples: Competitive experiments. *Environ. Sci. Pollut. Res.* **2017**, *24*, 1051–1059. [CrossRef]
60. Ayawei, N.; Ebelegi, A.N.; Wankasi, D. Modelling and Interpretation of Adsorption Isotherms. *J. Chem.* **2017**, *2017*, 11–23. [CrossRef]
61. Githinji, L.J.M.; Musey, M.K.; Ankumah, R.O. Evaluation of the fate of ciprofloxacin and amoxicillin in domestic wastewater. *Water Air Soil Pollut.* **2011**, *219*, 191–201. [CrossRef]
62. Mohammed, A.A.; Al-Musawi, T.J.; Kareem, S.L.; Zarrabi, M.; Al-Mabreh, A.M. Simultaneous adsorption of tetracycline, amoxicillin and ciprofloxacin by pistacho shell powder coates with zinc oxide nanoparticles. *Arab. J. Chem.* **2020**, *13*, 4629–4643. [CrossRef]
63. Shahrouzi, J.R.; Sakineh, M.; Ebadi, A.; Tiwfighi, F.; Bakhti, F. Investigation of effective parameters on adsorption of amoxicillin from aqueous medium onto activated carbon. *Adv. Environ. Technol.* **2019**, *2*, 107–114.
64. Zhi, D.; Yang, D.; Zheng, Y.; Yang, Y.; HE, Y.; Luo, L.; Zhou, Y. Current progress in the adsorption, transport and biodegradation of antibiotics in soil. *J. Environ. Manag.* **2019**, *251*, 109598–109605. [CrossRef] [PubMed]
65. Pezoti, O.; Cazetta, A.L.; Bedin, K.C.; Souza, L.S.; Martíns, A.C.; Silva, T.L.; Santos Junior, O.O.; Visentainer, J.V.; Almeida, V.C. NaOH-actived carbon of high surface area produced from guava seeds as a high-efficiency adsorbent for amoxicillin removal: Kinetic, isotherm and thermodynamic studies. *Chem. Eng. J.* **2016**, *288*, 778–788. [CrossRef]
66. Conde-Cid, M.; Fernández, D.; Núñez-Delgado, A.; Fernández-Sanjurjo, M.J.; Arias-Estévez, M.; Álvarez-Rodríguez, E. Influence of mussel shell, oak ash and pine bark on the adsorption and desorption of sulfonamides in agricultural soils. *J. Environ. Manag.* **2020**, *261*, 110221–110231. [CrossRef]
67. Foo, K.Y.; Hameed, B.H. Insights into the modeling of adsorption isotherm systems. *Chem. Eng. J.* **2010**, *156*, 2–10. [CrossRef]
68. Behnajady, M.A.; Bimeghdar, S. Synthesis of mesoporous NiO nanoparticles and their application in the adsorption of Cr (VI). *Chem. Eng. J.* **2014**, *239*, 105–113. [CrossRef]
69. Barceló, H.A.; Santos, S.C.; Botelho, C.M. Tannin-based biosorbents for environmental applications–A review. *Chem. Eng. J.* **2016**, *303*, 575–587. [CrossRef]
70. Homem, V.; Alves, A.; Santos, L. Amoxicillin removal from aqueous matrices by sorption with almond shell ashes. *Int. J. Environ. Anal. Chem.* **2010**, *90*, 1063–1084. [CrossRef]
71. Chauhan, M.; Saini, V.K.; Suthar, S. Ti-pillared montmorillonite clay for adsorptive removal of amoxicillin, imipramine, diclofenac-sodium, and paracetamol from water. *J. Hazard. Mater.* **2020**, *399*, 122832–122845. [CrossRef]

toxics

MDPI

Article

Colony-Forming Efficiency Assay to Assess Nanotoxicity of Graphene Nanomaterials

Hansol Won †, Sung-Hyun Kim †, Jun-Young Yang, Kikyung Jung, Jayoung Jeong, Jae-Ho Oh and Jin-Hee Lee *

Division of Toxicological Research, National Institute of Food and Drug Safety Evaluation, Ministry of Food and Drug Safety, 187, Osongsaengmyeong 2-Ro, Cheongju 28159, Korea; hanssol2@korea.kr (H.W.); tjdgus32@kakao.com (S.-H.K.); yangjy@korea.kr (J.-Y.Y.); kikyung@korea.kr (K.J.); 0jjy@korea.kr (J.J.); chopin68@korea.kr (J.-H.O.)

* Correspondence: tod98@korea.kr; Tel.: +82-43-719-5106; Fax: +82-43-719-5100

† These authors contributed equally to this work.

Abstract: The nano-market has grown rapidly over the past decades and a wide variety of products are now being manufactured, including those for biomedical applications. Despite the widespread use of nanomaterials in various industries, safety and health effects on humans are still controversial, and testing methods for nanotoxicity have not yet been clearly established. Nanomaterials have been reported to interfere with conventional cytotoxicity tests due to their unique properties, such as light absorption or light scattering. In this regard, the colony-forming efficacy (CFE) assay has been suggested as a suitable test method for testing some nanomaterials without these color-interferences. In this study, we selected two types of GNPs (Graphene nanoplatelets) as test nanomaterials and evaluated CFE assay to assess the cytotoxicity of GNPs. Moreover, for further investigation, including expansion into other cell types, GNPs were evaluated by the conventional cytotoxicity tests including the 3-(4,5-dimethylthiazol-2-yl)-5-(3-carboxymethoxyphenyl)-2-(4-sulfophenyl)-2H-tetrazolium (MTS), Cell Counting Kit-8 (CCK-8), and Neutral red uptake (NRU) assay using MDCK, A549 and HepG2 cells. The results of CFE assay suggest that this test method for three cell lines can be applied for GNPs. In addition, the CFE assay was able to evaluate cytotoxicity regardless more accurately of color interference caused by residual nanomaterials.

Keywords: graphene; cytotoxicity; CFE; interference

Citation: Won, H.; Kim, S.-H.; Yang, J.-Y.; Jung, K.; Jeong, J.; Oh, J.-H.; Lee, J.-H. Colony-Forming Efficiency Assay to Assess Nanotoxicity of Graphene Nanomaterials. *Toxics* **2022**, *10*, 236. https://doi.org/10.3390/toxics10050236

Academic Editor: Avelino Núñez-Delgado

Received: 6 April 2022
Accepted: 27 April 2022
Published: 5 May 2022

1. Introduction

In recent years, due to the rapid growth of nanotechnology, various manufacturing nanomaterials are being produced, and nanomaterials are used in various industries such as batteries, electrodes, cosmetics, displays and biomedical engineering [1–3]. The growth of the nano-industry affects our lives in a more prosperous manner and contributes to it by providing various benefits, however like a 'double-edged sword' it has the potential to induce human toxicity, both large and small when exposed to the body. Therefore, it is crucial to develop an accurate nanotoxicity evaluation method to understand the toxicity of these nanomaterials.

The Organization for Economic Cooperation and Development (OECD), European Union (EU) and other organizations stipulate the following for manufactured nanomaterials: 'Materials with a size less than 100 nm made for this purpose' [4,5]. As such, nanomaterials are nanoscopic in size, and the risk of nanomaterial products stem from its small size and the unique physicochemical properties of the nanomaterial. Taking the physical 'shape' as an example, carbon nanotube (CNT) nanomaterials with acicular structures such as asbestos or glass fibers have risks such as cancer-causing potential [6,7]. In addition, high surface reaction power and surface charge, due to their very small size, can contribute to allowing nanomaterials to be easily grouped and accumulated into cells [8,9].

Unlike general chemicals, nanomaterials have unique properties that make them nearly non-soluble; thus, during measurements, solid nanomaterials are detected in particular areas such as the bottom of a well, deposition on cell membranes and during intracellular uptake, which can interfere with the system and generate unreliable data [10]. Guadagnini et al. [11] also reported significant differences observed in nanomaterials interference for cytotoxicity analysis depends on the nature of nanomaterials. These problems can make it difficult to determine the exact cytotoxicity of nanomaterials, so a solution to the effects of nanomaterial interference is needed.

Colony forming efficiency (CFE) assay used to measure cellular ability to form colonies was described in OECD detailed review paper and Joint Research Centre (JRC) reports [12,13]. This in vitro assay can be used to determine cytotoxicity induced by nanomaterials. It can be performed with any adherent cells that are able to form colonies including human adult low calcium high temperature (HaCaT), Madin Darby canine kidney cell line (MDCK), human lung cancer cells (A549), human liver carcinoma cell line (HepG2) and immortalized mouse fibroblast cell line (Balb/3T3) cells. The great advantage of CFE assay is a label-free test that reduces the possibility of the incident of nanomaterials interferences. This testing method calculates cell viability by comparing the number of colonies in the vehicle control after treatment with toxicants.

We conducted a test to analyze the colony formation efficacy of various nanomaterials in MDCK cells through the OECD-JRC report [13]. In the present study, we tried to evaluate the CFE assay method for GNPs, a kind of carbon nanomaterial. In addition, we want to establish a GNP's CFE assay protocol based on A549 and HepG2 cells, which is different from the CFE conditions of MDCK cells proposed by the OECD.

In this study, the applicability of carbon-based graphene nanomaterials to a total of three cell lines was evaluated through CFE assay, an in vitro test method independent of the effect of color interference. Also, we aimed to compare the cytotoxicity assay of the conventional colorimetric cytotoxicity assay with that of the CFE assay.

2. Materials and Methods

2.1. Graphene Nanomaterials

Two types of GNPs (product No. 06-0225, product No. 06-0230) materials were purchased from Strem Chemicals (Newburyport, MA, USA). Their morphological images were confirmed by transmission electron microscopy (TEM; JEM-1200EX II, JEOL, Tokyo, Japan). The zeta potentials of the GNPs were measured using a Zetasizer Nano ZS instrument (Malvern Instruments, Malvern Hills, UK). To confirm the unique physicochemical properties of GNPs, this assay was measured in PBS and culture medium (DMEM contained with 10% FBS). In order to evaluate the dispersion stability of the test substance, the final working time was measured up to 72 h. To evaluate the dispersion stability of GNPs, a dynamic light scattering (DLS) was measured using a Zetasizer (Malvern). The levels of endotoxin were evaluated using an Endpoint Chromogenic Limulus Amoebocyte Lysate (LAL) QCL-1000 assay (Cambrex, Walkersville, MD, USA). Endotoxins were measured according to the protocols provided by the kit's manufacturer.

2.2. Preparation of Nanomaterials Suspensions

GNP's suspension was prepared by slightly modifying described methods [14,15]. Briefly, the GNPs stock (10× fold) solutions were dispersed in PBS and sonicated at 40 kHz with 100 W output power for 30 min in an ultra-sonicator (Saehan-Sonic, Seoul, Korea). Thereafter, Dulbecco's Modified Eagle's Medium (DMEM) (Life Technologies, Grand Island, NY, USA) supplemented with 10% fetal bovine serum (FBS) (Life Technologies), 100 U/mL penicillin (Life Technologies), and 100 μg/mL streptomycin (Life Technologies) was added to different working concentrations (Table 1). Initially, the concentration of GNPs was set based on a JRC report, which was previously evaluated by reference to the concentration of the same single-wall carbon nanotubes (swCNTs) [13]. The concentrations of two GNPs were finally set by performing a preliminary toxicity assessment based on the concentration

of the above carbon nanotubes and up-adjusting the test concentration according to the results.

Table 1. Test concentration of the two different carbon nanomaterials.

Nanomaterials	CAS RN	Test Concentration * (μg/mL)
GNPs-1 (300 m^2/g)	7782-42-5	1, 10, 100, 200, 400, 800
GNPs-2 (500 m^2/g)	7782-42-5	1, 10, 100, 200, 400, 800

* The concentration of GNPs was set based on a JRC report [13]. GNPs = graphene nanoplatelets.

2.3. Cell Culture

MDCK (product No. CCL-34), A549 (product No. CCL-185), and HepG2 (product No. HB-8065) cell lines were purchased from American Type Culture Collection (ATCC; Manassas, VA, USA). The cells were cultured in DMEM medium supplemented with 10% FBS, 100 U/mL penicillin and 100 μg/mL streptomycin. Three types of cells were sub-cultured every 2–4 days at about 80% confluence. For the experiments, cell density was adjusted according to the conditions of each cytotoxicity method and seeded on the 96 well culture plates or 60 × 15-mm Petri dish. Then, culture medium was replaced with a fresh medium and incubated in a humidified atmosphere condition of 5% CO_2 at 37 °C.

2.4. Colony Forming Efficiency Assay Methods

CFE assay was performed as previously described to study the cytotoxicity induced by two types of GNPs [13]. The cells were seeded at a density of 200 cells/dish (MDCK) in 3 mL complete culture medium at least in three replicates for each treatment. In the same procedure, 400 cells/dish for A549 cells and 200 cells/dish for HepG2 cells were inoculated, respectively. After 24 h, the treatment suspensions of nanomaterials and positive control (sodium chromate, Na_2CrO_4, product No. 307831, Sigma-Aldrich, St. Louis, MO, USA) were added to the cells. After 72 h of exposure, the medium was changed with a fresh complete culture medium. Considering the growth cycle of each cell line colony, after 5 days (MDCK), 8 days (HepG2) and 10 days (A549), each cell was fixed for 20 min with 3.7% (*v*/*v*) of formaldehyde solution (Sigma-Aldrich) in PBS without calcium, magnesium and sodium bicarbonate (Life Technologies, product No. 14190-250), and stained for 30 min with 0.4% (v/v) Giemsa solution (Sigma-Aldrich, product No. GS500) in ultrapure water. Colonies were manually scored under a stereomicroscope. The results were expressed as CFE (%) = [(average of treatment colonies/average of control colonies) × 100] and the corresponding standard error means [SEM% = SD/$\sqrt{}$ (number of treatments)].

$$\text{Colony Forming Efficiency } (\%) = \frac{\text{Average of treatment colonies} \times 100}{\text{Average of control colonies}} \quad (1)$$

2.5. Cytotoxicity Measurement of Colorimetric Based Assay

To confirm the difference between the existing tests measuring cytotoxicity of the test substance and the CFE assay, two types of GNPs were evaluated using three commonly used colorimetric cytotoxicity assays. The MTS assay; each cell was seeded at 3×10^4 cells/well in 96-well plates and cultured overnight and incubated for another 24 h. The conversion of MTS tetrazolium salt into its reduced formazan form was assessed with the CellTiter 96 AQueous Non-Radioactive Cell Proliferation Assay kit (Promega, Madison, WI, USA) following the manufacturer's protocol. The absorbance was read at 450 nm on a Synergy HT Multimode Microplate Reader (Bio-Tek Instruments, Winooski, VT, USA).

Cell Counting Kit-8 (CCK-8) assay; to evaluate the cell viability, cells were seeded into 96-well plates at a density of 1×10^4 cells/mL and incubated overnight to reach approximately 80% confluence. Followed by the addition of suspension containing either nanomaterials or positive control and then were incubated for 24 h at each different dose. After 24 h, the cell viability was measured using a CCK-8 assay kit (Dojindo Molecular Technologies, Gaithersburg, MD, USA).

Neutral red uptake (NRU) assay is a dye exclusion assay (Sigma-Aldrich, Cat #N2889). Briefly, each cell was seeded at 5×10^3 cells/well in 96-well plates for 24 h prior to the treatments. After nanomaterials suspension treatment, plates were incubated for 2 h with a supplemented medium containing 40 μg/mL of neutral red. Cells were subsequently washed twice with Dulbecco's Phosphate Buffered Saline (DPBS) and the dye was extracted with 200 μL destaining solution (ethanol, deionized water, and glacial acetic acid, 50:49:1 *v*/*v*). The absorbance was read at 540 nm using a microplate reader. Cell viability in terms of percentage of control was expressed in the same manner as for the MTS assay. All four types of test result data were expressed as mean ± SEM (n = 3) using GraphPad Prism V5.0 (GraphPad Software, San Diego, CA, USA).

3. Results

3.1. Physicochemical Characteristics of Graphene Nanomaterials

The morphological characteristics of graphene nanomaterials were confirmed through transmission electron microscopy (TEM) images (Figure 1). TEM images of graphene nanoplatelets (GNPs)-1 and GNPs-2 could not measure the average diameter, but according to the information provided by the manufacturer, the average diameter was <2 μm, and thickness was a few nanometers. Measurement of the zeta potential showed that two GNPs were negatively charged, with charge in phosphate buffered saline (PBS) or working solution. As a result of the dispersion stability measurement, the two substances showed a similar size distribution up to 72 h (Table 2). There was no statistical significance. Through the results of Limulus Amoebocyte Lysate (LAL) test, it was confirmed that all nanomaterials did not show contamination by endotoxin.

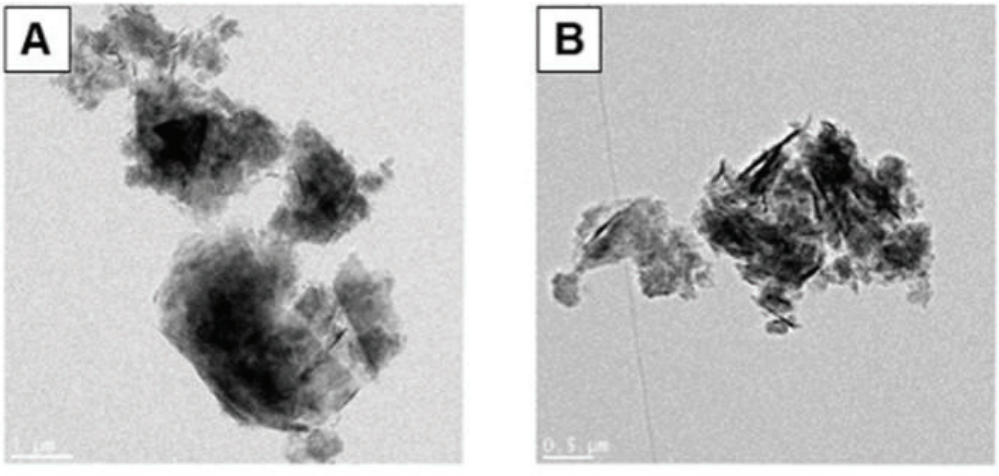

Figure 1. Morphological images of differential graphene nanomaterials observed by transmission electron microscopy. (**A**) GNPs-1 (300 m^2/g, bar = 1 μm) and (**B**) GNPs-2 (500 m^2/g, bar = 0.5 μm).

Table 2. Physicochemical characterization of the graphene nanomaterials.

Characterization	GNPs-1	GNPs-2
Average diameter (nm) *	<2 μm	<2 μm
	(a thickness of a few nanometers)	
Surface area (m^2/g) *	300	500
Zeta potential (mV) in PBS **	−30.01 ± 4.30	−33.32 ± 4.91
Zeta potential (mV) in DMEM **	−26.82 ± 0.69	−25.78 ± 0.81
Endotoxin (EU/mL)	<0.1	<0.1
Dispersion stability measurement using DLS (nm) **		
0 h	3018.00 ± 213.55	2929.00 ± 66.47
24 h	3116.67 ± 684.92	3074.50 ± 303.35
72 h	3416.00 ± 823.07	3467.00 ± 934.80
pH		
In DMEM	10.81	
In working solution **	8.87	8.56

Data are expressed as mean ± standard error of the mean (n = 6). * This data used material information provided by the manufacturer. ** Working concentration was 800 μg/mL (Measurement was performed by diluting × 100 fold in DW at the highest concentration). GNPs = graphene nanoplatelets, PBS = phosphate buffered saline, DMEM = Dulbecco's modified Eagle's medium, EU = endotoxin unit, DLS = Dynamic light scattering.

3.2. Cytotoxicity Evaluation of GNPs Using CFE Assay for Selected Cell Lines

The cytotoxicity of GNPs was evaluated by performing a CFE assay using three types of cell lines. A graph of the calculated CFE compared to the vehicle control group was presented in Figure 2 and used CFE dish images for each cell line was presented in Supplementary Materials (Figures S1–S3). First, the result of the colony forming ability test using MDCK cells at a concentration of 200 cells/dish was able to obtain cytotoxicity results in a dose-dependent manner in GNPs-1 and GNPs-2. It was confirmed that A549 cells with a concentration of 400 cells/dish, which are additional cell lines other than MDCK, were capable of optimal colony count at 10 days, and optimized at eight days of 200 cells/dish in HepG2 cells. Like the MDCK results, the results of colony formation tests using two cell lines confirmed that the cytotoxicity of nanomaterials was identified in a dose-dependent manner.

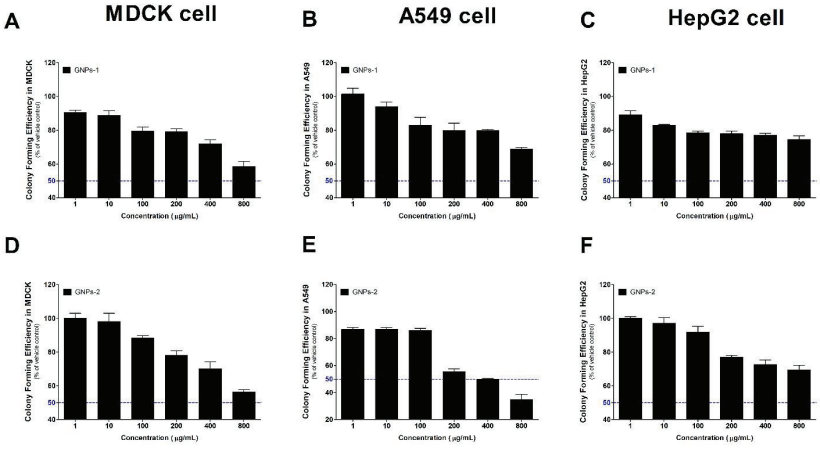

Figure 2. The colony-forming efficacy (CFE) assay results of graphene nanomaterials to MDCK, A549, and HepG2 cells. Results of GNPs-1 in (**A**) MDCK, (**B**) A549 and (**C**) HepG2 cells. Results of GNPs-2 in (**D**) MDCK, (**E**) A549, (**F**) HepG2 cells. Data are expressed as mean ± SEM (n = 3). Blue line; 50 = The half maximal.

3.3. Differences of Cytotoxicity between Colorimetric Assays

The in vitro cytotoxic effect of graphene nanomaterials was explored against MDCK, A549 and HepG2 cells in comparison with CFE assay and colorimetric cytotoxicity assay (Figure 3). Some data of the neutral red uptake (NRU) assay (red line) in the three cells showed cell viability higher than the viability value of the control group. In other words, it was observed that the cell viability rather increased as the concentration of graphene increased. In the cell counting kit-8 (CCK-8) assay results (purple line), a concentration-dependent cytotoxicity trend was observed at relatively low concentrations, but an increase-pattern in survival rate was observed with increasing optical density (OD) values at high concentrations. Especially, in A549 cells of GNPs-1 in Figure 3B, IC50 was observed at low-concentration, however cell viability showed a tendency to increase to more than 100% at high concentration. In the results of the 3-(4,5-dimethylthiazol-2-yl)-5-(3-carboxymethoxyphenyl)-2-(4-sulfophenyl)-2H-tetrazolium (MTS) assay (green line), the formazan measurement method based on mitochondrial activity, it showed a trend of concentration-dependent cell viability more sensitively than the other two methods. However, it appeared that cell viability increased when the OD value was increased at some high concentrations as shown in Figure 3B,F.

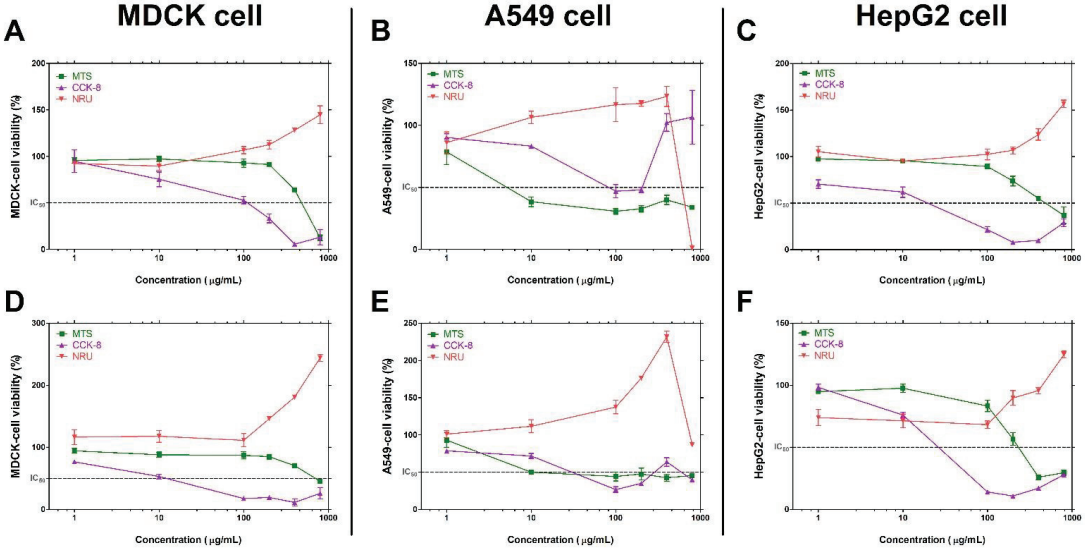

Figure 3. The comparison with results of colorimetric cytotoxicity assays treated with graphene nanomaterials. The cytotoxicity results of GNPs-1 in (**A**) MDCK, (**B**) A549 and (**C**) HepG2 cells. The cytotoxicity results of GNPs-2 in (**D**) MDCK, (**E**) A549, (**F**) HepG2 cells. Data are expressed as mean ± SEM (n = 3).

4. Discussion

Although the advantages of various nanomaterials enrich our society, it is essential to accurately evaluate the toxicity of nanomaterials to ensure the safety of workers in plants manufacturing the materials and consumers who consume products. Therefore, there is a need to develop a reliable toxicity analysis method for nanomaterials. Recently, the toxicity of nanomaterials has been identified and reported through various studies, and based on these research results, the OECD has revised the animal test guidelines such as inhalation toxicity evaluation prepared based on chemical substances by reflecting the content of nanomaterials.

Animal testing is also important in evaluating the toxicity of nanomaterials, but in vitro testing is a test method that may be appropriate for screening the toxicity of nanomaterials to various target organs under controlled conditions that cannot be performed in vivo

testing. Oberdorster et al. propose a portal-of-entry toxicity test for target organ toxicity such as lung, skin, endothelium, liver and kidney as an in vitro technique [16]. The OECD-JRC report exemplifies some test cases of nanomaterials, and a preemptive study was conducted [13]. Through this work, the OECD established and proposed a "test protocol" for a colony-forming efficacy assay based on MDCK cells. However, since the test method was verified only for MDCK cells, research was needed to apply it to various cells. To utilize the colony test for a variety of cell lines, Ponti et al. reported studies applying various adherent cells such as Caco-2, HepG2, etc., [17]. In our study, we established the applicability of the CFE assay using the alveolar epithelial cell line A549 and the hepatocyte cell line HepG2 cells as organ-derived cell lines closely related to the exposure and accumulation of nanomaterials. Based on the test results, different time-points are required to prepare a colony optimized for cells, so there is a limitation that a 'standardized number of cells' cannot be specified. However, in the end, it was confirmed that these cell lines could be used in the CFE test.

Other studies involving the testing of graphene cytotoxicity with CFE assay in vitro [18–20]. Our study performs validation of cell line expansion of swCNTs (Figure S4), and also reports the CFE evaluation results of carbon-based graphene nanomaterials that have not been reported in previous studies [13]. GNP is a type of carbon nanomaterial, which has recently attracted great attention in various fields including biomedical [21]. In general, as well known, nanomaterials were insoluble in almost solvents, and most readily form agglomerates as confirmed by transmission electron microscopy (Figure 1) [22]. Since the nanotoxicity can be accurately evaluated only when the nanomaterials used are uniformly dispersed, we tried to find a dispersion method optimized for nanomaterials. According to the papers reported on dispersion, 'serum protein' is known as a very useful dispersing agent [23,24]. In fact, it has been reported that the large aggregation of nanomaterials in a solvent was reduced by gentle aggregation in the final solution after dispersion using serum [25,26]. Therefore, by applying this method, the protein-corona coating operation was performed using FBS on the nanomaterial stock solution to induce the most homogeneous dispersion of the particles. In addition, since the mechanical dispersion operation of the ultrasonic disperser can contribute to the homogenization of the test material, the operation was additionally reflected [23].

The contrasting difference between the CFE assay and the conventional cytotoxicity assay for GNPs substances may suggest that the CFE assay was a reliable in vitro toxicity assay for GNPs [10,11,27]. Nanomaterials are either absorbed by cells or deposited on cell membranes or wells. These particles interact with cells or remain in culture plate wells despite multiple washing operations [17,28]. Traditional colorimetric-cytotoxicity assays use absorbance to evaluate the toxicity of test materials by calculating the OD values of the control and test groups and calculating the cytotoxicity in 'percentage (%)' [29–32]. If conventional absorbance-based colorimetric measurements were performed in the presence of such residual nanomaterials, incorrect results may be obtained through distortion of OD values. According to Guadagnini et al. (2015) [11], TiO_2 nanoparticles can cause false-negative results because they have the property of increasing absorbance when measured by a colorimetric method. Moreover, Wörle-Knirsch et al., Casey et al., Monteiro-Riviere et al. reported that the evaluation of carbon-based nanomaterials, which was also used in our study, may not be suitable for cytotoxicity evaluation due to color interference of the material [33–35]. As such, absorbance-based tests using nanomaterials are highly likely to cause distortion of results, such as increased cell viability in the presence of color interference. Additionally, if strong washing is performed to remove the remaining nanomaterials, there is a possibility that it may cause loss of cells attached to the bottom of the well and lower the viability of the original cells.

In order to avoid distortion of the measurement result due to residual nanomaterials, a method of transferring the supernatant to a new plate may be considered [36]. When this method is applied, the uptake state in the cell or the substances strongly attached to the outer membrane are excluded from the absorbance measurement so that distortion

is not induced. However, in the case of nanomaterials that dissolve rapidly and release metal ions, it can affect the color of the medium and induce distortion in the supernatant itself. For example, in the case of CuO nanoparticles, Cu ions chemically inactivate the intracellular formazan formation cascade in LDH analysis, which is one of the color-metric assays, resulting in false-negative results [26]. Therefore, the CFE assay is a label-free assay that counts the number of colonies in evaluating these kinds of nanomaterials that can affect the supernatant itself, so it can be a good alternative in vitro assay [37,38].

In conclusion, we reported CFE results using three types of cells for (GNPs, which have not been evaluated so far. This study successfully established applicability by applying the GNP's CFE assay to MDCK, A549 and HepG2 cells. Of course, nanomaterials have different shapes, sizes, colors, etc., so the appropriate test methods may be different, respectively. Because our study applied only two GNPs, there may be some limitations. Therefore, it is thought that more data accumulation of nanomaterials for the CFE test method is needed.

5. Conclusions

In this study, the toxicity evaluation of nano-graphene in three cell lines was successfully confirmed, and the optimal time zone was confirmed for each cell line. Currently, the CFE test method of nanomaterials is being prepared for OECD guidelines, so it is judged that these cell-specific established model studies can contribute to international standards or guidelines. However, further investigation is needed because a better understanding of the toxicity of these NP requires more information about immune activity and ROS generation potential.

Supplementary Materials: The following are available online at https://www.mdpi.com/article/10.3390/toxics10050236/s1, Figure S1: The culture dish images for Colony Forming Efficiency (CFE) evaluation of MDCK cell line treated with graphene nanomaterials, Figure S2: The culture dish images for Colony Forming Efficiency (CFE) evaluation of A549 cell line treated with graphene nanomaterials, and Figure S3: The culture dish images for Colony Forming Efficiency (CFE) evaluation of HepG2 cell line treated with graphene nanomaterials, Figure S4: The validation data for Colony Forming Efficiency (CFE) evaluation of (A) MDCK, (B) A549, and (C) HepG2 cell line treated with single wall carbon nanotubes (swCNTs).

Author Contributions: Conceptualization & experiments and analysis, H.W., J.-H.L. and S.-H.K.; with help (investigation etc.) of J.-Y.Y. and K.J.; writing—original draft preparation, H.W. and S.-H.K.; writing—review & editing, J.-H.L. and S.-H.K.; project administration and supervision, J.J. and J.-H.O. All authors have read and agreed to the published version of the manuscript.

Funding: This research was funded by the Ministry of Food and Drug Safety of Korea, grant number 20181MFDS401.

Institutional Review Board Statement: Not applicable.

Informed Consent Statement: Not applicable.

Data Availability Statement: The original contributions presented in the study are included in the article/Supplementary Material, further inquiries can be directed to the corresponding authors.

Conflicts of Interest: The authors declare that the research was conducted in the absence of any commercial or financial relationships that could be construed as a potential conflict of interest.

References

1. McNeil, S.E. Nanotechnology for the biologist. *J. Leukoc. Biol.* **2005**, *78*, 585–594. [CrossRef] [PubMed]
2. Zang, X.; Wang, T.; Han, Z.; Li, L.; Wu, X. Recent advances of 2D nanomaterials in the electrode materials of lithium-ion batteries. *Nano* **2019**, *14*, 1930001. [CrossRef]
3. Katz, L.M.; Dewan, K.; Bronaugh, R.L. Nanotechnology in cosmetics. *Food Chem. Toxicol.* **2015**, *85*, 127–137. [CrossRef] [PubMed]
4. Rasmussen, K.; Rauscher, H.; Kearns, P.; González, M.; Riego Sintes, J. Developing OECD test guidelines for regulatory testing of nanomaterials to ensure mutual acceptance of test data. *Regul. Toxicol. Pharmacol.* **2019**, *104*, 74–83. [CrossRef] [PubMed]
5. Rauscher, H.; Rasmussen, K.; Sokull-Klüttgen, B. Regulatory aspects of nanomaterials in the EU. *Chem. Ing. Tech.* **2017**, *89*, 224–231. [CrossRef]

6. Abdelgied, M.; El-Gazzar, A.M.; Alexander, W.T.; Numano, T.; Iigou, M.; Naiki-Ito, A.; Takase, H.; Hirose, A.; Taquahashi, Y.; Kanno, J. Carcinogenic effect of potassium octatitanate (POT) fibers in the lung and pleura of male Fischer 344 rats after intrapulmonary administration. *Part. Fibre Toxicol.* **2019**, *16*, 34. [CrossRef]
7. Kasai, T.; Umeda, Y.; Ohnishi, M.; Mine, T.; Kondo, H.; Takeuchi, T.; Matsumoto, M.; Fukushima, S. Lung carcinogenicity of inhaled multi-walled carbon nanotube in rats. *Part. Fibre Toxicol.* **2015**, *13*, 53. [CrossRef]
8. Jiang, J.; Oberdörster, G.; Biswas, P. Characterization of size, surface charge, and agglomeration state of nanoparticle dispersions for toxicological studies. *J. Nanoparticle Res.* **2009**, *11*, 77–89. [CrossRef]
9. Braakhuis, H.M.; Park, M.V.; Gosens, I.; De Jong, W.H.; Cassee, F.R. Physicochemical characteristics of nanomaterials that affect pulmonary inflammation. *Part. Fibre Toxicol.* **2014**, *11*, 18. [CrossRef]
10. Kroll, A.; Pillukat, M.H.; Hahn, D.; Schnekenburger, J. Interference of engineered nanoparticles with in vitro toxicity assays. *Arch. Toxicol.* **2012**, *86*, 1123–1136. [CrossRef]
11. Guadagnini, R.; Halamoda Kenzaoui, B.; Walker, L.; Pojana, G.; Magdolenova, Z.; Bilanicova, D.; Saunders, M.; Juillerat-Jeanneret, L.; Marcomini, A.; Huk, A. Toxicity screenings of nanomaterials: Challenges due to interference with assay processes and components of classic in vitro tests. *Nanotoxicology* **2015**, *9*, 13–24. [CrossRef] [PubMed]
12. OECD Detailed Review Paper on Cell Transformation Assays for Detection of Chemical Carcinogens. 2007. Available online: http://www.oecd.org/chemicalsafety/testing/37863750.pdf (accessed on 28 November 2016).
13. Kinsner-Ovaskainen, A.; Ponti, J.; Norlén, H.; Altmeyer, S.; Andreoli, C.; Bogni, A.; Chevillard, S.; De Angelis, I.; Chung, S.; Eom, I. Interlaboratory comparison study of the Colony Forming Efficiency assay for assessing cytotoxicity of nanomaterials. *Jt. Res. Cent.* **2014**, *EUR27009EN*, 1–80. [CrossRef]
14. Cho, W.; Duffin, R.; Bradley, M.; Megson, I.L.; MacNee, W.; Lee, J.K.; Jeong, J.; Donaldson, K. Predictive value of in vitro assays depends on the mechanism of toxicity of metal oxide nanoparticles. *Part. Fibre Toxicol.* **2013**, *10*, 55. [CrossRef] [PubMed]
15. Jeong, J.; Kim, S.; Lee, S.; Lee, D.; Han, Y.; Jeon, S.; Cho, W. Differential contribution of constituent metal ions to the cytotoxic effects of fast-dissolving metal-oxide nanoparticles. *Front. Pharmacol.* **2018**, *9*, 15. [CrossRef]
16. Oberdörster, G.; Maynard, A.; Donaldson, K.; Castranova, V.; Fitzpatrick, J.; Ausman, K.; Carter, J.; Karn, B.; Kreyling, W.; Lai, D. Principles for characterizing the potential human health effects from exposure to nanomaterials: Elements of a screening strategy. *Part. Fibre Toxicol.* **2005**, *2*, 8. [CrossRef]
17. Ponti, J.; Colognato, R.; Rauscher, H.; Gioria, S.; Broggi, F.; Franchini, F.; Pascual, C.; Giudetti, G.; Rossi, F. Colony forming efficiency and microscopy analysis of multi-wall carbon nanotubes cell interaction. *Toxicol. Lett.* **2010**, *197*, 29–37. [CrossRef]
18. Wang, J.; Wang, P.; He, Y.; Liu, X.; Wang, S.; Ma, C.; Tian, X.; Wang, J.; Wu, X. Graphene oxide inhibits cell migration and invasion by destroying actin cytoskeleton in cervical cancer cells. *Aging* **2020**, *12*, 17625–17633. [CrossRef] [PubMed]
19. Wu, J.; Yang, R.; Zhang, L.; Fan, Z.; Liu, S. Cytotoxicity effect of graphene oxide on human MDA-MB-231 cells. *Toxicol. Mech. Methods* **2015**, *25*, 312–319. [CrossRef]
20. Elkhenany, H.; Amelse, L.; Lafont, A.; Bourdo, S.; Caldwell, M.; Neilsen, N.; Dervishi, E.; Derek, O.; Biris, A.S.; Anderson, D.; et al. Graphene supports in vitro proliferation and osteogenic differentiation of goat adult mesenchymal stem cells: Potential for bone tissue engineering. *J. Appl. Toxicol.* **2015**, *35*, 367–374. [CrossRef]
21. Brownson, D.A.; Banks, C.E. Graphene electrochemistry: An overview of potential applications. *Analyst* **2010**, *135*, 2768–2778. [CrossRef]
22. Zhang, Y.; Chen, Y.; Westerhoff, P.; Hristovski, K.; Crittenden, J.C. Stability of commercial metal oxide nanoparticles in water. *Water Res.* **2008**, *42*, 2204–2212. [CrossRef] [PubMed]
23. Bihari, P.; Vippola, M.; Schultes, S.; Praetner, M.; Khandoga, A.G.; Reichel, C.A.; Coester, C.; Tuomi, T.; Rehberg, M.; Krombach, F. Optimized dispersion of nanoparticles for biological in vitro and in vivo studies. *Part. Fibre Toxicol.* **2008**, *5*, 14. [CrossRef] [PubMed]
24. Anders, C.B.; Chess, J.J.; Wingett, D.G.; Punnoose, A. Serum proteins enhance dispersion stability and influence the cytotoxicity and dosimetry of ZnO nanoparticles in suspension and adherent cancer cell models. *Nanoscale Res. Lett.* **2015**, *10*, 448. [CrossRef] [PubMed]
25. Jeong, J.; Lee, S.; Kim, S.; Han, Y.; Lee, D.; Yang, J.; Jeong, J.; Roh, C.; Huh, Y.S.; Cho, W. Evaluation of the dose metric for acute lung inflammogenicity of fast-dissolving metal oxide nanoparticles. *Nanotoxicology* **2016**, *10*, 1448–1457. [CrossRef] [PubMed]
26. Han, Y.; Lee, D.; Kim, S.; Lee, S.; Jeon, S.; Cho, W. High inflammogenic potential of rare earth oxide nanoparticles: The New Hazardous Entity. *Nanotoxicology* **2018**, *12*, 712–728. [CrossRef]
27. Holder, A.L.; Goth-Goldstein, R.; Lucas, D.; Koshland, C.P. Particle-induced artifacts in the MTT and LDH viability assays. *Chem. Res. Toxicol.* **2012**, *25*, 1885–1892. [CrossRef]
28. Costa, C.; Brandão, F.; Bessa, M.J.; Costa, S.; Valdiglesias, V.; Kiliç, G.; Fernández-Bertólez, N.; Quaresma, P.; Pereira, E.; Pásaro, E. In vitro cytotoxicity of superparamagnetic iron oxide nanoparticles on neuronal and glial cells. Evaluation of nanoparticle interference with viability tests. *J. Appl. Toxicol.* **2016**, *36*, 361–372. [CrossRef]
29. Aslantürk, Ö.S. *In Vitro Cytotoxicity and Cell Viability Assays: Principles, Advantages, and Disadvantages*; InTech: London, UK, 2018; Volume 2.
30. Han, X.; Gelein, R.; Corson, N.; Wade-Mercer, P.; Jiang, J.; Biswas, P.; Finkelstein, J.N.; Elder, A.; Oberdörster, G. Validation of an LDH assay for assessing nanoparticle toxicity. *Toxicology* **2011**, *287*, 99–104. [CrossRef]
31. Kamiloglu, S.; Sari, G.; Ozdal, T.; Capanoglu, E. Guidelines for cell viability assays. *Food Front.* **2020**, *1*, 332–349. [CrossRef]

32. Stockert, J.C.; Horobin, R.W.; Colombo, L.L.; Blázquez-Castro, A. Tetrazolium salts and formazan products in Cell Biology: Viability assessment, fluorescence imaging, and labeling perspectives. *Acta Histochem.* **2018**, *120*, 159–167. [CrossRef]
33. Wörle-Knirsch, J.; Pulskamp, K.; Krug, H. Oops they did it again! carbon nanotubes hoax scientists in viability assays. *Nano Lett.* **2006**, *6*, 1261–1268. [CrossRef] [PubMed]
34. Casey, A.; Herzog, E.; Davoren, M.; Lyng, F.; Byrne, H.; Chambers, G. Spectroscopic analysis confirms the interactions between single walled carbon nanotubes and various dyes commonly used to assess cytotoxicity. *Carbon* **2007**, *45*, 1425–1432. [CrossRef]
35. Monteiro-Riviere, N.; Inman, A.; Zhang, L. Limitations and relative utility of screening assays to assess engineered nanoparticle toxicity in a human cell line. *Toxicol. Appl. Pharmacol.* **2009**, *234*, 222–235. [CrossRef] [PubMed]
36. Kim, S.; Lee, D.H.; Choi, S.; Yang, J.; Jung, K.; Jeong, J.; Oh, J.H.; Lee, J.H. Skin Sensitization Potential and Cellular ROS-Induced Cytotoxicity of Silica Nanoparticles. *Nanomaterials* **2021**, *11*, 2140. [CrossRef]
37. Herzog, E.; Casey, A.; Lyng, F.M.; Chambers, G.; Byrne, H.J.; Davoren, M. A new approach to the toxicity testing of carbon-based nanomaterials—The clonogenic assay. *Toxicol. Lett.* **2007**, *174*, 49–60. [CrossRef] [PubMed]
38. Gellein, K.; Hoel, S.; Gellein, K.; Hoel, S.; Evje, L.; Syversen, T. The colony formation assay as an indicator of carbon nanotube toxicity examined in three cell lines. *Nanotoxicology* **2009**, *3*, 215–221. [CrossRef]

processes

MDPI

Article

Correlation between the Desiccator Method and 1 m^3 Climate Chamber Method for Measuring Formaldehyde Emissions from Veneered Particleboard

Jia Shao [1,2], Yang Chen [1], Ling Dong [2], Tangfeng Yuan [2], Zhongfeng Zhang [1] and Jijuan Zhang [1,*]

[1] College of Furniture and Art Design, Central South University of Forestry and Technology, Changsha 410004, China; 20211200365@csuft.edu.cn or richardshaojia@163.com (J.S.); 20191200262@csuft.edu.cn (Y.C.); t19990735@csuft.edu.cn (Z.Z.)
[2] Oppein Home Group INC, Guangzhou 510000, China; dongling@oppeinmail.com (L.D.); yuantangfeng@oppeinmail.com (T.Y.)
* Correspondence: t20050729@csuft.edu.cn; Tel.: +86-139-7511-9348

Abstract: To shorten the measuring time of formaldehyde emissions from wood-based panels and reduce the costs of quality control processes during industrial furniture production, more efficient methods for measuring formaldehyde emissions from wood-based panels need to be developed. In this study, the formaldehyde emissions from 18-mm-thick veneered particleboard were measured using the desiccator method and the 1 m^3 climate chamber method according to Chinese national standard GB/T17657-2013, and the correlation between these two methods was determined. Through a correlation analysis of 60 groups of data, the results indicated that the linear correlation coefficient (R) between two methods was 0.718, and the regression model was established, which by F and P values demonstrated a significant correlation at the 0.01 level of significance. As long as the quality of materials and the production processes remained consistent, the desiccator method was reliable enough for conducting routine quality control measurements of formaldehyde emissions from veneered boards of 18 mm thickness. In case of dispute, the results can be verified using the 1 m^3 climate chamber method for accuracy.

Keywords: desiccator method; climate chamber method; formaldehyde emissions; veneered particleboard; wood-based panels; correlation coefficient

Citation: Shao, J.; Chen, Y.; Dong, L.; Yuan, T.; Zhang, Z.; Zhang, J. Correlation between the Desiccator Method and 1 m^3 Climate Chamber Method for Measuring Formaldehyde Emissions from Veneered Particleboard. *Processes* **2022**, *10*, 1023. https://doi.org/10.3390/pr10051023

Academic Editors: Avelino Núñez-Delgado, Zhien Zhang, Elza Bontempi, Mario Coccia, Marco Race and Yaoyu Zhou

Received: 24 April 2022
Accepted: 16 May 2022
Published: 20 May 2022

1. Introduction

Panel-type furniture enterprises require a substantial amount of wood-based panels, such as particleboard, fiberboard, and plywood, as raw materials. In 2020, the total output of wood-based panels in China was over 300 million m^3, and the scale of China's wooden furniture market exceeded 600 billion yuan. Among them, solid wood furniture accounted for 41.8%; panel furniture accounted for 58.2%. These wood-based composites are usually bonded with formaldehyde-based adhesives, such as urea-formaldehyde resin, melamine-formaldehyde resin, and phenolic resin, which inevitably leads to formaldehyde release into the surrounding indoor environments [1]. Formaldehyde release from wood-based panels is a complicated process, which can be affected by several factors: the physical and chemical properties of the materials, such as formaldehyde content, component structure, chemical composition, density, thickness, and surface properties of the material; and environmental factors, such as temperature, relative humidity, air velocity, and air exchange rate [2–4]. Honggang Chen found that a high concentration of formaldehyde is toxic to the nervous system, immune system, and liver; it is carcinogenic to humans [5]. Formaldehyde has been classified as a potentially dangerous carcinogen and an important environmental pollutant by the World Health Organization and the United States Environmental Protection Agency. The testing methods of formaldehyde can be summarized in three categories: total amount

testing method, such as perforation; static emission testing method, such as desiccator; and dynamic emission testing method, such as chamber. The chamber method is widely used in the United States and Germany, and its testing technology of chamber is in a leading position in the world. The EU standards use chamber, gas analysis, and perforation methods. Japan is using the desiccator method [6–10]. The Chinese standard GB18580-2017 [11] stipulates that the measurement of formaldehyde emissions from wood-based panels shall be carried out in accordance with the 1 m^3 climate chamber method in the GB/T 17657-2013 standard, and the desiccator method, the perforator method, is for production quality control in enterprise [12]. The formaldehyde emission standards of wood-based panels in different countries are shown in Table 1 [13].

Table 1. Formaldehyde emission standards for wood-based panels in Europe, the USA, Japan, Australia, and China.

Country	Standard	Test Method	Board Class	Limit Value
Europe	EN13986: 2005	Perforator EN ISO 12460-5	E1-unfaced particleboard, MDF/HDF, OSB	≤8 mg/100 g *
		Chamber EN 717-1	E1-particleboard, MDF/HDF, OSB	≤0.1 ppm **
		Gas analysis EN 717-2	E1-unfaced plywood, solid wood panels, laminated veneer lumber (LVL)	≤3.5 mg/m^2 h
		Gas analysis EN 717-2	E1-coated, overlaid, or veneered particleboard, OSB, fibreboard, plywood, solid wood panels, LVL, cement-bonded particleboard	≤3.5 mg/m^2 h
USA	ANSI A 208.1 & 2	ASTM E1333 (chamber)	Particleboard/MDF	≤0.18 or 0.09 ppm/≤ 0.21 or 0.11 ppm
Japan	JIS A 5908 (2015) and 5905	JIS A 1460 (Desiccator)	F **/F ***(E0)/ F ****(SE0)	≤1.5 mg/L/ ≤0.5 mg/L/ ≤0.3 mg/L
Australia and New Zealand	AS/NZS 1859/1 (2017) and 2	AS/NZS 4266.16 (Desiccator)	E0-particleboard, MDF/E1-particleboard /E1/MDF	≤0.5 mg/L/ ≤1.5 mg/L/ ≤1.0 mg/L
China	GB18580-2017	GB/T 17657-2013 (chamber)	E1-MDF, particleboard, plywood, LVL, or veneered wood-based panel	≤0.124 mg/m^3

* E3 30–60 mg/100 g, E2 8–30 mg/100 g, E1 5–8 mg/100 g, E0 ≤ 3 mg/100 g, super E0 ≤ 1.5 mg/100 g. ** 0.05 ppm boards can be marked with an environmental label ("Blue Angel"), 0.03 ppm boards are about equal to the Japanese emission class F ****.

The climate chamber method considers the temperature, relative humidity, loading ratio, air exchange rate, and air speed on the sample surface; therefore, it most closely reflects real-world conditions. However, the climate chamber method is not suitable for routine enterprise production quality control because it is time consuming. The desiccator method is an internationally recognized method because it enables a much faster measurement of formaldehyde emissions from wood-based panels, and it is inexpensive and relatively easy to conduct, which has made it popular in Chinese furniture enterprises. This study sought to develop a relevant mathematical model for establishing a relationship between the desiccator method and the 1 m^3 climate chamber method. This model would make it convenient for enterprises to adopt desiccator methods for production quality control and to meet the requirements of the GB18580-2017 standard.

A significant number of experimental studies have been conducted to establish relationships between different formaldehyde-measuring methods. Chris Leffel determined the empirical equation y = 29.332x + 4.2569 to convert between the measured values obtained from the perforator method (y) and the American large climate chamber method (x) [14]. Yongliang Chi (2015) measured the formaldehyde emission of medium-density fiberboard (MDF) using the 9–11 L desiccator (A) and perforator (D) methods, and the statistical analysis results showed that there was a linear relationship between the two methods. The linear regression equation was D = 4.8953A + 2.3412, and its correlation coefficient (R^2) was 0.9960, indicating a significant correlation [15]. Yiqing Peng measured the formaldehyde emission of MDF using the 40 L desiccator, gas analysis, and perforator methods. Upon analysis of the results using SPSS software, a relevant regression model and linear equation were established, the results of which demonstrated a highly positive correlation between the three measurement methods [16]. Qionghui Zhao measured the formaldehyde emission of blockboard by two different methods, the desiccator method and the 1 m^3 climate chamber method and compared the results to elucidate the influence of different measurement methods on the results of measurement of formaldehyde emissions. The results showed that the two methods were consistent in the grade characterization of the panels, and there was a correlation between the standard curves of the two methods [17]. Xiaorong Lin and Xiyuan Liang took 20 different wood-based panel samples with different specifications and models, and the formaldehyde emissions from each sample were measured using the 1 m^3 climate chamber method and the desiccator method. Through comparative analysis, the formaldehyde emissions from the MDF, particleboard, and plywood samples measured using the 1 m^3 climate chamber method were in the range of 0.100–0.124 mg/m^3, while the emissions measured using the desiccator method were in the range of 0.5–0.7 mg/L. When the concentration of formaldehyde measured using the desiccator method reached 0.7 mg/L, the concentration measured using the climate chamber method was below the limit of 0.124 mg/m^3 [18]. These studies elucidated the correlations between the different formaldehyde measuring methods and provided an impetus for developing reliable and feasible quality control methods for the measurement of formaldehyde emissions from wood-based panels. In addition, the identification and analysis of the factors influencing the accuracy and reliability of different measurement methods could provide guidance to ensure the accuracy of the data obtained in this study.

Other studies have reported poor correlations between different methods of measuring formaldehyde emission. Previously, Jimei Wang and Zhijiang Ji conducted a comparative analysis on seven samples of plywood, particleboard, and blockboard, the results of which indicated that the concentration of formaldehyde emitted from the three types of wood-based panels differed depending on the method of measurement (i.e., perforator method, desiccator method, and climate chamber method); thus, there was no correlation or comparability between them [19]. The researchers attributed the lack of correlation to the poor uniformity of the wood-based panels themselves and to the differences in the production process at each manufacturer, making it difficult to conduct a unified correlation analysis. In addition, the data gathered were insufficient to accurately demonstrate a correlation between the results. Lastly, errors were inevitable because of the different measuring conditions of the enterprises, operation methods of operators, and other factors.

Since the implementation of the new Chinese national standard, the methods available to measure formaldehyde emissions have undergone continuous development and improvement in practice. To guide the formaldehyde measurement and quality control of wood-based panels, it was necessary to study the correlation between different measurement methods. However, all of the current studies were limited to a small range of laboratory-scale analyses and comparisons; most studies comprised only 15–30 groups of experiments. Thus, the amount of experimental data was not comprehensive enough to draw conclusions for establishing a reliable method for measuring formaldehyde emissions in industrial production. In this study, we increased the number of standardized measurements to 60 groups. We hypothesized that these additional data would make

the correlation studies more robust and provide a reliable and accurate reference for the rapid measurement of formaldehyde emissions for quality control during actual industrial production processes.

2. Materials and Methods

2.1. Materials

A total of 60 pieces of veneered particleboard were obtained from Oppein Home Group, Inc. The dimensions of the boards were 1220 mm × 2440 mm × 18 mm.

2.1.1. Sample Preparation

The 60 sample groups were numbered from 1 to 60. Each specimen was cut into two pieces with dimensions of 1220 mm × 1200 mm, as shown in the sample crosscut diagram in Figure 1. The pieces of each specimen were marked as X-1 and X-2, respectively (i.e., 1-1, 1-2, 2-1, 2-2, and so on), and the samples were wrapped with a plastic film that did not adsorb or release formaldehyde to be measured.

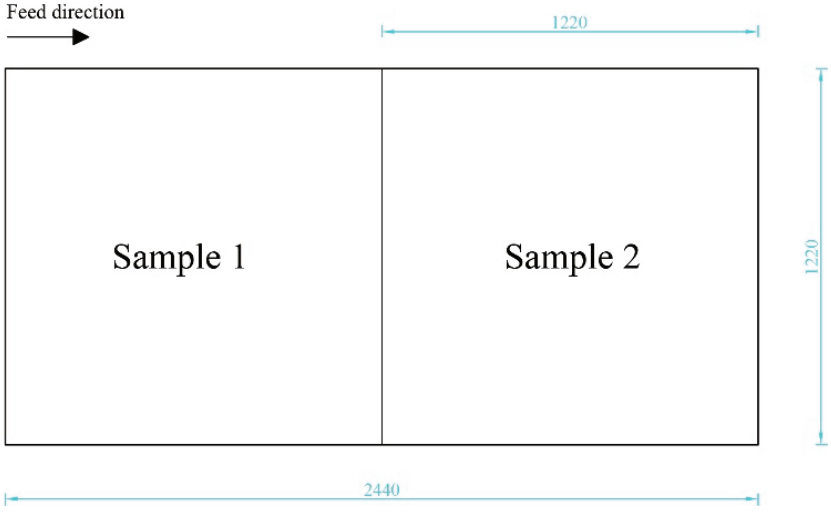

Figure 1. Sample preparation.

The samples whose formaldehyde emissions were measured using the 1 m^3 climate chamber method of GB/T17657-2013 comprised group A. Two pieces with dimensions of 500 mm × 500 mm × 18 mm were made, respectively from sample 1 and sample 2 according to the positions shown in Figures 2 and 3. The samples whose formaldehyde emissions were measured using the desiccator method of GB/T17657-2013 comprised group B. Ten pieces with dimensions of 150 mm × 50 mm × 18 mm were prepared from sample 1 and sample 2 according to the positions shown in Figures 2 and 3. An additional standby group was prepared, totaling 30 pieces. For example, the samples for the 1 m^3 climate chamber method were labeled 1-A1 and 1-A2, and the samples for the desiccator method were labeled 1-B1, 1-B2, and 1-B3. The other groups were named in the same way. The cutting edge and ends of each sample needed to be at least 50 mm from the plate edge.

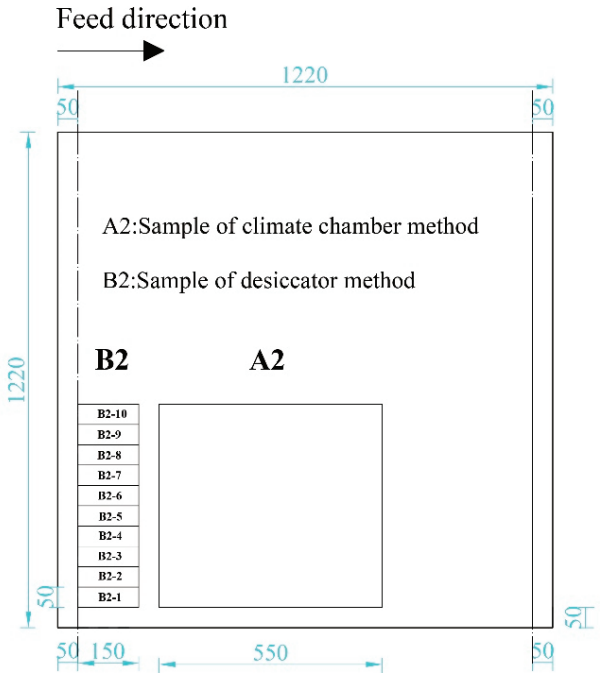

Figure 2. Sampling diagram of sample 1.

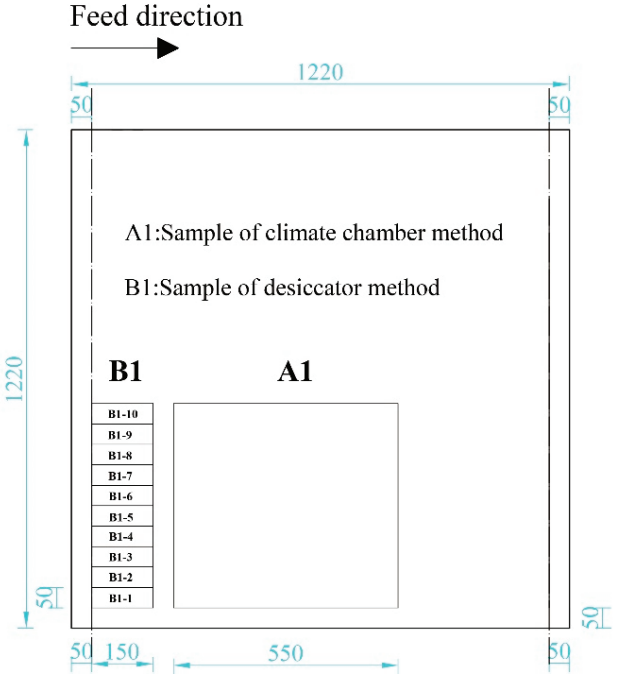

Figure 3. Sampling diagram of sample 2.

2.1.2. Reagents

Acetyl acetone (analytical purity), ammonium acetate (analytical purity), glacial acetic acid (analytical purity), and 10.1% formaldehyde standard solution (CH_2O).

2.2. Instruments and Equipment

The main equipment used in this study included a QWH-1000C 1 m^3 climate chamber (Hainate, Jinan, China), TY-210-4 formaldehyde balance chamber (Mingchi, Dongguan, China), UV-1500 UV spectrophotometer (ShouKe, Guangzhou, China), 723PC visible spectrophotometer (Shunyao Hengping, Shanghai, China), Model 501 constant-temperature water boiler (Aohua, Changzhou, China), QC-3 atmospheric sampler (Lubo, Qingdao, China), 608-H1 temperature and humidity detector (Testo, Titisee-Neustadt, Germany), and desiccator (diameter: 240 mm, volume: 9–11 L) (Lubo, Qingdao, China). The laboratory in which the tests were conducted was maintained at a constant temperature and humidity.

2.3. Measuring Methods

2.3.1. 1 m^3 Climate Chamber Method

The two pieces (e.g., 1-A1 and 1-A2) with dimensions of 500 × 500 mm of each sample were placed in a formaldehyde balance chamber at a temperature of 23 ± 1 °C and a relative humidity of 50 ± 5%. The distance between the samples was at least 25 mm to allow air to freely circulate throughout the chamber and to contact all surfaces of the samples. After 15 ± 2 days in the chamber, the edges of the samples were sealed with aluminum tape, except for 750 mm of the edge, which was not sealed. Then, the samples were placed in a 1 m^3 climate chamber at a temperature of 23 ± 0.5 °C, relative humidity of 50 ± 3%, and air exchange rate of 1.0 h^{-1}. The next day, the sampling and measurements began.

2.3.2. Desiccator Method

The dimensions (150 mm × 50 mm × 18 mm) of the samples to be measured using the desiccator method were chosen to ensure that the total surface area was close to 1800 cm^2. The samples were conditioned under standard conditions at a temperature of (20 ± 2) °C and a relative humidity of 65 ± 5% until they attained constant mass for 7 days and then started the test. Next, a crystallization dish containing 300 mL distilled water was added, and the samples were stored in the desiccator at 20 °C for 24 h to measure the concentration of formaldehyde in the distilled water. This test was repeated twice, and the average of the two results was reported.

3. Results

The formaldehyde emission results from each group of veneered particleboard samples measured by the desiccator method and the 1 m^3 climate chamber method are shown in Table 2.

Table 2. The measured results of formaldehyde emission from veneered particleboard by the desiccator method and the 1 m^3 climate chamber method.

Sample No.	Desiccator (mg/L)	Climate Chamber (mg/m^3)	Samples No.	Desiccator (mg/L)	Climate Chamber (mg/m^3)
1	0.24	0.018	31	0.07	0.011
2	0.23	0.017	32	0.21	0.012
3	0.64	0.020	33	0.34	0.019
4	0.26	0.022	34	0.25	0.013
5	0.41	0.020	35	0.30	0.015
6	0.45	0.020	36	0.30	0.012
7	0.38	0.022	37	0.28	0.018
8	0.57	0.032	38	0.42	0.016
9	0.52	0.026	39	0.30	0.015

Table 2. *Cont.*

Sample No.	Desiccator (mg/L)	Climate Chamber (mg/m^3)	Samples No.	Desiccator (mg/L)	Climate Chamber (mg/m^3)
10	0.49	0.030	40	0.39	0.018
11	0.50	0.029	41	0.38	0.019
12	0.59	0.030	42	0.27	0.023
13	0.50	0.019	43	0.47	0.015
14	0.60	0.021	44	0.40	0.014
15	0.66	0.012	45	0.38	0.015
16	0.45	0.019	46	0.47	0.021
17	0.52	0.013	47	0.31	0.014
18	0.63	0.019	48	0.35	0.016
19	0.49	0.014	49	0.02	0.006
20	0.70	0.020	50	0.03	0.007
21	0.50	0.014	51	0.03	0.009
22	0.52	0.020	52	0.02	0.011
23	0.61	0.020	53	0.02	0.008
24	0.51	0.018	54	0.03	0.006
25	0.30	0.013	55	0.02	0.007
26	0.26	0.010	56	0.10	0.011
27	0.28	0.012	57	0.05	0.008
28	0.33	0.014	58	0.02	0.010
29	0.42	0.021	59	0.09	0.008
30	0.28	0.011	60	0.02	0.008

4. Discussion

From the results provided in Table 1, the correlations between the two methods were analyzed using IBM SPSS Statistics 25 statistical software. The formaldehyde emission data obtained from the desiccator method were plotted on the abscissa, and the formaldehyde emission data obtained from the climate chamber method were plotted on the ordinate. The relationship between the two different measuring methods is depicted in Figure 4.

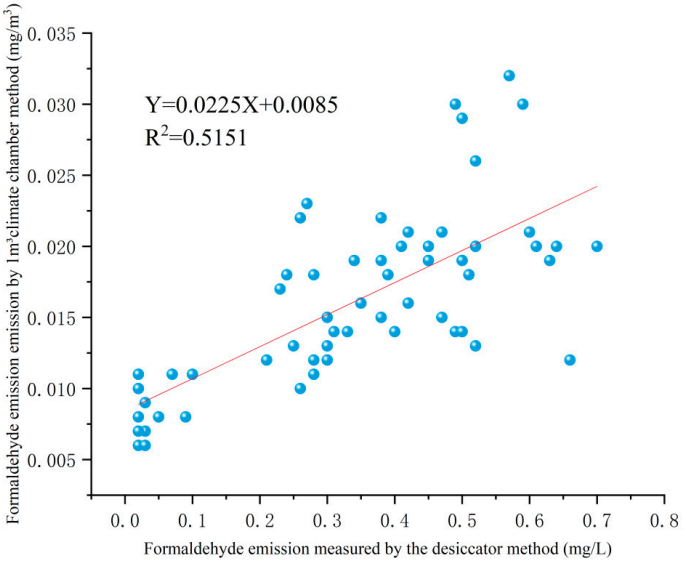

Figure 4. The relationship of formaldehyde emissions between the desiccator method and the climate chamber.

Regression analysis of the emission data obtained from the desiccator method and the climate chamber method was performed, and the correlation results are shown in Table 3. The regression model data are shown in Table 4, and the data from the analysis of variance (ANOVA) of the regression model are shown in Table 5.

Table 3. Correlation analysis of formaldehyde emissions between the desiccator and climate chamber.

		Desiccator	Climate Chamber
Desiccator	Pearson correlation	1	0.718 **
	Sig.(2-tailed)	/	0.000
	Number of cases	60	60
Climate Chamber	Pearson correlation	0.718 **	1
	Sig.(2-tailed)	0.000	/
	Number of cases	60	60

** At 0.01 (2-tailed), with a high correlation.

Table 4. Regression model of formaldehyde emissions between the desiccator and climate chamber.

Model [a]		Unstandardized Coefficients		Standardized Coefficients	*t*	Significance
		B	Standard Error	Beta		
1	(Constant)	0.009	0.001	/	7.623	0.000
	Desiccator	0.023	0.003	0.718	7.849	0.000

[a] Dependent Variable: 1 m^3 Climate Chamber.

Table 5. Variance analysis of regression model of formaldehyde emissions between desiccator and climate chamber.

Model	DOF	Sum of Squares	Mean Square	F	*p*
Regression	1	0.001	0.001	61.609	≤0.001
Residual	58	0.001	0	/	/
In total	59	0.002	/	/	/

As shown in Tables 2–4, the Pearson's linear correlation coefficient of the two methods (R) was 0.718, indicating that they were correlated. The F = 61.609 and $p \leq 0.001$ indicated that the regression equation of the fitted data was extremely significant when the confidence level was a = 0.01, and the data were linearly correlated. For the 60 groups of test data, the established regression model is shown in Table 3. Upon fitting the data, the regression equation of the correlation model was y = 0.0225x + 0.0085, and the coefficient of correlation (R^2) was 0.5151. This means that 51% of the variation is explained by this model of regression, and the other 49% of the variation is due to other factors or random variation.

Xiaorong L. and Xianyuan L. selected 20 wood-based panel samples with different specifications and models as the research object, and the formaldehyde emission of each sample was tested by the 1 m^3 climate chamber method and desiccator method, respectively. Through comparative analysis, it is found that the formaldehyde emission of MDF, particleboard, and plywood samples in the experiment varies in the range of 0.5–0.7 mg/L when the test value of the climate chamber method is 0.100–0.124 mg/m^3. When the concentration of the desiccator method reaches 0.7 mg/L, the concentration of the climate chamber method exceeds the limit requirement of ≤0.124 mg/m^3 [18]. The results reflect the correlation between the two formaldehyde measurement methods, but this experiment only selected 20 group samples to test in the laboratory; the experimental data are not extensive enough.

This research is combined with the specific situation in the production process of enterprises, selects the commonly used panels of enterprises as samples, carries out 60 groups of testing experiments, analyzes its correlation through more experimental data, and the reliability of the results is higher.

5. Conclusions

In this study, the desiccator and 1 m^3 climate chamber methods of GB/T17657-2013 were used to measure formaldehyde emissions from veneered particleboard. Statistical analysis of the emission data indicated that there was a linear relationship between the two methods. The linear regression equation upon fitting of the data was y = 0.0225x + 0.0085, and its coefficient of correlation (R^2) was 0.5151. The model, therefore, could explain 51% of the variation in the data using the two methods. However, the measurements were affected by many uncertain factors. Although the fitness of the linearity was low, regression analysis has an inherently low universal applicability. The methods in this study can be referenced to establish a linear regression model between different methods. The climate chamber method is not economically feasible for many factories; thus, a correlation with other methods is necessary. The established regression model makes it possible to use the desiccator method for routine control in factories, but only in the case of veneered particleboards. Future research is needed on other types of panels.

Author Contributions: Conceptualization, Z.Z.; methodology, J.S.; validation, L.D. and T.Y., data curation, Y.C.; writing—original draft preparation, J.S.; writing—review and editing, J.Z.; visualization, Y.C.; supervision, J.S.; project administration, J.S.; funding acquisition, J.Z. All authors have read and agreed to the published version of the manuscript.

Funding: This research was funded by the Chinese National Promotion Program of Forestry and Grassland Scientific and Technological Achievements, grant number 2020133139 and The Oppein Home Group INC, grant number 2020.

Institutional Review Board Statement: Not applicable.

Informed Consent Statement: Not applicable.

Data Availability Statement: Not applicable.

Conflicts of Interest: The authors declare no conflict of interest.

References

1. Yiping, L. Research on formaldehyde emission from wood-based panel and its detection method. *Technol. Innov. Appl.* **2019**, *28*, 125–126.
2. Yang, Y.; Li, L.Q.; Ma, W.W.; Ma, X.C.; Liu, B.; Chen, R.F.; Yan, J. Effect of relative humidity and temperature on formaldehyde emissions of plywood panels. *China Environ. Sci.* **2016**, *36*, 390–397.
3. Park, B.D.; Kang, E.C.; Lee, S.M.; Park, J.Y. Formaldehyde Emission of Wood-Based Composite Panels with Different Surface Lamination Materials Using Desiccator Method. *J. Korean Wood Sci. Technol.* **2016**, *44*, 600–606. [CrossRef]
4. Zhang, J.; Song, F.; Tao, J.; Zhang, Z.; Shi, S.Q. Research Progress on Formaldehyde Emission of Wood-Based Panel. *Int. J. Polym. Sci.* **2018**, *2018*, 9349721. [CrossRef]
5. Honggang, C.; Gang, S.; Shudong, Z. Harmful Effects of Formaldehyde and Measures for Reducing Formaldehyde Emission from Wood-based Panels. *China Wood Ind.* **2006**, *20*, 32–33.
6. Yu, C.W.F.; Crump, D.R. Testing for formaldehyde emission from wood-based products—A review. *Indoor Built Environ.* **1999**, *8*, 280–286. [CrossRef]
7. Zhu, H.O.; Lu, Z.G.; Li, X.; Zhang, J.; Yuan, M. Analysis on Test Methods for Determining Formaldehyde Emission from Wood-based Products. *China Wood Ind.* **2009**, *23*, 37–40.
8. Haofei, G.; Min, L.; Yiling, Z. Correlation analysis of formaldehyde emission of wood-based panels by different detection methods. *Wood Ind.* **2013**, *27*, 33–37.
9. Zhengguo, W.; Xinfang, D.; Long, G.; Han, J. Comparison on Formaldehyde Standards Between China, the EU, the United States, and Japan for Wood-based Panels. *World For. Res.* **2015**, *28*, 58–61.
10. Jufen, L. Comparative Analysis of the Limitation Requirement and Test Methods of Formaldehyde Emission in Furniture and Wood-Based Panel. *Furniture* **2016**, *37*, 101–106.
11. *GB18580-2017*; Indoor Decorating and Refurbishing Materials—Limit of Formaldehyde Emission of Wood-Based Panels and Finishing Products. China Standards Press: Beijing, China, 2017.
12. *GB/T 17657-2013*; Test Methods of Evaluating the Properties of Wood-Based Panels and Surface Decorated Wood-Based Panels. China Standards Press: Beijing, China, 2013.
13. Lubos, K.; Petar, A.; Pavlo, B.; Lubis, M.A.R.; Iswanto, A.H.; Reh, R.; Sedliacik, J.; Savov, V.; Taghiyari, H.R.; Papadopoulos, A.N.; et al. Recent progress in ultra-low formaldehyde emitting adhesive systems and formaldehyde scavengers in wood-based panels: A review. *Wood Mater. Sci. Eng.* **2022**, *4*, 1–20.

14. Chris, L. Comparison of formaldehyde emission limits for wood-based panels. *Wood-Based Panel Commun.* **2005**, *9*, 19–20.
15. Chi, Y. Study on the correlation between the drying method and perforation extraction method for the determination of formaldehyde emission in medium density fiberboard. *For. Mach. Woodwork. Equip.* **2015**, *3*, 19–21, 26.
16. Peng, Y. Study on the correlation between 40L dryer method and gas analysis method and perforation extraction method for determination of formaldehyde emission of medium density fiberboard. *For. Mach. Woodwork. Equip.* **2017**, *45*, 46–49.
17. Qionghui, Z. Comparison between the dryer method and the environmental chamber method for the detection of joinery board. *Build. Mater. Decor.* **2018**, *9*, 174–176.
18. Xiaorong, L.; Xianyuan, L.; Pengfei, H. Study on correlation between climate chamber method and desiccator method for formaldehyde emission measurement of wood-based panel. *China Wood-Based Panel* **2019**, *26*, 24–27.
19. Jimei, W.; Zhijiang, J.; Xiaoyan, W. Effect of test method on formaldehyde emission concentration value of artificial board. *Wood Work. Mach.* **2018**, *29*, 24–28.

toxics

MDPI

Article

Indoor Air Quality Considerations for Laboratory Animals in Wildfire-Impacted Regions—A Pilot Study

Adam Schuller [1], Ethan S. Walker [2], Jaclyn M. Goodrich [3], Matthew Lundgren [4] and Luke Montrose [5,*]

[1] Biomolecular Sciences Graduate Program, Boise State University, 1910 W University Drive, Boise, ID 83725, USA; adamschuller@u.boisestate.edu
[2] Center for Population Health Research, University of Montana, 32 Campus Drive, Missoula, MT 59812, USA; ethan.walker@mso.umt.edu
[3] Department of Environmental Health Sciences, University of Michigan School of Public Health, 1415 Washington Heights, Ann Arbor, MI 48109, USA; gaydojac@umich.edu
[4] Office of Research Compliance, Boise State University, 1910 W University Drive, Boise, ID 83725, USA; mattlundgren@boisestate.edu
[5] Department of Public Health and Population Science, Boise State University, 1910 W University Drive, Boise, ID 83725, USA
* Correspondence: lukemontrose@boisestate.edu; Tel.: +1-(208)-426-3979

Simple Summary: With increasing wildfires in the western US and around the world, it is important to take stock of impacts to humans as well as animals. Fires create smoke, and exposure to wildfire particles is known to negatively impact health. Therefore, we asked if smoke might get into buildings where animal research takes place. Our one-month study provides evidence that smoke does get inside an animal facility and levels can exceed ambient air quality standards that are set to protect public health. More work is needed to establish the impact that indoor smoke exposure might have on research animals, but we suggest these data warrant consideration for air quality monitoring and planning within animal facilities at risk for outdoor smoke events.

Abstract: Wildfire events are increasing across the globe. The smoke generated as a result of this changing fire landscape is potentially more toxic than air pollution from other ambient sources, according to recent studies. This is especially concerning for populations of humans or animals that live downwind of areas that burn frequently, given that ambient exposure to wildfire smoke cannot be easily eliminated. We hypothesized that a significant indoor air pollution risk existed for laboratory animal facilities located proximal to fire-prone areas. Here, we measured real time continuous outdoor and indoor air quality for 28 days at a laboratory animal facility located in the Rocky Mountain region. We demonstrated that during a wildfire event, the indoor air quality of this animal facility is influenced by ambient smoke events. The daily average indoor fine particulate matter value in an animal room exceeded the Environmental Protection Agency's ambient annual standard 14% of the time and exceeded the World Health Organization's ambient annual guideline 71% of the time. We further show that specialized cage filtration systems are capable of mitigating air pollution penetrance and could improve an animal's microenvironment. The potential effects for laboratory animal physiology that occur in response to the exposure levels and durations measured in this study remain to be determined; yet, even acute wildfire exposure events have been previously correlated with significant differences in gene regulatory and metabolic processes in vivo. We believe these findings warrant consideration for indoor laboratory animal facility air quality monitoring and development of smoke exposure prevention and response protocols, especially among facilities located downwind of fire-prone landscapes.

Keywords: air quality; lab animal; wildfire smoke

Citation: Schuller, A.; Walker, E.S.; Goodrich, J.M.; Lundgren, M.; Montrose, L. Indoor Air Quality Considerations for Laboratory Animals in Wildfire-Impacted Regions—A Pilot Study. *Toxics* **2022**, *10*, 387. https://doi.org/10.3390/toxics10070387

Academic Editors: Avelino Núñez-Delgado, Zhien Zhang, Elza Bontempi, Mario Coccia, Marco Race and Yaoyu Zhou

Received: 24 May 2022
Accepted: 10 July 2022
Published: 12 July 2022

1. Introduction

Extreme weather events are significant contributors to adverse health around the globe, and their occurrence has increased substantially with climate change [1]. In particular, wildfires are increasing in size and duration as global temperature increases [2]. This has been associated with a greater health cost burden, mortality, and morbidity world-wide [3–5]. The top five years for acres burned in the United States (US) since 1960 have all occurred in the last 15 years and wildfire events in 2020 and 2021 burned more than 15 million combined acres [6]. Consequently, wildfire smoke continues to be a major contributor of particulate matter (PM) in wildfire-prone regions despite downward trends in ambient air pollution elsewhere in the US [7]. Computational models suggest that wildfire smoke currently makes up 25% of total ambient air pollution in the US with estimates that this number could surpass 50% in the next 20 years [8,9].

Wildfire smoke is a complex mixture of chemicals that vary in composition depending on burning conditions and the proximity of the sampling location relative to the source [10]. Despite this, common constituent groups include volatile organic compounds, gaseous pollutants (e.g., carbon monoxide), polycyclic aromatic hydrocarbons, and PM [11]. The smoke from wildfires contains more fine (aerodynamic diameter < 2.5 μm) and ultrafine (aerodynamic diameter < 0.1 μm) PM relative to coarse (2.5 μm < aerodynamic diameter < 10 μm) PM, which is significant because these smaller particles pose greater risks to health given their ability to penetrate deep into the lung and contribute to disease pathology and mortality [12–14]. A growing body of data from both animal and human studies suggests that $PM_{2.5}$ from wildfire smoke can impact health more significantly than $PM_{2.5}$ from other sources, due in part to its propensity to produce reactive oxygen species [15–17]. Furthermore, the adverse impact of wildfire smoke exposure is not isolated to the pulmonary and cardiovascular systems, but can also affect other systems such as the central nervous system and reproductive organs [18,19].

Wildfire smoke air pollutants can infiltrate structures and impact indoor air quality as well as the health or disease risk of individuals within those structures. This has been observed in schools and commercial buildings [20,21], but has not been studied in other important settings, including laboratory animal facilities. Laboratory animal research is an integral part of many fields including toxicology, pharmacology, and other biomedical sciences. A major benefit of using model organisms in settings such as academia, contract research organizations (CROs), and governmental research institutions is better control of potentially confounding variables. The reproducibility of scientific studies requires the ability to replicate the specific conditions under which the research was carried out. Such conditions would include purposeful as well as inadvertent exposures. Laboratory animals are housed in a wide range of indoor facilities with diverse air quality management systems and are, thus, potentially vulnerable to inhalation exposures, including those that emanate from outside the facility (e.g., wildfire smoke).

Measurement of indoor air quality in animal facilities is not a new concept, but these data are not often collected or reported in the literature as part of the standard facility metrics (e.g., temperature, relative humidity, light/dark cycle, and air change rate) [22]. The sparse data that exist demonstrate that animals in confined spaces are susceptible to air pollution exposure from the macroenvironment (e.g., recirculated building exhaust air) and microenvironment (e.g., dust generated from cage bedding) [23–25]. Importantly, the most recent version of the Guide for the Care and Use of Laboratory Animals addresses multiple aspects of air quality, but focuses exclusively on air pollutants generated inside the facility and not on air pollutants that may infiltrate the facility from the ambient environment [26]. This leaves a significant gap in guidance related to monitoring changes in indoor air quality, or exposure-induced health effects, that might subsequently affect experimental data. To help address this gap, our group performed a pilot assessment of indoor air quality using low-cost sensors in a laboratory animal facility located in a wildfire-prone region of the US. Below, we will discuss the collected data, potential impacts on the animal research community, and offer some recommendations.

2. Materials and Methods

University and facility location: This pilot study was conducted for a 28-day period from 8 August to 4 September 2021 on the Boise State University campus located in Boise, Idaho (Figure 1). Idaho is a US state situated in the Rocky Mountain region with its capital city of Boise located in the Treasure Valley between the Owyhee and Boise Mountain ranges. The Boise metropolitan area is impacted by smoke generated from wildfires from within Idaho as well as British Columbia, Washington, Oregon and California, depending on weather patterns.

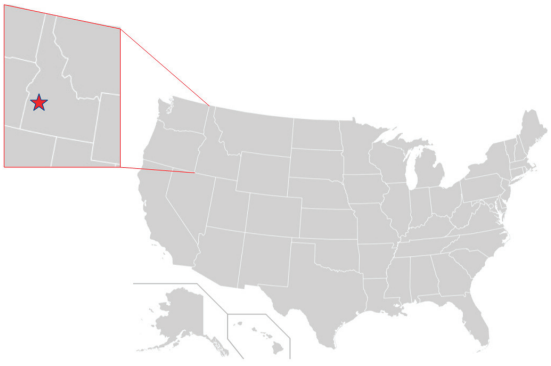

Figure 1. Location of Idaho within the United States and the city of Boise (red star) within the state of Idaho.

Facility characteristics: Air quality sensors were sited at the Boise State University vivarium. This 576 m^2 facility houses the majority of the animals on campus, which are primarily rodents. The vivarium's construction in 2015 was funded by a National Institutes of Health (NIH) award and thus was built to the NIH's stringent Design Requirements Manual (DRM) specifications [27]. The building heating ventilation and air conditioning (HVAC) filters used during the study period were Minimum Efficiency Rating Value (MERV) 15 filter; MERVs are derived from a test method developed by the American Society of Heating, Refrigerating and Air Conditioning Engineers (ASHRAE), and a rating of 15 is given to a filter that removes >85% of particles 0.3–1 μm and >90% of particles 1.0–10 μm [28]. The HVAC system also has a MERV 8 pre-filter for the removal of large dust particles. The air change rate during the study period was greater than 10 per hour.

Compliance authorization: The study does not directly involve animals so did not require Institutional Animal Care and Use Committee protocol approval. However, our research team worked closely with the Boise State University Office of Research Compliance at all stages including project development, implementation, and analysis.

Air quality monitoring: Air quality was monitored indoors and outdoors at the university vivarium. The PurpleAir PA-II (PurpleAir, Inc., Draper, UT, USA) was used and contains two PMS5003 sensors (Plantower, Beijing, China). The PMS5003 estimates particle mass concentrations on the principle of light scatter and these methods are elaborated on further by Sayahi et al. [29]. The PMS5003 reports both mass concentrations (including $PM_{2.5}$) and particle counts at 2-min intervals. Mass concentrations are calculated from particle count data using proprietary algorithms developed by the PMS5003 sensor manufacturer and are provided in two data series which are designated "CF = ATM" and "CF = 1", respectively [30]. Data from each monitor are transferred via Wi-Fi in real-time to a cloud account and are accessed by the research team. Outdoor data were collected from an established PurpleAir sensor named "Boise State Athletics" which is located on campus and approximately 1km from the animal facility. The indoor location was a negatively pressured animal room which typically houses mice and has no windows and one door. Note that during the course of this air quality study, there were no animals housed in

this room. Within the experimental room, two PurpleAir sensors were sited (Figure 2C). The first was located approximately 6 feet above the ground on a wall (Figure 2A). The second was located inside an empty (i.e., no animals or bedding) polycarbonate mouse cage mounted on a Tecniplast (West Chester, Pennsylvania, PA, USA) model GM80 rack with high efficiency particulate air (HEPA) supplied and exhausted air (Figure 2B).

Figure 2. Placement of indoor sensors including (**A**); indoor wall location, (**B**); indoor HEPA cage location, and (**C**); room where both indoor sensors were located.

Analysis: Analysis was conducted using R version 4.0.4 (The R Foundation for Statistical Computing, Austria). We calculated hourly mean $PM_{2.5}$ concentrations from the raw PurpleAir data collected at 2-min intervals. Prior to calculating hourly mean $PM_{2.5}$, we checked data completeness to ensure that each hour of data collection had at least 15 observations (≥50% of the expected 30 observations per hour at 2-min sampling intervals). Each hour of data had at least 25 observations, so no hourly observations were removed from data analysis. We evaluated agreement between the two identical sensors in each PurpleAir monitor by assessing differences and percent differences for the hourly $PM_{2.5}$ concentrations from the paired sensors within each monitor. Hourly observations (n = 4) were removed from the dataset if the $PM_{2.5}$ concentrations from the paired sensors were different by more than 5 $\mu g/m^3$ and had percent differences larger than two standard deviations [31]. Following this evaluation of sensor agreement, we used the mean hourly CF = 1 $PM_{2.5}$ concentration from paired sensors within each PurpleAir monitor for all subsequent analysis. The mean hourly $PM_{2.5}$ concentrations were corrected using an equation developed by the United States Environmental Protection Agency (EPA) that incorporates $PM_{2.5}$ and humidity data collected by the PurpleAir monitor. Only days with 12+ hours of hourly sampling data were included in statistical analyses. We calculated descriptive statistics for $PM_{2.5}$ concentrations (n, mean, sd, minimum [min], median, maximum [max]) for each PurpleAir monitor across all study days and for wildfire days and non-wildfire days. A suspected wildfire day was classified as a day with mean ambient 24-h $PM_{2.5}$ (as measured by the outdoor PurpleAir monitor) greater than 21 $\mu g/m^3$. A similar cut off to classify a wildfire day has been used previously in multiple studies [32,33]. This definition of a wildfire day assumes that the dominant source of ambient $PM_{2.5}$ during sampling is

from wildfire smoke, an assumption supported by an analysis of particulate air pollution in the Northwestern US from 1988 to 2016 [7].

We calculated infiltration efficiency (Finf) using a previously validated recursive modeling approach [34–36]. Finf is defined as the fraction of the outdoor $PM_{2.5}$ concentration that penetrates to the indoor environment and remains suspended [34]. It is presented as a unitless number between 0 and 1. We used paired hourly indoor and outdoor $PM_{2.5}$ concentrations from the PurpleAir monitors to calculate Finf. The Finf model is based on the assumption that indoor $PM_{2.5}$ is equal to a fraction of outdoor $PM_{2.5}$ from the current hour, a fraction of indoor $PM_{2.5}$ from the previous hour, and indoor $PM_{2.5}$ from the current hour. Data for the calculation were censored to exclude periods with indoor sources of $PM_{2.5}$ (i.e., periods with a rise in indoor $PM_{2.5}$ without a subsequent rise in outdoor $PM_{2.5}$) [34,35]. Censored data were then used in a linear model with indoor $PM_{2.5}$ ($indoor_t$) as the outcome variable, outdoor $PM_{2.5}$ ($outdoor_t$) and the previous hour's indoor $PM_{2.5}$ ($indoor_{t-1}$) as predictor variables, and intercept set to 0:

$$indoor_t = \alpha 1(outdoor_t) + \alpha 2(indoor_{t-1}) + 0$$

Model coefficients were then used to calculate F_{inf}:

$$F_{inf} = \alpha 1/(1 - \alpha 2)$$

We used this equation to calculate infiltration from the outdoor to indoor sampling locations across all study days and separately for wildfire and non-wildfire days. In addition, we multiplied 24-h outdoor PM $_{2.5}$ concentrations by the estimated Finf to estimate outdoor-generated indoor $PM_{2.5}$ concentrations [37,38]. We divided the outdoor-generated indoor $PM_{2.5}$ concentrations by the total 24-h indoor concentration to estimate the percentage of indoor $PM_{2.5}$ generated from outdoor sources [34]. If the infiltrated concentration was greater than the measured indoor concentration, we set the infiltrated concentration to equal the measured indoor concentration [34].

3. Results

For the 28-day study, which took place from 8 August–4 September 2021, corrected daily average concentrations of outdoor, indoor, and HEPA cage $PM_{2.5}$ are shown in Table 1. Outdoor air exhibited a higher daily average $PM_{2.5}$ concentration (26.2 $\mu g/m^3$) than both indoor air (8.9 $\mu g/m^3$) and HEPA cage air (3.1 $\mu g/m^3$) across all study days. This trend persisted even when separating wildfire event days (n = 12) and non-wildfire event days (n = 16). The indoor daily average $PM_{2.5}$ concentration was nearly three times higher on wildfire days compared to non-wildfire days. However, the HEPA cage $PM_{2.5}$ values were not different by wildfire day status and remained consistently low at approximately 3.0 $\mu g/m^3$.

Table 1. Outdoor, indoor, and HEPA cage $PM_{2.5}$ concentrations from 8 August–4 September 2021.

		Outdoor $PM_{2.5}$ ($\mu g/m^3$)	**Indoor $PM_{2.5}$ ($\mu g/m^3$)**	**HEPA Cage $PM_{2.5}$ ($\mu g/m^3$)**
	Sampling Days	**Mean (sd)** **Min, Median, Max**	**Mean (sd)** **Min, Median, Max**	**Mean (sd)** **Min, Median, Max**
All Study Days	28	26.2 (23.4) 6.4, 18.1, 92.6	8.9 (6.9) 3.3, 6.7, 27.9	3.1 (0.1) 2.6, 3.1, 3.2
Wildfire Day	12	45.0 (25.4) 23.3, 32.8, 92.6	13.9 (8.1) 7.9, 9.7, 27.9	3.0 (0.2) 2.6, 3.1, 3.2
Non-Wildfire Day	16	12.1 (4.3) 6.4, 11.2, 19.4	5.2 (1.4) 3.3, 5.0, 7.3	3.1 (0.1) 3.0, 3.1, 3.2

$PM_{2.5}$ = fine particulate matter; sd = standard deviation; HEPA = high efficiency purified air; min = minimum; max = maximum. Wildfire Day = day with mean 24-h outdoor $PM_{2.5}$ > 21 $\mu g/m^3$ during wildfire season. Only sampling days with >12 h of hourly data for both indoor and outdoor $PM_{2.5}$ are included in table.

Siting $PM_{2.5}$ sensors both indoors and outdoors at the animal facility allowed for the comparison of these data by three methods including difference, ratio, and Finf, which are shown in Table 2. The average $PM_{2.5}$ outdoor to indoor difference was greater for the HEPA cage (23.1 $\mu g/m^3$) as compared to the room indoor sensor (17.3 $\mu g/m^3$) and this trend was similar for the comparison of the ratio of indoor to outdoor $PM_{2.5}$. For both the room indoor sensor and the HEPA cage, the outdoor to indoor difference was highest on wildfire days (31.1 $\mu g/m^3$ and 42.0 $\mu g/m^3$, respectively). Finf values can range from 0 to 1, with values closer to 0 representing less infiltration of outdoor $PM_{2.5}$ to the indoor environment. Finf for the indoor location was 0.30 (95% Confidence Interval [CI] = 0.21 to 0.43) for all study days, 0.30 (95% CI = 0.17 to 0.50) for wildfire days, and 0.40 (95% CI = 0.29 to 0.54) for non-wildfire days. For the HEPA cage location, Finf model estimates were equal to 0, meaning Finf was equal to 0 and confidence intervals could not be calculated. Although Finf was slightly lower on wildfire days versus non-wildfire days, outdoor generated indoor $PM_{2.5}$ and percentage of indoor $PM_{2.5}$ generated outdoors were both higher on wildfire days compared to non-wildfire days (Table 2).

Table 2. Comparison of indoor and outdoor air quality data.

	Sampling Days	Outdoor–Indoor $PM_{2.5}$ Difference ($\mu g/m^3$)	Indoor/ Outdoor $PM_{2.5}$ Ratio	Infiltration Efficiency (95% CI)	Outdoor-Generated Indoor $PM_{2.5}$ ($\mu g/m^3$)	Percent (%) Indoor $PM_{2.5}$ Generated Outdoors
		Mean (sd) Min, Median, Max			Mean (sd) Min, Median, Max	Mean (sd) Min, Median, Max
All Study Days						
Indoor location	28	17.3 (16.8) 1.6, 11.4, 64.8	0.34	0.30 (0.21, 0.43)	7.7 (7.0) 1.9, 5.4, 27.8	80 (17) 37, 82, 100
HEPA cage location	28	23.1 (23.5) 3.2, 14.9, 89.7	0.12	NA*	NA*	NA*
Wildfire Day						
Indoor location	12	31.1 (17.6) 14.0, 24.0, 64.8	0.31	0.30 (0.17, 0.50)	13.1 (7.9) 6.8, 9.6, 27.8	94 (8) 74, 100, 100
HEPA cage location	12	42.0 (25.5) 20.1, 29.7, 89.7	0.07	NA*	NA*	NA*
Non-Wildfire Day						
Indoor location	16	6.9 (3.4) 1.6, 6.8, 12.8	0.43	0.40 (0.29, 0.54)	3.6 (1.3) 1.9, 3.4, 5.8	70 (14) 37, 72, 88
HEPA cage location	16	9.0 (4.3) 3.2, 8.0, 16.2	026	NA*	NA*	NA*

$PM_{2.5}$ = fine particulate matter; sd = standard deviation; CI = confidence interval; HEPA = high efficiency purified air; min = minimum; max = maximum. Wildfire Day = day with mean 24-h outdoor $PM_{2.5}$ > 21 $\mu g/m^3$ during wildfire season. Only sampling days with >12 h of hourly data for both indoor and outdoor $PM_{2.5}$ are included in table. NA* = model estimates were equal to 0, meaning infiltration efficiency was equal to 0 and confidence intervals could not be calculated.

During the 28-day sampling period, ambient air quality was negatively impacted and this resulted in exceedances of regulatory thresholds. In particular, there was one remarkable wildfire event which lasted several days in the middle of August where ambient $PM_{2.5}$ concentrations rose above 90 $\mu g/m^3$ (Figure 3). The outdoor $PM_{2.5}$ concentration exceeded the 24-h $PM_{2.5}$ thresholds set by both the WHO (61% of sampling days) and the EPA (18% of sampling days) (Table 3). By contrast, the HEPA cage $PM_{2.5}$ concentration did not exceed the annual or 24-h $PM_{2.5}$ thresholds set by the WHO or the EPA. The indoor room $PM_{2.5}$ concentration values were typically less than the 24-h WHO guideline and EPA standard and the EPA annual standard, except during the major wildfire event that occurred in the middle of August. During this 4-day smoke event, the indoor room $PM_{2.5}$ concentration exceeded all but the EPA 24-h standard.

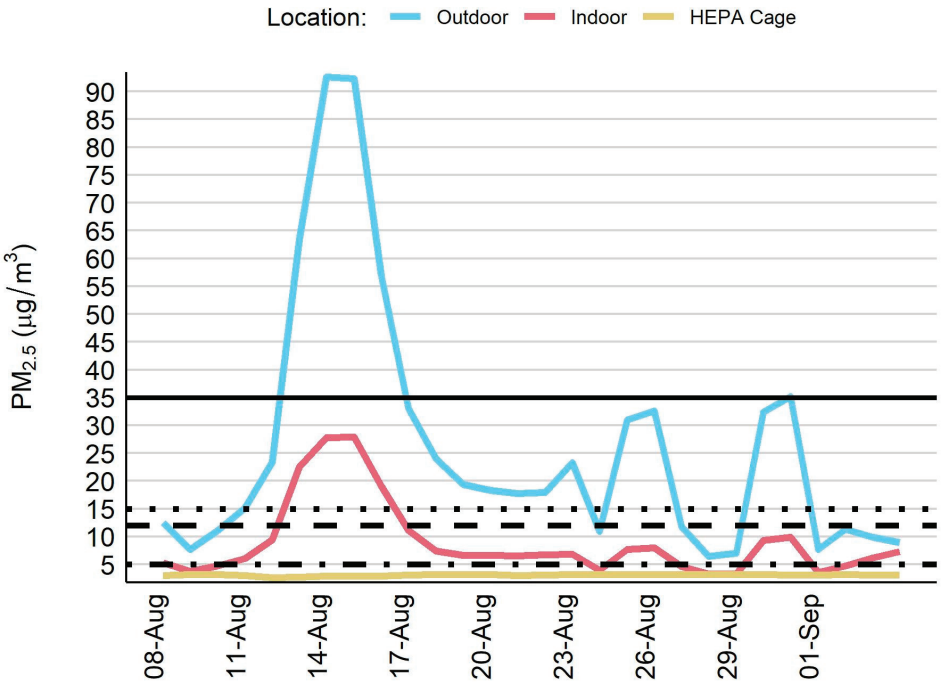

Figure 3. Time series plot for fine particulate matter across three sampling locations. $PM_{2.5}$ = fine particulate matter. Horizontal lines indicate $PM_{2.5}$ thresholds: United State Environmental Protection Agency–24-h standard of 35 µg/m^3 (solid line) and annual mean of 12 µg/m^3 (long dashes); World Health Organization–24-h guideline of 15 µg/m^3 (short dashes) and annual mean of 5 µg/m^3 (alternating short/long dashes).

Table 3. Number of days that sensor measurements surpassed EPA and WHO thresholds.

	Outdoor $PM_{2.5}$ (µg/m^3)	Indoor $PM_{2.5}$ (µg/m^3)	HEPA Cage $PM_{2.5}$ (µg/m^3)
Sampling Days, n	28	28	28
Days with $PM_{2.5}$ > 35 µg/m^3, n (%) [a]	5 (18)	0 (0)	0 (0)
Days with $PM_{2.5}$ > 12 µg/m^3, n (%) [a]	18 (64)	4 (14)	0 (0)
Days with $PM_{2.5}$ > 15 µg/m^3, n (%) [b]	17 (61)	4 (14)	0 (0)
Days with $PM_{2.5}$ > 5 µg/m^3, n (%) [b]	28 (100)	20 (71)	0 (0)

$PM_{2.5}$ = fine particulate matter. [a] United States Environmental Protection Agency National Ambient Air Quality Standard for $PM_{2.5}$ is 35 µg/m^3 for a 24-h period and 12 µg/m^3 for an annual period. [b] World Health Organization Air Quality Guideline for $PM_{2.5}$ is 15 µg/m^3 for a 24-h period and 5 µg/m^3 for an annual period. Only sampling days with >12 h of hourly data are included in table.

4. Discussion

In this pilot study we demonstrate the potential for ambient air pollution events caused by wildfires to impact indoor air quality within a facility that houses research animals in the western US. To our knowledge, there are no indoor $PM_{2.5}$ standards for public health, occupational health, or research animal health related to $PM_{2.5}$. Thus, we compared our observations to ambient $PM_{2.5}$ public health thresholds provided by the EPA and WHO. Our results show that outdoor $PM_{2.5}$ impacted indoor air quality in the research facility with a remarkable increase in indoor $PM_{2.5}$ during wildfire smoke events. This is notable

given that the animal facility and HVAC system in this pilot study are relatively new and utilize the recommended filters designed to capture $PM_{2.5}$.

We hypothesized that infiltration of smoke would be greatest on wildfire days. This would be consistent with others who have identified associations between seasonality and sources of pollution [39]. However, our data revealed that PM infiltration was higher during non-wildfire days within the wildfire season. Interestingly, this is in line with recent data collected by researchers in California who used crowdsourced low-cost sensor data to assess infiltration among residential homes [40]. Liang et al. speculate that infiltration on wildfire days is lower because of behavioral changes like shutting windows and running air conditioning, but it is not clear that these explanations would be relevant in an animal facility. Thus, more research is needed to understand the factors that contribute to changes in infiltration rates. Even though Finf was slightly lower during wildfire days versus non-wildfire days, it is important to reiterate that indoor air quality at the animal facility was adversely impacted by wildfire smoke. Indoor $PM_{2.5}$, outdoor generated indoor $PM_{2.5}$, and percentage of indoor $PM_{2.5}$ generated outdoors were all higher on wildfire days compared to non-wildfire days.

Studies of air pollution toxicology have been conducted in laboratory animals, and this body of evidence informs our presumption that wildfire smoke PM can also cause adverse health effects [41]. However, the biological importance and extent of physiologic effects specific to indoor wildfire smoke exposure remain largely uncharacterized. Without an indoor standard for $PM_{2.5}$, it is difficult to know whether the EPA or WHO ambient thresholds are overly protective or overly relaxed for animals. We speculate this would depend on several factors including animal species, age, and immune status as well as experimental study conditions such as exposure, outcome measure, and duration of study paradigm. The latter would be important especially in circumstances where animals might be episodically and chronically exposed (i.e., exposure to repeated wildfire seasons).

Our finding that wildfire smoke infiltrates animal facilities suggests it is plausible that unintended exposure to smoke could affect the reproducibility of study data. In this way laboratories impacted by smoke might struggle to replicate the findings from laboratories not impacted by smoke, or vice versa. One could argue that for experiments conducted during the wildfire season, "exposed" and "control" animals would both be exposed to the same background level of smoke, and thus any statistical differences may be attributed to the exposure of interest rather than to the wildfire smoke exposure. However, if smoke exposure and the experimental condition of interest acted synergistically to impact an outcome, this larger effect size could be wrongly attributed to the experimental treatment alone. Furthermore, it is particularly problematic to consider studies that use a staggered cohort design where some groups may be raised during fire season while others are not. In these cases, a single lab might struggle to reproduce their own findings from one animal cohort to the next. Smoke exposure could also impact animal breeding operations including breeding success, fertility, and the health of the offspring [19,42–44].

Smoke exposure for research animals is a timely and necessary challenge to consider in the US and around the world given that wildfire events continue to increase in frequency and duration concurrent with climate change. Facilities that house animals proximal to prime fire conditions are perhaps at the greatest risk for infiltration-related exposure. However, wildfire smoke is transient and health impacts have been reported in populations living great distances from wildfire events [45]. Some of these distant impacts may be attributed to the differential toxicity reported after "aging" of smoke, which is suggested to produce more oxidative stress [46,47].

Whether smoke exposure occurs locally or downstream of a wildfire event, there is a growing body of data indicating that adverse health outcomes are possible in humans [48] as well as animals [49]. As an example of human effects, a cohort exposed to an intense and long-duration wildfire smoke event in Seeley Lake, Montana, experienced persistent lung function decrements that were measurable two years following exposure [50]. In cell models, wildfire smoke PM has been shown to induce inflammation and cytotoxicity [51]. In

guinea pigs, short-term exposure to wildfire smoke can contribute to differential expression of inflammatory cytokines [52]. Effects of wildfire smoke may occur not only in the directly exposed animal but can be passed on to the subsequent generation. In primates, short-term perinatal exposure to wildfire smoke in California resulted in immune modulation that was observable into adolescence in the offspring [53]. Male rats exposed to wildfire smoke produce offspring with behavioral aberrancies, suggesting a potential for multi-generational effects [44]. Such effects could be passed through the germ line as we have demonstrated that prolonged exposure to wildfire smoke significantly alters the sperm epigenome of mice [54]. This and other intergenerational animal studies demonstrate the ability for an exposure to impact the parent generation, the offspring, and even in some cases subsequent generations through inter- and trans-generational inheritance [55]. Such exposure-induced effects within a breeding colony could impact future study outcomes.

With the backdrop of increasing wildfire activity and considering the potential for adverse health outcomes or study confounding, it would be advisable to measure indoor air quality in animal facilities where penetrance of wildfire smoke is possible. From an academic research perspective, the above advisement is consistent with a recent report produced by the University of California Systemwide Air Quality Protocol Working Group which stated "Accurate and reliable outdoor and indoor air quality monitoring and data sources are critical to decision-making related to regulatory compliance, and operational actions" [56]. In the commercial or industrial setting, the EPA suggests using new guidance from the American Society of Heating, Refrigerating, and Air-Conditioning Engineers (ASHRAE) titled "Planning framework for protecting commercial building occupants from smoke during wildfire events" which also suggests that one of the best ways to prepare for wildfire season is to "add the ability to monitor indoor $PM_{2.5}$" [57].

While our specific concern for wildfire smoke is novel and timely, the consideration of air quality more generally in an animal facility and its potential influence on experimental outcomes is not new; Besch reported on this in 1985 [58]. As early as 2003 there were calls for a more thorough description of air quality standards for laboratory animals [59]. Still, there exists no new metric or standard guideline for the measurement or reporting of air quality in laboratory animal facilities in the US. The Canadian Council on Animal Care (CCAC) has provided guidance on indoor air quality including ammonia, carbon dioxide, volatile organic compounds, and PM [60]. The 2019 guidance from the CCAC adopts the EPA's outdoor annual standard of 12 $\mu g/m^3$ as a maximum threshold for $PM_{2.5}$ in the laboratory animal environment. It is notable that this document does not discuss ambient episodes or sources (e.g., wildfires and smoke events). The lack of acknowledgement for ambient factors by the CCAC and the committee for the Guide for the Care and Use of Laboratory Animals is concerning. It is for this reason that we recommend implementation of air quality monitoring in animal facilities in wildfire-impacted areas to address both indoor and outdoor sources of poor air quality.

The collection of animal facility air quality data would help with decision making within individual facilities and further reporting of this data could inform broader policies and guidelines for laboratory animal environments across the globe. Facilities at risk of ambient exposure to wildfire smoke exposure events should employ active air monitoring programs and develop prudent internal standards and plans for how to deal with aberrant indoor air quality. Building managers, compliance personnel, and research staff should work collaboratively to determine if these air quality disruptions can be predicted and mitigated.

The necessity and scope of air quality mitigation measures will be entirely dependent on each individual facility. Facilities will need to consider the risk for elevated ambient levels of wildfire smoke, anticipated infiltration, and the type of animals or experiments that occur on site. The ASHRAE planning framework outlines several key steps that facilities can take to ensure HVAC systems and buildings are prepared for wildfire season [57]. In this pilot, we demonstrate that a HEPA filter air-supplied mouse rack is sufficient to mitigate exposure under the specific conditions that occurred during the sampling period.

More studies will need to be conducted to fully understand the impact that higher levels of infiltration would have on the HEPA filter rack system. However, filter racks may not be available in all facilities and may not be feasible for all species (e.g., large animals). Standalone HEPA filter air purification systems could be an alternative to enhance air quality in large or small animal rooms. Such filters have been shown to substantially reduce indoor air pollution in many settings [61], but the effectiveness in animal research facilities has not been explored. Circumstances including the size of the room, the number of air changes per hour, or the amount of make-up air being brought in from outside the facility could impact the effectiveness of an air purifier. Air quality sensors should be used to attain a baseline and to evaluate any benefits from modifications that are made.

5. Conclusions

Wildfire smoke exposure is increasing in certain parts of the US and throughout the world. In this pilot, we demonstrated that PM infiltration occurs in a laboratory animal facility during wildfire season. Universities and other institutions with laboratory animal operations that are at risk of ambient exposure to wildfire smoke should do an indoor air quality inventory, especially during fire season. Whenever possible these institutions should actively monitor the indoor conditions and mitigate infiltration, in order to protect the animals' health and reduce confounding and loss of confidence in study results.

Author Contributions: Conceptualization, L.M. and M.L.; methodology, L.M., E.S.W. and M.L.; formal analysis, E.S.W.; investigation, L.M. and A.S.; resources, M.L.; data curation, L.M. and E.S.W.; writing—original draft preparation, A.S.; writing—review and editing, L.M., M.L., J.M.G., E.S.W., A.S.; visualization E.S.W.; supervision, L.M.; project administration, L.M.; funding acquisition, M.L. All authors have read and agreed to the published version of the manuscript.

Funding: L.M. and A.S. were supported by the Boise State University COBRE (P20GM109095). E.S.W. was supported by the University of Montana Center for Population Health Research (P20GM130418).

Institutional Review Board Statement: Not applicable.

Informed Consent Statement: Not applicable.

Data Availability Statement: The data presented in this study are available on request from the corresponding author.

Conflicts of Interest: The authors declare no conflict of interest.

References

1. Sheehan, M.C. 2021 Climate and Health Review–Uncharted Territory: Extreme Weather Events and Morbidity. *Int. J. Health Serv. Plan. Adm. Eval.* **2022**, *52*, 189–200. [CrossRef] [PubMed]
2. Senande-Rivera, M.; Insua-Costa, D.; Miguez-Macho, G. Spatial and temporal expansion of global wildland fire activity in response to climate change. *Nat. Commun.* **2022**, *13*, 1208. [CrossRef] [PubMed]
3. Borchers-Arriagada, N.; Bowman, D.M.J.S.; Price, O.; Palmer, A.J.; Samson, S.; Clarke, H.; Sepulveda, G.; Johnston, F.H. Smoke health costs and the calculus for wildfires fuel management: A modelling study. *Lancet Planet. Health* **2021**, *5*, e608–e619. [CrossRef]
4. Xue, T.; Geng, G.; Li, J.; Han, Y.; Guo, Q.; Kelly, F.J.; Wooster, M.J.; Wang, H.; Jiangtulu, B.; Duan, X.; et al. Associations between exposure to landscape fire smoke and child mortality in low-income and middle-income countries: A matched case-control study. *Lancet Planet. Health* **2021**, *5*, e588–e598. [CrossRef]
5. Xu, J.-W.; Martin, R.V.; Evans, G.J.; Umbrio, D.; Traub, A.; Meng, J.; van Donkelaar, A.; You, H.; Kulka, R.; Burnett, R.T.; et al. Predicting Spatial Variations in Multiple Measures of Oxidative Burden for Outdoor Fine Particulate Air Pollution across Canada. *Environ. Sci. Technol.* **2021**, *55*, 9750–9760. [CrossRef]
6. Hoover, K.; Hanson, L.A. Wildfire Statistics. Congressional Research Service, IF10244, October 2021. Available online: https://sgp.fas.org/crs/misc/IF10244.pdf (accessed on 4 May 2022).
7. McClure, C.D.; Jaffe, D.A. US particulate matter air quality improves except in wildfire-prone areas. *Proc. Natl. Acad. Sci. USA* **2018**, *115*, 7901–7906. [CrossRef]
8. Burke, M.; Driscoll, A.; Heft-Neal, S.; Xue, J.; Burney, J.; Wara, M. The changing risk and burden of wildfire in the United States. *Proc. Natl. Acad. Sci. USA* **2021**, *118*, e2011048118. [CrossRef]
9. Ford, B.; Martin, M.V.; Zelasky, S.E.; Fischer, E.V.; Anenberg, S.C.; Heald, C.L.; Pierce, J.R. Future Fire Impacts on Smoke Concentrations, Visibility, and Health in the Contiguous United States. *GeoHealth* **2018**, *2*, 229–247. [CrossRef]

10. Kim, Y.H.; Warren, S.H.; Krantz, Q.T.; King, C.; Jaskot, R.; Preston, W.T.; George, B.J.; Hays, M.D.; Landis, M.; Higuchi, M.; et al. Mutagenicity and Lung Toxicity of Smoldering vs. Flaming Emissions from Various Biomass Fuels: Implications for Health Effects from Wildland Fires. *Environ. Health Perspect.* **2018**, *126*, 017011. [CrossRef]
11. Black, C.; Tesfaigzi, Y.; Bassein, J.A.; Miller, L.A. Wildfire smoke exposure and human health: Significant gaps in research for a growing public health issue. *Environ. Toxicol. Pharmacol.* **2017**, *55*, 186–195. [CrossRef]
12. Liu, Y.; Austin, E.; Xiang, J.; Gould, T.; Larson, T.; Seto, E. Health Impact Assessment of the 2020 Washington State Wildfire Smoke Episode: Excess Health Burden Attributable to Increased $PM_{2.5}$ Exposures and Potential Exposure Reductions. *GeoHealth* **2021**, *5*, e2020GH000359. [CrossRef] [PubMed]
13. Liu, J.C.; Wilson, A.; Mickley, L.J.; Dominici, F.; Ebisu, K.; Wang, Y.; Sulprizio, M.P.; Peng, R.D.; Yue, X.; Son, J.-Y.; et al. Wildfire-specific Fine Particulate Matter and Risk of Hospital Admissions in Urban and Rural Counties. *Epidemiology* **2017**, *28*, 77–85. [CrossRef] [PubMed]
14. Makkonen, U.; Hellén, H.; Anttila, P.; Ferm, M. Size distribution and chemical composition of airborne particles in south-eastern Finland during different seasons and wildfire episodes in 2006. *Sci. Total Environ.* **2010**, *408*, 644–651. [CrossRef] [PubMed]
15. Aguilera, R.; Corringham, T.; Gershunov, A.; Benmarhnia, T. Wildfire smoke impacts respiratory health more than fine particles from other sources: Observational evidence from Southern California. *Nat. Commun.* **2021**, *12*, 1493. [CrossRef]
16. Karthikeyan, S.; Balasubramanian, R.; Iouri, K. Particulate Air Pollution from Bushfires: Human Exposure and Possible Health Effects. *J. Toxicol. Environ. Health Part A* **2006**, *69*, 1895–1908. [CrossRef]
17. Williams, K.M.; Franzi, L.M.; Last, J.A. Cell-specific oxidative stress and cytotoxicity after wildfire coarse particulate matter instillation into mouse lung. *Toxicol. Appl. Pharmacol.* **2012**, *266*, 48–55. [CrossRef]
18. Rhew, S.H.; Kravchenko, J.; Lyerly, H.K. Exposure to low-dose ambient fine particulate matter PM2.5 and Alzheimer's disease, non-Alzheimer's dementia, and Parkinson's disease in North Carolina. *PLoS ONE* **2021**, *16*, e0253253. [CrossRef]
19. Willson, B.E.; Pinkerton, K.E.; Lasley, B.; Gee, N. Effect of wildfire smoke on pregnancy outcomes in the non-human primate. *Fertil. Steril.* **2019**, *112*, e13. [CrossRef]
20. Xiang, J.; Huang, C.-H.; Shirai, J.; Liu, Y.; Carmona, N.; Zuidema, C.; Austin, E.; Gould, T.; Larson, T.; Seto, E. Field measurements of PM2.5 infiltration factor and portable air cleaner effectiveness during wildfire episodes in US residences. *Sci. Total Environ.* **2021**, *773*, 145642. [CrossRef]
21. May, N.W.; Dixon, C.; Jaffe, D.A. Impact of Wildfire Smoke Events on Indoor Air Quality and Evaluation of a Low-cost Filtration Method. *Aerosol Air Qual. Res.* **2021**, *21*, 210046. [CrossRef]
22. Kacergis, J.B.; Jones, R.B.; Reeb, C.K.; Turner, W.A.; Ohman, J.L.; Ardman, M.R.; Paigen, B. Air Quality in an Animal Facility: Particulates, Ammonia, and Volatile Organic Compounds. *Am. Ind. Hyg. Assoc. J.* **1996**, *57*, 634–640. [CrossRef] [PubMed]
23. Hudda, N.; Durant, J.L.; Nemeth, A.; Mann, P.; Petitto, J.; Brugge, D.; Nephew, B.C. Bedding-generated particulate matter: Implications for rodent studies. *Inhal. Toxicol.* **2019**, *31*, 368–375. [CrossRef] [PubMed]
24. Besch, E.L. Animal Facility Ventilation Air Quality and Quantity. AIVC, 6 July 2013. Available online: https://www.aivc.org/resource/animal-facility-ventilation-air-quality-and-quantity (accessed on 2 January 2022).
25. Werth, S.; Schusterman, E.; Peterson, C.; Mitloehner, F. Air: Confined Animal Facilities and Air Quality Issues. In *Reference Module in Food Science*; Elsevier: Amsterdam, The Netherlands, 2017. [CrossRef]
26. National Research Council (US) Committee for the Update of the Guide for the Care and Use of Laboratory Animals. *Environment, Housing, and Management*; National Academies Press: Washington, DC, USA, 2011. Available online: https://www.ncbi.nlm.nih.gov/books/NBK54046/ (accessed on 2 January 2022).
27. Design Requirements Manual (DRM). Available online: https://orf.od.nih.gov/TechnicalResources/Pages/DesignRequirementsManual2016.aspx (accessed on 3 January 2022).
28. US EPA. What Is a MERV Rating? 19 February 2019. Available online: https://www.epa.gov/indoor-air-quality-iaq/what-merv-rating (accessed on 18 April 2022).
29. Sayahi, T.; Butterfield, A.; Kelly, K.E. Long-term field evaluation of the Plantower PMS low-cost particulate matter sensors. *Environ. Pollut.* **2019**, *245*, 932–940. [CrossRef]
30. Tryner, J.; L'Orange, C.; Mehaffy, J.; Miller-Lionberg, D.; Hofstetter, J.C.; Wilson, A.; Volckens, J. Laboratory evaluation of low-cost PurpleAir PM monitors and in-field correction using co-located portable filter samplers. *Atmos. Environ.* **2019**, *220*, 117067. [CrossRef]
31. Barkjohn, K.K.; Gantt, B.; Clements, A.L. Development and application of a United States-wide correction for $PM_{2.5}$ data collected with the PurpleAir sensor. *Atmos. Meas. Tech.* **2021**, *14*, 4617–4637. [CrossRef]
32. Doubleday, A.; Schulte, J.; Sheppard, L.; Kadlec, M.; Dhammapala, R.; Fox, J.; Isaksen, T.B. Mortality associated with wildfire smoke exposure in Washington state, 2006–2017: A case-crossover study. *Environ. Health* **2020**, *19*, 4. [CrossRef]
33. Zhou, X.; Josey, K.; Kamareddine, L.; Caine, M.C.; Liu, T.; Mickley, L.J.; Cooper, M.; Dominici, F. Excess of COVID-19 cases and deaths due to fine particulate matter exposure during the 2020 wildfires in the United States. *Sci. Adv.* **2021**, *7*, eabi8789. [CrossRef]
34. Allen, R.; Larson, T.; Sheppard, L.; Wallace, L.; Liu, L.-J.S. Use of Real-Time Light Scattering Data to Estimate the Contribution of Infiltrated and Indoor-Generated Particles to Indoor Air. *Environ. Sci. Technol.* **2003**, *37*, 3484–3492. [CrossRef]

35. Allen, R.; Wallace, L.; Larson, T.; Sheppard, L.; Liu, L.-J.S. Evaluation of the recursive model approach for estimating particulate matter infiltration efficiencies using continuous light scattering data. *J. Expo. Sci. Environ. Epidemiol.* **2007**, *17*, 468–477. Available online: https://www.nature.com/articles/7500539 (accessed on 10 February 2022). [CrossRef]
36. Semmens, E.O.; Noonan, C.W.; Allen, R.W.; Weiler, E.C.; Ward, T.J. Indoor particulate matter in rural, wood stove heated homes. *Environ. Res.* **2015**, *138*, 93–100. [CrossRef]
37. Ott, W.; Wallace, L.; Mage, D. Predicting Particulate (PM_{10}) Personal Exposure Distributions Using a Random Component Superposition Statistical Model. *J. Air Waste Manag. Assoc.* **2000**, *50*, 1390–1406. [CrossRef] [PubMed]
38. Diapouli, E.; Chaloulakou, A.; Koutrakis, P. Estimating the concentration of indoor particles of outdoor origin: A review. *J. Air Waste Manag. Assoc.* **2013**, *63*, 1113–1129. [CrossRef] [PubMed]
39. Barn, P.; Larson, T.I.; Noullett, M.; Kennedy, S.; Copes, R.; Brauer, M. Infiltration of forest fire and residential wood smoke: An evaluation of air cleaner effectiveness. *J. Expo. Sci. Environ. Epidemiol.* **2007**, *18*, 503–511. [CrossRef] [PubMed]
40. Liang, Y.; Sengupta, D.; Campmier, M.J.; Lunderberg, D.M.; Apte, J.S.; Goldstein, A.H. Wildfire smoke impacts on indoor air quality assessed using crowdsourced data in California. *Proc. Natl. Acad. Sci. USA* **2021**, *118*, e2106478118. [CrossRef] [PubMed]
41. Cho, C.-C.; Hsieh, W.-Y.; Tsai, C.-H.; Chen, C.-Y.; Chang, H.-F.; Lin, C.-S. In Vitro and In Vivo Experimental Studies of PM2.5 on Disease Progression. *Int. J. Environ. Res. Public Health* **2018**, *15*, 1380. [CrossRef] [PubMed]
42. Rubin, E.S.; Parker, P.B.; Garg, B.; Wu, D.; Peregrine, J.; Lee, D.; Amato, P.; Gibbins, K.J.; Baldwin, M.K.; O'Leary, T.; et al. Wildfire Smoke Exposure Is Associated with Decreased Total Motile Sperm Count. *Fertil. Steril.* **2021**, *116*, e89. [CrossRef]
43. Capitanio, J.P.; Del Rosso, L.A.; Gee, N.; Lasley, B.L. Adverse biobehavioral effects in infants resulting from pregnant rhesus macaques' exposure to wildfire smoke. *Nat. Commun.* **2022**, *13*, 1774. [CrossRef] [PubMed]
44. Sosedova, L.M.; Vokina, V.A.; Novikov, M.A.; Rukavishnikov, V.S.; Andreeva, E.S.; Zhurba, O.M.; Alekseenko, A.N. Paternal Biomass Smoke Exposure in Rats Produces Behavioral and Cognitive Alterations in the Offspring. *Toxics* **2020**, *9*, 3. [CrossRef]
45. O'Dell, K.; Bilsback, K.; Ford, B.; Martenies, S.E.; Magzamen, S.; Fischer, E.V.; Pierce, J.R. Estimated Mortality and Morbidity Attributable to Smoke Plumes in the United States: Not Just a Western US Problem. *GeoHealth* **2021**, *5*, e2021GH000457. [CrossRef]
46. Magzamen, S.; Gan, R.W.; Liu, J.; O'Dell, K.; Ford, B.; Berg, K.; Bol, K.; Wilson, A.; Fischer, E.V.; Pierce, J.R. Differential Cardiopulmonary Health Impacts of Local and Long-Range Transport of Wildfire Smoke. *GeoHealth* **2021**, *5*, e2020GH000330. [CrossRef]
47. Lindaas, J.; Farmer, D.K.; Pollack, I.B.; Abeleira, A.; Flocke, F.; Roscioli, R.; Herndon, S.; Fischer, E.V. Changes in ozone and precursors during two aged wildfire smoke events in the Colorado Front Range in summer 2015. *Atmos. Chem. Phys.* **2017**, *17*, 10691–10707. [CrossRef]
48. Adetona, O.; Reinhardt, T.E.; Domitrovich, J.; Broyles, G.; Adetona, A.; Kleinman, M.T.; Ottmar, R.D.; Naeher, L.P. Review of the health effects of wildland fire smoke on wildland firefighters and the public. *Inhal. Toxicol.* **2016**, *28*, 95–139. [CrossRef] [PubMed]
49. Sanderfoot, O.V.; Bassing, S.B.; Brusa, J.L.; Emmet, R.L.; Gillman, S.J.; Swift, K.; Gardner, B. A review of the effects of wildfire smoke on the health and behavior of wildlife. *Environ. Res. Lett.* **2021**, *16*, 123003. [CrossRef]
50. Orr, A.; Migliaccio, C.A.L.; Buford, M.; Ballou, S.; Migliaccio, C.T. Sustained Effects on Lung Function in Community Members Following Exposure to Hazardous $PM_{2.5}$ Levels from Wildfire Smoke. *Toxics* **2020**, *8*, 53. [CrossRef]
51. Jalava, P.I.; Salonen, R.O.; Hälinen, A.I.; Penttinen, P.; Pennanen, A.; Sillanpää, M.; Sandell, E.; Hillamo, R.; Hirvonen, M.-R. In vitro inflammatory and cytotoxic effects of size-segregated particulate samples collected during long-range transport of wildfire smoke to Helsinki. *Toxicol. Appl. Pharmacol.* **2006**, *215*, 341–353. [CrossRef]
52. Ramos, C.; Cañedo-Mondragón, R.; Becerril, C.; González-Ávila, G.; Esquivel, A.L.; Torres-Machorro, A.L.; Montaño, M. Short-Term Exposure to Wood Smoke Increases the Expression of Pro-Inflammatory Cytokines, Gelatinases, and TIMPs in Guinea Pigs. *Toxics* **2021**, *9*, 227. [CrossRef]
53. Black, C.; Gerriets, J.E.; Fontaine, J.H.; Harper, R.W.; Kenyon, N.J.; Tablin, F.; Schelegle, E.S.; Miller, L.A. Early Life Wildfire Smoke Exposure Is Associated with Immune Dysregulation and Lung Function Decrements in Adolescence. *Am. J. Respir. Cell Mol. Biol.* **2017**, *56*, 657–666. [CrossRef] [PubMed]
54. Schuller, A.; Bellini, C.; Jenkins, T.G.; Eden, M.; Matz, J.; Oakes, J.; Montrose, L. Simulated Wildfire Smoke Significantly Alters Sperm DNA Methylation Patterns in a Murine Model. *Toxics* **2021**, *9*, 199. [CrossRef]
55. Legoff, L.; D'Cruz, S.C.; Tevosian, S.; Primig, M.; Smagulova, F. Transgenerational Inheritance of Environmentally Induced Epigenetic Alterations during Mammalian Development. *Cells* **2019**, *8*, 1559. [CrossRef]
56. Wildfire Smoke/Air Quality | University Health Services. Available online: https://uhs.berkeley.edu/health-topics/wildfire-smoke-air-quality (accessed on 3 January 2022).
57. US EPA. Guidance Available to Prepare Schools, Commercial and Public Buildings for Wildfire Smoke. 15 June 2021. Available online: https://www.epa.gov/sciencematters/guidance-available-prepare-schools-commercial-and-public-buildings-wildfire-smoke (accessed on 4 January 2022).
58. Besch, E.L. Definition of Laboratory Animal Environmental Conditions. In *Animal Stress*; Moberg, G.P., Ed.; Springer: New York, NY, USA, 1985; pp. 297–315. [CrossRef]
59. National Research Council (US) Institute for Laboratory Animal Research. *Environmental Controls (US Guidance)*; National Academies Press: Washington, DC, USA, 2004. Available online: https://www.ncbi.nlm.nih.gov/books/NBK25409/ (accessed on 4 January 2022).

60. Canadian Council on Animal Care. Heating, Ventilation, and Air Conditioning: Addendum to the CCAC Guidelines on Laboratory Animal Facilities–Characteristics, Design and Development. 2019. Available online: http://www.aircuity.com/wp-content/uploads/CCAC-Documents-Combined.pdf (accessed on 2 May 2022).
61. Cheek, E.; Guercio, V.; Shrubsole, C.; Dimitroulopoulou, S. Portable air purification: Review of impacts on indoor air quality and health. *Sci. Total Environ.* **2020**, *766*, 142585. [CrossRef]

materials

MDPI

Article

Cu and As(V) Adsorption and Desorption on/from Different Soils and Bio-Adsorbents

Raquel Cela-Dablanca [1,*], Ana Barreiro [1], Gustavo Ferreira-Coelho [1], Claudia Campillo-Cora [2], Paula Pérez-Rodríguez [2], Manuel Arias-Estévez [2], Avelino Núñez-Delgado [1], Esperanza Álvarez-Rodríguez [1] and María J. Fernández-Sanjurjo [1]

[1] Department of Soil Science and Agricultural Chemistry, Engineering Polytechnic School, University of Santiago de Compostela, 27002 Lugo, Spain; ana.barreiro.bujan@usc.es (A.B.); gustavof.coelho@gmail.com (G.F.-C.); avelino.nunez@usc.es (A.N.-D.); esperanza.alvarez@usc.es (E.Á.-R.); mf.sanjurjo@usc.es (M.J.F.-S.)

[2] Soil Science and Agricultural Chemistry, Faculty of Sciences, University of Vigo, 32004 Ourense, Spain; ccampillo@uvigo.es (C.C.-C.); paulaperezr@uvigo.es (P.P.-R.); mastevez@uvigo.es (M.A.-E.)

* Correspondence: raquel.dablanca@usc.es

Abstract: This research is concerned with the adsorption and desorption of Cu and As(V) on/from different soils and by-products. Both contaminants may reach soils by the spreading of manure/slurries, wastewater, sewage sludge, or pesticides, and also due to pollution caused by mining and industrial activities. Different crop soils were sampled in A Limia (AL) and Sarria (S) (Galicia, NW Spain). Three low-cost by-products were selected to evaluate their bio-adsorbent potential: pine bark, oak ash, and mussel shell. The adsorption/desorption studies were carried out by means of batch-type experiments, adding increasing and individual concentrations of Cu and As(V). The fit of the adsorption data to the Langmuir, Freundlich, and Temkin models was assessed, with good results in some cases, but with high estimation errors in others. Cu retention was higher in soils with high organic matter and/or pH, reaching almost 100%, while the desorption was less than 15%. The As(V) adsorption percentage clearly decreased for higher As doses, especially in S soils, from 60–100% to 10–40%. The As(V) desorption was closely related to soil acidity, being higher for soils with higher pH values (S soils), in which up to 66% of the As(V) previously adsorbed can be desorbed. The three by-products showed high Cu adsorption, especially oak ash, which adsorbed all the Cu added in a rather irreversible manner. Oak ash also adsorbed a high amount of As(V) (>80%) in a rather non-reversible way, while mussel shell adsorbed between 7 and 33% of the added As(V), and pine bark adsorbed less than 12%, with both by-products reaching 35% desorption. Based on the adsorption and desorption data, oak ash performed as an excellent adsorbent for both Cu and As(V), a fact favored by its high pH and the presence of non-crystalline minerals and different oxides and carbonates. Overall, the results of this research can be relevant when designing strategies to prevent Cu and As(V) pollution affecting soils, waterbodies, and plants, and therefore have repercussions on public health and the environment.

Keywords: bio-adsorbents; heavy metals; soil pollution; release; retention

Citation: Cela-Dablanca, R.; Barreiro, A.; Ferreira-Coelho, G.; Campillo-Cora, C.; Pérez-Rodríguez, P.; Arias-Estévez, M.; Núñez-Delgado, A.; Álvarez-Rodríguez, E.; Fernández-Sanjurjo, M.J. Cu and As(V) Adsorption and Desorption on/from Different Soils and Bio-Adsorbents. *Materials* **2022**, *15*, 5023. https://doi.org/10.3390/ma15145023

Academic Editor: Teofil Jesionowski

Received: 2 June 2022
Accepted: 18 July 2022
Published: 19 July 2022

1. Introduction

The increasing spreading of metals and metalloids included in the group of the so-called "heavy metals" into the soil through fertilizers, manure/slurry, sewage sludge, irrigation with wastewater, pesticides, or mining and industrial activities has given rise to concerns about their impact on the environment in general and human health in particular [1–4]. These substances enter various environmental compartments (soil, water, and air), and affect different living beings (microbial, plant, and animal communities) and may have adverse effects on individual biological receptors and populations [5]. Their toxicity is affected by the difficulties of organisms to achieve their excretion, with a tendency to

bio-accumulate, and, even in cases where they do not have high concentrations in specific environments, they can reach harmful levels after passing through the food chain [6,7].

Arsenic is naturally present in certain minerals, but its presence as a pollutant in the environment can also be caused by certain human activities, such as mining, use of fossil fuels, pesticides, and herbicides. It is a semimetal or metalloid that can occur in inorganic form, with the As(III) species being the most frequent in reducing conditions, and As(V) in well-aerated media, while the organic forms (with As included in organic molecules) are quantitatively less important [8]. This element causes special concern due to its high toxicity, and it can be mobilized in the most frequent groundwater pH values, thus threatening drinking water resources [9]. It has associated chronic toxic effects, increasing the risks of developing cancers affecting the skin, lung, kidney, and liver [10,11]. Details regarding the effects of arsenic on toxicity and human health have been extensively documented in previous papers [12–16].

As regards Cu, it is an essential micronutrient for human beings and for plant development, but it is toxic when present at high concentrations [17,18]. It is less mobile than As, but high Cu concentrations can alter cell division in some plants, affect microbial activity, microorganism diversity, and soil ecosystem services [19–22], and cause damage to detritivore populations [23]. As regards the effects of Cu on human health, extensive reviews have been carried out in previous publications [24–27].

Soils can act as a sink for these pollutants and reduce their toxicity through adsorption, precipitation, or occlusion processes, mainly affected by soil organic matter, low crystallinity minerals, and acid–base and redox conditions [28,29].

The retention capacity of the soil can be an important factor in mitigating the toxic effects of these metals/metalloids, but, in the long term, soil adsorbent surfaces could be saturated, increasing the risk of passage to plants, water, and the food chain. To minimize this problem, different remediation strategies have been developed, mainly aimed at acting on the mobility of the pollutants [30], including the use of bio-adsorbent materials. In this regard, studies focusing on bio-adsorbents are of growing interest, as an efficient and low-cost alternative to retain the different contaminants present in soils and water. Generally, materials that are low cost and locally available in large quantities are considered a good choice to be assessed regarding their effectivity [31]. The food and agroforestry industries produce large amounts of waste and by-products, such as mussel shell, biomass combustion ash, and pine bark, which could be used for this purpose. Specifically, previous studies on pollutant retention onto biomass ash showed promising results in investigations focused on As [32,33] as well as on Cu [34,35].

In this view, the objective of this work is to study the retention of Cu and As(V) in cultivated soils with different characteristics, as well as the capacity of different by-products (oak ash, pine bark, and mussel shell) to immobilize these contaminants. The results of the research could be useful in program-appropriate practices to manage soils and low-cost by-products in order to reduce the risks of environmental contamination associated with the spreading of materials that contain both pollutants.

2. Materials and Methods

2.1. Soils and By-Products

For this research, six crop soils were selected, which were previously sampled at two areas of Galicia (NW Spain) subjected to intensive farming: S soils (sampled at Sarria, Lugo province) and AL soils (sampled at A-Limia, Ourense province). The samples were taken from the surface layer (0–20 cm), with each one being the result of combining 10 sub-samples collected in a zig-zag manner for each soil. These soils have been previously studied and described [36].

The forest by-products used in this study were oak ash from a local boiler at Lugo (Spain), pine bark (fraction less than 0.63 mm), a commercial product provided by Geolia (Madrid, Spain), and un-calcined mussel shell (<1 mm in diameter), supplied by Abonomar

S.L. (Illa de Arousa, Pontevedra province, Spain). A more complete description was previously published [37].

The methods used for the characterization of soils and by-products were the following: pH in water and 0.1 M KCl (soil:solution ratio 1:2.5), using a pH-meter (pH-model 2001 Crison, Spain); C and N by elemental analysis (CHNS Truspec, Leco, St. Joseph, MI, USA); available P by the Olsen method [38]; exchangeable cations, extracted with 1 M NH_4Cl [39] and quantified by atomic absorption/emission spectrometry; the effective cation exchange capacity (eCEC) was calculated as the sum of exchangeable Ca, Mg, Na, K, and Al; non-crystalline Al and Fe (Al_o, Fe_o) were extracted with ammonium oxalate acidified at pH 3. All determinations were performed in triplicate.

Tables 1 and 2 show the main characteristics of the soils and the three by-products used, respectively.

Table 1. Main characteristics of the six soils studied. Average values (n = 3) with coefficients of variation always lower than 5%.

Parameter	Units	Soil					
		3AL	19AL	50AL	6S	51S	71S
pH_{H2O}		4.74	4.80	4.49	6.33	7.06	6.24
pH_{KCl}		4.30	4.25	4.00	5.86	6.39	5.44
Ca_e	$cmol_c\ kg^{-1}$	2.24	1.53	5.94	12.86	9.89	12.79
Mg_e	$cmol_c\ kg^{-1}$	0.64	0.41	1.48	1.13	0.97	2.88
Na_e	$cmol_c\ kg^{-1}$	0.35	0.25	0.42	0.36	0.28	0.41
K_e	$cmol_c\ kg^{-1}$	1.00	1.27	1.14	0.61	1.40	1.20
Al_e	$cmol_c\ kg^{-1}$	1.68	0.61	2.66	0.00	0.01	0.11
eCEC	$cmol_c\ kg^{-1}$	5.92	4.08	11.64	14.96	12.54	17.38
Al saturation	%	28.43	15.00	22.83	0.00	0.05	0.06
P	$mg\ kg^{-1}$	117.90	225.43	135.90	71.42	120.03	96.77
N	%	0.31	0.09	0.84	0.23	0.19	0.48
C	%	3.39	1.07	10.92	1.98	1.75	6.88
OM	%	5.84	1.84	18.83	3.41	3.02	11.86
C/N		10.94	11.89	13.00	8.44	9.05	14.21
Sand	%	54.72	64.72	58.72	29.28	27.28	61.28
Silt	%	26.00	14.00	16.00	49.28	51.28	23.28
Clay	%	19.28	21.28	25.28	21.44	21.44	15.44
Al_o	$mg\ kg^{-1}$	5040.0	855.0	2995.0	18,377.5	15,755.7	50,593.5
Fe_o	$mg\ kg^{-1}$	2585.0	1150.0	1430.0	56,423.8	42377.4	73,095.9

Ca_e, Mg_e, Na_e, K_e, and Al_e = exchangeable concentrations of the elements; Al_o and Fe_o = Al and Fe concentration after extraction with ammonium oxalate.

Table 2. Main characteristics of the three by-products used. Average values (n = 3) with coefficients of variation always lower than 5%.

Parameter	Unit	Oak Ash	Pine Bark	Mussel Shell
C	%	13.23	48.70	11.43
N	%	0.22	0.08	0.21
C/N		60.13	608.75	55.65
pH_{H2O}		11.31	3.99	9.39
pH_{KCl}		13.48	3.42	9.04
Ca_e	$cmol_c\ kg^{-1}$	95.00	5.38	24.75
Mg_e	$cmol_c\ kg^{-1}$	3.26	2.70	0.72
Na_e	$cmol_c\ kg^{-1}$	12.17	0.46	4.37
K_e	$cmol_c\ kg^{-1}$	250.65	4.60	0.38
Al_e	$cmol_c\ kg^{-1}$	0.07	1.78	0.03
Al saturation	%	0.02	11.91	0.11
eCEC	$cmol_c\ kg^{-1}$	361.17	14.92	30.25
P-Olsen	$mg\ kg^{-1}$	462.83	70.45	54.17
Al_o	$mg\ kg^{-1}$	8323.00	315.00	178.33
Fe_o	$mg\ kg^{-1}$	4233.00	74.00	171.00

Ca_e, Mg_e, Na_e, K_e, and Al_e = exchangeable concentrations of the elements; Al_o and Fe_o = Al and Fe concentration after extraction with ammonium oxalate.

Table S1 (Supplementary Materials) shows data on BET surface areas for the six soils studied, evidencing that the values were higher for S soils. Of note, although higher surface area facilitates achieving higher adsorption of a variety of substances onto soils, other factors could be of even higher relevance, as previously stated for different pollutants [40].

In addition, Table S2 (Supplementary Materials) shows data on BET surface areas for the three by-products, evidencing that the highest value corresponded to oak ash (1.3336 $m^2\ g^{-1}$), followed by mussel shell (1.1318 $m^2\ g^{-1}$), and being much lower for pine bark (0.3320 $m^2\ g^{-1}$).

2.2. Adsorption and Desorption Experiments

To perform adsorption studies, batch-type experiments were carried out, stirring 1 g of each soil or by-product for 24 h with 40 mL of 0.005 M $CaCl_2$ and with different concentrations of Cu or As(V) (100, 200, 400, 800, and 1000 μmol L^{-1}), with each pollutant added individually. The solutions were prepared from analytical grade $Cu(NO_3)_2.3H_2O$ and Na_2HAsO_4 (Panreac, Barcelona, Spain). After 24 h of agitation, the samples were centrifuged (at 4000 rpm) and filtered. In the equilibrium solution, the dissolved organic carbon (DOC) was determined by means of UV-1201 spectroscopy (Shimadzu, Kyoto, Japan), the pH using a glass electrode (Crison, Madrid, Spain), and the concentrations of Cu or As using an ICP-MS equipment (Varian 820-NS, Palo Alto, CA, USA). The amount of Cu or As adsorbed was calculated by the difference between the added concentration and that remaining in the equilibrium solution.

Regarding desorption experiments, 40 mL of 0.005 M $CaCl_2$ was added to each of the samples used in the previous adsorption tests, then stirring for 24 h, centrifuging, filtering and quantifying Cu or As(V) in the equilibrium solution, following the same methodology indicated above.

2.3. Data Analysis and Statistical Treatment

The experimental adsorption data were checked as regards their fitting to the Freundlich (Equation (1)), Langmuir (Equation (2)), and Temkin (Equation (3)) models:

$$q_a = K_F C_{eq}^n \quad (1)$$

$$q_a = K_F C_{eq}^n \quad (2)$$

$$q_a = \beta \ln K_T + \beta \ln C_{eq} \quad (3)$$

where q_a is the amount of Cu or As(V) adsorbed in equilibrium (μmol kg^{-1}); C_{eq} is the concentration of Cu or As(V) present in the solution in the equilibrium (μmol L^{-1}); K_F is the Freundlich affinity parameter ($L^n\ \mu mol^{1-n}\ kg^{-1}$); n is the Freundlich linearity parameter (dimensionless); K_L is a Langmuir parameter related to the adsorption energy (L μmol^{-1}), and q_m is the Langmuir's maximum adsorption capacity (μmol kg^{-1}). In addition, β is calculated as RT/bt; bt is the Temkin isotherm constant; T is Temperature (K = 298°) (25 °C); R is the universal gas constant (8314 Pa m^3/mol K); and K_T is the Temkin isotherm equilibrium binding constant (L g^{-1}).

Desorption was expressed as the amount of Cu or As(V) desorbed (in μmol kg^{-1}, and also as percentage) with respect to the amount previously adsorbed.

The statistical software R version 3.1.3 and the *nlstools* package for R [41] were used to check the fittings to the adsorption models. The SPSS 15.0 software was used to carry out bivariate Pearson correlations between adsorption and desorption data and characteristics of the sorbent materials, and multiple linear regression analyses.

3. Results

3.1. Cu and As(V) Adsorption onto Soils

The adsorption curves for the soils and bio-adsorbents studied are shown in Figures 1 and 2, respectively.

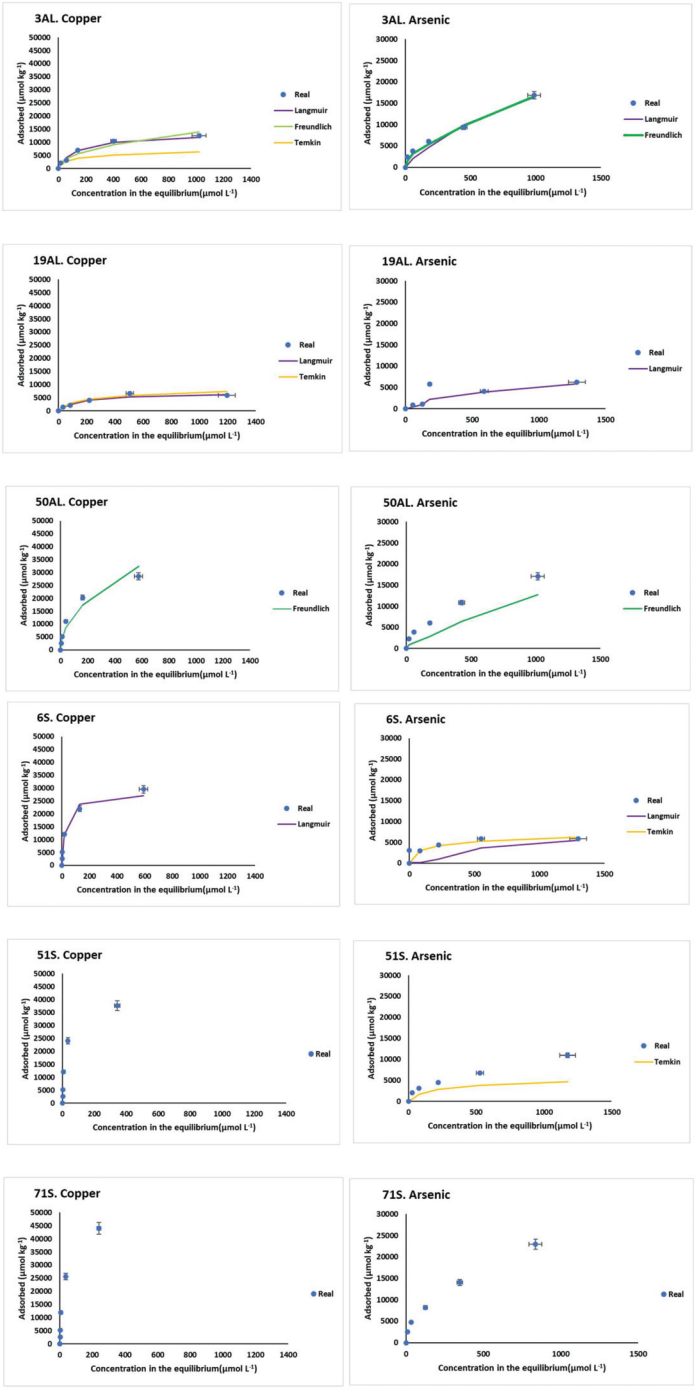

Figure 1. Cu and As(V) adsorption curves and selected graphical fittings to the various adsorption models for the six soils studied. Error bars represent twice the standard deviation of the mean (n = 3). When bars are not visible, they are smaller than the symbols.

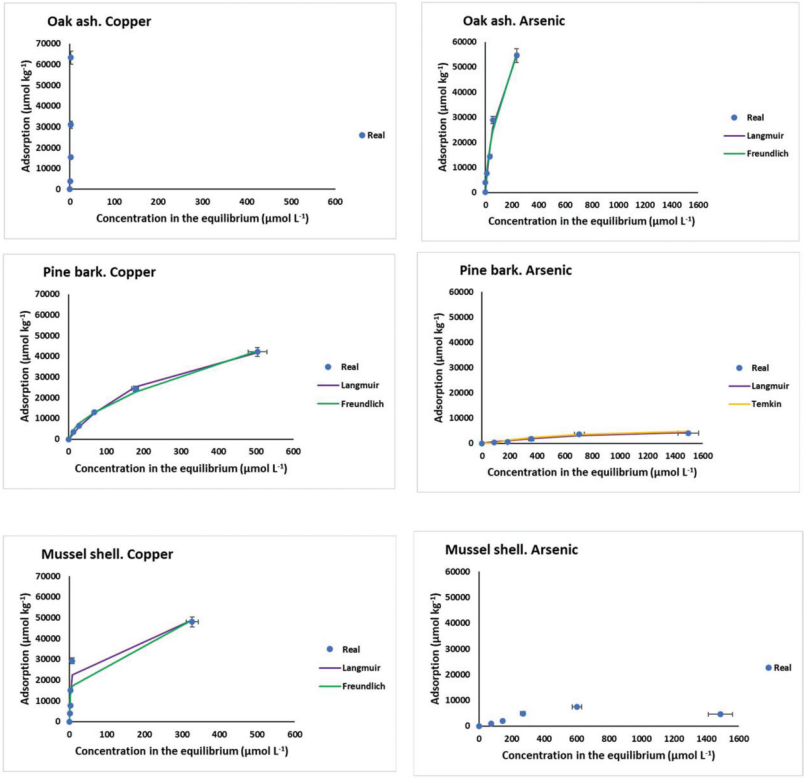

Figure 2. Cu and As adsorption curves and selected graphical fittings to the various adsorption models for the three bio-adsorbents studied. Error bars represent twice the standard deviation of the mean (n = 3). When bars are not visible, they are smaller than the symbols.

Figure 1 shows a variety of shapes in the adsorption curves, with differences between the AL and S soils. In fact, these curves show that overall Cu adsorption was higher for S soils (which have higher surface area) than for AL soils, while As(V) adsorption was similar for both kinds of soils.

Figure 2 shows that Cu and As(V) adsorption results were clearly higher for oak ash as compared to pine bark and mussel shell.

Figure 3 shows the results corresponding to Cu and As(V) adsorption onto the different soils (both in absolute value and percentage) as a function of the concentration added. Considering the absolute values, it is clear that the higher the Cu or As(V) concentrations added, the higher the adsorption for all soils, while the adsorbed percentage shows a decreasing trend. Adsorption was generally higher for Cu than for As, especially in S soils.

When the highest Cu or As(V) concentrations (1600 μmol L^{-1}) were added, Cu maximum adsorption values were reached in soils 51S and 71S (37,687 μmol kg^{-1} and 44,019 μmol kg^{-1}, respectively), while for As(V), the highest scores corresponded to soils 50AL and 71S (17,076 μmol kg^{-1} and 22,980 μmol kg^{-1}, respectively) (Figure 3). In contrast, the minimum Cu adsorption corresponded to soils 19AL and 3AL (5963 μmol kg^{-1} and 12,523 μmol kg^{-1}, respectively), while for As(V), the minima were for soils 19AL and 6S (6290 μmol kg^{-1} and 5868 μmol kg^{-1}, respectively).

Regarding percentage adsorption, within AL soils, the one with the highest organic matter content (soil 50AL, Table 1) adsorbed about 90% of Cu for the three lowest doses added, while this percentage dropped to 57% for the highest dose; however, for soil 19AL

(the one with the lowest organic matter content), Cu adsorption never exceeded 56%, being less than 12% for the highest dose. The progressive decrease in the adsorption rate affecting these three AL soils could be related to a saturation of the adsorption sites, many of which would be functional groups in organic compounds, and that decrease would be more pronounced for those soils with a lower organic matter content. In S soils, the adsorption was close to 100% for the three lowest doses of Cu added, decreasing to 82% in the soil with the highest organic matter content (soil 71S) and to 56% in soil 6S when the maximum Cu dose was added, again due to the saturation of the functional groups involved in adsorption, many of which lie in organic matter.

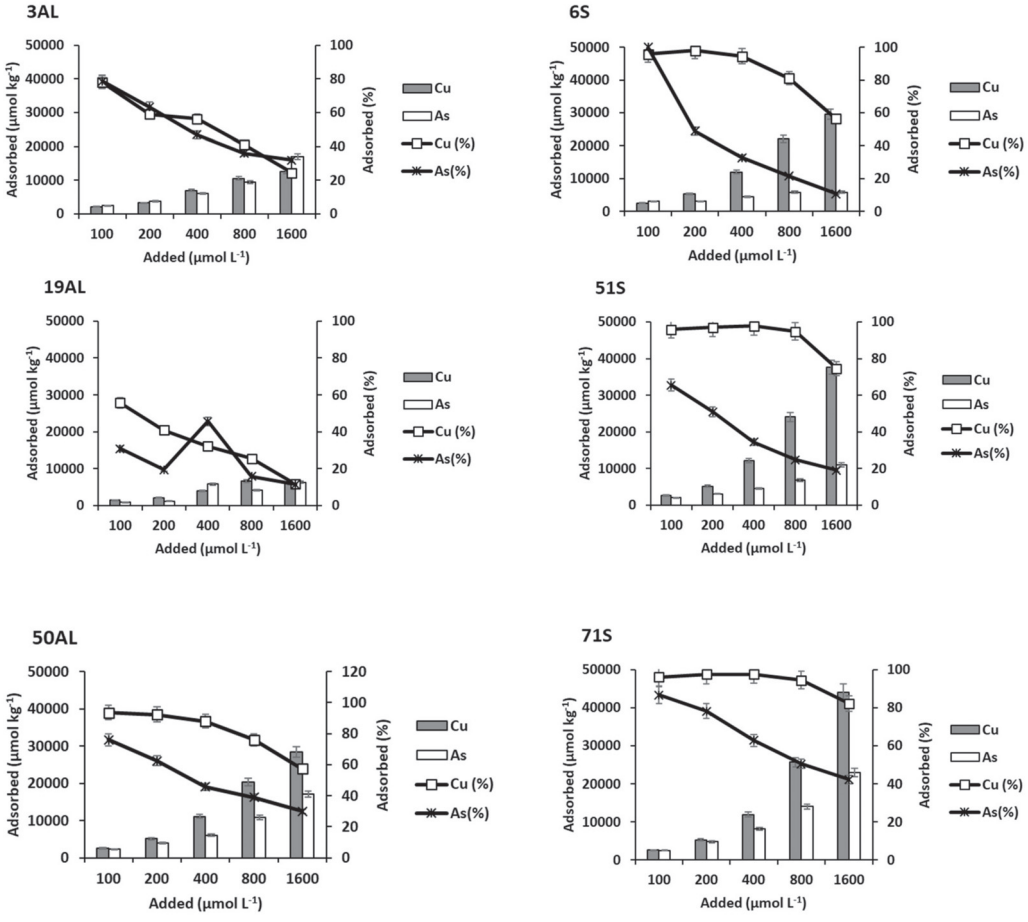

Figure 3. Cu and As (V) adsorption, expressed in μmol kg^{-1} and as percentage, for the soils studied, as a function of the pollutant concentrations added. Error bars represent twice the standard deviation of the mean (n = 3). When bars are not visible, they are smaller than the symbols.

Table 3 shows data corresponding to Cu and As(V) adsorption for the various initial concentrations added of both pollutants to the soils studied, in parallel to data corresponding to pH and DOC values in the equilibrium solution.

3.2. Cu and As(V) Desorption from Soils

Figure 4 shows the amounts of Cu and As(V) desorbed from the soils as a function of the concentrations added. As the added dose of each element increased, both the amount

and the percentage desorbed were higher. All AL soils had a similar desorption of both elements, while S-zone soils (with higher pH) desorbed much more As than Cu (Figure 4).

Table 3. Values of Cu and As(V) adsorption (Q) as well of pH and DOC in the equilibrium solution for the various Cu and As(V) initial concentrations (C_0) added to the soils.

		Cu			As(V)		
Soil	**C_0 μmol L^{-1}**	**Q μmol kg^{-1}**	**pH**	**DOC mg L^{-1}**	**Q μmol kg^{-1}**	**pH**	**DOC mg L^{-1}**
3AL	0.00	0.00	4.75	0.08	0.00	4.76	0.19
	100	2127.04	4.64	0.20	2394.39	4.78	0.19
	200	3225.97	4.46	0.13	3764.03	4.97	0.23
	400	6951.04	4.43	0.13	6037.21	5.17	0.16
	800	10,467.99	4.25	0.12	9344.48	5.37	0.17
	1600	12,523.80	4.10	0.10	16,882.19	5.92	0.16
19AL	0.00	0.00	4.71	0.20	0.00	5.00	0.08
	100	1433.70	4.57	0.13	888.39	5.19	0.14
	200	2088.81	4.45	0.19	1153.99	5.33	0.21
	400	3969.43	4.34	0.29	5778.18	5.74	0.09
	800	6659.33	4.27	0.17	4126.55	6.11	0.12
	1600	5963.30	4.07	0.28	6290.39	6.60	0.09
50AL	0.00	0.00	4.27	0.26	0.00	4.50	0.13
	100	2524.26	4.24	0.19	2272.59	4.37	0.18
	200	5106.61	4.13	0.26	3939.78	4.38	0.20
	400	11,086.25	4.03	0.28	6058.32	4.45	0.28
	800	20,244.49	3.79	0.34	10,856.87	4.66	0.23
	1600	28,481.45	3.69	0.23	17,075.78	4.89	0.22
6S	0.00	0.00	5.61	0.20	0.00	5.88	0.19
	100	2558.33	5.66	0.19	3048.25	5.87	0.12
	200	5253.62	6.26	0.13	3015.26	6.33	0.08
	400	12,030.50	5.57	0.15	4393.79	6.44	0.09
	800	22,000.77	5.07	0.13	5849.58	6.73	0.09
	1600	29,540.60	4.75	0.17	5866.52	6.88	0.06
51S	0.00	0.00	6.04	0.16	0.00	6.61	0.15
	100	2615.99	6.09	0.18	2016.28	6.80	0.14
	200	5202.90	6.06	0.19	3091.30	6.83	0.12
	400	12,205.87	5.93	0.14	4485.69	6.85	0.09
	800	24,061.91	5.55	0.13	6775.33	6.96	0.12
	1600	37,687.91	5.09	0.11	10,962.17	7.18	0.08
71S	0.00	0.00	5.49	0.29	0.00	6.00	0.11
	100	2618.82	5.53	0.20	2516.39	5.85	0.09
	200	5282.88	5.49	0.19	4786.28	5.84	0.13
	400	11,962.35	5.36	0.16	8174.64	5.84	0.14
	800	25,655.79	5.13	0.18	14,047.81	5.92	0.13
	1600	44,019.57	4.69	0.15	22,979.85	6.07	0.13

In relation to Cu, desorption was much higher from AL soils than from S soils (the latter having a higher surface area). The maximum percentage values for AL soils were between 39% of the soil with less organic matter (19AL) and 12% of the one containing most organic matter (soil 50AL), while the range for the S zone was narrower: between 15% (soil 6S) and 5% (soils 51S and 71S). In general, soils with low desorption values match those with high adsorption scores.

3.3. Cu and As(V) Adsorption onto the Three By-Products

Figure 5 shows Cu and As(V) adsorption onto the three by-products as a function of the concentration added. Adsorption was always much higher for Cu than for As(V), especially for pine bark and mussel shell, while for oak ash, the differences were clearly smaller, although becoming more evident as the added dose increased.

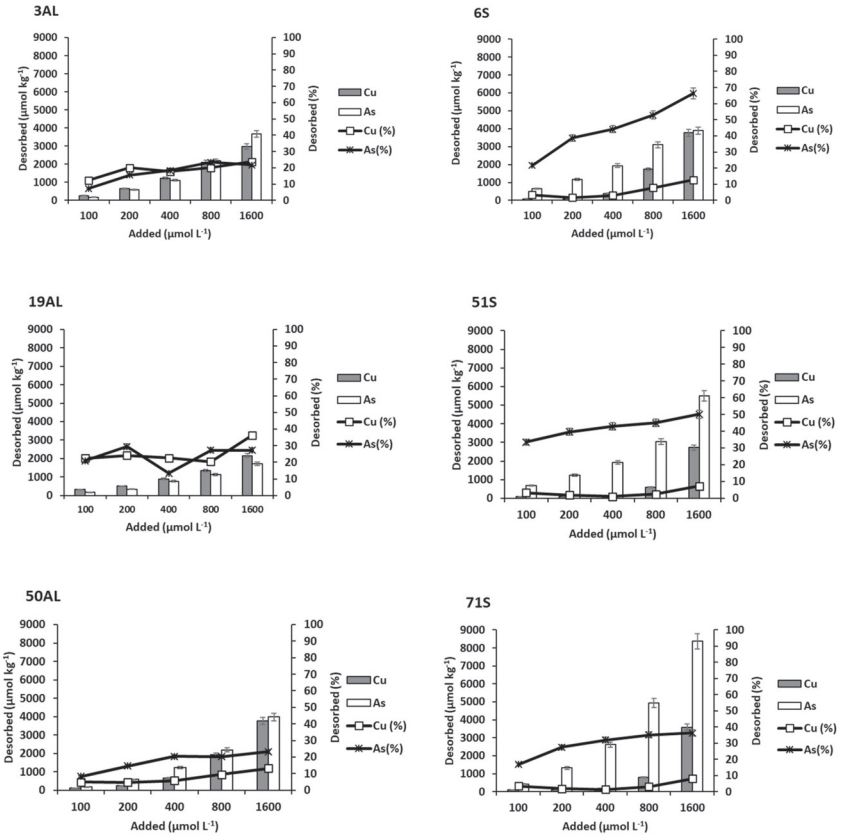

Figure 4. Cu and As (V) desorption, expressed in μmol kg^{-1} and as percentage, for the soils studied, as a function of the pollutant concentrations added. Error bars represent twice the standard deviation of the mean (n = 3). When bars are not visible, they are smaller than the symbols.

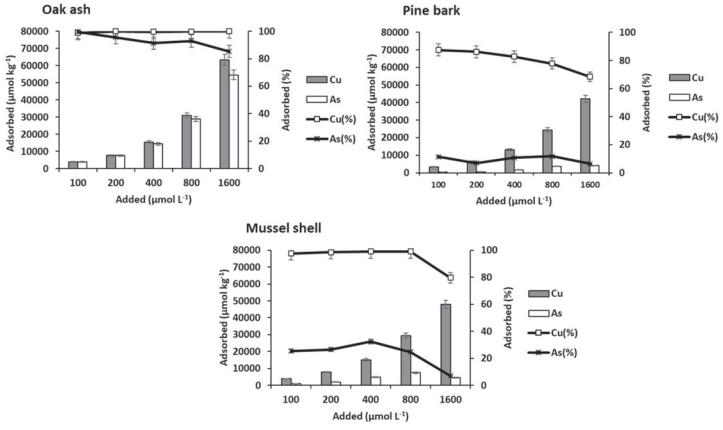

Figure 5. Cu and As (V) adsorption, expressed in μmol kg^{-1} and as percentage, for the three bio-adsorbents studied, as a function of the pollutant concentrations added. Error bars represent twice the standard deviation of the mean (n = 3). When bars are not visible, they are smaller than the symbols.

In relation to Cu, its adsorption increased in all cases as a function of the concentration of Cu added. At high doses of the pollutants, the differences among the by-products were more apparent, with the highest adsorption corresponding to oak ash, followed by mussel shell and pine bark. Mussel shell and especially oak ash have a pH clearly higher than that of pine bark (Table 2), which may influence the different adsorption on the three by-products. As the pH increases, the negative charge in the variable charge colloids rises, favoring cationic retention, as mentioned above for soils. In this sense, non-crystalline minerals, which provide a high variable charge, were much more abundant in oak ash than in mussel shell, which could explain why oak ash adsorbed more Cu.

3.4. Cu and As(V) Desorption from the Three By-Products

Figure 6 shows data corresponding to Cu and As(V) desorption from oak ash, pine bark, and mussel shell. For Cu, the desorption sequence was: pine bark > mussel shell ≥ oak ash (inverse to that of adsorption). Cu desorption was low from oak ash and mussel shell, with the maximum desorption value being 30.5 μmol kg^{-1} for oak ash and 70.16 μmol kg^{-1} for mussel shell. For pine bark, desorption rose remarkably when increasing the concentration of added Cu, with the minimum value being 246.66 μmol kg^{-1} and the maximum reaching 6188.55 μmol kg^{-1}. This by-product has a very high concentration of organic C, clearly higher than those of oak ash and mussel shell, with organic matter being responsible for retaining much of the Cu added.

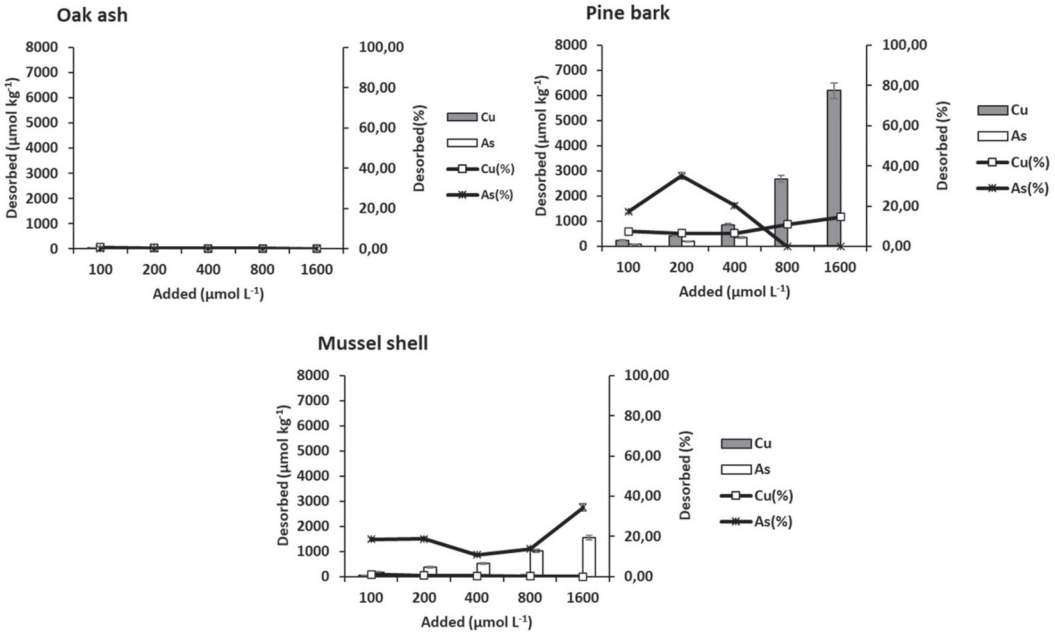

Figure 6. Cu and As (V) desorption, expressed in μmol kg^{-1} and as percentage, for the three bio-adsorbents studied, as a function of the pollutant concentrations added. Error bars represent twice the standard deviation of the mean (n = 3). When bars are not visible, they are smaller than the symbols.

3.5. Fitting of Cu and As(V) Experimental Data to Different Adsorption Models

Cu and As(V) adsorption can be partially fitted to the Langmuir (Table 4), Freundlich (Table 5), and Temkin (Table 6) models. The three models for both elements have R^2 values ranging between 0.784 and 0.999 for Langmuir, 0.845–0.999 for Freundlich, and 0.732–0.999 for Temkin.

Table 4. Fitting to the Langmuir model of experimental data corresponding to Cu and As(V) adsorption onto the soils and bio-adsorbents used.

Soil/Bio-Adsorbent		Langmuir Parameter				
		q_m (μmol kg^{-1})	Error-1	K_L (L μmol^{-1})	Error-2	R^2
3AL	Cu	13,400.09	3292.03	0.0075	0.003	0.935
	As(V)	27,759.87	9142.35	0.0014	0.0009	0.967
19AL	Cu	7020.96	1227.60	0.0065	0.003	0.958
	As(V)	9102.93	6017.42	0.0015	0.006	0.837
50AL	Cu	27,463.77	2525.40	0.021	0.003	0.992
	As(V)	25,379.96	4566.65	0.002	0.001	0.985
6S	Cu	28,242.77	6241.05	0.041	0.015	0.945
	As(V)	6457.63	295.59	0.010	0.002	0.992
51S	Cu	44,100.55	11,594.77	0.028	0.010	0.950
	As(V)	14,417.56	3161.04	0.002	0.001	0.962
71S	Cu	49,174.35	2524.46	0.033	0.005	0.996
	As(V)	32,341.86	6030.63	0.003	0.001	0.982
Oak ash	Cu	-	-	-	-	-
	As(V)	83,740.12	13,748.45	0.008	0.003	0.987
Pine bark	Cu	65,560.70	3016.86	0.0035	0.0003	0.999
	As(V)	7298.80	2723.54	0.0010	0.0007	0.958
Mussel shell	Cu	50,467.87	6290.40	0.1021	0.0364	0.959
	As(V)	6925.85	2393.08	-	-	0.784

q_m: maximum adsorption capacity; K_L: constant related to the intensity of interaction adsorbent/adsorbate; R^2: coefficient of determination; -: error too high for fitting.

Table 5. Fitting to the Freundlich model of experimental data corresponding to Cu and As(V) adsorption onto the soils and bio-adsorbents used.

Soil/Bio-Adsorbent		Freundlich Parameter				
		K_F (L^n μmol^{1-n} kg^{-1})	Error-1	n	Error-2	R^2
3AL	Cu	605.97	161.97	0.453	0.051	0.970
	As(V)	317.97	123.29	0.571	0.059	0.991
19AL	Cu	-	-	0.354	0.114	0.902
	As(V)	-	-	-	-	-
50AL	Cu	1420.25	290.32	0.492	0.047	0.969
	As(V)	396.35	71.49	0.546	0.028	0.997
6S	Cu	4334.21	1250.35	0.308	0.051	0.975
	As(V)	1302.36	548.87	0.219	0.066	0.938
51S	Cu	2042.58	750.21	0.527	0.103	0.845
	As(V)	332.74	77.00	0.491	0.035	0.996
71S	Cu	4695.40	1535.83	0.413	0.065	0.977
	As(V)	679.50	74.58	0.522	0.017	0.999
Oak ash	Cu	-	-	-	-	-
	As(V)	2481.83	963.55	0.568	0.076	0.986
Pine bark	Cu	1013.92	204.18	0.601	0.0342	0.997
	As(V)	-	-	0.649	0.1843	0.933
Mussel shell	Cu	9586.92	4114.71	0.282	0.084	0.899
	As(V)	-	-	-	-	-

K_F: parameter related to the adsorption capacity; n: parameter related to adsorbent heterogeneity; R^2: coefficient of determination; -: error too high for fitting.

Table 6. Fitting to the Temkin model of experimental data corresponding to Cu and As(V) adsorption onto the soils and bio-adsorbents used.

Soil/Bio-Adsorbent		Temkin Parameters				
		bt	**Error-1**	**K_t (L/g)**	**Error-2**	**R^2**
3AL	Cu	1249.03	329.44	0.16	0.08	0.915
	As(V)	-	-	-	-	-
19AL	Cu	1667.41	318.40	0.07	0.05	0.947
	As(V)	1574.12	721.31	-	-	0.764
50AL	Cu	-	-	0.38	0.058	0.979
	As(V)	-	-	0.06	0.034	0.941
6S	Cu	-	-	0.63	0.12	0.946
	As(V)	1163.51	187.13	0.17	0.10	0.975
51S	Cu	-	-	0.49	0.028	0.988
	As(V)	1111.30	457.70	0.06	0.034	0.942
71S	Cu	272.31	174.11	0.50	0.03	0.999
	As(V)	-	-	0.10	0.06	0.944
Oak ash	Cu	-	-	-	-	-
	As(V)	-	-	-	-	-
Pine bark	Cu	-	-	0.08	0.02	0.970
	As(V)	1690.37	258.54	0.01	0.00	0.956
Mussel shell	Cu	-	-	-	-	-
	As(V)	1565.52	849.08	-	-	0.732

bt: Temkin isotherm constant; *Kt*: Temkin isotherm equilibrium binding constant; R^2: coefficient of determination.

4. Discussion

4.1. Cu and As(V) Adsorption onto Soils

The influence of organic groups on Cu adsorption shown in the current research has already been pointed out by other authors [42], and, in the current study, it is supported by the significant and positive correlation obtained between Cu adsorption (when the maximum dose is added) and soil organic matter content ($r = 0.53$, $p < 0.05$). However, there are other factors that influence adsorption, as indicated by the fact that both the amount and the percentage of Cu adsorbed were always higher in S soils (which are those that have higher pH values, as well as a higher surface area) compared to AL soils. This would indicate that adsorption is a pH-dependent process and is related to the influence of this parameter on the solubility of metal ions and also on the ionization state of functional groups of adsorbent surfaces (variable charge components) [43,44]. In this sense, soils with a higher pH have more negative charges in the variable charge components, mainly in organic matter, but also in non-crystalline components, which are also much more abundant in S soils (Table 1).

The effect of non-crystalline Fe and Al minerals on Cu adsorption has been reported by several authors [45,46] and attributed to Cu-specific complexation and adsorption reactions onto non-crystalline oxy-hydroxides. Supporting the latter, in the present study, a significant ($p < 0.05$) and positive correlation was obtained between Cu adsorption and Fe_o ($r = 0.812$), and also with the sum of Fe_o and Al_o ($r = 0.819$), parameters that estimate the content of non-crystalline minerals. A significant and positive correlation was also found between Cu adsorption and eCEC ($p < 0.01$, $r = 0.946$). In addition, performing a successive steps regression, it was obtained that eCEC (in which organic matter and non-crystalline minerals are of great importance) explains 87% of Cu adsorption. This clear influence of eCEC is indicative of the importance of charges present in soil colloids for adsorption. It is also worth noting the decrease in pH in the equilibrium solution as the adsorption of Cu increases (Table 3), finding a significant and negative correlation between both parameters, with $p < 0.01$ for soils 51S ($r = -0.99$), 71S ($r = -0.99$), and 19AL ($r = -0.96$), and with

$p < 0.05$ for soils 3AL ($r = -0.94$), 50AL ($r = -0.96$), and 6S ($r = -0.897$), which could be related to the proton exchange taking place in the Cu adsorption process.

Regarding As(V), differences in adsorption were no so clear for S and AL soils (Figure 3). This would indicate that soil pH does not have such an obvious effect on As adsorption, compared to Cu. Several authors indicate that As(V) can be adsorbed over a wide range of pH. Specifically, Stanić et al. [47], using zeolite as adsorbent, reported a range between 4.0 and 11.0, and Mamindy-Pajany et al. [48] found 100% adsorption for As on hematite in a pH range between 2 and 11. However, other authors have reported ranges not as wide, such as 6–8 for alumina impregnated with La^{3+} and Y^{3+}, or a range of 2–4 for molybdenum-impregnated chitosan [49,50]. Recently, Yusof et al. [51] reported a range of 3–7 using palm oil combustion ash. It should be noted that, under oxidizing conditions and at a low pH, arsenate is dominant, mainly as $H_2AsO_4^-$, while as the pH increases the predominant species would be $HAsO_4^{2-}$ [52–54]. In acid soils, such as those in the AL zone of the current study, the $H_2AsO_4^-$ species would be adsorbed on variable-charge colloids, which would be positively charged due to protonation taking place at that low pH prevailing, and then adsorption could take place by means of electrostatic attraction. Within these colloids would be non-crystalline minerals [53], which are more abundant in soils 3AL and 50AL compared to 19AL, coinciding with the highest adsorption taking place in the former (Table 1 and Figure 3). Several authors have found that arsenates are strongly adsorbed to these kinds of Al (and especially Fe) compounds, and the adsorbed amounts can be significant even with low concentrations of As present in the liquid phase [55,56]. In the current study, the zone S soils have high concentrations of non-crystalline minerals of Fe and Al compounds (mainly oxy-hydroxide), and, although these soils have higher pH values than those of zone AL, it is below the pH of the zero point of charge (zpc) of these minerals (between 8.7 and 9.1) [57], with which these colloids would be positively charged, and adsorption could also occur by electrostatic attraction. Other colloids would present a negative charge at pH around 6, as would happen with soil organic matter. In these cases, adsorption can be performed through a cationic bridge and/or by ligand exchange. In relation to the latter, significant and positive correlations were found between the pH in the equilibrium solution and As adsorption in soils 3AL, 50AL, and 51S ($r = 0.987$, 0.992, and 0.997, respectively, $p < 0.01$) and in soil 71S ($r = 0.978$, $p < 0.05$) (Table 3). This increase in the equilibrium pH in the adsorption process is in line with findings previously reported [53,58], which would be justified by an exchange of ligands between the species $H_2AsO_4^-$ or $HAsO_4^{2-}$ and OH^- groups, which are released in the solution.

In addition, the influence of organic matter on the adsorption of As is also present. In the S zone, adsorption was higher in the soil with the highest organic matter content (soil 71S), compared with the other two (soils 51S and 6S). However, this influence is not as obvious as for Cu, since both 50AL and 3AL soils (with very different concentrations of organic C, Table 1) have a similar As adsorption capacity (Figure 1). As mentioned above, expressing As(V) adsorption as a percentage (Figure 3), a decrease is observed when the concentration added rises, which is due to the afore-mentioned saturation of the adsorbent surfaces. In AL soils, the As(V) adsorption percentage dropped from 75–80% to 30% (for soils 3AL and 50AL), and from 30–40% to 11% for the one with less organic matter content (19AL). In S soils, the largest decrease in the As(V) adsorption percentage, due to the rise in the concentration added, took place for soil 6S (from 100% to 10%).

4.2. Cu and As(V) Desorption from Soils

It should be borne in mind that different soil factors can influence the desorption of metals and metalloids. Several authors highlight the influence of pH on the desorption of heavy metals from soils [59,60], since, with increasing pH, Cu desorption would decrease linearly, which in the present study could explain, in part, the differences observed between the soils of the two zones. Liang et al. [61], studying Cu desorption in rice-growing soils, attributed the decrease in desorption to the rise in soil eCEC, and this influence of eCEC was again pointed out by Zhanget al. [62]. This coincides with that obtained for the soils of

the present study, since those with higher eCEC (S Soils) (Table 1) are those that desorbed less Cu (Figure 4).

Regarding As(V) (Figure 4), the high desorption taking place for all S soils (which are in the range of 3800–8400 μmol kg^{-1} for the maximum dose added) contrasts with the lower desorption found for AL soils (between 424 and 676 μmol kg^{-1}). This represents a percentage of desorption that did not exceed 40% in the AL zone, while in the S zone, the desorbed proportion reached maxima between 40 and 67%. Again, the soils showing the highest As desorption are those that adsorbed the least (Figures 3 and 4). By conducting a bivariate correlation study to find out how different soil parameters influence As(V) desorption, a significant ($p < 0.05$) and positive correlation was obtained with soil pH (r = 0.837) and non-crystalline Fe and Al compounds (r = 0.848). There is also a significant ($p < 0.05$), but negative (r = −0.875), correlation with the available phosphorus content. These results support the importance of pH in the desorption processes. As the pH increases, the positive charges on the colloidal surfaces (including those of the non-crystalline Fe and Al compounds) become negative, hindering the adsorption of As(V) in anionic form, causing the bonds to be more labile, while the opposite happens when acidity increases. This would explain the greater desorption of As(V) from S soils, with higher pH. A negative correlation with available P could indicate that arsenate ions compete with phosphate ions (which are often found bound to non-crystalline Fe and Al compounds with different adsorption energies), resulting in an increase in available P and an adsorption of As(V) with different holding forces. Results similar to these were found by Rahman et al. [63] studying the adsorption and release of As in contaminated soils, observing higher As(V) release as the pH increased, attributing it to electrostatic repulsion. These authors also pointed to the strong competition of arsenate with phosphate, which is much higher than with sulfate.

4.3. Cu and As(V) Adsorption onto the Three By-Products

According to Boim et al. [64], the decrease in Cu mobility as pH increases is due to the formation of insoluble complexes, and they also highlight the importance of non-crystalline Fe and Al oxy-hydroxides in the adsorption of Cu^{2+}. In a study carried out on vineyard soils amended with mussel shell [65], a decrease in the available Cu was observed, which was related to the increase in soil pH, although it could also be affected by the direct adsorption of Cu onto the added mussel shell [66]. Pine bark, the most acidic material among the three by-products, has abundant organic matter with different functional groups, some of which may have a negative charge even at pH values < 3 [67], which would explain the adsorption values of Cu being just slightly lower than those corresponding to mussel shell. These reactive functional groups present in pine bark are progressively saturated as the added Cu dose rises, as indicated by the decrease in the percentage of Cu adsorbed (decreasing from 87% to 68%) (Figure 5).

In contrast, oak ash and mussel shell adsorbed 100% of the amounts of contaminants added, except for the highest dose, where adsorption decreased to 79% for mussel shell. Furthermore, Table 7 shows that pH in the equilibrium solution decreased with the increasing concentration of adsorbed Cu, as mentioned for soils, obtaining a significant and negative correlation between both parameters, with r = −0.964 ($p < 0.01$) for oak ash and r = −0.840 ($p < 0.05$) for mussel shell. Šoštarić et al. [68] also found a decrease in pH after the adsorption of different metals onto apricot peels, which was caused by the release of H^+ due to strong competition with cationic metals, suggesting the intervention of ion exchange processes.

Table 7 also shows that, regarding the values of dissolved organic carbon (DOC), they tend to decrease for oak ash and pine bark when Cu adsorption rises. In fact, for pine bark, a significant negative correlation is obtained between DOC and adsorption (r = −0.844 and $p < 0.05$). This could be related to the high affinity between Cu and organic matter, forming organometallic complexes, which could move to the solid phase [69], this being another mechanism for Cu retention.

Table 7. Values of Cu and As(V) adsorption (Q, in μmol kg^{-1}) as well of of pH and DOC (in mg L^{-1}) in the equilibrium solution for the various Cu and As(V) initial concentrations (C_0, in μmol L^{-1}) added to the three by-products.

		Cu			As(V)		
Sorbent	**C_0**	**Q**	**pH**	**DOC**	**Q**	**pH**	**DOC**
Oak ash	0.00	0.00	12.21	0.37	0.00	11.99	0.40
	100	3953.65	12.19	0.42	3945.07	12.00	0.40
	200	7619.05	12.22	0.45	7639.94	12.05	0.41
	400	15,455.80	12.18	0.36	14,451.22	12.09	0.82
	800	31,008.12	12.16	0.36	28,892.20	12.05	0.49
	1600	63,284.57	12.09	0.33	54,610.45	11.96	0.50
Pine bark	0.00	0.00	4.58	0.526	0.00	5.94	0.28
	100	3300.95	3.91	0.46	442.89	5.69	0.31
	200	6564.22	3.9	0.52	556.30	5.63	0.33
	400	13,112.66	3.82	0.43	1725.85	5.45	0.34
	800	24,405.27	3.77	0.44	3669.51	5.47	0.37
	1600	42,152.96	3.61	0.39	4036.64	5.17	0.30
Mussel shell	0.00	0.00	7.44	0.12	0.00	7.05	0.08
	100	3903.02	7.50	0.16	1003.36	7.63	0.24
	200	7797.85	7.53	0.18	2025.12	7.90	0.16
	400	15,088.63	7.50	0.18	4889.31	8.13	0.19
	800	29,335.28	7.42	0.19	7427.29	8.20	0.16
	1600	48,033.56	6.18	0.15	4515.32	8.33	0.11

Regarding As(V), Figure 5 shows that oak ash is also the material with the highest adsorption, which increases as the concentration added rises. As(V) adsorption is much lower on mussel shell, and especially on pine bark. Given the high pH values corresponding to oak ash and mussel shell (Table 2), the predominant As species will be $HAsO_4^{2-}$ [52], and non-crystalline components will be negatively charged, meaning that the bond between the anionic As and these surfaces could take place by means of a cationic bridge. Oak ash contains, in addition to carbonates, oxides of Ca, Fe, and other elements, and these oxides would contribute to As(V) adsorption either by physical mechanisms or by chemical reactions [63]. As discussed above, the presence of a high concentration of oxalate-extractable Al and Fe (non-crystalline Fe and Al compounds) (Table 2) could also explain the high adsorption taking place on oak ash.

A variety of authors have found that arsenates are strongly adsorbed to these compounds (especially to non-crystalline Fe), and the amounts adsorbed can be relevant, even when low As concentrations are present in the liquid phase [55,56]. Furthermore, for oak ash and pine bark, the pH of the equilibrium solution shows a tendency to decrease as As(V) adsorption rises (Table 7), while pH increases in the case of mussel shell, with no significant correlation for any of the three by-products. Several studies have reported an increase in the equilibrium pH for As(V) adsorption due to exchange with OH^- groups, as explained above. The fact that in some cases this does not occur would indicate that other anions (SO_4^{2-}, PO_4^{3-}, or organic anions) are released, or that other mechanisms are involved in As adsorption, such as adsorption on calcite and Van der Waals forces, where OH^- groups are not released [70].

The good results regarding the retention of both pollutants in oak ash could also be reltated to its higher BET surface area (Table S1, Supplementary Materials), as previously pointed out for tetracycline antibiotics using the same three bio-adsorbents [71].

Other authors carried out studies using low-cost sorbents including ash, but some of them were clearly different materials compared to the oak ash used in the current work. As an example, Tsang et al. [72] found good results for coal fly ash as regards As stabilisation, although not successful for Cu retention. Mitchell et al. [73] found a reduction in soluble As and Cu by means of cementitious aggregation of wood ashes, although the authors indicate

that the extent is metal(loid)-specific when amended to soils. Park et al. [74] studied fly and bottom ash from wood pellet thermal power plants, finding that these by-products have a high potential for heavy metal removal, although the authors focused specifically on Cd. In addition, the quality of the bio-adsorbents is relevant, as shown by Lucchini et al. [75] working with ash derived from Cu-based preservative-treated wood, where the authors reported that these by-products can lead to extremely high Cu concentrations in soil and negatively affect plant growth.

In view of the layout of some of the isotherm graphs, it could be considered that the concentrations of some of the sorbents and/or the concentration range of the sorbates were not optimal, influencing the accuracy of the fitting of various models. In this regard, we have published previous papers dealing with these and other aspects related to Cu and As adsorption/desorption studies, using similar values to those of the current work for molar concentrations of these pollutants, which facilitates the easier comparison of retention efficacy, although other concentrations and ranges would be cleary interesting for future investigation, to shed further and more specific light on the overall processes. As examples, the references [76–78] correspond to some of these papers.

4.4. Cu and As(V) Desorption from the Three By-Products

According to [79], Cu binds to OC occupying high-affinity sites when Cu activity is low, but if that activity increases, Cu would also occupy low-affinity sites, which would facilitate desorption, and this could explain the obvious increase in desorption taking place only in pine bark as the concentration of Cu added rises. In relation to the percentage desorbed (Figure 6), a gradual increase is observed for pine bark as the dose of Cu added rises, reaching a maximum value of 15%. For oak ash and mussel shell, desorption rates were very low, not exceeding 2% in any case.

Regarding As(V), the desorption sequence was: mussel shell $\geq$ pine bark> oak ash. For mussel shell, As(V) desorption increases as the added concentration rises (Figure 6), ranging from 186.25 to 1556.26 μmol kg^{-1}, which corresponds to a value of 34% as maximum desorption. For pine bark, desorption reaches 35%, while for oak ash As(V) desorption was practically zero, probably due to the strong adsorption taking place at its high pH values, especially adsorption on the Fe and Al oxy-hydroxides very abundant in this by-product (Table 2), as indicated above. This shows the excellent adsorption capacity of oak ash for both Cu and As(V).

4.5. Fitting of Cu and As(V) Experimental Data to Different Adsorption Models

Table 4 shows that the Langmuir q_m parameter, related to adsorption capacity, is generally higher for Cu than for As(V), and for soils and by-products having higher pH values. In addition, among the most acidic soils and sorbents, q_m is higher for those with higher organic matter content, which will be the ones requiring higher concentrations of these elements to become saturated [80]. The q_m values obtained for Cu are significantly correlated with the N content (r = 0.838, $p < 0.01$), N being related to organic matter, which corroborates the role of organic substances in Cu adsorption. Regarding As(V), q_m values are significantly and positively correlated with the cation exchange capacity (r = 0.905), Ca (r = 0.864), K (r = 0.913), and pH_{KCl} (r = 0.71), which could suggest that the As adsorbed is in anionic form, with adsorption taking place through a cationic bridge on the negatively charged components of variable charge (mainly organic matter and non-crystalline minerals).

As regards the Langmuir K_L parameter, its value was higher for Cu than for As(V), which suggests a higher adsorption energy for Cu [81]. K_L is significantly and positively correlated with pH in water (r = 0.95, $p < 0.01$, for Cu, and r= 0.74, $p < 0.05$, for As), indicating an increase in the retention energy with increasing negative soil charge.

The values of the Freundlich parameter K_F parameter, related to the multilayer adsorption capacity of a given adsorbent [82], were also much higher for Cu than for As(V) (Table 5). In general, the highest K_F values were found in those soils and by-

products having higher pH, with a significant correlation ($p < 0.01$) between K_F and pH_{H2O} (r = 0.941 and 0.85 for Cu and As, respectively) and also between K_F and a parameter closely related to soil pH, especially in soils with variable charge, which is eCEC (r = 0.89 and 0.88 for Cu and As, respectively). The *n* Freundlich parameter indicates the reactivity and heterogeneity of the active sites of the adsorbent, with Table 5 showing that the *n* value is always lower than 1 (specifically, it varies between 0.219 and 0.649), except for Cu adsorption on oak ash. This indicates the existence of non-linear and concave adsorption curves, with heterogeneous adsorption surfaces, which leads to a decrease in adsorption sites as the added metal/metalloid concentration increases [83], which coincides with the decrease in the adsorbed percentage as the dose of Cu and As added increases.

Temkin's model is related to the adsorption energy and is characterized by a uniform distribution of binding energies up to a maximum level [84]. It is also assumed that this energy decreases linearly with surface coverage due to adsorbent–adsorbate interactions. The Temkin parameters in the current study show R^2 values generally >0.80. According to [85], values of the Temkin constant (*bt*) lower than 20 KJ mol^{-1} would indicate the existence of physical adsorption processes. Table 4 shows that, in general, *bt* values are always higher, which would justify the presence of chemisorption reactions [84]. According to [86], these high *bt* values would indicate a high degree of interaction between both pollutants (As and Cu) and the adsorbents used in the present study.

5. Conclusions

In the soils and by-products used in this study, adsorption was higher for Cu than for As(V). In the soils, pH and organic matter content were the most influential factors as regards Cu adsorption, which increased with both parameters. In addition, Cu in cationic form would be adsorbed by binding to the negatively charged sites generated by raising the pH in the variable charge components (mainly organic matter and low-crystallinity minerals). Regarding As(V) adsorption, the influence of pH and organic matter was not so clear, since, at a low pH, As in anionic form binds to the positively charged colloids, while at higher pHs, other mechanisms intervene, such as cationic bridges or ligand exchange. For As(V) and, to a lesser extent, for Cu, the percentage of adsorption decreases with increasing dose of the added pollutant, indicating the saturation of the adsorption sites. Regarding desorption, in soils with more acidic pH (AL soils), Cu and As desorption were similar, while in soils with higher pH (S soils), more As is desorbed. Overall, oak ash performed as an excellent Cu and As(V) adsorbent and could be used in soil and water decontamination processes, possibly due to its high pH and content of carbonates, oxides, and non-crystalline minerals. Mussel shell and pine bark could also be used to retain Cu, but its capacity to adsorb As was low and its desorption was high. The adsorption data for both elements can be partially fitted to the Langmuir, Freundlich, and Temkin models. The values of the different parameters of the equations indicate a higher adsorption energy for Cu onto the sorbent surfaces, compared to As(V), and the existence of heterogeneous adsorbent surfaces with the gradual saturation of the adsorption sites, as well as the predominance of chemisorption reactions. In addition, the high correlations obtained among the different parameters of the equations and parameters of the sorbents support the influence of pH, exchange cations, as well as organic matter and non-crystalline Fe and Al oxy-hydroxides in Cu and As(V) adsorption. These results can be considered relevant to program an appropriate management of soils affected by Cu and As(V) pollution, as well as the use of low-cost bio-adsorbents, such as those tested in this study. In future research, soils with different characteristics could be evaluated, as well as other bio-adsorbents and/or study conditions, and on the other hand, complementary studies could be designed in order to advance the elucidation of the mechanisms that intervene in the adsorption processes of both contaminants in the sorbent materials under consideration.

Supplementary Materials: The following supporting information can be downloaded at: https://www.mdpi.com/article/10.3390/ma15145023/s1, Table S1: Data corresponding to the BET surface area results for the six soils studied. Mean values (n = 3) with coefficients of variation always <5%; Table S2. Data corresponding to the BET surface area results for the three bio-adsorbent materials studied. Mean values (n = 3) with coefficients of variation always <5%.

Author Contributions: Conceptualization, M.J.F.-S., E.Á.-R., A.N.-D., M.A.-E. and P.P.-R.; methodology, M.J.F.-S., E.Á.-R., A.N.-D., M.A.-E. and P.P.-R.; software, R.C.-D., A.B., G.F.-C. and C.C.-C.; validation, M.A.-E., A.N.-D., E.Á.-R., A.N.-D. and M.J.F.-S.; formal analysis, R.C.-D.; investigation, R.C.-D., A.B., G.F.-C. and C.C.-C.; resources, E.Á.-R., M.J.F.-S. and M.A.-E.; data curation, R.C.-D., A.B., M.J.F.-S. and E.Á.-R.; writing—original draft preparation, R.C.-D., A.B., M.J.F.-S. and E.Á.-R.; writing—review and editing, A.N.-D.; visualization, R.C.-D., A.B., G.F.-C., C.C.-C., P.P.-R., M.A.-E., A.N.-D., E.Á.-R. and M.J.F.-S.; supervision, M.J.F.-S.; project administration, E.Á.-R., M.J.F.-S. and M.A.-E.; funding acquisition, E.Á.-R., M.J.F.-S. and M.A.-E. All authors have read and agreed to the published version of the manuscript.

Funding: This work was supported by the Spanish Ministry of Economy and Competitiveness (grant numbers RTI2018-099574-B-C21 and RTI2018-099574-B-C22), with European Regional Development Funds (FEDER in Spain).

Institutional Review Board Statement: Not applicable.

Informed Consent Statement: Not applicable.

Data Availability Statement: Not applicable.

Conflicts of Interest: The authors declare no conflict of interest. The funders had no role in the design of the study; in the collection, analyses, or interpretation of data; in the writing of the manuscript, or in the decision to publish the results.

References

1. Coelho, G.F.; GonÇalves, A.C.; Nóvoa-Muñoz, J.C.; Fernández-Calviño, D.; Arias-Estévez, M.; Fernández-Sanjurjo, M.J.; Álvarez-Rodríguez, E.; Núñez-Delgado, A. Competitive and non-competitive cadmium, copper and lead sorption/desorption on wheat straw af-fecting sustainability in vineyards. *J. Clean. Prod.* **2016**, *139*, 1496–1503. [CrossRef]
2. Qin, F.; Shan, X.; Wei, B. Effects of low-molecular-weight organic acids and resi-dence time on desorption of Cu, Cd, and Pb from soils. *Chemosphere* **2004**, *57*, 253–263. [CrossRef] [PubMed]
3. Keshavarzi, A.; Kumar, V. Spatial distribution and potential ecological risk assess-ment of heavy metals in agricultural soils of Northeastern Iran. *Geol. Ecol. Landsc.* **2019**, *4*, 87–103. [CrossRef]
4. Baltas, H.; Sirin, M.; Gokbayrak, E.; Ozcelik, A.E. A case study on pollution and a human health risk assessment of heavy metals in agricultural soils around Sinop province, Turkey. *Chemosphere* **2020**, *241*, 125015–125025. [CrossRef]
5. Komárek, M.; Vaněk, A.; Ettler, V. Chemical stabilization of metals and arsenic in contaminated soils using oxides—A review. *Environ. Pollut.* **2013**, *172*, 9–22. [CrossRef]
6. Delgadillo-López, A.E.; González-Ramírez, C.A.; Prieto-García, F.; Villagómez-Ibarra, J.R.; Acevedo-Sandoval, O. Fitorremediación: Una alternativa para eliminar la contaminación. *Trop. Subtrop. Agroecosyst.* **2011**, *14*, 597–612.
7. Zaynab, M.; Al-Yahyai, R.; Ameen, A.; Sharif, Y.; Ali, L.; Fatina, M.; Khan, K.A.; Li, S. Health and environmental effects of Heavy metals. *J. King Saud Univ. Sci.* **2022**, *34*, 101653–101661. [CrossRef]
8. Doušová, B.; Grygar, T.; Martaus, A.; Fuitová, L.; Koloušek, D.; Machovič, V. Sorption of AsV on aluminosilicates treated with FeII nanoparticles. *J. Colloid Interface Sci.* **2006**, *302*, 424–431. [CrossRef]
9. Podgorski, J.; Berg, M. Global threat of arsenic in groundwater. *Science* **2020**, *368*, 845–850. [CrossRef]
10. Smedley, P.L.; Kinninburgh, D.G. A review of the source, behaviour and distribution of arsenic in natural waters. *Appl. Geochem.* **2002**, *17*, 517–568. [CrossRef]
11. Sharma, A.K.; Tjell, J.C.; Sloth, J.J.; Holm, P.E. Review of arsenic contamination, exposure through water and food and low cost mitigation options for rural areas. *Appl. Geochem.* **2014**, *41*, 11–33. [CrossRef]
12. Martín-Peinado, F.J.; Romero Freire, A.; Arco Lázaro, E.; Sierra Aragón, M.; Ortiz-Bernad, I.; Abbaslou, H. Assessment of arsenic toxicity in spiked soils and water solutions by the use of bioassays. *Span. J. Soil Sci.* **2012**, *2*, 45–56. [CrossRef]
13. Abdul, K.S.M.; Jayasinghe, S.S.; Chandana, E.P.S.; Jayasumana, C.; De Silva, P.M.C.S. Arsenic and human health effects: A review. *Environ. Toxicol. Pharmacol.* **2015**, *40*, 828–846. [CrossRef]
14. Bhowmick, S.; Pramanik, S.; Singh, P.; Mondal, P.; Chatterjee, D.; Nriagu, J. Arsenic in groundwater of West Bengal, India: A review of human health risks and assessment of possible intervention options. *Sci. Total Environ.* **2018**, *612*, 148–169. [CrossRef]
15. Majumder, S.; Banik, P. Geographical variation of arsenic distribution in paddy soil, rice and rice-based products: A meta-analytic approach and implications to human health. *J. Environ. Manag.* **2019**, *233*, 184–199. [CrossRef]

16. Fatoki, J.O.; Badmus, J.A. Arsenic as an environmental and human health antagonist: A review of its toxicity and disease initiation. *J. Hazard. Mater. Adv.* **2022**, *5*, 100052–100063. [CrossRef]
17. Gómez-Armesto, A.; Carballeira-Díaz, J.; Pérez-Rodríguez, P.; Fernández-Calviño, D.; Arias-Estévez, M.; Nóvoa-Muñoz, J.C.; Álvarez-Rodriguez, E.; Fernández-Sanjurjo, M.J.; Núñez-Delgado, A. Copper content and distribution in vineyard soils from Betanzos (A Coruña, Spain). *Span. J. Soil Sci.* **2015**, *5*, 60–71. [CrossRef]
18. Okereafor, U.; Makhatha, M.; Mekuto, L.; Uche-Okereafor, N.; Sebola, T.; Mavumengwana, V. Toxic Metal Implications on Agricultural Soils, Plants, Animals, Aquatic life and Human Health. *Int. J. Environ. Res. Public Health* **2020**, *17*, 2204. [CrossRef]
19. Díaz-Raviña, M.; Calvo de Anta, R.; Bååth, E. Tolerance (PICT) of the bacterial communities to copper in vineyard soils from Spain. *J. Environ. Qual.* **2007**, *36*, 1760–1764. [CrossRef]
20. Fernández-Calviño, D.; Soler-Rovira, P.; Polo, A.; Díaz-Raviña, M.; Arias-Estévez, M.; Plaza, C. Enzyme activities in vineyard soils long-term treated with copper based fungicides. *Soil Biol. Biochem.* **2010**, *42*, 2119–2127. [CrossRef]
21. Fernández-Calviño, D.; Martín, A.; Arias-Estévez, M.; Bååth, E.; Díaz-Raviña, M. Microbial community structure of vineyards soils with different pH and copper content. *Appl. Soil Ecol.* **2010**, *46*, 276–282. [CrossRef]
22. Kumar, A.; Tripti; Maleva, M.; Kiseleva, I.; Maiti, S.K.; Morozova, M. Toxic metal(loid)s contamination and potential human health risk assessment in the vicinity of century-old copper smelter, Karabash, Russia. *Environ. Geochem. Health* **2020**, *42*, 4113–4124. [CrossRef]
23. Daoust, C.M.; Bastien, C.; Deschênes, L. Influence of soil properties and aging on the toxicity of copper on compost worm and barley. *J. Environ. Qual.* **2006**, *35*, 558–567. [CrossRef] [PubMed]
24. Stern, B.R. Essentiality and Toxicity in Copper Health Risk Assessment: Overview, Update and Regulatory Considerations. *J. Toxicol. Environ. Health—Part A* **2010**, *73*, 114–127. [CrossRef] [PubMed]
25. Taylor, A.A.; Tsuji, J.S.; Garry, M.R.; McArdle, M.E.; Goodfellow, W.L., Jr.; Adams, W.J.; Menzie, C.A. Critical Review of Exposure and Effects: Implications for Setting Regulatory Health Criteria for Ingested Copper. *Environ. Manag.* **2020**, *65*, 131–159. [CrossRef] [PubMed]
26. Boudebbouz, A.; Boudalia, S.; Bousbia, A.; Habila, S.; Boussadia, M.I.; Gueroui, Y. Heavy metals levels in raw cow milk and health risk assessment across the globe: A systematic review. *Sci. Total Environ.* **2021**, *751*, 141830–141845. [CrossRef] [PubMed]
27. Pereira-Covre, W.; Ramos, S.J.; Pereira, W.V.S.; Souza, E.S.; Martins, G.C.; Teixeira, O.M.M.; Amarante, C.B.; Nunes-Dias, Y.; Rodrigues-Fernandes, A. Impact of copper mining wastes in the Amazon: Properties and risks to environment and human health. *J. Hazard. Mater.* **2022**, *421*, 126688–126701. [CrossRef] [PubMed]
28. Bigalke, M.; Weyer, S.; Wilcke, W. Copper isotope fractionation during complexation with insolubilized humic acid. *Environ. Sci. Technol.* **2010**, *44*, 5496–5502. [CrossRef]
29. Caporale, A.G.; Violante, A. Chemical Processes Affecting the Mobility of Heavy Metals and Metalloids in Soil Environments. *Curr. Pollut. Rep.* **2016**, *2*, 15–27. [CrossRef]
30. Kumar, M.; Seth, A.; Singh, A.K.; Rajput, M.S.; Sikandar, M. Remediation strategies for heavy metals contaminated ecosystem: A review. *Environ. Sustain. Indic.* **2021**, *12*, 100155–100168. [CrossRef]
31. Cutillas-Barreiro, L.; Ansias-Manso, L.; Fernández-Calviño, D.; Arias-Estévez, M.; Nóvoa-Muñoz, J.C.; Fernández-Sanjurjo, M.J.; Álvarez-Rodríguez, E.; Núñez-Delgado, A. Pine Bark as bio-adsorbent for Cd, Cu, Ni, Pb and Zn: Batch-type and stirred flow chamber experiments. *J. Environ. Manag.* **2014**, *114*, 258–264. [CrossRef]
32. Rivas-Pérez, I.M.; Paradelo-Núñez, R.; Nóvoa-Muñoz, J.C.; Arias-Estévez, M.; Fernández-Sanjurjo, M.J.; Álvarez-Rodríguez, E.; Núñez-Delgado, A. As(V) and P Competitive Sorption on Soils, By-Products and Waste Materials. *Int. J. Environ. Res. Public Health* **2015**, *12*, 15706–15715. [CrossRef]
33. Seco-Reigosa, N.; Bermúdez-Couso, A.; Garrido-Rodríguez, B.; Arias-Estévez, M.; Fernández-Sanjurjo, M.J.; Álvarez-Rodríguez, E.; Núñez-Delgado, A. As(V) retention on soils and forest by-products and other waste materials. *Environ. Sci. Pollut. Res.* **2013**, *20*, 6574–6583. [CrossRef]
34. Rajfur, M.; Kłos, A.; Wacławek, M. Sorption of copper(II) ions in the biomass of alga *Spirogyra* sp. *Bioelectrochemistry* **2012**, *87*, 65–70. [CrossRef]
35. Xu, L.; Cui, H.; Zheng, X.; Liang, J.; Xing, X.; Yao, L.; Chen, Z.; Zhou, J. Adsorption of Cu^{2+} to biomass ash and its modified product. *Water Sci. Technol.* **2017**, *1*, 115–125. [CrossRef]
36. Conde-Cid, M.; Álvarez-Esmorís, C.; Paradelo-Núñez, R.; Nóvoa-Muñoz, J.C.; Arias-Estévez, M.; Álvarez-Rodríguez, E.; Fernández-Sanjurjo, M.J.; Núñez-Delgado, A. Occurrence of tetracyclines and sulfonamides in manures, agricultural soils and crops from different areas in Galicia (NW Spain). *J. Clean. Prod.* **2018**, *197*, 491–500. [CrossRef]
37. Conde-Cid, M.; Fernández-Calviño, D.; Nóvoa-Muñoz, J.C.; Núñez-Delgado, A.; Fernández-Sanjurjo, M.J.; Arias-Estévez, M.; Álvarez-Rodríguez, E. Experimental data and model prediction of tetracycline adsorption and desorption in agricultural soils. *Environ. Res.* **2019**, *177*, 108607–108620. [CrossRef]
38. Olsen, S.R.; Sommers, L.E. Phosphorus. Methods of soil analysis, Part 2. In *Chemical and Microbiological Properties*; Page, A.L., Miller, R.H., Keeney, D.R., Eds.; EEUU: Madison, WI, USA, 1982.
39. Peech, L.; Alexander, L.T.; Dean, L.A. *Methods of Soil Analysis for Soil-Fertility Investigations*; Cir. Nº 757; USDA: Washington, DC, USA, 1947.

40. Álvarez-Esmorís, C.; Conde-Cid, M.; Fernández-Sanjurjo, M.J.; Núñez-Delgado, A.; Álvarez-Rodríguez, E.; Arias-Estévez, M. Environmental relevance of adsorption of doxycycline, enrofloxacin, and sulfamethoxypyridazine before and after the removal of organic matter from soils. *J. Environ. Manag.* **2021**, *287*, 112354–112364. [CrossRef]
41. Baty, F.; Ritz, C.; Charles, S.; Brutsche, M.; Flandrois, J.-P.; Delignette-Muller, M.-L. Toolbox for Nonlinear Regression in R: The Package nlstools. *J. Stat. Softw.* **2015**, *66*, 1–21. [CrossRef]
42. Shaheen, S.M.; Shams, M.S.; Khalifa, M.R.; El-Daly, M.A.; Rinklebe, J. Various soil amendments and wastes affect the (im)mobilization and phytoavailability of potentially toxic elements in a sewage effluent irrigated sandy soil. *Ecotoxicol. Environ. Saf.* **2017**, *142*, 375–387. [CrossRef]
43. Tunali, S.; Ahmet, Ç.; Tamer, A. Removal of lead and copper ions from aqueous solutions by bacterial strain isolated from soil. *Chem. Eng. J.* **2006**, *115*, 203–211. [CrossRef]
44. Patra, A.S.; Ghorai, S.; Sarkar, D.; Das, R.; Sarkar, S.; Pal, S. Anionically functionalized guar gum embedded with silica nanoparticles: An efficient nanocomposite adsorbent for rapid adsorptive removal of toxic cationic dyes and metal ions. *Bioresour. Technol.* **2017**, *225*, 367–376. [CrossRef] [PubMed]
45. Agbenin, J.O.; Olojo, L.A. Competitive adsorption of copper and zinc by a Bt horizon of a savanna Alfisol as affected by pH and selective removal of hydrous oxides and organic matter. *Geoderma* **2004**, *119*, 85–95. [CrossRef]
46. Palleiro, L.; Patinha, C.; Rodríguez-Blanco, M.L.; Tableda-Castro, M.M.; Tableda-Castro, M.T. Metal fractionation in topsoils and bed sediments in the Mero River rural basin: Bioavailability and relationship with soil and sediment properties. *Catena* **2016**, *144*, 34–44. [CrossRef]
47. Stanić, T.; Daković, A.; Živanović, A.; Tomašević-Čanović, M.; Dondur, V.; Milićević, S. Adsorption of arsenic (V) by iron (III)-modified natural zeolitic tuff. *Environ. Chem. Lett.* **2009**, *7*, 161–166. [CrossRef]
48. Mamindy-Pajany, Y.; Hurel, C.; Marmier, N.; Roméo, M. Arsenic (V) adsorption from aqueous solution onto goethite, hematite, magnetite and zero-valent iron: Effects of pH, concentration and reversibility. *Desalination* **2011**, *281*, 93–99. [CrossRef]
49. Wasay, S.A.; Tokunaga, S.; Park, S. Removal of Hazardous Anions from Aqueous Solutions by La(lll)- and Y(lll)-lmpregnated Alumina. *Sep. Sci. Technol.* **1996**, *31*, 1501–1514. [CrossRef]
50. Dambies, L.; Guibal, E.; Roze, A. Arsenic(V) sorption on molybdate-impregnated chitosan beads. *Colloids Surf. A Physicochem. Eng. Asp.* **2000**, *170*, 19–31. [CrossRef]
51. Yusof, M.S.M.; Othman, M.H.D.; Wahab, R.A.; Jumbri, K.; Razak, F.I.A.; Kurniawan, T.A.; Samh, R.A.; Mustafa, A.; Rahman, M.A.; Jaafar, J.; et al. Arsenic adsorption mechanism on palm oil fuel ash (POFA) powder suspension. *J. Hazard. Mater.* **2020**, *383*, 121214–121224. [CrossRef]
52. Rakhunde, R.; Jasudkar, D.; Deshpande, L.; Juneja, H.D.; Labhasetwar, P. Health effects and significance of arsenic speciation in water. *Int. J. Environ. Sci. Res.* **2012**, *1*, 92–96.
53. Inchaurrondo, N.; Di Luca, C.; Mori, F.; Pintar, A.; Žerjav, G.; Valiente, M.; Palet, C. Synthesis and adsorption behavior of mesoporous alumina and Fe-doped alumina for the removal of dominant arsenic species in contaminated waters. *J. Environ. Chem. Eng.* **2019**, *7*, 102901–102915. [CrossRef]
54. Das, T.K.; Bezbaruah, A.N. Comparative study of arsenic removal by iron-based nanomaterials: Potential candidates for field applications. *Sci. Total Environ.* **2021**, *764*, 142914. [CrossRef]
55. Hiemstra, T.; Van Riemsdijk, W.H. A surface structural approach to ion adsorption: The charge distribution. The charge distribution model. *J. Colloid Interface Sci.* **1996**, *179*, 488–508. [CrossRef]
56. Tabelin, C.B.; Corpuz, R.D.; Igarashi, T.; Villacorte-Tabelin, M.; Alorro, R.D.; Yoo, K.; Raval, S.; Ito, M.; Hiroyoshi, N. Acid mine drainage formation and arsenic mobility under strongly acidic conditions: Importance of soluble phases, iron oxyhydroxides/oxides and nature of oxidation layer on pyrite. *J. Hazard. Mater.* **2020**, *399*, 122844–122860. [CrossRef]
57. Ewbank, J.L.; Kovarik, L.; Kenvin, C.C.; Sievers, C. Effect of preparation methods on the performance of Co/Al_2O_3 catalysts for dry reforming of methane. *Green Chem.* **2014**, *16*, 885–896. [CrossRef]
58. Yasinta, J.; Victor Emery, D.; Mmereki, D. A Comparative Study on Removal of Hazardous Anions from Water by Adsorption: A Review. *Int. J. Chem. Eng.* **2018**, *2018*, 3975948. [CrossRef]
59. Ören, A.H.; Kaya, A. Factors affecting adsorption characteristics of Zn^{2+} on two natural zeolites. *J. Hazard. Mater.* **2006**, *131*, 59–65. [CrossRef]
60. Korchagin, J.; Moterle, D.F.; Escosteguy, P.A.V.; Bortoluzzi, E.C. Distribution of copper and zinc fractions in a Regosol profile under centenary vineyard. *Environ. Earth Sci.* **2020**, *79*, 439. [CrossRef]
61. Liang, M.; Renkou, X.; Jun, J. Adsorption and desorption of Cu(II) and Pb(II) in paddy soils cultivated for various years in the subtropical China. *J. Environ. Sci.* **2010**, *22*, 689–695. [CrossRef]
62. Zhang, J.; Liu, Y.; Sun, Y.; Wang, H.; Cao, X.; Li, X. Effect of soil type on heavy metals removal in bioelectrochemical system. *Bioelectrochemistry* **2020**, *136*, 107596–107605. [CrossRef]
63. Rahman, M.S.; Clark, M.W.; Yee, L.H.; Comarmond, M.J.; Payne, T.E.; Burton, E.D. Effects of pH, competing ions and aging on arsenic(V) sorption and isotopic exchange in contaminated soils. *Appl. Geochem.* **2019**, *105*, 114–124. [CrossRef]
64. Boim, A.G.; Rodrigues, S.M.; dos Santos-Araújo, S.N.; Pereira, E.; Alleoni, L.R. Pedotransfer functions of potentially toxic elements in tropical soils cultivated with vegetable crops. *Environ. Sci. Pollut. Res.* **2018**, *25*, 12702–12712. [CrossRef]

65. Fernández-Calviño, D.; Cutillas-Barreiro, L.; Núñez-Delgado, A.; Fernández-Sanjurjo, M.J.; Álvarez-Rodríguez, E.; Nóvoa-Muñoz, J.C.; Arias-Estévez, M. Cu Immobilization and Lolium perenne Development in an Acid Vineyard Soil Amended with Crushed Mussel Shell. *Land Degrad. Dev.* **2017**, *28*, 762–772. [CrossRef]
66. Farouq, R.; Yousef, N.S. Equilibrium and kinetics studies of adsorption of copper (II) ions on natural biosorbent. *Int. J. Chem. Eng. Appl.* **2015**, *6*, 319–324. [CrossRef]
67. Kosmulski, M. pH-dependent surface charging and points of zero charge. IV. Update and new approach. *J. Colloid Interface Sci.* **2009**, *337*, 439–448. [CrossRef]
68. Šoštarić, T.D.; Petrović, M.S.; Pastor, F.T.; Lončarević, D.R.; Petrović, J.T.; Milojković, J.V.; Milojković, J.V.; Stojanović, M.D. Study of heavy metals biosorption on native and alkali-treated apricot shells and its application in wastewater treatment. *J. Mol. Liq.* **2018**, *259*, 340–349. [CrossRef]
69. Vítková, M.; Komárek, M.; Tejnecký, V.; Šillerová, H. Interactions of nano-oxides with low-molecular-weight organic acids in a contaminated soil. *J. Hazard. Mater.* **2015**, *293*, 7–14. [CrossRef]
70. Boddu, V.M.; Abburi, K.; Talbott, J.L.; Smith, E.D. Removal of hexavalentchromium from waste water using a new composite chitosan biosorbent. *Environ. Sci. Technol.* **2003**, *37*, 4449–4456. [CrossRef]
71. Conde-Cid, M.; Fernández-Sanjurjo, M.J.; Ferreira-Coelho, G.; Fernández-Calviño, D.; Arias-Estevez, M.; Núñez-Delgado, A.; Álvarez-Rodríguez, E. Competitive adsorption and desorption of three tetracycline antibiotics on bio-sorbent materials in binary systems. *Environ. Res.* **2020**, *190*, 110003. [CrossRef]
72. Tsang, D.C.W.; Yip, A.C.K.; Olds, W.E.; Weber, P.A. Arsenic and copper stabilisation in a contaminated soil by coal fly ash and green waste compost. *Environ. Sci. Pollut. Res.* **2014**, *21*, 10194–10204. [CrossRef]
73. Mitchell, K.; Moreno-Jimenez, E.; Jones, R.; Zheng, L.; Trakal, L.; Hough, R.; Beesley, L. Mobility of arsenic, chromium and copper arising from soil application of stabilised aggregates made from contaminated wood ash. *J. Hazard. Mater.* **2020**, *393*, 122479. [CrossRef] [PubMed]
74. Park, J.H.; Eom, J.H.; Lee, S.L.; Hwang, S.W.; Kim, S.H.; Kang, S.W.; Yun, J.J.; Cho, J.S.; Lee, Y.H.; Seo, D.C. Exploration of the potential capacity of fly ash and bottom ash derived from wood pellet-based thermal power plant for heavy metal removal. *Sci. Total Environ.* **2020**, *740*, 140205. [CrossRef] [PubMed]
75. Lucchini, P.; Quilliam, R.; DeLuca, T.; Vamerali, T.; Jones, D.L. Increased bioavailability of metals in two contrasting agricultural soils treated with waste wood-derived biochar and ash. Environ. *Sci. Pollut. Res.* **2014**, *21*, 3230–3240. [CrossRef] [PubMed]
76. Seco-Reigosa, N.; Cutillas-Barreiro, L.; Nóvoa-Muñoz, J.C.; Arias-Estévez, M.; Fernández-Sanjurjo, M.J.; Álvarez-Rodríguez, E.; Núñez-Delgado, A. Mixtures including wastes from the mussel shell processing industry: Retention of arsenic, chromium and mercury. *J. Clean. Prod.* **2014**, *84*, 680–690. [CrossRef]
77. Ramírez-Pérez, A.M.; Paradelo, M.; Nóvoa-Muñoz, J.C.; Arias-Estévez, M.; Fernández-Sanjurjo, M.J.; Álvarez-Rodríguez, E.; Núñez-Delgado, A. Heavy metal retention in copper mine soil treated with mussel shells: Batch and column experiments. *J. Hazard. Mat.* **2013**, *248–249*, 122–130. [CrossRef] [PubMed]
78. Osorio-López, C.; Seco-Reigosa, N.; Garrido-Rodríguez, B.; Cutillas-Barreiro, L.; Arias-Estévez, M.; Fernández-Sanjurjo, M.J.; Álvarez-Rodríguez, E.; Núñez-Delgado, A. As(V) adsorption on forest and vineyard soils and pyritic material with or without mussel shell: Kinetics and fractionation. *J. Taiwan Inst. Chem. Eng.* **2014**, *45*, 1007–1014. [CrossRef]
79. Amery, F.; Degryse, F.; Van Moorleghem, C.; Duyck, M.; Smolders, E. The dissociation kinetics of Cu-dissolved organic matter complexes from soil and soil amendments. *Anal. Chim. Acta* **2010**, *670*, 24–32. [CrossRef]
80. Febrianto, J.; Kosasih, A.N.; Sunarso, J.; Ju, Y.; Indraswati, N.; Ismadji, S. Equilibrium and kinetic studies in adsorption of heavy metals using biosorbent: A summary of recent studies. *J. Hazard. Mater.* **2009**, *162*, 616–645. [CrossRef]
81. Khezami, L.; Capart, R. Removal of chromium(VI) from aqueous solution by activated carbons: Kinetic and equilibrium studies. *J. Hazard. Mater.* **2005**, *123*, 223–231. [CrossRef]
82. Bhaumik, R.; Mondal, N.K.; Das, B.; Roy, P.; Pal, K.C.; Das, C.; Banerjee, A.; Datta, K. Eggshell Powder as an Adsorbent for Removal of Fluoride from Aqueous Solution: Equilibrium, Kinetic and Thermodynamic Studies. *E-J. Chem.* **2012**, *9*, 1457–1480. [CrossRef]
83. Sukul, P.; Lamshöft, M.; Zühlke, S.; Spiteller, M. Sorption and desorption of sulfadiazine in soil and soil-manure systems. *Chemosphere* **2008**, *73*, 1344–1350. [CrossRef]
84. Vijayalakshmi, K.; Devi, B.M.; Latha, S.; Gomathi, T.; Sudha, P.N.; Venkatesan, J.; Anil, S. Batch adsorption and desorption studies on the removal of lead (II) from aqueous solution using nanochitosan/sodium alginate/microcrystalline cellulose beads. *Int. J. Biol. Macromol.* **2017**, *104*, 1483–1494. [CrossRef]
85. Eftekhari, M.; Gheibi, M.; Azizi-Toupkanloo, H.; Hossein-Abadi, Z.; Khraisheh, M.; Fathollahi-Fard, A.M.; Tian, G. Statistical optimization, soft computing prediction, mechanistic and empirical evaluation for fundamental appraisal of copper, lead and malachite green adsorption. *J. Ind. Inf. Integr.* **2021**, *23*, 100219–100240. [CrossRef]
86. Uchechukwu, O.F.; Azubuike, O.S.; Okan, E.N. Biosorption of Cd^{2+}, Ni^{2+} and Pb^{2+} by the shell of pentaclethra macrophylla: Equilibrium isotherm studies. *J. Sci. Technol. Environ. Inform.* **2015**, *13*, 26–35. [CrossRef]

materials

MDPI

Article

Pitting and General Corrosion Susceptibilities of Materials for High Level Radioactive Waste (HLW) Disposal

Brent Verhoeven [1], Walter Bogaerts [2], Pieter Van Aken [1], Roberto Gaggiano [3], Jan Baeyens [1], Barbara Rossi [4,5] and Raf Dewil [1,4,*]

[1] Department of Chemical Engineering, Process and Environmental Technology Lab, KU Leuven, J. De Nayerlaan 5, 2860 Sint-Katelijne-Waver, Belgium
[2] Department of Materials Engineering, KU Leuven, Kasteelpark Arenberg 44, 3001 Leuven, Belgium
[3] RD&D Department, ONDRAF/NIRAS, Kunstlaan 14, 1210 Brussels, Belgium
[4] Department of Engineering Science, University of Oxford, Parks Road, Oxford OX1 3PJ, UK
[5] Department of Civil Engineering, Materials and Structures, KU Leuven, J. De Nayerlaan 5, 2860 Sint-Katelijne-Waver, Belgium
* Correspondence: raf.dewil@kuleuven.be

Abstract: The disposal of high-level radioactive waste (HLW) in deep stable geological formations is accepted at an international level to be the most promising option for its long-term management. The supercontainer concept is currently being considered as the Belgian reference design, wherein the waste will be stored in geological stable clay formations. The outer barrier of the supercontainer is the envelope, which should be made of a corrosion-resistant material as it will be in contact with the aggressive species leaching from the host rock (i.e., chloride) and diffusing through the cementitious barriers of the disposal system. Polarization measurements are carried out to study the pitting susceptibility and the uniform corrosion of possible candidate materials in chloride-rich concrete pore solutions, aerated by high-purity oxygen. The tests are carried out at a deep soil-representative temperature of 60 °C. All materials showed high pitting resistance in aerated concrete pore solutions and can withstand chloride concentrations up to 1 M. Regular 316L and LDX2304 stainless steel also showed good corrosion resistance and can serve as a more economical alternative. The pH of the used pore solutions did affect the measured corrosion rate irrespective of the alloying elements inside the steel grades.

Keywords: radioactive waste; disposal; deep geological formations; supercontainer; pitting; corrosion susceptibility; steel alloys

Citation: Verhoeven, B.; Bogaerts, W.; Van Aken, P.; Gaggiano, R.; Baeyens, J.; Rossi, B.; Dewil, R. Pitting and General Corrosion Susceptibilities of Materials for High Level Radioactive Waste (HLW) Disposal. *Materials* **2022**, *15*, 6464. https://doi.org/10.3390/ma15186464

Academic Editors: Avelino Núñez-Delgado, Elza Bontempi, Marco Race, Zhien Zhang, Yaoyu Zhou and Mario Coccia

Received: 20 July 2022
Accepted: 28 August 2022
Published: 17 September 2022

1. Introduction

Currently, geological disposal is internationally accepted to be the most promising option for the long-term management of high-level and/or long-lived radioactive waste (HLW). To ensure a proper sequestration of the waste, a stable geological formation is required to serve as a natural barrier. In Belgium, clay formations are favored [1,2] because of their lower water permeability, limited diffusivity and absence of preferential migration pathways for solutes. Apart from this natural barrier, the disposal system includes multiple engineered barriers: radioactive waste containers are placed in concrete shafts (galleries) in the underground facility, and the container itself (containing vitrified radioactive waste or spent fuel assemblies) consists of multiple material layers. All recommendations from the Contained Environment Concept (CEC) and even earlier designs of the Engineered Barrier System (EBS) have been addressed in the current reference design of the supercontainer (Figure 1) [3]. It consists of a carbon steel inner pack (overpack) containing the waste canister (A), surrounded by a buffer (B) and a stainless steel envelope as the outer layer (C) [4]. The intention of the CEC is to achieve and preserve a durable (long-term) favorable chemical environment in the immediate vicinity of the overpack, at least for the duration

of the thermal phase (several hundred to thousands of years). Portland Cement-based concrete has hence been chosen as the material for the buffer to provide a highly alkaline chemical environment, in which the external surface of the overpack will be passivated. The main function of the envelope is preventing the infiltration of pore water from the host rock through the concrete galleries into the concrete buffer. Therefore, the envelope should have high pitting resistance, but even more importantly, a low uniform corrosion rate when it is in contact with this pore water that contains chlorides, sulfides and thiosulfates (originated from the clay host formation). Such contaminants are considerably aggressive to stainless steels and nickel-based alloys [5–16]. The concrete barriers of the disposal facility create alkaline conditions ensuring good passivation of the envelope, while elevated temperatures are expected because of the remaining heat dissipation from the nuclear waste [2]. Apart from the corrosion resistance in this harsh environment, the envelope should provide mechanical strength to ensure the reliability and possible retrievability of the supercontainer. The retrievability determines the possibility to retrieve the waste containers after they have been disposed in the repository in case the repository does not perform according to the expectations.

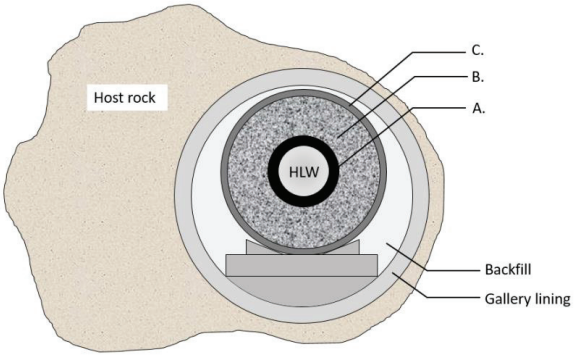

Figure 1. Cross-section of the "supercontainer" reference concept with its main components: (A) carbon steel liner (overpack), (B) concrete reinforcement (buffer) and (C) envelope liner.

The concrete environment is often simulated using pore solutions in lab-scale tests. Saturated $Ca(OH)_2$ (pH 12.5 at 25 °C) and a mixture of KOH/NaOH (pH 13.5 at 25 °C) are the commonly applied pore solutions seen in the literature. Li et al. [17] and Luo et al. [18] highlighted that stainless steels showed better passivation in saturated $Ca(OH)_2$ than in KOH/NaOH mixtures. This is mainly due to the higher Cr^{3+} content in the passive film at pH 12.5. Regardless of the strong passivated behavior in these alkaline conditions, the presence of chlorides enhances the pitting corrosion of stainless steels.

Traditional austenitic stainless steels and lean low wt. % Ni duplex stainless steels are common alloys for applications in concrete. Several studies have reported the corrosion behavior of these alloys in simulated pore solutions. Gastaldi et. al. [19] found that AISI 304 L and LDX2101 were susceptible to pitting corrosion in saturated $Ca(OH)_2$ at only 6000 ppm Cl^-. According to Blanco et al. [20], AISI 304 L appears to show pitting susceptibility at an even lower concentration, i.e., 3000 ppm Cl^-.

Moser et. al. [21] argued that LDX2101 has better pitting resistance than AISI 316L in saturated $Ca(OH)_2$. At chloride concentrations of 0.5 M, both alloys showed pits at the surface, while LDX2304 did not show such pitting corrosion. Only at chloride concentrations of 1 M Cl^- did all studied lean duplex steels fail in terms of pitting corrosion [21]. Traditional duplex steels, such as DX2205, showed improved pitting corrosion resistance, even at concentrations above 1 M Cl^- [20–22]. So far, most studies performed in pore solutions have assessed corrosion behavior at ambient temperatures. It has been suggested that temperature strongly influences the pitting resistance of stainless steel. If the tem-

perature increases, pitting potentials considerably decrease [2,19–21]. Pedeferri et al. [22] and Gastaldi et al. [15] performed potentiostatic and potentiodynamic measurements on stainless steels in saturated $Ca(OH)_2$ at 40 °C. According to the research conducted by Gastaldi et al., austenitic stainless steels (AISI 304 L, AISI 316L) and lean duplex stainless steels (LDX2101, LDX2304) showed pitting at 40 °C with 3 wt. % Cl^- [15].

At the envelope surface, a temperature of 60–80 °C is expected, which is created by the heat dissipation of the enclosed radioactive waste. In addition, pitting is expected to become important because of the high chloride concentrations expected at the envelope liner, originating from the host formation. To further develop the supercontainer, and more specifically select a suitable material for the envelope, the corrosion behavior of stainless steels and nickel-based alloys should be studied in this temperature range in a chloride-rich concrete environment. Very few studies have attempted to define the corrosion behavior and the pitting susceptibility of stainless steels in pore solutions at elevated temperatures, and before now, no study has performed corrosion tests at temperatures of 60 °C. Research on corrosion behavior in chloride-contaminated pore solutions is often limited to austenitic and lean duplex stainless steels. The aim of this study is to investigate the corrosion behavior of more resistant (superaustenitic) stainless steels and nickel-based alloys in concrete pore solutions at a temperature of 60 °C. The stainless steels and nickel-based grades under scrutiny are listed in Table 1 and will be further discussed. One zirconium grade was also included, i.e., Zircaloy 702 (abbreviated as Zr702), as it shows excellent corrosion resistance in high-pH environments due to the formation of insoluble oxides [23]. Table 1 also provides the pitting resistance equivalent number, PREN, as calculated according to Equation (1).

$$PREN = Cr\% + 3.3 * (Mo\% + 0.5 * W\%) + 16 * N\% \quad (1)$$

Table 1. Chemical composition and PREN values of all tested materials.

Common Denomination	UNS	Cr	Ni	Mo	PREN
316L	S31603	16–18	10–14	2–3	24
Alloy 825	N08825	19.5–23.5	38–46	2.5–3.5	28
904 L	N08904	19–23	23–28	4–5	32
254SMO	S31254	19.5–20.5	17.5–18.5	6–6.5	42
Al-6XN	N08367	20–22	23.5–25.5	6–7	43
Alloy 31	N08031	26–28	30–32	6–7	48
LDX2304	S32304	21.5–24.5	3–5.5	0.05–0.6	22
DX2205	S31803	21–23	4.5–6.5	2.5–3.5	31
SDX2507	S32750	24–26	6–8	3–5	38
SDX100	S32760	24–26	6–8	3–4	37
C-276	N10276	15.5–16.5	Ca. 57	15–17	-
C-4	N06455	16	Ca. 65	16	-
C-22	N06022	20–22.5	Ca. 56	12.5–14.5	-
C-2000	N06200	22–24	Ca. 67	15–17	-
Zr702	R60702	-	-	-	-

2. Materials and Methods

Accelerated corrosion tests were conducted on different stainless steels and nickel-based alloys. All tested materials with their chemical compositions and PREN values (pitting resistance equivalent number) are listed in Table 1. Every alloy is tested as a sheet under cold-rolled conditions. AISI 316L has a low PREN value and is considered as the reference material.

To simulate the concrete environment, the tests were performed in saturated $Ca(OH)_2$ and a mixture of KOH/NaOH at 60 °C. The pH values of the simulated pore solutions were 12.5 and 13.5, respectively (measured at 25 °C). For testing pitting susceptibility, a high chloride concentration of 35400 ppm (1 M) was added to the pore solution. In addition, the

uniform corrosion rates were studied using Tafel extrapolation [12]. All test solutions were aerated with oxygen (summarized in Table 2).

Table 2. Experimental conditions.

Type of Pore Solution	pH	Temperature	Chloride	Type of Aeration
Sat. $Ca(OH)_2$ NaOH/KOH mixt.	12.5 13.5	60 °C	35400 ppm	1 L/min O_2

A three-electrode set-up was used to perform electrochemical corrosion tests (see Figure 2). Before each test, the sample was immersed for at least 1 h [24]. All alloys were imbedded in cold epoxy resin and polished with a diamond suspension (1 μm). A rubber gasket was compressed in the sample area to avoid crevice corrosion. A Hg/HgO reference electrode (20% KOH, +98 mV versus SHE) was used due to its electrochemical stability in alkaline solutions.

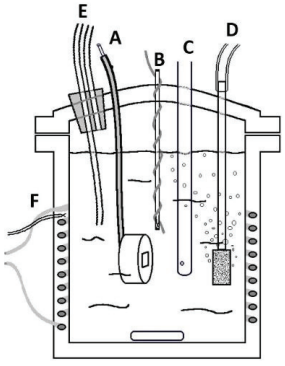

Figure 2. Setup of the electrochemical cell with (A) the working electrode; (B) the counter electrode; (C) the reference electrode; (D) gas bubbler; (E) gas outlet; and (F) electrical heating.

Cyclic polarization plots were used to measure the uniform corrosion rate and check the pitting susceptibility of each alloy in the test electrolyte. All polarization measurements were conducted using a scan rate of 250 mV/h. Every measurement was started 100 mV below the measured open-circuit potential. The scan direction was reversed if the apex potential was reached (+750 mV versus Hg/HgO) or if the current density exceeded 5 mA/cm^2 [24]. Tafel extrapolation for additional information on the general corrosion behavior was conducted on the linear parts of the anodic and cathodic curves. Extrapolation should start 50–100 mV away from the open-circuit potential [12]. After checking normality with Q-Q plots, Kruskal–Wallis and Dunn test statistics were applied to get a better understanding of the data derived [25–27]. Additionally, a principal component analysis (PCA) provides a survey of any correlation found between the added alloying elements (within a grade) and their corresponding corrosion resistance.

3. Results

3.1. Pitting Susceptibility

The results of the cyclic potentiodynamic measurements in saturated $Ca(OH)_2$ with 1 M Cl^- at 60 °C are presented in Figure 3. Every measurement was repeated three times and showed a similar behavior. As can be seen by the absence of hysteresis loops, no pitting corrosion was found for all tested stainless steels. This result is somewhat counterintuitive, especially for the lean duplex LDX2304 and AISI 316L (reference material).

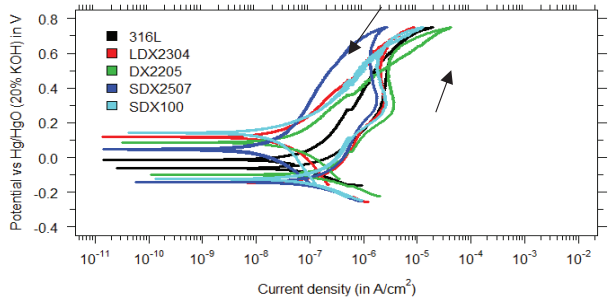

(A)

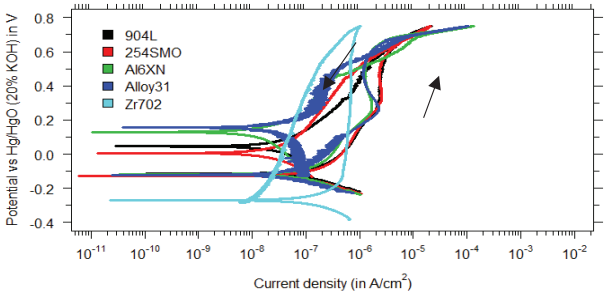

(B)

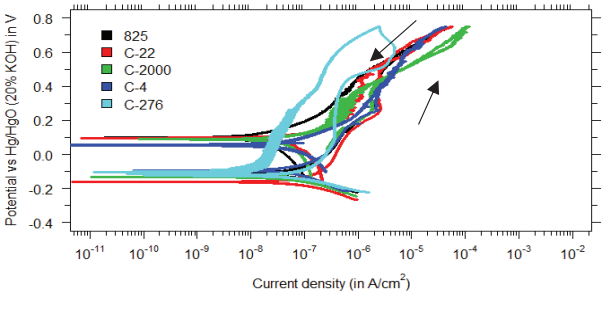

(C)

Figure 3. Polarization curves in saturated $Ca(OH)_2$ (pH 12.5) with 1 M Cl^- for (**A**) regular, duplex and super duplex stainless steels; (**B**) superaustenitics and zirconium-based alloys; and (**C**) nickel—based alloys.

The fact that no pitting corrosion was observed for those leaner grades is in contrast with the findings of previous studies [18,20], where LDX2304 failed due to pitting corrosion at much lower chloride concentrations. A possible explanation might be that other studies were influenced by the occurrence of crevice corrosion, in which case the pitting tests performed cannot be validated. Additional uncertainty arises with the high scan rates used in other studies during potentiodynamic tests. The polarization tests of Gastaldi et al. [19] and Moser et al. [21] used high scan rates of 1200 mV/h and 3600 mV/h, respectively. ASTM standards propose a scan rate of 600 mV/h for anodic polarization curves performed on stainless steel alloys [24]. The possible interference of higher scan rates and anodic polarization curves cannot be ruled out. The exhaustive review of Esmailzadeh et al. describes the effect of the scan rate on the observed pitting potential [28]. The lower scan rates applied during anodic polarization result in lower pitting potentials. This correlation

is interesting because it suggests that in the present measurements, materials are expected to fail because of the low scan rate of 250 mV/h. Another explanation for the absence of pits in the current study is the surface treatment applied. Esmailzadeh et al. suggested that polished working electrodes may relate to higher pitting resistance [28]. Ezuber found that the AISI 304 performance is significantly lower in chloride-contaminated solutions if the sample surface roughness increases [29]. In the current study, polished test specimens (up to 1 μm diamond suspension) have been used, while Moser et al. tested samples in their as-received condition [21]. Gastaldi et al. did not specify any surface treatment besides the pickling of their samples before immersing them in the test electrolyte [19].

The results for the regular duplex stainless steels are consistent with previous findings. Traditional duplex DX2205 did not show any pitting behavior in saturated $Ca(OH)_2$ at 1 M Cl^-. This is in agreement with the findings of Mesquita et al. and Elsener et al. [30,31]. More resistant materials in the experimental matrix, such as super duplex, superaustentic and nickel-based alloys, are even more promising for pitting resistance than DX2205, especially given their high PREN value (see Table 2). Bertolini et al. reported a high pitting resistance of superaustenitic 254SMO in chloride-contaminated saturated $Ca(OH)_2$, even at an elevated temperature (±40 °C) [32]. The report of Nürnberger confirms that SDX100 and other superaustenitic materials (such as alloy 926) are more resistant in harsh concrete environments [33]. The results presented in this paper form one of the first investigations to explore the corrosion behavior of nickel-based alloys in simulated pore solutions. Hastelloy C-series and Alloy 825, as expected by their high PREN value, did not show any pitting susceptibility in saturated $Ca(OH)_2$ with 1 M Cl^-.

Another striking finding is the strong passive behavior of Zr702 (Zircaloy 702) in saturated $Ca(OH)_2$ with 1 M Cl^-. Unlike other polarization curves, where a current increase is observed around 200–300 mV versus the Hg/HgO electrode (probably due to dissolution of chromium as chromate), Zr702 does not show any significant current increase at high oxidizing potentials in the tested environment. This finding is consistent with the review of corrosion resistance of zirconium in ASM handbooks [34], where great performance in strong alkalis and high chloride concentrations is reported.

Figure 4A–C display the polarization curves of all materials in a mixture of KOH/NaOH with a high chloride content of 1 M. The absence of any hysteresis loops in the cyclic polarization curves is again remarkable. No pitting corrosion was observed on any of the test specimens. This is a significant outcome, especially given the less passive behavior of the protective film reported at pH 13.5 [17,18]. Most research on chloride-induced pitting in concrete pore solutions has been carried out in saturated $Ca(OH)_2$, and the literature on higher pH is limited. Elsener et al. found that the DX2205 stainless steel did not pit in a 0.1 M NaOH solution (pH = 13), even when 5 M Cl^- was added [26]. Because higher pH values increase pitting resistance [35], it can be expected that duplex DX2205 will also show similar pitting resistance in KOH/NaOH pore solutions (and will also not pit in 5 M Cl^-) [31]. No studies were found wherein other grades of stainless steel, besides DX2205, were tested in high-alkaline pore solution (pH > 13) with chloride contamination.

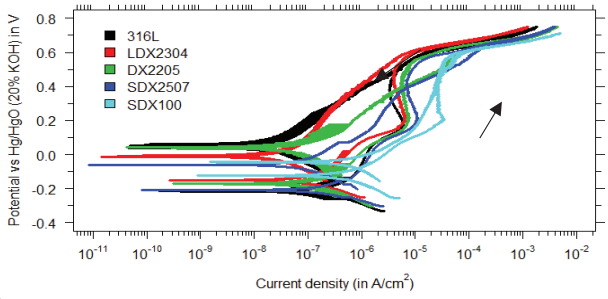

(A)

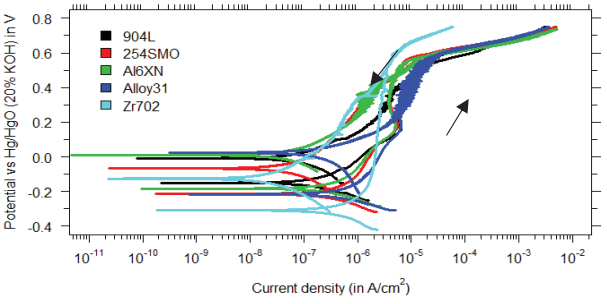

(B)

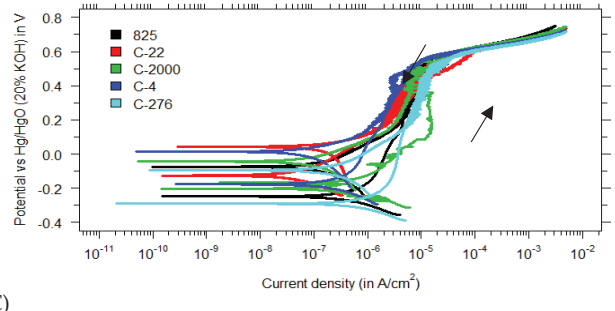

(C)

Figure 4. Polarization curves in a KOH/NaOH mixture (pH 13.5) with 1 M Cl^- for (**A**) regular, duplex and super duplex stainless steels; (**B**) superaustenitics and zirconium-based alloys; and (**C**) nickel—based alloys.

3.2. Uniform (General) Corrosion Rates

3.2.1. Tafel-Extrapolated Results in Simulated Pore Solutions

All corrosion rates have been determined by Tafel extrapolation. Several studies have provided insights into the importance of performing a Tafel extrapolation at least 50–100 mV away from the open-circuit potential [12]. The results in saturated $Ca(OH)_2$ (pH 12.5) and KOH/NaOH mixtures (pH 13.5) with 1 M Cl^- (at 60 °C) are presented in Figure 5. The corrosion rates, determined by the Tafel slopes, vary between 0.44 and 4.2 µm/y.

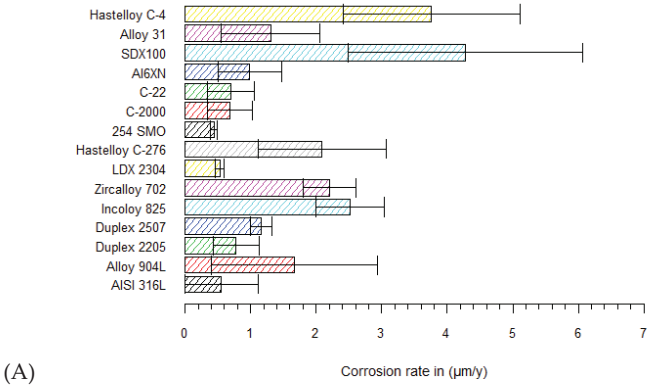

(A)

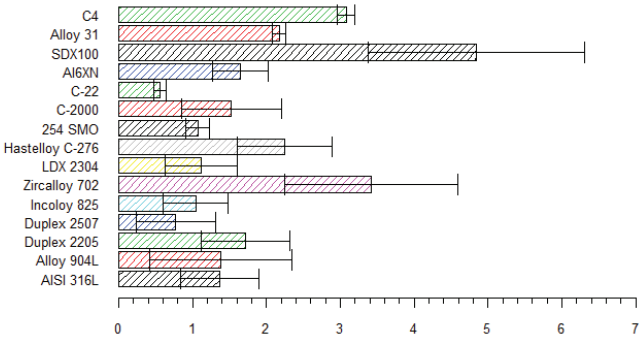

(B)

Figure 5. Uniform corrosion rates calculated by Tafel extrapolation in (**A**) pH 12.5 with 1 M Cl^-; and (**B**) pH 13.5 with 1 M Cl^-.

A remarkable finding of the measured corrosion rates is the high rate of Hastelloy® C-4 and SDX100 in saturated $Ca(OH)_2$ (Figure 5A). Superaustenitic 254SMO shows the lowest corrosion rate, with 1 M Cl^-. The reference material AISI 316L in saturated $Ca(OH)_2$ (at 60 °C) corroded at a uniform rate of 0.56 µm/y. In the KOH/NaOH mixture (pH 13.5, Figure 5B), AISI 316L had an average measured corrosion rate of 1.46 µm/y. Again, Hastelloy C-4 and SDX100 showed high corrosion rates in pH 13.5, together with Zircaloy 702. Surprisingly, another Hastelloy grade (e.g., C-22) showed the lowest corrosion rate in pH 13.5.

Studies of stainless steels in alkaline conditions at elevated temperature with high chloride contents are limited. However, in the Cobecoma report [2], results of stainless steels in alkaline conditions have been found without chloride contamination. A corrosion rate of 0.5 µm/y was reported for stainless steels in simulated pore solutions at 80 °C. A study of Blackwood et al. has reported on experiments with AISI 304 L to check the effects of temperature on uniform corrosion rates in concrete pore solutions without any chloride addition (pH = 13) [36]. At temperatures of 50 °C and 80 °C, the corrosion rates were 0.18 and 0.82 µm/y, which are in line with the rates reported in Figure 5A. The measured corrosion rate of AISI 316L in pH 13.5 (with 1 M Cl^- at 60 °C~1.46 µm/y) is in the same range as the 0.6 µm/y reported by Mcdonald et al. in alkaline conditions (pH 13.3) with 0.5 M Cl^- at ambient temperature [37]. Yet, the outcome for the reference material 316L is different to that found by Fujisawa et al., where a corrosion rate of 0.3 nm/y was claimed for AISI 304 L in pore solution (pH 12.8). A possible explanation for this rather low rate could be the testing procedure, as Fujisawa et al. used immersion tests to determine the

corrosion rate. Immersion tests are known to be more accurate and favored in determining the uniform corrosion rate [12], but often are not feasible because of their long duration.

Zircaloy 702 had a corrosion rate of 2.2 μm/y. This confirms earlier statements in the ASM Handbook suggesting a corrosion rate well below 25 μm/y in strong alkaline solutions [34]. Yau et al. found corrosion rates in alkaline conditions that were in a lower range, i.e., between 0.06 and 0.17 μm/y [38]. It is moreover important to mention that these corrosion rates were also determined by immersion tests. No studies were carried out on superaustenitic and nickel-based alloys. Other geological disposal concepts studying the corrosion behavior of Hastelloy C-series are difficult to compare because other pore–water properties were applied [39,40].

3.2.2. Comparison of the Measured Corrosion Rates

Before any statistical analysis was performed, the normal distribution of the measured uniform corrosion rates was checked by a Q-Q plot (Figure 6). Theoretical quantiles of standard normal distribution have been generated (*x*-axis) and compared with the experimental quantiles of the dataset with the measured corrosion rates (*y*-axis). Points falling along a straight line give strong evidence that the dataset is normally distributed. The grey area on the Q-Q plot in Figure 6 represents a 95% confidence interval. If data points fall out of the grey area, the data are not normally distributed. In Figure 6, the Q-Q plot for uniform corrosion rates in the saturated $Ca(OH)_2$ and KOH/NaOH mixture are presented. It can be concluded that, because many data points are not in the 95% confidence area for both pore solutions, the dataset is not normally distributed.

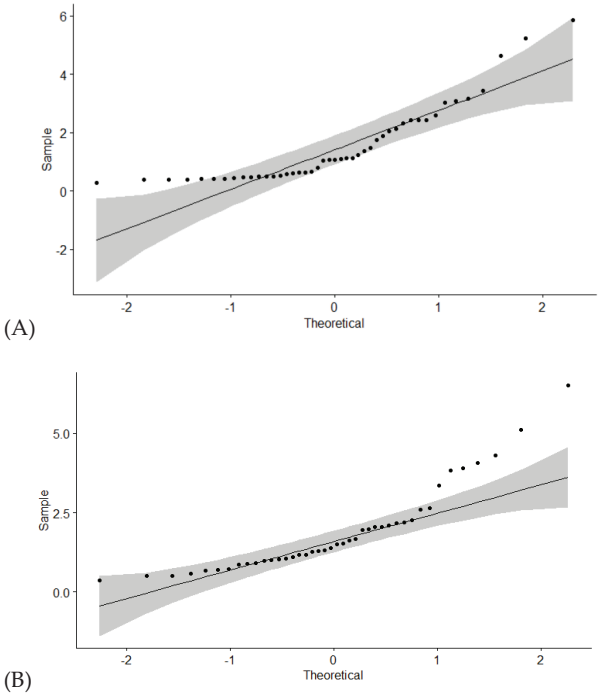

Figure 6. Q-Q plots used to check normal distribution of the measured uniform corrosion rates in (**A**) pH 12.5 with 1 M Cl^-; and (**B**) pH 13.5 with 1 M Cl^-.

Alternatively, a Kruskal–Wallis test was performed on the corrosion data. The Kruskal–Wallis test is a non-parametric statistical test (specifically developed for not normally distributed data) and is used to check if any statistical difference is present between

alloys [41]. The output of the Kruskal–Wallis test is one *p*-value for the whole dataset. A low *p*-value (<0.05) indicates statistical differences within the dataset. In our analysis, *p*-values of 0.001 and 0.025 were determined for the results in saturated $Ca(OH)_2$ and a KOH/NaOH mixture, respectively. This suggests that statistical differences are present between the grades in the tested environments. A following test, the Dunn test, was used to check which alloys are statistically better than others. The results of the Dunn test are *p*-values for every possible comparison (between alloys), and if *p*-values are below 0.025, a significant difference is found.

In saturated $Ca(OH)_2$ with a high chloride content (1 M Cl^-), five materials showed different statistical *p*-values in combination with other grades according to the Dunn test (Table 3). Superaustenitic 254SMO, Hastelloy C-2000 and C-22, austenitic 316L and lean duplex 2304 stainless steel are found in several combinations with a *p*-value < 0.025. Interestingly, these five grades had a surprisingly low corrosion rate in saturated $Ca(OH)_2$, as reported in Figure 5A. Superaustenitic 254SMO compared to Hastelloy C-276 had a corresponding *p*-value of 0.009, which is significant. It is apparent from Figure 5A that the uniform rate of 254SMO is lower than that of Hastelloy C-276. Even when taking into account the standard deviation, their difference is statistically significant using the Dunn test. For all the other significant *p*-values (and combinations), the same methodology was used for interpretation. 254SMO shows better resistance to uniform corrosion than Hastelloy C-4, Alloy 825, Zr702 and super duplex SDX100. The other four grades (i.e., Hastelloy C-22, Hastelloy C-2000, AISI 316L, LDX2304) showed similar behaviors to the tested 254SMO, and also have multiple comparisons with *p*-values <0.025.

Table 3. Results of the Dunn test for saturated $Ca(OH)_2$ with a high chloride content.

Compared Materials	*p*-Value of Dunn Test ($p < 0.025$)
254SMO–Hastelloy C-276	0.009
254SMO–Hastelloy C-4	0.0008
254SMO–Alloy 825	0.004
254SMO–Zr702	0.007
254SMO–SDX100	0.001
Hastelloy C-22–Hastelloy C-276	0.002
Hastelloy C-22–904L	0.01
Hastelloy C-22–Alloy 825	0.0008
Hastelloy C-22–Hastelloy C-4	0.0001
Hastelloy C-22–SDX2507	0.02
Hastelloy C-22–Alloy 31	0.015
Hastelloy C-22–Zr702	0.0014
Hastelloy C-22–SDX100	0.0002
316L–Hastelloy C-4	0.005
316L–Alloy 825	0.017
316L–SDX100	0.005
LDX2304–Hastelloy C-4	0.016
LDX2304–Alloy 825	0.004
LDX2304–SDX100	0.005
Hastelloy C-2000–Hastelloy C-4	0.007
Hastelloy C-2000–SDX100	0.009

The Dunn test results indicate that these five grades have a significantly low corrosion rate. The five grades with their significant comparisons are again summarized below, ranked according to their increasing (uniform) corrosion rates.

254. SMO < C-276/C-4/Alloy 825/Zr702/SDX100
Hastelloy C-2000 < C-4/SDX100
Hastelloy C-22 < C-276/904 L/Alloy 825/C-4/SDX2507/Alloy 31/SDX100
AISI 316L < C-4/Alloy 825/SDX100
LDX2304 < C-4/Alloy 825/SDX100

The same statistical test was applied to the corrosion data for pH 13.5 (mixture KOH/NaOH). Every comparison with a *p*-value < 0.025 includes super duplex SDX100, Zircaloy 702 or Hastelloy C-22. In Figure 5B, it can be observed that SDX100 and Zr702 show the highest uniform corrosion rates of all tested grades. For comparisons wherein a *p*-value < 0.025 is obtained and containing SDX100 or Zr702, the Dunn test showed a significantly lower rate for the other grades (mentioned in the comparison with SDX100 or Zr702) and, therefore, these alloys are more interesting as an envelope material in the Belgian disposal plan. The Dunn test highlights that the high corrosion rates of SDX100 and Zr702, presented in Figure 5B, are statistically significant. It is apparent (Table 4) that many comparisons are possible with Hastelloy C-22. Figure 5B illustrates that Hastelloy C-22 has the lowest corrosion rate in the KOH/NaOH mixture (pH 13.5). The Dunn test showed that the C-22 grade has a significantly lower corrosion rate than Duplex 2205, superaustenitic Al6XN, Alloy 31, Hastelloy C-4 and C-276.

Table 4. Results of the Dunn test for the KOH/NaOH mixture with high chloride content.

Compared Materials	*p*-Value of Dunn Test ($p < 0.025$)
SDX2507–SDX100	0.001
254SMO–SDX100	0.006
316L–SDX100	0.02
Alloy 825–SDX100	0.006
Hastelloy C-22–SDX100	0.0002
LDX2304–SDX100	0.007
SDX2507–Zr702	0.004
254SMO–Zr702	0.02
Alloy 825–Zr702	0.02
Hastelloy C-22–Zr702	0.0006
LDX2304–Zr702	0.02
Hastelloy C-22–Duplex 2205	0.02
Hastelloy C-22–Al6XN	0.02
Hastelloy C-22–Alloy 31	0.01
Hastelloy C-22–Hastelloy C-4	0.02
Hastelloy C-22–Hastelloy C-276	0.004

Table 4 presents the outcome of the Dunn test in pH 13.5. SDX100 and Zircaloy 702 showed statistically higher corrosion rates than other tested grades. Hastelloy C-22, however, showed a promising behavior with a lower uniform corrosion rate than other candidate materials, again ranked according to increasing (uniform) corrosion rate:

SDX2507/254SMO/316L/Alloy825/Hastelloy C-22/LDX2304 < SDX100;
SDX2507/254SMO/Alloy825/Hastelloy C-22/LDX2304 < Zircaloy 702;
Hastelloy C-22 < Duplex 2205/Al6XN/Alloy 31/Hastelloy C-4/Hastelloy C-276.

With the use of Dunn tests, significant differences between the measured uniform corrosion rates of the tested grades are identified. In pH 12.5 (saturated $Ca(OH)_2$), five grades showed a significantly lower corrosion rate: 254SMO, Hastelloy C-2000, Hastelloy C-22, AISI 316L and LDX2304. Those grades are marked in green in Figure 7A, representing materials with a low corrosion rate. Hastelloy C-276, Hastelloy C-4, Alloy 825, Zr702 and SDX100 showed a significantly higher corrosion rate compared to 254SMO and, therefore, these grades are marked in red in Figure 7A. The same methodology was followed for the other comparisons. SDX2507 did not show a statistical difference with any other tested grade in the Dunn test, and is marked in orange. By combining the statistics and uniform corrosion rates, a better understanding of the performance of the tested grades in pH 12.5 is obtained. The Dunn test reveals that SDX100 and Zircaloy 702 showed a significantly higher corrosion rate in pH 13.5, and in addition, Hastelloy C-22 showed a statistically low corrosion rate. Materials that performed better than SDX100 and Zircaloy 702 are marked in green in Figure 7B. Grades that show a higher rate than Hastelloy C-22 (according to the

Dunn test) are marked in red. Only one material, Hastelloy C-2000, was not found in any significant comparison, and is marked orange.

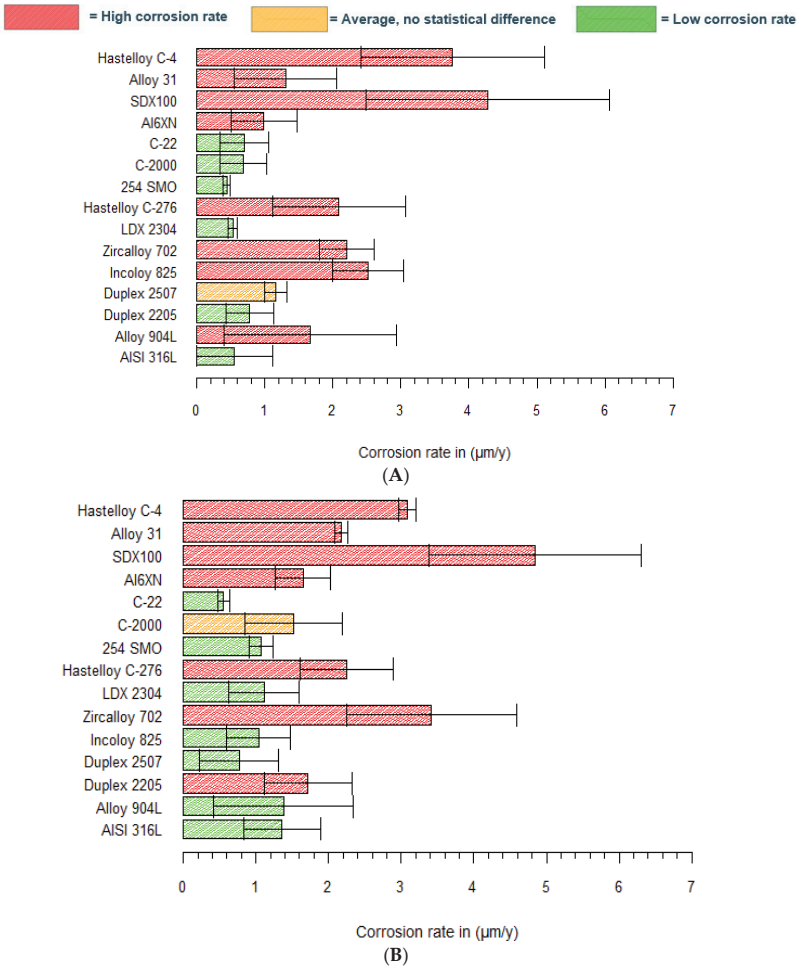

Figure 7. Uniform corrosion rates calculated by Tafel extrapolation, including the statistics of the Dunn tests for (**A**) pH 12.5 with 1 M Cl^-; and (**B**) pH 13.5 with 1 M Cl^-.

Because the envelope material should have a low uniform corrosion rate in the disposal plan, materials marked green are interesting for further consideration. Tested grades, marked in red, should be avoided because of their higher corrosion rate. Hastelloy C-22 showed a very low uniform corrosion rate in both test solutions. Implementation, however, can be limited because of its higher cost, and other grades marked in green (e.g., 316L, LDX2304 and 254SMO) can be used as a cheaper alternative.

3.2.3. Effect of Alloying Elements and pH on the Measured Corrosion Rate

A principal component analysis was performed to check the correlation between alloying elements, the pH of the used pore solution, and the calculated corrosion rates. This statistical procedure computes principal components and uses these to get a better visualization of the variation within the dataset. In general, two first principal components are used because, usually, they represent the largest part of the variation within the data.

The values of the first principal component are mentioned on the *x*-axis, and the second component on the *y*-axis. The PCA analysis was performed in R Studio [42] and is presented in Figure 8. Alloying elements, pH and corrosion rates are represented as vectors in the biplot. If vectors have the same direction, a correlation is found. Similar directions indicate that the correlation is directly proportional. If the directions are opposed, an inversely proportional correlation is found. Vectors (and parameters) that make an angle of (almost) 90 °C on the bi-plot are not correlated. In Figure 8, the main components of stainless steel and nickel-based alloys (chromium, nickel and molybdenum) make an angle of almost 90 °C with vector corrosion rate. Therefore, little or no correlation is found between the alloying element. This result (for both pH values) is somewhat unexpected, because, especially for the chromium, a large body of the literature reports higher resistance due to increasing chromium content [43–45]. The vector "pH", on the contrary, does have the same direction as the vector that represents the corrosion rate. Hence, the PCA analysis suggests a proportional correlation between both parameters. This implies that the corrosion rates measured at pH 13.5 are significantly higher than at pH 12.5. This is consistent with the studies of Li and Luo et al., who found that this adverse effect is because of a lower Cr^{3+} content inside the passive film at pH 13.5 [17,18].

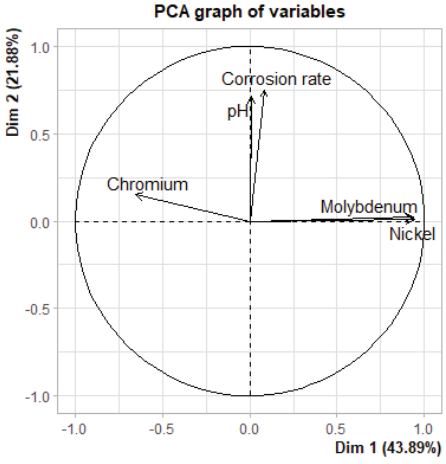

Figure 8. Biplot of the PCA—analysis to check the influence of alloying elements and the pH of the pore solution on the measured uniform corrosion rate.

To check the developed correlations of the PCA analysis, an additional Spearman test was performed (Table 5) [46]. The results of the Spearman test are in good agreement with the PCA biplot, and confirm that there is no significant effect of the alloying elements on the corrosion rate. All three alloying elements showed a high *p*-value (>0.1). Hence, the null hypothesis (no effect of tested parameter on corrosion behavior) cannot be rejected. For the pH of the pore solution, a *p*-value of 0.07 was found. A common practice is to reject the null hypothesis only if the *p*-value is lower than 0.05, although some studies suggest that 0.1 can also be used as a threshold value [47]. If a significance level of 10% (*p*-value = 0.1) is used, the null hypothesis can be rejected. By doing so, the Spearman test proves that the pH of the pore solution affects the corrosion behavior. The positive rho (ρ) coefficient suggests that the correlation between pH and the corrosion rate is proportional, similar to what was found by the PCA. However, the somewhat low value of the rho (ρ) coefficient implies that this significant effect is rather weak.

Table 5. A Spearman correlation test on the uniform corrosion rates.

Parameter	*p*-Value Spearman	Spearman Correlation Coefficient
Chromium	0.85	0.02
Molybdenum	0.28	0.12
Nickel	0.13	0.17
pH	0.07	0.2

4. Conclusions

The aim of this paper was to study the corrosion behaviors of austenitic, super-austenitic and nickel-based alloys in contaminated pore solutions. These materials are considered as possible construction materials for the envelope of the Belgian supercontainer for the disposal of highly active radioactive waste. The study explored the pitting susceptibility and general corrosion of the promising materials under aerobic conditions.

In general, in an aerobic environment (without the presence of any reduced sulfur), good pitting resistance was observed for all tested candidate materials. No pitting corrosion was observed for LDX2304 and AISI 316L in high chloride pore solutions at 60 °C, which is somewhat surprising due to their low PREN value. Tafel extrapolation was used to calculate uniform corrosion rates. Corrosion rates of 0.44–4.2 μm/y were found in pore solutions containing 1 M Cl^- at an elevated temperature of 60 °C. These corrosion rates agree with other electrochemical studies, but are much higher than corrosion rates calculated by gas measuring cells (long-term immersion tests) [48]. The statistical evaluations (Kruskal–Wallis and Dunn tests) suggest that significant differences are present between the tested materials. 254SMO, C-22, AISI 316L and LDX2304 showed excellent uniform corrosion resistance in both pore solutions, and therefore, these materials are interesting for further research. However, with the higher standard deviation, caution must be applied, as comparison of Tafel extrapolated corrosion rates becomes quite difficult.

It was not possible to find a significant correlation between the main alloying elements and the measured corrosion rates. This was a surprising finding, especially because a beneficial effect of chromium on corrosion resistance is often reported in the literature [43–45]. The pH of the pore solution, however, did affect the corrosion behavior. This is confirmed by the PCA biplot and the Spearman test (significance level 10%). The effect was directly proportional, thus candidate materials showed a higher corrosion rate in pore solutions with higher alkalinity. A possible explanation for this may be the more protective behavior of passive layers at pH 12.5 compared to pH 13.5.

The question was raised whether lean duplex and traditional austenitic grades also perform well in more aggressive environments, as expected under sulfur-rich anaerobic conditions, which will be the topic of a follow-up paper.

Author Contributions: Conceptualization, P.V.A., W.B., R.G. and R.D.; methodology, B.V., P.V.A., W.B., R.G., J.B., B.R. and R.D.; software, B.V.; validation, B.V. and J.B.; writing—original draft preparation, B.V.; writing—review and editing, P.V.A., W.B, R.G., J.B., B.R. and R.D.; supervision, P.V.A., W.B., R.G., B.R. and R.D.; project administration, P.V.A., W.B., R.G., R.D.; funding acquisition, R.G. and R.D. All authors have read and agreed to the published version of the manuscript.

Funding: The authors would like to thank the Belgian Agency for Radioactive Waste and Enriched Fissile Materials (ONDRAF/NIRAS) for the financial support, as well as the Private Foundation De Nayer for funding the electrochemical test equipment.

Institutional Review Board Statement: Not applicable.

Informed Consent Statement: Not applicable.

Data Availability Statement: The data used to support the findings of this study are included within the article.

Conflicts of Interest: The authors declare no conflict of interest. The funders had no role in the design of the study; in the collection, analyses, or interpretation of data; in the writing of the manuscript, or in the decision to publish the results.

References

1. Dehandschutter, B.; Sintubin, M.; Vandenberghe, N.; Vandycke, S.; Gaviglio, P.; Wouters, L. Fracture analysis in the Boom clay (URF, Mol, Belgium). *Aardkd. Meded.* **2002**, *12*, 245–248.
2. Kursten, B.; Druyts, F.; Gens, R. The Belgian Supercontainer concept–corrosion issues. In *Sulphur-Assisted Corrosion in Nuclear Disposal Systems*; CRC Press: Boca Raton, FL, USA, 2020; pp. 1–18.
3. Kursten, B.; Smart, N.R.; Senior, N.A.; Macdonald, D.D.; Caes, S.; De Souza, V.; Gaggiano, R. Overview of anaerobic corrosion of carbon steel radioactive waste packages in alkaline media in support of the Belgian supercontainer concept. *Mater. Corros.* **2021**, *72*, 32–51. [CrossRef]
4. Bel, J.J.; Wickham, S.M.; Gens, R.M. Development of the Supercontainer design for deep geological disposal of high-level heat emitting radioactive waste in Belgium. *MRS Online Proc. Libr. (OPL)* **2006**, *932*, 122.1. [CrossRef]
5. Xia, D.; Song, S.; Zhu, R.; Behnamian, Y.; Shen, C.; Wang, J.; Luo, J.; Lu, Y.; Klimas, S. A mechanistic study on thiosulfate-enhanced passivity degradation of Alloy 800 in chloride solutions. *Electrochim. Acta* **2013**, *111*, 510–525. [CrossRef]
6. Naghizadeh, M.; Nakhaie, D.; Zakeri, M.; Moayed, M.H. Effect of thiosulfate on pitting corrosion of 316ss: I. critical pitting temperature and pit chemistry. *J. Electrochem. Soc.* **2014**, *162*, C71. [CrossRef]
7. Zanotto, F.; Grassi, V.; Balbo, A.; Monticelli, C.; Zucchi, F. Stress corrosion cracking of LDX 2101® duplex stainless steel in chloride solutions in the presence of thiosulphate. *Corros. Sci.* **2014**, *80*, 205–212. [CrossRef]
8. Chasse, K.R.; Raji, S.; Singh, P.M. Effect of chloride ions on corrosion and stress corrosion cracking of duplex stainless steels in hot alkaline-sulfide solutions. *Corrosion* **2012**, *68*, 932–949. [CrossRef]
9. Xia, D.H.; Zhu, R.K.; Behnamian, Y.; Luo, J.L.; Lin, C.J.; Klimas, S. Understanding the interaction of thiosulfate with Alloy 800 in aqueous chloride solutions using SECM. *J. Electroanal. Chem.* **2015**, *744*, 77–84. [CrossRef]
10. Xia, D.H.; Zhu, R.K.; Behnamian, Y.; Shen, C.; Luo, J.L.; Lu, Y.C.; Klimas, S. pH effect on sulfur-induced passivity degradation of alloy 800 in simulated crevice chemistries. *J. Electrochem. Soc.* **2014**, *161*, C201. [CrossRef]
11. Bhattacharya, A.; Singh, P.M. Electrochemical behaviour of duplex stainless steels in caustic environment. *Corros. Sci.* **2011**, *53*, 71–81. [CrossRef]
12. Stansbury, E.E.; Buchanan, R.A. *Fundamentals of Electrochemical Corrosion*; ASM International: Almere, The Netherlands, 2000.
13. Xiao, Y.; Tang, J.; Wang, Y.; Lin, B.; Nie, Z.; Li, Y.; Normand, B.; Wang, H. Corrosion behavior of 2205 duplex stainless steel in NaCl solutions containing sulfide ions. *Corros. Sci.* **2022**, *200*, 110240. [CrossRef]
14. Araneda, A.A.B.; Kappes, M.A.; Rodríguez, M.A.; Carranza, R.M. Pitting corrosion of Ni-Cr-Fe alloys at open circuit potential in chloride plus thiosulfate solutions. *Corros. Sci.* **2022**, *198*, 110121. [CrossRef]
15. Feng, X.; Zhang, T.; Zhu, R.; Chen, Z.; Lu, X. Pitting initiation on 304 stainless steel in a chloride-contaminated pore solution under alternating temperature conditions. *Corros. Rev.* **2022**, *40*. [CrossRef]
16. Giebel, B. Austenitic, Duplex, and Lean Duplex Stainless Steel Critical Pitting Temperature in Simulated Concrete Environment. Bachelor's Thesis, The University of Akron, Akron, OH, USA, 2022.
17. Li, B.; Zhang, W. Electrochemical and corrosion behavior of 2205 duplex stainless steel in simulated concrete pore solution. *Int. J. Electrochem. Sci.* **2017**, *12*, 8432–8446. [CrossRef]
18. Luo, H.; Su, H.; Dong, C.; Li, X. Passivation and electrochemical behavior of 316L stainless steel in chlorinated simulated concrete pore solution. *Appl. Surf. Sci.* **2017**, *400*, 38–48. [CrossRef]
19. Gastaldi, M.; Bertolini, L. Effect of temperature on the corrosion behaviour of low-nickel duplex stainless steel bars in concrete. *Cem. Concr. Res.* **2014**, *56*, 52–60. [CrossRef]
20. Blanco, G.; Bautista, A.; Takenouti, H. EIS study of passivation of austenitic and duplex stainless steels reinforcements in simulated pore solutions. *Cem. Concr. Compos.* **2006**, *28*, 212–219. [CrossRef]
21. Moser, R.D.; Singh, P.M.; Kahn, L.F.; Kurtis, K.E. Chloride-induced corrosion resistance of high-strength stainless steels in simulated alkaline and carbonated concrete pore solutions. *Corros. Sci.* **2012**, *57*, 241–253. [CrossRef]
22. Elsener, B.; Addari, D.; Coray, S.; Rossi, A. Stainless steel reinforcing bars–reason for their high pitting corrosion resistance. *Mater. Corros.* **2011**, *62*, 111–119. [CrossRef]
23. Dong, C.; Luo, H.; Xiao, K.; Sun, T.; Liu, Q.; Li, X. Effect of temperature and Cl^- concentration on pitting of 2205 duplex stainless steel. *J. Wuhan Univ. Technol.-Mater. Sci. Ed.* **2011**, *26*, 641–647. [CrossRef]
24. *ASTM G5-94*; Standard Reference Test Method for Making Potentiostatic and Potentiodynamic Anodic. American Society for Testing and Materials International (ASTM): West Conshohocken, PA, USA, 2004; 94, pp. 1–12. [CrossRef]
25. Kelly, R.G.; Scully, J.R.; Shoesmith, D.; Buchheit, R.G. *Electrochemical Techniques in Corrosion Science and Engineering*; CRC Press: Boca Raton, FL, USA, 2002.
26. Ostertagova, E.; Ostertag, O.; Kováč, J. Methodology and application of the Kruskal-Wallis test. In *Applied Mechanics and Materials*; Trans Tech Publications Ltd.: Zurich, Switzerland, 2014; Volume 611, pp. 115–120.
27. Dinno, A.; Dinno, M.A. *Package 'Dunn. Test'*; The Comprehensive R Archive Network (CRAN) Repository: Vienna, Austria, 2017; Volume 10, pp. 1–7.

28. Esmailzadeh, S.; Aliofkhazraei, M.; Sarlak, H. Interpretation of cyclic potentiodynamic polarization test results for study of corrosion behavior of metals: A review. *Prot. Met. Phys. Chem. Surf.* **2018**, *54*, 976–989. [CrossRef]
29. Ezuber, H.; Alshater, A.; Nisar, S.O.; Gonsalvez, A.; Aslam, S. Effect of surface finish on the pitting corrosion behavior of sensitized AISI 304 austenitic stainless steel alloys in 3.5% NaCl solutions. *Surf. Eng. Appl. Electrochem.* **2018**, *54*, 73–80. [CrossRef]
30. Mesquita, T.J.; Chauveau, E.; Mantel, M.; Kinsman, N.; Roche, V.; Nogueira, R.P. Lean duplex stainless steels—The role of molybdenum in pitting corrosion of concrete reinforcement studied with industrial and laboratory castings. *Mater. Chem. Phys.* **2012**, *132*, 967–972. [CrossRef]
31. Elsener, B.; Addari, D.; Coray, S.; Rossi, A. Nickel-free manganese bearing stainless steel in alkaline media—Electrochemistry and surface chemistry. *Electrochim. Acta* **2018**, *56*, 4489–4497. [CrossRef]
32. Bertolini, L.; Bolzoni, F.; Pastore, T.; Pedeferri, P. Behaviour of stainless steel in simulated concrete pore solution. *Br. Corros. J.* **1996**, *31*, 218–222. [CrossRef]
33. Nürnberger, U. Stainless steel reinforcement—A survey. Überblick, Nichtrostende Betonstähle–Ein, and Armatures en Acier Inoxydable–Un Aperçu. *Otto-Graf-J.* **2005**, *16*, 111.
34. Korb, L.J.; Olson, D.L. *ASM Metals Handbook*; Corrosion Houston; ASM International: Almere, The Netherlands, 1987; Volume 13.
35. Klapper, H.S.; Stevens, J.; Wiese, G. Pitting corrosion resistance of CrMn austenitic stainless steel in simulated drilling conditions—Role of pH, temperature, and chloride concentration. *Corrosion* **2013**, *69*, 1095–1102. [CrossRef]
36. Blackwood, D.J.; Gould, L.J.; Naish, C.C.; Porter, F.M.; Rance, A.P.; Sharland, S.M.; Smart, N.R.; Thomas, M.I.; Yates, T. The localised corrosion of carbon steel and stainless steel in simulated repository environments. *AEAT/ERRA* **2002**, *318*.
37. McDonald, D.B.; Sherman, M.R.; Pfeifer, D.W.; Virmani, Y.P. Stainless steel reinforcing as corrosion protection. *Concr. Int.* **1995**, *17*, 65–70.
38. Yau, T.L.; Webster, R.T. Corrosion of zirconium and hafnium. In *Metals Handbook*, 9th ed.; ASM International: Almere, The Netherlands, 1987; Volume 13.
39. King, F.; Padovani, C. Review of the corrosion performance of selected canister materials for disposal of UK HLW and/or spent fuel. *Corros. Eng. Sci. Technol.* **2011**, *46*, 82–90. [CrossRef]
40. Hua, F.; Rebak, R.B.; Gordon, G.M.; Mon, K. Degradation in Modes of Alloy 22 in Yucca Mountain Repository Conditions. Paper Presented at the CORROSION, San Diego, CA, USA, 12–16 March 2006.
41. Dinno, A. Nonparametric pairwise multiple comparisons in independent groups using Dunn's test. *Stata J.* **2015**, *15*, 292–300. [CrossRef]
42. Lê, S.; Josse, J.; Husson, F. FactoMineR: An R package for multivariate analysis. *J. Stat. Softw.* **2008**, *25*, 1–18. [CrossRef]
43. Yu, Y.; Shironita, S.; Souma, K.; Umeda, M. Effect of chromium content on the corrosion resistance of ferritic stainless steels in sulfuric acid solution. *Heliyon* **2018**, *4*, e00958. [CrossRef]
44. Fauvet, P. Corrosion issues in nuclear fuel reprocessing plants. In *Nuclear Corrosion Science and Engineering*; Woodhead Publishing: Sawston, UK, 2012; pp. 679–728.
45. Outokumpu. *The Effects of Alloying Elements*; Outokumpu: Helsinki, Finland, 2017.
46. Mann, P.S. *Introductory Statistics*; John Wiley & Sons: Hoboken, NJ, USA, 2007.
47. Ugoni, A. On the subject of hypothesis testing. *COMSIG Rev.* **1993**, *2*, 45. [PubMed]
48. Fujisawa, R.; Kurashige, T.; Inagaki, Y.; Senoo, M. Gas generation behavior of transuranic waste under disposal conditions. *MRS Online Proc. Libr. (OPL)* **1999**, *556*, 1199. [CrossRef]

processes

MDPI

Article

Azithromycin Adsorption onto Different Soils

Raquel Cela-Dablanca [1,*], Ana Barreiro [1], Lucía Rodríguez-López [2], Paula Pérez-Rodríguez [2], Manuel Arias-Estévez [2], María J. Fernández-Sanjurjo [1], Esperanza Álvarez-Rodríguez [1] and Avelino Núñez-Delgado [1]

[1] Department Soil Science and Agricultural Chemistry, Engineering Polytechnic School, Universidad Santiago de Compostela, 27002 Lugo, Spain
[2] Soil Science and Agricultural Chemistry, Faculty Sciences, University of Vigo, 32004 Ourense, Spain
* Correspondence: raquel.dablanca@usc.es

Abstract: The antibiotic azithromycin (AZM) is one of the most persistent in the environment, with potential to cause serious health and environmental problems. As some polluting discharges containing this antibiotic can reach the soil, it is clearly relevant determining the ability of soils with different characteristics to retain it. In this research, AZM adsorption and desorption were studied for a variety of soils, using batch-type experiments. The results show that, at low doses of antibiotic added (less than or equal to 50 μmol L^{-1}), the adsorption always reached 100%, while when higher concentrations were added (between 200 and 600 μmol L^{-1}) the highest adsorption corresponded to soils with higher pH values. Adsorption data were fitted to the Linear, Langmuir and Freundlich models, with the latter showing the best fit, in view of the determination coefficient. No desorption was detected, indicating that AZM is strongly adsorbed to the soils evaluated, suggesting that the risks of environmental problems due to this contaminant are minimized for these edaphic media. These results can be considered relevant with respect to risk assessment and possible programming of measures aimed at controlling environmental contamination by emerging contaminants, especially from the group of antibiotics, and in particular from AZM.

Keywords: antibiotic; emerging contaminants; adsorption; desorption; environment

Citation: Cela-Dablanca, R.; Barreiro, A.; Rodríguez-López, L.; Pérez-Rodríguez, P.; Arias-Estévez, M.; Fernández-Sanjurjo, M.J.; Álvarez-Rodríguez, E.; Núñez-Delgado, A. Azithromycin Adsorption onto Different Soils. *Processes* **2022**, *10*, 2565. https://doi.org/10.3390/pr10122565

Academic Editor: Jesús M. Marín-Benito

Received: 18 October 2022
Accepted: 25 November 2022
Published: 2 December 2022

1. Introduction

Azithromycin (AZM) is a semi-synthetic broad spectrum antibiotic belonging to the subclass of second-generation macrolides [1]. It is used to treat bacterial infections in infants and in people with weaker immune systems, among other diseases [2]. In the US, AZM is among the first-line agents prescribed for infectious diseases [3]. In 30 European countries, this group of antimicrobials together with beta-lactams, lincosamides, streptogramins and tetracyclines accounted for 83.5% of total antibiotic sales in 2013 [4]. This antibiotic is on the DU75 list (among the 75% of the most consumed antibiotics) in 24 of 46 countries in the European area [5]. In addition, during 2020 the use of AZM increased significantly in Spain [6].

When AZM, as well as other antibiotics and other emerging contaminants, reach the environment through polluting discharges, it is considered a cause of concern, especially taking into account the high concentrations detected in aquatic environments [7–10]. In fact, there are several routes for antibiotics to reach the environment as pollutants, but the main one is through wastewater [11]. The cause is that, after their administration as drugs, these antimicrobials are partially metabolized and released through urine and feces [12]. Specifically regarding AZM, 75% of it is excreted after being administered [13], reaching wastewater treatment plants.

The efficacy of these treatment plants is dependent on factors such as the type of treatment, or the nature and properties of the antibiotic to be treated. Specifically, AZM belongs to a group of antibiotics of special relevance in view of its prevalence in the

environment, due to its persistence and resistance to biological degradation [14]. The effectiveness of different treatments applied in wastewater treatment plants to retain this antibiotic was studied by Mirzaei et al. [15], finding that the efficiency of one of the treatments ranged from 0% to 74.9%, while another treatment was not effective in removing AZM. In addition, in a study carried out in twelve wastewater plants in China [16], it was found that AZM was one of the antibiotics that appeared most frequently, and it was affected by the lowest elimination rate efficiency, specifically 6.3%.

Antibiotics that cannot be eliminated after wastewater treatment persist in these waters and/or end up in the sludge generated by this treatment, reaching agricultural soils through the application of irrigation wastewaters and/or biosolids [17]. In a study by Rodríguez-Mozaz et al. [18], the authors found the presence of AZM in a range of 45.2–597.5 ng L^{-1}, with Portugal showing the highest concentrations of this antibiotic, while the minimum values were obtained in Cyprus. In North America, Europe and elsewhere, the use of biosolids as agricultural soil amendment is permitted [19], and specifically, in the EU-27, 53% of the total sludge produced is recycled in agriculture directly or after composting [20]. In some countries such as Denmark, France, the Walloon region of Belgium, Ireland, Spain and the United Kingdom, more than half of the sludge production ends up on agricultural land, while in other countries such as Finland, the Netherlands, Slovakia, Greece and Slovenia, the amounts are less than 5% [21].

The persistence of antibiotics in these sludges can lead to contamination of the soil and other environmental compartments, such as surface water and groundwater by leaching or runoff processes, or even enter the food chain through vegetables grown in contaminated soils [22]. Walters et al. [23] carried out a study on the persistence of antibiotics in mixtures of biosolids with soils and found that AZM had a half-life of 408–3466 days. Of special concern as regards health risks related to the presence of antibiotics in soil are the emergence and spread of antibiotic resistance in pathogenic bacteria [24].

The characterization of the retention and release processes of these antibiotics in soils amended with biosolids is essential to evaluate their transport and the risks associated with their presence [25]. The behavior of these contaminants in the soil depends on edaphic characteristics, such as organic carbon and clay contents, texture and pH [26] and on antibiotics properties, such as hydrophobicity, solubility and molecular structure [27] and their degrees of ionization [28]. The dissociation constant (pK_a) is a parameter to predict the ionization state of a molecule with respect to pH [29]. The antibiotic AZM has two pk_a values, pk_{a1} = 8.74 and pk_{a2} = 9.45, causing that in most soils the molecule behaves as cation [30], however, some authors indicate only one pk_a value, being 7.25 [31] or 8.96 [32]. This antibiotic presents multi-basic amines, having pk_a values that could allow suffering protonation in a rather specific (physiological) pH range [33].

It is also interesting to determine and bear in mind the sensitivity of these molecules to different environmental conditions that could affect their degradation [34].

Taking all of the above into account, the objective of this work is to determine AZM adsorption and desorption on/from soils with different physical-chemical properties. This will be key to evaluating the risk that the presence of this antibiotic may pose in the soil environment, as well as, due to its eventual mobility, the risk of pollution affecting to other different environmental compartments.

2. Materials and Methods

2.1. Soils

A total of 21 soils were selected for the study, all of them previously sampled at different areas of Galicia (NW Spain). Six of the soils correspond to plots planted with corn/maize (designated with codes from M1 to M6), while twelve soils were from vineyards (from VO1 to VO5 -Ourense province-, and from VP1 to VP7 -Pontevedra province), and three were forest soils, of which one was pine forest (FP), another eucalyptus (FE) and another oak (*Q. robur*) (FR). These soils were selected based on their pH values and organic

matter contents. Table S1 (Supplementary Material) shows some characteristics of the areas where the soil samples were collected.

Each soil sample was made up of 10 subsamples collected in a zig-zag pattern in the surface layer (0–20 cm). Once collected, the samples were dried at 40 °C to constant weight, and then sieved through a 2 mm diameter sieve and stored until analysis. The soils used in this work were previously characterized by Cela-Dablanca et al. [35]. Table S2 (Supplementary Material) shows the main physical-chemical properties of the selected soils.

2.2. Chemical Reagents

The AZM used was supplied by Sigma-Aldrich (Barcelona, Spain). Figure S1 (Supplementary Material) shows the molecular structure of AZM. Potassium phosphate (purity $\geq$ 99.5%) and acetonitrile (purity $\geq$ 99.9%) used for HPLC were supplied by Fisher Scientific (Madrid, Spain) and $CaCl_2$ (95% purity) by Panreac (Barcelona, Spain). To carry out HPLC determinations, all solutions were prepared with milliQ water (Millipore, Madrid, Spain).

2.3. Sorption and Desorption Experiments

Batch-type experiments were carried out to study the adsorption/desorption of AZM on/from the different soils. For this, 2 g of each sample were weighed, then adding 5 mL of a solution with different concentrations of the antibiotic (2.5, 5, 10, 20, 30, 40, 50, 200, 400, and 600 μmol L^{-1}), also containing 0.005 M $CaCl_2$ as background electrolyte. The suspensions were shaken in the dark for 48 h (time enough to reach equilibrium, according to previous kinetic tests) using a rotary shaker. These suspensions were then centrifuged at 4000 rpm for 15 min (G force: 1931.91). The resulting supernatants were filtered through 0.45 μm nylon syringe filters. Finally, the antibiotic concentrations in the equilibrium solution were determined by HPLC-UV with a LPG 3400 SD equipment (Thermo-Fisher, Waltham, MA, USA). The quantification method, as well as further details regarding adsorption and desorption experiments, are shown in Supplementary Material.

2.4. Data Treatment

The experimental data obtained in the adsorption/desorption tests were adjusted to the Freundlich (Equation (1)), Langmuir (Equation (2)) and Linear (Equation (3)) models [36].

$$q_e = K_F C_{eq}^n \quad (1)$$

$$q_e = \frac{K_L\, C_{eq} q_m}{1 + K_L C_{eq}} \quad (2)$$

$$q_e = K_d C_{eq} \quad (3)$$

where q_e (expressed in μmol kg^{-1}) is the amount of antibiotic retained onto the soil (calculated as the difference between the concentration added and that remaining in the equilibrium solution); K_F (Ln μmol^{1-n} kg^{-1}) is the Freundlich constant related to the adsorption capacity; C_{eq} (μmol L^{-1}) is the concentration of antibiotic present in the solution at equilibrium; n (dimensionless) is a parameter of the Freundlich model associated with the degree of heterogeneity of the adsorption; K_L (L μmol^{-1}) is the Langmuir adsorption constant; q_m (μmol kg^{-1}) is the maximum adsorption capacity according to the Langmuir model; and K_d (L kg^{-1}) is the partition coefficient in the linear model.

In addition, soil properties were correlated with the parameters obtained in the adjustments to the adsorption models, determining the Pearson correlation coefficients.

The SPSS Statistics 21 software was used to carry out the adjustment of the data derived from the adsorption experiments to the Langmuir, Freundlich and Linear models, as well as any further statistical analysis.

3. Results and Discussion

3.1. Adsorption

Figure 1 shows relations among equilibrium concentrations and AZM adsorption for the different soils. The results indicate that the corn/maize soils have a maximum adsorption value of 1256.77 μmol kg^{-1}, similar to that found in vineyard soils, which specifically reach 1229.38 and 1318.21 μmol kg^{-1} in granite soils and in slate/schist soils, respectively. Regarding forest soils, AZM adsorption is much lower than in crop soils, with maximum value (228.84 μmol kg^{-1}) found in the eucalyptus soil sample. Regarding the minimum adsorption scores, for the highest AZM concentration added they were the following: 754.04 μmol kg^{-1} in soils with corn cultivation, 690.96 μmol kg^{-1} in granite vineyard soils, 401.27 μmol kg^{-1} in slate/schist vineyard soils, and 187.29 μmol kg^{-1} in forest soils.

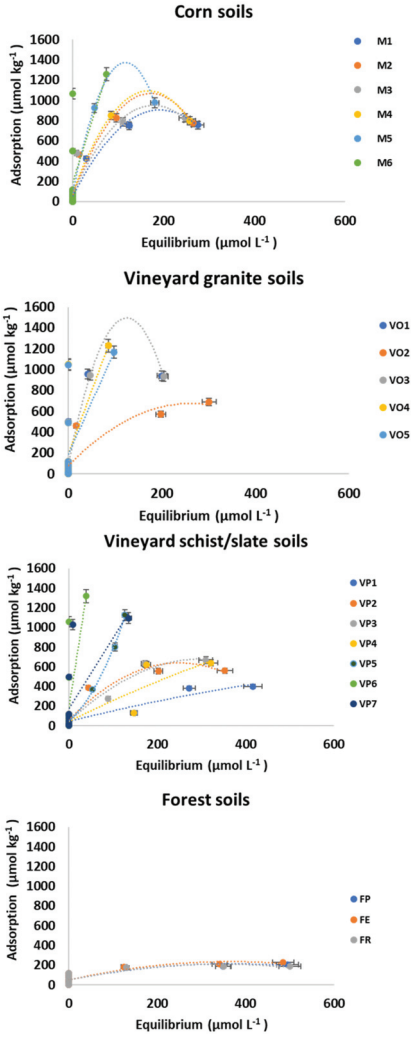

Figure 1. AZM adsorption curves for the different soils studied. M: corn/maize soils, VO: vineyard soils (Ourense Province), VP: vineyard soils (Pontevedra province), FP: forest soil (*P. pinaster*), FE: forest soil (*E. nitens*), FR: forest soil (*Q. robur*), 1–7: different soil samples. Error bars indicate standard deviation.

Figure 2 shows that the percentage adsorption values were 100% for all the soils when the antibiotic concentrations added were in the range of 2.5–50 μmol L^{-1}, while marked differences are observed among the different soils when the highest AZM concentrations (200–600 μmol L^{-1}) were added. To note that, in general, in this last range of concentrations added the percentage of adsorption decreases as the concentration of antibiotic added increases, probably due to the saturation of the adsorption sites [37]. Considering specific values, most maize soils show high adsorption percentages, ranging between 52.29% and 100%, very close to those obtained in granite vineyard soils, which range between 47.92% and 100%. Adsorption on slate/schists vineyard soils varied over a broader range (from 26.12% to 100%). On the other hand, forest soils were those that presented the lowest adsorption scores (between 13.25% and 37.27%).

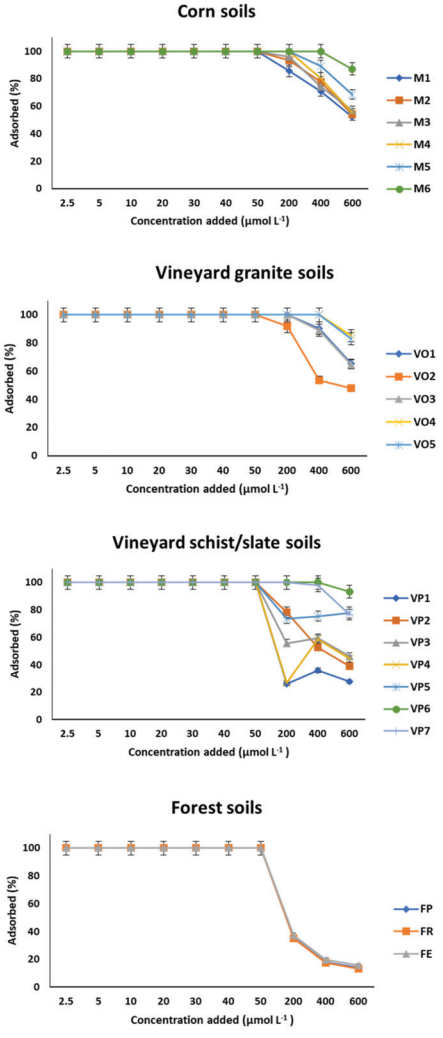

Figure 2. AZM adsorption percentages for the soils studied, as a function of the AZM concentration added. M: corn/maize soils, VO: vineyard soils (Ourense Province), VP: vineyard soils (Pontevedra province), FP: forest soil (*P. pinaster*), FE: forest soil (*E. nitens*), FR: forest soil (*Q. robur*), 1–7: different soil samples. Error bars indicate standard deviation.

When comparing adsorption data with soil characteristics (Table S2, Supplementary Material) it is clear that the soils showing higher adsorption were those having higher pH values (M5, M6, VP6 and VP7). In fact, adsorption data were correlated with soil properties, indicating that AZM adsorption correlates positively and significantly with soil pH (r = 0.562 and $p < 0.01$) (Table 1). To note that pH is one of the parameters having greater influence on antibiotic-adsorbent interactions, since it simultaneously affects the chemical speciation of the pollutants and adsorbent surfaces [38]. Both antibiotics and soil components have functional groups that may suffer protonation/deprotonation, depending on the pH of the solution. This makes it possible for there to have positive, negative or neutral charges on the reactive surfaces, and therefore allows the formation of different types of bonds [39]. The pK_a of AZM is approximately between 8.6–9.5, so in an acid medium this antibiotic is protonated [40]. In the pH range of the soils included in this study (4.68–8.02), AZM has positively charged functional groups, thus favoring electrostatic interactions with the negatively charged surfaces of minerals and organic matter [41,42].

Table 1. Correlations between AZM adsorption values and soil properties. OM: organic matter; Al_{ox}: Non-crystalline aluminum (extracted with ammonium oxalate).

Soil Property	Correlation Coefficient (r)	Significance Level (p)
pH	0.562	0.01
OM	0.530	0.05
Al_{ox}	−0.43	0.05

Soil organic matter and the non-crystalline Fe and Al components have variable charge, with negative charge increasing as the pH rises, favoring higher AZM adsorption to these charged surfaces, as AZM is mainly present as a divalent cation. For this reason, forest soils, despite the fact that they have a high content of both organic matter and non-crystalline minerals, present low AZM adsorption when the antibiotic is added at concentrations above 200 μmol L^{-1}. This is due to the fact that their pH is very low and there are few negative charges. However, soils having lower organic matter and non-crystalline minerals contents (M5, M6, VO4, VP6, VP7), show higher adsorption than forest soils, because they have a pH >5.8 and higher presence of negative charges. This would explain the significant ($p < 0.05$) and negative correlation obtained between the maximum adsorption of each soil with the organic matter content (r = −0.53) and the total non-crystalline Al extracted with ammonium oxalate (r = −0.43) (Table 1). Other authors also found no positive correlations between non-crystalline Fe components and AZM adsorption [43]. However, in our study we not found any correlations (positive or negative) with this parameter. The high AZM adsorption obtained in the current study for various agricultural soils (Figures 1and 2) is consistent with that found in other researches carried out with high concentrations of this antibiotic in amended crop soils, which on the other hand showed that this drug does not cause toxicity in crops or soil microorganisms [44,45].

The adsorption data were fitted to the Linear, Freundlich and Langmuir models, which are the most commonly used to establish equilibrium relations between an adsorbent and an adsorbate, or between the amount adsorbed to a solid phase and that which remains in solution at a given temperature under equilibrium conditions [30].

Table 2 shows the adsorption parameters obtained from the fit of the experimental data to the Freundlich, Langmuir and Linear adsorption models.

Taking into account the values of the coefficient of determination (R^2), it can be considered that the model showing a better fit was the Freundlich equation, with R^2 greater than 0.85 for the 33% soils, while the Langmuir model obtained a R^2 value > 0.85 for 23% of the soils, and for the Linear model this porcentage decrease until 9%. However, in the Freundlich and in the Langmuir model, very high error values were associated with the estimation of the parameters in many cases, so they would not satisfactorily explain AZM adsorption in these soils. To note that some authors indicate that AZM follows linear

adsorption models in soils amended with biosolids [46], although the soils in the current study have higher pH values.

Table 2. Fitting of the adsorption data to the Freundlich, Langmuir and Linear models. K_F expressed in L^n μmol^{1-n} kg^{-1}; n is dimensionless; K_L expressed in L μmol^{-1}; q_m expressed in μmol kg^{-1}; K_d expressed in L kg^{-1}; -: error values too high for fitting.

	Freundlich					Langmuir					Linear		
Soil	K_F	**Error**	n	**Error**	R^2	K_L	**Error**	q_m	**Error**	R^2	K_d	**Error**	R^2
M1	95.986	50.522	0.387	0.103	0.89	0.028	0.012	901.315	100.849	0.94	3.403	0.55	0.67
M2	341.346	94.081	0.161	0.057	0.95	0.097	0.037	852.124	60.454	0.96	3.653	0.77	0.52
M3	354.449	72.119	0.159	0.042	0.97	0.167	0.058	837.409	49.227	0.97	4.026	0.72	0.62
M4	-	-	-	-	-	-	-	-	-	-	3.787	0.9	0.44
M5	-	-	-	-	-	-	-	995.768	258.357	0.8	6.309	1.42	0.49
M6	9.471	0	1.136	0.073	0.31	-	-	1600	0	0.31	16.97	5.08	0.31
VO1	-	-	-	-	-	-	-	-	-	-	5.456	1.43	0.39
VO2	314.979	91.637	0.128	0.057	0.94	0.143	0.085	-	-	0.94	2.532	0.41	0.66
VO3	-	-	-	-	-	-	-	-	-	-	5.376	1.35	0.42
VO4	9.219	0	1.101	0.072	0.31	-	-	1600	0	0.31	14.46	4.36	0.31
VO5	8.87	0	1.066	0.073	0.27	-	-	1554.29	0	0.27	11.99	3.78	0.27
VP1	-	-	0.829	0.365	0.79	-	-	-	-	-	1.08	0.13	0.79
VP2	203.771	95.973	0.178	0.089	0.93	0.041	0.026	608.522	66.977	0.93	1.952	0.32	0.65
VP3	-	-	0.552	0.182	0.91	-	-	-	-	-	2.546	0.26	0.86
VP4	-	-	0.872	0.418	0.77	-	-	-	-	-	2.149	0.29	0.77
VP5	-	-	1.326	0.213	0.98	-	-	-	-	-	8.274	0.4	0.97
VP6	10.24	0	1.327	0.082	0.36	-	-	1600	0	0.36	33.87	9.59	0.36
VP7	-	-	-	-	–	-	-	1099.382	190.379	0.84	8.581	2.56	0.3
FP	-	-	-	-	–	-	-	209.883	80.292	0.44	0.493	0.11	0.2
FR	-	-	-	-	–	-	-	192.928	73.297	0.4	0.466	0.11	0.1
FE	-	-	-	-	–	-	-	242.635	87.674	0.54	0.559	0.11	0.33

The values of the distribution coefficient of the linear model (K_d), a parameter related to the adsorption intensity, range between 3.403 and 16.973 L kg^{-1} in maize soils, between 2.532 and 14.463 L kg^{-1} in vineyard granite soils, between 1.080 and 33.867 L kg^{-1} in slate/schists vineyards, and between 0.466 and 0.599 L kg^{-1} in forest soils. The lower values of forest soils indicate greater AZM mobility in them [47]. These values are higher than those obtained in previous studies for sulfonamides [48], but lower than those obtained for tetracyclines [49], indicating that interactions with these soils that give rise to AZM adsorption are stronger than those of sulfonamides and weaker than those of tetracyclines. As for the values of the Freundlich affinity coefficient (K_F), related to the soil adsorption capacity, they indicate that corn and vineyard soils on granite are the ones with the highest affinity for AZM adsorption.

Bearing in mind that the lower the value of n, the more heterogeneous the adsorption surface [50], and also that values of this parameter being between 1 and 10 indicate favorable conditions for adsorption [51], the fact that some of the maize and vineyard soils in this study are the ones with the lowest n values would indicate that they are the ones with a more heterogeneous surface. As comparison, Bao et al. [52] obtained lower n values for tetracycline in forest than in agricultural soils. Regarding the Langmuir model, the lowest values of the q_m parameter (the maximum Langmuir's adsorption capacity) corresponded to some of the forest soils, which would confirm that these soils are the ones with the lowest adsorption capacity.

3.2. Desorption

The desorbed AZM concentrations were lower than the detection limit in all the soils studied and for all the antibiotic concentrations added. These results indicate that AZM is adsorbed very strongly onto these soils, causing that the retention process could be

considered almost not reversible under the conditions of this study. These results are consistent with previous research indicating strong AZM adsorption in both biosolids [42] and biosolids-amended soils [30].

4. Conclusions

When AZM concentrations of up to 50 μmol L^{-1} are added to the soils used in this research, its adsorption was 100% in all of them, while when the concentration added was equal to or greater than 200 μmol L^{-1}, some differences were observed, with those soils having higher pH showing higher adsorption. Adsorption data fitted better to the Freundlich model, in the sense of presenting higher determination coefficients. Regarding AZM desorption, its concentrations were always lower than the detection limit, indicating that the antibiotic was adsorbed in a very strong manner to the soils studied. These results can be considered relevant in terms of assessment of risks of pollution due to AZM, both in soils and in other environmental compartments to which the antibiotic could migrate. It should be noted that, although AZM is present in the environment at lower concentrations than those found in this research, its consumption has clearly increased in recent years, which makes the current work relevant as regard increasing the knowledge on the factors that influence this fact, and facilitating the future development of solutions to the problem. In addition, taking into account that desorption is practically absent from the soils studied, it is suggested that these edaphic environments could help to prevent AZM leaching/transportation to other environmental compartments such as water bodies, especially in case that the adsorption capacity of these soils could be increased by means of low-cost sorbents.

Supplementary Materials: The following supporting information can be downloaded at: https://www.mdpi.com/article/10.3390/pr10122565/s1. Table S1: Basic details corresponding to the different soils used in this work. M: maize (corn) soils; VO: vineyard soils (Ourense province); VP: vineyard soils (Pontevedra province); F: forest soils; Table S2: Values corresponding to the basic parameters determined in the various soils studied. M: maize (corn) soils; VO: vineyard soils (Ourense province); VP: vineyard soils (Pontevedra province); F: forest soils. OC: organic carbon; OM: organic matter; N: nitrogen; eCEC: effective cation exchange capacity; Alox and Feox: Al and Fe extracted with ammonium oxalate; Alpir and Fepir: Al and Fe extracted with sodium pyrophosphate. Average values (n = 3), with coefficients of variation always <5%; Table S3: AZM adsorption expressed in μmol kg^{-1} (and in percentage between brackets), for the soils studied, as a function of the concentration of antibiotic added. M: maize (corn) soils; VO: vineyard soils (Ourense province); VP: vineyard soils (Pontevedra province); F: forest soils. Average values (n = 3), with coefficients of variation always <5%; Figure S1: Molecular structure of AZM; Figure S2. Molecular structure of AZM with amine groups selected; Figure S3: Selected chromatograms corresponding to AZM adsorption onto soils.

Author Contributions: Conceptualization, E.Á.-R., M.J.F.-S., A.N.-D. and M.A.-E.; methodology, E.Á.-R., M.J.F.-S., A.N.-D., M.A.-E., R.C.-D. and A.B.; software, E.Á.-R., L.R.-L., P.P.-R. and R.C.-D.; validation, E.Á.-R., M.J.F.-S., A.N.-D., M.A.-E. and A.B.; formal analysis, R.C.-D., L.R.-L. and P.P.-R.; investigation, E.Á.-R., M.J.F.-S., R.C.-D., L.R.-L., P.P.-R. and A.B.; resources, E.Á.-R., M.J.F.-S. and M.A.-E.; data curation, E.Á.-R., M.J.F.-S., A.N.-D. and A.B.; writing—original draft preparation, E.Á.-R., M.J.F.-S., A.B. and R.C.-D.; writing—review and editing, A.N.-D.; visualization, E.Á.-R., M.J.F.-S., A.N.-D., M.A.-E., R.C.-D., L.R.-L., P.P.-R. and A.B.; supervision, E.Á.-R., M.J.F.-S. and A.B.; project administration, E.Á.-R., M.J.F.-S. and M.A.-E.; funding acquisition, E.Á.-R., M.J.F.-S. and M.A.-E. All authors have read and agreed to the published version of the manuscript.

Funding: This research was funded by Spanish Ministry of Science, Innovation and Universities, grant numbers RTI2018-099574-B-C21 and RTI2018-099574-B-C22.

Institutional Review Board Statement: Not applicable.

Informed Consent Statement: Not applicable.

Data Availability Statement: Not applicable.

Conflicts of Interest: The authors declare no conflict of interest. The funders had no role in the design of the study; in the collection, analyses, or interpretation of data; in the writing of the manuscript, or in the decision to publish the results.

References

1. Maier, M.L.V.; Tjeerdema, R.S. Azithromycin sorption and biodegradation in a simulated California river system. *Chemosphere* **2018**, *190*, 471–480. [CrossRef] [PubMed]
2. Bakheit, A.H.H.; Al-Hadiya, B.M.H.; Abd-Elgalil, A.A. Chapter One—Azithromycin. In *Profiles of Drug Substances, Excipients and Related Methodology*; Brittain, H.G., Ed.; Elsevier: Amsterdam, The Netherlands, 2014; Volume 39, pp. 1–40. [CrossRef]
3. Goossens, H. Antibiotic consumption and link to resistance. *Clin. Microbiol. Infect.* **2009**, *15*, 12–15. [CrossRef] [PubMed]
4. ECDC Antimicrobial Consumption Interactive Database (ESAC-Net). Available online: http://ecdc.europa.eu/en/healthtopics/antimicrobial_resistance/esac-net-database/Pages/database.aspx (accessed on 29 July 2022).
5. World Health Organization. *WHO Report on Surveillance of Antibiotic Consumption: 2016–2018 Early Implementation*; World Health Organization: Geneva, Switzerland, 2018; Licence: CC BY-NC-SA 3.0 IGO.
6. Gonzalez-Zorn, B. Antibiotic use in the COVID-19 crisis in Spain. *Clin. Microbiol. Infect.* **2021**, *27*, 646–647. [CrossRef] [PubMed]
7. Zuccato, E.; Gastiglioni, S.; Bagnati, R.; Melis, M.; Fanelli, R. Source, occurrence and fate of antibiotics in the Italian aquatic environment. *J. Hazard. Mater.* **2010**, *179*, 1042–1048. [CrossRef]
8. Cardoso, O.; Porcher, J.M.; Sanchez, W. Factory-discharged pharmaceuticals could be a relevant source of aquatic environment contamination: Review of evidence and need for knowledge. *Chemosphere* **2014**, *115*, 20–30. [CrossRef]
9. Santás-Miguel, V.; Díaz-Raviña, M.; Martín, A.; García-Campos, E.; Barreiro, A.; Núñez-Delgado, A.; Fernández-Sanjurjo, M.J.; Álvarez-Rodríguez, E.; Arias-Estévez, M.; Fernández-Calviño, D. Medium-term influence of tetracyclines on total and specific microbial biomass in cultivated soils of Galicia (NW Spain). *Span. J. Soil Sci.* **2020**, *10*, 218–232. [CrossRef]
10. Barreiro, A.; Cela-Dablanca, R.; Nebot, C.; Rodríguez-López, L.; Santás-Miguel, V.; Arias-Estévez, M.; Fernández-Sanjurjo, M.; Núñez-Delgado, A.; Álvarez-Rodríguez, E. Occurrence of Nine Antibiotics in Different Kinds of Sewage Sludge, Soils, Corn and Grapes After Sludge Spreading. *Span. J. Soil Sci.* **2022**, *12*, 10741–10753. [CrossRef]
11. Rizzo, L.; Manaia, C.; Merlin, C.; Schwartz, T.; Dagot, C.; Ploy, M.C.; Michael, I.; FattaKassinos, D. Urban wastewater treatment plants as hotspots for antibiotic resistant bacteria and genes spread into the environment: A review. *Sci. Total Environ.* **2013**, *447*, 345–360. [CrossRef]
12. Kümmerer, K. The presence of pharmaceuticals in the environment due to human use–present knowledge and future challenges. *J. Environ. Manag.* **2009**, *90*, 2354–2366. [CrossRef]
13. Zuckerman, J.M. The newer macrolides: Azithromycin and clarithromycin. *Infect. Dis. Clin. N. Am.* **2000**, *14*, 449–462. [CrossRef]
14. Martínez-Polanco, M.P.; Valderrama-Rincón, J.A.; Martínez-Rojas, A.J.; Luna-Wandurraga, H.J.; Díaz-Báez, M.C.; Bustos-López, M.C.; Valderrama-Rincon, J.D. Degradation of high concentrations of azithromycin when present in a high organic content wastewater by using a continuously fed laboratory-scale UASB bioreactor. *Chemosphere* **2022**, *287*, 132191. [CrossRef]
15. Mirzaei, R.; Mesdaghinia, A.; Hoseini, S.S.; Yunesian, M. Antibiotics in urban wastewater and rivers of Tehran, Iran: Consumption, mass load, occurrence, and ecological risk. *Chemosphere* **2019**, *221*, 55–66. [CrossRef]
16. Zhang, X.; Zhao, H.; Dú, J.; Qu, Y.; Shen, C.; Tan, F.; Chen, J.; Quan, X. Ocurrence, removal, and risk assessment of antibiotics in 12 wastewater treatment plants from Dalian, China. *Environ. Sci. Pollut. Res.* **2017**, *24*, 16478–16487. [CrossRef]
17. Topp, E.; Renaud, J.; Sumarah, M.; Sabourin, L. Reduced persistence of the macrolide antibiotics erythromycin, clarithromycin and azithromycin in agricultural soil following several years of exposure in the field. *Sci. Total Environ.* **2016**, *562*, 136–144. [CrossRef] [PubMed]
18. Rodriguez-Mozaz, S.; Vaz-Moreira, I.; Varela Della Giustina, S.; Llorca, M.; Barceló, D.; Schubert, S.; Berendonk, T.U.; Michael-Kordatou, I.; Fatta-Kassinos, D.; Martinez, J.L.; et al. Antibiotic residues in final effluents of European wastewater treatment plants and their impact on the aquatic environment. *Environ. Int.* **2020**, *140*, 105733. [CrossRef] [PubMed]
19. O'Connor, G.A.; Elliot, H.A.; Basta, N.T.; Bastian, R.K.; Pierzynski, G.M.; Sims, R.C.; Smith, J.E. Sustainable Land Application. *J. Environ. Qual.* **2005**, *34*, 7–17. [CrossRef]
20. Kelessidis, A.; Stasinakis, A.S. Comparative study of the methods used for treatment and final disposal of sewage sludge in European countries. *Waste Manag.* **2012**, *32*, 1186–1195. [CrossRef] [PubMed]
21. Milieu Ltd.; WRc; RPA. Environmental, Economic and Social Impacts of the Use of Sewage Sludge on Land. Final Report, Part III: Project Interim Reports. DG ENV.G.4./ ETU/2008/0076r. 2010. Available online: http://ec.europa.eu/environment/archives/waste/sludge/pdf/part_iii_report.pdf (accessed on 2 May 2022).
22. Pan, M.; Chu, L.M. Fate of antibiotics in soil and their uptake by edible crops. *Sci. Total Environ.* **2017**, *599–600*, 500–512. [CrossRef]
23. Walters, E.; McClellan, K.; Halden, R.U. Occurrence and loss over three years of 72 pharmaceuticals and personal care products from biosolids-soil mixtures in outdoor mesocosms. *Water Res.* **2010**, *44*, 6011–6020. [CrossRef]
24. Arun, S.; Kumar, R.M.; Ruppa, J.; Mukhopadhyay, M.; Ilango, K.; Chakraborty, P. Occurrence, sources and risk assessment of fluoroquinolones in dumpsite soil and sewage sludge from Chennai, India. *Environ. Toxicol. Pharmacol.* **2020**, *79*, 103410. [CrossRef] [PubMed]
25. Berthod, L.; Roberts, G.; Sharpe, A.; Whitley, D.C.; Greenwood, R.; Mills, G.A. Effect of sewage sludge type on the partitioning behaviour of pharmaceuticals: A meta-analysis. *Environ. Sci. Water Res. Technol.* **2016**, *2*, 154–163. [CrossRef]

26. OECD Guideline for the Testing of Chemicals: Adsorption–Desorption Using a Batch Equilibrium Method. Available online: http://www.epa.gov/scipoly/sap/meetings/2008/october/106_adsorption_desorption_using.pdf. (accessed on 16 June 2022).
27. Kemper, N. Veterinary antibiotics in the aquatic and terrestrial environment. *Ecol. Indic.* **2008**, *8*, 1–13. [CrossRef]
28. Ribeiro, A.R.; Schmidt, T.C. Determination of acid dissociation constants (pKa) of cephalosporin antibiotics: Computational and experimental approaches. *Chemosphere* **2017**, *169*, 524–533. [CrossRef] [PubMed]
29. Demiralay, E.Ç.; Koç, D.; Daldal, Y.D.; Çakır, C. Determination of chromatographic and spectrophotometric dissociation constants of some beta lactam antibiotics. *J. Pharm. Biomed. Anal.* **2012**, *71*, 139–143. [CrossRef] [PubMed]
30. Sidhu, H.; D′Angelo, E.; O′Connor, G. Retention-release of ciprofloxacin and azithromycin in biosolids and biosolids-amended soils. *Sci. Total Environ.* **2019**, *650*, 173–183. [CrossRef] [PubMed]
31. Babić, S.; Horvat, A.J.M.; Pavlović, D.M.; Kaštelan-Macan, M. Determination of pKa values of active pharmaceutical ingredients. *TrAC Trends Anal. Chem.* **2007**, *26*, 1043–1061. [CrossRef]
32. Zrnčić, M.; Babić, S.; Pavlović, D.M. Determination of thermodynamic pKa values of pharmaceuticals from five different groups using capillary electrophoresis. *J. Sep. Sci.* **2015**, *38*, 1232–1239. [CrossRef]
33. Derendorf, H. Excessive lysosomal ion-trapping of hydroxychloroquine and azithromycin. *Int. J. Antimicrob. Agents* **2020**, *55*, 106007. [CrossRef]
34. Rodríguez-López, L.; Santás-Miguel, V.; Núñez-Delgado, A.; Álvarez-Rodríguez, E.; Pérez-Rodríguez, P.; Arias-Estévez, M. Influence of pH, Humic Acids, and Salts on the Dissipation of Amoxicillin and Azithromycin Under Simulated Sunlight. *Span. J. Soil Sci.* **2022**, *12*, 10438. [CrossRef]
35. Cela-Dablanca, R.; Nebot, C.; López, L.R.; Fernández-Calviño, D.; Arias-Estévez, M.; Núñez-Delgado, A.; Fernández-Sanjurjo, M.J.; Álvarez-Rodríguez, E. Efficacy of different waste and by-products from forest and food industries in the removal/retention of the antibiotic cefuroxime. *Processes* **2021**, *9*, 1151. [CrossRef]
36. Ayawei, N.; Ebelegi, A.N.; Wankasi, D. Modelling and Interpretation of Adsorption Isotherms. *J. Chem.* **2017**, *2017*, 3039817. [CrossRef]
37. Chu, B.; Goyne, K.W.; Anderson, S.H.; Lin, C.-H.; Udawatta, R.P. Veterinary antibiotic sorption to agroforestry buffer, grass buffer and cropland soils. *Agrofor. Syst.* **2010**, *79*, 67–80. [CrossRef]
38. Figueroa-Diva, R.A.; Vasudevan, D.; MacKay, A.A. Trends in soil sorption coefficients within common antimicrobial families. *Chemosphere* **2010**, *79*, 786–793. [CrossRef] [PubMed]
39. Sun, H.; Shi, X.; Mao, J.; Zhu, D. Tetracycline sorption to coal and soil humic acids: An examination of humic structural heterogeneity. *Environ. Toxicol. Chem.* **2010**, *29*, 1934–1942. [CrossRef]
40. Balarak, D.; Mahvi, A.H.; Shahbaksh, S.; Wahab, A.; Abdala, A. Adsorptive removal of azithromycin antibiotic from aqueous solution by Azolla Filiculoides-based activated porous carbon. *Nanomaterials* **2021**, *11*, 3281. [CrossRef]
41. Peterson, J.W.; O´Meara, T.A.; Seymour, M.D.; Wang, W.; Gu, B. Sorption mechanisms of cephapirin, a veterinary antibiotic, onto quartz and feldspar minerals as detected by Raman spectroscopy. *Environ. Pollut.* **2009**, *157*, 1849–1856. [CrossRef]
42. Chen, H.; Ma, L.Q.; Gao, B.; Gu, C. Effects of Cu and Ca cations and Fe/Al coating on ciprofloxacin sorption onto sand media. *J. Hazard. Mater.* **2013**, *252–253*, 375–381. [CrossRef]
43. Gravesen, C.; Judy, J.D. Effect of biosolids characteristics on retention and release behavior of azithromycin and ciprofloxacin. *Environ. Res.* **2020**, *184*, 109333. [CrossRef]
44. Sidhu, H.; O′Connor, G.; Ogram, A.; Kumar, K. Bioavailability of biosolids-borne ciprofloxacin and azithromycin to terrestrial organisms: Microbial toxicity and earthworm responses. *Sci. Total Environ.* **2019**, *650*, 18–26. [CrossRef]
45. Sidhu, H.; O′Connor, G.; Kruse, J. Plant toxicity and accumulation of biosolidsborne ciprofloxacin and azithromycin. *Sci. Total Environ.* **2019**, *648*, 1219–1226. [CrossRef]
46. Lemić, J.; Kovačević, D.; Tomašević-Čanović, M.; Kovačević, D.; Stanić, T.; Pfend, R. Removal of atrazine, lindane and diazinone from water by organo-zeolites. *Water Res.* **2006**, *40*, 1079–1085. [CrossRef]
47. Deng, J.-C.; Jiang, X.; Lü, X.; Yu, G.-F.; Wang, F.; Zhang, B. Atrazine Adsorption Behavior on a Fluvo-Aquic Soil as Influenced by Contact Periods. *Pedosphere* **2007**, *17*, 786–791. [CrossRef]
48. Conde-Cid, M.; Ferreira-Coelho, G.; Fernández-Calviño, D.; Núñez-Delgado, A.; Fernández-Sanjurjo, M.J.; Arias-Estévez, M.; Álvarez-Rodríguez, E. Single and simultaneous adsorption of three sulfonamides in agricultural soils: Effects of pH and organic matter content. *Sci. Total Environ.* **2020**, *744*, 140872. [CrossRef] [PubMed]
49. Conde-Cid, M.; Fernández-Calviño, D.; Nóvoa-Muñoz, J.C.; Núñez-Delgado, A.; Fernández-Sanjurjo, M.J.; Arias-Estévez, M.; Álvarez-Rodríguez, E. Experimental data and model prediction of tetracycline adsorption and desorption in agricultural soils. *Environ. Res.* **2019**, *177*, 108607. [CrossRef] [PubMed]
50. Kong, W.; Li, C.; Dolhi, J.M.; Li, S.; He, J.-Z.; Qiao, M. Characteristics of oxytetracycline sorption and potential bioavailability in soils with various physical–chemical properties. *Chemosphere* **2012**, *87*, 542–548. [CrossRef] [PubMed]
51. Mohapatra, M.; Rout, K.; Mohapatra, B.; Anand, S. Sorption behavior of Pb(II) and Cd(II) on iron ore slime and characterization of metal ion loaded sorbent. *J. Hazard. Mater.* **2009**, *166*, 1506–1513. [CrossRef] [PubMed]
52. Bao, Y.; Zhou, Q.; Wan, Y.; Yu, Q.; Xie, X. Effects of Soil/Solution Ratios and Cation Types on Adsorption and Desorption of Tetracycline in Soils. *Soil Sci. Soc. Am. J.* **2010**, *74*, 1553–1561. [CrossRef]

applied sciences

MDPI

Article

Enhanced Photocatalytic Performance of $Bi_2O_2CO_3$ Loaded Activated Carbon for Toluene Removal in Air

Xiaoyan Wang [1], Lu Chen [1], Changfu Li [1], Yongchao Xiao [1], Yuchen Gao [1], Yaochun Liu [2], Yuanhua Lin [3,*] and Junping Ding [1,*]

[1] China Astronaut Research and Training Center, Beijing 100094, China
[2] Foshan (Southern China) Institute for New Materials, Foshan 528200, China
[3] State Key Laboratory of New Ceramics and Fine Processing, School of Materials Science and Engineering, Tsinghua University, Beijing 100084, China
* Correspondence: linyh@mail.tsinghua.edu.cn (Y.L.); djp15@tsinghua.org.cn (J.D.); Tel.: +86-10-6636-5775 (J.D.)

Featured Application: This work may provide potential applications in indoor air purification for the removal of volatile organic compounds.

Abstract: Activated carbon (AC) is one of the most used air purification materials with excellent adsorption capacity for volatile organic compounds (VOCs). In this work, $Bi_2O_2CO_3$ (BOC) nanomaterials, as a photocatalysis component, are grown on the surface of the AC to construct BOC/AC composites. The as-synthesized composites were characterized by scanning electron microscopy (SEM), X-ray diffraction (XRD), and N_2 adsorption/desorption measurements. The results demonstrate that flower-like BOC can be grown in situ on the surface of AC. The photocatalytic properties for the removal of gaseous toluene (50.0 ppm) in air over the BOC/AC composites were investigated under simulated sunlight illumination. The results show that the BOC/AC photocatalyst can effectively degrade toluene to CO_2 and H_2O, with more than 90% degradation in 3 h. The excellent photocatalytic performance of the BOC/AC composite catalyst can be ascribed to the synergistic effect of the adsorption ability of AC and photocatalytic activity of both BOC nanosheets and AC. This work may provide useful guidance for indoor air purification, particularly for harmful trace gases such as VOCs.

Keywords: $Bi_2O_2CO_3$; activated carbon; in situ; toluene removal; photocatalyst

Citation: Wang, X.; Chen, L.; Li, C.; Xiao, Y.; Gao, Y.; Liu, Y.; Lin, Y.; Ding, J. Enhanced Photocatalytic Performance of $Bi_2O_2CO_3$ LoadedActivated Carbon for Toluene Removal in Air. *Appl. Sci.* **2022**, *12*, 12500. https://doi.org/10.3390/app122312500

Academic Editors: Elza Bontempi, Marco Race, Avelino Núñez-Delgado, Vlasoula Bekiari, Zhien Zhang, Yaoyu Zhou and Mario Coccia

Received: 28 October 2022
Accepted: 2 December 2022
Published: 6 December 2022

1. Introduction

People usually stay indoors for the majority of the time (ca. 85~90%) during the day; thus receiving exposure to indoor air pollution from a variety of trace harmful gases such as volatile organic compounds (VOCs). Among the different VOCs, benzene, toluene, and xylene (BTX) can pose a risk of adverse health effects following long term exposure and may result in considerable harm to human health, with a high risk of developing asthma, cancers, heart disease, and lymphoma/leukemia, etc. [1–4]. Therefore, the efficient and economic disposal of BTX in the indoor environment is highly desired and has received considerable attention from researchers in recent years.

Adsorption technology is considered as a simple, economical, efficient, and environmentally friendly method for removing VOCs [5]. With adsorbents, no additional energy is needed because they are able to absorb VOCs by surface molecules at room temperature [6]. As a synthetic adsorbent, activated carbon (AC) is widely used for BTX removal due to its advantages of low costs, high adsorption capacity, high efficiency and multifunction [7–13]. Nevertheless, the process that AC removes gaseous pollutants is only a physical adsorption. If the active adsorption sites are saturated, generally AC can adsorb almost no more BTX and thus needs to be exchanged or regenerated. According to recent reports, AC can only act as a photocatalyst for the degradation of organic contaminants under UV

irradiation [14–18]. Therefore, the introduction of narrow bandgap catalytic materials is highly necessary to expand the solar absorption spectrum to the visible light region [19,20].

Among all the visible light driven photocatalysts, layered structured $Bi_2O_2CO_3$ (BOC), one of the bismuth-containing Aurivillius compounds with alternative stacking of $(Bi_2O_2)^{2+}$ thin layers separated by CO_3^{2-} groups [21–23], has been explored as a promising visible light active photocatalyst [24–26]. Furthermore, the layered structure can easily lead to the formation of 2D morphologies, such as sheet-/plate-like morphologies, which may result in excellent photocatalytic performance. In our previous work, we demonstrated the effective photocatalytic removal of toluene in air utilizing (002) oriented BOC nanosheets, which led to an almost complete degradation of toluene into CO_2 and H_2O [27,28]. These results demonstrate the promising potential of utilizing layered BOC nanostructures as photocatalyst for removing VOCs. In this work, we aim to combine the advantages of both AC and BOC as a composite catalyst for the removal of toluene in air by fabricating AC modified with BOC nanomaterials. On one hand, the AC can adsorb toluene effectively due to its large surface area. On the other hand, BOC nanostructures can function as photocatalyst for the in-situ degradation of toluene.

2. Materials and Methods

2.1. Materials

All the chemical reagents in this work were analytical-grade and used without any further purification: Bi_2O_3 (99.99%, Aladdin Industrial Corporation, Shanghai, China), HNO_3 solution (GR, Sinopharm Chemical Reagent Co., Ltd., Shanghai, China) and Na_2CO_3 (RA, Sinopharm Chemical Reagent Co., Ltd., Shanghai, China).

2.2. Synthesis of $Bi_2O_2CO_3$

In a typical experiment, 2.325 g Bi_2O_3 was dissolved in 450 mL 1 mol/L of HNO_3 solution under ultrasonication conditions. The obtained suspension was kept at 20 °C in a water bath for 1 h. Subsequently, 400 mL 0.6 mol/L Na_2CO_3 solution was added into the above suspension at a speed of 30 mL/min, until a uniform solution with pH of about 7 was reached under magnetic stirring. Then, the as-obtained powder sample was centrifuged, washed with de-ionized water and ethyl alcohol for several times, and dried at 70 °C in an oven. Finally, the powdered $Bi_2O_2CO_3$ (labeled as BOC) sample was obtained.

The synthesis process of $Bi_2O_2CO_3$ nanomaterials follows Equations (1)–(6). CO_3^{2+} is formed via a hydrolysis reaction process between Na_2CO_3 and H_2O. Bi_2O_3 is dissolved in dilute nitric acid to generate $(Bi_2O_2)^{2+}$. Then, a reaction occurs between $(Bi_2O_2)^{2+}$ and CO_3^{2+} to synthesize $Bi_2O_2CO_3$. Most of the H^+ is neutralized by CO_3^{2+} to generate CO_2 and H_2O. Only a small part of the H^+ is combined with OH^- to form H_2O. Na^+ and NO_3^- are washed off by de-ionized water.

$$HNO_3 \rightarrow H^+ + NO_3^- \quad (1)$$

$$Bi_2O_3 \xrightarrow{HNO_3} {Bi_2O_2}^{2+} + 2OH^- \quad (2)$$

$$Na_2CO_3 \xrightarrow{H_2O} 2Na^+ + {CO_3}^{2-} \quad (3)$$

$${Bi_2O_2}^{2+} + {CO_3}^{2-} \rightarrow Bi_2O_2CO_3 \downarrow \quad (4)$$

$$2H^+ + {CO_3}^{2-} \rightarrow H_2O + CO_2 \quad (5)$$

$$H^+ + OH^- \rightarrow H_2O \quad (6)$$

2.3. Synthesis of BOC/AC Composites

2.325 g Bi_2O_3 was dissolved in 450 mL 1 mol/L HNO_3 solution under ultrasonication condition. The obtained suspension was kept at 20 °C in a water bath. Then, 400 mL 0.6 mol/L Na_2CO_3 solution was added into the above suspension at a speed of 30 mL/min, while stirring at a speed of 300 r/min. At the same time, different amounts (50 g, 100 g,

150 g, and 200 g) of honeycomb activated carbon (4~60 mesh, iodine value of 1050 mg/g) were added. The suspension was kept in 20 °C water bath for 6 h. Then, the product was washed with de-ionized water and ethyl alcohol several times. The as-obtained powder sample was centrifuged and dried at 70 °C in an oven. Finally, the BOC/AC composites (labeled as BOC/AC_50, BOC/AC_100, BOC/AC_150, and BOC/AC_200, respectively) were obtained.

2.4. Characterization

The X-ray diffraction (XRD) measurements were performed on a diffractometer (D8-Advance, Bruker, Karlsruhe, Germany) with monochromatized Cu Kα (λ = 1.54056 nm) radiation at a scanning speed of 0.15°/s. The microstructure of the as-obtained samples was characterized using scanning electron microscopy (SEM, JSM-7001F, JEOL, Tokyo, Japan) operated at a voltage of 5 kV. The composition of chemical elements was performed using an X-ray fluorescence (XRF, Thermo Scientific, Niton, UK).

The N_2 adsorption/desorption measurements were performed on an automated gas sorption analyzer (AutosorbiQ2, Quantachrome, Boynton Beach, FL, USA) at P/Po = 0.99 and the specific surface areas were estimated using the Brunauer–Emmet–Teller (BET) method. Before analysis, all samples were dried at 90 °C for 1 h and degassed by vacuum at 200 °C for 24 h.

2.5. Photocatalytic Activity Test

2.5.1. Photocatalytic Activity Test of $Bi_2O_2CO_3$

To prepare the sample for photocatalytic toluene removal performance in air, 0.025 g BOC was dispersed into 150 mL de-ionized water under ultrasonication for 15 min. The suspension was filtered using a 0.1 μm nylon membrane through a vacuum pump. The photocatalytic performances of the BOC samples were evaluated by toluene removal in air using a gas phase photocatalytic testing system developed by our group (China Patent, NO.202210103256.X). The reactor is a stainless steel canister and the BOC membrane was placed at the bottom of the reactor. The gas product in the reactor was analyzed at regular time intervals, using a gas chromatograph (GC), equipped with two flame-ionization detectors (FID) [28]. Toluene analysis was performed with one FID loaded with an Rt-Q-Bond Plot column (30 m × 0.25 mm, film thickness 10 μm), while CO_2 analysis was performed by the other FID loaded with a packed column (TDX-01, 3 m × 3 mm) followed by a methanizer CO_2 concentration. The gas samples were fed to the GC online through an automatic gas sampling valve.

2.5.2. Photocatalytic Activity of BOC/AC Composites

The photocatalytic performances of the BOC/AC composites were investigated using a similar system to that described in Section 2.5.1. To imitate practical applications, the stainless steel canister was replaced by a 60 L Tedlar polyvinyl fluoride (PVF) pocket in a thermostatic test chamber and kept at a constant temperature (e.g., 20 °C). Then, 3 g BOC/AC particulates was placed on the dish and into the pocket. The incident light can pass through the PVF film to the BOC/AC surface. The structure is illustrated in Figure 1.

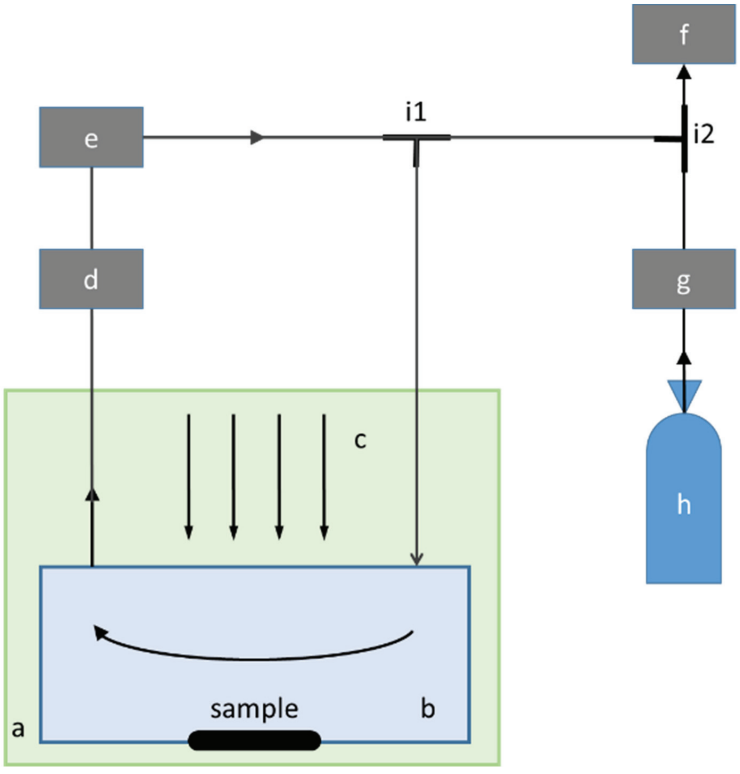

Figure 1. Schematic illustration of gas-phase photocatalysis testing system. (**a**) Thermostatic test chamber, (**b**) PVF pocket, (**c**) light source, (**d**) gas delivery pump, (**e**) gas chromatograph (GC), (**f**) vacuum pump, (**g**) gas mass flow meter, (**h**) toluene gas, and (i1–i2) three-port value.

To test the photocatalytic activity, the reaction reactor was first vacuumized by pump. Then, 60 L toluene gas (50.0 ppm in air) was injected as the target indoor pollutant. This required about 12 min. After that, the reaction reactor was kept in the dark for 0.5 h to reach the adsorption/desorption equilibrium. A 300 W xenon lamp (CEL-HXF300, Beijing China Education AuLight Technology Co., Ltd., Beijing, China) was used as the simulated sunlight source. The gas product in the reactor was analyzed at regular time intervals using GC. In addition, the toluene gas in the pocket could not flow completely to the automatic gas sampling valve of the GC at 0 min because the pipe diameter of the valve is relatively small and the gas delivery pump has just started. Thus, the toluene concentration is low. This means that the first point (at t = 0) is not 100% for all studies.

3. Results and Discussion

3.1. Characterization and Properties of $Bi_2O_2CO_3$

The crystal structure of the BOC nanomaterials prepared by chemical method was analyzed by XRD. As displayed in Figure 2, all diffraction peaks of the sample can be well indexed to the single phase of tetragonal $Bi_2O_2CO_3$ (JCPDS 41-1488) with good crystallinity, without any other impurity peaks. Moreover, the average crystal size of the BOC nanosheets was estimated to be ca. 80 nm using the XRD patterns.

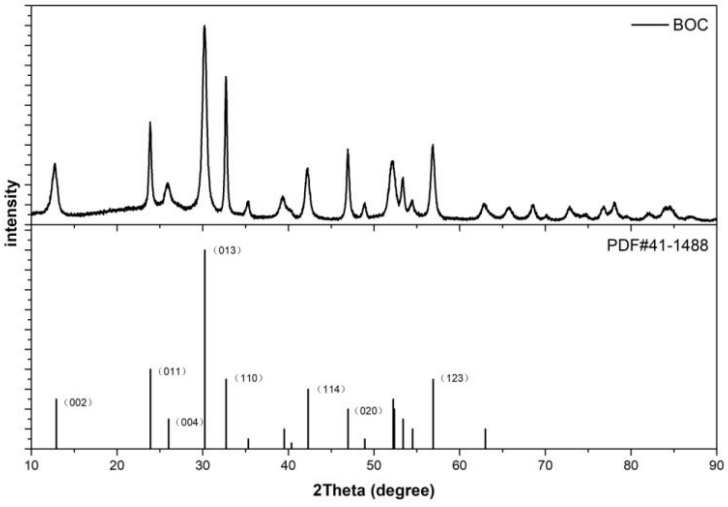

Figure 2. XRD patterns of the as-synthesized $Bi_2O_2CO_3$.

The morphology of the BOC sample was investigated by SEM. As shown in Figure 3, the BOC has a flower-like shape assembled by nanosheets during the crystallization process, with lateral sizes of several micrometers and a thickness of a few nanometers. Thus, the flower-like shape can provide more reactive sites owing to the unique layered structure of $Bi_2O_2CO_3$ [29,30].

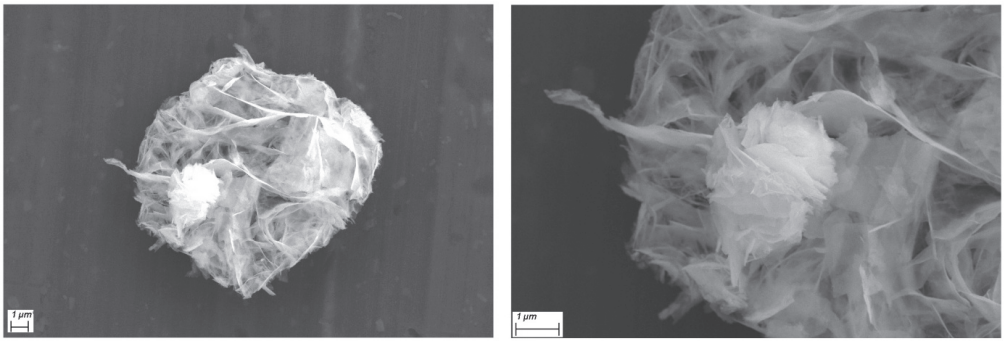

Figure 3. SEM images of $Bi_2O_2CO_3$.

The photocatalytic activity of the BOC sample for removing gaseous toluene in air was investigated at a concentration of 50.0 ppm (450 mL) under irradiation by a Xe lamp as the light source. As displayed in Figure 4, the pristine BOC sample demonstrated an excellent photocatalytic efficiency for toluene removal with a degradation rate as high as 96.8% over 3 h.

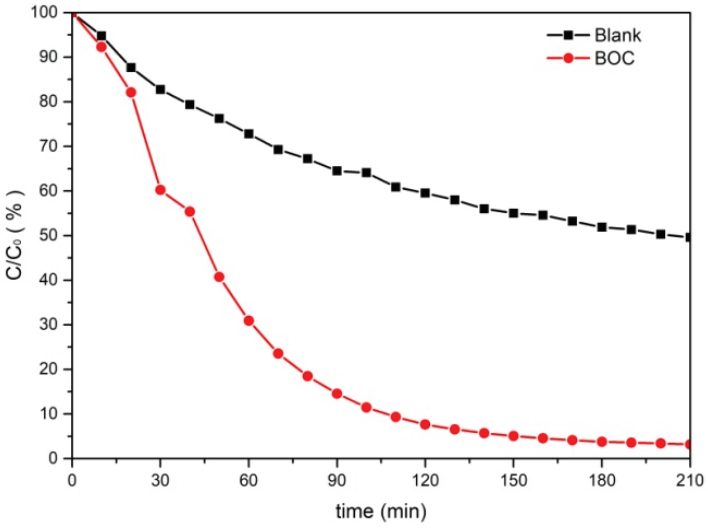

Figure 4. The photocatalytic property of $Bi_2O_2CO_3$ for toluene removal in air. The blank control experiment was performed under light illumination in the absence of catalyst.

3.2. Characterization and Propertiesof BOC/AC Composites

3.2.1. Microstructure Analysis

The microstructures of the BOC/AC and AC samples were characterized by SEM. As shown in Figure 5, the BOC/AC_50 and BOC/AC_100 samples have flower-like BOC grown on the surface of AC, with a size of ca. 5 μm (Figure 5a,b). These results demonstrate the successful growth of BOC on the surface of AC via an in-situ crystallization process. The BOC/AC_150 and BOC/AC_200 have cylinder-like morphology with a length of ca. hundreds of nanometers (Figure 5c,d). Figure 5e,f show the morphologies of the pristine AC sample, which has a porous structure with high specific surface area and good adsorption ability [31–33].

The surface area, pore volume, and pore diameter results of the as-prepared samples are shown in Figure S1 and listed in Table 1. The BOC/AC_100 sample has the highest BET surface area among all BOC/AC and AC samples, possibly because of the flower-like BOC on the surface of the AC. This is highly beneficial for promoting the photocatalytic performance by providing an abundance of active reaction sites. All samples show similar pore volume and pore diameter (1.5 nm), which is due to the use of the same matrix of AC. For these composite materials, activated carbon has excellent adsorption capability for toluene gas and $Bi_2O_2CO_3$ photocatalysis can in situ mineralize the adsorbed toluene to CO_2 and H_2O under light illumination.

3.2.2. Structure and Composition Analysis

The XRD patterns of the BOC/AC and AC are presented in Figure 6. All BOC/AC samples show similar XRD patterns (Figure 6a). In Figure 6b–d, the enlarged local XRD patterns clearly show that the peak intensity increased for BOC/AC_50 and BOC/AC_100 near $2\theta = 30.2^\circ$ and 32.7°, which are the characteristic peaks of $Bi_2O_2CO_3$ (JCPDS: 41-1488), corresponding to the (013) and (110) facets, respectively. The energy dispersive spectroscopy (EDS) elemental mapping images (Figure 7) of BOC/AC_100 sample further proves the successful growth of $Bi_2O_2CO_3$ on the surface of AC and the homogeneous elemental distribution of Bi, C, and O elements in the $Bi_2O_2CO_3$ nanosheets. To quantify the composition of different chemical elements in the composite, XRF analysis was performed, which showed that the ratio of C: O: Bi was about 94.3: 4.0: 1.7 wt.%.

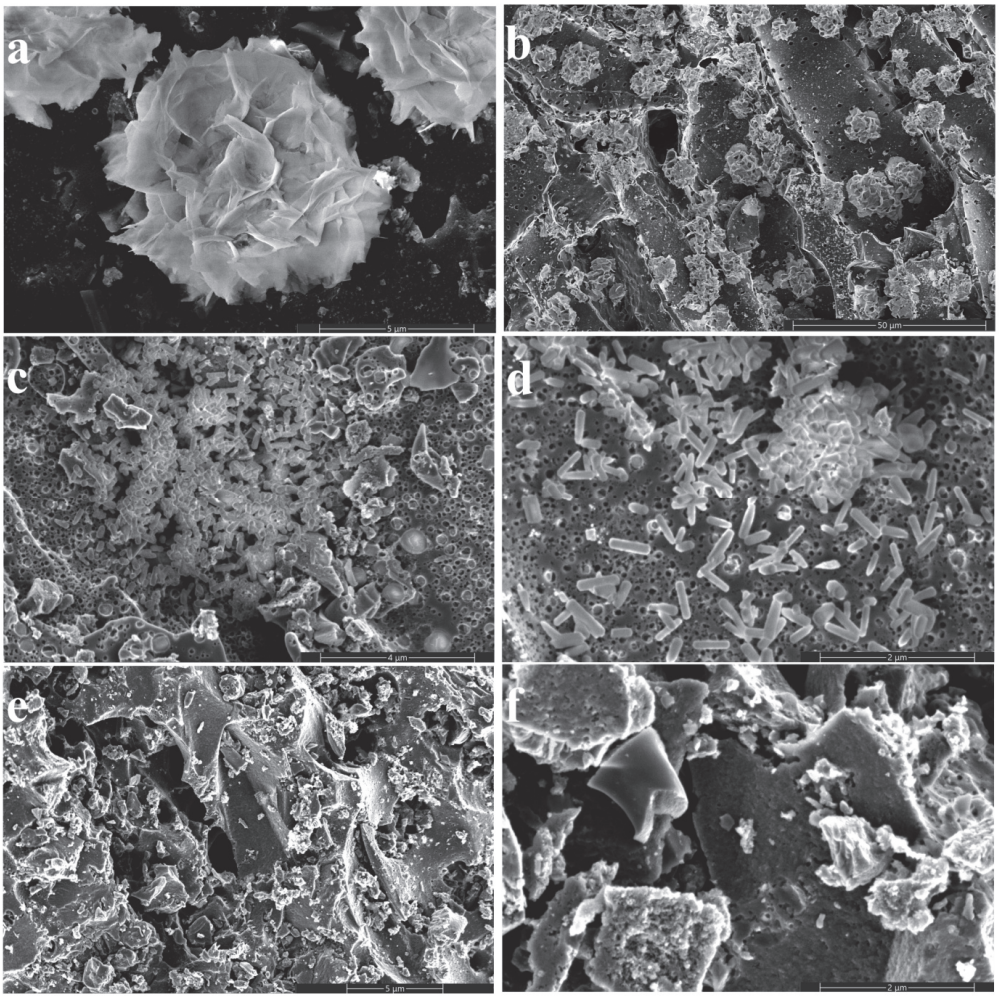

Figure 5. SEM images of BOC/AC_50 (**a**), BOC/AC_100 (**b**), BOC/AC_150 (**c**), BOC/AC_200 (**d**), and activated carbon (**e**,**f**).

Table 1. Surface area, pore volume, and pore diameter of BOC/AC.

	AC	BOC/AC_50	BOC/AC_100	BOC/AC_150	BOC/AC_200
Surface area (m^2/g)	953.8	931.8	955.3	951.2	851.4
Single point adsorption total pore volume (cm^3/g)	0.34	0.33	0.36	0.34	0.32
Average pore diameter (4V/A by BET) (nm)	1.44	1.43	1.52	1.45	1.48

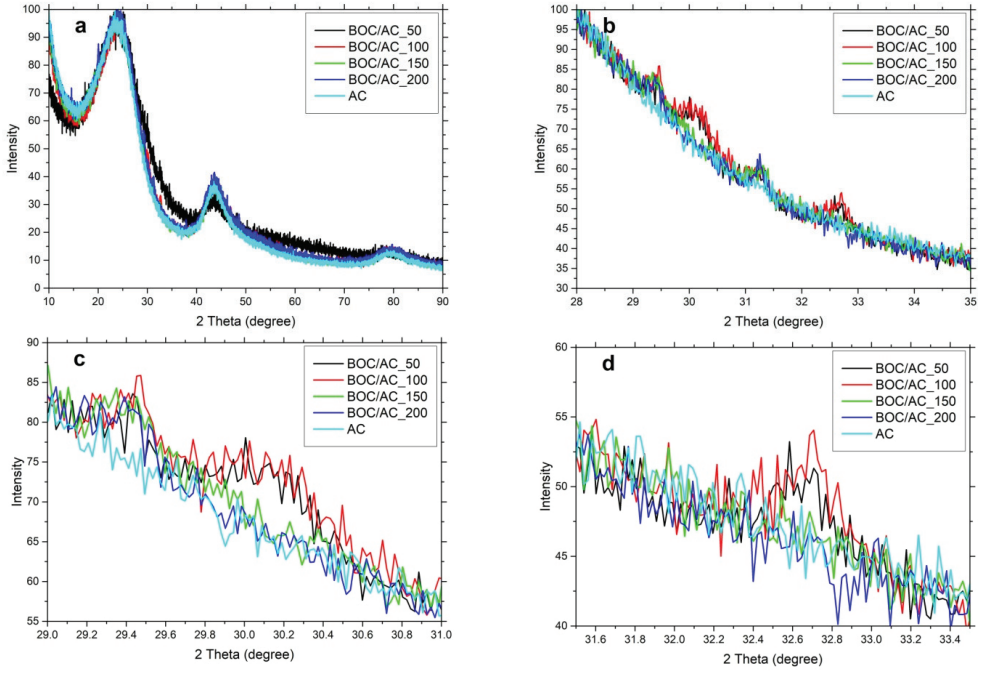

Figure 6. XRD patterns (**a**) and enlarged local XRD patterns (**b**–**d**) of the as-synthesized BOC/AC and AC.

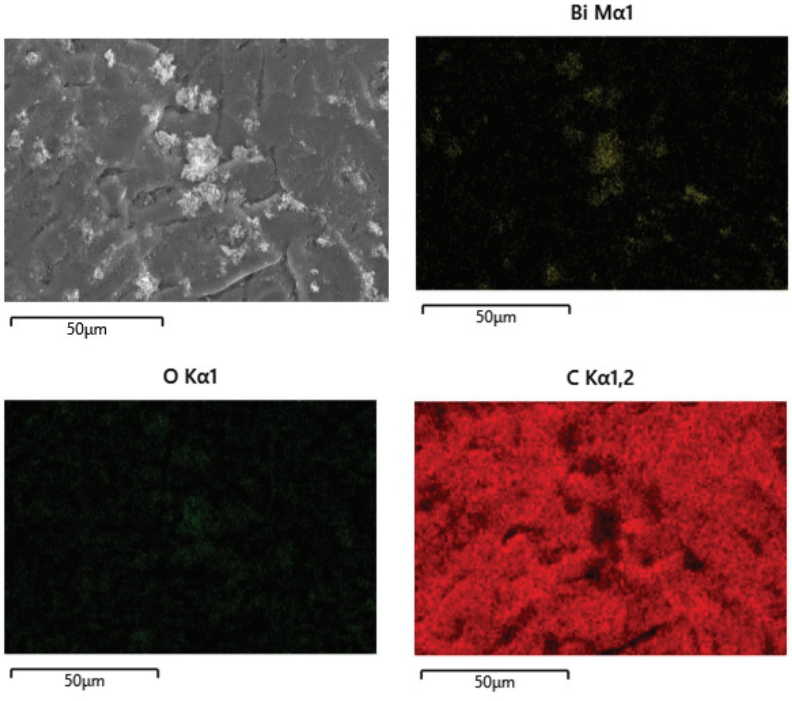

Figure 7. EDS element mapping images of BOC/AC_100.

3.2.3. Photocatalytic Properties

The photocatalytic properties of the degradation of gaseous toluene (50.0 ppm) in air over the BOC/AC composites were investigated under light illumination. As shown in Figure 8a, all samples demonstrated good removal efficiency of more than 90%. Among the BOC/AC composites, BOC/AC_100 shows the optimal efficiency with a removal rate of up to 92.2% in 3 h. The performances are comparable and higher than previously reported typical composite photocatalysts such as N-TiO_2/zeolite [34] and Fe_2O_3/In_2O_3 composite [35], showing the promising potential application of BOC/AC composite catalysts. In previous works, other methods have been used for the removal of toluene from the air, such as biofiltration [36], post-plasma catalytic technology [37], and corona discharge [38]. Compared with those methods, which are usually expensive and complex, the present BOC/AC composite has the advantages of being green and low-cost. The products of toluene degradation were detected using GC. The results demonstrate that CO_2 is the main product (Figures 8b and S2) with the highest productivity of 82.5 mg/m^3 in 3 h for BOC/AC_100, and another main product should be H_2O, on the basis that toluene is hydrocarbon. More reactive sites are provided for BOC/AC_100 due to the flower-like $Bi_2O_2CO_3$ on the surface of BOC/AC_50 and BOC/AC_100, which leads to enhanced photocatalytic performance. The photocatalytic process of the optimal sample (BOC/AC_100 composite) was investigated further. As shown in Figures 8c and S3, the toluene was completely removed in 7 h. Furthermore, the concentration of CO_2 increased significantly and reached 105.2 mg/m^3 (Figure 8d), which indicated the continuous degradation of toluene. However, the production rates of CO_2 were merely 38.3 mg/m^3 in 3 h and 55.4 mg/m^3 in 7 h for pristine AC. As we mentioned in the introduction, AC acts mainly as an adsorbent. Moreover, according to previous works, AC can also act as a photocatalyst for the degradation of organic contaminants. However, it is only active under UV irradiation with low catalytic efficiency. These results clearly show that the degradation rate of toluene is enhanced after the in-situ growth of BOC on the surface of the AC. This is attributed to the synergistic effect of the adsorption ability of AC and photocatalytic activity of both BOC and AC, demonstrating the advantage of the composite material.

The stability of BOC/AC composites (BOC/AC_100) for photocatalytic removal of toluene was evaluated by performing three experimental cycles under light illumination. As shown in Figure 8e, highly stable photocatalytic efficiency was maintained for BOC/AC_100, reaching as high as 90% for toluene removal after three cycles, which demonstrated the excellent recyclability of BOC/AC for photocatalytic toluene degradation.

In addition, we investigated the toluene removal efficiency using different amounts of BOC/AC_100 (1 g, 1.5 g, 2 g, and 3 g). As shown in Figure 8f, the photocatalytic activity was enhanced as the amount of catalyst increased, reaching the highest efficiency when 3 g of BOC/AC_100 was used.

A proposed photocatalytic reaction mechanism over the BOC/AC composites for the degradation of gaseous toluene under light irradiation can be explained as follows (Figure 9). First, the honeycomb AC matrices adsorb and capture the toluene molecules. Then, under light illumination, the electrons are excited from the valence band (VB) to the conduction band (CB) in the surface of $Bi_2O_2CO_3$ loaded Activated Carbon, leaving holes in the VB. The AC can function as electron acceptors to reduce the recombination rate of electron–hole pairs. Consequently, the excited electrons on CB in $Bi_2O_2CO_3$ can be easily transferred to the surface of AC, thus promoting the separation and migration of photo-generated charge carriers.

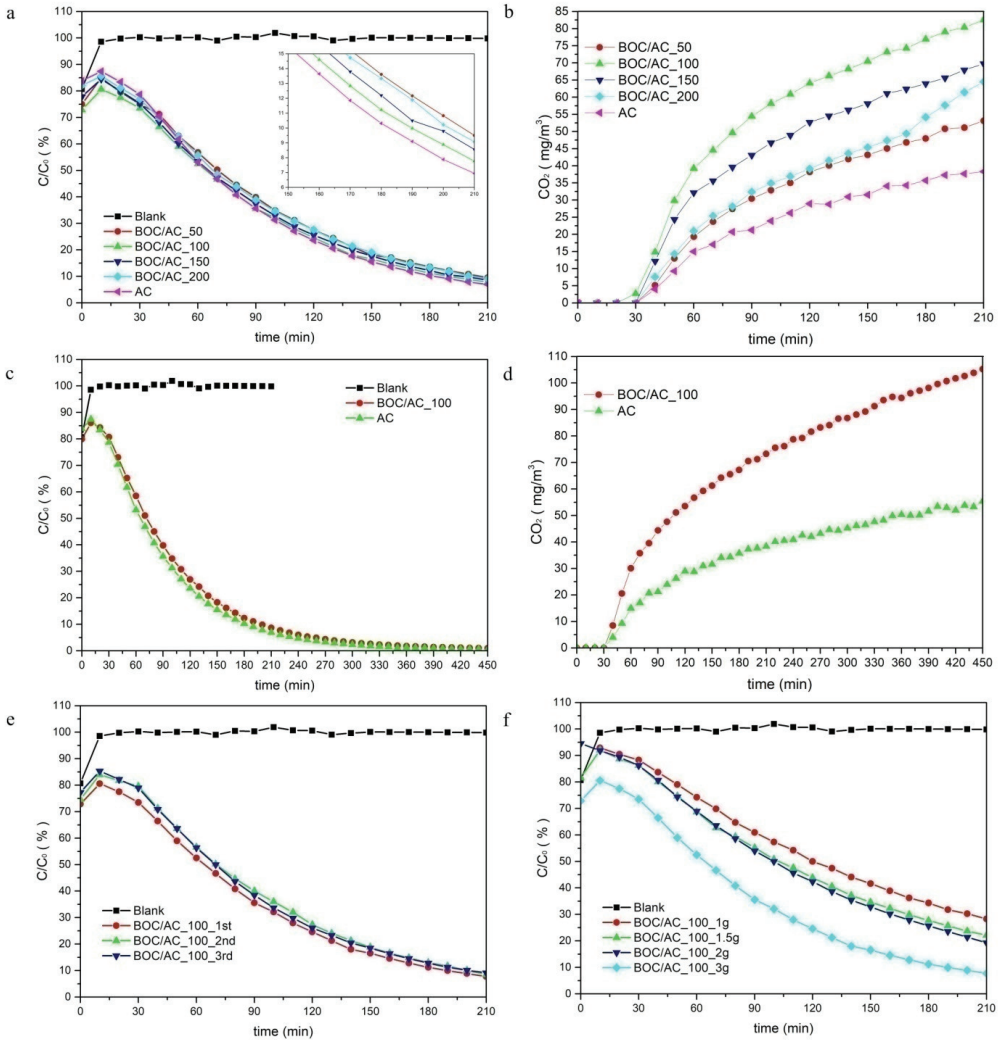

Figure 8. The photocatalytic performance of the BOC/AC samples for toluene removal in air (**a**), theCO_2 productivity of the samples (**b**), the property of BOC/AC_100 and AC for toluene removal (**c**), CO_2 productivity of BOC/AC_100 and AC (**d**), the stability of BOC/AC_100 for three cycles (**e**), and the toluene removal efficiency of the different amounts of BOC/AC_100 (**f**).

The photo-excited electrons (e^-) on the BOC and AC could reduce the O_2 adsorbed on the surface to active species of superoxide anions ($\bullet O^{2-}$). Consequently, the $\bullet O^{2-}$ active oxidizing species can oxidize toluene into intermediate products and finally into CO_2 and H_2O [39]. Meanwhile, the photo-generated holes (h^+) left on the BOC oxidize H_2O on their surface into another highly active species of hydroxyl radicals (•OH). Finally, the produced $\bullet O^{2-}$ and •OH, with strong oxidizing ability, can efficiently degrade the intermediates into CO_2 and H_2O, which are not harmful.

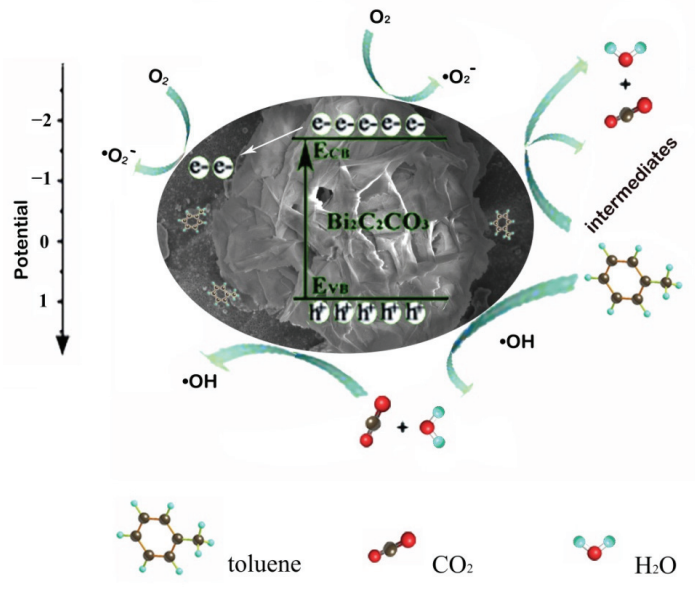

Figure 9. Photocatalytic mechanism of toluene removal using BOC/AC composite.

4. Conclusions

In summary, a novel BOC/AC nanocomposite photocatalyst was fabricated by in-situ growth of flower-shaped BOC nanosheets on the surface of activated carbon through a facile chemical method. The as-synthesized BOC/AC nanocomposite demonstrated excellent removal efficiency for toluene, with more than 90% degradation in 3 h, which is comparable and even higher than reported catalysts. Moreover, CO_2 and H_2O were confirmed as the major products. We also found that the catalytic activity was highly dependent on the loading content of BOC, with the highest performance obtained for 100 g loading. Furthermore, toluene could be completely removed after 7 h. Importantly, the photocatalytic efficiency remains constant after three cycles, demonstrating the good recyclability of the BOC/AC for photocatalytic toluene removal. The excellent photocatalytic degradation activity of the BOC/AC composite catalyst can be attributed to the synergistic effect of the adsorption ability of AC and the photocatalytic activity of both the BOC nanosheets and the AC. This work may provide useful guidance for indoor air purification, particularly for trace harmful gases such as VOCs.

Supplementary Materials: The following supporting information can be downloaded at: https://www.mdpi.com/article/10.3390/app122312500/s1, Figure S1: N2 adsorption− desorption isotherms (a) and pore size distributions (b) of AC and BOC/AC composites. Figure S2: Chromatograms of organic products at 3 h for BOC/AC_100 (a) and AC (b). Figure S3: Chromatograms of organic products at 7 h for BOC/AC_100 (a) and AC (b); Figure S4: Spectrum of the xenon lamp used.

Author Contributions: Investigation, X.W., L.C. and J.D.; Methodology, X.W., C.L., Y.G. and Y.L. (Yaochun Liu); Supervision, Y.L. (Yuanhua Lin) and J.D.; Writing and original draft, X.W. and L.C.; Review and editing, Y.L. (Yaochun Liu) and Y.X. All authors have read and agreed to the published version of the manuscript.

Funding: This research received no external funding.

Institutional Review Board Statement: Not applicable.

Informed Consent Statement: Not applicable.

Data Availability Statement: Not applicable.

Conflicts of Interest: The authors declare no conflict of interest.

References

1. Salthammer, T.; Uhde, E. (Eds.) *Organic Indoor Air Pollutants: Occurrence, Measurement, Evaluation*; WILEY-VCH: Weinheim, Germany, 2009.
2. Adan, O.C.G.; Samson, C.R. *Fundamentals of Mold Growth in Indoor Environments and Strategies for Healthy Living*; Wageningen Academic Publishers: Utrecht, The Netherlands, 2011.
3. Abadi, M.B.H.; Shirkhanloo, H.; Rakhtshah, J. Air pollution control: The evaluation of TerphApm@MWCNTs as a novel heterogeneous sorbent for benzene removal from air by solid phase gas extraction. *Arab. J. Chem.* **2020**, *13*, 1741–1751. [CrossRef]
4. Zhang, X.; Gao, B.; Fang, J.; Zou, W.; Dong, L.; Cao, C.; Zhang, J.; Li, Y.; Wang, H. Chemically activated hydrochar as an effective adsorbent for volatile organic compounds (VOCs). *Chemosphere* **2019**, *218*, 680–686. [CrossRef] [PubMed]
5. Liu, S.; Wei, W.; Wu, S.; Zhang, F.; Cheng, H. Efficient dichloromethane and toluene removal via lignin derived oxygen and nitrogen-containing activated carbons with well-developed micro-mesopore structure. *Diam. Relat. Mater.* **2022**, *124*, 108922. [CrossRef]
6. Saqlain, S.; Zhao, S.; Kim, S.Y.; Kim, Y.D. Enhanced removal efficiency of toluene over activated carbon under visible light. *J. Hazard. Mater.* **2021**, *418*, 126317. [CrossRef]
7. Kim, K.D.; Park, E.J.; Seo, H.O.; Jeong, M.G.; Kim, Y.D.; Lim, D.C. Effect of thin hydrophobic films for toluene adsorption and desorption behavior on activated carbon fiber under dry and humid conditions. *Chem. Eng. J.* **2012**, *200*, 133–139. [CrossRef]
8. Baur, G.B.; Beswick, O.; Spring, J.; Yuranov, I.; Kiwi-Minsker, L. Activated carbon fibers for efficient VOC removal from diluted streams: The role of surface functionalities. *Adsorption* **2015**, *21*, 255–264. [CrossRef]
9. Baytar, O.; Ahin, O.S.; Horoz, S.; Kutluay, S. High-performance gas-phase adsorption of benzene and toluene on activated carbon: Response surface optimization, reusability, equilibrium, kinetic, and competitive adsorption studies. *Environ. Sci. Pollut. Res.* **2020**, *27*, 26191–26210. [CrossRef] [PubMed]
10. Kutluay, S.; Baytar, O.; Ahin, O.S. Equilibrium, kinetic and thermodynamic studies for dynamic adsorption of benzene in gas phase onto activated carbon produced from Elaeagnus angustifolia seeds. *J. Environ. Chem. Eng.* **2019**, *7*, 102947. [CrossRef]
11. Zhang, G.; Lei, B.; Chen, S.; Xie, H.; Zhou, G. Activated carbon adsorbents with micro-mesoporous structure derived from waste biomass by stepwise activation for toluene removal from air. *J. Environ. Chem. Eng.* **2021**, *9*, 105387. [CrossRef]
12. Liu, X.; Zhu, H.; Gong, L.; Jiang, L.; Lin, D.; Yang, K. New insights into hierarchical pore size and level of concentration in efficient removal of toluene vapor by activated carbon. *Sci. Total Environ.* **2022**, *853*, 158719. [CrossRef]
13. Lei, B.; Liu, B.; Zhang, H.; Yan, L.; Xie, H.; Zhou, G. CuO-modified activated carbon for the improvement of toluene removal in air. *J. Environ. Sci.* **2020**, *88*, 122–132. [CrossRef] [PubMed]
14. Velasco, L.F.; Fonseca, I.M.; Parra, J.B.; Lima, J.C.; Ania, C.O. Photochemical behaviour of activated carbons under UV irradiation. *Carbon* **2012**, *50*, 249–258. [CrossRef]
15. Velo-Gala, I.; Lopez-Penalver, J.J.; Sanchez-Polo, M.; Rivera-Utrilla, J. Activated carbon as photocatalyst of reactions in aqueous phase. *Appl. Catal. B-Environ.* **2013**, *142*, 694–704. [CrossRef]
16. Velasco, L.F.; Gomis-Berenguer, A.; Lima, J.C.; Ania, C.O. Tuning the surface chemistry of nanoporous carbons for enhanced nanoconfined photochemical activity. *ChemCatchem* **2015**, *7*, 3012–3019. [CrossRef]
17. Velo-Gala, I.; L'opez-Peñalver, J.J.; S'anchez-Polo, M.; Rivera-Utrilla, J. Role of activated carbon surface chemistry in its photocatalytic activity and the generation of oxidant radicals under UV or solar radiation. *Appl. Catal. B-Environ.* **2017**, *207*, 412–423. [CrossRef]
18. Velasco, L.F.; Maurino, V.; Laurenti, E.; Fonseca, I.M.; Lima, J.C.; Ania, C.O. Photoinduced reactions occurring on activated carbons. A combined photooxidation and ESR study. *Appl. Catal. A-Gen.* **2013**, *452*, 1–8. [CrossRef]
19. Li, S.; Zhao, Z.; Li, J.; Liu, H.; Liu, M.; Zhang, Y.; Su, L.; Pérez-Jiménez, A.I.; Guo, Y.; Yang, F.; et al. Mechanically Induced Highly Efficient Hydrogen Evolution from Water over Piezoelectric SnSe nanosheets. *Small* **2022**, *18*, 2202507. [CrossRef]
20. Li, S.; Zhao, Z.; Liu, M.; Liu, X.; Huang, W.; Sun, S.; Jiang, Y.; Liu, Y.; Zhang, J.; Zhang, Z. Remarkably enhanced photocatalytic performance of Au/$AgNbO_3$heterostructures by coupling piezotronics with plasmonic effects. *Nano Energy* **2022**, *95*, 107031. [CrossRef]
21. Taylor, P.; Sunder, S.; Lopata, V.J. Structure, spectra, and stability of solid bismuth carbonates. *Can. J. Chem.* **1984**, *62*, 2863–2873. [CrossRef]
22. Chen, R.; So, M.H.; Yang, J.; Deng, F.; Che, C.-M.; Sun, H. Fabrication of bismuth subcarbonate nanotube arrays from bismuth citrate. *Chem. Commun.* **2006**, *21*, 2265–2267. [CrossRef]
23. Zhang, Q.; Yuan, S.; Xu, B.; Xu, Y.; Cao, K.; Jin, Z.; Ohno, T. A facile approach to build $Bi_2O_2CO_3$/PCNnanohybridphoto catalysts for gaseous acetaldehyde efficient removal. *Catal. Today* **2018**, *315*, 184–193. [CrossRef]
24. Madhusudan, P.; Ran, J.; Zhang, J.; Yu, J.; Liu, G. Novel urea assisted hydrothermal synthesis of hierarchical $BiVO_4$/$Bi_2O_2CO_3$ nanocomposites with enhanced visible-light photocatalytic activity. *Appl. Catal. B-Environ.* **2011**, *110*, 286–295. [CrossRef]
25. Fan, H.; Zhou, H.; Li, H.; Liu, X.; Ren, C.; Wang, F.; Li, W. Novel Ag_2CrO_4/$Bi_2O_2CO_3$ heterojunction: Simple preparation, wide visible light absorption band and excellent photocatalytic activity. *Chem. Phys.* **2019**, *517*, 60–66. [CrossRef]
26. Bai, P.; Tong, X.; Wan, J.; Gao, Y.; Xue, S. Flower-like $Bi_2O_2CO_3$-mediated selective oxidative coupling processes of amines under visible light irradiation. *J. Catal.* **2019**, *374*, 257–265. [CrossRef]

27. Ding, J.; Wang, H.; Luo, Y.; Xu, Y.; Liu, J.; Lin, Y. Oriented $Bi_2O_2CO_3$ Nanosheets with Enhanced Photocatalytic Performance for Toluene Removal in Air. *Catalysts* **2020**, *10*, 389. [CrossRef]
28. Ding, J.; Wang, H.; Luo, Y.; Xu, Y.; Liu, J.; Gao, Y.; Lin, Y. Carbon Quantum Dots Modified(002) Oriented $Bi_2O_2CO_3$ Composites with Enhanced Photocatalytic Removal of Toluene in Air. *Nanomaterials* **2020**, *10*, 1795. [CrossRef]
29. Huang, H.; Li, X.; Wang, J.; Dong, F.; Chu, P.K.; Zhang, T.; Zhang, Y. Anionic Group Self-Doping as a Promising Strategy: Band-Gap Engineering and Multi-Functional Applications of High-Performance CO_3^{2-}-Doped $Bi_2O_2CO_3$. *ACS Catal.* **2015**, *5*, 4094–4103. [CrossRef]
30. Ding, J.; Wang, H.; Xu, H.; Qiao, L.; Luo, Y.; Lin, Y.; Nan, C. Synthesis and broadband spectra photocatalytic properties of $Bi_2O_2(CO_3)_{1-x}S_x$. *Materials* **2018**, *11*, 791. [CrossRef]
31. Muthirulan, P.; Devi, C.N.; Sundaram, M.M. Synchronous role of coupled adsorption and photocatalytic degradation on CAC–TiO_2 composite generating excellent mineralization of alizarin cyanine green dye in aqueous solution. *Arab. J. Chem.* **2017**, *10*, 1477–1483. [CrossRef]
32. Alalm, M.G.; Tawfik, A.; Ookawara, S. Enhancement of photocatalytic activity ofTiO_2 by immobilization on activated carbon for degradation of pharmaceuticals. *J. Environ. Chem. Eng.* **2016**, *4*, 1929–1937. [CrossRef]
33. Elizalde-Gonz´alez, M.P.; García-Díaz, E.; Sabinas-Hern'andez, S.A. Novel preparation of carbon-TiO_2composites. *J. Hazard. Mater.* **2013**, *263*, 73–83. [CrossRef] [PubMed]
34. Wei, Z.; Sun, J.; Xie, Z.; Liang, M.; Chen, S. Removal of gaseous toluene by the combination of photocatalytic oxidation under complex light irradiation of UV and visible light and biological process. *J. Hazard. Mater.* **2010**, *177*, 814–821. [CrossRef] [PubMed]
35. Zhang, F.; Li, X.; Zhao, Q.; Zhang, Q.; Tadé, M.; Liu, S.F. Abrication of α-Fe_2O_3/In_2O_3 composite hollow microspheres: A novel hybrid photocatalyst for toluene degradation under visible light. *J. Colloid Interface Sci.* **2015**, *457*, 18–26. [CrossRef] [PubMed]
36. Darlington, A.B.; Dat, J.F.; Dixon, M.A. The Biofiltration of Indoor Air: Air Flux and Temperature Influences the Removal of Toluene, Ethylbenzene, and Xylene. *Environ. Sci. Technol.* **2001**, *35*, 240–246. [CrossRef]
37. Durme, J.V.; Dewulf, J.; Demeestere, K.; Leys, C.; Langenhove, H.V. Post-plasma catalytic technology for the removal of toluene from indoor air: Effect of humidity. *Appl. Catal. B-Environ.* **2009**, *87*, 78–83. [CrossRef]
38. Durme, J.V.; Dewulf, J.; Sysmans, W.; Leys, C.; Langenhove, H.V. A batement and degradation pathways of toluene in indoor air by positive corona discharge. *Chemosphere* **2007**, *68*, 1821–1829. [CrossRef]
39. Hennezel, O.; Pichat, P.; Ollis, D.F. Benzene and toluene gas-phase photocatalytic degradation over $H_2O$and HCL pretreated TiO_2: By-products and mechanisms. *J. Photochem. Photobiol. A-Chem.* **1998**, *118*, 197–204. [CrossRef]

MDPI
St. Alban-Anlage 66
4052 Basel
Switzerland
www.mdpi.com

MDPI Books Editorial Office
E-mail: books@mdpi.com
www.mdpi.com/books

Academic Open
Access Publishing

mdpi.com

ISBN 978-3-7258-0828-1